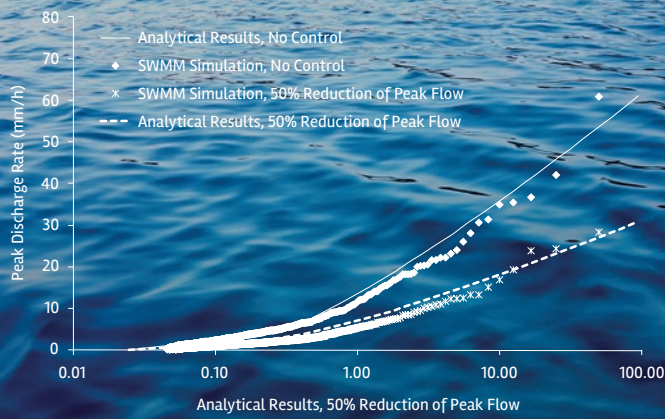


Statistical Analysis of Hydrologic Variables

Methods and Applications



Edited by

Ramesh S. V. Teegavarapu, Ph.D., P.E.
Jose D. Salas, Ph.D.
Jery R. Stedinger, Ph.D.



ENVIRONMENTAL &
WATER RESOURCES
INSTITUTE

Statistical Analysis of Hydrologic Variables

Methods and Applications

Edited by
Ramesh S.V. Teegavarapu
Jose D. Salas
Jery R. Stedinger

Prepared by the Task Committee on
Statistical Applications in Hydrology of the
Surface Water Hydrology Technical Committee of the
Environmental and Water Resources Institute.



Published by the American Society of Civil Engineers

Library of Congress Cataloging-in-Publication Data

Names: Teegavarapu, Ramesh S. V., 1970– editor. | Salas, J. D. (Jose D.), editor. | Stedinger, Jerry R., editor. | American Society of Civil Engineers, sponsoring body. | Environmental and Water Resources Institute (U.S.), sponsoring body.

Title: Statistical analysis of hydrologic variables : methods and applications / edited by Ramesh S.V. Teegavarapu, Jose D. Salas, Jerry R. Stedinger.

Description: Reston, Virginia : American Society of Civil Engineers, 2019. | “Prepared by Members of the ASCE EWRI Statistical Distributions in Hydrology Task Committee, sponsored by Environmental and Water Resources Institute (EWRI).” | Includes bibliographical references and index.

Identifiers: LCCN 2018045155| ISBN 9780784415177 (hardcover: alk. paper) | ISBN 9780784481875 (PDF)

Subjects: LCSH: Hydrologic cycle—Mathematical models. | Hydrologic models. | Groundwater flow—Mathematical models.

Classification: LCC GB848 .S73 2019 | DDC 551.4801/1-dc23

LC record available at <https://lccn.loc.gov/2018045155>

Published by American Society of Civil Engineers

1801 Alexander Bell Drive

Reston, Virginia 20191-4382

www.asce.org/bookstore | ascelibrary.org

Any statements expressed in these materials are those of the individual authors and do not necessarily represent the views of ASCE, which takes no responsibility for any statement made herein. No reference made in this publication to any specific method, product, process, or service constitutes or implies an endorsement, recommendation, or warranty thereof by ASCE. The materials are for general information only and do not represent a standard of ASCE, nor are they intended as a reference in purchase specifications, contracts, regulations, statutes, or any other legal document. ASCE makes no representation or warranty of any kind, whether express or implied, concerning the accuracy, completeness, suitability, or utility of any information, apparatus, product, or process discussed in this publication, and assumes no liability therefor. The information contained in these materials should not be used without first securing competent advice with respect to its suitability for any general or specific application. Anyone utilizing such information assumes all liability arising from such use, including but not limited to infringement of any patent or patents.

ASCE and American Society of Civil Engineers—Registered in U.S. Patent and Trademark Office.

Photocopies and permissions. Permission to photocopy or reproduce material from ASCE publications can be requested by sending an e-mail to permissions@asce.org or by locating a title in the ASCE Library (<http://ascelibrary.org>) and using the “Permissions” link.

Errata: Errata, if any, can be found at <https://doi.org/10.1061/9780784415177>.

Copyright © 2019 by the American Society of Civil Engineers.

All Rights Reserved.

ISBN 978-0-7844-1517-7 (print)

ISBN 978-0-7844-8187-5 (PDF)

Manufactured in the United States of America.

Contents

Preface	vii
Chapter 1 Introduction	1
References	4
Chapter 2 Statistical Analysis of Precipitation Extremes.....	5
2.0 Introduction	5
2.1 Ground-, Radar-, and Satellite-based Measurements	6
2.2 Fitting of Probability Distributions for Rainfall Extremes.....	9
2.3 Precipitation Frequency Analysis: Development of Cumulative Distribution Functions	10
2.4 Probability Distributions for Characterizing Precipitation Data	11
2.5 Estimation of Distribution Parameters.....	16
2.6 Frequency Factors	18
2.7 Goodness-of-Fit Tests for Normal Distributions.....	20
2.8 Goodness-of-Fit Tests for Other Distributions	20
2.9 Regional Frequency Analysis	21
2.10 Illustrative Examples.....	22
2.11 Fitting of a Parametric Frequency Curve for Rainfall Extremes	26
2.12 Extreme Rainfall Frequency Analysis in the United States	28
2.13 Probable Maximum Precipitation.....	30
2.14 Rainfall Frequency Analysis: Uncertainty and Variability Issues	31
2.15 Stationarity Issues.....	37
2.16 Homogeneity	42
2.17 Detection of Changes in Moments	44
2.18 Nonparametric Methods	45
2.19 Nonparametric Test for Independence	49
2.20 Partial Duration Series.....	50
2.21 Statistical Characterization of Interevent Time Definition of Storm Events	51
2.22 Incorporation of Climate Variability Cycles and Climate Change into Rainfall Frequency Analysis	51
2.23 Use of Future Data Sources for Frequency Analysis.....	52
2.24 Descriptive Indexes for Precipitation Extremes	53
2.25 Standard Precipitation Index	54
2.26 Trends Based on GCM Model Simulations.....	56
2.27 Hydrologic Design for the Future	57
2.28 Summary and Conclusions	57
References	57
Appendix: Cumulative Probability Plots of Precipitation Data Using Different Plotting Position Formulae	69

Chapter 3 Evapotranspiration and Evaporative Demand.....	71
3.0 Introduction	71
3.1 Evapotranspiration and Evaporative Demand: A Physical Primer.....	73
3.2 Models and Observations of ET and E_0	78
3.3 The Reference Evapotranspiration Concept.....	101
3.4 Trends in ET and E_0	116
3.5 Summary	134
Acknowledgments.....	135
References	135
Chapter 4 Infiltration and Soil Water.....	145
4.0 Scope and Introduction.....	145
4.1 Infiltration and Soil–Water Dynamics: Description and Measurement.....	148
4.2 Spatial and Temporal Variability of Soil Water and Infiltration.....	156
4.3 Scaling and Estimation of Soil Hydraulic Properties and Infiltration	160
4.4 Uncertainty in Measurement and Space–Time Estimation.....	166
4.5 Links between Infiltration and Runoff at Different Scales.....	168
4.6 Suggestions for Advancing Infiltration Science and Practice.....	170
List of Terms.....	172
Acknowledgments and Caveat	173
References	174
Chapter 5 Probability Distributions in Groundwater Hydrology.....	179
5.0 General	179
5.1 Definitions.....	180
5.2 Basic Notation and Key Statistics	182
5.3 Frequently Used PDFs in Groundwater Hydrology	183
5.4 Illustrative Examples	190
5.5 Conclusions	201
References	201
Chapter 6 Modeling Streamflow Variability.....	203
6.0 Introduction	203
6.1 Stochastic Features of Streamflow Time Series.....	203
6.2 Modeling of Streamflow Time Series.....	209
6.3 Modeling of Complex River Systems.....	222
6.4 Software Tools	228
6.5 Further Remarks.....	228
References	229
Chapter 7 Flood Frequency Analysis in the United States	233
7.0 General	233
7.1 Evolution of <i>Bulletin 17B</i>	234
7.2 Characteristics of the LP3 Distribution	236
7.3 Estimation Procedures for Complete Samples.....	245
7.4 Estimation Procedures with Historical Information and Low Outliers.....	249
7.5 Incorporation of Climate Change and Climate Variability into Flood Frequency Analysis.....	257
7.6 Closing Remarks	261

Appendix 7A: Plotting Positions for Use with Low Outliers and Historical Information.....	262
Appendix 7B: Expected Moments Algorithm	263
References	264
Chapter 8 Low Flows and Droughts	269
8.0 Introduction	269
8.1 Low Flow and Drought Definitions	270
8.2 Empirical Frequency Analysis of Low Flows	273
8.3 Probability Distribution of Low Flows.....	274
8.4 Regional Analysis of Low Flows	283
8.5 Analysis of Autocorrelated Low Flows.....	288
8.6 Statistical Characterization of Multiyear Droughts.....	299
8.7 Regional Analysis of Droughts	319
8.8 Effects of Hydraulic Structures on Low Flows	321
8.9 Closing Remarks	323
References	326
Chapter 9 Probabilistic Models for Urban Stormwater Management.....	333
List of Symbols.....	333
9.0 General	335
9.1 Analytical Probabilistic Stormwater Models	336
9.2 Performance Modeling for BMP Pollutant Removal with Uncertainty Analysis	360
9.3 Summary	374
Acknowledgments	375
References	376
Chapter 10 Analysis of Water Quality Random Variables.....	381
Glossary	381
10.0 General	383
10.1 Special Characteristics of Water Quality Random Variables	383
10.2 Practical Applications of Water Quality Distributions	384
10.3 The Normal Distribution.....	385
10.4 Tests for Normality and Transformations	386
10.5 The Log–Normal Distribution	387
10.6 Other Continuous Distributions: Gamma, Weibull, and Beta	388
10.7 The Binomial and Hypergeometric Distributions	389
10.8 Other Discrete Distributions and Microbiological Variables	390
10.9 Nonparametric Representations	391
10.10 Censored Observations	394
10.11 Water Quality Populations of Interest Defined	396
10.12 Probability Sampling	397
10.13 Time Series and Stochastic Processes.....	397
10.14 Importance of Serial Correlation	398
10.15 Seasonality and Flow Effects	400
10.16 Multivariate Characterization	401
10.17 Summary	402
References	403

Chapter 11 Multivariate Frequency Distributions in Hydrology	407
11.0 General.....	407
11.1 Multivariate Distributions in Hydrology	408
11.2 Conventional Multivariate Distributions Used in Hydrology.....	412
11.3 Copula Method and Its Use in Hydrology.....	416
11.4 Illustrative Examples.....	443
References	485
Chapter 12 Hydrologic Record Events.....	491
Glossary.....	491
12.0 General.....	492
12.1 Parametric Properties of Hydrologic Records	494
12.2 Nonparametric Statistical Properties of Hydrologic Records	501
12.3 Flood Envelope Curves: Application of the Theory of Records.....	508
12.4 Applications of the Theory of Records: Case Studies.....	522
12.5 Conclusions.....	532
References	533
Index.....	537

Preface

The Environmental and Water Resources Institute (EWRI), the American Society of Civil Engineers' (ASCE) Task Committee on "statistical distributions in hydrology," envisioned the development of a comprehensive monograph addressing uses and applications of statistical distributions in hydrology. This Task Committee was organized by the EWRI's Surface Water Hydrology Technical Committee (SWHTC) of the Watershed Council. Over several years the members of this committee struggled to determine the appropriate scope and contents of this monograph. Dr. Ahmed Nazeer led the initial vision and development of the monograph's outline and content. Subsequently, Dr. Veronica Webster, in collaboration with professors Jose D. Salas and Jerry R. Stedinger, continued the effort and expanded the book's scope with the addition of selected chapters. She also supervised the writing and review of the various chapters. More recently, the SWHTC asked Dr. Ramesh Teegavarapu to take the lead in collaboration with Professors Salas and Stedinger, to re-review the chapters and complete the final steps needed for publication.

Each chapter of this book went through a peer review process by independent reviewers and the editorial team. The monograph is intended to be a standalone reference document that compiles state-of-the-art statistical methods for analyzing and describing critical variables that are part of the hydrological cycle. The monograph addresses the pressing problem of the dynamics of hydrological processes under stationary and nonstationary conditions. Developing a monograph addressing the statistical analysis of key variables in the hydrological cycle was a major undertaking, particularly as the field is evolving rapidly with a corresponding expansion of its literature. While efforts were made to be comprehensive, gaps remain to be filled. These gaps should be addressed in future hydrologic research. Nevertheless, the authors and the editors hope that this monograph, which addresses uses and applications of statistical methods, will be valuable to students, educators, researchers, and practicing hydrologists and water resource specialists. We sincerely thank the lead authors and coauthors of the chapters and the peer reviewers who have provided enormous help in the development of this monograph. We also thank EWRI for supporting the task committee's activities and helping with publication.

—Editorial Team
Ramesh S.V. Teegavarapu
José D. Salas
Jerry R. Stedinger

CHAPTER 1

Introduction

Ramesh S.V. Teegavarapu
Jose D. Salas
Jery R. Stedinger

Characterizing and understanding the variability of hydroclimatological processes and measurements are essential for assessing the performance of water resources infrastructure and its management and for planning successful and efficient water resources projects. Spatial and temporal resolution of data are increasing with an expanding set of data sources, including remote and land-based instruments with real-time reporting. The analyzed data provide invaluable insights into the temporal and spatial dynamics of hydrological processes that represent the hydrological cycle. Historical data combined with future projections of anthropogenic and climate changes provide ample opportunities to evaluate trends and change points in the time series to develop realistic hydrologic designs and water and environmental systems management alternatives. The assessment of climate variability also relies on the evaluation of patterns and variations of historical hydroclimatological data. Hence a need exists for clear understanding and application of various data analysis methods, ranging from simple exploratory analysis to more comprehensive statistical methods.

This book aims to provide appropriate statistical methods for analyzing and modeling various parts of the hydrological cycle. Following this introductory chapter, the monograph contains 11 chapters, 2 through 12. Many chapters describe a key process in the hydrological cycle, such as precipitation, evaporation, infiltration and soil water, groundwater, and streamflow. Some chapters are devoted primarily to analyzing extreme events such as floods and low flows and droughts. Also, because watersheds and river basins often include built infrastructure and conveyances, Chapter 9 is dedicated to the hydrologic cycle that takes place in urban areas, such as precipitation and runoff, and stormwater collection and management. Most chapters emphasize the quantitative aspects of the movement of water. Chapter 10 considers the probabilistic and statistical issues related to the water quality component of the hydrologic cycle. Furthermore, because various components of the hydrologic cycle are interrelated, Chapter 11 considers the use of multivariate distributions in hydrology. Whenever possible, authors have provided examples and applications of techniques and models using real data, guidelines for data assessment, and discussion of model limitations.

Chapter 2 discusses applications of statistical methods for analysis of precipitation extremes, including a discussion about precipitation measurement and statistical estimation issues. The chapter describes probability distributions used to characterize precipitation extremes at different temporal and spatial scales and as a time series. Illustrative examples of fitting different distributions to precipitation data at different temporal scales are also presented. The chapter ends with a discussion of precipitation under a changing climate and sustainable climate change-sensitive hydrologic design that considers potential changes in the frequency of occurrences and magnitudes of precipitation extremes.

Evapotranspiration (ET) is a major component of the hydrologic cycle that needs to be described accurately for hydrologic modeling and water resources management. Chapter 3 explains the basics of ET, including physical processes, energy, water balance, and eddy covariance methods to estimate ET. Use of remote sensing in estimating ET via energy balance procedures along with uncertainty and limitations of different methods are discussed. The reference evapotranspiration concept is elaborated, and Penman–Monteith and ASCE standardized reference methods are described. The chapter also discusses methods for deriving reference ET from different data sources and understanding its variability. Trend analysis of ET and evaporative demand using nonparametric trends tests and discussion of drivers influencing these two components are presented. Infiltration is a key component influencing runoff processes and is discussed in Chapter 4. Processes affecting infiltration and soil water, along with conventional methods of handling rainfall infiltration and losses, are discussed. Challenges include addressing the spatial and temporal variability of infiltration, its measurement, and soil-specific factors affecting infiltration. Methods for estimation of soil hydraulic properties and infiltration are also discussed. Uncertainty in the measurement of infiltration and inverse methods of parameter estimation are dealt with in detail. The chapter ends with recommendations for addressing different issues related to measurements across different scales and use of systems approaches and risk assessments. Chapter 5 deals with use and applications of probabilistic distributions for characterizing subsurface hydrology-specific variables. The chapter discusses probability distribution functions that can be used to develop probabilistic models of hydraulic conductivity; groundwater residence time and age, including gamma distributions for characterizing residence time and age; and exponential, lognormal, and log–gamma distributions for hydraulic conductivity. Discussions address statistical homogeneity and independence of observations. Illustrative examples using real data show the applicability of different probability distributions.

Streamflow is another major component of the hydrological cycle. Chapter 6 describes the analysis of streamflows at various temporal scales, including monthly and annual, and spatial scales involving one or multiple sites. Various temporal models are considered, particularly those within the autoregressive and moving average (ARMA) framework for annual flows and extensions thereof for seasonal flows. Likewise, product models with discrete and continuous parts are formulated for intermittent flows. A discussion considers models that can reproduce long-term persistence, including the fractional Gaussian noise and fractional ARMA, as well as shifting mean models. Such models can generate shifting patterns such as those arising from low-frequency components of atmospheric and oceanic processes. In addition, modeling and generation of seasonal streamflows at multiple sites may require the application of multivariate models, temporal and spatial disaggregation models, and nonparametric schemes, depending on the complexity of the system. The chapter ends with a discussion of software tools and common applications of the various models and techniques discussed.

Extreme events such as floods and droughts are a major concern in engineering hydrology. Chapter 7 explains the methods employed for flood risk estimation in the United States, based on the log–Pearson type III (LP3) distribution. The chapter gives a detailed description of the LP3. Sometimes low outliers may distort a distribution fit to a flood record. A relatively new estimation method, called the expected moments algorithm, effectively employs the entire data set, including the gauged record, historical information, low outliers, and regional skew information. *Bulletin 17B* has been the standard manual for flood frequency analysis in the United States since 1982. The chapter reviews *Bulletin 17B*'s evolution and the changes in the long-awaited new manual, *Bulletin 17C*. The chapter ends with a detailed discussion of how climate variability and change can be incorporated into flood frequency analysis.

Extreme low flows and droughts are also important elements of the hydrologic cycle. Chapter 8 begins with key definitions, followed by applications of lognormal, LP3, and general extreme value (GEV) distributions, including regional frequency studies of low flows. Often the time series of low

flows are autocorrelated because of the effect of surface and groundwater storages and then discrete and continuous autocorrelated models are necessary for predicting low flows. The chapter includes various modeling alternatives such as simple Markov chains, discrete ARMA, and gamma auto-regressive processes. A mathematical algorithm is presented for determining return periods and risk of low flow variables and then extended to estimate the return period and risk of multiyear droughts. Several examples illustrate the use of the methods. The chapter ends with a discussion of the effects of anthropogenic and climatic variability and change on the analysis and modeling of low flows and droughts.

Impervious surfaces and extensive drainage systems characterize urban areas, which leads to faster flow response and greater amounts of runoff reaching the streams. Also, runoff from urban areas contains sediments and water contaminants. Many techniques and modeling tools are available for estimating precipitation rates, runoff characteristics, erosion, and water quality loads, including the effect of management practices. Furthermore, given the random nature of many of the hydrologic and hydraulic variables involved in urban watersheds and related best management practices, some applications of probability theory have been developed in the past decades to help in the analysis, management, and planning of urban hydraulic systems. Chapter 9 has been written for this purpose, as a complement to traditional approaches.

Most of the statistical analysis and probability distributions included in Chapters 2 through 9 can be applied to water quality variables as well. Chapter 10 gives a comprehensive presentation of many water quality random variables. It includes the most commonly used distributions; nonparametric approaches; how to deal with censored observations that are typically encountered in data; problems related to water quality; seasonal effects on water quality characteristics; the effect of autocorrelated observations, which sometimes require using time series analysis and models; and the inherent nature of water quality that is characterized by variables arising from physical, chemical, and biological measurements, which requires using multivariate distributions.

As stated in other chapters, description of the hydrological cycle generally involves many random variables that are defined at temporal and spatial scales. Chapter 11 is devoted specifically to deal with such multivariate problems and the applications of multivariate probability distribution functions. After introducing the basic concepts for analyzing multiple variables, a review is made of the typical applications reported in literature of multivariate distributions in hydrometeorology and hydrology. The chapter provides details on two fundamental approaches: conventional multivariate distributions (often based upon normal distributions) and the copula method. Examples and specifics of conventional distributions are discussed, particularly bivariate distributions, such as the bivariate normal, lognormal, exponential, and Gumbel distributions. In addition, the concepts and types of copulas and the selection and generation methods based on copulas are discussed in some detail. The end of the chapter includes three applications for copula modeling of peak flow and volume, storm duration and depth, and regional flood risk management.

Some chapters deal with extreme events such as extreme precipitation in Chapter 2 and extreme floods in Chapter 7. The last chapter, Chapter 12, deals with such extreme value problems but from a different perspective. It deals with “record events,” that is to say, an event that exceeds all previous events that occurred in the record. And “no matter how large the magnitude of the flood record event may be, it will eventually be broken” (Glick 1978), thus “the probability of the largest observed flood will be exceeded is 1” (Vogel et al. 2019, authors of Chapter 12). To understand the theoretical framework and implications and use of such types of statements, reading the final chapter is worthwhile. The chapter’s authors indicate that “there are surprisingly few water resources studies that have applied the theory of records.” The chapter includes parametric and nonparametric approaches to statistical analyses of hydrologic records, gives some examples using flood envelope curves, and provides a probabilistic interpretation of such curves. The chapter ends with applications of regional envelope curves for flood studies in Italy and the United States and precipitation studies in Austria.

The editors of this book are very pleased with the material that the chapter authors have contributed. The book should be of great interest to individuals concerned with the theory and applications of probabilistic methods in hydrology and water resources in general, with a particular component of the hydrological cycle, or with a specific issue such as extreme events. We encourage readers to pursue issues further by looking through the references (e.g. Singh 2017) or looking up subsequent journal papers and reports. Readers are invited to contact the authors and coauthors of the various chapters to pursue more advanced issues or issues that were omitted, perhaps because of space constraints. We are in a world that is becoming technically more sophisticated and aims to describe hydrologic phenomena more completely. To treat a process that we know varies over time as constant, or to ignore uncertainty in estimated parameters as if no uncertainty were present, is to describe reality incompletely or without appropriate care. This book is part of our profession's effort to encourage the use of probability models and statistics to more completely characterize hydrologic processes; such efforts should support the advancement of hydrologic science and improve the design process by developing more complete descriptions of all the interacting processes that affect the safety and efficient operation of water resource projects.

References

- Glick, N. 1978. "Breaking records and breaking boards." *Am. Math. Month.* **85** (1): 2–26.
Singh, V. P. (editor-in-chief). 2017. *Handbook of applied hydrology*, 2nd ed. New York: McGraw-Hill Education.
Vogel, R. M., A. Castellarin, N. C. Matalas, J. F. England Jr., and A. Zafirakou. 2019. "Hydrologic record events." In *Statistical analysis of hydrologic variables: Methods and applications*. Reston, VA: ASCE.

CHAPTER 2

Statistical Analysis of Precipitation Extremes

Ramesh S. V. Teegavarapu, Ph.D., P.E.
Chandra S. Pathak, Ph.D., P.E.

2.0 INTRODUCTION

Precipitation is the key hydrologic variable linking the atmosphere with land surface processes and plays a dominant role in the terrestrial hydroclimatic system. Accurate measurements of precipitation on various space and time scales are important not only to weather forecasters and climate scientists, but also to many decision makers, including hydrologists, agriculturalists, and industrialists ([Ebert et al. 2007](#)). Excessive and insufficient precipitation can cause significant damage to life and property through hydrological extremes such as floods and droughts, respectively. Prediction of such phenomena largely depends on how accurate estimation of precipitation is and its resolution at different spatial and temporal scales. Even though rain gauges are the conventional instruments for direct measurement of rainfall, sparse network or no coverage over land or ocean and remote land areas limits their utility over these regions. The absence of gauges in remote regions clearly indicates the need for remotely sensed (radar and satellite) measurements by which rainfall estimation can be monitored as well. Remote sensing provides advantages in terms of availability of data in real time and complete area coverage irrespective of terrain or climate. For these reasons, the complex error structure, and high variability exhibited by intermittent measurement through sparse rain gauges, identifying true rainfall fields has been recognized to be difficult. To overcome these issues, ground-based radar measurement adjusted with rain gauges was found to be more representative of the true rainfall field. Also, as an alternative, satellite-based precipitation estimation techniques have been developed ([Huffman et al. 2003](#), [Sene 2009](#)). A few sections of this chapter are adopted from [Teegavarapu \(2012a\)](#).

The widespread availability and easy accessibility of satellite-based precipitation estimates ([Teegavarapu 2012a](#)) have also enhanced hydrological modeling and forecasting procedures at the watershed scale. Before satellite-based precipitation products can become fully accepted, rainfall estimates from this source must be assessed to understand their strengths and limitations so that they can be interpreted correctly. Future precipitation estimates will be dominated by radar- and satellite-based observations with dependence on the ground truth (i.e., rain gauge). The main focus of this chapter is on statistical analysis of precipitation data with emphasis on extremes. Statistical methods used for analysis of bias in precipitation measurements and design of rain gauge networks are also discussed. Precipitation occurs in various forms such as rain, snow, hail, drizzle, sleet, and others. Appropriate measurement methods and procedures ([Strangeways 2007](#)), when adopted, are expected to provide water equivalents that can be used to analyze precipitation time series, characteristics, and extremes. This chapter does not elaborate on these methods and measures. The next three sections provide a brief introduction about precipitation measurements.

2.1 GROUND-, RADAR-, AND SATELLITE-BASED MEASUREMENTS

Ground-based measurements refer to the conventional and direct ways of measuring precipitation, and these are generally carried out by a network of rain gauges. Radar measurements are sometimes considered to be ground based because of the location of the radar unit. In this chapter, radar-based estimates are treated separately because their operation is primarily meant to obtain data of spatially varying precipitation. Satellite-based measurement is an emerging method for estimating precipitation. [Sene \(2009\)](#) and [Kidder and Haar \(1995\)](#) document the available satellite-based precipitation estimates derived from different algorithms.

2.1.1 Systematic and Random Errors

Precipitation measurements, like any measurements, are prone to systematic and random errors. The field of metrology (the science of measurement) provides an exhaustive treatment of different types of errors and their manifestations in different measurement settings. Systematic errors are mainly due to measuring instruments (instrument-related systematic errors) ([Rabinovich 2005](#)). These errors can be corrected but cannot be eliminated. In some situations, systematic errors are qualified as errors made by human participants ([Rabinovich 2005](#)), and they are mainly due to the individual characteristics of the observer. Systematic errors due to wind undercatch, splashing, evaporation, and wetting losses are also common. Random errors are mainly due to imprecision in measurement and unknown wind fields responsible for losses ([Vieux 2006](#)), irregularities of topography and microclimatic variations around the gauge site, and inadequate network density to account for the natural spatial variability of rainfall ([WMO 2009](#)).

2.1.2 Precipitation Measurements and Networks

More than 150,000 nonrecording rain gauges are in operation throughout the world ([Servuk and Klemm, 1989](#)). In addition, several different types of gauges differ in catch area, height and material used, and other aspects. [Servuk and Klemm \(1989\)](#) and [Strangeways \(2003, 2007\)](#) indicate that more than 50 types of manually read gauges exist in the world. These estimates may not reflect current figures, and variations in the types are not easy to document. However, these numbers and types of gauges show the diversity in the configuration of rain gauges around the world. Recording gauges measure precipitation at discrete intervals of time and thus provide the time distribution of rainfall for a given storm event or within a time frame of consideration. Typically, recording gauges are electronically controlled, and the information about rainfall measurements is transmitted through telemetric devices. Human intervention is minimal in measurement and collection of the data. Examples of these types of gauges include tipping bucket, weighing bucket, and float gauges. A tipping bucket precipitation gauge is a recording rain gauge that works by measuring water volume through the use of a lightweight, dual-compartment tipping device. The time of each tipping of the bucket is recorded and can be resampled at discrete intervals of time. A weighing bucket rain gauge has a reservoir for collecting precipitation and a recording mechanism to register the amount of precipitation. The reservoir itself rests on a scale, and the weight of the collected precipitation is converted into a precipitation amount and recorded. The float-type rain gauge provides temporal distribution of precipitation data using a float mechanism located inside the rainfall collection reservoir. Nonrecording gauges are typically standard recording gauges and are manually operated. These gauges do not provide temporal distribution of rainfall. Human involvement is critical in the collection and reporting of measured precipitation. As no automatic recording devices are attached, precipitation measurement readings must be taken manually at regular time intervals.

Snowfall is much more difficult to measure than rainfall ([Strangeways 2007](#)). [Strangeways \(2007\)](#) describes conventional rain gauges and optical precipitation gauges, measurements of snow depth and weight, and the use of gamma ray attenuation in detail. [Dingman \(2008\)](#) documents

different methods for measurement of snow, which include standard methods using rulers, universal gauges, radar, snow stakes, snow surveys and pillows, acoustic and radioactive gauges, and airborne microwave and radar- and satellite-based measurements. Once the snow pack depth or amount of snowfall is measured, snow water equivalent (SWE) can be easily obtained.

Precipitation monitoring network density is simply the number of rain gauges per given area of a specific region. The World Meteorological Organization ([Sevruk and Hamon 1984](#)) provides recommendations for minimum network density of precipitation networks for hydrometeorological purposes. Design of optimal monitoring networks requires a critical assessment of information to be gained about the heterogeneity of the precipitation process among sampling locations. The design of a monitoring network is aimed at capturing and characterizing the spatial variability of the precipitation across a specific region. This generally should be the primary objective. However, other secondary objectives related to placement of gauges can be due to other reasons such as (1) validation of modeling efforts, (2) precipitation measurements required to derive inputs for a hydrological simulation model, and (3) requirement of a precipitation monitoring effort for a specific hydrologic or hydraulic project. The design of the network depends on several factors that include (1) placement of rain gauges to maximize the information obtained from them, (2) existing network of rain gauges, (3) monetary cost involved in the placement (relocation and installation) of the rain gauges, and (4) feasibility of installation of a rain gauge at a location within a specific region. The number of stations required in a specific region (e.g., watershed or basin) can be determined by conceptually simple methods based on the variance of rainfall measurements in space or variants thereof. The variance of rainfall is calculated based on the existing number of rain gauges in the region. [Rakhecha and Singh \(2009\)](#) discuss three variance-based methods and report methods by [Rycroft \(1949\)](#), [Ganguli et al. \(1951\)](#), and [Ahuja \(1960\)](#). All these methods use the concept of variance in space and allowable variance in the estimate of mean rainfall to determine the optimum number of rain gauges. A geostatistical approach discussed by [Teegavarapu et al. \(2015\)](#) and [Vieux \(2006\)](#) uses information about the spatial variability of variables of interest (e.g., solar radiation and rainfall) with the help of semi-variograms.

2.1.3 Radar-Based Rainfall Estimates

The use of radar technology to estimate precipitation (rainfall) began in the early 1960s ([Meischner 2005](#)). During the early 1990s, the use of this technology proliferated as the National Oceanic and Atmospheric Administration (NOAA) installed many radars across the United States as part of the Weather Surveillance Radar 88-Doppler (WSR 88-D) or NEXt Generation RADar (NEXRAD) program initiated by the National Weather Service (NWS). Several types of weather radars are in use throughout the world. They are sometimes classified based on frequency and wavelength characteristics. Exhaustive discussion about radar-based precipitation measurements can be obtained from reference books by [Meischner \(2005\)](#), [Strangeways \(2007\)](#), and [Raghavan \(2003\)](#). [Meischner \(2005\)](#) provides a comprehensive assessment of radar-based precipitation networks, estimation, use of radar data for hydrometeorological applications, and recent advances in the radar measurement of precipitation. The reader is referred to [Vieux \(2001\)](#) and [Collier \(1989\)](#) for initial development of radar-based precipitation networks and their evolution. The NEXRAD system was initially prototyped in 1988 at the National Severe Storms Laboratory in Norman, Oklahoma, and deployed for use nationally in 1992 under the controlling agencies of the NWS, the US Air Force, and the Federal Aviation Administration. Currently, more than 150 WSR-88D radars are in operation across most of the United States. Figure 2-1 shows the location of these radar sites in the United States and the US territories. Weather radars can locate and follow precipitation within a range of 200 to 400 km, depending on radio propagation conditions and the nature of the weather system.

There is a statistical tradeoff between rainfall measurement data collected by rain gauges and weather radar. Rain gauges can provide precise point values of rainfall depth and intensity but cannot economically provide the spatial distribution of rainfall. Whereas rain gauges are appropriate

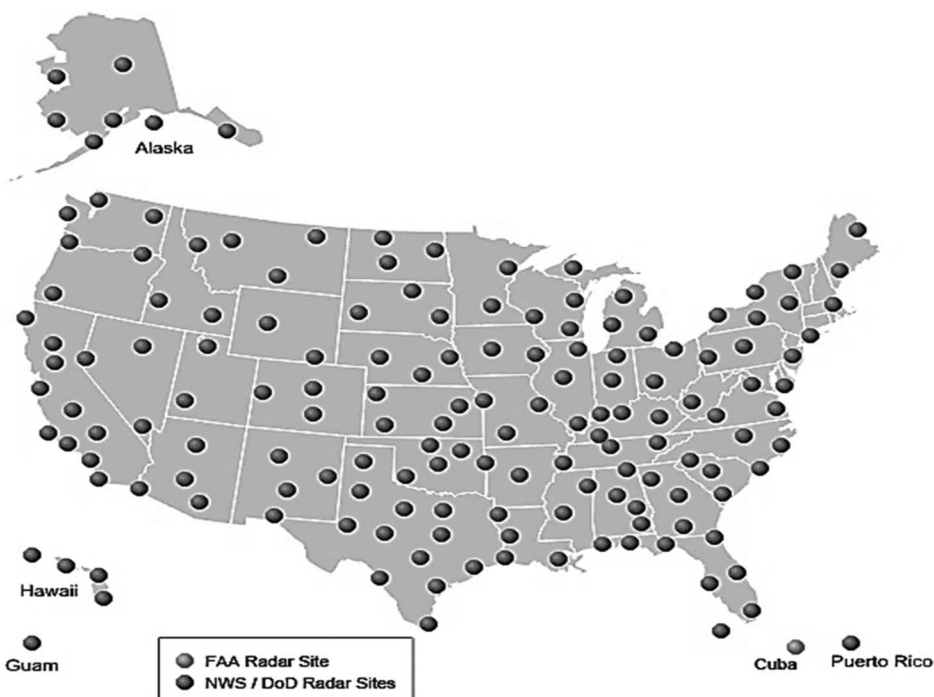


Figure 2-1. NEXRAD ground-based radar network—Doppler WSR-88D radar covering the United States.

Source: <http://radar.weather.gov/>.

for frontal-related rainfall events, they often do not represent the timing and orientation of the frontal systems well. Gauges can also miss highly variable convective rainfall events altogether. Radar data provides complete spatial coverage of rainfall amounts unobtrusively using a predetermined grid resolution (usually $4 \text{ km} \times 4 \text{ km}$) (Figure 2-1). WSR-88D precipitation estimates are based on the Precipitation Processing System (PPS) (Fulton et al. 1998). This algorithm preprocesses incoming reflectivity data, applies certain quality control measures, converts the reflectivity to rainfall rates, and provides estimates of accumulations. NEXRAD rainfall data are limited by relying on the measurement of raindrop reflectivity, which factors such as raindrop size and signal reflection by other objects can affect. Because the reflected signal measured by the radar is proportional to the sum of the sixth power of the diameter of the raindrops in a given volume of atmosphere, small changes in the size of raindrops can dramatically affect the radar's rainfall estimate. For this reason, a radar reflectivity (Z) and rainfall rate (R) is initially developed and used to estimate rainfall for a given reflectivity value. Drop size distributions vary for different rainfall characteristics. Thus, many empirical $Z-R$ relationships have been developed to account for observed precipitation in different climate areas and meteorological conditions. Bedient et al. (2008) offer an extensive account of $Z-R$ equations. Teegavarapu and Pathak (2012) provide different methods for obtaining optimal $Z-R$ relationships. NEXRAD data provide rainfall products with two primary spatial resolutions ($4 \text{ km} \times 4 \text{ km}$ Cartesian; $2 \text{ km} \times 1\text{-degree azimuth-range}$). Hoblit et al. (1999) and Hoblit and Curtis (2000) discuss applications of radar rainfall data adjustments applied to radar rainfall data products derived from NEXRAD. Teegavarapu et al. (2016) provide a comprehensive framework for assessment of biases in radar-based precipitation estimates. According to Wilson and Brandes (1979), better rainfall estimates are obtained from bias-adjusted radar rainfall data than can be achieved with either rain gauge networks or radar rainfall data alone. Readers can obtain additional

information on this subject from many other authors (Huebner et al. 2003, Teegavarapu 2012a, Raghavan 2003, Meischner 2005). Radar-derived rainfall data generally are scaled to match the volume measured at coincident rain gauges using some form of bias adjustment technique (Wilson and Brandes, 1979). Vieux and Vieux (2005a, b) describe statistical interpretation of bias-adjusted radar rainfall data accuracy for hydrologic modeling or urban stormwater and sanitary sewer hydraulic modeling purposes. Because the existing horizontal-polarization radar technology cannot differentiate among backscattering targets, many features can introduce spurious rainfall into any field of estimates. These features include anomalous propagation, ground clutter, insects, migrating birds, and metallic chaff. Beam blockages by terrain features, trees, or buildings near the radar antenna can reduce or eliminate reflectivity and rainfall estimates over portions of the geographic radar umbrella.

2.1.4 Satellite-Based Precipitation Estimation

In recent decades, satellite-based measurement of precipitation has affected the field of hydrometeorological observation networks that focus on accurate spatial measurement of precipitation; however, this chapter does not provide a comprehensive discussion about methods of satellite-based measurement of precipitation, instruments, and their workings. Strangeways (2007) describes precipitation estimation by cloud indexing and bispectral and life-history methods and from passive and active microwave measurements. Mekonnen and Hossain (2009) discuss the most recent advances in satellite-based rainfall estimation and its utility in hydrologic modeling. Sene (2009) provides brief descriptions of algorithms used to obtain satellite-based precipitation estimations.

The Tropical Rainfall Measuring Mission (TRMM) (TRMM 2011) is a joint US–Japanese satellite mission to monitor tropical and subtropical precipitation. The TRMM Multi-Satellite Precipitation Analysis (TMPA) provides a calibration-based sequential scheme for combining precipitation estimates from multiple satellites, and gauge analyses where feasible, at fine scales ($0.25^\circ \times 0.25^\circ$ at three-hour intervals). TMPA is available both after and in real time, based on calibration by the TRMM combined instrument and TRMM microwave imager precipitation products, respectively. Only the after-real-time product incorporates gauge data at present. The dataset covers the latitude band 50°N–S (Huffman et al. 2003) for the period from 1998 to 2015. The Global Precipitation Measurement (GPM) mission is an international network of satellites that provide the global observations of rain and snow. GPM, initiated by National Aeronautics and Space Administration (NASA) and the Japan Aerospace Exploration Agency (JAXA) as a global successor to TRMM, comprises a consortium of international space agencies, including the Centre National d'Études Spatiales (CNES), the Indian Space Research Organization (ISRO), the National Oceanic and Atmospheric Administration (NOAA), the European Organization for the Exploitation of Meteorological Satellites (EUMETSAT), and others (GPM 2018). The reader is directed to the website, <http://pmm.nasa.gov/GPM> for more details about GPM. The GPM's array of satellites is expected to provide precipitation measurements every 2 to 4 hours across the globe. The measurements are based on advanced active/passive microwave sensors and provide greater sensitivity to light rain and falling snow. GPM will also provide an exhaustive description of space–time variability of global precipitation and insights into storm structure and large-scale atmospheric processes.

2.2 FITTING OF PROBABILITY DISTRIBUTIONS FOR RAINFALL EXTREMES

Rainfall measurements are available at different temporal resolutions from various sources. Temporal variations of extreme rainfall events for different durations are often analyzed as a part of rainfall frequency analysis, which leads to the development of design storm events using depth–duration–frequency (DDF) curves. Once the rainfall extremes are extracted from a long-term series,

probability distributions are used to characterize these extremes. The following steps are used to fit and evaluate probability distributions to rainfall data. Before the steps are executed, historical precipitation data at a site are evaluated for any problems associated with missing data and homogeneity and stationarity issues. A computational code is required to sequentially search the historical precipitation data to obtain the extreme value's data for different durations.

1. Obtain extreme rainfall depth data for different durations for each year. The series of depths is referred to as the annual maximum series (AMS).
2. Obtain the empirical cumulative distribution functions (CDFs) for the AMS for each duration.
3. Develop a hypothesis for the CDF underlying the data.
4. Estimate the parameters for the hypothesized distribution function.
5. Select a goodness-of-fit test along with a level of significance.
6. Evaluate the validity of the hypothesized distribution of data using a goodness-of-fit test.
7. Repeat Steps 3 to 6 if the hypothesized distribution does not fit the data.

Before statistical analysis, the rainfall depths are converted to annual extreme value (AEV) series or peak over threshold (POT) series. AEV series is usually used because it simplifies the statistical analysis. These rainfall series should satisfy these four conditions ([Ashkar 1996](#)): (1) randomness, (2) independence, (3) homogeneity, and (4) stationarity. Annual extreme rainfall events are considered random and independent. Homogeneity and stationarity are two main issues that need to be thoroughly addressed when dealing with extreme precipitation data. When these four conditions are satisfied for any time series of extremes, then the series of observations (i.e., sample) can be regarded as independent and identically distributed (IID). Tests for IID can include evaluation of distributions of subsamples, scatter plot of observations, and lag-1 observations and assessment of the location-dispersion ellipsoid ([Meucci 2009](#)). IID is confirmed when the distributions of subsamples obtained by split samples are similar, the scatter plot shows no correlation between successive observations, and finally the location-dispersion ellipsoid is circular.

2.3 PRECIPITATION FREQUENCY ANALYSIS: DEVELOPMENT OF CUMULATIVE DISTRIBUTION FUNCTIONS

A quantile plot (i.e., referred to as an empirical CDF plot) provides a graph of the ordered data and the corresponding estimated cumulative probabilities ([Chin 2006](#), Millard and Neerchel 2001, [Wilks 2006](#)). The estimated probabilities are defined as the plotting positions, and several formulae are available for obtaining these probabilities. [Blom \(1958\)](#) and [Cullen and Frey 1999](#)) describe a general expression, which is provided in Equation (2-1) to develop empirical CDFs.

$$P_i(X < x_i) = \frac{i - a}{n - 2a + 1} \quad \forall i$$

for i = 1, 2, ..., n and x₁ < x₂ < x₃ < ... < x_n (2-1)

where x_1, x_2, \dots, x_n are the sample values ranked in ascending order; i is an index that refers to the rank of each sample; P_i is the cumulative probability; X is the random variable of interest and n is the total number of sample values. Table 2-1 provides different values of parameter a for obtaining different plotting position formulae based on Equation (2-1). The appendix provides an example of cumulative probability plots using different plotting position formulae for annual extreme rainfall depths for a duration of 1 hour. Normal and Weibull probability plots for the same data are also shown in Figures A-1 to A-3 in the appendix. [Makkonen \(2006\)](#) investigates several plotting position

Table 2-1. Values of Constant a for Different Plotting Position Formulae.

Plotting Position Formula	a
Weibull (1939)	0.000
Blom (1958)	0.375
Cunnane (1978)	0.400
Gingorten (1963)	0.440
Hazen (1930)	0.500
Tukey (1962)	0.333
Chegodayev or Leivikov (1955)	0.300

formulae and concludes that the Weibull plotting position formula predicts much shorter return periods of extreme events than the other commonly used plotting position methods. The California plotting position formula ([California State Department 1923](#)), equal to $\frac{i}{n}$, is one of the first formulae developed. [Cunnane \(1978\)](#) evaluates different formulae using two criteria: (1) unbiasedness and (2) minimum variance. Based on these two criteria, Cunnane notes that the Weibull formula is biased and plots the largest values of a sample at too small a return period. Blom's formula for normally distributed data and Gingorten's formula for data distributes according to extreme value type I ([Chow et al. 1988](#)). [Yevjevich \(1972\)](#) makes a similar recommendation for the Gingorten formula. [Hosking et al. \(1985\)](#) provide a plotting position formula as $\frac{i-0.35}{n}$.

2.4 PROBABILITY DISTRIBUTIONS FOR CHARACTERIZING PRECIPITATION DATA

Understanding hydrometeorological and hydroclimatological processes is critical for deciding the type of distribution appropriate for characterizing precipitation data ([Shuttleworth 2012](#)). Several probability distributions are appropriate for characterizing extreme precipitation at different temporal scales. Regional frequency analysis ([Madsen et al. 2002](#)) for spatially available rainfall observations is characterized using appropriate probability distributions. Generally, distributions that are asymmetric and skewed to the right (i.e., negatively skewed) are used. The skewness is mainly owing to the range of values observed for the hydrologic process variable. Positively skewed values for hydrologic variables (i.e., precipitation) are bounded on the left by the lower boundary of the ranges. Distributions (e.g., Gaussian) that can characterize variables on the entire real line of variables can be mathematically fit to precipitation data. Selection of probability distributions is crucial for those variables that are physically constrained to be nonnegative. Fitting a Gaussian distribution to precipitation data is practically possible, yet the probabilities obtained from the use of this distribution are not feasible. Some of the distributions used in past studies include Gaussian distribution for annual totals ([Naoum and Tsanis 2003](#)); Weibull and exponential for daily rainfall ([Duan et al. 1995](#), [Burgueño et al. 2005](#)); Gumbel or extreme value type 1 distribution for annual precipitation extremes ([Hershfield 1961](#); generalized extreme value (GEV) distribution for 5-, 10-, and 15-min, daily, and hourly annual maximum series ([Bonnin et al. 2006](#)) and 1-, 2-, 6-, 12-, 24-, 48-, 72-, and 96-h precipitation extremes ([Teegavarapu et al. 2013](#)); gamma for daily rainfall amounts ([Groisman et al. 1999](#)); and Pearson type-III for full records of daily precipitation data and kappa for wet-day daily rainfall ([Hanson and Vogel 2008](#)). [Shuttleworth \(2012\)](#) indicates that selection of a particular probability distribution is as much an art as a science and is a decision that is aided by experience but influenced by personal preference. The following sections briefly describe a few commonly used distributions for characterizing precipitation.

2.4.1. Normal Distribution

Normal or Gaussian distributions are not generally applicable to characterizing hydrologic variables as the normally distributed random variables vary from $-\infty$ to $+\infty$. Assigning probabilities to negative variable values—however small the values are—is theoretically possible but illogical. However, several studies have used normal distributions to characterize extreme annual rainfall values. The symbols μ_x and σ_x represent the mean and standard deviation of the series. Equation (2-2) gives the probability density function of the normal distribution.

$$f(x) = \frac{1}{\sigma_x \sqrt{2\pi}} \exp\left[-\frac{1}{2}\left(\frac{x - \mu_x}{\sigma_x}\right)^2\right] \quad (2-2)$$

2.4.2. Log-Normal Distribution

The log-normal distribution can be used to characterize the distribution of extreme values using logarithmic transformation (i.e., $y = \log_e x$ or $y = \log_{10} x$). Equation (2-3) gives the probability density function (PDF) of the log-normal distribution.

$$f(x) = \frac{1}{x \sigma_y \sqrt{2\pi}} \exp\left[-\frac{(y - \mu_y)^2}{2\sigma_y^2}\right], \quad x > 0 \quad (2-3)$$

The variable y is the log-transformed extreme value, and μ_y and σ_y are the mean and standard deviation of the transformed series. Log-normal distributions can be used for characterizing annual precipitation totals and extremes.

2.4.3 Three-Parameter Log-Normal Distribution

A three-parameter log-normal distribution function is similar to the density function provided by Equation (2-4) with an additional parameter referred to as the threshold parameter. The transformation $y = \log_e(x - \gamma)$ or $\log_{10}(x - \gamma)$ with the threshold parameter, γ , is used for the three-parameter log-normal distribution. When the threshold parameter is associated with location and when it equals zero, the distribution reduces to a two-parameter log-normal distribution (Millard and Neerchal 2000).

2.4.4 Extreme Value Type I Distribution

Equation (2-4) gives the general form of the extreme value PDF.

$$f(x) = \frac{1}{a} \exp\left\{\pm \frac{x - b}{a} - \exp\left[\pm \frac{x - b}{a}\right]\right\}, \\ -\infty < x < \infty, \quad \infty < b < \infty, \quad a > 0 \quad (2-4)$$

where a and b are scale and location parameters and b is the mode of the distribution. The minus sign in \pm is used for maximum values. The distribution is also referred to as type I or Gumbel's distribution.

2.4.5 Extreme Value Type III Distribution

Equation (2-5) gives the probability density function for the extreme value type III, which is generally used for characterizing extreme values bounded on the left by zero (Chin 2006). The distribution is also referred to as a Weibull distribution.

$$f(x) = ax^{a-1}b^{-a} \exp\left[-\left(\frac{x}{b}\right)^a\right], \quad x \geq 0, \quad a, b > 0 \quad (2-5)$$

2.4.6 Generalized Extreme Value Distribution

The GEV distribution is based on extreme-value type I, II, and III distributions for maxima (Chin 2006). Equation (2-6) gives the CDF for the GEV. The variables ao , bo , and co in Equation (2-6) are the location, scale, and shape parameters of the distribution.

$$F(x) = \begin{cases} \exp\left\{-\left[1 - \frac{co(x-ao)}{bo}\right]^{\frac{1}{co}}\right\} & co \neq 0 \\ \exp\left\{-\exp\left[-\frac{(x-ao)}{bo}\right]\right\} & co = 0 \end{cases} \quad (2-6)$$

2.4.7 Gamma Type III Distribution

The general form of the one-parameter gamma distribution (Chin 2006, Millard and Neerchal 2000) is given by

$$f(x) = \frac{1}{\Gamma(\alpha)} x^{\alpha-1} e^{-x}, \quad x \geq 0 \quad (2-7)$$

The variable α is the mean, and Γ is the gamma function. The PDF of a Pearson type III distribution is given by

$$f(x) = \frac{1}{\beta^\alpha \Gamma(\alpha)} (x-\gamma)^{\alpha-1} e^{-(x-\gamma)/\beta}, \quad x \geq \gamma \quad (2-8)$$

The variable γ is the lower bound of the distribution, β is the scale parameter, and α is the shape parameter. The log-Pearson type III distribution essentially has the same probability density function with the data being logarithmically transformed.

2.4.8 Exponential Distribution

The general form of the exponential distribution with one parameter (λ) is given by

$$f(x) = \begin{cases} \lambda e^{-\lambda x} & x \geq 0 \\ 0 & x < 0 \end{cases} \quad (2-9)$$

The parameter ($\lambda > 0$) is also referred to as the rate of distribution. The mean of the exponential distribution $E[X]$ is equal to $\frac{1}{\lambda}$.

2.4.9 Other Distributions

A few other distributions such as generalized logistic (GLO), generalized normal (GNO) and generalized Pareto (GPA), five-parameter Wakeby, and kappa (Park and Jung 2002) are also appropriate for characterizing precipitation extremes. The exponential distribution is used for characterizing daily precipitation data in several studies. Servuk and Geiger (1981) provide details of several distributions that are appropriate to characterize rainfall extremes. These distributions should be evaluated along with the others discussed previously in this chapter before selecting a specific distribution to characterize extreme rainfall values. Tables 2-2 lists studies using different probability distributions to characterize precipitation at different durations. Note that the list is by no means exhaustive and the studies reported are carried out in different parts of the world.

Table 2-2. Studies Using Different Probability Distributions to Characterize Precipitation at Different Temporal Scales.

Temporal scale	Distribution type	Reference
Daily	Two-parameter gamma	Aksoy (2000)
Monthly	Exponential	Alexandersson (1985)
Monthly	Normal, gamma, Weibull	Alghazali and Alawadi (2014)
Seasonally	Weibull and gamma	Alonge and Afullo (2012)
Monthly	Gamma, log-normal, normal	Angelidis et al. (2012)
Daily	Generalized extreme value and generalized log-normal	Benabdesselam and Amarchi (2013)
Yearly	Gumbel and Weibull	Berthe et al. (2015)
Daily	Generalized extreme value	Bertoldo et al. (2015)
Monthly	Gamma two-parameter and Pearson type III	Blain (2011)
Daily	Gamma	Blain and Meschiatti (2015)
Hourly	Generalized extreme value	Carreau et al. (2013)
Daily	Normal	Chen et al. (2012)
Annually	Generalized extreme value	Chikobvu and Chifurira (2015)
Monthly	Gamma and log-normal	Cho et al. (2004)
Daily	Generalized extreme value	Chun and Wheater (2012)
Monthly	Weibull and generalized extreme value	Clarke (2002)
Annually	Generalized extreme value	Crisci et al. (2002)
Hourly	Generalized Pareto, exponential, and gamma	Dan'azumi et al. (2010)
Quarterly	Gamma	Dikko et al. (2013)
Daily	Weibull and gamma	Duan et al. (1998)
Daily	Gamma and Tweedie	Dunn (2004)
Hourly	Generalized extreme value	Dyrrdal et al. (2015)
Daily, 2-day, 5-day, 10-day, annually	Generalized extreme value	Feng et al. (2007)
Monthly	Gamma three, generalized extreme value, generalized Pareto, Wakeby	Fischer et al. (2012)
Annually	Log-normal	Foster et al. (2006)
Monthly	Gamma, normal, log-normal	Gasiorek and Musial (2015)
Daily	Gamma	Goyal et al. (2013)
Monthly	Gamma and Wakeby	Guttman et al. (1993)
Daily	Two-parameter gamma, Pearson type III, kappa	Hanson and Vogel (2008)
Monthly	Gamma	Husak et al. (2007)
Hourly, daily, annually	Wakeby, generalized extreme value function, and two-parameter Weibull	Kang and Yusof (2013)
Daily	Mixed exponential	Kannan and Farook (2015)
Monthly	Normal and gamma	Kasperska-Wolowicz et al. (2016)
Daily	Generalized exponential, gamma, and Weibull	Kazmierczak and Kotowski (2015)
Annually	Weibull	Kotei et al. (2013)

Table 2-2. Studies Using Different Probability Distributions to Characterize Precipitation at Different Temporal Scales. (Continued)

Temporal scale	Distribution type	Reference
Daily	Normal, gamma, and stretched exponential	Krakauer et al. (2015)
Daily	Log-normal	Kronenberg et al. (2014)
Annually	Generalized extreme value	Kysely and Picek (2007)
Areal	Gumbel	Lebel and Laborde (1988)
Yearly	Generalized extreme value	Lehmann et al. (2013)
Daily	Gamma	Li et al. (2012)
Daily, monthly, annually	Exponential, gamma, Weibull, skewed normal, mixed exponential, and hybrid exponential/Pareto	Li et al. (2013)
Daily	Generalized extreme value, Burr, Weibull	Li et al. (2015)
Daily	Exponential, gamma, mixed-exponential, and log-normal	Liu et al. (2011)
Annually	Normal, two-parameter log-normal, three-parameter log-normal Gumbel, two-parameter gamma, Pearson type III, and log-Pearson type III	Mahdavi et al. (2010)
Monthly	Log-skew-normal and log-skew-t	Marchenko and Genton (2010)
Monthly	Log-skew-normal alpha-power	Martinez-Florez et al. (2013)
Annual maximum	Burr, generalized extreme value, and log-Pearson III	Mayooran and Laheetharan (2014)
Daily	Generalized extreme value	Min et al. (2009)
Monthly	Gamma	Modley (1973)
Daily	Weibull and gamma	Neykov et al. (2014)
Daily	Three-parameter mixed-exponential, single-parameter exponential, Gamma, Weibull	Nguyen and Mayabi (1990)
Monthly and yearly	Normal	Nyatsume et al. (2014)
Hourly	Generalized extreme value and log-normal	Overeem et al. (2008)
Daily	Generalized extreme value	Ozcan et al. (2013)
Annually	Wakeby	Öztekin (2007)
Daily	Generalized extreme value	Panagoulia et al. (2014)
Daily	Gumbel and generalized extreme value	Papalexiou and Koutsoyiannis (2006)
Daily	Gamma, Pareto, log-normal, Weibull, and gamma	Papalexiou et al. (2013)
Daily and 2-day	Wakeby	Park et al. (2001)
Daily	Normalized gamma	Penide et al. (2013)
Daily	Normal	Raheem et al. (2015)
Daily	Gamma	Rana et al. (2014)

(Continued)

Table 2-2. Studies Using Different Probability Distributions to Characterize Precipitation at Different Temporal Scales. (Continued)

Temporal scale	Distribution type	Reference
6-hour	Generalized extreme value	Rulfová et al. (2016)
Hourly	Gumbel and generalized extreme value	Saito and Matsuyama (2015)
Daily	Generalized extreme value and generalized Pareto	Santos et al. (2016)
Monthly	Weibull	Schonwiese et al. (2003)
Monthly, daily	Weibull	Selker and Haith (1990)
Daily	Log-normal and gamma	Sharma and Singh (2010)
Daily	Wakeby	Su et al. (2009)
Daily	Exponential, gamma, Weibull, and log-normal	Suhaila et al. (2011)
Monthly	Log-normal or gamma and log-skew-elliptical	Sun et al. (2015)
1-hour–72 hours	Generalized extreme value	Teegavarapu et al. (2013)
Daily	Gamma	Vlček and Huth (2009)
Monthly	Generalized extreme value, extreme value	Vivekanandan (2014)
Daily	Gumbel	Vivekanandan and Roy (2013)
Monthly	Gamma	Volkova et al. (2014)
Hourly and daily	Exponential, Weibull, gamma, generalized gamma, log-normal, and Johnsons' bounded distribution	Wakazuki (2011)
2-hour and daily	Generalized extreme value	Wallis et al. (2007)
Daily	Gamma	Wang et al. (2008)
Daily	Weibull	Wilks (1988)
Daily	Gamma, log-normal, and mixed exponential	Wilson and Toumi (2005)
Annually, seasonally, and monthly	Generalized extreme value, three-parameter log-normal, Pearson type III, and log-Pearson type III	Yue and Hashino (2007)

2.5 ESTIMATION OF DISTRIBUTION PARAMETERS

Parameter estimation involves estimation of population parameters from the sample data. Three commonly used methods include the method of moments (MOM), the maximum likelihood method, and the L-moments method. MOM is the easiest, and the maximum likelihood and L-moment methods are computationally intensive and require iterative approaches. Six characteristics of the estimation methods are important: Small (1990) describes these as (1) consistency, (2) lack of bias, (3) efficiency, (4) sufficiency, (5) robustness, and (6) practicality.

2.5.1 Method of Moments

As the name suggests, MOM indicates that parameters of the distribution can be estimated using the moments of the distribution. These estimates are unbiased estimates of mean, standard deviation,

and skewness. The estimates are obtained from the sample data, and they are assumed to be equal to the population parameters.

$$\hat{\mu}_x = \frac{1}{no} \sum_{j=1}^{no} x_j \quad (2-10)$$

$$\hat{\sigma}_x^2 = \frac{1}{no - 1} \sum_{j=1}^{no} (x_j - \hat{\mu}_x)^2 \quad (2-11)$$

$$\hat{g}_x = \frac{no}{(no - 1)(no - 2)} \frac{\sum_{j=1}^{no} (x_j - \hat{\mu}_x)^3}{\hat{\sigma}_x^3} \quad (2-12)$$

2.5.2 Maximum Likelihood Estimation Method

The maximum likelihood estimation (MLE) method is the most common method for estimating parameters. A likelihood function (L°) given by Equation (2-13), or a log-likelihood function, is maximized. The variable np is the number of parameters, no is the number of observations, j is the index for the observation number, and $f_X()$ is the PDF. Partial derivatives of the likelihood function (L°) with respect to different parameters ($\theta_1, \theta_2, \dots, \theta_{np}$) are obtained using Equation (2-14) to solve a set of equations. In some cases, maximizing the logarithm of the likelihood function (referred to as log-likelihood function) is easier (Millard and Neerchal 2000). The solutions of these equations provide the estimated parameter values.

$$L^\circ(\theta_1, \theta_2, \dots, \theta_{np}) = \prod_{j=1}^{no} f_X(x_j | \theta_1, \theta_2, \dots, \theta_{np}) \quad (2-13)$$

$$\frac{\partial L^\circ}{\partial \theta_{jp}} = 0, \quad jp = 1, \dots, np \quad (2-14)$$

2.5.3 L-Moments Approach

Hosking (1990) proposed the concept of L-moments as linear combinations of probability-weighted moments (PWM). Greenwood et al. (1979) described the theory of probability-weighted moments. Equation (2-15) describes the PWM. The variable ω_r is the r^{th} order PWM, and $F_X(x)$ is the CDF of x . Hosking and Wallis (1997) define the unbiased sample estimators of PWMs as ϕ_1, ϕ_2, ϕ_3 , and ϕ_4 , which are the four L-moments. Unbiased sample estimates of the PWM for any distribution can be obtained using Equations (2-15) to (2-19).

$$\omega_r = \int_{-\infty}^{+\infty} x [F_X(x)]^r f_X(x) dx \quad (2-15)$$

$$\phi_1 = \omega_0 \quad (2-16)$$

$$\phi_2 = 2\omega_1 - \omega_0 \quad (2-17)$$

$$\phi_3 = 6\omega_2 - 6\omega_1 + \omega_0 \quad (2-18)$$

$$\phi_4 = 20\omega_3 - 30\omega_2 + 12\omega_1 - \omega_0 \quad (2-19)$$

The values of ω_0 , ω_1 , ω_2 , and ω_3 are obtained by equating them to derived constants (bc_0 , bc_1 , bc_2 , and bc_3) from the sample using Equations (2-20) to (2-23).

$$bc_0 = \frac{1}{no} \sum_{j=1}^{no} x_j \quad (2-20)$$

$$bc_1 = \frac{1}{no(no-1)} \sum_{j=2}^{no} (j-1)x_j \quad (2-21)$$

$$bc_2 = \frac{1}{no(no-1)(no-2)} \sum_{j=3}^{no} (j-1)(j-2)x_j \quad (2-22)$$

$$bc_3 = \frac{1}{no(no-1)(no-2)(no-3)} \sum_{j=4}^{no} (j-1)(j-2)(j-3)x_j \quad (2-23)$$

The ratios of ϕ_2 and ϕ_1 , ϕ_3 and ϕ_2 , and ϕ_4 and ϕ_2 are defined as L-coefficient of variation, L-skewness, and L-kurtosis, respectively. These ratios are referred to as L-moment ratios. Table 2-3 gives parameters for different probability distributions and associated L-moments (Hosking and Wallis, 1997, Chin, 2006) to obtain these parameters. Notation for the parameters is adopted from Chin (2006). The coefficients of L-variation, L-skewness, and L-kurtosis provide measures of dispersion, symmetry, and peakedness, respectively.

The use of best-fitting distribution for each data sample provides frequency estimates that are too sensitive to sampling variations in the data and the period of record available (WMO 2009). Procedures involving a combination of regionalization of some parameters and split-sample Monte-Carlo evaluation of different estimation methods are often used (WMO 2009, ASCE 1996).

2.6 FREQUENCY FACTORS

Frequency factors (Chin 2006, Rakhecha and Singh 2009) are available for several distributions, and they can be used to obtain the magnitude of an event for a specific return period, T . Frequency factors are used in the method proposed by Chow (1951), referred to as the frequency method or the general frequency equation for hydrologic frequency analysis. The general equation is given as

$$x_T = \bar{x} + K_T s \quad (2-24)$$

where x_T is the magnitude of an event for a return period T , and K_T , \bar{x} , and s are the frequency factor, mean, and standard deviation values calculated based on the sample, respectively.

The frequency factors depend on the type of distribution used. In general, for two-parameter distributions, the factors depend on the return period. Chow et al. (1988) and Chin (2006) provide

Table 2-3. Moments of Distributions and Corresponding L-Moments.

Distribution	Parameters	Moments	L-moments
Normal	μ_X, σ_X	$\mu_X = \mu_X$ $\sigma_X = \sigma_X$	$\phi_1 = \mu_X$ $\phi_2 = \frac{\sigma_X}{\pi^{1/2}}$
Log-normal ($Y = \ln X$)	μ_Y, σ_Y	$\mu_Y = \mu_Y$ $\sigma_Y = \sigma_Y$	$\phi_1 = \exp\left(\mu_Y + \frac{\sigma_Y^2}{2}\right)$ $\phi_2 = \exp\left(\mu_Y + \frac{\sigma_Y^2}{2}\right) \operatorname{erf}\left(\frac{\sigma_Y}{2}\right)$
Exponential (two-parameter)	ξ, η	$\mu_X = \xi + \frac{1}{\eta}$ $\sigma_X = \sqrt{\xi + \frac{1}{\eta^2}}$	$\phi_1 = \xi + \frac{1}{\eta}$ $\phi_2 = \frac{1}{2\eta}$
Gumbel	ξ, α	$\mu_X = \xi + 0.5772\alpha$ $\sigma_X^2 = 1.645\alpha^2$	$\phi_1 = \xi + 0.5772\alpha$ $\phi_2 = 0.6931\alpha$
Generalized extreme value	ξ, α, κ	$\mu_X = \xi + \frac{\alpha}{\kappa}[1 - \Gamma(1 + \kappa)]$ $\sigma_X^2 = \left(\frac{\alpha}{\kappa}\right)^2 \{\Gamma(1 + 2\kappa) - [\Gamma(1 + \kappa)]^2\}$	$\phi_1 = \xi + \frac{\alpha}{\kappa}[1 - \Gamma(1 + \kappa)]$ $\phi_2 = \frac{\alpha}{\kappa}(1 - 2^{-\kappa})\Gamma(1 + \kappa)$

Note: Euler's constant = 0.5772.

the factors for normal and gamma (Pearson type III) and extreme value type I distributions, which are given by Equations (2-25), (2-27), and (2-29), respectively.

$$K_T = w - \frac{2.515517 + 0.802853w + 0.010328w^2}{1 + 1.432788w + 0.189269w^2 + 0.001308w^3} \quad (2-25)$$

$$w = \left[\ln\left(\frac{1}{p^2}\right) \right]^{\frac{1}{2}}, \quad 0 < p \leq 0.5 \quad (2-26)$$

In Equation (2-26), the value of p is the exceedance probability, and when the value of p is greater than 0.5, then p is substituted with $1-p$ with modification of sign for the value of K_T .

$$K_T = \frac{1}{3k} \{[(x'_T - k)k + 1]^3 - 1\} \quad (2-27)$$

$$k = \frac{g_x}{6} \quad (2-28)$$

$$K_T = -\frac{\sqrt{6}}{\pi} \left\{ 0.5772 + \ln \left[\ln \left(\frac{T}{T-1} \right) \right] \right\} \quad (2-29)$$

Chow et al. (1988) present the frequency factor relationship for log-Pearson type III distribution provided by Kite (1977) and Equation (2-30). The z value is equal to frequency factor (K_T) when g_x (skewness coefficient) equals zero, and when g_x does not equal zero, then K_T is defined by Equation (2-29). Equation (2-28) gives the value of k .

$$K_T = z + (z^2 - 1)k + \frac{1}{3}(z^3 - 6z)k^2 - (z^2 - 1)k^3 + zk^4 + \frac{1}{3}k^5 \quad (2-30)$$

2.7 GOODNESS-OF-FIT TESTS FOR NORMAL DISTRIBUTIONS

Precipitation data at different temporal scales can be tested for normality using several goodness-of-fit tests. These tests include Lilliefors ([Lilliefors 1967](#)), Jarque–Bera ([Jarque and Bera 1987](#)), chi-square (χ^2) ([Corder and Foreman 2009](#)), and Kolmogorov–Smirnov (KS) ([Massey 1967](#), Smirnov 1939, [Thode 2002](#), [Sheskin 2003](#)) goodness-of-fit tests along with visual checks using normal probability plots. Visual checks confirm normality if the CDF appears as a straight line in the probability plot ([Benson 1962](#)). Visual assessments of probability plots give a preliminary indication of the normality of the sample data. As visual tests using probability plots are not robust and no objective measure of the straightness of a probability plot is available ([Mage 1982](#)), goodness-of-fit tests such as chi-square, Kolmogorov–Smirnov, Anderson–Darling ([Anderson and Darling 1954](#)), Lilliefors, Shapiro–Wilks ([Shapiro and Wilk 1965](#)), and D’Agostino–Pearson ([Pearson 1931](#), [D’Agostino et al. 1990](#)) should be used. One major limitation of the KS method is that population parameters are required for the test as opposed to sample parameters. [Steinskog et al. \(2007\)](#) suggest that the Jarque–Bera and the Shapiro–Wilks tests for normality are good alternatives to the KS test based on a power comparison of eight different tests. [Coin \(2008\)](#) reports an extension of the Shapiro–Wilks test that is not affected by the presence of one or a few outliers in the dataset. Several modifications to the KS test have been made recently that overcome this limitation of the test. The preferred tests are D’Agostino–Pearson, Anderson–Darling, and Lilliefors. Precipitation data frequently may not conform to normality. Transformations of data are often used to achieve normality. Different transformations such as logarithmic, square, square-root, and several others described by [Helsel and Hirsch \(2002\)](#) and [Box and Cox \(1964\)](#) can be used. The Box–Cox transformation parameter is obtained by using an optimization formulation that maximizes the objective function defined by a log–likelihood function ([Wilks 2011](#)). The Environmental Protection Agency ([USEPA 2000](#)) provides guidelines for tests for normality along with stipulations on the sample size (n). These are the Shapiro–Wilks test ($n \leq 5,000$), Filliben’s statistic ($n \leq 100$), skewness and kurtosis tests ($n > 50$), the studentized range test ($n \leq 1,000$), Geary’s test ($n > 50$), Lilliefors–Kolmogorov–Smirnov test ($n > 50$), and the chi-square test (χ^2 test). For the chi-square test the recommended number of observations should be at least five in each bin. If the expected frequencies are less than five, or when the number of classes is small, then the χ^2 test with Yates ([Yates 1934](#)) corrections can be applied ([Vidakovic 2011](#)).

2.8 GOODNESS-OF-FIT TESTS FOR OTHER DISTRIBUTIONS

Two common goodness-of-fit tests used for evaluation of other distributions include the KS and chi-square tests ([Sheskin 2003](#)). The KS test is recommended when the number of samples is less than 30. The chi-square test is more sensitive to the number of bins (i.e., intervals) used. [Filliben \(1975\)](#) proposes another test that can be used, which is the probability-plot correlation coefficient (PPCC) test. The test ([Filliben 1975](#), [Dingman 2008](#)) involves calculation of the correlation coefficient between each sample value and the values that would exist at the corresponding exceedance probabilities if the data were from a specific distribution. A distribution quantile function ([Stedinger et al. 1992](#)) can be used to calculate values associated with specific exceedance probability for the proposed distribution. The hypothesis that the data are not from a specific distribution is not rejected if the correlation coefficient is closer to 1. Critical values of the correlation coefficient for the PPCC approach as a function of sample size are available for rejecting or accepting the hypothesis that data are from a specific distribution.

2.8.1 Quantitative Measures

Two indexes defined by Equations (2-31) and (2-32), the mean absolute deviation index (MADI) and the mean square deviation index (MSDI) proposed by [Jain and Singh \(1987\)](#), can be used to measure the relative goodness of fit when several distributions are evaluated for the data. The MADI and the MSDI are given by

$$MADI = \frac{1}{N} \sum_{i=1}^N \left| \frac{x_i - z_i}{x_i} \right| \quad (2-31)$$

$$MSDI = \frac{1}{N} \sum_{i=1}^N \left(\frac{x_i - z_i}{x_i} \right)^2 \quad (2-32)$$

where, x_i is the observed value (i.e., extreme precipitation) and z_i is the estimated value of extreme precipitation obtained for a specific exceedance probability. The empirical probability of exceedance is obtained from the Gringorten formula. The non-exceedance cumulative probability using the Gringorten formula is given by Equation (2-33).

$$P(X < x_i) = \frac{i - 0.44}{n + 0.12} \quad (2-33)$$

The distribution providing the smallest values of two indexes can be selected as the best distribution characterizing the extreme precipitation data.

2.8.2 L-Moment Diagrams

Use of L-moment analysis and L-moment ratio diagrams are widely accepted approaches for evaluation of goodness of fit of statistical distributions of observations. [Hosking \(1990\)](#) and [Hosking and Wallis \(1997\)](#) introduced the concepts of L-moments. L-moment ratios are approximately unbiased compared with conventional moment ratios, which can exhibit enormous downward bias, even for very large samples ([Vogel and Fennessey 1994](#), [Hanson and Vogel 2008](#)). L-moment ratio diagrams provide a convenient visual way to view the characteristics of sample data compared with theoretical probability distributions ([Hanson and Vogel, 2008](#)). The L-moment diagrams using L-kurtosis vs. L-skewness and L-coefficient of variation vs. L-skewness are useful for comparison of goodness of fit for a range of multiple-parameter distributions. Use of L-moment ratio diagrams for a selection of distributions for precipitation data is evident from studies by [Lee and Maeng \(2003\)](#), [Park and Jung \(2002\)](#), [Pilon et al. \(1991\)](#), and [Hanson and Vogel \(2008\)](#).

2.9 REGIONAL FREQUENCY ANALYSIS

In many situations, data available at a site (i.e., at one rain gauge) may not be adequate for frequency analysis of extreme precipitation. Therefore, data from several rain gauges in a region can be used for the analysis in a procedure referred to as regional or pooled frequency analysis. The analysis based on the “index storm” approach is beneficial for quantile estimations of extreme precipitation events with the help of data augmentation for data-scarce sites. Regional frequency analysis ([Hosking and Wallis 1997](#)) requires delineation of a region that is classified according to a homogeneous pooling

group using a classification method and a homogeneity criterion. Once the homogeneous group is established, the augmented data are used for fitting a statistical distribution. Parameter estimation for a specific distribution can be carried out using maximum likelihood or L-moments estimation methods.

2.10 ILLUSTRATIVE EXAMPLES

This section presents two examples that involve fitting probability distributions to daily and annual extreme values of precipitation data.

Example 2-1: Daily Precipitation Time Series

Precipitation data at different temporal resolutions other than annual extremes of peaks over a specific threshold can be characterized by different probability distributions. Exponential and gamma distributions are generally found to be best fits for precipitation depths at the daily temporal resolution and interevent times (Adams and Howard 1986, Adams et al. 1986, Adams and Papa 2000). Daily precipitation data series are used to illustrate this point. A typical precipitation frequency distribution of daily rainfall values is positively skewed with a large number of lower magnitude events and fewer higher magnitude events (Shuttleworth 2012). Figures 2-2 and 2-3 show the histogram and CDF plot for daily precipitation data from a site in Louisville, Kentucky. The time series consists of approximately 66% zero values.

Figure 2-4 shows that the gamma distribution with two parameters provides the best fit for the data. MLE and MOM are used for parameter estimations for exponential and gamma distributions. The likelihood function becomes unbounded because of the presence of zero values in the daily

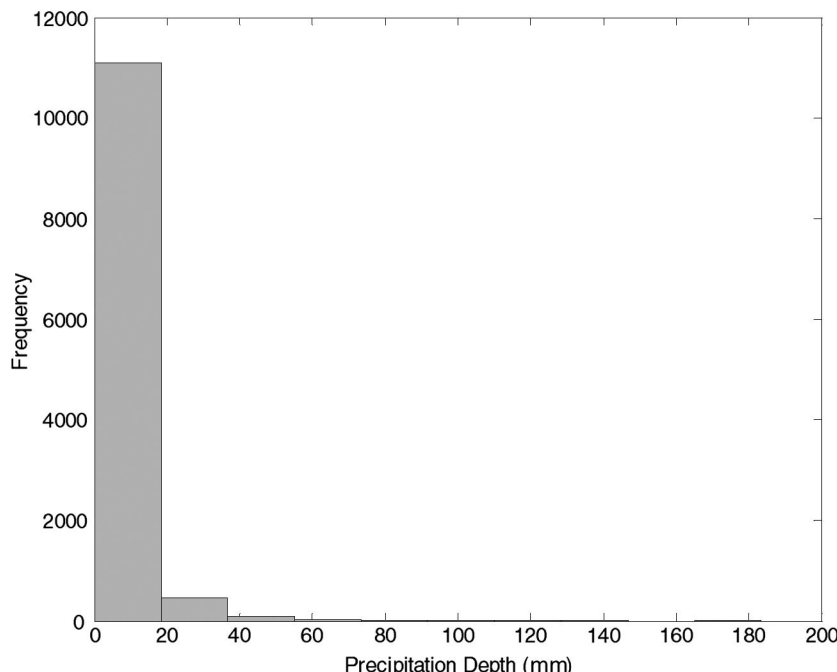


Figure 2-2. Histogram of daily precipitation time series.

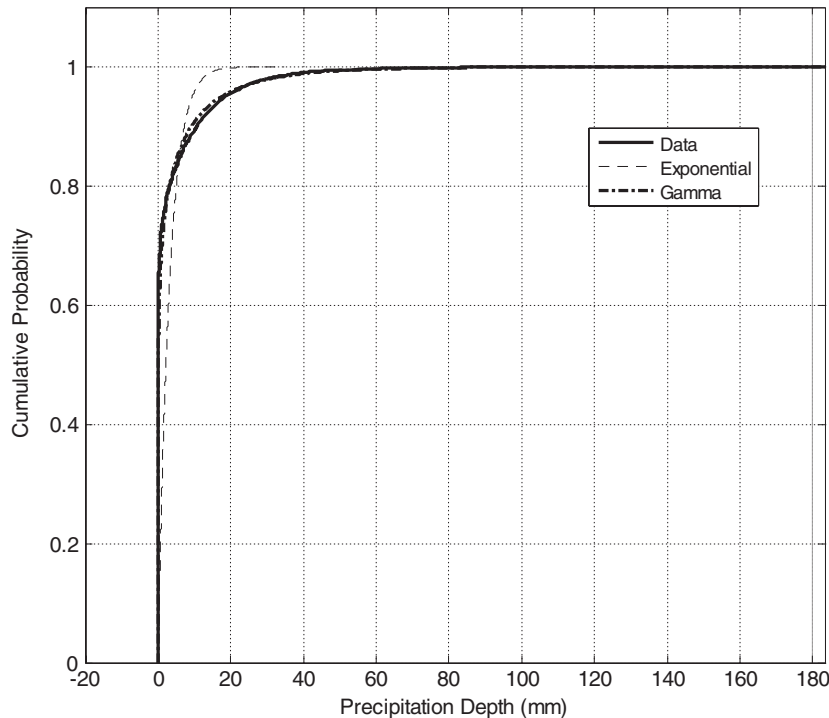


Figure 2-3. CDF function plots of daily precipitation data using exponential and gamma distributions.

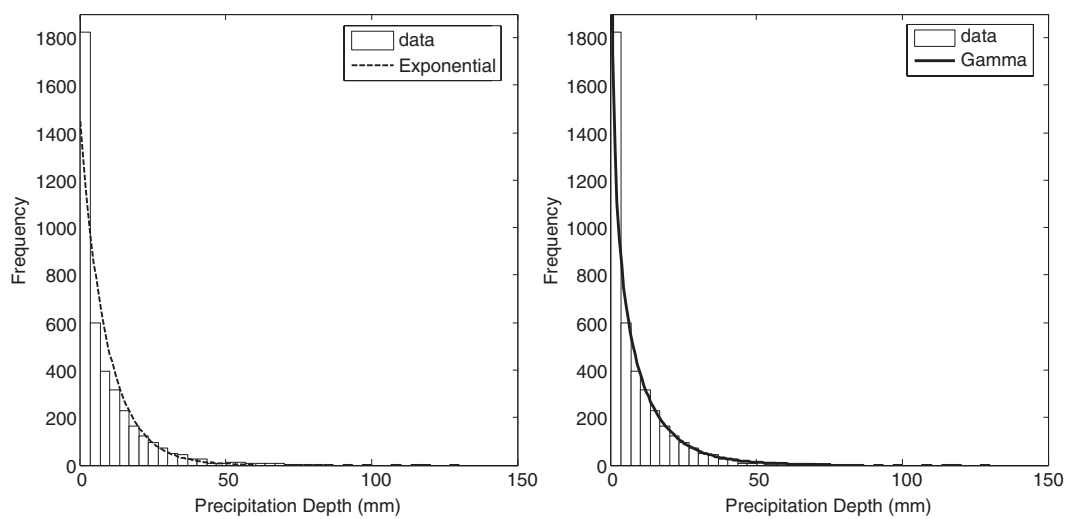


Figure 2-4. Probability density functions superimposed over histograms of nonzero daily precipitation data using exponential and gamma distributions.

precipitation data series. Probability distributions for nonzero precipitation data can be developed as shown in Figure 2-4 with the scaled exponential and gamma distributions superimposed over histograms. Figure 2-4 shows that the gamma distribution fits well for the nonzero daily precipitation data.

Example 2-2: Annual Extremes for Different Durations

Annual precipitation extreme values for different durations available at a rain gauge in the state of Florida are used to illustrate the fitting of several distributions using the maximum log-likelihood parameter estimation procedure. Table 2-4 provides details of the rainfall extremes.

Table 2-4. Annual Precipitation Extreme (mm) at a Rain Gauge in the State of Florida.

Duration (Hours)								
1	2	6	12	24	48	72	96	120
28	47	79	127	153	155	155	155	155
65	81	89	89	93	129	143	168	196
48	63	64	64	84	101	103	111	128
55	70	70	71	77	118	121	125	133
47	66	90	90	103	105	117	126	134
42	74	122	153	212	345	400	401	402
62	84	105	117	163	169	170	170	170
59	61	63	63	66	79	104	107	108
61	102	248	271	274	274	274	279	279
75	97	109	110	132	146	146	154	180
57	96	97	97	98	98	100	104	105
71	90	92	93	108	141	141	148	224
54	69	70	79	90	99	105	126	134
61	65	68	80	96	120	120	120	167
75	105	108	108	117	118	147	178	212
50	58	117	159	177	330	386	388	388
28	32	44	49	63	63	64	71	78
60	74	74	74	74	87	91	111	130
92	109	110	110	139	144	163	168	171
50	56	119	119	140	152	166	181	181
69	92	97	98	98	100	118	125	146
44	58	88	89	90	106	114	131	132
33	44	44	46	63	76	88	111	119
61	75	75	75	75	81	90	95	95
58	71	71	77	112	131	131	141	141
52	74	79	85	99	105	105	105	139
40	54	71	118	144	144	155	155	155
51	56	81	114	137	145	145	145	160
46	48	71	86	86	86	89	99	102
48	61	61	61	94	107	109	109	130
41	56	74	94	122	135	147	147	147
58	66	84	86	91	109	112	114	135
53	84	86	86	86	86	130	130	130
41	43	48	48	69	107	130	142	173
53	66	74	76	76	89	97	97	102
56	79	86	89	157	165	165	165	165
48	71	89	94	97	122	137	147	147

Table 2-4. Annual Precipitation Extreme (mm) at a Rain Gauge in the State of Florida. (Continued)

		Duration (Hours)						
1	2	6	12	24	48	72	96	120
64	64	76	76	79	79	99	140	147
48	61	66	66	66	66	66	71	71
46	64	81	107	114	150	155	160	163
48	76	86	107	130	132	135	137	137
43	58	86	91	99	109	112	112	124
41	69	157	211	224	224	224	229	234
58	61	66	66	91	114	114	117	117
51	51	56	56	56	79	99	107	112
51	66	69	71	86	89	107	107	109
43	46	46	74	104	109	109	109	142
30	56	56	56	79	81	81	84	114
48	58	94	97	97	163	165	173	173
25	46	64	107	124	132	132	150	150
36	61	74	84	86	86	91	97	99
64	66	76	79	150	196	196	208	218
69	69	71	71	117	137	140	150	178
61	84	86	86	97	135	157	178	188
53	74	84	84	86	124	130	132	152
33	48	58	94	152	170	170	175	175
64	66	74	79	130	142	160	160	191
64	79	89	89	89	97	132	137	145
43	61	107	130	175	244	246	246	272

Source: Data from the National Climatic Data Center.

Figure 2-5 shows the fitted and empirical probability distributions. The GEV distribution was found to be appropriate for characterizing the distributions of extreme precipitation depths of all durations. This was confirmed by visual evaluation of CDF plots based on data and fitted GEV parameters and goodness-of-fit tests. The chi-square goodness-of-fit test suggests null hypothesis is true for all distributions characterizing rainfall extremes for a duration of 96 h.

A recent survey of rainfall frequency estimation methods by Svensson and Jones (2010) indicates that the GEV is the most-used distribution for rainfall extremes in nine countries (Canada, Sweden, France, Germany, United States, South Africa, New Zealand, Australia, and the United Kingdom). Svensson and Jones (2010) indicate that in large parts of New Zealand, the regional shape parameter in the GEV is negative and a general increase occurs in this parameter value with the increase in duration. In some countries, the Gumbel distribution is used, partly because the estimation of a shape parameter from short records is not justified for individual sites. L-moment estimators compare favorably with those from MLE methods, particularly for small sample sizes (15 to 25 samples) for the GEV distribution (Hosking et al. 1985). Many researchers attribute short records (around 15 to 25 years) for negative shape parameters for the GEV distribution.

Conclusions based on a detailed study of the use of the GEV distribution and parameters for extreme rainfall characterization for different durations (Teegavarapu and Goly 2011, Teegavarapu et al. 2013) using several rain gauges in the state of Florida follow.

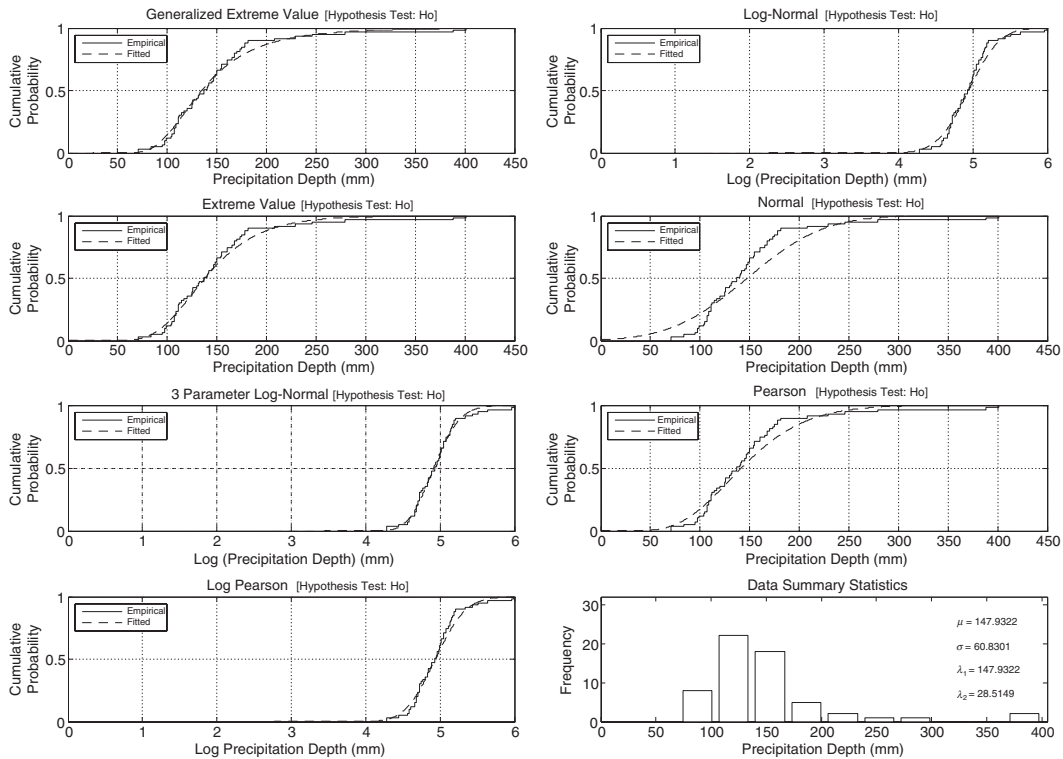


Figure 2-5. Fitted and empirical CDF plots of extreme precipitation values for a duration of 96 h.

- GEV distribution was found to be the best distribution for characterizing extreme precipitation events for all durations based on several goodness-of-fit tests and visual comparison of CDF plots.
- Shape parameter of GEV distributions showed spatial and temporal variations. However, no specific pattern in space was identified.
- Evaluation of the shape parameter for two sets of data from two different sources suggested that mostly positive shape parameters values were obtained for the duration of 24 h.
- Assessment of spatial variability of GEV distribution parameters suggests no distinct patterns or clusters of negative or positive shape parameters are evident.

2.11 FITTING OF A PARAMETRIC FREQUENCY CURVE FOR RAINFALL EXTREMES

Observed rainfall data are rarely used directly in hydrologic design for various reasons. The main reasons include (1) lack of data at a region of interest and temporal resolution required, (2) the existence of data gaps in chronological records, and (3) lack of homogeneous observations due to changes in the observation network over time and space. A design rainfall intensity defined for a given duration and frequency is commonly used in the single-event hydrologic simulation. Intensity-duration-frequency (IDF) curves are developed by local or regional water management agencies to aid hydrologic and water resources design professionals. The use of design precipitation to estimate floods is particularly valuable in those situations where flood records are not available or

not long enough at the site of interest or are not homogeneous owing to changes of watershed characteristics such as urbanization and channelization (WMO 2009). Figure 2-6 shows a typical IDF curve for a region in Florida.

IDF curve development and characterization of regional rainfall extremes are areas of continuing research as evidenced by many recent studies (e.g., Madsen et al. 2002). IDF curves can be developed from historical annual maxima for different durations using Weibull formula (Chin 2006). Alternatively, IDF curves can be developed by assuming that the historical extremes can be best characterized by extreme value type I (Gumbel's distribution) and using a frequency factor-based analysis. IDF curves can be represented by one of the generalized functional forms (Dingman, 2008, WMO 2010):

$$I = \frac{A}{(D + C)^B} \quad (2-34)$$

$$I = \frac{AT}{D^e + C} \quad (2-35)$$

$$I = \frac{A}{(D - C)^e} \quad (2-36)$$

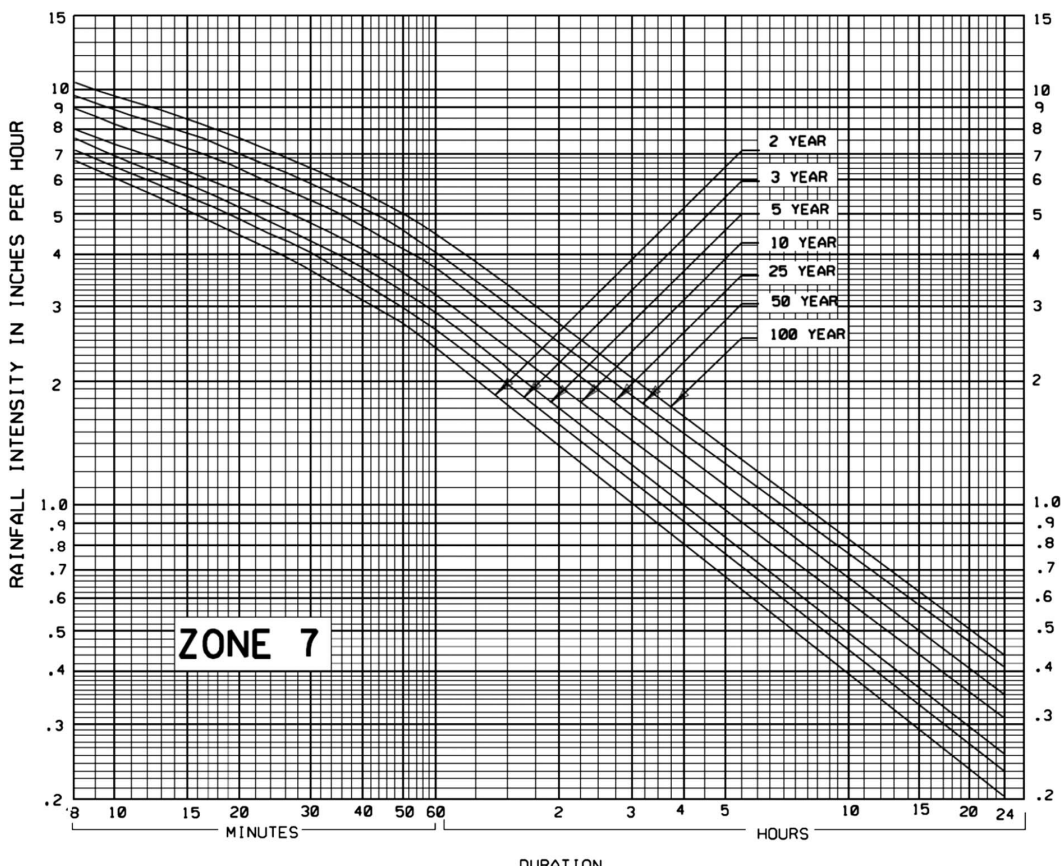


*Figure 2-6. Typical IDF curve for a region in South Florida.
Source: Florida Department of Transportation.*

$$I = \frac{A + B \log(T)}{(1 + D)^e} \quad (2-37)$$

In Equations (2-34) to (2-37), I is the average intensity; D is the duration; T is the return period; and A , B , e , and C are constants that are region specific and can be derived by optimal function approximation or regression using observed precipitation data. Examples of these functional relationships can be found in studies by [Chen \(1983\)](#), [Bell \(1969\)](#), [Kothyari and Garde \(1992\)](#), [Alia \(2000\)](#), and [Pagliara and Vitti \(1993\)](#). Polynomial equations of orders greater than three can be used to approximate the IDF curves. For example, the Australian Bureau of Meteorology uses sixth-order polynomials for functional approximations of IDF curves.

The point rainfall depths for a given duration and return period obtained from IDF curves should be adjusted using areal reduction factors to obtain the average depth over a drainage area. The reduction factor is a function of area and duration ([Dingman 2008](#)). The US National Weather Service (USNWS) provides depth area reduction curves applicable for the United States that were approximated by an empirical functional form by [Eagleson \(1972\)](#) and described by [Dingman \(2008\)](#). The functional form is given by

$$K(D, A) = 1 - \exp(-1.1 D^{0.25}) + \exp(-1.1 D^{0.25} - 0.01 A) \quad (2-38)$$

where

$K(D, A)$ = reduction factor that is a function of duration,

D = hours and area, and

A = square miles (m^2).

Equation (2-38) for reduction factors provides slightly higher values for durations less than 6 hours compared with original curves provided by the US NWS.

The temporal distribution of rainfall within design storms based on IDF curves is generally obtained from empirical methods. Different empirical methods are available: (1) the triangular method, (2) the alternating-block method, and (3) Natural Resources Conservation Service (NRCS) 24 h hyetographs ([Chin 2006](#)). Four distributions (type I, IA, II, and III) were developed by the NRCS ([SCS 1986](#)) for four geographical regions of the United States.

2.12 EXTREME RAINFALL FREQUENCY ANALYSIS IN THE UNITED STATES

This section provides a brief review of rainfall frequency analysis efforts in the United States. Exhaustive details of frequency distributions applicable for US precipitation data for different durations are discussed in two technical documents referred to as HYDRO-35 ([Frederick et al. 1977](#)) and TP-40 ([Hershfield 1961](#)) developed by the US NWS. The frequency distributions evaluated for use in HYDRO-35 are the Pearson type III, the log-Pearson type III, and the Gumbel or extreme value type I (referred to as the Fisher-Tippett type I). The predictions from the 1-, 6-, and 24 h durations were compared to determine the percentage of observations that equaled or exceeded calculated values. The analysis showed no significant differences in the results obtained. The Gumbel (extreme value type I) distribution was then chosen for use in HYDRO-35, because it was also the method adopted in the previous studies.

DDF maps were developed using both the 60 min and 24 h durations and for several other intermediate durations for TP-40. In the case of HYDRO-35, 15 min and 60 min durations were used to develop DDF maps. The studies (TP-40 and HYDRO-35) provided similar results for precipitation data for a 2-year return period. For example, for the Florida peninsula, the intensities presented in TP-40 and HYDRO-35 were in general similar. However, the HYDRO-35 study considered the

intensity of thunderstorms prevalent in a tropical climate and higher values for rainfall intensity for the interior portion of the peninsula. In many areas TP-40 is still used for durations greater than 1 h, and HYDRO-35 is used for durations less than or equal to 1 h. Bonnin et al. (2006) documented the ongoing development of NOAA Atlas 14 Volume 2, which currently contains precipitation frequency estimates with associated confidence limits for select areas of the United States. The atlas also provides information related to temporal distributions and seasonality and is divided into volumes based on geographic sections of the country. The atlas is intended to be the official documentation of precipitation frequency estimates and associated information for the entire United States. Figure 2-7 shows the status of development of Atlas 14 volume 2 for the United States (<http://hdsc.nws.noaa.gov/hdsc/pfds/index.html>). The schematic is accurate as of October 2016. The atlas supersedes precipitation frequency estimates in Technical Paper No. 40 (Hershfield 1961), HYDRO-35 (Frederick et al. 1977), and Technical Paper No. 49 (Miller 1964).

In Atlas 14, the precipitation depth–frequency relationships are developed for different durations (15 min, 30 min, 1 h, 2 h, 3 h, 6 h, 12 h, 1 day, 2 days, 3 days, 4 days, 7 days, 10 days, 20 days, 30 days, 45 days, and 60 days), and the extremes are based on AMS. Several distributions are analyzed, and they include three-parameter generalized extreme value, normal, generalized Pareto, generalized logistic, Pearson type III, four-parameter kappa, and five-parameter Wakeby. The frequency analysis methods used for development of NOAA Atlas 14 are based on the assumption of a stationary climate. Parametric and nonparametric tests (e.g., Mann–Kendall) tests are used to evaluate if statistically significant trends are present in the annual maximum series. Tests based on the work completed so far for Atlas 14 have shown very little observable or geographically consistent temporal trends in the precipitation data (NOAA 2016).

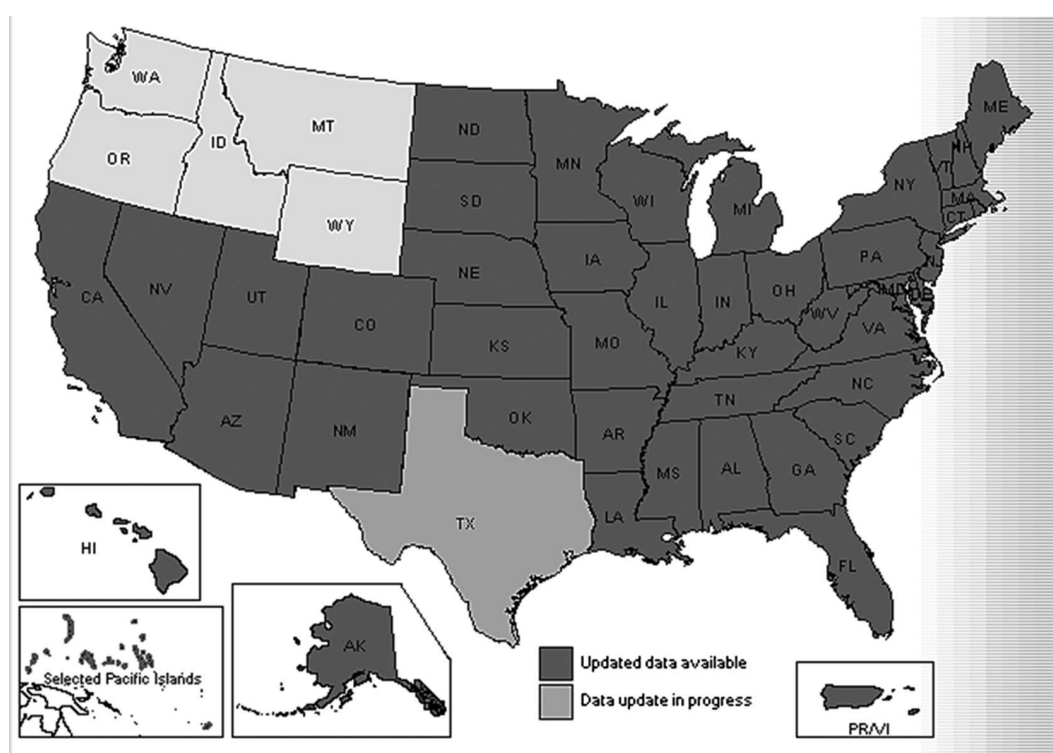


Figure 2-7. Status of precipitation frequency atlas for the United States.

Source: Hydrometeorological Design Studies Center, NOAA (2016).

2.13 PROBABLE MAXIMUM PRECIPITATION

The probable maximum precipitation (PMP) is defined by WMO (1994) as the theoretically greatest depth of precipitation for a given duration that is physically possible over a storm area of a given size under particular geographical conditions at a specified time of the year. It is widely used in the design of dams and other large hydraulic systems, for which a very rare event could have disastrous consequences. PMP refers to the quantity of precipitation that approximates the physical upper limit for a given duration over a particular basin (WMO 1994). The estimation of PMP is possible using one of the methods provided by WMO (1986). These methods include (1) the storm model approach, (2) maximization and transposition of actual storms, (3) generalized depth-area-duration relationships, and (4) statistical analysis of extreme rainfall totals. PMP is commonly estimated by using storm transposition and maximization. This approach is based on the assumptions (1) that precipitation can be expressed as the product of the available moisture and the combined effect of the storm efficiency and inflow of wind and (2) that the most effective combination of storm efficiency and inflow wind can be estimated from outstanding storms on record (WMO 1994). To determine PMP for a given project basin, depth-area-duration analyses for the region of interest are required. In the absence of this information, individual storm studies should be undertaken, and the selection of the likely critical rainfall duration for the project design of interest should be reasonably determined (WMO 1994). For relatively large drainage basins, dividing the region into subbasins and determining the maximum flood hydrographs for each subbasin may be necessary before conducting storm analyses (WMO 1994). By considering large storms occurring within a meteorologically homogenous region, overcoming the obstacle of shortness of rainfall records is possible; however, it is important to consider that individual storms do not always have the same probability of occurrence over all sections of their transposition zone, especially if variations in orographic features exist within the transposition zone. The US Weather Bureau (1976) and Kennedy et al. (1988) report advances in the evaluation of orographic effects for use in storm transposition and synthesis (WMO 1994, 2009).

A common method for selecting storms for analysis involves determining the meteorologically homogeneous region that encompasses the project basin and extracting the dates of the occurrence of major rainfalls from available rainfall station records (WMO 1994, 2009). Next, the synoptic features of the major storms are examined to determine whether a storm may be transposed to the project basin (WMO 1994); this may be accomplished via methods proposed by WMO (1986). After selecting the major storms, the storms are maximized such that the percentage by which a particular storm's rainfall would have increased if the meteorological characteristics of the storm approached estimated upper physical limits (WMO 1994).

The reader is referred to Weisner (1970) and the US Weather Service (WMO 1986) for published methods of storm maximization and to WMO (1986) and Hansen et al. (1982) for studies relevant to the orientation of maximized storms. With maximized storm data, estimating the highest rainfall depth for any selected duration for the project basin or relevant subbasins is possible (WMO 1994). If critical meteorological data are missing, then PMP estimates should be determined by way of analogy to PMP in climatologically similar regions with available data (WMO 1994). However, special care should be taken to account for significant topographic, orographic, and meteorological differences between climatologically comparable regions. Statistical procedures may be of utility in determining PMP in such scenarios and are described in WMO (1986). Hershfield (1965) provides a statistical method to determine PMP if times series data of observed rainfall of a given duration are available. The PMP value is given by

$$PMP = \bar{X}_{no} + K_m S_{no} \quad (2-39)$$

The variable \bar{X}_{no} refers to the times series mean of observed annual extreme precipitation for a specified time interval, K_m is a modification coefficient, and S_{no} is the standard deviation of the time series. The variable K_m is defined by Equation (2-40) (Hershfield, 1965) as

$$K_m = \frac{X_{max} - \bar{X}_{no-1}}{S_{no-1}} \quad (2-40)$$

where

X_{max} = largest (first-ranked) item in the ranked observed series,

\bar{X}_{no-1} = mean of the series excluding X_{max} , and

S_{no-1} = standard deviation of the series excluding X_{max} .

2.14 RAINFALL FREQUENCY ANALYSIS: UNCERTAINTY AND VARIABILITY ISSUES

Variability is introduced into rainfall frequency analysis because of various factors, including (1) lack of reasonable length of data, (2) missing data, (3) lack of stationarity, (4) nonhomogeneous nature of storm events, (5) temporal window from which extreme values are considered, and finally (6) partial duration series (PDS). The following are a few initial preliminary data analysis steps that can evaluate the influence of some of these factors on precipitation frequency analysis.

1. Check and confirm the validity of all assumptions relevant to homogeneity, independence, randomness, and stationarity of time series of precipitation extremes.
2. Collect all metadata related to the rain gauge observations that are useful for assessing some of the assumptions indicated in item 1.
3. Evaluate the completeness of precipitation data series. If data are missing for short periods in annual maximum duration series, data available before and after the missing periods can be used. However, the conditions related to what is an acceptable missing period need to be established.
4. Use statistical tests to assess the existence or nonexistence of trends in the annual duration series and variance of precipitation time series. Shifts in mean and variance values can be tested for using data from two segments of the time series. In general, each data segment should contain at least 30 years of data.
5. Assess the spatial variation of trends (increasing or decreasing) at different rain gauge locations. This is an essential exercise if a regional frequency analysis needs to be conducted for the development of isopluvial curves of rainfall intensity.

2.14.1 Sample Adjustment Factors

Precipitation data are archived or compiled based on rain gauge observations for a specific duration. For example, when daily extremes are used for extreme value analysis, these values are based on fixed 24-hour period measurements rather than a moving window of 24 h. Data collected at predefined fixed time intervals may not include the true maximum accumulations for those periods equal or close to the sampling period. Empirically derived corrections factors ([von Storch and Zwiers 1999](#)) are often used to address this issue. Adjustment factors for rainfall recorded at fixed intervals are recommended. Adjustment factors ([Weiss 1964](#), [Young and McEnroe 2003](#)) are often based on average values of the ratios of true maximum and the maximum value of accumulation in a fixed time interval. These factors are referred to as sampling adjustment factors (SAFs).

2.14.2 Length of Historical Data

Guidelines for the minimum number of sample data (minimum number of annual extreme rainfall depths) used for analysis are not available in the literature. Data length is always a contentious issue in statistical analysis. The size of the sample (data length) should be large enough to warrant the estimation of parameters of the underlying probability distribution with the required reliability

(Adams and Papa 2000). A threshold number of years greater than 10 years is typically used. Use of data less than this specific threshold is not advisable for analysis. A minimum of 25 years of data is generally acceptable for statistical analysis of extreme values (Gupta 2008, Servuk and Geiger 1981). Different methods are available (e.g., Sokolov et al. 1976) to confirm the adequacy of data length. Summary statistics of observations from a gauge with an incomplete record can be compared with a nearby gauge with complete data. Sample record lengths have a substantial effect on the power of statistical tests (Yue et al. 2002, Yue and Pilon 2004) and therefore reasonable lengths exceeding 40 years are found satisfactory (Servuk and Geiger 1981, WMO 2010). Availability of long-term precipitation data is critical for rainfall frequency analysis for determining statistically based rainfall estimates of reasonable reliability, especially for extreme rainfalls with high return periods, such as those greater than 100 years (WMO 2010).

2.14.3 Missing Data and Rainfall Statistics Preservation

Continuous precipitation data without any gaps are needed for hydrologic modeling. Precipitation data gaps of different lengths are often unavoidable due to random and systematic errors. Incorrect recording and transcription of precipitation data create gaps in the data to be filled and cast doubt on the reliability of data for statistical and trend analysis (Hosking and Wallis 1998). The following section provides a brief overview of missing data estimation methods for precipitation records.

2.14.4 Missing Rainfall Records: Estimation Methods

Deterministic weighting and stochastic interpolation methods have been used for the spatial construction of rainfall fields or estimating missing rainfall data at points in space. Weighting methods belong to a class of spatial interpolation techniques such as inverse distance (Simanton and Osborn 1980, Wei and McGuinness 1973), nonlinear deterministic, and stochastic interpolation methods (e.g., kriging). Regression and time series analysis methods belong to data-driven approaches. Global interpolation methods that use trend surface analysis and regression provide several advantages compared with deterministic weighting techniques. Trend surface analysis uses a polynomial equation of spatial coordinates to approximate points with known values. These methods and their several variants are briefly discussed in the next few sections.

The inverse distance weighting method (IDWM) is the most commonly used approach for estimating missing data and is often referred to as the US NWS method (ASCE 1996). In the field of quantitative geography, IDWM is used for spatial interpolation (O'Sullivan and Unwin 2003). Hodgson (1989) modified IDWM to include a learned search approach that reduces the number of distance calculations. To incorporate topographical aspects, Shepard (1968) proposed a modified IDWM that is referred to as a barrier method. Variance-dependent surface interpolation methods, belonging to the general family of kriging, have been applied to hydrological interpolation problems (Vieux, 2001, Grayson and Blöschl, 2001). These interpolation schemes are based on the principle of minimizing the estimate of variance at points where measurements are unavailable. Kriging in various forms has been used to estimate missing precipitation data at stations and to interpolate precipitation from point measurements (Dingman 2008, Vieux 2006). Ashraf et al. (1997) compared interpolation methods (kriging, inverse distance, and co-kriging) to estimate missing precipitation values. They indicate that kriging provides the smallest root mean square error (RMSE). Krajewski (1987) has employed co-kriging of radar and rain gauge data to estimate mean areal precipitation. Seo et al. (1990a, b) describe the use of co-kriging and indicator kriging for interpolating rainfall data.

Teegavarapu and Chandramouli (2005), Teegavarapu (2012b), Teegavarapu (2016) and Teegavarapu et al. (2017) report several limitations and advantages of using deterministic and stochastic spatial interpolation techniques to estimate missing precipitation data at a base station (i.e., a station with missing data) using data at all other stations. They indicate that all interpolation

techniques would provide inaccurate estimates of missing precipitation data in two situations: (1) when precipitation is measured at one or more stations, but no precipitation actually occurred at the base station, and (2) when precipitation occurs at the base station, but no precipitation is measured or occurred at all other stations. In case 1, all spatial interpolation techniques will produce a positive estimate, whereas in reality zero precipitation is recorded at the base station. Estimating missing precipitation data is impossible in the second case because point observations are used to estimate the missing value at the base station using spatial interpolation algorithms alone. All interpolation techniques produce a zero estimate for situations encountered in case 2. Data from other sources (e.g., radar-based estimates) can be used in these situations to estimate the missing values. However, the reliability of radar-based precipitation measurements is a contentious issue ([Teegavarapu 2008](#)).

Limitations of spatial interpolation methods have been reported in recent studies. [Vieux \(2006\)](#) points out several limitations of IDWM, with a major one being the “tent pole effect” that leads to greater estimates closer to the point of interest. [Grayson and Blöschl \(2001\)](#) list several limitations of Thiessen polygons and inverse-distance methods. They suggest that these methods should not be recommended for spatial interpolation considering their limitations. However, they recommend thin splines and kriging for interpolating hydrologic variables. The Thiessen polygon approach has the major limitation of not providing a continuous field of estimates when used for spatial interpolation ([O’Sullivan and Unwin 2003](#)). [Brimicombe \(2003\)](#) indicates that the main point of contention in applying IDWM to spatial interpolation is selecting the number of relevant observation points used for the spatial interpolation. Correlation weighting techniques and artificial neural network (ANN) methods are proved conceptually to be superior deterministic approaches compared with traditional IDWM and its variants. The kriging estimation method (KEM) is considered a reliable interpolation technique ([O’Sullivan and Unwin 2003](#)), but is plagued by several limitations. These include selecting the appropriate semi-variogram, and assignment of arbitrary values to the sill and nugget parameters, distance intervals, and observation value-insensitive variance estimates. [Teegavarapu and Chandramouli \(2005\)](#) revisited distance weighting methods often used for estimating missing rainfall records. Conceptual revisions of the methods address two main issues relating to the definition of distance used in the calculations and selection process of the nearby gauges. Universal functional approximators such as ANNs are used for fitting a semi-variogram model using the raw data in ordinary kriging to estimate missing precipitation data by [Teegavarapu \(2007b\)](#). The use of ANN eliminates the need for predefined authorized semi-variogram models to capture the spatial variation of data and the trial and error process involved in estimation of semi-variogram parameters. [Teegavarapu \(2007a\)](#) recently discussed the association rule mining (ARM)-based spatial interpolation approach to improve the precipitation estimates provided by deterministic and stochastic spatial interpolation techniques. Considerable improvements in the estimates were achieved when the ARM is used in conjunction with other interpolation techniques.

Range and cluster-based optimization methods in space and time were developed by [Teegavarapu and Bajaj \(2008\)](#). Optimization models using mixed-integer linear and nonlinear programming formulations are developed for estimation of missing precipitation data at a gauge. These formulations use binary variables for selection of rain gauges that participate in the spatial interpolation process and also in the process of selection of an optimum cluster of rain gauges for estimation of missing data. Several variants of these mathematical programming formulations ([Teegavarapu 2012b](#), [Teegavarapu et al. 2017](#)) are proposed to improve the estimates of missing precipitation data. Optimal functional forms using genetic programming and algorithms were implemented by [Teegavarapu et al. \(2009\)](#). The variants investigated in their study provide improved estimates of precipitation data compared with those obtained from traditional distance-based weighting methods. [Teegavarapu and Pathak \(2008\)](#) propose and investigate a nonlinear mathematical programming model using binary variables to infill missing precipitation records using radar

(NEXRAD)-based rainfall estimates. The model identifies the cluster of radar data values that can be used for infilling the rain gauge records.

Infilling methods may introduce significant biases when the gaps constitute more than 20% of the data. Teegavarapu et al. (2011) indicate that bias introduced by infilling methods could alter the statistics of the data. Teegavarapu and Nayak (2017) show that use of filled precipitation data may lead to under- and overestimation of higher- and lower-end extremes. Spatial interpolation becomes inevitable when temporal autocorrelations at several lags are negligible, thus eliminating the possibility of using time series models for infilling. In many instances, gauges that are selected as single best estimators based on Euclidean distance or other statistical distances should be used for infilling extreme values. Schuenemeyer and Drew (2010) indicate that any statistical inference made from data with more than 15% missing observations should be interpreted with caution. Estimation of missing extreme precipitation data is difficult and should not be carried out by global interpolation methods. In many instances, gauges that are selected as single best estimators based on Euclidean distance or other statistical distances should be used for infilling extreme values. Infilling of precipitation data at a site should focus on preservation of site-specific and regional statistics. Regional statistics are mainly defined as site-to-site relationships, spatial correlations, and variability across the region. Figure 2-8 shows the CDF plots based on precipitation data and filled precipitation data using interpolation methods. The missing data in this example are only 25% of the total data available. Figure 2-8 clearly shows that the data filled using a naïve method utilizing the mean of all observations in the region do not preserve the statistics.

Comparative analysis of distributions of filled and nonfilled data can be carried out using different nonparametric statistical hypothetical tests, including (1) two-sample KS (Smirnov 1939, Sheskin 2003), (2) Ansari-Bradley (Ansari and Bradley 1960), and 3) Wilcoxon rank-sum (Wilcoxon 1945, Hollander and Wolfe 1999). The null hypothesis (H_0) is that observed and estimated precipitation data are from the same continuous distribution. The alternative hypothesis

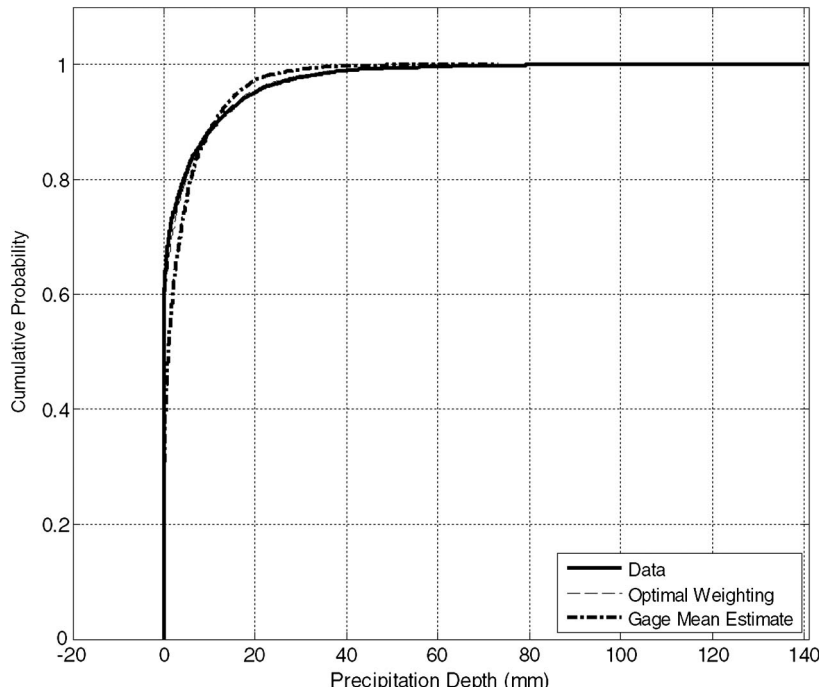


Figure 2-8. CDF plots of precipitation data and filled data using two interpolation methods.

(H_a) is that these two datasets are from different continuous distributions. The hypothesis tests are carried out at a statistical significance level of 5%. The Ansari–Bradley (AB) test is used to evaluate the hypothesis (null hypothesis: H_o) that two independent samples of observed and filled data come from the same distribution against the alternative (alternative hypothesis: H_a) that they come from distributions with the same median and shape but different dispersions (e.g., variances). The rank-sum test can be used to evaluate the null hypothesis that observed and filled data are independent samples from identical continuous distributions with equal medians, against the alternative that they do not have equal medians. The test is equivalent to a Mann–Whitney U-test. The Wilcoxon rank-sum test is a nonparametric alternative to the t-test. Teegavarapu (2013b) demonstrates the utility of these tests for evaluating the similarity of filled and nonfilled precipitation dataset distributions.

Infilling of missing data in a long precipitation data series introduces the following complexities when conducting rainfall frequency analysis:

1. Local and global spatial interpolation methods underestimate higher-magnitude events and overestimate lower-magnitude events.
2. Site-specific statistics and regional (site-to-site) relationships are modified.
3. Transition probabilities that characterize persistence and wet-to-wet, wet-to-dry, dry-to-wet, and dry-to-dry states are altered and homogeneity of the precipitation time series is disturbed.

2.14.5 Statistical Corrections of Spatially Interpolated Missing Precipitation Data Estimates

Teegavarapu (2009, 2012b) recommend correction procedures based on single best estimator (SBE) to implement after initial spatial interpolation estimates are obtained. Teegavarapu (2013b) provides an optimal single best estimator for correction of spatially interpolated estimates. The correction procedures improve site-specific and regional statistics and reduce under- and overestimations. Bias correction methods used in climate change studies can be used for correcting spatially interpolated precipitation data. The next two sections discuss two quantile mapping procedures for correction of estimates.

2.14.5.1 Quantile Mapping

The quantile-based mapping method is widely used for correcting the biases in both downscaled precipitation and temperature datasets obtained from general circulation model (GCM) simulations. The quantile-mapping method (Panofsky and Brier 1968) is widely used in numerous hydrologic simulations and climate change impact studies (Wood et al. 2002, Hayhoe et al. 2004, Maurer and Hidalgo 2008). Although this method tries to adjust all the moments of the estimated data, the major drawback is its dependence on a stationarity assumption for corrections. The method uses the observed CDF of data from the training period to correct data from the test period with an assumption that the future distribution of data follows that of past observed data. The correction method is expressed as

$$\theta_i^{bce} = F_o^{-1}(F_e^v(\theta_i^e)) \quad \forall i \quad (2-41)$$

where the variable F_o is the CDF of the observed data derived from the training dataset and F_e^v is the CDF from the testing dataset based on estimated precipitation data.

Figure 2-9 illustrates the application of the method, with these CDFs shown in Figure 2-9a and Figure 2-9b. The variable θ_i^{bce} is the bias-corrected estimate of precipitation for any time interval i from the testing dataset obtained by following two steps: (1) estimated values of precipitation are used to develop a CDF, and the non-exceedance probability $F_e^v(\theta_i^e)$ is obtained for each value of θ_i^e as

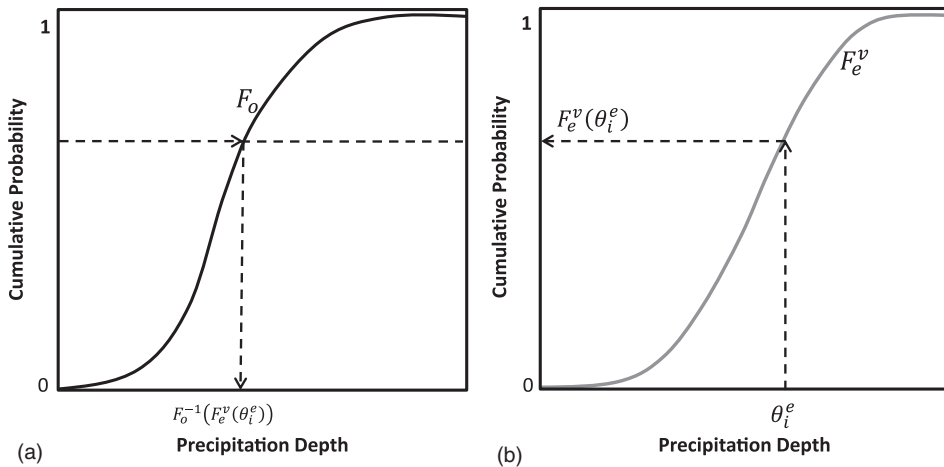


Figure 2-9. Quantile-matching bias correction method for precipitation estimates.

Source: [Teegavarapu \(2013b\)](#).

shown in Figure 2-9b; and (2) corrected estimate (θ_i^{bce}) using the inverse of the observed CDF for the value of nonexceedance probability is obtained in step 1 as shown in Figure 2-9a.

2.14.5.2 Equi-Ratio Quantile Matching

The limitation associated with the stationarity assumption in quantile matching is addressed by the equidistant matching method (EQM) developed by [Li et al. \(2010\)](#). The EQM incorporates the information from the CDF built based on estimated data from the training period, rather than assuming that the CDF from the observed dataset from the training data is valid for the test dataset ([Li et al. 2010](#)). The difference between the observed data and the estimated data for a given probability is assumed not to change in the future. The proposed method, referred to as equi-ratio quantile matching (ERQM), is a minor variant of the existing EQM in which multiplicative scaling factors are considered as substitutes for additive factors. Figure 2-10 shows the method. The first step in the ERQM method is the same as for the quantile matching method (Figure 2-10b). However, in

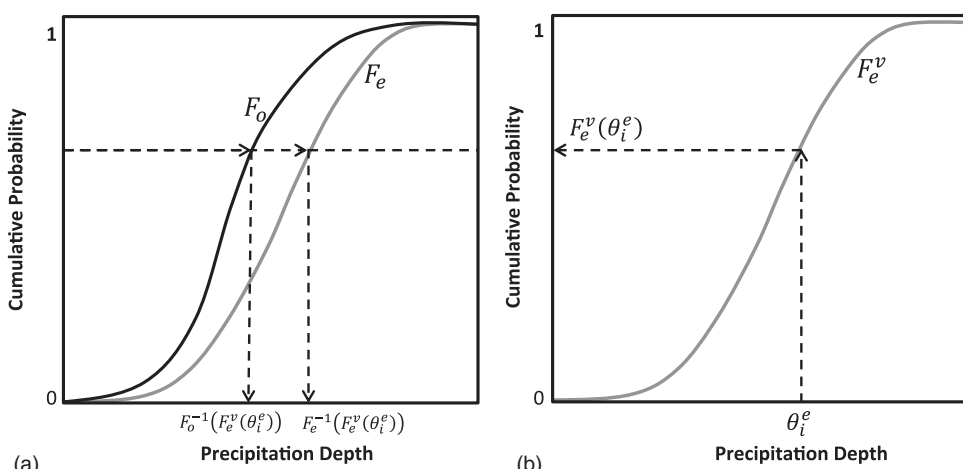


Figure 2-10. ERQM bias correction method for precipitation estimates.

Source: [Teegavarapu \(2013b\)](#).

the second step (Figure 2-10a), the ratio of $F_o^{-1}(F_e^v(\theta_i^e))$ and $F_e^{-1}(F_e^v(\theta_i^e))$ is obtained for a given nonexceedance probability value obtained from step 1. F_e^{-1} is the inverse of the CDF of estimated values from test dataset. Equation (2-42) gives the corrected precipitation estimate in any time interval

$$\theta_i^{bce} = \theta_i^e \frac{F_o^{-1}(F_e^v(\theta_i^e))}{F_e^{-1}(F_e^v(\theta_i^e))} \quad \forall i \quad (2-42)$$

2.15 STATIONARITY ISSUES

According to [WMO \(2009\)](#), stationarity means that, excluding random fluctuations, the data series is invariant with respect to time. Precipitation extremes are evaluated as block maxima or a single extreme value per year. Annual precipitation extremes time series should be checked for stationarity. This is an important element of the statistical analysis conducted after the initial phase of the data collection. Trend analyses should be conducted for all available annual extreme data for all durations, and tests for statistically significant trends should be based on Mann–Kendall or other tests. According to [Ashkar \(1996\)](#), two important forms of nonstationarity in a time series (e.g., streamflow time series) are jumps and trends. Another impact form is the existence of cycles that are associated with long-term climatic oscillations. Statistical tests for detecting stationarity include the Mann–Whitney test for jumps and Wald–Wolfowitz test for trends ([Bobee and Ashkar 1991](#)).

[Betancourt \(2009\)](#) argues that systems for management of water throughout the developed world have been designed and operated under the paradigm of hydrologic stationarity (HS). The stationarity assumption suggests that hydrologic variables have time-invariant probability density functions whose properties can be estimated from the instrumental record ([Betancourt 2009](#)). Given the magnitude and time lags of climate change associated with the buildup of greenhouse gases, stationarity may indeed be dead ([Milly et al. 2008](#)). A viable successor to stationarity must encompass principles and methods for identifying nonstationary probabilistic models of relevant environmental variables and for using such models to optimize water systems ([Betancourt 2009](#), [Milly et al. 2008](#)). Nonstationary hydrologic variables can be handled stochastically to describe the temporal evolution of their means and variances, with estimates of uncertainty.

2.15.1 Trend Analysis

Trend analysis of precipitation extremes at different temporal scales can be carried out using two well-known nonparametric tests: (1) Spearman's rho (ρ) test and (2) the Mann–Kendall test. Discussion about these tests can be found in [Teegavarapu and Oishi \(2016\)](#) and [Teegavarapu \(2018\)](#). Applications of the Mann–Kendall test are more documented in the literature compared to Spearman's test. However, in many cases the power of both tests is the same.

2.15.2 Spearman's Rank Correlation Coefficient (ρ) Test

Spearman's rho test, a nonparametric test, can be used to evaluate the association between two ranked variables. The test can be used to assess a possible linear association between the time and the precipitation data. The null hypothesis (H_0) $\rho=0$ and the alternative hypothesis (H_a) $\rho \neq 0$ are defined. The Spearman's rank correlation coefficient R_s is calculated as

$$R_s = 1 - \frac{6 \sum_{i=1}^n (D_i - i)^2}{n(n^2 - 1)} \quad (2-43)$$

where

R_s = Spearman's rank correlation coefficient,

D_i = rank of the i^{th} observation, and

n = total length of the time series data.

The significance of the correlation can be tested using a table of critical values (one-tailed or two-tailed test values) when the number of data pairs is less than 30. The null hypothesis is rejected if the absolute value of R_s is greater than the critical value given in the table. If the number of data pairs is greater than 30 (Gauthier 2001), a statistic (Z_s), which is also referred to as the "t statistic," is calculated by

$$Z_s = R_s \sqrt{\frac{n-2}{1-R_s^2}} \quad (2-44)$$

where Z_s is Student's t -distribution with $(n-2)$ degrees of freedom. A critical value for Z_s can be obtained if t at a 0.05 significance level in Student's t -distribution table is defined as $(n-2, 1-\alpha/2)$. If $|Z_s| > (n-2, 1-\alpha/2)$, (H_0) is rejected, and it can be concluded that a significant trend exists in the time series.

2.15.3 Mann–Kendall Test

The nonparametric Mann–Kendall and Sen's slope tests can be used to assess the existence of trends in the time series data, especially rainfall extremes. Details of the tests presented, along with the notation, are adopted from Dullo et al. (2017). For both methods, the dataset is not required to be normally distributed as they are distribution-free tests. The methods are less sensitive to extreme events and missing data points (Partal and Kahya 2006, Yilmaz and Perera 2015). For the Mann–Kendall test, the null hypothesis (H_0) represents the case in which there is no trend in the record, while the alternative hypothesis (H_a) indicates the existence of an upward or downward monotonic trend in the recorded events. The test statistic (S) required for the Mann–Kendall test is obtained as

$$S = \sum_{k=1}^{n-1} \sum_{j=k+1}^n sgn(x_j - x_k) \quad (2-45)$$

where x_j and x_k are measurements obtained at times j and k , and n is the number of observed events. The function $sgn()$ is defined as

$$sgn(x_j - x_k) = \begin{cases} +1 & \text{if } (x_j - x_k) > 0 \\ 0 & \text{if } (x_j - x_k) = 0 \\ -1 & \text{if } (x_j - x_k) < 0 \end{cases} \quad (2-46)$$

The variance of the test statistics (S) is calculated by

$$Var(S) = \frac{[n(n-1)(2n+5) - \sum_{i=1}^m t_i(t_i-1)(2t_i+5)]}{18} \quad (2-47)$$

where

n = number of observations,

m = total number of tied groups, and

t_i = number of ties of extent i .

The standardized test statistics (z) is computed using

$$z = \begin{cases} \frac{S-1}{\sqrt{\text{Var}(S)}} & \text{if } S > 0 \\ 0 & \text{if } S = 0 \\ \frac{S+1}{\sqrt{\text{Var}(S)}} & \text{if } S < 0 \end{cases} \quad (2-48)$$

The null hypothesis (H_0) is accepted if $|z| \leq z_{\alpha/2}$, where α is a user-specified level of significance (Partal and Kahya 2006). Following Yilmaz and Perera (2015), 0.01, 0.05, and 0.1 can be used as levels of significance that correspond to 99%, 95%, and 90% confidence levels, respectively.

To quantify the magnitude of the trend detected by the Mann–Kendall test, Sen’s slope estimator can be used. According to Sen (1968), the slope of the lines (Q_i) connecting N distinct pairs is computed as

$$Q_i = \frac{Y_j - Y_k}{j - k} \quad \text{for } i = 1, \dots, N \quad (2-49)$$

where Y_j and Y_k are data values corresponding to j and k ($j > k$), respectively. After arranging the values of Q_i ’s in ascending order of magnitude, the median of the slopes (Sen’s slope estimator) (Q_{med}) is computed as

$$Q_{med} = \begin{cases} Q_{(N+1)/2} & \text{if } N \text{ is odd} \\ \frac{Q_{(N/2)} + Q_{(N+2)/2}}{2} & \text{if } N \text{ is even} \end{cases} \quad (2-50)$$

2.15.4 Application of Spearman’s Rho and Mann–Kendall Tests

This section discusses an illustrative example of the Spearman’s rho and Mann–Kendall tests. The two nonparametric trend tests were applied to a 45-min duration precipitation annual extreme time series obtained from a site in Florida. Figure 2-11 shows a plot of observations and Spearman’s hypothesis test results. Figure 2-12 shows trend analysis using the Mann–Kendall test and estimation of Theil–Sen slope. The shorter line is the one based on Theil–Sen slope.

2.15.5 Parametric Trend Analysis: Regression

Linear regression is one of the parametric procedures that can be used for assessing linear trends. If observations are available with respect to time, a linear regression given by Equation (2-51) can be developed. An ordinary least squares method can be used to estimate the parameters (slope: β , intercept: α). The residual (or error) is represented by $\varepsilon(t)$. The null hypothesis $H_0: \beta = 0$ and alternative hypothesis $H_a: \beta \neq 0$ are evaluated using the t statistic.

$$y(t) = \beta \cdot t + \alpha + \varepsilon(t) \quad (2-51)$$

Several assumptions need to be met before the results from the parametric model can be used for making any conclusions about trends in the data. The assumptions include (1) residuals are independent, (2) residuals are normally distributed, and (3) residuals are identically distributed. Residuals based on observed and estimated data are estimated for each time interval using the regression equation. They are evaluated for any systematic bias, time-dependent bias, signs of heteroscedasticity, and normality of residuals. A residual (e_i) is calculated for each time interval i and

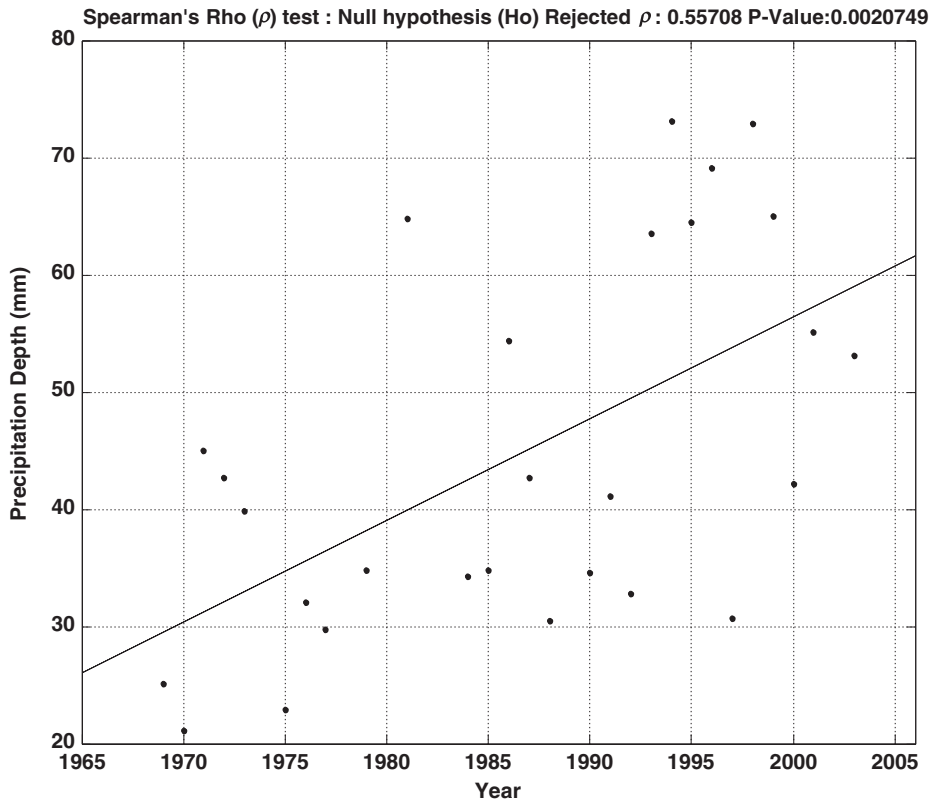


Figure 2-11. Trend analysis results using the nonparametric Spearman's rho test.

is given by Equation (2-52). The residuals (e_i) are obtained using Equation (2-52) based on estimated values ($\theta_{e,i}$) from Equation (2-51) and observed values ($\theta_{o,i}$).

$$e_i = \theta_{o,i} - \theta_{e,i} \quad \forall i \quad (2-52)$$

Visual evaluation procedures via several plots will reveal many properties of the residuals. Probability plots of residuals can be evaluated for normality. Table 2-5 provides a few visual and statistical tests for evaluation of residuals.

Normality of residuals can be evaluated using a histogram of residuals, normal probability plot, quantile-quantile plot, or goodness-of-fit hypothesis tests. Independence of residuals can be evaluated using an autocorrelation function, and constant variance (homoscedasticity) of residuals can be checked using the Tukey-Anscombe plot, which shows the variation of residual values with respect to estimated (fitted) values. The Durbin-Watson (DW) test can be used to evaluate the presence of serial correlation. The DW test statistic, based on Equation (2-53), is compared with a critical value that in turn is based on sample size.

$$d = \frac{\sum_{i=2}^N (e_i - e_{i-1})^2}{\sum_{i=1}^N e_i^2} \quad (2-53)$$

The Ljung-Box Q test (Ljung and Box 1978), a portmanteau test, can be used to check the null hypothesis that no autocorrelation exists in a series of residuals for a prespecified number of lags (L)

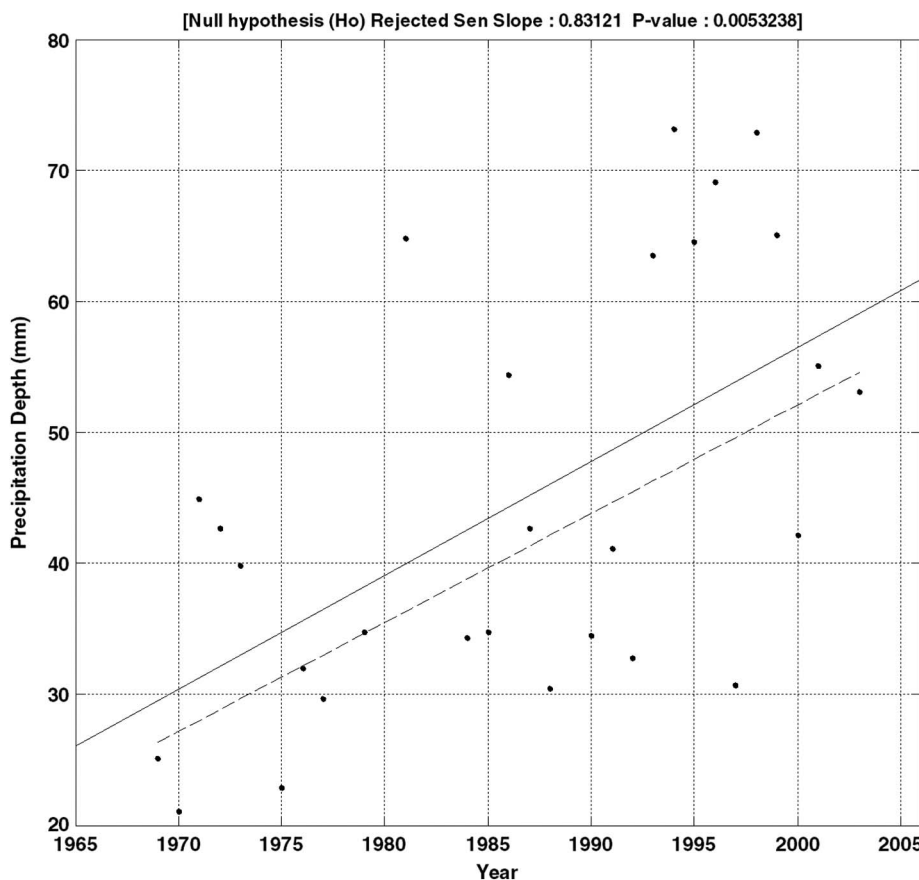


Figure 2-12. Trend analysis results using the nonparametric Mann–Kendall test with Theil–Sen slope-based line.

Table 2-5. Tests for Evaluation of Residuals.

Test or plot	Evaluation	Requirement
Time series plot of residuals	Time dependency	Random variation and no structured pattern in the variation of residuals with time.
Autocorrelation plot (autocorrelogram)	Check for serial correlation at different temporal lags	Low or negligible correlation at all lags
Probability plot (normal)	Normality of residuals	Linear plot of residuals
Histogram	Visual check for normality	Gaussian distribution
Durbin–Watson test	Test for serial correlation	No serial correlation

against the alternative that the serial correlation coefficient, $\rho(k)$, for lags up to L , is nonzero. The variable n is the length of time series. The test statistic, Q , is calculated as

$$Q = n(n + 2) \sum_{k=1}^L \left(\frac{\rho(k)^2}{(n - k)} \right) \quad (2-54)$$

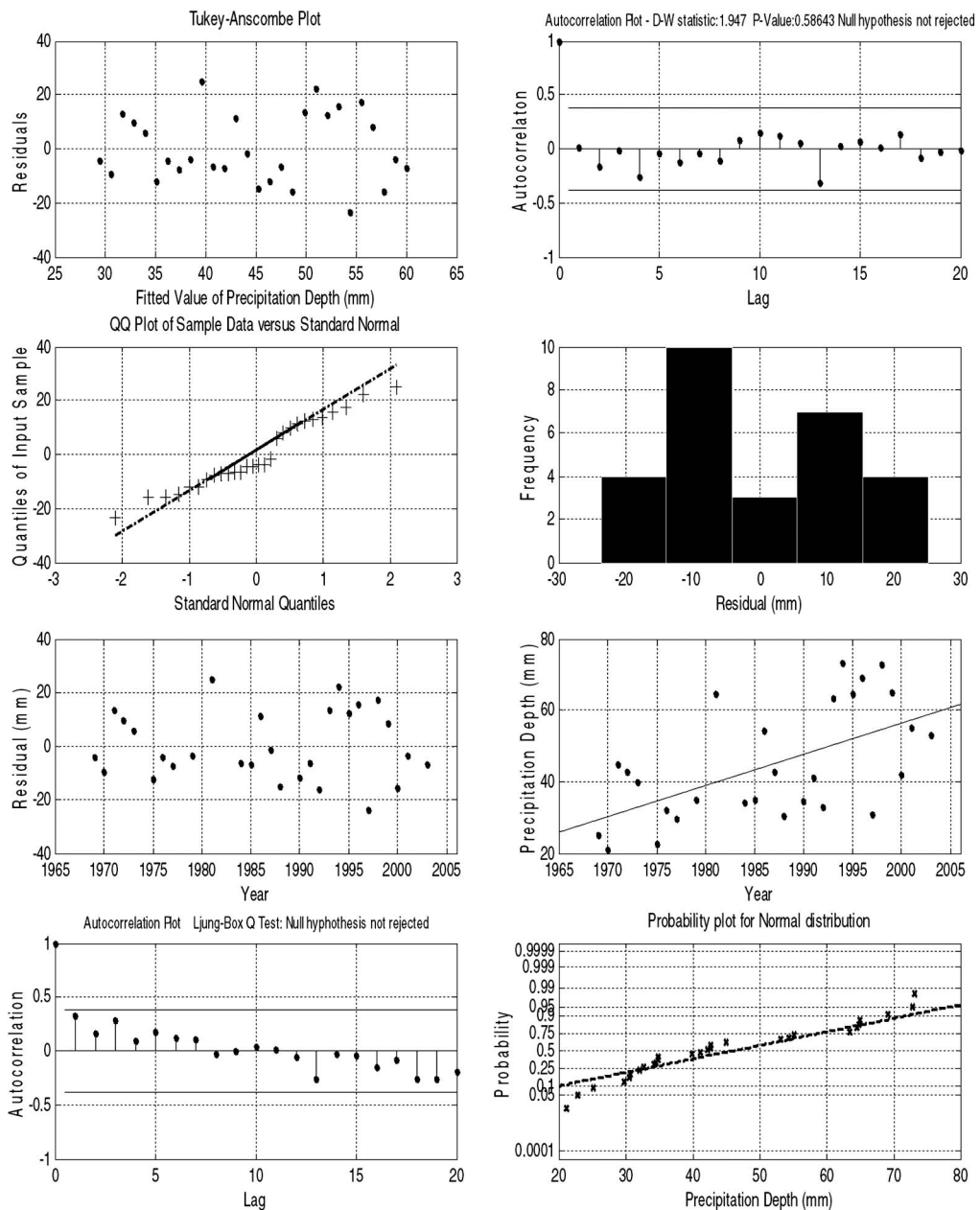


Figure 2-13. Visual evaluation of parametric trend analysis using different plots.

The number of lags used for the test will affect the test's power; appropriate values recommended by Box et al. (1994) can be used. Figure 2-13 shows the results from the Ljung–Box Q test for the precipitation time series.

2.16 HOMOGENEITY

Like any other hydrologic time series, precipitation time series often exhibit spurious (nonclimatic) jumps and/or gradual shifts due to changes in station location, environment (exposure),

instrumentation, or observing practices ([WMO 2009](#)). Homogeneity means that all elements of the data series originate from a single population ([WMO 2009](#)). Observation stations (i.e., rain gauges) are moved from one location to another, and these locational changes may lead to discontinuities in extremes, trends, and observations influenced by local weather and other regional climatic influences. All these factors affect the homogeneous nature of the long-term time series of precipitation data and bias studies of extremes. Guidelines on analysis of extreme events developed by [WMO \(2009\)](#) provide real-life examples of nonhomogeneities and stress the need for complete station history metadata (data about data) for resolving these issues. If observations at a station or a set of stations are suspect, carefully identified reference stations can be used for evaluation. Mass curves can be developed using the observations at the station suspected of problems and the reference station.

Graphical methods for detecting nonhomogeneity include moving average plots using smoothing methods ([McCuen 2003](#)). Collecting causal information in the process of analysis is also important to evaluate the reasons for nonhomogeneity. Often metadata about observations and information about the stations (or measuring instruments) are extremely helpful for deciphering any nonhomogeneity in the data. Associating different rainfall-producing mechanisms (slow-moving frontal systems, hurricane events, and summer convective storms) to rainfall depths in specific years for specific storm durations is important. Spatial summary statistics for all stations should be used to assess the regional or global variability of rainfall in a region. This analysis will help to establish or confirm if the storm events produced by meteorological processes are similar in nature. This will also strictly satisfy the homogeneity requirement of statistical analysis of extreme events. [Miller \(1972\)](#) points out that in the case of extreme precipitation, nonhomogeneity tends to be difficult to decipher, while it is easier to in yearly precipitation totals.

The Mann–Whitney U statistic is commonly used to decide whether observations of a hydrologic variable are from the same population. To apply the Mann–Whitney test, the raw data sequences with n elements should be divided into two sample groups with n_1 and n_2 elements, respectively. The raw dataset is then ranked from lowest to highest, including tied rank values where appropriate. The equations related to the Mann–Whitney U statistic are as follows ([Bobee and Ashkar 1991](#), [Corder and Foreman 2009](#)):

$$U_i = n_1 n_2 + \frac{n_i(n_i + 1)}{2} - \sum R_i \quad (2-55)$$

$$\bar{x}_u = \frac{n_1 n_2}{2} \quad (2-56)$$

$$S_u = \sqrt{\frac{n_1 n_2 (n_1 + n_2 + 1)}{12}} \quad (2-57)$$

$$Z^* = \frac{U_i - \bar{x}_u}{S_u} \quad (2-58)$$

where

S_u = standard deviation,

$\sum R_i$ = sum of all the ranks from the sample of interest,

U_i = U statistic from the sample of interest, and

\bar{x}_u = mean.

The index i refers to either sample 1 or 2, and the smaller of the two U-statistic values calculated is used for the test. The variable U_i can be examined for significance using a table of critical values provided by [Corder and Foreman \(2009\)](#). The variable Z^* is the z-score for a normal approximation

of the data when the number of samples exceeds that available from the table of critical values. The null hypothesis, which is homogeneity, for the observations is rejected if the calculated Z^* statistic is greater than the selected critical value at the 0.05 significance level obtained from the standard normal distribution table. Several other tests are available for assessment of homogeneity of time series. These tests include Pettitt's test (Pettitt 1979), Buishand's test (Buishand 1982), Alexandersson's standard normal homogeneity test (Alexandersson 1986), and von Neumann's ratio test (von Neumann 1941). Buishand and Alexandersson have used the tests that were named after them for evaluating the homogeneity of rainfall records.

2.17 DETECTION OF CHANGES IN MOMENTS

Statistical analyses can be conducted to assess the changes in moments based on historical data. The data are split into two datasets (sample populations) and compared. Initially, the sample populations are checked to see if they fit a specific probability distribution (e.g., normal or log-normal distribution), and then the sample variances (S_1^2, S_2^2) are also checked to see if they were equal or unequal. Probability plots on normal or log-normal paper generally are used to check the hypothesized distributions visually. Goodness-of-fit tests can also be used for more comprehensive checks.

In a few studies, annual precipitation totals were characterized using normal and gamma distributions. Thompson (1999) indicates that annual precipitation tends to follow a normal distribution, particularly in humid climates, and existence of low values in arid and semi-arid climates can be characterized by positively skewed distributions. However, the time dependence of these values may violate the assumption of independence due to persistence at interannual time scales. Droughts and wet years are examples of multiyear persistence (Thompson 1999). Naoum and Tsanis (2003) report that annual rainfall amounts can be characterized using a normal distribution for the island of Crete in Greece. When data seem to follow normal distributions, a few goodness-of-fit tests are applicable. The Kolmogorov-Smirnov test can be used to ensure the validity of hypothesized data distributions. The Anderson-Darling test, which is sensitive to the tails of the distribution, can also be used. For datasets with equal variances, a comparison can be made using a t-test. For datasets with unequal variances, a comparison can be made using Satterthwaite's modified t-test (Satterthwaite 1964, McBean and Rovers 1998). Sample means (\bar{x}_1, \bar{x}_2) can then be calculated for the datasets and checked to see if they were statistically different at a specified significance level using hypothesis tests. A significance level of 0.05 can be used. F-tests are required to ascertain if the variances were equal or not equal. A t-test can then be used to make inferences about differences in sample mean values. Gilbert (1987) and Ott (1995) discuss the procedures for these tests in detail. Table 2-6 summarizes statistical hypothesis tests used for the assessment of changes in trend for normally distributed data.

Inferences about changes in the mean values can be made using a parametric hypothesis test (e.g., t-test). The use of t-tests requires several conditions that need to be met before any inferences can be made about population means. The assumptions for a two-sample unpaired t-test are (1) normality, (2) independence of observations, and (3) equal variances. Two different types of t-tests can be used based on the knowledge about sample variances. Equations (2-59) and (2-60) identify the t-test statistic calculations when the sample variances based on two different sampling periods are equal.

$$t = \frac{\bar{x}_1 - \bar{x}_2}{\sqrt{\frac{n_1+n_2}{n_1 n_2} \left(\frac{(n_1-1)S_1^2 + (n_2-1)S_2^2}{n_1+n_2-2} \right)}} \quad (2-59)$$

Table 2-6. Hypothesis Tests Used to Assess Changes in Moments for Normally Distributed Data.

<i>Statistical hypothesis tests</i>	<i>Purpose of the test</i>	<i>Null hypothesis</i> (H_0)	<i>Alternative hypothesis</i> (H_o)
Kolmogorov-Smirnov Lilliefors Chi-square Anderson-Darling Jarque-Bera	Goodness of fit	Data follows the hypothesized distribution (i.e., normal)	Data does not follow the hypothesized distribution
F-test	Equality of population variances	$\sigma_1^2 = \sigma_2^2$	$\sigma_1^2 \neq \sigma_2^2$
Two-sample unpaired t-test (Equal variance – Student's two-sample t-test) (Unequal variance – Satterthwaite's two-sample unpaired t-test)	Equality of hypothesized population means	$\mu_1 = \mu_2$	$\mu_1 \neq \mu_2$

Equation (2-60) defines the degrees of freedom (df).

$$df = n_1 + n_2 - 2 \quad (2-60)$$

where

n_1 = number of samples in dataset 1,

n_2 = number of samples in dataset 2,

S_1^2 and S_2^2 = variances, and

\bar{x}_1 and \bar{x}_2 = mean values of datasets 1 and 2, respectively.

Equations (2-61) and (2-62) define the t-test statistic used for unequal variances. The test is referred to as Satterthwaite's modified t-test (Satterthwaite, 1946). The degrees of freedom (df) for this t-test are given by

$$t = \frac{\bar{x}_1 - \bar{x}_2}{\sqrt{\frac{S_1^2}{n_1} + \frac{S_2^2}{n_2}}} \quad (2-61)$$

$$df = \frac{\left[\frac{S_1^2}{n_1} + \frac{S_2^2}{n_2} \right]^2}{\frac{S_1^4}{n_1^2(n_1-1)} + \frac{S_2^4}{n_2^2(n_2-1)}} \quad (2-62)$$

2.18 NONPARAMETRIC METHODS

Several nonparametric techniques can be used to characterize and analyze precipitation extremes. The following section discusses a technique that can be used to evaluate data characteristics with no assumptions made about the distribution of the data.

2.18.1 Kernel Density Estimation

Kernel density estimation (KDE) is a nonparametric alternative to using a histogram to characterize the distribution of sample data. Compared with parametric estimators, the parameters to be estimated from nonparametric data estimators have no fixed structure and depend on all the data points to reach an estimate. The main reasons for using a kernel density estimator in place of a histogram are (1) histograms do not provide a smooth representation of the data. (2) The shapes of the histograms depend on the end points of bins. The selection of the number of bins is subjective even though a few rules of thumb are available. And (3) the visual representation of the data distribution also depends on the width of the bins. No clear guidelines are available for selection of the widths. Shimazaki and Shinomoto (2007, 2010) provide approaches for optimum bin width in case of histograms and bandwidth for kernel density estimation functions. The use of optimum bin width eliminates the limitations associated with subjective bin selection. Kernel estimators center a kernel function (K) at each data point. Adoption of a smooth kernel function can overcome the limitations of the histograms. The contribution of data point x_i to the estimate at some point x depends on how far apart x_i and x are from each other. The extent of this contribution is dependent upon the shape of the kernel function adopted and the width (bandwidth, h) assigned.

The estimated density at any point x is

$$\hat{f}_h(x) = \frac{1}{nh} \sum_{i=1}^n K\left(\frac{x - x_i}{h}\right) \quad (2-63)$$

Several kernel functions are available for use with KDE. These are uniform, triangular, biweight, triweight, Epanechnikov, normal, Cauchy, and others. Teegavarapu (2016a), Teegavarapu and Goly (2011), and Teegavarapu et al. (2013) have used kernel density estimates to evaluate precipitation extremes at different durations in two Atlantic multidecadal oscillation (AMO) phases. In these studies, a Gaussian kernel was used to develop KDE for assessing the extreme precipitation events in AMO phases. Equation (2-64) gives the Gaussian kernel function.

$$K\left(\frac{x - x_{ip}}{h}\right) = \frac{1}{\sqrt{2\pi}} \exp\left(-\frac{1}{2} \left(\frac{x - x_{ip}}{h}\right)^2\right) \forall ip \quad (2-64)$$

Kernel density estimates using a Gaussian smoothing function and optimal bandwidth (h) are used to characterize precipitation extremes and their temporal occurrences in two phases of AMO. The bandwidth parameter (h) controls the smoothness of the probability density curve, and different bandwidths are experimented with before an optimal one is selected to represent kernel density estimates. The histograms of precipitation data for different durations are superimposed on kernel density estimates with appropriate scaling to evaluate the match between the two and to confirm the use of correct bandwidth.

2.18.2 Characterization of Extreme Precipitation Events

Bootstrap sampling methods and the generation of confidence intervals can help in making inferences about the sample statistics when limited numbers of datasets related to precipitation extremes are available due to missing data or other reasons. A bootstrap sampling method (Efron and Tibshirani 1993) is used to obtain samples from data. This study adopts the general procedure of bootstrap methodology and notation used by Davison and Hinkley (1997). The sample values y_1, y_2, \dots, y_n are thought of as the outcomes of independent and identically distributed (*iid*) random variables Y_1, Y_2, \dots, Y_n , whose CDF is denoted by F . The estimate of F , denoted by \hat{F} , is obtained using data y_1, y_2, \dots, y_n . The following steps from Davison and Hinkley (1997) are used to obtain bootstrap sampling confidence intervals:

- Bootstrap (re) samples $y_1^*, y_2^*, \dots, y_n^*$ $\sim \hat{F}$ are obtained from the original samples allowing repetitions.
- \hat{F} , an estimator of F , is obtained nonparametrically using an empirical distribution function of the original data, i.e., by placing a probability of $1/n$ at each data value from samples y_1, y_2, \dots, y_n .
- Sample mean statistic $\hat{\theta}^*$ is computed from bootstrap samples $y_1^*, y_2^*, \dots, y_n^*$.
- The previous steps are repeated N times, to obtain N sample means $\hat{\theta}_1^*, \hat{\theta}_2^*, \dots, \hat{\theta}_N^*$. The practical size of N depends on the tests to be run on the data.

The sizes of N that Chernick (2007) recommends are 1,000 and 10,000 for evaluating the sample statistic and confidence intervals, respectively. The current study uses these values. After N samples are obtained, normally approximated confidence intervals are computed for the uncertainty assessment. If $\hat{\theta}$ (estimated mean of original data) is approximately normal, then $\hat{\theta} \sim N(\theta + \beta, \nu)$.

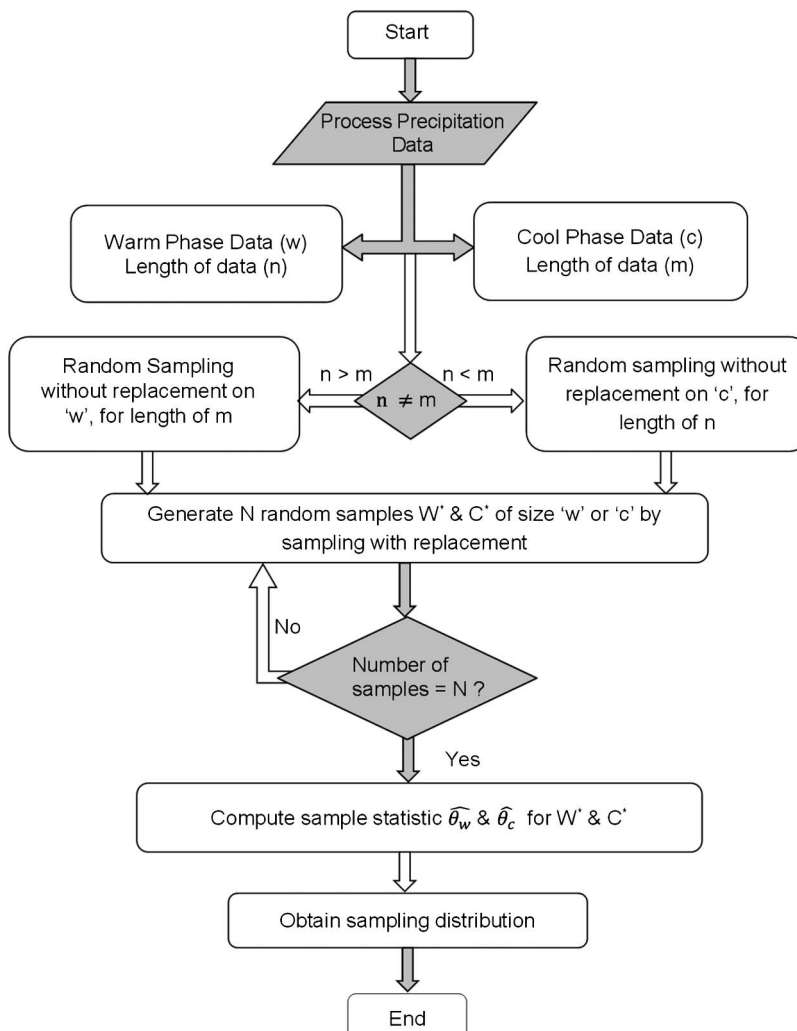


Figure 2-14. Schematic of random sampling without replacement and bootstrap sampling.
Source: Teegavarapu et al. (2013).

The confidence interval (CI) of θ for known bias ($\beta = \beta(F)$) and variance ($\nu = \nu(F)$) (Davidson and Hinkley 1997) is given by

$$CI = \hat{\theta} - \beta \pm Z_{\alpha} \cdot \nu^{1/2} \quad (2-65)$$

where

$$\beta(F) \doteq \beta(\hat{F}) \doteq b = \bar{\theta^*} - \hat{\theta} \quad (2-66)$$

$$\nu(F) \doteq \nu(\hat{F}) \doteq \nu = \frac{1}{N-1} \sum_{i=1}^N (\hat{\theta}_i^* - \bar{\theta^*})^2 \quad (2-67)$$

at 95% confidence interval, $\alpha = 0.025$, $Z_{\alpha} = -1.96$.

The variable $\bar{\theta^*}$ is the mean of $\hat{\theta}_1^*, \hat{\theta}_2^*, \dots, \hat{\theta}_N^*$, and Z_{α} is the α quantile of the standard normal distribution.

Teegavarapu et al. (2013) have used bootstrap sampling methods to evaluate precipitation extremes in two phases of AMO. The multidecadal temporal phases of AMO are not of equal length. A comparative analysis of extremes in two phases may be biased if the number of observations is

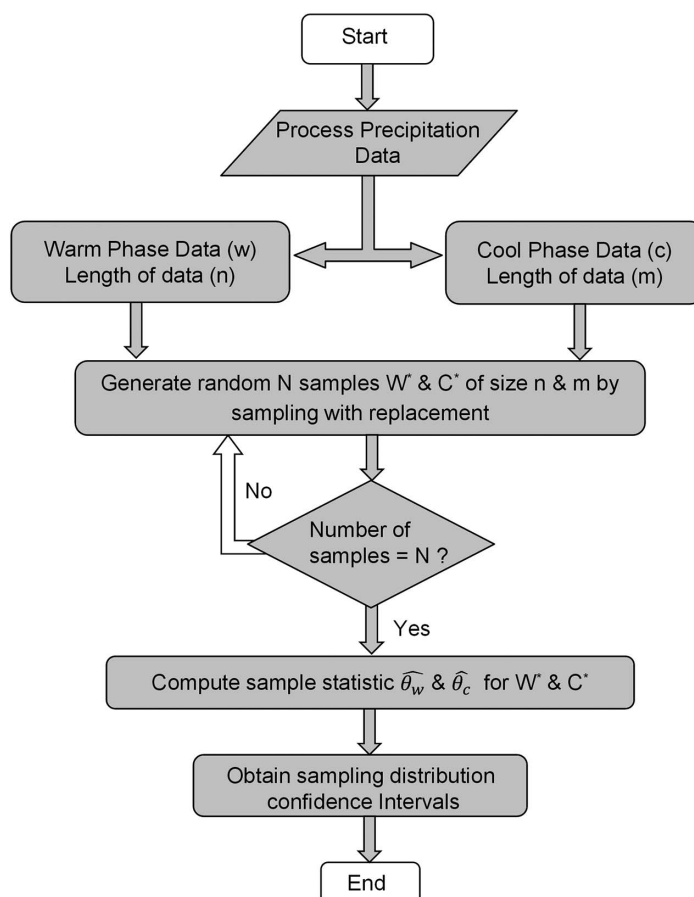


Figure 2-15. Bootstrap sampling approach for determining confidence intervals.
Source: Teegavarapu et al. (2013).

higher in one phase than the other. To avoid bias because of this, a resampling technique such as bootstrap sampling method is used to obtain samples from data in phase with a higher number of observations than the other phase. The number of samples drawn is restricted to a lower number of datasets from two phases. Given two datasets, an AMO warm phase (sample size, n) and an AMO cool phase (sample size, m), simple random sampling without replacement has been performed on two datasets to obtain equal datasets of the length x [$x = \min(n, m)$]. Once datasets of equal length of x are obtained, bootstrap sampling is used to obtain sample distribution. Random sampling without replacement is repeated several times along with bootstrap sampling in the second step. Figure 2-14 illustrates an approach combining random sampling without replacement and with replacement. The distributions of sample statistics (e.g., means) developed from the final step are evaluated using kernel density estimates. Figure 2-15 illustrates the bootstrap sampling method used for obtaining confidence intervals.

2.19 NONPARAMETRIC TEST FOR INDEPENDENCE

This section presents details of two nonparametric tests for evaluating independence of sample values of a time series.

2.19.1 Runs Test

The runs test, also referred to as the Wald–Wolfowitz test ([Wald and Wolfowitz 1943](#)), is a nonparametric test that can be used to examine a sample's randomness. No parametric equivalent of this test exists. [Nott \(2006\)](#) uses the runs test to confirm nonrandomness in a time series. The runs test can be used to decide if a dataset is derived based on a random process. A run is generally defined as a series of increasing values or as a series of decreasing values. The initial step in the runs test is to list the values in a sequential order and count the number of runs. The number of increasing (or decreasing) values is the length of the run. In a random dataset, the probability that the $(i + 1)^{th}$ value is larger or smaller than the i^{th} value follows a binomial distribution, which forms the basis of the runs test ([NIST 2011](#)). The next step in the runs test is to compute the sequential differences ($Y_i - Y_{i-1}$). Positive values indicate an increasing value, whereas negative values indicate a decreasing value. In other terms, if $Y_i > Y_{i-1}$, a unit value (one) is assigned for an observation and a 0 (zero) otherwise. The series is then transformed to a series of 1s and 0s. To determine if the number of runs is the correct number for a series that is random, let n be the number of observations, n_1 be the number above the mean, n_2 be the number below the mean, and R be the observed number of runs. Then, using combinatorial methods, the probability $P(R)$ can be established and the mean and variance of R can be derived ([Cromwell et al. 1994](#), [Gibbons 1997](#)). When n is relatively large (>20) the distribution of R is approximately normal.

$$\bar{x}_R = \frac{2n_1 n_2}{n_1 + n_2} + 1 \quad (2-68)$$

$$S_R = \sqrt{\frac{2n_1 n_2 (2n_1 n_2 - n_1 - n_2)}{(n_1 + n_2)^2 (n_1 + n_2 - 1)}} \quad (2-69)$$

$$Z^* = \frac{R + h - \bar{x}_R}{S_R} \quad (2-70)$$

where

Z^* = z-score for a normal approximation of the data,

R = number of runs ([Corder and Foreman 2009](#)), and

h = correction for continuity, ± 0.5 ,

where

$$h = +0.5 \quad \text{if } R < \frac{2n_1 n_2}{(n_1 + n_2 + 1)} \quad (2-71)$$

$$h = -0.5 \quad \text{if } R > \frac{2n_1 n_2}{(n_1 + n_2 + 1)} \quad (2-72)$$

The null hypothesis is rejected if the calculated Z_N value is greater than the selected critical value obtained from the standard normal distribution table at the 0.05 significance level. In other words, the time series is decided to be nonrandom.

2.19.2 Ranked von Neumann Test

The ranked von Neumann test or a ranked version of von Neumann's ratio test, a nonparametric test, can be used for testing the randomness in a sequence of observations. Equation (2-73) gives the test statistic, where the null and alternative hypotheses are the data are independent and the data are not independent, respectively. The variable n refers to the number of sample data and r_i is the rank of the data when the values are arranged from smallest to largest.

$$V_o = \frac{12}{n(n^2 - 1)} \sum_{i=2}^N (r_i - r_{i-1})^2 \quad (2-73)$$

The test statistic is compared with a critical value $V_{n,\alpha}$ at a significance level of α from the table provided by [Bartels \(1982\)](#). If the value of V_o is less than $V_{n,\alpha}$, then the null hypothesis is rejected. The power of the test is expected to be diminished when ranks are tied.

2.20 PARTIAL DURATION SERIES

The annual extreme value series is often referred to as the block maxima series and is generally used for frequency analysis. In case of the annual extreme series, the maximum value can be obtained from a calendar year or a water year basis. However, extreme values over a prespecified threshold are also used for analysis. These series are referred to as partial duration series (PDS). One limitation of annual series is that they may omit a value that is lower than the maximum value in a specific year that is higher than all other values in a series. The partial duration series overcomes this limitation by selecting all extreme values above a threshold. In some instances, the number of extreme values adopted from a PDS is the same as the number of years of data available. Analysis of annual maximum series provides estimates of the average period between years when a particular value is exceeded. This is generally referred to as average recurrence interval (ARI).

The partial duration series provides the average period between cases of a specific magnitude. The information obtained from the PDS is the annual exceedance probability (AEP). [Laurenson \(1987\)](#) provides the definitions for ARI and AEP. In the context of precipitation analysis, ARI refers to the average, or expected, value of the periods between exceedances of a given rainfall total accumulated over a given duration. AEP refers to the probability that a given rainfall total accumulated over a given

duration will be exceeded in any one year. The peaks over threshold value are first assessed for independence of observations. Several flood frequency analysis studies ([Stedinger 2000](#)) using PDS have identified the advantages of using such series. One of the difficulties associated with the use of the PDS for rainfall frequency analysis is the subjective selection of the threshold.

2.21 STATISTICAL CHARACTERIZATION OF INTEREVENT TIME DEFINITION OF STORM EVENTS

[Adams and Howard \(1986\)](#) critically evaluated the use of design storms based on IDF curves for stormwater management. The analytical probabilistic models for stormwater management models prescribed by [Adams and Papa \(2000\)](#) describe the need for identification of individual storms using an interevent time definition. The interevent time definition (IETD) is defined as the minimum temporal spacing without rainfall required to consider two rainfall events as belonging to different events ([Adams and Papa 2000](#)). Rainfall volumes, durations, intensities, and interevent times can be characterized using exponential or gamma distributions ([Behera et al. 2010](#)) for use in analytical probabilistic models. The statistics of storm event characteristics are influenced by the values of the IETD.

2.22 INCORPORATION OF CLIMATE VARIABILITY CYCLES AND CLIMATE CHANGE INTO RAINFALL FREQUENCY ANALYSIS

Evaluation of extreme precipitation events that considers magnitude, duration, and geographical location is crucial for the design of hydrologic systems and long-term operation of water resource systems. Several studies confirm the link between internal modes of climate variability and extreme precipitation events at different spatial and temporal scales ([Teegavarapu 2016a](#)). Some of the major internal modes of climate variability affecting precipitation around the globe are AMO, the El Niño southern oscillation (ENSO), the Pacific decadal oscillation (PDO), and the north Atlantic oscillation (NAO). Teleconnections such as ENSO and AMO cycles or phases influence rainfall patterns and droughts in several parts of the continental United States and others regions of the world. Higher precipitation totals (especially for long temporal durations greater than 24 hours) have been attributed to different phases of these oscillations in the state of Florida ([Teegavarapu et al. 2013](#)). [Teegavarapu et al. \(2013\)](#) also evaluated GEV, log-normal, three-parameter log-normal, Pearson, and log-Pearson distributions for characterizing extreme precipitation data. GEV with a flexible three-parameter model was found to be most appropriate for characterizing 24-hour duration precipitation extremes in the region. Figure 2-16 shows depth duration curves for four sites in Florida for two phases of AMO. [Teegavarapu et al. \(2013\)](#) suggest the following key points in the development of design storms using extreme precipitation datasets considering the influences of oceanic and atmospheric oscillations:

- The conventional wisdom of using an entire dataset of available precipitation extremes for determination of design storms is now debatable considering the influences of different phases of oscillations on the whole or parts of a region spatially and temporally.
- Multiple teleconnections influencing regional hydrology simultaneously in different temporal windows may increase or decrease the frequency and magnitudes of extreme precipitation events and influence intraannual temporal occurrences of extremes.
- Emphasis should be placed on those temporal windows in which the combined influences of two or more teleconnections may lead to rare extremes, and data selection for design should be representative of these extremes.

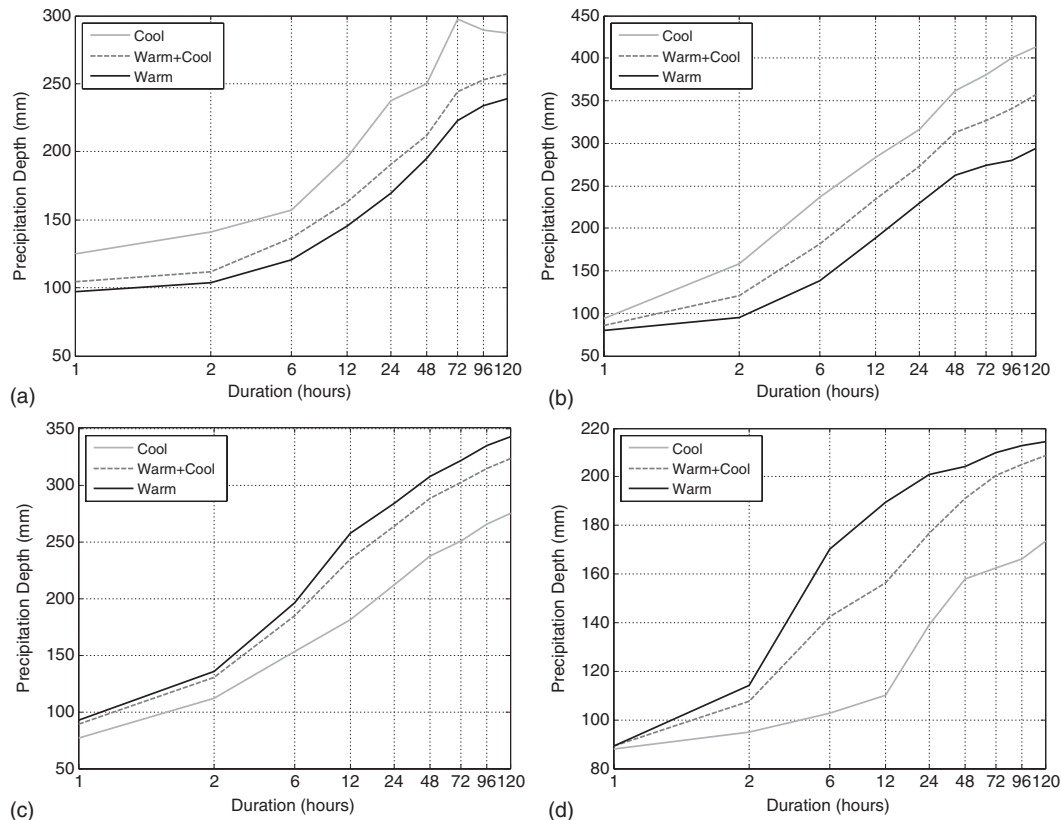


Figure 2-16. Depth duration curves during AMO warm, cool, and combined phases (cool and warm) for four stations in (a) north Florida, (b) Key West, (c) Palm Beach, and (d) Lake Okeechobee.

Source: Teegavarapu et al. (2013).

- The idea of using site-specific extremes for design confined to one specific region is not new. However, consideration of region-specific influences of climate variability at different spatial and temporal scales is advocated for hydrologic design.

Future rainfall frequency analysis methods should consider the influences of teleconnections to understand the regional and temporal variability of rainfall extremes. Long-term, high-quality, and reliable climate records of finer (with a daily or higher) temporal resolution are required for assessing changes in extremes. Brunet et al. (2008) discuss guidelines for the development of datasets of these characteristics. WMO (2010) discusses (1) development of datasets for the analysis of extremes, (2) use of descriptive indexes and extreme-value theory concepts to evaluate extreme events, (3) assessment of trends and other statistical approaches for evaluating changes in extremes, and (4) understanding of observed changes and model-projected changes in extremes.

2.23 USE OF FUTURE DATA SOURCES FOR FREQUENCY ANALYSIS

Hydrological design based on design storms will benefit from the emerging sources of rainfall measurement such as radar and satellite. The use of radar data for estimation of PMP is often dismissed due to the shorter length of data compared with the long-term data that are available from rain gauges (Collier and Hardaker 2007). The utility of radar data is also being questioned for use in

frequency analysis of extremely rare events due to lack of reasonable data length of 10 years. In spite of all these limitations associated with the available length of radar data, these data are now used extensively for extreme rainfall analysis and other hydrologic modeling applications (Pathak and Teegavarapu 2018). Collier and Hardaker (1996) developed methods to estimate maximum rainfall totals to obtain realistic estimates of PMP. Cluckie et al. (1987) developed depth-area-duration curves using radar-based rainfall data. Cluckie and Pessoa (1990) characterize actual storms for the development of PMP estimates using radar-based precipitation data. Reliable radar data are now available in many parts of the world at a temporal resolution that is adequate for frequency analysis for hydrologic design. One concern with radar is that the evolving technology suggests no consistency in methods used for obtaining reflectivity data. Often the fine temporal resolution radar-based precipitation data are useful in analyzing short-duration storms. The satellite data temporal resolution, however coarse, is still the only reasonably accurate rainfall data available for analysis in regions of the world with extremely low rain gauge density and also in regions where radar-based rainfall estimates are not available (Teegavarapu 2012a). Radar-based precipitation data are often corrected for bias with the help of rain gauge data. To analyze the bias, different performance measures, skill scores, and distributions of radar and rain gauge data are analyzed.

2.24 DESCRIPTIVE INDEXES FOR PRECIPITATION EXTREMES

Descriptive indexes for precipitation extremes were developed by the Expert Team on Climate Change Detection and Indexes (ETCCDI) and are described by WMO (2009). These indexes describe specific characteristics of extremes, including frequency, amplitude, and persistence (WMO 2009). Table 2-7 provides eleven indexes for precipitation developed by ETCCDI. The indexes can be used for long-term changes in precipitation extremes. According to the WMO technical regulations, standard normals are averages of climatological data computed for the following consecutive periods of 30 years: January 1, 1901 to December 31, 1930, January 1, 1931 to December 31, 1960, and so forth. Climate normals are required for calculation of a few indexes provided in Table 2-10. These climatological baseline periods are nonoverlapping. The current WMO normal period (Lu 2006) is 1981 to 2010. Teegavarapu et al. (2011) use two indexes to evaluate long-term trends in extreme precipitation data at several locations in Florida. They indicate the existence of missing data in the

Table 2-7. Descriptive Indexes for Precipitation Extremes.

Index	Description
RX1day	Maximum one-day precipitation
RX5day	Maximum five-day precipitation
SDII	Simple daily intensity index
R10mm	Count of precipitation days with RR greater than 10 mm
R20mm	Count of precipitation days with RR greater than 20 mm
Rnnmm	Count of days with RR greater than a threshold value
CDD	Consecutive dry days ($RR < 1 \text{ mm}$)
CWD	Consecutive wet days ($RR \geq 1 \text{ mm}$)
R95pTOT	Total precipitation due to wet days (> 95th percentile)
R99pTOT	Total precipitation due to extremely wet days (> 99 percentile)
PRCPTOT	Total precipitation in wet days (> 1 mm)

Note: RR = observed daily rainfall.

time series and express concern that infilling procedures might introduce biases in the trends. Teegavarapu et al. (2012) report similar conclusions related to missing data and indexes.

2.25 STANDARD PRECIPITATION INDEX

Standard precipitation index (SPI) (McKee et al. 1993, McKee et al. 1995) calculation involves fitting a probability distribution (generally a gamma distribution) to one-, three-, six-, and 12-month precipitation totals and then using standard normal distribution to obtain SPI values. SPI is widely used by drought planners for quantifying precipitation deficits (WMO 2012). The probability density function of a two-parameter gamma distribution is given by

$$f(x) = \frac{1}{\beta^\alpha \Gamma(\alpha)} (x)^{\alpha-1} e^{-(x)/\beta} \quad (2-74)$$

The parameters of gamma distribution can be estimated by the maximum likelihood method. Precipitation data may contain zero values, and in such instances, gamma function is undefined (McKee et al. 1993, McKee et al. 1995). However, alternative procedures suggested by Thom (1966) can be used to estimate cumulative probability values based on incomplete gamma distribution functions (Edwards and McKee 1997).

$$\hat{\alpha} = \frac{1}{4A} \left(1 + \sqrt{1 + \frac{4A}{3}} \right) \quad (2-75)$$

$$\hat{\beta} = \frac{\bar{x}}{\hat{\alpha}} \quad (2-76)$$

where

$$A = \ln(\bar{x}) - \frac{\sum \ln(x)}{n} \quad (2-77)$$

n = number of precipitation observations

Based on the estimated parameters ($\hat{\alpha}, \hat{\beta}$), the cumulative probability of an observed precipitation value can be obtained by

$$F(x) = \frac{1}{\hat{\beta}^{\hat{\alpha}} \Gamma(\hat{\alpha})} \int_0^x t^{\hat{\alpha}-1} e^{-t/\hat{\beta}} dt \quad (2-78)$$

Letting $= x/\hat{\beta}$, Equation (2-77) becomes the incomplete gamma function:

$$F(x) = \frac{1}{\Gamma(\hat{\alpha})} \int_0^x t^{\hat{\alpha}-1} e^{-t} dt \quad (2-79)$$

Because the gamma function is undefined for $x = 0$ and a precipitation distribution may sometimes contain zero values, the cumulative probability then can be expressed as

$$D(x) = p + (1 - p)F(x) \quad (2-80)$$

where p is the probability of a zero value.

If m is the number of zeros in a precipitation time series, the value of p can be estimated by m/n (Thom 1966). The Z value can be computationally estimated using a rational approximation provided by Abramowitz and Stegun (1972) that converts cumulative probability to the standard normal random variable (Z):

$$Z = - \left(t - \frac{c_0 + c_1 t + c_2 t^2}{1 + d_1 t + d_2 t^2 + d_3 t^3} \right) \quad 0 < D(x) \leq 0.5 \quad (2-81)$$

$$Z = \left(t - \frac{c_0 + c_1 t + c_2 t^2}{1 + d_1 t + d_2 t^2 + d_3 t^3} \right) \quad 0.5 < D(x) \leq 1.0 \quad (2-82)$$

$$t = \sqrt{-2 \ln(D(x))} \quad 0 < D(x) \leq 0.5 \quad (2-83)$$

$$t = \sqrt{-2 \ln(1 - D(x))} \quad 0.5 < D(x) \leq 1.0 \quad (2-84)$$

The values of c_0 , c_1 , d_1 , d_2 , d_3 are 2.515517, 0.802853, 0.010328, 1.432788, 0.189269, and 0.001308, respectively. The maximum absolute error possible (Abramowitz and Stegun 1972) due to rational approximation is 4.5×10^{-4} . Figure 2-17 shows an example calculation of SPI for two-month precipitation totals.

The empirical cumulative probabilities are obtained by sorting the precipitation data in increasing order of magnitude (Panofsky and Brier 1958). The smooth curve shown in Figure 2-17b is the cumulative distribution function of the fitted two-parameter gamma distribution, and the curve with markers is the empirical cumulative distribution function of the precipitation data. Figure 2-17c shows the cumulative probability distribution of a standard normal random variable. SPI can be obtained

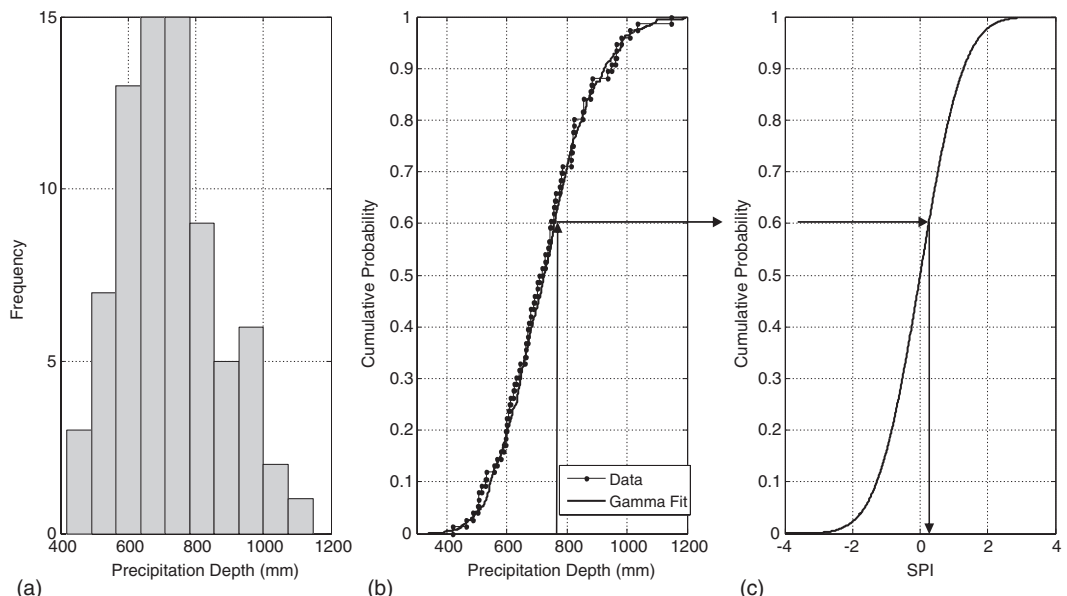


Figure 2-17. Illustration of two-month SPI calculation using fitted gamma distribution.

using the two-month precipitation value shown in Figure 2-17b. [Guttman \(1994\)](#) suggests that 50 to 60 years (or more) are preferred for calculation of SPI. Distributions other than gamma can also be used to characterize the precipitation data. [Guttman \(1999\)](#) evaluates several candidate distributions, including two-parameter gamma, three-parameter Pearson type III, three-parameter GEV, four-parameter kappa, and five-parameter Wakeby. [Guttman's \(1999\)](#) study concludes that the Pearson type III distribution is the “best” universal model, that the reliability of the SPI is sample -size dependent, and that SPIs with time scales longer than 24 months may be unreliable considering data limitations. SPI values can be used to define wet and dry conditions based on the classification system proposed by [McKee et al. \(1993\)](#) as extremely wet (2 or higher), very wet (1.5 to 1.99), moderately wet (1.0 to 1.49), near normal (−0.99 to 0.99), moderately dry (−1.0 to −1.49), severely dry (−1.5 to −1.99), and extremely dry (−2 and less). [Goly and Teegavarapu \(2014\)](#) used 3 month SPI values calculated using gridded precipitation data from the state of Florida for evaluation of variations in drought occurrences in two phases of AMO and ENSO.

2.26 TRENDS BASED ON GCM MODEL SIMULATIONS

Precipitation events of a specific magnitude that lead to catastrophic floods are under scrutiny by many research studies aiming to understand the influence of climate change and variability on these events. According to [IPCC \(2007a\)](#), the observed increases in the frequency of heavy precipitation events (frequency or proportion of total precipitation from heavy falls) over most areas are indicated *likely* based on the trends in the later part of the twentieth century, especially after 1960. The human contribution to the trends in these events is described as *most likely*. Also, the [IPCC \(2007b\)](#) suggests that the increases in the frequency of these events are *very likely* based on the projections from different climate change model projections for the 21st century considering the greenhouse gas emissions scenarios described in Special Report on Emission Scenarios (SRES) ([IPCC 2007a](#)). SRES are replaced by Representative Concentration Pathways (RCPs) in 2014. Hydrologic variable trends based on downscaled GCM simulations can be evaluated using the statistical concepts discussed in this chapter. Downscaled precipitation data at a temporal scale of one month are currently available from several climate change models ([Teegavarapu 2012a](#)). However, GCM-based projections are not available for precipitation datasets at finer spatial and temporal resolutions for all regions that are essential for hydrologic design. [Benestad et al. \(2008\)](#), [Fowler et al. \(2007\)](#), and [Fung et al. \(2010\)](#) discuss the inability of climate change models to reproduce precipitation extremes accurately and the limitations of downscaling models in replicating the spatial and temporal variability. One important and critical assumption of stationarity used in frequency analysis is no longer valid when the analysis is carried out with such datasets. In general, frequency analysis methods always require the assumption of a stationary climate. Several statistical tests are used to see if statistically significant trends are present in the AMS or the PDS of observations used for frequency analysis. For example, the precipitation frequency analysis carried out by NOAA for Atlas 14 assumes a stationary climate.

Precipitation frequency analysis studies now focus on the evaluation of climate change impacts on trends of extreme rainfall. If the detailed statistical analysis shows no or little observable change in trends over time, the assumption of a stationary climate is not detrimental to precipitation frequency analysis. The impacts of potential changes in climate on precipitation frequency estimates remain uncertain. The uncertainty is mainly owing to the documented large differences among climate model projections with respect to the expected changes in extreme precipitation frequencies and magnitudes. Further research is also needed to determine how to adjust precipitation frequency estimates for future climate change.

2.27 HYDROLOGIC DESIGN FOR THE FUTURE

The single most critical input to the hydrologic design used in a single event or continuous modeling approaches is precipitation. Hydrologic designs continue to rely on the assumption of stationarity even though it is no longer valid (Milly et al. 2008). Future changes in climate that may alter the frequency of precipitation extremes would have consequences for stormwater management infrastructure, particularly when stormwater detention and conveyance facilities are designed under the stationarity assumption. Urban drainage design practices are expected to be revised by incorporating climate change factors (Arnbjerg-Nielsen 2012), analyzing trends in precipitation extremes (Teegavarapu 2018) and their frequencies (de Toffol et al. 2009), evaluating impacts of changing extremes using downscaled precipitation data from GCMs (Grum et al. 2006), and designing frameworks for risk and uncertainty management (Arnbjerg-Nielsen 2011). Design storms derived using IDF relationships (Adams and Howard 1986) are still widely employed for the design of stormwater conveyance systems in engineering practice. An adaptive approach is to upgrade existing infrastructure with changing IDF relationships over time, evolving temporal precipitation distributions and evaluating economic options to minimize cost and improve the reliability of the hydrologic structures. Alternatively, a sustainable hydrologic design that identifies a compromise between current and future climate-based conditions can be devised (Teegavarapu 2013b, Kolokytha et al. 2016).

2.28 SUMMARY AND CONCLUSIONS

Statistical analysis of precipitation extremes is the main focus of this chapter. In setting the stage for precipitation data analysis, measurement and collection of precipitation data using rain gauges and radar is also provided. The availability of continuous precipitation data without any gaps and missing extreme observations is critical for the statistical analysis of data to obtain design rainfall for stormwater management systems. This chapter also provides a brief review of deterministic and stochastic interpolation methods for estimation of missing precipitation data. Statistical analysis of extreme precipitation data is clearly explained, and the procedures that lead to the development of IDF curves and isopluvial contours based on spatial interpolation are discussed. Assessment of extreme precipitation data under a changing climate and uncertainties associated with future climate change-based trends in extreme precipitation are also discussed.

References

- Abramowitz, M., and I. A. Stegun. 1972. *Handbook of mathematical functions*. New York: Dover.
- Adams, B. J., H. G. Fraser, C. D. D. Howard, and M. S. Hanafy. 1986. "Meteorological data analysis for urban drainage system design." *J. Environ. Eng.* **112** (5): 827–848.
- Adams, B. J., and C. D. D. Howard. 1986. "Pathology of design storms." *Can. Water Resour.* **11** (3): 49–55.
- Adams, B. J., and F. Papa. 2000. *Urban stormwater management planning with analytical probabilistic models*. New York: Wiley.
- Ahuja, P. R. 1960. *Planning for precipitation network for water resources development in India: WMO flood control series no. 15*, 106–112. Geneva: WMO.
- Aksoy, H. 2000. "Use of gamma distribution in hydrological analysis." *Turk. J. Eng. Environ. Sci.* **24** (2000): 419–428.
- Alexandersson, H. 1985. "A simple stochastic model of the precipitation process." *J. Clim. Appl. Meteorol.* **24** (12): 1285–1295.
- Alexandersson, H. 1986. "A homogeneity test applied to precipitation data." *J. Climatol.* **6** (6): 661–675.
- Alghazali, N. O. S., and D. A. H. Alawadi. 2014. "Fitting statistical distributions of monthly rainfall for some Iraqi stations." *Civ. Environ. Res.* **6** (6): 40–46.

- Alia, Y. 2000. "Regional rainfall depth-duration frequency equations for Canada." *Water Resour. Res.* **36** (7): 1767–1778.
- Alonge, A. A., and T. J. Afullo. 2012. "Seasonal analysis and prediction of rainfall effects in eastern South Africa at microwave frequencies." *Prog. Electromagn. Res. B* **40**: 279–303.
- Anderson, T. W., and D. A. Darling. 1954. "A test of goodness of fit." *J. Am. Stat. Assoc.* **49** (268): 765–769.
- Angelidis, P., F. Maris, N. Kotovinos, and V. Hrissanthou. 2012. "Computation of drought index SPI with alternative distribution functions." *Water Resour. Manage.* **26** (9): 2453–2473.
- Ansari, A., and R. Bradley. 1960. "Rank sum tests for dispersion." *Ann. Math. Stat.* **31** (4): 1174–1189.
- Arnbjerg-Nielsen, K. 2011. "Past, present, and future design of urban drainage systems with focus on Danish experiences." *Water Sci. Technol.* **63** (3): 527–535.
- Arnbjerg-Nielsen, K. 2012. "Quantification of climate change effects on extreme precipitation used for high resolution hydrologic design." *Urban Water J.* **9** (2): 57–65.
- ASCE. 1996. *Hydrology handbook*. New York: ASCE.
- Ashkar, F. 1996. "Extreme floods." In *Hydrology of disasters*, edited by V. P. Singh. Dordrecht, Netherlands: Kluwer Academic.
- Ashraf, M., J. C. Loftis, and K. G. Hubbard. 1997. "Application of geostatistics to evaluate partial weather station network." *Agric. For. Meteorol.* **84** (3–4): 255–271.
- Bartels, R. 1982. "The rank version of von Neumann's ratio test for randomness." *J. Am. Stat. Assoc.* **77** (377): 40–46.
- Bedient, P. B., W. C. Huber, and B. E. Vieux. 2008. *Hydrology and floodplain analysis*. 4th ed., 816. Upper Saddle River, NJ: Prentice-Hall.
- Behera, P., Y. Guo, R. S. V. Teegavarapu, and T. Branham. 2010. "Evaluation of antecedent storm event characteristics for different climatic regions based on interevent time definition (IETD)." In *Proc., World Environmental and Water Resources Congress: Challenges of Change*, edited by R. Palmer. Reston, VA: ASCE.
- Bell, F. C. 1969. "Generalized rainfall-duration-frequency relationships." *J. Hydraul. Div.* **95** (HY1): 311–327.
- Benabdesselam, T., and H. Amarchi. 2013. "Regional approach for the estimation of extreme daily precipitation on north-east area of Algeria." *Int. J. Water Resour. Environ. Eng.* **5** (10): 573–583.
- Benestad, R. E., I. Hanssen-Bauer, and D. Chen. 2008. *Empirical-statistical downscaling*. Hackensack, NJ: World Scientific.
- Benson, M. A. 1962. "Plotting positions and economics of engineering planning." *J. Hydraul. Div.* **88** (6): 57–71.
- Berthe, K. A., B. Abdramane, and S. Reichenbach. 2015. "Gumbel Weibull distribution function for Sahel precipitation modeling and predicting: Case of Mali." *Afr. J. Environ. Sci. Technol.* **9** (5): 405–412.
- Bertoldo, S., C. Lucianaz, and M. Allegretti. 2015. "Extreme rainfall event analysis using rain gauges in a variety of geographical situations." *Atmos. Clim. Sci.* **5** (2): 82–90.
- Betancourt, J. 2009. "Coping with non-stationarity in water and ecosystem management." In *Proc., 9th Annual SAHRA Meeting*, Tucson, AZ: SAHRA.
- Blain, G. C. 2011. "Standardized precipitation index based on Pearson type III distribution." *Rev. Bras. Meteorol.* **26** (2): 167–180.
- Blain, G. C., and M. C. Meschiatti. 2015. "Inadequacy of the gamma distribution to calculate the standardized precipitation index." *Rev. Bras. Eng. Agríc. Ambient* **19** (12): 1129–1135.
- Blom, G. 1958. *Statistical estimates and transformed beta-variables*. New York: Wiley.
- Bobee, B., and F. Ashkar. 1991. *The gamma family and derived distributions applied in hydrology*. Littleton, CO: Water Resources Publications.
- Bonnin, G. M., D. Martin, B. Lin, T. Parzybok, M. Yekta, and D. Riley. 2006. *Precipitation-frequency atlas of the United States: Atlas 14*. Silver Spring, MD: NOAA.
- Box, G. E. P., and D. R. Cox. 1964. "An analysis of transformations." *J. R. Stat. Soc. Series B* **26** (2): 211–252.
- Box, G. E. P., G. M. Jenkins, and G. C. Reinsel. 1994. *Time series analysis: Forecasting and control*. 3rd ed. Englewood Cliffs, NJ: Prentice-Hall,
- Brimicombe, A. 2003. *GIS, environmental modeling and engineering*. London: Taylor and Francis.
- Brunet, M. O., O. Saladié, P. Jones, J. Sigró, E. Aguilar, A. Moberg, D. Lister, A. Walther, and C. Almarza. 2008. *A case-study/guidance on the development of long-term daily adjusted temperature datasets*. WCDMP-66. Geneva: WMO.
- Buishand, T. A. 1982. "Some methods for testing the homogeneity of rainfall records." *J. Hydrol.* **58** (1-2): 11–27.

- Burgueño, A., M. D. Martínez, X. Lana, and C. Serra. 2005. "Statistical distributions of the daily rainfall regime in Catalonia (northeastern Spain) for the years 1950-2000." *Int. J. Climatol.* **25** (10): 1381–1403.
- California State Department. 1923. *Flow in California streams*. Sacramento, CA: California State Dept.
- Carreau, J., L. Neppel, P. Arnaud, and P. Cantet. 2013. "Extreme rainfall analysis at ungauged sites in the south of France: Comparison of three approaches." *J. Soc. Fr. Statistique* **154** (2): 119–138.
- Chegodaev, N. N. 1953. *Computation of runoff on small catchments*. Moscow, Russia: Transzhedorizdat.
- Chen, C. L. 1983. "Rainfall intensity-duration-frequency formulas." *J. Hydraul. Eng.* **109** (12): 1603–1621.
- Chen, M., C. Lin, Y. Wu, P. Wu, S. Lung, and H. Su. 2012. "Effects of extreme precipitation to the distribution of infectious diseases in Taiwan, 1994-2008." *PLOS One* **7** (6): 1–8.
- Chernick, M. R. 2007. *Bootstrap methods: A guide for practitioners and researchers*. Hoboken, NJ: Wiley.
- Chikobvu, D., and R. Chifurira. 2015. "Modelling of extreme minimum rainfall using generalized extreme value distribution for Zimbabwe." *S. Afr. J. Sci.* **111** (9–10): 1–8.
- Chin, D. 2006. *Water resources engineering*. Upper Saddle River, NJ: Prentice Hall.
- Cho, H., K. P. Bowman, and G. R. North. 2004. "A comparison of gamma and lognormal distributions for characterizing satellite rain rates from the tropical rainfall measuring mission." *J. Appl. Meteorol.* **43** (11): 1586–1597.
- Chow, V. T. 1951. "A general formula for hydrologic frequency analysis." *Trans. Am. Geophys. Union* **32** (2): 231–237.
- Chow, V. T., D. R. Maidment, and L. W. Mays. 1988. *Applied hydrology*. Singapore: McGraw-Hill.
- Chun, K. P., and H. S. Wheater. 2012. "An extreme analysis for the 2010 precipitation event at the south of Saskatchewan Prairie." *Global Nest J.* **14** (3): 311–324.
- Clarke, R. T. 2002. "Estimating trends in data from the Weibull and a generalized extreme value distribution." *Water Resour. Res.* **38** (6): 25-1–25-10.
- Cluckie, I. D., P. P. Ede, M. D. Owens, and A. C. Bailey. 1987. "Some hydrological aspects of weather radar research in the United Kingdom." *Hydrol. Sci.* **32** (3): 329–346.
- Cluckie, I. D., and M. L. Pessoa. 1990. "Dam safety: An evaluation of some procedures for design flood estimation." *Hydrol. Sci.* **35** (5): 547–569.
- Coin, D. 2008. "Testing normality in the presence of outliers." *Stat. Methods Appl.* **17** (1): 3–12.
- Collier, C. G. 1989. *Applications of weather radar systems: A guide to uses of radar data in meteorology and hydrology*. New York: Wiley.
- Collier, C. G., and P. J. Hardaker. 1996. "Estimating probable maximum precipitation using a storm model approach." *J. Hydrol.* **183** (3–4): 277–306.
- Collier, C. G., and P. J. Hardaker. 2007. "Using radar in hydrometeorology." In *Weather radar: Principles and advanced applications*, edited by P. Meischner. Berlin: Springer.
- Corder, W. G., and D. I. Foreman. 2009. *Nonparametric statistics for non-statisticians*. Hoboken, NJ: Wiley.
- Crisci, A., B. Gozzini, F. Meneguzzo, S. Pagliara, and G. Maracchi. 2002. "Extreme rainfall in a changing climate: Regional analysis and hydrological implications in Tuscany." *Hydrol. Processes* **16** (6): 1261–1274.
- Cromwell, J. B., W. C. Labys, and M. Terraza. 1994. *Univariate tests for time series models*, 07–99. London: Sage.
- Cullen, A. C., and H. C. Frey. 1999. *Probabilistic techniques in exposure assessment*. New York: Plenum.
- Cunnane, C. 1978. "Unbiased plotting-positions: Rev." *J. Hydrol.* **37** (3–4): 205–222.
- D'Agostino, R. B., A. Belanger, and R. B. D'Agostino Jr. 1990. "A suggestion for using powerful and informative tests of normality." *Am. Stat.* **44** (4): 316–321.
- Dan'azumi, S., S. Shamsudin, and A. A. Rahman. 2010. "Probability distribution of rainfall depth at hourly time-scale." *Int. Scholar. Sci. Res. Innov.* **4** (12): 670–674.
- Davison, A. C., and D. V. Hinkley. 1997. *Bootstrap methods and their applications*. Cambridge, UK: Cambridge University Press.
- de Toffol, S., A. N. Laghari, and W. Rauch. 2009. "Are extreme rainfall intensities more frequent? Analysis of trends in rainfall patterns relevant to urban drainage systems." *Water Sci. Technol.* **59** (9): 1769–1776.
- Dikko, H. G., I. J. David, and H. R. Bakari. 2013. "Modeling the distribution of rainfall intensity using quarterly data." *J. Math.* **9** (1): 11–16.
- Dingman, S. L. 2008. *Physical hydrology*. Long Grove, IL: Waveland.
- Duan, J., J. Selker, and G. E. Grant. 1998. "Evaluation of probability density functions in precipitation models for the Pacific Northwest." *J. Am. Water Resour. Assoc.* **34** (3): 617–627.

- Duan, J., A. K. Sikka, and G. E. Grant. 1995. "A comparison of stochastic models for generating daily precipitation at the H. J. Andrews Experimental Forest." *Northwest Sci.* **69** (4): 318–329.
- Dullo, T. T., A. J. Kalyanapu, and R. S. V. Teegavarapu. 2017. "Evaluation of changing characteristics of temporal rainfall distribution within 24-hour duration storms and their influences on peak discharges: Case study of Asheville, North Carolina." *J. Hydrol. Eng.* **22** (11): 05017022.
- Dunn, P. K. 2004. "Occurrence and quantity of precipitation can be modelled simultaneously." *Int. J. Climatol.* **24** (10): 1231–1239.
- Dyrrdal, A. V., A. Lenkoski, T. L. Thorarinsdottir, and F. Stordal. 2015. "Bayesian hierarchical modeling of extreme hourly precipitation in Norway." *Environmetrics* **26** (2): 89–106.
- Eagleson, P. S. 1972. "Dynamics of flood frequency." *Water Resour. Res.* **8** (4): 878–898.
- Ebert, E. E., J. E. Janowiak, and C. Kidd. 2007. "Comparison of near real-time precipitation estimates from satellite observations and numerical models." *Bull. Am. Meteorol. Soc.* **88** (1): 47–64.
- Edwards, D. C., and T. B. McKee. 1997. *Characteristics of 20th century drought in the United States at multiple time scales*. Climatology Rep. No. 97-2, Fort Collins, CO: Colorado State Univ.
- Efron, B. 1979. "Bootstrap methods: Another look at the jackknife." *Ann. Stat.* **7** (1): 1–26.
- Efron, B., and G. Gong. 1983. "A leisurely look at the bootstrap, the jackknife, and cross validation." *Am. Stat.* **37** (1): 36–48.
- Efron, B., and R. Tibshirani. 1993. *An Introduction to the Bootstrap*. London: Chapman and Hall.
- Evans, M., N. Hastings, and B. Peacock. 2002. *Statistical distributions*. New York: Wiley.
- Feng, S., S. Nadarajah, and Q. Hu. 2007. "20th international congress on modelling and simulation." In Vol. 85 of *Proc., 20th Int. Congress on Modelling and Simulation*, 599–613.
- Filliben, J. J. 1975. "The probability plot correlation coefficient test for normality." *Technometrics* **17** (1): 111–117.
- Fischer, T., B. Su, Y. Luo, and T. Scholten. 2012. "Probability distribution of precipitation extremes for weather index-based insurance in the Zhujiang River Basin, South China." *J. Hydrometeorol.* **13** (3): 1023–1037.
- Foster, J., M. Bevis, and W. Raymond. 2006. "Precipitable water and the lognormal distribution." *J. Geophys. Res.* **111** (D15): 1–11.
- Fowler, H. J., S. Blenkinsop, and C. Tebaldi. 2007. "Linking climate change modeling to impacts studies—Recent advances in downscaling techniques for hydrological modeling." *Int. J. Climatol.* **27** (12): 1547–1578.
- Frederick, R. H., V. A. Myers, and E. Auciello. 1977. *Five-to 60-minute precipitation frequency for the eastern and central United States*. HYDRO-35 Rep. Silver Spring, MO: National Weather Service.
- Fulton, R. A., J. P. Breidenbach, D. J. Seo, D. A. Miller, and T. O'Bannon. 1998. "The WSR-88D rainfall algorithm." *Weather Forecasting* **13** (2): 377–395.
- Fung, F., A. Lopez, and M. New. 2010. *Modelling the impact of climate change on water resources*. Hoboken, NJ: Wiley.
- Ganguli, M. K., R. Rangarajan, and G. M. Panchang. 1951. "Accuracy of mean rainfall estimates: Data of Domodar catchment." *Irrig. Power J.* **8** (2): 278.
- Gąsiorek, E., and E. Musiał. 2015. "Evaluation of the precision of standardized precipitation index (SPI) based on years 1954–1995 in Lodz." *J. Ecol. Eng.* **16** (4): 49–53.
- Gauthier, T. D. 2001. "Detecting trends using Spearman's rank correlation coefficient." *Environ. Forensic* **2** (4): 359–362.
- Gibbons, J. D. 1997. *Nonparametric methods for quantitative analysis*. Columbus, OH: American Sciences.
- Gilbert, R. O. 1987. *Statistical methods for environmental pollution monitoring*. New York: Van Nostrand Reinhold.
- Goly, A., and R. S. V. Teegavarapu. 2014. "Individual and coupled influences of AMO and ENSO on regional precipitation characteristics and extremes." *Water Resour. Res.* **50** (6): 4686–4709.
- Goyal, M. K., D. H. Burn, and C. S. P. Ojha. 2013. "Precipitation simulation based on k-nearest neighbor approach using gamma kernel." *J. Hydrol. Eng.* **15** (5): 481–487.
- GPM (Global Precipitation Measurement). 2019. "Global precipitation measurement." Accessed December 2018. <https://pmm.nasa.gov/GPM>.
- Grayson, R., and G. Blöschl. 2001. *Spatial patterns in catchment hydrology: Observations and modeling*. Cambridge, UK: Cambridge University Press.
- Greenwood, J. A., J. M. Landwehr, N. C. Matalas, and J. R. Wallis. 1979. "Probability weighted moments: Definition and relation to parameters of several distributions expressable in inverse form." *Water Resour. Res.* **15** (5): 1049–1054.

- Gringorten, I. I. 1963. "A plotting rule for extreme probability paper." *J. Geophys. Res.* **68** (3): 813–814.
- Groisman, P. Y., et al. 1999. "Changes in the probability of heavy precipitation: Important indicators of climatic change." *Clim. Change* **42** (1): 243–283.
- Grum, M., A. T. Jørgensen, R. M. Johansen, and J. J. Linde. 2006. "The effect of climate change on urban drainage: An evaluation based on regional climate model simulation." *Water Sci. Technol.* **54** (6–7): 9–15.
- Gupta, R. 2008. *Hydrology and hydraulic systems*. Long Grove, IL: Waveland.
- Guttman, N. B. 1994. "On the sensitivity of sample L moments to sample size." *J. Clim.* **7** (6): 1026–1029.
- Guttman, N. B. 1999. "Accepting the standardized precipitation index: A calculation algorithm." *J. Am. Water Resour. Assoc.* **35** (2): 311–322.
- Guttman, N. B., J. R. M. Hosking, and J. R. Wallis. 1993. "Regional precipitation quantile values for the continental United States computed from L-moments." *J. Clim.* **6** (12): 2326–2340.
- Hansen, E. M., L. C. Schreiner, and J. F. Miller. 1982. *Application of probable maximum precipitation estimates: United States east of the 105th meridian*. Hydrometeorological Rep. No. 52. Washington, DC: National Weather Service.
- Hanson, L. and R. Vogel. 2008. "The probability distribution of daily rainfall in the United States." In *Proc., World Environmental and Water Resources Congress*, 1–10.
- Hayhoe, H., et al. 2004. "Emissions pathways, climate change, and impacts on California." *Proc. Natl. Acad. Sci.* **101** (12): 422–427.
- Hazen, A. 1930. *Flood flows: A study of frequencies and magnitudes*. New York: Wiley.
- Helsel, D. R., and R. M. Hirsch. 2002. "Statistical methods in water resources." In *Hydrologic analysis and interpretation*. Reston, VA: US Geological Survey.
- Hershfield, D. M. 1961. *Rainfall frequencies atlas of the United States for durations from 30 minutes to 24 hours and return periods from 1 to 100 years*. Technical Paper No. 40. Washington, DC: US Weather Bureau.
- Hershfield, D. M. 1965. "Method for estimating probable maximum rainfall." *J. Am. Water Assoc.* **57** (8): 965–972.
- Hoblit, B., and D. Curtis. 2000. "Next generation rainfall data." In *Proc., ASCE Watershed and Operations Management 2000 Conf.* Reston, VA: ASCE.
- Hoblit, B. C., B. E. Vieux, A. W. Holder, and P. B. Bedient. 1999. "Prediction with precision." *Civ. Eng.* **69** (11): 40–43.
- Hodgson, M. E. 1989. "Searching methods for rapid grid interpolation." *Prof. Geogr.* **41** (1): 51–61.
- Hollander, M., and D. A. Wolfe. 1999. *Nonparametric statistical methods*. Hoboken, NJ: Wiley.
- Hosking, J. R. M. 1990. "L-moments: Analysis and estimation of distributions using linear combination of order statistics." *J. R. Stat. Soc. Ser. B (Methodol.)* **52** (1): 105–124.
- Hosking, J. R. M., and J. R. Wallis. 1997. *Regional frequency analysis: An approach based on l-moments*. Cambridge, UK: Cambridge University Press.
- Hosking, J. R. M., J. R. Wallis, and E. F. Wood. 1985. "Estimation of the generalized extreme value distribution by the method of probability-weighted moments." *Technometrics* **27** (3): 251–261.
- Huebner, R. S., C. S. Pathak, and B. C. Hoblit. 2003. "Development and use of a NEXRAD database for water management in south Florida." In *Proc., ASCE World Water and Environmental Resources Congress*. Reston, VA: ASCE.
- Huffman, G. J., R. F. Adler, E. F. Stocker, D. T. Bolvin, and E. J. Nelkin. 2003. "Analysis of TRMM 3-hourly multi-satellite precipitation estimates computed in both real and post-real time." In *Proc., 12th Conf. Satellite Meteorology and Oceanography*. Washington, DC: American Meteorological Society.
- Husak, G. J., J. Michaelsen, and C. Funk. 2007. "Use of the gamma distribution to represent monthly rainfall in Africa for drought monitoring applications." *Int. J. Climatol.* **27** (7): 935–944.
- IPCC (Intergovernmental Panel on Climate Change). 2007a. *Climate change 2007: The physical science basis. Contribution of working group I to the fourth assessment report of the Intergovernmental Panel on Climate Change*, edited by S. Solomon, et al., 1–18. Cambridge, UK: Cambridge University Press.
- IPCC. 2007b. "Summary for policymakers." In *Climate change 2007: The physical science basis. Contribution of working group I to the fourth assessment report of the Intergovernmental Panel on Climate Change*, edited by S. Solomon, et al. Cambridge, UK: Cambridge University Press.
- Jain, D., and V. P. Singh. 1987. "Comparison of some flood frequency distributions using empirical data." In *Hydrologic frequency model*, edited by V. P. Singh, 467–485. Dordrecht, Netherlands: D. Reidel Publishing.
- Jarque, C. M., and A. K. Bera. 1987. "A test for normality of observations and regression residuals." *Int. Stat. Rev.* **55** (2): 163–172.

- Kang, H. M., and F. Yusof. 2013. "Determination of best-fit distribution and rainfall events in Damansara and Kelantan, Malaysia." *Matematika* **29** (1): 43–52.
- Kannan, K. S., and A. J. Farook. 2015. "Stochastic simulation of precipitation using Markov chain-mixed exponential model." *Appl. Math. Sci.* **9** (65): 3205–3512.
- Kasperska-Wołowicz, W., K. Smarzyńska, Z. Miatkowski, T. Bolewski, and R. Farat. 2016. "Monthly precipitation patterns in a region vulnerable to climate-related hazards—A case study from Poland." *Water* **8** (9): 362.
- Kazmierczak, B., and A. Kotowski. 2015. "The suitability assessment of a generalized exponential distribution for the description of maximum precipitation amounts." *J. Hydrol.* **525** (2015): 345–351.
- Kennedy, M. R., H. J. Pearce, R. P. Canterford, and L. J. Mintz. 1988. "The estimation of generalized probable maximum precipitation in Australia." In *Proc., Workshop on Spillway Design Floods*, 79. Hobart, Australia: ANCOLD.
- Kidder, S. G., and T. H. V. Haar. 1995. *Satellite meteorology: An introduction*. San Diego: Academic Press.
- Kite, G. W. 1977. *Frequency and risk analysis in hydrology*. Fort Collins, CO: Water Resources Publications.
- Kolokytha, E., C. O. Galvao, and R. Teegavarapu. 2016. "Climate change impacts and water resource management and planning" In *Sustainable water resources planning and management under climate change*, edited by E. Kolokytha, S. Oishi, and R. Teegavarapu, Singapore: Springer.
- Kotei, R., N. Kyei-Baffour, E. Ofori, and W. A. Agyare. 2013. "Establishment of rainfall intensity-duration-frequency (IDF) curves for Mampong-ashanti municipal area of the Ashanti Region in Ghana." *J. Eng. Appl. Sci.* **8** (9): 693–698.
- Kothiyari, U. C., and R. J. Garde. 1992. "Rainfall intensity-duration-frequency formula for India." *J. Hydraul. Eng.* **118** (2): 323–336.
- Krajewski, W. F. 1987. "Co-kriging of radar and rain gage data." *J. Geophys. Res.* **92** (D8): 9571–9580.
- Krakauer, N. Y., S. M. Pradhanang, J. Panthi, T. Lakhankar, and A. K. Jha. 2015. "Probabilistic precipitation estimation with a satellite product." *Climate* **3** (2): 329–348.
- Kronenberg, R., J. Franke, and C. Bernhofer. 2014. "Comparison of different approaches to fit log-normal mixtures on radar-derived precipitation data." *Meteorol. Appl.* **21** (3): 743–754.
- Kysely, J., and J. Picek. 2007. "Regional growth curves and improved design value estimates of extreme precipitation events in the Czech Republic." *Clim. Res.* **33** (3): 243–255.
- Laurenson, E. M. 1987. "Back to basics on flood frequency analysis." *Civ. Eng. Trans.* **29** (2): 47–53.
- Lebel, T., and J. P. Laborde. 1988. "A geostatistical approach for areal rainfall statistics assessment." *Stochastic Hydrol. Hydraul.* **2** (4): 245–261.
- Lee, S. H., and S. J. Maeng. 2003. "Frequency analysis of extreme rainfall using Lmoment." *Irrig. Drain.* **52** (3): 219–230.
- Lehmann, E. A., A. Phatak, S. Soltyk, J. Chia, R. Lau, and M. Palmer. 2013. "Bayesian hierarchical modelling of rainfall extremes." In *Proc., 20th Int. Congress Modelling and Simulation*, 2806–2812. Adelaide, Australia: Australian Mathematical Sciences Institute.
- Leivikov, M. L. 1955. *Meteorology, hydrology, and hydrometry*. 2nd ed. Moscow, Russia: Sel'khozgiz.
- Li, H., J. Sheffield, and E. F. Wood. 2010. "Bias correction of monthly precipitation and temperature fields from Intergovernmental Panel on Climate Change AR4 models using equidistant quantile matching." *J. Geophys. Res.* **115**: D10101.
- Li, L., L. Zhao, Y. Gong, F. Tian, and Z. Wang. 2012. "Probability distribution of summer daily precipitation in the Huaihe Basin of China based on gamma distribution." *Acta Meteorol. Sin.* **26** (1): 72–84.
- Li, Z., F. Brissette, and J. Chen. 2013. "Finding the most appropriate precipitation probability distribution for stochastic weather generation and hydrological modeling in Nordic watersheds." *Hydrol. Processes* **27** (25): 3718–3729.
- Li, Z., Z. Li, W. Zhao, and Y. Wang. 2015. "Probability modeling of precipitation extremes over two river basins in northwest of China." *Adv. Meteorol.* **2015**: 1–13.
- Lilliefors, H. W. 1967. "On the Kolmogorov-Smirnov test for normality with mean and variance unknown." *J. Am. Stat. Assoc.* **62** (318): 399–402.
- Liu, Y., W. Zhang, Y. Shao, and K. Zhang. 2011. "A comparison of four precipitation distribution models used in daily stochastic models." *Adv. Atmos. Sci.* **28** (4): 809–820.
- Ljung, G. M., and G. E. P. Box. 1978. "On a measure of a lack of fit in time series models." *Biometrika* **65** (2): 297–303.

- Longobardi, A., and P. Villani. 2009. "Trend analysis of annual and seasonal rainfall time series in the Mediterranean area." *Int. J. Climatol.* **30** (10): 1538–1546.
- Lu, X. 2006. *Guidance on the development of regional climate scenarios for application in climate change vulnerability and adaptation assessments within the framework of national communications from parties not included in Annex I to the United Nations Framework Convention on Climate Change*. New York: National Communications Support Programme, UNDP–UNEP–GEF.
- Madsen, H., P. S. Mikkelsen, D. S. Rosbjerg, and P. Harremoes. 2002. "Regional estimation of rainfall intensity-duration-frequency curves using generalized least squares regression of partial duration series statistics." *Water Resour. Res.* **38** (11): 21-1–21-11.
- Mage, D. T. 1982. "An objective graphical method for testing normal distributional assumptions using probability plots." *Am. Stat.* **36** (2): 116–120.
- Mahdavi, M., K. Osati, S. A. N. Sadeghi, B. Karimi, and J. Mobaraki. 2010. "Determining suitable probability distribution models for annual precipitation data (a case study of Mazandaran and Golestan Provinces)." *J. Sustainable Dev.* **3** (1): 159–168.
- Makkonen, L. 2006. "Plotting positions in extreme value analysis." *J. Appl. Meteor. Climatol.* **45** (2): 334–340.
- Marchenko, Y. V., and M. G. Genton. 2010. "Multivariate log-skew-elliptical distributions with applications to precipitation data." *Environmetrics* **21** (3–4): 318–340.
- Martínez-Flórez, G., S. Vergara-Cardozo, and L. M. González. 2013. "The family of log-skew-normal alpha-power distributions using precipitation data." *Rev. Colomb. Estadística* **36** (1): 43–57.
- Massey, F. J., Jr. 1967. "The Kolmogorov-Smirnov test for goodness-of-fit." *J. Am. Stat. Assoc.* **46** (253): 68–78.
- Maurer, E. P., and H. G. Hidalgo. 2008. "Utility of daily vs. monthly largescale climate data: An intercomparison of two statistical downscaling methods." *Hydrol. Earth Syst. Sci.* **12** (2): 551–563.
- Mayooran, T., and A. Laheetharan. 2014. "The statistical distribution of annual maximum rainfall in Colombo District." *Sri Lankan J. Appl. Stat.* **15** (2): 107–130.
- McBean, A. E., and F. A. Rovers. 1998. *Statistical procedures for analysis of environmental monitoring data and risk assessment*. Upper Saddle River, NJ: Prentice Hall.
- McCuen, R. H. 2003. *Hydrologic analysis and design*. Upper Saddle River, NJ: Prentice-Hall.
- McKee, T. B., N. J. Doesken, and J. Kleist. 1993. "The relationship of drought frequency and duration to time scale." In *Proc., 8th Conf. on Applied Climatology*, 179–184. Boston: American Meteorological Society.
- McKee, T. B., N. J. Doesken, and J. Kleist. 1995. "Drought monitoring with multiple timescales." In *Proc., 9th Conf. on Applied Climatology*, 233–236. Boston: American Meteorological Society.
- Meischner, P. 2005. *Weather radar: Principles and Advanced Applications: Physics of earth and space environments*. New York: Springer.
- Mekonnen, G., and F. Hossain, eds. 2010. *Satellite rainfall applications for surface hydrology*. New York: Springer.
- Meucci, A. 2009. *Risk and asset allocation*. Berlin: Springer.
- Millard, S. P., and N. K. Neerchal. 2000. *Environmental statistics with S-plus*. Boca Raton, FL: CRC Press.
- Miller, J. F. 1964. *Two-to ten-day precipitation for return periods of 2 to 100 years in the contiguous United States*. Technical Rep. No. 49. Washington, DC: US Weather Bureau.
- Miller, J. F. 1972. "Physiographically adjusted precipitation frequency maps: Distribution of precipitation in mountainous areas." *World Meteorol. Org.* **326** (11): 264–277.
- Milly, P. C. D., J. Betancourt, M. Falkenmark, R. M. Hirsch, Z. W. Kundzewicz, D. P. Lettenmaier, and R. J. Stouffer. 2008. "Stationarity is dead: Whither water management." *Science* **319** (5863): 573–574.
- Min, S., X. Zhang, F. W. Zwiers, P. Friederichs, and A. Hense. 2009. "Signal detectability in extreme precipitation changes assessed from twentieth century climate simulations." *Clim. Dyn.* **32** (1): 95–111.
- Modley, D. A. 1973. "Gamma distribution probability model for Asian summer monsoon monthly rainfall." *Mon. Weather Rev.* **101** (2): 160–176.
- Naoum, S., and I. K. Tsanis. 2003. "Temporal and spatial variation of annual rainfall on the island of Crete, Greece." *Hydrol. Processes* **17** (10): 1899–1922.
- Neykov, N. M., P. N. Neytchev, and W. Zucchini. 2014. "Stochastic daily precipitation model with a heavy-tailed component." *Nat. Hazards Earth Syst. Sci.* **14** (9): 2321–2335.
- Nguyen, V., and A. Mayabi. 1990. "Probabilistic analysis of summer daily rainfall for the Montreal region." *Can. Water Resour. J.* **15** (3): 65–80.
- NIST (National Institute of Standards and Technology). 2011. "NIST/SEMATECH ehandbook of statistical methods." Accessed December 2012. <http://www.itl.nist.gov/div898/handbook/>.

- NOAA. 2016. "NOAA's weather service, Hydrometeorological design study center: Frequently asked questions." Accessed October 2016. <http://www.nws.noaa.gov/oh/hpsc/FAQ.html>.
- Nott, J. 2006. *Extreme events: A physical reconstruction and risk assessment*. Cambridge, UK: Cambridge University Press.
- Nyatuame, M., V. Owusu-Gyimah, and F. Ampiah. 2014. "Statistical analysis of rainfall trend for Volta region in Ghana." *Int. J. Atmos. Sci.* **2014**: 1–11.
- O'Sullivan, D., and D. J. Unwin. 2003. *Geographical information analysis*. Hoboken, NJ: Wiley.
- Ott, W. R. 1995. *Environmental statistics and data analysis*. Boca Raton, FL: CRC Press.
- Overeem, A., A. Buishand, and I. Holleman. 2008. "Rainfall depth-duration-frequency curves and their uncertainties." *J. Hydrol.* **348** (1–2): 124–134.
- Ozcan, O., B. Bookhagen, and N. Musaoglu. 2013. "Analyzing spatiotemporal patterns of extreme precipitation event in southeastern Anatolia." *Int. Arch. Photogramm. Remote Sens. Spatial Inform. Sci.* **7**: 195.
- Öztekin, T. 2007. "Wakeby distribution for representing annual extreme and partial duration rainfall series." *Meteorol. Appl.* **14** (4): 381–387.
- Pagliara, S., and C. Vitti. 1993. "Discussion of rainfall intensity-duration-frequency formula for India." *J. Hydraul. Eng.* **119** (8): 962–966.
- Panagoulia, D., P. Economou, and C. Caroni. 2014. "Stationary and nonstationary generalized extreme value modelling of extreme precipitation over a mountainous area under climate change." *Environmetrics* **25** (1): 29–43.
- Panofsky, H. A., and G. W. Brier. 1968. *Some application of statistics to meteorology*. University Park, PA: Penn State University Press.
- Papalexiou, S. M., and D. Koutsoyiannis. 2006. "A probabilistic approach to the concept of probable maximum precipitation." *Adv. Geosci.* **7**: 51–54.
- Papalexiou, S. M., D. Koutsoyiannis, and C. Makropoulos. 2013. "How extreme is extreme? An assessment of daily rainfall distribution tails." *Hydrol. Earth Syst. Sci.* **17** (2): 851–862.
- Park, J. S., and H. S. Jung. 2002. "Modelling Korean extreme rainfall using a kappa distribution and maximum likelihood estimate." *Theor. Appl. Climatol.* **72** (1–2): 55–64.
- Park, J. S., H. S. Jung, R. S. Kim, and J. H. Oh. 2001. "Modelling summer extreme rainfall over Korean peninsula using Wakeby distribution." *Int. J. Climatol.* **21** (11): 1371–1384.
- Partal, T., and E. Kahya. 2006. "Trend analysis in Turkish precipitation data." *Hydrol. Processes* **20** (9): 2011–2026.
- Pathak, C., and R. S. V. Teegavarapu. 2018. *Radar rainfall data estimation and use*. Reston, VA: ASCE.
- Pearson, E. S. 1931. "Note on tests for normality." *Biometrika* **22** (3–4): 423–424.
- Penide, G., V. V. Kumar, A. Protat, and P. T. May. 2013. "Statistics of drop size distribution parameters and rain rates for stratiform and convective precipitation during the north Australian wet season." *Mon. Weather Rev.* **141** (9): 3222–3237.
- Pettitt, A. N. 1979. "A non-parametric approach to the change-point problem." *Appl. Stat.* **28** (2): 126–135.
- Pilon, P. J., K. Adamowski, and Y. Alila. 1991. "Regional analysis of annual maxima precipitation using L-moments." *Atmos. Res.* **27** (1–3): 81–92.
- Rabinovich, G. S. 2005. *Measurement errors and uncertainties: Theory and practice*. New York: Springer.
- Raghavan, S. 2003. *Radar meteorology*. Dordrecht, Netherlands: Springer.
- Raheem, M. A., W. B. Yahya, and K. O. Obisesan. 2015. "A Markov chain approach on pattern of rainfall distribution." *J. Environ. Stat.* **7** (1): 1–13.
- Rakhecha, P. R., and V. P. Singh. 2009. *Applied hydrometeorology*. New Delhi: Springer.
- Rana, A., K. Foster, T. Bosshard, J. Olsson, and L. Bengtsson. 2014. "Impact of climate change on rainfall over Mumbai using distribution-based scaling of global climate model projections." *J. Hydrol. Reg. Stud.* **1** (1): 107–128.
- Rulfová, Z., A. Buishand, M. Roth, and J. Kysely. 2016. "A two-component generalized extreme value distribution for precipitation frequency analysis." *J. Hydrol.* **534**: 659–668.
- Rycroft, H. B. 1949. "Random sampling of rainfall." *J. South Afr. For. Assoc.* **18** (1): 71–81.
- Saito, H., and H. Matsuyama. 2015. "Probable hourly precipitation and soil water index for 50-yr recurrence interval over the Japanese archipelago." *SOLA* **11**: 118–123.
- Salas, J. D.-J. 1993. "Analysis and modeling of hydrological time series." In *Handbook of hydrology*, edited by D. R. Maidment. New York: McGraw-Hill.

- Santos, E. B., P. S. Lucio, and C. M. S. Silva. 2016. "Estimating return periods for daily precipitation extreme events over the Brazilian Amazon." *Theor. Appl. Climatol.* **126** (3–4): 585–595.
- Satterthwaite, F. E. 1946. "An approximate distribution of estimates of variance components." *Biom. Bull.* **2** (6): 110–114.
- Schonwiese, C.-D., J. Grieser, and S. Tromel. 2003. "Secular change of extreme monthly precipitation in Europe." *Theor. Appl. Climatol.* **75** (3–4): 245–250.
- Schuenemeyer, J. H., and L. J. Drew. 2010. *Statistics for earth and environmental scientists*. New York: Wiley.
- SCS (Soil Conservation Service). 1986. *Urban hydrology for small watersheds: Technical Release No. 55*. Washington, DC: US Dept. of Agriculture.
- Selker, J. S., and D. A. Haith. 1990. "Development and testing of single-parameter precipitation distributions." *Water Resour. Res.* **26** (11): 2733–2740.
- Sen, P. K. 1968. "Estimates of the regression coefficient based on Kendall's Tau." *J. Am. Stat. Assoc.* **63** (324): 1379–1389.
- Sene, K. 2009. *Hydrometeorology: Forecasting and applications*. New York: Springer.
- Seo, D.-J., W. F. Krajewski, and D. S. Bowles. 1990a. "Stochastic interpolation of rainfall data from rain gages and radar using cokriging. 1: Design of experiments." *Water Resour. Res.* **26** (3): 469–477.
- Seo, D.-J., W. F. Krajewski, A. Azimi-Zonooz, and D. S. Bowles. 1990b. "Stochastic interpolation of rainfall data from rain gages and radar using cokriging. 2: Results." *Water Resour. Res.* **26** (5): 915–924.
- Servuk, B., and H. Geiger. 1981. *Selection of distribution types for extremes of precipitation*. Rep. No. 15. Geneva: World Meteorological Organization.
- Servuk, B., and W. R. Hamon. 1984. *International comparison of national precipitation gages with a reference pit gage*. Instruments and Observing Methods Rep. No. 17. Geneva: World Meteorological Organization.
- Servuk, B., and S. Klemm. 1989. "Types of standard precipitation gages." In *WMO/IAHS/ETH International Workshop on Precipitation Measurement*. St. Moritz.
- Shapiro, S. S., and M. B. Wilk. 1965. "An analysis of variance test for normality (complete samples)." *Biometrika* **52** (3–4): 591–611.
- Sharma, M. A., and J. B. Singh. 2010. "Use of probability distribution in rainfall analysis." *New York Sci. J.* **3** (9): 40–49.
- Shepard, D. 1968. "A two-dimensional interpolation function for irregularly spaced data." In *Proc., 23rd National Conf. on Association for Computing Machinery*, 517–524. New York: ACM.
- Sheskin, D. J. 2003. *Handbook of parametric and nonparametric statistical procedures*. Boca Raton, FL: Chapman and Hall/CRC.
- Shimazaki, H., and S. Shinomoto. 2007. "A method for selecting the bin size of a time histogram." *Neural Comput.* **19** (6): 1503–1527.
- Shimazaki, H., and S. Shinomoto. 2010. "Kernel bandwidth optimization in spike rate estimation." *J. Comput. Neurosci.* **29** (1–2): 171–182.
- Shuttleworth, W. J. 2012. *Terrestrial hydrometeorology*. Hoboken, NJ: Wiley.
- Simanton, J. R., and H. B. Osborn. 1980. "Reciprocal-distance estimate of point rainfall." *J. Hydraul. Eng. Div.* **106** (7): 1242–1246.
- Small, M. J. 1990. "Probability distributions and statistical estimation." In *Uncertainty: A guide to dealing with uncertainty in quantitative risk and policy analysis*, edited by M. G. Morgan and M. Henrion. Cambridge, MA: Cambridge University Press.
- Sokolov, A. A., S. E. Rantz, and M. Roche. 1976. *Floodflow computation: Methods compiled from world experience, studies and reports in hydrology*. Rep. No. 22. Paris: UNESCO.
- Srnirnov, N. V. 1939. "Estimate of derivation between empirical distribution functions in two independent samples." [In Russian.] *Bull. Moscow Univ.* **2**: 3–16.
- Stedinger, J. 2000. "Flood frequency analysis and statistical estimation of flood risk." In *Inland flood hazards: Human, riparian, and aquatic communities*, edited by E. E. Whol. Cambridge, UK: Cambridge University Press.
- Steinskog, J. D., D. B. Tjøstheim, and N. G. Kvamstø. 2007. "A cautionary note on the use of the Kolmogorov-Smirnov test for normality." *Mon. Weather Rev.* **135** (3): 1151–1157.
- Stedinger, J. R., R. M. Vogel, and E. Foufoula-Georgiou. 1992. "Frequency analysis of extreme events." In *Handbook of hydrology*, edited by D. Maidment. New York: McGraw-Hill.

- Strangeways, I. 2003. *Measuring the natural environment*. 2nd ed. Cambridge, UK: Cambridge University Press.
- Strangeways, I. 2007. *Precipitation: Theory, measurement and distribution*. Cambridge, UK: Cambridge University Press.
- Su, B., Z. W. Kundzewicz, and T. Jiang. 2009. "Simulation of extreme precipitation over the Yangtze River Basin using Wakeby distribution." *Theor. Appl. Climatol.* **96** (3–4): 209–219.
- Suhaila, J., K. Ching-Yee, Y. Fadhilah, and F. Hui-Mean. 2011. "Introducing the mixed distribution in fitting rainfall data." *Open J. Mod. Hydrol.* **1** (2): 11–22.
- Sun, Y., K. P. Bowman, M. G. Genton, and A. Tokay. 2015. "A Matern model of the spatial covariance structure of point rain rates." *Stochastics Environ. Res. Risk Assess.* **29** (2): 411–416.
- Svensson, C., and D. Jones. 2010. "Review of rainfall frequency estimation methods." *J. Flood Risk Manage.* **3** (4): 296–313.
- Teegavarapu, R. S. V. 2007a. "Estimation of missing precipitation data using soft computing based spatial interpolation techniques." In *Proc., AGU Fall Meeting*, H13H–1683. Washington, DC: AGU.
- Teegavarapu, R. S. V. 2007b. "Use of universal function approximation in variance dependent surface interpolation technique: An application in hydrology." *J. Hydrol.* **332** (1–2): 16–29.
- Teegavarapu, R. S. V. 2009. "Estimation of missing precipitation records integrating surface interpolation techniques and spatio-temporal association rules." *J. Hydroinf.* **11** (2): 133–146.
- Teegavarapu, R. S. V. 2012a. *Floods in changing climate: Extreme precipitation*. Cambridge, UK: Cambridge University Press.
- Teegavarapu, R. S. V. 2012b. "Spatial interpolation using non-linear mathematical programming models for estimation of missing precipitation records." *Hydrol. Sci.* **57** (3): 383–406.
- Teegavarapu, R. S. V. 2013a. "Climate change-sensitive hydrologic design under uncertain future precipitation extremes." *Water Resour. Res.* **49** (11): 7804–7814.
- Teegavarapu, R. S. V. 2013b. "Statistical corrections of spatially-interpolated missing precipitation data estimates." *Hydro. Processes* **28** (11): 3789–3808.
- Teegavarapu, R. S. V. 2016a. "Climate variability and changes in precipitation extremes and characteristics." In *Sustainable water resources planning and management under climate change*, edited by E. Kolokytha, S. Oishi, and R. Teegavarapu. Basel, Switzerland: Springer.
- Teegavarapu, R. S. V. 2016b. "Spatial and temporal estimation and analysis of precipitation." In *Handbook of applied hydrology*. New York: McGraw Hill.
- Teegavarapu, R. S. V. 2018. *Trends and changes in hydroclimatic variables: Links to climate variability and change*. New York: Elsevier.
- Teegavarapu, R. S. V., A. Aly, C. S. Pathak, J. Ahlquist, H. Fuelberg, and J. Hood. 2017. "Infilling missing precipitation records using variants of spatial interpolation and data-driven methods: Use of optimal weighting parameters and nearest neighbor-based corrections." *Int. J. Climatol.* **38** (2): 776–793.
- Teegavarapu, R. S. V., and P. Bajaj. 2008. "Optimal spatial weighting methods for estimation of missing rain gauge records." In *Proc., World Environmental and Water Resources Congress*, Reston, VA: ASCE.
- Teegavarapu, R. S. V., and V. Chandramouli. 2005. "Improved weighting methods, deterministic and stochastic data-driven models for estimation of missing precipitation records." *J. Hydrol.* **312** (1–4): 191–206.
- Teegavarapu, R. S. V., and A. Goly. 2011. *Assessment of spatial and temporal variation of extreme precipitation events in coastal basins of SFWMD region*. SFWMD Final Report. West Palm Beach, FL: South Florida Water Management District.
- Teegavarapu, R. S. V., A. Goly, and J. Obeysekera. 2013. "Influences of Atlantic multidecadal oscillation phases on spatial and temporal variability of regional precipitation extremes." *J. Hydrol.* **495**: 74–93.
- Teegavarapu, R. S. V., A. Goly, C. Viswanathan, and P. Behera. 2012. "Precipitation extremes and climate change: Evaluation using descriptive WMO indices." In *Proc., World Environmental and Water Resources Conf.* Reston, VA: ASCE.
- Teegavarapu, R. S. V., A. Goly, and Q. Wu. 2016. "Comprehensive framework for assessment of radar-based precipitation estimates." *J. Hydrol. Eng.* **22** (5): E4015002.
- Teegavarapu, R. S. V., and A. Nayak. 2017. "Evaluation of long-term trends in extreme precipitation: Implications of infilled historical data and temporal-window based analysis." *J. Hydrol.* **550**: 616–634.

- Teegavarapu, R. S. V., A. Nayak, and C. Pathak. 2011. "Assessment of long-term trends in extreme precipitation: Implications of in-filled historical data and temporal window-based analysis." In *Proc., World Environmental and Water Resources Congress*.
- Teegavarapu, R. S. V., and S. Oishi. 2016. *Evaluation of trends and variability in sea level, temperature and precipitation of Japan: Links to climate variability and change*. Kobe, Japan: Kobe Univ.
- Teegavarapu, R. S. V., and C. Pathak. 2008. "Infilling of rain gage records using radar (NEXRAD) data: Influence of spatial and temporal variability of rainfall processes." In *Proc., World Environmental and Water Resources Conf.*, edited by R. W. Babcock and R. Walton. Reston VA: ASCE.
- Teegavarapu, R. S. V., and C. Pathak. 2012. "Development of optimal Z-R relationships, weather radar and hydrology." *Int. Assoc. Hydrol. Sci.* **351**: 75–80.
- Teegavarapu, R. S. V., C. S. Pathak, J. R. Mecikalski, and J. Srikishen. 2015. "Optimal solar radiation sensor network design using spatial and geostatistical analyses." *J. Spatial Sci.* **61** (1): 69–97.
- Teegavarapu, R. S. V., M. Tufail, and L. Ormsbee. 2009. "Optimal functional forms for estimation of missing precipitation records." *J. Hydrol.* **374** (1–2): 106–115.
- Thode, H. J. 2002. *Testing for normality*. New York: Marcel Dekker.
- Thom, H. C. S. 1966. *Some methods of climatological analysis*. WMO No. 199 Technical Note No. 81. Geneva: World Meteorological Organization.
- Thompson, S. A. 1999. *Hydrology for water management*. Dordrecht, Netherlands: Balkema.
- Tukey, J. W. 1962. "The future of data analysis." *Ann. Math. Stat.* **33** (1): 1–67.
- US Weather Bureau. 1976. *Hydrometeorology*. Reports 55A, 56, and 57. Washington, DC: US Weather Bureau.
- USEPA. 2000. *Guidance for data quality assessment: Practical methods for data analysis*. EPA QA/G-9. Washington, DC: Environmental Protection Agency.
- Vidakovic, B. 2011. *Statistics for bioengineering sciences with MATLAB and WinBUGS support*. New York: Springer.
- Vieux, B. E. 2006. *Distributed hydrologic modeling using GIS Water Science and Technology Library*. Dordrecht, Netherlands: Kluwer Academic.
- Vieux, B. E. 2006. "Rain gauge network optimization study." Rep. West Palm Beach, FL: South Florida Water Management District (SFWMD).
- Vieux, B. E., and J. E. Vieux. 2005a. "Rainfall accuracy considerations using radar and rain gage networks for rainfall-runoff monitoring." In *Effective modeling of urban water systems*. Monograph 13, edited by W. James, K. N. Irvine, E. A. McBean, and R. E. Pitt. Guelph, Canada: CHI.
- Vieux, B. E., and J. E. Vieux. 2005b. "Statistical evaluation of a radar rainfall system for sewer system management." *J. Atmos. Res.* **77** (1–4): 322–336.
- Vivekanandan, N. 2014. "Rainfall frequency analysis using L-moments of probability distributions." *Int. J. Comput. Appl. Eng. Technol.* **3** (3): 248–256.
- Vivekanandan, N., and S. K. Roy. 2013. "Assessment of probable maximum precipitation using Gumbel distribution and Hershfield method." *Bonfring Int. J. Data Min.* **3** (1): 1–5.
- Vlček, O., and R. Huth. 2009. "Is daily precipitation gamma-distributed? Adverse effects of an incorrect use of the Kolmogorov-Smirnov test." *Atmos. Res.* **93** (2009): 759–766.
- Vogel, R. M., and N. M. Fennessey. 1994. "Flow-duration curves 2. New interpretation and confidence-intervals." *J. Water Resour. Plann. Manage.* **120** (4): 485–504.
- Volkova, T., A. Longobardi, and N. Krasnogorskaya. 2014. "Application of the stochastic model for precipitation generation in the complex orographic region (Bashkortostan Republic, Russian Federation)." *WSEAS Trans. Environ. Dev.* **10** (1): 434–443.
- von Neumann, J. 1941. "Distribution of the ratio of the mean square successive difference to the variance." *Ann. Math. Stat.* **12** (4): 367–395.
- von Storch, H., and F. W. Zwiers. 1999. *Statistical analysis in climate research*. Cambridge, MA: Cambridge University Press.
- Wakazuki, Y. 2011. "New distribution functions for hourly and daily precipitation intensities during the snowless season in Japan." *J. Meteorolog. Soc. Jpn.* **89** (1): 29–45.
- Wald, A., and J. Wolfowitz. 1943. "An exact test for randomness in the non-parametric case based on serial correlation." *Ann. Math. Stat.* **14** (4): 378–388.

- Wallis, J. R., M. G. Schaefer, B. I. Barker, and G. H. Taylor. 2007. "Regional precipitation-frequency analysis and spatial mapping for 24-hour and 2-hour durations for Washington State." *Hydrol. Earth Syst. Sci.* **11** (1): 415–442.
- Wang, W., X. Chen, P. Shi, and P. H. A. J. M. Van Gelder. 2008. "Detecting changes in extreme precipitation and extreme streamflow in the Dongjiang River Basin in southern China." *Hydrol. Earth Syst. Sci.* **12** (1): 207–221.
- Wei, T. C., and J. L. McGuinness. 1973. *Reciprocal distance squared method, a computer technique for estimating area precipitation*. Tech. Rep. ARS-Nc-8. North Central Region, OH: US Agricultural Research Service.
- Weibull, W. 1939. "A statistical theory of the strength of materials." In *Ingenjörs Vetenskaps Akademien Handlingar*. Vol. **151**. Stockholm, Sweden: Generalstabens Litografiska Anstalts Förlag.
- Weisner, C. J. 1970. *Hydrometeorology*. London: Chapman & Hall.
- Weiss, L. L. 1964. "Ratio of true to fixed-interval maximum rainfall." *J. Hydraul. Eng.* **90** (1): 77–82.
- Wilks, D. S. 1988. "Rainfall intensity, the Weibull distribution, and estimation of daily surface runoff." *J. Appl. Meteorol.* **28** (1): 52–58.
- Wilks, D. S. 2006. *Statistical methods in the atmospheric sciences*. San Diego: Academic Press.
- Wilson, J., and E. Brandes. 1979. "Radar measurement of rainfall: A summary." *Bull. Am. Meteorol. Soc.* **60** (9): 1048–1058.
- Wilson, P. S., and R. Toumi. 2005. "A fundamental probability distribution for heavy rainfall." *Geophys. Res. Lett.* **32** (14): 1–4.
- WMO (World Meteorological Organization). 1986. *Manual for estimation of probable maximum precipitation*. Operational Hydrology Rep. No. 1, WMO No. 332. Geneva: WMO.
- WMO. 1994. *Guide to hydrological practices: Data acquisition and processing, analysis, forecasting and other applications*. Geneva: WMO.
- WMO. 2009. *Guide to hydrological practices: Volume II management of water resources and application to hydrological practices*: WMO-No. 168. Geneva: WMO.
- WMO. 2010. *Guidelines on analysis of extremes in a changing climate in support of informed decisions for adaptation*. Geneva: WMO.
- WMO. 2012. *Standard precipitation index user guide*: WMO-No. 1090. Geneva: WMO.
- Wood, A. W., E. P. Maurer, A. Kumar, and D. P. Lettenmaier. 2002. "Long-range experimental hydrologic forecasting for the eastern United States." *J. Geophys. Res.* **107** (D20): ACL-6.
- Yates, F. 1934. "Contingency table involving small numbers and the χ^2 test." *J. R. Stat. Soc. 1 (suppl.)* **1** (2): 217–35.
- Yevjevich, V. 1972. *Probability and statistics in hydrology*. Highlands Ranch, CO: Water Resources Publications.
- Yilmaz, A. G., and B. J. C. Perera. 2015. "Spatiotemporal trend analysis of extreme rainfall events in Victoria, Australia." *Water Resour. Manage.* **29** (12): 4465–4480.
- Young, B. C., and B. M. McEnroe. 2003. "Sampling adjustment factors for rainfall recorded at fixed time intervals." *J. Hydrol. Eng.* **8** (5): 294–296.
- Yue, S., and M. Hashino. 2007. "Probability distribution of annual, seasonal and monthly precipitation in Japan." *Hydrol. Sci. J.* **52** (5): 863–877.
- Yue, S., and P. Pilon. 2004. "A comparison of the power of the t test, Mann-Kendall and bootstrap tests for trend detection." *Hydrol. Sci.* **49** (1): 21–37.

APPENDIX: CUMULATIVE PROBABILITY PLOTS OF PRECIPITATION DATA USING DIFFERENT PLOTTING POSITION FORMULAE

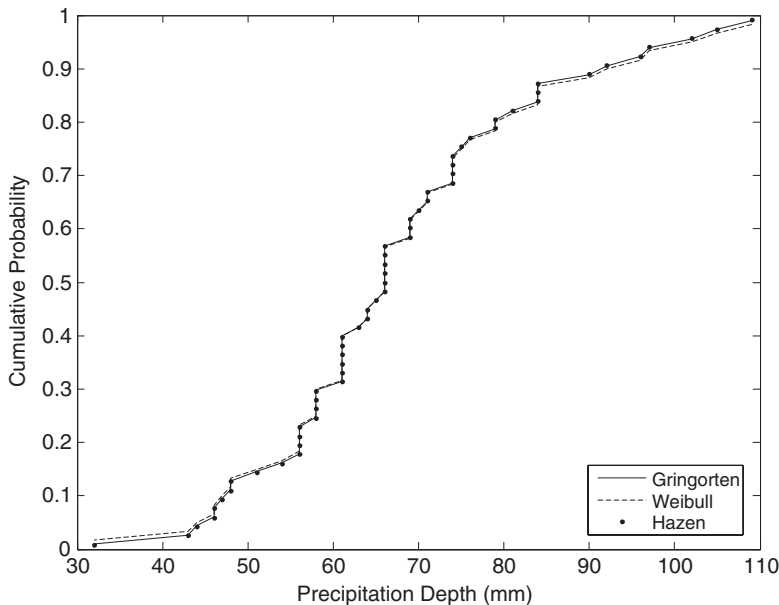


Figure A-1. Cumulative probability plots using different plotting position formulae for annual extreme rainfall depths for a duration of 1 h.

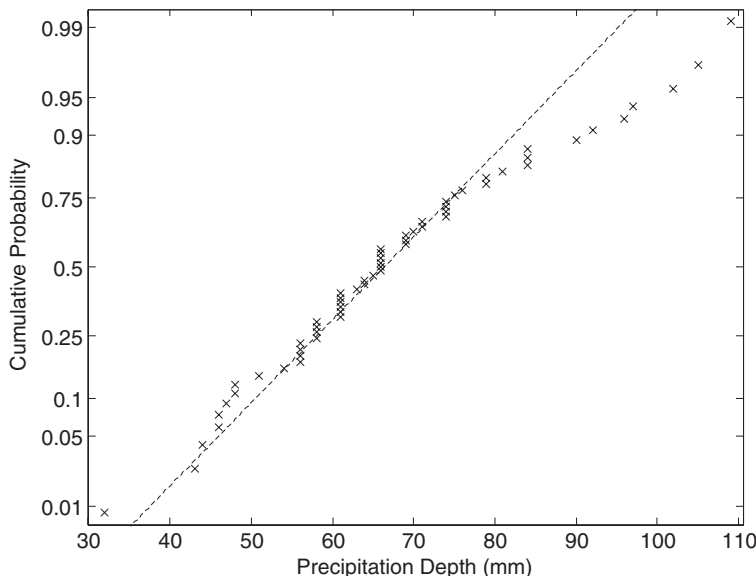


Figure A-2. Probability plot on normal probability paper for annual extreme rainfall depths for a duration of 2 h.

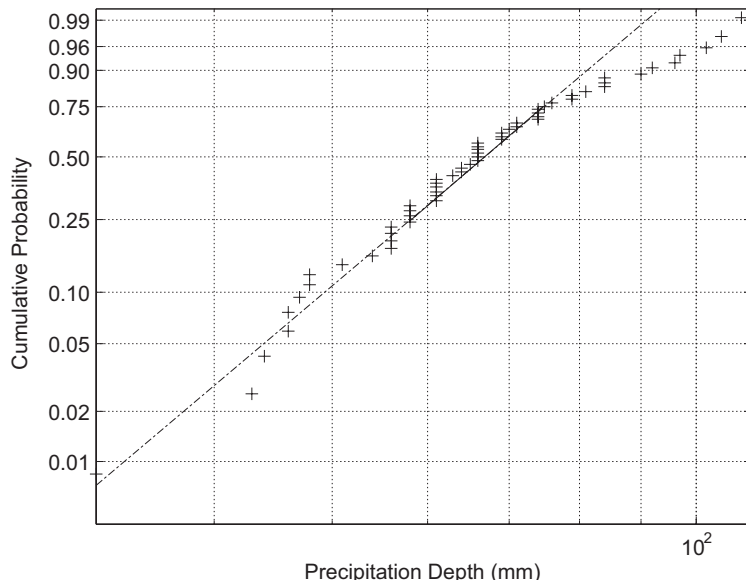


Figure A-3. Weibull probability plot for annual extreme rainfall depths for a duration of 2 h.

CHAPTER 3

Evapotranspiration and Evaporative Demand

Mike Hobbins
Gabriel Senay
Prasanna H. Gowda
Guleid Artan

3.0 INTRODUCTION

Evapotranspiration (ET) comprises the sum of fluxes of moisture from the terrestrial surface to the atmosphere or, more specifically, evaporation from ground and water surfaces and transpiration from vegetative canopies. Invisible, and indivisible enough to warrant the conflated term “evapotranspiration,” ET plays a critical role in regulating the earth’s hydrologic, climatic, and ecological dynamics at most time and space scales, while varying significantly across all of them. As a primary component of the land-surface water budget, ET consumes more than half of the solar energy received by the land surface (Trenberth et al. 2009) and returns about 60% of global land precipitation (P) to the atmosphere, or about $65,000 \text{ km}^3 \text{ year}^{-1}$ (Jung et al. 2010). In warm, humid land climates, as much as 50% of P may be water from upwind ET (Gash and Shuttleworth, 2007). In the United States, agricultural irrigation covers approximately 55 million ac (around $224,000 \text{ km}^2$, an area larger than the state of Utah), accounts for more than 80% of the water consumed, and has associated water rights worth more than \$200 billion (Rick Allen, Western States ET workshop 2012). Thus, ET should be considered an essential climate variable in the global water and energy cycle and in ecosystem performance; its accurate estimation is a national economic necessity. Further, an examination of changes in ET under a changing climate is crucial for food security: worldwide, the agricultural sector accounts for about two thirds of water withdrawals and 90% of water consumption.

3.0.1 Motivation

Despite its importance within global and local hydrologic cycles, ET remains difficult to estimate at scales useful to water managers, primarily due to the essentially uncertain nature of the distribution of limiting soil and vegetative moisture. As a result, hydrologists quantifying ET are often constrained to using the concept of *atmospheric evaporative demand* (E_0) to describe ET ’s upper limit; the ideal flux of E_0 has become central to hydrology in three primary uses. The first two use E_0 to derive ET through some parameterization of moisture availability (Θ), as typified by, first, land surface models (LSMs) used in such applications as river forecasting, and second, in field-scale irrigation scheduling. To provide E_0 in this latter use, the reference crop ET (ET_{rc}) concept is replacing the traditional evaporation pan; its estimation forms a central theme of this chapter. The

final use of E_0 is as a climatological indicator: in the crucial context of analyzing the impacts of climate change and variability, ET remains among the most sensitive of fluxes. Hydroclimatologists have found in E_0 an informative measure of the dryness of the lower atmosphere and, given a long worldwide history of observations (in the form of pan evaporation and increasingly ET_{rc}), attention has recently turned to the diagnostic potential of the E_0 record.

The many uses of and estimation techniques for ET and E_0 vary along many axes. Users need ET and E_0 estimates in operations at various timescales—daily (e.g., reservoir operations); weekly (e.g., drought monitoring and irrigation scheduling); and seasonal (e.g., demand forecasting by water utilities)—and to meet scientific needs at scales that run the gamut from instantaneous to secular. Flux types vary from the supply side, or actual ET , to the demand side, where E_0 measures range from pan evaporation (E_{pan}) observations to estimates of the traditional potential evaporation (E_p) to ET_{rc} . Driving philosophies are generally observational or synthetic, rarely statistical. Estimation scales vary from point (e.g., evaporation pans or lysimeters) to basinwide (e.g., basin budget-derived ET) and further to regional (e.g., remotely sensed ET). Formulations within each flux type range in complexity from simple temperature-based empirical models to more complex physically based parameterizations requiring estimates of a suite of meteorologic and hydrologic variables to model the radiative and advective dynamics at the land surface–atmosphere interface.

A clear need exists for operationally and physically sound measures of ET and E_0 —measures that rely on appropriate forcings, are well calibrated to reasonable parameter values, and yield accurate results over the whole spatiotemporal domain, with any biases eliminated or minimized. Explicating the most important statistical considerations incumbent on end users seeking to achieve these goals motivates this chapter. However, the very nature of ET —and of its estimation and observation techniques, most of which are diagnostic, not prognostic—constrains the extent to which its treatment within the context of statistical distributions and stochastic techniques is possible or, in practice, desirable. Statistical distributions apply peripherally to the estimation of ET and E_0 , but they are rarely intrinsic to the estimation of the fluxes themselves.

3.0.2 Chapter Contents

This chapter’s central theme is an examination of statistical issues arising in observing ET and in one of the most common procedures for estimating ET from its companion theoretical flux E_0 pertaining to operational practitioners and elucidating fundamental questions in the field.

The goals of the chapter are twofold: first to discuss functional ET estimation with a statistical perspective including uncertainties in observations, model, and data; the drivers of variability of ET and E_0 ; and trends in both fluxes and their drivers; and second, the role of statistical distributions in the estimation of ET and E_0 and the significance of detected trends.

We primarily examine two types of uncertainty in this chapter: aleatory and epistemic. In aleatory uncertainty, the outputs reflect the effects of inherent randomness in the driving variables of ET or E_0 models. This treatment of drivers as random variables lies at the heart of Section 3.3.6, where a first-order, second-moment uncertainty analysis examines the variability of an outcome as a result of the natural randomness of its inputs. In epistemic uncertainty, our understanding of the necessary physics, or of their representation in the model, is uncertain. In this context, we will discuss the limitations of E_0 parameterizations based on air temperature (T) as opposed to more fully physically descriptive parameterizations, as in Section 3.2.7, and the resolution of the pan evaporation paradox, described in Section 3.4.2.5.

In terms of science, there is an a priori clear choice of modeling approach—physically based models best represent the physics of ET and E_0 —but in terms of accuracy in practice a different answer may apply, and, indeed, the addition of more variables, more parameters, and therefore the concomitant added uncertainty may perhaps not be worth the added physical representativeness. Resolution of this conflict between science and practice is a crucial step in selecting an ET -estimation procedure.

Due to space constraints, here we do not discuss evaporation from lakes and reservoirs, nor, owing to the limited audience among operational hydrologists, do we discuss small-scale instrumented measures of ET —such as sap-flux measurement, weighing lysimetry, and techniques that examine point or small-scale ET by close examination of the microphysics near the evaporating surface, such as Bowen ratio methods and scintillometry. Although eddy covariance techniques incur significant instrumentation burdens, Section 3.2.5 discusses them as they contribute to climate modeling and constraining global ET estimation efforts.

As hydrologic fluxes, ET and E_0 are best estimated by observation. ET is most often observed at a point, back-calculated as a residual of large-scale fluxes or modeled (Section 3.2). A short primer on the physics of ET and E_0 that underpins these direct physical measures and provides the necessary background for the rest of the chapter is provided in Section 3.1. Beyond a few point observations that are mainly useful to the research community (e.g., lysimeters, eddy covariance stations, and Bowen ratio stations), or the local irrigation community (e.g., evaporation pans), few methods of direct estimation of ET are available at the time and space scales relevant to water managers, hydrologists, or engineers. These practitioners are then mainly left with estimating ET as a basin-scale water-balance residual, for which we examine the uncertainties in Section 3.2.4, or from remote sensing platforms, a typical application of which we examine in Section 3.2.6.

Most land-based operational formulations derive ET by scaling E_0 down by some metric of Θ , yielding ET values between zero for dry conditions and E_0 for unlimited moisture. In Section 3.3, we describe such a model that relies on sound physical representations of the soil and vegetation dynamics at the micro-scale combined with bulk surface characteristics: the concept of ET_{rc} from the Penman–Monteith equation (Monteith 1965). Clearly, any such formulations require a well-calibrated estimation or observation of E_0 : one for which the user can know or can determine which input variable is most important to the specific location and time frame and which may be ignored. To this end, we perform first a point-based sensitivity analysis of ET_{rc} from weather station data (Section 3.3.5) and then, using gridded input data, we report a rigorous first-order, second-moment uncertainty analysis that studies the drivers of temporal and spatial variability of ET_{rc} (Section 3.3.6).

Given the increasing interest in secular changes in ET and E_0 , we discuss trend analyses—in terms of their quantification, their climatologic implications, and the statistical implications of their proper estimation, including the treatment of autocorrelation in assessing trends’ significance (Section 3.4.1).

3.1 EVAPOTRANSPIRATION AND EVAPORATIVE DEMAND: A PHYSICAL PRIMER

A summary treatment of the physics of ET and E_0 is necessary for a more complete understanding of this chapter’s material: more complete treatments are available in books [e.g., Brutsaert (1982)], chapters [e.g., Shuttleworth (1993)], and other manuals [e.g., Allen et al. (1998)]. In this section, we discuss the physical drivers of the evaporative process and common parameterizations thereof, setting up subsequent discussion of E_0 as a maximal estimator of ET .

3.1.1 Physical Measures of ET and E_0

Most operational hydrologic applications require estimates of actual ET , so the question we seek to answer is “How much water is supplied from the land surface to the atmosphere under prevailing meteorologic, radiative, and hydrologic conditions?” However, in general, Θ is limited to a degree that is unknown at operationally useful scales. Thus, the answer often becomes more complicated and requires asking a further pair of questions: first, “ignoring limitations on Θ , how much water could be supplied from the earth’s surface to meet the demand for it in the atmosphere?” and second, “How do we then account for limited Θ at the evaporating surface?” Answering this first new

question yields the conceptual flux of E_0 ; answering the second converts E_0 to ET . Following, then, we examine the drivers of, or limits to, ET , quickly invoking the concept of E_0 .

3.1.2 Drivers or Limits to ET : Introducing E_0

In basic concept, the physics of ET can be expressed as a function of Θ and some parameterization $g(\dots)$ of net available surface energy for evaporation (Q_n), wind speed (U_z) at a given height above the evaporating surface (T), and actual vapor pressure (e_a):

$$ET = f(\Theta, g(Q_n, U_z, T, e_a, \lambda)). \quad (3-1)$$

where λ is the latent heat of vaporization (approximately $2.5 \times 10^6 \text{ J kg}^{-1}$) used to convert ET and ET -related fluxes (E_0, E_p, ET_{rc} , and E_{pan}) between mass fluxes and energy fluxes ($\lambda ET, \lambda E_0, \lambda E_p, \lambda ET_{rc}$, and λE_{pan}). Note that in this chapter, we discuss mass fluxes in units of mm day^{-1} and their energy flux equivalents in units of W m^{-2} : to convert ET and ET -related fluxes from the former to the latter, we multiply by $\lambda/86,400$, where 86,400 is the number of seconds in a day.

The availability of water for evaporation Θ , whether in soil moisture, vegetation, open water, or ice, provides a hydrologic limit. The remaining meteorologic and radiative variables in Equation (3-1) are here combined into the function $g(\dots)$, and together drive the supply of energy to the surface and the ability of the overpassing air to transport moisture, respectively providing the energetic and advective limits to ET .

3.1.2.1 Moisture Availability Limit

The Θ limit describes the availability of water (or ice) to evaporate, as follows:

$$ET \leq \frac{\partial \Theta}{\partial t}, \quad (3-2)$$

where $\partial \Theta / \partial t$ is the time rate of change of moisture availability in units of mass flux.

ET is then always constrained to the lowest of the Θ limit [Equation (3-2)] and the function $g(\dots)$. However, the quantity or spatial distribution of Θ at the land surface is very poorly characterized, rendering direct estimation or observation of ET difficult on spatial scales useful to hydrologists or water managers. The state of the atmosphere is easier to characterize as atmospheric quantities—at least the fluxes of momentum, moisture storage, and energy near the surface—are better mixed and so are more easily and accurately sampled. To circumvent the difficulty in estimating Θ , we estimate a rate of ET for which this surface moisture limit does not apply—we idealize a wet surface—and consider this the rate of ET constrained only by atmospheric limits. We call this idealized rate of ET the evaporative demand E_0 [Equation (3-3)].

Essentially, in turning to E_0 we simplify the question from “What is ET under ambient conditions?” to “If unlimited water were available, how much could the atmosphere extract?” We answer this latter question from one of two different perspectives: one looking down from the atmosphere; another looking up from an idealized soil and plant surface. Each perspective results in a slightly different conceptualization of E_0 , but the relationship among ET , E_0 , and their meteorological and radiative drivers may be summarized thus:

$$\lambda ET \leq \lambda E_0 = g(Q_n, U_z, T, e_a). \quad (3-3)$$

In Section 3.2.1, we address the first conceptualization, that of potential evaporation E_p , as first defined by Penman (1948). Section 3.2.8.2 addresses observational E_0 from E_{pan} . Section 3.3 addresses the second theoretical flux, ET_{rc} . Whichever flux is estimated, we then adjust E_0 , using by some parameterization of Θ that accounts for our lack of specific knowledge of it, and thereby

estimate ET . How this is achieved is central to hydrologic modeling and depends on the application for which the ET estimate is desired.

Many physically sound ET formulations originate in [Penman's \(1948\)](#) treatment (Section 3.2.1). Following, we briefly summarize his approach to estimating the advective and radiative limits. While the specific approaches are not followed for all formulations, they remain instructive as the basis of all physically based ET -from- E_0 approaches.

3.1.2.2 Advective Driver

The advective limit describes the ability of the dynamic boundary layer to absorb and bear away moisture, as follows:

$$\lambda ET \leq (e_{sat} - e_a) \cdot f(U_z); \quad (3-4)$$

where e_a is previously defined and e_{sat} represents the saturated vapor pressure, both estimated from the Clausius–Clapeyron equation using T for e_{sat} and dewpoint (T_{dew}) for e_a , and $f(U_z)$ is a vapor transfer function (see the following) in $\text{W m}^{-2} \text{ Pa}^{-1}$. The right-hand side (RHS) of Equation (3-4) is also known as the drying power of the air (E_A) in W m^{-2} . Note that with zero advection, ET is limited to diffusion only.

The proper and accurate parameterization of the advective component is the sine qua non of any physically based ET or E_0 model ([Hobbins et al. 2001a, b](#); [Sugita et al. 2001](#)). $f(U_z)$ describes the variation of vapor transfer of the air as a function of U_z . [Brutsaert and Stricker \(1979\)](#), Equation 17 give an example of a more complete expression for $f(U_z)$ under neutral conditions (i.e., a stable atmospheric boundary layer):

$$f(U_z) = \frac{2.89 \times 10^{-4} a_v k^2 U_z}{T \ln \left[\frac{z_v - d_0}{z_{0v}} \right] \ln \left[\frac{z_m - d_0}{z_{0m}} \right]}, \quad (3-5)$$

where

a_v = ratio of eddy diffusivity to eddy viscosity under neutral conditions,

k = von Kármán constant of value 0.4 (-),

z_{0m} and z_{0v} = roughness lengths (m) for momentum and water vapor, respectively,

z_m and z_v = heights (m) at which momentum and vapor pressure (i.e., U_z and e_a) are measured, respectively (typically 2 m above the surface, although sometimes higher), and

d_0 = zero-plane displacement height (m).

However, on operational spatiotemporal scales, the confounding effects of atmospheric instability acting over short time periods and the onerous data requirements rule out such theoretical formulations. In his development of the concept of E_p as ET from a free water surface, [Penman \(1948\)](#) made various assumptions relating to the time step and micro-scale physics of the boundary layer and suggested for $f(U_z)$ an empirical, linear function of U_2 (m sec^{-1}), or wind speed measured at a 2 m height (i.e., $z_m = 2$), still commonly used:

$$f(U_z) \approx f(U_2) = (a + bU_2) \frac{86,400}{\lambda} = 0.263(1 + 0.528U_2) \frac{86,400}{\lambda} \quad (3-6)$$

which, for $f(U_2)$ in $\text{W m}^{-2} \text{ Pa}^{-1}$, gives E_A in W m^{-2} .

Most studies since [Penman's \(1948\)](#) seminal work on pan evaporation has developed new $f(U_z)$ relations [e.g., [Hobbins et al. 2001a](#), who calibrated $f(U_2)$ across the contiguous US (CONUS)], or selected from existing parameterizations. On the other hand, some models of ET and E_0 parameterize the advective component without an explicit function of U_z to address data uncertainty

(e.g., Morton 1983). The enduring practical value of the Penman (1948) wind function and others based on Penman is demonstrated in what is probably the most precisely metered experiment on the physics of E_{pan} , in which Lim et al. (2012) provide observed wind functions. They couple Fick's (1995) Law of Diffusion with boundary layer theory and account for an observed temperature depression in the thin layer at the water surface that provokes a temperature difference between the water surface and the air (most models simply use the air temperature for T). Their results indicate good agreement with Thom et al.'s (1981) envelope of theoretical curves, particularly with Penman's (1948) $f(U_2)$.

In general, parameterization choices are generally predicated on the modeler's preference, the region of application, how such factors as the temporal resolution of modeling and consequent assumptions on vertical stability at small scales (Katul and Parlange 1992, Parlange and Katul 1992a, b) or at large scales (Sugita et al. 2001) coincide with modeling goals, or on data availability and quality (Kohler and Parmele 1967, Morton 1983).

3.1.2.3 Radiative Driver

The radiative driver describes the availability of energy to drive the evapotranspiration process (with no source for the latent heat flux to drive the mass transfer, ET cannot take place) and thus describes an upper limit on ET :

$$\lambda ET \leq Q_n, \quad (3-7)$$

where Q_n is a function of the energy fluxes and storages described by the instantaneous energy balance, which is shown in Figure 3-1, and as follows:

$$\frac{\partial W}{\partial t} = (1 - \alpha)R_d + L_d - L_u - H - \lambda ET - G - C + A_d, \quad (3-8)$$

where all fluxes (RHS) and time rates of change of heat storage (left-hand side, LHS) are in flux units (W m^{-2}), with positive fluxes into the evaporating surface and negative out. $\partial W/\partial t$ is the time rate of change of heat storage in the evaporating layer (positive increase), α is the surface albedo (-) to shortwave radiation, R_d is the downward shortwave radiation incident at the surface, L_d and L_u are

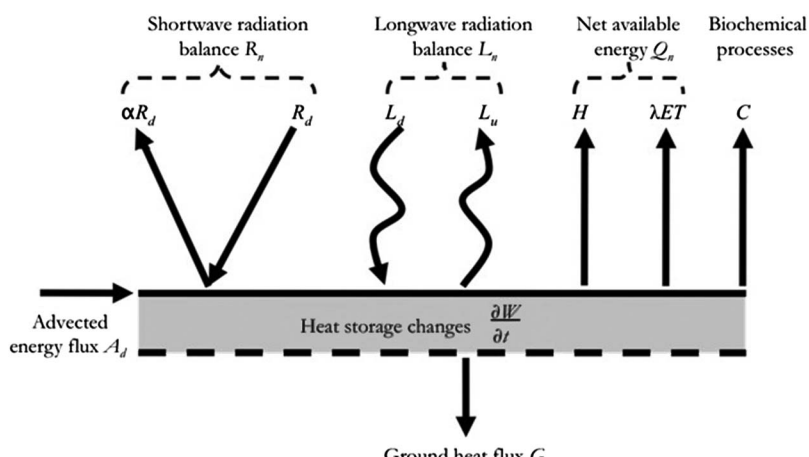


Figure 3-1. Instantaneous energy balance at an evaporating surface. All fluxes and heat-storage changes are in flux units (W m^{-2}). The gray rectangle represents the control volume to and from which all fluxes pass and within which all heat-storage changes are considered.

respectively the longwave radiation fluxes inward to and outward from the surface, H is the sensible heat flux by diffusion from the surface, λET is the latent heat flux equivalent of actual evapotranspiration, G is the heat flux conducted into the soil (or ground heat flux) from below the evaporating layer, C is the energy absorbed by biochemical processes in vegetation, and A_d is heat advected into the control volume.

All E_0 flux types require accurate estimation of Q_n , which is most often estimated as the net radiative balance, itself consisting of the two largest terms in Equation (3-9): the net shortwave radiation (R_n) and net longwave radiation (L_n) fluxes, respectively the difference of R_d less the reflected upward shortwave radiation R_u [determined as R_d multiplied by α ; see Equation (3-8)] and L_d less L_u . Whether or not the remaining terms in $Q_n - G, \partial W/\partial t, C$, and A_d —appear is a function of data availability, time step, and their relevance to the conceptual flux (E_p, E_{pan} , and ET_{rc}) make specific assumptions as to the nature of the evaporating surface: an extensive free-water surface for E_p , an evaporation pan filled with water for E_{pan} , and a ground surface and vegetated canopy for ET and ET_{rc}). Estimation of G requires knowledge of soil temperature and moisture content and so is generally neglected under the assumption that over daily or longer time periods it is generally orders of magnitude lower than the net radiative balance (see also [Allen et al. 1998](#)). For heavily vegetated areas, a zero G is a tenable assumption. In bare soil conditions, however, G may be considerable, constituting as much as 30% of the net radiative balance. When required, G may be estimated as a function of T ([Shuttleworth 1993](#)). $\partial W/\partial t$ is important in open-water evaporation, particularly for small water bodies at shorter time scales or as the size and heat capacity of the water body increases, but outside of the discussion of E_{pan} (Section 3.2.8.2), we do not discuss open-water evaporation and so neglect it. A_d may be advected into the control volume by air in the case of ET and ET_{rc} or may include larger fluxes owing to flows into and out of water bodies and P onto water bodies in the case of E_p . For a free-water surface such as a lake, A_d —comprising sensible heat from P and the balance between the heat contents of outflow and inflow—may be significant and must be considered. C is generally negligible compared with the radiative and latent heat fluxes of interest—on the order of 2% of Q_n ([Shuttleworth 1993](#))—and so is most often neglected. These smallest terms— C and A_d —are neglected in this chapter.

The remaining terms are conflated into groups that are more conceptually malleable. The radiation terms are gathered into R_n and L_n . The net radiation at the surface is then $R_n + L_n$. Most conveniently, $R_n, L_n, G, \partial W/\partial t$, and the smaller heat fluxes C and A_d are conceived of as together [LHS in Equation (3-9)] providing Q_n , which, due to the predominance of the R_n and L_n terms, we refer to as a radiative driver. Q_n is then partitioned into the processes of latent (λET) and sensible (H) heat fluxes [RHS in Equation (3-6)], as follows:

$$R_n + L_n - G = Q_n = \lambda ET + H. \quad (3-9)$$

Complete knowledge of the net radiative balance requires extensive instrumentation not generally available on an operational basis; as a result, much parameterization is required. The various methodologies for estimating the radiative components of the various formulations of E_0 also pertain to the estimation of ET . Expressions for L_n at the surface are available in [Shuttleworth \(1993\)](#) and [Allen et al. \(1998\)](#), among others. Absent explicit estimates for each longwave component, effective net emissivity is estimated to account for the effects of atmospheric composition, including such factors such as clouds, dust, and concentrations of greenhouse gases such as water vapor and carbon dioxide. While most applications assume atmospheric concentrations are constant, in rigorous trend analyses or climate modeling, each of these constituents has its own emissivity and concentration (see Section 3.4.2.3).

Important to note is that in this scheme and in the absence of direct measurements, the shortwave and longwave radiation balances are most often entirely parameterized by T, e_a , and either observed sunshine hours by the Angström formula (e.g., [Allen et al. 1998](#)) or percent cloud cover

(CC) by the Savinov–Angström equation (e.g., Brutsaert 1982), with no actual radiative flux measurements used. Thus, there is significant potential for bias, both in the modeling framework and due to the threshold problems [e.g., the Campbell–Stokes sunshine recorder indicates only that the sun is shining or not, relative to a threshold value of R_d of $\sim 120 \text{ W m}^{-2}$ (Stanhill and Cohen 2001)—compared with a typical theoretical maximum value of $1,367 \text{ W m}^{-2}$ for the top of the atmosphere—which significantly limits information that may be inferred on shortwave fluxes].

3.2 MODELS AND OBSERVATIONS OF ET AND E_0

In this section we examine physical models and observations of ET and E_0 . We begin by highlighting Penman’s (1948) seminal treatment, which introduced the concept E_0 as a limit to ET and outlined long-term measures of ET at its drivers’ limits. We summarize a measure of large-scale ET that is based on its complementarity with E_0 . We explore the following observational approaches to estimating ET : those leading directly to ET estimates without an intermediate step of estimating E_0 , derivation of ET as a residual of a basin-scale water balance in a procedure often used to generate observations for ground-truthing and calibrating other ET -estimation techniques; direct observations of the evaporative flux from canopies in eddy covariance techniques; and remotely sensed observations of ET , used for various large-scale needs, such as water rights, irrigation imagery, and drought analysis. Then we address epistemic uncertainty by warning against the use of T -based, or nonphysically based, E_0 parameterizations. We close with a summary of the main issues relating to observations of E_0 .

3.2.1 Penman’s Legacy: Physical Models of E_0

Like Penman (1948) before us, we seek to quantify the demand in the atmosphere for water from the land surface or, equivalently, the capacity of the atmosphere to extract this water. This then is the original E_p approach to E_0 , wherein the surface is assumed to supply moisture at a rate sufficient to meet the atmospheric demand and so is often referred to as a wet or free-water surface.

Penman (1948) describes the meteorologic limits on ET as a sink strength that meters the atmosphere’s ability to absorb and bear away moisture (the advective limit) and the source strength that meters the energy available for evapotranspiration (the radiative limit). Prior to his work, ET had been calculated using an aerodynamic method when the supply of energy to provide the latent heat was not limiting and using an energy budget method when the vapor transport mechanism was not limiting. Penman’s genius was to recognize that normally both of these factors are limiting, whereas Θ was essentially unknowable. He combined the two meteorologic limits in a “Combination Equation” to estimate evaporation for “a reproducible surface of known properties,” which is to say, a surface moist enough that ET is constrained only by radiative and advective limits. The Penman approach takes into consideration the similarity of flux profiles of U_z , specific humidity, and potential temperature in the dynamic sublayer above a saturated surface. This results in a convex linear combination of ET rates driven by the surface energy budget (i.e., the radiative driver in the first term on the RHS below) and by the vapor transfer (i.e., the advective driver in the second term):

$$\lambda E_p = \frac{\Delta}{\Delta + \gamma} Q_n + \frac{\gamma}{\Delta + \gamma} E_A \quad (3-10)$$

where

λE_p , Q_n [Equation (3-9)] and E_A are in W m^{-2} ,

E_A is parameterized as $f(U_z)(e_{sat} - e_a)$,

e_{sat} and e_a are in Pa,

Δ (Pa K⁻¹) is the slope of the saturated vapor pressure curve (de_{sat}/dT) at T (K), and γ is the psychrometric constant (Pa K⁻¹).

Shuttleworth (1993) shows formulations for Δ , γ , and λ .

The Penman (1948) combination equation for E_p has over the years shown itself remarkably robust and has launched many improvements and offspring. These offspring equations generally tune the advective driver, particularly to improve the characterization of the diffusion process in a local or specific setting, or adapt the equation by setting the advective driver, which is generally far smaller than the radiative driver, to a constant, resulting in an expression that is a function only of the radiative driver (called radiation-based equations). An important example of the latter is the Priestley–Taylor expression for partial equilibrium conditions (Priestley and Taylor 1972), used to estimate ET from regional-scale wet surfaces, or wet environment evaporation (E_w):

$$\lambda E_w = \alpha_{PT} \frac{\Delta}{\Delta + \gamma} Q_n \quad (3-11)$$

where λE_w is in W m⁻², and α_{PT} is the dimensionless Priestley–Taylor parameter (generally estimated in the range of 1.28 to 1.32 and mostly depending on vegetation type and surface roughness) that accounts for departure from purely radiative forcing. This is a flexible estimator of maximal ET : Fisher et al. (2005) scale E_w down to provide estimates of ET by parameterizing α_{PT} as a function of Θ : they recommend its use in large-scale ecosystem models, due in part to its limited parameter set. Alternatively, Fisher et al. (2008) keep α_{PT} constant and scale E_w down to ET using considerations of plant physiology, which they show works well at the global scale.

A significant development from Penman (1948) is the “big-leaf” Penman–Monteith approach (Monteith 1965), in which a saturated surface is no longer assumed and ET is estimated for observed conditions parameterized by two varying resistances— aerodynamic and stomatal—against which vapor diffuses from the leaf interior to the dynamic boundary layer. A carefully specified case of Penman–Monteith ET provides a measure of E_0 known as reference crop ET (ET_{rc}), wherein ET is estimated for a specific surface and then generalized for actual Θ conditions. The ET_{rc} approach addresses the question asked from the soil/plant perspective: “Given well-defined, ideal surface, or reference, conditions, what could the land surface supply to the atmosphere?” The formalized answer to this question defines ET_{rc} as a reference supply that can then be used as a starting estimate against which additional assumptions regarding prevailing soil- and vegetation-moisture conditions and vegetation mix and phenology are applied to scale down for ET . This approach to ET estimation has become the standard in the agricultural sector worldwide (Allen et al. 1998) and is described in Section 3.3, particularly in relation to uncovering the dynamics driving its space–time variability.

A common observational approach to E_0 relies on evaporation pans, which was the instrumentation Penman (1948) used to verify his combination approach; Section 3.2.8 examines these more closely. Recent work has adjusted both the advective and radiative drivers in theoretical combination approaches to synthesize observations of E_{pan} from standardized (US Class-A) pans (Linacre 1994, Rotstain et al. 2006). Thom et al. (1981), Stanhill (2002), Roderick et al. (2009a, b), and Lim et al. (2012) supply more detail on evaporation pans.

Given the differing surface conditions for these three approaches, we should not be surprised that E_p , ET_{rc} , and E_{pan} yield different estimates of E_0 .

3.2.2 Energy and Water Limits to ET : The Budyko Framework

The analysis of limitations of ET has permitted an informative examination by Budyko (1974), who visualized the variation of large-scale, long-term climatology as a function of the energy limit and the water limit. Budyko (1974) specifies time scales long enough that steady-state conditions may be assumed to prevail over areas large enough that the influences of climate on the land surface may be

assumed to be fully developed. He defines two indices to represent the resulting behavior: the dryness index Φ , defined as an E_0 rate generally estimated from the Priestley–Taylor equation [Equation (3-11)] and normalized by P , i.e., $\Phi = E_0/P$, and the evaporative index ε , defined as a similarly normalized ET rate (i.e., $\varepsilon = ET/P$). The “Budyko curve” is then an empirical parabolic relationship between the two:

$$\varepsilon_B = \sqrt{\Phi \tanh\left(\frac{1}{\Phi}\right)(1 - \cosh \Phi + \sinh \Phi)} \quad (3-12)$$

wherein ET is asymptotic to two limits (see Figure 3-2): the water limit at the arid end of the hydroclimatologic spectrum, where it is defined by P , and the energy limit at the humid end, where ET is defined by long-term E_0 . Figure 3-2 shows the Budyko curve, along with other prior and succeeding relations. Budyko showed agreement between the ET estimated by his relations and that estimated by basin budgets to within 10%.

Figure 3-2 also indicates the behavior of 229 basins across Australia within the Budyko framework using data reported fully in [Donohue et al. \(2010\)](#). Clearly, while the overall shape of the Budyko relation was preserved—the observed data approach both asymptotes—a great deal of scatter remains. Indeed, the [Turc \(1954\)](#) curve appears to better approximate these data than does the [Budyko \(1974\)](#) curve.

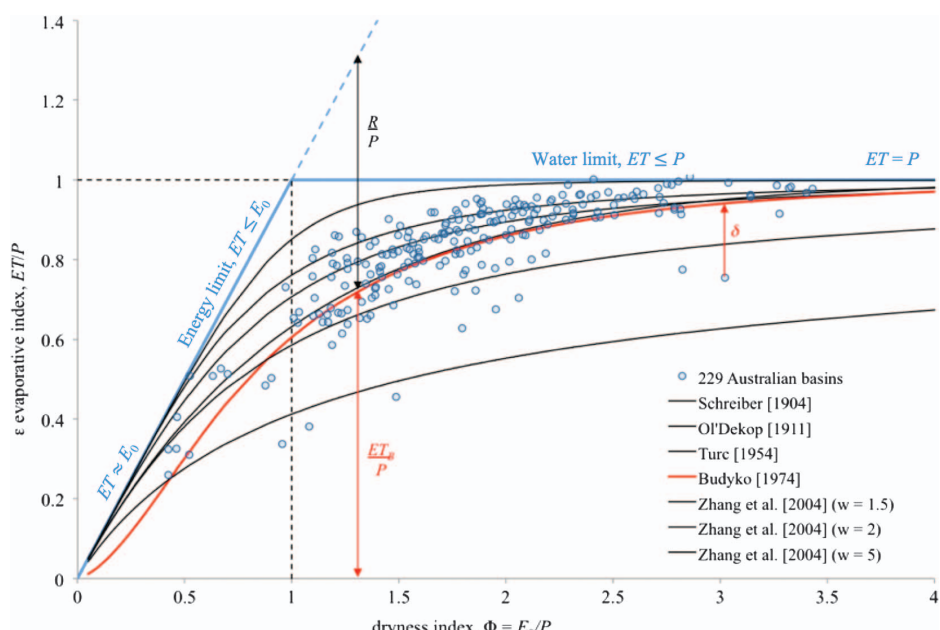


Figure 3-2. The Budyko concept in theory and applied to a set of basins. The blue lines denote the water and energy limits on ET, to which all relations describing the behavior of ET are asymptotic. Blue circles indicate the long-term, large-scale behavior observed at 229 Australian basins [from [Donohue et al. \(2010\)](#), personal communication, [2011]]. Various ideal relations between ε and Φ are shown as black lines [[Schreiber \(1904\)](#), [Ol'dekop \(1911\)](#), [Turc \(1954\)](#), [Zhang et al. \(2004\)](#)] for various values of model parameter (w) and a red line ([Budyko 1974](#)). The red dotted line indicates the ET-estimation error δ at a single basin using [Budyko \(1974\)](#).

The so-called Budyko scatter (δ) is the difference between Budyko-estimated evaporative index ε_B and basin-observed evaporative index ε :

$$\delta = \varepsilon - \varepsilon_B = \frac{ET - ET_B}{P} \quad (3-13)$$

where ET_B is ET defined by the Budyko relation (Figure 3-2). Greater δ has been observed at shorter time scales (Zhang et al., 2008), due to contravention of the steady-state assumption, and at smaller spatial scales (Budyko 1974, Donohue et al. 2007, Oudin et al. 2008), due to local effects dominating the regional climate signal. Various attempts to reduce and/or explain δ have involved examination of soil and topographic characteristics of the basin (Fu 1981). Oudin et al. (2008) find significant improvements in smaller catchments through examining land cover. Donohue et al. (2010) examine the role of vegetation dynamics in improving the predictive accuracy in the Budyko framework at smaller spatiotemporal scales and conclude that no generally applicable broad-scale ecohydrological relation exists and that physically based models must also account for water storage in addition to vegetative models to improve ET estimation.

Szilágyi and Jozsa (2009) highlight the Budyko framework's ecological promise, demonstrating a conceptual linkage between Porporato et al.'s (2004) implementation of the coupled long-term water-energy balance and the complementary relationship between ET and E_0 (discussed in Section 3.2.3). They show that derivation of some ecosystem characteristics—specifically mean effective relative soil moisture and maximum soil-water storage available to plants—was possible using meteorological and radiative data alone, permitting prediction of changes in the mean rooting depth of vegetation in response to changing climatic forcings.

That techniques based on the Budyko (1974) framework are still used is testament to its robustness, both as a lesson in the limits to ET and as an ET predictor—when properly implemented and calibrated, in ungauged basins absent local climatologic knowledge of ET .

3.2.3 Complementarity of Regional ET and E_0

As scales of analysis increase, the moisture from a homogeneous surface and the overpassing air become physically coupled through the partitioning of Q_n into latent (λET) and sensible (H) heat fluxes into a well-mixed boundary layer, leading to feedback mechanisms linking E_0 and regional-scale ET . For a given radiative input to an evaporating surface of regional scale (scale lengths on the order of 1 km), reductions in surface moisture supply lead to reductions in λET , which liberates a portion of the surface energy budget q_2 as H into the overpassing air, which increases its VPD (i.e., $e_{sat} - e_a$) and hence λE_0 by an amount q_1 . Conversely, increasing the moisture available for evaporation has the opposite effect: λET increases and λE_0 decreases. This is known as the “complementary relationship in regional evapotranspiration.” First proposed by Bouchet (1963), its most basic expression is

$$ET = k_{CR}E_w - E_0, \quad (3-14)$$

where

k_{CR} = complementarity constant,

E_w = evaporation rate for a regional-scale wet surface (i.e., a moisture-unlimited ET rate that only varies as a function of Q_n), and

E_0 is specified by Bouchet (1963) as E_p .

In its most simple form, all the energy liberated is assumed to increase E_0 (so $q_2 = q_1$), so k_{CR} takes a value of 2. However, Kahler and Brutsaert (2006) show that k_{CR} varies with the specific measure of E_0 : using E_{pan} for E_0 leads to an asymmetric complementarity with k_{CR} in the range of 2 to 5, reflecting the effectiveness of heat transfer between the pan and its surroundings.

Although they conclude that pans are more sensitive to changes in aridity than their surroundings, this inference must be weighed against their use of daily E_{pan} observations, which are often too noisy to be of diagnostic use (Roderick et al. 2009a, see Section 3.2.8.2). Symmetrical complementarity (i.e., where $k_{CR} = 2$) should only be expected in the unlikely situation of no heat exchange between the instrument measuring E_0 (e.g., an evaporation pan) and its surroundings (Szilágyi 2007). Asymmetry notwithstanding, the complementary relationship has been observed around the world (e.g., Davenport and Hudson 1967) and established as observational fact across CONUS using E_{pan} observations for E_0 and deriving ET from basinwide water balances [Equation (3-16)] (Hobbins et al. 2004, Ramírez et al. 2005). Figure 3-3 graphically represents the relation for $k_{CR} = 2$ and conditions of constant energy availability.

The most widely used models of the complementary relationship are based on the Advection-Aridity (AA) approach of Brutsaert and Stricker (1979). This approach forms the basis of modeling in Section 3.4.2; it is summarized here as it elucidates the conceptual basis of the complementary relationship at the heart of the resolution of the so-called evaporation paradox. The model combines the complementary relationship hypothesis between E_p and ET with the effects of regional advection on E_p . In this model, E_w is calculated based on derivations of the concept of equilibrium evapotranspiration under conditions of minimal advection, first proposed by Priestley and Taylor (1972), and E_p is calculated by combining information from the energy budget and water-vapor transfer in the Penman (1948) equation [Equation (3-10)]. ET is then calculated with Equation (3-14) with $k_{CR} = 2$, which results in the following expression, where the two driving dynamics are clear: the first term on the RHS represents the influence of the energy budget and the second term the local wetness:

$$\lambda ET = (2\alpha_{PT} - 1) \frac{\Delta}{\Delta + \gamma} Q_n - \frac{\gamma}{\Delta + \gamma} f(U_z)(e_{sat} - e_a). \quad (3-15)$$

Recognizing the variability in estimates of α_{PT} , Hobbins et al. (2001a) recalibrate it for use in the AA model across CONUS resulting in a value of $\alpha_{PT} = 1.3177$. The $f(U_z)$ in the formulation of E_A in the expression for E_p was calibrated regionally and seasonally (i.e., for each month across each of the 344 hydrologic accounting units in CONUS), following procedures detailed in Hobbins et al. (2001a). So calibrated, the AA model was then used to generate the CONUS-wide ET surfaces examined for autocorrelation in Section 3.4.1 and for trends in Section 3.4.2.1.

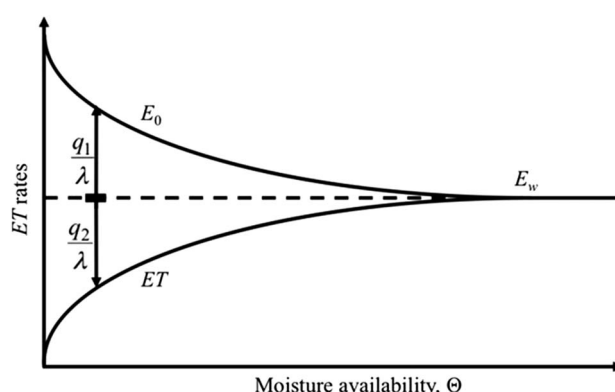


Figure 3-3. The complementary relationship between E_0 and regional ET for $k_{CR} = 2$ and under ideal conditions of constant energy availability.

Note that the distinction between ET -estimation methods based on the complementary relationship and on traditional paradigms lies in the conception of the advective component (E_A). Traditional paradigms consider the overpassing air decoupled from the surface and therefore conceive of E_A as independent of ET : a higher E_A indicates that ET from the region upwind is lower and vice versa with E_A approaching zero as E_p approaches E_w under equilibrium conditions. In this paradigm, E_0 drives ET , but does not respond to it, and does not vary with Θ . However, in the complementary relationship, E_A depends on ET . Under this proper treatment of regional-scale advection, E_A then reflects the effects of regional advection on ET after the evaporating surface has been brought into equilibrium with the overpassing air by the feedbacks across regional-scale land-surface/atmosphere interfaces. In the complementary relationship hypothesis, E_A over a region is greater when less evaporation into the air has occurred (due to a regional drying trend) and the boundary layer has been well mixed, decreased when regional ET is increased (due to regional wetting).

The utility of the complementary relationship has been amply demonstrated. Hobbins et al. (2001a, 2004) show that for a wide variety of climatic regimes, ET and its trends are estimated better by models that invoke the complementary relationship than by traditional ground-based paradigms because they implicitly account for the soil moisture-dependence of E_0 and the input data reflect surface conditions regardless of the origins of the water and degree of anthropogenic disturbance. This is further discussed in the context of the resolution of the evaporation paradox in Section 3.4.2.5. Szilágyi et al. (2011) combine a complementary relationship model with remotely sensed (Moderate Resolution Imaging Spectroradiometer; MODIS) land surface temperature data in a calibration-free approach that generates good estimates of monthly ET across large-scale homogeneous landscapes at scales as fine as 1 km.

3.2.4 Water-balance Estimates of ET

Deriving a basin water balance is the process whereby water fluxes (ET , Precipitation, groundwater recharge, surface and subsurface runoff), and storage changes are balanced across hydrologic basins or watersheds. The calculation can be done at any temporal scale (hours to years) and spatial scale (plots to large watersheds) for which fluxes and storage changes are known. Basin water balances can be lumped by considering the whole basin as a unit or distributed by calculating the water balance at the level of basin subunits. The water-balance equation for basins under natural conditions (i.e., with no significant transbasin water transfers) is solved for water-balance-derived ET (ET^{WB}), as follows:

$$ET^{WB} = P - Q - G_L + \Delta S \quad (3-16)$$

where

Q = streamflow, here defined as the sum of the surface and subsurface runoff fluxes recorded by the streamgauge,

G_L = water lost to regional groundwater unrecorded at streamgauges, and

ΔS = basinwide average change of S (i.e., $S_t - S_{t-1}$, where S_t is the sum of the water stored in lakes, rivers, and the saturated and unsaturated zones of the soil at the end of period t).

All fluxes are in units of time-rate changes of depth (mm day^{-1} for consistency with rest of this chapter, but general to all time units). Usually the proportion of the subsurface runoff [term G_L in Equation (3-16)]—through movement of the regional aquifer system—that bypasses the stream gauging station can be ignored in the water-balance calculation. When the water-balance calculation is carried out for annual values and for multiple years, the ΔS term can be considered small enough to be ignored. In the United States, the US Geological Survey (USGS) archives water data across “water years”—12-month periods that start on October 1 of the previous year—to minimize the

effects of interannual basinwide moisture storage changes (for the southern hemisphere a different start date for the water year would be appropriate). For basins with significant transbasin water transfers, calculating ET^{WB} with Equation (3-16) would introduce substantial errors.

Assuming that the measurement errors of each term in Equation (3-16) are independent and random and given that each term has an uncertainty (measured here as variance) σ^2 , then the uncertainty associated with estimating ET^{WB} may be estimated from [Lesack \(1993\)](#):

$$\sigma_{ET^{WB}} = \sqrt{\sigma_{\Delta S}^2 + \sigma_P^2 + \sigma_Q^2 + \sigma_{G_L}^2}. \quad (3-17)$$

Traditionally, Q is measured with rating curves based on flow stage at streamgauges. Water measured at a stream discharge station is the combined surface and subsurface runoff from all areas upstream of the streamgauge. [Sauer and Meyer \(1992\)](#) find that the uncertainty for individual discharge measurements by stage gauges ranges from 2% to 20% of estimated discharge, with most uncertainty errors in the range of 3% to 6%. P is most often measured from tipping-bucket raingauges and/or Doppler radar for rainfall (and snow pillows for measuring snow-water equivalent, SWE, in mountain snowpacks). Although these techniques generally underestimate the true P (e.g., owing to wind-driven undercatch by raingauges, or underestimation of high-elevation P by raingauges sited at lower elevations in regions with significant orographic effects), the uncertainty of measured P is generally negatively correlated with the observation time scale and the density of the network ([Dingman 2002](#)). [Habib et al. \(2001\)](#) and [Ciach \(2003\)](#) report rainfall estimated with raingauge network had uncertainties of 6.4% and 4.9% for a 5-min rainfall and 2.3% and 2.9% for a 15-min averaged rainfall, respectively. The uncertainty due to the density of observing raingauges is small if the density of the gauges exceeds one raingauge per 15 km radius (or 710 km²) ([Seed and Austin 1990](#)). The aforementioned instrumental and network measurement uncertainty can be translated to uncertainties in water-balance components (if the measurements are assumed to be normally distributed, a flux's 95% confidence intervals for the mean will be $\bar{X} \pm \sigma/1.96$, where σ and \bar{X} are the standard deviation and mean value of the flux, respectively). For example, the annual P and Q of Coose Basin in the southeastern United States are 1,270 mm year⁻¹ and 440 mm year⁻¹, respectively. The uncertainties of measured P and Q were reported as 8% (102 mm year⁻¹) and 5% (22 mm year⁻¹), respectively. Thus, the annual ET^{WB} is 1,270 – 440 = 830 mm year⁻¹, with an uncertainty $\sigma_{ET^{WB}}$ of $(102 + 22)^{1/2} = 104$ mm year⁻¹.

When the basin water-balance calculation is carried out on subannual time scales, the ΔS term cannot be assumed to be negligible. Furthermore, depending on basin size and hydrologic and geologic characteristics, not all of the excess water available for Q during any given day or month will actually leave the basin during the same time period; delays can be as long as several months. Typically, about half of the water available for Q in any given month runs off in that month in most mid-size basins (< 5,000 km²), with the residual fraction becoming part of Q only in the following months. Consequently, soil-water moisture should be considered a state variable to track through time in Equation (3-16). In such cases, E_p replaces the ET^{WB} term and Equation (3-16) is rewritten as

$$\Delta S = P - Q - G_L - \eta E_p \quad (3-18)$$

where η is a moisture extraction function. [Dyck \(1983\)](#) summarizes some of the moisture extraction functions currently in use. The simplest η function is SM / SM_{fc} , where SM is soil-moisture water content during the simulation period and SM_{fc} is the soil's field capacity (maximum water that could remain in the root zone after three days of drainage). In these cases, the water-balance estimation proceeds in the following multistep process:

1. If the calculations are made for periods of complete years, then ΔS is small compared with P , Q , and ET^{WB} and is set to zero;

2. If the calculation starts at the end of the dry season, SM is assumed to be zero, whereas if the calculation starts in the wet season, initial SM is set to the water-holding capacity and water-balance calculations are made up to the end of the simulation period;
3. The basin water-balance calculation is restarted with the initial basin water storage set equal to the water storage found at the end of the previous calculation, then the calculation is repeated until the difference between the end water storages of two successive calculations is insignificant.

3.2.5 Eddy Covariance Estimates of ET and Global Observation Efforts

The eddy covariance technique estimates ET directly from fine-scale micrometeorological and radiative observations at sensors mounted above vegetative canopies on “flux towers” and is the subject of significant research efforts worldwide. While this data- and instrument-intensive technique is primarily a research tool, its goals are to inform mesoscale models and global climate models (GCMs) and to generate global estimates of fluxes (ET and carbon dioxide, CO_2), so operational hydrologists and students should gain at least a passing familiarity with it.

The primary source and curator of eddy covariance data from around the globe is FLUXNET, an international network of long-term flux towers, generally consisting of eddy covariance equipment and sensors of meteorologic, radiative, and soil thermal parameters that together measure carbon, energy, and water fluxes at 0.5–5 km^2 scales over various ecosystems and climates (Figure 3-4). The primary motivations for the use of FLUXNET data are threefold: ground-truthing existing modeling approaches, estimating forest ecosystem-scale fluxes, and improving the estimation of global ET .

Point estimates of land/atmosphere exchanges, including water vapor, from in situ eddy covariance stations can constrain estimates of regional ET derived from spatial interpolation of meteorological and radiative observations of drivers, and can act as ground truth for particular ecosystems.

Forests play a crucial role in local and regional water supplies and in altering regional and global climate, but forest exchanges on the ecosystem scale are difficult to measure. This has limited our understanding of forest function in relation to climate change—including changes in water and carbon fluxes and their roles in carbon sequestration. For this reason, the eddy covariance stations of the AmeriFlux network that comprise the North and South American component of FLUXNET and the EUROFLUX stations of its counterpart in Europe are located in research forests. Flux data gathered there are now finding their way into ecosystem models (Fisher et al. 2005).

FLUXNET aims to provide global estimates of ecosystem fluxes, including ET . Traditionally, global ET estimates have demonstrated a tension between simple, easily applicable but unrealistic models [e.g., the Thorntwaite (1948) model] and complex models requiring significant parameterization, with the latter being increasingly favored (Fisher et al. 2008). Flux tower estimates of ET should assist in GCM and mesoscale modeling by providing good parameterizations of processes that operate at subgrid variability (Aubinet et al. 1999). FLUXNET eddy covariance data have permitted global ET estimation (e.g., Fisher et al. 2008, Jung et al. 2010) and could indicate the best global-scale ET model to predict change in land surface exchange due to climate change (Fisher et al. 2005).

The eddy covariance technique attempts to close the energy budget in Equation (3-8), defining $\partial W/\partial t$ as the rate of change of heat storage between the soil surface and the eddy covariance instrumentation and assuming that C and A_d terms are negligible, so

$$\lambda ET + H = (1 - \alpha)R_d + L_d - L_u - \frac{\partial W}{\partial t} - G. \quad (3-19)$$

where all terms are measured at eddy covariance flux towers (Wilson et al. 2002). The exchange of gases between the biosphere and the atmosphere are directly measured by high-frequency sampling

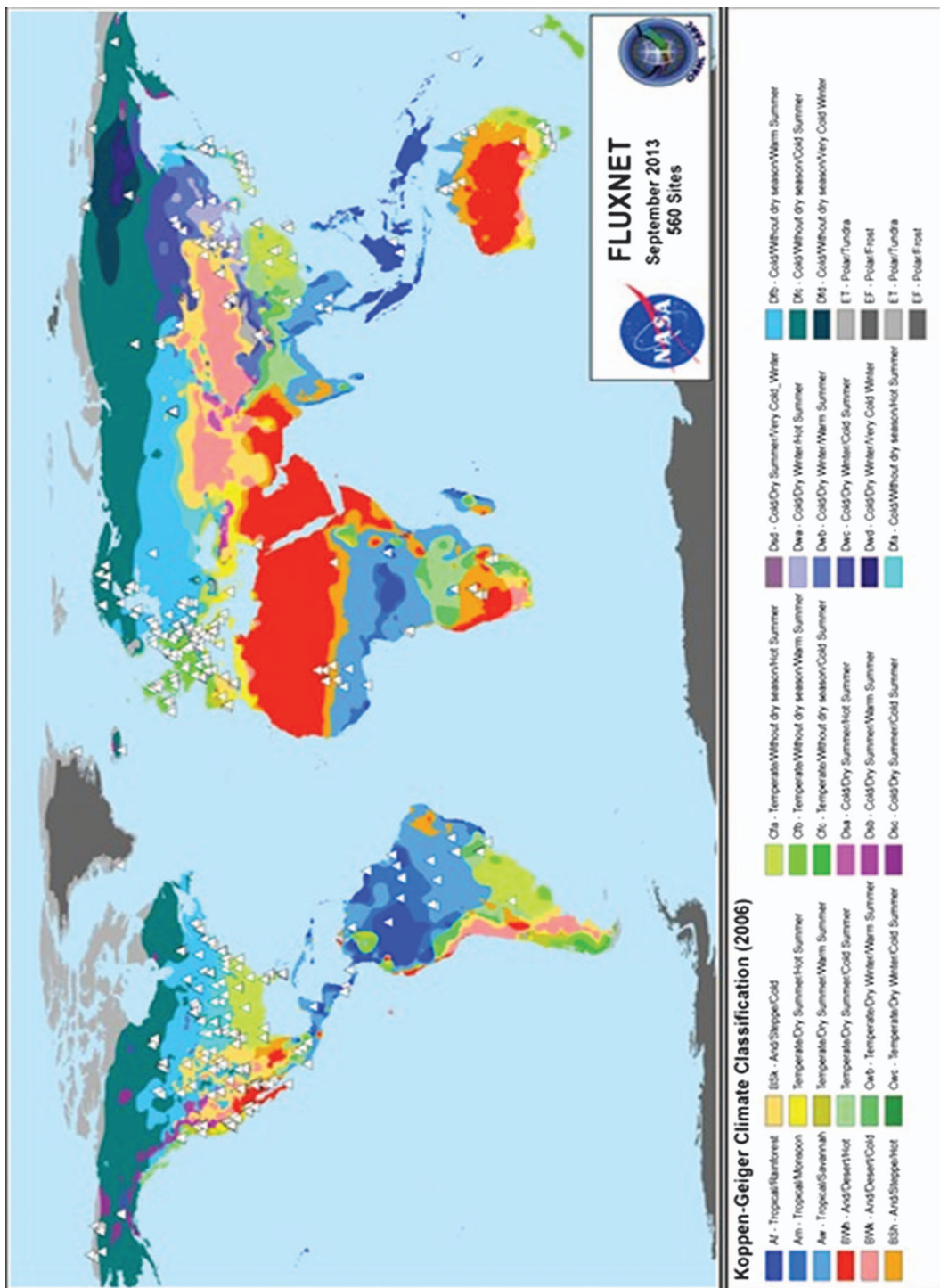


Figure 3-4. The global distribution of FLUXNET eddy covariance towers across the Koppen-Geiger Climatic Classification [map from the National Aeronautics and Space Administration (NASA), http://fluxnetornl.gov/sites/default/files/Koeppen-Geiger_FLUXNET_fullsize-9-13.png; accessed November 22, 2013].

of atmospheric eddies for their vertical velocity and gas concentrations (CO_2 or, in the case of ET estimation, water vapor) and averaging over more than about 30 min. The underlying physics stems from the conservation equation for a scalar in a control volume with axes defined as the horizontal prevailing wind direction x , the horizontal direction y orthogonal to x , and the vertical direction z , as follows (Aubinet et al. 1999):

$$\frac{\partial \rho_s}{\partial t} + u \frac{\partial \rho_s}{\partial x} + v \frac{\partial \rho_s}{\partial y} + w \frac{\partial \rho_s}{\partial z} = S + D \quad (3-20)$$

where

ρ_s = scalar density (water-vapor density for ET estimation);

u , v , and w = wind velocity components in directions x , y , and z , respectively;

S = source/sink term for the scalar; and

D = molecular diffusion.

Using Reynolds decomposition, in which each velocity component (e.g., u) and the water-vapor density (ρ_s) are considered as a deviation u' around a time average \bar{u} (i.e., $u = \bar{u} + u'$ and $\rho_s = \bar{\rho}_s + \rho_s'$), and assuming no horizontal eddy flux convergence, yields the following expression for the estimation of ET from eddy covariance instrumentation:

$$\int_0^{h_m} S dz = \overline{w' \rho_s'} + \int_0^{h_m} \frac{\partial \bar{\rho}_s}{\partial t} dz + \int_0^{h_m} \bar{u} \frac{\partial \bar{\rho}_s}{\partial x} dz + \int_0^{h_m} \bar{w} \frac{\partial \bar{\rho}_s}{\partial z} dz \quad (3-21)$$

where the LHS represents the ET flux from the ecosystem, and the terms on the RHS represent the eddy flux at height h_m , storage of water vapor between the soil surface and instrument height, and horizontal and vertical fluxes of water vapor, respectively. The rightmost three terms may decay to zero in conditions of atmospheric stationarity and horizontal homogeneity (which may be contravened). The water-vapor storage term is low at night as transpiration from the canopy is low. The horizontal advection term may be significant under sloping terrain at night (owing to drainage) and in heterogeneous terrain. The vertical advection term (last term on the right) may be zero over short crops, but whether this is true for forests remains unresolved, and it may be particularly significant on calm nights.

A typical EUROFLUX instrumentation setup comprises a three-axis sonic anemometer that measures u , v , w , and T fluctuations and a closed-path infrared gas analyzer (IRGA) that measures ρ_s , both operating at high frequencies (~20 Hz) (Aubinet et al. 1999). A suite of micrometeorological measurements often accompanies these, typically including global and net radiation ($R_n + L_n$), photosynthetic photon flux density, atmospheric pressure P_a , precipitation P , relative humidity RH , G , various soil and vegetation temperatures, and soil-water contents at various soil depths. Lower-frequency meteorological measurements are also made to characterize the prevailing meteorological conditions, to correct and quality control eddy covariance measurements (particularly to close the energy budget using radiation and energy storage terms), to gap-fill eddy covariance measurements, and to provide input data to soil vegetation atmosphere transfer (SVAT) models for calibration and validation.

Aubinet et al. (1999) describe a set of standardized procedures and tests to quality check the recorded data for errors and inconsistencies. Raw data analyses test the data as recorded for discontinuities and for anomalous spikes, higher moment statistics, and absolute limits. A stationarity test of the measurement process ensures that this assumption—central to the eddy covariance technique—is not contravened. An integral turbulence test ensures that data are recorded under the assumed turbulent conditions. This test should highlight any additional turbulence caused by the sensors or by heterogeneous sources of surface temperature and moisture.

Although closure of the energy balance is considered an important test of the technique and data, many workers report a long-standing general lack of closure at most sites of about 10% to 30%: Wilson et al. (2002) report a mean closure error of 20% for 50 site years of data from 22 sites, and Fisher et al. (2005) report errors of 10% in general. These closure errors imply that either λET and H are underestimated or Q_n is overestimated. Energy balance closure errors are observed across all vegetation types and climates, including the conditions of flat, homogeneous terrain with short crop cover that are ideal for the eddy covariance technique, with the greatest errors observed under less turbulent nighttime conditions but declining with increasing turbulent intensity (friction velocity) (Wilson et al. 2002).

Many hypotheses have been proposed to explain the energy balance closure error (Aubinet et al. 1999, Fisher et al. 2005, Wang and Dickinson 2012), primarily the following: errors in the estimation of radiation fluxes or heat storage terms; flux sources or “footprints” that are assumed to be spatially representative but that may in fact be heterogeneous (e.g., forested/clear) or that may vary with day, year, and wind direction; systemic bias or poor response times in instrumentation; neglected energy sinks within the control volume, such as melting of precipitation or dew, or conduction of heat to intercepted rain; and the occurrence of nonvertical or nonturbulent fluxes, such as advection or subsidence, that are unaccounted for in the energy balance and hard to detect with sonic anemometry (in particular, sonic anemometers are poor at resolving fine-scale, weak, high-frequency eddies that are particularly prevalent at night) and that tend to lead to underestimation of ET at night, as the relation of error to U_z is stronger under the stable conditions that prevail at night than under unstable conditions.

Gaps in the data record—for example, from poor weather conditions and sensor failures—may comprise up to around 30% of data and introduce around 5% uncertainty in annual ET totals (Wang and Dickinson 2012). Such data gaps may be filled by time interpolation in a single observed time series, parameterizing missing data by known relationships to gathered data, or by use of neural networks to infill by unknown combinations with gathered data (Aubinet et al. 1999).

In this section, we have only summarized the physics of the technique, its main agents, and the sources of error and uncertainty; more interested readers are encouraged to seek out the seminal sources cited herein.

3.2.6 Remote Sensing and Energy Balance Modeling of ET

ET is often poorly characterized in environmental modeling, despite the fact that it is a landscape primary process and direct indicator of the status of ecological, biological, and hydrological conditions. Recent results using MODIS land surface temperature data (T_s , also abbreviated in remote sensing literature as LST) and model-assimilated weather data from the National Oceanic Atmospheric Administration (NOAA) suggest that realistic estimates of seasonal plant water use can be made successfully (Senay et al. 2013). Because transpiration is directly determined by stomatal conductance, both water stress due to hot, dry spells and increased water use can be detected earlier and more readily than with traditional vegetation indexes such as the Normalized Difference Vegetation Index (NDVI). Furthermore, serious gaps in our knowledge of the spatial and temporal variation of ET across the landscape may be filled by using available remote sensing data and atmospheric model outputs.

Many researchers have used surface energy balance methods (Jackson et al. 1981; Moran et al. 1996; Bastiaanssen et al. 1998, 2005; Kustas and Norman 2000; Roerink et al. 2000; Su 2002; Allen et al. 2007a, b; Su et al. 2005; Anderson et al. 2007) to estimate agricultural crop-water use and terrestrial ET . Gowda et al. (2008) and Kalma et al. (2008) present comprehensive summaries of the various surface energy balance models. The approach of most energy balance models requires solving the energy balance [Equation (3-8)] at the land surface, where λET is calculated as the residual of net radiation ($R_n + L_n$) less H and G .

Here, we summarize the implementation of Senay et al.’s (2007, 2011) Simplified Surface Energy Balance (SSEB) modeling approach. The SSEB works similarly to the more complex surface energy

balance models in the sense that T_s is used as a primary scalar. However, whereas in the complex models the temperature scalar is applied in an aerodynamic estimation of H that is in turn subtracted from estimates of $R_n + L_n$ and G to determine actual λET , the SSEB temperature scalar is multiplied directly by the estimate of maximum ET . The SSEB approach estimates actual λET using the relative ET fractions scaled from thermal imagery in combination with a spatially explicit maximum ET_{rc} .

3.2.6.1 Materials and Methods

The SSEB model combines remote sensing data with weather data to derive estimates of ET . Herein, we validate these modeled estimates against ET derived from water-balance data.

Remote Sensing Data

Global T_s and NDVI data from the Terra MODIS sensor are available from the Land Processes Distributed Active Archive Center (LPDAAC) website (https://lpdaac.usgs.gov/lpdaac/products/modis_products_table). Here, we use the eight-day average MODIS T_s in combination with the 16-day NDVI dataset.

Weather Data Sets

Global daily ET_{rc} produced using six-hourly Global Data Assimilation System (GDAS) datasets were used (Kanamitsu, 1989). Senay et al. (2008) detail the data sources and modeling of a global ET_{rc} on an operational basis. GDAS is generated at a one-degree resolution (~ 100 km near the equator). However, ET_{rc} is downscaled to 10 km using a simple spatial statistical relationship (Senay et al. 2007) with a climatology of E_p from the International Water Management Institute.

In addition, high-resolution (4-km), monthly T from the Parameter-Elevation Regressions on Independent Slopes Model (PRISM) was used in combination with the T_s to calculate the ET fraction according to Equation (3-22) (<http://www.prism.oregonstate.edu/>; Daly et al 1994).

Rainfall (P) and Streamflow (Q) Data

Annual total P data were aggregated from daily data provided by NOAA's New Precipitation product, a blend of station and Next-Generation Radar (NEXRAD) data. Annual Q data were acquired from the USGS at the HUC-8 (eight-digit hydrologic unit) level for the ET validation procedure (<http://waterwatch.usgs.gov/>).

ET Modeling Approach with the SSEB

Figure 3-5 shows the schematic representation of the SSEB modeling framework. NDVI datasets were used to visually select hot and cold pixels for each T_s image period (more details will be provided later in this section). For each of the 46 eight-day image dates in a year eight-day ET

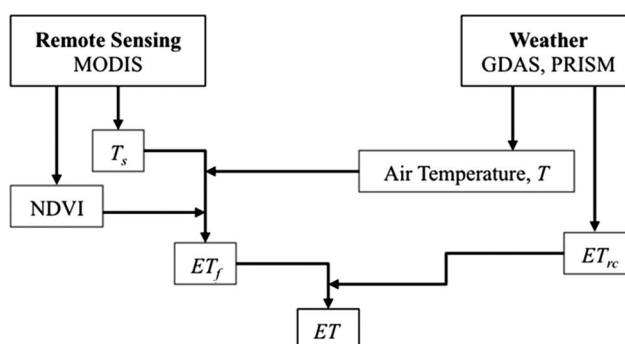


Figure 3-5. Data sources and ET-estimation workflow diagram.

fractions are generated for each year. Each eight-day ET fraction is multiplied by ET_{rc} generated independently using the GDAS weather dataset.

The main principle behind Senay et al.'s (2007, 2011) SSEB approach is the combination of ET_{rc} and T_s data for ET estimation. The surface energy balance is first solved for a reference crop condition (assuming full vegetation cover and unlimited water supply) using the standardized Penman–Monteith equation (Allen et al. 1998). The ET fraction (ET_f) accounts for differences in water availability in the landscape and is used to adjust ET_{rc} based on the T_s and T of the pixel [Equation (3-22)].

In the SSEB model formulation, ET_f is calculated from T_s and T_a datasets based on the assumptions that hot pixels experience little or no ET (Bastiaanssen et al. 1998, Allen et al. 2007a) and cold pixels represent “maximum” ET and with the simplified assumption that ET can be scaled between these two values in proportion to the difference between T_s and T_a . Jackson et al. (1981), Menenti and Choudhury (1993), and Moran et al. (1996) also apply the linearity assumption, though not in combination with the hot- and cold-pixel approaches of the Surface Energy Balance Algorithm for Land (SEBAL; Bastiaanssen et al. 1998) or Mapping Evapotranspiration at High Resolution with Internalized Calibration (METRIC) (Allen et al. 2007a) models.

In principle, instantaneous T_s at satellite overpass time can be used to identify hot and cold pixels, which in turn can be used to calculate the proportions of ET in each pixel. The hot and cold pixels are selected using an NDVI image as a guide to identify dry bare areas ($NDVI < 0.2$) for the hot pixels. Similarly, the cold pixels are selected from well-watered, well-vegetated areas with $NDVI > 0.7$. The major innovation in the revised application of the SSEB approach is the inclusion of T_a data in the calculation of ET_f .

The ET fraction (ET_f) is calculated for each pixel by applying Equation (3-22) to each of the eight-day T_s grids:

$$ET_f = \frac{\delta T_h - \delta T_x}{\delta T_h - \delta T_c} = \frac{(T_s - T)_h - (T_s - T)_x}{(T_s - T)_h - (T_s - T)_c}, \quad (3-22)$$

where the subscripts h and c refer to the hot and cold pixels, and x to the pixel in question.

The basic principle that relates instantaneous satellite measurements to daily and weekly ET estimation is the fact that ET_f is stable throughout the day (Allen et al. 2007a). By extension, eight-day ET_f generated from the available eight-day MODIS thermal datasets represent the average ET_f for the period. Because the ET_f s are average representations of the period, the day-to-day variability of ET is captured by the magnitude of ET_{rc} , which is largely driven by the $R_n + L_n$ and advection forcings experienced by the modeling unit (i.e., the pixel).

The basic approach to calculating ET is a two-step process: ET is simply a product of the ET fraction (ET_f) and maximum crop ET [ET_m ; Equations (3-22) and (3-23)],

$$ET = ET_f \cdot ET_m, \quad (3-23)$$

where ET_m is the maximum crop ET for the location. A proportional relationship exists between clipped grass ET_{rc} and other cover types. For example, Allen (2010, personal communication) suggests the use of a factor of 1.2 to estimate the maximum ET for crops such as alfalfa, corn, and wheat, as they are aerodynamically rougher than the clipped grass reference and have greater leaf area and thus greater canopy conductance (Allen et al. 1998). We recommend a calibration and validation process to determine this coefficient.

In this study, we focused on using the eight-day MODIS data stream because of its impressive spatial and temporal coverage for many agrohydrological applications from crop monitoring to hydrologic water-balance studies at a basin scale. The eight-day coverage from MODIS allows the filling of cloudy pixels by previous or next eight-day ET_f in the generation of the ET time series. As

the MODIS data stream only started in March 2000, the ET climatology will be rather short term, but its usefulness will be unique for hydrologic and crop-monitoring purposes. Specifically, hydrologists will be able to estimate difficult water-balance terms such as groundwater recharge and withdrawal and monitor crop water use dynamics in different parts of the world under changing climate and land use/land cover conditions.

ET Validation Using a Water-Balance Approach

Although [Gowda et al. \(2009\)](#) successfully validate the Landsat-based SSEB ET model using lysimeter data, MODIS-based ET is more difficult to validate using such data because of its coarse spatial resolution (i.e., 1 km). In this study, we used a water balance approach to evaluate how the SSEB ET compares with the annual difference between P and Q at the HUC-8 level and assumed negligible net storage changes at the annual time scale and the watershed level. Thus, this comparison does not account for interbasin transfers for irrigation. Subbasins with runoff coefficients (Q to P) of > 0.5 were excluded from the analysis to reduce the inclusion of subbasins with large regional flows, in other words, subsurface runoff joining from other subbasins. The median of five years of P , Q , and ET were used for this exercise. Scatterplots were created of annual SSEB-derived ET against the difference between P and Q for each of 1,789 watersheds. The coefficient of determination (R^2) and slope of the linear relation were calculated by regressing ET on the difference between P and Q .

3.2.6.2 Results

The SSEB model has been implemented in different parts of the world for water budget analyses and drought monitoring. Figure 3-6 shows sample model outputs showing 2009 annual total ET distribution in the United States, the Euphrates and Tigris region of Iraq, and the Horn of Africa. The SSEB model has been validated using data from four lysimeters in the Texas High Plains with an R^2 of 0.84 for daily total comparisons ([Gowda et al. 2009](#)) and was also compared with other well-established ET models such as METRIC ([Allen et al. 2007a](#)), against which it provides comparable performance ([Senay et al. 2011](#)).

According to Figure 3-6, the SSEB-derived ET captures well the spatial distribution of continental-scale ET with higher ET being mapped in high rainfall and irrigated regions while low ET dominates the arid and semi-arid regions. Furthermore, wetland areas and tree-covered regions with access to groundwater are shown as high ET .

Furthermore, Figure 3-7 shows preliminary results from recent verification against a water balance approach. The median annual difference between P and Q for the period between 2005 and 2009 was used in this study to compare with modeled median ET at a watershed scale.

The strong R^2 (0.73) and near-unity slope in Figure 3-7 demonstrate that the SSEB method is capable of simulating ET in diverse ecosystems. Some of the scatter δ here may be caused by ET met from water sources other than P , such as irrigation or wetlands, or contravene the assumptions of negligible regional inflow or net storage changes. The uncertainty level in these assumptions must be checked, particularly in small watersheds. Section 3.2.4 provides a more detailed discussion on basin water balance calculation and uncertainty analysis.

3.2.6.3 Discussion

As an important climatic and ecological variable, ET can be used both in absolute and relative terms. While water-balance calculations and facility designs for irrigation water delivery require quantitative estimation of ET , drought monitoring and early warning applications can be served with relative estimates.

Relative ET estimates are generated using statistical approaches to detect anomalous periods and seasons during the growing season. A commonly used anomaly calculation is to derive percent deviations from the mean or median years. Due to limited availability of historical remotely sensed data, currently we can generate anomalies using the past 11 years (2000–2010) from MODIS-based

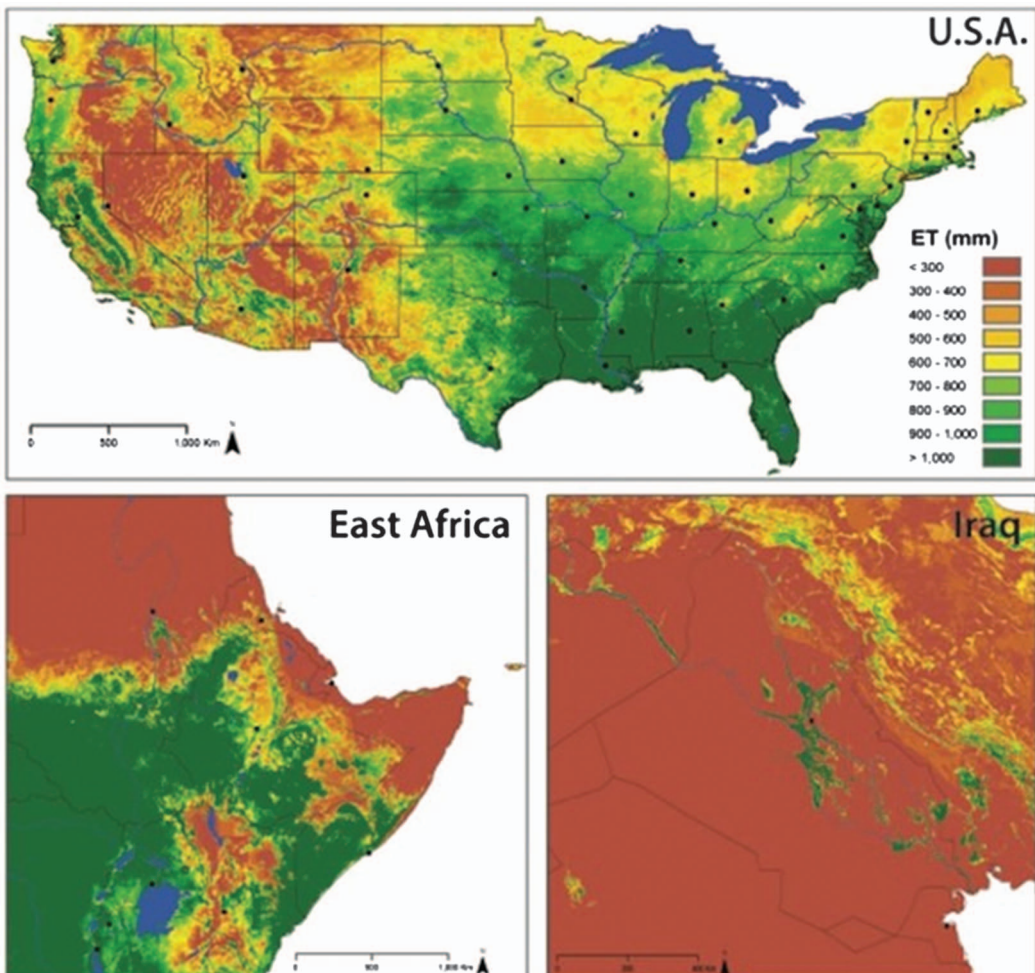


Figure 3-6. Annual ET depths (mm) for 2009 for three study regions demonstrating the spatial distribution of ET; green indicates high water use in high rainfall and irrigated/wetland regions and brown indicates low water use in arid regions.

ET datasets as percent deviation or ratio in relation to the mean or median [Equation (3-24)]. Generally, the median is preferred to avoid the influence of extreme values for the relatively small sample sizes.

$$ET'(\%) = \frac{ET_i}{ET_{50}} * 100\% \quad (3-24)$$

Here ET' is the ET anomaly expressed as a percentage; ET_i is the cumulative ET or discrete-period ET for the year i in question; and ET_{50} is the median cumulative ET for the same period. For example, ET_i for the growing period from June to September may amount to 500 mm. If ET_{50} is 550 mm for the same period and location, then ET' would be 91%, indicating a drier than normal condition.

Although anomalies can be generated from statistical analyses of current ET datasets in relation to historical ET , ET projections can also be made using the SSEB model. The separation of T_s and

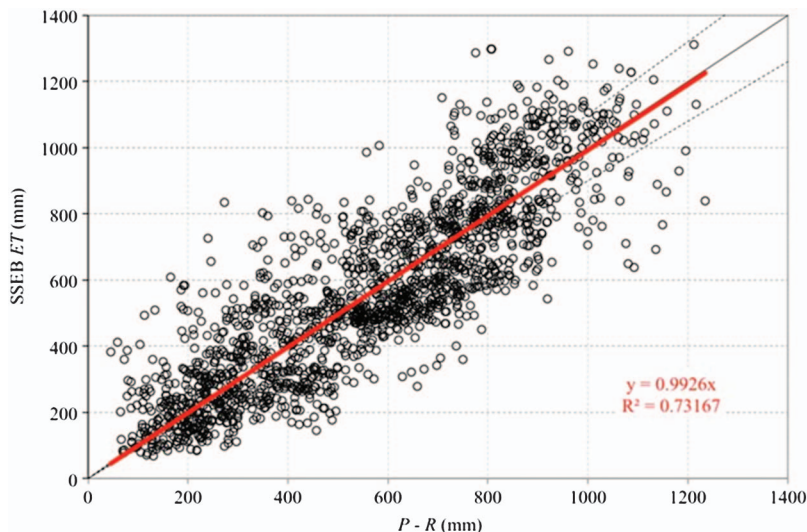


Figure 3-7. Verification of SSEB-derived annual ET against watershed annual water balance (P less Q) using 1,789 HUC-8 watersheds across CONUS. Also shown are the line of best fit and its equation and R^2 (red line and inset text), the 1:1 line of perfect correspondence (black solid line), and HUC-8 basins with less than 10% prediction errors (between black dashed lines).

weather datasets in the SSEB algorithm enables the model to simulate projected vegetation-water use under different climate-change scenarios. The SSEB ET model effectively separates the impact of radiative forces from that of water supply. While ET fractions are mainly influenced by soil moisture, ET_{rc} is under unlimited water conditions and is thus strictly influenced by energy and aerodynamic forces. Potentially, ET may be estimated for a certain land cover or landscape of mixed land-cover types under changing climatic conditions. For this purpose, ET_{rc} projections that are created using statistical and probabilistic manipulations can be used.

In examining an example model (SSEB) of the remote sensing of ET, we find that T_s data for calculating ET_f , which responds to variations in water supply mainly drives the variability within the SSEB ET model. The ET magnitude is determined by ET_{rc} driven by weather datasets. With a simple model setup, the SSEB ET model demonstrates that explaining the spatial variability of ET fairly accurately is possible. At an annual time scale, SSEB ET explained 73% of the spatial variability of the difference between P and Q in 1,789 HUC-8 level watersheds across CONUS.

3.2.7 T-Based E_0 Formulations: A Warning

Since the earliest attempts to parameterize E_0 (Penman 1948), interest in models that use minimal data sources as drivers has lingered for example, the Thornthwaite (1948) and Hamon (1961) formulations of E_p and the Hargreaves (Hargreaves and Samani 1985) and Blaney-Criddle (Blaney and Criddle 1950) formulations for ET_{rc} —despite complete physical descriptions being concurrently available. Such minimalist estimators are generally motivated by the scarcity of data describing radiation, wind, or humidity, relying instead on T (often in the form of daily maximum and minimum T , T_{max} and T_{min} , respectively). With light data requirements, they are easily implemented, as T data are widely available in time and space. The theory underpinning T -based equations holds that T affects (or reflects) both the advective and radiative drivers that are explicitly treated in more physically based (and hence more data-intensive) formulations. Formulations may differ in their details but generally make the same basic assumptions about the relation between T and radiative forcing, while neglecting the effects of advective forcing.

The fatal flaw of T -based parameterizations of E_0 is their lack of rigorous physical underpinning. Most minimal E_0 parameterizations are developed for agricultural or ongoing operational uses and therefore focus on capturing short-term E_0 variability. However, Shuttleworth (1993) recommends against the use of T -based formulations other than the Blaney–Criddle and Hargreaves equations and even then, never at temporal resolutions finer than monthly. Despite this warning, E_0 parameterizations based solely on T have become dangerously ubiquitous and reached beyond this initial setting. They may be obscured deep within larger models used in a predictive mode, such as for water-resources planning under climate-change scenarios (e.g., Mahmoud et al. 2011), or in diagnostic analyses of ongoing droughts, or secular analyses such as of drought trends (e.g., the Palmer Drought Severity Index, PDSI, in Dai et al. 2004), where their inherent biases from dependence on long-term T trends may lead to questionable conclusions. Clearly, trends in T -based E_0 will be a function solely of trends in T : under global warming, therefore, T -based E_0 can only rise, in contrast to worldwide observations of declining E_0 (e.g., Roderick et al. 2009a). Here we warn against their use in such settings.

As an example of the short-term variability of E_0 , Figure 3-8a presents observed E_0 derived from E_{pan} observations. Clearly, E_{pan} increases with T , but with an interstation variability at each T that results from the physical interplay of all physical E_{pan} drivers. The best that can be said for the T -based E_0 parameterizations that drive the PDSI hydrology component (Figure 3-8b) or from Thornthwaite (1948, Figure 3-8c) is that on a monthly basis they are of the same order of magnitude as E_0 observations. However, neither T -based E_p parameterization replicates the variability in E_0 observed in the warmer stations (for, say, $T > 10^\circ\text{C}$). Further, above about 25°C , Thornthwaite E_p increases in a physically unrealistic manner, while PDSI E_p suppresses this rapid increase in the warmest stations and months by switching to a different parameterization (see Supporting Information in Hobbins et al. 2008), which leads to decreases in E_p above about 35°C —another phenomenon not observed in nature.

The importance of including all drivers in estimating E_0 is demonstrated more rigorously in Hobbins et al. (2012), who decompose the variability of a physically based estimator of E_0 (synthetic E_{pan} —shown to be a good estimator of E_0), finding that for nearly 50% of CONUS, T was not the most significant driver of annual E_{pan} variability and that which driver dominated varied with season and region. A similar analysis is conducted for the fully physical Penman–Monteith ET_{rc} in Section 3.3.6. Such conclusions are supported from a different methodology: that of neuro-fuzzy

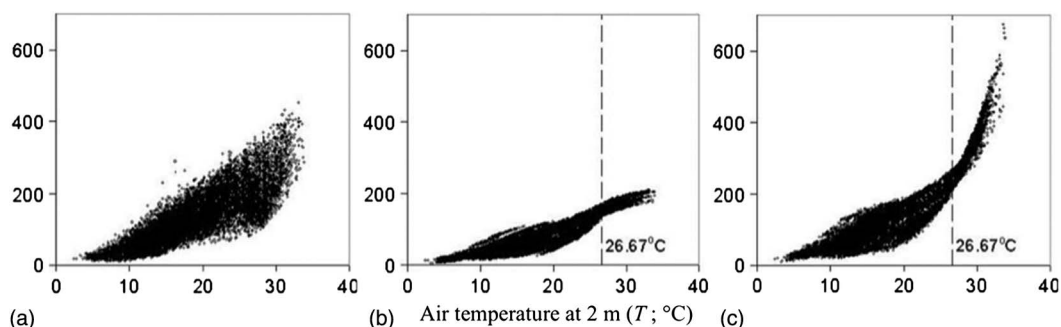


Figure 3-8. Empirical and forced T responses of E_0 parameterizations compared across Australia and New Zealand [source: Hobbins et al. (2008)]. Vertical axes are monthly E_p depths across 35 stations for 1975 to 2004 estimated by (a) E_{pan} observations, (b) the operational PDSI E_p parameterization (see Supporting Information in Hobbins et al. 2008, and (c) the Thornthwaite (1948) parameterization. Horizontal axes are the corresponding mean monthly T ($^\circ\text{C}$). The dashed vertical lines in (b) and (c) indicate the threshold (26.67°C) above which E_p growth is suppressed in PDSI E_p .

E_0 -estimation techniques: [Kişi \(2006\)](#) finds that, in estimating daily E_{pan} at two California stations, using a full set of drivers far outperformed using T alone.

In outlining research needs relating to secular variability and trends in ET and E_0 , [Ohmura and Wild \(2002\)](#) state, “The direction of the evaporation trend is not determined by temperature alone. That a warmer atmosphere does not necessarily produce more evaporation can be seen in the fact that hemispheric evaporation is much more substantial in winter than in summer under the present climate.” They call for analyses of ET in the context of both its radiative and advective components.

The over-simplicity of relying on T generally constrains long-term E_0 to increase with warming, with significant deleterious effects on water-balance assessment ([Hobbins et al., 2008](#)), whereas the advective driver ignored in T -based formulations— U_z , specifically—is responsible for most of the long-term trends in E_{pan} in Australia ([Roderick et al. 2007](#)). Early warnings against using T -based E_0 from GCMs were sounded by [McKenney and Rosenberg \(1993\)](#), who show that GCM-driven trends in T -based E_0 often had different signs from physically based (i.e., Penman-based) E_0 . When only T was permitted to vary, all E_0 measures trended positively, but the increases in T -based E_0 measures were an order of magnitude greater than those in physically based measures. When all variables (i.e., R_d , e_a , U_2 , leaf area index, and stomatal resistance) were permitted to vary, many of the physically based measures showed declines, indicating that the sensitivities of physically based E_0 measures to T are greatly mediated by sensitivities to their other driving variables. [Donohue et al. \(2010\)](#) draw the same conclusions in using both T -based and physically based E_0 measures to match observed E_0 trends in Australia; they also find that E_0 trends were best estimated by physical measures.

To compare T -based and physically based E_0 as drivers of a simple LSM in trend analyses, [Hobbins et al. \(2008\)](#) ran the hydrology model of the PDSI ([Palmer 1965](#)) at both water-limited and energy-limited meteorological stations, driving it by the T -based E_p measure traditionally used in the PDSI (shown in Figure 3-8b) and by the E_{pan} observation-based E_p (shown in Figure 3-8a). Their work was motivated by the IPCC’s ([2007](#)) predictions of drying in mid-latitude continental interiors undergoing warming, which were predicated to a large part on work underpinned by long-term studies using the PDSI but that flew in the face of contradictory observations of long-term increases in observed soil moisture (SM) ([Robock et al. 2005](#)). The 30-year trends observed in the E_{pan} -based E_0 measures were in line with global declines in E_0 (see Section 3.4.2.2), but different from the mostly positive trends in T -based E_0 : at almost 50% of the stations the two trend directions were opposite. The resulting trends in ET and SM depended on hydroclimatology: in water-limited areas, trends in ET followed trends in P , regardless of E_0 type. In energy-limited areas, trends in ET were a function of trends in E_0 . The populations of SM trends between the two runs bore no relation to each other: at 20% of stations—primarily in agricultural regions toward the energy limit to ET —the trends were opposite.

More recently, [Lofgren et al. \(2011\)](#) warn that, to preserve the physical linkage between T and surface latent heat flux, GCM predictions of T -based E_0 should not be used to drive LSMs. They compare physically based and T -based parameterizations of E_0 in driving large-scale lake budgets. They use data from GCM scenarios to force the Large Basin Runoff Model (LBRM) applied to Great Lakes hydrology, finding that the T -based E_0 currently used in the LBRM leads to far greater ET increases than does a fully physical E_0 . The latter leads to lower decreases, and even increases, in net basin supply and so to higher lake levels. E_0 and ET from the lakes were correlated with T only for the mean annual cycle, and they infer that R_d is the strongest influence on E_0 . This is supported by [Hobbins et al. \(2012\)](#), who show that on an annual scale, T , q , and R_d vie for top billing as the greatest contributor to the variability in a full physical description of E_0 across the Great Lakes region.

In summary, if modeling or preserving variability in E_0 is at stake, T -based E_0 —and other hydroclimatologic analyses derived from it—should be avoided at all time scales, in a diagnostic sense in estimating E_0 itself, in a prognostic sense in using E_0 so-derived to predict land surface hydrologic conditions or fluxes, and in studies of long-term hydrologic trends.

3.2.8 Observed E_0

Operational hydrologists rely heavily on the concept of land surface modeling to mediate their E_0 estimates to the ET fluxes necessary to balance water budgets. LSMs parameterize the dynamics of energetic, hydrologic, pedologic, and biologic fluxes and storages operating across the land surface-atmosphere interface to convert meteorological data to land-surface flux estimates, such as ET . This ET-LSM paradigm underpins much of operational hydrology, not least streamflow (Q) simulation and prediction and analyses of the effects of climate change and variability on the hydrosphere (including drought). As an example, the National Weather Service River Forecast System (NWSRFS) at the nation's 13 River Forecast Centers use the Sacramento Soil Moisture Accounting (Sac-SMA) model (Burnash et al. 1973) in their Q simulation and forecast operations. In the NWSRFS, Q is simulated by driving the Sac-SMA model by observed P and T and forecast by driving the model with forecast P and T from National Weather Service (NWS) Numerical Weather Predictor models. The NWSRFS accounts for ET by driving the Sac-SMA model with monthly climatologic E_0 acting on the available moisture in two stocks representing soil moisture content. E_0 is derived from atlases of observed long-term (1956–1970) mean E_{pan} observations (Farnsworth and Thompson 1982, Farnsworth et al. 1982), spatially and temporally interpolated for each basin.

Traditional users of E_{pan} —the agricultural community—have moved toward ET_{rc} to meet their irrigation scheduling needs. However, partly because the international record is so geographically diverse and long lasting and because the measure itself is simple and intuitive, climatologists and other analysts taking a longer, or secular, view of hydroclimatic variability and change have recently started to acknowledge the diagnostic potential of the E_0 record as an informative measure of the dryness of the lower atmosphere, and E_{pan} provides the best E_0 observation. However, some early analyses have been prone to problematic implementation of E_0 . An example of the problematic estimation of E_0 —and consequent derivation of ET —in the analysis of the impacts of global climate change and variability on the hydrologic cycle, and of drought in particular, is that of the PDSI (Palmer 1965). The PDSI model, which is so central to much of current drought-monitoring practice in the United States (US Drought Monitor 2011) and to worldwide, long-term drought trend analyses (Dai et al. 2004), uses a T -based parameterization of E_0 to drive its LSM and thereby derive ET —to significant deleterious effect (see Section 3.2.7). In fact, E_{pan} has recently been recognized as a valuable metric of E_0 for analyses of climate change and variability (e.g., Roderick and Farquhar 2002; Roderick et al. 2009a, b; Ohmura and Wild 2002; Brutsaert and Parlange 1998; Hobbins et al. 2004). Thus, robust examination of long-term trends and variability in the hydrologic cycle must address the question, “what drives the variability of E_{pan} and are we capturing said variability?” Hobbins et al. (2012) directly address this question.

Recognizing the issue of spatial scale is important. E_{pan} is effectively a zero-dimensional point estimate of E_0 . It is thus subject to forcing from ET from the region surrounding the pan through the dynamics underpinning the complementary relationship (see Section 3.2.3), but the moisture evaporated from the pan is too small to force regional ET in turn. (Were the pan replaced instead by a regional-scale wet surface, this would affect ET , and E_0 and ET would converge, as shown in Section 3.2.3.) Thus, the proper treatment of the diagnostic power of E_{pan} invokes assumptions inherent in the complementary relationship regarding the homogeneity of the region upwind of the pan and whether the overlying boundary layer is well mixed. Given that pans are often sited where they are hostage to the effects of land-use changes, affecting both the long-term time-series trends and the uniformity of surface conditions of the land upwind (and hence of the boundary-layer mixing), these assumptions—specific to the use of observed E_{pan} as an estimator of regional E_0 —are prone to contravention (see Section 3.2.8.2).

Evaporation pans are extraordinarily informative hydroclimatologic indicators, both as to variations in both the radiative driver (e.g., global dimming), where uncovering the dynamics of trends in E_0 have led to resolution of the pan evaporation paradox (Section 3.4.2.5), and as to the advective driver, where a near-global stilling phenomenon has been uncovered (Section 3.4.2.3) in

pursuit of an explanation for declining E_{pan} (Section 3.4.2.2). Unfortunately, while interest in the global record of E_{pan} is rising, ongoing institutional support of the observation networks is declining.

3.2.8.1 Observed E_0 Types

Observations of E_0 are made using instruments that expose a water reservoir to the air and then measure the loss to evaporation over a given period—these may be sited above the ground in the case of evaporation pans or sunk into the ground. US Class A evaporation pans are the most commonly used and widely accepted evaporimeters, but smaller-diameter pans are commonly used in China (McVicar et al. 2005). Of the sunken pans, Colorado pans are perhaps the most widely known. Other smaller evaporimeters (or atmometers), such as the Piche evaporimeter (Piche 1872, de Vries and Venema 1953), are gaining renewed interest as cheaper, reliable replacements to pans for use in, for example, metering ET_{rc} in irrigation scheduling. It was against observations from evaporation pans that Penman (1948) verified estimates of his new meteorological parameter—potential evaporation (E_p). Bridging the gap between such purely physical models and instrumented observations are synthetic estimates that attempt to emulate the performance of instrumentation, such as the PenPan formulation (Linacre 1994, Rotstayn et al. 2006) that adjusts the Penman (1948) equation for E_p to better characterize the enhanced radiative and advective dynamics of US Class A evaporation pans. Simple, nonphysical estimators also exist that parameterize E_0 using T alone; we warn against their use in Section 3.2.8.2.

The affordability and simplicity of the US Class-A evaporation pan has led to its use worldwide over many decades to meter E_0 in agricultural settings (it has been adopted by the World Meteorological Organization as the international standard) and more recently as a metric of long-term hydrologic and atmospheric change and variability (e.g., Brutsaert and Parlange 1998; Ohmura and Wild 2002; Roderick and Farquhar 2002; Hobbins et al. 2004, 2008). The standard US Class A evaporation pan is clearly specified (e.g., Strangeways 2001); it is refilled (or emptied) to the same depth at the same time daily. E_{pan} for the preceding 24 h period is then derived as the change in successive water level not caused by P , or

$$E_{pan_i} = \Delta WL_i + P_i \quad (3-25)$$

where P_i is precipitation accumulated at a nearby tipping-bucket raingauge over the previous 24 h period, and ΔWL_i is the change in water depth over the same period, negative for an increase in depth (from significant P into the pan) and positive for a depth decrease over the previous period. E_{pan} so measured physically integrates all driving variables and is scaled by a pan coefficient that accounts for the effects of the instrumentation—extra radiation intercepted by the pan sides, extra turbulence at the pan edges, and the presence or absence of a bird guard—and then represents a physical measure of E_0 at a point.

3.2.8.2 Pan Evaporation: Uncertainty Sources and Limitations

Evaporation pans have been widely used to measure evaporative demand since well before the term itself was coined. Their primary use has always been as a decision-support tool for irrigation scheduling: basically, irrigators supply water to meet E_0 while accounting for crop phenology and type, thereby maximizing uptake by their crops but minimizing waste. As the physical feedbacks between the land surface and the atmosphere are implicit in pan measurements, they adapt to changing land use, land cover, and hydroclimatology: thus so can the irrigation regime. Indeed, long-term E_{pan} time series are increasingly recognized as a valuable metric of climate change and variability. However, for farmers, hydrologists, and climatologists alike, the practical use of E_{pan} measurements has important sources of uncertainty and limitations, discussed next.

Appropriate Time Scale

The appropriate time scale for E_{pan} is a balance between the season and the operational requirements. The primary purpose of pans in the agricultural sector is to schedule irrigation on short time scales. Due to their negligible thermal mass, vegetated surfaces are energetically more or less at an instantaneous steady state such that incoming and outgoing energy fluxes balance instantly; in evaporation pans, however, heat is stored in the water body for later release, with significant effect on the diurnal and inter-daily variations of E_{pan} (Molina Martínez et al. 2006). This deviation from a steady state by the instrumentation generates deviations from the evaporative dynamics of the vegetation the pan is modeling and has important implications for the appropriate time scale at which E_{pan} data may be used to estimate E_0 accurately.

The deviation from a steady state is a function of period of integration of observations and varies with season and prevailing climatic regime. For an instrumented pan in Australia, Roderick et al. (2009a) show that the change in heat storage comprises a large proportion of λE_{pan} at shorter time scales: it is by far the dominant contributor to the daily energy balance (it can be nearly five times λE_{pan} itself), so the daily observed E_{pan} rate cannot be said to represent daily E_0 . Weekly heat storage change terms may be larger, but their relations to weekly E_{pan} fluxes are far smaller: they are at their largest—up to 40% of the weekly λE_{pan} flux—in the fall and winter, as E_{pan} approaches and reaches its annual minimum. During summer months of higher E_{pan} and lower weekly heat storage changes, the steady-state assumption appears good. On a monthly time step, the heat storage change term represents no greater than 8% of the monthly λE_{pan} —highest again in winter. Depending on one's comfort level, this may be the appropriate time scale at which the steady-state assumption can be said to hold in winter. In summary, the period across which the heat storage term is integrated must be long enough that it does not dominate the λE_{pan} flux accumulated across the same period.

Fortunately, most E_{pan} applications in the operational field (irrigation scheduling) would be made during the spring-to-fall period when λE_{pan} is higher and the heat storage changes are lower as a proportion: thus, λE_{pan} may be assumed to represent E_0 at finer time scales more appropriate to operational requirements. In a climatological setting, this point is moot, as relevant time steps of analyses are long enough to assume steady-state conditions.

Space and Time Limitations to E_{pan} Observations

In the United States, using E_{pan} data to estimate long-term regional trends is constrained by the spatiotemporal distribution of the pans and the physical representativeness of the data. First, the spatial and seasonal bias in the E_{pan} record yields either a spatially limited but year-round dataset or one that is spatially complete but seasonally limited: warm-season pans are located throughout CONUS, but annual pans are limited only to areas free from seasonal freezing. Second, E_{pan} estimates are subject to the vagaries of ambient conditions: many pans are situated in urbanized areas or where local climatological conditions are influenced by upwind spatial heterogeneity. In observing average changes in E_{pan} at a particular site, we may simply be observing the long-term effects of upwind land-use changes—for example, urbanization, irrigation, or deforestation—and may therefore misdiagnose local effects as long-term, regional-scale climatological trends.

E_{pan} Errors under Heavy Precipitation Events

The very nature of evaporation pans generates errors in E_{pan} observations under heavy P events, when splashout—water leaving the pan through splashes over the rim—can account for a significant proportion of raingauge-recorded P input to a pan: 8% to 9%, according to Thom et al. (1981). Not accounting for splashout results in overestimation of E_{pan} for rainy days, and as the error is cumulative it retains its relative importance across any aggregation period.

Further inconsistencies can occur with respect to installation, construction materials, maintenance procedures, and whether or not bird guards and/or paint are used. Variations in the albedo of

the pan directly affect the amount of shortwave radiation absorbed by a pan and hence its energy budget: such variations may also arise due to material aging over the life of a pan.

Homogeneity of E_{pan} Data Series

In multidecadal networks of pans, various adverse impacts create discontinuities (also known in the literature as heterogeneities, breaks, or mean shifts) in the recorded data of various origins: operational impacts include changes in instrumentation, observing procedure, personnel, or station location; local impacts include changes in the land use or land cover in the area immediately surrounding the station, such as urbanization, afforestation, deforestation, or irrigation; large scale impacts include changes in the physical dynamics of the evaporative process themselves, whether because of the variability inherent in the processes, or because of climate forcing, anthropogenic or otherwise. Therefore, before long-term records of E_{pan} (or any hydroclimatologic variable, for that matter) may be used, the data must be homogenized; that is, the artificial signals of operational discontinuities must be removed, leaving only variations in data that result from the variability inherent in the physical dynamics of the process metered. [Peterson et al. \(1998\)](#) provide the basic motivation for homogenization of in situ climatologic data, stating, “The difference in trends between homogeneity-adjusted and unadjusted data can be enormous at an individual station and very significant in regional analyses.” Ideally, metadata—data about the data—would be used to identify potential discontinuities: they are supposed to record the time and nature of operational changes to the station recording the data, some of which will generate discontinuities. Whether local forcings should also be filtered out is a function of the purposes to which the homogenized data will be put.

The flexibility of choice of homogenization procedure is constrained primarily by the temporal completeness of the data, the quality of the metadata, and the purpose of the adjusted data. Across CONUS, E_{pan} data are notable for their incompleteness: at any given station seasonal and multiyear gaps exist where either no data are recorded or insufficient data are recorded to generate the annual, seasonal, or monthly totals of interest. The US pans’ metadata—maintained by the National Climatic Data Center (NCDC) ([NCDC 2011](#)) as lists of dates and coordinates attached to each pan’s online data—do not report all potential sources of discontinuities and often break a pan’s record into subperiods without distinguishing among them. In some cases, subperiods may be distinguished by changes in the recorded latitude and longitude (in degrees and whole minutes) and elevation, allowing pan-location changes to be inferred to a limited precision.

Guided, Semi-Objective Homogenization of CONUS E_{pan}

Compared with trusting the raw (unhomogenized) data completely, homogenizing based on the metadata alone is often a poor improvement. Seeking further potential discontinuities that may not have been reported in the metadata but that are subjectively evident may be necessary. For climatological analyses, climatically driven trends should not be filtered out as sources of heterogeneity, so resolving understandings of both the physical dynamics and the statistical properties of the dataset may be incorporated into a middle-ground approach that combines objective rigor and subjective judgment.

To homogenize the US E_{pan} dataset for hydroclimatic trend analyses in [Hobbins et al. \(2004\)](#), [Hobbins \(2004\)](#) developed a task-specific methodology to meet the requirement that the effects of potentially changing regional climatic drivers be preserved in the dataset and to resolve the issues of incomplete E_{pan} records and less-than-useful metadata. The a priori assumption of nonstationarity obviated many standard, off-the-shelf homogeneity tests that would filter out the very trends sought. Ideally, the effects of local discontinuities would also be removed; however, distinguishing them from the regional variations of interest is not possible. Thus, a homogeneity test was developed that incorporated objective statistical analyses and subjective judgment.

[Hobbins \(2004\)](#) identified three types of discontinuities in the unadjusted data. First, all location changes recorded in the metadata were assumed to result in discontinuities and were adjusted.

Second, some metadata-recorded changes of unknown type were assumed to have resulted in discontinuities, but not all—a reflection of the possibility that some station changes may be unrelated to pan operation (e.g., changes in ancillary instrumentation). Finally, abrupt changes were apparent in the recorded time series, but not recorded in the metadata: the assumption is that some of these discontinuities may be significant. The second and third discontinuity types are tested statistically, and those whose effects are significant are adjusted. Thus, the process homogenizes all statistically confirmed discontinuities and all physical shifts in the pan.

The *t*-test is used to determine whether two samples from periods bounded by discontinuities are likely to have come from the same underlying population, that is, that the discontinuity between them is insignificant. Where the *t*-test implies a statistically significant difference in the mean across the candidate discontinuity, the earlier data are homogenized to the latest (in time) subperiod of the dataset (or subseries) according to the following equation:

$$E_{pan}^A = \mu_2 + E_{pan} - \mu_1 \quad (3-26)$$

where E_{pan}^A indicates the homogenized, or adjusted, data, and E_{pan} its unhomogenized equivalent, and μ_1 and μ_2 refer to the E_{pan} sample means before and after the candidate discontinuity, respectively.

[Hobbins \(2004\)](#) applies this guided, semi-objective homogeneity test to 230 pans' records, resulting in the removal of 326 abrupt data shifts across 75% of the pans, of which 280 were due to changes in pan location and 46 were due to unspecified changes. In this manner, 43% of annual data (at the pans recording year-round E_{pan}) and 55% of warm-season data were homogenized. While the assumptions inherent in the *t*-test—that the mean and variance of the data in the subperiods are stationary—runs counter to the assumption of trends in the data, this source of error is conservative as trends at a given pan tend to be underestimated when they are derived from data thus homogenized. In a comparison of trend results for pre- and post-adjustment data across all pans some differences were noted in the details: the proportions of decreasing trends remained fairly static: annual 57% to 64%, warm season 62% to 60%; the numbers of significant trends in the annual data dropped from 64% to 27% and from 56% to 19% in the warm-season data. However, these differences were not together significant enough to confuse or change the conclusions of the trend analysis for which the homogenization technique was developed ([Hobbins et al. 2004](#)).

Objective Homogeneity Tests

Subjective methods by experienced climatologists may be further informed by such objective techniques as double mass curves ([Kohler 1949](#)) between two stations, or parallel cumulative sums among several reference stations ([Rhoades and Salinger, 1993](#)). [Peterson et al. \(1998\)](#) list and motivate further objective homogeneity tests applicable to hydrometeorological data series. Objective tests make different assumptions and can yield different results but, in general, whichever discontinuity detection and adjustment procedures are used, they are convergent: that is, for a given station, differently adjusted time series will be more similar to each other than they are to the unadjusted time series.

Further examples of objective homogeneity tests—used to generate homogeneous E_{pan} data records for climatological studies in Australia—are the bivariate test ([Potter 1981](#)) used by [Kirono and Jones \(2007\)](#) and the RHTest ([Wang and Feng 2004](#)) used by [Jovanovic et al. \(2008\)](#). Both [Kirono and Jones \(2007\)](#) and [Jovanovic et al. \(2008\)](#) surmise that the Australia-wide negative trends in E_{pan} uncovered by [Roderick and Farquhar \(2004\)](#) might be artifacts of uncorrected discontinuities. However, given the worldwide ubiquity of negative trends in E_{pan} ([Roderick et al. 2009a](#)) and that the trends noted in [Roderick and Farquhar \(2004\)](#) are supported by physical synthesis ([Roderick et al. 2007](#)), the need for a combined statistical and physical approach to homogeneity is clear: statistical heterogeneities should be confirmed physically using a physical model such as the PenPan model of

synthetic E_{pan} (Rotstayn et al. 2006). Using such a physical model to verify results of homogenization may address questions as to the accuracy of the results, against what data this accuracy should be measured, and whether or not the errors involved in homogenization are larger than the trends themselves.

3.3 THE REFERENCE EVAPOTRANSPIRATION CONCEPT

In the agricultural sector, accurate quantification of actual ET from crops (crop ET , ET_c) is crucial for optimizing water-use efficiency, particularly in estimating crop-water demand for irrigation scheduling purposes. To estimate ET_c , we largely rely on the concept of ET_{rc} , in which we estimate ET for a reference crop under strictly specified conditions: this ET_{rc} rate then represents the evaporation from an extensive surface of adequately watered, actively growing crop—grass or alfalfa—of uniform height, subject only to the advective and radiative constraints on ET (see Section 3.1.2). Various coefficients are then applied to account for the differences of crop types, soil types, phenology, and so on between this reference estimate and the prevailing conditions to thereby derive ET_c [Equation (3-29)], which is a measure of the water requirements of a given crop under prevailing conditions.

Such approaches have been codified internationally by the UN Food and Agriculture Organization in Paper 56 (FAO-56, Allen et al. 1998) and across CONUS by the ASCE as the ASCE Standardized Reference ET Equation (Allen et al. 2005b). As a result, the approach has been adopted worldwide in the agricultural sector to estimate ET_c . Beyond its use in estimating ET_c , the ET_{rc} concept is now finding a place in analysis of agricultural drought and, in combination with remotely sensed LST (see Section 3.2.6), in estimating landscape-scale ET in the USGS National Water Census.

In this section, we start with the broader perspective of the most common physically descriptive direct estimator of ET —the Penman–Monteith (P-M) approach; we summarize the concept of ET_{rc} ; then we conduct an empirical sensitivity analysis of ET_{rc} at one site; and finally, we rigorously decompose the time and space variability of ET_{rc} across CONUS.

3.3.1 Penman–Monteith Approach to ET

First, recall that in estimating ET directly surface characteristics are not constrained but instead vary with actual land cover, including vegetation, bare soil, and open water. The P-M model of ET is the most accepted, physically conceptualized, direct estimator of ET (as opposed to remotely sensed estimates or estimates derived from water balances or E_0 -driven LSMs). The P-M model is a Penman (1948)-based combination equation—in other words, a weighted combination of radiative and advective drivers—that is modified to include in its advective driver a parameterization of the fine-scale diffusive characteristics of the plants and the surface under variable Θ conditions. In the P-M model, the fluxes of λET and H are assumed to originate from a combination of bare soil and plant canopy acting as a combined single “big leaf” (see, e.g., Shuttleworth 1993). Water vapor diffuses first from the stomates of the canopy against a bulk stomatal resistance r_s , and then against an aerodynamic resistance r_a from the canopy to the height in the atmospheric boundary layer at which T , R_n , and e_a are measured. H diffuses only from the canopy (i.e., not from within the stomates) and thus diffuses only against r_a . Land cover determines r_a (e.g., through crop height), while Θ restrictions are reflected in r_s , which increases under drier conditions. Together, r_a and r_s reflect both the availability of moisture to evaporate and the process of vapor transfer into the atmosphere, thus their specifications require some characterization of the soil and canopy and their Θ and U_z . For the general case of ET estimation, Brutsaert (1982) describes the parameter r_a . While the r_s concept has been proven useful in simulations and as a diagnostic of conditions of water stress, it remains the primary constraint on the use of the P-M formulation for ET [Equation (3-27)]. This constraint is due to unknown distribution of intracanopy radiative heating, spatial variability of

vapor sources on diurnal and seasonal cycles, seasonality of plant physiology, moisture stress at the roots, and species-specific physiology; no usable soil, plant, or atmospheric parameterizations have been developed for r_s (Brutsaert 1982).

The general P-M formulation for ET is as follows:

$$\lambda ET = \frac{\Delta}{\Delta + \gamma \left(1 + \frac{r_s}{r_a}\right)} Q_n + \frac{\frac{\rho_a c_p}{r_a}}{\Delta + \gamma \left(1 + \frac{r_s}{r_a}\right)} (e_{sat} - e_a), \quad (3-27)$$

where

λET and Q_n are in W m^{-2} ,

Δ and γ are in Pa K^{-1} ,

e_{sat} and e_a are in Pa,

ρ_a is the density of moist air in kg m^{-3} ,

c_p is the specific heat of moist air in $\text{J kg}^{-1} \text{K}^{-1}$, and

r_s and r_a are in sec m^{-1} .

Q_n is derived from the surface energy budget as $R_n + L_n - G$, where R_n and L_n are previously defined and G is a function of T . Formulations for these parameters may be found in Shuttleworth (1993) and Allen et al. (1998).

3.3.2 The ASCE Standardized Reference ET Equation

The ASCE Standardized Reference ET Equation (Allen et al. 2005b), herein known as ASCE05, was developed from the P-M formulation [Equation (3-27)] and has been widely adopted in the United States. It was an attempt to resolve uncertainties that arise from the variety of ET_{rc} model inputs and their applications across the United States and to standardize both ET_{rc} estimation and the determination of crop coefficients for agriculture and landscape use. The ASCE05 formulation of ET_{rc} is derived as a specific instance of the P-M ET model for the following reference conditions: a hypothetical, well-watered short crop of height 0.12 m (similar to clipped, cool-season grass) or a 0.50 m tall crop (similar to full-cover alfalfa); a stomatal resistance r_s of 70 s m^{-1} ; and an albedo α of 0.23. The formulation is as follows:

$$ET_{SZ} = \frac{0.408\Delta}{\Delta + \gamma(1 + C_d U_2)} (R_n + L_n - G) \frac{86,400}{10^6} + \frac{\gamma \frac{C_n}{T}}{\Delta + \gamma(1 + C_d U_2)} U_2 \frac{(e_{sat} - e_a)}{10^3}, \quad (3-28)$$

where ET_{SZ} is the standardized reference ET for grass (ET_{os}) or alfalfa (ET_{rs}) crop surfaces (mm day^{-1} or mm hour^{-1} for daily or hourly time steps, respectively). The 0.408 coefficient is in units of $\text{m}^2 \text{mm MJ}^{-1}$. Other terms on the RHS convert quantities from units used in this chapter to those required in the ASCE05 ET_{SZ} expression: $(86,400/10^6)$ converts R_n , L_n , and G from W m^2 to $\text{MJ m}^{-2} \text{day}^{-1}$; $(1/10^3)$ converts e_a and e_{sat} from Pa to kPa. Values of the numerator constant C_n ($\text{K mm sec}^3 \text{Mg}^{-1} \text{day}^{-1}$ or $\text{K mm sec}^3 \text{Mg}^{-1} \text{hour}^{-1}$ for daily or hourly time steps, respectively) and the denominator constant C_d (sec m^{-1}) specific to time step and the choice of grass or alfalfa, and the derivation of all other variables, are detailed in Allen et al. (2005b), which provides terms standardized for application of ASCE05.

3.3.3 Derivation of ET_c from Reference ET

Estimates of ET_{rc} represent evaporation from soil and transpiration by plants under specific conditions (see Section 3.3.2) and therefore provide an upper limit on ET_c , constrained only by

the advective and radiative drivers of ET . The remaining driver—the moisture required for ET_c —may be supplied by water stored in the soil profile, precipitation, and/or irrigation. Irrigation is required when the ET_c exceeds P and soil water available in the root zone. ET_c is used to optimize water-use efficiency in daily irrigation scheduling programs, water-demand models, and other applications (Marek et al. 2010). Its accurate quantification is crucial but highly dependent on the characterization of site location and the representation of topography, wind obstructions, buildings, roads, hills, drainage, and waterways. In the ET_{rc} paradigm, ET_c can be estimated as

$$ET_c = ET_{rc} K_c K_s, \quad (3-29)$$

where K_c is a crop coefficient that varies by crop development stage (ranges from 0 to 1), and K_s is a water-stress coefficient also ranging from 0 to 1.

K_s is equal to 1 when the depth of readily available water in the root zone (RAW) is greater than or equal to water shortage relative to field capacity (D_r) and for $D_r > RAW$, K_s can be estimated as (Allen et al. 2005a)

$$K_s = \frac{(TAW - D_r)}{(TAW - RAW)}, \quad (3-30)$$

where TAW is the total available soil water in the root zone. A K_s value of 1 can be assumed for fully irrigated conditions.

K_c represents an integration of the effects of four characteristics that distinguish a given crop from the reference crop: crop height, which affects aerodynamic resistance and vapor transfer; canopy–soil albedo, which affects R_n ; canopy resistance to vapor transfer; and evaporation from soil (Allen et al. 1998). K_c is mainly derived directly from studies of the soil-water balance determined from cropped fields or from lysimeters. K_c values are estimated under optimal agronomical conditions, that is, with no issues pertaining to water stress, disease, weed/insect infestation, or salinity.

3.3.4 Sources of Uncertainty in ET_c Estimation

ET_c estimation has many sources of uncertainty: errors in the measurement of weather data and adoption of different methods for estimating ET_{rc} ; errors in the identification of crop-growth stages; differences in the crop varieties due to rapid advances in plant breeding and genomics; errors in the selection of reference ET weather stations to represent the climatic conditions of a field of interest; and errors in the ET_{rc} map due to interpolation. Traditionally, point measurements of ET_{rc} input parameters from the nearest weather station have been used to represent the surrounding area, with ET_{rc} calculated from that station either used directly or interpolated between weather stations for deriving ET_{rc} at a point of interest, the assumption being that weather conditions for the reference crop surface are similar to those in the surrounding region and for the crop in question. However, the sensitivity of ET_{rc} to each of its drivers varies in space (Irmak et al. 2006), as demonstrated for the ASCE05 ET_{rc} formulation in Section 3.3.6.

Variability in K_c over large regions is another source of ET_c uncertainty, which results from spatial variability in ET_{rc} and the use of different ET_{rc} formulations and different reference crops. No consensus exists regarding the suitability of any single ET_{rc} formulation or reference crop for all climatic and geographic conditions, resulting in different values for ET_{rc} and consequently for K_c . Other equations in the literature for estimating ET_{rc} range from physically conceptualized models, such as the Kimberly Penman equation [Equation 4.2.33 in Shuttleworth (1993)], which parameterizes the vapor transfer function by the day of year, to T -based formulations such as the Hargreaves equation (Hargreaves and Samani 1985), which characterizes weather-scale variability using only daily minimum and maximum T (in Section 3.2.7, we address the dangers of T -based

models). Colorado uses the Blaney–Ciddle approach, whereas Texas uses the P–M equation, while in the Pacific Northwest the US Bureau of Reclamation favors the Kimberly Penman equation calibrated in Kimberly, ID. Further, different US states and regions use different reference crops to develop crop coefficients (e.g., Idaho uses alfalfa, whereas Texas uses grass). Consequently, K_c developed for a crop type in one region may not be directly applicable to the same crop type in another region. Therefore, before published K_c values are used, their compatibility with respect to climatic region, reference crop, and ET_{rc} formulation should be ensured (Sammis et al. 2011). However, modifying K_c for compatibility with irrigation–water management may add uncertainty, as statistical approaches are used to develop relationships between, or correction factors for, reported K_c values. Overall, a combination of one or more of these uncertainties can lead to inaccurate ET_c estimation and consequently result in either over-application of water or lower yield due to plant stress. Both can cause decline in producers' net profit and, in the case of over-irrigation, waste limited freshwater supplies.

3.3.5 Observed Sensitivity Analysis of ET_{rc}

Estimation of ET_{rc} requires four input weather parameters— R_d , U_2 , T , and RH —each of which has a high spatial variability. ET_{rc} can be accurately calculated from meteorological data recorded from weather stations with properly instrumented sensors measuring conditions at a reference crop surface (grass or alfalfa), under the prevailing assumption that the weather conditions on the reference crop surface would be similar to that in the surrounding region. If such networks are sufficiently dense, they can effectively capture the spatial variability in ET_{rc} . For example, real-time ET_{rc} and/or ET_c estimates are available for growers for irrigation scheduling in many parts of the world from such networks as the California Irrigation Management Information System or the Texas High Plains ET (TXHPET) Network. However, such networks incur significant installation and operational costs: as a result, more sophisticated geostatistical techniques have been developed (Goovaerts 2000) to perform spatial interpolation of either climatic data or daily ET_{rc} (Courault and Monestiez 1999, Kurtzman and Kadmon 1999). Producers can obtain ET_{rc} values by using geographic coordinates of their fields with interpolated ET_{rc} maps. However, high variation in T , U_2 , wind direction and other weather parameters due to both local effects such as topography (Huard 1993, Goovaerts 2000), land use (Seguin et al. 1982, Li et al. 2010), elevation (Dodson and Marks 1997), soil properties (López-Granados et al. 2005), and regional effects such as atmospheric circulation patterns (Knapp 1992, Buishand and Brandsma 1997) make it difficult to use one predetermined spatial interpolation technique and/or fitting model for interpolating and mapping ET_{rc} over the region. This underscores the necessity for a structural analysis of the dataset (Courault and Monestiez 1999) at a daily time step to select a suitable interpolation technique and a model for creating accurate ET_{rc} maps. The various interpolation techniques available in the literature have inherent advantages and disadvantages.

In this section, we examine the effects of three of the aforementioned weather parameters (T , U_2 , and R_d) to indicate the necessity of accurate data and properly maintained sensors. For this work, data for 1991 to 2008 were collected from the Bushland weather station located in the High Plains of Texas ($35^{\circ} 11' N$, $102^{\circ} 06' W$, 1,170 m elevation) and managed by the TXHPET Network per ASCE guidelines (Allen et al. 2005b). The typical summer growing season in the region is May to October. ET_{rc} for grass (ET_{os}) and alfalfa (ET_{rs}) were calculated using the ASCE05 equation [Equation (3-28)]. The sensitivity of ASCE05 ET_{rc} (Allen et al. 2005b) was quantified with respect to T , U_2 , and R_d measured at a 2-m height. Sensitivity analyses of each variable were conducted by estimating its sensitivity coefficients, β (in mm per unit change), following Smajstrla et al. (1987) and Irmak et al. (2006) as

$$\beta_X = \frac{\Delta ET_{rc}}{\Delta X}, \quad (3-31)$$

where β_X is the sensitivity coefficient of ET_{rc} with respect to one variable (X), keeping all other variables constant; ΔX is the perturbation in T , U_2 , or R_d in increments of 1 K, 1 $m s^{-1}$, and 25 $W m^{-2}$, respectively; and ΔET_{rc} is the response in ET_{rc} .

The sensitivity coefficients β were calculated for ET_{os} and ET_{rs} and graphed to determine sensitivity of T , U_2 , and R_d over different cropping seasons (see Figure 3-9). These figures illustrate an annual cycle in the sensitivity to the driving data, with β dramatically increased during the summer growing season, when individual drivers significantly affect ET_{rc} estimates. This is of major concern to producers and groundwater management districts in the Texas High Plains, where corn, cotton, and sorghum are the major irrigated summer crops. Further, these effects are compounded when two or more variables covary. These results indicate that, with respect to the variability of ET_{rc} , U_2 is generally the most significant driver, followed by T . However, errors in the solar radiation data

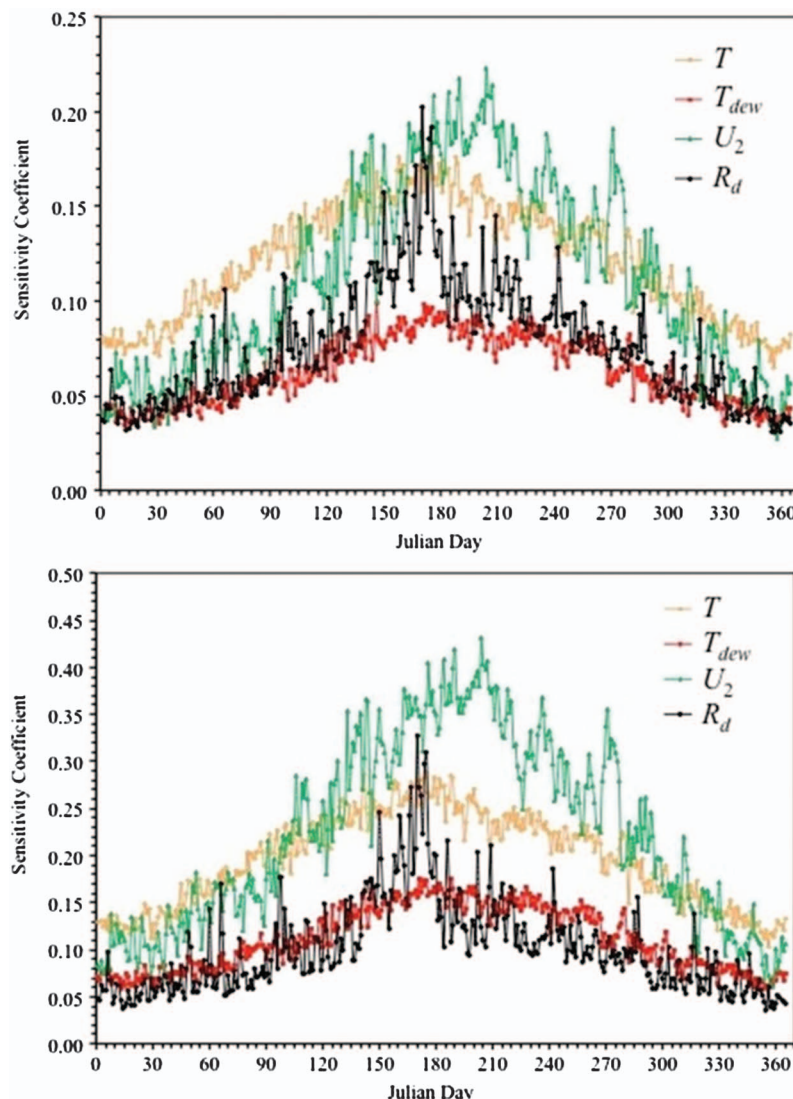


Figure 3-9. The annual cycles of daily average sensitivity coefficients for (top) ET_{os} and (bottom) ET_{rs} for T (brown), T_{dew} (red), U_2 (green), and R_d (black).

during the mid-summer growing period also significantly affect ET estimation. For example, a 1-cm increase in seasonal crop ET demand in the Texas Panhandle due to errors in the measurement of climate variables could result in wasting more than 20 million m^3 of groundwater resources annually (Marek et al. 2010). Therefore, producers need accurate ET_{rc} data during the summer to manage their irrigated crops. The adverse effects on producers' profits of error in estimating ET could be significant. Considering the need for accurate climate data measured at a reference crop site to estimate ET_{rc} and ET_c accurately, application of coarser and relatively less accurate ET_{rc} maps available through the North American Land Data Assimilation System (NLDAS) may be limited to regional and continental-scale applications. In the following section, we decompose the variability of ET_{rc} in such an application.

3.3.6 Method of Moments Variability Analysis of ET_{rc}

Whether the purpose for estimating ET or E_0 is operational (e.g., irrigation scheduling, river forecasting, reservoir operations) or research oriented (e.g., climate change impact analyses, ecological research), in terms of science the a priori optimal models are physically based, as these best represent the physics of ET . However, in terms of accuracy in practice and of practice itself, the answer may lie in a different model. Model choice, therefore, may be a tradeoff between the concomitant addition of more variables, more parameters, and therefore more uncertainty against any potential added physical representativeness. A rigorous variability analysis is a valuable tool in assisting the modeler in finding this balance.

The variability (or uncertainty) in a hydrologic response, whether modeled or observed, is driven by the variabilities (or uncertainties) of its drivers. (Parameterizations of the physics in the model and in the model's parameter values also drive response uncertainty.) The principles of Gaussian error propagation are often used to quantify the effects of driver uncertainty on a predicted or modeled variable. The uncertainties in a model's drivers—in their observations or, if modeled, in their representations—propagate through the model to generate uncertainties in its response or output. Both variability and uncertainty imply a distribution in model outcomes around a mean or an assumed condition. Typically, the normal (Gaussian, hence the name) distribution is assumed for the drivers, with the drivers' standard deviations used to represent their statistical uncertainty. The drivers may be assumed to be independent or uncorrelated, or they may not be, with the complexity rising under the latter assumption. Gaussian error propagation is the effect of uncertainty or error in driving variables on the outcome of a function.

Such techniques have found utility in various hydrologic models. For example, Fisher et al. (2005) use this technique to assess estimates of eddy covariance-derived E_0 from five models from a wide range of simplicity of formulation and driver suites: T and Q_n in the Priestley–Taylor formulation [Equation (3-11)], T and VPD in the McNaughton–Black formulation, combinations of advective and radiative drivers in the Penman and P-M formulations [Equations (3-10) and (3-27), respectively], and a combination equation for evaporation from the soil and transpiration from the vegetation considered separately and then combined in the Shuttleworth–Wallace formulation. They assume that covariances among drivers were negligible, in other words, that the drivers were independent or uncorrelated. They found that much of the overestimation of E_0 by the Shuttleworth–Wallace formulation was because of the uncertainty in estimating a single parameter, canopy stomatal resistance. The performance of these E_0 measures in then estimating ET (applying an Θ function) depended on their specific formulations and driver sets: for example, the Penman equation's performance was highly sensitive to U_z . In fact, the simplest model—the Priestley–Taylor equation—performed remarkably well in estimating ET when its α_{PT} parameter was calibrated to local surface conditions and/or SM ; indeed, Fisher et al. (2008) recommend it for ecosystem models run at larger scales and for assessing global ET trends.

Fisher et al.'s (2005, 2008) findings demonstrate the dangers of model over-decomposing the uncertainties and variabilities into their drivers is vital to operational hydrologists as doing so

permits uncertainty reduction by improvements in the drivers and appropriate model selection and model parameter evaluation. Understanding what drives the variability of a hydrologic response is therefore crucial as it permits prioritization of these efforts.

Following, we examine the variability of E_0 as measured by the ASCE05 ET_{rc} formulation. (For ease of presentation, ET_{rc} is in units of W m^{-2} throughout Section 3.3.6.) The central question we seek to answer is this: “What drives the spatial and temporal variability of E_0 across CONUS?” This method assumes a known relationship between the drivers and a modeled response—here the ET_{rc} from the ASCE05 ET_{rc} model (Allen et al. 2005b) described in Section 3.3.2—and attributes the response variability to each driver, through a Gaussian error propagation technique known as the method of moments. In this technique a functional relationship $f(X_i, i = 1 \dots n)$ among all n drivers X_i and a model output—here ET_{rc} —is known; one or more statistical moments of ET_{rc} are sought and are estimated using approximations of $f(X_i)$. This method may be said to be a derived distribution approach in that the statistics of the distribution of the dependent variable are derived from the distributions of the independent variables via the functional relationship. Such an analysis identifies which drivers—by dint of their own uncertainty or variability—introduce the greatest error and thus require the most correction effort, and which are essential to strike the correct balance between the competing demands of parameter parsimony and physical representation.

Which member of the family of methods is used depends on which statistical moment of the response variable is required and the order of approximation to $f(X_i)$. Here we make a first-order approximation and, as we are interested in examining the variability of E_0 in relation to the variabilities in its drivers, we use the second moment to estimate the variance (mean is the first moment, the variance the second moment about the mean, skewness the third, and kurtosis the fourth). Thus, the member of the family of methods we use herein is the “first-order, second-moment analysis.” Computational tractability may become a limiting issue in estimating higher moments of the response variable.

For a given model using spatially distributed drivers, output variability results from drivers’ variability at a point in space across multiple realizations (e.g., multiple years of data) and spatial uncertainty for a single realization of drivers owing to each driver’s spatial correlation structure and the cross-correlations among drivers. While we do not consider the drivers’ spatial correlation structures here—this is determined by the NLDAS assimilation algorithms—Buttafuoco et al. (2010) show that to accurately assess model output uncertainty, modeling the drivers’ spatial correlation correctly is crucial for distinguishing between uncertainties owing to the drivers and those owing to the model.

Following, in Section 3.3.6.1, we describe the use of the ASCE05 ET_{rc} model to estimate spatially distributed ET_{rc} data series used in the subsequent variability analysis. Then, in Section 3.3.6.2, we map the variability of ET_{rc} across CONUS. In section 3.3.6.3 we outline the concept used to decompose ET_{rc} variability into contributions from its drivers using a first-order, second-moment variability analysis. In Section 3.3.6.4 we quantify the contributions to ET_{rc} of each of the drivers, summarizing the results in a series of maps demonstrating for various time frames the power of each driver in determining the variability of ET_{rc} across CONUS and identifying which driver dominates ET_{rc} variability.

3.3.6.1 Driving ET_{rc} with NLDAS Data

Although we use the ASCE05 equation for ET_{rc} (Allen et al. 2005b), the results of our variability analysis on ET_{rc} are representative of the physics of E_0 and may be generalized to most physically based E_0 estimates that take a similar form to the Penman combination equation. We drive the ASCE05 ET_{rc} model [Equation (3-28)] with the following four meteorological and radiation variables drawn from NLDAS (Mitchell et al. 2004): T , q , U_{10} , and R_d . (P_a and L_d are also available from NLDAS, but ASCE05 eschews these inputs. While doing so affects the variability in our output ET_{rc} , we wish to adhere to the ASCE05 formulation and input suite so that our results remain general.) The drivers are hourly reanalysis surfaces aggregated to daily means. The results shown in Figures 3-10 to 3-16 are for 30 years (1980–2009) of daily, NLDAS-forced analyses distributed across

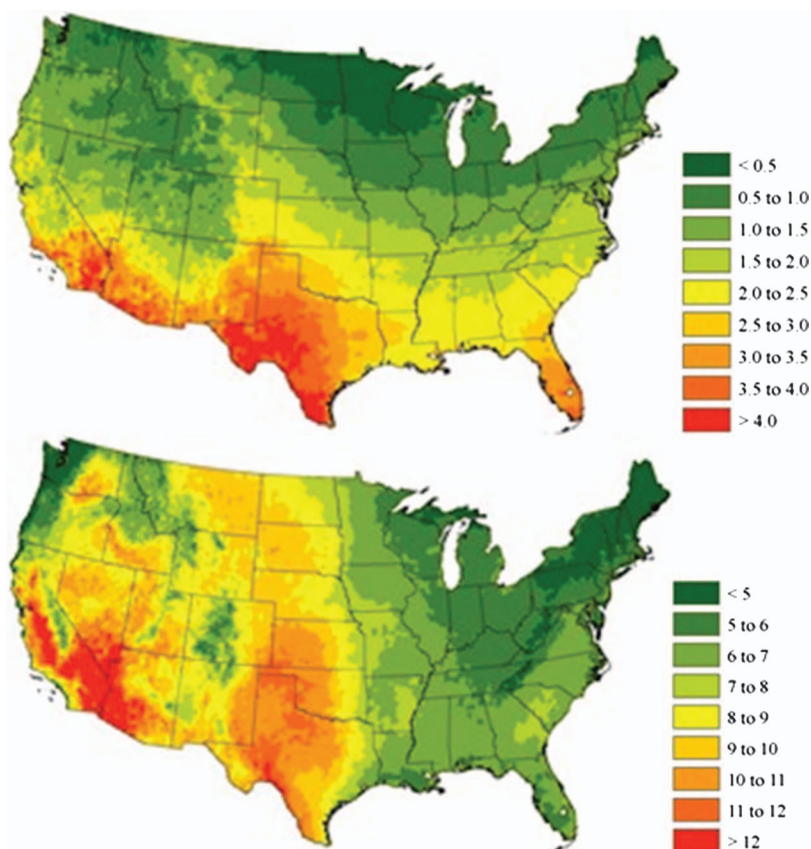


Figure 3-10. 30-year climatologic mean ET_{rc} as estimated by the ASCE05 formulation forced by NLDAS data, 1980–2009, at the daily time frame and aggregated across (top) January and (bottom) July (mm day^{-1}). Note the different scales and units for each panel.

CONUS at a 0.125° resolution. Similar results may be obtained for time frames as short as the smallest time step of the dataset (in this case, individual days).

Figure 3-10 shows mean monthly ASCE05-derived ET_{rc} from the 30 year daily reanalysis. As expected, ET_{rc} is highest in regions that are sunniest, warmest, driest, and/or windiest, although totals vary widely in magnitude and spatial distribution.

3.3.6.2 Mapping the Variability of ET_{rc}

Figure 3-11 shows the coefficient of variation (CV) of daily ET_{rc} over two monthly time frames. There is intra-annual change of variability in ET_{rc} ; in January, the area of greatest variability of daily ET_{rc} is in the northern High Plains, west into Montana, and also in eastern Washington and pockets of the inter-mountain West, while the southern states have uniformly low variability; in July, the pattern more closely resembles that of the annual time frame (not shown), excepting that the western United States has almost uniformly low variability.

3.3.6.3 The First-Order, Second-Moment Variability Analysis Framework

Following, we describe a first-order, second-moment variability analysis performed to decompose the variability in ET_{rc} into the variabilities in all model drivers. Variability in this context refers to the variances of the response $\sigma_{ET_{rc}}^2$ and its four drivers σ_X^2 . This technique requires the analytical

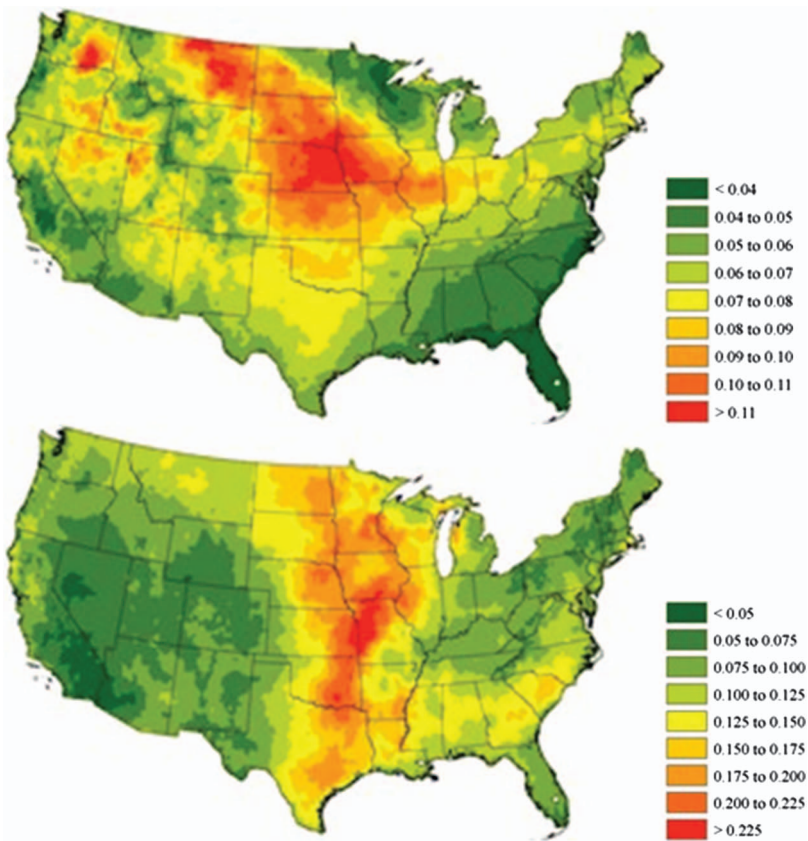


Figure 3-11. Coefficient of variation of ET_{rc} at daily time frames across (top) January and (bottom) July. Note the different scales between panels.

derivation of the sensitivities of the model to its drivers, empirical observation of the variabilities in each of the drivers varying alone and together in pairs and combining these sensitivities and variabilities in an expression of the overall variability of ET_{rc} .

The variability in ASCE05-derived ET_{rc} results from the variabilities in each member of its set of drivers— T , q , U_{10} , and R_d , each assumed to be a random variable with a distribution of known mean and variance—acting independently and covarying with the others.

We define γ as the vector of all partial derivatives (i.e., the sensitivities of ET_{rc} to its drivers) and γ^T as its transpose:

$$\gamma^T \stackrel{\text{def}}{=} \left[\frac{\partial ET_{rc}}{\partial T} \frac{\partial ET_{rc}}{\partial q} \frac{\partial ET_{rc}}{\partial U_{10}} \frac{\partial ET_{rc}}{\partial R_d} \right], \quad (3-32)$$

in which the partial derivatives are evaluated at all drivers' means across the relevant time frame. We further define C as the covariance matrix, describing the variances σ_X^2 of, and covariances $\sigma_{X,Y}$ between, the driving variables:

$$C \stackrel{\text{def}}{=} \begin{bmatrix} \sigma_T^2 & \sigma_{T,q} & \sigma_{T,U_{10}} & \sigma_{T,R_d} \\ \sigma_{q,T} & \sigma_q^2 & \sigma_{q,U_{10}} & \sigma_{q,R_d} \\ \sigma_{U_{10},T} & \sigma_{U_{10},q} & \sigma_{U_{10}}^2 & \sigma_{U_{10},R_d} \\ \sigma_{R_d,T} & \sigma_{R_d,q} & \sigma_{R_d,U_{10}} & \sigma_{R_d}^2 \end{bmatrix}. \quad (3-33)$$

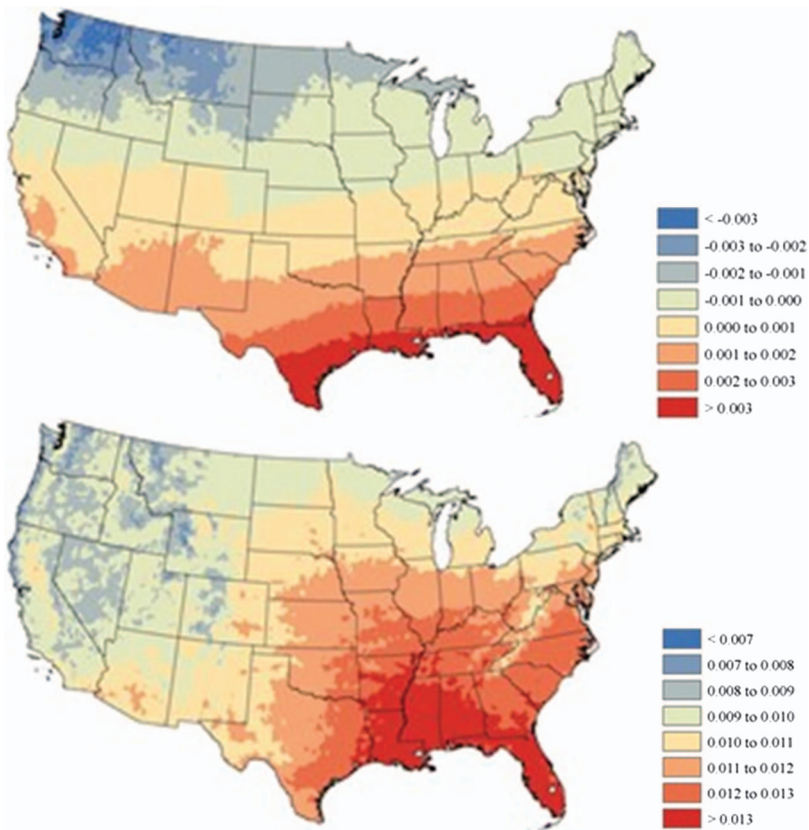


Figure 3-12. Sensitivity of ET_{rc} to mean R_d ($\partial ET_{rc} / \partial R_d$) at the daily time frame across (top) January and (bottom) July ($(mm\ month^{-1})$ ($W\ m^{-2}$) $^{-1}$). Note the different scales and units for each panel.

Then, $\sigma^2_{ET_{rc}}$ expands completely into the full expression for the variability in ET_{rc} expressed as contributions from all of its components, as follows:

$$\sigma^2_{ET_{rc}} = \gamma^T C \gamma = \left\{ \begin{array}{l} \frac{\partial ET_{rc}}{\partial T}^2 \sigma_T^2 + \frac{\partial ET_{rc}}{\partial T} \frac{\partial ET_{rc}}{\partial q} \sigma_{T,q} + \frac{\partial ET_{rc}}{\partial T} \frac{\partial ET_{rc}}{\partial U_{10}} \sigma_{T,U_{10}} + \frac{\partial ET_{rc}}{\partial T} \frac{\partial ET_{rc}}{\partial R_d} \sigma_{T,R_d} + \\ \frac{\partial ET_{rc}}{\partial q}^2 \sigma_q^2 + \frac{\partial ET_{rc}}{\partial q} \frac{\partial ET_{rc}}{\partial T} \sigma_{q,T} + \frac{\partial ET_{rc}}{\partial q} \frac{\partial ET_{rc}}{\partial U_{10}} \sigma_{q,U_{10}} + \frac{\partial ET_{rc}}{\partial q} \frac{\partial ET_{rc}}{\partial R_d} \sigma_{q,R_d} + \\ \frac{\partial ET_{rc}}{\partial U_{10}}^2 \sigma_{U_{10}}^2 + \frac{\partial ET_{rc}}{\partial U_{10}} \frac{\partial ET_{rc}}{\partial T} \sigma_{U_{10},T} + \frac{\partial ET_{rc}}{\partial U_{10}} \frac{\partial ET_{rc}}{\partial q} \sigma_{U_{10},q} + \frac{\partial ET_{rc}}{\partial U_{10}} \frac{\partial ET_{rc}}{\partial R_d} \sigma_{U_{10},R_d} + \\ \frac{\partial ET_{rc}}{\partial R_d}^2 \sigma_{R_d}^2 + \frac{\partial ET_{rc}}{\partial R_d} \frac{\partial ET_{rc}}{\partial T} \sigma_{R_d,T} + \frac{\partial ET_{rc}}{\partial R_d} \frac{\partial ET_{rc}}{\partial q} \sigma_{R_d,q} + \frac{\partial ET_{rc}}{\partial R_d} \frac{\partial ET_{rc}}{\partial U_{10}} \sigma_{R_d,U_{10}} \end{array} \right\} \quad (3-34)$$

In Equation (3-34), each line on the RHS represents the contributions to the variability in ET_{rc} due to the inclusion of a single driver in the ET_{rc} parameterization: the first term on each line represents the variability arising from the driver considered varying independently of other drivers and each of the next three terms represents the variability arising from that driver covarying with each of the other drivers. When the independent variables are uncorrelated, the expression devolves to simple Gaussian error propagation. However, we cannot assume that the four meteorological and radiative drivers are uncorrelated.

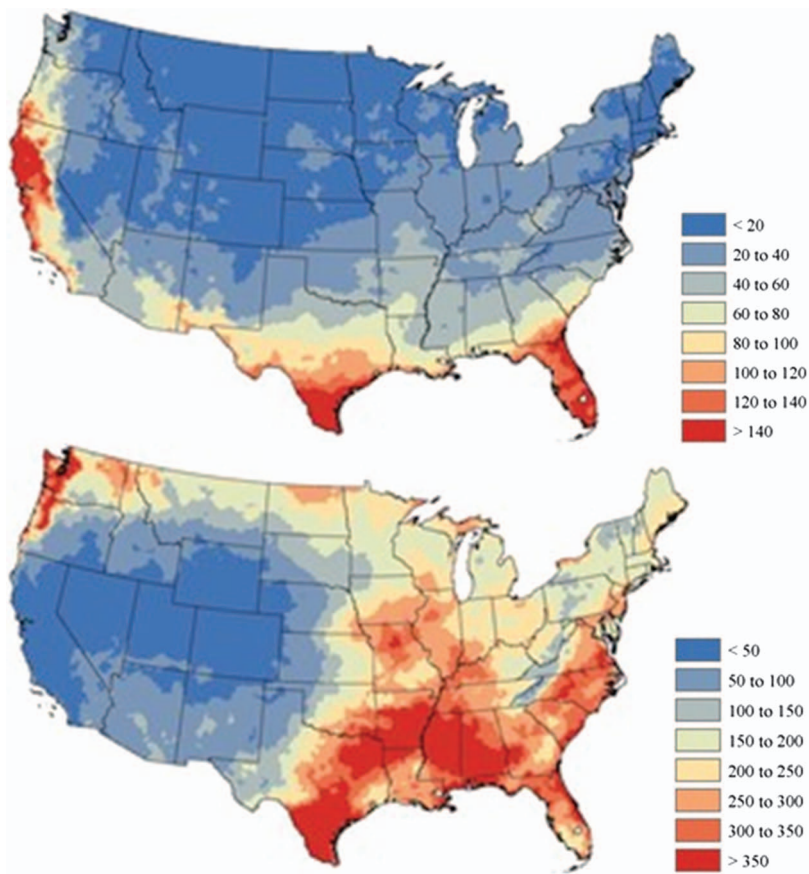


Figure 3-13. Variance of NLDAS R_d ($\sigma_{R_d}^2$ in $W^2 m^{-4}$) at the daily time frame across (top) January and (bottom) July. Note the different scales for each panel.

All σ_X^2 and $\sigma_{X,Y}$ are derived empirically from the 30-year NLDAS reanalysis dataset (e.g., Figures 3-13 and 3-14). The sensitivities of ET_{rc} to each of its drivers ($\partial ET_{rc}/\partial X$) are derived analytically from the model formulation by first expressing ET_{rc} as a differentiable expression with respect to each of its four drivers, as detailed in Hobbins (2016).

Each sensitivity expression is estimated at the means of all drivers that appear in the partial derivative as overbarred variables. Figure 3-12 shows an example of these sensitivities. Recalling that all σ_X^2 and $\sigma_{X,Y}$ are quantified through time-series analysis, we can now decompose the contribution to the overall variability in $\sigma_{ET_{rc}}^2$ from each driver.

Figures 3-13 and 3-14 show examples spatial patterns of variance and covariance: Figure 3-13 maps $\sigma_{R_d}^2$ and Figure 3-14 maps $\sigma_{R_d,T}$. The patterns and magnitudes of the variance of R_d differ between time frames as different regions are influenced by different weather systems at any given moment and at any point from season to season. Away from the coasts, the western half and northeast of CONUS display the least variability in R_d , while the West and Gulf Coasts and the southeast generally display the greatest variance. Positive covariances indicate that two variables vary in the same direction. Negative covariances indicate that the two variables are negatively correlated, with a decrease in one associated with an increase in the other. Modeled annually (not shown), R_d and T vary together across the vast majority of CONUS: clearer skies are associated with higher T , and cloudier skies with lower T . In winter, when cold snaps associated with high pressure outbreaks dominate covariance, T and R_d exhibit negative covariance: clearer skies are associated with lower T .

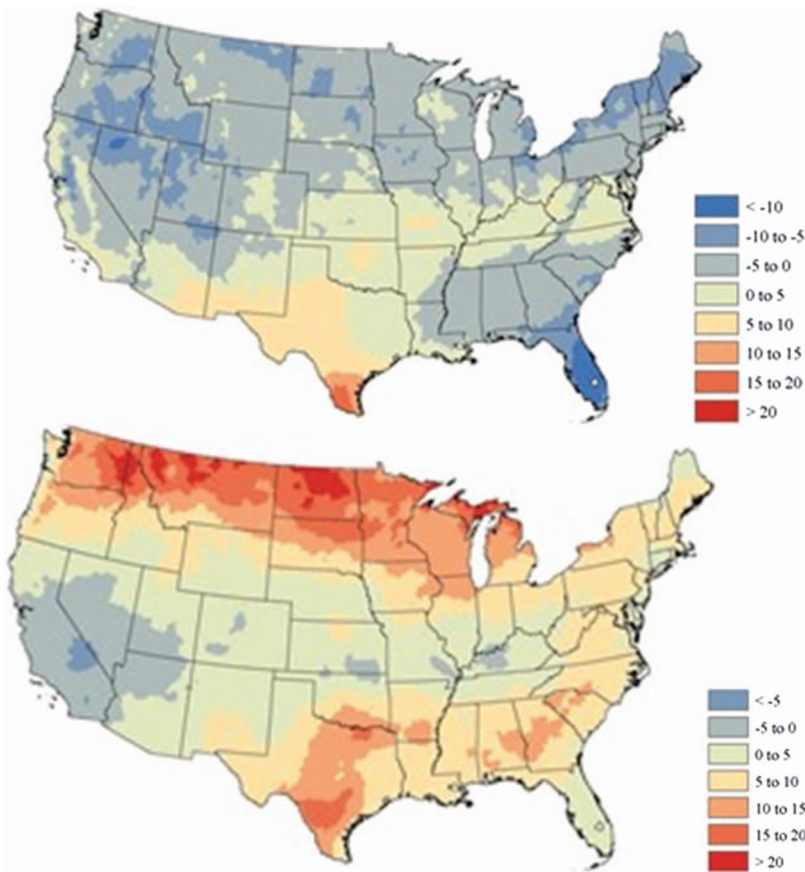


Figure 3-14. Covariances of R_d with T , $\sigma_{R_d,T}$ ($W m^{-2} K$), as observed from NLDAS data at the daily time frame across (top) January and (bottom) July. Note the different scales for each panel.

In summer, except in the far southwest, the covariance pattern is positive: clearer skies and a sun higher in the sky allow for more solar heating, resulting in higher T . For many pairs of drivers, however, drawing meaningful conclusions regarding covariance is difficult, and magnitudes can be slight.

It is important to recognize that sensitivities, variances, and covariances interact to affect the magnitude of variability in ET_{rc} : they can both augment and mitigate ET_{rc} variability. Taking the parts of the expression for the overall decomposition in overall ET_{rc} variability [Equation (3-34)] that pertain to R_d and T , for example

$$\sigma_{ET_{rc}}^2 \sim f \left\{ \frac{\partial ET_{rc}}{\partial T} \sigma_T^2, \frac{\partial ET_{rc}}{\partial R_d} \sigma_{R_d}^2, 2 \frac{\partial ET_{rc}}{\partial T} \frac{\partial ET_{rc}}{\partial R_d} \sigma_{T,R_d} \right\}, \quad (3-35)$$

It is clear that the contribution to $\sigma_{ET_{rc}}^2$ from T and R_d acting alone (the first two terms on the RHS) can only be positive (i.e., augment $\sigma_{ET_{rc}}^2$). The same is true for the contributions from all drivers considered acting alone. However, whether the contribution to $\sigma_{ET_{rc}}^2$ of R_d and T acting in concert is to augment or to mitigate depends on the signs of $\partial ET_{rc}/\partial R_d$, $\partial ET_{rc}/\partial T$, and $\sigma_{R_d,T}$. For instance, as shown in Figure 3-14, in July R_d and T covary negatively across the southwest and California, while both $\partial ET_{rc}/\partial R_d$ (see Figure 3-12) and $\partial ET_{rc}/\partial T$ (not shown) are everywhere positive in this time frame, leading to a negative RHS third term. This implies that, at least in this region in July, the effect of R_d and T acting in concert is to mitigate the overall variability in daily ET_{rc} .

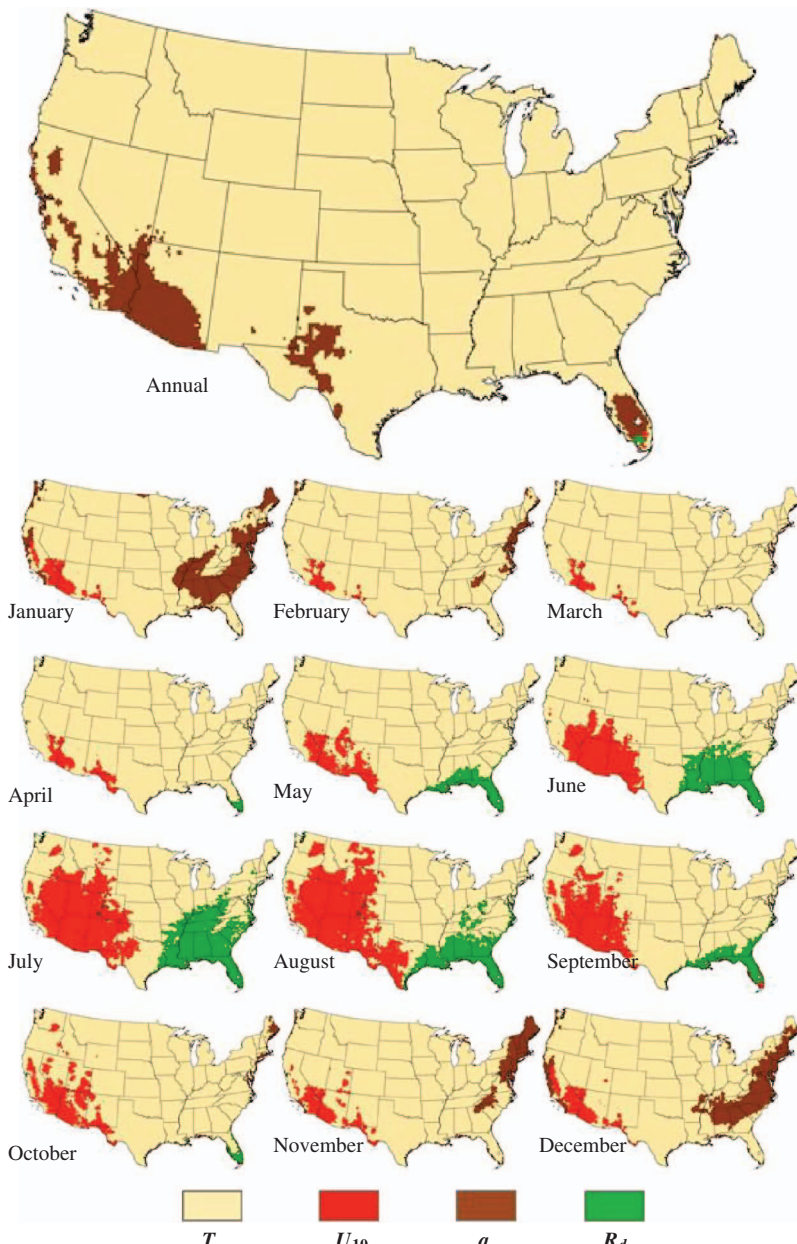


Figure 3-15. The dominant drivers of variability in annual ET_{rc} and daily ET_{rc} by month.
Source: [Hobbins \(2016\)](#), used with permission.

3.3.6.4 Quantifying Variability Contributions from Drivers

As Equation (3-34) shows, the contribution to the variability in ET_{rc} of any single variable X is a function of terms comprising contributions due to its own variability σ^2_X and to the variability arising from its covariance with all other m ($m = n - 1$) variables Y . The variance terms (i.e., the first term in each line) are always positive and so always act to augment ET_{rc} variability; the covariances between variables and sensitivities (i.e., the components of the remaining terms in each line) are often negative (e.g., see Figure 3-14), in which case they act to mitigate ET_{rc} variability. Here we

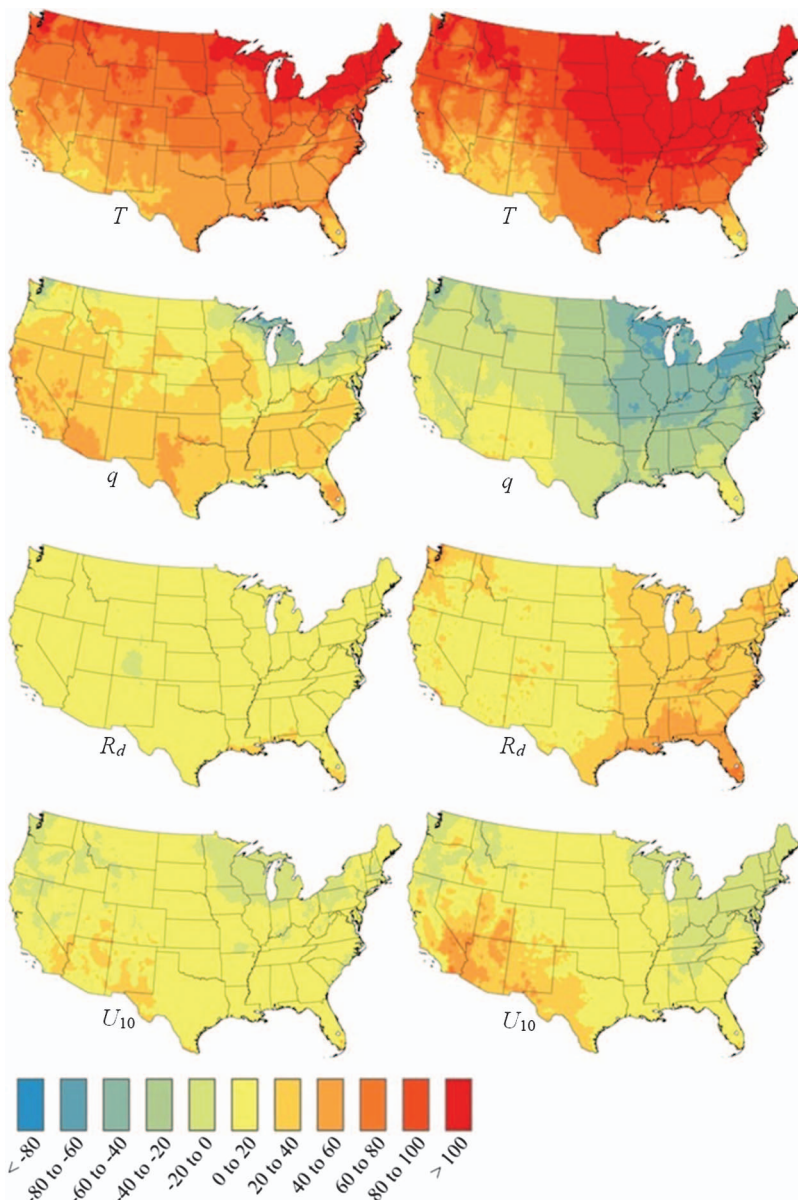


Figure 3-16. Each driver's percentage contribution to variability of (left column) annual ET_{rc} and (right column) daily ET_{rc} across the growing season (MJASO—May, June, July, August, September, October). Drivers are indicated.

Source: [Hobbins \(2016\)](#). Used with permission.

define the contribution to overall ET_{rc} variability from any single variable X as the magnitude of the sum of augmenting and mitigating terms (B_X), as follows:

$$B_X \stackrel{\text{def}}{=} \frac{\partial ET_{rc}}{\partial X} \left[\frac{\partial ET_{rc}}{\partial X} \sigma_X^2 + \sum_{i=1}^m \left(\frac{\partial ET_{rc}}{\partial Y_i} \sigma_{X,Y_i} \right) \right]. \quad (3-36)$$

Note here that although covariances are commutative (i.e., $\sigma_{X,Y} = \sigma_{Y,X}$), in estimating B_X , we distinguish between identically defined covariance terms to prevent double counting of their contributions.

The overall variability in ET_{rc} from all n drivers ($n = 4$ here) is then

$$\sigma_{ET_{rc}}^2 = \sum_{x=1}^n B_X. \quad (3-37)$$

We then define a variable's power (Θ_X), or its relative strength among all contributors to ET_{rc} variability, by normalizing its contribution by the sum of contributions for all drivers, as follows:

$$\Theta_X \stackrel{\text{def}}{=} \frac{B_X}{\sum_{x=1}^n B_X}. \quad (3-38)$$

By mapping which variable is top ranked [$\max(\Theta_X)$ for all X], Figure 3-15 demonstrates which drivers contribute the greatest variability to ET_{rc} and that this dominance varies significantly across time and space. When modeled on an annual basis (i.e., annual ET_{rc} totals derived from mean annual drivers), T dominates across the vast majority of CONUS (94.4% by area); q dominates across the Sonoran Desert in the southwest (5.4%), parts of west Texas, and southern Florida; while R_d and U_{10} account for small areas (0.06% of CONUS) in southern Florida. Such observations at the annual time frame may underpin the common misconception that T is a suitable driver for ET_{rc} at all time frames (see Section 3.2.7); however, the figures for daily ET_{rc} for each month demonstrate the spatiotemporal volatility of the leading contributors to variability as the top-ranked drivers clearly change seasonally across CONUS. In the vital late-spring and summer months, R_d becomes the top-ranked driver across the southeast, while U_{10} dominates in the west, with T ranked top elsewhere. Domination by q is limited to the winter months in the northeast, Mid-Atlantic states, and some areas along the Pacific Coast.

Figure 3-16 indicates the relative proportions of ET_{rc} variability contributed by each driver across the annual and daily (across MJJASO) time frames. It uncovers transitory shifts in dominant variability driver that demonstrate the importance of regional and seasonal analyses. Note that while variability contributions sum to 100% across the complete set of four drivers, a given driver's contributions may exceed 100%: these will be offset by variability reductions (negative values) of other drivers. R_d is much more important at the daily scale than at the annual scale, particularly in eastern CONUS; this is similar to U_{10} in the southwest. In general, q contributes to annual ET_{rc} variability; however, it tends to reduce daily ET_{rc} variability where T makes the greatest contributions, particularly in the east and north. Many unexplored ways to examine such datasets using these methodologies remain. Smaller-scale analyses are possible that reflect the seasonal and regional demands, such as the all-important growing and water-supply seasons in the western United States. Other E_0 formulations and driver sets may uncover different phenomena: for instance, in using T , q , U_{10} , R_d , L_d , and P_a from NLDAS to drive synthetic E_{pan} from the PenPan model (Rotstayn et al. 2006), Hobbins et al. (2012) find a bloom of significant variability contribution from U_{10} in the late spring and summer across the Colorado Plateau and Great Basin, a finding with significant implications in determining model type for monitoring or forecasting E_0 across that part region.

These results underscore the importance of such regional and seasonal analyses of E_0 and the dangers of a one-size-fits-all oversimplification in the number and type of drivers. In summary, the simplicity afforded by parameter parsimony can no longer be substituted for accuracy.

3.4 TRENDS IN ET AND E_0

Few of climate change's effects on life on Earth will be more immediate than those involving the hydrosphere. To understand the future effects of an altered hydrologic cycle, hydrologists and water managers turn to predictions from global and regional climate models, but first it is essential to establish a baseline for such modeling by rigorously examining past changes both in assessing their direction, magnitude, and significance and in identifying their drivers.

The hydroclimatologic research community has recently come to recognize E_{pan} as a valuable metric of E_0 for such analyses: E_{pan} is a long and widely observed flux that responds to radiative, meteorologic, and hydrologic forcings acting globally and at regional and local scales. Trends in these forcings can be teased out of E_{pan} trends. The worldwide long-term time series of E_{pan} offers a proxy for long-term climatic trends in its drivers (Roderick et al. 2009a, b), so decomposing E_{pan} trends may prove useful beyond the hydrologic community. Compared with the number of studies in E_0 trends, few of ET itself exist. This dearth of direct observational analysis of ET trends (Jung et al. 2010) is primarily due to the difficulties inherent in calculating secular time series of ET and the complications of scale (Hobbins 2004), leaving most ET trend studies generally in the context of E_0 at a point particularly E_{pan} (e.g., Peterson et al. 1995; Brutsaert and Parlange 1998; Ohmura and Wild 2002; Roderick and Farquhar 2002, 2004, 2005; Hobbins et al. 2004; Roderick et al. 2007, 2009a)—and not ET at a regional scale. Therefore, a need exists for analyses of trends in ET on regional spatial scales useful in the resolution of water-management issues raised by an increasingly variable hydroclimate.

In following sections, then, we detail the use of the Mann–Kendall test, commonly used in hydrologic trends analyses. This will raise issues relating to the treatment of the effects of serial correlation on the significance of trends: we propose a simple, intuitive technique to adjust the critical bounds of test statistics to better assess the significance of trends that are autocorrelated. For a case study of these techniques, we use a 42-year annual time series of ET derived using Brutsaert and Stricker's (1979) AA model of the complementary relationship in regional ET . Hobbins et al. (2001a, b; 2004) describe the derivation of this data series, so here the following suffices: such a data series meets the need to estimate ET trends across unmetered regions and requires no surface parameterizations; distributed input fields are derived at a spatial resolution as close to the smallest physically defensible under the complementary relationship paradigm that computational power limitations will allow; and as the analysis is not limited to stations, trends in ET and its components may be represented at various spatial breakdowns.

Here, we summarize the recent literature on constraints on and observations of observed secular trends in ET and its drivers (i.e., the radiative and advective dynamics). We summarize recent studies that have observed trends in ET and E_0 across CONUS and examine such trends as indicators of climatic change by decomposing them into the trends in their drivers. We identify sources of consensus and of controversy—in particular, in explaining the falling E_{pan} phenomenon in relation to trends in the meteorologic, radiative, and hydrologic drivers of ET , we discuss the evaporation paradox and its resolution.

3.4.1 Trend Analysis Techniques

Various methods may be used to examine temporal trends in hydrologic time series, falling broadly into parametric and nonparametric types. The former relies on assumptions regarding the underlying distribution of a population sampled by independent, normally distributed observations to estimate the parameters of the process. An example is ordinary least squares (OLS) linear regression, which we use in Section 3.4.2 to make direct comparisons to the work of others. Hirsch et al. (1992) cover OLS linear regression applied to hydrologic data. Nonparametric tests examine measurements of a process made in nominal, or ordinal, scales (e.g., the rank of an observation in a

sample) but make no assumptions as to the underlying distribution of the population. They are thought to represent the statistics of nonnormally distributed data better than parametric tests (Yue et al. 2002). A typical nonparametric test used in hydrology is the Mann–Kendall test, which is covered in Salas (1993). Following, we examine the effects of autocorrelation on the power of this test, and we use the test to estimate trends in *ET* (Section 3.4.2.1) and its drivers (Section 3.4.2.4).

Autocorrelation and the Power of the Mann–Kendall Test

The Mann–Kendall test statistic (*Z*-statistic) is nondimensional, measuring the direction of a succession of data with time and thereby offering information as to the direction of observed trends of a time series and a measure of their significance, but providing no quantification of the magnitude of the trend. The *Z*-statistic is used to test the null hypothesis (H_0) that the data are identically distributed random observations and not time dependent—in other words, that no trend exists. Ordinarily—that is, assuming no autocorrelation in the time series beyond that directly resulting from trends— H_0 of no trend cannot be rejected at the α -significance level if *Z* lies outside the $1 - \alpha/2$ quantile of the standard normal distribution. Otherwise, H_0 must be rejected at the α -significance level in favor of the alternative hypothesis (H_a) of a positive (or negative) trend if *Z* exceeds the critical value of *U* in a positive (or negative) direction.

Crucially, the power of the Mann–Kendall test—the probability of correctly rejecting H_0 and identifying an existing trend—varies with sample size, trend magnitude, significance level, and the time-series' variability and autocorrelation (Yue et al. 2002): indeed, one of the primary assumptions in the application of nonparametric tests remains that of serial independence (or lack of autocorrelation). The impact of autocorrelation on the test's power is also a function of trend magnitude, sample size, and autocorrelation magnitude (Yue and Wang 2002), increasingly so for lower sample sizes and lower trend magnitudes. For low sample sizes, Yue and Wang (2002) suggest $n < 50$, positive autocorrelation increases the probability of trends being detected; that is, one is more likely to reject H_0 and conclude that a trend exists, falsely or not; negative autocorrelation decreases the probability of detection, that is, one is more likely to accept H_0 and conclude that no trend exists—again, falsely or not.

Given that *ET* is a function of a range of hydrologic (*SM*), meteorologic (*T*, U_z , and e_a), and radiative (R_d and L_d) drivers that may exhibit strong persistence and be influenced by periodic phenomena such as the El Niño–Southern Oscillation (ENSO), one should be prepared to account for the effects of autocorrelation when examining *ET* trends. Here we examine these effects using an annual *ET* dataset (water years 1953 to 1994, so $n = 42$) derived according to the principles of the complementary relationship (Section 3.2.3). First, we test for the significance of autocorrelation. Traditionally, this involves the application of confidence limits to the correlogram, which displays the autocorrelation ρ_j of a time series across a range of time lags j . The limits for the γ confidence level (or α significance level; $\gamma = 1 - \alpha$) are defined by $(-U_{1-\alpha/2}/\sqrt{n}, U_{1-\alpha/2}/\sqrt{n})$. For a given α , values of ρ_j within these limits indicate no autocorrelation at lag j ; values of ρ_j outside these limits indicate significant autocorrelation: positive above and negative below. Figure 3-17 plots these results for the annual *ET* data series in the manner of a correlogram, but displayed spatially rather than the more familiar temporal domain, with “correlomap” representing ρ_j of annual *ET* across CONUS.

Our initial suspicion of autocorrelation in annual *ET* is confirmed: at lag 1, 64% of CONUS shows a significant positive ρ , particularly in the western and eastern thirds; at lag 2, this ρ has decayed markedly within the central third and to about 50% of each of eastern and western thirds; at still higher lags, the positive ρ decays further, all but disappearing by lag 4, at which point negative ρ begins to appear in isolated, transitory pockets. Further correlomaps (not shown) express no apparent spatial structure. The bottom panel summarizes these findings, showing the areal proportions of CONUS with significant ρ_j (positive or negative) for $j = 1 \dots 12$.

Trends may be masked by time-series variability, with test power reduced by large variability, increased for low variability. For a given α , the test becomes more powerful at detecting stronger

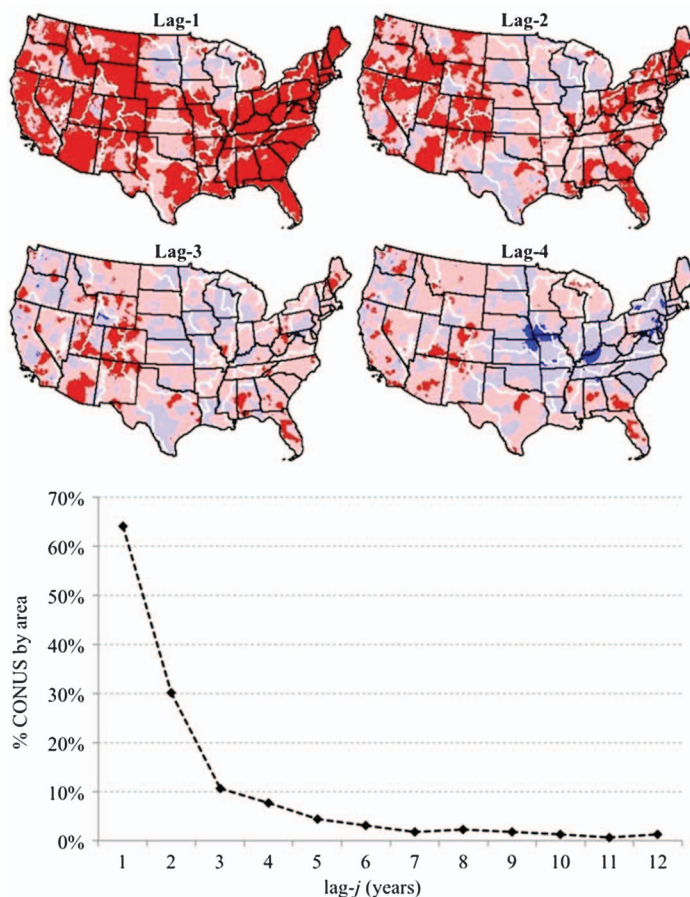


Figure 3-17. Autocorrelation in annual ET mapped and summarized across CONUS: (top) shows sign and significance of ρ_j for $j = 1 \dots 4$ (dark colors indicate 95% significance: red positive, blue negative), states, and USGS HUC-2 level regions; (bottom) shows the areal proportions of CONUS with 95% significant positive or negative ρ_j for $j = 1 \dots 12$.

absolute (i.e., either upward or downward) trends than at detecting smaller ones, including in nonnormally distributed time series often found in hydrology. However, for some distributions, the relationship between power and absolute trend is weak (e.g., for log-normally distributed time series— P and Q , often—the power remains constantly low across the range of trends), thereby complicating analyses of trends, or for sites that have different distributions or different shape parameter values for a given distribution. For greater α (or smaller confidence levels), the power increases across the range of trends, but more so for greater absolute trends than for smaller. This squares with the idea that trends are more likely to be rejected at lower α , more likely to be identified at higher α .

Figure 3-18 demonstrates the effects of varying α and ρ on the power of the Mann–Kendall test, summarizing results from 50,000 simulations of a first-order autoregressive [AR(1)] process ($n = 42$) with added white noise and lag-1 autoregression coefficients φ_1 ranging from -1.0 to $+1.0$. Clearly, negative φ_1 reduces the variance of the Z population around a zero mean, leading to increasingly constrictive limits for increasingly negative φ_1 , and a Z population that, while normal, has very low variance. The opposite is true for series with positive φ_1 : the variance of the Z population is increased around a zero mean, leading to increasingly divergent limits for increasingly

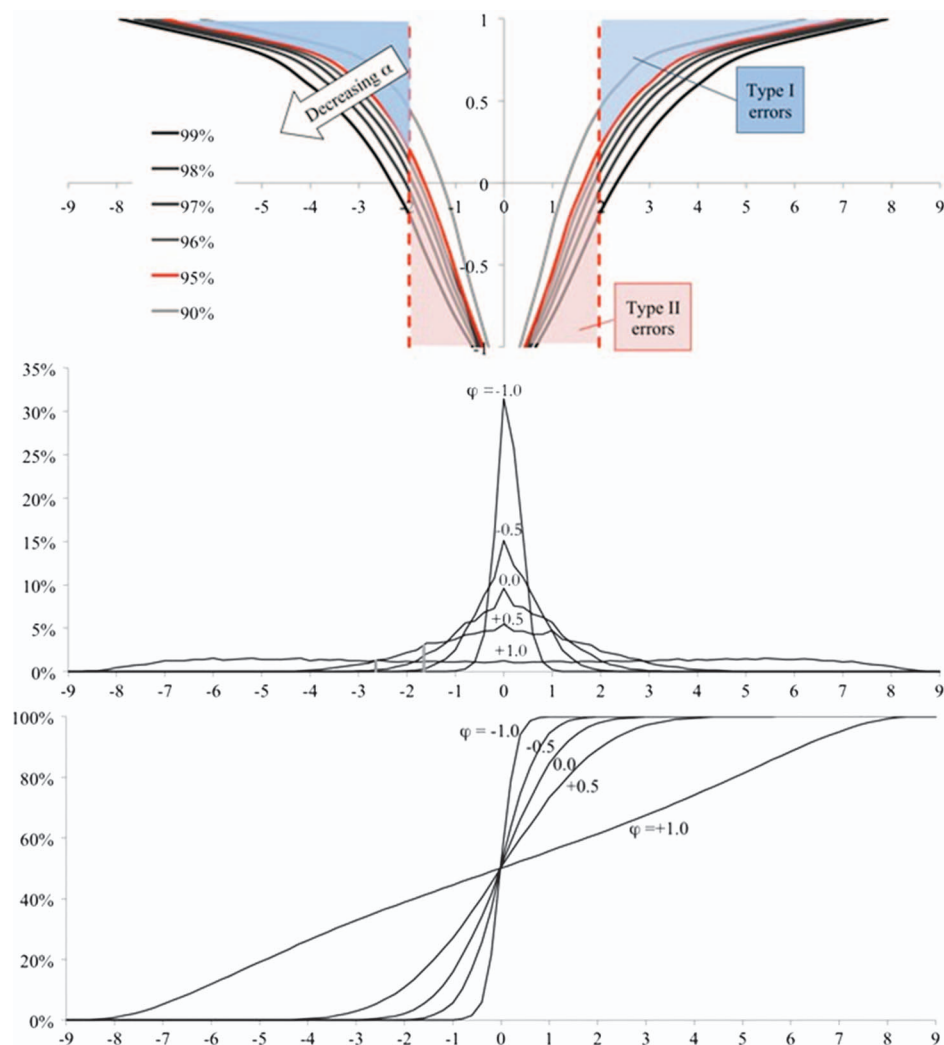


Figure 3-18. The effects of autocorrelation on the power of the Mann-Kendall test: (top) shows critical Z-statistics for various φ_1 (y-axis) and α , and regions of Type-I errors and Type-II errors invoked by the use of 95% limits for uncorrelated series (red dashed lines) in series that are autocorrelated; the lower two panels show for a given α (95%) the empirical (middle) and cumulative (bottom) densities of Z-statistics, with frequencies on the y-axes. All panels share common x-axes showing a range of Z-statistics (dimensionless).

positive φ_1 , and the appearance of a more uniformly distributed Z population. As indicated by the variety of limits across confidence limits ranging from 90% to 99%, lowering the confidence (or raising α) has the obvious effect of increasing the probability of detecting a trend, but increasingly so for increasingly positive—or decreasingly negative—autocorrelations.

Falsely assuming a process is uncorrelated may lead to errors of a type dependent on the actual autocorrelation in the series, as follows: (1) an increased probability of Type-I errors (i.e., rejecting H_0 when it is true) for series with positive autocorrelation and (2) an increased probability of Type-II errors (i.e., accepting H_0 when it is false) for series with negative autocorrelation. Thus, assuming zero autocorrelation in a time series leads to underdetection of trends in negatively autocorrelated series and overdetection of trends in positively autocorrelated series.

Having shown that a series under study is significantly autocorrelated, it remains to account for this autocorrelation in the trend analyses. Typically, use of the Mann–Kendall test in the detection of trends in autocorrelated time series has involved first rendering the time series uncorrelated by applying a process known as “pre-whitening.” This most commonly takes the form of reducing the raw data by subtraction of an autocorrelated trend, the parameters of which are estimated from the raw data. The trend is commonly an autoregressive lag- p [AR(p)] process, which may be expressed in its most general form—one that allows for a trend in the mean and autocorrelation in the series—as follows:

$$x_i = \mu(i) + \sum_{j=1}^p \varphi_j(x_{i-j} - \mu(i-j)) + \varepsilon_i \quad (3-39)$$

where

x_i = i 'th value of x in the time series,

μ = time-series mean,

j = time-index,

p = order of the autoregressive process,

φ_j = autoregressive coefficients, and

ε_i = uncorrelated series independent of x_{i-j} which, if random and normally distributed is called “white noise.”

$\mu(i)$ and $\mu(i-j)$ are deterministic functions of the time indexes i and j , which is to say that they represent a generalized—and therefore potentially nonstationary—mean, or a trend in the mean. An x_i series generated using no deterministic function in the mean—in other words, one with constant μ , or a stationary time series—will still exhibit short-term trends that result solely from autocorrelation. Conversely, an x_i series generated using a nonstationary mean $\mu(i)$ and zero autocorrelation will still exhibit autocorrelation solely due to the trend in the mean. Writing the x_i series in this fashion [Equation (3-39)] illustrates the interconnectedness or intractability of trends and autocorrelation, demonstrating that to define a trend in the presence of autocorrelation is essentially to distinguish between autocorrelation and nonstationary means—a distinction that is, to a great degree, subjective. Pre-whitening significantly affects trend calculations, lowering any trend if positive autocorrelation is removed and inflating it if negative: thus, the slope estimated from a pre-whitened series is not the estimate of the true slope of the series. [Yue and Wang \(2002\)](#) conclude that pre-whitening may be of little use in a practical, water-resource management-oriented contexts, where the true trend is of more interest than the statistically “purer” one.

3.4.2 Trends in ET and E_0 and the Evaporation Paradox

In general, changes in ET have been examined through either estimates of a mass balance in basinwide water budgets (Section 3.2.4) or of the energy balance through a mixture of modeling and observations, while changes in E_0 have most commonly been explained using observations. Other techniques drive land-surface or climate models with long-term reanalyses. Here we do not thoroughly examine projected future changes in ET , as this—the domain of GCMs—is a fast-moving field. Rather, we highlight a few influential studies picking out robust changes observed and predicted in the hydrologic cycle as they pertain to ET and E_0 . Analyses of E_0 trends have taken different approaches and used different E_0 formulations, yielding results that depend significantly on the region under analysis and, to a lesser extent, on the model (e.g., [Chen et al. 2005](#)). Here, we discuss E_{pan} for the following reasons: It is a physically observable flux, its long-standing and worldwide observations yield the most widely distributed set of trends analyses, and analyses of E_{pan} trends have uncovered phenomena central both to E_0 and to its drivers. In any case, few conclusions are drawn from studies of E_{pan} that do not also relate to other E_0 estimators. We demonstrate here

that examining trends in ET and E_0 and in their driving dynamics in the light of their complementary relationship (Section 3.2.3) permits resolution of the evaporation paradox, until recently a major source of conceptual uncertainty.

3.4.2.1 Trends in ET

Despite incomplete data records and often contrasting regional trends, the empirical evidence from a raft of hydrologic fluxes (including ET) and stocks points to an ongoing and future intensification of the global hydrologic cycle under warming, although evidence exists that intensification of ET fluxes has become constrained in *SM-limited* regions of the world (Jung et al. 2010). Much of the question regarding past (and future) ET trends revolves around the role ET plays in increased global Q , which results from increased ocean evaporation and, on land, increased P and/or decreased ET (Labat et al. 2004). In a hydrologic cycle of increased intensity, Q may increase in the face of increasing ET due to the increase in P far exceeding that of ET (Huntington 2008). While the accelerated hydrologic cycle should increase renewable freshwater resources and thereby mitigate the growth of water-stressed populations, Oki and Kanae (2006) warn that under the increased variability in fluxes, withdrawals for irrigation may be unable to keep pace with food requirements. To mediate the inevitable conflicts and competition, it is essential accurately assess past changes in ET , understand what drives them, and project future rates under a changing climate.

Global Observations

The development of global, long-term datasets of ET and related surface heat fluxes is vital in providing physical evidence-based constraints on climate models and evaluating the effects of climate change on the hydrologic cycle. The necessary quantification of the energy budget and its partitioning—including that at the surface for ET —has resulted in a multifaceted effort using data from many different platforms and modeling approaches. Interested readers are encouraged to turn to Wang and Dickinson's (2012) comprehensive review of the observation, modeling, and variabilities of global terrestrial ET estimation wherein they highlight the uncertainties and constraints of developing such estimates from techniques that fall into three broad theoretical approaches: Monin–Obukhov Similarity Theory, Bowen ratio, and P-M. Following we summarize results from a few recent influential studies estimating global terrestrial ET .

A signal example of the use of combinations of approaches and data sources is the LandFlux project of the Global Energy and Water Cycle Experiment (GEWEX), which uses remotely sensed radiation-related observations and verifies them using data from FLUXNET eddy covariance towers. GEWEX—a research program of the World Climate Research Programme—is an international collaboration of researchers observing and modeling the Earth's hydrologic cycle with a goal to improve by an order of magnitude our ability to model and predict P and ET patterns.

An influential data-driven study of recent (1982–2008) global ET changes (Jung et al. 2010) combines observations from FLUXNET, meteorological stations, and remote sensing platforms, and results from an ensemble of LSMs. It notes a globally averaged increase in ET of $+7.1 \pm 1.0 \text{ mm year}^{-1}$ decade $^{-1}$ from 1982 to 1997, but that a “switch” occurred in the late 1990s, after which no global increase occurs in ET (although not dated precisely, they estimate this switch as having occurred in 1998, the year of a major El Niño event). This finding is supported by Vinukollu et al.'s (2011) examination of the uncertainties in global terrestrial ET as estimated by three physically based models—the Surface Energy Balance System (Su et al. 2005), a modified P-M equation, and a variation of the Priestley–Taylor equation—forced by remotely sensed and observational net radiation ($R_n + L_n$) and meteorological datastreams. As to what drives this decline in the acceleration of global ET in the face of a more vigorous hydrologic cycle, Jung et al. (2010) point to SM limitation in the southern hemisphere (particularly Africa and Australia), with other possible mechanisms being increasing CO_2 leading to stomatal closure, land-use change, and decreasing U_z (stilling). Beyond the question of whether natural variability or climate change is behind these dynamics, they

raise a vital question, “Are we reaching a limit to the energy- and T -driven acceleration of the global hydrologic cycle?” If so, this could lead to declines in productivity and in the terrestrial carbon sink and increasing land-surface warming and intensifying regional land–atmosphere feedbacks as a growing surface energy budget is partitioned increasingly toward H .

Vinukollu et al. (2011) highlight the uncertainties in global terrestrial ET estimation—earlier work had reported uncertainties in terrestrial ET that approached 50% of its long-term annual mean—and find that even though radiation datasets displayed large differences between components and temporal inconsistencies in satellite sensors and retrieval algorithms, the uncertainty in ET estimates was significantly greater than that of radiation sets, and that this is primarily due to ET model choice. They conclude that uncertainties and inconsistencies in drivers (especially R_n and T) and the lack of SM data prevent firm conclusions regarding global terrestrial ET trends.

Current Global Climatology

GCM-modeling results support observation-based trends. Simulations of twentieth-century climate with mid-range CO_2 emission scenarios show that by 2050 in the global mean an increasing T (by 2.3°C) will increase many hydroclimatologic fluxes: P (by 5.2%), ET (by 5.2%), and Q (by 7.3%) (Huntington 2006). Increasing sea surface temperatures and the salinity of the upper layer of the ocean both imply an increase in oceanic ET , or at least an increase in net evaporation (i.e., $ET - P$, the net flux of water from the surface to the atmosphere; over land, the inverse ($P - ET$) provides a measure of Q to the oceans). Held and Soden (2006) find decreasing convective mass fluxes but increasing horizontal moisture transport and decreasing horizontal H transport outside of the tropics. In the global mean and over multiples of years, P is balanced by ET , but regionally the $ET - P$ difference increases with lower tropospheric water vapor: wet regions get wetter and dry regions get drier—a response that has been reported in many climate change impact studies—and the variance of $ET - P$ increases, increasing the intensity of both floods and droughts. Their general conclusion—that the residence time of atmospheric water vapor increases with warming and leads to a weakening atmospheric circulation—supports work by Bosilovich et al. (2005) for a simulated twentieth-century climate, who find that the hydrologic intensity, as measured by annual P , increases. Simply put, the fluxes (P and ET) are growing, but so are stocks (water vapor in the atmosphere). In line with observations, simulated oceanic P increased, but terrestrial P declined (mainly in the tropics), whereas terrestrial ET declined with the recycling of continental moisture. An exception to these trends was North America, where both P and ET increased, leading to increases in moisture recycling. The global increasing trends in P , ET , total precipitable water, and residence time were all significant. However, no broad agreement exists as to implications for terrestrial ET .

While GCMs are useful for establishing likely long-term mean conditions under various forcing scenarios, as deterministic models they do not offer information regarding the uncertainty of their forecasts. Instead, the range of multiple models’ results is taken as a proxy for climate prediction uncertainty, a substitution that requires the models themselves be independent. However, algorithms, errors, data, and techniques are shared among models. Thus, relying on the intermodel range for uncertainty underestimates the true range of uncertainty (Allen and Ingram 2002). Modeling climate in a probabilistic manner would allow for accurate risk assessment and planning of infrastructure. To reduce the uncertainty associated with conclusions drawn from GCM results, improved spatial resolution and temporal extents of observed data are required, and a better process-level understanding of complex feedbacks such as atmospheric water vapor (the atmosphere’s dominant greenhouse gas) and changes in cloudiness, cloud type and properties, and snow cover (Cess 2005). This is an ongoing issue: for instance, it has recently been suggested that this feedback is, in fact, negative; Soden et al. (2005) refute this, using remote sensing bands to confirm that RH is preserved in the upper troposphere, in accordance with GCM-modeling practice, and thereby resolving the modeling uncertainty regarding the water-vapor feedback. The modeling uncertainty in cloud feedback mechanisms remains.

Regional ET Trends across CONUS

Following we examine ET trends across CONUS, first as observed by basin budgets (derived as described in Section 3.2.4), then modeled from radiation and meteorological observations and by a large-scale LSM. In contrast to the global picture of decreasing terrestrial ET around the globe, observations over CONUS show that P is increasing faster than Q , with an implied increase in ET that is supported by basin-budget observational studies over the last half of the twentieth century (Szilágyi et al. 2001, Brutsaert 2006, Milly and Dunne 2001, Walter et al. 2004, Huntington 2006). Szilágyi et al. (2001) note a 3% increase in annual ET^{WB} in six basins covering more than 50% of CONUS. While these basin-derived ET trend rates are uncertain due to the large interannual variability in the estimates, particularly surface storage terms that are considered stationary (Walter et al. 2004), the fact that trends are positive in all basins is notable. In the Mississippi River basin, over the last half of the twentieth century, Milly and Dunne (2001) observe increasing P (+1.78 mm year $^{-2}$) leading to increasing Q (+0.95 mm year $^{-2}$) and ET (+0.95 mm year $^{-2}$). Brutsaert (2006) reports increasing ET (+0.39 mm year $^{-2}$ to 1.89 mm year $^{-2}$) from CONUS river basins, in line with an increase in mean ET (+0.44 mm year $^{-2}$) estimated from pans and global average trends in R_n and T . Walter et al. (2004) expect soil-limited ET periods to decrease, and thus energy limits to increasingly dominate. They also observe a statistically significant increasing trend (+1.04 mm year $^{-2}$) in basin-derived ET across the six large basins of CONUS. Hobbins (2004) explores the spatial variability of trends in ET^{WB} more closely, and demonstrate a heterogeneous pattern, shown in Figure 3-19, which indicates their distribution, direction, and significance in 655 minimally disturbed basins. Note that these basins are much smaller than those examined in Szilágyi et al. (2001) and Walter et al. (2004). Few basins show annual ET trends that are significant at the 95% level (as measured by the Mann-Kendall statistic): only 2.9% are significantly decreasing, and 9.0% are significantly increasing. Of the remaining basins, 43.2% are decreasing, and 44.9% are increasing. Broadly, basins in the midwest and south show decreasing ET , whereas those in the High Plains and desert southwest show increasing ET . The rest of CONUS is a heterogeneous mix of increasing and decreasing ET , with neither predominating. In Section 3.4.2.3 trends in the driving dynamics of this ET dataset—in other

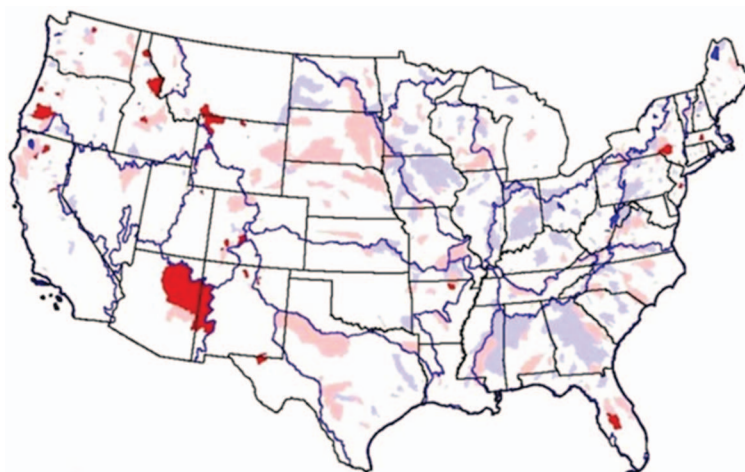


Figure 3-19. Trends in annual basin-budget ET in 655 basins in the Hydro-Climatic Data Network of minimally disturbed watersheds (Slack and Landwehr 1992). Trends are measured by the Mann-Kendall test statistic, with statistical significance assessed at the 95% confidence level. Annual fluxes of P and Q are from PRISM (PRISM 2004) and USGS (Hydrophere 1996), respectively. Dark colors show statistically significant trends: red increasing, blue decreasing. Also shown are the state and USGS HUC-2 level region boundaries.

Source: Hobbins (2004).

words, Q_n and E_A —are examined independently to see if, when combined with proper regard to physics, they predict these observed ET trends.

To examine trends in modeled ET , Szilágyi (2001) and Szilágyi et al. (2001) use Morton et al.'s (1985) WREVAP model of the complementary relationship in regional ET (Section 3.2.3) to produce some of the first studies to determine long-term, large-scale ET trends across CONUS. Szilágyi (2001) estimates ET at 210 stations across CONUS and shows that monthly complementary relationship-derived ET increased by 2% to 3% in 1961 to 1990 (+2.5% for annual ET , +3% for warm-season ET), with the strongest—and only statistically significant trends—in the eastern third of CONUS (+4% for annual ET ; +4.5% for warm-season ET). Then using E_{pan} observations as the E_p input to the complementary relationship, Szilágyi et al. (2001) note that an 11% increase in P over their period of interest agrees with the increase in ET : a 6% increase in modeled ET in the warm season (May–October) and a 3% increase in annual ET^{WB} . They find that, in general, the overstated increase in complementary relationship-derived ET was due to an assumption that the radiative budget remained constant across the period, whereas it has in fact increased while the advective budget remained nearly constant. Hobbins (2004) uses Brutsaert and Stricker's (1979) AA complementary relationship model over the period common to Szilágyi (2001) and Szilágyi et al. (2001) and finds that CONUS-wide, annual ET had increased by 5.5%, supporting, but exceeding, their findings. Differences may relate to the difference in methodologies and to the fact that Hobbins (2004) made no assumptions about stationarity in either the advective or radiative dynamics. Modeling differences aside, the increases in ET estimated by complementary relationship models are in line with long-term increases in T , P , and Q , and they support Brutsaert and Parlange's (1998) notion of an accelerated hydrologic cycle over CONUS. Further, they show great potential in determining and decomposing ET trends (Section 3.4.2.4) and resolving the evaporation paradox (Section 3.4.2.5).

Examining trends in the Mississippi River basin for the last half of the twentieth century using mass and energy balances from the Community Land Model 3.0 (CLM3.0) model with reanalysis forcings from the National Centers for Environmental Prediction (NCEP) and National Center for Atmospheric Research (NCAR) added to observations of P , T , and CC , Qian et al. (2007) confirm the observations of Milly and Dunne (2001), Szilágyi (2001), and Szilágyi et al. (2001). In the mass balance (i.e., water budget), increased P (+0.86 mm year⁻²) led to increased Q (+0.68 mm year⁻²) and ET (+0.21 mm year⁻²). In the energy budget, observed increased cloudiness decreased R_n and H and increased L_n , while λET increased (+0.025 W m⁻² year⁻¹) due to wetter surface conditions. A sensitivity analysis showed that P trends dominate ET trends, while T and R_n trends have little effect. This might be expected for water-limited areas: indeed, in eastern and central parts of the basin, increased P led primarily to increased Q ; in the western parts of the basin, increased P led to increased ET —a distinction expected for water-limited areas (western basin) versus energy-limited areas (central and eastern basin). Qian et al. (2007) also find ubiquitous, though not statistically significant, positive ET trends.

Milly and Dunne (2001), Hobbins et al. (2004), and Brutsaert (2006) observe E_{pan} declining as ET increases, in line with the complementary relationship (see Section 3.2.3), and R_n decreasing due to reductions in R_d . Decreasing R_n and increasing λET implies a negative H trend (-0.11 W m⁻² year⁻¹) and surface cooling, as confirmed by observations (Milly and Dunne 2001). In their energy balance, Qian et al. (2007) find an H trend of -0.018 W m⁻² year⁻¹: in the same direction as Milly and Dunne (2001) but an order of magnitude greater. Trends in H are clearly a significant source of uncertainty in energy-balance estimates.

3.4.2.2 Trends in E_o

Worldwide studies of trends in E_{pan} are notable for their consensus: E_{pan} appears to be declining almost globally over the last 30 to 50 years. Roderick et al. (2009a) and Fu et al. (2009) summarize these studies: briefly, studies that examine trends at multiple (>10) pans, from the United States

(Peterson et al. 1995, Lawrimore and Peterson 2000, Hobbins et al. 2004), India (Chattopadhyay and Hulme 1997), China (Liu et al. 2004; Liu and Zeng 2004; Qian et al. 2006; Xu et al. 2006a, b; Wang et al. 2007; Zhang et al. 2007; Zuo et al. 2006), the former Soviet Union (Peterson et al. 1995, Golubev et al. 2001), Venezuela (Quintana-Gomez 1998), Thailand (Tebakari et al. 2005), Australia (Roderick and Farquhar 2004, Kirono and Jones 2007, Jovanovic et al. 2008), and New Zealand (Roderick and Farquhar 2005) indicate mean declines in annual E_{pan} ranging up to $-24.9 \text{ mm year}^{-2}$, with most studies reporting declines in the range of -2 to $-4.5 \text{ mm year}^{-2}$. Given some exceptions to the downward trend in smaller sets of pans, a conservative estimate of the overall trend would be about 2 mm year^{-2} , or 60 mm year^{-1} across the period 1961 to 2003. In energetic terms, this is equivalent to a decline in radiative forcing of $0.16 \text{ W m}^{-2} \text{ year}^{-1}$ for a total reduction of about 4.8 W m^{-2} over the same period. Roderick et al. (2009a) set this in a climate-change context, stating that this exceeds the radiative forcing at the top of the atmosphere that would result from an instantaneously doubled atmospheric CO₂ concentration [$3\text{--}7 \text{ W m}^{-2}$ from IPCC (2007)], and that the trend is an order of magnitude higher than the trend in the top-of-atmosphere imbalance, which Hansen et al. (2005) estimate at $0.02 \text{ W m}^{-2} \text{ year}^{-1}$ for 1961 to 2003, or about 0.8 W m^{-2} by 2003.

Across CONUS, Hobbins et al. (2004) examine long-term trends in observed annual E_{pan} at 44 pans and warm-season E_{pan} at 228 pans. Prior to their homogenization (described in Section 3.2.8.2), the datasets are characterized by their lack of completeness in time and, more importantly, recurrent heterogeneities that could have introduced spurious biases into analyses of long-term trends. Of the annual pans, 64% indicated decreasing E_{pan} trends, including nine of the 12 pans with significant (90%) trends. Of the warm-season pans, 60% indicated decreasing E_{pan} , including 36 of the 43 pans with significant trends. Of the 228 warm-season pans, 60% show decreasing E_{pan} ; of the 43 pans with significant trends, 84% are decreasing. Warm-season E_{pan} was observed decreasing across most of CONUS but with exceptions in the northwest, the northeast, around the Gulf of Mexico, South Carolina, and southern Florida.

3.4.2.3 Drivers of Trends in ET and E_0

Changes in ET may be due to changes in hydroclimatic drivers—in other words, the radiative and advective drivers of the evaporative process that also affect E_0 —and much recent attention has turned to such changes, particularly Q_n and U_z . Other change drivers include Θ , seasonality, land-cover changes, and consumptive use. Here we summarize such changes, focusing particularly on the radiative and advective drivers. In the following sections we see how these drivers' trends combine under the complementary relationship to resolve trends in ET and E_0 (Section 3.4.2.4) that sometimes appear paradoxical (Section 3.4.2.5).

Terrestrially, Q is increasing faster than P , which raises the question as to what is suppressing ET . Gedney et al. (2006) associate Q increases with a direct effect of increased atmospheric CO₂ through a detection and attribution technique known as “optimal fingerprinting” and find that among potential causes—climate change and variability, deforestation, and solar dimming—elevated atmospheric CO₂ is suppressing ET from plants by increasing their water-use efficiency, leading them to transpire less for the same CO₂ uptake. However, this mechanism is far from certain, particularly with respect to the conflicting effects of warming and increased CO₂ concentrations alone or in combination (Huntington 2008). Opposing drivers are warmer canopies (due to decreased conductance) raising the VPD between the canopy and the atmosphere and so increasing transpiration and increased T driving plants to increase evaporative cooling.

Changing seasonality increases ET (Huntington 2006): growing seasons are lengthening due to earlier onset and are associated with higher T in spring and fall (e.g., Serrat-Capdevila et al. 2011). Dependent on region, longer seasons may also correlate with earlier snowmelt, decreases in spring snow cover, and lengthening of the frost-free season. FLUXNET-derived T - ET relations across various vegetation types in North America and Europe display sensitivities on the order of 20 mm K^{-1} . In energy-limited areas, ET increases with T during the twentieth century.

Local land-cover change affects ET through changes in evaporation of intercepted P , transpiration from new cover, or evaporation from bare ground. Changes in Q depend on original and replacement species, plantation age, and hydroclimate, among other factors (Farley et al. 2005). Transpiration changes result from changes in water availability (rooting characteristics), the radiative driver (albedo affecting leaf-level R_n , leaf area), and the advective driver (stomatal conductance, turbulence). Hydrologically, deforestation and afforestation are not reverse processes: changes due to deforestation also result from soil disturbance, deposition of slash and litter, and, of course, the duration of the process; compared with afforestation, deforestation is almost instantaneous. As grasslands are replaced with either shrublands or forest, ET tends to increase more than Q decreases, due to the greater capacity for transpiration from increased leaf area and increased evaporation from interception (particularly from conifers' needle-shaped leaves in wetter regions), but also to replacement species' use of deeper water unavailable to the rooting systems of original species (particularly the faster-growing, deeper roots of eucalypts in drier regions). This phenomenon may be transitory, lasting until steady state is reached between surface ET and water at depth.

Human-induced ET changes in CONUS may arise particularly from irrigation from groundwater, but evidence from regions where this is not a factor in the hydrologic cycle supports a climatological explanation in addition to any anthropogenic impacts. Milly and Dunne (2001) show that ET increased due primarily to increased P and then to human water use. However, across CONUS, consumptive use is poorly modeled—it has long been derived from periodic reports accumulated from county agricultural agencies—although this should change with the advent of the National Water Census, which will institute near-real-time reporting on a spatially distributed basis.

A great deal of recent attention has been paid to trends in E_0 as driven by trends in their radiative and advective drivers. In the case of the former, this has mostly focused on R_d and the concept of “global dimming” and subsequent “rebrightening,” and in the case of the latter, to changes in U_z and the newer concept of “global stilling.” Clearly, any trends in the radiative and advective drivers also affect ET , and this interplay is examined in Section 3.4.2.4.

Dimming

Changes in the radiation budget occur in both longwave and shortwave radiation fluxes. In terms of longwave radiation, emissions from increasing concentrations of greenhouse gases such as methane, CO_2 , and water vapor have contributed to a radiative imbalance at the top of the atmosphere of $0.9 \pm 0.5 \text{ W m}^{-2}$ (Trenberth and Fasullo 2010) and so to atmospheric warming—the “greenhouse effect.” Changes in R_d are due to changes external to the atmosphere system (solar variability), but also to changes in atmospheric transmission and reflection due to atmospheric composition, cloudiness, and their interactions.

Stanhill and Cohen (2001) review the instrumented R_d trends across the second half of the twentieth century and find evidence of global dimming. Briefly, globally averaged R_d has declined by $2.7\% \text{ decade}^{-1}$ for a total (by 2000) of 20 W m^{-2} .

To determine the cause of dimming, Stanhill and Cohen (2001) express R_d following Darnell et al.’s (1992) model, wherein R_d at the evaporating surface is parameterized by proceeding from knowledge of the extraterrestrial irradiance at the top of the atmosphere R_{toa} and then accounting for scattering, absorption, and reflection of this flux as a function of dust, aerosols, clouds, and humidity through which it has to pass, using an additive system of transmissivities (τ) to yield R_d , as follows:

$$R_d = R_{toa} \exp(-\tau_r + \tau_g + \tau_w + \tau_a + \tau_c) \quad (3-40)$$

where

τ_r and τ_g account for Rayleigh scattering and permanent gas absorption;

τ_w accounts for the effects of atmospheric water vapor; and

τ_a and τ_c account for the effects of aerosols and clouds.

R_{toa} is calculated as a function of solar constant, latitude, relative Earth–sun distance, solar declination, and sunset-hour angle (see Shuttleworth 1993, Allen et al. 1998). R_{toa} is stable compared with other factors: a maximum change across 300 years of only 5.4 W m^{-2} is associated with sun-spot activity but is, in fact, observed as increasing somewhat over the last 150 years; satellite data indicate short-term variations associated with the 11-year solar cycle at an amplitude of only 1.36 W m^{-2} or 0.1%. Variations in τ_r , τ_g , and τ_w may be neglected as primary sources of the observed R_d changes as changes in the atmospheric composition (assuming that all gases radiatively active in the solar spectrum in the atmosphere are known) and the increase of the global mean depth of water vapor ($\sim 25 \text{ mm}$) under global warming are insufficient. This leaves the effects of aerosols in the troposphere on atmospheric heating profiles and the size, lifespan, and radiation properties of clouds, parameterized through τ_a and τ_c .

Natural and anthropogenic aerosols in the troposphere include organic carbon, sulfates, nitrates (all of which scatter visible light) and black carbon (from industrial activity and biomass burning, and which absorbs visible light), sea salt, and dust. Unlike CO_2 , aerosols are neither well mixed globally nor long lived, so their effects on radiation forcing are regional. A direct radiative effect occurs through shortwave scattering and longwave absorption and re-emission, while indirect radiative effects affect the cloud droplet size and number and thereby modify cloud formation, precipitation efficiency, and reflectivity. Indirect effects include both positive (warming of the Earth-atmosphere system) and negative (cooling) radiative-forcing effects: increased cloud condensation nuclei from anthropogenic pollution increase cloud reflection of shortwave radiation (the Twomey effect) and cloud lifetime effects reduce radiative forcing (cooling the Earth-atmosphere system) by increasing CC and cloud optical depth (although this may depend on hydroclimatology: the indirect effect has been shown to increase the cloud reflectivity and CC in humid conditions, but reduce CC absent such conditions (Qian et al. 2006); carbonaceous aerosols and dust increase radiative forcing at the top of the atmosphere (particularly in high-albedo regions), reducing RH , CC, and cloud optical depth, and thereby amplifying the warming; and possible, if unlikely, effects that increases P due to large aerosols acting as condensation nuclei, leading to lower CC, and so to increased R_d (Lohmann and Feichter 2005). CC has increased only 1% in the last 50 to 80 years, or, depending on region, decreased about 1% to $3\% \text{ decade}^{-1}$, but (assumed) large uncertainties associated with this measure result from the very crude gauging of the effects on the radiative changes due to cloud that CC represents. Empirically, even a 4% decrease in CC over 40 years should lead to only about a 2% decrease in R_d , so again, only around $0.5\% \text{ decade}^{-1}$ for this potential cause of R_d reduction—much lower than the observed $2.7\% \text{ decade}^{-1}$ decrease in R_d (Stanhill and Cohen 2001). More attention is being turned to the effects of aviation and high-altitude cirrus clouds on the reduction in R_d —another aerosol indirect effect. Other smaller effects include those from volcanoes, solar forcing, land use, stratospheric ozone, and dust-on-snow and chemical interactions with greenhouse gases potentially altering their radiative properties.

The scale of the reduction in R_d due to the various aerosol loadings and effects is still under discussion (e.g., combined direct- and indirect-forced R_n reductions at the surface of up to -20 W m^{-2} are reported (Nazarenko and Menon 2005) with estimates of aerosol-induced reductions often orders of magnitude less than the observed reduction in R_d through the atmosphere (Stanhill and Cohen 2001). For example, for sulfate aerosols, the average of nine studies' estimates of direct forcing is -0.44 W m^{-2} ($+/- 0.13 \text{ W m}^{-2}$ standard error), and for 14 studies of indirect forcing 1.28 W m^{-2} ($+/- 1.12 \text{ W m}^{-2}$) (Stanhill and Cohen 2001). But this 140-year accumulation represents an annual decrease of only 2% of the rate observed for the last 40 years. As a comparison, L_d forcing related to greenhouse gases (GHGs) is 2.45 W m^{-2} .) Regardless of the scale of reduction in R_d due to a particular aerosol effect, reductions have been assumed to follow the same spatial distribution as either the industrial activity that generates aerosols or the pollution paths that concentrate and transport them. Stanhill and Cohen (2001) conclude that aerosols and cloud cover and their indirect interactions are the most likely causes of global dimming, but that they are the most complex and difficult to quantify.

Hydrologic sensitivity to the atmospheric radiation balance motivates intensive ongoing research efforts into modeling aerosols' direct and indirect effects. The hydrologic effects of aerosols range from the obvious—reductions in the R_n (particularly in the direct-beam component of R_d) that may lead to a suppression of the hydrologic cycle, even in the face of a warming climate—to suppression of low-intensity P due to the cloud lifetime effect (although modeling studies do not simulate observations well). Further aerosol effects include those on convection, and thus on both floods and droughts, and changes in distant regions, for example, a southward shift of the Intertropical Convergence Zone that may result in Sahelian drought (Lohmann and Feichter 2005). Nazarenko and Menon (2005) demonstrate that modeling the combined effects of both GHG-forcing and aerosol effects together replicates the dimming and rebrightening that is observed; neither dynamic does alone. Romanou et al. (2007) cast doubt on the reported rebrightening trend, given its short period (1984–2000) within such shorter-term (~decadal) variability from cloud cover changes from ENSO. The sensitivity of λET to aerosol forcing relative to that of the net heat flux is due to the regionality of aerosol-forced R_d changes: the combined effect of all forcings is a small reduction in global mean λET . Romanou et al. (2007) warn that any brightening that may occur would have the same effect on surface warming as GHG forcing but result in twice the impact on the hydrologic cycle.

Data since 1990 indicate a reverse of the dimming, or rebrightening, in many regions (Wild et al. 2005). This generalized turnaround is supported on a global scale by satellite observations (Pinker et al. 2005) and by the earthshine method (using the brightness of the Earth's reflection from the moon as a proxy for Earth's planetary albedo). Wild et al. (2005) attribute Eastern European rebrightening to the reduction in industrial output following regional regime change there in the late 1980s and, in general, other rebrightening to the implementation of clean-air regulations reducing atmospheric aerosol pollution. They anticipate a stronger greenhouse signal to be observed from a brighter atmosphere, after the direct and indirect dimming effects of the aerosols are alleviated. However, Alpert et al. (2005) cast doubt on dimming as a global phenomenon, instead associating it with large urban regions and latitudes where industrial activity is at its global height and where the dimming is at its peak, as opposed to equatorial regions where brightening is often observed in sparsely populated areas. They cite uncertainty in the understanding of the effects of air pollution on the atmospheric energy balance, in the use of correlation between the human population and the sorts of industrial activity that will affect aerosol optical depth, and other effects of urban areas, including heat island effects and albedo changes. Their results are also in agreement with Pinker et al. (2005), who observe persistently increasing solar radiation over the ocean and over the tropics, using satellite data. Complicating this developing picture, Qian et al. (2006) find decreasing trends in R_d over much of China for 1954 to 2001, but also that the upturn in R_d in the mid 1990s observed elsewhere in the world was also noted in China, under no such air quality improvement.

Observational uncertainties, identifying which way the aerosol indirect effect should affect R_d and the regional versus global issues raised by Qian et al. (2006) all point to the need for resolution of the issue of aerosols' effects on the hydrologic cycle: it is a field ripe for further observational and modeling study. Needed is a better understanding and parameterization of aerosol dynamics and effects in GCMs, requiring resolution of various uncertainties: aerosol measurement accuracy, their variation in optical properties, the extent to which a sample represents their spatiotemporal distribution, their short atmospheric lifetimes, and, significantly, the interactions between aerosols and clouds (Stanhill and Cohen 2001).

Stilling

Consensus is growing that land-surface U_z is declining worldwide—the “stilling” phenomenon. Observations from Australia (Roderick et al. 2007, Rayner 2007), China (Xu et al. 2006a, b; McVicar et al. 2008), Italy (Pirazzoli and Tomasin 2003), the United States (Klink 1999, Hobbins et al. 2004, Pryor et al. 2007), Canada (Tuller 2004), and the Tibetan Plateau (Shenbin et al. 2006, Zhang et al.

2007) support the argument that stilling is neither solely a observational quality problem, nor an isolated or regional one.

The direct effect of U_z is to modify eddy diffusivity: increasing U_z leads to increasing eddy diffusivity and increasing turbulence, which, all else equal, increase E_0 and lead to a complementary decrease in ET . Ozdogan and Salvucci (2004) suggest four further reasons to explain the strong correlation of changes in U_2 and E_p that they observe: first, the oasis effect, wherein irrigation affects local wind circulation in both magnitude and direction; second, and akin to the findings of Alpert and Mandel (1986), that the growth of irrigated crops results in increased surface roughness over large distances; third, that their U_z instrumentation is affected by local shielding, either by crop growth or by trees planted specifically to reduce U_z over the crops; and fourth, that U_z is decreasing due to climatological factors acting on regional or larger scales unrelated to local ET changes.

Across CONUS, strong regional patterns of statistically significant trends outside the range of instrumentation variability are evident (Pryor et al. 2007), with eastern CONUS experienced stilling but the west experiencing both increasing and declining U_z . Unfortunately, trends in wind fields from reanalyses products, such as those from NCEP–NCAR, are generally not consistent with those observed at pans (Rayner 2007) or meteorological stations (McVicar et al. 2008). Neither reanalyses nor gradients derived from daily P_a surfaces have proved useful in attributing U_z trends to large atmospheric circulation changes, suggesting that daily U_z at the surface is not dominated by large-scale atmospheric patterns. For the United States, homogeneous, high-quality data sets are needed to determine whether U_z changes are a regional-scale climatic effect or a local one—for example, from urbanization or vegetation growth, or from changing local hydrometeorology (e.g., Ozdogan and Salvucci 2004).

In Australia, development of high-quality U_z datasets is underway. McVicar et al. (2008) generated new $0.01^\circ U_2$ grids for Australia that show for a recent 33-year period the stilling phenomenon otherwise undetected in reanalyses: stilling is evident across nearly 90% of Australia (significant in 57% by area), with an areal mean trend of $-0.009 \text{ m s}^{-1} \text{ year}^{-1}$.

3.4.2.4 Decomposition of Trends in ET and E_0 in the Complementary Relationship

Following is a first-order determination of the trends in ET^{WB} [derived as the $P-Q$ difference; see Equation (3-16)] and E_0 (observed as E_{pan}) in terms of their hydroclimatic drivers, in other words, the radiative and advective components just examined in terms of dimming and stilling, respectively (Section 3.4.2.3). Here, the driving equations for ET and E_0 are examined in a general sense that encodes both components' dynamics—the regional E_A in the vapor transfer component and the energy flux driving the system in the radiative component Q_n —acting under any paradigm, including that of the complementary relationship (Section 3.2.3).

Starting from a general functional expression $\lambda ET = f[Q_n(t), E_A(t), \Delta(t), \gamma(t)]$ and assuming that E_A and Q_n are independent functions but that Δ and γ are stationary, λET can be expressed as $f[Q_n(t), E_A(t), \Delta, \gamma]$. Therefore, a general expression for temporal trends in ET as a function of trends in its components, regardless of the actual formulation of ET (i.e., either the complementary relationship or the traditional paradigm; see Section 3.2.3 for the distinction) is

$$\lambda \frac{dET}{dt} = \frac{\partial ET}{\partial Q_n} \frac{dQ_n}{dt} + \frac{\partial ET}{\partial E_A} \frac{dE_A}{dt}, \quad (3-41)$$

noting that for trends in E_0 , dET and ∂ET may be replaced by dE_0 and ∂E_0 , respectively.

Following, we first turn to the decomposition of trends in E_0 (as represented by E_{pan}) into its driving trends—radiative and advective—as this is the most intuitively tractable and corresponds most closely with previous discussion (Section 3.4.2.3) of changes in the radiative and advective drivers of the evaporative process (dimming and stilling, respectively). Then we similarly examine

the decomposition of trends in ET . This latter decomposition will first require some validating examination of the complementary relationship. When trends in the radiative and advective drivers are examined together as drivers of trends in ET and E_0 under complementarity, the evaporation paradox will resolve (Section 3.4.2.5).

Decomposition of Trends in E_0

Roderick et al. (2007) use synthetic E_{pan} from the PenPan model of Rotstain et al. (2006) to attribute long-term trends in observed E_{pan} in Australia to trends in its drivers, finding that U_2 dominates. Eslamian et al. (2011) find that, at five stations in semi-arid climates in Iran, P-M ET_{rc} (Monteith 1965) is most sensitive to T and RH , whereas Bois et al. (2005) find that U_2 and R_d were the most effective drivers at stations in France. Tang et al. (2011) attribute temporal trends in P-M ET_{rc} in northeastern China, finding that ET_{rc} decreased at 1 mm year^{-2} —the same direction and order of magnitude as E_{pan} trends observed worldwide (see Roderick et al. 2009a)—driven by U_2 , Q_n , and then e_a , but that rising T tended to drive ET_{rc} up.

In a rigorous attribution study on a regional scale, Roderick et al. (2007) decomposed the observed, generally declining, trends in monthly E_{pan} at 41 Australian stations for a recent 30-year period using the PenPan formulation of synthetic E_{pan} , which permitted examination of the relative influence of all physical drivers on the observed E_{pan} trends. In the mean, the E_{pan} trend across all stations of $-2.0 \text{ mm year}^{-2}$ was found to result from a superposition of an increase in E_{pan} of 0.6 mm year^{-2} due to increasing Q_n , with a decrease in E_{pan} of $-2.6 \text{ mm year}^{-2}$ due to a decreasing advective component (E_A), which may be further decomposed (assuming first-order independence of U_2 , T , and VPD) to reveal that changes due to both T and VPD were about 0.0 mm year^{-2} , but that the change due to U_2 was $-2.7 \text{ mm year}^{-2}$.

Some regional differences emerged: for example, the decreasing radiative driver in northwestern Australia was in line with the dimming observed across much of the world, but not with the generality of Australian observations. However, the decline in U_2 (mean $dU_2/dt = -0.01 \text{ m s}^{-1} \text{ year}^{-1}$) was similar to worldwide trends in U_2 , which show stilling across most land surfaces. While finding similar results, Rayner (2007) surmises that, as some U_2 trends are discontinuous or uncorrelated with nearby stations, at least some changes are locally driven. Roderick et al.'s (2009b) results—notably, that T trends were found not to be a significant driver of E_{pan} trends—further underscore the dangers of relying on T -based E_0 parameterizations (see Section 3.2.7). They suggest that, given pans' long-term worldwide ubiquity and the utility of their attribution technique, pans may have a role as long-term repositories of radiometric information for periods predating accurate and direct radiometry.

Fu et al. (2009) suggest future research avenues in E_0 trends. Uncertainties in E_{pan} trends must be clarified and the role of homogenization of the record must be quantified. Regional differences in E_0 trends must be examined and their regional controls established across other regions, including over the ocean, where trends in E_0 may differ significantly from those on land, due to oceanic heat storages. Trends in observed E_{pan} and ET_{rc} should be compared and any differences between the two explained. The globally observed negative E_{pan} trends have been shown generally to result from decreases in radiative or advective forcing (Fu et al. 2009, Roderick et al. 2009a), or—considering the complementarity of regional ET and E_{pan} —an increase in actual ET , or a combination of all three dynamics (Hobbins et al. 2004). As these trends are so widespread, these stark results bear further analysis. A more formal, global-scale meta-analysis would pull all of these data together to uncover regional differences in trends and drivers.

In the context of these effects of component trends on ET trends, the critical difference between complementary relationship models and traditional paradigms (i.e., those in which ET is a function of E_0 mediated by Θ) lies in their functional relationship to trends in the advective component (E_A). In the traditional paradigm—one that ignores the complementarity between ET and E_0 described in Section 3.2.3—trends in ET are a positive function of trends in E_0 and therefore a positive function of trends in E_A . Feedbacks between the surface and the dynamic boundary layer are ignored: E_0 is a

driver of ET , not a response to it, and more moisture is presumed to evaporate into the air simply as a result of the air being drier [i.e., in Equation (3-41), $\partial ET / \partial E_A > 0$]. In complementary relationship-based estimates of ET this causality is reversed as E_A responds to the feedback between regional advection and ET : when these feedbacks have brought the land surface and atmosphere into equilibrium, a greater E_A is diagnostic of less evaporation into the air. Thus, in contrast to traditional paradigms, under the complementary relationship hypothesis, ET trends are a negative function of E_A trends [i.e., in Equation (3-41), $\partial ET / \partial E_A < 0$].

Formulating the complementary relationship by the AA model described in Equation (3-15), the influence of trends in regional E_A on trends in ET is made evident by substituting the appropriate terms for the partial derivatives in Equation (3-41), yielding

$$\lambda \frac{dET}{dt} = (2\alpha_{PT} - 1) \frac{\Delta}{\Delta + \gamma} \frac{dQ_n}{dt} - \frac{\gamma}{\Delta + \gamma} \frac{dE_A}{dt}. \quad (3-42)$$

Figure 3-20 shows the effects of trends in the two components (dQ_n/dt and dE_A/dt) combined in the complementary relationship. The first cause of ET trends, a long-term change in E_A in the absence of a change in the energy budget, is akin to moving both ET and E_0 in the same direction along the paired curves (red arrows marked E_0'' and ET''). Under the complementary relationship, increasing the wetness of an evaporating surface decreases E_A and moves the $ET-E_0$ pair to the right toward their curves' convergence (shown), whereas decreasing wetness moves the pair to the left and divergence.

The second cause—a long-term change in Q_n in the absence of a change in wetness—shifts both the horizontal line representing E_w and the curve representing E_0 upward in the case of increasing Q_n , or downward in the case of decreasing Q_n . Correspondingly, the curve representing ET shifts in a similar direction (arrows marked E_0' and ET'). E_w is predominantly a function of Q_n and is therefore unaffected by changes in basin wetness alone.

Clearly, these two dynamics do not occur in isolation, but respond to all or any of the causes discussed in Section 3.4.2.3. For instance, the effect of a long-term decrease in the available energy,

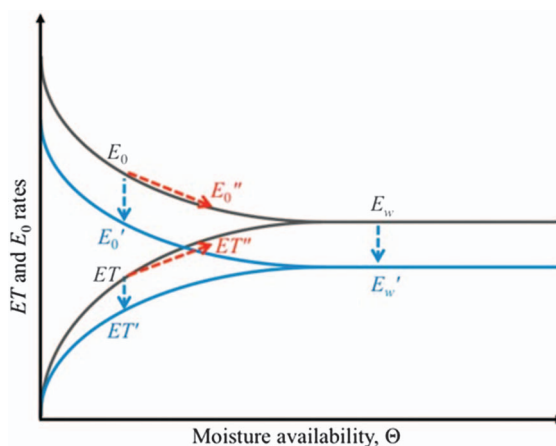


Figure 3-20. Schematic representation of the effects of trends or changes in the driving dynamics of ET under the complementary relationship. Undisturbed conceptual relations between ET, E_0 , and E_w are shown in grey across a notional range of surface Θ . Changes in ET, E_0 , and E_w due to trends (decreases shown) in advective forcing (E_A) and radiative forcing (Q_n) are shown in red and blue, respectively (opposite-sign changes in E_A and Q_n result in changes in the opposite directions to the arrows shown).

indicated here by a negative trend in Q_n , may be an increase in soil moisture and thereby a decrease in VPD in the overpassing air, which leads, in turn, to a negative trend in regional E_A .

Trends in Drivers of Observed ET^{WB}

Following, we demonstrate the power of the complementary relationship hypothesis over the traditional paradigm in analyzing long-term ET trends. This leads to resolution of the evaporation paradox (Section 3.4.2.5). We examine trends in annual observations of ET^{WB} and its Q_n and E_A components in 655 minimally disturbed basins across CONUS (Table 3-1).

Of these combinations of trends, 48.7% (rows 1, 2, 7, and 8) display trends in ET^{WB} that can be explained by both the traditional paradigm that holds that E_0 is independent of ET and by the complementary relationship between ET and E_0 . However, the trends in 43.2% (row 4 and the empty row 5) of basins can only be explained as a result of the complementary relationship. In these basins, the trends in E_A and Q_n are both negative, indicating a decrease in E_A of the overpassing air (through a decrease in either VPD or $f(U_2)$), which under the complementary relationship tends to reflect increasing regional ET and a decrease in the local radiative flux, which tends to decrease local ET . The balance of these trends results in an increase in local ET . Applying these two component trends in the context of the monotonically increasing relationship between ET and E_0 central to the traditional paradigm could only produce a decrease in ET^{WB} . As observations confound these expectations, the observations have heretofore been described as paradoxical. Trends in the remaining 8.1% (rows 3 and 6) basins are explicable within the context of the traditional paradigm, but not in the context of the complementary relationship. Possible explanations for these latter contradictory basins are as follows: (1) the trends are insignificant, that is, the indicated trend statistics represent the mean of a noisy dataset and no contradictory dynamic is in fact at work, and (2) although all three components represent the spatially integrated mean for each basin, the Q_n and E_A data result from spatial interpolation from observations that may have been made at some distance from the basins, while ET trend data are derived from a mixture of basinwide observations (Q) and spatially interpolated, modeled data (P).

In summary, at the regional scale useful to water managers and climate modelers, making the familiar assumption that ET can be calculated as a function of some soil moisture measure

Table 3-1. Long-Term Trend Directions in Annual ET^{WB} , Q_n , and E_A for 42 years in 655 Hydrologically Undisturbed Basins across CONUS, Denoted by the Sign of the Mann–Kendall Test Statistic [i.e., $\text{sign}(Z(\dots))$, where the Ellipsis is E_A , Q_n , or ET^{WB}].

% of basins	$\text{sign}(Z(\dots))$			Explained by . . . ?	
	E_A	Q_n	ET^{WB}	CR	Trad
1	0.3	+	+	✓	✓
2	2.8	–	+	✓	✓
3	7.6	+	–	✗	✓
4	43.2	–	–	✓	✗
5	0	+	+	✓	✗
6	0.5	–	+	✗	✓
7	2.4	+	–	✓	✓
8	43.2	–	–	✓	✓

Note: The right-hand columns indicate whether the combinations of trend directions for Q_n and E_A explain the trend direction in ET^{WB} within the context of the complementary relationship hypothesis (CR) or a traditional relationship (Trad) between ET and E_0 : ✓ = explained; ✗ = not explained. Bordered cells indicate trend combinations that have been described as paradoxical.

constrained below an E_0 estimate that is itself independent of ET —as is done in many traditional basin-scale models—is physically indefensible. Combining the radiative and advective fluxes in the context of the complementary relationship explains observed ET trends better than the traditional paradigm: 91.9% of the basinwide trends were explained by the complementary relationship as opposed to only 56.8% by the traditional paradigm. The 43.2% of trends explained under the complementary relationship but not under the traditional paradigm constitute the subset of basins exhibiting what was previously considered paradoxical behavior. Any estimation procedure that ignores the complementary effects of regional advection is therefore fundamentally flawed. To predict ET trends, one must also make reference to the dynamics of the two components that constitute both ET rates and how they combine within the complementary relationship to draw complete conclusions, particularly in areas where the signal from trends in the regional advective component outweighs that from the local radiative component.

3.4.2.5 Resolution of the Evaporation Paradox

In Sections 3.4.2.1 and 3.4.2.2, we report observations of increasing ET over the global land surface but decreasing E_0 . In Section 3.4.2.4, we observe how the directions of 43.2% of CONUS-observed ET^{WB} trends appear to contradict the traditional paradigm of ET dynamics (i.e., in which land surface–atmosphere feedbacks are ignored and E_0 is treated as independent of Θ and ET). Reverse trends were also observed between E_{pan} and ET in the southeastern United States, but in the opposite directions: increasing E_{pan} and decreasing ET (Golubev et al. 2001). How ET and E_0 trends may be in opposite directions has fed into talk of an “evaporation paradox.” Other expressions of this paradox, also known as the “pan evaporation paradox,” are numerous and include observations of decreasing E_{pan} that seem to contradict increases in observed P (e.g., Cong et al. 2009) and cloudiness and in GCM-derived ET (e.g., Brutsaert and Parlange 1998), and increases in T (e.g., Roderick and Farquhar 2002). However defined, this apparent paradox is not ubiquitous: for example, decreasing E_{pan} was observed in parallel with decreasing ET in Siberia (Golubev et al. 2001) and northern European Russia (Peterson et al. 1998, Golubev et al. 2001). In their rigorous global study of ET trends, (Jung et al. 2010) observe that the relative directions of changes in ET and E_0 depended on SM availability, with opposite direction trends observed in SM-limited regions, but same direction trends (positive) in non-SM-limited regions (e.g., south India, China). In Section 3.4.2.4, we examine the paradox as expressed in its most essential form: between ET trends and trends in its drivers. We demonstrate how these trends in ET^{WB} —paradoxical and parallel trends in ET^{WB} —are explainable given a full understanding of the interrelations of the fluxes of E_{pan} and ET and of their drivers.

The previously noted seemingly paradoxical behavior has provoked a heuristic argument by Brutsaert and Parlange (1998) in favor of the complementary relationship. They argue that E_{pan} has not been treated correctly as an indicator of climate change, but that in nonhumid (water-limited) environments E_{pan} is not a good predictor of ET , as it does not behave proportionally. Traditionally, in nonwater-limited environments a pan coefficient of order one is used to convert E_{pan} to E_p , but when water becomes limited, the traditional conception of E_p as a constant fraction of E_{pan} breaks down, and the complementarity between ET and E_{pan} becomes obvious.

Roderick and Farquhar (2002) observe the pan evaporation paradox by noting that the global mean T has increased by $0.15^\circ \text{decade}^{-1}$ over the last 50 years; that the expected increase in evaporation from terrestrial open water bodies due to drier air at the surface and evident in an increase in E_{pan} does not occur; and that, in fact, E_{pan} is decreasing. They propose and examine two explanations to resolve the paradox: (1) the complementary relationship between E_0 and ET and (2) a decrease in Q_n at the Earth’s surface (“dimming”), due, in part, to an increase in the concentration of aerosols. They conclude that the complementary relationship explanation is not completely satisfactory for the following two reasons: (1) that E_{pan} in nonwater-limiting environments is also decreasing, that is, E_{pan} and ET are decreasing together, and (2) that VPD across

CONUS has remained stationary over the last 50 years. However, the central tenet of Roderick and Farquhar (2002) is that E_{pan} trends are a function of radiative component trends (dQ_n/dt) only, not advective component trends (dE_A/dt), and therefore the complementary relationship is not an important dynamic in determining trends in E_{pan} or, by extension, in ET . This is in marked contrast to Szilágyi et al. (2001), who assume exactly the opposite: that no Q_n trends exist and that ET trends are due solely to E_A trends.

Perhaps in an attempt to force the science to resolve these contradictory assumptions and explanations, Ohmura and Wild (2002) suggest that ET trends are what is important and that E_{pan} is only relevant if it offers clues as to their direction. Hobbins et al. (2004) resolve the differences between Roderick and Farquhar (2002) and Szilágyi et al. (2001) by showing that neither Q_n nor VPD can be assumed to have remained stationary. Their study uses spatially coincident observations of ET^{WB} and E_{pan} from across all climatic regimes in CONUS and thereby provides the heretofore missing empirical evidence, showing that ET and E_{pan} are complementary under constant radiative input, but also that, under declining (or increasing) Q_n , both E_{pan} and ET can be expected to decline (or increase) together without contravening complementarity.

Figure 3-20 shows this resolution, indicating the effects of the two previously competing explanations for the changes in E_{pan} with relation to ET : decreases in the energetic input to the surface and the complementary relationship acting to depress E_0 and raise ET . Decreasing the energetic driver alone (through the effects of dimming) decreases both ET and E_0 (and, given sufficient moisture supply, E_w). The complementary relationship hypothesis dictates that decreasing E_A alone, whether through decreases in U_z (stilling) or decreases in VPD [as observed by Hobbins et al. (2004) across 75% of CONUS] decreases E_0 and is as a result of the increase in ET (and vice versa for increasing E_A alone). Whether acting in isolation or together, neither explanation contradicts the other, and both must be considered together as a robust resolution of the paradox: together they explain all relative changes in ET and E_0 at various time and space scales. In our examination of the trends in ET^{WB} as a function of both of its components (Q_n and E_A , see Table 3-1), the traditional paradigm explained ET^{WB} trends in a little more than half of the basins, while the complementary relationship explained ET^{WB} trends in more than 90% of them, the difference being the 43% of the basins whose ET^{WB} trends would heretofore have been described as paradoxical.

The resolution of the evaporation paradox is not merely a nice distinction for climatologists. The purported existence of the paradox has been used by climate-change naysayers to cast doubt on “climate alarmists’ illusionary world of ‘unprecedented’ global warming” (CSCDGC 2003). However, here we have shown that the seemingly paradoxical behavior is no more than the consequence of the dependence of E_0 on ET that lies at the heart of the complementary relationship and is demonstrated to link trends in the two fluxes.

3.5 SUMMARY

This chapter has hewn as closely as possible to discussion of the statistical matters and variability/uncertainty thrown up by the estimation of the flux of actual ET and of its companion ideal flux, E_0 . The latter, conceptual rate is limited only by energy availability and/or the ability of the overpassing air to bear moisture away, thereby defining the maximal ET rate. It has three primary functions: assisting in irrigation management and agricultural estimates of ET , driving LSMs to estimate ET , and indicating hydroclimatologic change. Given that applications of statistics in ET estimation are limited and further given different models and modeling philosophies, some explication of the physics of the measures was required; we strove to keep this discussion succinct. In our survey of ET and E_0 topics, whether physical or statistical, we have cast the analyses in terms of statistics, variability, and uncertainty.

With regard to observations of ET , we outlined an uncertainty analysis of ET estimated as a residual of water budgets, provided as an example of the remote sensing of ET a review of the SSEB model and its application with a MODIS-based thermal dataset, and summarized the physics and sources of error and uncertainty in the eddy covariance technique and its concomitant global ET estimation efforts.

For modeled E_0 we mentioned the main sources of uncertainty, distinguishing between formulations based on physics and those based on simple empirical relationships to other drivers. This distinction is one of the central themes of the chapter, as it relates both to capturing the variability and trends in E_0 and using E_0 to force long-term hydroclimatology studies. A classical sensitivity analysis of one of the most commonly used E_0 measures in agriculture—Penman-Monteith ET_{rc} —was performed. We have underlined the implications for modelers of E_0 (and often hence ET), who must choose the optimal parameterization for E_0 from a plethora of models, ranging from those based solely on T to more complete physically based parameterizations of both radiative and advective dynamics. Optimal parameterizations strike a balance between parameter parsimony and accurate physical representation. We have summarized various studies that underscore the importance of using the best E_0 metric: one for which the best available information is available, including data streams, parameter estimates, and physical formulations. Ideally, these would be physically based formulations; few regions exist in the world where the supporting data remain unavailable. A first-order, second-moment uncertainty analysis of ET_{rc} has answered the crucial question, “Where in space and time can one effectively model E_0 with T alone?” and outlined the implications for E_0 parameterization choice, both in short-term variability and long-term trends.

We examined secular trends in both ET as an essential hydrologic variable and E_0 as a physical indicator of hydroclimatology. We suggested an approach to account for autocorrelation in time series of ET in estimating trend significance. We examined the roles that trends in E_0 's primary forcings—radiation and advection—play in determining its trends, and what these trends can tell us about the changing state of an anthropogenically warming hydrologic cycle. We resolved the so-called evaporation paradox as no more than these two drivers covarying, sometimes in concert, sometimes in opposition, but always within the realm of a thorough physical understanding of evaporation physics. Here again, secular analyses raised concerns regarding the choice of E_0 driving philosophy.

In this chapter we have striven to provide important information about a heretofore missing link in surface hydrology and have made it available to water managers, climatologists, and ecologists, or to any student of the surface hydrologic cycle. In the final analysis, the choice of modeling philosophy and the particular E_0 model used depend to a large degree on the purpose for the E_0 estimate to be produced, the availability of the calibrating data across the region of interest, and the preference of the modeler; here we have attempted to inform that modeler.

ACKNOWLEDGMENTS

The NLDAS data used were acquired as part of the mission of NASA's Earth Science Division and archived and distributed by the Goddard Earth Sciences Data and Information Services Center. MH was supported by a grant from the National Integrated Drought Information System.

References

- Allen, M. R., and W. J. Ingram. 2002. "Constraints on future changes in climate and the hydrologic cycle." *Nature* **419** (6903): 224–232.
- Allen, R. G., L. S. Pereira, D. Raes, and M. Smith. 1998. *Crop evapotranspiration: Guidelines for computing crop water requirements: FAO irrigation and drainage paper 56*. Rome: Food and Agricultural Organization of the United Nations.

- Allen, R. G., L. S. Pereira, M. Smith, D. Raes, and J. L. Wright. 2005a. "FAO-56 dual crop coefficient method for estimating evaporation from soil and application extensions." *J. Irrig. Drain. Eng.* **131** (1): 1–13.
- Allen, R. G., M. Tasumi, A. T. Morse, R. Trezza, W. Kramber, I. Lorite, and C. W. Robison. 2007a. "Satellite-based energy balance for mapping evapotranspiration with internalized calibration (METRIC)—Applications." *J. Irrig. Drain. Eng.* **133** (4): 395–406.
- Allen, R. G., M. Tasumi, and R. Trezza. 2007b. "Satellite-based energy balance for mapping evapotranspiration with internalized calibration (METRIC)—Model." *J. Irrig. Drain. Eng.* **133** (4): 380–394.
- Allen, R. G., I. A. Walter, R. Elliott, T. Howell, D. Itenfisu, and M. Jensen. 2005b. *The ASCE standardized reference evapotranspiration equation*, 59. Baltimore, MD: EWRI Task Committee on Standardization of Reference Evapotranspiration.
- Alpert, P., P. Kishcha, Y. J. Kaufman, and R. Schwarzbard. 2005. "Global dimming or local dimming?: Effect of urbanization on sunlight availability." *Geophys. Res. Lett.* **32** (17): L17802.
- Alpert, P., and M. Mandel. 1986. "Wind variability—An indicator for a mesoclimatic change in Israel." *J. Climate Appl. Meteor.* **25** (11): 1568–1576.
- Anderson, J., M. Norman, J. R. Mecikalski, J. A. Otkin, and W. P. Kustas. 2007. "A climatological study of evapotranspiration and moisture stress across the continental United States based on thermal remote sensing: 1. Model formulation." *J. Geophys. Res.* **112**: D10117.
- Aubinet, M., et al. 1999. "Estimates of the annual net carbon and water exchange of forests: The EUROFLUX methodology." *Adv. Ecol. Res.* **30**: 114–175.
- Bastiaanssen, W. G. M., M. Menenti, R. A. Feddes, and A. A. M. Holtslag. 1998. "A remote sensing surface energy balance algorithm for land (SEBAL): 1. Formulation." *J. Hydrol.* **212**: 198–212.
- Bastiaanssen, W. G. M., E. J. M. Noordman, H. Pelgrum, G. Davids, B. P. Thoreson, and R. G. Allen. 2005. "SEBAL model with remotely sensed data to improve water-resources management under actual field conditions." *J. Irrig. Drain. Eng.* **131** (1): 85–93.
- Blaney, H. F., and W. D. Criddle. 1950. *Determining water requirements in irrigated areas from climatological and irrigation data*. SCS-Tech. Rep. No. 96. Washington, DC: US Dept. of Agriculture Soil Conservation Service.
- Bois, B., P. Pieri, C. Van Leeuwen, and J. P. Gaudillere. 2005. "Sensitivity analysis of the Penman–Monteith evapotranspiration formula and comparison of empirical methods used in viticulture soil water balance." In *Proc., 14th Int. GESCO Viticulture Congress*, 187–193. Geisenheim, Germany: Groupe d'Etude des Systemes de Conduite de la vigne (GESCO).
- Bosilovich, M. G., S. D. Schubert, and G. K. Walker. 2005. "Global changes of the water cycle intensity." *J. Clim.* **18** (10): 1591–1608.
- Bouchet, R. J. 1963. "Évapotranspiration réelle et potentielle, signification climatique." [In French.] *IAHS Publ.* **62**: 134–142.
- Brutsaert, W. 1982. *Evaporation into the atmosphere: Theory, history, and applications*, 299. Dordrecht, Netherlands: D. Reidel.
- Brutsaert, W. 2006. "Indications of increasing land surface evaporation during the second half of the 20th century." *Geophys. Res. Lett.* **33** (20): L20403.
- Brutsaert, W., and M. Parlange. 1998. "Hydrologic cycle explains the evaporation paradox." *Nature* **396** (6706): 30–30.
- Brutsaert, W., and H. Stricker. 1979. "An advection-aridity approach to estimate actual regional evapotranspiration." *Water Resour. Res.* **15** (2): 443–450.
- Budyko, M. I. 1974. *Climate and life: International Geophysics Series*. Vol. 18, 508. New York: Academic Press.
- Buishand, T. A., and T. Brandsma. 1997. "Comparison of circulation classification schemes for predicting temperature and precipitation in the Netherlands." *Int. J. Climatol.* **17** (8): 875–889.
- Burnash, R. J. E., R. L. Ferral, and R. A. McGuire. 1973. *A generalized streamflow simulation system*. Rep. No. 204. Sacramento, CA: Joint Federal–State River Forecast Center.
- Buttafuoco, G., T. Caloiero, and R. Coscarelli. 2010. "Spatial uncertainty assessment in modelling reference evapotranspiration at regional scale." *Hydrol. Earth Syst. Sci. Discuss.* **14** (11): 2319–2327.
- Cess, R. D. 2005. "Water vapor feedback in climate models." *Science* **310** (5749): 795–796.
- Chattopadhyay, N., and M. Hulme. 1997. "Evaporation and potential evapotranspiration in India under conditions of recent and future climate change." *Agric. For. Meteorol.* **87** (1): 55–73.

- Chen, D., G. Gao, C.-Y. Xu, J. Guo, and G. Ren. 2005. "Comparison of the Thornthwaite method and pan data with the standard Penman-Monteith estimates of reference evapotranspiration in China." *Clim. Res.* **28** (2): 123–132.
- Ciach, G. J. 2003. "Local random errors in tipping-bucket rain gauge measurements." *J. Atmos. Oceanic Technol.* **20** (5): 752–759.
- Cong, Z. T., D. W. Yang, and G. H. Ni. 2009. "Does evaporation paradox exist in China?" *Hydrol. Earth Syst. Sci.* **13** (3): 357–366.
- Courault, D., and P. Monestiez. 1999. "Spatial interpolation of air temperature according to atmospheric circulation patterns in southeast France." *Int. J. Climatol.* **19** (4): 365–378.
- CSCDGC (Center for the Study of Carbon Dioxide and Global Change). 2003. "Fifty years of pan evaporation and solar radiation data: What do they tell us about climate change?" *CO₂ Sci. Mag.* **6** (2).
- Dai, A., K. E. Trenberth, and T. Qian. 2004. "A global dataset of Palmer Drought Severity Index for 1870–2002: Relationship with soil moisture and effects of surface warming." *J. Hydrometeorol.* **5** (6): 1117–1130.
- Daly, C., R. P. Neilson, and D. L. Phillips. 1994. "A statistical-topographic model for mapping climatological precipitation over mountainous terrain." *J. Appl. Meteorol.* **33** (2): 140–158.
- Darnell, W. L., W. F. Staylor, S. K. Gupta, N. A. Ritchey, and A. C. Wilber. 1992. "Seasonal variation of surface radiation budget derived from International Satellite Cloud Climatology Project C1 data." *J. Geophys. Res.* **97** (D14): 15,741–15,760.
- Davenport, D. C., and J. P. Hudson. 1967. "Local advection over crops and fallow. 1: Changes in evaporation rates along a 17-km transect in the Sudan Gezira." *Agric. Meteorol.* **4** (5): 339–352.
- de Vries, D. A., and H. J. Venema. 1953. "Some considerations on the behaviour of the Piche evaporimeter." *Neth. J. Agric. Sci.* **5–6** (1): 225–34.
- Dingman, S. L. 2002. *Physical hydrology*, 646. 2nd ed. Upper Saddle River, NJ: Prentice Hall.
- Dodson, R., and D. Marks. 1997. "Daily air temperature interpolated at high spatial resolution over a large mountainous region." *Clim. Res.* **8** (1): 1–20.
- Donohue, R. J., T. R. McVicar, and M. L. Roderick. 2010. "Assessing the ability of potential evaporation formulations to capture the dynamics in evaporative demand within a changing climate." *J. Hydrol.* **386** (1–4): 186–197.
- Donohue, R. J., M. L. Roderick, and T. R. McVicar. 2007. *Correcting long-term AVHRR reflectance data using the vegetation cover triangle*. CSIRO Land and Water Science Rep. No. 26/07. Canberra, Australia: CSIRO.
- Dyck, S. 1983. *Overview on the present status of the concepts of water balance models*. IAHS Publication 148. Wallingford, UK.
- Eslamian, S., M. J. Khordadi, and J. Abedi-Koupai. 2011. "Effects of variations in climatic parameters on evapotranspiration in the arid and semi-arid regions." *Global Planet. Change* **78** (3–4): 188–194.
- Farley, K. A., E. G. Jobbágy, and R. B. Jackson. 2005. "Effects of afforestation on water yield: A global synthesis with implications for policy." *Global Change Biol.* **11** (10): 1565–1576.
- Farnsworth, R. K., and E. S. Thompson. 1982. *Mean monthly, seasonal, and annual pan evaporation for the United States*. NOAA Technical Rep. No. NWS 34. Washington, DC: Office of Hydrology, National Weather Service, US Dept of Commerce.
- Farnsworth, R. K., E. S. Thompson, and E. L. Peck. 1982. *Evaporation atlas for the contiguous 48 United States*. NOAA Technical Rep. No. NWS 33. Washington, DC: Office of Hydrology, National Weather Service, US Dept of Commerce.
- Fick, A. 1995. "On liquid diffusion." *J. Membr. Sci.* **100** (1): 33–38.
- Fisher, J. B., T. A. DeBiase, Y. Qi, M. Xu, and A. H. Goldstein. 2005. "Evapotranspiration models compared on a Sierra Nevada forest ecosystem." *Environ. Modell. Software* **20** (6): 783–796.
- Fisher, J. B., K. P. Tu, and D. B. Baldocchi. 2008. "Global estimates of the land-atmosphere water flux based on monthly AVHRR and ISLSCP-II data, validated at 16 FLUXNET sites." *Remote Sens. Environ.* **112** (3): 901–919.
- Fu, B. P. 1981. "On the calculation of the evaporation from land surface." [In Chinese.] *Sci. Atmos. Sin* **5**: 23–31.
- Fu, G., S. P. Charles, and J. Yu. 2009. "A critical overview of pan evaporation trends over the last 50 years." *Clim. Change* **97** (1–2): 193–214.
- Gash, J. H. C., and W. J. Shuttleworth. 2007. "Introduction." In *Evaporation: Benchmark papers in hydrology*, No. 2, 521. Wallingford, UK: IAHS Press.

- Gedney, N., P. M. Cox, R. A. Betts, O. Boucher, C. Huntingford, and P. A. Stott. 2006. "Detection of a direct carbon dioxide effect in continental river runoff records." *Nature* **439** (7078): 835–838.
- Golubev, V. S., J. H. Lawrimore, P. Y. Groisman, N. A. Speranskaya, S. A. Zhuravin, M. J. Menne, T. C. Peterson, and R. W. Malone. 2001. "Evaporation changes over the contiguous United States and the former USSR: A reassessment." *Geophys. Res. Lett.* **28** (13): 2665–2668.
- Goovaerts, P. 2000. "Geostatistical approaches for incorporating elevation into the spatial interpolation of rainfall." *J. Hydrol.* **228** (1–2): 113–129.
- Gowda, P. H., J. L. Chavez, P. D. Colaizzi, S. R. Evett, T. A. Howell, and J. A. Tolk. 2008. "ET mapping for agricultural water management: Present status and challenges." *Irrig. Sci.* **26** (3): 223–237.
- Gowda, P. H., G. B. Senay, T. A. Howell, and T. H. Marek. 2009. "Lysimetric evaluation of simplified surface energy balance approach in the Texas high plains." *Appl. Eng. Agric.* **25** (5): 665–669.
- Habib, E., W. F. Krajewski, and A. Kruger. 2001. "Sampling errors of tipping-bucket rain gauge measurements." *J. Hydrol. Eng.* **6** (2): 159–166.
- Hamon, W. R. 1961. "Estimating potential evapotranspiration." *J. Hydraul. Div.* **87** (HY3): 107–120.
- Hansen, J., et al. 2005. "Earth's energy imbalance: Confirmation and implications." *Science* **308** (5727): 1431–1435.
- Hargreaves, G. H., and Z. A. Samani. 1985. "Reference crop evapotranspiration from temperature." *Appl. Eng. Agric.* **1** (2): 96–99.
- Held, I. M., and B. J. Soden. 2006. "Robust responses of the hydrological cycle to global warming." *J. Clim.* **19** (21): 5686–5699.
- Hirsch, R. M., D. R. Helsel, T. A. Cohn, and E. J. Gilroy. 1992. "Statistical analysis of hydrologic data." In *Handbook of hydrology*, edited by D. R. Maidment, 551. New York: McGraw-Hill.
- Hobbins, M. T. 2004. "Regional evapotranspiration and pan evaporation: Complementary interactions and long-term trends across the conterminous United States." Ph.D. dissertation, Hydrologic Science and Engineering Program, Civil Engineering Dept., Colorado State Univ.
- Hobbins, M. T. 2016. "The variability of ASCE standardized reference evapotranspiration: A rigorous, CONUS-wide decomposition and attribution." *Trans. ASABE* **59** (2): 561–576.
- Hobbins, M. T., A. Dai, M. L. Roderick, and G. D. Farquhar. 2008. "Revisiting the parameterization of potential evaporation as a driver of long-term water balance trends." *Geophys. Res. Lett.* **35** (12): L12403.
- Hobbins, M. T., J. A. Ramírez, and T. C. Brown. 2001a. "The complementary relationship in estimation of regional evapotranspiration: An enhanced advection-aridity model." *Water Resour. Res.* **37** (5): 1389–1403.
- Hobbins, M. T., J. A. Ramírez, and T. C. Brown. 2004. "Trends in pan evaporation and actual evapotranspiration across the conterminous US: Paradoxical or complementary?" *Geophys. Res. Lett.* **31** (13): L13503.
- Hobbins, M. T., J. A. Ramírez, T. C. Brown, and L. H. J. M. Claessens. 2001b. "The complementary relationship in estimation of regional evapotranspiration: The CRAE and advection-aridity models." *Water Resour. Res.* **37** (5): 1367–1387.
- Hobbins, M. T., A. Wood, D. Streubel, and K. Werner. 2012. "What drives the variability of evaporative demand across the conterminous United States?" *J. Hydrometeorol.* **13** (4): 1195–1214.
- Huard, F. 1993. "Approches théoriques de la spatialisation des variables climatiques à partir de la discréétisation du relief français." Ph.D. dissertation, Université de Caen (in French).
- Huntington, T. G. 2006. "Evidence for intensification of the global water cycle: Review and synthesis." *J. Hydrol.* **319** (1–4): 83–95.
- Huntington, T. G. 2008. "CO₂-induced suppression of transpiration cannot explain increasing runoff." *Hydro. Processes* **22** (2): 311–314.
- Hydrosphere Data Products. 1996. *Hydrodata USGS daily values*, Vol. 8.0. Boulder, CO: Hydrosphere Data Products.
- IPCC (Intergovernmental Panel on Climate Change). 2007. "Climate change 2007: The physical science basis." In *Proc., Contribution of Working Group I to the 4th Assessment Report of the Intergovernmental Panel on Climate Change*, edited by S. Solomon, et al. Cambridge, UK: Cambridge University Press.
- Irmak, S., J. O. Payero, D. L. Martin, A. Irmak, and T. A. Howell. 2006. "Sensitivity analyses and sensitivity coefficients of standardized daily ASCE-Penman-Monteith equation." *J. Irrig. Drain. Eng.* **32** (6): 564–578.
- Jackson, R. D., D. B. Idso, R. J. Reginato, and P. J. Pinter Jr. 1981. "Canopy temperature as a crop water stress indicator." *Water Resour. Res.* **17** (4): 1133–1138.

- Jovanovic, B., D. A. Jones, and D. Collins. 2008. "A high quality monthly pan evaporation dataset for Australia." *Clim. Change* **87** (3–4): 517–535.
- Jung, M., et al. 2010. "Recent decline in the global land evapotranspiration trend due to limited moisture supply." *Nature* **467** (7318): 951–954.
- Kahler, D. M., and W. Brutsaert. 2006. "Complementary relationship between daily evaporation in the environment and pan evaporation." *Water Resour. Res.* **42** (5): W05413.
- Kalma, J. D., T. R. McVicar, and M. F. McCabe. 2008. "Estimating land surface evaporation: A review of methods using remotely sensed surface temperature data." *Surv. Geophys.* **29** (4–5): 421–469.
- Kanamitsu, M. 1989. "Description of the NMC global data assimilation and forecast system." *Weather Forecasting* **4** (3): 335–342.
- Katul, G. G., and M. B. Parlange. 1992. "A Penman-Brutsaert model for wet surface evaporation." *Water Resour. Res.* **28** (1): 121–126.
- Kirono, D. G. C., and R. N. Jones. 2007. "A bivariate test for detecting inhomogeneities in pan evaporation time series." *Aust. Meteorol. Mag.* **56** (2): 93–103.
- Kişi, Ö. 2006. "Daily pan evaporation modelling using a neuro-fuzzy computing technique." *J. Hydrol.* **329** (3–4): 636–646.
- Klink, K. 1999. "Climatological mean and interannual variance of United States surface wind speed, direction, and velocity." *Int. J. Climatol.* **19** (5): 471–488.
- Knapp, P. A. 1992. "Correlation of 700-mb height data with seasonal temperature trends in the Great Basin (western USA): 1947–1987." *Clim. Res.* **2**: 65–71.
- Kohler, M. A. 1949. "On the use of double-mass analysis for testing the consistency of records and for making adjustments." *Bull. Am. Meteorol. Soc.* **30** (5): 188–195.
- Kohler, M. A., and L. H. Parmele. 1967. "Generalized estimates of free-water evaporation." *Water Resour. Res.* **3** (4): 997–1005.
- Kurtzman, D., and R. Kadmon. 1999. "Mapping of temperature variables in Israel: A comparison of different interpolation methods." *Clim. Res.* **13** (1): 33–43.
- Kustas, W. P., and J. M. Norman. 2000. "A two-source energy balance approach using directional radiometric temperature observations for sparse canopy covered surfaces." *Agron. J.* **92** (5): 847–854.
- Labat, D., Y. Goddérus, J. L. Probst, and J. L. Guyot. 2004. "Evidence for global runoff increase related to climate warming." *Adv. Water Resour.* **27** (6): 631–642.
- Lawrimore, J., and T. C. Peterson. 2000. "Pan evaporation trends in dry and humid regions of the United States." *J. Hydrometeorol.* **1** (6): 543–546.
- Lesack, L. F. W. 1993. "Water balance and hydrologic characteristics of a rain forest catchment in the Central Amazon Basin." *Water Resour. Res.* **29** (3): 759–773.
- Li, J., D. D. Richter, A. Mendoza, and P. Heine. 2010. "Effects of land-use history on soil spatial heterogeneity of macro- and trace elements in the southern Piedmont USA." *Geoderma* **156** (1–2): 60–73.
- Lim, W. H., M. L. Roderick, M. T. Robbins, S. C. Wong, P. J. Groeneveld, F. Sun, and G. D. Farquhar. 2012. "The aerodynamics of pan evaporation." *Agric. For. Meteorol.* **152**: 31–43.
- Linacre, E. T. 1994. "Estimating US class A pan evaporation from few climate data." *Waters Int.* **19** (1): 5–14.
- Liu, B., M. Xu, M. Henderson, and W. Gong. 2004. "A spatial analysis of pan evaporation trends in China, 1955–2000." *J. Geophys. Res.* **109**: D15102.
- Liu, C. M., and Y. Zeng. 2004. "Changes of pan evaporation in the recent 40 years in the Yellow River Basin." *Water Int.* **29** (4): 510–516.
- Lofgren, B. M., T. S. Hunter, and J. Wilbarger. 2011. "Effects of using air temperature as a proxy for potential evapotranspiration in climate change scenarios of Great Lakes basin hydrology." *J. Great Lakes Res.* **37** (4): 744–752.
- Lohmann, U., and J. Feichter. 2005. "Global indirect aerosol effects: A review." *Atmos. Chem. Phys.* **5** (3): 715–737.
- López-Granados, F., M. Jurado-Expósito, J. M. Peña-Barragán, and L. García-Torres. 2005. "Using geostatistical and remote sensing approaches for mapping soil properties." *Eur. J. Agron.* **23** (3): 279–289.
- Mahmoud, M. I., H. V. Gupta, and S. Rajagopal. 2011. "Scenario development for water resources planning and watershed management: Methodology and semi-arid region case study." *Environ. Modell. Software* **26** (7): 873–885.

- Marek, T. H., T. A. Howell, R. L. Snyder, D. Porter, and T. Scherer. 2010. "Crop coefficient development and application to an evapotranspiration network." In *Proc., 5th Decennial National Irrigation Symp.* St. Joseph, MI: American Society of Agricultural and Biological Engineers.
- McKenney, M. S., and N. J. Rosenberg. 1993. "Sensitivity of some potential evapotranspiration estimation methods to climate change." *Agric. For. Meteorol.* **64** (1–2): 81–110.
- McVicar, T. R., L. T. Li, T. G. Van Niel, M. F. Hutchinson, X. M. Mu, and Z. H. Liu. 2005. *Spatially distributing 21 years of monthly hydrometeorological data in China: Spatio-temporal analysis of FAO-56 crop reference evapotranspiration and pan evaporation in the context of climate change*. CSIRO Land and Water Technical Rep. No. 8/05. Canberra, Australia: CSIRO.
- McVicar, T. R., T. G. Van Niel, L. T. Li, M. L. Roderick, D. P. Rayner, L. Ricciardulli, and R. J. Donohue. 2008. "Wind speed climatology and trends for Australia, 1975–2006: Capturing the stilling phenomenon and comparison with near-surface reanalysis output." *Geophys. Res. Lett.* **35** (20): L20403.
- Menenti, M., and B. J. Choudhury. 1993. "Parameterization of land surface evaporation by means of location dependent potential evaporation and surface temperature range." In *Proc., Yokohama Symp. Exchange Processes at the Land Surface for a Range of Space and Time Scales: IAHS Publication No. 212*. London: IAHS.
- Milly, P. C. D., and K. A. Dunne. 2001. "Trends in evaporation and surface cooling in the Mississippi River basin." *Geophys. Res. Lett.* **28** (7): 1219–1222.
- Mitchell, K. E., et al. 2004. "The multi-institution North American Land Data Assimilation System (NLDAS): Utilizing multiple GCIP products and partners in a continental distributed hydrological modeling system." *J. Geophys. Res.* **109** (D7): D07S90.
- Molina Martínez, J. M., V. Martínez Alvarez, M. M. González-Real, and A. Baille. 2006. "A simulation model for predicting hourly pan evaporation from meteorological data." *J. Hydrol.* **318** (1–4): 250–261.
- Monteith, J. L. 1965. "Evaporation and environment." *Symp. Soc. Exp. Biol.* **19**: 205–234.
- Moran, M. S., A. F. Rahman, J. C. Washburne, D. C. Goodrich, M. A. Weltz, and W. P. Kustas. 1996. "Combining the Penman-Monteith equation with measurements of surface temperature and reflectance to estimate evaporation rates of semiarid grassland." *Agric. For. Meteorol.* **80** (2–4): 87–109.
- Morton, F. I. 1983. "Operational estimates of areal evapotranspiration and their significance to the science and practice of hydrology." *J. Hydrol.* **66** (1–4): 1–76.
- Morton, F. I., F. Ricard, and S. Fogarasi. 1985. *Operational estimates of areal evapotranspiration and lake evaporation—Program WREVAP*. Paper 24. Ottawa, Canada: National Hydrologic Research Institute.
- Nazarenko, L., and S. Menon. 2005. "Varying trends in surface energy fluxes and associated climate between 1960 and 2002 based on transient climate simulations." *Geophys. Res. Lett.* **32** (22): L22704.
- NCDC (National Climatic Data Center). 2011. "Multi-network metadata system." Accessed November 16, 2011. <https://mi3.ncdc.noaa.gov/>.
- Ohmura, A., and M. Wild. 2002. "Is the hydrological cycle accelerating?" *Science* **298** (5597): 1345–1346.
- Oki, T., and S. Kanae. 2006. "Global hydrological cycles and world water resources." *Science* **313** (5790): 1068–1072.
- Ol'dekop, E. M. 1911. *On evaporation from the surface of river basins: Transactions on meteorological observations*. [In Russian.] Tartu, Estonia: Univ. of Tartu.
- Oudin, L., V. Andréassian, J. Lerat, and C. Michel. 2008. "Has land cover a significant impact on mean annual streamflow? An international assessment using 1508 catchments." *J. Hydrol.* **357** (3–4): 303–316.
- Ozdogan, M., and G. D. Salvucci. 2004. "Irrigation-induced changes in potential evapotranspiration in southeastern Turkey: Test and applications of Bouchet's complementary hypothesis." *Water Resour. Res.* **40** (4): W04301.
- Palmer, W. C. 1965. *Meteorological drought*. Research Paper 45. Washington, DC: Dept. of Commerce.
- Parlange, M. B., and G. G. Katul. 1992a. "An advection-aridity evaporation model." *Water Resour. Res.* **28** (1): 127–132.
- Parlange, M. B., and G. G. Katul. 1992b. "Estimation of the diurnal variation of potential evaporation from a wet bare soil surface." *J. Hydrol.* **132** (1–4): 71–89.
- Penman, H. L. 1948. "Natural evaporation from open water, bare soil, and grass." *Proc., R. Soc. London, Ser. A* **193** (1032): 120–145.
- Peterson, T. C., et al. 1998. "Homogeneity adjustments of in-situ atmospheric climate data: A review." *Int. J. Climatol.* **18** (13): 1493–1517.

- Peterson, T. C., V. S. Golubev, and P. Y. Groisman. 1995. "Evaporation losing its strength." *Nature* **377** (6551): 687–688.
- Piche, E. M. 1872. "Note sur l'atmismomètre, instrument destiné à mesurer l'évaporation." [In French.] In *Bulletin Hebdomadaire de l'Association Scientifique de France*, 166–167.
- Pinker, R. T., B. Zhang, and E. G. Dutton. 2005. "Do satellites detect trends in surface solar radiation?" *Science* **308** (5723): 850–854.
- Pirazzoli, P. A., and A. Tomasin. 2003. "Recent near-surface wind changes in the central Mediterranean and Adriatic areas." *Int. J. Climatol.* **23** (8): 963–973.
- Porporato, A., E. Daly, and I. Rodriguez-Iturbe. 2004. "Soil water balance and ecosystem response to climate change." *Am. Nat.* **164** (5): 625–632.
- Potter, K. W. 1981. "Illustration of a new test for detecting a shift in mean in precipitation series." *Mon. Weather Rev.* **109** (9): 2040–2045.
- Priestley, C. H. B., and R. J. Taylor. 1972. "On the assessment of surface heat flux and evaporation using large-scale parameters." *Mon. Weather Rev.* **100** (2): 81–92.
- PRISM Climate Group. 2004. "Parameter-elevation regressions on independent slopes model." Corvallis: OR: Oregon State Univ. Accessed November 11, 2018. <http://www.prismclimate.org>.
- Pryor, S. C., R. J. Barthelmie, and E. S. Riley. 2007. "Historical evolution of wind climates in the USA." *J. Phys.: Conf. Ser.* **75**: 012065.
- Qian, T., A. Dai, and K. E. Trenberth. 2007. "Hydroclimatic trends in the Mississippi River basin from 1948 to 2004." *J. Clim.* **20** (18): 4599–4614.
- Qian, Y., D. P. Kaiser, L. R. Leung, and M. Xu. 2006. "More frequent cloud-free sky and less surface solar radiation in China from 1955 to 2000." *Geophys. Res. Lett.* **33** (1): L01812.
- Quintana-Gomez, R. A. 1998. "Changes in evaporation patterns detected in northernmost South America." In *Proc., 7th Int. Meeting on Statistical Climatology*, 97. Whistler, Canada: Institute of Mathematical Statistics.
- Ramirez, J. A., M. T. Hobbins, and T. C. Brown. 2005. "Observational evidence of the complementary relationship in regional evaporation lends strong support for Bouchet's hypothesis." *Geophys. Res. Lett.* **32** (15): L15401.
- Rayner, D. P. 2007. "Wind run changes: The dominant factor affecting pan evaporation trends in Australia." *J. Clim.* **20** (14): 3379–3394.
- Rhoades, D. A., and M. J. Salinger. 1993. "Adjustment of temperature and rainfall records for site changes." *Int. J. Climatol.* **13** (8): 899–913.
- Robock, A., M. Mu, K. Vinnikov, I. V. Trofimova, and T. I. Adamenko. 2005. "Forty-five years of observed soil moisture in the Ukraine: No summer desiccation (yet)." *Geophys. Res. Lett.* **32** (3): L03401.
- Roderick, M. L., and G. D. Farquhar. 2002. "The cause of decreased pan evaporation over the past 50 years." *Science* **298** (5597): 1410–1411.
- Roderick, M. L., and G. D. Farquhar. 2004. "Changes in Australian pan evaporation from 1970 to 2002." *Int. J. Climatol.* **24** (9): 1077–1090.
- Roderick, M. L., and G. D. Farquhar. 2005. "Changes in New Zealand pan evaporation since the 1970s." *Int. J. Climatol.* **25** (15): 2031–2039.
- Roderick, M. L., M. T. Hobbins, and G. D. Farquhar. 2009a. "Pan evaporation trends and the terrestrial water balance. I: Principles and observations." *Geogr. Compass* **3** (2): 746–760.
- Roderick, M. L., M. T. Hobbins, and G. D. Farquhar. 2009b. "Pan evaporation trends and the terrestrial water balance. II: Energy balance and interpretation." *Geogr. Compass* **3** (2): 761–780.
- Roderick, M. L., L. D. Rotstayn, G. D. Farquhar, and M. T. Hobbins. 2007. "On the attribution of changing pan evaporation." *Geophys. Res. Lett.* **34** (17): L17403.
- Roerink, G. J., Z. Su, and M. Menenti. 2000. "S-SEBI: A simple remote sensing algorithm to estimate the surface energy balance." *Phys. Chem. Earth Part B* **25** (2): 147–157.
- Romanou, A., B. Liepert, G. A. Schmidt, W. B. Rossow, R. A. Ruedy, and Y. Zhang. 2007. "20th century changes in surface solar irradiance in simulations and observations." *Geophys. Res. Lett.* **34** (5): L05713.
- Rotstayn, L. D., M. L. Roderick, and G. D. Farquhar. 2006. "A simple pan-evaporation model for analysis of climate simulations: Evaluation over Australia." *Geophys. Res. Lett.* **33** (17): L17715.
- Salas, J. D. 1993. "Analysis and modeling of hydrologic time series." In *Handbook of hydrology*, edited by D. R. Maidment, 551. New York: McGraw-Hill.

- Sammis, T. W., J. Wang, and D. R. Miller. 2011. "The transition of the Blaney-Criddle formula to the Penman-Monteith equation in the Western United States." *J. Serv. Climatol.* **5** (1): 1–11.
- Sauer, V. B., and R. W. Meyer. 1992. *Determination of error in individual discharge measurements*. USGS Open File Rep. 92-144. Reston, VA: USGS.
- Schreiber, P. 1904. "Über die beziehungen zwischen dem niederschlag und der wasserfhrung der flüsse in Mittleeuropa." [In German.] *Meteorol. Z.* **21**: 441–452.
- Seed, A. W., and G. L. Austin. 1990. "Sampling errors for raingauge-derived mean areal daily and monthly rainfall." *J. Hydrol.* **118** (1–4): 163–173.
- Seguin, B., S. Baelz, J. M. Monget, and V. Petit. 1982. "Utilisation de la thermographie IR pour l'estimation de l'évaporation régionale. II: Résultats obtenus à partir de données satellites." [In French.] *Agronomie* **2** (2): 113–115.
- Senay, G. B., S. Bohms, R. K. Singh, P. H. Gowda, N. M. Velpuri, H. Alemu, and J. P. Verdin. 2013. "Operational evapotranspiration mapping using remote sensing and weather datasets: A new parameterization for the SSEB approach." *J. Am. Water Resour. Assoc.* **49** (3): 577–591.
- Senay, G. B., M. E. Budde, and J. P. Verdin. 2011. "Enhancing the simplified surface energy balance (SSEB) approach for estimating landscape ET: Validation with the METRIC model." *Agric. Water Manage.* **98** (4): 606–618.
- Senay, G. B., M. E. Budde, J. P. Verdin, and A. M. Melesse. 2007. "A coupled remote sensing and simplified surface energy balance approach to estimate actual evapotranspiration from irrigated fields." *Sensors* **7** (6): 979–1000.
- Senay, G. B., J. P. Verdin, R. Lietzow, and A. M. Melesse. 2008. "Global daily reference evapotranspiration modeling and evaluation." *J. Am. Water Resour. Assoc.* **44** (4): 969–979.
- Serrat-Capdevila, A., R. L. Scott, W. J. Shuttleworth, and J. B. Valdés. 2011. "Estimating evapotranspiration under warmer climates: Insights from a semi-arid riparian system." *J. Hydrol.* **399** (1–2): 1–11.
- Shenbin, C., L. Yunfeng, and A. Thomas. 2006. "Climatic change on the Tibetan Plateau: Potential evapotranspiration trends from 1961–2000." *Clim. Change* **76** (3–4): 291–319.
- Shuttleworth, W. J. 1993. "Evaporation." In *Handbook of hydrology*, edited by D. R. Maidment, 551. New York: McGraw-Hill.
- Slack, J. R., and J. M. Landwehr. 1992. *Hydro-Climatic Data Network (HCDN): A US Geological Survey streamflow data set for the United States for the study of climate variations, 1874–1988*. USGS Open File Rep. No. 92-632. Reston, VA: USGS.
- Smajstrla, A. G., F. S. Zazueta, and G. M. Schmidt. 1987. "Sensitivity of potential evapotranspiration to four climatic variables in Florida." *Proc. Soil Crop Sci. Soc. Florida* **46**: 21–26.
- Soden, B. J., D. L. Jackson, V. Ramaswamy, M. D. Schwarzkopf, and X. Huang. 2005. "The radiative signature of upper tropospheric moistening." *Science* **310** (5749): 841–844.
- Stanhill, G. 2002. "Is the Class A evaporation pan still the most practical and accurate meteorological method for determining irrigation water requirements?" *Agric. For. Meteorol.* **112** (3): 233–236.
- Stanhill, G., and S. Cohen. 2001. "Global dimming: A review of the evidence for a widespread and significant reduction in global radiation with discussion of its probable causes and possible agricultural consequences." *Agric. For. Meteorol.* **107** (4): 255–278.
- Strangeways, I. 2001. "Back to basics: The 'met. enclosure': Part 7—Evaporation." *Weather* **56** (12): 419–427.
- Su, H., M. F. McCabe, E. F. Wood, Z. Su, and J. Prueger. 2005. "Modeling evapotranspiration during SMACEX: Comparing two approaches for local and regional scale prediction." *J. Hydrometeorol.* **6** (6): 910–922.
- Su, Z. 2002. "The surface energy balance system (SEBS) for estimation of turbulent heat fluxes." *Hydrol. Earth Syst. Sci.* **6** (1): 85–100.
- Sugita, M., J. Usui, I. Tamagawa, and I. Kaihotsu. 2001. "Complementary relationship with a convective boundary layer to estimate regional evapotranspiration." *Water Resour. Res.* **37** (2): 353–365.
- Szilágyi, J. 2001. "Modeled areal evaporation trends over the conterminous United States." *J. Irrig. Drain. Eng.* **127** (4): 196–200.
- Szilágyi, J. 2007. "On the inherent asymmetric nature of the complementary relationship of evaporation." *Geophys. Res. Lett.* **34** (2): L02405.
- Szilágyi, J., and J. Jozsa. 2009. "Complementary relationship of evaporation and the mean annual water-energy balance." *Water Resour. Res.* **45** (9): W09201.

- Szilágyi, J., J. Józsa, and Á. Kovács. 2011. "A calibration-free evapotranspiration mapping (CREMAP) technique." In *Evapotranspiration*, edited by L. Labedzki. Accessed November 11, 2018. <https://www.intechopen.com/books/evapotranspiration/a-calibration-free-evapotranspiration-mapping-cremap-technique>.
- Szilágyi, J., G. G. Katul, and M. B. Parlange. 2001. "Evapotranspiration intensifies over the conterminous United States." *J. Water Resour. Plann. Manage.* **127** (6): 354–362.
- Tang, B., L. Tong, S. Kang, and L. Zhang. 2011. "Impacts of climate variability on reference evapotranspiration over 58 years in the Haihe river basin of north China." *Agric. Water Manage.* **98** (10): 1660–1670.
- Tebakari, T., J. Yoshitani, and C. Suvanpimol. 2005. "Time-space trend analysis in pan evaporation over Kingdom of Thailand." *J. Hydrol. Eng.* **10** (3): 205–215.
- Thom, A. S., J.-L. Thony, and M. Vauclin. 1981. "On the proper employment of evaporation pans and atmometers in estimating potential transpiration." *Q. J. R. Meteorolog. Soc.* **107** (453): 711–736.
- Thorntwaite, C. W. 1948. "An approach toward a rational classification of climate." *Geogr. Rev.* **38** (1): 55–94.
- Trenberth, K. E., and J. T. Fasullo. 2010. "Tracking earth's energy." *Science* **328** (5976): 316–317.
- Trenberth, K. E., J. T. Fasullo, and J. Kiehl. 2009. "Earth's global energy budget." *Bull. Am. Meteorol. Soc.* **90** (3): 311–324.
- Tuller, S. E. 2004. "Measured wind speed trends on the west coast of Canada." *Int. J. Climatol.* **24** (11): 1359–1374.
- Turc, L. 1954. "Le bilan d'eau des sols: Relation entre les précipitations, l'évaporation et l'écoulement." [In French.] *Annales Agronomiques Série A* **5**: 491–595.
- US Drought Monitor. 2011. "Current US drought monitor." Accessed November 16, 2011. <https://droughtmonitor.unl.edu>.
- Vinukollu, R. K., R. Meynadier, J. Sheffield, and E. F. Wood. 2011. "Multi-model, multi-sensor estimates of global evapotranspiration: Climatology, uncertainties and trends." *Hydrol. Processes* **25** (26): 3993–4010.
- Walter, M. T., D. S. Wilks, J.-Y. Parlange, and R. L. Schneider. 2004. "Increasing evapotranspiration from the conterminous United States." *J. Hydrometeorol.* **5** (3): 405–408.
- Wang, K., and R. E. Dickinson. 2012. "A review of global terrestrial evapotranspiration: Observation, modeling, climatology, and climatic variability." *Rev. Geophys.* **50** (2): RG2005.
- Wang, X. L., and Y. Feng. 2004. "RHtestsV3 user manual." Accessed November 18, 2011. <http://cccma.seos.uvic.ca/ETCCDMI/software.shtml>.
- Wang, Y., T. Jiang, O. Bothe, and K. Fraedrich. 2007. "Changes of pan evaporation and reference evapotranspiration in the Yangtze River basin." *Theor. Appl. Climatol.* **90** (1–2): 13–23.
- Wild, M., H. Gilgen, A. Roesch, A. Ohmura, C. N. Long, E. G. Dutton, B. Forgan, A. Kallis, V. Russak, and A. Tsvetkov. 2005. "From dimming to brightening: Decadal changes in solar radiation at Earth's surface." *Science* **308** (5723): 847–850.
- Wilson, K., et al. 2002. "Energy balance closure at FLUXNET sites." *Agric. For. Meteorol.* **113** (1–4): 223–243.
- Xu, C.-Y., L. Gong, J. Tong, and D. Chen. 2006a. "Decreasing reference evapotranspiration in a warming climate—A case of Changjiang (Yangtze) river catchment during 1970–2000." *Adv. Atmos. Sci.* **23** (4): 513–520.
- Xu, C.-Y., L. Gong, J. Tong, D. Chen, and V. P. Singh. 2006b. "Analysis of spatial distribution and temporal trend of reference evapotranspiration and pan evaporation in Changjiang (Yangtze River) catchment." *J. Hydrol.* **327** (1–2): 81–93.
- Yue, S., P. Pilon, and G. Cavadias. 2002. "Power of the Mann-Kendall and Spearman's rho tests for detecting monotonic trends in hydrologic series." *J. Hydrol.* **259** (1–4): 254–271.
- Yue, S., and C. Y. Wang. 2002. "Applicability of prewhitening to eliminate the influence of serial correlation on the Mann-Kendall test." *Water Resour. Res.* **38** (6): 4-1–4-7.
- Zhang, L., K. Hickel, W. R. Dawes, F. H. S. Chiew, A. W. Western, and P. R. Briggs. 2004. "A rational function approach for estimating mean annual evapotranspiration." *Water Resour. Res.* **40** (2): W02502.
- Zhang, L., N. Potter, K. Hickel, Y. Q. Zhang, and Q. X. Shao. 2008. "Water balance modeling over variable time scales based on the Budyko framework—Model development and testing." *J. Hydrol.* **360** (1–4): 117–131.
- Zhang, Y., C. Liu, Y. Tang, and Y. Yang. 2007. "Trends in pan evaporation and reference and actual evapotranspiration across the Tibetan plateau." *J. Geophys. Res.* **112**: D12110.
- Zuo, H. C., Y. Bao, C. J. Mang, and Y. Q. Hu. 2006. "An analytic and numerical study on the physical meaning of pan evaporation and its trend in recent 40 years." [In Chinese.] *Chin. J. Geophys.* **49** (3): 607–616.

CHAPTER 4

Infiltration and Soil Water

Timothy R. Green
Roger E. Smith
Richard E. Green

4.0 SCOPE AND INTRODUCTION

Water is essential for life, and “soils sustain life” (<https://www.soils.org/>) — largely by retaining water and nutrients in the biotic zone. This chapter addresses the critical hydrological processes of surface infiltration and soil–water flow and storage. First, we lay a basic groundwork for understanding soil hydraulic properties and processes of water infiltration, soil–water retention, and redistribution. Next, concepts of natural variability and statistical distributions are introduced. Both continuum theory (diffuse flow) and preferred flow processes are discussed within a representative volume and across heterogeneous landscapes, where patterns emerge. This leads to spatial scaling of processes and variables and effective upscaled parameter estimation. These concepts and methods culminate in the quantification of uncertainty in measurements and spatial estimates of soil–water and infiltration flux.

4.0.1 Central Role of Infiltration in Hydrology

Figure 4-1 highlights the central roles of infiltration and soil–water processes in the broader context of hydrological interactions over space and time. The process of infiltration, where rainwater enters the soil surface, partitions atmospheric precipitation of water on the land surface between overland flow (a direct form of runoff) and soil–water intake at a point or discrete area. Surface runoff and run-on of overland flow may be controlled by intake rates limited at the soil surface, or by filling the soil with water above infiltration-limiting strata. Likewise, irrigation water by various delivery methods (e.g., sprinkler, drip, or ponded) is partitioned, even though rates are controlled to reduce runoff from the application area. Natural and artificial surface water bodies infiltrate into the subsurface at rates controlled by the media underlying the water body, including liners intended to reduce infiltration losses. From point to watershed scales, the process of infiltration is a key to flux partitioning between overland flow and soil water and potentially to groundwater. Components of the resulting water balance need to be estimated or predicted for water resource and land management.

Infiltration and soil–water processes interact with other biophysical processes at different scales in space and time (left panel in Figure 4-1). These interactions, combined spatial variability and uncertainty about the soil properties and state variables (right panel in Figure 4-1), complicate hydrologic predictions and present the need for applications of statistics and stochastic methods.

Figure 4-2 illustrates a timeline for advances in infiltration and soil–water research, including key advances in the areas of physical measurements, theory, and statistical models. Simple

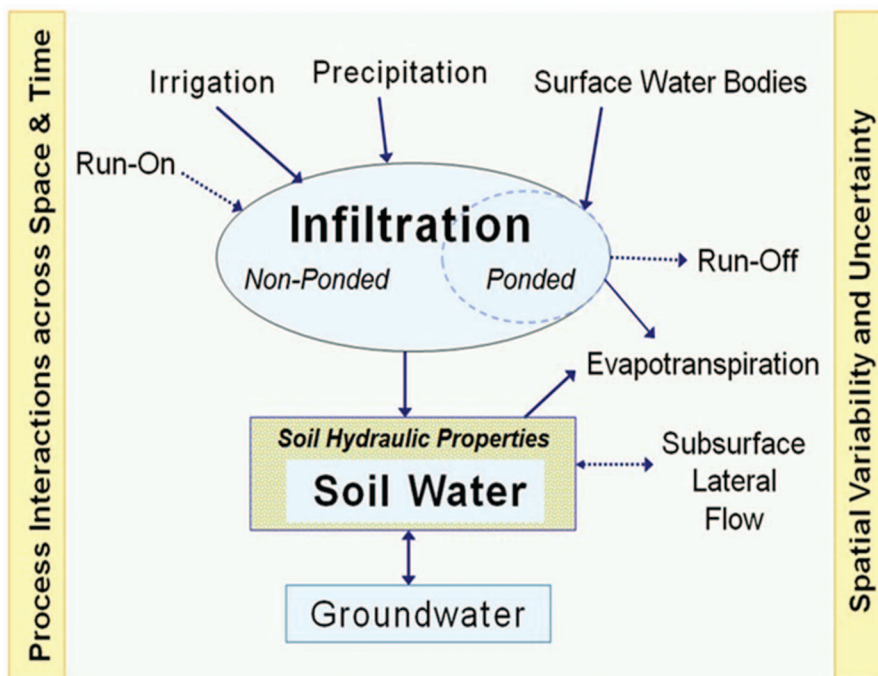


Figure 4-1. Schematic, infiltration-centric view of hydrological process interactions across space and time, where spatial variability and uncertainty are implicit. Infiltration is a flux of water at the soil surface, while soil water is a distributed storage of water. Soil hydraulic properties control the processes of surface infiltration, soil water redistribution, and groundwater recharge or capillary rise.

Infiltrometers have been used for more than a century to measure infiltration processes, followed by a mathematical model for vertical infiltration (Green and Ampt 1911) that is used to this day. Even so, statistical methods for quantifying natural variability did not emerge widely until the middle of the twentieth century, as analytical solutions were being derived for the dynamics of vertical infiltration at a point. Scale issues related to measurements, simulations, and different applications of hydrological theory arose mainly near the end of the twentieth century. Simultaneously, new technologies for automated soil–water measurements were being developed and applied, which made measurements of spatial variability in soil–water content more broadly feasible.

4.0.2 Process Interactions Affecting Infiltration and Soil Water

Infiltration capacity (f_c , also called *infiltrability*) is the maximum rate of infiltration that can occur at a given time; it is both state and scale dependent. A primary control and negative feedback on infiltrability is the near-surface soil moisture (water content). Actual infiltration rate (f) may change from rainfall-controlled to soil-controlled as the soil wets up during an infiltration rainfall (or irrigation) event. An exception to this rule is when a dry surface is hydrophobic or water-repellent (Bughici and Wallach 2016, Wallach et al. 2013), and the water repellency decreases as the surface soils wet. Hydrophobic conditions are common in deserts, where organic residues accumulate on the ground surface, and following forest or grass fires. Thus, initial or antecedent soil moisture state controls infiltrability in a highly transient manner that is occasionally nonmonotonic (rising and falling over time).

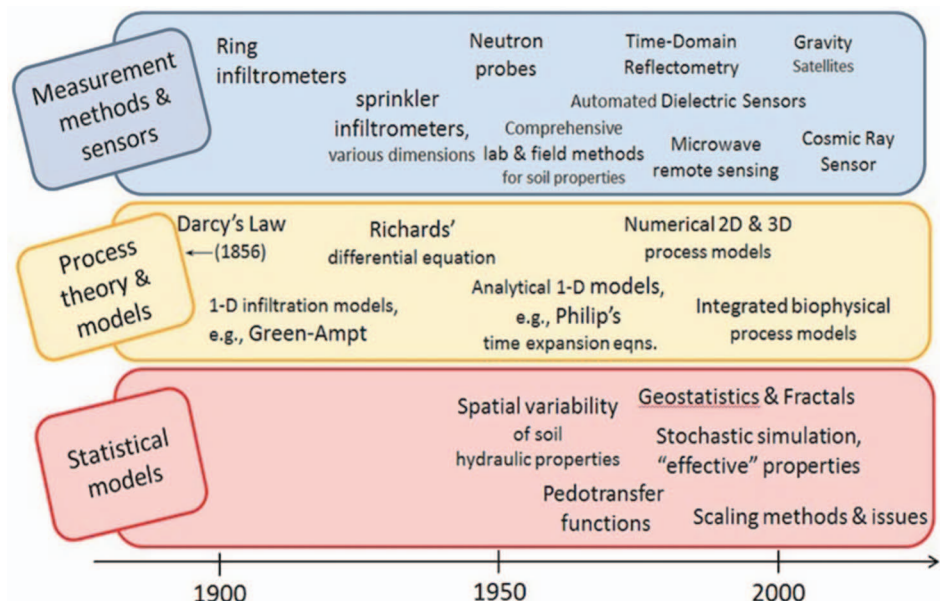


Figure 4-2. Timeline of infiltration and soil–water research contributions showing when statistical considerations became a focus of infiltration and soil hydrology research. Time periods of different activities are approximate.

Scale dependence occurs due to spatial variability of infiltration, which allows runoff from one location to run on to a neighboring location where it may infiltrate (Blöschl and Sivapalan 1995). The effective or average infiltration over an area may change depending upon the internal variability, and the total variance tends to increase with the size of the area (e.g., fractal behavior). Spatial variability may cause internal runoff to initiate sooner, due to low infiltrability of some areas. However, the internal runoff tends to infiltrate more readily in neighboring high-infiltrability locations within an area of interest. As a result, the net or effective infiltrability tends to increase with soil spatial variability.

The effective infiltrability of an area is further complicated by spatial correlation (e.g., patchiness) and connectivity of patterns, which may increase the net runoff and decrease the net infiltration. This is the case when fine sediments, including clay particles, are deposited along pathways of concentrated overland flow to create a semi-permeable surface seal. Vegetation patches, such as clumps of grass or shrubs, also contribute to spatial variability when soils beneath vegetation are more permeable than adjacent bare soils. Such vegetation patches often occur in subareas of microtopographic highs, such that the overall areal infiltrability increases after ponding, as the water stage rises and inundates more vegetation patches. Thus, spatial variations and patterns within the landscape provide controls on infiltration dynamics in space and time.

4.0.3 Variability and Uncertainty of Infiltration and Soil Water

As noted previously, surface properties that control infiltrability of water are highly variable in space and time. All of the main factors of soil formation—parent materials, biota, topography, climate, and time (Jenny 1946)—interact to determine the current soil hydraulic properties and their spatial patterns. Soil–water status further interacts with the soil properties to control the temporal variability of infiltration. Obviously, we are left with a high degree of uncertainty. Statistical methods should then be invoked, even in the most process-based quantification, to estimate and predict infiltration rates and the corresponding soil–water contents across space and time.

4.1 INFILTRATION AND SOIL-WATER DYNAMICS: DESCRIPTION AND MEASUREMENT

This section provides some historical context, basic principles, and equations used to describe and quantify soil–water dynamics and infiltration. Plant canopy interception of rainfall and soil-surface sealing are discussed and illustrated without incorporating these added complexities into the analyses. Methods and instruments for measuring infiltration and soil–water content are then discussed in light of the theory, but not in a comprehensive manner. All these topics lay the foundation for exploring spatial and temporal variability of infiltration and soil moisture.

4.1.1 History: Engineering Treatment of Rainfall Infiltration and Losses

Physical understanding of the movement of water into and within the soil has developed mainly in the last century ([Assouline 2013](#)). The factors that affect uncertainty and variability in soil water and infiltration are the same, but the emphases of the two branches of knowledge are different. For example, two Australian scientists, [Green and Ampt \(1911\)](#), published an equation for vertical infiltration rate into a soil column, describing soil–water infiltration in terms of capillary suction at the wetting front, with a gradient decreasing in time as the wetting front moves deeper into the soil. Three decades later, [Horton \(1939\)](#) began to quantify infiltration with equations that also describe a temporally decreasing rate. While the general understanding of the processes was similar, Green and Ampt were interested in water movement in the soil, whereas Horton was concerned with losses from rain and the production of runoff. Horton was aware of Green and Ampt's work, but he thought that the decrease in infiltrability with time was related to other processes, such as swelling and fine particles filling pore spaces ([Horton 1936](#)). While understanding of the dynamics of both soil–water movement and infiltration has made enormous strides in the last half-century, the uncertainty and variability of natural soil properties often seem overwhelming. In this section the underlying description of unsaturated soil–water flow and its relation to infiltration is presented to lay the groundwork for possible treatment of the variability and uncertainties involved. Like many aspects of engineering in the sphere of natural conditions, even in the presence of these factors, estimates must be made, and planning must proceed.

4.1.2 Plant Canopy Interception of Rainfall

Before rainfall or sprinkler irrigation contacts the ground or soil surface, a fraction of the ground area is often filtered by the aboveground plant canopy. The effective leaf area may be quantified by the leaf area index (LAI , $m^2 m^{-2}$) as the leaf area per unit ground area. For a closed canopy, the LAI will exceed unity, and much larger values are possible. [Scurlock et al. \(2001\)](#) summarize a global dataset, where $LAI > 8$ in 14% of sampled areas. Leaf area affects the interception of both light (solar radiation) and water (rainfall), which affect soil evaporation and the net rainfall available for soil infiltration. Our current focus on infiltration begs the question, "How might canopy interception affect the infiltration amount?" This can be answered for an individual infiltration event and over longer time periods, such as a crop season.

For small leaf areas, canopy interception is usually negligible (within rainfall estimation error), but as LAI increases, the maximum interception storage per ground area (depth) may be on the order of 1 mm for annual crops or >8 mm for dense forests ([Herwitz 1985](#)). Water stored on leaves and stems is available for evaporative loss after the rain ceases. If the canopy is dry before a rainfall event, the interception depth (potential storage) is subtracted from the total rainfall for that event. For small events, the fraction of intercepted rainfall that is evaporated may be large, even negating any net infiltration. Over a crop season, such as a wheat crop in Australia ([Leuning et al. 1994](#)), [Kozak et al. \(2007\)](#) show that the cumulative canopy interception may comprise approximately one-third of the cumulative rainfall (Figure 4-3).

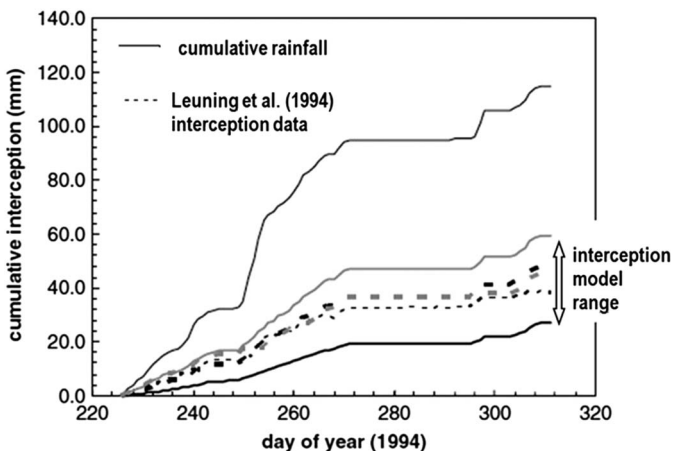


Figure 4-3. Cumulative canopy interception (dashed lines show different datasets, and other bounding lines show modeled interception) and cumulative rainfall (upper black line) versus time within a crop season for wheat in Wagga Wagga, New South Wales, Australia. The double arrow and “interception model range” indicate a range of simulated cumulative interception.

Source: Experimental data from Leuning et al. (1994); figure taken from Kozak et al. (2007).

The amount of interception depends upon the climate and crop, and its estimation can vary greatly among canopy interception models. Nonetheless, this example highlights the potential importance of interception storage. Figure 4-4 illustrates the potential impacts on cumulative infiltration and other water balance components. This example considers only plant canopy interception, but Kozak et al. (2007) also explore plant residue interception as additional interception storage. They investigate models that include interception, but many hydrological infiltration models do not consider canopy interception. In the following sections, “rainfall” may be considered to be the “net rainfall” after interaction with the canopy.

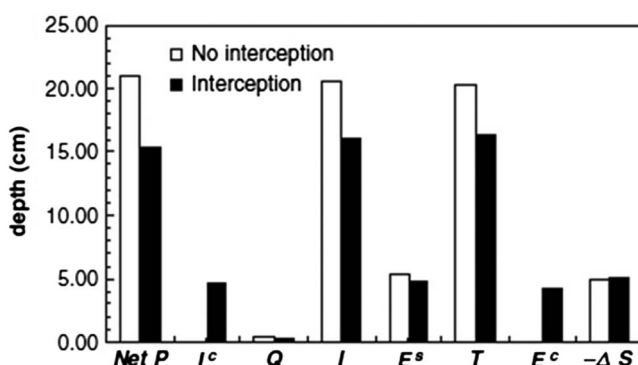


Figure 4-4. Simulated seasonal water balance components with and without simulated canopy interception for a wheat crop in Australia. In this figure, Net P is precipitation reaching the soil surface, I^c is canopy interception, Q is surface runoff, I is soil–water infiltration, E^s and E^c are evaporation from soil and canopy, T is plant transpiration, and $-\Delta S$ is the negative change in water storage over the season.

Source: Experimental data from Leuning et al. (1994), and figure from Kozak et al. (2007).

4.1.3 Local Processes of Soil Water and Infiltration

4.1.3.1 Capillary Pressure Head and Saturation

Our current understanding of infiltration of rainfall (or sprinkler irrigation) is based on the same theory that describes soil–water flow. Soil is a porous medium in which the intake and movement of water can be described by conservation of mass (continuity) and Darcy's Law. Water exists in unsaturated soil at the intersection of soil particles within the pore space and is lower in pressure head, ψ (m), than the soil–air phase due to the capillary properties of the air–water interface. Water content θ ($\text{m}^3 \text{ m}^{-3}$) increases with increasing ψ . In terms of normalized water content, or “effective saturation” Θ , the relation of water content to soil–water pressure may be expressed as follows (Smith 1990):

$$\Theta = \frac{\theta - \theta_o}{\theta_s - \theta_o} = \left[1 + \left(\frac{\Psi}{P} \right)^a \right]^{-\frac{1}{a}} \quad (4-1)$$

in which λ , P , and a are parameters, and the subscripts s and o denote saturation and residual water contents, respectively. van Genuchten (1980) introduced a similar relation earlier. The parameters in Equation (4-1), however, have graphical meaning (see Figure 4-5).

4.1.3.2 Wetting and Water Transfer Processes

Darcy's Law is fundamentally empirical but demonstrable, stating that water moves from higher to lower hydraulic head locations in the soil, where the total hydraulic head (m) is $H = \psi - z$, and z (m) is measured downward from the soil surface. Darcy's Law states that the soil–water flux is proportional to the total head gradient $\partial H / \partial z$ and a coefficient called the soil–water *hydraulic conductivity* (K) (m s^{-1}).

$$q = K(\psi, \theta) \nabla H \quad (4-2)$$

in which q is the flux (vector) (m s^{-1}). The units of q relate to a volume (m^3) of water crossing a unit area (m^2) per unit time (s). K can be treated as either a function of ψ or θ through the relations shown in Figure 4-5. The value of K when θ is at its maximum (saturated) and when ψ is near 0 is called the *saturated hydraulic conductivity*, K_s .

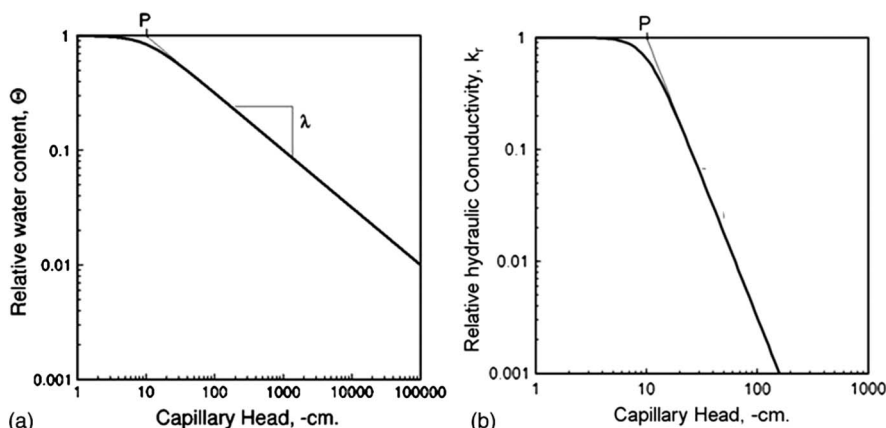


Figure 4-5. Generalized description of the variation of (a) relative soil–water content and (b) relative hydraulic conductivity versus soil capillary (pressure) head.

Rainfall at the soil surface causes water to move into the soil in response to the hydraulic head gradient of soil water. This gradient includes the depth of surface water, if any, as in irrigation. When, as a result of continuous rainfall the soil surface becomes saturated, the surface hydraulic head can increase only to a maximum ponding height allowed by surface detention storage. Consequently, the local gradient may limit intake rate as described in Equation (4-2) and thus create local *rainfall infiltration excess* and *Hortonian overland flow* (Horton 1936). This is surface-controlled infiltration, dependent on the rate of rainfall exceeding infiltrability. Runoff can also occur when a surface soil underlain by a soil of limiting permeability or a bedrock creates soil saturation that can reach the surface. This runoff mechanism is generally called *saturation excess overland flow* (Dunne and Black 1970, Freeze 1974).

4.1.3.3 Infiltrability and Cumulative Infiltration

The rate at which rainfall can enter the soil, determined by the surface value of q [Equation (4.2)], is called the *infiltrability*, f_c (m s^{-1}). At the beginning of any rainstorm in which rainfall rates exceed surface soil-saturated hydraulic conductivity is always an initial part of the storm where infiltrability exceeds rainfall, and all rainfall enters the soil. For storms where rainfall intensity continues to be greater than K_s for sufficient time, the infiltrability will decrease until it controls the soil-water intake. This point is often called the ponding time. As shown in the following and elsewhere (Smith et al. 2002), the description of the onset of ponding (and thus runoff) is made robust and parsimonious by describing infiltrability in terms of cumulative infiltration, I (m), or total volume (m^3) of water per unit surface area (m^2). Given the dependence of water flow processes on spatially variable soil properties, ponding will clearly occur at various times over different parts of a catchment. Some efforts have been made to describe and anticipate the effects of this variability (e.g., Smith and Goodrich 2000).

4.1.4 Infiltration Dynamics

As mentioned previously, water moves from higher to lower H regions in a continuous soil. This can result from different wetness or from changes in elevation. It can also occur when roots use water and create local areas of low pressure head around the roots. Plants can bring water up from the water table by creating an upward gradient of H . Likewise, water redistributes in response to head gradients after the end of a rainfall. A wetted zone near the surface will dry at the surface due to evaporation, but water will also continue to move downward into the soil with accompanying reduction in saturation near the surface. The movement of soil water in the vertical case is described by mass conservation in the form of differential continuity, plus Darcy's Law [Equation (4-2)], referred to generally as Richards' Equation, to which we now turn.

4.1.4.1 Richards' Equation

Here we refer to vertical flow, in which gravity plays a part. Simply combining an expression for mass conservation,

$$\frac{\partial \theta}{\partial t} - \frac{\partial q}{\partial z} = 0, \quad (4-3)$$

with Darcy's Law [Equation (4-2)] yields Richards' Equation:

$$\frac{\partial \theta}{\partial t} = \frac{\partial}{\partial z} \left(K(\psi) \frac{\partial \Psi}{\partial z} - K(\psi) \right) \quad (4-4)$$

In this expression z (m) is measured downward from the soil surface, and t (s) is time.

4.1.4.2 Boundary and Initial Conditions

For rainfall rate, r , on an initially unsaturated soil, the boundary condition will be the influx that is equal to r , so long as the soil can respond by adjusting the surface value of ψ to satisfy the flux boundary condition:

$$r = -q = K(\psi) \left(1 - \frac{\partial \psi}{\partial z} \right) \Big|_{z=0} \quad (4-5)$$

For values of $r > K_s$, a point is reached where the surface head gradient cannot satisfy Equation (4-4) for $\psi < 0$, and the boundary condition changes to a surface head boundary condition:

$$\psi(z=0) = d \quad (4-6)$$

where d is the depth of water on the surface (initially $d = 0$). The time this occurs is called *ponding time*, which marks the inception of runoff and soil-controlled infiltration rates. Head boundary conditions also occur when water appears suddenly on the soil surface in quantities greater than can be imbibed, such as on soil under furrow irrigation or in channels during flood-wave advance.

Lower boundary conditions vary with local situations, but a general one for natural conditions is either *gravity drainage* ($d\psi/dz = 0$) or a *water table* ($\psi = 0$) at some large value of z . For deep soils, the lower boundary condition is not critical. For shallow soils or where a limiting soil interface occurs, the lower boundary is crucial. At large scales in hydrology the soil depth and the water table both exhibit variability that can be important.

4.1.4.3 Numerical Solution

Many methods of approximation to the description of infiltration using Equation (4-4) have been developed and cannot all be presented here (see, e.g., Smith et al. 2002). Figure 4-6 illustrates the general infiltration behavior under significant values of r ($r > K_s$). Ponding occurs more rapidly for larger values of r .

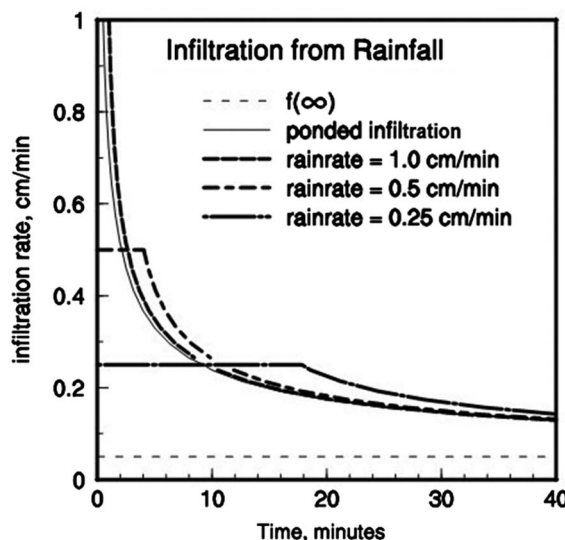


Figure 4-6. Infiltration rate (f) as a function of time for instantaneous ponding and three rainfall rates, showing the effect of steady rainfall rate on ponding time.

The methods for numerical solution of Equation (4-4) are not described here, but accurate solution involves careful choice of numerical increment size to match the scale of spatial and temporal variations, plus careful selection of methods to minimize errors of mass conservation (e.g., Smith et al. 2002, Appendix III) and numerical dispersion.

4.1.4.4 Theoretical and Conceptual Approximations

Philip (1957) derived a simple equation for infiltration under ponded boundary conditions:

$$I = St^{1/2} + At \quad (4-7)$$

in which I is the cumulative infiltration, S is defined as soil *sorptivity* ($\text{m s}^{-1/2}$), A is an empirical constant (m s^{-1}) proportional to the field-saturated hydraulic conductivity, and here t is the time (s) from the start of an infiltration event. Neglecting gravity [i.e., $A = 0$, Equation (4-7)] is a valid description for the early-time behavior shown in Figure 4-6, which exhibits the square root of time behavior proportional to S . This is an important approximation for infiltration analysis when the storm is intense and short. It also is important for design of field experiments to define infiltration properties, because sorptivity may be measured relatively easily (Chong and Green 1979, Smith 1999, Talsma and Parlange 1972).

The simplest analytical solution of Equation (4-3) for infiltration was that of Green and Ampt (1911), referred to previously:

$$f = K_s + \frac{G(\Delta\theta)K_s}{I} \quad (4-8)$$

where f is infiltration rate; K_s is the saturated hydraulic conductivity; and G is the capillary drive, a bulk parameter representing soil capillary strength, defined as the integral under the relative hydraulic conductivity and capillary pressure head relation (Figure 4-5b). The factor $\Delta\theta$ is a variable—the *saturation deficit*—defined as $\theta_s - \theta_i$, where θ_i is the *initial water content* of the surface soil region. This relation can be derived from Richards' Equation (4-4) under the assumption that the rapidly varying $K(\theta)$ is a step function.

Further mathematical advances in the solution of Equation (4-4) (e.g., Parlange and Smith 1976, Talsma and Parlange 1972) have resulted in a more accurate description of the infiltration behavior under rainfall conditions for both short and long times and for general soil properties:

$$I = G \Delta\theta \ln\left(\frac{f}{f - K_s}\right) \quad (4-9)$$

Equation (4-8) or (4-9) may be converted to relations of $f(t)$ or $I(t)$ by substituting $f = dI/dt$. Smith et al. (2002) summarized the various forms of these equations. Time-based forms, $t(f)$ and $t(I)$, result directly, but explicit expressions for $f(t)$ and $I(t)$ given a time of ponding require special approximation techniques.

4.1.5 Soil-Surface Sealing

The hydraulic properties of the soil surface may be altered by the mechanical impact of water drops (McIntyre 1958) and by biochemical processes. Mechanical energy is often sufficient to disturb soil aggregates and separate clay particles from the bulk soil. These finer particles settle last after surface ponding of water and its suspended sediment, resulting in a fine layer of lower-permeability material commonly called a *surface seal* or *crust* (Assouline 2004, Bosch and Onstad 1988, Eisenhauer et al. 1992, Fox and Le Bissonnais 1998). In fact, this material is a permeable surface

skin that impedes infiltration relative to the bulk soil without a seal or crust (Moore 1981). Various investigators have addressed the topic of surface sealing of bare soil, and some models implement a surface impedance layer (Ahuja 1983, Baumhardt et al. 1990, Cresswell et al. 1992, Mein and Larson 1973, Smith et al. 1999).

Live vegetation and plant residue that cover the soil surface can protect it from sealing (Duley 1939). Consequently, when plant residue covers only part of the area, the fraction of ground area covered can affect infiltration significantly (Ruan et al. 2001). To further complicate matters, microtopography interacts with spatially variable bare-soil surface crusting, which affects the net infiltration (Fox et al. 1998), and tillage may (temporarily) remove a surface seal (Logsdon et al. 1993). Crusting of bare or partially covered surface soils cannot be ignored in some cases (Ruan et al. 2001), but we will not consider these effects henceforth.

4.1.6 Methods of Measuring Soil Water Content

The Soil Science Society of America has published a comprehensive manual describing a variety of laboratory and field methods for measuring soil–water content and other soil hydraulic variables (Klute 1986). Details of these methods cannot be given here. In the laboratory, soil sample water contents are measured most often by weighing before and after drying. Various dielectric methods are available based on the dielectric properties of water in field soils. One popular method is time domain reflectometry (TDR), using insertion probes to obtain an estimate of soil–water content based on the return (reflection) of a radio frequency signal applied to the probes (Schwartz et al. 2009a, b). Other dielectric sensors measure the resonance frequency of a circuit, which depends upon the electrical capacitance and its sensitivity to water content (its dielectric constant or permittivity). Examples of some commercial capacitance-based dielectric sensors include Sentek downhole probes (Evett et al. 2006, Fares and Alva 2000, Paltineanu and Starr 1997, Schwank and Green 2007, Schwank et al. 2006, Starr and Rowland 2007), Stevens Hydra Probes (Logsdon et al. 2010, Seyfried and Grant 2007), and the Decagon ECH₂O family of soil–water sensors (Saito et al. 2009).

The backscattering of neutrons by soil water is used in the *neutron probe* method, where aluminum or plastic tubes are inserted into the soil, and readings are taken at known distances into the tube. This method gets the integrated value of an influence volume near the tube (Evett et al. 2006). Gamma ray attenuation can also be used to measure the water content between two parallel tubes (Rousseva et al. 1988). Methods are available to measure soil–water pressure head, but they are generally difficult or impractical to apply in the field. Soil–water tensiometers are usable in the field, but their range of applicability is limited to higher pressures (higher water contents).

Spatial measurements of soil–water content are rare due to the cost of measurement systems and difficulty collecting samples or measurements rapidly at multiple locations. However, TDR systems have been mounted on vehicles for rapid measurements over a field or small watershed (e.g., Green and Erskine 2004, Western and Grayson 1998, Western et al. 1999, Western et al. 2004), as shown in Plate 4-1. A few studies have used dedicated in-ground dielectric sensors installed at multiple locations to measure temporal dynamics in a spatial network (e.g., De Lannoy et al. 2006, Green and Erskine 2011, Lin 2006).

4.1.7 Surface Flux Measurements

Infiltration studies are most satisfying if the conditions of interest can be replicated and the results carefully measured. This is true for both irrigation applications and for rainfall situations. Empirical infiltration models require calibration in all cases and duplicating the infinite variety of rainfall rate patterns is impossible in any case. Thus the infiltrated depth approximation (Smith et al. 2002) described in Section 4.3.2 is useful for developing parameters for the infiltration model based on surface boundary conditions that may practically be created in the field. Thus, information from a ponded surface condition or from a controlled uniform flux application may obtain the same

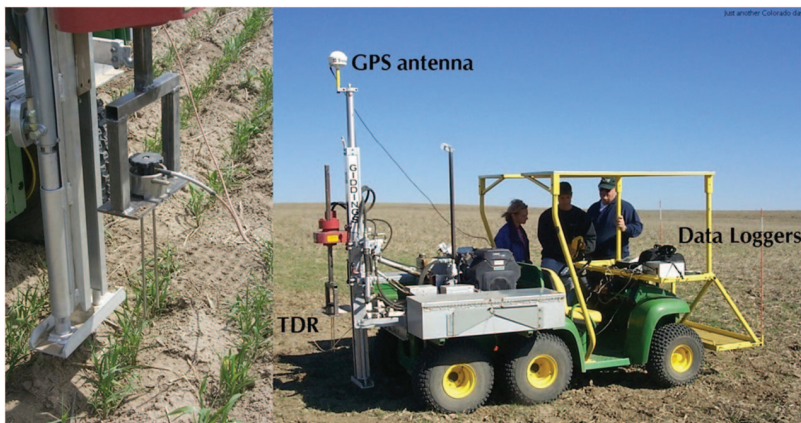


Plate 4-1. A TDR system (TraseBE) is mounted on an all-terrain vehicle (John Deere Gator), where the TDR rods (30 cm here) are inserted into the soil with a custom-made bracket attached to a hydraulic soil coring machine (Giddings). A global positioning system (Trimble) is used to navigate to measurement locations, and TDR-estimated soil water content is recorded along with the spatial coordinates on a handheld data collector for "on-the-go" (actually stop-and-go) measurements. This system used for collecting spatial maps of soil water (e.g., [Green and Erskine 2004](#)) was based on a similar system designed by [Western and Grayson \(1998\)](#).

physically based parameters. However, performing an infiltration simulation until the late-time, asymptotic (theoretical) value K_s is reached is not usually practical. Other means are more time and cost effective. Given the power of modern computer hardware and simulation software, inverse modeling or parameter identification methods are practical to determine accurate values of in situ soil infiltration parameters, provided sufficiently simple and appropriate boundary conditions are maintained.

4.1.7.1 Tension Infiltrometer Methods

In the last few decades, a method for making measurements of surface-soil behavior has been developed ([White et al. 1992](#)), which allows measurement of soil influx from a small disc source under surface water pressure heads from 0 to -20 cm (approximately). The disc must be in continuous soil contact over its surface area, for which a fine sand contact material may be required. Various mathematical approximations for this three-dimensional but symmetrical geometry are available ([Smith et al. 2002](#)), but the inverse modeling approach is the most accurate (e.g., Hydrus2D, [Simunek et al. 1999](#)).

4.1.7.2 Ponded and Rainfall Infiltration and Sorptivity

Ponded upper boundary infiltration may be simulated by simply pouring water into a containing ring pushed into the surface soil. However, several practical difficulties arise. First, like the tension infiltrometer, the flow is not one-dimensional vertical, but is in fact three dimensional, unless the ring is pushed very deep. This is difficult if not impossible to achieve without creating boundary gaps that allow shortcut flow paths. Water infiltration rates are difficult to measure based on the change in water elevation. This can be much improved using a Marriott siphon, as for the disc permeameter. The multidimensionality can be mitigated somewhat by an outer buffer ring (i.e., double-ring infiltrometer) so that measurement is confined to a center portion, which should generally be one dimensional at smaller time scales. [Lai and Ren \(2007\)](#) found that lateral flow could be affected by the size of the infiltrometer and suggested that the outer ring diameter should be larger than 80 cm.

Rainfall can be simulated with various devices, but uniformity over a given test area is difficult to accomplish. As for the infiltrometers, a buffer area is required if one-dimensional flow is to be presumed. Then, measurements are generally confined to observing the onset of runoff and then estimating the difference between rainfall rate and runoff rate. The runoff rate measured in this test integrates $r - f$ over the time necessary for the flow to reach a measuring device off site, so the value of $f(t)$ cannot be determined before runoff occurs and is sometimes difficult to determine after runoff begins.

Sorptivity (S) is one of the most prominent hydrologic parameters in the early infiltration process, and estimation of S is one of the more satisfactory field measurements that can be made. Sorptivity can be obtained either from in situ soil–water redistribution measurements (Chong et al. 1981, 1982a, b) or constant-rate simulated rainfall (Chong 1983). However, the simplest field method of measuring S is based on Equation (4-7), using a single-ring ponded infiltrometer (Talsma 1969). By inserting the infiltrometer carefully into the soil, S can be estimated rather quickly and simply by measuring the time required for a given depth of water to infiltrate. Like other ring-containment methods, care must be taken to minimize soil disturbance at the ring boundary during insertion. The measurement and interpretation are straightforward, however, and many measurements can be made in an area to determine spatial variability (Smith 1999).

Sorptivity is very sensitive to surface conditions, water content, and soil management. Various applications of sorptivity have been discussed (Chong and Green 1979, 1983). It has been applied for characterizing soil compaction (Gardner and Chong 1989, Walker and Chong 1986) and calculating incipient ponding time, t_p , in surface runoff (Kutilek 1980). Because t_p is related to runoff potential of the soil, S has also been related to the USDA runoff curve number (Chong and Teng 1986).

4.2 SPATIAL AND TEMPORAL VARIABILITY OF SOIL WATER AND INFILTRATION

Variability of atmospheric conditions (weather), soils, terrain, land cover, and management produce variability of infiltration rates and soil–water contents in space and time. From the previous section, we also know that the flux and storage of water in soils are nonlinearly related. In this section, we address the combined spatial and temporal variability of soil water and infiltration in terms of physical and statistical distributions. Finally, we touch upon the topic of temporal variability of soil hydraulic properties.

4.2.1 Vertical Soil Heterogeneity Effects on Infiltration

For simplicity and clarity, the infiltration equations given in Section 4.1 were based on uniform soil profiles and their mathematical approximants. In reality, sediment deposition (parent materials) and soil development over time result in layered soil profiles. Even when textural stratification is not pronounced, hydraulic properties change with depth. Clay-sized particles tend to move from the surface soils (A-horizon) and accumulate in the layers beneath (B-horizon). As a result, K_s is generally greatest near the surface, with the exception of surface soil sealing (see Section 4.1.5). Beven (1984) approximates the vertical profile variation using exponential decay functions for K_s and θ_s . The resulting equations were solved explicitly for $I(I)$, meaning that $I(t)$ must be solved iteratively. Details of the derivation and solution are left for the interested reader to explore.

The resulting equations fit field experimental data in layered soils well (Childs and Bybordi 1969). Subsequently, the exponential decrease in K_s has been used in other models, particularly TopModel (for saturation flow) (Ambroise et al. 1996). However, this approach may be problematic for large heterogeneous catchments.

4.2.2 Observations of Space–Time Variability

Although the concept of infiltration varying spatially over a landscape or watershed is well known, detailed measurements remain rare. To quote Keith Watson (Watson 1965), “It is apparent therefore that two, rather opposite, sources of information on the infiltration problem are available. On one hand theoretical and laboratory analyses on restricted models have provided valuable insights into the physical process; on the other hand, there is a large body of *qualitative* information available on such factors (as entrapped air, sub-surface cracking, cover variability and soil variation and stratification with depth) on infiltration into field soils. Between these extremes it is possible to make some progress towards a greater quantitative understanding of infiltration in field soils by field experiments.”

Indeed, some progress has been made in the last five decades following Watson’s premise and examples, but these are limited. A few notable examples are given here to illustrate spatial variability over a field or small catchment.

An early study that is often cited regarding spatial variability of infiltration and associated soil hydraulic properties was conducted on a 150 ha agricultural field in the central valley of California (Nielsen et al. 1973). Despite being cited more than 1,300 times to date, many may not be familiar with details of this study (Nielsen et al. 1973 published in *Hilgardia*, because the paper had not been readily available in digital libraries until recently). Twenty infiltration plots were installed over different soil units comprising primarily clay loam and silty clay. Percent clay in 480 samples from soil profiles was approximately normally distributed (mean = 45.2%, standard deviation = 10.5%). Ponded infiltration was maintained until soil–water pressure stabilized to 1.83 m depth. The resulting statistical distribution of K_s (or field-saturated K) over 20 plots at six depths was skewed, and the data were approximated by a log-normal distribution. The steady infiltration rate after 20 days ranged from 0.5 to 45.7 cm d⁻¹ (0.021 to 1.90 cm h⁻¹). Soil–water content measurements were normally distributed (mean and standard deviation of 0.433 and 0.046 m³m⁻³, respectively).

Tricker (1981) conducted a “reconnaissance survey” of spatial patterns by soil type, slope, and land use in a 3,600 ha catchment in the United Kingdom. The survey was used to stratify 23 sampling areas, and “representative” areas were sampled by clustering 10 random single-ring infiltration measurements within each 20 m² area. At $t = 1$ h, rates varied within a wide range of 0 to 250 cm h⁻¹. The total variance included considerable intra-site and inter-site variance, despite their systematic landscape stratification. In that landscape, land cover (quantified by litter depth) explained 60% of the variance, and soil physical variables (e.g., texture and A-horizon thickness) were not significant explanatory variables.

In two other studies, the spatial variability of field infiltration was quantified by fitting Philip’s infiltration Equation (4-7) to measurements. Sharma et al. (1980) measured infiltration at 26 locations in a 9.6 ha grassland catchment in Oklahoma, named “R-5” that is now well documented (Heppner and Loague 2008, Loague and Gander 1990, Loague and Kyriakidis 1997, Mirus et al. 2011). Sharma et al. (1980) noted that $I(t)$ became linear (steady flow) for $t > 45$ min in most cases and that fitted values of A were approximately equal to 0.33 $f(t = 1\text{ h})$. The distributions of both S and A were approximately log-normal, and S and A were linearly correlated ($R = 0.81$). Berndtsson (1987) fits Philip’s equation and another model to double-ring infiltrometer data collected at 52 sample locations in a 19 km² catchment in northern Tunisia (Berndtsson and Larson 1987). Table 4-1 shows the resulting statistics for the parameter values, S and A , which were moderately cross-correlated ($R = 0.56$). Frequency distributions for both parameters were approximately exponential with many low values and tails extending through the maxima in Table 4-1.

More recently, Green et al. (2009) collected single-ring steady infiltration measurements in randomly clustered patterns of 15 points within 10 landscape positions, which were stratified based on topographic attributes within a wheat field in Colorado, USA (Figure 4-7). Figure 4-8

Table 4-1. Statistical Properties of Philips' Infiltration Parameters [Equation (4-7)]. Based on Spatially Distributed Samples.

Study	Parameter	n	Mean	Median	Std. Dev.	Max.	Min.	CV (%)
Sharma +	S ($\text{mm h}^{-0.5}$)	26	50	43	25	106	9.5	49
	A (mm h^{-1})	26	15	14	9	44	1.5	60
Berndtsson	S ($\text{mm h}^{-0.5}$)	52	60	40	60	250	0*	99
	A (mm h^{-1})	52	60	35	60	300	0*	106

Source: Berndtsson (1987) and Sharma et al. (1980).

*0 values reported by Berndtsson were due to negative fitted values of A.

Note: S is sorptivity, and A is a constant related to field-saturated hydraulic conductivity. CV is the coefficient of variation. Mean is the arithmetic mean, and n is the number of samples.

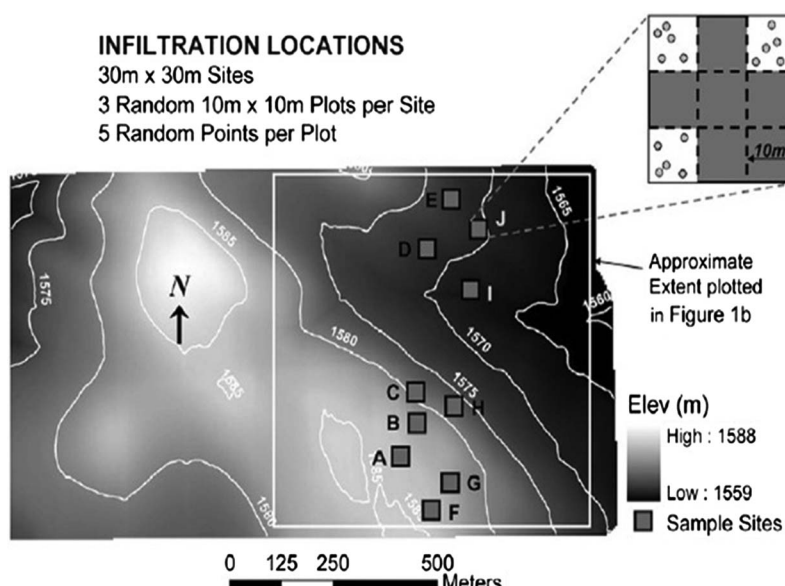


Figure 4-7. Site map for 150 single-ring steady infiltration measurements. Inset shows a schematic for 15 randomly located points nested within three 10 m × 10 m plots within each "site" or landscape position in a wheat field in Colorado.

Source: Green et al. (2009).

shows the measured steady infiltration rates, illustrating the variations within and among sites. At each infiltration site, measured late-time infiltration rates were very linear with t (see R^2 values in Table 4-2), indicating quasi-steady flow. The coefficient of variation (CV) ranged from 0.26 to 0.63 for intra-site samples, and CV = 0.51 among all 150 samples, with a range of late-time infiltration spanning three orders of magnitude ($0.2, 166 \text{ cm h}^{-1}$). This range is common even in this type of agricultural field. In Section 4.3, we discuss these spatial data in terms of autocorrelation structure and spatial persistence.

4.2.3 Temporal Variability of Soil Hydraulic Properties

Spatial variability of K near the soil surface measured under ponded and tension infiltration was found to vary temporally in a cultivated field (Logsdon and Jaynes 1996). This type of space-time

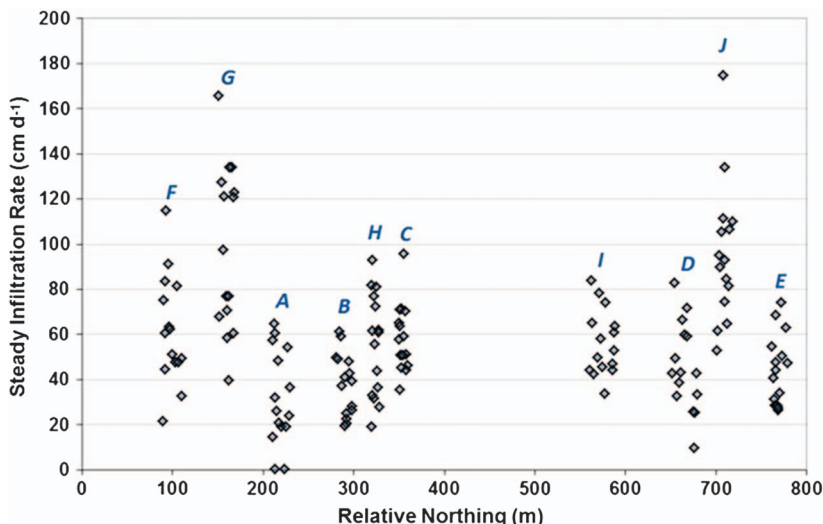


Figure 4-8. Quasi-steady infiltration rates versus the relative nothing (distance due North) to illustrate variability within and among sites (A–J) shown in Figure 4-7.

Table 4-2. Statistics of Steady Infiltration Rates Measured.

Site	Steady Infiltration Rate (cm d ⁻¹)					R ^{2†}	
	Mean	SD [‡]	CV	Min.	Max.	Mean	SD [‡]
A	30.70	19.25	0.63	0.20	61.47	0.984	0.025
B	37.52	12.04	0.32	21.49	58.12	0.986	0.018
C	60.98	17.60	0.29	38.61	116.01	0.991	0.015
D	47.62	19.51	0.41	11.83	93.02	0.992	0.019
E	37.97	13.61	0.36	22.58	63.26	0.997	0.002
F	68.43	26.28	0.38	24.61	120.40	0.993	0.007
G	100.99	34.64	0.34	45.71	165.72	0.995	0.003
H	57.25	23.42	0.41	19.79	89.66	0.991	0.007
I	51.81	13.23	0.26	32.28	73.99	0.997	0.002
J	83.89	24.30	0.29	49.58	141.63	0.994	0.004
All [§]	57.72	29.43	0.51	0.20	165.72	0.992	0.006

Source: Green et al. (2009).

[†]Coefficient of determination or variance explained by the linear regression fit.

[‡]Note small sample sizes of $n = 15$ per site.

[§]Results from all 150 infiltrometers.

variability appears to be the norm rather than the exception, based on previous reviews of the literature (Green et al. 2003, Strudley et al. 2008). However, direct effects of tillage on soil hydraulic properties may be rather transient, as surface soils can reconsolidate after just two wet-dry cycles (Mapa et al. 1986). Therefore, site- or soil-specific temporal variability of soil properties is extremely difficult to quantify, but some general trends may be expected within the following time scales:

- Days to weeks: large changes after disturbance, such as tillage, followed by relaxation toward the undisturbed condition due to reconsolidation;

- Weeks to annual cycles: seasonal changes with climate and weather patterns (e.g., freezing in winter and desiccation in summer), systematic soil–water-nutrient management, crop rotation, and traffic patterns; and
- Years to decades: long-term management and climate feedbacks on soil chemistry, biota, and physical soil development.

Each of these time scales requires careful consideration when designing monitoring and management programs. Short-term variations can be dominant in many cases, but long-term effects may require long-term monitoring, which is challenging to maintain.

4.3 SCALING AND ESTIMATION OF SOIL HYDRAULIC PROPERTIES AND INFILTRATION

Soil hydraulic properties and the associated infiltration and soil–water redistribution processes they control may be “scaled” to represent flow rates and storages at different spatial scales. The term “scaling” is used broadly in soil physics, leading to possible confusion. Here, we try to differentiate universal or nondimensional properties, which result from parameter normalization, from spatial scaling. The latter scaling emerges from characterizing bulk process behaviors over a range of spatial scales containing variability of the underlying soil properties and processes (Section 4.2). Another topic that relates to estimation of soil hydraulic properties is the use of surrogate data in *pedotransfer* functions.

4.3.1 Pedotransfer Functions

Although infiltration and soil hydraulic properties can be estimated directly from field and laboratory measurements (c.f., Section 4.1.7), flux measurements are expensive and often challenging to collect. Consequently, relationships called *pedotransfer functions* (PTFs) have been developed between soil hydraulic properties and more readily available information, such as soil texture. Hierarchical PTFs (e.g., Rosetta) and Root Zone Water Quality Model, or RZWQM ([Ahuja et al. 2000](#)) use cascading levels of information to estimate hydraulic properties with increasing accuracy. In this approach, soil bulk density or porosity may be added to basic soil texture as input to a PTF. Likewise, soil–water retention at discrete pressures, such as 1/3 bar (33 kPa) may improve the PTF. For example, a universal PTF across soil classes has been used to estimate K_s from the “effective porosity” (θ_s – to determine accurate values of in situ soil infiltration parameters θ_{33}), where θ_s is saturated water content and θ_{33} is the water content at 33 kPa, as shown in Figure 4-9 ([Ahuja et al. 2010](#)). Although this log–log linear or power-law relationship explains most of the variance among soil classes ($R^2 = 0.96$), variability within a given soil class or among some adjacent classes may not fit this simple PTF, and the relationship does not hold for aggregated clay Oxisols and Ultisols. Moreover, [Fang et al. \(2010\)](#) found that values of K_s calibrated to match measured soil moisture in a loamy soil did not follow this functional relationship well, and this PTF substantially overestimated K_s for $(\theta_s - \theta_{33}) > 0.3$.

4.3.2 Dimensionless Relationships in Infiltration Processes

Expressing infiltrability f_c as a function of I produces a robust relation that collapses the various relations of Figure 4-5 into a single parsimonious relation independent of rainfall. The relationship $f_c(I)$, which describes infiltrability both before and after ponding, has been termed the infiltrated depth approximation ([Smith et al. 2002](#)). Outside of a small perturbation in the region near ponding, based on careful solutions to Equation (4-4), it is a very close approximation (Figure 4-10). Others have referred to this approach as the time compression approximation ([Assouline 2013](#)).

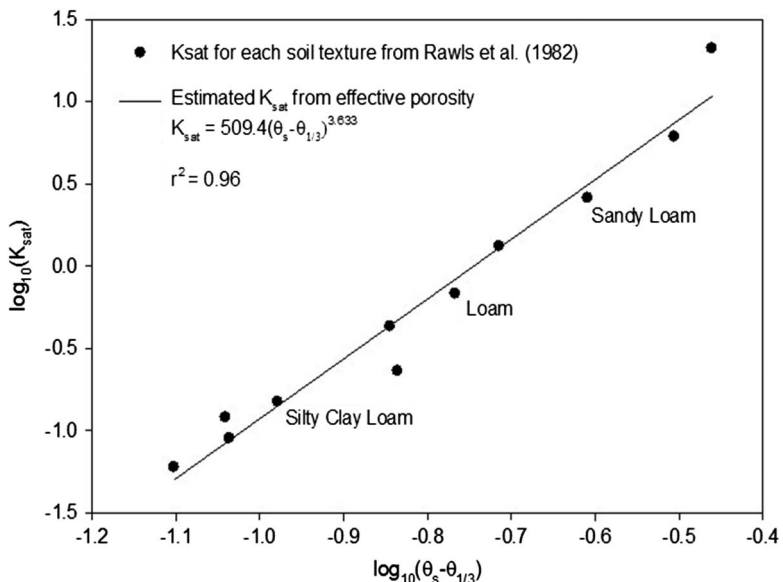


Figure 4-9. Log-log relationship between saturated hydraulic conductivity K_{sat} and effective porosity ($\theta_s - \theta_{33}$), where θ_s is saturated water content and $\theta_{1/3}$ (θ_{33}) is the water content at 1/3 bar (33 kPa).

Source: Ahuja et al. (2010).

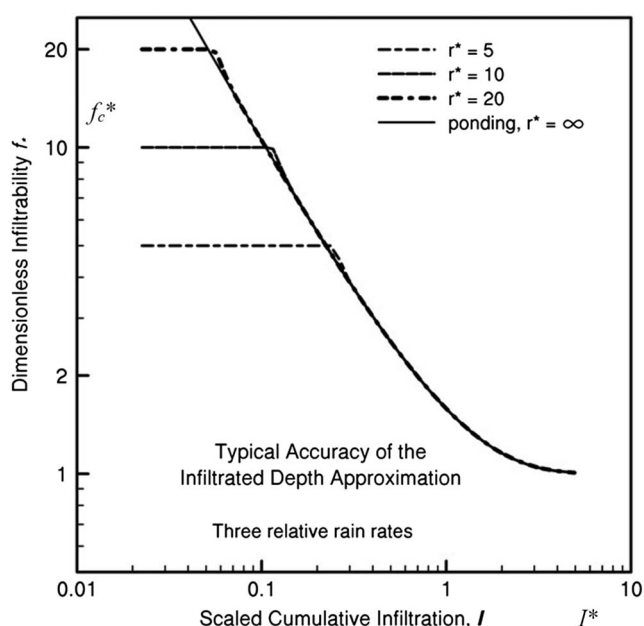


Figure 4-10. Dimensionless infiltrability (f_c^*) converges for different dimensionless rain rates (r^*) when plotted against dimensionless or scaled cumulative infiltration (I^*). Normalization [Equation (4-10)] makes all dimensional curves in Figure 4-6 approximately equal after ponding occurs.

The infiltration and soil–water processes have several scaling variables, which can reduce the parametric diversity and simplify expressions and measurement. Dimensionless variables are especially useful in characterizing variability across the landscape. One important soil scale parameter is saturated hydraulic conductivity, K_s , with which one may describe relative hydraulic conductivity, as shown in Figure 4-5b. The practical lower limit of soil–water content, θ_r , and the upper limit, θ_s , are useful for expressing normalized water content, Θ (Equation (4-1)). For infiltration, each of the theoretically derived expressions contains the basic capillary head parameter G , defined previously in Equation (4.8). The parameter G combined with the saturation deficit $\Delta\theta$ forms a basic parameter, C (m) used for normalization. Sorptivity, S , could also be treated as a normalization parameter, were gravity to be ignored (e.g., horizontal flow). In summary, the dimensionless values for infiltrability, infiltrated depth, and time are

$$f_c^* = \frac{f_c}{K_s}; \quad I^* = \frac{I}{C}; \quad t^* = \frac{t K_s}{C}, \quad (4-10)$$

where $C = G \Delta\theta$.

Dimensionless values used here express the relations illustrated in Figure 4-10.

4.3.3 Geostatistical Scaling Methods and Examples

Spatial autocorrelation functions and variograms are common statistical measures of how a measured variable (e.g., steady infiltration or soil moisture) is related to itself at different separation or lag distances. The geostatistical literature is too extensive to cover here, other than by sharing some examples. [Green and Erskine \(2004\)](#) use variogram analysis to explore the spatial statistical structure and “persistence” of soil moisture. Spatial persistence can be quantified by the Hurst exponent (η) which is linearly related to the fractal dimension. Here, we prefer η because it is independent of the dimensionality of the space explored (number of physical dimensions). [Burrough \(1981\)](#) showed how these coefficients can be estimated from a variogram as follows:

$$2\gamma(h) = E[\{\nu(x + h) - \nu(x)\}^2] = \sigma^2 h^{2\eta} \quad (4-11)$$

where (h) is the semi-variance of any spatially variable field $\nu(x)$ as a function of lag distance h between pairs of points and $E[\cdot]$ is the expected value. On the right-hand side, σ^2 is the variance of ν ($h = 1$) for fractional Brownian noise. By fitting the simple power-law equation, we obtain an empirical value of the Hurst exponent, η . If the variogram model is linear, $\eta = 0.5$. Values of $\eta > 0.5$ indicate “persistence” in the observed spatial field, which is analogous to temporal persistence (long memory) observed in time series of some geophysical phenomena ([Hurst 1951](#)).

In the spatial context, persistence means that the increase in variance with lag distance h is greater than linear, rather than leveling off as h increases. The power-law variogram is nonstationary (no sill) for all $\eta > 0$, but practically, a constant variance or sill is approached as $\eta \rightarrow 0$.

[Green and Erskine \(2004\)](#) used a mobile TDR (see Plate 4-1) to sample the top 30 cm at around 500 locations in radial patterns within a wheat field in Colorado (Figure 4-11a). Using the variogram analysis described previously, they demonstrated simple fractal-like behavior in the spatial auto-correlation of TDR measurements (e.g., Figure 4-11b). For the example data shown, the power-law model fit the experimental variogram well, indicating fractal behavior and spatial structure in the data over hundreds of meters. The fitted value of $\eta = 0.48$ indicates slight anti-persistence with no apparent sill out to at least 400 m.

Returning to the spatial infiltration data ([Green et al. 2009](#)), those sparser data were analyzed for monofractal and multifractal behavior over a range of different spatial extents (i.e., maximum lag distances). Although 150 locations comprise a relatively large sample for infiltration, it was considered “sparse data” for fractal analysis, so landscape slope and other terrain attributes were

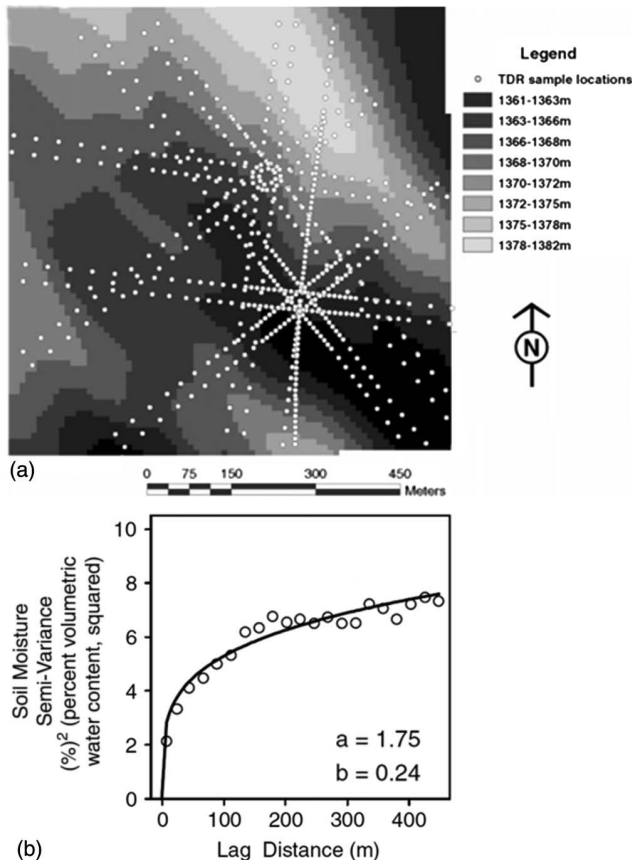


Figure 4-11. (a) Map of TDR measurement locations (dots) overlaid on the surface elevation (grayscale) of a wheat field in Colorado, and (b) the resulting experimental semi-variogram of soil water content (percent volumetric) in the top 300 mm (circles represent data averages of binned data pairs) fit with a power-law model (line) for one sampling date, June 30, 1999.

Source: Green and Erskine (2004, Figure 9).

used as surrogates to see if the sparse data displayed artifacts that were not present in the “dense” topographic data (5 m grid). Figure 4-12 shows estimates of η versus the maximum lag distance for (a) sparse infiltration and slope data compared with (b) dense slope data. Based on the colocated sparse data, the values of η for slope and infiltration were anti-correlated, and both displayed distinct effects of the domain or extent of the data window analyzed. Based on the dense slope data over each of the two strips (West and East) sampled within the wheat field (planted and fallow), these effects were not entirely due to the sample locations or data sparseness. Green et al. (2009) concluded that maximum spatial persistence occurred in measured infiltration at hillslope scales (approximately 200 m) with values of η decreasing rapidly at smaller and larger scales. The physical interpretation is that hillslope-scale processes affecting soil erosion, deposition, and development may account for the observed deviations from pure fractal behavior.

4.3.4 Effective Parameters of Heterogeneous Soil

Scale-invariant parameters are desired to simulate infiltration and soil–water redistribution processes over all spatial scales. While great progress has been made toward estimating scale-invariant properties and processes, the spatial variability of real-world soils complicates things (Ahuja and Garrison 1996).

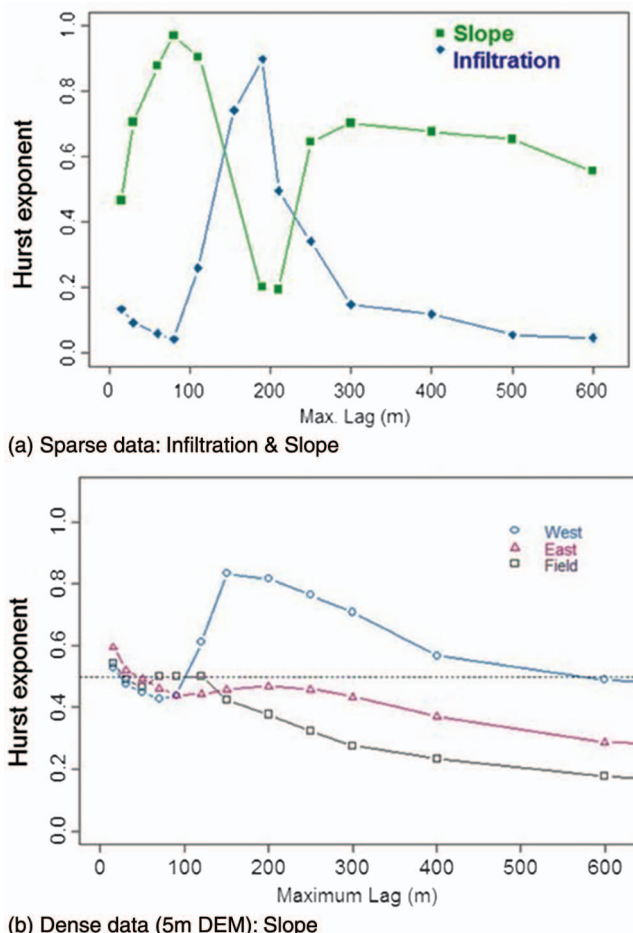


Figure 4-12. Fractal results of Green et al. (2009) for spatial measurements of single-ring steady infiltration rates at 150 locations (see Figures 4-7 and 4-8), where the Hurst exponent (η) of a monofractal model is plotted against the maximum "lag" distance between pairs of measured values (i.e., excluding all pairs with greater lag distances). For comparison, η values were computed for terrain slope values using (a) "sparse data" only at the locations of infiltration measurements and (b) "dense data" for all 5 m grid cells from the digital elevation model (DEM) over the whole field ("Field") and regionalized samples from the "West" and "East" strips encompassing sites A-E and F-J, respectively (see Figure 4-7).

Numerical experiments by Smith and Diekkruger (1996) illustrate the expected effects of the larger-scale effective ensemble retention and conductivity relations of soils made up of a log-normal distribution of the parameters used to describe soil hydraulic relations given previously in Equation (4-1). In simplest terms, random distributions of P increase the effective or ensemble value of a and tend to decrease the ensemble value of λ .

Smith and Goodrich (2000) illustrated theoretical expectations for the upscaled or areal infiltration rate patterns of areas composed of randomly varying infiltration characteristics. The parameter K_s is important in Equations (4-8) and (4-9), and K_s commonly exhibits approximately log-normal distributions in space (e.g., Nielsen et al. 1973, Figure 16). These distributions were simulated using a physically based runoff model and a Latin-hypercube simulation method, as well as using spatial sampling with and without spatial autocorrelation. Briefly, Latin-hypercube numerical simulation

samples parameter values in equal intervals from assumed cumulative distributions to derive the simulated output distribution of interest. Figure 4-13 illustrates the general nature of their results under constant rates of rainfall. A log-normal distribution of K_s results in a reduction in the late-time asymptotic value of f_c . Depending on the variance of K_s , some fraction of the area will have K_s greater than rainfall rate. In addition, the increased variability of ponding time will result in a gradual development of runoff, as the figure shows, rather than a single time at which the entire area will begin contributing to runoff. This can be observed and is intuitively expected.

Figure 4-14 also shows how the infiltration rate is related to I for different values of dimensionless rainfall rate (r^*) on an area where the coefficient of variation of K_s is 0.6 (similar to observed variability from Green et al. 2009). Spatial variability blurs the onset of ponding and smooths the transition to decreased rates of infiltration over time compared with the homogeneous case ($CV_{K_s} = 0$). Modeling such variability in K_s has demonstrated improvements in watershed modeling (Smith and Goodrich 2000).

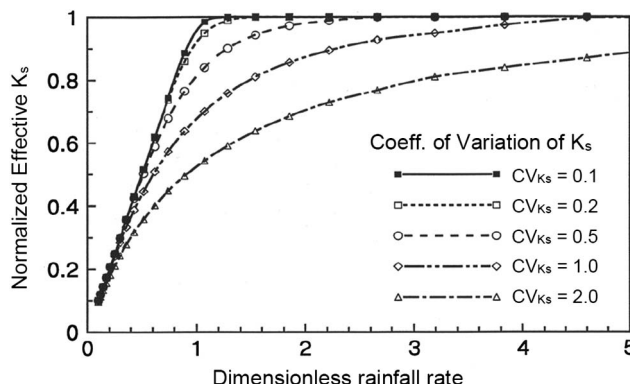


Figure 4-13. Effective K_s (normalized) over a heterogeneous area versus dimensionless rainfall rate (r/K_s) plotted for different values of the coefficient of variation of K_s (CV_{K_s}).

Source: Smith and Goodrich (2000, Figure 2).

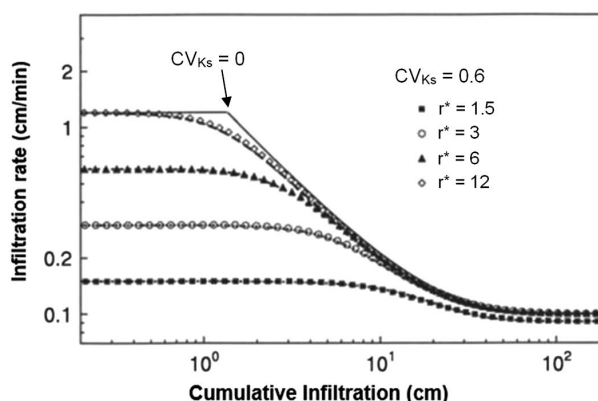


Figure 4-14. Infiltration rate (flux) versus cumulative infiltration for different values of dimensionless rainfall rate ($r^ = r/K_s$) for an example value of the coefficient of variation of K_s ($CV_{K_s} = 0.6$). The solid line ($CV_{K_s} = 0$) represents the relationship for a homogeneous area with distinct incipient ponding.*

Source: Smith and Goodrich (2000, Figure 3b).

4.4 UNCERTAINTY IN MEASUREMENT AND SPACE-TIME ESTIMATION

Estimation of infiltration (flux) and soil–water content (storage) at the scales of interest in space and time is essential. Issues range from basic science across disciplines to management of resources and environmental policy. From these topics, sources of uncertainty include

- Measurement error at the *support scale* (size of each sample or zone of influence),
- Parameter estimation error for a given infiltration model,
- Structural errors in the governing equation or model due to unresolved process interactions and due to processes active in the field but absent in the model,
- Higher dimensionality of the actual process compared with the model (this is closely related to the previous point),
- Uncertainty of driving forces, particularly weather and management variables, and
- Subscale space–time variability and inference of statistical distributions with limited data.

Some of these sources of uncertainty are combined within or dispersed among the following subsections.

4.4.1 Local Measurement Uncertainty

Rainfall intensity and duration are critical driving variables for estimating incipient ponding and subsequent decreasing infiltration rates. Chapter 2 covers details of precipitation estimation. Here, we highlight some basic potential errors associated with

- Rain gauge catch (underestimation bias), which is worsened by high winds commonly associated with convective storms;
- Temporal aggregation of recorded data typical of some meteorological networks (e.g., in the Colorado Agricultural Meteorological nETwork (CoAgMet, <http://ccc.atmos.colostate.edu/~coagmet/>) data are aggregated to hourly amounts);
- Sparse spatial measurements, where the meteorological station may be a considerable distance from the area of interest and the spatial variability of precipitation is not well known ([Sivapalan and Bloschl 1998](#));
- Temporal gaps (missing data) or poor-quality precipitation data; and
- Variable or changing states of precipitation, most notably from liquid to solid state, but also thermodynamic differences within phases.

The temperature of infiltrating water affects the dynamic viscosity of water, which affects infiltration rate ([Musgrave 1955](#)). Likewise, the chemical composition of irrigation water may affect soil–water infiltration through flocculation and dispersion of clay minerals, for example. Even though some of the thermodynamic and chemical effects may be predictable in theory, large potential uncertainty exists in estimating water quality characteristics, if they are measured at all.

Initial soil–water content is an important factor for infiltration [e.g., Equation (4.8)], and $\theta(t)$ is typically inferred from dielectric sensors. TDR or capacitance probes are sensitive to soil temperature and electrical conductivity among other measurement factors. We can account for some of these factors ([Green and Erskine 2011](#), [Schwartz et al. 2009a](#)), but only with partial confidence even in the best measurement programs. In practice, water content estimated from automated electrical sensors, including some of our national networks (<http://www.wcc.nrcs.usda.gov/scan/>), may be highly uncertain.

Soil hydraulic properties may be our greatest source of uncertainty for predicting infiltration at the local scale, mainly due to a lack of data. Detailed hydraulic property data underlying the soil

characteristic curves in Figure 4-4 are rare, especially for $K(\theta)$ or $K(\psi)$. As noted earlier, field-based measurement of sorptivity [S, Equation (4-7)] is more feasible for many points within an area of interest.

4.4.2 Inverse Methods and Parameter Estimation

Even with the simplest models, the model parameters are estimated by fitting measured data to the model responses. Some parameter estimation methods could be as simple as minimizing the sum of squared errors or root mean squared error between measurements and the equation for $I(t)$. In other cases, more sophisticated parameter estimation methods may be used, which provide optimal parameters and some measure of parameter uncertainty (Abbaspour et al. 2004, Doherty and Johnston 2003, Fang et al. 2010, Minasny and McBratney 2002). Such information can be used in forward modeling of infiltration and soil–water processes, ultimately providing estimates of their uncertainty.

4.4.3 Model Process Uncertainty and Preferential Flow

The word *model* itself indicates that the real-world process is simulated by an idealized conceptual and mathematical approximation. Total uncertainty of model results can be quantified by comparisons with relevant data, but the breakdown of error sources between measured data, model structure, and parameter values is generally not known. For example, one may lump all of the differences between simulated and observed data into parameter estimation error, simply because the model is assumed to represent the processes and their interactions.

Preferential flow (PF) paths into and through soils are often neglected, even though PF may dominate water and chemical fluxes under certain conditions, including ponding. Thus, if PF occurs at any time during an infiltration event, model structural error (process omission) may become the dominant source of uncertainty. To be clear, PF includes a broad class of processes by which flow paths bypass some or most of the soil matrix. Common forms of PF are

1. Soil macropore flow (e.g., root and earthworm holes with effective diameters greater than the largest matrix pore; Beven and Germann 1982) and natural pipes on hillslopes (e.g., 10 cm diameter conduits in the near subsurface; Wilson 2011);
2. Flow fingering due to hydraulic instabilities (Jury et al. 2011), which are usually induced by wetting of a fine-textured layer over a dry coarser layer. Fingering has been identified and induced in laboratories under quantifiable and repeatable conditions (Selker et al. 1992), but detecting and quantifying fingering in the field is difficult; flow instability may also be linked to water repellency (Bughić and Wallach 2016); and
3. Focusing of variably saturated flow by structured heterogeneity in the porous media, including lateral subsurface flow in sloping unsaturated soil (Zaslavsky and Sinai 1981).

The latter mechanism (number 3) requires neither macropores nor an impeding layer in terms of K_s , because fine-scale layers with different water retention and hydraulic properties cause anisotropy in upscaled unsaturated K . That is, effective values of K parallel to layering exceed values perpendicular to layering, and the unsaturated anisotropy exceeds the anisotropy at saturation.

4.4.4 Statistical Inference

In the end, flux and storage at different scales should be estimated along with confidence intervals. In some cases, one may want to know the *subgrid variability* or variance within a defined spatial zone. Spatial *moments* (mean, variance, etc.) may be used to characterize complex spatial patterns at different times (synoptic views) or average moisture states. In this way, the outcome of complex processes and their interactions in space and time may be summarized by lumped statistical distributions. Likewise, the various sources of uncertainty outlined here may propagate to the distributions of flux and storage needed directly for risk assessment. Other process models may

“consume” these statistical distributions to produce *derived distributions* of land–atmosphere and ecological variables of interest.

4.5 LINKS BETWEEN INFILTRATION AND RUNOFF AT DIFFERENT SCALES

As noted in Section 4.0 and Figure 4-1, infiltration and soil–water processes interact with each other and with other hydrological processes over a range of space–time scales. At the time scale of a surface runoff event, the interactions with runoff, run-on, and subsurface lateral flow can be very important.

4.5.1 Runoff, Run-On, and Process Interactions

Scaling of infiltration is complicated by the types of spatial variability illustrated previously (including K_s varying by orders of magnitude) and interactions among subareas along flow paths (Wood 1995). For infiltration excess overland flow, runoff from upslope may infiltrate downslope on soil surfaces with higher infiltration capacities, which can make the average infiltrability of a full hillslope or large area greater than the arithmetic mean. It can also be reduced if flow paths occur on soils with surface seals, so that the total variance, spatial correlation, and connectivity all need to be estimated. For the saturation excess mechanism of overland flow generation, surface infiltrability is rarely the limiting factor, and other complexities, such as subsurface pipes caused by animal burrows, tree roots, and subsurface erosion, make the net infiltration and runoff more difficult to predict.

This chapter has primarily addressed diffuse infiltration of rainfall or other distributed sources of water. Moving up in scale to a large watershed, concentration of runoff into streams and lakes forms areas of focused infiltration. Surface water infiltration is most important in arid to semi-arid regions where groundwater levels may be low and hydraulic gradients are downward, at least most of the time. For example, ephemeral streams emerging from mountainous areas flow into seasonally dry channels that transmit water readily through coarse-textured streambeds (Constantz et al. 2013, Constantz et al. 2002). Such streambed infiltration is highly variable in space and time, but significant for regional water resources. Upscaling of these fluxes remains a challenge.

In a lumped watershed model, or one in which all land areas are connected to a stream or other water body, subarea interactions between infiltration and runoff are not considered. Only runoff at the outlet or stream is estimated. However, spatially variable infiltration and routing of runoff along hillslope areas includes quantification of overland flow moving on and off of each simulated area. Thus, run-on and runoff may occur simultaneously. This simple definition encompasses a more restricted definition by Nahar et al. (2004): “The run-on process can be defined as the infiltration of surface water that, as it moves downslope, encounters areas where moisture deficit has not yet been satisfied. In such cases, water available for infiltration includes rainfall and water supply from upslope areas.”

4.5.2 Recent Advances in Simulating Space–Time Infiltration and Soil Water

Several research studies have explored the potential effects of spatial patterns of landscape properties and space–time precipitation on the resulting patterns of infiltration and soil water. Here we highlight a study that combined geostatistical scaling of rainfall and soil variables with spatial infiltration process modeling to derive statistical (multifractal) patterns of infiltration.

Meng et al. (2006) used a universal multifractal (UM) model (Schertzer and Lovejoy 1987) to generate high-resolution rainfall events and soil spatial patterns as input to the process-based Hortonian Infiltration and Run-Off/On (HIRO₂) model. HIRO₂ (fully described in Meng et al. 2008) is a grid-based spatial hydrology model for rainfall infiltration and runoff events that computes $f(\mathbf{x}, t)$, $I(\mathbf{x}, t)$, and $\theta \Delta z(\mathbf{x}, t)$, where Δz is the active soil profile depth and $\mathbf{x} = [x, y]$ horizontal location.

Meng et al. (2006) generated multiple rainfall and K_s fields with the desired characteristics by systematically varying the three scaling parameters. Figure 4-15 shows three fields of K_s , for example,

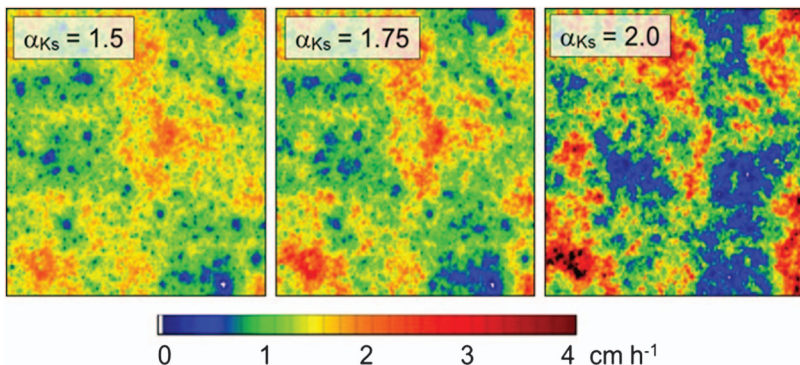


Figure 4-15. Generated fields of saturated soil hydraulic conductivity (K_s) illustrating the effects of the Levy index (α_{K_s}) in the universal multifractal model.

Source: Meng et al. (2006).

by varying the Levy index for K_s ($\alpha_{K_s} = 1.5, 1.75$, and 2.0). Schertzer and Lovejoy (1987) described the nature of singularity as “most of the space becomes inactive (darker blue in Figure 4-15), while the increasingly sparse active regions (dark red) become infinitely active.” To the eye, patches of low K_s (blue) and high K_s (red) intensify as $\alpha_{K_s} \rightarrow 2$, which indicates an increasing degree of multifractal behavior, rather than changes in sparseness and heterogeneity (Lavallée et al. 1993).

Figure 4-16 shows the temporal progression of pairs of spatial fields of rainfall and infiltration rate for a few snapshots during a rainfall event. Here, space–time rainfall patterns over the field area of interest resulted from generating a larger fractal pattern of rainfall and moving it at a specified mean advective velocity of the storm, then using only the spatial area overlaying the area of interest at each time. At early times of 2 and 10 min after rainfall began, the spatial fields of infiltration mimic those of rainfall rate, because rainfall controls i . At 50 min, features of both the rainfall and K_s fields are apparent as the control on infiltration began to change from rainfall to soils. At 90 min, the infiltration pattern is clearly soil dominated, as seen by the static spatial pattern of K_s . Watershed topography also affects the pattern via infiltration of run-on water.

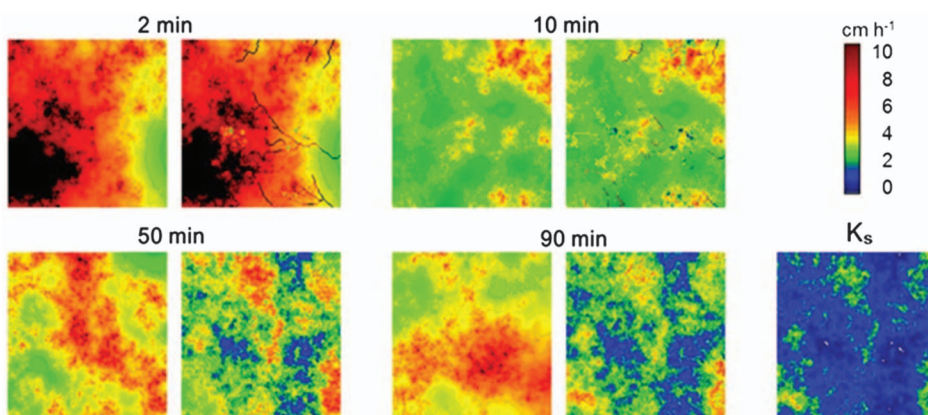


Figure 4-16. Synoptic views of paired rainfall (left field) and infiltration rate (right field) at times of 2, 10, 50, and 90 min after the beginning of a rainfall event, where rainfall is simulated as a universal multifractal model in space with advection in time, and infiltration fields are simulated with the process-based HIRO₂ model. Soil saturated hydraulic conductivity (K_s) is a single realization of a universal multifractal model (see Figure 4-15).

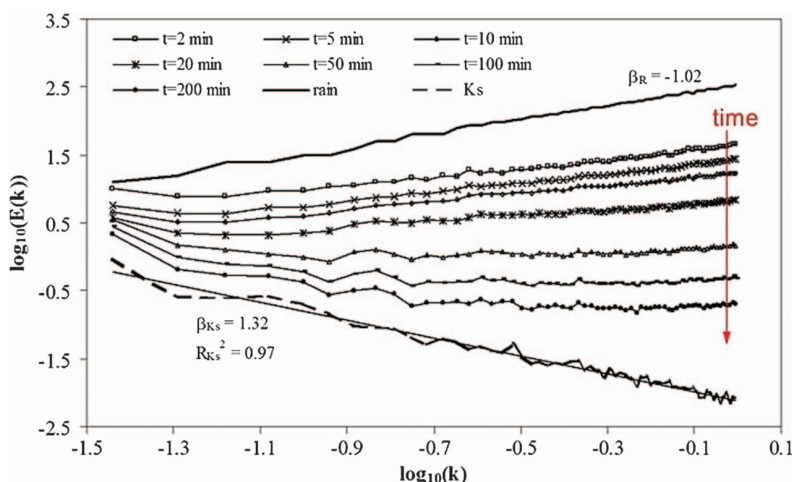


Figure 4-17. Power spectra of rainfall (thick, solid line), saturated soil hydraulic conductivity (K_s ; dashed line; thin solid linear regression fit), and simulated infiltration rate (lines with symbols), showing the temporal progression from nonscaling (in this example), rainfall-controlled infiltration to scaling, soil-controlled infiltration (after Meng et al. 2006). $E(k)$ is the power spectrum of each variable, k is the wavenumber, β is the spectral exponent, and t is the time in min after rainfall began for each spatial field of infiltration.

Figure 4-17 plots the power spectra of these spatial fields, including more times, and shows the graphical progression from rainfall-controlled spatial patterns (nonscaling in this case) at early times to soil-controlled patterns (scaling) at late times in the infiltration/runoff event. A negative slope of the power spectrum indicates scaling behavior. Thus, the UM model was useful for generating input fields and analyzing the space-time structure of the HIRO₂ model output $i(\mathbf{x}, t)$, illustrated here, as well as $I(\mathbf{x}, t)$ and $\theta \Delta z(\mathbf{x}, t)$. Obviously, these examples are theoretical and based on a research-level computer model that would not be used for most practical problems. The insights gained about process interactions in space and time provide a consistent understanding of how point-scale infiltration processes may relate to infiltration and runoff processes over larger, heterogeneous areas.

In addition to scaling properties of infiltration with dynamic effects of run-on, the spatial variability affects areal averages of infiltration rate and cumulative infiltration with time. In other words, characteristics of the internal variability of rainfall, soils, and topography can affect the average responses over a spatial field or watershed.

4.6 SUGGESTIONS FOR ADVANCING INFILTRATION SCIENCE AND PRACTICE

In this chapter, we discussed a rich history of quantifying water infiltration into soils and associated flow and storage of water in soils (soil moisture). Analytical equations have been derived to describe infiltration and soil-water processes, and some of these have been made dimensionless to provide more universal equations (e.g., Figure 4-10 shows a log-log relationship between scaled infiltrability f_c^* and scaled cumulative infiltration I^*). However, spatial and temporal variability remain difficult to quantify, as soil moisture and infiltration display fractal and multifractal behaviors. While geostatistical characterization of space-time patterns and statistical inference may have disappointed some after a surge of interest and promise in the 1980s, spatial statistics and scaling methods remain essential for quantifying variability, often at nested scales, across landscapes. The problems that we

need to address are usually greater than our individual measurement scales, so spatial estimation and averaging or upscaling are essential.

Infiltration and soil–water redistribution in the subsurface are estimated and predicted using equations with scale-dependent effective parameters, which may be derived explicitly from governing equations and some knowledge or assumptions about the subscale variability. More commonly, constant model parameter values are used and calibrated to fit observed fluxes (e.g., runoff) and state variables (e.g., soil moisture). Whether simple analytical equations or complex numerical models of the processes and space–time patterns are used, these models must be linked to field observations to gain verity and instill confidence in the model predictions. This brings us back to measurements and inference (based on indirect measurements) of water flux and storage in space and time.

4.6.1 Advances in Measurement across Scales

Most of the past and current methods measure soil moisture and infiltration over very limited spatial scales, where each sample is typically at the submeter scale and rarely above the length scale of an adult human. In fact, the largest scale of controlled infiltration experiments has been with sprinkler-simulated rainfall on plots up to about 100 m^2 but usually smaller. These costly, isolated research experiments may be a thing of the past given reductions and redirections of limited research funding.

In contrast, creative thinking and technological advances are likely to yield relatively low-cost techniques to infer soil moisture in the near surface. One example is COSMOS (see timeline in Figure 4-2), where the scattering of cosmic radiation is measured at a ground-based station to infer near-surface soil moisture over areal scales of hundreds of m^2 (Desilets et al. 2010, Zreda et al. 2008, Zreda et al. 2012) and penetration depths of approximately 0.3 m (Franz et al. 2012), depending on other sources of hydrogen in the measurement zone (air, soils, and vegetation). Another example is optical cable buried in the near surface at multiple depths. Each cable can estimate soil temperature accurately at the meter scale (Tyler et al. 2010), and soil moisture may be inferred between cables (Steededunne et al. 2010). Real-time measurements with high temporal resolution make inferring water fluxes possible, and ongoing research may lead to accuracies useful for estimating infiltration rates over large areas within instrumented fields. Of course, these example methods are still being explored, and their applications will be limited to research studies for some time.

Ground, airborne, and satellite remote sensing of soil moisture may provide much broader spatial measurements (Famiglietti et al. 2008) limited to the near surface (i.e., a few centimeters) at regular temporal intervals. The temporal frequency is limited by the flight time and intervals between overpasses, but this too is improving. The authors hold little hope for accurately estimating infiltration processes from remote sensing, but we expect to see rapid advances in various methods of areal (also aerial) surveillance related to inferring near-surface soil moisture. We also recognize that gravity methods (e.g., GRACE satellite mission, Rodell et al. 2007) are promising for vertically integrated water storage and changes over time, but the current spatial resolution (approximately 400 to 600 km, Chen et al. 2005) of GRACE satellite data is a major limitation.

On a more optimistic note, automated data collection across a range of scales has resulted in exponential growth of data acquisition and storage. Consequently, “data mining” is a discipline in itself, and we are likely to gain specific and broad knowledge from the wealth of data now being collected. The powers of observation remain paramount in scientific discovery, and we stress the value of carefully designed measurements and monitoring. Some level of consistency, even uniformity, is needed across sites to allow for rigorous multilocation synthesis of data.

4.6.2 Systems Approaches for Simulating Process Interactions

Infiltration and soil–water flow and storage were addressed largely in isolation here to avoid confusion. As Figure 4-1 illustrates, however, process interactions in the context of whole systems in space and time cannot be neglected. Certain dominant behaviors may emerge only from studying infiltration in a relatively broad sphere of geographical, biological, and chemical influences, and its

spatial context. The illustration of multiscaling infiltration (Meng et al. 2006) was purely physiographical, but the combination of terrain (watershed topography), soil variability, and rainfall patterns in space and time required a detailed hydrological model to act as a spatial transfer function from which patterns of infiltration could be explored.

Other models incorporate water interactions with plant growth and projected climate change (e.g., WAVES, Crosbie et al. 2010, Green et al. 2007) and various agricultural system components, for example, RZWQM (Ma et al. 1998), including agricultural management (Fang et al. 2012), soil heterogeneity (Ahuja et al. 2010), and macroporosity (Malone et al. 2001). Continued improvements and applications of agro-ecosystem models over a range of landscapes and watershed scales will enhance our understanding of potential interactions between soil hydrological processes and biological processes. Ideally, the computed process interactions will improve predictions of infiltration and soil–water distributions over a range of scales.

4.6.3 Computer Decision Aids and Risk Assessments

How does one make informed water resources decisions given all of the complex space–time interactions noted here? Like it or not, policy and management decisions require “simple answers to simple questions” (anonymous, but often stated). “Simple questions” may be well posed, usually after considerable thought and synthesis of knowledge, but “simple answers” are rare or potentially wrong. The challenge is to condense very complex system behaviors into response functions and statistical distributions that summarize available information.

A probability density function (pdf) and its integral, a cumulative density function (cdf) of the derived distribution of interest (e.g., $\theta(x, t)$ inferred from measurements or model results), contains valuable information for threshold analysis and risk assessment. Regional assessments of vulnerability to groundwater contamination have used this general approach (e.g., Loague et al. 1996). When societal values can be quantified in terms that relate to physical variables, decision making becomes relatively straightforward.

Computer systems may incorporate very complex statistical and process models that are not fully exposed to users, while providing elegant and clean (visually simple) user interfaces as decision aids. This topic (also known as “decisions support systems”) could be a chapter or book of its own, but suffice it to say that modern computing technologies (local and web based) enable powerful decision aids driven by rigorous scientific methods and rich data.

LIST OF TERMS

Acronyms

COSMOS	Cosmic-ray Soil Moisture Observing System (ground-based sensors)
GRACE	Gravity Recovery and Climate Experiment (satellite mission)
HIRO ₂	Hortonian Infiltration and Run-Off/On model
PTF	pedotransfer function
RZWQM	Root Zone Water Quality Model (also RZWQM2)
WAVES	Water, Atmosphere, Vegetation, Energy, and Solutes model
UM	universal multifractal model

Symbols

A	empirical constant ($m s^{-1}$) of the Philips infiltration Equation (4-7)
C	basic scaling parameter (m)
CV	coefficient of variation = standard deviation \div mean value of a variable (-)
CV_{K_s}	coefficient of variation of saturated hydraulic conductivity (-)

d	depth of water (m)
E	expected value operator
f	infiltration rate (m s^{-1})
f_c	infiltrability or infiltration capacity (m s^{-1})
f_c^*	scaled infiltrability (-)
G	capillary drive parameter, defined as the integral under the relative hydraulic conductivity and capillary pressure head relation (m)
h	lag distance (m) between pairs of points
H	total hydraulic head (m)
I	cumulative infiltration (m); $i = dI/dt$
I^*	scaled cumulative infiltration (-)
K	hydraulic conductivity (m s^{-1})
K_s	saturated hydraulic conductivity (m s^{-1})
LAI	leaf area index ($\text{m}^2 \text{ m}^{-2}$)
q	Darcy flux vector (m s^{-1})
r	rainfall rate (m s^{-1})
r^*	dimensionless rain rate = r/K_s (-)
R^2	coefficient of determination for linear regression
S	soil sorptivity ($\text{m s}^{-1/2}$)
t	time (s)
t^*	scaled time (-)
t_p	time to incipient ponding (s)
$v(\mathbf{x})$	spatially variable field function
\mathbf{x}	horizontal location, $\mathbf{x} = (x, y)$
z	vertical distance (m) measured downward from the soil surface
Δz	active soil profile depth (m)
θ	soil-water content ($\text{m}^3 \text{ m}^{-3}$)
$\Delta\theta$	saturation deficit ($\text{m}^3 \text{ m}^{-3}$) equal to $= \theta_s - \theta_i$
θ_i	initial soil-water content ($\text{m}^3 \text{ m}^{-3}$) for the saturation deficit
θ_s	saturated soil-water content ($\text{m}^3 \text{ m}^{-3}$)
$\theta_s - \theta_{33}$	effective porosity ($\text{m}^3 \text{ m}^{-3}$)
θ_{33}	water content ($\text{m}^3 \text{ m}^{-3}$) at 33 kPa (1/3 bar)
λ, P, a	parameters of the water retention model, Equation (4-1)
Θ	effective saturation (-), Equation (4-1)
α	Levy index (α_{K_s} is the Levy index of K_s) of the universal multifractal (-)
$\gamma(h)$	semi-variance (units of the spatial variable squared)
η	Hurst exponent (-)
σ^2	variance of v ($h = 1$) for fractional Brownian noise
ψ	pressure head (m)

ACKNOWLEDGMENTS AND CAVEAT

Professor She-Kong Chong (emeritus faculty, Southern Illinois University) provided valuable input to the discussion of sorptivity, for which we are grateful. Dr. Benjamin Mirus (US Geological Survey) provided very detailed and helpful review comments on an earlier draft of this chapter.

The topic of this chapter could comprise a full book, which made it difficult to pick and choose the contents. Many noteworthy studies could not be included here. Instead, we offer a sampling of work biased by our own experience and knowledge of the literature.

References

- Abbaspour, K. C., C. A. Johnson, and M. T. van Genuchten. 2004. "Estimating uncertain flow and transport parameters using a sequential uncertainty fitting procedure." *Vadose Zone J.* **3** (4): 1340–1352.
- Ahuja, L. R. 1983. "Modeling infiltration into crusted soils by the Green-Ampt approach." *Soil Sci. Soc. Am. J.* **47** (3): 412–418.
- Ahuja, L. R., and A. Garrison. 1996. "Real world infiltration." In *Proc., USDA-ARS Workshop*, 262. Pingree Park, CO: Colorado Water Resources Research Institute.
- Ahuja, L. R., L. Ma, and T. R. Green. 2010. "Effective soil properties of heterogeneous areas for modeling infiltration and redistribution." *Soil Sci. Soc. Am. J.* **74** (5): 1469–1482.
- Ahuja, L. R., K. W. Rojas, J. D. Hanson, M. D. Shaffer, and L. Ma. 2000. *Root zone water quality model: Modeling management effects on water quality and crop production*, 372. Highland Ranch, CO: Water Resources Publications.
- Ambroise, B., K. Beven, and J. Freer. 1996. "Toward a generalization of the TOPMODEL concepts: Topographic indices of hydrological similarity." *Water Resour. Res.* **32** (7): 2135–2145.
- Assouline, S. 2004. "Rainfall-induced soil surface sealing: A critical review of observations, conceptual models, and solutions." *Vadose Zone J.* **3** (2): 570–591.
- Assouline, S. 2013. "Infiltration into soils: Conceptual approaches and solutions." *Water Resour. Res.* **49** (4): 1755–1772.
- Baumhardt, R. L., M. J. M. Romkens, F. D. Whisler, and J. Y. Parlange. 1990. "Modeling infiltration into a sealing soil." *Water Resour. Res.* **26** (10): 2497–2505.
- Berndtsson, R. 1987. "Application of infiltration equations to a catchment with large spatial variability in infiltration." *Hydrol. Sci. J.* **32** (3): 399–413.
- Berndtsson, R., and M. Larson. 1987. "Spatial variability of infiltration in a semi-arid environment." *J. Hydrol.* **90** (1–2): 117–133.
- Beven, K. 1984. "Infiltration into a class of vertically non-uniform soils." *Hydrol. Sci. J.* **29** (4): 425–434.
- Beven, K., and P. Germann. 1982. "Macropores and water flow in soils." *Water Resour. Res.* **18** (5): 1311–1325.
- Blöschl, G., and M. Sivapalan. 1995. "Scale issues in hydrological modeling—A review." *Hydrol. Processes* **9** (3–4): 251–290.
- Bosch, D. D., and C. A. Onstad. 1988. "Surface seal hydraulic conductivity as affected by rainfall." *Trans. ASAE* **31** (4): 1120–1127.
- Bughici, T., and R. Wallach. 2016. "Formation of soil-water repellency in olive orchards and its influence on infiltration pattern." *Geoderma* **262**: 1–11.
- Burrough, P. A. 1981. "Fractal dimensions of landscape and other environmental data." *Nature* **294** (5838): 240–242.
- Chen, J. L., C. R. Wilson, J. S. Famiglietti, and M. Rodell. 2005. "Spatial sensitivity of the gravity recovery and climate experiment (GRACE) time-variable gravity observations." *J. Geophys. Res. B: Solid Earth* **110** (B8): 1–8.
- Childs, E. C., and M. Bybordi. 1969. "The vertical movement of water in stratified porous material 1. Infiltration." *Water Resour. Res.* **5** (2): 446–459.
- Chong, S. K. 1983. "Calculation of sorptivity from constant-rate rainfall infiltration measurement." *Soil Sci. Soc. Am. J.* **47** (4): 627–630.
- Chong, S. K., and R. E. Green. 1979. "Application of field-measured sorptivity for simplified infiltration prediction." In *Proc., Hydrologic Transport Modeling Symp*, 88–96. Chicago: American Society of Agricultural Engineers.
- Chong, S. K., and R. E. Green. 1983. "Sorptivity measurement and its application." In *Proc., National Conf. on Advances in Infiltration*, 82–91. Chicago: American Society of Agricultural Engineers.
- Chong, S. K., R. E. Green, and L. R. Ahuja. 1981. "Simple in situ determination of hydraulic conductivity by power function descriptions of drainage." *Water Resour. Res.* **17** (4): 1109–1114.
- Chong, S. K., R. E. Green, and L. R. Ahuja. 1982a. "Determination of sorptivity based on in-situ soil water redistribution measurements." *Soil Sci. Soc. Am. J.* **46** (2): 228–230.
- Chong, S. K., R. E. Green, and L. R. Ahuja. 1982b. "Infiltration prediction based on estimation of Green-Ampt wetting front pressure head from measurements of soil water redistribution." *Soil. Sci. Soc. Am. J.* **46** (2): 235–239.
- Chong, S. K., and T.-M. Teng. 1986. "Relationship between the runoff curve number and hydrologic soil properties." *J. Hydrol.* **84** (1–2): 1–7.

- Constantz, J., C. A. Eddy-Miller, J. D. Wheeler, and H. I. Essaid. 2013. "Streambed exchanges along tributary streams in humid watersheds." *Water Resour. Res.* **49** (4): 2197–2204.
- Constantz, J., A. E. Stewart, R. Niswonger, and L. Sarma. 2002. "Analysis of temperature profiles for investigating stream losses beneath ephemeral channels." *Water Resour. Res.* **38** (12): 52-1–52-13.
- Cresswell, H. P., D. E. Smiles, and J. Williams. 1992. "Soil structure, soil hydraulic properties and the soil-water balance." *Aust. J. Soil Res.* **30** (3): 265–283.
- Crosbie, R., J. McCallum, G. Walker, and F. Chiew. 2010. "Modelling climate-change impacts on groundwater recharge in the Murray-Darling Basin, Australia." *Hydrol. J.* **18** (7): 1639–1656.
- De Lannoy, G. J. M., N. E. C. Verhoest, P. R. Houser, T. J. Gish, and M. Van Meirvenne. 2006. "Spatial and temporal characteristics of soil moisture in an intensively monitored agricultural field (OPE3)." *J. Hydrol.* **331** (3–4): 719–730.
- Desilets, D., M. Zreda, and T. P. A. Ferré. 2010. "Nature's neutron probe: Land surface hydrology at an elusive scale with cosmic rays." *Water Resour. Res.* **46** (11): W11505.
- Doherty, J., and J. M. Johnston. 2003. "Methodologies for calibration and predictive analysis of a watershed model." *J. Am. Water Resour. Res.* **39** (2): 251–265.
- Duley, F. L. 1939. "Surface factors affecting the rate of intake of water by soils." *Soil Sci. Soc. Am. Proc.* **4**: 60–64.
- Dunne, T., and R. D. Black. 1970. "Partial area contributions to storm runoff in a small New England watershed." *Water Resour. Res.* **6** (5): 1296–1311.
- Eisenhauer, D. E., D. F. Heermann, and A. Klute. 1992. "Surface sealing effects on infiltration with surface irrigation." *Trans. ASAE* **35** (6): 1799–1807.
- Evett, S. R., J. A. Tolk, and T. A. Howell. 2006. "Soil profile water content determination: Sensor accuracy, axial response, calibration, temperature dependence, and precision." *Vadose Zone J.* **5** (3): 894–907.
- Famiglietti, J. S., D. Ryu, A. A. Berg, M. Rodell, and T. J. Jackson. 2008. "Field observations of soil moisture variability across scales." *Water Resour. Res.* **44** (1): W01423.
- Fang, Q. X., T. R. Green, M. Liwang, R. H. Erskine, R. W. Malone, and L. R. Ahuja. 2010. "Optimizing soil hydraulic parameters in RZWQM2 under fallow conditions." *Soil Sci. Soc. Am. J.* **74** (6): 1897–1993.
- Fang, Q. X., R. W. Malone, L. Ma, D. B. Jaynes, K. R. Thorp, T. R. Green, and L. R. Ahuja. 2012. "Modeling the effects of controlled drainage, N rate and weather on nitrate loss to subsurface drainage." *Agric. Water Manage.* **103**: 150–161.
- Fares, A., and A. K. Alva. 2000. "Evaluation of capacitance probes for optimal irrigation of citrus through soil moisture monitoring in an entisol profile." *Irrig. Sci.* **19** (2): 57–64.
- Fox, D. M., and Y. Le Bissonnais. 1998. "Process-based analysis of aggregate stability effects on sealing, infiltration, and interrill erosion." *Soil Sci. Soc. Am. J.* **62** (3): 717–724.
- Fox, D. M., Y. Le Bissonnais, and P. Quetin. 1998. "The implications of spatial variability in surface seal hydraulic resistance for infiltration in a mound and depression microtopography." *Catena* **32** (2): 101–114.
- Franz, T. E., M. Zreda, T. P. A. Ferre, R. Rosolem, C. Zweck, S. Stillman, X. Zeng, and W. J. Shuttleworth. 2012. "Measurement depth of the cosmic ray soil moisture probe affected by hydrogen from various sources." *Water Resour. Res.* **48** (8): W08515.
- Freeze, R. A. 1974. "Streamflow generation." *Rev. Geophys.* **12** (4): 627–647.
- Gardner, B. D., and S. K. Chong. 1989. "Hydrologic response of compacted forest soils." *J. Hydrol.* **112** (3–4): 327–334.
- Green, T. R., L. R. Ahuja, and J. G. Benjamin. 2003. "Advances and challenges in predicting agricultural management effects on soil hydraulic properties." *Geoderma* **116** (1–2): 3–27.
- Green, T. R., B. C. Bates, S. P. Charles, and P. M. Fleming. 2007. "Physically based simulation of potential effects of carbon dioxide altered climates on groundwater recharge." *Vadose Zone J.* **6** (3): 597–609.
- Green, T. R., G. H. Dunn, R. H. Erskine, J. D. Salas, and L. R. Ahuja. 2009. "Fractal analyses of steady infiltration and terrain on an undulating agricultural field." *Vadose Zone J.* **8** (2): 310–320.
- Green, T. R., and R. H. Erskine. 2004. "Measurement, scaling, and topographic analyses of spatial crop yield and soil water content." *Hydrol. Processes* **18** (8): 1447–1465.
- Green, T. R., and R. H. Erskine. 2011. "Measurement and inference of profile soil-water dynamics at different hillslope positions in a semiarid agricultural watershed." *Water Resour. Res.* **47** (12): W00H15.
- Green, W. A., and W. A. Ampt. 1911. "Studies on soil physics: 1. The flow of air and water through soils." *J. Agric. Sci.* **4** (1): 1–24.

- Heppner, C. S., and K. Loague. 2008. "Characterizing long-term hydrologic-response and sediment-transport for the R-5 Catchment." *J. Environ. Qual.* **37** (6): 2181–2191.
- Herwitz, S. R. 1985. "Interception storage capacities of tropical rainforest canopy trees." *J. Hydrol.* **77** (1–4): 237–252.
- Horton, R. A. 1936. "Hydrologic interrelations of water and soils." *Proc. Soil Sci. Soc. Am.* **1**: 401–429.
- Horton, R. A. 1939. "Analysis of runoff-plot experiments with varying infiltration capacity." *Trans. AGU* **20**: 693–711.
- Hurst, H. E. 1951. "Long-term storage capacity of reservoirs." *Trans. ASAE* **116**: 770–808.
- Jenny, H. 1946. "Arrangement of soil series and types according to functions of soil-forming factors." *Soil Sci.* **61** (5): 375–392.
- Jury, W. A., et al. 2011. "Kirkham's legacy and contemporary challenges in soil physics research." *Soil Sci. Soc. Am. J.* **75** (5): 1589–1601.
- Klute, A. 1986. *Methods of soil analysis. Part 1: Physical and mineralogical methods*, 1188. Madison, WI: American Society of Agronomy.
- Kozak, J. A., L. R. Ahuja, T. R. Green, and L. W. Ma. 2007. "Modelling crop canopy and residue rainfall interception effects on soil hydrological components for semi-arid agriculture." *Hydrol. Processes* **21** (2): 229–241.
- Kutilek, M. 1980. "Constant-rainfall infiltration." *J. Hydrol.* **45** (3–4): 289–303.
- Lai, J., and L. Ren. 2007. "Assessing the size dependency of measured hydraulic conductivity using double-ring infiltrometers and numerical simulation." *Soil Sci. Soc. Am. J.* **71** (6): 1667–1675.
- Lavallée, D., S. Lovejoy, D. Schertzer, and P. Ladoy. 1993. "Nonlinear variability of landscape topography: Multifractal analysis and simulation." In *Fractal in geography*, edited by L. De Cola and N. Lam, 158–192. Englewood Cliffs, NJ: Prentice-Hall.
- Leuning, R., A. G. Condon, F. X. Dunin, S. Zegelin, and O. T. Denmead. 1994. "Rainfall interception and evaporation from soil below a wheat canopy." *Agric. For. Meteorol.* **67** (3–4): 221–238.
- Lin, H. 2006. "Temporal stability of soil moisture spatial pattern and subsurface preferential flow pathways in the shale hills catchment." *Vadose Zone J.* **5** (1): 317–340.
- Loague, K., R. L. Bernknopf, R. E. Green, and T. W. Giambelluca. 1996. "Uncertainty of groundwater vulnerability assessments for agricultural regions in Hawaii: Review." *J. Environ. Qual.* **25** (3): 475–490.
- Loague, K., and G. A. Gander. 1990. "R-5 revisited: 1. Spatial variability of infiltration on a small rangeland catchment." *Water Resour. Res.* **26** (5): 957–971.
- Loague, K., and P. C. Kyriakidis. 1997. "Spatial and temporal variability in the R-5 infiltration data set: Déjà vu and rainfall-runoff simulations." *Water Resour. Res.* **33** (12): 2883–2895.
- Logsdon, S. D., T. R. Green, M. Seyfried, S. R. Evett, and J. Bonta. 2010. "Hydra Probe and twelve-wire probe comparisons in fluids and soil cores." *Soil Sci. Soc. Am. J.* **74** (1): 5–12.
- Logsdon, S. D., and D. B. Jaynes. 1996. "Spatial variability of hydraulic conductivity in a cultivated field at different times." *Soil Sci. Soc. Am. J.* **60** (3): 703–709.
- Logsdon, S. D., J. Jordahl, and D. L. Karlen. 1993. "Tillage and crop effects on ponded and tension infiltration rates." *Soil Tillage Res.* **28** (2): 179–189.
- Ma, L. W., H. D. Scott, M. J. Shaffer, and L. R. Ahuja. 1998. "RZWQM simulations of water and nitrate movement in a manured tall fescue field." *Soil Sci.* **163** (4): 259–270.
- Malone, R. W., M. J. Shipitalo, L. Ma, L. R. Ahuja, and K. W. Rojas. 2001. "Macropore component assessment of the root zone water quality model (RZWQM) using no-till soil blocks." *Trans. ASAE* **44** (4): 843–852.
- Mapa, R. B., R. E. Green, and L. Santo. 1986. "Temporal variability of soil hydraulic-properties with wetting and drying subsequent to tillage." *Soil Sci. Soc. Am. J.* **50** (5): 1133–1138.
- McIntyre, D. S. 1958. "Permeability measurements of soil crusts formed by raindrop impact." *Soil Sci.* **85** (4): 185–189.
- Mein, R. G., and C. L. Larson. 1973. "Modeling infiltration during a steady rain." *Water Resour. Res.* **9** (2): 384–394.
- Meng, H., T. R. Green, J. D. Salas, and L. R. Ahuja. 2008. "Development and testing of a terrain-based hydrologic model for spatial Hortonian infiltration and run-off/on." *Environ. Modell. Software* **23** (6): 794–812.
- Meng, H., J. D. Salas, T. R. Green, and L. R. Ahuja. 2006. "Scaling analysis of space-time infiltration based on the universal multifractal model." *J. Hydrol.* **322** (1–4): 220–235.
- Minasny, B., and A. B. McBratney. 2002. "Uncertainty analysis for pedotransfer functions." *Eur. J. Soil Sci.* **53** (3): 417–429.

- Mirus, B. B., B. A. Ebel, C. S. Heppner, and K. Loague. 2011. "Assessing the detail needed to capture rainfall-runoff dynamics with physics-based hydrologic response simulation." *Water Resour. Res.* **47** (3): W00H10.
- Moore, I. D. 1981. "Effects of surface sealing on infiltration." *Trans. ASAE* **24** (6): 1546–1552.
- Musgrave, G. W. 1955. "How much of the rain enters the soil?" In *The yearbook of agriculture*, 151–159. Washington, DC: USDA.
- Nahar, N., R. S. Govindaraju, C. Corradini, and R. Morbidelli. 2004. "Role of run-on for describing field-scale infiltration and overland flow over spatially variable soils." *J. Hydrol.* **286** (1–4): 36–51.
- Nielsen, D. R., J. W. Biggar, and K. T. Erh. 1973. "Spatial variability of field-measured soil-water properties." *Hilgardia* **42** (7): 215–259.
- Paltineanu, I. C., and J. L. Starr. 1997. "Real-time soil water dynamics using multisensor capacitance probes: Laboratory calibration." *Soil Sci. Soc. Am. J.* **61** (6): 1576–1585.
- Parlange, J.-Y., and R. E. Smith. 1976. "Ponding times for variable rainfall rates." *Can. J. Soil Sci.* **56** (2): 121–123.
- Philip, J. R. 1957. "The theory of infiltration 4: Sorptivity and algebraic infiltration equations." *Soil Sci. Soc. Am. J.* **84** (3): 257–264.
- Rawls et al. (1982).
- Rodell, M., J. Chen, H. Kato, J. S. Famiglietti, J. Nigro, and C. R. Wilson. 2007. "Estimating groundwater storage changes in the Mississippi River basin (USA) using GRACE." *Hydrogeol. J.* **15** (1): 159–166.
- Rousseva, S. S., L. R. Ahuja, and G. C. Heathman. 1988. "Use of a surface gamma-neutron gauge for insitu measurement of changes in bulk-density of the tilled zone." *Soil Tillage Res.* **12** (3): 235–251.
- Ruan, H. X., L. R. Ahuja, T. R. Green, and J. G. Benjamin. 2001. "Residue cover and surface-sealing effects on infiltration: Numerical simulations for field applications." *Soil Sci. Soc. Am. J.* **65** (3): 853–861.
- Saito, T., H. Fujimaki, H. Yasuda, and M. Inoue. 2009. "Empirical temperature calibration of capacitance probes to measure soil water." *Soil Sci. Soc. Am. J.* **73** (6): 1931–1937.
- Schaap, M. G., F. J. Leij, and M. T. van Genuchten. 2001. "Rosetta: A computer program for estimating soil hydraulic parameters with hierarchical pedotransfer functions." *J. Hydrol.* **251** (3–4): 163–176.
- Schertzer, D., and S. Lovejoy. 1987. "Physical modeling and analysis of rain and clouds by anisotropic scaling multiplicative processes." *J. Geophys. Res.* **92**: 9693–9714.
- Schwank, M., and T. R. Green. 2007. "Simulated effects of soil temperature and salinity on capacitance sensor measurements." *Sensors* **7** (4): 548–577.
- Schwank, M., T. R. Green, C. Mätzler, H. Benedickter, and H. Flühler. 2006. "Laboratory characterization of a commercial capacitance sensor for estimating permittivity and inferring soil water content." *Vadose Zone J.* **5** (3): 1048–1064.
- Schwartz, R. C., S. R. Evett, and J. M. Bell. 2009a. "Complex permittivity model for time domain reflectometry soil water content sensing. II: Calibration." *Soil Sci. Soc. Am. J.* **73** (3): 898–909.
- Schwartz, R. C., S. R. Evett, M. G. Pelletier, and J. M. Bell. 2009b. "Complex permittivity model for time domain reflectometry soil water content sensing. I: Theory." *Soil Sci. Soc. Am. J.* **73** (3): 886–897.
- Scurlock, J. M. O., G. P. Asner, and S. T. Gower. 2001. "Global leaf area index data from field measurements, 1932–2000." Data set. Oak Ridge National Laboratory Distributed Active Archive Center, Oak Ridge, TN, USA. <http://www.daac.ornl.gov>.
- Selker, J., J. Y. Parlange, and T. Steenhuis. 1992. "Fingered flow in two dimensions: 2. Predicting finger moisture profile." *Water Resour. Res.* **28** (9): 2523–2528.
- Seyfried, M. S., and L. E. Grant. 2007. "Temperature effects on soil dielectric properties measured at 50 MHz." *Vadose Zone J.* **6** (4): 759–765.
- Sharma, M. L., G. A. Gander, and C. G. Hunt. 1980. "Spatial variability of infiltration in a watershed." *J. Hydrol.* **45** (1–2): 101–122.
- Simunek, J., M. Sejna, and M. T. van Genuchten. 1999. *The HYDRUS-2D software package for simulating two-dimensional movement of water, heat, and multiple solutes in variably saturated media. Version 2.0*. IGWMC - TPS - 53. Golden, CO: Colorado School of Mines.
- Sivapalan, M., and G. Bloschl. 1998. "Transformation of point rainfall to areal rainfall: Intensity-duration frequency curves." *J. Hydrol.* **204** (1–4): 150–167.
- Smith, R. E. 1990. "Analysis of infiltration through a two-layer soil profile." *Soil Sci. Soc. Am. J.* **54** (5): 1219–1227.
- Smith, R. E. 1999. "Technical note: Rapid measurement of soil sorptivity." *Soil Sci. Soc. Am. J.* **63** (1): 55–57.

- Smith, R. E., C. Corradini, and F. Melone. 1999. "A conceptual model for infiltration and redistribution in crusted soils." *Water Resour. Res.* **35** (5): 1385–1393.
- Smith, R. E., and B. Diekkruger. 1996. "Effective soil water characteristics and ensemble soil water profiles in heterogeneous soils." *Water Resour. Res.* **32** (7): 1993–2002.
- Smith, R. E., and D. C. Goodrich. 2000. "Model for rainfall excess patterns on randomly heterogeneous areas." *J. Hydrol. Eng.* **5** (4): 355–362.
- Smith, R. E., K. Smettem, P. Broadbridge, and D. A. Woolhiser. 2002. *Infiltration theory for hydrologic applications*. Washington, DC: American Geophysical Union.
- Starr, J. L., and R. Rowland. 2007. "Soil water measurement comparisons between semi-permanent and portable capacitance probes." *Soil Sci. Soc. Am. J.* **71** (1): 51–52.
- Steededunne, S. C., M. Rutten, D. M. Krzeminska, M. B. Hausner, S. W. Tyler, J. Selker, T. A. Bogaard, and N. C. Van de Giesen . 2010. "Feasibility of soil moisture estimation using passive distributed temperature sensing." *Water Resour. Res.* **46**: W03534.
- Strudley, M. W., T. R. Green, and J. C. Ascough II. 2008. "Tillage effects on soil hydraulic properties in space and time: State of the science." *Soil Tillage Res.* **99** (1): 4–48.
- Talsma, T. 1969. "In-situ measurement of sorptivity." *Aust. J. Soil Res.* **7** (3): 269–276.
- Talsma, T., and J.-Y. Parlange. 1972. "One-dimensional vertical infiltration." *Aust. J. Soil Res.* **10** (2): 143–150.
- Tricker, A. S. 1981. "Spatial and temporal patterns of infiltration." *J. Hydrol.* **49** (3–4): 261–277.
- Tyler, S. W., J. S. Selker, M. B. Hausner, C. E. Hatch, T. Torgersen, C. E. Thodal, and S. G. Schladow. 2010. "Environmental temperature sensing using Raman spectra DTS fiber-optic methods." *Water Resour. Res.* **46**.
- van Genuchten, M. T. 1980. "A closed-form equation for predicting the hydraulic conductivity of unsaturated soils." *Soil Sci. Soc. Am. J.* **44** (5): 892–898.
- Walker, J., and S. K. Chong. 1986. "Characterization of compacted soil using sorptivity measurements." *Soil Sci. Soc. Am. J.* **50** (2): 288–291.
- Wallach, R., M. Margolis, and E. R. Gruber. 2013. "The role of contact angle on unstable flow formation during infiltration and drainage in wettable porous media." *Water Resour. Res.* **49** (10): 6508–6521.
- Watson, K. K. 1965. "A statistical treatment of the factors affecting the infiltration capacity of a field soil." *J. Hydrol.* **3** (1): 58–65.
- Western, A. W., and R. B. Grayson. 1998. "The Tarrawarra data set: Soil moisture patterns, soil characteristics and hydrological flux measurements." *Water Resour. Res.* **34** (10): 2765–2768.
- Western, A. W., R. B. Grayson, and T. R. Green. 1999. "The Tarrawarra project: High resolution spatial measurement, modelling and analysis of soil moisture and hydrological response." *Hydrolog. Processes* **13** (5): 633–652.
- Western, A. W., S.-L. Zhou, R. B. Grayson, T. A. McMahon, G. Blöschl, and D. J. Wilson. 2004. "Spatial correlation of soil moisture in small catchments and its relationship to dominant spatial hydrological processes." *J. Hydrol.* **286** (1–4): 113–134.
- White, I., M. J. Sully, and K. M. Perroux. 1992. "Measurement of surface-soil hydraulic properties: Disk permeameters, tension infiltrometers, and other techniques." In *Advances in measurement of soil physical properties: SSSA special publication no. 30*, edited by G. C. Topp, 69–103. Madison, WI: Soil Science Society of America.
- Wilson, G. 2011. "Understanding soil-pipe flow and its role in ephemeral gully erosion." *Hydrolog. Processes* **25** (15): 2354–2364.
- Wood, E. F. 1995. "Scaling behaviour of hydrological fluxes and variables: Empirical studies using a hydrological model and remote sensing data." In *Scale issues in hydrological modeling*, edited by J. Kalma and M. Sivapalan, 89–104. Chichester, UK: Wiley.
- Zaslavsky, D., and G. Sinai. 1981. "Surface hydrology. I—Explanation of phenomena." *J. Hydraul. Div.* **107**: 1–16.
- Zreda, M., D. Desilets, T. P. A. Ferré, and R. L. Scott. 2008. "Measuring soil moisture content non-invasively at intermediate spatial scale using cosmic-ray neutrons." *Geophys. Res. Lett.* **35** (21).
- Zreda, M., W. J. Shuttleworth, X. Zeng, C. Zweck, D. Desilets, T. Franz, and R. Rosolem. 2012. "COSMOS: The cosmic-ray soil moisture observing system." *Hydrolog. Earth Syst. Sci.* **16** (11): 4079–4099.

CHAPTER 5

Probability Distributions in Groundwater Hydrology

Hugo A. Loáiciga

5.0 GENERAL

Groundwater hydrology is a discipline of the earth sciences concerned with the quantitative study of water flow, water storage, chemical transport, and related processes in the subsurface. Groundwater hydrologists measure properties of soils and rocks to gain an understanding of subsurface hydrologic processes and to construct predictive models of groundwater phenomena. Those properties include, but are not limited to, porosity, permeability, hydraulic conductivity, specific storage, specific yield, and dispersivity. Because of the complex nature of geologic materials, measurements of these properties exhibit variability even in strata considered to be homogeneous on account of their origin and basic features (such as mineral composition and textural properties). For example, hydraulic conductivity measurements made at different locations in an aquifer exhibit substantial variability. Figure 5-1 exemplifies this, showing a plot of 201 measurement of hydraulic conductivity made in cohesive sediments of lacustrine origin underlying Mexico City.

The measurements of hydraulic conductivity shown in Figure 5-1 vary over five orders of magnitude. Those measurements—and those of other aquifer properties—can be analyzed using the laws of probability and statistics to obtain a proper description of the property (or variable) under study that goes beyond the calculation of its average, standard deviation, or other indicators of central tendency, dispersion, and asymmetry. The fitting of an aquifer property with a proper probability density function (pdf) is a necessary step—after its measurement in the field or in the laboratory—to arrive at a complete description of its probabilistic characteristics. Analysts can then use the fitted pdf in various analyses and design modes that provide a wider range of options than those available when the property is treated deterministically (i.e., as a nonrandom entity).

The previous paragraph should not suggest that all soil and rock properties vary over a wide numerical range. The porosity of soil and rocks, for example, takes values between 0 and 1. Table 5-1 shows the range of porosity of common rocks. Therefore, in the probabilistic analysis of porosity one must employ probability density functions defined over a finite domain, or use truncated probability functions (see, e.g., Loáiciga et al. 1992).

This chapter presents (1) several pdfs commonly used in groundwater hydrology and (2) examples of how pdfs are used to interpret aquifer properties and groundwater variables in a probabilistic manner. Several of the examples rely on hydraulic conductivity data. This is because hydraulic conductivity is an aquifer property that controls the movement of groundwater and dissolved chemicals in a fundamental manner. Besides its importance in groundwater hydrology, its variability is well suited for probabilistic analysis. In addition, hydraulic conductivity has been more extensively measured *in situ* or in the laboratory than any other aquifer property of relevance in groundwater hydrology. For

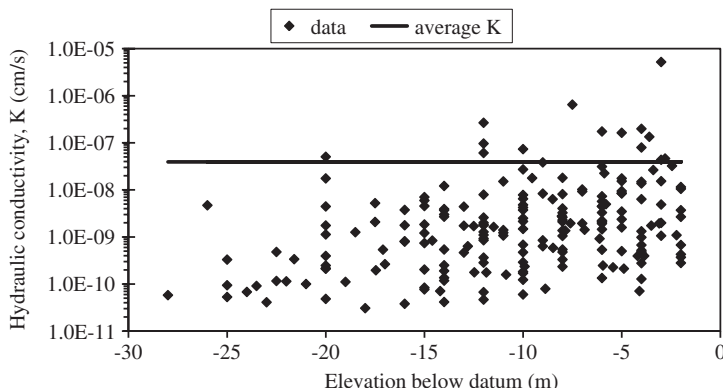


Figure 5-1. Measurement of hydraulic conductivity (K) in the lacustrine sediments underlying Mexico City. The horizontal line is the average, 3.94×10^{-8} cm/s.

Table 5-1. Range of Porosity in Near-Surface Common Rocks.

Rock type	Range of porosity (%)
Igneous:	
basalt	0.22–22.06
granite	1.11–3.98
Sedimentary:	
sandstone	1.62–26.40
breccia	0.78–18.73
limestone	0.27–4.36
Metamorphic:	
gneiss	0.30–2.23
marble	0.31–2.02

Source: [Krynyne and Judd \(1957\)](#).

this reason, datasets that can be analyzed with the methods of this chapter are more common for hydraulic conductivity than for any other aquifer property. This makes the hydraulic conductivity an attractive property to work with when describing probabilistic methods amenable to the characterization of aquifer properties. This chapter uses the symbol K to represent a generic aquifer property or groundwater variable, although it is customarily used to represent the hydraulic conductivity. Some of the material presented in this chapter has been borrowed from the works of the author and collaborators (Loáiciga 2004, 2008a, 2008b, 2014; Loáiciga and Leipnik 2005; Loáiciga et al. 2006).

5.1 DEFINITIONS

5.1.1 Probability Density Function

A pdf, in the univariate case, is a mathematical formula that assigns a nonnegative value to any number contained in the domain of the pdf. They are functions of the form $f(x)$, in which x denotes any value at which the function f is calculated. The set of x values over which the function f is defined is called the domain of the pdf. The pdf integrated over its entire domain yields a value of 1. When

integrated over part of its domain, it produces a probability between 0 and 1. The mathematical formula of a pdf may take many forms. Among the best known and more widely used ones are the uniform, normal (or Gaussian), the log-normal, the gamma and log-gamma, beta, exponential, Weibull, Gumbel, student *t*, and the chi-squared pdfs. In some pdfs the *x* values are strictly integer values. These pdfs are more commonly referred to as probability distributions. The binomial, Poisson, and geometric probability distributions are commonly used.

5.1.2 Correlation Coefficient

Consider two random variables X_1 and X_2 with expected values (or means) μ_1 and μ_2 , and variances σ_1^2 and σ_2^2 , respectively, that are correlated with correlation coefficient ρ . The following formula defines the latter:

$$\rho = \frac{E[(x_1 - \mu_1)(x_2 - \mu_2)]}{\sigma_1 \sigma_2} \quad (5-1)$$

where the symbol E denotes the expectation operator. The correlation coefficient ρ is a normalized measure of the degree of statistical association between two random variables. Its magnitude falls in the range $[-1, 1]$. A value of -1 means perfect negative correlation, a value of $+1$ denotes perfect positive correlation, and a value of zero means that the variables X_1 and X_2 are uncorrelated.

5.1.3 Spatial Correlation

Spatial correlation is a measure of the degree of statistical association among measurements of an aquifer property made at different locations in an aquifer. Positively correlated measurements occur when the spatial correlation between two measurements of the property K_1 and K_2 made at locations x_1 and x_2 , respectively, ranges between 0 and 1. The closer the spatial correlation is to 1, the greater the degree of statistical association between the measurements K_1 and K_2 .

5.1.4 Correlation Scale

Correlation scale is the distance between two points x_1 and x_2 beyond which the aquifer property K_1 (at x_1) and K_2 (at x_2) cease to be spatially correlated.

5.1.5 Statistical Homogeneity and Independence

Statistical homogeneity and independence of measurements are conditions that must be met when attempting to fit a pdf to a sample of measurements of an aquifer property. Statistical homogeneity implies the pdf of the property in question is the same everywhere in the aquifer or portion of aquifer in which measurements are made with a similar device or method. In this case, the measurements exhibit a constant average and a spread of values about the average devoid of spatial trends or spatial periodic patterns. Independence of measurements implies the value of the measured property at any location in an aquifer is not related in a probabilistic sense to any other of its values measured at other locations in the same aquifer. Independent measurements are uncorrelated. Property measurements can be statistically homogeneous and correlated simultaneously. In the latter instance, one must resort to geostatistics, a discipline concerned with the study of spatially correlated variables (Journel and Huijbregts 1978, Dagan 1989, Loáiciga 2010). From a physical standpoint, statistical homogeneity is approximated in the field when geological processes produce unconsolidated deposits (clays, silts, sands, gravels, or combinations of these) or consolidated deposits (also called bedrock aquifers) of similar texture, porosity characteristics, and mineral composition. Independence requires physical separations among property measurement locations that ensure the vanishing of any statistical dependence among its values. Measurement locations so chosen produce samples of measurements that are uncorrelated. The minimal spatial separation among measurements must exceed the correlation scale of the saturated hydraulic conductivity. The correlation scale can be estimated using geostatistical procedures (Loáiciga 2010).

5.2 BASIC NOTATION AND KEY STATISTICS

A sample of n measurements of an aquifer property K is assumed available for statistical inference. The individual measurements are denoted by K_1, K_2, \dots, K_n , or, symbolically, by, K_j , where $j = 1, 2, \dots, n$. The natural logarithm of K is denoted by $Y = \ln K$. The sample of Y values is denoted by $Y_j (= \ln K_j)$, where $j = 1, 2, \dots, n$. The logarithmic transformation is commonly applied to permeability, hydraulic conductivity, or other aquifer properties that are frequently found to be log-normally distributed. That is, the property is rendered normally distributed (and thus symmetric) upon undergoing the logarithmic transformation. The following subsections introduce several important statistics that describe the central tendency, the degree of spread about a measure of central tendency, and the skewness of data. The statistics are necessary in fitting pdfs to measurements of aquifer properties.

5.2.1 The Sample Average

Calculate the sample average of the property K using the following formula:

$$\bar{K} = \frac{1}{n} \sum_{j=1}^n K_j \quad (5-2)$$

The sample average \bar{K} is an estimate of the unknown population average of K , or μ_K . The sample average is a measure of the central tendency of the data it represents.

The sample average of the log property Y is calculated with the following equation:

$$\bar{Y} = \frac{1}{n} \sum_{j=1}^n Y_j \quad (5-3)$$

The sample average \bar{Y} is an estimate of the unknown population average of Y , or μ_Y .

5.2.2 The Geometric Mean

Calculate the sample geometric mean of K (denoted by \bar{K}_G) with the following equation:

$$\bar{K}_G = e^{\bar{Y}} \quad (5-4)$$

The sample geometric mean is an estimate of the (unknown) population geometric mean, $K_G = \exp(\mu_Y)$. The geometric mean is sometimes used as an effective saturated hydraulic conductivity in groundwater hydrology. The effective saturated hydraulic conductivity is a parameter that relates the average groundwater specific discharge to the average hydraulic gradient.

5.2.3 The Standard Deviation and Variance

Calculate the sample standard deviation of the property K as follows

$$\bar{\sigma}_K = \sqrt{\frac{1}{n-1} \sum_{j=1}^n (K_j - \bar{K})^2} \quad (5-5)$$

The sample's standard deviation $\bar{\sigma}_K$ is an estimate of the unknown population standard deviation of K , or σ_K . The sample variance of the property K is equal to $\bar{\sigma}_K^2$. The sample standard deviation measures the spread of the data about its average.

The sample standard deviation of the log property ($\bar{\sigma}_Y$) is calculated as follows:

$$\bar{\sigma}_Y = \sqrt{\frac{1}{n-1} \sum_{j=1}^n (Y_j - \bar{Y})^2} \quad (5-6)$$

The sample standard deviation $\bar{\sigma}_Y$ is an estimate of the unknown population standard deviation of Y , σ_Y . The sample variance of log conductivity equals $\bar{\sigma}_Y^2$.

5.2.4 The Coefficient of Skew

The sample coefficient of skew measures the degree of asymmetry of a set of measurements of the property K . It may take positive or negative values. The larger the absolute value of coefficient of skew is the more asymmetric is the pdf of the property K . A symmetric pdf, such as the normal pdf, has a coefficient of skew equal to zero. The sample coefficient of skew is calculated using the following equation:

$$C_{sK} = \frac{n}{(n-1)(n-2)} \sum_{j=1}^n \left(\frac{K_j - \bar{K}_j}{\bar{\sigma}_K} \right)^3 \quad (5-7)$$

The sample coefficient of skew of the log property Y is calculated as follows:

$$C_{sY} = \frac{n}{(n-1)(n-2)} \sum_{j=1}^n \left(\frac{Y_j - \bar{Y}_j}{\bar{\sigma}_Y} \right)^3 \quad (5-8)$$

If the log property Y is normally distributed, then its coefficient of skew equals zero. In this instance the sample coefficient of skew of the log property Y tends toward zero. In practice, if $-0.05 \leq C_{sY} \leq 0.05$, then the log property Y can be assumed to be normally distributed, or equivalently, that the property K follows a log-normal pdf. Otherwise, that is, if $|C_{sY}| > 0.05$, use a skewed pdf to fit the log property Y .

The average, standard deviation, and coefficient of skew can be calculated expeditiously and accurately using functions available in commercial spreadsheets and numerical software such Microsoft Excel and MATLAB.

5.3 FREQUENTLY USED PDFS IN GROUNDWATER HYDROLOGY

This chapter presents several pdfs that have been used to model aquifer properties or groundwater processes. The following sections include several applications.

5.3.1 The Log-Normal pdf

The log-normal pdf has been found to fit many types of data well, including aquifer properties such as permeability and hydraulic conductivity. [Freeze \(1975\)](#) provides early impetus for using the log-normal pdf as a statistical model to fit hydraulic conductivity data. Over time, the log-normal pdf has been accepted as a viable model for describing various aquifer properties (see a discussion of this topic in [Loáiciga et al. 2006](#)). Attractive features of the log-normal pdf in the modeling of some aquifer properties are (1) it can fit positively skewed data, (2) the parameters of a normally

distributed log property Y [symbolically $Y \sim N(\mu_Y, \sigma_Y^2)$] are the population mean μ_Y and the population variance σ_Y^2 , which are estimable using the standard sample estimators for the mean and previously introduced variance. Moreover, the quantiles of Y can be obtained straightforwardly from tabulated quantiles of the standard normal pdf $N(0, 1)$ or from statistical software. The log-normal pdf, however, cannot be used to model either skewed log data or negatively skewed aquifer data. Although the log-normal pdf allows positive lower bounds on aquifer data, it does not allow upper bounds. In contrast, the log-gamma pdf, a generalization of the gamma pdf, can fit skewed data, with upper and lower bounds, or with upper or lower bounds.

Properties of the Log-Normal pdf

Let K and θ denote an aquifer property and its lower bound, respectively, and $Y = \ln(K - \theta)$ be the log property. Evidently, $K = \exp(Y) + \theta$. The three-parameter log-normal pdf is given by the following formula (μ_Y denotes the population mean of the log property Y):

$$f_K(s) = \frac{1}{(s - \theta)\sigma_Y\sqrt{2\pi}} \exp\left[-\frac{1}{2}\left(\frac{\ln(s - \theta) - \mu_Y}{\sigma_Y}\right)^2\right] s > \theta \quad (5-9)$$

in which the lower bound θ is nonnegative due to physical feasibility. The lower bound θ is generally assumed equal to zero in most applications of the log-normal pdf in groundwater hydrology. The log-normal pdf in equation (5-9) implies several formulas for the property K , the log property Y , and their parameters, which follow. In these equations, for the sake of simplicity, the population means of K and Y are replaced by their sample averages \bar{K} and \bar{Y} , respectively. The population standard deviations of K and Y are replaced by their sample estimates and $\bar{\sigma}_K$ and $\bar{\sigma}_Y$, respectively. C_{SK} denotes the population and sample coefficient of skew of the property K .

Expected Value of the Property K

$$\bar{K} = e^{\left(\bar{Y} + \frac{\bar{\sigma}_Y^2}{2}\right)} + \theta \quad (5-10)$$

The expected value is estimated by the sample average written in Equation (5-2).

Median of the Property K ($K_{0.50}$)

$$K_{0.50} = e^{\bar{Y}} + \theta \quad (5-11)$$

The geometric mean of the property K equals $K_G = \theta + \exp(\bar{Y})$, usually with $\theta = 0$, which implies the geometric mean and the median of log-normally distributed K data are equal to each other.

Equation (5-11) is convenient for estimating the lower bound θ . To do so, the sample estimator $\bar{K}_{0.50}$ is obtained and then substituted in Equation (5-11), which is then solved for an estimate of θ . Alternatively, Equation (5-10) could also be used to estimate θ . If the sample size is large (say, more than 30 values of hydraulic conductivity) and K conformed exactly to a log-normal pdf, then the estimators of θ from either equation will converge to the same value as the sample size increases. The common assumption in practical applications in groundwater hydrology is that $\theta = 0$.

Mode of the Property K

The mode (K_M) is the most likely value of K :

$$K_M = e^{\bar{Y} - \sigma_Y^2} + \theta \quad (5-12)$$

Equations (5-10), (5-11), and (5-12) show that $K_M < K_{0.50} < \bar{K}$.

Variance of the Property K (σ_K^2)

The following formula provides a relation between the variance of the property K and its log property Y :

$$\sigma_K^2 = e^{2\bar{Y} + \bar{\sigma}_Y^2} \cdot (e^{\bar{\sigma}_Y^2} - 1) \quad (5-13)$$

The variance of K is estimated by the square of the sample standard deviation in Equation (5-5).

Coefficient of Variation of K (C_{vK})

For $\theta = 0$:

$$C_{vK} = \frac{\sigma_K}{\bar{K}} = (e^{\bar{\sigma}_Y^2} - 1)^{\frac{1}{2}} \quad (5-14)$$

The coefficient of variation is a dimensionless ratio that measures the magnitude of the standard deviation of K relative to its mean. The larger the coefficient of variation is, the larger is the variability of K about its mean.

Coefficient of Skew of the Property K (C_{sk})

$$C_{sk} = \frac{E[K - \bar{K}]^3}{\sigma_K^3} = \frac{e^{3\bar{\sigma}_Y^2} - 3\bar{\sigma}_Y^2 + 2}{C_{vK}^3} \quad (5-15)$$

in which C_{vk} is given by Equation (5-14). The C_{sk} in Equation (5-15) is always positive. It is estimated with Equation (5-7).

Quantiles of the Property K

For $0 < p < 1$, $P(K \leq K_p) = p$ defines the p -th quantile (K_p) of property K . K_p is given by

$$K_p = e^{(\bar{Y} + z_p \bar{\sigma}_Y) + \theta} \quad (5-16)$$

In Equation (5-16) z_p denotes the p -th quantile of the standard normal variate with zero mean and unit variance, which is readily obtained with ubiquitous software such as Microsoft Excel, using the function $z_p = \text{norm.s.inv}(p)$. The quantile K_p can be obtained directly as follows:

$$K_p = e^{Y_p} + \theta \quad (5-17)$$

where the p -th quantile Y_p of the log property Y can be obtained with the $\text{norm.inv}(p, \bar{Y}, \bar{\sigma}_Y)$ function of Microsoft Excel.

5.3.2 The Gamma pdf and Its Special Case the Exponential pdf

The gamma pdf is a versatile model that is used in many fields of science and engineering, groundwater hydrology included. Loáiciga (2004) proposes the gamma pdf as an alternative to the log-normal pdf in an analysis of stochastic groundwater flow and solute transport. Loáiciga and Leipnik (2005) apply the gamma pdf to model water-quality variables.

Properties of the Gamma pdf

The pdf of a three-parameter gamma-distributed aquifer property K is

$$g_K(s) = \frac{\left(\frac{s-\theta}{\beta}\right)^\alpha |s-\theta|^{-1} e^{-\left(\frac{s-\theta}{\beta}\right)}}{\Gamma(\alpha)} \quad s \geq \theta \text{ if } \beta > 0, \quad s \leq \theta \text{ if } \beta < 0 \quad (5-18)$$

in which α and β are shape and scale parameters, respectively, and $\alpha > 0$; θ is a lower bound of the variable K when $\beta > 0$ and an upper bound when $\beta < 0$. Most applications in groundwater hydrology assume that $\theta = 0$. Γ denotes the gamma function:

$$\Gamma(\alpha) = \int_0^{\infty} e^{-\nu} \nu^{\alpha-1} d\nu \quad (5-19)$$

The gamma function is widely tabulated and programmed in commercial software (Microsoft Excel, MATLAB, or MATHEMATICA). The domain of the gamma pdf is $[-\infty, \theta]$ when $\beta < 0$, which contains negative numbers and thus violates the nonnegativity of positive-valued aquifer properties. Noteworthy is that when $\theta = 0$, $\alpha = 1$, and $\beta > 0$, the gamma pdf in Equation (5-18) becomes the exponential pdf with parameter $\lambda = 1/\beta$. The exponential pdf is given by

$$h_K(s) = \lambda e^{-\lambda s} \quad s \geq 0; \lambda > 0 \quad (5-20)$$

The next subsection presents a summary of the properties of the gamma pdf for positive or negative scale parameter β .

Expected Value (Mean) of the Property K

$$\bar{K} = \alpha \beta + \theta \quad (5-21)$$

Median of the Property K

$$K_{0.50} = \psi_{0.50} \beta + \theta \quad (5-22)$$

in which $\psi_{0.50}$ must be obtained from the integral equation:

$$\frac{1}{\Gamma(\alpha)} \int_0^{\psi_{0.50}} e^{-\nu} \nu^{\alpha-1} d\nu = \frac{1}{2} \quad (5-23)$$

The integral on the left-hand side of Equation (5-23) is called the incomplete gamma function $\gamma(\alpha, \psi_{0.50})$ (see, e.g., Gradshteyn and Ryzhik 1994), so that Equation (5-23) can be shortened to

$$\frac{\gamma(\alpha, \psi_{0.50})}{\Gamma(\alpha)} = \frac{1}{2} \quad (5-24)$$

The left-hand side of Equation (5-24) can be evaluated using the GAMMA.INV(probability, alpha, beta) function in Microsoft Excel, with probability = $1/2$, alpha = α , and beta = $\beta = 1$, which returns the value of $\psi_{0.50}$.

Mode of the Property K

when $\alpha > 1$,

$$K_M = (\alpha - 1) \cdot \beta + \theta, \quad (5-25)$$

and it is equal to θ when $0 < \alpha \leq 1$.

Variance of the Property K

$$\sigma_K^2 = \alpha \beta^2 \quad (5-26)$$

Coefficient of Variation of the Property K

$$C_{vK} = \frac{|\alpha^{\frac{1}{2}} \cdot \beta|}{|\alpha \beta + \theta|} \quad (5-27)$$

Coefficient of Skew of the Property K

$$C_{sK} = \frac{2 \alpha \beta^3}{\sigma_K^3} \quad (5-28)$$

in which the sign of the skew is determined by that of the shape parameter β . $C_{sK} > 0$ when $\beta > 0$, in which case the pdf is positively skewed with lower bound θ . $C_{sK} < 0$ when $\beta < 0$, in which case the pdf is negatively skewed with upper bound θ .

Moment Estimators of the α , β , and θ Parameters

These are deducible from the various properties of the previously described gamma pdf. The moment estimators are

$$\alpha = \frac{4}{C_{sK}^2} \quad (5-29)$$

$$\beta = \frac{\bar{\sigma}_K C_{sK}}{2} \quad (5-30)$$

$$\theta = \bar{K} - 2 \frac{\bar{\sigma}_K}{C_{sK}} \quad (5-31)$$

in which \bar{K} , $\bar{\sigma}_K$, and C_{sK} , in Equations (5-29) through (5-31) represent the sample estimators of the mean, variance, and coefficient of skewness of the property K , respectively.

Quantiles of the Property K

For $0 < p < 1$, $P[K \leq K_p] = p$ defines the p -th quantile. In particular, $K_{0.50}$ equals the median. In general, K_p is given by the following equation:

$$K_p = \bar{K} + \left[\frac{\Psi_q C_{sK}}{2} - \frac{2}{C_{sK}} \right] \sigma_K \quad (5-32)$$

in which ψ_q must be obtained from the following integral equation ($0 < p < 1$):

$$\frac{1}{\Gamma(\alpha)} \int_0^{\psi_q} e^{-v} v^{\alpha-1} dv = p \quad \text{if } C_{sK} > 0 \quad (\text{i.e., } \beta > 0) \quad (5-33)$$

with $\alpha = 4/C_{sK}^2$, or from

$$\frac{1}{\Gamma(\alpha)} \int_0^{\psi_q} e^{-v} v^{\alpha-1} dv = 1 - p \quad \text{if } C_{sK} < 0 \quad (\text{i.e., } \beta < 0) \quad (5-34)$$

in which $\alpha = 4/C_{sK}^2$. All the special functions used in the previous equations related to the gamma pdf are available in commercial software and their calculation is expeditious. In particular, the left-hand side of Equations (5-33) and (5-34) can be evaluated using the GAMMA.INV(probability, alpha, beta) function in Microsoft Excel, with probability $q = p$ (if $C_{sK} > 0$) or $1 - p$ (if $C_{sK} < 0$), alpha = α , and beta = $\beta = 1$, which returns the value of ψ_q . In the limit $C_{sK} \rightarrow 0$, the factor within brackets in Equation (5-32) tends to the standard normal quantile z_p . Specifically,

$$\lim_{C_{sK} \rightarrow 0} \left[\frac{\psi_q C_{sK}}{2} - \frac{2}{C_{sK}} \right] \rightarrow z_p \quad (5-35)$$

so that the quantile K_p in Equation (5-35) becomes $K_p = \bar{K} + z_p \bar{\sigma}_K$. In other words, the gamma pdf approaches the normal pdf when the coefficient of skew tends to zero.

5.3.3 The Log-Gamma pdf

A variant of the gamma pdf is the log-gamma pdf (also called log-Pearson type III), which U.S. federal agencies use to fit annual streamflow peaks at gauged sites (see, e.g., [US Geological Survey 1982](#)). When using the log-gamma pdf, the assumption is that the logarithm of the property K (i.e., $Y = \ln(K)$) follows the gamma pdf in Equation (5-18) with the shape and scale parameters replaced by α_Y and β_Y , respectively. In this instance, $\theta = \theta_Y$ in Equation (5-18) denotes the lower bound of Y when $\beta_Y > 0$, or its upper bound when $\beta_Y < 0$. The log property Y has the following gamma pdf:

$$g_Y(s) = \frac{\left(\frac{s-\theta_Y}{\beta_Y}\right)^{\alpha_Y} |s-\theta_Y|^{-1} e^{-\left(\frac{s-\theta_Y}{\beta_Y}\right)}}{\Gamma(\alpha_Y)} \quad (5-36)$$

such that $s \geq \theta_Y$ if $\beta_Y > 0$, or $s \leq \theta_Y$ if $\beta_Y < 0$.

Evidently, $K = \exp(Y)$, which is positive with lower or upper bound $\exp(\theta_Y)$ depending on whether $\beta_Y > 0$ or $\beta_Y < 0$, respectively. The pdf of the log-gamma distributed K is

$$h_K(s) = \frac{\left(\frac{\ln(s)-\theta_Y}{\beta_Y}\right)^{\alpha_Y} |\ln(s)-\theta_Y|^{-1} e^{-\left(\frac{\ln(s)-\theta_Y}{\beta_Y}\right)}}{s \Gamma(\alpha_Y)} \quad (5-37)$$

in which $s \geq e^{\theta_Y}$ if $\beta_Y > 0$, or $0 < s \leq e^{\theta_Y}$ if $\beta_Y < 0$. Key properties of the log-gamma-distributed property K are derivable from its pdf (5-37). These are presented next.

Expected Value of the Property K

$$\bar{K} = \frac{e^{\theta_Y}}{(1 - \beta_Y)^{\alpha_Y}} \quad (5-38)$$

Geometric Mean of the Property K

$$K_G \equiv e^{E(Y)} = e^{\alpha_Y \beta_Y + \theta_Y} \quad (5-39)$$

Median of the Property K

$$K_{0.50} = e^{\psi_{0.50} \beta_Y + \theta_Y} \quad (5-40)$$

in which $\psi_{0.50}$ is obtained from the solution of the integral Equation (5-24).

Mode of the Property K

When $\alpha > 1$,

$$\bar{K}_M = e^{\left[(\alpha_Y - 1) \frac{\beta_Y}{\beta_Y + 1} + \theta_Y \right]} \quad (5-41)$$

The mode equals e^{θ_Y} if $0 < \alpha_Y \leq 1$.

Variance of the Property K

$$\sigma_K^2 = \bar{K}^2 \cdot \left[\left(\frac{(1 - \beta_Y)^2}{(1 - 2 \beta_Y)} \right)^{\alpha_Y} - 1 \right] \quad (5-42)$$

in which \bar{K} (the expected value of K) is given by Equation (5-38).

Coefficient of Variation of the Property K

$$C_{vK} = \left[\left(\frac{(1 - \beta_Y)^2}{(1 - 2 \beta_Y)} \right)^{\alpha_Y} - 1 \right]^{\frac{1}{2}} \quad (5-43)$$

Coefficient of Skew of the Property K

$$C_{sK} = \frac{\left(\frac{(1 - \beta_Y)^3}{(1 - 3 \beta_Y)} \right)^{\alpha_Y} - 3 \left(\frac{(1 - \beta_Y)^2}{(1 - 2 \beta_Y)} \right)^{\alpha_Y} + 2}{C_{vK}^3} \quad (5-44)$$

in which C_{vK} is given by Equation (5-43).

Moment Estimators of the Log Parameters α_Y , β_Y , and θ_Y

Moment estimators are obtained by resorting to the fact that $Y = \ln(K)$ is gamma distributed. Letting \bar{Y} , σ_Y , and C_{sY} be the mean, standard deviation, and coefficient of skew of Y , respectively, one obtains

$$\alpha_Y = \frac{4}{C_{sY}^2} \quad (5-45)$$

$$\beta_Y = \frac{\bar{Y} C_{sY}}{2} \quad (5-46)$$

$$\theta_Y = \bar{Y} - 2 \frac{\bar{\sigma}_Y}{C_{sY}} \quad (5-47)$$

in which \bar{Y} , $\bar{\sigma}_Y$, and C_{sY} represent in equations the sample estimators of the mean, variance, and coefficient of skew of the log property Y , respectively, in Equations (5-45) to (5-47).

Quantiles of the Property K

For $0 < p < 1$, $P[K \leq K_p] = p$ defines the p -th quantile (K_p) of the property K . In particular, $K_{0.50}$ equals the median. In general, K_p is given by the following equation:

$$K_p = \exp \left[\bar{Y} + \left(\frac{\psi_q C_{sY}}{2} - \frac{2}{C_{sY}} \right) \cdot \bar{\sigma}_Y \right] \quad (5-48)$$

in which ψ_q must be obtained from the following integral equations ($0 < p < 1$):

$$\frac{1}{\Gamma(\alpha_Y)} \int_0^{\psi_q} e^{-v} v^{\alpha_Y-1} dv = p \quad \text{if } C_{sY} > 0 \quad (\text{i.e., } \beta_Y > 0) \quad (5-49)$$

in which $\alpha_Y = 4/C_{sY}^2$, or

$$\frac{1}{\Gamma(\alpha_Y)} \int_0^{\psi_q} e^{-v} v^{\alpha_Y-1} dv = 1 - p \quad \text{if } C_{sY} < 0 \quad (\text{i.e., } \beta_Y < 0) \quad (5-50)$$

in which $\alpha_Y = 4/C_{sY}^2$. The left-hand side of Equations (5-49) and (5-50) can be evaluated using the GAMMA.INV(probability, alpha, beta) function in Microsoft Excel, with probability $q = p$ (if $C_{sY} > 0$) or $1 - p$ (if $C_{sY} < 0$), alpha = α_Y , and beta = $\beta = 1$, which returns the value of ψ_q .

In the limit $C_{sY} \rightarrow 0$ the factor within brackets in Equation (5-48) tends to the standard normal quantile z_p . Specifically,

$$\lim_{C_{sY} \rightarrow 0} \left[\frac{\psi_q C_{sY}}{2} - \frac{2}{C_{sY}} \right] \rightarrow z_p \quad (5-51)$$

so that the quantile K_p in Equation (5-48) becomes

$$K_p = \exp(\bar{Y} + z_p \bar{\sigma}_Y) \quad (5-52)$$

Therefore, the log-gamma pdf approaches the log-normal pdf when the coefficient of skew tends to zero (compare Equation (5-52) with Equation (5-16), after setting $\theta = 0$ in the latter equation).

5.4 ILLUSTRATIVE EXAMPLES

The following sections present applications of the log-normal, gamma, log-gamma, and exponential pdfs to various groundwater problems, including fitting aquifer data, groundwater flow, and water quality.

5.4.1 Application of the Log-Normal pdf to Hydraulic Conductivity Data

The hydraulic conductivity data shown in Figure 5-1 has an average $\bar{K} = 3.94 \times 10^{-8}$ cm/s, and standard deviation $\bar{\sigma}_K = 3.70 \times 10^{-7}$, which implies an extraordinarily large coefficient of variation $C_{vK} = 9.4$. The coefficient of skew equals 13.7, testimony to acutely right-skewed hydraulic conductivity data. The K data were log-transformed to produce the log-conductivity data Y in an attempt to reduce the asymmetry and facilitate fitting a pdf to the hydraulic conductivity data. The sample average (\bar{Y}), standard deviation ($\bar{\sigma}_Y$), and coefficient of skew (C_{sY}) of the log conductivity data equal -20.30 , 2.08 , and 0.592 , respectively. Although the skew coefficient was reduced by the log transformation, a histogram of the Y data shown in Figure 5-2 confirms that it is right skewed.

If the log conductivity Y were normally distributed, its pdf would be (setting $\theta = 0$):

$$f_Y(y) = \frac{1}{2.08\sqrt{2\pi}} \exp\left[-\frac{1}{2}\left(\frac{y - (-20.3)}{2.08}\right)^2\right] \quad (5-53)$$

Figure 5-3 graphs Equation (5-53). The graphed normal pdf is symmetric. The log conductivity data is right skewed. Assuming the log conductivity Y is sufficiently close to a normal pdf, and then using Equations (5-16) or (5-17) to estimate quantiles of the hydraulic conductivity K , is customary in applications. For example, if the lower quartile ($K_{0.25}$) and upper quartile ($K_{0.75}$) of the hydraulic conductivity were needed in a simulation study of groundwater flow and chemical and heat transport, these two values could be approximated as follows (using Equation (5-16) with $\theta = 0$):

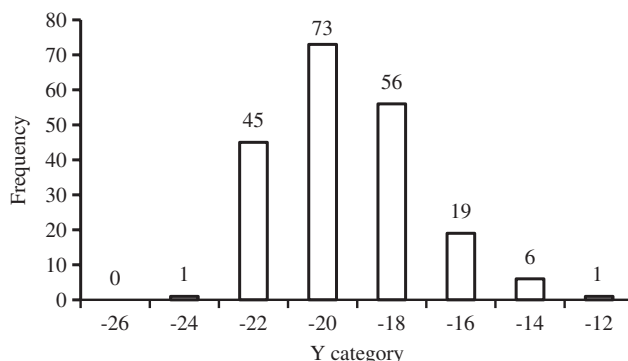


Figure 5-2. Histogram of the log conductivity data Y graphed in Figure 5-1.

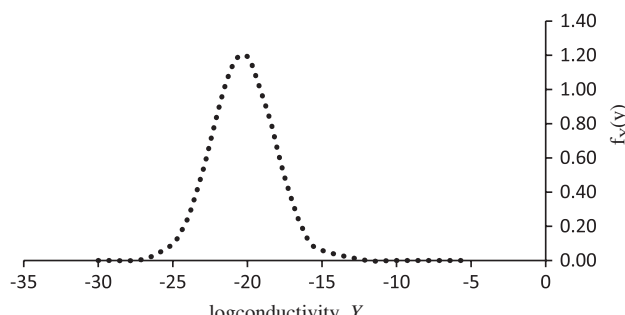


Figure 5-3. Graph of the normal pdf fitted to the log conductivity data graphed in Figure 5-1.

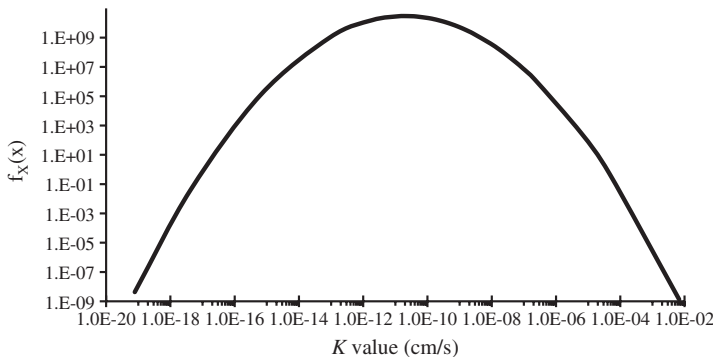


Figure 5-4. The log-normal pdf fitted to the hydraulic conductivity data K shown in Figure 5-1.

$$K_{0.25} = e^{\bar{Y} + z_{0.25}\bar{\sigma}_Y} = e^{-20.3 + (-0.6745) \cdot 2.08} = 3.75 \times 10^{-10} \text{ cm/s} \quad (5-54)$$

$$K_{0.75} = e^{\bar{Y} + z_{0.75}\bar{\sigma}_Y} = e^{-20.3 + 0.6745 \cdot 2.08} = 6.21 \times 10^{-9} \text{ cm/s} \quad (5-55)$$

Under the assumption that hydraulic conductivity K is approximately log-normally distributed, its pdf is

$$f_K(x) = \frac{1}{x(2.08)\sqrt{2\pi}} \exp\left[-\frac{1}{2}\left(\frac{\ln(x) - (-20.3)}{2.08}\right)^2\right] \quad (5-56)$$

Equation (5-56) is graphed in Figure 5-4. Because of the wide range of the hydraulic conductivity and the complexity of Equation (5-56)—relative to the normal pdf Equation (5-53)—the latter formula is easier to work with when making calculations on hydraulic conductivity values.

5.4.2 Application of the Log-Gamma pdf to Fit Hydraulic Conductivity Data

The previous section's example showed how the logarithmic transformation of hydraulic conductivity data can reduce its asymmetry and a normal pdf can be fitted to the log conductivity data reasonably well. One can go one step further and fit an asymmetric pdf to the skewed log conductivity data. Furthermore, one can carry out a formal statistical goodness-of-fit test to ascertain whether or not the proposed (asymmetric) pdf is an acceptable match to the hydraulic conductivity data. With these two aims, that is, fitting a pdf and testing the fit, the log-gamma pdf (5-37) was fitted to the hydraulic conductivity data graphed in Figure 5-1. Recall that the sample average, standard deviation, and coefficient of skew of log conductivity are $\bar{Y} = -20.3$, $\bar{\sigma}_Y = 2.08$, and $C_{sY} = 0.592$, respectively. These were used to calculate the log-gamma parameters $\alpha_Y = 11.4$, $\beta = 0.616$, and $\theta_Y = -27.3$ using Equations (5-45), (5-46), and (5-47), respectively. Because C_{sY} is positive, the hydraulic conductivity has a lower bound equal to $\exp(\theta_Y) = 1.39 \times 10^{-12}$. The log-gamma pdf of hydraulic conductivity K is

$$h_K(s) = \frac{\left(\frac{\ln(s) - (-27.3)}{0.616}\right)^{11.4} |\ln(s) - (-27.3)|^{-1} e^{-\left(\frac{\ln(s) - (-27.3)}{0.616}\right)}}{s \Gamma(11.4)} \quad (5-57)$$

Equation (5-57) is graphed in Figure 5-5.

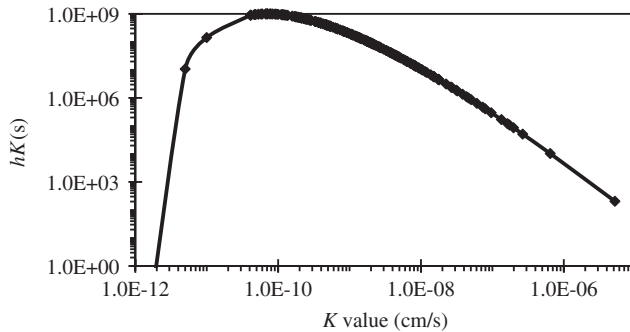


Figure 5-5. The log-gamma pdf fitted to the hydraulic conductivity K data shown in Figure 5-1.

Use Equation (5-48) to calculate the quantiles of a log-gamma distributed property. Suppose the quantiles of log conductivity $K_{0.25}$, $K_{0.50}$, and $K_{0.75}$, are wanted. The values $\psi_{q=p}$ for $p = 0.25$, 0.50 , and 0.75 equal 8.98 , 11.1 , and 13.5 , respectively. Calculate the values of the desired quantiles using Equation (5-48): $K_{0.25} = 3.43 \times 10^{-10}$, $K_{0.50} = 1.25 \times 10^{-9}$, and $K_{0.75} = 5.45 \times 10^{-9}$ cm/s.

Goodness-of-Fit Testing: The Chi-Squared Test

The chi-squared goodness-of-fit test is a formal procedure used to accept or reject a proposed pdf to fit specific data. The procedure can be used for any type of data. Herein it is used in conjunction with aquifer properties, such as the hydraulic conductivity. The following steps must be implemented in applying the chi-squared test:

Step 1. Calculate R saturated hydraulic conductivity (or other groundwater variable) quantiles, denoted by $K_{\Delta p} < K_{2\Delta p} < \dots < K_{R\Delta p}$, using the appropriate equation for quantile calculation. The notation $K_{r\Delta p}$ implies the probability corresponding to the quantile is $r \cdot \Delta p$, in which $r = 1, 2, \dots, R$, and the probability increment Δp is defined by Equation (5-58). A suitable range for R is $4 \leq R \leq 9$. The quantiles $K_{r\Delta p}$, $r = 1, 2, \dots, R$, are chosen so that they define $R + 1$ equal-probability, nonoverlapping intervals of hydraulic conductivity:

$$P(K_{r\Delta p} \leq K \leq K_{(r+1)\Delta p}) = P(K < K_{\Delta p}) = P(K > K_{R\Delta p}) = \Delta p \quad (5-58)$$

for $r = 1, 2, \dots, R - 1$, in which

$$\Delta p = \frac{1}{R + 1} \quad (5-59)$$

is the probability of each of the $R + 1$ intervals of saturated hydraulic conductivity defined by the quantiles $K_{r\Delta p}$, $r = 1, 2, \dots, R$. The quantiles satisfy the probability statement:

$$P(K \leq K_{r\Delta p}) = r \cdot \Delta p \quad r = 1, 2, \dots, R \quad (5-60)$$

Step 2. The expected number of K measurements that fall in any of the $R + 1$ (equal-probability) intervals equals $n \cdot \Delta p$, in which n is the number of K measurements available. This number compares with the actual number of K measurements observed in the r -th interval, n_r , $r = 1, 2, \dots, R + 1$. Calculate the test statistic:

$$D = \frac{1}{n \cdot \Delta p} \sum_{r=1}^{R+1} (n_r - n \cdot \Delta p)^2 \quad (5-61)$$

Step 3. Determine the chi-squared critical value associated with a 5% significance level and $R - f$ degrees of freedom, $\chi^2_{0.05, R-f}$. The number of degrees of freedom of the chi-squared critical value is customarily R . However, $f = 2$ parameters ($\bar{Y}, \bar{\sigma}_Y$) must be estimated from the K data for the log-normal pdf (with lower bound equal to zero), and $f = 3$ parameters ($\alpha_Y, \beta_Y, \theta_Y$) must be estimated from data for the log-gamma pdf. Therefore, the number of degrees of freedom of the chi-squared critical value becomes $R - f$. The chi-squared critical value is tabulated in the technical literature. It can also be obtained using commercial software. Using Microsoft Excel the function CHISQ.INV.RT(0.05, $R - f$) returns the critical value $\chi^2_{0.05, R-f}$. The software MATLAB returns the critical value $\chi^2_{0.05, R-f}$ using the command chi2inv(0.95, $R-f$).

Step 4. If the test statistic D exceeds $\chi^2_{0.05, R-f}$, reject the fitted pdf as a suitable probability model for the K data. Otherwise, accept the fitted pdf as a suitable probability model for the K data.

Calculation Example on How to Fit and Test the Log-Gamma pdf

The goodness of fit of the log-gamma pdf to the K data shown in Figure 5-1 is assessed. The statistics pertaining to the K data are found at the beginning of Section 5.4.2. Choose $R = 9$. Quantify nine quantiles $K_{\Delta p} < K_{2\Delta p} < \dots < K_{9\Delta p}$ using Equation (5-48), which define $R + 1 = 9 + 1 = 10$ equal-probability intervals. The probability associated with each interval is $\Delta p = 1/10 = 0.10$ so that the expected number of K measurements in each interval is $n \cdot \Delta p = 201 \times 0.10 = 20.1$. The number of measurements observed in each interval is counted from the K sample. The test statistic [D , Equation (5-61)] is calculated and the chi-squared critical value determined. Table 5-2 summarizes the results.

The test statistic $D = 6.91 < \chi^2(0.05, 9 - 3 = 6) = 12.59$. Thus, the log-gamma pdf is accepted as a suitable probability model for the K data used in this example. Figure 5-6 summarizes in graphical form the key features of this example.

Goodness-of-fit tests other than the chi-square test are available. [Benjamin and Cornell \(1970\)](#) and [Gilbert \(1987\)](#) review several goodness-of-fit tests.

Table 5-2. Results of the Goodness-of-Fit Test for the Data in Figure 5-1 and the Log-Gamma pdf.

Interval number r	Upper limit of interval cm/s	Expected number $n \cdot \Delta p$	Observed number n_r	$(n_r - n \cdot \Delta p)^2 / (n \cdot \Delta p)$
1	$K_{0.1} = 1.248 \times 10^{-10}$	20.10	24	0.757
2	$K_{0.2} = 2.559 \times 10^{-10}$	20.10	20	0.000
3	$K_{0.3} = 4.494 \times 10^{-10}$	20.10	14	1.851
4	$K_{0.4} = 7.505 \times 10^{-10}$	20.10	19	0.060
5	$K_{0.5} = 1.245 \times 10^{-9}$	20.10	16	0.836
6	$K_{0.6} = 2.119 \times 10^{-9}$	20.10	28	3.105
7	$K_{0.7} = 3.859 \times 10^{-9}$	20.10	19	0.060
8	$K_{0.8} = 8.097 \times 10^{-9}$	20.10	22	0.180
9	$K_{0.9} = 2.433 \times 10^{-8}$	20.10	20	0.000
10	∞	20.10	19	0.060
Test statistic $D =$				6.91
$\chi^2(0.05, 6) =$				12.59

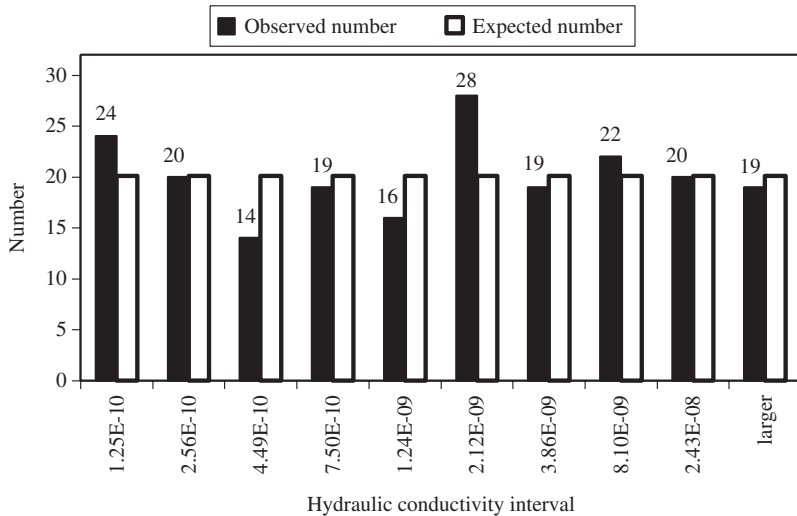


Figure 5-6. Histogram of the observed and expected numbers of K values (cm/s) in 10 equal-probability ($\Delta p = 0.10$) intervals. The expected number of K values equals 20.1 and is represented by the white bars.

5.4.3 Application of the Exponential Function to Hydraulic Conductivity Data

The exponential pdf has found applications in many fields of inquiry, including groundwater hydrology. Its pdf is

$$h_K(s) = \lambda e^{-\lambda s} \quad s \geq 0, \lambda > 0 \quad (5-62)$$

The parameter λ can be estimated from the sample average of the property (say, hydraulic conductivity), \bar{K} , as follows:

$$\bar{\lambda} = \frac{1}{\bar{K}} \quad (5-63)$$

The p -th quantile of the exponential pdf is

$$K_p = \frac{1}{\lambda} \ln \left(\frac{1}{1-p} \right) \quad (5-64)$$

Table 5-3 lists the hydraulic conductivity values measured with constant-head permeameter in a silty sand. The exponential pdf was fitted to the K data in Table 5-3 to yield $h_K(s) = 0.538 \exp(-0.538 s)$ with sample average $\bar{K} = 1.86$ and parameter $\bar{\lambda} = 0.538$.

Table 5-4 summarizes the results of the chi-squared test implement to assess the goodness-of-fit of the exponential pdf to the hydraulic conductivity data in Table 5-3. The test statistic $D = 1.23 < \chi^2(0.05, 4 - 1 = 3) = 7.81$. The exponential pdf is accepted as a suitable model for the data in Table 5-3. Figure 5-7 graphs the results of the chi-square test.

Table 5-3. Measurements of Hydraulic Conductivity in Silty Sand Obtained with Constant-Head Permeameter.

Sample number	Sample identification code	K (m/day)
1	GB1-2	0.14
2	GB1-4	3.52
3	GB1-6	1.12
4	GB1-7	4.58
5	GB2-1.5	2.42
6	GB2-3	0.23
7	GB3-2	5.36
8	GB3-3.5	0.63
9	GB3-5	2.51
10	GB4-3	0.72
11	GB4-4	0.95
12	GB5-4	1.21
13	GB5-6	0.76
Average $\bar{K} =$		1.86
$\bar{\lambda} =$		0.538

Source: Data from [Loáiciga \(2008b\)](#).

Table 5-4. Results of the Chi-Squared Goodness-of-Fit test Applied to the Data in Table 5-3 and the Exponential pdf.

Interval number r	Interval of K	Δp	$n \Delta p$	n_r	$(n_r \cdot n \cdot \Delta p)^2 / (n \cdot \Delta p)$
1	< 0.41	0.2	2.6	2	0.36
2	0.41–0.95	0.2	2.6	4	1.96
3	0.95–1.70	0.2	2.6	2	0.36
4	1.70–2.99	0.2	2.6	2	0.36
5	> 2.99	0.2	2.6	3	0.16
Test statistic $D =$					1.23
$\chi^2 (0.05, 3) =$					7.81

5.4.4 Application of the Gamma pdf to Residence Time and Age of Groundwater

The residence time of a groundwater particle (t_1) extends from the moment when the particle enters a groundwater flow system until it exits. In contrast, the age of a water particle (t_2) moving in groundwater is the time elapsed since the particle entered the groundwater flow system (see [Loáiciga 2004](#)). Let L be the total distance traveled by a groundwater particle in its journey through an aquifer, and K denote the hydraulic conductivity of the aquifer. Groundwater flow is assumed to take place under a constant hydraulic gradient g . The aquifer's porosity is n . The residence time of a groundwater particle equals the total travel distance L divided by the average groundwater velocity. The latter is obtained from Darcy's law. The residence time is then given by Equation (5-65):

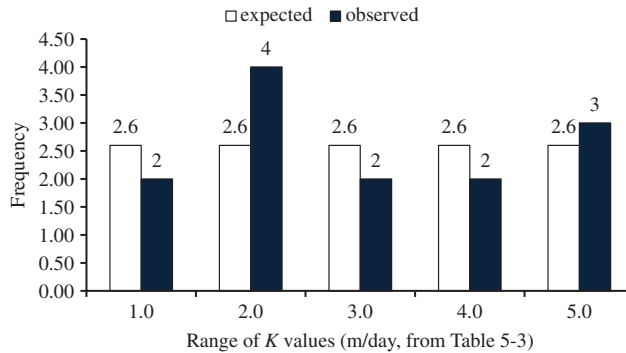


Figure 5-7. Example histogram of K data from Table 5-3 indicative of an exponential pdf.

$$t_1 = \frac{n L}{g K} \quad (5-65)$$

L and K are random variables. L and K are independent random variables. A gamma pdf is proposed to characterize the probabilistic characteristics of K . Therefore, the proposed pdf of K is a two-parameter gamma distribution:

$$f_K(x) = \frac{x^{a_2-1} e^{-\frac{x}{b_2}}}{\Gamma(a_2) b_2^{a_2}} \quad a_2 > 1; b_2 > 0; x \geq 0 \quad (5-66)$$

in which a_2 and b_2 are the shape and scale parameters of the gamma distribution, respectively, and $\Gamma(\cdot)$ denotes the gamma function, which defined as follows:

$$\Gamma(u) = \int_0^{\infty} e^{-v} v^{u-1} dv \quad (5-67)$$

The distribution of the total travel distance L is modeled herein by a two-parameter gamma distribution:

$$f_L(y) = \frac{y^{a_1-1} e^{-\frac{y}{b_1}}}{\Gamma(a_1) b_1^{a_1}} \quad a_1 > 1; b_1 > 0; y \geq 0 \quad (5-68)$$

The hydraulic conductivity K and total travel distance L have expected values $a_1 \cdot b_1$ and $a_2 \cdot b_2$, respectively. Equation (5-65) implies that the residence time is the scaled ratio of two independent gamma variables, in which the scaling ratio is the constant $n/g \equiv a > 0$. [Loáiciga \(2004\)](#) derives the pdf $f(t_1)$ of the residence time t_1

$$f_1(t) = \frac{\Gamma(a_1 + a_2)}{\Gamma(a_1) \Gamma(a_2)} \left(a \frac{b_1}{b_2} \right)^{a_2} \frac{t^{a_1-1}}{\left(t + a \frac{b_1}{b_2} \right)^{a_1+a_2}} \quad t \geq 0; a = n/g \geq 0 \quad (5-69)$$

The average residence time is derived from Equation (5-69) (letting $\beta = ab_1/b_2$):

$$T_1 = \int_0^{\infty} t f_1(t) dt = a \frac{b_1}{b_2} \frac{a_1}{(a_2 - 1)} \quad (5-70)$$

The average turnover time (T) of groundwater storage is defined as the storage (V) divided by the average rate of aquifer recharge (or discharge, R). Recharge into an aquifer displaces existing groundwater, so that the average time that it takes the recharge to replace the groundwater already in storage equals T . A plausible connection between T and T_1 is intuitive. The key to deciphering this connection is the groundwater age. The age of a groundwater particle (t_2) moving through an aquifer is the time elapsed since the particle entered the aquifer. Its pdf is denoted by $f_2(t)$. The latter pdf may not be specified independently of $f_1(t)$, the pdf of the residence time, because t_1 and t_2 are interdependent. Such interdependency is deducible from basic mass-balance considerations, as shown in [Loáiciga \(2004\)](#), who proved that the pdf of the groundwater age, $f_2(t)$ is (with $\beta = ab_1/b_2$):

$$f_2(t) = \frac{1}{T} (1 - F_1(t)) = \frac{1}{T} \left[1 - \frac{\Gamma(a_1 + a_2)}{\Gamma(a_1)\Gamma(a_2)} \frac{t^{a_1}}{a_1 \beta^{a_1}} \cdot {}_2F_1\left(a_1 + a_2, a_1; a_1 + 1; -\frac{t}{\beta}\right) \right] \quad (5-71)$$

in which $F_1(t)$ is the cumulative distribution function of the residence time (this is equal to the integral of $f_1(t)$); ${}_2F_1$ denotes Gauss's hypergeometric function ([Gradshteyn and Ryzhik 1994](#)); T is the expected turnover time of groundwater storage introduced previously. Differentiating in Equation (5-71) produces the following relationship between $f_1(t)$ and $f_2(t)$:

$$f_1(t) = -T \frac{df_2(t)}{dt} \quad (5-72)$$

Equation (5-72) allows us to write the average residence time as follows:

$$T_1 = \int_0^\infty t f_1(t) dt = -T \int_0^\infty t \frac{df_2(t)}{dt} dt = T \quad (5-73)$$

Equation (5-73) states that the average residence time equals the average turnover time, that is, $T_1 = T$. T_1 was given in Equation (5-70). The equality $T_1 = T = V / R$ introduces a constraint involving T_1 , V , and R . For example, if the average recharge rate R is known, the storage volume must be $V = T_1 R$. If V and R are known, then, from Equation (5-70), $a \cdot b_1 \cdot a_1/[b_2 (a_2 - 1)] = T_1 = V/R$, which imposes a constraint on the gamma parameters a_1 , a_2 , b_1 , and b_2 .

Taking into consideration the pdf $f_2(t)$ given in Equation (5-71), the expected groundwater age is (with $\beta = a b_1/b_2$, in which $a_2 > 2$ to achieve convergence to a finite T_2):

$$T_2 = \frac{1}{T} \int_0^\infty t \left[1 - \frac{\Gamma(a_1 + a_2)}{\Gamma(a_1)\Gamma(a_2)} \frac{t^{a_1}}{a_1 \beta^{a_1}} {}_2F_1\left(a_1 + a_2, a_1; a_1 + 1; -\frac{t}{\beta}\right) \right] dt \quad (5-74)$$

The average age of groundwater expressed by Equation (5-74) must be calculated numerically.

The results presented in this section demonstrate the flexibility of the gamma pdf in modeling basic groundwater processes analytically. The next section expands on the power of the gamma pdf to model real-world data.

5.4.5 Application of the Gamma pdf to Model Water Quality of Springs: Correlated Gamma Variables

Spring water in Las Palmas Creek, Santa Barbara, California, was tested to study the ratio of fecal coliforms (FC) to fecal streptococcus (FS) in it. FC and FS are enteric bacteria, that is, they live in

the intestinal tract of warm-blooded animals and are frequently used as indicators of fecal contamination of water bodies (Loáiciga and Leipnik 2005). Loáiciga and Leipnik (2005) fit FC and FS values with univariate gamma pdfs, allowing for correlation between them. The ratio FC/FS was determined from each pair of FC and FS values obtained from a single water sample. This procedure yielded 38 experimental values of FC/FS. The FC/FS ratio is of interest because, under suitable conditions, it may be used to discern the origin of enteric bacteria. In Las Palmas Creek, a FC/FS ratio in the interval [0, 0.4] was deemed of equine origin, while a FC/FS ≥ 3.0 was considered to be human in origin. The range $0.4 < \text{FC}/\text{FS} < 4.0$ was associated with mixed origin (i.e., humans, horses, and wildlife; Loáiciga and Leipnik 2005). If the sources of enteric bacteria are correctly identified, management actions are taken to counter the contamination of the spring water. Letting $X_1 \equiv \text{FC}$ and $X_2 = \text{FS}$, the correlated (four-parameter) gamma pdfs are

$$f(x_1) = \frac{x_1'^{\gamma\alpha_1-1} e^{-\frac{x_1'}{b_1}}}{\Gamma(\gamma\alpha_1)b_1^{\gamma\alpha_1}} \quad x_1 \geq \xi_1 \text{ if } b_1 > 0, \quad x_1 \leq \xi_1 \text{ if } b_1 < 0 \quad (5-75)$$

$$f(x_2) = \frac{x_2'^{\gamma\alpha_2-1} e^{-\frac{x_2'}{b_2}}}{\Gamma(\gamma\alpha_2)b_2^{\gamma\alpha_2}} \quad x_2 \geq \xi_2 \text{ if } b_2 > 0, \quad x_2 \leq \xi_2 \text{ if } b_2 < 0 \quad (5-76)$$

in which $x_j' = x_j - \xi_j$, $j = 1, 2$; $\gamma\alpha_1$ and $\gamma\alpha_2$ are the marginal shapes of the pdfs of X_1 and X_2 , respectively; (b_1, b_2) and (ξ_1, ξ_2) are scale and location parameters, respectively; and γ is a (collective) shape parameter of the bivariate distribution of X_1 and X_2 . $\alpha_1, \alpha_2, \gamma$ are positive. The correlation coefficient ρ is defined in terms of the means (μ_1, μ_2) and variances (σ_1^2, σ_2^2) of X_1 and X_2 , respectively, and a parameter β is introduced by Loáiciga and Leipnik (2005) to induce statistical dependence between X_1 and X_2 :

$$\rho = \frac{\mu_{1,2}}{\sigma_1\sigma_2} = \frac{E[(x_1 - \mu_1)(x_2 - \mu_2)]}{\sigma_1\sigma_2} = \frac{\beta\gamma}{\sigma_1\sigma_2} = \frac{\beta}{b_1b_2\sqrt{\alpha_1\alpha_2}} \quad (5-77)$$

The sample estimator of the correlation coefficient is (see Priestly 1989, Shumway and Stoffer 2010):

$$\bar{\rho} = \frac{1}{\bar{\sigma}_1\bar{\sigma}_2} \cdot \frac{1}{n} \sum_{j=1}^n (x_{1j} - \bar{X}_1)(x_{2j} - \bar{X}_2) \quad (5-78)$$

where (\bar{X}_1, \bar{X}_2) and $(\bar{\sigma}_1, \bar{\sigma}_2)$ are the sample estimators of the means and standard deviations of $X_1 = \text{FC}$, and $X_2 = \text{FS}$.

The goal of this application is to present the pdf of the ratio $Z = X_1/X_2 = \text{FC}/\text{FS}$. This pdf allows a characterization of Z , and, thus, of the origin of enteric bacteria in a probabilistic manner. Loáiciga and Leipnik (2005) derive the ratio pdf of the two correlated gamma variables, which is as follows (with $\xi_1 = \xi_2 = 0$):

$$g(z) = \sum_{n=0}^{\infty} \sum_{k=0}^n \sum_{j=0}^n (-1)^{n+k+j} \left(\frac{\beta}{b_1^{\alpha_1} b_2^{\alpha_2}} \right)^n \binom{-\gamma}{n} \binom{n}{k} \binom{n}{j} \left(\frac{b_1^{-(\gamma\alpha_1+k)}}{b_2^{\gamma\alpha_2+j}} \right) \cdot \frac{\Gamma(\lambda_{1,2}) \cdot z^{\lambda_1+k-n-1}}{\Gamma(\lambda_1 - n + k) \cdot \Gamma(\lambda_2 - n + j) \cdot z^{\lambda_{1,2}}} \quad (5-79)$$

in which $\lambda_j = \alpha_j(n + \gamma)$, $j = 1, 2$; $\lambda_{1,2} = \lambda_1 + \lambda_2 + k + j - 2n$:

$$z' = \frac{z}{b_1} + \frac{1}{b_2} \quad (5-80)$$

and

$$\binom{\lambda}{k} = \frac{\lambda(\lambda - 1) \dots (\lambda - k + 1)}{k!} \quad (5-81)$$

is the binomial coefficient for any real λ and nonnegative integer k . The estimated parameters in the Las Palmas Creek study were $\hat{b}_1 = \hat{b}_2 = 1.0$; $\hat{\alpha}_1 = 2.471$; $\hat{\alpha}_2 = 8.245$; $\hat{\beta} = 1.417$; $\hat{\gamma} = 0.35$, and $\hat{\rho} = 0.40$.

Figure 5-8 shows the empirical ($\text{obs} \times 100$) and calculated ($\text{model} \times 100$) frequencies of the ratio FC/FS in Las Palmas Creek, Santa Barbara, California (1999–2000). The empirical frequency in each range was calculated by dividing the number of observations within the range by the sample size (=38) and then scaling it by 100 for ease of interpretation. The model frequency in each range was calculated by integrating Equation (5-79) and then scaling it by 100 for ease of interpretation. In Figure 5-8, the range labeled 0.1 equals the interval [0.0, 0.1], that labeled 0.2 = [0.1, 0.2], and so on. The last range is ≥ 2.0 . Figure 5-8 shows an overall excellent agreement between the empirical and calculated probabilities. The observed and model-calculated probabilities $P(Z \leq 0.4)$ were 71.1% and 66.1%, respectively, which provides strong evidence of the predominance of equine fecal bacteria in Las Palmas Creek. A chi-squared goodness-of-fit test was implemented to ascertain the suitability of the pdf $g(z)$ [Equation (5-79)] for the ratio $Z = \text{FC}/\text{FS}$ to describe the FC/FS data. The chi-square statistic $\chi^2(0.05, 32) = 46.19$, larger than the test statistic $D = 24.70$. Thus, the null hypothesis of a gamma ratio distribution was not rejected at a 5% significance level. The P -value in this case was approximately 0.85, which demonstrates the robustness of the fit of the model probability to the empirical data.

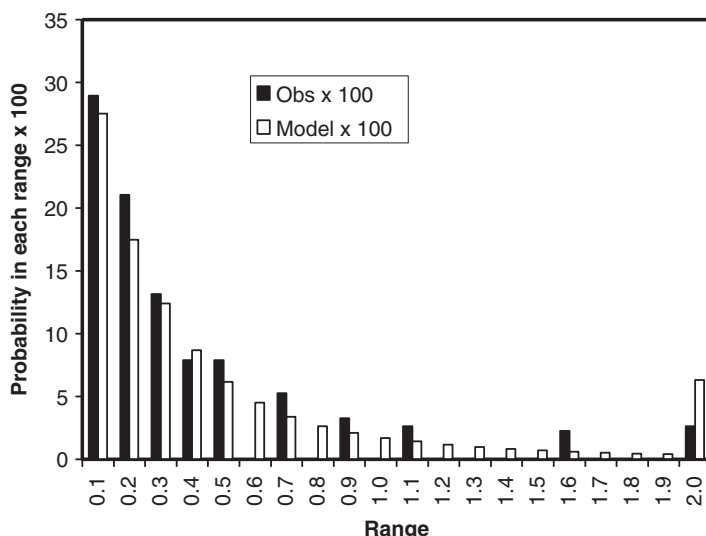


Figure 5-8. Empirical ($\text{obs} \times 100$) and calculated ($\text{model} \times 100$) frequencies of the ratio FC/FS at Las Palmas Creek, Santa Barbara, California (1999–2000). FC = fecal coliform concentration; FS = fecal streptococcus concentration.

5.5 CONCLUSIONS

This chapter has reviewed several pdfs commonly used in groundwater hydrology. The reviewed pdfs were illustrated with examples or data processes that demonstrated the richness of application possibilities in groundwater hydrology.

This chapter's examples show that probabilistic modeling of asymmetric aquifer properties, such as the hydraulic conductivity, can be accomplished with the log-gamma pdf with a flexibility that is unmatched by alternative pdfs.

The gamma pdf was shown to exhibit remarkable flexibility to model groundwater processes, such as residence time and age.

Many other applications of pdfs in groundwater hydrology are available that this chapter did not review. One of them is multivariate pdfs, which are used to model several random variables simultaneously. Other statistical methods in groundwater hydrology involve spatial correlation (geostatistics) and random fields. These were not pursued herein.

References

- Benjamin, J. R., and C. A. Cornell. 1970. *Probability, statistics, and decisions for civil engineers*. New York: McGraw-Hill.
- Dagan, G. 1989. *Flow and transport in porous formations*. Berlin: Springer.
- Freeze, R. A. 1975. "A stochastic conceptual analysis of one-dimensional groundwater flow in nonuniform homogeneous media." *Water Resour. Res.* **11** (5): 725–741.
- Gilbert, R. O. 1987. *Statistical methods for environmental pollution monitoring*. New York: Van Nostrand Reinhold.
- Gradshteyn, I. S., and I. M. Ryzhik. 1994. *Tables of integrals, series, and products*. 5th ed. San Diego: Academic Press.
- Journel, A., and C. Huijbregts. 1978. *Mining geostatistics*. New York: Academic Press.
- Krynnine, D. P., and W. R. Judd. 1957. *Principle of engineering geology and geotechnics*. New York: McGraw-Hill.
- Loáiciga, H. A. 2004. "Residence time, groundwater age, and solute output in steady-state groundwater systems." *Adv. Water Resour.* **27** (7): 681–688.
- Loáiciga, H. A. 2008a. *Standard guideline for estimating the effective saturated hydraulic conductivity*. ASCE 51-2008. Reston, VA: ASCE.
- Loáiciga, H. A. 2008b. *Standard guideline for fitting saturated hydraulic conductivity using probability functions*. ASCE/EWRI 50-2008. Reston, VA: ASCE.
- Loáiciga, H. A. 2010. *Standard guideline for the geostatistical estimation and block-averaging of homogeneous and isotropic saturated hydraulic conductivity*. ASCE/EWRI 54-10. Reston, VA: ASCE.
- Loáiciga, H. A. 2014. "Probability distributions in groundwater hydrology: Methods and applications." *J. Hydrol. Eng.* **20** (5): 04014063.
- Loáiciga, H. A., and R. B. Leipnik. 2005. "Correlated gamma variables in the analysis of microbial densities in water." *Adv. Water Resour.* **28** (4): 329–335.
- Loáiciga, H. A., J. Michaelsen, and P. F. Hudak. 1992. "Truncated distribution in hydrologic analysis." *Water Resour. Bull.* **28** (5): 853–863.
- Loáiciga, H. A., W. W.-G. Yeh, and M. A. Ortega-Guerrero. 2006. "Probability density functions in the analysis of hydraulic conductivity data." *J. Hydrol. Eng.* **11** (5): 442–450.
- Priestly, M. B. 1989. *Spectral analysis and time series*. London: Academic Press.
- Shumway, R. H., and D. S. Stoffer. 2010. *Time series analysis and its applications*. 3rd ed. New York: Springer.
- USGS (US Geological Survey). 1982. *Interagency advisory committee on water data*. Bulletin 17B. Reston, VA: USGS.

CHAPTER 6

Modeling Streamflow Variability

A. Cancelliere

6.0 INTRODUCTION

The term streamflow refers to the component of the hydrological cycle that transfers along the surface of the earth precipitation excess (i.e., not evaporated) in a watershed to the oceans. In a given point of the hydrographic network, streamflows are the result of the routing of runoff from the upstream watershed through storage mechanisms and of the subsurface and groundwater flow. Thus, streamflow variability stems from the variability of the climate forcing (precipitation and evaporative demand from the atmosphere) and from the dynamics of subsurface and groundwater flow. Streamflows can be investigated at different time scales, according to the purpose of the analysis. Broadly speaking, time scales of interest can range from hourly to daily for flood analysis, from daily to yearly for water management problems (e.g., water supply, hydroelectric production, navigation, recreational use, pollution control, etc.), up to decades and more to investigate long-term variability in the hydrological cycle. In the present chapter, methods for the stochastic analysis and modeling of streamflow variability are illustrated, with a specific focus on water management purposes. In particular, stochastic features describing variability of streamflow time series at time scales ranging from weekly to yearly are presented, and the main stochastic models that can be applied to reproduce such variability are illustrated.

6.1 STOCHASTIC FEATURES OF STREAMFLOW TIME SERIES

When analyzing streamflow variability at time scales ranging from weekly to yearly, different stochastic features can be identified, whose origin can be related to the complex mechanisms leading to the streamflow's formation. In general terms, different features may arise, or become more evident, as the time scale of aggregation changes. At longer time scales, sources of variability in streamflows include natural and/or anthropogenic changes in watershed geomorphology, soil and land use characteristics, river network, and development of water diversions or transfers from other basins. Changes or long-term variability in climate may also induce variability in streamflows. Such features are generally detected at yearly time scales and may also include long-term memory in the series.

Seasonality, in the form of a distinct pattern repeating from year to year, becomes apparent when data are aggregated at a subyearly time scale. Such pattern is clearly inherited from periodicity in the meteorological and hydrological drivers (mainly precipitation and temperatures) behind the streamflow formation due to the rotation of the Earth around the sun.

Short-term memory, in other words, the tendency to observe high streamflows followed by high streamflows and low values followed by low values, is mainly due to the dynamics of the

transformation of precipitation into streamflows. This is generally more evident at subyearly time scales, though in many cases streamflows exhibit short-term memory also at yearly time scales. Streamflows may also exhibit long-term memory or long-term dependence, a characteristic that has been found in many geophysical time series.

Finally, intermittency, in other words, temporary lack of streamflow, is due to characteristics of the meteorological drivers but is also affected by the complex storage mechanisms underlying the rainfall–streamflow transformation. For instance, in arid or semi-arid climates, intermittent streamflows can be observed at different time scales ranging from weekly to (in extreme cases) yearly.

In what follows, some of the aforementioned features are described, and basic statistical tools for their characterization are illustrated.

6.1.1 Autocorrelation

With reference to a time series, the autocorrelation function (ACF) measures dependence in time, namely how past values affect present values. The term memory is frequently adopted to describe such feature of streamflows, and from a physical standpoint, the time dependence often observed in streamflow series can be ascribed, apart from memory in meteorological forcing, which is generally less evident, to the complex storage mechanisms involved in the transformation of precipitation into streamflows. Therefore, basins with large surface storage in the form of lakes, swamps, snow and glaciers, or significant subsurface and groundwater flows are generally characterized by significant autocorrelation. With reference to a stationary sample series x_t , $t = 1, 2, \dots, n$, the autocorrelation r_k at lag k can be estimated as (Brockwell and Davis 2002):

$$r_k = \frac{\sum_{t=1}^{n-k} (x_{t+k} - \bar{x})(x_t - \bar{x})}{\sum_{t=1}^n (x_t - \bar{x})^2} \quad (6-1)$$

where $\bar{x} = \sum_{t=1}^n x_t / n$ is the sample mean of the series.

The plot of r_k with k generally reveals a decreasing pattern, because the influence of past values on present ones is expected to decrease with time lag. Fast rate of decay to zero of the autocorrelogram indicates short memory in the series, while a relatively slow decreasing pattern may suggest the presence of long-term persistence or long memory in the process. From a mathematical standpoint, a process is said to have short memory if the autocorrelation function is absolutely summable, whereas in the opposite case long memory arises (Beran 1994).

Due to the sampling variability of the autocorrelation function, its pattern will generally oscillate around zero even at large lags. Then statistical tests can be employed to assess whether nonzero values are due to sampling variability of the autocorrelation or to the presence of time dependence. Under the zero autocorrelation hypothesis, approximate and asymptotic 95% for r_k bounds are given by $\pm 1.96/\sqrt{n}$ (Brockwell and Davis 1991).

Figure 6-1 shows two examples of annual autocorrelation functions, along with the related 95% bounds (dashed lines). The figure at the top shows a slow decaying autocorrelation of the annual flows of the White Nile River at Mongalla, South Sudan, which is indicative of high persistence in the series. In contrast, the figure on the bottom shows a fast decaying autocorrelation of annual streamflows of Yakima river at Cle Elum, Washington State, with values not statistically significant for lags greater than 1.

6.1.2 Seasonality

Like most hydroclimatic series, streamflow series exhibit seasonal (or periodic) patterns at time scales less than a year. Such short-term periodic behavior is generally due to the annual revolution of the Earth around the sun, which induces seasonal patterns in all hydroclimatic processes. Seasonality results in nonstationarity of streamflows at subannual time scales, in the sense that different probability distributions should be assumed for the different seasons. Generally, this is evident in

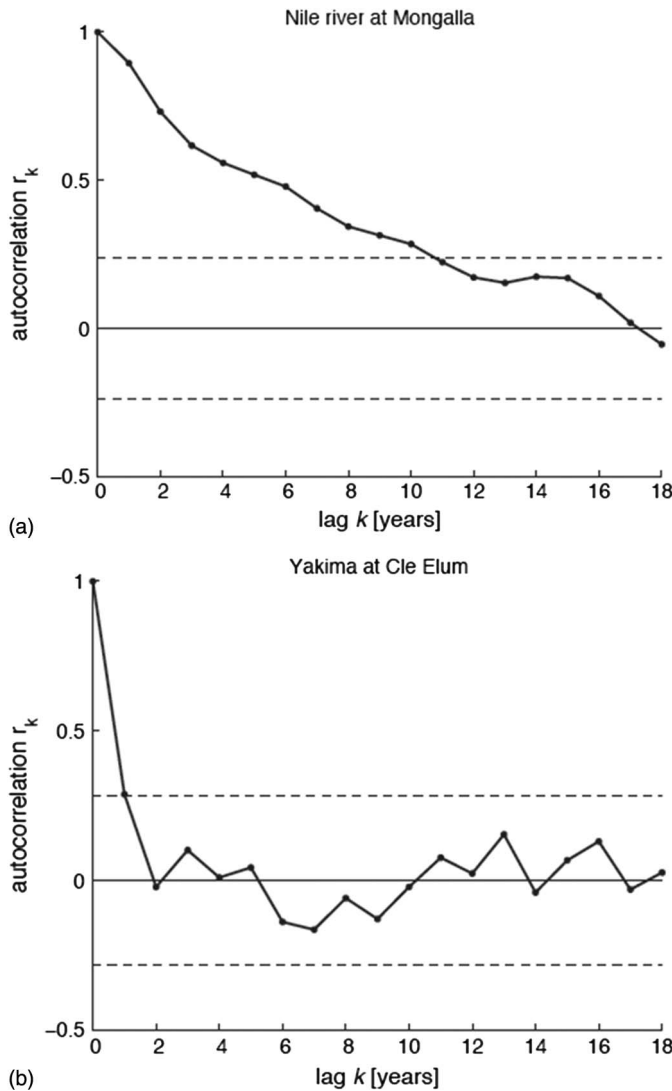


Figure 6-1. Autocorrelation functions of annual streamflows of the Nile River at Mongalla (a) and of Yakima river at Cle Elum (b).

Source: Data from Salas et al. (1995). (a) Data from Bonneville Power Plant Administration, (b) personal communication.

terms of statistical characteristics such as mean, variances, and so on. For instance when analyzing streamflows at monthly time scales, mean, variances, and other statistics computed separately for each month will generally exhibit a distinct periodic behavior throughout the year, which is indicative of the periodic stochastic nature of the series. The simplest way to investigate periodicity in seasonal series of streamflows is by computing basic statistics for the different seasons. With reference to a seasonal streamflow series $x_{\nu,\tau}$, where $\nu = 1, \dots, n$ indicates the year, n is the number of available years of observations and $\tau = 1, \dots, \omega$ indicates the season (for monthly series $\omega = 12$), the seasonal mean, variances, and skewness coefficients can be computed as

$$\bar{x}_\tau = \frac{\sum_{\nu=1}^n x_{\nu,\tau}}{n} \quad (6-2)$$

$$s_{\tau}^2 = \frac{\sum_{\nu=1}^n (x_{\nu,\tau} - \bar{x}_{\tau})^2}{n} \quad (6-3)$$

$$G_{\tau} = \frac{\sum_{\nu=1}^n (x_{\nu,\tau} - \bar{x}_{\tau})^3 / n}{s_{\tau}^3} \quad (6-4)$$

Furthermore, periodic lag- k autocorrelation and autocovariances can be computed respectively as

$$r_{k,\tau} = \frac{\sum_{\nu=1}^n (x_{\nu,\tau} - \bar{x}_{\tau})(x_{\nu,\tau-k} - \bar{x}_{\tau})}{\sum_{t=1}^n (x_{\nu,\tau} - \bar{x}_{\tau})^2} \quad (6-5)$$

$$c_{k,\tau} = \frac{1}{n} \sum_{\nu=1}^n (x_{\nu,\tau} - \bar{x}_{\tau})(x_{\nu,\tau-k} - \bar{x}_{\tau}) \quad (6-6)$$

where cyclic conditions are assumed, namely $x_{\nu,\tau-k} = x_{\nu-1,\omega-k+\tau}$ for $\tau - k \leq 0$. The plot of the aforementioned statistics versus the season τ will generally reveal a periodic pattern.

Periodicity can also be investigated making use of the periodogram of the series, namely the discrete Fourier transform of the sample autocovariance function (e.g., Brockwell and Davis 2002):

$$I_n(\lambda_k) = \frac{1}{n} \sum_{s=1}^n \sum_{t=1}^n (x_s - \bar{x})(x_t - \bar{x}) e^{-i(s-t)\lambda_k} \quad (6-7)$$

where λ_k are the Fourier frequencies $2\pi k/n$ and n is the length of the sample. The plot of the periodogram versus the frequency λ_k represents a useful diagnostic tool, because the presence of a distinct peak in the plot at frequency λ_k will indicate periodicity in the series, with period $2\pi/\lambda$ expressed in the same units as the aggregation time scale of the original time series (for instance months). As an example, in Figure 6-2, the periodogram of the monthly streamflow series of Salso river at Pozzillo is plotted against the frequency λ_k . From the plot, a peak at frequency $\lambda_k = \pi/6$ is clearly evident that corresponds to a period of 12 months, as expected.

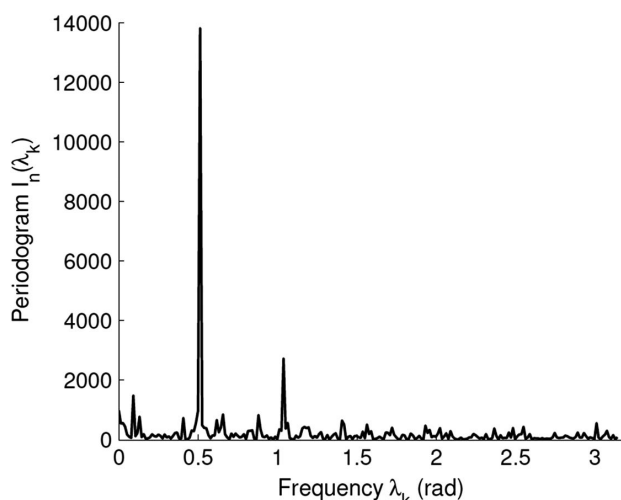


Figure 6-2. Periodogram of Salso at Pozzillo monthly streamflows.

Source: Data from Indelicato et al. (1989) and further updates.

6.1.3 Storage-Related Statistics and Hurst Effect

Long-term variability in streamflows can also be characterized in terms of reservoirs' storage-related statistics. With reference to a series of observations, x_t , $t = 1, \dots, n$, cumulative departures from the mean (partial sums) can be computed as

$$S_j = S_{j-1} + (x_j - \bar{x}) \quad j = 1, \dots, n \quad (6-8)$$

where \bar{x} is the sample mean and $S_0 = 0$. The series S_j is the basis to compute storage-related statistics under the assumption of a constant draft equal to the long-term mean. In particular, the plot of S_j versus j enables derivation of the minimum reservoir capacity C_n needed to supply a demand equal to the long-term mean, according to the well-known sequent peak algorithm (e.g., Klemeš 1987).

The range is defined as

$$R_n^* = \max(S_0, S_1, \dots, S_n) - \min(S_0, S_1, \dots, S_n) \quad (6-9)$$

whereas the rescaled range is

$$R_n^{**} = R_n^*/s \quad (6-10)$$

where s is the sample standard deviation of the series. Both the range and rescaled range are related to C_n and therefore have been widely studied and used as a measure of long-term variability in streamflow series. In particular, the question of their variability with the sample size has been investigated since the pioneering work by Hurst (1951), who, while studying the long-term storage requirements for the Nile river, analyzes several geophysical time series including streamflows and finds empirically that R_n^{**} is proportional to n^H , with $H > 1/2$. However, from a theoretical standpoint, it can be shown that, asymptotically, $H = 1/2$ for normal independent processes (Feller 1951) and for autoregressive processes (Mandelbrot and Van Ness 1968). Such contrast between theoretical findings and empirical evidence, often termed Hurst phenomenon or Hurst effect, suggests that the independence or autoregressive assumption for geophysical series (and streamflow in particular) may not be adequate to model long-term variability, giving rise to the need for more complex tools (Mandelbrot 1965). Since Hurst's work, the quest for an explanation has sparked the interest of many researchers (see, e.g., Bras 1985, Hipel and McLeod 1994). Among the possible causes of the observed discrepancy, variability with time of the mean (Boes and Salas 1978), presence of trends (Bhattacharya et al. 1983), preasymptotic behavior due to limited length of observed records (Salas et al. 1979), and long-term memory and scaling dynamics of natural processes (Mandelbrot and Wallis 1968) have been suggested as explanations of the Hurst phenomenon.

Estimators of the H exponent have been proposed by many authors either through parametric and nonparametric approaches, since Hurst's original estimator K (Hurst 1951, 1956):

$$K = \frac{\log(\bar{R}_n^{**})}{\log(n/2)} \quad (6-11)$$

Estimates of H can be obtained as the slope of the fitting line, in a log-log scale, of the plot of R_n^{**} versus $n/2$ (Wallis and Matalas 1970). Other estimators are based on assuming a stochastic structure for the underlying series. To this end, estimators based on an autoregressive moving average (ARMA) process (Siddiqui 1976, Grimaldi 2004, Piccolo 1990) or on Hurst–Kolmogorov dynamics (Koutsoyiannis 2003) can be adopted. The practical implications of the presence of the Hurst effect in streamflow series are obviously related to reservoir storage problems either for design or management. Exponents H greater than $1/2$ would imply that larger reservoir storages are required with respect to the case of independent or autocorrelated streamflow series. However, Klemeš et al. (1981) analyzes the practical implications of long-term memory in reservoir design, concluding that

given the uncertainties in available socioeconomic and hydrologic data, use of long-memory models cannot be justified. Nonetheless, long memory influences the statistical significance of observed trends in hydroclimatological series, and therefore apparent trends may arise due to persistence in the series (Cohn and Lins 2005). To this end, models able to reproduce the Hurst effect have been proposed to describe long-term variability in climate, thus providing an explanation of the apparent nonstationarities observed in many hydrometeorological series (Koutsoyiannis 2002, 2011).

Example 6-1: Analysis of Variability Features of Poudre River Streamflows

Figure 6-3 shows the plot of the yearly (top) and monthly (bottom) streamflows of the Poudre River at Mouth of the Canyon. The yearly plot indicates a relatively large variability from year to year while the monthly plot exhibits a clear periodic (seasonal) pattern in the streamflows.

To characterize the seasonal features, monthly means, standard deviations, and skewness have been computed from Equations (6-2), (6-3), and (6-4), respectively. Figure 6-4 plots the results. All statistics change significantly from month to month, which confirms the distinct seasonal pattern of the underlying monthly series. In particular, the monthly means indicate larger flows during the

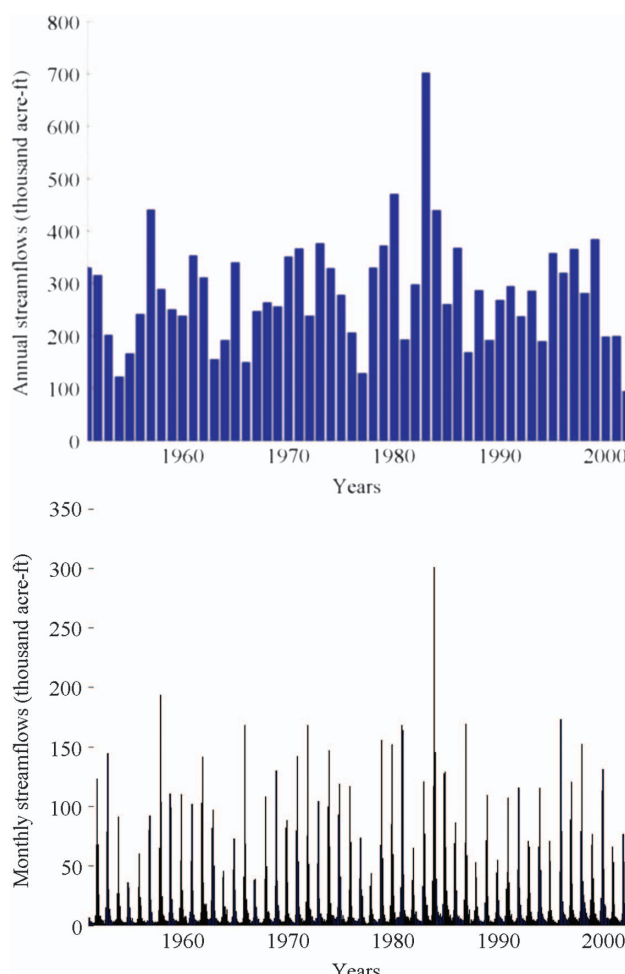


Figure 6-3. Poudre River at Mouth of the Canyon river flows (1951–2002) aggregated at an annual time scale (top) and a monthly time scale (bottom).

Source: Data from Northern Colorado Water Conservancy District.

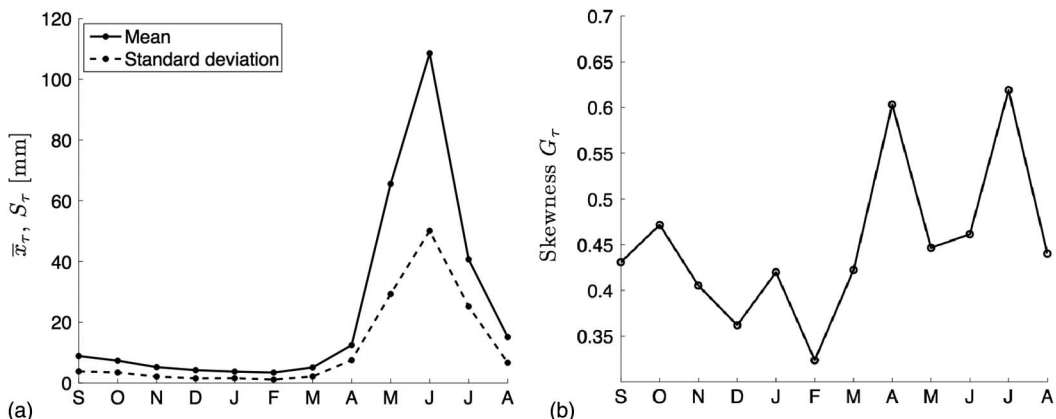


Figure 6-4. Seasonal means, standard deviations (a) and skewness (b) for Poudre River at Mouth of the Canyon monthly flows (1951–2002).

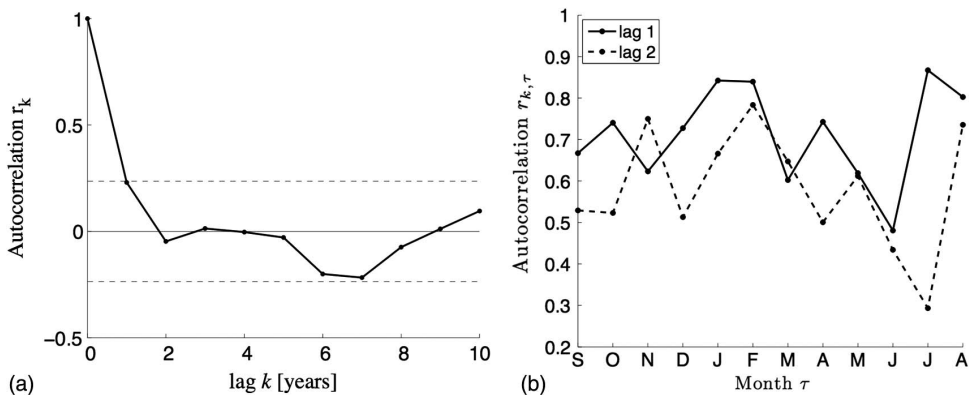


Figure 6-5. Annual (a) and lag-1 and lag-2 monthly correlations (b) for streamflows of the Poudre River at Mouth of the Canyon.

spring–summer months and very low flows during the fall and winter, which is distinctive of a streamflow regime driven by snowmelt.

Furthermore, the autocorrelation features of the series at the annual and monthly time scales have been determined using Equations (6-1) and (6-5), respectively. Figure 6-5 shows the results. In panel (a), the autocorrelation r_k at annual time scale is shown versus the lag k and the approximate confidence bounds at 95% level. Panel (b) shows the monthly correlations for lags 1 and 2. From the figure a relatively weak autocorrelation structure can be observed for the Poudre River annual time series, which suggests a weak memory of the process from one year to the other. However, as expected, stronger month-to-month correlations are observed at the monthly time scale. Furthermore, distinctive periodic patterns of monthly correlations can also be observed.

6.2 MODELING OF STREAMFLOW TIME SERIES

Stochastic modeling of streamflow series has become one of the standard tools for approaching several engineering problems, since the pioneering work of Thomas and Fiering (1962) and

[Yevjevich \(1963\)](#). The availability of mathematical models that can reproduce the main probabilistic features of streamflows at different time scales, and their evolution with time, provides useful information for simulation and forecasting studies. Several types of models have been proposed in literature and have been successfully applied to water resources problems, differing according to the features they intend to reproduce (e.g., autocorrelation, seasonality, intermittency, and long memory) and for the type of approach, either parametric or nonparametric. Furthermore, when the interest lies in modeling complex river systems, the need to account for other features arises. In what follows, the main types of models that have been proposed for modeling univariate streamflow series are briefly illustrated. For further details, the reader is referred to [Salas \(1993\)](#), [Hipel and McLeod \(1994\)](#), and [Sveinsson and Salas \(2017\)](#). Section 6.4 presents the main methodologies available to model complex river systems.

6.2.1 ARMA Models

Among the several modeling schemes proposed to reproduce stochastic variability of streamflows, the class of autoregressive moving average models have found probably the most widespread applications. Among the reasons for their success are their ability to reproduce virtually any observed autocorrelation function and their relative simplicity. Furthermore, their structure can be linked to simple conceptual rainfall–streamflow models (e.g., [Fiering 1967](#), [Salas and Smith 1981](#), [Salas and Obeysekera 1992](#)). With reference to a nonseasonal time series X_t , the general form of an ARMA(p, q) model is

$$X_t = \mu + \sum_{i=1}^p \phi_i(X_{t-i} - \mu) - \sum_{j=1}^q \theta_j \varepsilon_{t-j} + \varepsilon_t \quad (6-12)$$

where ϕ_1, \dots, ϕ_p are the p autoregressive parameters, $\theta_1, \dots, \theta_q$ are the q moving average parameter, μ is a parameter representing the mean of the process, and ε_t is a white noise (not autocorrelated) process with mean zero and variance σ_ε^2 . In practice, generally low-order ARMA models have been employed for modeling annual streamflows or seasonal flows after seasonal standardization. For instance, letting $p = 1$ and $q = 0$, the well-known lag-1 autoregressive model AR(1) is obtained:

$$X_t = \mu + \phi(X_{t-1} - \mu) + \varepsilon_t \quad (6-13)$$

whose variance and autocorrelation function $\rho(h)$ are given by

$$\text{Var}[X_t] = \frac{\sigma_\varepsilon^2}{(1 - \phi^2)} \quad (6-14)$$

$$\rho(h) = \phi^h \quad (6-15)$$

Similarly, by letting $p = 1$ and $q = 1$, the ARMA(1, 1) is obtained:

$$X_t = \mu + \phi(X_{t-1} - \mu) - \theta \varepsilon_{t-1} + \varepsilon_t \quad (6-16)$$

whose variance and autocorrelation function are given by

$$\text{Var}[X_t] = \frac{1 - 2\phi\theta + \theta^2}{1 - \phi^2} \sigma_\varepsilon^2 \quad (6-17)$$

$$\rho(1) = \frac{(1 - \phi\theta)(\phi - \theta)}{1 - 2\phi\theta + \theta^2} \quad (6-18)$$

$$\rho(h) = \rho(1)\phi^h, \quad h > 1 \quad (6-19)$$

For the general case of the ARMA(p, q) model, expressions for the variance and autocorrelation function can be derived making use of the so-called infinite moving average (MA) representation valid if the process is causal, namely if $1 - \phi_1 z - \dots - \phi_p z^p \neq 0$ for all $|z| \leq 1$ (Brockwell and Davis 2002):

$$\rho(h) = \frac{\sum_{j=0}^{\infty} \psi_j \psi_{j+h}}{\sum_{j=0}^{\infty} \psi_j^2} \quad (6-20)$$

where the coefficients ψ_j are given by the recursive equation:

$$\psi_j - \sum_{k=1}^p \phi_k \psi_{j-k} = \theta_j, \quad j = 0, 1, \dots \quad (6-21)$$

and $\theta_0 = 1$ and $\theta_j = 0$ for $j > q$ and $\psi_j = 0$ for $j < 0$.

Similarly, the variance of the process is given by

$$\text{Var}[X_t] = \sigma_e^2 \sum_{j=0}^{\infty} \psi_j^2 \quad (6-22)$$

Although in some cases Equations (6-20) and (6-22) may be used to derive analytical expressions of the autocorrelation and variance of an ARMA(p, q) model, in practice, they are generally computed numerically by truncating the infinite sums to an appropriate value.

Several methods have been proposed to estimate the parameters of an ARMA(p, q) model. Generally, the mean μ is estimated as the sample mean \bar{x} . The remaining parameters can be estimated either by method of moments (MOM) or by least square (LS) or maximum likelihood (ML) procedures.

For example for the AR(p) and low-order ARMA(p, q), MOM can be employed for deriving analytical solutions for the parameter estimators. The Yule–Walker equation can be used to derive MOM estimators for the parameters ϕ_1, \dots, ϕ_p of an AR(p) model (Brockwell and Davis 2002) as a function of the estimator r_k of $\rho(h)$:

$$r_{|k|} = \phi_1 r_{|k-1|} + \dots + \phi_p r_{|k-p|} \quad (6-23)$$

Writing the aforementioned equations for $k = 1, \dots, p$, a linear system of p equations can be solved for the p unknown autoregression parameters. Once the ϕ_j s are estimated, the variance of the noise σ_e^2 can be estimated as

$$\hat{\sigma}_e^2 = s^2 \left(1 - \sum_{j=1}^p \phi_j r_j \right) \quad (6-24)$$

where s^2 is the sample variance of the available observations.

As a particular case, the following estimators are easily derived for the two parameters ϕ_1 and σ_e^2 of an AR(1) model:

$$\hat{\phi}_1 = r_1 \quad (6-25)$$

$$\hat{\sigma}_e^2 = s^2 (1 - r_1^2) \quad (6-26)$$

Likewise, for the ARMA(1, 1) model, the following MOM estimators can be derived (Salas 1993):

$$\hat{\phi}_1 = \frac{r_2}{r_1} \quad (6-27)$$

$$\hat{\sigma}_e^2 = \frac{s^2(1 - \hat{\phi}_1^2)}{(1 - 2\hat{\phi}_1\hat{\theta}_1 + \hat{\theta}_1^2)} \quad (6-28)$$

$$\hat{\theta}_1 = \frac{-b \pm \sqrt{b^2 - 4(r_1 - \hat{\phi}_1)^2}}{2(r_1 - \hat{\phi}_1)} \quad (6-29)$$

where $b = 1 - 2\hat{\phi}_1 r_1 + \hat{\phi}_1^2$.

As the orders p and q of ARMA models increases, MOM estimators are more difficult to derive in closed form. In such cases, the system of equations obtained by equating the theoretical autocorrelations [given by Equation (6-20)] with the corresponding sample estimates can be solved numerically for the parameters ϕ_1, \dots, ϕ_p and $\theta_1, \dots, \theta_q$.

As an alternative to MOM, ML methods can be employed for parameter estimation of ARMA models based on searching the set of parameters that maximize the likelihood function. To this end, Gaussian likelihood is generally assumed, and numerical optimization is applied to find the maximum (Brockwell and Davis 2002). Approximate maximum likelihood estimates can also be found by minimizing the sum of squared residuals (Salas 1993):

$$SSR(\phi_1, \dots, \phi_p, \theta_1, \dots, \theta_q) = \sum \hat{\varepsilon}_t^2 \quad (6-30)$$

where $\hat{\varepsilon}_t$ are the residuals obtained from Equation (6-12) as a function of the observations.

Furthermore, the Hannan–Rissanen algorithm (Hannan and Rissanen 1982) can be employed, which yields estimates in a least square sense, and they can be used directly or as starting solution for numerical optimization. The basic idea behind the Hannan–Rissanen algorithm is to consider the ARMA process as a multiple linear regression of X_t on $X_{t-1}, X_{t-2}, \dots, X_{t-p}$ and on the residuals $\varepsilon_{t-1}, \varepsilon_{t-2}, \dots, \varepsilon_{t-q}$. Because the latter are unknown, first a high-order $AR(p^*)$ model with $p^* > \max(p, q)$ is fitted to the zero mean observations, for instance using the Yule–Walker equations. Based on such a model, the residuals are computed as

$$\varepsilon_t^* = X_t - \phi_1^* X_{t-1} - \phi_2^* X_{t-2} - \dots - \phi_{p^*}^* X_{t-p^*} \quad (6-31)$$

Then, the preliminary estimates of the ARMA(p, q) model parameters can be found by regressing X_t on $X_{t-1}, X_{t-2}, \dots, X_{t-p}$ and on the residuals $\varepsilon_{t-1}^*, \varepsilon_{t-2}^*, \dots, \varepsilon_{t-q}^*$ in other words, by minimizing the following sum of squares:

$$\begin{aligned} SSQ(\phi_1, \dots, \phi_p, \theta_1, \dots, \theta_q) = & \sum_{t=p^*+1}^n (X_t - \phi_1 X_{t-1} - \phi_2 X_{t-2} - \dots - \phi_p X_{t-p} \\ & - \theta_1 \varepsilon_{t-1}^* - \theta_2 \varepsilon_{t-2}^* - \dots - \theta_q \varepsilon_{t-q}^*)^2 \end{aligned} \quad (6-32)$$

Once the autoregressive and moving average parameters have been determined, the Hannan–Rissanen estimate of the white noise variance is

$$\hat{\sigma}_e^2 = \frac{SSQ}{n - p^*} \quad (6-33)$$

6.2.2 Modeling of Seasonal Series

As mentioned previously, modeling of streamflows at time scales smaller than a year requires accounting for the periodic stochastic nature of the underlying time series. Broadly speaking, two main modeling approaches can be employed to model such periodicity. The first is based on removing the periodic components and applying a stationary model to the resulting residuals. This procedure is often referred to as “deseasonalization.” The second approach is based on models that are intrinsically periodic stochastic and therefore do not require removing the periodicity from the series in advance.

6.2.2.1 Deseasonalization

The term deseasonalization refers to the removal of deterministic periodic components from a time series. Although in principle, the resulting residuals should be independent and identically distributed (i.i.d.), in practice, deseasonalization is generally limited to a few stochastic features of the time series, and therefore the residuals cannot strictly be considered i.i.d.

Among deseasonalization techniques, perhaps the simplest is to operate a seasonal standardization of the series using the periodic mean and variance as (e.g., Grimaldi 2004):

$$y_t = \frac{x_{\nu,\tau} - \mu_\tau}{\sigma_\tau} \quad (6-34)$$

where y_t , $t = (\nu - 1)\omega + \tau$ is the zero-mean, unit-variance residual series and μ_τ and σ_τ^2 , $\tau = 1, \dots, \omega$, are the periodic (seasonal) means and variances, respectively. Although the computed residuals will have zero mean and unit variance, seasonal patterns in higher-order moments and in the autocorrelation structure will remain.

As the time scale of the analysis decreases (e.g., weekly or daily), the number of “seasons” increases and so will the number of means and variances to be considered in Equation (6-34). Furthermore, high-frequency variations of seasonal statistics due to sample variability will yield irregular patterns of the statistics versus the season. Then, to reduce the number of deseasonalization parameters, one may smooth the seasonal statistics using, for example, Fourier series. For illustration, with reference to the seasonal means \bar{x}_τ , $\tau = 1, \dots, \omega$, a linear combination of sine and cosine curves are fitted to the \bar{x}_τ . The fitted means $\hat{\mu}_\tau$ are given by

$$\hat{\mu}_\tau = A_0 + \sum_{k=1}^{n_\omega} \left(A_k \cos \frac{2\pi k \tau}{\omega} + B_k \sin \frac{2\pi k \tau}{\omega} \right) \quad (6-35)$$

where n_ω is the number of coefficients, $A_0 = \frac{1}{\omega} \sum_{\tau=1}^{\omega} \bar{x}_\tau$, and the Fourier coefficients A_k and B_k are given by

$$A_k = \frac{2}{\omega} \sum_{\tau=1}^{\omega} \bar{x}_\tau \cos \frac{2\pi k \tau}{\omega} \quad (6-36)$$

$$B_k = \frac{2}{\omega} \sum_{\tau=1}^{\omega} \bar{x}_\tau \sin \frac{2\pi k \tau}{\omega} \quad (6-37)$$

The same approach can be applied with reference to seasonal standard deviations, or to any other seasonal statistics. The advantage of these procedure is that, generally, a small number of Fourier components n_ω is enough to capture the intraannual variability of the statistics and therefore the overall number of parameters can be significantly reduced.

Alternatively, normal quantile transformation (NQT) can be employed, which is a particular case of an equal probability transformation, or probability integral transform. NQT has been used in several hydrological studies and is fully described in [Krzysztofowicz \(1997\)](#) and [Montanari \(2005\)](#). It is based on fitting ω cumulative distribution functions (cdf) $F_\tau(x)$ to the series $x_{\nu,\tau}$ for fixed $\tau = 1, \dots, \omega$ and by computing the deseasonalized value y_t as the value of a standard normal random variable with the same nonexceedence probability of $x_{\nu,\tau}$:

$$y_t = \Phi^{-1}(F_\tau(x_{\nu,\tau})) \quad (6-38)$$

where the notation $\Phi^{-1}()$ is the inverse of the standard normal cumulative distribution function. The same approach can also be applied using the empirical distribution functions of $x_{\nu,\tau}$ for fixed τ , instead of the fitted cdf $F_\tau(x)$.

All of the aforementioned approaches will yield zero mean and unit variance residuals. In addition, the NQT will yield residuals identically distributed according to a standard normal. Then, nonseasonal models (e.g., ARMA) can be applied to the residuals either for generation or forecasting purposes. The generated residuals can then be transformed back in the original domain ([McLeod and Hipel 1978](#)). However, the limitation of the referred approaches is that the season-to-season correlations may not be adequately modeled.

6.2.2.2 Periodic Models

As already mentioned, the deseasonalization procedures described in Section [6.3.3](#) will not remove periodic components in the autocorrelation function, and therefore, when a distinct periodic behavior in the autocorrelation is observed, other modeling strategies should be employed. From a physical standpoint, seasonality in the autocorrelation may arise from different prevailing storage mechanisms in the rainfall–streamflow transformation within the year, especially in the case of ephemeral/intermittent streamflows. Several models that explicitly account for seasonal components have been suggested, such as the class of periodic autoregressive moving average (PARMA) and the seasonal autoregressive integrated moving average. With reference to a seasonal streamflow series $X_{\nu,\tau}$, $\tau = 1, \dots, \omega$, the general form of a PARMA(p, q) model is ([Salas 1993](#)):

$$X_{\nu,\tau} = \mu_\tau + \sum_{i=1}^p \phi_{i,\tau}(X_{\nu,\tau-i} - \mu_\tau) - \sum_{j=1}^q \theta_{j,\tau}\varepsilon_{\nu,\tau-j} + \varepsilon_{\nu,\tau} \quad (6-39)$$

where μ_τ is the seasonal means, $\varepsilon_{\nu,\tau}$ is a zero mean seasonal white noise process with seasonal variances $\sigma_{\varepsilon\tau}^2$ that are uncorrelated with $X_{\nu,\tau-1}, X_{\nu,\tau-2}, \dots, X_{\nu,\tau-p}$, and $\phi_{j,\tau}$ and $\theta_{j,\tau}$ are the seasonal $p\omega$ autoregressive and $q\omega$ moving average parameters. For instance, by letting $p = 1$ and $q = 0$ in Equation [\(6-39\)](#) the lag-1 periodic autoregressive PAR(1) model is obtained:

$$X_{\nu,\tau} = \mu_\tau + \phi_\tau(X_{\nu,\tau-1} - \mu_\tau) + \varepsilon_{\nu,\tau} \quad (6-40)$$

in which the notation $\phi_\tau = \phi_{1,\tau}$ is used for simplicity. Similarly, for $p = 1$ and $q = 1$ in Equation [\(6-39\)](#) the PARMA(1,1) model is obtained:

$$X_{\nu,\tau} = \mu_\tau + \phi_\tau(X_{\nu,\tau-1} - \mu_\tau) - \theta_\tau\varepsilon_{\nu,\tau-1} + \varepsilon_{\nu,\tau} \quad (6-41)$$

Seasonal variances and autocorrelation functions can be derived for the general case of the PARMA(p, q) model using the infinite moving average representation of the process as

$$\sigma_\tau^2 = \sum_{j=0}^{\infty} \psi_{j,\tau}^2 \quad (6-42)$$

$$\rho_{h,\tau} = \frac{\sum_{j=0}^{\infty} \psi_{j,\tau} \psi_{j+h,\tau}}{(\sigma_{\tau} \sigma_{\tau-h})^2} \quad (6-43)$$

where the coefficients $\psi_{j,\tau}$ are given by the following recursions:

$$\begin{aligned} \psi_{0,\tau} &= 0 \\ \psi_{j,\tau} &= \sum_{k=1}^p \phi_{k,\tau} \psi_{j-k,\tau} - \theta_{j,\tau} \\ \psi_{j,\tau} &= 0 \text{ for } j < 0 \text{ and } \theta_{j,\tau} = 0 \text{ for } j > q \end{aligned} \quad (6-44)$$

Although in some cases Equations (6-42) and (6-43) may be used to derive analytical expressions of the autocorrelation and variance of a PARMA(p, q) model, in practice, they are generally computed numerically by truncating the infinite sums to an appropriate value.

Estimation of the parameters for PARMA(p, q) models can be carried out in a similar fashion as for the ARMA models (see Section 6.3.2). The periodic means μ_{τ} are generally estimated using the seasonal sample means of Equation (6-2) as

$$\hat{\mu}_{\tau} = \bar{x}_{\tau} \quad (6-45)$$

Analytical expressions of the parameters' estimators can be derived by the method of moments for low-order PARMA models. For instance, the parameters $\phi_{1,\tau}$ and $\sigma_{\varepsilon\tau}^2$ for the PARMA(1) case are given by (Salas 1993)

$$\hat{\phi}_{1,\tau} = \left(\frac{s_{\tau}}{s_{\tau-1}} \right) r_{1,\tau} \quad (6-46)$$

$$\hat{\sigma}_{\varepsilon\tau}^2 = s_{\tau}^2 - s_{\tau-1}^2 r_{1,\tau}^2 \quad (6-47)$$

where s_{τ}^2 and $r_{1,\tau}$ are the seasonal variances and lag-1 autocorrelation given by Equations (6-3) and (6-5), respectively.

Similarly, for the case of the PARMA(1, 1) model, the following system of equations can be employed for estimating the parameters $\phi_{1,\tau}$, $\theta_{1,\tau}$, and $\sigma_{\varepsilon\tau}^2$ by MOM (Salas et al. 1982):

$$\hat{\phi}_{1,\tau} = \frac{c_{2,\tau}}{c_{1,\tau-1}} \quad (6-48)$$

$$\hat{\theta}_{1,\tau} = \hat{\phi}_{1,\tau} + \frac{(s_{\tau}^2 - \hat{\phi}_{1,\tau} c_{1,\tau})}{\hat{\phi}_{1,\tau} s_{\tau-1}^2 - c_{1,\tau}} - \frac{(\hat{\phi}_{1,\tau+1} s_{\tau}^2 - c_{1,\tau+1})}{(\hat{\phi}_{1,\tau} s_{\tau-1}^2 - c_{1,\tau}) \hat{\theta}_{1,\tau+1}} \quad (6-49)$$

$$\hat{\sigma}_{\varepsilon\tau}^2 = \frac{\hat{\phi}_{1,\tau+1} s_{\tau-1}^2 - c_{1,\tau+1}}{\hat{\theta}_{1,\tau+1}} \quad (6-50)$$

where $c_{h,\tau}$ are the seasonal autocovariances given by Equation (6-6).

Alternatively, approximate ML estimates of the parameters $\phi_{1,\tau}$ and $\theta_{1,\tau}$ can be obtained by minimizing the sum of the square of the residuals $\sum_{\nu=1}^n \sum_{\tau=1}^{\omega} \varepsilon_{\nu,\tau}^2$. The variance of the noise term can then be estimated as $\hat{\sigma}_{\varepsilon\tau}^2 = (1/n) \sum_{\nu=1}^n \varepsilon_{\nu,\tau}^2$.

As an alternative to PARMA models, seasonal autoregressive integrated moving average (SARIMA) models can also be employed to model seasonal streamflows series, especially for

forecasting (e.g., Valipour 2015, Moeeni and Bonakdari 2016, Fernández et al. 2009, Modarres 2007). With reference to the seasonal series $X_t, t = (\nu - 1)^*\omega + \tau$, a SARIMA(p, d, q) \times (P, D, Q) process is defined such that the differenced series, $Y_t = (1 - B)^d(1 - B^{\omega})^D X_t$ follows the ARMA process defined as

$$\phi(B)\Phi(B^{\omega})Y_t = \theta(B)\Theta(B^{\omega})\varepsilon_t \quad (6-51)$$

where in the Box-Jenkins notation, B is the backward shift operator such that $B^k X_t = X_{t-k}$, $\phi(B) = (1 - \phi_1 B - \phi_2 B^2 - \dots - \phi_p B^p)$, $\Phi(B^{\omega}) = (1 - \Phi_1 B^{\omega} - \Phi_2 B^{2\omega} - \dots - \Phi_P B^{P\omega})$, $\theta(B) = (1 - \theta_1 B - \theta_2 B^2 - \dots - \theta_q B^q)$, $\Theta(B^{\omega}) = (1 - \Theta_1 B^{\omega} - \Theta_2 B^{2\omega} - \dots - \Theta_Q B^{Q\omega})$, and ε_t is a zero-mean white noise process with variance σ_{ε} . In applications, D is rarely more than one and the orders p, q, P, Q of the polynomials are generally limited to 0–3. Identification of SARIMA processes is generally carried out by finding the values of d and D such that the differenced series $Y_t = (1 - B)^d(1 - B^{\omega})^D X_t$ does not exhibit seasonal components. Then, the autocorrelations of Y_t at lags multiple than ω can be analyzed to estimate the orders P, Q . If $r(k)$ is the sample autocorrelation of Y_t , P and Q should be chosen such that $r(\omega k)$, $k = 1, 2, \dots$ is compatible with the autocorrelation function (ACF) of an ARMA(P, Q) model. Finally the orders p and q are selected by trying to match $r(1), r(2), \dots, r(\omega - 1)$ with the ACF of an ARMA(p, q) model (Brockwell and Davis 2002).

6.2.3 Product Models for Intermittent Flows

Streamflows in arid and semi-arid regions may be intermittent at subannual time scales (daily to months), exhibiting a pattern of alternating sequence of zero/nonzero flows. The resulting flow process generally presents higher coefficients of variation and skewness with respect to perennial flows in humid or temperate regions, which can hinder the applicability of traditional modeling schemes such as ARMA or PARMA. To model the sequence of zero and nonzero flows, the product of two mutually independent processes can be considered: a discrete binary one aimed at reproducing the occurrences of zero and nonzero values and a continuous one for modeling the nonzero flows, namely:

$$X_{\nu,\tau} = Q_{\nu,\tau} Z_{\nu,\tau} \quad (6-52)$$

where $Q_{\nu,\tau}$ is a binary Bernoulli (0,1) periodic process, $Z_{\nu,\tau}$ is a periodic autocorrelated process [e.g., PARMA(p, q)], and the two processes are generally assumed to be mutually independent.

Different approaches have been proposed for modeling the alternating binary sequence $Q_{\nu,\tau}$ of zero and nonzero flow occurrences. For example, Chebaane et al. (1995) propose periodic discrete autoregressive PDAR(1) for modeling the discrete component $Q_{\nu,\tau}$. It can be written as

$$Q_{\nu,\tau} = V_{\nu,\tau} Q_{\nu,\tau-1} + (1 - V_{\nu,\tau}) U_{\nu,\tau} \quad (6-53)$$

where $V_{\nu,\tau}$ and $U_{\nu,\tau}$ are mutually independent, nonautocorrelated periodic Bernoulli processes with $P[V_{\nu,\tau} = 1] = \gamma_{\tau}$, $P[U_{\nu,\tau} = 1] = \delta_{\tau}$, and $Q_{\nu,0} = Q_{\nu,\omega}$. Estimation of the parameters γ_{τ} and δ_{τ} of the PDAR model given by Equation (6-53) can be made by matching the transition probabilities as (Chebaane et al. 1995)

$$\hat{\gamma}_{\tau} = \frac{n_{0_{\tau-1}} n_{11_{\tau}} - n_{1_{\tau-1}} n_{01_{\tau}}}{n_{1_{\tau-1}} n_{0_{\tau-1}}} \quad (6-54)$$

and

$$\hat{\delta}_{\tau} = \frac{n_{1_{\tau-1}} n_{01_{\tau}}}{n_{1_{\tau-1}} n_{01_{\tau}} - n_{0_{\tau-1}} n_{10_{\tau}}} \quad (6-55)$$

where $n_{ij_{\tau}}$, $i = 0, 1$, $j = 0, 1$ is the number of all the combinations of flow (1)/no flow (0) transitions at season τ , and $n_{0_{\tau-1}} n_{10_{\tau}}$ and $n_{1_{\tau-1}} n_{10_{\tau}}$ are the numbers of flow and no flow observations,

respectively. For instance, n_{11_τ} is the number of times a nonzero flow occurs at season τ following a nonzero flow at season $\tau - 1$, while n_{01_τ} is the number of times a nonzero flow occurs at season τ following a zero flow at season $\tau - 1$. In some particular cases (e.g., when $n_{1_{\tau-1}}n_{01_\tau} - n_{0_{\tau-1}}n_{10_\tau} \leq 0$) these estimators may yield unfeasible solutions, then, the alternative estimators derived by Chebaane et al. (1995) for such particular cases can be employed. Likewise, two state periodic Markov chains for modeling daily streamflows has been proposed among others by Aksoy (2003). Because the continuous component $Z_{\nu,\tau}$ of Equation (6-52) cannot be observed, the parameters of the corresponding PARMA model can be carried out by relating the first and second order moments of the three processes $X_{\nu,\tau}$, $Q_{\nu,\tau}$, and $Z_{\nu,\tau}$ as (Chebaane et al. 1995)

$$\mu_\tau(X) = \mu_\tau(Q)\mu_\tau(Z) \quad (6-56)$$

$$\sigma_\tau^2(X) = \mu_\tau(Q)\sigma_\tau^2(Z) + \mu_\tau^2(Z)\sigma_\tau^2(Q) \quad (6-57)$$

$$\begin{aligned} \rho(k)_\tau(X) = & \left\{ \rho(k)_\tau(Q)\sigma_\tau(Q)\sigma_{\tau-k}(Q)[\rho(k)_\tau(Z)\sigma_\tau(Z)\sigma_{\tau-k}(Z) + \mu_\tau(Z)\mu_{\tau-k}(Z)] \right. \\ & \left. + \mu_\tau(Q)\mu_{\tau-k}(Q)\rho_{k,\tau}(Z)\sigma_\tau(Z)\sigma_{\tau-k}(Z) \right\} / \sigma_\tau(X)\sigma_{\tau-k}(X) \end{aligned} \quad (6-58)$$

where $\mu_\tau()$, $\sigma_\tau^2()$, and $\rho_{k,\tau}()$ represent the periodic expected values, variances, and the lag k autocorrelation for the corresponding variable at season τ . For instance, Chebaane et al. (1995) derive MOM estimators for the parameters assuming a PARMA(1) model for the process $Z_{\nu,\tau}$.

6.2.4 Modeling of Long-Term Variability

Several hydroclimatic processes aggregated at yearly time scales exhibit apparent nonstationarities in the form of cycles, changes in the mean and other statistics, or shifting patterns from one stationary state to another, thus departing from the traditional hypothesis that the basic statistical parameters do not change with time. Such series are generally characterized by Hurst exponents greater than 0.5 (see Section 6.2.4) and slowly decreasing autocorrelograms, and therefore application of traditional modeling schemes such as ARMA models poses some limitations. As a consequence, over the years, a great deal of statistical hydrology literature emerged aimed at developing alternative models and estimation techniques that may represent more closely the behavior of hydrologic time series.

Several physical and stochastic underlying mechanisms and related modeling schemes have been proposed to explain the behavior of such series, among which scale invariance, long memory, and nonstationarity of the mean are probably those that have found most widespread consensus (Bras and Rodriguez-Iturbe 1985, Salas 1993). Nonetheless, no general agreement has been reached over the preferable modeling approach, while time series analysis modelers recognize that distinguishing between long memory and changes in regimes is generally difficult given the length of the available time series (see, e.g., Banerjee and Urga 2005, Smith 2005). A recent work on long memory can be found in Koutsogiannis (2016).

In what follows, three types of models possessing the previously mentioned mechanisms, namely fractional Gaussian noise (FGN), fractionally integrated moving average (FARMA), and shifting mean (SL) are illustrated in some detail.

6.2.4.1 Fractional Gaussian Noise

Mandelbrot (1965) and Mandelbrot and Wallis (1968) introduce the FGN model for preserving the Hurst phenomenon. The model assumes that hydrometeorological series exhibit scale-invariant behavior when aggregated at any time scale greater than annual. More precisely, let us consider a

process X_i , defined at a basic time scale, and the corresponding aggregated process $Z_i^{(k)}$, defined at a time scale k , i.e.,

$$Z_i^{(k)} = \sum_{l=(i-1)k+1}^{ik} X_l, \quad i = 1, 2, \dots \quad (6-59)$$

Then we assume that the aggregated process $Z_i^{(k)}$ exhibits scale-invariant properties, namely,

$$(Z_i^{(k)} - k\mu) \underline{=} d \left(\frac{k}{l}\right)^H (Z_i^{(l)} - l\mu) \quad (6-60)$$

where k and l are two generic time scales, μ is the mean of the X_i process, and the symbol $\underline{=}$ stands for equality in distribution. Equation (6-60) states that the process maintains the same statistical behavior at different aggregation time scales, provided that a proper scaling multiplicative coefficient $(k/l)^H$ is applied.

If the process X_i is Gaussian, Equation (6-60) is a discrete FGN. Because in principle different distributions for X_i can be defined, alternative names have been proposed, e.g., simple scaling signal (SSS) (Koutsoyiannis 2003) or Hurst–Kolmogorov model (HK) (Koutsoyiannis 2011). Bras and Rodriguez-Iturbe (1985), for example, show that the process defined by Equation (6-60) preserves the Hurst behavior with Hurst coefficient H . Furthermore, the autocorrelation ρ_h does not depend on the time scale and, for large time lags, is a power function of h . Therefore, the autocorrelation function is not absolutely summable, and the FGN possesses long memory, at least in mathematical sense. From a practical standpoint, FGN series cannot be operationally obtained but only approximated. Mandelbrot and Wallis (1969) propose two approximations consisting of weighting averages of independent Gaussian variables. Approximations of FGN by means of ARMA processes have been suggested by O’Connell (1974) and illustrated in detail by Bras and Rodriguez-Iturbe (1985). More recently, Koutsoyiannis (2011) provides simple algorithms to generate FGN or SSS processes.

6.2.4.2 Long Memory Models

The presence of long memory in hydroclimatic series and in streamflow series in particular has been examined by several authors, especially in an attempt to explain the Hurst effect. As a consequence, some models capable of representing many of the previously referred properties have been proposed in literature and have been applied successfully to various fields, such as geophysical phenomena and econometric series. A class of models possessing long memory has been introduced independently by Granger and Joyeux (1980) and Hosking (1981). It generalizes the autoregressive integrated moving average (ARIMA) process by allowing noninteger values for the degree of differencing d . These processes are usually referred to as fractionally differenced autoregressive moving average FARMA(p, d, q), although some authors prefer using the acronyms ARIMA(p, d, q), FARIMA(p, d, q), or ARFIMA(p, d, q). An advantage of FARMA(p, d, q) models is that, because they are combinations of ARMA(p, q) processes with fractionally integrated long-memory processes, by varying the autoregressive and moving average components, one can combine short- and long-memory effects, thus reproducing the autocorrelation structure of natural processes that exhibit both short- and long-term persistence.

Consider that Y_t is a fractionally differenced autoregressive process FARMA(p, d, q) with $-0.5 < d < 0.5$ that satisfies the following difference equation:

$$\Phi(B) \nabla^d Y_t = \Theta(B) \varepsilon_t \quad (6-61)$$

where Y_t has zero mean, B is the backward operator $B^k X_t = X_{t-k}$, $\nabla^d = (1 - B)^d$ is the differencing operator, $\Phi(B)$ and $\Theta(B)$ are the p -order autoregressive and q -order moving average polynomials,

respectively (refer to Section 6.3.3), and ε_t is a white noise term with zero mean and variance σ_ε^2 . The differencing operator may be defined by means of the binomial expansion as

$$\nabla^d = (1 - B)^d = \sum_{j=0}^{\infty} \pi_j B^j \quad (6-62)$$

where $\pi_0 = 1$, $\pi_j = \frac{\Gamma(j-d)}{\Gamma(j+1)\Gamma(-d)}$, $j = 1, 2, \dots$, and $\Gamma(\cdot)$ is the complete gamma function. The autocovariance function of the process Y_t is given by (Brockwell and Davis 1991)

$$\gamma_Y(h) = \sum_{k=-\infty}^{\infty} \gamma^*(k) \gamma_X(h-k) \quad (6-63)$$

where $\gamma^*(\cdot)$ is the autocovariance function of the ARMA process $\Phi(B)W_t = \Theta(B)\varepsilon_t$ with $W_t = \nabla^d Y_t$, and $\gamma_X(\cdot)$ is the autocovariance of a fractionally differenced noise X_t , namely (Brockwell and Davis 1991)

$$\gamma_X(h) = \sigma_\varepsilon^2 \frac{\Gamma(1-2d)}{\Gamma^2(1-d)} \prod_{0 < k \leq h} \frac{k-1+d}{k-d} \quad (6-64)$$

It can be shown that the autocorrelation function of the process Y_t for large h behaves as

$$\rho_Y(h) = Ch^{2d-1} \quad (6-65)$$

where C is a constant and therefore the FARMA(p, d, q) process possesses long memory provided $d > 0$. Furthermore, the d exponent is related to the Hurst coefficient H by the relationship $d = H - 0.5$, which shows that for $d > 0$ FARMA models are able to preserve the Hurst phenomenon.

Estimation of the parameters of a FARMA(p, d, q) model cannot be carried out by means of traditional ARMA estimation techniques such as the method of moments because the process does not admit a finite state representation. Therefore, the attention has been devoted mainly to maximum likelihood estimators. To this end, exact (Gaussian) and approximated likelihood have been applied. Sowell (1992) and Cheung and Diebold (1994) explore use of exact Gaussian likelihood, but, due to numerical difficulties, Whittles' approximation of the Gaussian likelihood in the frequency domain is generally preferred (Fox and Taqqu 1986, Montanari et al. 1997). With reference to a mean subtracted observed sample y_1, \dots, y_n , fitting a FARMA(p, d, q) model requires estimating a total of $p + q + 2$ parameters, namely $p + q$ autoregressive and moving average polynomial coefficients, the fractional exponent d , and the variance of the noise term σ_ε . Setting $\beta = (d, \phi_1, \dots, \phi_p, \theta_1, \dots, \theta_q)$, the Whittles approximation of the Gaussian likelihood can be expressed as (Brockwell and Davis 1991)

$$l_W(\beta) = \ln \left(\frac{1}{n} \sum_{j=1}^n \frac{I_n(\lambda_j)}{f_Y(\lambda_j; \beta)} \right) + \frac{1}{n} \sum_{j=1}^n n \ln f_Y(\lambda_j; \beta) \quad (6-66)$$

where λ_j are the Fourier frequencies $2\pi j/n$, $I_n(\lambda_j)$ is the periodogram of the observations [Equation (6-7)], and $f_Y(\lambda)$ is the spectral density of the FARMA model, which is given by

$$f_Y(\lambda) = \frac{\sigma_\varepsilon^2}{2\pi} \frac{|\Theta(e^{-i\lambda})|^2}{|\Phi(e^{-i\lambda})|^2} |2 \sin(\lambda/2)|^{-2d} \quad (6-67)$$

Note that the Whittle approximation is asymptotically valid even in the non-Gaussian case and therefore can be employed even in the case of nonnormal distributed data. Minimization of

Equation (6-66) with respect to β and σ_e will lead to estimates of the parameters. In practice, such minimization must be carried out numerically and initial values of the parameters are required. Preliminary estimates of d can be obtained by estimating the Hurst exponent \hat{H} from the available sample and by letting $\hat{d} = \hat{H} - 0.5$. Then, a preliminary filtered series y_t^* can be computed by applying the differencing filter of Equation (6-62) to y_t . Finally, because such filtered series will follow an ARMA(p, q) process identical to the ARMA components of the original FARMA process y_t , traditional ARMA estimation procedures can be applied to get preliminary estimates of $(\hat{\phi}_1, \dots, \hat{\phi}_p, \hat{\theta}_1, \dots, \hat{\theta}_q, \hat{\sigma}_e)$.

6.2.4.3 Shifting Mean Models

Many hydroclimatic series exhibit apparent shifts in one or more of their statistical properties. For instance, Figure 6-6 shows the plot of the annual average flows of the Niger River at Koulikoro, which exhibits an apparent random oscillatory behavior compatible with a shifting of mean levels. Shifting behavior of the mean has also been suggested as a possible explanation of the Hurst phenomenon since the pioneering work by [Hurst \(1957\)](#), who used a deck of cards to run a rough simulation experiment in an attempt to devise a model that would explain what he had observed in natural time series. Since then, models with nonstationary means have been proposed by several authors including [Klemeš \(1974\)](#), [Potter \(1976\)](#), [Boes and Salas \(1978\)](#), [Salas and Boes \(1980\)](#), and [Sveinsson et al. \(2003\)](#).

A general definition of a shifting mean (SM) process is as follows:

$$X_t = M_t + Z_t \quad (6-68)$$

where M_t is a process that assumes constant values (levels) during variable time spans and Z_t is a noise term. Then, different models can be built depending on the definition of the M_t and Y_t processes. For instance, one may assume that Z_t and M_t are mutually independent, Z_t an i.i.d. process with mean μ_Z and variance σ_Z^2 , and M_t such that

$$M_t = M_{t-1} \text{ with probability } 1 - p$$

$$M_t = \xi_t \text{ with probability } p$$

where ξ_t is drawn from some distribution with zero mean and variance σ_ξ^2 . Thus the aforementioned process consists of the superposition of an i.i.d. process with a varying levels process, where each level remains constant for a time span distributed according to a geometric distribution. [Fortin et al. \(2004\)](#) show that the aforementioned model can be reformulated as a hidden Markov model.

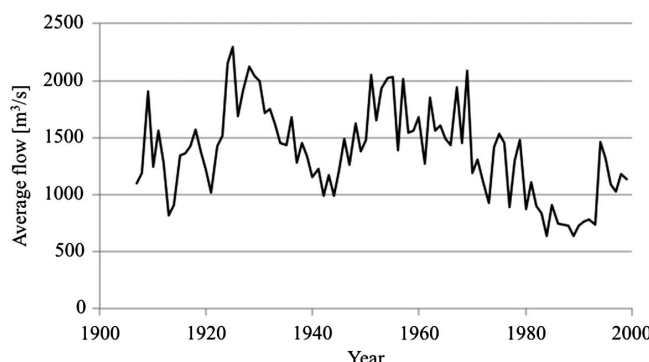


Figure 6-6. Annual average flows for the Niger River at Koulikoro.

Source: Data from [Sveinsson et al. \(2003\)](#).

Mean, variance, and lag- h autocorrelation of the SM model have been derived by [Salas and Boes \(1980\)](#) as

$$\begin{aligned}\mu_X &= \mu_Z \\ \sigma_X^2 &= \sigma_Y^2 + \sigma_M^2 \\ \rho_h &= \frac{\sigma_M^2(1-p)^h}{\sigma_Y^2 + \sigma_M^2}\end{aligned}$$

Fitting an SM model to a series of observations requires estimating the four parameters μ_Z , σ_Y^2 , σ_M^2 , and p . Using the method of moments, the following estimators can be derived, as a function of the sample mean \bar{X} , variance s^2 , and lag-1 and lag-2 autocorrelation coefficients r_1 and r_2 of the observed series ([Salas and Boes 1980](#), [Sveinsson et al. 2003](#)):

$$\begin{aligned}\hat{\mu}_Y &= \bar{X} \\ \hat{\sigma}_M^2 &= s^2 \frac{r_2^2}{r_1} \\ \hat{\sigma}_Y^2 &= s^2 - \hat{\sigma}_M^2 \\ \hat{p} &= 1 - \frac{r_2}{r_1}\end{aligned}$$

Note that the parameter estimates are feasible only if $r_1 > r_2 > r_1^2$. Due to sample variability of the autocorrelogram, infeasible parameters may result, and adjusting procedures such as those proposed by [Sveinsson et al. \(2003\)](#) can be employed.

Several authors have proposed alternate formulations of SM models. For instance, [Sveinsson et al. \(2003\)](#) propose an SM model where the levels alternate between high and low values. [Ballerini and Boes \(1985\)](#) show that by choosing appropriate distributions for the M_t and Z_t processes, an SM process that exhibits a Hurst exponent greater than 0.5 may be devised. A model with several levels spanning with different time scales has been proposed by [Koutsoyiannis \(2002\)](#) to approximate a fractional Gaussian noise process with Hurst exponent greater than 0.5.

6.2.5 Modeling of Streamflows by Nonparametric Methods

Traditional parametric streamflow modeling has focused on models capable of reproducing several key statistical features of observed data, including mean, variances, autocorrelation, and cross correlations. Despite that parametric models have found widespread use for data generation and forecasting, in some cases drawbacks such as the need to transform the original data to normal and the nonlinearity of the hydrologic system may limit their application. The aforementioned difficulties have sparked an increasing attention to nonparametric models aimed at overcoming some of the drawbacks of traditional parametric models.

Unlike parametric models, nonparametric methods are not based on fixing some functional form either to express the link between successive values or the probability density function, but rather, they directly use the observations to generate new data, thus implicitly preserving statistical features sometimes difficult to reproduce by means of parametric approaches.

Techniques such as block bootstrapping ([Kunsch 1989](#), [Vogel and Shallcross 1996](#)), k -nearest neighbors resampling (KNNR) ([Lall and Sharma 1996](#); [Mehrotra and Sharma 2006](#), [Prairie et al. 2007](#)), and conditional density estimate ([Sharma et al. 1997](#)) have been developed, with the objective of generating random synthetic series resembling different features of observed samples without the need of prior selection of the model's functional form. Nonparametric approaches have also been

proposed to account for information from paleohydrological reconstructed data ([Gangopadhyay et al. 2009](#), [Henley et al. 2013](#)). Other applications of nonparametric models relate to spatial and temporal disaggregation that will be discussed in some detail in Section [6.4](#).

Bootstrapping is a generation technique based on resampling in a random fashion from an observed series. When resampling involves one value at a time (simple bootstrapping), it can be applied to uncorrelated series because the time dependence structure of the observations will not be preserved. Block bootstrapping, however, is based on resampling sequences of values, thus preserving up to a certain lag the autocorrelation function of the obervations. Bootstrapping, however, suffers the drawback of generating values that are identical to the original observations except for the order. To overcome such drawbacks, hybrid models have been proposed based on a combination of parametric and resampling approaches ([Srinivas and Srinivasan 2001, 2005, 2006](#); [Kim and Valdés 2005](#)), or more elaborate schemes based on KNNR or conditional density estimate.

KNNR (e.g., [Lall and Sharma 1996](#), [Mehrotra and Sharma 2006](#), [Prairie et al. 2007](#)) generates new values according to the closeness of the distance estimated from current and past known values and the historical counterparts. For instance, by considering a limited number of sequences of observations (neighbors) close in the Euclidean sense to given values, a new value is generated by random extraction from the observations among the successors of the selected neighbors. The method requires the selection of the k nearest neighbors and the corresponding weights w_i that generally decrease with increasing distance. [Lall and Sharma \(1996\)](#) propose $k = \sqrt{N}$, where N is the number of observations, and the weights are given by

$$w_i = \frac{1/i}{\sum_{j=1}^k 1/j}, \quad i = 1, \dots, k \quad (6-69)$$

[Prairie et al. \(2006\)](#) propose improvements to the KNNR method, who adopt a local polynomial regression where the innovations are sampled using KNNR. [Salas and Lee \(2009\)](#) propose two approaches based on a k -nearest neighbor resampling algorithm with gamma kernel perturbations for simulating seasonal flows while preserving annual variability.

Conditional density methods ([Sharma et al. 1997](#), [Sharma and O'Neill 2002](#)) are based on the idea that in general terms the generation of a value X_t at time t , based on past values $X_{t-1}, X_{t-2}, \dots, X_{t-p}$ can be pursued by sampling from the conditional probability density function $f(X_t | X_{t-1}, X_{t-2}, \dots, X_{t-p})$. Then, instead of assuming a parametric form for such conditional density, the latter is estimated from the sample by means of nonparametric kernel density estimation methods. For instance, [Sharma et al. \(1997\)](#) propose the following Gaussian kernel density estimator:

$$\hat{f}(x) = \sum_{t=1}^n K\left(\frac{x - x_t}{h}\right) \quad (6-70)$$

where $K()$ is a kernel function that must integrate to 1 and h is a parameter called bandwidth.

6.3 MODELING OF COMPLEX RIVER SYSTEMS

Stochastic modeling of streamflows at different sites within a complex river system is often required for planning and management purposes, including reservoirs design and operation, low flow and drought analysis, performance assessment of water supply systems under uncertain streamflows, streamflow forecasting, water allocation problems among different users, and so on. Modeling such complex systems requires accounting for some statistical features stemming from the topological structure of the river network. For instance, preservation of autocorrelations and cross-correlations

is crucial to properly account for the joint occurrence of low or high flows in the different branches of the river system. Additivity of generated streamflows at merging branches of the river system is another important issue that must be considered in streamflow generation of complex river networks. Furthermore, often the streamflow simulation requires the preservation of statistics at different time scales (e.g., seasonal and annual), which generally cannot be accomplished by simply building a model at the smaller time scale (e.g., monthly) and by aggregating the generated values at the larger time scales (e.g., yearly). To account for the aforementioned features, several modeling schemes have been proposed, generally based on the combination of univariate or multivariate models and spatial and temporal disaggregation procedures. In what follows, multivariate ARMA and PARMA models and parametric and nonparametric disaggregation schemes are discussed. Then, the role of alternative modeling schemes, based on the combination of the aforementioned is discussed.

6.3.1 Modeling of Multivariate Time Series

Nonseasonal ARMA models can be extended to the case of joint generation of multiple time series by considering instead of a scalar-valued random variable X_t , a vector-valued time series \mathbf{X}_t . More specifically, for m sites, let us define by $\mathbf{X}_t = X_t^{(1)}, X_t^{(2)}, \dots, X_t^{(m)}$ the vector of streamflows at time t at the different sites $j = 1, \dots, m$. Then, the multivariate extension of the ARMA(1, 1) model denoted as MARMA(1, 1) is

$$\mathbf{Y}_t = \Phi_1 \mathbf{Y}_{t-1} - \Theta_1 \underline{\varepsilon}_{t-1} + \mathbf{B} \underline{\varepsilon}_t \quad (6-71)$$

where \mathbf{Y}_t is a zero-mean vector $\mathbf{Y}_t = \mathbf{X}_t - \underline{\mu}$, $\underline{\mu}$ is the vector of the means of \mathbf{X}_t , Φ_1 and Θ_1 are $m \times m$ autoregressive and moving average square matrices, \mathbf{B} is an $m \times m$ matrix, and $\underline{\varepsilon}_t$ is an uncorrelated, zero-mean and unit variance white noise $m \times 1$ vector such that $E[\underline{\varepsilon}_t \underline{\varepsilon}_t^T] = \mathbf{I}$ where \mathbf{I} is the identity matrix and $E[\underline{\varepsilon}_t \underline{\varepsilon}_{t-k}^T] = 0$ for $k \neq 0$.

Extension to the multivariate autoregressive moving average model MARMA(p, q) considers p autoregressive and q moving average terms and can be written as ([Salas 1993](#))

$$\mathbf{Y}_t = \sum_{i=1}^p \Phi_i \mathbf{Y}_{t-i} - \sum_{j=1}^q \Theta_j \underline{\varepsilon}_{t-j} + \mathbf{B} \underline{\varepsilon}_t \quad (6-72)$$

where $\Phi_i, i = 1, \dots, p$ and $\Theta_i, i = 1, \dots, q$ are $m \times m$ autoregressive and moving average square matrices.

The method of moments can be employed to estimate parameter matrices of low-order MARMA(p, q) models. For instance, with reference to the multivariate lag-1 autoregressive MAR(1) model the following estimators are available for Φ_1 and \mathbf{B} ([Matalas 1967](#)):

$$\hat{\Phi}_1 = \hat{\mathbf{M}}_1 \hat{\mathbf{M}}_0^{-1} \quad (6-73)$$

$$\hat{\mathbf{B}} \hat{\mathbf{B}}^T = \hat{\mathbf{M}}_0 - \hat{\Phi}_1 \hat{\mathbf{M}}_1^T \quad (6-74)$$

where $\hat{\mathbf{M}}_0$ and $\hat{\mathbf{M}}_1$ are the lag-zero and lag-1 cross-covariance matrices of the observations \mathbf{X}_t . Solving for $\hat{\mathbf{B}}$ in Equation (6-74) can be carried out by using several methods ([Salas 1993](#)), and adjustment procedures are also available to overcome numerical problems that may arise (see, e.g., [Bras and Rodriguez-Iturbe 1985](#)).

As the orders p and q increase, estimation of the parameter matrices of the full multivariate ARMA(p, q) model is often a complicated task due to numerical difficulties that generally arise. Therefore, alternative and simpler formulations have been proposed, such as the contemporaneous ARMA (CARMA) ([Matalas 1967](#), [Camacho et al. 1987](#), [Salas 1993](#)), which assumes a diagonal form for the matrices $\Phi_i, i = 1, \dots, p$ and $\Theta_j, j = 1, \dots, q$. Such an assumption leads to a dramatic

simplification of the estimation procedures because it enables decoupling of the model into m ARMA models that can be estimated in an univariate fashion, while estimation of the matrix \mathbf{B} , whose role is to model jointly the series, can be carried out by the method of moments as a function of the cross-correlation matrices at different observation lags. However, the drastic reduction of the number of parameters limits the model's capabilities to preserve all the cross-correlations at several lags.

With reference to a CARMA(1, 1) model, the elements of the matrix $\mathbf{G} = \mathbf{B}\mathbf{B}^T$ can be estimated as (Stedinger et al. 1985a)

$$\hat{g}^{(ij)} = \frac{m_0^{(ij)}(1 - \hat{\phi}^{(i)}\hat{\phi}^{(j)})}{1 - \hat{\phi}^{(i)}\hat{\theta}^{(j)} - \hat{\phi}^{(j)}\hat{\theta}^{(i)} + \hat{\theta}^{(i)}\hat{\theta}^{(j)}} \quad (6-75)$$

where $\hat{\phi}^{(i)}$ and $\hat{\theta}^{(i)}$ are the autoregressive and moving average parameters of the univariate ARMA(1, 1) model fitted to site (i) , and $m_0^{(ij)}$ is the lag-zero cross-correlation between site i and j . Once the matrix \mathbf{G} is found, \mathbf{B} can be estimated by solving the matrix equation $\mathbf{G} = \mathbf{B}\mathbf{B}^T$ (Bras and Rodriguez-Iturbe 1985).

Periodic models such as PARMA(p, q) can also be extended to the multivariate case by considering matrix parameters. For instance, the multivariate version of the PAR(1) [Equation (6-40)] is given by (Salas and Pegram 1977, Salas 1993)

$$\mathbf{Y}_{v,\tau} = \Phi_{1,\tau} \mathbf{Y}_{v,\tau-1} + \mathbf{B}_\tau \boldsymbol{\varepsilon}_{v,\tau} \quad (6-76)$$

where $\mathbf{Y}_{v,\tau}$ is a zero-mean vector $\mathbf{Y}_{v,\tau} = \mathbf{X}_{v,\tau} - \underline{\mu}_\tau$, $\underline{\mu}_\tau$ is the seasonal vector of the means of $\mathbf{X}_{v,\tau}$, $\Phi_{1,\tau}$ is the ω -periodic $m \times m$ autoregressive matrix, \mathbf{B}_τ is a periodic $m \times m$ matrix, and $\boldsymbol{\varepsilon}_{v,\tau}$ is an uncorrelated, zero-mean and unit-variance white noise $m \times 1$ vector, i.e., such that $\mathbf{E}[\boldsymbol{\varepsilon}_{v,\tau} \boldsymbol{\varepsilon}_{v,\tau}^T] = \mathbf{I}$ and \mathbf{I} is the identity matrix with $\mathbf{E}[\boldsymbol{\varepsilon}_{v,\tau} \boldsymbol{\varepsilon}_{v,\tau-k}^T] = 0$ for $k \neq 0$.

Likewise the general multivariate PARMA(p, q) is defined as

$$\mathbf{Y}_{v,\tau} = \sum_{i=1}^p \Phi_{i,\tau} \mathbf{Y}_{v,\tau-i} - \sum_{i=1}^q \Theta_{i,\tau} \boldsymbol{\varepsilon}_{v,\tau-i} + \mathbf{B}_\tau \boldsymbol{\varepsilon}_{v,\tau} \quad (6-77)$$

where $\Phi_{i,\tau}, i = 1, \dots, p$ are the p ω -periodic $m \times m$ autoregressive matrices and $\Theta_{i,\tau}, i = 1, \dots, q$ are the q ω -periodic $m \times m$ moving average matrices.

As in the case of nonseasonal modeling, multivariate PARMA can also be formulated in a contemporaneous fashion, by assuming diagonal autoregressive and moving average matrices $\Phi_{i,\tau}$ and $\Theta_{i,\tau}$ (Bartolini et al. 1988). Then, the model in Equation (6-77) can be decoupled into m univariate PARMA, whose autoregressive and moving average periodic components can be estimated in an univariate setting. Estimation of the periodic matrices \mathbf{B}_τ can be pursued similarly to the nonseasonal case by the method of moments. For instance, estimators for the elements $g_\tau^{(ij)}$ of the matrix $\mathbf{G}_\tau = \mathbf{B}_\tau \mathbf{B}_\tau^T$ have been derived by Haltiner and Salas (1988) for the case of PARMA(1, 1) and by Rasmussen et al. (1996) for the case of PARMA(2, 2).

To reduce the number of parameters when the number of sites increases, contemporaneous PARMA (CPARMA) models have also been proposed in which the matrices $\Phi_{i,\tau}$ and $\Theta_{i,\tau}$ are assumed to be diagonal. This leads to strictly preserving only the contemporaneous cross-correlation among sites, while the preservation of cross-correlations at different time lags (which sometimes can be neglected) is not ensured. Efstratiadis et al (2014) describe recent advances on the subject.

6.3.2 Disaggregation Models

Joint modeling of streamflows at different sites based on multivariate ARMA or PARMA models suffers the drawback of not preserving statistics at different scales of aggregation, either in time

(e.g., monthly streamflows aggregated at yearly scale) or space (merging branches in complex river systems). This is so, particularly for low-order models. Thus, several disaggregation models have been proposed to preserve statistics at different scales of aggregation. For instance, [Valencia and Schaake \(1973\)](#) propose a model to disaggregate annual values at m sites into corresponding seasonal values such that seasonal values at each site sums up to the corresponding annual value. The model has the form

$$\mathbf{Y} = \mathbf{AX} + \mathbf{B}\boldsymbol{\varepsilon} \quad (6-78)$$

where

\mathbf{X} = zero-mean,

m = vector of annual values at the m sites,

\mathbf{Y} = zero-mean $m\omega$ vector of seasonal values (ω number of seasons) at the m sites,

\mathbf{A} and $\mathbf{B} = m\omega \times m$ and $m\omega \times m\omega$ parameter matrices respectively, and

$\boldsymbol{\varepsilon} = m\omega$ vector of uncorrelated noises.

The parameter matrices \mathbf{A} and \mathbf{B} can be estimated by the method of moments as

$$\hat{\mathbf{A}} = \mathbf{S}_{YX} \mathbf{S}_{XX}^{-1} \quad (6-79)$$

$$\hat{\mathbf{B}} \hat{\mathbf{B}}^T = \mathbf{S}_{YY} - \hat{\mathbf{A}} \mathbf{S}_{XY} \quad (6-80)$$

where \mathbf{S}_{WZ} is the covariance matrix between the generic vectors \mathbf{W} and \mathbf{Z} . Whereas the model can preserve seasonal autocorrelation and cross-correlation among the sites, it does not preserve autocorrelation between the first season of a year and any preceding season. To overcome such limitation, [Mejia and Rousselle \(1976\)](#) propose an enhancement of the aforementioned model by introducing an additional term,

$$\mathbf{Y} = \mathbf{AX} + \mathbf{B}\boldsymbol{\varepsilon} + \mathbf{C}\mathbf{Z} \quad (6-81)$$

where \mathbf{C} is a parameter matrix and \mathbf{Z} is a vector of seasonal values from the previous year for each site. For instance, \mathbf{Z} may contain only the last season from the previous year, in which case \mathbf{Z} is a $n \times 1$ vector and \mathbf{Z} is a $n\omega \times n$ matrix. Estimators for the matrices \mathbf{A} , \mathbf{B} , and \mathbf{C} based on MOM are given by [Lane \(1982\)](#) and [Salas \(1993\)](#).

[Stedinger and Vogel \(1984\)](#) propose an alternative scheme, which enables preserving the cross-correlations at annual scale as

$$\mathbf{Y}_t = \mathbf{AX}_t + \boldsymbol{\varepsilon}_t \quad (6-82)$$

$$\boldsymbol{\varepsilon}_t = \mathbf{C}\boldsymbol{\varepsilon}_{t-1} + \zeta_t \quad (6-83)$$

where $\boldsymbol{\varepsilon}_t$ is independent of \mathbf{X}_t and ζ_t is a noise term with covariance matrix $\mathbf{S}_{\zeta\zeta}$.

Drawbacks of the aforementioned models include the relatively large number of parameters, which may become an issue especially when the number of sites is large and the available sample size is small. Furthermore, when the orginal data are preliminarily transformed to account for nonnormality, additivity is not guaranteed anymore (in the real space data). Thus, models with reduced number of parameters have been proposed and adjustments techniques to preserve the additivity of seasonal values at the annual time scale ([Stedinger et al. 1985](#), [Grygier and Stedinger 1988](#), [Lane and Frevert 1990](#), [Koutsoyiannis and Manetas 1996](#)). Simple stepwise disaggregation schemes have been proposed by [Santos and Salas \(1992\)](#) to reduce the overall number of parameters while preserving key features in the temporal and spatial disaggregation.

Alternatively, nonparametric techniques can be employed to disaggregate streamflows at different sites spatially and temporally. This includes simple disaggregation techniques (e.g., Acharya and Ryu 2013, Portela and Silva 2016) and more sophisticated methods. Nonparametric disaggregation (NPD) is based on sampling from the conditional distribution of the vector of disaggregated variables $\mathbf{Y} = (Y_1, Y_2, \dots, Y_m)$ given the aggregated value X , $f(\mathbf{Y}|X) = f(\mathbf{Y}, X)/f(X)$, where $f(\mathbf{Y}, X)$ is the joint probability density function of \mathbf{Y} and X and $f(X)$ is the marginal density of X . NPD requires first a rotation of the lower-level variable vector \mathbf{Y} into a new vector space $\mathbf{Z} = (Z_1, Z_2, \dots, Z_m)^T$:

$$\mathbf{Z} = \mathbf{R}\mathbf{Y} \quad (6-84)$$

where \mathbf{R} is a $m \times m$ rotation matrix obtained through the Gram Schmidt Orthonormalization such that the last element of the rotated variable is $Z_m = X/\sqrt{m}$. Details on the algorithm to compute \mathbf{R} can be found in Tarboton et al. (1998). The NPD model is based on generating \mathbf{Z} first and then backrotating into \mathbf{Y} from Equation (6-84) so that $\mathbf{Y} = \mathbf{R}^{-1}\mathbf{Z}$.

Tarboton et al. (1998) propose multivariate kernel density estimates to generate Z_1, Z_2, \dots, Z_{d-1} and $Z_d = X/\sqrt{d}$. Prairie et al. (2007) propose a similar approach based on a k -nearest neighbor technique instead of a multivariate kernel density that enables circumventing the complications associated with the latter approach as the dimensionality of the problem increases. Lee et al. (2010) highlight the similarity of NPD with the adjusting procedure proposed by Koutsoyiannis and Manetas (1996) and suggest some enhancements based on genetic algorithms to preserve cross-boundary correlations (i.e., correlation between the first season with the last season from the previous year) and to avoid generation of negative values and repetition of temporal and spatial historical flow patterns. Models based on copula have also been recently proposed for disaggregating monthly flows (Li et al. 2013, Hao and Singh 2013).

6.3.3 Modeling Strategies for Complex River Systems

As already mentioned, when modeling complex river systems, a key requisite is that the generation of series at the different sites should reflect the topology of the river network in terms of cross-correlation, additivity, and proportionality, in the sense that flows at a downstream site should be represented as the sum of tributary river flows and channel losses/gains. Furthermore, that statistics at different times scales (e.g., monthly and annual) be preserved and that the sum of seasonal values add up to the corresponding annual flows are often desirable. At the same time, as the number of sites increases, so does the complexity of the model, generally leading to difficulties related to its implementation and calibration. None of the models proposed so far can satisfy all of these requisites, and therefore, a preferable approach is to put in place proper modeling strategies based on the use of a combination of different models as the system requires.

When the interest lies in modeling a complex river system at different sites, application of a seasonal multivariate model (e.g., traditional multivariate PARMA or multivariate contemporaneous PARMA) would preserve the statistics (e.g., means, variances, autocorrelations, and cross-covariances) of the different sites but would not satisfy the additivity requisite. However, application of disaggregation schemes to the whole system could become cumbersome due to the relatively large number of sites. Therefore, a preferable approach is to use multivariate models to simulate flows at key sites (e.g., stations farthest downstream along a main stream) first and then use one or more disaggregation schemes to disaggregate such generated values into flows at the other sites. To this end, no general rule exists and the modeler should use his or her judgment and expertise to choose a modeling strategy that can meet as much as possible the simulation requirements. In the following example, such a modeling strategy is better illustrated with reference to a real case.

Example 6-2: Disaggregation Strategy for Modeling Upper Colorado River System

This example is taken from [Salas et al. \(2006\)](#) and shows a spatiotemporal disaggregation modeling and generation approach applied to the monthly streamflow data of the Upper Colorado River basin.

Figure 6-7 shows the stations' locations in the basin. In this example, the disaggregation approach will be illustrated with reference to part of the Upper Colorado Basin. In principle, only a multivariate PARMA or CPARMA model could be fitted to monthly flows at all stations. Though this would preserve the cross-correlations at the different sites, the additivity between upstream and downstream sites would not be ensured and, furthermore, the statistics at the annual scale would not be preserved. For instance, application of a monthly multivariate model would not ensure that the flows (at the monthly time scale, let alone at the annual one) at station 8 would be equal to the sum of flows at stations 7, 6, and 2. However, application of a combined multivariate-disaggregation approach will preserve the aforementioned features, as described in the following.

The map shows that stations 8 and 16 control two major sources for the Upper Colorado Basin and therefore can be both considered key stations for stepwise disaggregation. Further upstream, stations 2, 6, 7, 11, 12, 13, 14, and 15 are the control stations for the tributaries. Therefore these stations are considered substations. Then the key stations can be modeled so that the annual flows of the key stations will be added together to form one series of annual data as an artificial index station. The artificial index station data can be fitted with an ARMA(1, 1) model and then a disaggregation model (either a Valencia and Schaake or a Mejia and Rousselle scheme) can be applied to disaggregate the annual flows of the index station into the annual flows at the key stations. The key station to substation disaggregation can be done using two groups. The first group contains key station 8 and substations 2, 6, and 7. The second group contains key station 16

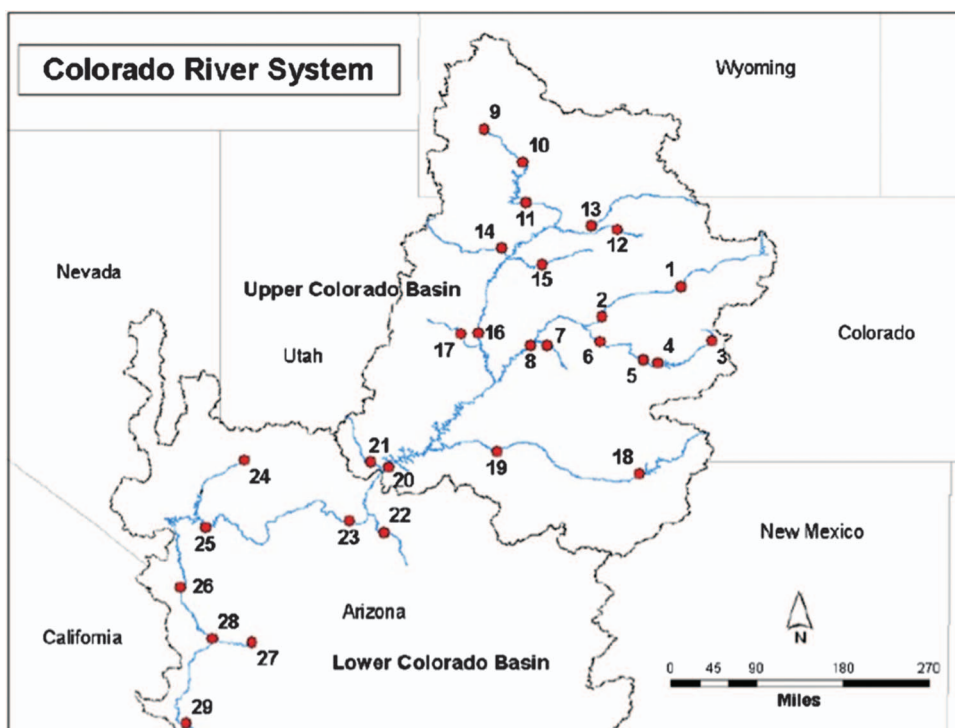


Figure 6-7. Upper Colorado River disaggregation example.

Source: ASCE and Salas (2006).

and substations 11, 12, 13, 14, and 15. Similarly, the same two groups used for spatial grouping are adopted for temporal disaggregation.

Note how the resulting generated series will preserve additivity at downstream sites 8 and 16 because the artificial index station represents the sum of the flows. Furthermore, the stepwise spatiotemporal disaggregation approach will ensure the preservation of additivity at the key stations and the preservation of statistics at both annual and monthly time scales.

6.4 SOFTWARE TOOLS

Several software tools are available for stochastic modeling of streamflow series among which, general purpose time series analysis codes can be employed for many modeling problems. In principle, such general purpose software tools are attractive because they are well documented and offer a wide range of analysis and modeling capabilities. In general, a distinction can be made between software specifically oriented toward statistical analysis and general mathematical platforms for which specific statistical and time series analysis toolboxes are available. Examples of the former categories include Statistica (<http://www.statsoft.com>), SPSS (<http://www-01.ibm.com/software/analytics/spss/>), Statgraphics (<http://www.statgraphics.com>), ITSM (Brockwell and Davis 2002), and others, whereas examples of the latter category are Matlab (<https://www.mathworks.com>) and Mathematica (<https://www.wolfram.com/mathematica>). Besides commercially oriented software, attention to open source software is increasing, for which many tools are continually produced and made available by developers from all over the world. One example is R software (<http://www.r-project.org>), an open source framework for statistical analysis, and related tools (e.g., McLeod et al. 2012). Most of the aforementioned software, however, does not account for issues that are peculiar to streamflow modeling, such as periodicity, cross-correlation, model validation through storage-related and drought statistics, spatial and temporal disaggregation, and other features as discussed in some previous sections. However, specifically designed software has also been developed to support stochastic modeling of streamflows for water engineering problems. Such software tools have the advantage that the underlying models' estimation, verification, and validation procedures involve features that are unique to hydrological time series and streamflows in particular. Examples of hydrological time series oriented software include SAMS (Salas et al. 2006), LAST (Lane and Frevert 1990), and SPIGOT (Grygier and Stedinger 1990).

6.5 FURTHER REMARKS

Streamflow analysis and modeling is one of the key steps for a successful water resources management. The different sources of variability in streamflows must be properly modeled to assess their impacts on water resources availability. In this chapter, several well-known analysis and modeling approaches have been presented, and references to some recently emerging techniques have been provided. The presented models have found widespread application for many water resources management problems, such as streamflow and drought forecasting, reservoir sizing, performance assessment of water supply systems, and many others.

As in many engineering modeling exercises, the selection of the appropriate streamflow modeling strategy should be carried out following a "problem-driven" approach. The modeler should be aware of the features of streamflow variability to account for given the specific purpose of the analysis. Answer to questions such as "what are the temporal scales of interest," "is modeling different sections of the river system necessary," "is preservation of statistics at different temporal scales a key aspect," "is long-term persistence an important feature to be considered (e.g., for

reservoir sizing)," "is intermittency significant in the streamflow series," and some others, may guide the modeler in choosing the most appropriate methodology. Data availability may also play a key role in model selection. Sometimes different approaches may be adopted, and the choice can be made on the basis of cross-validation procedures that can help to highlight which specific feature of interest is best preserved by each methodology (Stedinger and Taylor 1982). To this end, only a clear understanding of the purpose of the analysis and of the corresponding most relevant streamflow features can ensure successful modeling. Finally, the issue of nonstationarity, resulting from the effects of some anthropogenic and oceanic and atmospheric driving factors, is becoming a topic of some interest in the field (e.g., Koutsoyiannis 2016, Sveinsson and Salas 2017).

References

- Acharya, A., and J. H. Ryu. 2013. "Simple method for streamflow disaggregation." *J. Hydrol. Eng.* **19** (3): 509–519.
- Aksoy, H. 2003. "Markov chain-based modeling techniques for stochastic generation of daily intermittent streamflows." *Adv. Water Resour.* **26** (6): 663–671.
- Ballerini, R., and D. C. Boes. 1985. "Hurst behavior of shifting level processes." *Water Resour. Res.* **21** (11): 1642–1648.
- Banerjee, A., and G. Urga. 2005. "Modelling structural breaks, long memory and stock market volatility: An overview." *J. Econom.* **129** (1): 1–34.
- Bartolini, P., J. D. Salas, and J. Obeysekera. 1988. "Multivariate periodic ARMA(1,1) processes." *Water Resour. Res.* **24** (8): 1237–1246.
- Beran, J. 1994. *Statistics for long-memory processes*. Vol. 61. Boca Raton, FL: Chapman & Hall/CRC.
- Bhattacharya, R., V. K. Gupta, and E. Waymire. 1983. "Hurst effect under trends." *J. Appl. Probab.* **20** (3): 649–662.
- Boes, D., and J. D. Salas. 1978. "Nonstationarity of the mean and the Hurst phenomenon." *Water Resour. Res.* **14** (1): 135–143.
- Bras, R. L., and I. Rodriguez-Iturbe. 1985. *Random functions and hydrology*. New York: Dover.
- Brockwell, P. J., and R. A. Davis. 1991. *Time series: Theory and methods*. New York: Springer.
- Brockwell, P. J., and R. A. Davis. 2002. *Introduction to time series and forecasting*. New York: Springer.
- Camacho, F., A. McLeod, and K. Hipel. 1987. "Multivariate contemporaneous arma model with hydrological applications." *Stochastics Hydrol. Hydraul.* **1** (2): 141–154.
- Chebaane, M., J. Salas, and D. Boes. 1995. "Product periodic autoregressive processes for modeling intermittent monthly streamflows." *Water Resour. Res.* **31** (6): 1513–1518.
- Cheung, Y.-W., and F. X. Diebold. 1994. "On maximum likelihood estimation of the differencing parameter of fractionally-integrated noise with unknown mean." *J. Econom.* **62** (2): 301–316.
- Cohn, T. A., and H. F. Lins. 2005. "Nature's style: Naturally trendy." *Geophys. Res. Lett.* **32** (23): L23402.
- Efstratiadis, A., Y. Dialynas, S. Kozanis, and D. Koutsoyiannis. 2014. "A multivariate stochastic model for the generation of synthetic time series at multiple time scales reproducing long term persistence." *Environ. Model. Software* **62**: 139–152.
- Feller, W. 1951. "The asymptotic distribution of the range of sums of independent random variables." *Ann. Math. Stat.* **22** (3): 427–432.
- Fernández, C., J. A. Vega, T. Fontebel, and E. Jiménez. 2009. "Streamflow drought time series forecasting: A case study in a small watershed in North West Spain." *Stochastics Environ. Res. Risk Assess.* **23** (8): 1063–1070.
- Fiering, M. B. 1967. *Streamflow synthesis*. Cambridge, MA: Harvard University Press.
- Fortin, V., L. Perreault, and J. Salas. 2004. "Retrospective analysis and forecasting of streamflows using a shifting level model." *J. Hydrol.* **296** (1): 135–163.
- Fox, R., and M. S. Taqqu. 1986. "Large-sample properties of parameter estimates for strongly dependent stationary Gaussian time series." *Ann. Stat.* **14** (2): 517–532.
- Gangopadhyay, S., B. L. Harding, B. Rajagopalan, J. J. Lukas, and T. J. Fulp. 2009. "A nonparametric approach for paleohydrologic reconstruction of annual streamflow ensembles." *Water Resour. Res.* **45** (6): W06417.
- Granger, C. W., and R. Joyeux. 1980. "An introduction to long-memory time series models and fractional differencing." *J. Time Ser. Anal.* **1** (1): 15–29.
- Grimaldi, S. 2004. "Linear parametric models applied to daily hydrological series." *J. Hydrol. Eng.* **9** (5): 383–391.

- Grygier, J. C., and J. R. Stedinger. 1988. "Condensed disaggregation procedures and conservation corrections for stochastic hydrology." *Water Resour. Res.* **24** (10): 1574–1584.
- Grygier, J. C., and J. R. Stedinger. 1990. *SPIGOT: A synthetic streamflow generation package, technical description, version 2.5*. Ithaca, NY: Cornell Univ.
- Haltiner, J. P., and J. D. Salas. 1988. "Development and testing of a multivariate, seasonal ARMA(1, 1) model." *J. Hydrol.* **104** (1): 247–272.
- Hannan, E. J., and J. Rissanen. 1982. "Recursive estimation of mixed autoregressive-moving average order." *Biometrika* **69** (1): 81–94.
- Hao, Z., and V. Singh. 2013. "Modeling multisite streamflow dependence with maximum entropy copula." *Water Resour. Res.* **49** (10): 7139–7143.
- Henley, B. J., M. A. Thyre, and G. Kuczera. 2013. "Climate driver informed short-term drought risk evaluation." *Water Resour. Res.* **49** (5): 2317–2326.
- Hipel, K. W., and A. I. McLeod. 1994. *Time series modelling of water resources and environmental systems*. Vol. 45. Dordrecht, Netherlands: Elsevier Science.
- Hosking, J. R. 1981. "Fractional differencing." *Biometrika* **68** (1): 165–176.
- Hurst, H. E. 1951. "Long-term storage capacity of reservoirs." *Trans. Am. Soc. Civ. Eng.* **116** (2447): 770–799.
- Hurst, H. E. 1956. "Methods of using long-term storage in reservoirs." *Proc. Inst. Civ. Eng.* **5** (5): 519–543.
- Hurst, H. E. 1957. "A suggested statistical model of some time series which occur in nature." *Nature* **180** (4584): 494–494.
- Indelicato, S., V. Tamburino, S. Barbagallo, and G. Mazzola. 1989. *Risorse idriche nei grandi serbatoi artificiali siciliani. I contributo*. [In Italian.] Catania, Italy: CSEI.
- Kim, T.-W., and J. B. Valdés. 2005. "Synthetic generation of hydrologic time series based on nonparametric random generation." *J. Hydrol. Eng.* **10** (5): 395–404.
- Klemeš, V. 1974. "Hurst phenomenon: A puzzle?" *Water Resour. Res.* **10** (4): 675–688.
- Klemeš, V. 1987. "One hundred years of applied storage reservoir theory." *Water Resour. Manage.* **1** (3): 159–175.
- Klemeš, V., R. Srikanthan, and T. McMahon. 1981. "Long- memory flow models in reservoir analysis: What is their practical value?" *Water Resour. Res.* **17** (3): 737–751.
- Koutsoyiannis, D. 2002. "The Hurst phenomenon and fractional Gaussian noise made easy." *Hydrol. Sci. J.* **47** (4): 573–595.
- Koutsoyiannis, D. 2003. "Climate change, the Hurst phenomenon, and hydrological statistics." *Hydrol. Sci. J.* **48** (1): 3–24.
- Koutsoyiannis, D. 2011. "Hurst-Kolmogorov dynamics and uncertainty." *J. Am. Water Resour. Assoc.* **47** (3): 481–495.
- Koutsoyiannis, D. 2016. "Generic and parsimonious stochastic modeling for hydrology and beyond." *Hydrol. Sci. J.* **61** (2): 225–244.
- Koutsoyiannis, D., and A. Manetas. 1996. "Simple disaggregation by accurate adjusting procedures." *Water Resour. Res.* **32** (7): 2105–2117.
- Krzysztofowicz, R. 1997. "Transformation and normalization of variates with specified distributions." *J. Hydrol.* **197** (1–4): 286–292.
- Kunsch, H. R. 1989. "The jackknife and the bootstrap for general stationary observations." *Ann. Stat.* **17** (3): 1217–1241.
- Lall, U., and A. Sharma. 1996. "A nearest neighbor bootstrap for resampling hydrologic time series." *Water Resour. Res.* **32** (3): 679–693.
- Lane, W. L. 1982. "Corrected parameter estimates for disaggregation schemes." In *Statistical analysis of rainfall and runoff*, edited by V. Singh, 505–530. Littleton, CO: Water Resources Publications.
- Lane, W. L., and D. Frevert. 1990. *Applied stochastic techniques user manual*. Denver: US Bureau of Reclamation.
- Lee, T., J. Salas, and J. Prairie. 2010. "An enhanced nonparametric streamflow disaggregation model with genetic algorithm." *Water Resour. Res.* **46** (8).
- Li, C., V. P. Singh, and A. K. Mishra. 2013. "Monthly river flow simulation with a joint conditional density estimation network." *Water Resour. Res.* **49** (6): 3229–3242.
- Mandelbrot, B. B. 1965. "Une classe de processus stochastiques homothétiques à soi; application à la loi climatologique de hehurst." [In French.] *CR Acad. Sci. Paris* **260**: 3284–3277.

- Mandelbrot, B. B., and J. W. Van Ness. 1968. "Fractional Brownian motions, fractional noises and applications." *SIAM Rev.* **10** (4): 422–437.
- Mandelbrot, B. B., and J. R. Wallis. 1968. "Noah, Joseph, and operational hydrology." *Water Resour. Res.* **4** (5): 909–918.
- Mandelbrot, B. B., and J. R. Wallis. 1969. "Computer experiments with fractional Gaussian noises. Part 1: averages and variances." *Water Resour. Res.* **5** (1): 228–241.
- Matalas, N. C. 1967. "Mathematical assessment of synthetic hydrology." *Water Resour. Res.* **3** (4): 937–945.
- McLeod, A. I., and K. W. Hipel. 1978. "Simulation procedures for Box-Jenkins models." *Water Resour. Res.* **14** (5): 969–975.
- McLeod, A. I., H. Yu, and E. Mahdi. 2012. "Time series analysis with r." Vol. **30** of *Handbook of statistics*. Dordrecht, Netherlands: Elsevier.
- Mehrotra, R., and A. Sharma. 2006. "Conditional resampling of hydrologic time series using multiple predictor variables: A k-nearest neighbour approach." *Adv. Water Resour.* **29** (7): 987–999.
- Mejia, J. M., and J. Rousselle. 1976. "Disaggregation models in hydrology revisited." *Water Resour. Res.* **12** (2): 185–186.
- Modarres, R. 2007. "Streamflow drought time series forecasting." *Stochastic Environ. Res. Risk Assess.* **21** (3): 223–233.
- Moeeni, H., and H. Bonakdari. 2016. "Forecasting monthly inflow with extreme seasonal variation using the hybrid sarima-ann model." *Stochastic. Environ. Res. Risk Assess.* **31** (8): 1–14.
- Montanari, A. 2005. "Deseasonalisation of hydrological time series through the normal quantile transform." *J. Hydrol.* **313** (3–4): 274–282.
- Montanari, A., R. Rosso, and M. S. Taqqu. 1997. "Fractionally differenced arima models applied to hydrologic time series: Identification, estimation, and simulation." *Water Resour. Res.* **33** (5): 1035–1044.
- O'Connell, P. 1974. "Stochastic modelling of long-term persistence in streamflow sequences." Ph.D. thesis, Imperial College, Univ. of London.
- Piccolo, D. 1990. "A distance measure for classifying arima models." *J. Time Ser. Anal.* **11** (2): 153–164.
- Portela, M. M., and A. T. Silva. 2016. "Disaggregation modelling of annual flows into daily streamflows using a new approach of the method of fragments." *Water Resour. Manage.* **30** (15): 5589–5607.
- Potter, K. W. 1976. "Evidence of nonstationarity as a physical explanation of the Hurst phenomenon." *Water Resour. Res.* **12** (5): 1047–1052.
- Prairie, J., B. Rajagopalan, U. Lall, and T. Fulp. 2007. "A stochastic nonparametric technique for space-time disaggregation of streamflows." *Water Resour. Res.* **43** (3).
- Prairie, J. R., B. Rajagopalan, T. J. Fulp, and E. A. Zagona. 2006. "Modified k-nn model for stochastic streamflow simulation." *J. Hydrol. Eng.* **11** (4): 371–378.
- Rasmussen, P. F., J. D. Salas, L. Fagherazzi, J.-C. Rassam, and B. Bobée. 1996. "Estimation and validation of contemporaneous parma models for streamflow simulation." *Water Resour. Res.* **32** (10): 3151–3160.
- Salas, J. D. 1993. "Analysis and modeling of hydrologic time series." Chap. 19 in *Handbook of hydrology*, edited by D. Maidment. New York: McGraw-Hill.
- Salas, J. D., and D. C. Boes. 1980. "Shifting level modelling of hydrologic series." *Adv. Water Resour.* **3** (2): 59–63.
- Salas, J. D., D. C. Boes, and R. A. Smith. 1982. "Estimation of arma models with seasonal parameters." *Water Resour. Res.* **18** (4): 1006–1010.
- Salas, J. D., D. C. Boes, V. Yevjevich, and G. G. S. Pegram. 1979. "Hurst phenomenon as a pre-asymptotic behavior." *J. Hydrol.* **44** (1–2): 1–15.
- Salas, J. D., and T. Lee. 2009. "Nonparametric simulation of single-site seasonal streamflows." *J. Hydrol. Eng.* **15** (4): 284–296.
- Salas, J. D., and J. Obeysekera. 1992. "Conceptual basis of seasonal streamflow time series models." *J. Hydrol. Eng.* **118** (8): 1186–1194.
- Salas, J. D., and G. G. S. Pegram. 1977. "A seasonal multivariate multilag autoregressive model in hydrology." In *Proc., 3rd Int. Symp. Theoretical and Applied Hydrology*. Fort Collins, CO: Colorado State Univ.
- Salas, J. D., N. Saada, and C. Chung. 1995. *Stochastic modeling and simulation of the Nile River system monthly flows*. Technical Rep. No. 5. Fort Collins, CO: Colorado State Univ.
- Salas, J. D., and R. A. Smith. 1981. "Physical basis of stochastic models of annual flows." *Water Resour. Res.* **17** (2): 428–430.

- Salas, J. D., O. Sveinsson, W. Lane, and D. Frevert. 2006. "Stochastic streamflow simulation using SAMS-2003." *J. Irrig. Drain. Eng.* **132** (2): 112–122.
- Santos, E. G., and J. D. Salas. 1992. "Stepwise disaggregation scheme for synthetic hydrology." *J. Hydraul. Eng.* **118** (5): 765–784.
- Sharma, A., and R. O'Neill. 2002. "A nonparametric approach for representing interannual dependence in monthly streamflow sequences." *Water Resour. Res.* **38** (7): 5-1–5-10.
- Sharma, A., D. G. Tarboton, and U. Lall. 1997. "Streamflow simulation: A nonparametric approach." *Water Resour. Res.* **33** (2): 291–308.
- Siddiqui, M. 1976. "The asymptotic distribution of the range and other functions of partial sums of stationary processes." *Water Resour. Res.* **12** (6): 1271–1276.
- Smith, A. 2005. "Level shifts and the illusion of long memory in economic time series." *J. Bus. Econ. Stat.* **23** (3): 321–335.
- Sowell, F. 1992. "Maximum likelihood estimation of stationary univariate fractionally integrated time series models." *J. Econom.* **53** (1): 165–188.
- Srinivas, V., and K. Srinivasan. 2001. "A hybrid stochastic model for multiseason streamflow simulation." *Water Resour. Res.* **37** (10): 2537–2549.
- Srinivas, V., and K. Srinivasan. 2005. "Hybrid moving block bootstrap for stochastic simulation of multi-site multi-season streamflows." *J. Hydrol.* **302** (1): 307–330.
- Srinivas, V., and K. Srinivasan. 2006. "Hybrid matched-block bootstrap for stochastic simulation of multiseason streamflows." *J. Hydrol.* **329** (1): 1–15.
- Stedinger, J. R., D. P. Lettenmaier, and R. M. Vogel. 1985a. "Multisite arma(1, 1) and disaggregation models for annual streamflow generation." *Water Resour. Res.* **21** (4): 497–509.
- Stedinger, J. R., D. Pei, and T. A. Cohn. 1985b. "A condensed disaggregation model for incorporating parameter uncertainty into monthly reservoir simulations." *Water Resour. Res.* **21** (5): 665–675.
- Stedinger, J. R., and M. R. Taylor. 1982. "Synthetic streamflow generation: 1. Model verification and validation." *Water Resour. Res.* **18** (4): 909–918.
- Stedinger, J. R., and R. M. Vogel. 1984. "Disaggregation procedures for generating serially correlated flow vectors." *Water Resour. Res.* **20** (1): 47–56.
- Sveinsson, O. G. B., and J. D. Salas. 2017. "Time series analysis and models." In *Handbook of applied hydrology*. 2nd ed., edited by V. P. Singh. New York: McGraw-Hill.
- Sveinsson, O. G. B., J. D. Salas, D. C. Boes, and R. A. Pielke Sr. 2003. "Modeling the dynamics of long-term variability of hydroclimatic processes." *J. Hydrometeorol.* **4** (3): 489–505.
- Tarboton, D. G., A. Sharma, and U. Lall. 1998. "Disaggregation procedures for stochastic hydrology based on nonparametric density estimation." *Water Resour. Res.* **34** (1): 107–119.
- Thomas, H., and M. Fiering. 1962. "Mathematical synthesis of streamflow sequences for the analysis of river basins by simulation." In *Design of water resources systems*, edited by A. Mass, et al., 459–493. Cambridge, MA: Harvard University Press.
- Valencia, R. D., and J. C. Schaake. 1973. "Disaggregation processes in stochastic hydrology." *Water Resour. Res.* **9** (3): 580–585.
- Valipour, M. 2015. "Long-term runoff study using sarima and arima models in the United States." *Meteorol. Appl.* **22** (3): 592–598.
- Vogel, R. M., and A. L. Shallcross. 1996. "The moving blocks bootstrap versus parametric time series models." *Water Resour. Res.* **32** (6): 1875–1882.
- Wallis, J. R., and N. C. Matalas. 1970. "Small sample properties of h and k-estimators of the Hurst coefficient h." *Water Resour. Res.* **6** (6): 1583–1594.
- Yevjevich, V. 1963. *Fluctuations of wet and wry years. Part 1: Research data assembly and mathematical models*. Hydrology Paper No. 1. Fort Collins, CO: Colorado State Univ.

CHAPTER 7

Flood Frequency Analysis in the United States

Veronica L. Webster (formerly Veronica Webster Griffis)
Jery R. Stedinger

7.0 GENERAL

A large portion of the US population, infrastructure, and industry is located in flood-prone areas. Floods cause an average of nearly 100 deaths and cost roughly US\$2.3 billion annually. While hydrologic and hydraulic engineers cannot stop floods from occurring, they should seek structural or nonstructural strategies to reduce the risk of large economic losses, social disruption, and loss of life. To identify plans that are economically and socially rational requires an estimate of the risk of flooding. Accurate estimates of the magnitude and frequency of flood flows are needed for the design of water-use and water-control projects, for floodplain definition and management, and for the design of transportation infrastructure such as bridges and roads. This chapter evaluates the methods currently employed and recently recommended for use in the United States for flood frequency analysis.

To describe the possible magnitudes of future flood flows and their frequency, one could use either the empirical distribution represented by the data, or an analytic probability distribution fit to the data. In practice the true distribution that describes flood events is not known, and thus use of an empirical distribution may be appealing. However, using a reasonable analytic distribution has several advantages (Stedinger et al. 1993):

1. It presents a smooth interpretation of the empirical distribution. As a result, quantiles and other statistics computed using the fitted distribution should be more accurate than those computed with the empirical distribution.
2. It provides a compact and easy-to-use representation of available data.
3. It is likely to provide a more realistic description of the range of values that a random variable may assume and their likelihood, in other words, probability of occurrence. For example, by using the empirical distribution one implicitly assumes that no values larger or smaller than the sample maximum or minimum can occur. This is unreasonable for flood series.
4. Often one needs to estimate the likelihood of extreme events that lie outside the range of the sample (either in terms of magnitude or in terms of frequency). Such extrapolation makes little sense with the empirical distribution.

Distributions commonly employed to model annual maximum flood series include the log-Pearson type III, generalized extreme value, log-normal, and generalized logistic distributions; see Stedinger et al. (1993), Kotegoda and Rosso (1997), Hosking and Wallis (1997) and references therein).

For the selected analytic distribution, one must estimate its parameters so that the fitted distribution is consistent with the available data. Several parameter estimation methods are available, including maximum likelihood, method of moments, L-moments, and Bayesian inference. Maximum likelihood methods have the most theoretical appeal and, for many problems, generate asymptotically the most efficient estimators possible. They are also very flexible. Method of moment estimators have a long history of use, are often easy to employ, and have intuitive appeal. They summarize the available data by its sample average and often the sample variance; the parameters of the analytic distribution are then selected to reproduce those statistics. In several classic cases, method of moments and maximum likelihood estimators are equivalent. (This is true for the binomial, Poisson, normal, and exponential distributions with complete samples.) Still other methods continue to be developed, often for special situations, and are in some cases very attractive. L-moments are commonly employed for regional analysis of hydrologic variables such as rainfall and floods ([Hosking and Wallis 1997](#)).

Bayesian inference represents a different statistical point of view for parameter estimation. In a Bayesian statistical framework the unknown parameters are viewed as random variables whose distribution is derived, conditional on the available data interpreted through the likelihood function and prior information provided by the analyst. The use of prior information raises interesting issues about what is known about a distribution from sources beyond the dataset that may be available for a site. Such information is often subjective. This use of subjective information is attractive to some groups, while others find it troubling. Bayesian methods are experiencing a resurgence of interest with the recent development of Monte–Carlo Markov–Chain (MCMC) methods that provide a Bayesian analysis of a range of problems which were previously intractable; see, for example, [Gelman et al. \(1995\)](#), [Reis and Stedinger \(2005\)](#), [Renard \(2011\)](#), or [Viglione et al. \(2013\)](#).

The current methodology recommended for flood frequency analysis by US federal agencies is presented in *Bulletin 17B* ([IACWD 1982](#)). Under the assumption that annual maximum flood series are a sample of independent and identically distributed events, *Bulletin 17B* fits a log–Pearson type III (LP3) distribution to a flood series. The recommended technique is to fit a Pearson type III (P3) distribution to the logarithms of the flood series using the method of moments (MOM). Estimates of the mean, standard deviation, and skew coefficient of the sample data’s logarithms are computed using traditional moment estimators. However, because the data available at a site are generally limited to less than 100 years, and is often less than 30 years in length, the skewness estimator can be particularly unstable. Therefore, *Bulletin 17B* recommends combining the at-site skew with regional skew information to obtain a more accurate skewness estimator. *Bulletin 17B* includes several additional procedures to adjust sample moments and improve flood quantile estimates. The following sections discuss three major features of the *Bulletin*: regional skew coefficients, low outliers and the conditional probability adjustment, and historical flood peaks.

Because of the importance of the LP3 distribution in the United States, this chapter focuses primarily on the characteristics of the LP3 distribution and its applicability in flood frequency analysis, the value of regional skew information, and recommended procedures for low outlier adjustment and the incorporation of historical flood information. Innovations in the new *Bulletin 17C* are outlined. Uncertainty and variability in flood control projects and possible methods to incorporate climate variability and climate change into flood frequency analyses are also discussed.

7.1 EVOLUTION OF BULLETIN 17B

Bulletin 17B ([IACWD 1982](#)) describes uniform flood frequency techniques recommended for use by US federal agencies. Although now 35 years old, *Bulletin 17B* is the most recent document in a series of publications by the US government attempting to provide a uniform and accurate method for

estimating flood quantiles ([Griffis and Stedinger 2007a](#)). The development of a uniform procedure for flood frequency analysis began as part of a larger movement to improve water management practices. In the mid-1960s it became apparent that uniform flood frequency methods were needed for the development of a national flood insurance program in the United States and to facilitate the interaction among various levels of government and private enterprise that share water resource systems ([Thomas 1985](#)).

Prior to the 1960s, the United States lacked a national policy for prioritizing water projects. Congress and the Bureau of the Budget (BoB) required that all projects pass an economic feasibility test (i.e., that benefits would exceed costs) as outlined in Circular A-47 ([Caulfield 2000](#)). All agencies involved in water resources planning were required to submit details of their programs to the BoB for review.

In the early 1960s, Congress began advocating uniform standards for the evaluation and formulation of water projects by federal agencies. The movement toward uniform procedures began in July 1961 when President John Kennedy proposed the Water Resources Planning Act. Although the Act was not finalized until 1965, a Water Resources Council (WRC) was formed in October 1961 as stipulated in the president's bill. The charge of the council was to review current policies, standards, and procedures for the formulation and evaluation of water projects and to develop new uniform standards to be employed by all federal agencies. The new standards were completed by May 1962 and submitted to President Kennedy for review. Shortly afterward, the new standards were published as *Senate Document No. 97*, and *Circular A-47* was annulled ([Holmes 1979](#), pp. 43–44, [Caulfield 2000](#)).

Under the direction of the BoB, the uniform standards outlined in *Senate Document No. 97* were intended to facilitate coordination of interagency water projects with three main objectives: economic development, preservation of natural resources, and the well-being of the people ([Coffey 2005](#), personal communications). With regard to these objectives, on August 10, 1966, the BoB for President Lyndon Johnson submitted a report with recommendations for the development of a national flood-damage abatement program. Published as *House Document No. 465*, the report led to the National Flood Insurance Act of 1968.

Recommendation 2 of *House Document No. 465* was for the WRC to establish a panel consisting of hydrologists, statisticians, and economists to "present a set of techniques for frequency analyses that are based on the best of known hydrological and statistical procedures." The WRC did so in September 1966 under the direction of the BoB. In December 1967, the WRC published *Bulletin 15*, "A Uniform Technique for Determining Flood Flow Frequencies"; this was the first set of uniform flood frequency techniques to be employed by all federal agencies ([Water Resources Council 1967](#)).

[Benson \(1968\)](#) discusses the analysis employed in developing *Bulletin 15*. Six procedures were considered and ultimately the LP3 distribution with a regional skew coefficient was recommended. The procedures considered were the most common techniques employed by federal agencies at that time, including graphical distribution-free methods and various statistical distributions; *Bulletin 13*, "Methods of Flow Frequency Analysis," published in April 1966, describes those methods ([Inter-agency Committee on Water Resources 1966](#)).

Bulletin 15 was a significant step toward the development of a uniform procedure for flood frequency analysis; however, it was not as uniform as originally intended ([Thomas 1985](#), p. 324). Uniform procedures were not specified for the treatment of outliers or the estimation of the regional skew, and no recommendation was made for the use of historical data.

In the years following, *Bulletin 15* evolved in response to efforts that aimed to improve various aspects of the recommended techniques. *Bulletin 17*, "Guidelines for Determining Flood Flow Frequency," was published in March 1976, and was quickly succeeded by *Bulletin 17A*, published in June 1977. The latter version included a clarification that the computation of weighted moments reflecting available historical information was to be employed before weighting the sample skew with a regional skew; this is the only significant difference between *Bulletin 17* and *17A* ([Thomas 1985](#)). However, discrepancies still existed in the treatment of low outliers, and thus *Bulletin 17B* was

published in September 1981. *Bulletin 17B* also includes a revised weight for skew estimation (Thomas 1985). *Bulletin 17B*, last revised in March 1982, is the methodology currently recommended for flood frequency analysis by federal agencies in the United States.

7.2 CHARACTERISTICS OF THE LP3 DISTRIBUTION

The LP3 distribution is an extension of the Pearson type III family of distributions, one of several families of distributions proposed by the statistician Pearson as a model of random variables (Bobee and Ashkar 1991). The LP3 distribution is used extensively in hydrologic applications and is currently recommended for use by US federal agencies for flood frequency analyses as described by *Bulletin 17B*, but its properties are not always well understood. The primary goals of this section are (1) to provide a clear and concise presentation of the characteristics of the LP3 distribution, including L-moments, product moments in both real space and log space, and their relationship, and (2) to define combinations of the log space skew and the log space standard deviation that are consistent with the characteristics of real US flood data and for which the LP3 distribution is a reasonable model of the distribution of annual maximum flood series from unregulated watersheds.

7.2.1 Log Space Characteristics

The LP3 distribution describes a random variable Q whose logarithms are P3 distributed. Thus, $Q = \exp(X)$ if a base-e conversion is employed. To simplify the discussion, all results presented in this section use base-e natural logarithms, although any base could be employed; *Bulletin 17B* employs base-10 common logarithms. [If $Y = \log_{10}(Q)$, then $Y = \log_{10}(e)$ and $X = 0.4343 Y$; thus, Y has a scaled version of the X distribution with the same skew.]

The P3 distribution has shape, scale, and location parameters α , β , and τ with the probability density function

$$f_X(x) = \frac{1}{|\beta| \Gamma(\alpha)} \left[\frac{x - \tau}{\beta} \right]^{\alpha-1} \exp \left[-\frac{x - \tau}{\beta} \right] \quad (7-1)$$

defined for $\alpha > 0$ and $(x - \tau)/\beta > 0$, where $\Gamma(\alpha)$ is the complete gamma function.

The parameters of the P3 distribution are functions of the first three population moments (μ_x , σ_x , and γ_x):

$$\alpha = \frac{4}{\gamma_x^2}; \beta = \frac{\sigma_x \gamma_x}{2}; \tau = \mu_x - 2 \frac{\sigma_x}{\gamma_x} \quad (7-2)$$

By definition the standard deviation σ_x is positive; therefore, the skewness coefficient γ_x and the parameter β must have the same sign. For a positively skewed distribution, β is positive and τ is the lower bound of the P3 distribution with an unbounded tail for larger quantiles. For a negatively skewed distribution, β is negative and τ is the upper bound of the P3 distribution that is unbounded below. The existence of an upper bound for flood flows with the LP3 distribution can be a concern (Gilroy 1972). This issue is addressed later in this section.

Figure 7-1 illustrates the shape of the P3 density function for four values of the population skew coefficient γ_x with mean $\mu_x = 1$ and lower bound $\tau = 0$. Only cases with positive skew coefficients are shown; the shape and scale of the P3 density function are the same for negative values of γ_x when μ_x and σ_x are held constant. However, the location parameter τ changes from a lower bound to an upper bound as the resultant distribution with negative skew is the reverse reflection about the mean of the distribution with positive skew of the same magnitude.

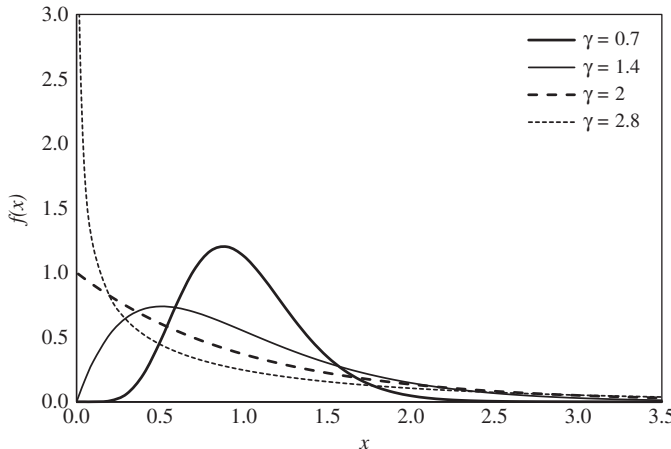


Figure 7-1. Probability density function for P3 distribution with $\tau = 0$; $\mu_x = 1$; and $\gamma_x = 0.7, 1.4, 2.0$, and 2.8 .

7.2.2 Real Space Characteristics

The LP3 distribution has the following probability density function:

$$\begin{aligned} f_Q(q) &= \frac{1}{|\beta|q\Gamma(\alpha)} \left[\frac{\ln q - \tau}{\beta} \right]^{\alpha-1} \exp\left[-\frac{\ln q - \tau}{\beta}\right] \\ &= \frac{1}{|\beta|\Gamma(\alpha)} \frac{\exp(\tau/\beta)}{q^{1+1/\beta}} \left[\frac{\ln q - \tau}{\beta} \right]^{\alpha-1} \end{aligned} \quad (7-3)$$

where $\ln Q = X$ has a P3 distribution with parameters α , β , and τ . The density function is defined for $\alpha > 0$, $0 < q \leq \exp(\tau)$ for $\gamma_x < 0$, and $\exp(\tau) \leq q$ for $\gamma_x > 0$. When γ_x goes to 0, the LP3 distribution converges to a log-normal distribution.

The r^{th} noncentral moment of Q is

$$E[Q^r] = e^{r\tau} \left(\frac{1}{1 - r\beta} \right)^\alpha \quad (7-4)$$

for $\beta < 1/r$ (Bobee, 1975, Equation 13; Johnson et al. 1994, pp. 383–384). Using Equation (7-4) the product moments of Q are

$$\begin{aligned} \mu_Q &= e^\tau \left(\frac{1}{1 - \beta} \right)^\alpha && \text{for } \beta < 1 \\ \sigma_Q^2 &= e^{2\tau} \left[\left(\frac{1}{1 - 2\beta} \right)^\alpha - \left(\frac{1}{1 - \beta} \right)^{2\alpha} \right] && \text{for } \beta < 1/2 \\ \gamma_Q &= \frac{E[Q^3] - 3\mu_Q E[Q^2] + 2\mu_Q^3}{\sigma_Q^3} && \text{for } \beta < 1/3 \end{aligned} \quad (7-5)$$

The product moments are infinite for values of β outside of these ranges.

Using Equation (7-5), the real space $C_v = \sigma_Q/\mu_Q$ can be computed from

$$C_v = \left[\left(1 + \frac{\beta^2}{1 - 2\beta} \right)^\alpha - 1 \right]^{1/2} = \left[\left(1 + \frac{[\sigma_x \gamma_x]^2}{4[1 - \sigma_x \gamma_x]} \right)^{4/\gamma_x^2} - 1 \right]^{1/2} \quad (7-6)$$

for $\beta < 1/2$ or $\sigma_x \gamma_x < 1$, and $\gamma_x \neq 0$. When γ_x goes to 0, the LP3 distribution converges to a log-normal distribution for which the real space C_v and real space skew γ_Q are computed as follows:

$$C_v = [\exp(\sigma_x^2) - 1]^{1/2} \quad (7-7)$$

$$\gamma_Q = 3C_v + C_v^3 \quad (7-8)$$

Figure 7-2 illustrates the shape of the LP3 density function for different combinations of α and β with $m = \exp(\tau)$. (Recall $\alpha = 4/\gamma_x^2$.) Bobee (1975) and Bobee and Ashkar (1991) also illustrate these forms of the LP3 density function; however, a different parameterization is employed herein resulting in a permutation of the patterns. Table 7-1 summarizes the various forms of the density function resulting from different combinations of α and β . The shape of the density function at the bound $\exp(\tau)$ is always controlled by α (or $|\gamma_x|$). The density function at $q = \exp(\tau)$ is infinite at the upper/lower bound when $0 < \alpha < 1$ ($|\gamma_x| > 2$) and does not have a tail when $1 < \alpha < 2$ ($1.414 < |\gamma_x| < 2$). When $2 < \alpha$ ($|\gamma_x| < 1.414$), the form of the density function at $q = \exp(\tau)$ at the bound ranges from a short tail to a long, thin tail as α increases from two to larger values.

For $\beta > 0$, corresponding to $\gamma_x > 0$, $\exp(\tau)$ is the lower bound of the LP3 distribution and the distribution is unbounded above. The r^{th} moment of Q only exists for $\beta < 1/r$, independent of α , and thus β affects the thickness of the upper tail. Figure 7-2 illustrates as cases P1 to P3 the LP3 density functions with $\beta > 0$, which emulate the corresponding P3 density functions for each range of γ_x .

For $\beta < 0$, corresponding to $\gamma_x < 0$, the LP3 distribution has a lower bound of 0 and an upper bound of $\exp(\tau)$. As illustrated in Figure 7-2, $\beta < 0$ yields several forms of the LP3 density function. This occurs because q is now allowed to approach 0, unlike for $\beta > 0$ when q must exceed $\exp(\tau)$. For $\beta < 0$, the LP3 density function in Equation (7-3) is a function of $q^{-1/(1+\beta)}$. Therefore, for $\beta < -1$, the density function is inversely proportional to q^p for negative p and thus goes to infinity when q goes to 0. For $-1 < \beta < -1/2$, the density function is proportional to q^p , where p is between 0 to 1; this causes the density function to go to 0 quasi-linearly when q goes to 0. For $-1/2 < \beta < 0$, the density function is proportional to a power of q greater than 1, and has a thin tail as q goes to 0. Thus, β controls the shape of the density function at $q = 0$.

When considering the shape of the LP3 distribution in log space as in Figure 7-1, the mean and standard deviation are not of concern because they only affect the location and scale of the distribution, respectively, and not the shape. When converting from log space (Figure 7-1) to real space (Figure 7-2), the mean only affects the scale of the LP3 distribution. However, the standard deviation through the value of β affects the shape of the distribution in real space. As Figure 7-2 illustrates, the shape of the LP3 distribution in real space is a complex function of both α and β and is thus a function of the log space standard deviation σ_x and the log space skew γ_x ; see Equation (7-2).

While Figure 7-2 clearly shows the relationship between γ_x and the LP3 parameters α and β , less clear is how σ_x relates to the various forms of the LP3 density function. Regions P1 to P3 and N1 to N9 in Figure 7-3 represent the combinations of σ_x and γ_x , which result in the 12 forms of the LP3 density function previously shown in Figure 7-2.

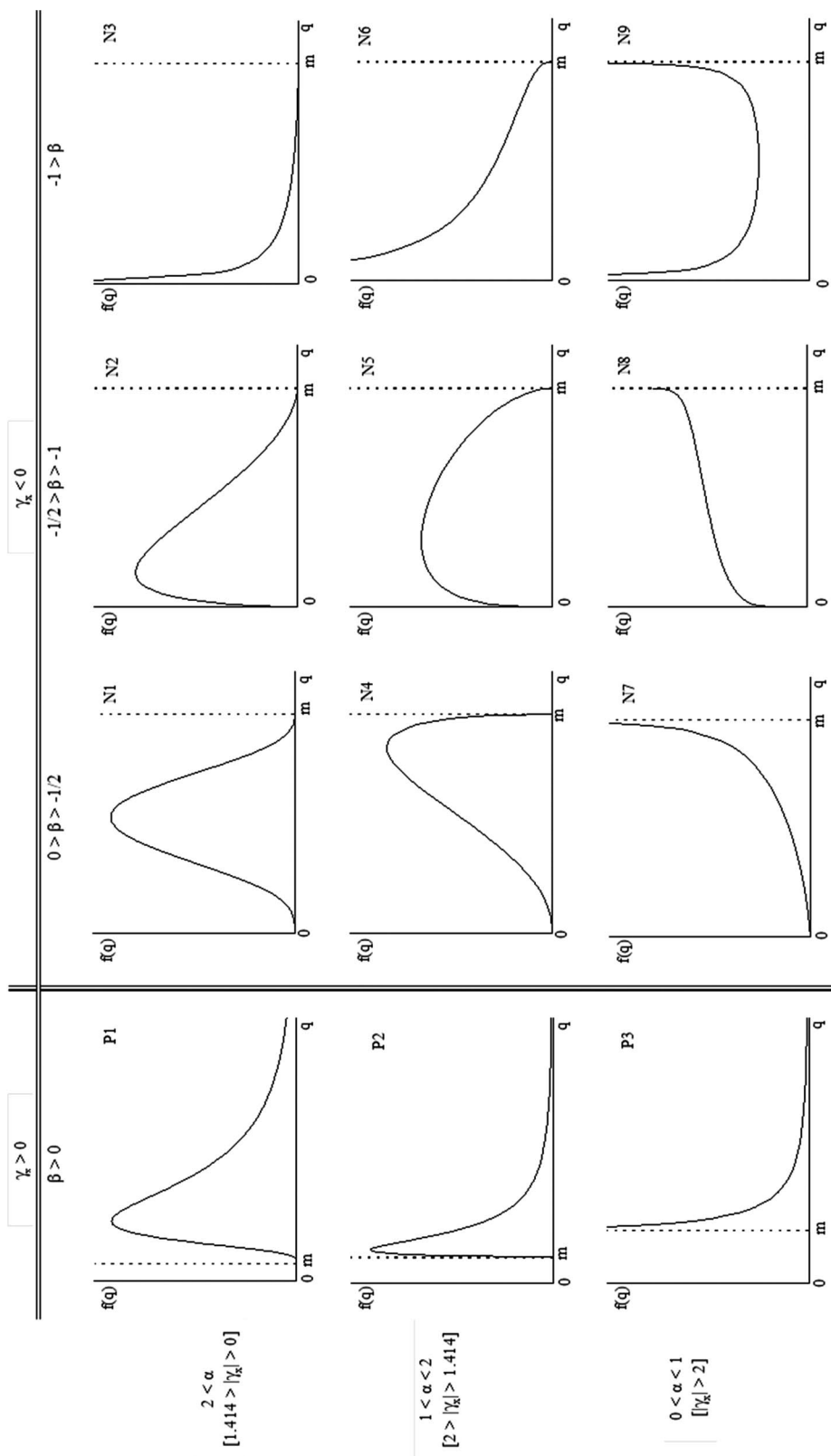


Figure 7-2. Probability density function for LP3 distribution with $m = \exp(\tau)$ and various combinations of α and β .

Table 7-1. Shape of LP3 Density Function for Different Combinations of α and β .

		$\gamma_x > 0$	$\gamma_x < 0$		
		$\beta > 0$	$0 > \beta > -1/2$	$-1/2 > \beta > -1$	$-1 > \beta$
$2 < \alpha$ ($1.414 > \gamma_x $)	P1. Long, thin upper tail; thin lower tail	N1. Bell shape, thin upper tail	N2. Thin upper tail	N3. Reverse J-shape (infinite at zero)	
$1 < \alpha < 2$ ($2 > \gamma_x >$ 1.414)	P2. Mode close to lower bound, no lower tail	N4. Mode close to upper bound, no upper tail	N5. No tails*	N6. No tail at upper bound	
$0 < \alpha < 1$ ($ \gamma_x > 2$)	P3. Reverse J-shape (infinite at lower bound), thick upper tail	N7. J-shape (infinite at upper bound)	N8. No tails, infinite at upper bound	N9. U-shape (infinite at zero and upper bound)*	

*Bobee (1975) subdivides these cases into two classes, but neither is of interest here.

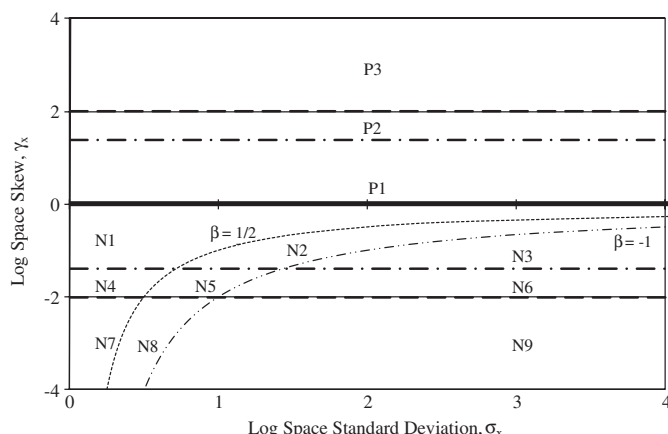


Figure 7-3. Log space skew versus log space standard deviation as a function of LP3 parameters α and β (with base-e transformations).

7.2.3 LP3 Model for Annual Flood Series

Concerns have been raised regarding how appropriate the LP3 distribution is as a model of annual maximum flood series. One concern is the existence of an upper bound for flood flows when modeled by the LP3 distribution. Another issue is the range of LP3 parameter values that is reasonable. In this section, parameter values for the LP3 distribution that are thought to produce reasonable flood-like distributions are juxtaposed with the observed characteristics of real flood series using statistics in both log space and real space. The analysis demonstrates that the characteristics of real US flood data across the 14 regions delineated by the US Geological Survey fall well within the range of parameters for which the LP3 distribution is thought to produce reasonable flood-like distributions.

Log Space Model. In the literature, log space skews for floods are commonly restricted to the range ± 1.0 (Chowdury and Stedinger 1991, Spencer and McCuen 1996, Cohn et al. 1997,

Whitley and Hromadka 1999, McCuen 2001). Although a log space population skew of $\gamma_x = \pm 1.0$ would seem to be very extreme, having sample skews on the order of -1.0 is not uncommon. For a partition of the United States into 14 regions, Landwehr et al. (1978) report mean regional log space skew values in the range $(-0.4, +0.3)$. Hardison (1974) reports mean regional log space skew values in the range $(-0.5, +0.6)$, with a standard error for individual station estimators of 0.55 (corresponding to a mean square error $MSE(G_R)$ of 0.302). Thus, a range of $(-1.0, +1.0)$ for the log space skew is certainly within the distribution of site-to-site variability reported by Hardison.

Subsequent work by Tasker and Stedinger (1986) indicates $MSE(G_R) = 0.302$ is most likely too large; in that study, their regional log space skew has an MSE of 0.11. Several recent studies report values of the same order (Rasmussen and Perry 2000; Pope et al. 2001; Martins and Stedinger 2002; Reis et al. 2003, 2004, 2005; Feaster et al. 2009; Gotvald et al. 2009; Weaver et al. 2009). A log space skew range of $(-1.0, +1.0)$ is consistent with $MSE(G_R)$ on the order of 0.100 and a mean within $(-0.4, +0.4)$. But is the LP3 density function a reasonable model for annual maximum flood series with log space skews in this range?

Real Space Model. The shape of the LP3 density function is a complex function of α and β and thus the log space standard deviation σ_x and skew γ_x . Therefore, reasonable ranges of values for both σ_x and γ_x should be considered. In flood frequency analysis, a long thin upper tail is viewed as physically reasonable, representing increasingly infrequent combinations of hydrologic factors that contribute to increased runoff. The theory of extremes provides insight as to what is reasonable: if the probability distribution of the largest floods in a year is a distribution that looks exponential or Pareto-like with a long upper tail, then the annual maximum would have a Gumbel-like distribution with a long upper tail and a shorter lower tail (Kotegoda and Rosso 1997, pp. 428–440).

First consider the shape of the LP3 density function for positive γ_x (corresponding to $\beta > 0$) as illustrated in Figure 7-2. The shape of the density function is appropriate with $0 < \gamma_x < 1.414$ (case P1). With $1.414 < \gamma_x < 2$ (case P2), the upper tail is still reasonable representing increasingly unlikely combinations of rainfall possibilities and watershed states that result in ever larger annual maximum floods, but the mode is very close to the lower bound and the density function goes to zero rapidly at the lower bound; however, this is not necessarily a concern in flood frequency analysis wherein the larger quantiles are of interest.

With $\gamma_x > 2$ (case P3), while the upper tail is perhaps reasonable, the density function is infinite at the lower bound, suggesting that low-flow values are infinitely more likely than other values; again, this is not a reasonable model for annual maximum flood series. A similar problem exists with $-1.414 < \gamma_x < 0$ and $\beta < -1$ (case N3) at zero.

In cases N1 and N2 of Figure 7-2 with $-1.414 < \gamma_x < 0$ and $-1 < \beta < 0$, the density function has a very short tail at the upper bound, but overall the shape is reasonable. Still, the use of a distribution with an upper bound to model flood series is a concern because one cannot say with certainty that the upper bound will not be exceeded (Gilroy 1972) and imagining or anticipating a finite upper bound just beyond the range of floods historically experienced makes little physical sense in unregulated natural watersheds. National experience indicates that substantially larger floods can occur, though they are increasingly infrequent. In the remaining cases (N4–N9), with $\gamma_x < -1.414$ and $\beta < 0$, the LP3 density function is either infinite at the upper bound or does not have an upper tail and therefore is not a physically reasonable model for flood series.

Overall, evaluation of the shape of the LP3 density function in Figure 7-2 indicates that distributions with log space skews $|\gamma_x| \leq 1.414$ are physically reasonable descriptions of floods provided $\beta > -1$. Although γ_x as large as $+2.0$ may also yield a reasonable shape of the LP3 density function, Buckett and Oliver (1977), Griffis (2006), and Griffis and Stedinger (2007b) suggest that log space skew values should be restricted to $|\gamma_x| \leq 1.414$ for the shape of the log space density function to be reasonable for modeling flood flows. An interest here is to determine reasonable combinations

of σ_x and γ_x . Because $\beta = (\sigma_x \gamma_x)/2$, the proposed ranges for γ_x and β jointly determine a reasonable range for σ_x .

Reasonable Values of the Real Space C_v and Skew γ_Q . For a partition of the United States into 14 regions, Landwehr et al. (1978) analyze the sampling properties of the real space C_v and skew γ_Q employing a total of 1,351 observed flood sequences. Using the regional data provided by Landwehr et al. (1978), results in Griffis and Stedinger (2007b) indicate that 95% of the estimates of real space C_v in the United States are within (0.1, 1.8), and that 95% of the real space sample estimates of skew in the United States are within (0.1, 3.7). Adjusting the computed sample skew ranges for bias, Griffis and Stedinger (2007b) suggest that a reasonable range for the true population skew γ_Q is (0.1, 6.2), which is a larger interval because sample skewness estimators are bounded (Kirby 1974).

Using Equations (7-5) and (7-6), one can compute combinations of the log space standard deviation σ_x and the log space skew γ_x that correspond to real space C_v values of 0.1 and 1.8 and real space skew γ_Q values of 0.1 and 6.2. Figure 7-4 illustrates these combinations. Also shown in the figure are the 14 regional means reported by Landwehr et al. (1978) with a correction for bias in the mean values of the skew and a 90% confidence interval for the true mean of the log space skew. These values are clustered together with an average σ_x of approximately 0.6 and an average γ_x of -0.1. The curves for $\beta = -1/2$ and -1 are included in Figure 7-4 to relate the realistic combinations of σ_x and γ_x to the forms of the LP3 density function represented in Figures 7-2 and 7-3. The shaded region indicates the combinations of σ_x and γ_x that result in reasonable values for both the real space C_v and γ_Q , and also yield appropriate probability density functions (pdfs). This range is generally dominated by the value of γ_Q ; it is restricted by the upper bound on C_v only for $-0.4 > \gamma_x > -0.9$. For $\gamma_x < -0.9$, the value of σ_x is further restricted by the need for β to be greater than -1 for the pdf to be reasonable, but as expected, real data do not plot near that region of the parameter space.

Figure 7-4 shows that a log space skew of -1.4 combined with σ_x in the range of 0.6 to 1.4 yields reasonable C_v values of 0.4 to 0.9 and real space skews that are certainly within reasonable bounds ($\gamma_Q \geq 0$). For a log space skew of $+1.4$, reasonable values of $\gamma_Q \leq 6.2$ are only obtained when $\sigma_x \leq 0.3$, yielding $C_v \leq 0.4$. Log space skews $\gamma_x > 1.4$ must be paired with smaller, less common values of the C_v to obtain reasonable values of the real space skew. This suggests that $\gamma_x = 1.4$ is indeed an extreme value and a reasonable upper bound for hydrologic applications of the LP3 distribution in the United States.

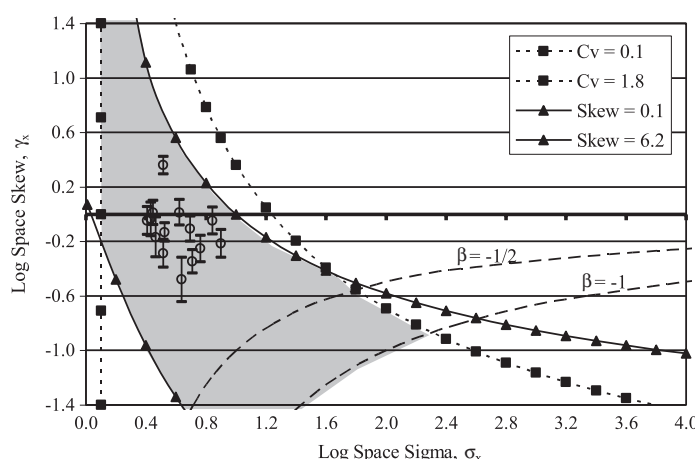


Figure 7-4. Log space skew versus log space standard deviation (with base-e transformations) as a function of real space C_v and skew; \circ represents Landwehr et al. (1978) regional data with 90% confidence intervals for the true mean log space skew.

Overall, analysis of the mathematical characteristics of the LP3 distribution in relation to what would be expected of an annual maximum flood series in the United States indicates that surely $|\gamma_x| \leq 2$, although $|\gamma_x| \leq 1.414$ is more realistic. If a hydrologist believes $|\gamma_x| > 1.414$ is needed to describe a flood series, then perhaps another distribution would provide a more realistic description of the data. Within the parameter ranges Figure 7-4 describes, the LP3 distribution with a log transformation of the data as recommended by *Bulletin 17B* is certainly a reasonable model for annual maximum flood series at most locations in the United States and other parts of the world where zero annual maximums are rare. However, if annual maximum series frequently hit a true lower bound, such as zero for annual floods, then a different model may be appropriate for frequency analysis, or one can model only the values above some threshold (Griffis et al. 2004).

7.2.4 L-Moments

In addition to traditional product moments, the shape of a distribution can be described in terms of the L-moment ratios τ_3 (L-skewness) and τ_4 (L-kurtosis):

$$\begin{aligned}\tau_3 &= \frac{6\beta_2 - 6\beta_1 + \beta_0}{2\beta_1 - \beta_0} \\ \tau_4 &= \frac{20\beta_3 - 30\beta_2 + 12\beta_1 - \beta_0}{2\beta_1 - \beta_0}\end{aligned}\quad (7-9)$$

where $\beta_k = E\{[X F(X)]^k\}$ are called probability-weighted moments (Hosking and Wallis 1997). L-moment ratio diagrams have been recommended to choose between probability distributions in regional frequency analyses (see Stedinger et al. 1993, Peel et al. 2001, and references therein). Many studies indicate that the generalized extreme value (GEV) and log-normal (LN) distributions are consistent with observed values of τ_3 and τ_4 computed with regional flood data. The log-normal distribution is a special case of the LP3 distribution for $\gamma_x = 0$. However, L-moments for the LP3 distribution were not available until recently (Griffis and Stedinger 2007b).

Hosking and Wallis (1997) provide the following approximation for τ_4 for the LP3 distribution when $\gamma_x = 0$ accurate to within 0.0005:

$$\tau_4 = 0.12282 + 0.77518\tau_3^2 + 0.12279\tau_3^4 - 0.13638\tau_3^6 + 0.11368\tau_3^8 \quad (7-10)$$

For the LP3 distribution with $\gamma_x \neq 0$, Griffis and Stedinger (2007b) develop the needed expressions for τ_4 as a function of τ_3 of the form:

$$\tau_4 = a + b\tau_3 + c\tau_3^2 + d\tau_3^3 \quad (7-11)$$

For a given τ_3 , with the coefficients in Table 7-2, the approximations yield values of τ_4 accurate to within 0.008 over the range $\tau_{3(\min)} \leq \tau_3 \leq 0.9$, wherein Table 7-2 specifies the minimum value $\tau_{3(\min)}$ for each value of γ_x ; these are obtained as σ_x approaches 0.

Figure 7-5 presents the L-moment ratio diagram for the LP3 distribution relative to other well-known distributions computed using approximations provided by Hosking and Wallis (1997). The light gray region represents the $\tau_4-\tau_3$ space covered by the LP3 distribution with $|\gamma_x| \leq 1.4$; the darker gray region represents the $\tau_4-\tau_3$ space corresponding to the reasonable combinations of σ_x and γ_x identified in Figure 7-4. The product-moment skew of the LN distribution is also shown suggesting how the skew of the LP3 distribution relates to the L-skew τ_3 . The curve labeled OLB represents that overall lower bound for the $\tau_4-\tau_3$ space given by $\frac{1}{4}(5\tau_3^2 - 1) \leq \tau_4$ (Hosking 1990).

Table 7-2. Coefficients of the Cubic Approximation in Equation (7-11) of τ_4 as a Function of τ_3 for the LP3 Distribution for Select Values of the Log Space Skew.

Log space skew, γ_x	Coefficient				τ_3 (min)
	a	b	c	d	
-1.4	0.0602	-0.1673	0.8010	0.2897	-0.2308
-1.0	0.0908	-0.1267	0.7636	0.2562	-0.1643
-0.5	0.1166	-0.0439	0.6247	0.2939	-0.0740
0.0	0.1220	0.0238	0.6677	0.1677	0.0000
0.5	0.1152	0.0639	0.7486	0.0645	0.0774
1.0	0.1037	0.0438	0.9327	-0.0951	0.1701
1.4	0.0776	0.0762	0.9771	-0.1394	0.2366

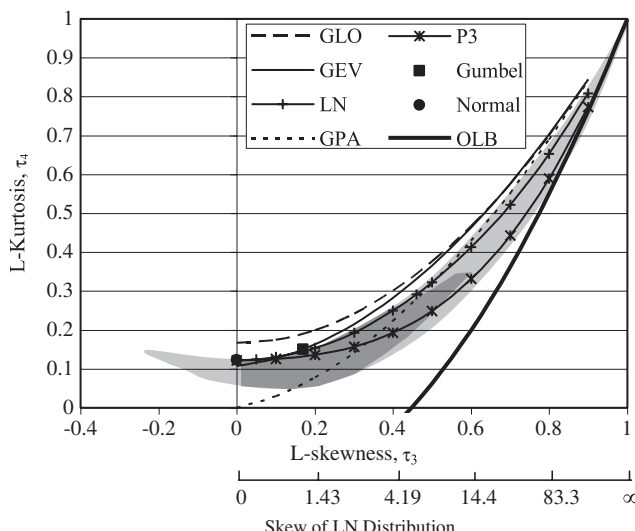


Figure 7-5. L-moment ratio diagram including generalized logistic (GLO), generalized extreme value (GEV), log-normal (LN), generalized Pareto (GPA), Pearson type III (P3), Gumbel, normal, and log-Pearson type III (LP3). The light gray region represents LP3 distribution with $|\gamma_x| \leq 1.414$, the dark gray region has restricted values of σ_x and γ_x as shown in Figure 7-4. The curve labeled OLB represents the overall lower bound for $\tau_4-\tau_3$ space.

Figure 7-5 shows that the L-skew of the LP3 distribution can be negative when the log space skew is negative and σ_x is small; however, these negative L-skew values are avoided for realistic combinations of σ_x and γ_x . With the same value of τ_3 , thinner tailed distributions can be obtained using the LP3 distribution with $\gamma_x < 0$. The $\tau_4-\tau_3$ space covered by the LP3 distribution lies slightly beneath the $\tau_4-\tau_3$ curve for the GEV distribution in the area around the Gumbel distribution, which is the region of interest; it is also below the generalized logistic (GLO) distribution. Overall, because the LP3 distribution has two shape parameters α and β , the L-moment ratios cover a two-dimensional space, and thus the LP3 distribution appears more flexible than the GEV and LN distributions. Moreover, the LP3 distribution recognizes that floods are nonnegative, whereas fitted GEV and GLO distributions with shape parameter $\kappa \geq 0$, and sometimes $\kappa < 0$, assign nonzero probabilities to negative flows.

7.3 ESTIMATION PROCEDURES FOR COMPLETE SAMPLES

The hydrologic literature has explored several parameter estimation methods for the LP3 distribution, including the MOM in both log space and real space, maximum likelihood estimators (MLE), and the method of mixed moments (MXM). [Bobee and Ashkar \(1991\)](#) provide a detailed review of these and other less common estimation techniques for use with the LP3 distribution and estimation techniques for other members of the gamma family. [Johnson et al. \(1994, pp. 355–378\)](#) and the references provided therein discuss estimation techniques for the gamma distribution. This section discusses the log space MOM estimator with regional skew information recommended by *Bulletin 17B*. An example is provided for a complete sample; additional procedures for low outlier adjustment and the incorporation of historical flood information are not employed. Section 7.4 addresses those issues and changes to appear in *Bulletin 17C*.

Another parameter estimation technique that has received attention in the hydrologic literature is the method of L-moments (see Section 7.2.4). L-moment estimators have been shown to be effective for regional analyses (see previous citations) but are generally not optimal for the analysis of a single set of data ([Landwehr et al. 1979](#), [Martins and Stedinger 2000](#)), and thus are not considered here.

7.3.1 Log Space Method of Moments

The parameters of the LP3 distribution can be estimated using log space MOM by fitting a P3 distribution to the logarithms of the flood peaks, denoted $\{X_1, \dots, X_N\}$. Estimates of the population mean μ_x , standard deviation σ_x , and skew coefficient γ_x of the logarithms of the station data are computed using traditional moment estimators:

$$\begin{aligned}\bar{X} &= \frac{1}{N} \sum_{i=1}^N X_i \\ S_x &= \left[\frac{1}{N-1} \sum_{i=1}^N (X_i - \bar{X})^2 \right]^{1/2} \\ G_x &= \frac{N}{(N-1)(N-2)S_x^3} \sum_{i=1}^N (X_i - \bar{X})^3\end{aligned}\quad (7-12)$$

The parameters of the P3 distribution (α , β , and τ) are then estimated by equating the sample product moments (\bar{X} , S_x , and G_x) to the population moments (μ_x , σ_x , and γ_x), resulting in the following parameter estimators:

$$\hat{\alpha} = \frac{4}{G_x^2}; \hat{\beta} = \frac{S_x G_x}{2}; \hat{\tau} = \bar{X} - \hat{\alpha} \hat{\beta} = \bar{X} - 2 \frac{S_x}{G_x} \quad (7-13)$$

The p^{th} quantile of the fitted distribution can be written as $X_p = \bar{X} + S_x K_p(G_x)$. Here $K_p(G_x)$ is a frequency factor that is the p^{th} quantile of a standard P3 variate with skew coefficient G_x , mean 0, and variance 1. The flood flow Q with cumulative probability p is then $Q_p = \exp(X_p)$. With this parameterization computing the values of α , β , or τ is not necessary.

Because of its computational ease, the log space moment method is appealing and is presumably why [Beard \(1962\)](#) suggests its use in the *Bulletin*. The only complication was the need for frequency factors that were later tabulated by [Benson \(1968\)](#) and are provided in the *Bulletin*; [Kirby \(1972\)](#) provides an excellent approximation. Today they can be computed directly with built-in functions in

many software packages, including Microsoft Excel and MATLAB ([Mathworks 2012](#)). Log space MOM is the parameter estimation technique currently recommended in *Bulletin 17B*, but with a slight modification to incorporate regional skew information to improve the accuracy of the skewness estimator. This procedure is discussed as follows.

7.3.2 Log Space Method of Moments with Regional Skew

The data available at a given site are generally limited to less than 100 years and often less than 30 years in length. Such short records produce skewness estimators that are sensitive to extreme events. The accuracy of the station skewness estimator should be improved by combining it with a regional skewness estimator obtained by pooling data from nearby sites ([Hardison 1974](#)). *Bulletin 17B* recommends combining the sample skew G_x and the regional skew G_R to obtain a weighted skew:

$$G_w = WG_x + (1 - W)G_R \quad (7-14)$$

where

$$W = \text{MSE}(G_R)/[\text{MSE}(G_x) + \text{MSE}(G_R)] \quad (7-15)$$

Here $\text{MSE}(G_x)$ is the estimated mean square error (equal to variance plus bias squared) of the sample skew, and $\text{MSE}(G_R)$ is the mean square error of the regional skew. Estimates of the regional skew and its variance are obtained from a separate regional analysis such as that described by [McCuen \(1979\)](#) or [Reis et al. \(2005\)](#).

Bulletin 17B recommends approximating $\text{MSE}(G_x)$ as a function of the sample skew G_x and the record length N using the equation provided therein. That equation is based on the Monte Carlo study reported in [Wallis et al. \(1974\)](#) and yields relative errors as large as 10% within the hydrologic region of interest ([Griffis, 2003](#)). [Griffis et al. \(2004\)](#) provide the relatively more precise approximation:

$$\text{MSE}(G_x) = \left[\frac{6}{N} + a(N) \right] \left[1 + \left(\frac{9}{6} + b(N) \right) \gamma_x^2 + \left(\frac{15}{48} + c(N) \right) \gamma_x^4 \right] \quad (7-16)$$

where $a(N)$, $b(N)$, and $c(N)$ are corrections for small samples:

$$\begin{aligned} a(N) &= -\frac{17.75}{N^2} + \frac{50.06}{N^3} \\ b(N) &= \frac{3.93}{N^{0.3}} - \frac{30.97}{N^{0.6}} + \frac{37.1}{N^{0.9}} \\ c(N) &= -\frac{6.16}{N^{0.56}} + \frac{36.83}{N^{1.12}} - \frac{66.9}{N^{1.68}} \end{aligned} \quad (7-17)$$

This approximation was developed for record lengths $N \geq 10$ and population skews $|\gamma_x| \leq 1.414$. Within that range, the maximum relative error was -0.62% . Therefore, this approximation is substantially more accurate than the approximation provided by *Bulletin 17B* and is consistent with the asymptotic variance for G_x provided by [Bobee \(1973\)](#). [Griffis and Stedinger \(2009\)](#) provide similar approximations of the bias and variance of skew estimators.

The *Bulletin 17B* inverse-MSE weighting scheme was adopted from [Tasker \(1978\)](#) but was extended to address bias in the sample skew estimate. Equation (7-14), with the weight in Equation (7-15), minimizes the MSE of the skewness estimator provided G is unbiased and

independent of G_x (Griffis 2003); however, it need not yield the minimum MSE quantile estimator. Griffis and Stedinger (2009) investigate an alternative weighting scheme that minimizes the MSE of the quantile estimator; however, they observe only modest improvements in the MSE of quantile estimates.

Griffis et al. (2004) illustrate the value of regional skew information for reducing the MSE of estimates of the 99th percentile. They observe a 22% reduction in the MSE of the 99th percentile estimates when a regional skew of 0 with the *Bulletin* skew estimation error of 0.302 (Hardison, 1974, and IACWD, 1982) is employed in samples of size 10; a 7.5% reduction is observed in samples of size 100. Greater reductions occur when a more informative regional skew is employed. They observe reductions of 31% and 18% in sample sizes of 10 and 100, respectively, when a regional skew of 0 is employed with an estimation error of 0.100, a value derived by Tasker and Stedinger (1986). Rasmussen and Perry (2000), Pope et al. (2001), Martins and Stedinger (2002), and Reis et al. (2003, 2004, 2005) obtain similar values for the variance of the regional skew more recently, using statistically efficient and relatively unbiased methods.

Using a Monte Carlo analysis, Griffis and Stedinger (2007c) quantitatively evaluate the efficiency of the *Bulletin 17B* MOM estimator with regional skew information relative to real space method of moments, method of mixed moments, traditional MLEs, and an MLE/Bayesian procedure with a prior to reflect regional skew information. They evaluate the relative performance of the parameter estimation methods using the MSE of estimates of the 100-year event ($Q_{0.99}$) for several cases chosen to reflect the reasonable parameter values identified in Figure 7-4. Overall, their results demonstrate that the log space method of moments estimator is robust and performs well when employed with informative regional skew information.

Only a modest range of log space skewness values is physically reasonable for natural unregulated watersheds and is particularly likely in the United States given our hydrologic experience (see Section 7.2). Therefore, a regional model of the skew is likely to be highly informative, and as the Monte Carlo results of Griffis et al. (2004) and Griffis and Stedinger (2007c) show, that information is quite valuable. Within this limited range of skew values, the LP3 distribution is more flexible than a two-parameter log-normal distribution but should not deviate too far from that reasonable two-parameter model. Thus, instead of employing the method of mixed moments to avoid use of the skew, using the method of moments with physically and hydrologically reasonable skew information is sensible. Furthermore, use of the log space method of moments estimator is advantageous as it allows regional skew information to be easily incorporated into a fairly simple and widely accepted parameter estimation method.

In addition, use of a log transformation of the data, as employed by *Bulletin 17B*, makes sense because large flood values would dominate real space sample moment estimates. However, the log transformation will give low outliers an increased weight, which is a concern in flood frequency analysis wherein the larger events are the primary interest. Furthermore, the log transformation cannot be applied to zero flood years. To account for low outliers and zero flood years, *Bulletin 17B* recommends performing a conditional probability adjustment (Jennings and Benson, 1969). Alternatively, one could employ the expected moments algorithm (EMA) originally developed by Cohn et al. (1997) for incorporating historical information in flood frequency analyses and later extended by Griffis et al. (2004) to handle low outliers and to employ regional skew information. EMA is a direct generalization of the MOM procedures recommended by *Bulletin 17B* that can deal with censored data. Section 7.4 discusses these procedures further, and they are the basis of the *Bulletin 17C* that is under review.

Example 7.1

This example illustrates the use of log space MOM with regional skew information to fit an LP3 distribution to a complete sample and to estimate design events, such as the magnitude of the 100-year flood event. The sample data employed herein is the record of annual flood peaks from 1928 to 1971 for Little River at Linden, North Carolina, USGS gauging station number 02103500.

Table 7-3. Annual Flood Peaks for Little River at Linden, North Carolina.

Date	Q (ft ³ /s)						
1951	1,300	1956	2,590	1971	3,540	1931	4,980
1940	1,710	1953	2,610	1932	3,590	1949	5,260
1933	1,760	1941	2,840	1939	3,600	1955	5,370
1962	1,930	1946	2,840	1966	3,640	1936	5,630
1934	2,280	1967	2,950	1963	3,850	1954	5,770
1969	2,400	1943	2,970	1959	4,320	1952	5,860
1970	2,400	1947	3,010	1958	4,340	1929	6,160
1935	2,470	1942	3,060	1937	4,500	1965	7,400
1968	2,490	1960	3,180	1948	4,500	1930	10,300
1938	2,500	1957	3,310	1944	4,860	1928	13,000
1950	2,580	1961	3,320	1964	4,940	1945	13,500

Table 7-3 provides the sorted sample data. To simplify the analysis, this example does not consider the presence of historical data and possible low outliers.

Here Q represents the true annual flood peaks and is assumed to follow an LP3 distribution, and X represents the base-e logarithms of the annual peaks and follows a P3 distribution. The sample contains $N = 44$ observations. In log space, the maximum observation is 9.51 and the minimum observation is 7.17. The sample moments of the logarithms calculated using Equation (7-12) are $\bar{X} = 8.210$, $S_x = 0.500$, and $G_x = 0.653$.

To improve the estimate of the skew, a weighted skew is then computed using Equation (7-14) with the weight given by Equation (7-15). The MSE of the sample skew is computed to be 0.171 using Equation (7-16) with the correction factors given by Equation (7-17). A regional skew of +0.4 is obtained from the *Bulletin 17B* skew map. As the skew map was used, an MSE of 0.302 is assumed for the regional skew as recommended by *Bulletin 17B*. The resulting weighted skew is 0.561. This is significantly closer to the value of the at-site sample skew than the regional skew because the MSE of the sample skew is nearly half that of the regional skew. Conversely, if the regional skew is assigned an MSE of 0.100 (Tasker and Stedinger 1986), the resulting weighted skew would be 0.493. Decreasing the MSE of the regional skew effectively increases the weight on the value of the regional skew in Equation (7-14). The result is a weighted skew coefficient closer in value to the more accurate regional skew.

The final fitted LP3 distribution matches the estimated moments in log space [and corresponding parameters calculated using Equation (7-13)]:

$$\bar{X} = 8.210, S_x = 0.500, \text{ and } G_x = 0.561$$

$$(\hat{\alpha} = 12.7, \hat{\beta} = 0.140, \text{ and } \hat{\tau} = 6.43)$$

The magnitude of the 100-year event (or 99th percentile of the fitted distribution) is computed as $Q_{0.99} = \exp[\bar{X} + S_x K_{0.99}(G_x)] = 14,403.3 \text{ ft}^3/\text{s}$, wherein the frequency factor $K_{0.99}(G_x)$ has a value of 2.728 given $G_x = 0.561$. Repeating these computations for a range of percentiles with cumulative probabilities $0 < p < 1$, corresponding to exceedance probabilities $1 - p$, yields the frequency curve illustrated in Figure 7-6. For comparison, the frequency curve obtained using $MSE(G_R) = 0.302$ per *Bulletin 17B* is plotted relative to the curve obtained using $MSE(G_R) = 0.100$, per Tasker and Stedinger (1986), to illustrate the difference. The sample data points are also included in the figure; these points were plotted using Blom's plotting position formula, $i/(N+1)$ for the i^{th} largest observation.

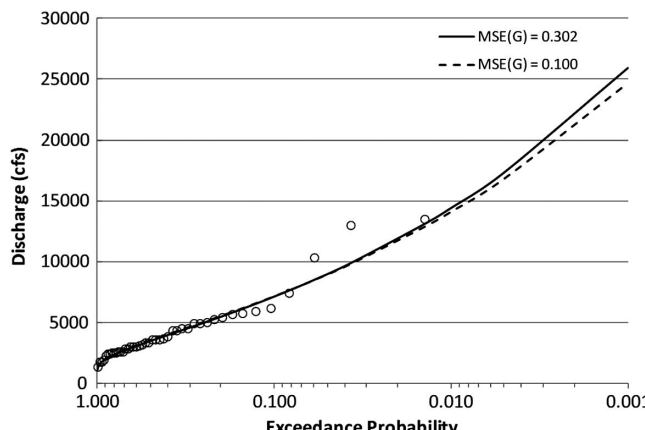


Figure 7-6. Frequency curve for Little River at Linden, North Carolina.

7.4 ESTIMATION PROCEDURES WITH HISTORICAL INFORMATION AND LOW OUTLIERS

In addition to using regional skew information, *Bulletin 17B* recommends special procedures for handling zero flows, low outliers, and historical peaks. This section briefly describes those procedures. The expected moments algorithm (EMA), originally developed by Cohn et al. (1997) to incorporate historical information in flood frequency analyses, and the extension by Griffis et al. (2004) to handle low outliers and to employ regional skew information, is also discussed.

7.4.1 Low Outliers

Bulletin 17B defines outliers as “data points which depart significantly from the trend of the remaining data.” The *Bulletin* uses a log transformation of the data; therefore, one or more unusual low-flow values can distort the entire fitted frequency distribution. Thus, low outliers are censored to improve the reliability of the larger flood quantile estimates of interest. Furthermore, the log transformation cannot be applied to zero flood years.

Low outliers are identified in log space by using the mean and standard deviation of the complete sample to specify a “truncation level”:

$$X_L = \bar{X} - K_N S \quad (7-18)$$

which is defined by the one-sided 10% significance level for a P3 distribution with zero skew (i.e., a two-parameter log-normal distribution). This is a Grubbs–Beck test. *Bulletin 17B* tabulates the 10% frequency factors K_N for the smallest observation in a sample drawn from a normal distribution as a function of sample size (for $10 \leq N \leq 149$). Sample values below the truncation level are considered to be outliers.

Bulletin 17B recommends a conditional probability adjustment (CPA) of the frequency curve when low outliers are identified, when the record contains zero flood years, or when a recording threshold results in a truncated dataset. These critical events are censored from the record of size N and a P3 distribution $F(x)$ is fit to the r retained logarithms of the flood flows that exceeded the truncation level X_L . CPA was developed by Jennings and Benson (1969) to account for the removal of zero-flow events from the record before fitting the LP3 distribution.

The probability that a given event exceeds the truncation level is estimated as $p_e = r/N$. The formula for conditional probability expressed in terms of exceedance probabilities indicates that the

flood flows exceeded with a probability $p \leq p_e$ in any year are obtained by solving $p = p_e(1 - F(x))$ to obtain $F(x) = 1 - p/p_e$. Whereas the CPA method defines a legitimate distribution, it is generally replaced with an approximating LP3 distribution; this is necessary to combine the computed station skew with regional skew information and to employ the procedures that compute confidence intervals for quantiles. Also, *Bulletin 17B* recommends performing CPA to adjust for any low outliers, missing values from incomplete records, and/or zero flood years before employing the historical flood algorithm, which would use the adjusted sample moment estimates. The new EMA ([Cohn et al. 1997](#), [Griffis et al. 2004](#)) solves these problems: EMA provides a direct fit of the LP3 distribution to the entire dataset, simultaneously employing historical and regional skew information and adjusting for any low outliers, missing values from an incomplete record, and/or zero flood years. Section [7.4.3](#) discusses EMA further.

The distribution $F(x)$ fit to the uncensored data is employed to compute three quantiles $Q_{0.99}$, $Q_{0.90}$, and $Q_{0.50}$, which will be exceeded with probabilities $p = 0.01$, 0.10 , and 0.50 . These three quantiles are then used to compute the three “synthetic” moments for a new P3 distribution according to

$$\begin{aligned} G_{syn} &= -2.50 + 3.12 \left[\log_{10} \left(\frac{Q_{0.99}}{Q_{0.90}} \right) \right] / \left[\log_{10} \left(\frac{Q_{0.90}}{Q_{0.50}} \right) \right] \\ S_{syn} &= \log_{10}(Q_{0.99}/Q_{0.50})/(K_{0.99} - K_{0.50}) \\ M_{syn} &= \log_{10}(Q_{0.50}) - K_{0.50}S_{syn} \end{aligned} \quad (7-19)$$

where $K_{0.99}$ and $K_{0.50}$ are P3 frequency factors computed using the synthetic skew G_{syn} (provided by the first equation) for cumulative probabilities of 0.99 and 0.50 , respectively. Here the term synthetic is used to refer to the moments of an approximating P3 distribution. The approximation for the synthetic skew is said to be appropriate for skew coefficients on the interval $(-2.0, +2.5)$ ([IACWD, 1982](#)). However, [Griffis \(2003\)](#) demonstrates that the absolute error in the computed skew is unnecessarily large (~4%) for $|\gamma_x| \leq 0.2$, which is in the center of the hydrologic region of interest.

In the absence of historical flood information, the final fitted distribution used to estimate the frequency of the r above threshold values is given by the synthetic mean and standard deviation and a weighted skew obtained by combining the synthetic skew with a regional skew using Equation [\(7-14\)](#). When historical flood information is available, the procedures become more complicated as the *Bulletin*'s recommended procedures for incorporating historical peaks are performed separately from the procedures for low outlier identification and the subsequent adjustment of the fitted distribution, and the order in which these procedures are performed is dependent on the value of the skew. [Griffis and Stedinger \(2007a\)](#) discuss these issues in more detail.

7.4.2 Historical Flood Information

In addition to regional skew information, historical flood information can be used to increase the effective record length at a site. Historical information includes written records such as newspaper accounts of exceptionally large floods and flood markers such as flood lines on buildings. Figure [7-7](#) shows a flood record that contains both historical and systematic (or gauged) data. In most cases the historical record would end when a stream gauge was installed; however, historical information could also include data for a stream in which a gauge was removed or lost and then perhaps reestablished. As Figure [7-7](#) illustrates, only the exceptionally large peaks are recorded in the historical period because they exceeded some perception threshold, or because the event was large enough to leave physical evidence. The historical threshold, denoted T , corresponds to “the discharge above which some sort of permanent flood record would be created” ([Cohn et al. 1997](#)). The magnitudes of any annual peak floods in the historical period that failed to exceed T are not

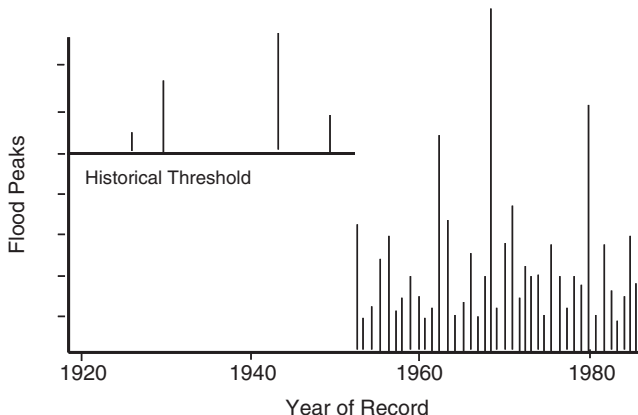


Figure 7-7. Flood record with both historical and systematic data.

Note: Units = log(cfs).

recorded. In this way, historical information represents a censored sample, which is the term used in statistics to describe a sample where an observation must exceed a threshold to be recorded. The magnitudes of all floods in the systematic period are known.

The logarithms of the flood record illustrated in Figure 7-7 can be expressed as the union of four sets (Cohn et al. 1997):

$$\{X\} = \{X_S^>\} \cup \{X_H^>\} \cup \{X_S^<\} \cup \{X_H^<\} \quad (7-20)$$

where

$\{X_S^>\}$ = logarithms of floods greater than T , which occurred during the systematic record and whose magnitudes were measured by stream gauge (of which there were $N_S^>$ values);

$\{X_H^>\}$ = logarithms of floods greater than T , which occurred during the historical period (of which there were $N_H^>$ values);

$\{X_S^<\}$ = logarithms of floods less than T , which occurred during the systematic period and whose magnitudes were measured by stream gauge (of which there were $N_S^<$ values); and

$\{X_H^<\}$ = logarithms of floods less than T , which occurred during the historical period and thus were not measured, except that their magnitudes are known not to exceed T (of which there were $N_H^<$ values).

In addition, if low outliers are identified using a low outlier threshold such as Equation (7-18), then the set $\{X_S^<\}$ can be expressed as

$$\{X_S^<\} = \{X_L^<\} \cup \{X_L^>\} \quad (7-21)$$

where

$\{X_L^<\}$ = logarithms of floods, which occurred during the systematic period and are less than X_L (of which there were $N_L^<$ values); and

$\{X_L^>\}$ = logarithms of floods that occurred during the systematic period and are greater than X_L but less than $\log(T)$ (of which there were $N_L^>$ values).

To use historical information, *Bulletin 17B* recommends computing adjusted sample moments in which the values in the systematic record below the historical flood threshold are used to represent unobserved floods in the historical period for computing the moment estimators for the entire period. The problem with the *Bulletin 17B* approach is that it places too much reliance upon the observed systematic flood peaks, which are conceptually replicated as many times as necessary to represent the below-threshold peaks during the historical period, whereas historical peaks above the

threshold are assigned a weight of one. In the extreme case that a historical perception threshold was never exceeded, the *Bulletin 17B* approach cannot use that information.

The adjusted sample mean is computed as

$$\tilde{M} = \frac{W\Sigma X_L^> + \Sigma X_S^> + \Sigma X_H^>}{N_H + N_S - W \cdot N_L^<} \quad (7-22)$$

where the historic record length $N_H = N_H^< + N_H^>$, the systematic record length $N_S = N_S^< + N_S^> = (N_L^< + N_L^>) + N_S^>$, and

$$W = (N_H^< + N_S^<)/N_S^< \quad (7-23)$$

Thus, the effective total record length is $N_H^> + N_S^> + WN_S^< = N_H + N_S$. And, the denominator $(N_H + N_S - W \cdot N_L^<)$ in Equation (7-22) appropriately reflects the effective number of years of record associated with the sample mean and the historic peaks. Appendix 7A provides plotting positions consistent with the previously described paradigm.

7.4.3 Expected Moments Algorithm

Cohn et al. (1997) originally developed the EMA to incorporate historical information in flood frequency analyses. The algorithm employs an iterative procedure for computing parameter estimates using censored data. The process begins with an initial set of parameter estimates obtained using the systematic stream gauge record and then updates the parameters using the known magnitudes of historical peaks and the expected contribution to the moment estimators of the below-threshold floods.

EMA can also include regional skew information and censored low outliers represented by an additional perception threshold. Griffis et al. (2004) describe the performance of the EMA with regional skew information and low outliers and discuss the advantages of EMA over the *Bulletin's* conditional probability adjustment. EMA uses historical information more efficiently than the *Bulletin 17B* procedures (Cohn et al. 1997, England et al. 2003, Griffis 2008) and can incorporate a much wider range of flood information, including thresholds that were never exceeded, or floods whose values are described by ranges. Appendix 7B describes the EMA procedure in more detail.

Example 7-2

This example illustrates censoring of low outliers and the application of subsequent procedures, namely CPA and EMA, to adjust the distribution fit to the retained observations. The sample data considered herein comprise the record of annual flood peaks from 1929 to 1973 for Back Creek near Jones Springs, West Virginia, USGS gauging station number 01614000. These data are employed in *Bulletin 17B* to illustrate the use of CPA. Table 7-4 provides the sorted sample data. Data are unavailable for 1932 through 1938, except for 1936, for which a value of 22,000 ft³/s was estimated using data from a nearby site. The *Bulletin* indicates that this flow value could be treated as historical data; however, it was omitted from the dataset as the example provided therein was only to illustrate the application of CPA. To simplify the discussion in this example, the presence of historical data will also not be considered.

Here Q represents the true annual flood peaks and is assumed to follow an LP3 distribution, and X represents the base-e logarithms of the annual peaks and follows a P3 distribution. The sample contains $N = 38$ observations. In log space, the maximum observation is 10.02 and the minimum observation is 6.284. The sample moments of the logarithms calculated using Equation (7-12) are $\bar{X} = 8.570$, $S_x = 0.646$, and $G_x = -0.731$.

Low Outlier Identification. Equation (7-18) is used to compute the truncation level $X_L = 6.852$ in log space, equivalent to 946 ft³/s in real space. One low outlier is identified with a real space value of

Table 7-4. Annual Flood Peaks for Back Creek near Jones Springs, West Virginia.

Date	Q (ft ³ /s)						
1969	536	1946	4,020	1963	5,190	1971	8,360
1947	1,600	1931	4,060	1973	5,210	1929	8,750
1950	3,010	1941	4,160	1965	5,600	1951	9,150
1940	3,130	1949	4,230	1954	6,200	1953	9,820
1958	3,240	1962	4,380	1939	6,300	1955	10,700
1957	3,420	1948	4,460	1970	6,680	1930	15,500
1960	3,740	1968	4,640	1942	6,700	1972	18,700
1944	3,880	1966	4,670	1959	6,800	1943	22,400
1956	3,880	1961	4,700	1967	7,080		
1964	3,960	1952	5,100	1945	8,050		

536 ft³/s, which is three times smaller than the next smallest observation of 1,600 ft³/s. This value is censored from the record, reducing the sample size from $N = 38$ to $r = 37$. The probability of an observation exceeding the truncation level is given by $p_e = 37/38 = 0.974$. The sample moments of the 37 above-threshold observations are estimated using Equation (7-12): $\bar{X} = 8.632$, $S_x = 0.529$, and $G_x = 0.631$.

Conditional Probability Adjustment. Following *Bulletin 17B* procedures, the sample moments of the above-threshold observations are used in the equation $F(x) = 1 - p/p_e$ to compute the logarithms of the flood flows with exceedance probabilities $p = 0.50$, 0.10 , and 0.01 , which yields the real space values: $Q_{0.50} = 5,214.6$ ft³/s, $Q_{0.90} = 11,213.1$ ft³/s, and $Q_{0.99} = 24,140.8$ ft³/s. Forcing the fitted P3 distribution through these three quantiles, the synthetic moments M_{syn} , S_{syn} , and G_{syn} of the unconditional P3 distribution are estimated using Equation (7-19):

$$M_{syn} = 8.614, S_{syn} = 0.533, \text{ and } G_{syn} = 0.625.$$

wherein the frequency factors $K_{0.99} = 2.772$ and $K_{0.50} = -0.104$ needed to compute M_{syn} and S_{syn} are obtained using $G_{syn} = 0.625$.

The MSE of the synthetic skew coefficient is computed to be 0.188 using Equation (7-16) with the correction factors in Equation (7-17). The synthetic skew G_{syn} is substituted for the sample skew G_x in Equation (7-14) to obtain a weighted skew for the adjusted sample. A regional skew of +0.5 with an MSE of 0.302 is obtained from the *Bulletin 17B* skew map. The resulting weighted skew is 0.577.

Following *Bulletin 17B* procedures, the final fitted LP3 distribution has the following sample moments in log space [and corresponding parameters calculated using Equation (7-13)]:

$$\begin{aligned} \bar{X} &= 8.614, S_x = 0.533, \text{ and } G_x = 0.577. \\ (\hat{\alpha}) &= 12.0, \hat{\beta} = 0.154, \text{ and } \hat{\tau} = 6.77 \end{aligned}$$

Expected Moments Algorithm. The sample record consists of $N_s = 38$ observations in which one low outlier was identified ($N_L^* = 1$) using Equation (7-18). No historic information is considered in this example ($N_H = 0$). The initial moments ($\hat{\mu}_1, \hat{\sigma}_1, \hat{\gamma}_1$) used in the EMA are the sample moments of the entire systematic record computed using Equation (7-12):

$$\hat{\mu}_1 = 8.570, \hat{\sigma}_1 = 0.646, \text{ and } \hat{\gamma}_1 = -0.731.$$

The first iteration $i = 1$ computes the parameters $(\hat{\alpha}_{i+1}, \hat{\beta}_{i+1}, \hat{\tau}_{i+1})$ of the P3 distribution using these initial sample moments in Equation (7-2):

$$\hat{\alpha}_2 = 7.483, \hat{\beta}_2 = -0.236 \text{ and } \hat{\tau}_2 = 10.34.$$

The sample moments updated with the expected contribution of the low outlier used in place of its actual value are then computed using Equations (7-32), (7-34), and (7-35) as detailed in Appendix 7B. Here the expected contribution from the low outlier is computed using the censoring threshold X_c equal to 7.378, which is the value in log space of the smallest retained observation. In each iteration of the EMA, the skew estimate is also updated using the regional skew information. Here the sample skew is weighted with the regional skew using an equivalent record length n_i computed using Equation (7-36) assuming $MSE(G_R) = 0.302$ is consistent with use of the map skew. The MSE of the sample skew with N_s years of data is estimated at each iteration using Equation (7-16). Successive iterations repeat the calculations until the moments differ by less than 0.01% from the results of the previous iteration. Table 7-5 presents the iterative results of the EMA. The EMA converged in eight iterations for this sample yielding moments' estimates

$$\bar{X} = 8.596, S_x = 0.566, \text{ and } G_w = 0.377.$$

These values represent the log space sample moments of the final fitted LP3 distribution using EMA, for which the corresponding parameters calculated using Equation (7-13) are

$$\hat{\alpha} = 28.1, \hat{\beta} = 0.107, \text{ and } \hat{\tau} = 5.594.$$

Figure 7-8 shows the frequency curves obtained using CPA and EMA and the sample data plotted using Blom's plotting position formula. In addition, the frequency curve obtained using the standard log space method of moments procedure with regional skew information is included for comparison. The latter curve, labeled MOM, represents the distribution fit to the data using all observed values with no adjustments to account for the low outlier. The MOM curve was obtained using the unadjusted sample mean $\bar{X} = 8.570$, the unadjusted sample standard deviation $S_x = 0.646$, and a weighted skew $G_w = -0.236$ obtained by combining the unadjusted sample skew $G_x = -0.731$ with the regional skew using Equation (7-14).

The LP3 distributions fit using the two low outlier adjustment estimation procedures, CPA and EMA yield similar estimates within the data. However, the LP3 distribution fit using EMA provides slightly smaller estimates of the upper quantiles beyond the 100-year event (exceedance

Table 7-5. Iterative Parameter Adjustment Using EMA for Back Creek, West Virginia.

Iteration	α	β	τ	μ	σ	γ
1	—	—	—	8.570	0.646	-0.731
2	7.48	-0.236	10.34	8.588	0.589	0.150
3	178	0.044	0.733	8.594	0.571	0.339
4	34.9	0.097	5.223	8.595	0.567	0.371
5	29.1	0.105	5.538	8.596	0.567	0.376
6	28.2	0.107	5.585	8.596	0.566	0.377
7	28.1	0.107	5.592	8.596	0.566	0.377
8	28.1	0.107	5.594	8.596	0.566	0.377

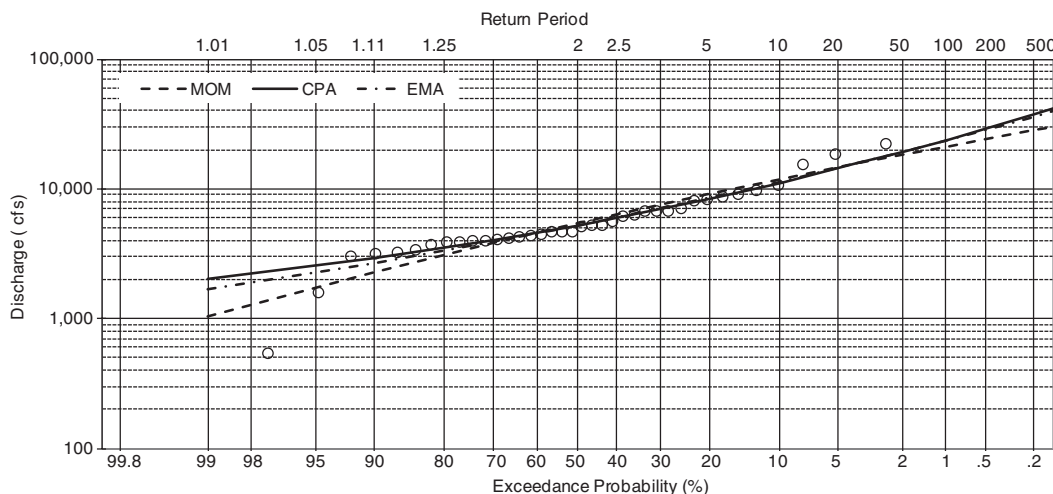


Figure 7-8. Frequency curves for Back Creek, West Virginia, obtained using CPA and EMA to adjust for the removal of one low outlier.

probability < 0.01) than the LP3 distribution fit using CPA. This would be rectified if the unusually small 1,600 ft³/s value used as the upper bound for the censored 536 ft³/s observation was also treated as a low outlier; then both would be represented as ≤ 3040 ft³/s. The LP3 distribution fit by MOM overestimates all of the sample values within the middle of the data and provides a relatively low estimate of the largest observation and quantiles beyond the data; this suggests the value of the low outlier adjustment.

7.4.5 What's Next: *Bulletin 17C*

Bulletin 17, adopted in 1976, and then *Bulletin 17B*, adopted in 1982, have guided US flood frequency analysis computations. With the great progress in statistical methods since the mid-1980s, the time has clearly come for a revised *Bulletin* that makes use of those advances.

Bulletin 17B (pp. 27–28) itself includes a list of issues recommended for additional research; *Bulletin 17C* specifically addresses the following four topics ([England et al. 2016](#)):

- Flood-frequency distribution selection and fitting procedures,
- Identification and treatment of outliers,
- Treatment of historical information, and
- Confidence limits for the Pearson type III distribution.

Topics left to be addressed by other studies include treatment of mixed distributions, precipitation as a measure of flood potential, flood risk at ungauged sites or sites with limited records and impacts of urbanization and reservoirs. [Lamontagne et al. \(2012\)](#) describe improvements in regional skew estimation.

With regard to distribution selection, the LP3 distribution with three parameters is highly flexible, and evidence has generally demonstrated that it provides reasonable descriptions of the distribution of flood flows (Figure 7-5, and results in [Griffis and Stedinger, 2007b](#), [Cohn et al. 2016](#)). The key issue is how to fit an LP3 distribution efficiently to provide accurate estimates of flood quantiles and of flood risk.

As discussed previously, a wide range of methods have been proposed, and log space moments, while not always the best, generally do well ([Griffis and Stedinger 2007c](#)). However, it is clear that when flood records contain zero and almost zero “flood” flows, the whole distribution of the annual

flood series is not well described by an LP3 distribution, and the log space method of moments implicitly gives too much weight to the smallest values (because of the log transformation, zeros would have a value of negative infinity, while unusually small flood flows have logarithms that fall far to the left of other values). *Bulletin 17B* tries to deal with this problem by using a Grubbs–Beck low outlier test for normal data to identify “outliers” that were dropped from the moment analysis; then the conditional moment adjustment discussed previously could be used with an LP3 distribution fit to retained flood values. Unfortunately, some flood records can contain many zeros and unusually small flood flows, and the Grubbs–Beck test is constructed to look to see if the smallest observation in a normal sample is unusually small. However, if a flood record has k zero flood values, then the smallest nonzero flood value should be distributed as the $(k+1)^{\text{th}}$ smallest value in the sample, not the smallest.

In addition to consideration of what has historically been called “outliers,” some records do not include the smallest values because of the use of crest-stage gauges, where some flows are not large enough to be recorded. The recording threshold can change through time when different instruments were employed. Even more important, historical and physical paleoflood records can provide a tremendous amount of information on the risk of large floods. Use of EMA can capture that information, while the method of weighted moments in *Bulletin 17B* generally does not do as well and works with only a single threshold ([Cohn et al. 1997](#)).

A major motivation for a *Bulletin 17C* was adoption of EMA as the appropriate extension of the method of log moments to deal with historical and paleoflood records. EMA allows multiple exceedance thresholds and use of ranges to describe observations. EMA can provide a direct fit of the LP3 distribution using the entire dataset, simultaneously employing regional skew information and a wider range of historical flood and threshold-exceedance information, while adjusting for any low outliers, missing values from an incomplete record, or zero flood years. No need exists to change the basic rules of the frequency analysis by use of a new distribution, or to adopt a radically different fitting procedure. Still with log space method of moments estimators, unusually small values can distort the fitted distribution, while zeros should not occur at all. Figure 7-8 provides an example wherein representing the smallest flood as less than the second smallest flood results in an important difference in the fitted distribution (MOM versus EMA or CPA). Because EMA represents zeros and unusual small flows as less than the smallest retained value (i.e., a censored value with that upper bound), the smallest retained value must not be an unusually small value given the distribution of the larger flood flows, whose distribution is what is important.

Hydrologists have understood this for a long time; they have used “professional judgement” to ignore the smaller values in many records. A general problem is that the smallest observations in a record can distort the exceedance probabilities assigned to the large floods of interest. *Bulletin 17C* now calls such small values potentially influential low floods (PILFs). *Bulletin 17C* includes a new multiple Grubbs–Beck outlier test (MGBT) for identifying PILFs ([Cohn et al. 2013](#)). [Spencer and McCuen \(1996\)](#) and [Lamontagne and Stedinger \(2015\)](#) discuss such tests and their use. [Cohn et al. \(2016\)](#) and [Lamontagne et al. \(2016\)](#) report extensive studies on the impact on robustness and quantile estimation precision of the identification of PILFs with the MGBT followed by use of EMA. Depending on the total sample size, and the rank of different observations, a sequential test identifies smaller observations that may be unusually influential in the fitting process; then, with EMA those PILFs are described as being smaller than the smallest retained observation. This makes the resulting EMA–MGBT fitting procedure very robust in that unusually small annual floods are not allowed to distort the distribution fit to the larger flood values. And what is remarkable is this: the identification of PILFs and their representation as less-than values generally does not diminish the precision of flood quantile estimators when the log space skew is zero or greater, while it *increases* the precision of quantile estimators when the log skew is less than zero. An increase occurs because the log space method of moments is not the optimal estimation procedure.

Thus, the EMA–MGBT generally makes flood frequency analysis based on the LP3 distribution with EMA both more accurate and more robust. In addition, EMA can deal with regional skew and

with historical and paleoflood information, and low flows, with a range of thresholds. The MGBT and the EMA computations are computationally involved; however, EMA–MGBT computer codes are available from the US Geological Survey and the US Army Corps of Engineers. These codes also include uncertainty analyses that provide accurate confidence intervals for computed flood quantiles based on the information considered in the computation, observed flood flows, floods described as less than a threshold or within an interval, regional skew information, and historical flood data.

7.5 INCORPORATION OF CLIMATE CHANGE AND CLIMATE VARIABILITY INTO FLOOD FREQUENCY ANALYSIS

The current techniques for flood frequency analysis presented in *Bulletin 17B* assume annual maximum floods are stationary, and thus the distribution of flood flows is not significantly affected by climatic trends or cycles (Olsen et al. 1999, Hirschboeck et al. 2000). However, the current scientific consensus is that indeed trends are occurring in flood risk (Georgakakos et al. 2014). Hirsch and Archfield (2015) observe that floods may not be larger, just more frequent, whereas in the past increased frequency can be a temporary and natural oscillation rather than a trend. Moreover, what is often overlooked is that despite the possibility of trends in streamflow statistics, short records give us only limited precision of the value of those statistics in the first place (Stedinger and Griffis 2011). This section considers how the *Bulletin 17B* framework can be modified to account for predictable variations in flood records due to climatic variability.

Climatic patterns that may result in long-term variability in flood risk include the Pacific decadal oscillation (PDO) and the Northern Atlantic oscillation (NAO) (Olsen et al. 1999, Garbrecht and Piechotab2006). These patterns exhibit low-frequency variability with shifts that last on the order of decades. For the Upper Mississippi River Basin, Olsen et al. (1999) relate annual maximum flows to PDO and NAO using linear regressions and find PDO and NAO explain little of the variation in flood peaks. Using nonparametric tests on monthly data for stations across the United States, Tootle et al. (2005) identify significant differences in streamflow between the cold and warm phases of both the PDO and NAO at several stations.

Another climatic pattern that may affect the magnitude of annual maximum flood flows is the El Niño–southern oscillation (ENSO). However, these events occur over a relatively short time frame (generally 12 to 18 months) and thus are not expected to result in long-term changes in flood risk. For the Upper Mississippi River Basin, Olsen et al. (1999, p. 1511) observe that “as long as the frequency and intensity of El Niño events are not changing over time, flood frequency analysis naturally accounts for climate variability associated with El Niño events.” Nevertheless, ENSO events can impact flood risk in a given year. Tootle et al. (2005) identify significant differences in monthly streamflow between the cold (La Niña) and warm (El Niño) phases in Florida, the Southwest, and the Pacific Northwest. Kiem et al. (2003), Grantz et al. (2005), Twine et al. (2005), Tootle et al. (2006), and Ward et al. (2014) also investigate the influence of ENSO on streamflow. The results of these studies indicate that incorporating effects of ENSO into forecasts of flood risk in any year can be worthwhile to adjust reservoir flood-storage requirements. Alternative approaches are discussed as follows.

7.5.1 Block Adjustment versus Parametric Adjustment

Two approaches for incorporating ENSO forecasts into computations of flood risk are block and parametric adjustments of the distribution parameters. Each approach has advantages and disadvantages.

Block adjustment is a simple approach wherein the flood events are categorized according to whether they occurred when the ENSO phase was warm, neutral, or cold, and a separate distribution

is fit to each category. Hamlet and Lettenmaier (1999) employ this approach in developing a probabilistic streamflow forecast model. Hirschboeck et al. (2000) discuss potential causes of mixed distributions that may be enhanced by ENSO teleconnections. In essence, categorizing the flood series in this way is analogous to mixtures of distributions employed when floods arise from different types of events, such as snowmelt versus rainstorms (see Waylen and Woo 1982). However, unless the individual categories are composed of events with distinctly different distributions, it would be better to develop one model for the entire flood series using a parametric approach so that fewer parameters need be estimated and more data are available to do so; if one categorizes the data, how should one proceed if one category contains relatively few observations?

Parametric adjustment is a more sophisticated approach. It adds relatively few parameters to the standard model. With this approach, one would attempt to develop a relationship relating climate indices to variations in the statistical properties of floods. This could be accomplished by regressing the distribution parameters on climatic indices describing ENSO; indexes such as the Niño-3.4 sea surface temperature (SST) anomalies, the Southern Oscillation Index (SOI), or the Multivariate ENSO Index (MEI) could be employed (Piechota et al. 2006). Kashelikar and Griffis (2008) and Kashelikar (2009) consider regressing the P3 location parameter on Niño-3.4 SST anomalies at sites throughout the United States; Fritsch (2012), Salvadori and Griffis (2013), and Salvadori (2013) extend that body of work to consider estimation of the P3 location and scale parameters as a function of MEI, as well as indices associated with NAO, PDO, and the Atlantic multidecadal oscillation (AMO). Li and Tan (2015) include an additional index to describe human development in a basin.

Time-dependent models of distribution parameters could be employed in a similar fashion to reflect observed trends in stream flows. Several studies have suggested such an approach. For example, Strupczewski et al. (2001) employ time-dependent parameters of a P3 distribution; Coles (2001, p. 106) and El Adlouni et al. (2007) consider GEV models with time-dependent parameters. The next section discusses three possible parametric approaches that employ climate indices describing ENSO.

7.5.2 INCORPORATION OF ENSO EFFECTS USING PARAMETRIC RELATIONSHIPS

To incorporate the effects of ENSO into flood frequency forecasts, Kashelikar and Griffis (2008) introduce a regression model to relate parameters of the P3 distribution (μ , σ , and γ) to an appropriate climate index, such as the SST anomalies. A model for the mean μ is

$$\mu_t = \beta_0 + \beta_1 c_t + \varepsilon_t \quad (7-24)$$

Here μ_t is the mean computed using the logarithms of flood peaks observed over the 10-year period ending at time t (i.e., μ_t is the mean of the logarithms $X_{t-9}, X_{t-8}, \dots, X_t$), β_0 and β_1 are regression parameters, and ε_t is the independent model error. The ENSO state and intensity are represented by the climate index c_t observed at time t . Use of a 10-year moving window to compute the mean avoids dampening of the climate signal.

Using the model in Equation (7-24), a one-year ahead forecast of the mean to year $T+1$ would be

$$\hat{\mu}_{T+1} = \beta_0 + \beta_1 \hat{c}_{T+1} \quad (7-25)$$

wherein \hat{c}_{T+1} is a forecasted value of the climate index. A similar approach could be used to update (forecast) the value of the standard deviation σ , and possibly the skew γ of the P3 distribution, such that the logs of the flood peaks would be modeled as $X_t \sim P3[\mu(t), \sigma(t), \gamma(t)]$. The updated parameters would then be used to forecast flood risk for the next year.

Coles (2001, pp. 105–108) employs a similar approach to account for nonstationarity in annual maximum sea levels due to ENSO. Let $GEV(\xi, \alpha, \kappa)$ denote the GEV distribution with location parameter ξ , scale parameter α , and shape parameter κ (Stedinger et al. 1993). Coles suggests

modeling the annual maximum sea level Z_t in year t as a function of the Southern Oscillation Index in year t , $\text{SOI}(t)$, using the GEV distribution so that

$$Z_t \sim \text{GEV}(\xi(t), \alpha, \kappa) \quad (7-26)$$

where

$$\xi(t) = \beta_0 + \beta_1 \text{SOI}(t) + \varepsilon_t \quad (7-27)$$

Coles notes that similar expressions could be used to model $\alpha(t)$ and $\kappa(t)$, although with limited data estimating parameters for the model of $\kappa(t)$ with adequate precision would be difficult.

A model wherein nonstationarity is expressed in terms of both the mean and the standard deviation is particularly appropriate for flood statistics. Using the LP3 model as recommended by *Bulletin 17B*, the logs of the flood peaks X_t could then be modeled as $X_t \sim P3[\mu(t), \sigma(t), \gamma]$, wherein $\mu(t)$ and $\sigma(t)$ are modeled as functions of a climate index such as SST. But one might believe that the coefficient of variation C_v of the flood distribution remains constant over time. In this case, if the mean scales with changes due to ENSO, then a corresponding change in the standard deviation must also occur. The model $X_t \sim P3[\mu(t), \sigma(t), \gamma]$ could capture this; however, estimating additional parameters for $\sigma(t)$ could be difficult with limited data. Moreover, not clear is whether this would ensure a constant real space C_v . An alternative approach would be to use the model

$$X_t \sim P3[\mu(t), \sigma, \gamma] \quad (7-28)$$

where

$$\mu(t) = \beta_0 + \beta_1 \text{SST}(t) + \varepsilon_t \quad (7-29)$$

Here the standard deviation and skew of $X = \ln(Q)$ are independent of time; as a result the coefficients of variation and skewness of Q will also be independent of time. This is an advantageous characteristic that follows from modeling the logarithm of the flows.

Overall, the model in Equations (7-28) and (7-29) is a reasonable approach to incorporate climate variability due to ENSO into forecasts of flood risk described by a time-varying LP3 distribution. A similar approach may be used to incorporate the effects of climate change in the flood estimates by regressing the LP3 parameters on alternative climatic indices, such as those describing the PDO and NAO (e.g., [Fritsch 2012](#), [Salvadori and Griffis 2013](#), [Salvadori 2013](#)).

Example 7-3

This example illustrates the application of ENSO climate index-parameter relationships for one-year ahead forecasts of flood risk obtained using the LP3 distribution. The sample data employed herein is the record of annual flood peaks from 1930 to 2005 for New River near Galax, Virginia, USGS gauging station number 03164000. Table 7-6 provides the sorted sample data. Note that data at this site are available beginning in 1930. However, as SST anomalies are only available beginning in 1950, the flood peak in 1941 is the earliest value needed to compute sample means over a 10-year window for use in Equation (7-29). To simplify the analysis, the presence of historic data and possible low outliers are not considered in this example. In addition, regional skew information is not employed to improve the estimate of the skew coefficient.

Here Q represents the true annual flood peaks and is assumed to follow an LP3 distribution, and X represents the natural logarithms of the annual peaks and follows a P3 distribution. The sample contains $N = 65$ observations. In log space, the maximum observation is 11.42 and the minimum observation is 8.73. The sample moments of the logarithms calculated using Equation (7-12) are

Table 7-6. Annual Flood Peaks for New River Near Galax, Virginia.

Year	Q (ft ³ /s)						
1988	6,200	1969	14,600	2003	24,400	1957	33,300
2000	7,510	1986	14,800	1960	24,900	1996	34,700
1971	8,340	1942	15,000	1998	25,600	1979	37,300
1941	8,940	1943	15,400	1975	26,200	1945	38,000
1968	9,350	1948	15,400	1980	26,500	1951	38,000
1985	10,500	1953	15,900	1976	26,600	1990	39,800
2002	11,100	1947	16,400	1961	26,900	1959	40,700
2005	11,600	1954	16,400	1974	27,200	1973	42,800
1967	12,000	1982	17,200	1970	27,400	2004	43,900
1964	12,600	1962	18,700	1977	28,400	1994	48,500
1950	13,200	1956	19,600	1991	28,400	1992	49,500
1999	13,400	1981	19,800	1949	30,000	1989	54,100
1944	13,600	1946	22,000	1966	30,500	1995	68,700
1958	13,700	1984	22,000	1983	30,500	1978	91,000
1997	14,200	1965	22,500	1972	30,700		
2001	14,300	1955	23,900	1993	31,300		
1952	14,500	1987	24,300	1963	31,500		

$\bar{X} = 9.990$, $S_x = 0.550$, and $G_x = 0.060$. An estimate of the flood risk (i.e., the LP3 quantile with specified cumulative probability p) using traditional log space MOM procedures would then be computed as

$$\hat{Q}_p = \exp\{\bar{X} + S_x K_p(G_x)\}$$

For example, the estimate of the 100-year event ($p = 0.99$) for use in water resources planning and management in year 2006 would be

$$\hat{Q}_{0.99} = \exp\{9.990 + 0.550(2.370)\} = 80,368.4 \text{ ft}^3/\text{s}.$$

This would be a reasonable estimate based on the available record, assuming the influence of ENSO on flood risk is negligible.

To incorporate the effects of ENSO, one first needs to estimate the regression parameters in Equation (7-29). Table 7-7 shows the needed SST anomalies in year t and the corresponding sample means of the logarithms computed over a 10-year window ending in year t . Ordinary least squares regression of $\mu(t)$ on $\text{SST}(t)$ yields regression parameters $\beta_0 = 10.04$ and $\beta_1 = 0.082$; β_1 is significantly different from zero at the 5% level. A one-year ahead forecast of the mean is obtained using these regression parameters in Equation (7-25):

$$\hat{\mu}_{T+1} = 10.04 + 0.082 \hat{c}_{T+1}$$

wherein \hat{c}_{T+1} is the forecasted value of the SST anomaly. To illustrate the value of the proposed model, consider two possible values of the SST anomaly: $\hat{c}_{T+1} = 0.2$, corresponding to a mild El Niño event, and $\hat{c}_{T+1} = 1.2$, corresponding to a strong El Niño event. These anomalies yield forecasted means of 10.06 and 10.14, respectively.

Table 7-7. SST Anomalies and Corresponding 10-Year Means for New River Near Galax, Virginia.

Year	$\mu(t)$	SST(t)	Year	$\mu(t)$	SST(t)	Year	$\mu(t)$	SST(t)
1950	9.880	-0.777	1969	9.898	0.687	1988	9.946	-0.820
1951	9.910	-0.083	1970	9.906	-0.260	1989	9.962	-0.830
1952	9.896	-0.133	1971	9.885	-0.770	1990	9.972	0.163
1953	9.887	0.507	1972	9.896	0.333	1991	9.976	0.113
1954	9.879	-0.740	1973	9.913	-0.393	1992	9.990	1.307
1955	9.887	-0.933	1974	9.920	-0.617	1993	9.995	0.867
1956	9.887	-0.507	1975	9.925	-0.623	1994	10.008	-0.213
1957	9.906	0.427	1976	9.931	-0.420	1995	10.025	-0.323
1958	9.893	0.330	1977	9.938	-0.060	1996	10.031	-0.597
1959	9.917	-0.080	1978	9.968	-0.567	1997	10.024	0.357
1960	9.923	-0.217	1979	9.979	0.173	1998	10.026	1.613
1961	9.932	-0.070	1980	9.983	-0.043	1999	10.018	-0.587
1962	9.929	-0.727	1981	9.981	-0.357	2000	10.003	-0.223
1963	9.942	-0.020	1982	9.977	0.300	2001	9.997	0.030
1964	9.927	-1.023	1983	9.983	1.877	2002	9.988	0.163
1965	9.930	0.233	1984	9.984	-0.210	2003	9.989	-0.327
1966	9.941	-0.227	1985	9.971	-0.930	2004	9.999	-0.097
1967	9.926	-0.617	1986	9.964	-0.283	2005	9.990	0.227
1968	9.906	-0.927	1987	9.967	1.120			

A one-year ahead forecast of the flood risk using the proposed model to incorporate the effects of ENSO is then obtained using the forecasted mean combined with the sample standard deviation and skew coefficient computed for the entire period of record. For example, the estimate of the 100-year event ($p = 0.99$) for use in water resources planning and management in year 2006 would be $\hat{Q}_{0.99} = \exp\{10.06 + 0.550(2.370)\} = 85,902.7 \text{ ft}^3/\text{s}$ given a forecasted SST anomaly of 0.2. This estimate is 5,534.4 ft^3/s greater than the estimate obtained using the traditional model wherein the mean is averaged over the entire period of record. A greater difference between the two models is observed when the SST anomaly corresponds to a strong ENSO event. The one-year ahead estimate of the 100-year event is 93,243.6 ft^3/s given an SST anomaly of 1.2, which is 12,875.3 ft^3/s greater than that obtained using the traditional model.

Figure 7-9 provides frequency curves that represent the forecasted flood magnitudes corresponding to various probabilities of exceedance at New River for the year 2006. The frequency curve labeled MOM was obtained using a traditional LP3 model wherein log space moments are computed using the entire period of record. The MOM curve yields smaller estimates of flood magnitude for all exceedance probabilities as compared with the estimates obtained using the proposed model with $\text{SST}(2006) = 0.2$ and $\text{SST}(2006) = 1.2$. These results clearly indicate the impact of ENSO events on flood risk. The sample data plotted using Blom's plotting position formula are also shown for comparison.

7.6 CLOSING REMARKS

Flood frequency analyses continue to improve as records get longer, flood frequency analysis methods get better, and greater computing power and computer software are available for analyses. This chapter has described in detail the flood frequency analysis methods that have been used in the United States with the *Bulletin 17-17A-17B* series starting in 1976. *Bulletin 17C* should soon be

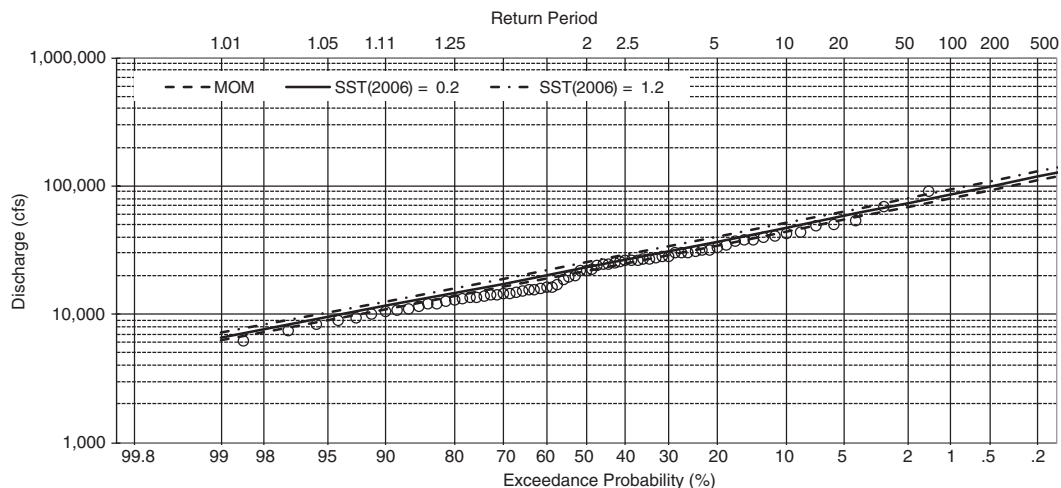


Figure 7-9. Frequency curves representing one-year ahead forecast for year 2006 at New River near Galax, Virginia. Forecasts obtained using traditional method of moments model (MOM) and a proposed model to incorporate ENSO effects assuming $SST(2006) = 0.2$ and 1.2 .

officially adopted representing a significant advance in flood frequency methods and our ability to represent a broader range of flood data both at site and regional. In addition, it provides much better estimates of the uncertainty in estimated flood quantiles and distribution parameters. Moreover, *Bulletin 17C* is fully implemented in computer codes with documentation available from the US Geological Survey and the US Army Corps of Engineers. This reduces the opportunity for errors and makes the best methods available to hydrologists conducting flood risk studies. A future challenge is changes that will occur in flood distributions due to climate variability and climate change. This chapter has also discussed how those concerns might be addressed.

APPENDIX 7A: PLOTTING POSITIONS FOR USE WITH LOW OUTLIERS AND HISTORICAL INFORMATION

Bulletin 17B includes plotting positions for historical flood data, but [Hirsch and Stedinger \(1987\)](#) provide a framework for more precise plotting positions that are applicable with multiple historical flood thresholds. In their framework, the exceedance probability q_e of the historical threshold may be estimated by $Z/(N_S + N_H)$, where $Z = N_S^> + N_H^>$ is the number of flood events that exceeded the perception threshold over the entire period (historic and systematic) of length $N_S + N_H$. If the Z observations that exceeded the historical flood threshold are ranked from $j = 1, \dots, Z$, plotting positions approximating the exceedance probabilities within the interval $(0, q_e)$ are given by

$$p_j^Z = q_e \left(\frac{j - a}{Z + 1 - 2a} \right) \quad (7-30)$$

Plotting positions within $(q_e, 1)$ for the remaining $N_S^<$ below threshold floods are then

$$p_j = q_e + (1 - q_e) \left(\frac{j - a}{N_S^< + 1 - 2a} \right) \quad (7-31)$$

for $j = 1, \dots, N_S^<$ ([Stedinger et al. 1993](#), pp. 18.41–18.42).

APPENDIX 7B: EXPECTED MOMENTS ALGORITHM

The EMA for low outlier adjustment, and the incorporation of regional skew information and historical information in flood frequency analyses with the LP3 distribution includes the following steps:

Step 1. Using all observations in the systematic record $\{X_S\}$, compute initial estimates of the sample moments $(\hat{\mu}_1, \hat{\sigma}_1, \hat{\gamma}_1)$.

Step 2. For $i = 1, 2, \dots$, the parameters of the P3 distribution $(\hat{\alpha}_{i+1}, \hat{\beta}_{i+1}, \hat{\tau}_{i+1})$ are estimated using the previously computed sample moments.

$$\hat{\alpha}_{i+1} = 4/\hat{\gamma}_i^2; \quad \hat{\beta}_{i+1} = \frac{1}{2}\hat{\sigma}_i\hat{\gamma}_i; \quad \hat{\tau}_{i+1} = \hat{\mu}_i - \hat{\alpha}_{i+1}\hat{\beta}_{i+1}$$

Step 3. Estimate new sample moments $(\hat{\mu}_{i+1}, \hat{\sigma}_{i+1}, \hat{\gamma}_{i+1})$ using expected moments such as

$$\hat{\mu}_{i+1} = \frac{\sum X_S^> + \sum X_L^> + N_L^<E[X_L^<] + \sum X_H^> + N_H^<E[X_H^<]}{N_S + N_H} \quad (7-32)$$

where $E[X_L^<]$ is the expected value of an observation in the systematic period known to have a value below the low outlier threshold X_L , and $E[X_H^<]$ is the expected value of the logarithm of an event in the historic period that failed to exceed the perception threshold T . The expected values are conditional expectations given that $X < X_c$ and $X < Y = \log(T)$, respectively. Here X_c denotes the EMA censoring threshold, which is defined as the smallest retained observation. Use of the smallest retained observation rather than X_L to define the possible range of censored values made the EMA algorithm less sensitive to the distribution of low outliers (Griffis 2003). With the current parameter estimates $(\hat{\alpha}_{i+1}, \hat{\beta}_{i+1}, \hat{\tau}_{i+1})$, the conditional expectation $E[X_L^<]$ is expressed in terms of the incomplete gamma function (Cohn et al. 1997):

$$E[X_L^<] = \tau + \beta \frac{\Gamma\left[\frac{X_c - \tau}{\beta}, \alpha + 1\right]}{\Gamma\left[\frac{X_c - \tau}{\beta}, \alpha\right]} \quad (7-33)$$

The expression for the conditional expectation $E[X_H^<]$ is equivalent to Equation (7-33), except the censoring threshold X_c is replaced by the logarithm of the perception threshold $Y = \log(T)$.

The second and third moments are estimated using

$$\begin{aligned} \hat{\sigma}_{i+1}^2 &= \frac{1}{N_S + N_H} \left\{ c_2 \left[\sum (X_S^> - \hat{\mu}_{i+1})^2 + \sum (X_L^> - \hat{\mu}_{i+1})^2 + \sum (X_H^> - \hat{\mu}_{i+1})^2 \right] \right. \\ &\quad \left. + N_L^<E[(X_L^< - \mu)^2] + N_H^<E[(X_H^< - \mu)^2] \right\} \end{aligned} \quad (7-34)$$

$$\begin{aligned} \hat{\gamma}_{i+1} &= \frac{1}{(N_S + N_H + n)\hat{\sigma}_{i+1}^3} \left\{ c_3 \left[\sum (X_S^> - \hat{\mu}_{i+1})^3 + \sum (X_L^> - \hat{\mu}_{i+1})^3 + \sum (X_H^> - \hat{\mu}_{i+1})^3 \right] \right. \\ &\quad \left. + N_L^<E[(X_L^< - \mu)^3] + N_H^<E[(X_H^< - \mu)^3] + nG\hat{\sigma}_{i+1}^3 \right\} \end{aligned} \quad (7-35)$$

wherein $c_2 = (N_S + N_H^>)/(N_S + N_H^> - 1)$, $c_3 = (N_S + N_H^>)^2/[(N_S + N_H^> - 1)(N_S + N_H^> - 2)]$, and n = additional years of record assigned to the regional skew. Here $\hat{\gamma}_{i+1}$ is a weighted skewness estimator. To ensure that EMA is consistent with *Bulletin 17B* when no low outliers are identified [i.e., $\hat{\gamma}_{i+1} = G_W$ in Equation (7-14)], the required value of n is

$$n = (N_S + N_H) \frac{MSE(\hat{\gamma})}{MSE(G_R)} \quad (7-36)$$

In this sense, n is the regional skew weight measured in years.

The expected contribution of the values below the low outlier threshold X_L to the second and third central moments ($m = 2$ and 3, respectively) is (Cohn et al. 1997)

$$E[(X_L^< - \mu)^m] = \sum_{j=0}^m \binom{m}{j} \beta^j (\tau - \mu)^{m-j} \frac{\Gamma\left[\frac{X_c - \tau}{\beta}, \alpha + j\right]}{\Gamma\left[\frac{X_c - \tau}{\beta}, \alpha\right]} \quad (7-37)$$

The expression for the expected contribution of the unobserved values in the historic period $E[(X_H^< - \mu)^m]$ is equivalent to Equation (7-37), except the censoring threshold X_c is replaced by the logarithm of the perception threshold $Y = \log(T)$.

Step 4. Convergence. In general, steps 2 and 3 are repeated until the parameter estimators for the P3 mean, standard deviation, and skew values converge. It is recommended, however, that EMA be employed first with all available data, both systematic and historical data, and regional skew information, to obtain initial estimates of the mean and standard deviation. To do so, steps 2 and 3 should be repeated until the moment estimators converge, wherein Equations (7-32), (7-34), and (7-35) are computed by including any possible low outliers in the set $\{X_L^>\}$; the terms involving the expected contribution from low outliers are omitted from the computations. Once the estimators converge, those values should then be used in Equation (7-18) to define the low outlier threshold, wherein the systematic record length N_S is used to define the frequency factor K_N . If low outliers are identified, then the EMA analysis should be repeated (steps 2 and 3 to convergence) treating the low outliers as censored observations that are known to be smaller than the smallest observation retained.

References

- Beard, L. R. 1962. *Statistical methods in hydrology*. Civil Works Investigation Project No. CW-151. Washington, DC: USACE.
- Benson, M. A. 1968. "Uniform flood-frequency estimating methods for federal agencies." *Water Resour. Res.* **4** (5): 891–908.
- Bobee, B. 1973. "Sample error of T-year events computed by fitting a Pearson type 3 distribution." *Water Resour. Res.* **9** (5): 1264–1270.
- Bobee, B. 1975. "The log Pearson type III distribution and its application in hydrology." *Water Resour. Res.* **11** (5): 681–689.
- Bobee, B., and F. Ashkar. 1991. *The gamma family and derived distributions applied in hydrology*. Littleton, CO: Water Resources Publications.
- Buckett, J., and F. R. Oliver. 1977. "Fitting the Pearson type 3 distribution in practice." *Water Resour. Res.* **13** (5): 851–852.
- Caulfield, H. P. 2000. "Early guidelines for water resource evaluation." *Water Resour. Update* **116** (1): 14–17.
- Chowdury, J. U., and J. R. Stedinger. 1991. "Confidence interval for design floods with estimated skew coefficient." *J. Hydraul. Eng.* **117** (7): 811–831.

- Cohn, T. A., N. A. Barth, J. F. England Jr., B. A. Faber, R. R. Mason, and J. R. Stedinger. 2016. *Evaluation of recommended revisions to Bulletin 17B*. Reston, VA: USGS.
- Cohn, T. A., J. F. England, C. E. Berenbrock, R. R. Mason, J. R. Stedinger, and J. R. Lamontagne. 2013. "A generalized Grubbs-Beck test statistic for detecting multiple potentially influential low outliers in flood series." *Water Resour. Res.* **49** (8): 5047–5058.
- Cohn, T. A., W. L. Lane, and W. G. Baier. 1997. "An algorithm for computing moments-based flood quantile estimates when historical flood information is available." *Water Resour. Res.* **33** (9): 2089–2096.
- Coles, S. 2001. *An introduction to statistical modeling of extreme values*. London: Springer.
- El Adlouni, S., T. B. Ouarda, X. Zhang, R. Roy, and B. Bobee. 2007. "Generalized maximum likelihood estimators for the nonstationary generalized extreme value model." *Water Resour. Res.* **43** (3): W03410.
- England, J. F., Jr., T. A. Cohn, B. A. Faber, J. R. Stedinger, W. O. Thomas Jr., A. G. Veilleux, J. E. Kiang, and R. R. Mason. 2016. "Guidelines for determining flood flow frequency." Bulletin 17C. Accessed November 8, 2016.
- England, J. F., Jr., J. D. Salas, and R. D. Jarrett. 2003. "Comparisons of two moments-based estimators that use historical and paleoflood data for the log-Pearson Type III distribution." *Water Resour. Res.* **39** (9): SWC-5-1–SWC-5-16.
- Feaster, T. D., A. J. Gotvald, and J. C. Weaver. 2009. *Magnitude and frequency of rural floods in the southeastern United States, 2006, Volume 3, South Carolina*. US Geological Survey Scientific Investigations Rep. No. 2009-5156. Reston, VA: USGS.
- Fritsch, C. E. 2012. "Evaluation of flood risk in response to climate variability." M.S. thesis, Dept. of Civil and Environmental Engineering, Michigan Technology Univ.
- Garbrecht, J. D., and T. C. Piechota. 2006. "Water resources and climate." In *Climate variations, climate change, and water resources engineering*, edited by J. D. Garbrecht and T. C. Piechota, 19–33. Reston, VA: ASCE.
- Gelman, A., J. B. Carlin, H. S. Stern, and D. B. Rubin. 1995. *Bayesian data analysis*. Boca Raton, FL: Chapman & Hall/CRC.
- Georgakakos, A., P. Fleming, M. Dettinger, C. Peters-Lidard, T. C. Richmond, K. Reckhow, K. White, and D. Yates. 2014. "Water resources." In *Climate change impacts in the United States: The third national climate assessment*, edited by J. M. Melillo, et al., 69–112. Washington, DC: US Global Change Research Program.
- Gilroy, E. J. 1972. *The upper bound of a log-Pearson type 3 random variable with negatively skewed logarithms*. Reston, VA: USGS.
- Gotvald, A. J., T. D. Feaster, and J. C. Weaver. 2009. *Magnitude and frequency of rural floods in the southeastern United States, 2006, Volume 1, Georgia*. US Geological Survey Scientific Investigations Rep. No. 2009-5043. Reston, VA: USGS.
- Grantz, K., B. Rajagopalan, M. Clark, and E. Zagona. 2005. "A technique for incorporating large-scale climate information in basin-scale ensemble streamflow forecasts." *Water Resour. Res.* **41** (10): W10410.
- Griffis, V. W. 2003. "Evaluation of log-Pearson type 3 flood frequency analysis methods addressing regional skew and low outliers." M.S. thesis, School of Civil and Environmental Engineering, Cornell Univ.
- Griffis, V. W. 2006. "Flood frequency analysis: Bulletin 17, regional information, and climate change." Ph.D. dissertation, School of Civil and Environmental Engineering, Cornell Univ.
- Griffis, V. W. 2008. "EMA with historical information, low outliers, and regional skew." In *Proc., World Water and Environmental Resources Congress*, edited by R. W. Babcock and R. Walton. Reston, VA: ASCE.
- Griffis, V. W., and J. R. Stedinger. 2007a. "Evolution of flood frequency analysis with Bulletin 17." *J. Hydrol. Eng.* **12** (3): 283–297.
- Griffis, V. W., and J. R. Stedinger. 2007b. "Log-Pearson type 3 distribution and its application in flood frequency analysis. I: Distribution characteristics." *J. Hydrol. Eng.* **12** (5): 482–491.
- Griffis, V. W., and J. R. Stedinger. 2007c. "Log-Pearson type 3 distribution and its application in flood frequency analysis. II: Parameter estimation methods." *J. Hydrol. Eng.* **12** (5): 492–500.
- Griffis, V. W., and J. R. Stedinger. 2009. "Log-Pearson type 3 distribution and its application in flood frequency analysis. III: Sample skew and weighted skew estimators." *J. Hydrol. Eng.* **14** (2): 121–130.
- Griffis, V. W., J. R. Stedinger, and T. A. Cohn. 2004. "LP3 quantile estimators with regional skew information and low outlier adjustments." *Water Resour. Res.* **40** (7): W07503.
- Hamlet, A. F., and D. P. Lettenmaier. 1999. "Columbia River streamflow forecasting based on ENSO and PDO climate signals." *J. Water Resour. Plann. Manage.* **125** (6): 333–341.
- Hardison, C. H. 1974. "Generalized skew coefficients of annual floods in the United States and their application." *Water Resour. Res.* **10** (4): 745–752.

- Hirsch, R. M., and S. A. Archfield. 2015. "Flood trends: Not higher but more often." *Nat. Clim. Change* **5** (3): 198–199.
- Hirsch, R. M., and J. R. Stedinger. 1987. "Plotting positions for historical floods and their precision." *Water Resour. Res.* **23** (4): 715–727.
- Hirschboeck, K. K., L. L. Ely, and R. A. Maddox. 2000. "Hydroclimatology of meteorologic floods." In *Inland flood hazards*, edited by E. E. Wohl, 39–72. Cambridge, MA: Cambridge University Press.
- Holmes, B. H. 1979. *History of federal water resource programs and policies, 1961–1970: Miscellaneous Publication No. 1379*. Washington, DC: Dept. of Agriculture.
- Hosking, J. R. M. 1990. "L-moments: Analysis and estimation of distributions using linear combinations of order statistics." *J. R. Stat. Soc. Ser. B (Methodol.)* **52** (1): 105–124.
- Hosking, J. R. M., and J. R. Wallis. 1997. *Regional frequency analysis: An approach based on L-moments*. Cambridge, MA: Cambridge University Press.
- House Document No. 465. 1966. "A unified national program for managing flood losses." In *Proc., 89th Congress, 2d Session*. Washington, DC: US Government Printing Office.
- IACWD (Interagency Committee on Water Data). 1982. *Guidelines for determining flood flow frequency: Bulletin 17B*. Washington, DC: IACWD.
- IACWD. 1966. *Methods of flow frequency analysis: Bulletin 13*. Washington, DC: IACWD.
- Jennings, M. E., and M. A. Benson. 1969. "Frequency curves for annual flood series with some zero events or incomplete data." *Water Resour. Res.* **5** (1): 276–280.
- Johnson, N. L., S. Kotz, and N. Balakrishnan. 1994. *Continuous univariate distributions*, Vol. 1. 2nd ed. New York: Wiley.
- Kashelikar, A. S. 2009. "Identification of teleconnections and improved flood risk forecasts using Bulletin 17B." M.S. thesis, Dept. of Civil and Environmental Engineering, Michigan Technology Univ.
- Kashelikar, A. S., and V. W. Griffis. 2008. "Forecasting flood risk with Bulletin 17B LP3 model and climate variability." In *Proc., World Water and Environmental Resources Congress*, edited by R. W. Babcock and R. Walton. Reston, VA: ASCE.
- Kiem, A. S., S. W. Franks, and G. Kuczera. 2003. "Multi-decadal variability of flood risk." *Geophys. Res. Lett.* **30** (2): 1035.
- Kirby, W. 1972. "Computer-oriented Wilson-Hilferty transformation that preserves the first three moments and the lower bound of the Pearson type 3 distribution." *Water Resour. Res.* **8** (5): 1251–1254.
- Kirby, W. 1974. "Algebraic boundness of sample statistics." *Water Resour. Res.* **10** (2): 220–222.
- Kottekoda, K. T., and R. Rosso. 1997. *Statistics, probability and reliability for civil and environmental engineers*. New York: McGraw-Hill.
- Lamontagne, J., and J. Stedinger. 2015. "Examination of the Spencer-McCuen outlier-detection test for log-Pearson type 3 distributed data." *J. Hydrol. Eng.* **21** (3): 04015069.
- Lamontagne, J. R., J. R. Stedinger, C. Berenbrock, A. G. Veilleux, J. C. Ferris, and D. L. Knifong. 2012. "Development of regional skews for selected flood durations for the Central Valley Region, California, based on data through water year 2008." US Geological Survey Scientific Investigations Rep. 2012-5130. Accessed November 6, 2016. <https://pubs.usgs.gov/sir/2012/5130/>.
- Lamontagne, J. R., J. R. Stedinger, X. Yu, C. A. Whealton, and Z. Xu. 2016. "Robust flood frequency analysis: Performance of EMA with multiple Grubbs-Beck outlier tests." *Water Resour. Res.* **52** (4): 3068–3084.
- Landwehr, J. M., N. C. Matalas, and J. R. Wallis. 1978. "Some comparisons of flood statistics in real and log space." *Water Resour. Res.* **14** (5): 902–920.
- Landwehr, J. M., N. C. Matalas, and J. R. Wallis. 1979. "Probability weighted moments compared with some traditional techniques in estimating Gumbel parameters and Quantiles." *Water Resour. Res.* **15** (5): 1055–1064.
- Li, J., and S. Tan. 2015. "Nonstationary flood frequency analysis for annual flood peak series, adopting climate indices and check dam index as covariates." *Water Resour. Manage.* **29** (15): 5533–5550.
- Martins, E. S., and J. R. Stedinger. 2000. "Generalized maximum likelihood GEV quantile estimators for hydrologic data." *Water Resour. Res.* **36** (3): 737–744.
- Martins, E. S., and J. R. Stedinger. 2002. "Efficient regional estimates of LP3 skew using GLS regression." In *Proc., 2002 Conf. on Water Resources Planning and Management*. Reston, VA: ASCE.
- Mathworks. 2012. *MATLAB and statistics toolbox release 2012b*. Natick, MA: MathWorks.
- McCuen, R. H. 1979. "Map skew." *J. Water Resour. Plann. Manage.* **105** (WR2): 269–277.

- McCuen, R. H. 2001. "Generalized flood skew: Map versus watershed skew." *J. Hydraul. Eng.* **6** (4): 293–299.
- Olsen, J. R., J. R. Stedinger, N. C. Matalas, and E. Z. Stakhiv. 1999. "Climate variability and flood frequency estimation for the Upper Mississippi and Lower Missouri Rivers." *J. Am. Water Resour. Assoc.* **35** (6): 1509–1523.
- Peel, M. C., Q. J. Wang, R. M. Vogel, and T. A. McMahon. 2001. "The utility of L-moment ratio diagrams for selecting a regional probability distribution." *Hydrolog. Sci.* **46** (1): 147–155.
- Piechota, T. C., J. D. Garbrecht, and J. M. Schneider. 2006. "Climate variability and climate change." In *Climate variations, climate change, and water resources engineering*, edited by J. D. Garbrecht and T. C. Piechota, 19–33. Reston, VA: ASCE.
- Pope, B. F., G. D. Tasker, and J. C. Robbins. 2001. *Estimating the magnitude and frequency of floods in rural basins of North Carolina—Revised*. Water-Resources Investigations Rep. No. 01-4207. Reston, VA: USGS.
- Rasmussen, P. P., and C. A. Perry. 2000. *Estimation of peak streamflows for unregulated rural streams in Kansas*. Water-Resources Investigation Rep. No. 00-4079. Reston, VA: USGS.
- Reis, D. S., Jr., and J. R. Stedinger. 2005. "Bayesian MCMC flood frequency analysis with historical information." *J. Hydrol.* **313** (1–2): 97–116.
- Reis, D. S., Jr., J. R. Stedinger, and E. S. Martins. 2003. "Bayesian GLS regression with application to LP3 regional skew estimation." In *Proc., World Water and Environmental Resources Congress*. P. Bizer and P. DeBarry. Reston, VA: ASCE.
- Reis, D. S., Jr., J. R. Stedinger, and E. S. Martins. 2004. "Operational Bayesian GLS regression for regional hydrologic analyses." In *Critical Transitions in Water and Environmental Resources Management: Proc., World Water and Environmental Resources Congress*, edited by G. Sehlke, et al. Reston, VA: ASCE.
- Reis, D. S., Jr., J. R. Stedinger, and E. S. Martins. 2005. "Bayesian generalized least squares regression with application to log Pearson type 3 regional skew estimation." *Water Resour. Res.* **41** (10): W10419.
- Renard, B. 2011. "A Bayesian hierarchical approach to regional frequency analysis." *Water Resour. Res.* **47** (11).
- Salvadori, N. M. 2013. "Evaluation of non-stationarity in annual maximum flood series of moderately impaired watersheds in the upper midwest and northeastern United States." M.S. thesis, Dept. of Civil and Environmental Engineering, Michigan Technology Univ.
- Salvadori, N., and V. W. Griffis. 2013. "Evaluation of the influence of climate variability on flood risk in moderately impaired watersheds." In *Proc., World Water and Environmental Resources Congress*. Reston, VA: ASCE.
- Spencer, C. S., and R. H. McCuen. 1996. "Detection of outliers in Pearson type III Data." *J. Hydraul. Eng.* **1** (1): 2–10.
- Stedinger, J. R., and V. W. Griffis. 2011. "Getting from here to where? Flood frequency analysis and climate." *J. Am. Water Resour. Assoc.* **47** (3): 506–513.
- Stedinger, J. R., R. M. Vogel, and E. Foufoula-Georgiou. 1993. "Frequency analysis of extreme events." In *Handbook of hydrology*, 18.1–18.66. New York: McGraw-Hill.
- Strupczewski, W. G., V. P. Singh, and W. Feluch. 2001. "Non-stationary approach to at-site flood frequency modeling. I: Maximum likelihood estimation." *J. Hydrol.* **248** (1–4): 123–142.
- Tasker, G. D. 1978. "Flood frequency analysis with a generalized skew coefficient." *Water Resour. Res.* **14** (2): 373–376.
- Tasker, G. D., and J. R. Stedinger. 1986. "Estimating generalized skew with weighted least squares regression." *J. Water Resour. Plann. Manage.* **112** (2): 225–237.
- Thomas, W. O., Jr. 1985. "A uniform technique for flood frequency analysis." *J. Water Resour. Plann. Manage.* **111** (3): 321–337.
- Tootle, G. A., T. M. Hunter, and T. C. Piechota. 2006. "Pacific oceanic/atmospheric variability and the Wind River range. Examining the confluence of environmental and water concerns." In *Proc., World Environmental and Water Resources Congress*, edited by R. Graham. Reston, VA: ASCE.
- Tootle, G. A., T. C. Piechota, and A. Singh. 2005. "Coupled oceanic-atmospheric variability and US streamflow." *Water Resour. Res.* **41** (12): W12408.
- Twine, T. E., C. J. Kucharik, and J. A. Foley. 2005. "Effects of El Niño-southern oscillation on the climate, water balance, and streamflow of the Mississippi River Basin." *J. Clim.* **18** (22): 4840–4861.
- Viglione, A., R. Merz, J. L. Salinas, and G. Blöschl. 2013. "Flood frequency hydrology: 3. A Bayesian analysis." *Water Resour. Res.* **49** (2): 675–692.
- Wallis, J. R., N. C. Matalas, and J. R. Slack. 1974. "Just a moment!" *Water Resour. Res.* **10** (2): 211–219.

- Ward, P. J., B. Jongman, M. Kummu, M. D. Dettinger, F. C. S. Weiland, and H. C. Winsemius. 2014. "Strong influence of El Niño southern oscillation on flood risk around the world." *Proc. Nat. Acad. Sci.* **111** (44): 15659–15664.
- Waylen, P., and M.-K. Woo. 1982. "Prediction of annual floods generated by mixed processes." *Water Resour. Res.* **18** (4): 1283–1286.
- Weaver, J. C., T. D. Feaster, and A. J. Gotvald. 2009. *Magnitude and frequency of rural floods in the southeastern United States, 2006, Volume 2, North Carolina*. US Geological Survey Scientific Investigations Rep. No. 2009-5158. Reston, VA: USGS.
- Whitley, R., and T. V. Hromadka. 1999. "Approximate confidence intervals for design floods for a single site using a neural network." *Water Resour. Res.* **35** (1): 203–209.
- WRC (Water Resources Council). 1967. *A uniform technique for determining flood flow frequencies: Bulletin 15*. Washington, DC: Hydrology Subcommittee of the Interagency Advisory Committee on Water Data.
- WRC. 1976. *Guidelines for determining flood flow frequency: Bulletin 17*. Washington, DC: Hydrology Subcommittee of the Interagency Advisory Committee on Water Data.
- WRC. 1977. *Guidelines for determining flood flow frequency: Bulletin 17A*, Washington, DC: Hydrology Subcommittee of the Interagency Advisory Committee on Water Data.

CHAPTER 8

Low Flows and Droughts

Jose D. Salas
Charles N. Kroll
Antonino Cancelliere
Bonifacio Fernández
Jose A. Raynal
Dong R. Lee

8.0 INTRODUCTION

In other chapters, some features of the hydrologic cycle dealing with the occurrence of extreme events such as extreme maximum precipitation and extreme maximum floods have been addressed. This chapter addresses another feature of the hydrologic cycle that deals with the opposite extreme or the other end of the spectrum, in other words, the occurrence of periods of low flows and drought. Whereas a flood is quite visible and generally gets prompt attention from the public, the media, and other institutions, a drought may not receive similar attention because it may take a while before its impacts and consequences become noted. The effects of periods of low flows and drought can be quite significant and sometimes devastating to the environment and to society. In the following sections we describe some concepts and definitions associated with low flow and drought phenomena and present some tools for analyzing them. Because of the random nature of such phenomena, the methods are based on probabilistic and stochastic concepts. Several problems in water resources and environmental engineering require the estimation of some low flow quantities and the estimation of drought properties. For example, the design of the storage capacity of a reservoir for water supply (conservation) is related to the occurrence of periods of low flows and drought. Low-flow characteristics of streams are commonly used in the planning and management of water resources systems, such as in designing water supply works, analyzing environmental impacts of water resources development, modeling stream water quality, regulating instream water uses, and improving the general understanding of natural regulated stream systems (Tasker 1987). Also, certain water quality standards are based on specific low-flow quantiles.

Low flow at a site is often characterized by an index of low flow. For example, a widely used index of low flow is the 7 day, 10 year low flow, which is the discharge having a 10 year return period derived from a frequency curve of the lowest average flow for seven consecutive days in a year (Riggs 1980). In some cases, low-flow data may be serially uncorrelated. In those cases, one may apply the usual procedures of frequency analysis and estimate useful statistics such as return period and risk. However, when the time series of low flows are time dependent, the usual frequency analysis assuming independence does not apply nor do the methods for estimating the return period and risk. In this chapter we consider both cases. In addition, this chapter includes characterizing droughts by stochastic methods. Drought is generally a complex phenomenon, which may involve a wide range

of temporal and spatial scales, and several hydrometeorological variables such as precipitation, temperature, soil moisture, streamflow, groundwater levels, and water storages may be necessary for drought identification and characterization depending on the particular problem at hand. In addition, many other variables may be necessary for drought forecasting (e.g., Wong et al. 2013) and to quantify drought impacts and consequences on the environment and society. As the title of the chapter implies, the emphasis here is based on streamflow as the key variable of analysis, and in the case of drought characterization the focus is on multiyear droughts. A vast amount of literature is available for analyzing various aspects of droughts such as definition, identification, prediction, impacts, adaptation, and management (e.g., Alley 1984, Frick et al. 1990, Guttmann 1998, Wilhite 2000, Svoboda 2000, Heim 2002, Panu and Sharma 2002, Salas et al. 2005, Bond et al. 2008, Mishra and Singh 2010, Sheffield et al. 2012a).

Following this introductory section, the next section describes definitions of low flow and drought. Then Section 8.2 introduces some elementary concepts and procedures for determining the frequency analysis of low flows using empirical methods, and Section 8.3 describes in some detail frequency analysis using traditional univariate distribution functions including the case of intermittent low-flow data. Section 8.4 includes the case of regional analysis of low flows. Section 8.5 describes the analysis of autocorrelated low flows based on low-order discrete and continuous stochastic models, and Section 8.6 discusses the characterization of multiyear droughts based on analytical approximations. The sections include the estimation of return periods of low flows and droughts, respectively. The case of regional droughts is briefly discussed in Section 8.7, and the effects of hydraulic structures on low flows are briefly described in Section 8.8. The chapter ends with a section of closing remarks, which includes some concepts and references on the effect of climate variability on low flows and droughts.

8.1 LOW FLOW AND DROUGHT DEFINITIONS

Before statistically characterizing low flows and droughts, it is necessary to define them precisely. Since both terms relate to those conditions where streamflow reaches some undesirable levels, there are some similarities as well. In the following two sections, we include definitions that have been suggested in literature, and indicate those cases where some similarities and differences arise between them.

8.1.1 Definitions of Low Flows

Several definitions of low flows are found in the hydrologic literature. Two of the most popular ones utilized in practice are called *low flow* and *low-flow duration*. Sometimes the terms *low-flow volume*, *low-flow discharge*, and *low-flow stage* are utilized to emphasize that the underlying variable is either volume, discharge, or stage, respectively. The term low flow refers to the minimum flow of a stream over a consecutive number of days that may occur during a given time period (generally a year). The term low-flow duration is defined as the number of consecutive days in which the flow (series) is below a certain *threshold value* or *crossing level*. In either case, the referred quantities are random variables so one must describe them in frequency terms.

The definition of low flow depends on the specified time duration d and the T_u , as shown in Figure 8-1. Assuming a daily streamflow hydrograph, typical values of d are 1 day, 5 days, 7 days, 10 days, and higher, depending on the problem, while the unit time period T_u is generally a year or a fraction of a year (e.g., the dry season). The year is the unit time period most commonly used for most problems involving low-flow analysis (U.S. Army Corps of Engineers 1964). Figure 8-1 shows schematically the definition of flow volume v_i and low-flow discharge q_i for the specified time duration d . Thus, one can obtain m values of v_1, \dots, v_m and q_1, \dots, q_m from the daily hydrograph.

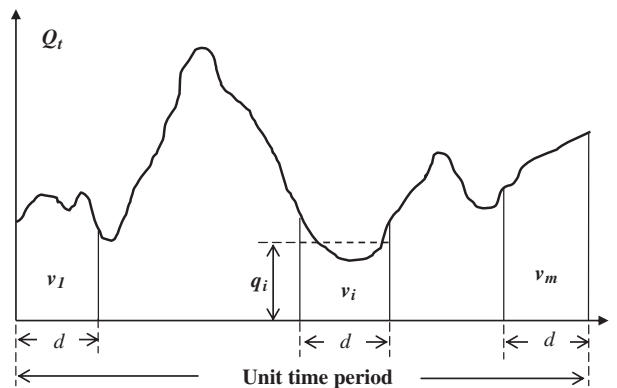


Figure 8-1. Definitions of time interval, d , unit time period T_u , flow volume v , and flow discharge q .
Source: Salas et al. (2018).

For example, assuming $d = 10$ days and $T_u = 365$ days, one can get $m = 356$ values of both v_i and q_i (considering overlapping). Thus, the low-flow volume for the given year, say year 1, is $V_1 = \min(v_1, \dots, v_m)$ and the low-flow discharge is $y_1 = \min(q_1, \dots, q_m)$. Considering N years of record (i.e., total number of time periods T_u) we will have the sequences of low-flow volumes V_1, \dots, V_N and low-flow discharges y_1, \dots, y_N that can be used for frequency analysis. Example 8-1 illustrates some of these concepts.

Another type of low-flow index has been used in hydrologic practice where the duration of low flows (and related quantities) is the variable of concern. *Low-flow duration* is defined as the number of consecutive time intervals (e.g., days) in which the flow series is below a certain *threshold* or *crossing level*. The low-flow spell has an associated *low-flow volume* (or cumulative flow deficit), which is the accumulated flow below the crossing level. The *low-flow intensity* is defined as the ratio of the low-flow volume and the duration of the low-flow spell. This type of analysis is called “low-flow duration analysis” (US Army Corps of Engineers 1975, Viessman et al. 1989). This is also referred to as “low-flow spells frequency analysis” (Shaw 1988).

Referring to Figure 8-2, let us assume that Q_t is a daily flow hydrograph (although the time interval may be hours, days, weeks, etc.) A low flow occurs when Q_t is below the crossing level (discharge) Q_o for a consecutive number of days or duration d . The figure shows four low-flow spells during the unit period T_u . In general, we may have m low-flow episodes during the unit time

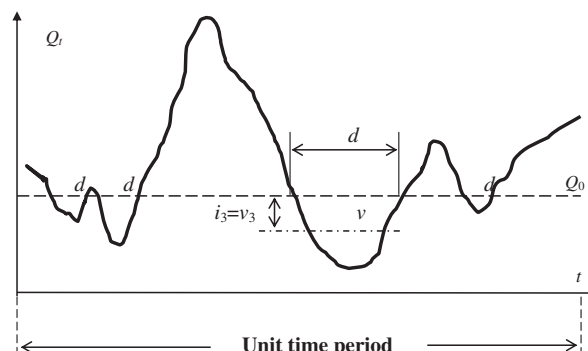


Figure 8-2. Definition of low-flow duration d , low-flow deficit v , and low-flow intensity i relative to the threshold discharge Q_o . The graph shows four episodes of low flows.
Source: Salas et al. (2018).

period T_u , with durations, d_1, \dots, d_m , low-flow deficits v_1, \dots, v_m , and low-flow intensities i_1, \dots, i_m . Note, however, that in some cases, low-flow spells may not occur in a particular year, and in those cases, the low-flow variables equal zero. Generally for most water resources applications we are interested in the maximum values, in other words, the longest dry period D , the largest deficit V , and the largest intensity I , each of which is a random variable. Thus, for N years of data available and $T_u = 1$ year, we will have the sequences of low-flow durations, D_1, \dots, D_N , low-flow deficits V_1, \dots, V_N , and low-flow intensities I_1, \dots, I_N . The frequency analysis of each sequence will provide the information needed to make probability statements about the variable of interest.

The various aforementioned low-flow definitions are particularly useful in perennial rivers. However, in streams of semi-arid and arid regions where the flow regime may be intermittent and zero values of flows may occur, appropriate adjustments may be needed for determining the corresponding frequency distribution as outlined in Section 8.3.2. In addition, other characteristics of low flows such as the duration of zero flows (e.g., considering $Q_o = 0$ in Figure 8-2) may be of interest, and determining the frequency distribution of the longest duration of zero flows (per year) may be needed. Also another way of analyzing low flows in streams of intermittent flow regime may be selecting an appropriate time scale of the hydrograph under consideration, for example, weekly instead of daily, so as to avoid the zero flow values, then the low-flow analysis for such a scale can be performed as described previously.

8.1.2 Definition of Drought

A drought is a complex phenomenon that evolves through time and space in a random fashion. It may be characterized by its initiation, duration, magnitude (accumulated deficit), intensity, termination, and spatial extent. These characteristics may be determined by comparing a water supply time series with a water demand series. Because water supply quantities such as streamflows are stochastic variables the corresponding drought characteristics are also random and must be described using stochastic methods. Let us consider a stochastic water supply series denoted by x_t , $t = 1, 2, \dots$ and a constant water demand threshold denoted by x_0 . Following the drought definition that Yevjevich (1967) suggests, a drought event is taken as a succession of consecutive periods (run) in which the water supply x_t remains below x_0 where the run is preceded and succeeded by water supply that is equal to or bigger than x_0 . Thus, the drought length L (or negative run length) is the number of consecutive time intervals (e.g., years) in which $x_t < x_0$, preceded and followed by (at least one period where) $x_t \geq x_0$. Figure 8-3 schematically shows this drought definition. In addition, the drought magnitude or accumulated deficit (run sum) is the total deficit throughout the drought duration [i.e., $D = \sum_{j=t}^{t+L-1} (x_0 - x_j)$], and the drought intensity is the mean deficit over the drought duration, (i.e., $I = D/L$). Furthermore, $d_0 \geq 0$ represents any given drought magnitude, and $i_0 > 0$ represents any given value of the intensity. To analyze the severity of droughts and the associated risks, we need to specify the drought event under consideration. For instance, one may consider only the duration of a drought regardless of the magnitude, or drought duration with a certain degree of deficit, or duration and a given intensity, and so on.

Worth noting are the similarity and differences between the definitions of low-flow duration (deficit and intensity) depicted in Figure 8-2 and the definition of drought duration (magnitude and intensity) shown in Figure 8-3. The similarity of the definitions is fairly obvious, but the main difference is in the ensuing analysis of the data arising from both definitions (figures). While the low-flow duration (and magnitude and intensity) in Figure 8-2 yields a maximum value per year, and the set of maximums is analyzed using frequency analysis methods (Sections 8.2 and 8.3), the drought length/duration (and magnitude and intensity) in Figure 8-3 give information that can be analyzed statistically but generally. Because of the small number of drought events that can be obtained from the underlying flow series, the analysis involves analytical approximations and stochastic simulation (Section 8.6). Furthermore, also note that in some cases where low flows are autocorrelated also, stochastic modeling approaches may have to be applied (Section 8.5).

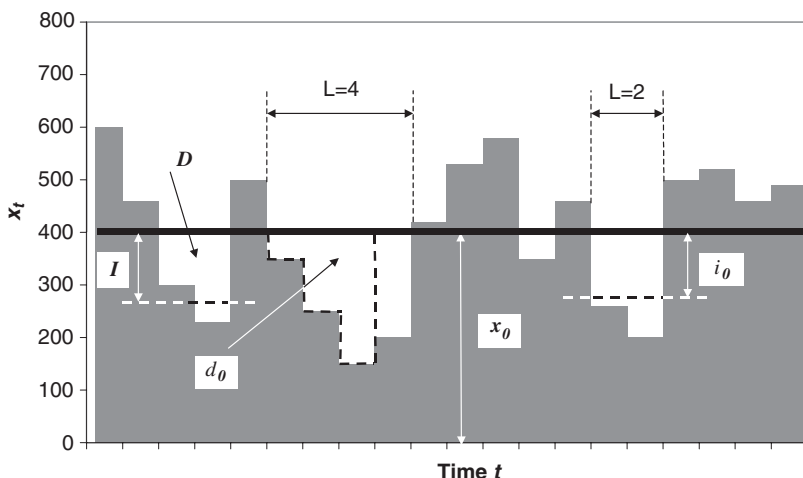


Figure 8-3. Water supply x_t , water demand x_0 , and drought properties: (a) duration L , (b) magnitude (accumulated deficit) D , and (c) intensity I . Also specific drought magnitude and intensity thresholds d_0 and i_0 are shown.

Source: Salas et al. (2005).

8.2 EMPIRICAL FREQUENCY ANALYSIS OF LOW FLOWS

The empirical frequency distribution of low flows may be determined using a certain plotting position formula. The procedure is straight forward but will be summarized here for completeness. Let us assume that the sample of the low-flow variable of interest is denoted as y_1, \dots, y_N , where N is the sample size. We will also assume that the sample has been arranged from the smallest value to the largest one so that y_1 represents the minimum and y_N the maximum. Then, an estimate of the cumulative probability corresponding to the ordered value y_i is given by $i/(N + 1)$, which is the Weibull plotting position formula. The literature has suggested alternative plotting position formulas (e.g., Stedinger et al. 1993), but for the purpose of this chapter we will use the Weibull formula. Because we assumed that the sample is ordered from the smallest to the largest, one can write

$$F(i) = P(Y \leq y_i) = i/(N + 1), \quad i = 1, \dots, N \quad (8-1)$$

in which $F(i)$ is the nonexceeding probability. Thus Equation (8-1) gives the estimate of the cumulative distribution function (CDF). This distribution is also referred to as the empirical CDF or empirical frequency curve.

This formula is quite simple, but one must be aware of special cases where appropriate interpretation and adjustments may be necessary. For instance, if the sample is a random sample in the sense that the sequence of observations is independent (uncorrelated), then one can use the nonexceedance probability $F(i) = q$ to determine the return period of the value of interest. Per illustration, if we are concerned with determining the return period of, say y_i , one can calculate it by $T = 1/F(i) = 1/q$. Note that sometimes $F(i) = q$ has been called the exceedance probability, particularly in relation to low flows. However, in this chapter we will stick to the usual terminology and jargon commonly found in statistical literature, which is $F(i) = P(Y \leq y_i) = q = \text{nonexceedance probability}$. Also, in cases where the observations are autocorrelated, applying the methods outlined in Section 8.5 instead may be useful, and where the sample has been censored, appropriate adjustments may be necessary as described in Section 8.3.2. In addition, the foregoing plotting position formula may provide a quick estimate of the probabilities of low-flow events and return

periods, but generally employing appropriate probabilistic or stochastic methods is better. This is even more so in the analysis of multiyear droughts where even records of 100 years may not be enough for estimating drought properties reliably. This is the case, for example, for determining the return period of multiyear droughts or for characterizing critical droughts. In these cases, applying approximate analytical techniques or stochastic simulations such as those described in Sections 8.5 and 8.6 may be necessary.

8.3 PROBABILITY DISTRIBUTION OF LOW FLOWS

When a historical streamflow record is available at a site of interest, low streamflow quantiles can be estimated via frequency analysis. The standard procedure is to pick a probability distribution that adequately describes the low streamflow series, to estimate the parameters of the probability distribution, and then to estimate the relevant quantile from the distribution. The following sections describe fitting univariate distributions, how to handle sites with intermittent (nonperennial) streamflows, and the regionalization of low flows and droughts.

8.3.1 Fitting of Univariate Distributions

The most challenging issue with estimating low-flow quantiles at sites with historical records is the choice of an appropriate probability distribution to describe the low-flow series. The few studies that investigate fitting probability distributions to low-flow series do not reach a consensus as to the best probability distribution to employ in practice. [Tasker \(1987\)](#) uses a bootstrap resampling experiment at 20 Virginia rivers to analyze how the three-parameter Weibull (W3), log-Pearson type III (LP3), log-Boughton, and Box-Cox distributions reproduce streamflow quantiles, recommending the W3 and LP3 distributions. [Condie and Nix \(1975\)](#) recommend the W3 distribution for best describing the lower bound of Canadian rivers. [Vogel and Kroll \(1989\)](#) employ a regional probability plot correlation coefficient (PPCC) test at rivers in Massachusetts to compare various probability distributions, recommending the two- and three-parameter log-normal (LN2 and LN3), LP3, and W3 distributions. [Onöz and Bayazit \(2001\)](#) use a PPCC test to examine the fit of probability to low flows at a several European rivers and recommend the use of the general extreme value (GEV) distribution.

[Pearson \(1995\)](#) employs an L-moment analysis of 1 day annual minimum flows at more than 500 New Zealand rivers, concluding that no single two- or three-parameter distribution provides an adequate fit. [Vogel and Wilson \(1996\)](#) also employ L-moment diagrams to examine 1 day annual minimum flows at more than 1,400 river sites across the United States and recommend the use of the three-parameter Pearson (P3) distribution based on a visual interpretation of the L-moment diagrams. [Kroll and Vogel \(2002\)](#) use an L-moment weighted distance measure to compare the fit of probability distributions to 7 day annual minimum flows at more than 1,500 river sites across the United States. They recommend the LN3 distribution at perennial sites and the P3 at intermittent sites due to patterns in the shift of L-moment ratios.

In this section, we illustrate the applications of the log-Pearson type III, log-normal three-parameter (log-normal 3), the Weibull, and the GEV models for fitting the distribution of low-flow variables. The fitting procedure is essentially based on the method of moments (MOM), although the literature proposes several other methods, such as the maximum likelihood and probability weighted moments. Detailed examples are included and in most cases the fitted and empirical CDFs are compared graphically.

8.3.1.1 Fitting the Log-Pearson Type III Distribution

Only a limited number of probability distributions are commonly fit to low-flow series, and in the United States this is typically the LP3 distribution. The Committee on Surface-Water Hydrology of

the Hydraulics Division (ASCE 1980) recommends fitting low-flow series with the LP3. In addition, in *Bulletin 17*, the US Water Resources Council recommends the LP3 distribution to describe annual maximum flows (USIAC 1982), and its common use to describe low flows is by default. The LP3 has also been employed in several USGS studies. The LP3 is a flexible distribution and converges to an LN2 distribution when the log skew approaches zero. Typically, the LP3 is parameterized by the method of moments. Whereas weighted skew maps and generalized least squares regression estimators of the skew have been recommended for flood flow series, no such tools have been recommended for low flows, and typically at-site skew estimators are employed, even though they have been shown to have high bias and variance in small samples (Stedinger et al. 1993).

If one defines a d day low streamflow series as x_1, x_2, \dots, x_N , and the logarithm of this series as y_1, y_2, \dots, y_N , i.e., $y_i = \ln(x_i)$, the log space moments of the series are

$$\hat{\mu}_y = \frac{1}{N} \sum_{i=1}^N y_i \quad (8-2)$$

$$\hat{\sigma}_y = \sqrt{\frac{\sum_{i=1}^N (y_i - \hat{\mu}_y)^2}{N-1}} \quad (8-3)$$

$$\hat{\gamma}_y = \frac{N \sum_{i=1}^N (y_i - \hat{\mu}_y)^3}{(N-1)(N-2)\hat{\sigma}_y^3} \quad (8-4)$$

The quantile of interest can then be estimated as

$$\hat{x}_q = \exp(\hat{\mu}_y + K_q \hat{\sigma}_y) \quad (8-5)$$

where K_q is the frequency factor that may be obtained from tables (e.g., USIAC 1982) or can be estimated approximately using the Wilson–Hilferty transformation as

$$K_q = \frac{2}{\hat{\gamma}_y} \left(1 + \frac{z_q \hat{\gamma}_y}{6} - \frac{\hat{\gamma}_y^2}{36} \right)^3 - \frac{2}{\hat{\gamma}_y} \quad (8-6)$$

in which z_q is the inverse standard normal variate such that $P(Z \leq z_q) = q$ where $Z \sim N(0, 1)$. This approximation is generally considered adequate when $0.01 \leq q \leq 0.99$ and $|\gamma| < 2$ (Kirby 1972). When $\hat{\gamma}_y \rightarrow 0$, $K_q \rightarrow z_q$, and the LP3 distribution turns into an LN2 distribution.

Example 8-1: Estimation of the 7 Day, 10 Year Low Streamflow, $\times 7,10$ Based on the Log-Pearson Type III Distribution

Table 8-1 contains 7 day annual minimum flows for Penns Creek at Penns Creek, PA (USGS #01555000), for the 76 year period from 1930 to 2005. The 7 day annual minimum is the lowest average daily streamflow over a 7 day period during the water year. The water year for low streamflow series typically begins during the high flow period of the year so that a single low-flow period is not included in two consecutive years. Here the water year was defined as April 1 to March 31.

Using these data, the following statistics were calculated based on Equations (8-2), (8-3), and (8-4), respectively: $\hat{\mu}_y = 4.13$, $\hat{\sigma}_y = 0.43$, $\hat{\gamma}_y = 0.77$. To estimate the 7 day low streamflow that has a

Table 8-1. 7 Day Annual Minimum Flows for Penns Creek at Penns Creek, PA.

Year	7 day min (ft ³ /s)						
1930	30	1949	55	1968	56	1987	60
1931	46	1950	73	1969	69	1988	58
1932	39	1951	54	1970	63	1989	84
1933	82	1952	47	1971	62	1990	171
1934	70	1953	43	1972	79	1991	52
1935	44	1954	42	1973	84	1992	82
1936	35	1955	52	1974	88	1993	72
1937	69	1956	166	1975	78	1994	117
1938	56	1957	47	1976	85	1995	51
1939	37	1958	61	1977	103	1996	107
1940	61	1959	43	1978	72	1997	82
1941	46	1960	65	1979	151	1998	39
1942	67	1961	43	1980	50	1999	50
1943	48	1962	33	1981	65	2000	62
1944	56	1963	42	1982	57	2001	53
1945	89	1964	31	1983	57	2002	55
1946	78	1965	34	1984	81	2003	221
1947	70	1966	24	1985	49	2004	204
1948	47	1967	93	1986	66	2005	44

nonexceedance probability of $1/10 = 0.1$, in other words, the 10th percentile of the distribution of annual minimum flows, the appropriate frequency factor is the inverse of the standard normal variate with a nonexceedance probability of 10%, in other words, $P(Z \leq z_{0.1}) = 0.1$. Employing a table for a standard normal distribution, $z_{0.1} = -1.282$. Using this value, the frequency factor obtained from Equation (8-6) is $K_q = K_{0.1} = -1.17$. From this the $x_{7,10}$ can be estimated from Equation (8-5) as

$$\hat{x}_{7,10} = \hat{x}_{0.1} = \exp[4.13 + (-1.17) \times 0.43] = 37.6 \text{ ft}^3/\text{s}$$

Note that if one instead fits a two-parameter log-normal distribution to the 7 day annual minimum flows, then

$$\begin{aligned}\hat{x}_{7,10} &= \hat{x}_{0.10} = \exp[\hat{\mu}_y + z_{0.10}\hat{\sigma}_y] = \exp[4.13 + (-1.282) \times 0.43] = 35.8 \text{ ft}^3/\text{s} \\ \hat{x}_{7,10} &= \hat{x}_{0.10} = \exp[\hat{\mu}_y + z_{0.10}\hat{\sigma}_y] = \exp[4.13 + (-1.282) \times 0.43] = 35.8 \text{ ft}^3/\text{s}\end{aligned}$$

8.3.1.2 Fitting the Three-Parameter Log-Normal Distribution (LN3)

The probability density function of the LN3 distribution is

$$f(x) = \frac{1}{(x - x_0)\sigma_y\sqrt{2\pi}} \exp\left[-\frac{[\ln(x - x_0) - \mu_y]^2}{2\sigma_y^2}\right], \quad x_0 < x < \infty \quad (8-7)$$

where x_0 , σ_y , and μ_y are the location, scale, and shape parameters, respectively. The CDF, defined as $F(x) = \int_{x_0}^x f(x) dx$, cannot be integrated explicitly, thus, numerical procedures or tables for the normal distribution must be used to calculate either probabilities for a given value of x or quantiles for a given probability.

The moment estimators of the parameters of the LN3 distribution are (Yevjevich 1972)

$$\hat{\mu}_y = \frac{1}{N} \sum_{i=1}^N \ln(x_i - \hat{x}_0), \quad (8-8)$$

$$\hat{\sigma}_y = \left[(1/N) \sum_{i=1}^N [\ln(x_i - \hat{x}_0) - \hat{\mu}_y]^2 \right]^{1/2}, \quad (8-9)$$

$$\hat{x}_0 = \hat{\mu}_x \left[1 - \frac{\hat{\eta}_x \omega^{1/3}}{(1 - \omega^{2/3})} \right], \quad (8-10)$$

in which

$$\hat{\eta}_x = \frac{\hat{\sigma}_x}{\hat{\mu}_x} \quad (8-11)$$

and

$$\omega = \frac{1}{2} [-\hat{\gamma}_x + (\hat{\gamma}_x^2 + 4)^{1/2}] \quad (8-12)$$

where $\hat{\mu}_x$, $\hat{\sigma}_x$, and $\hat{\gamma}_x$ are respectively the mean, standard deviation, and the skewness coefficient of the x 's. Note that the moment solution requires that $\hat{\gamma}_x > 0$.

Example 8-2: Estimation of the 1 Day, 10 Year Low Flow $\times 1,10$ Based on the LN3 Distribution
Table 8-2 gives the 1 day low flows for the San Pedro River at the Villalba gauging station in Mexico for 1939–1991. The results are obtained following the method of moments procedure described previously. Using the data of Table 8-2 the following 1 day low flow statistics are obtained:

$$\begin{aligned} \hat{\mu}_x &= \frac{1}{N} \sum_{i=1}^N x_i = 0.3306 \text{ m}^3/\text{s} \\ \hat{\sigma}_x &= \left[\frac{1}{N} \sum_{i=1}^N (x_i - \hat{\mu}_x)^2 \right]^{1/2} = 0.1465 \text{ m}^3/\text{s} \\ \hat{\gamma}_x &= \frac{N}{(N-1)(N-2)\hat{\sigma}_x^3} \sum_{i=1}^N (x_i - \hat{\mu}_x)^3 = 0.5853 \end{aligned}$$

Equations (8-11) and (8-12) give $\hat{\eta}_x = 0.4431$ and $\omega = 0.7493$, respectively.

Then applying Equations (8-10), (8-8), and (8-9) gives the moment estimates of the parameters of the LN3 distribution for the 1 day low flows for the San Pedro River, respectively,

Table 8-2. 1 Day Low Flows for the San Pedro River at Villalba, Mexico, for 1939–1991.

Year	x (m^3/s)	Year	x (m^3/s)	Year	x (m^3/s)
1939	0.6220	1957	0.0790	1975	0.4090
1940	0.6850	1958	0.1150	1976	0.5070
1941	0.4520	1959	0.4010	1977	0.4160
1942	0.3050	1960	0.2620	1978	0.2500
1943	0.6480	1961	0.2620	1979	0.4190
1944	0.4850	1962	0.1850	1980	0.3000
1945	0.4470	1963	0.2290	1981	0.7040
1946	0.4850	1964	0.3570	1982	0.4430
1947	0.4310	1965	0.1390	1983	0.3670
1948	0.3920	1966	0.3300	1984	0.1770
1949	0.2260	1967	0.3390	1985	0.3097
1950	0.2640	1968	0.3280	1986	0.3905
1951	0.1950	1969	0.3480	1987	0.4417
1952	0.1840	1970	0.2080	1988	0.3846
1953	0.1320	1971	0.3090	1989	0.2740
1954	0.1400	1972	0.3770	1990	0.1750
1955	0.2450	1973	0.3950	1991	0.1288
1956	0.1500	1974	0.2740		

Source: CONAGUA (2016).

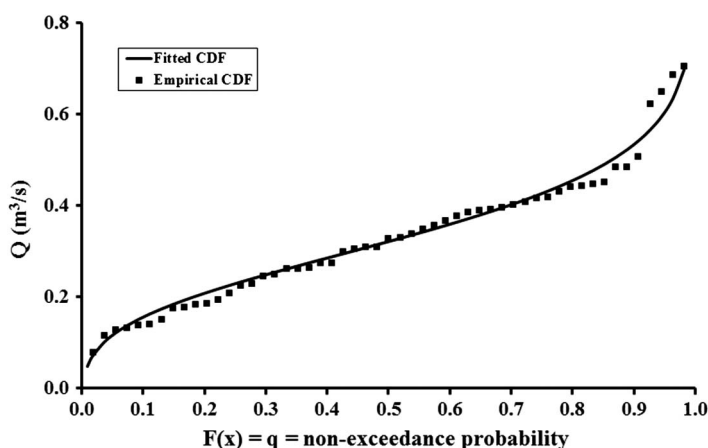


Figure 8-4. Empirical and fitted frequency curves for the 1 day low flows of the San Pedro River in Mexico, based on MOM estimates of the parameters of the LN3 distribution.

$\hat{x}_0 = -0.4296 \text{ m}^3/\text{s}$, $\hat{\mu}_y = -0.287$, and $\hat{\sigma}_y = 0.1945$. Figure 8-4 shows the graphical fitting of the LN3 distribution using the MOM. Then the 10 year 1 day low flow is

$$\begin{aligned}\hat{x}_{1,10} &= \hat{x}_{0.1} = \hat{x}_0 + \exp(\hat{\mu}_y + z_{0.1}\hat{\sigma}_y) = -0.4296 + \exp[-0.287 \\ &\quad + (-1.2816)(0.1945)] = 0.155 \text{ m}^3/\text{s}\end{aligned}$$

where $z_{0.1} = -1.282$ is the 10% quantile of the standard normal distribution.

8.3.1.3 Fitting the Extreme Value Type III (Weibull) Distribution

The probability density function of the Weibull distribution is (Gumbel 1958)

$$f(x) = \frac{k}{(\nu - \varepsilon)} \left(\frac{x - \varepsilon}{\nu - \varepsilon} \right)^{k-1} \exp \left[- \left(\frac{x - \varepsilon}{\nu - \varepsilon} \right)^k \right], \quad \varepsilon \leq x < \infty. \quad (8-13)$$

where ε , k , and ν are the location, scale, and shape parameters, respectively, such that $k > 0$ and $(\nu - \varepsilon) > 0$. Likewise, the cumulative probability distribution function is

$$F(x) = 1 - \exp \left[- \left(\frac{x - \varepsilon}{\nu - \varepsilon} \right)^k \right] \quad (8-14)$$

Kite (1988) shows that based on the method of moments the parameters may be estimated by

$$\hat{\varepsilon} = \hat{\mu}_x + \hat{\sigma}_x [1 - \Gamma(1 + 1/k)] B_k \quad (8-15)$$

$$\hat{\nu} = \hat{\varepsilon} - B_k \hat{\sigma}_x \quad (8-16)$$

$$\hat{k} = \frac{1}{a_0 + a_1 \hat{\gamma}_x + a_2 \hat{\gamma}_x^2 + a_3 \hat{\gamma}_x^3 + a_4 \hat{\gamma}_x^4 + a_5 \hat{\gamma}_x^5 + a_6 \hat{\gamma}_x^6} \quad (8-17)$$

where the approximation is valid in the range $-1.04 \leq \hat{\gamma}_x \leq 2$, $B_k = [\Gamma(1 + 2/k) - \Gamma^2(1 + 1/k)]^{-1/2}$

$\Gamma(\cdot)$ = complete gamma function

$$a_0 = 0.277597$$

$$a_1 = 0.323127,$$

$$a_2 = 0.061656,$$

$$a_3 = -0.020235,$$

$$a_4 = -0.007321,$$

$$a_5 = 0.005578,$$

$$a_6 = -0.001094, \text{ and}$$

$\hat{\mu}_x$, $\hat{\sigma}_x^2$, and $\hat{\gamma}_x$ = sample mean, variance, and skewness coefficient, respectively.

Example 8-3: Estimating the 1 Day, 10 Year Low Flow $\times 1,10$ Based on the Weibull Distribution

We will use the 1 day low flow data for the San Pedro River at Villalba, Mexico, for 1939–1991 (Table 8-2). The results are obtained using the MOM procedures described previously. From Example 8-2, the sample mean, standard deviation, and skewness coefficient are $\hat{\mu}_x = 0.3306 \text{ m}^3/\text{s}$, $\hat{\sigma}_x = 0.1465 \text{ m}^3/\text{s}$, and $\hat{\gamma}_x = 0.5853$, respectively. Then, applying the MOM procedure gives $\hat{k} = 2.0693$, $B_k = [\Gamma(1 + 2/k) - \Gamma^2(1 + 1/k)]^{-1/2} = [0.9863 - (0.8858)^2]^{-1/2} = 2.2269$, $\hat{\varepsilon} = \hat{\mu}_x + \hat{\sigma}_x [1 - \Gamma(1 + 1/k)] B_k = 0.3306 + (0.1465)(1 - 0.8858)(2.2269) = 0.0417$, and $\hat{\nu} = \hat{\varepsilon} - B_k \hat{\sigma}_x = 0.0417 - (2.2269)(0.1465) = 0.3678$.

Thus, the moment estimates of the parameters of the Weibull distribution for the 1 day low-flow sample data of the San Pedro River are $\hat{\varepsilon} = 0.0417 \text{ m}^3/\text{s}$, $\hat{k} = 2.0693$, and $\hat{\nu} = 0.3678 \text{ m}^3/\text{s}$. Figure 8-5 shows the corresponding fitted distribution.

Then from Equation (8-14), the q -th quantile may be written as

$$x_q = \varepsilon + (\nu - \varepsilon)[- \ln(1 - q)]^{1/k}$$

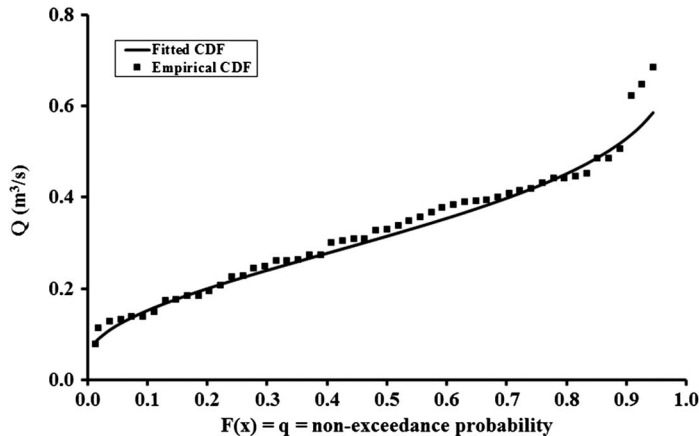


Figure 8-5. Empirical and fitted frequency curves for the San Pedro River at Villalba (Mexico), based on MOM estimates of the parameters of the Weibull distribution.

so that the 10 year, 1 day low flow is

$$\hat{x}_{1,10} = \hat{x}_{0.1} = 0.0417 + (0.3678 - 0.0417)[- \ln(1 - 0.1)]^{1/2.0693} = 0.152 \text{ m}^3/\text{s}$$

8.3.1.4 Fitting the General Extreme Value Distribution

The GEV has been applied to many hydrologic events for a long time (e.g., [NERC 1975](#)). Various forms and parameterizations of the GEV have been utilized in practice. Here we will follow that utilized by [Raynal-Villasenor \(2013\)](#), where the probability density function is defined as

$$f(x) = \frac{1}{\alpha} \exp\{-[1 - \beta(\omega - x)/\alpha]^{1/\beta}\} [1 - \beta(\omega - x)/\alpha]^{(1/\beta)-1} \quad (8-18)$$

in which ω is the location parameter, α is the scale parameter, and β is the shape parameter. Also $-\infty < x \leq \omega - \alpha/\beta$ for $\beta < 0$ and $\omega - \alpha/\beta \leq x < \infty$ for $\beta > 0$. Likewise, the cumulative probability distribution function is

$$F(x) = 1 - \exp\{-[1 - \beta(\omega - x)/\alpha]^{1/\beta}\} \quad (8-19)$$

The moments estimators of the GEV distribution are

$$\hat{\omega} = \hat{\mu} - \frac{\hat{\alpha}}{\hat{\beta}} \Gamma(1 + \hat{\beta}) + \frac{\hat{\alpha}}{\hat{\beta}}, \quad (8-20)$$

$$\hat{\alpha} = \frac{|\hat{\beta}| \hat{\sigma}}{\sqrt{\Gamma(1 + 2\hat{\beta}) - \Gamma^2(1 + \hat{\beta})}}, \quad (8-21)$$

and the shape parameter (β) may be estimated by [Raynal-Villasenor \(2013\)](#)

$$\begin{aligned}\hat{\beta} = & 0.24662 + 0.286678\hat{\gamma} + 0.072454\hat{\gamma}^2 + 0.010176\hat{\gamma}^3 + 0.000816\hat{\gamma}^4 \\ & + 0.000037\hat{\gamma}^5\end{aligned}\quad (8-22a)$$

for $\beta < 0$ and $-19.0 < \hat{\gamma} \leq -1.1396$ and

$$\begin{aligned}\hat{\beta} = & 0.279434 - 0.333535\hat{\gamma} + 0.048305\hat{\gamma}^2 + 0.024414\hat{\gamma}^3 + 0.003765\hat{\gamma}^4 \\ & - 0.000263\hat{\gamma}^5\end{aligned}\quad (8-22b)$$

for $\beta > 0$ and $-1.1396 \leq \hat{\gamma} < 11.35$. Note that L-moment estimators are often used to parameterize the GEV distribution (see Stedinger et al. 1993 for fitting procedures), because L-moment estimators can have better properties than MOM estimators for real-space distribution with three or more parameters.

Example 8-4: Estimation of the 1 Day, 10 Year Low Flow $\times 1.0.1$ Based on the GEV Distribution

The 1 day low-flow data for the San Pedro River in Mexico for 1939–1991 are also used in this example (Table 8-2). The estimation results have been obtained using the previously described procedures. The following statistics have already been obtained in Examples 8-2 and 8-3 as $\hat{\mu}_x = 0.3306$, $\hat{\sigma}_x = 0.1465 \text{ m}^3/\text{s}$, and $\hat{\gamma}_x = 0.5853$. Then Equations (8-22b), (8-20), and (8-21) give, respectively, $\hat{\beta} = 0.4965$, $\hat{\omega} = 0.3668 \text{ m}^3/\text{s}$, and $\hat{\alpha} = 0.158 \text{ m}^3/\text{s}$.

Figure 8-6 shows the fitted distribution for the GEV. From Equation (8-19) one may find that the 10 year, 1 day low flow is

$$\begin{aligned}\hat{x}_{1,10} = & \hat{x}_{0.1} = \omega + \frac{\alpha}{\beta} \left\{ \left[-\ln \left(1 - \frac{1}{T} \right) \right]^\beta - 1 \right\} \\ = & 0.3668 + \frac{0.158}{0.4965} \left\{ \left[-\ln \left(1 - \frac{1}{10} \right) \right]^{0.4965} - 1 \right\} = 0.153 \text{ m}^3/\text{s}\end{aligned}$$

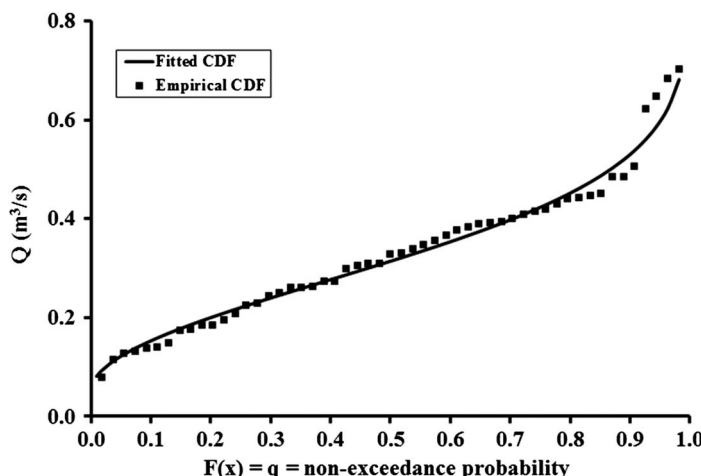


Figure 8-6. Empirical and fitted frequency curves for the low flows of the San Pedro River in Mexico, based on MOM estimates of the parameters of the GEV distribution.

Note that the value obtained is practically the same as that obtained using the Weibull distribution because it may be shown that the two distributions are equivalent.

Furthermore, as a matter of comparison we fitted the log-Pearson type III distribution, using the procedure outlined in Section 8.3.1.1 and obtained $\hat{x}_{0.1} = 0.156 \text{ m}^3/\text{s}$. Thus, the estimates based on the Weibull, GEV, LN3, and LP3 distributions are respectively 0.152, 0.153, 0.155, and 0.156—in other words, they are very close. Note, however, that the sample size in this case is $N = 53$. The results may have a wider variation for small sample sizes, smaller values of the nonexceedance probability q , and for datasets with larger skews.

8.3.2 Case of Intermittent Flows

A common issue in hydrology is intermittent streamflows, where the hydrologic record contains values recorded as zero. This typically occurs when the catchment area is small, the region is arid, precipitation is stored for long periods as snow or ice, or the groundwater storage is depleted during periods of little or no precipitation. When the streamflow is recorded as zero, it may actually be zero, or may be too small to be measured by the recording instrumentation.

Typical hydrologic frequency analyses, which often rely on log-transformed distributions, must be adapted to handle intermittent flows. Even when a real-spaced probability distribution, such as the GEV, is employed, a truncation of the lower tail of the distribution at zero is still a problem. While several techniques have been proposed to address this situation in regional frequency analyses, the most common is the use of a conditional probability adjustment (e.g., Haan 1992, USIAC 1982). This method, which represents the streamflow series as a mixed distribution with a point mass at zero and a continuous distribution to describe the nonzero observations, was originally recommended by Jennings and Benson (1969) for flood frequency analysis. While an argument could be made to employ a truncated distribution to describe the nonzero observations, with the truncation point at the measurement detection limit, typically a nontruncated distribution is used.

Assume one is confronted with the typical problem of estimating some streamflow quantile, x_q , where q is the probability of the streamflow X to be less than or equal to x_q can be written as

$$P(X \leq x_q) = F(x_q) = q \quad (8-23)$$

If one has a streamflow series of length N , of which N_0 of the values are reported as zero, an estimator of the probability of a zero flow is

$$\hat{q}_0 = P(X = 0) = \frac{N_0}{N} \quad (8-24)$$

If $q \leq \hat{q}_0$, then $\hat{x}_q = 0$. If instead $q > \hat{q}_0$, then one calculates an adjusted probability q_a as

$$q_a = \frac{q - \hat{q}_0}{1 - \hat{q}_0} \quad (8-25)$$

and then determines the q_a^{th} percentile of the distribution of the nonzero observations as

$$P(X_{NZ} \leq x_q) = q_a \quad (8-26)$$

where X_{NZ} is the variable defining flows greater than zero, in other words, nonzeros.

Table 8-3. 7 Day Annual Minimum Flows for Twelve Mile Creek near Waxhaw, NC (USGS #02146900).

Year	7 day min						
1961	0.400	1972	0.833	1983	0.000	1994	2.600
1962	0.500	1973	1.414	1984	2.000	1995	1.943
1963	0.529	1974	2.314	1985	0.553	1996	3.900
1964	6.071	1975	7.614	1986	0.094	1997	1.414
1965	3.371	1976	1.743	1987	0.096	1998	2.943
1966	0.543	1977	1.561	1988	1.031	1999	0.299
1967	2.471	1978	1.714	1989	6.371	2000	0.461
1968	0.014	1979	3.471	1990	1.287	2001	0.041
1969	1.686	1980	0.291	1991	3.600	2002	0.070
1970	0.000	1981	0.681	1992	2.843	—	—
1971	6.686	1982	1.157	1993	1.130	—	—

Example 8-5: Estimation of the 7-Day 10-Year Minimum Flows for the Case of Zero Flood Years

Table 8-3 gives the 7 day average annual minimum streamflows for Twelve Mile Creek near Waxhaw, North Carolina (USGS gauge #02146900), from 1961 to 2002. For two years (1970 and 1983), the 7 day annual minimum was recorded as zero. Assume one wishes to estimate $x_{7,10}$, in other words, the 7 day, 10 year annual minimum streamflow using a log-Pearson type III distribution. The $x_{7,10}$ is the 10th percentile of the distribution of 7 day annual minimums, in other words, $q = 0.1$.

Using information from Table 8-3, we have $N = \text{record length} = 42$ and $N_0 = \text{number of years when 7 day annual minimum flows equals zero} = 2$. Then, Equations (8-24) and (8-25) give

$$\hat{q}_0 = \frac{N_0}{N} = \frac{2}{42} = 0.0476 \quad \text{and} \quad q_a = \frac{q - \hat{q}_0}{1 - \hat{q}_0} = \frac{0.1 - 0.0476}{1 - 0.0476} = 0.055.$$

The $x_{7,10}$ is thus estimated as the 5.5th percentile of the distribution of the nonzero 7 day annual minimums. Using the nonzero 7 day annual minimum flows and Equation (8-2), (8-3), and (8-4) we get $\hat{\mu}_y = 0.0022$, $\hat{\sigma}_y = 1.439$, and $\hat{\gamma}_y = -1.089$, respectively. Also applying the Wilson-Hilferty transformation [Equation (8-6)] where $z_q = -1.598$ is the 5.5th percentile of the standard normal distribution, we obtain the frequency factor $K_q = -1.812$. Thus, the $\hat{x}_{7,10}$ is estimated as $\hat{x}_{7,10} = \hat{x}_{0.10} = \exp[0.0022 - 1.812 \times 1.439] = 0.074 \text{ ft}^3/\text{s}$.

8.4 REGIONAL ANALYSIS OF LOW FLOWS

Regional hydrologic analysis refers to the use of information from one or more gauged river sites to improve the estimation of a hydrologic statistic or parameter at the site of interest. In these situations, the site of interest typically has either no streamflow measurements (ungauged) or a limited record (partially gauged). Regional analysis typically involves selecting a homogeneous region of gauged sites that is similar to the site of interest and then employing that region of sites for estimation at the ungauged or partially gauged site.

8.4.1 Methods for Selecting Homogeneous Regions

For many low streamflow studies, determining a homogeneous region within which low streamflow processes are similar is beneficial. This is especially true when one has limited historical streamflow data at the site of interest, and information from other sites in the region must be transferred to the site of interest to improve low streamflow estimators at the site of interest. Low streamflow estimation techniques such as regional regression and index flow are based on a homogeneous region. [Hosking and Wallis \(1997\)](#) state that, “Of all the stages in a regional frequency analysis involving many sites, the identification of homogeneous regions is usually the most difficult and requires the greatest amount of subjective judgment.”

Although techniques have been developed to determine homogeneous regions when historical streamflow records are available at the site of interest, such as L-moment techniques ([Hosking and Wallis 1997](#)), streamflow data are not available at ungauged and partially gauged river sites. Thus, even if homogeneous regions were developed, one may have a problem determining which region the site of interest should include.

If contiguous regions are developed, then a site is placed into a region based on its geographic location. These regions are often developed based on drainage basins. For instance, the USGS has broken the conterminous United States into 18 regions containing the drainage areas of major basins and then subdivided these regions into 221 subregions based on smaller drainage areas. This classification is the basis of hydrologic unit codes (HUCs) by which watersheds are catalogued ([USGS 2010a](#)), and often state-based hydrologic studies develop regions based on a combination of HUCs and state boundaries.

For discontiguous regions, an allocation rule is required to place an ungauged or partially gauged site within a specific region. These rules must be based on watershed characteristics that can be measured at the ungauged or partially gauged site. The methods presented as follows identify several techniques that have been applied to develop homogeneous regions for low streamflow estimation.

[Hayes \(1992\)](#) uses a residual pattern approach to develop homogeneous regions. In this technique a global regression model between the flow characteristic of interest and watershed characteristics is first developed for all sites in a region, and the residuals from this model are mapped and generalized into homogeneous regions. One drawback of this approach is that the initial regression model, which was developed using all potential sites, may be incorrect for the specific region developed, creating an incorrect grouping of sites. Typically, with this technique, contiguous regions are developed, and thus placing an ungauged site in a region is based on its geographic location.

Another technique is the use of multivariate statistics to determine homogeneous regions. [Nathan and McMahon \(1990\)](#) compare several low-flow regionalization techniques, including cluster analysis, multiple regression, and principal component analysis. Their analysis recommends a weighted cluster analysis that creates groups that minimize the sum of squared errors between observations and the group’s weighted mean (Ward’s method). This method creates discontiguous regions, and thus a method for placing ungauged sites in a region is necessary. [Nathan and McMahon \(1990\)](#) suggest using Andrews curves for a decision rule, though [Laaha and Blöschl \(2006a\)](#) suggest that discriminant analyses and classification trees may also be used.

Still another approach is to use classification and regression tree (CART) models. These were first applied to the problem of low streamflow regionalization by [Laaha and Blöschl \(2006a\)](#). With this supervised classification technique, the initial heterogeneous domain is broken into several more homogeneous groups by maximizing the homogeneity of low flows and catchment characteristics simultaneously within each group. Usually the homogeneity is measured in terms of minimizing the variance of the low-flow statistic of interest. [Laaha and Blöschl \(2006a\)](#) note that the benefits of this technique include its nonparametric structure, the interpretability of small groupings, its ability to handle nonlinear relationships, and the lack of sensitivity to unusual sites (outliers). One major problem with this technique is that with large trees interpreting relationships is difficult. Once a regression tree has been developed, it can be employed to place ungauged sites in a region.

[Young et al. \(2000\)](#) and Laaha and Blöschl ([2006a, b](#)) examine a final approach, which is to use seasonality to group sites. This method assumes that the time of occurrence of low flows indicates the dominant hydrologic processes and thus can be used to determine low-flow regions. While [Young et al. \(2000\)](#) find the spatial variability of low-flow seasons to be relatively small in the United Kingdom, Laaha and Blöschl ([2006a, b](#)) find the spatial variability of low-flow seasonality to be very high in Austria, a humid, mountainous region. Ideally with this method regions are spatially contiguous, and thus placing an ungauged site in a region is based on its location.

[Laaha and Blöschl \(2006a\)](#) compare all four of the aforementioned regionalization methods to estimate the specific discharge exceeded 95% of the time at 325 watersheds in Austria. After determining homogeneous regions, they develop regional regression models in each region and perform a delete-one cross-validation to compare the regionalization techniques. They find that regions based on seasonality create the best groupings in Austria, though note that this may be the result of the wide variety of differences in seasonal low-flow processes within the study area. They also note that all methods appear to underestimate specific discharge at wet catchments.

8.4.2 Methods for Regional Analysis and Estimation

Several common methods have been applied to estimate low streamflow statistics at a site of interest using regional information. As mentioned previously, these techniques are commonly employed where little or no streamflow data are available at the site of interest. This section discusses two such techniques: low streamflow regional regression and baseflow correlation.

8.4.2.1 Regional Regression

When no historic streamflow record is available at the site of interest, a regional regression model may be developed. In this technique, a relationship is developed between the streamflow statistic of interest and watershed characteristics at gauged sites within the region, and then watershed characteristics at the ungauged site are employed to determine a streamflow estimate at the site of interest. Typically, these models have the following form:

$$Q_{d,T} = e^{\beta_0} X_1^{\beta_1} X_2^{\beta_2} \dots e^{\varepsilon} \quad (8-27)$$

where

$Q_{d,T}$ = d day,

T = year low streamflow statistic,

X_i = watershed characteristics,

β_i = model parameters to be estimated, and

ε = model error term. The form of this model is consistent with a theoretically based low streamflow watershed model derived from hillslope discharge models ([Vogel and Kroll 1992](#)).

When the logarithm of this equation is taken, one obtains a linear relationship:

$$\ln(Q_{d,T}) = \beta_0 + \beta_1 \ln(X_1) + \beta_2 \ln(X_2) + \dots + \varepsilon \quad (8-28)$$

The parameters of this equation can then be estimated using ordinary, weighted, or generalized least squares regression procedures ([Stedinger and Tasker 1986](#)). For ordinary least squares parameter estimators to be efficient, the model residuals need to be independent and homoscedastic (constant variance). Weighted least squares is employed to address heteroscedasticity (nonconstant variance) of the model residuals, while generalized least squares can be employed to address both heteroscedasticity and the lack of independence of the model residuals. [Kroll and Stedinger \(1998\)](#) show that if the model error variance in the regional regression model is large, which is typical for

low-flow regional regression, the model error variance overwhelms the time sampling error, and ordinary least squares produces similar parameter estimators as generalized least squares.

Low-flow regional regression models have been developed for many regions throughout the world, including Europe (e.g., [Gustard et al. 1989](#), [Laaha and Blöschl 2007](#)), Australia ([Nathan and McMahon 1992](#)), and the United States (e.g., [Thomas and Benson 1970](#), [Kroll et al. 2004](#)). One challenging aspect of developing low-flow regional regression models is determining the appropriate catchment characteristics to use as explanatory variables in the models. Whereas a theoretically derived model is available ([Vogel and Kroll 1992](#)), a common approach is using stepwise regression procedures ([Tallaksen and van Lanen 2004](#)). Such procedures are useful when the number of potential explanatory variables is large to help determine the significant variables to include in the final model ([Kroll et al. 2004](#)). [Tallaksen and van Lanen \(2004\)](#) and [Kroll et al. \(2004\)](#) list some catchment characteristics commonly employed in low-flow models, including drainage area, annual average rainfall, soil index, mean basin elevation, and summer precipitation. Hydrogeologic indexes, such as the baseflow index ([Institute of Hydrology 1980](#)) or baseflow recession constant ([Vogel and Kroll 1996](#), [Tallaksen 1995](#)) have been shown to greatly improve low streamflow regional regression models ([Kroll et al. 2004](#)), though often these indexes are difficult to obtain at ungauged river sites.

In most instances, the standard errors associated with low-flow regression models have been relatively high ([Vogel and Kroll 1992](#), [Smakhtin 2001](#)). One reason may be low-flow processes are too complex to be described with a linear or log-linear model. Another reason may be that important explanatory variables have been excluded from these models, and/or the watershed characteristics employed as explanatory variables have not been of high quality. Regardless of these issues, regional regression is still a common technique applied in low streamflow estimation.

Typically, a statistical computing package is employed to develop regression models, especially when ordinary least squares regression procedures are used to determine parameter estimators. [Hirsch et al. \(1993\)](#) provide an excellent review of regression analysis, including the formulas used in linear regression, a procedure for developing and testing a regression model, confidence and prediction intervals, model diagnostics, and model selection. The US Geological Survey ([USGS 2010a](#)) has the publicly available software package GLSNet to perform generalized least squares regression procedures (e.g., [Stedinger and Tasker 1986](#), [Kroll and Stedinger 1998](#)).

8.4.2.2 Baseflow Correlation

The baseflow correlation (or baseflow regression) method is a data transfer technique where information is transferred from a nearby long-record gauge to a short-record gauge. Baseflow correlation can be performed with only a minimal number of streamflow measurements at the partial record site (i.e., 5–15 measurements). One key assumption is the streamflow at the short- and long-record sites is under baseflow conditions, meaning that all contributions to streamflow are from groundwater discharge, which is typically considered to be at least three days after the peak of the hydrograph.

The baseflow correlation method was proposed by [Stedinger and Thomas \(1985\)](#) and has several assumptions. The first assumption of the baseflow correlation method is a linear relationship between y_i , the logarithm of the d day annual minimum flows at an ungauged site, and those at a gauged site, x_i :

$$y_i = \alpha + \beta x_i + \varepsilon_i, \quad (8-29)$$

where α and β are regression model parameters, and ε_i are independent normal error terms with a mean of zero and a constant variance, σ_ε^2 (i.e., $\varepsilon_i \sim N(0, \sigma_\varepsilon^2)$).

Second, because annual minimum flows are not available for the ungauged site, the relationship between d day annual minimum flows is assumed to be similar to the relationship between

instantaneous baseflows. In a large simulation experiment, [Zhang and Kroll \(2007b\)](#) find that this is generally a reasonable assumption, though in some cases wide variations occur. Thus, the linear relationship between baseflow measurements at the ungauged site, \tilde{y}_i , and corresponding baseflows at the gauged site, \tilde{x}_i , is given by

$$\tilde{y}_i = \alpha + \beta \tilde{x}_i + \varepsilon_i, \quad (8-30)$$

where $\varepsilon_i \sim N(0, \sigma_e^2)$.

The third assumption is that the annual minimum streamflows are described by an LP3 distribution. By this assumption, the logarithm of $Q_{7,10}$ at the ungauged site can be estimated by

$$\ln(\hat{Q}_{7,10}) = \hat{\mu}_y + K_y \hat{\sigma}_y \quad (8-31)$$

where

$\hat{\mu}_y$ = estimator of the log-space mean,

$\hat{\sigma}_y$ = estimator of the log-space variance, and

K_y = associated frequency factor for the LP3 distribution.

The frequency factor is a function of the log-space skew of the 7 day annual minimum flows and the percentile of interest. In the baseflow correlation method, the frequency factor for the ungauged site, K_y , is assumed equal to the frequency factor for the gauged site, K_x , an assumption [Zhang and Kroll \(2007b\)](#) find has little impact on the performance of this method. Thus, only estimators of $\hat{\mu}_y$ and $\hat{\sigma}_y$ are required; [Stedinger and Thomas \(1985\)](#) suggest the unbiased estimators:

$$\hat{\mu}_y = a + b m_x \quad (8-32)$$

$$\hat{\sigma}_y^2 = b^2 s_x^2 + s_e^2 \left(1 - \frac{s_x^2}{(L-1)s_x^2} \right) \quad (8-33)$$

where

m_x and s_x^2 = log-space mean and variance of the 7 day annual minimum flows at the gauged site, respectively,

s_x^2 = sample variance of the logarithms of the concurrent flows at the gauged site;

L = number of concurrent baseflow measurements, and

a , b , and s_e^2 = ordinary least squares estimators of the parameters α , β , and σ_e^2 estimated using baseflow measurements at the ungauged site as a function of the concurrent flows at the gauged site.

[Stedinger and Thomas \(1985\)](#) derive the variance of the $Q_{7,10}$ estimator as

$$\begin{aligned} \text{Var}[\ln(\hat{Q}_{7,10})] &\cong \frac{s_e^2}{L} + \frac{(m_x - m_{\tilde{x}})^2 s_e^2}{(L-1)s_{\tilde{x}}^2} + \frac{b^2 s_x^2}{n} + \frac{K_y^2}{4\hat{\sigma}_y^2} \left(\frac{4b^2 s_x^4 s_e^2}{L s_{\tilde{x}}^2} + \frac{2b^4 s_x^4}{n} + \frac{2s_e^4}{L} \right) \\ &\quad + \frac{2bs_x^2(m_x - m_{\tilde{x}})K_y s_e^2}{L \hat{\sigma}_y^2 s_{\tilde{x}}^2} \end{aligned} \quad (8-34)$$

where $m_{\tilde{x}}$ is the sample mean of the logarithms of the flows at the gauged site. [Stedinger and Thomas \(1985\)](#) examine the performance of baseflow correlation with 20 pairs of streamflow sites. [Reilly and Kroll \(2003\)](#) expand this analysis to more than 1,300 streamflow sites in the United States and find this method to perform well if nearly independent baseflow measurements were obtained. Reilly and Kroll suggest choosing one baseflow measurement from at least 10 consecutive streamflow recessions and

choosing a long-record site within 200 km of the short-record site. [Zhang and Kroll \(2007b\)](#) examine the tradeoffs between the number of required streamflows and the correlation coefficient between the baseflows at the two sites. [Zhang and Kroll \(2007a\)](#) showed that when only five measurements are available, employing multiple long-record sites can improve the performance of this technique.

8.5 ANALYSIS OF AUTOCORRELATED LOW FLOWS

To quantify the return period and risk of low flows events it is convenient to analyze the time series dependence structure of low flows. For this purpose, the mathematical models to be applied may consider the low flow as a continuous or discrete variable, depending of the complexity of the temporal dependence. In any case, some simple models are described in this section along with illustrative examples. Likewise, the estimation of return period and risk are described for the case of discrete variables.

8.5.1 Modeling of Autocorrelated Low Flows

Time series of low flows may be time dependent (autocorrelated) due to the effect of ground water, lake regulations, wetland storage, and channel storage. Several models representing the dependence structure of this type of process have been proposed in the hydrological literature (e.g., [Salas 1993](#)). One of the simplest models is the first-order autoregressive, which is generally adequate for modeling hydrologic processes having short-term time dependence. For processes with a more complex autocorrelation structure, autoregressive moving average (ARMA) models may be more applicable. Also, extensions or modifications thereof, for example, the gamma autoregressive (GAR) model ([Fernández and Salas 1990](#)) may be useful. Furthermore, shifting mean (SM) models ([Sveinsson et al. 2003](#)) may be necessary where long-term climate variability affects hydrological processes. In addition, where the hydrological process is a discrete autocorrelated variable defined by a finite number of states, then Markov chain models and discrete autoregressive (DAR) and discrete ARMA (DARMA) models may be useful (e.g., [Salas 1993](#)). In this section, we provide some details of the simple models.

8.5.1.1 Simple Markov Chain

A simple model for representing the dependence structure of low flows is the Markov-dependent process with two states and a homogeneous transition probability matrix, i.e., a simple Markov chain (e.g., [Fernández and Salas 1999a, 1999b](#)). The two states may represent above or below a critical level. Let Y_t represent a time series of low flows and Y_0 a certain threshold (e.g., the sample mean or a particular quantile). Consider the states $Y_t < Y_0$ and $Y_t \geq Y_0$ and for convenience we will denote those states as zero and one, respectively. A simple Markov chain that represents the sequence of zeros and ones is defined by its transition probability matrix: $p_{00} = P(Y_t < Y_0 | Y_{t-1} < Y_0)$, $p_{01} = P(Y_t \geq Y_0 | Y_{t-1} < Y_0)$, $p_{10} = P(Y_t < Y_0 | Y_{t-1} \geq Y_0)$, and $p_{11} = P(Y_t \geq Y_0 | Y_{t-1} \geq Y_0)$. It follows that $p_{00} + p_{01} = 1$ and $p_{10} + p_{11} = 1$. Furthermore, $p_0 = P(Y_t < Y_0)$ and $p_1 = P(Y_t \geq Y_0)$ are the unconditional probabilities of states 0 and 1, respectively, and $p_0 + p_1 = 1$.

Thus, to characterize the simple Markov chain estimating the transition probabilities is necessary. [Jackson \(1975\)](#) shows that maximum likelihood estimates of such transition probabilities can be obtained from a sample of the underlying process as follows. Let N_{ij} be the number of transitions from state i to state j . Then

$$\hat{p}_{01} = \frac{N_{01}}{N_0} = \frac{N_{01}}{N_{00} + N_{01}} \quad (8-35)$$

$$\hat{p}_{10} = \frac{N_{10}}{N_1} = \frac{N_{10}}{N_{10} + N_{11}} \quad (8-36)$$

And the remaining elements are $\hat{p}_{00} = 1 - \hat{p}_{01}$ and $\hat{p}_{11} = 1 - \hat{p}_{10}$.

Although \hat{p}_{01} and \hat{p}_{10} may be calculated by counting the occurrence of zeros and ones from the available sample, the procedure is reliable only if a large number of occurrences of zeros and ones can be obtained from the available record. However, for the typical lengths of hydrologic records and for the cases where Y_0 is small (such as for low-flow studies), zeros are rare with a small probability of occurrence, consequently the foregoing procedure for estimating the probability matrix based on Equations (8-35) and (8-36) is unreliable. An alternative procedure is to assume a bivariate distribution function for (Y_t, Y_{t-1}) , so that p_{00} can be determined from

$$p_{00} = P(Y_t < Y_0 | Y_{t-1} < Y_0) = \frac{P(Y_t < Y_0 \text{ and } Y_{t-1} < Y_0)}{P(Y_{t-1} < Y_0)}$$

For instance, for a bivariate normal distribution, [Cramer and Leadbetter \(1967\)](#) give

$$p_{00} = p_0 + \frac{1}{2\pi p_0} \int_0^\rho \frac{\exp[-Y_0^2/(1+z)]}{\sqrt{1-z^2}} dz \quad (8-37)$$

in which ρ = lag-one serial correlation coefficient of Y_t . In addition, the following relationship, proposed by [Sen \(1976\)](#), completes the transition probabilities:

$$p_{10} = P(Y_t < Y_0 | Y_{t-1} \geq Y_0) = \frac{p_0}{1-p_0} (1-p_{00}) \quad (8-38)$$

Figure 8-7 shows the relationship among p_{00} , p_0 , and ρ obtained from Equation (8-37) by numerical integration, which can be used as a first approximation for calculating the transition

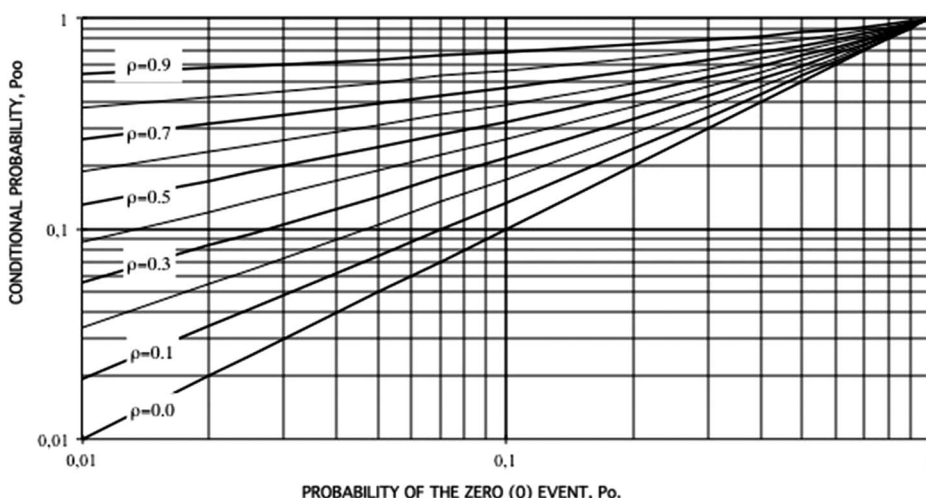


Figure 8-7. Relationship among p_{00} , p_0 , and ρ obtained by numerical integration for a bivariate normal process.

Source: [Fernández and Salas \(1999a\)](#).

probabilities. Also, Example 8-7 illustrates the estimation of transition probabilities for the Parana River 7 day low flows.

For the case of low flows, the focus is on computing the probability that $Y_t < Y_0$ occurs for the first time at the n^{th} time step, f_{n,Y_0} , where Y_0 is the critical event. This represents a sequence of state one during the first $n-1$ time steps and state zero at the n^{th} time step, in other words,

States:	1,	1,	1,	1,	1,	1,	0
Time step:	1,	2,	3,	4,	(n-2),	(n-1),	n

Then, the probability f_{n,Y_0} , can be calculated as

$$\begin{aligned}
 f_{0,Y_0} &= 0 \\
 f_{1,Y_0} &= p_0 \\
 f_{2,Y_0} &= p_1 p_{10} = (1 - p_0) p_{10} \\
 &\dots \\
 f_{n,Y_0} &= p_1 p_{11}^{n-2} p_{10} = (1 - p_0) p_{11}^{n-2} p_{10}, \quad n \geq 2
 \end{aligned} \tag{8-39}$$

The probability f_{n,Y_0} will be useful for calculating the return period and risk as we will see in Section 8.6.2.

8.5.1.2 Autoregressive Moving Average Models

The family of ARMA models has been widely used for modeling hydroclimatic processes at various time scales, such as annual streamflows (e.g., [Salas et al. 1980](#), [Loucks et al. 1981](#), [Salas 1993](#)). The ARMA(p, q) model is defined as ([Box and Jenkins 1976](#))

$$\begin{aligned}
 Y_t &= \mu + \sum_{j=1}^p \phi_j (Y_{t-j} - \mu) + \varepsilon_t - \sum_{j=1}^q \theta_j \varepsilon_{t-j} \\
 \phi(B)(Y_t - \mu) &= \theta(B)\varepsilon_t
 \end{aligned} \tag{8-40}$$

where

μ , ϕ 's, θ 's, and $\sigma^2(\varepsilon)$ = parameters of the model,

p = order of the autoregressive terms, and

q = order of the moving average terms, $\phi(B) = -\phi_1 B^1 - \phi_2 B^2 - \dots - \phi_p B^p$, $\theta(B) = -\theta_1 B^1 - \theta_2 B^2 - \dots - \theta_q B^q$, and $B^i Z_t = Z_{t-i}$.

Particular models derived from Equation (8-40) are the ARMA($p, 0$) or autoregressive AR(p) and the ARMA($0, q$) or moving average MA(q) models. These models assume that the variable Y_t is normally distributed, hence their applications to modeling hydroclimatic time series generally require that the underlying data be converted to normal by some appropriate transformation (e.g., [Box and Cox 1964](#)). However, some models with ARMA-type dependence structure are applicable to skewed marginal distributions. Some of these models can accommodate variables with gamma-marginal distribution functions, such as GAR models. Also, for processes consisting of discrete-valued random variables there are discrete DARMA models, which are more suitable for modeling

persistence characteristics with longer memory than simple Markov chain models. Low-order models are most widely used for modeling streamflow time series (Salas et al. 2001). Some of them are described in the following subsections.

8.5.1.3 The ARMA(1, 1) Model

The ARMA(1,1) model is defined as (Box and Jenkins 1976, Salas and Pielke 2003)

$$Y_t = \mu + \phi_1(Y_{t-1} - \mu) + \varepsilon_t - \theta_1\varepsilon_{t-1} \quad (8-41)$$

where μ , ϕ_1 , θ_1 , and σ_ε^2 are model parameters. It is a Gaussian stationary-dependent process with a continuous valued variable Y_t . It may be shown that the lag- k autocorrelation function of the ARMA(1, 1) process is $\rho_k(Y) = b\phi_1^{k-1}$, $k \geq 1$ where $b = (1 - \phi_1\theta_1)(\phi_1 - \theta_1)/(1 + \theta_1^2 - 2\phi_1\theta_1) = \rho_1(Y)$. In the case that $\theta_1 = 0$, Model (8-41) becomes the AR(1) process, and its autocorrelation function is $\rho_k(Y) = \phi_1^k$, $k \geq 1$. Note that the parameters of the ARMA(1, 1) and AR(1) models are constrained, which in turn implies certain relationships between $\rho_2(Y)$ and $\rho_1(Y)$ (Box and Jenkins 1976).

8.5.1.4 First-Order Gamma-Autoregressive Model

The GAR(1) model assumes that the underlying series is Markov dependent with a gamma marginal distribution, thus the model does not require variable transformation. Lawrence and Lewis (1981) develop the first-order gamma-autoregressive model, which is defined as

$$Y_t = \phi Y_{t-1} + \varepsilon_t \quad (8-42)$$

where

Y_t = gamma-dependent variable at time t ,

ϕ = autoregression coefficient, and

ε_t = independent variable.

The only difference with the well-known AR(1) model is that Y_t has a marginal distribution given by the three-parameter gamma density function,

$$f_Y(y) = \frac{\alpha^\beta (y - \lambda)^{\beta-1} \exp[-\alpha(y - \lambda)]}{\Gamma(\beta)}, \quad (8-43)$$

in which λ , α , and β are the location, scale, and shape parameters, respectively. Thus, a noise term ε_t must be found so that when incorporated into the autoregressive Equation (8-42), it will produce a variable Y_t that is gamma distributed as in Equation (8-43). Gaver and Lewis (1980) find that for integer values of β , the noise ε of Equation (8-42) is given by

$$\varepsilon = \lambda(1 - \phi) + \sum_{j=1}^{\beta} \eta_j \quad (8-44)$$

where

$\eta_j = 0$ with probability ϕ ,

$\eta_j = \exp(\alpha)$ with probability $(1 - \phi)$, and

$\exp(\alpha)$ = an exponentially distributed random variable with expected value $1/\alpha$.

This approach is valid for skewness coefficient less than or equal to 2. In addition, Lawrence (1982) finds another solution for noninteger values of β based on the shot-noise process used by Weiss (1977). In this case, ε can be obtained by

$$\varepsilon = \lambda(1 - \phi) + \eta \quad (8-45)$$

and

$$\begin{aligned} \eta &= 0 \quad \text{if } M = 0 \\ \eta &= \sum_{j=1}^M E_j \phi^{U_j} \quad \text{if } M > 0 \end{aligned} \quad (8-46)$$

in which M is a discrete random variable Poisson distributed with mean value equal to $-\beta \ln(\phi)$. The set (U_j) comprises independent identically distributed (iid) random variables with uniform $(0, 1)$ distribution and the set (E_j) comprises iid random variables exponentially distributed with mean $1/\alpha$.

The estimation of model parameters, in other words, λ , α , β , and ϕ , can be made by the method of moments ([Fernández and Salas 1990](#)). The population moments of the underlying variable, Y_b , may be expressed as a function of the parameters of the GAR(1) model as

$$\mu = \lambda + (\beta/\alpha) \quad (8-47a)$$

$$\sigma^2 = \beta/\alpha^2 \quad (8-47b)$$

$$\gamma = 2/\sqrt{\beta} \quad (8-47c)$$

$$\rho_1 = \phi \quad (8-47d)$$

where μ , σ^2 , γ , and ρ_1 are the population mean, variance, skewness coefficient, and lag-one autocorrelation coefficient of Y_b , respectively. These moments can be estimated based on the sample Y_1, Y_2, \dots, Y_N , using the well-known relationships:

$$m = \frac{1}{N} \sum_{i=1}^N Y_i \quad (8-48a)$$

$$s^2 = \frac{1}{N-1} \sum_{i=1}^N (Y_i - m)^2 \quad (8-48b)$$

$$g_1 = \frac{N}{(N-1)(N-2)s^3} \sum_{i=1}^N (Y_i - m)^3 \quad (8-48c)$$

$$r_1 = \frac{1}{(N-1)s^2} \sum_{i=1}^{N-1} (Y_i - m)(Y_{i+1} - m) \quad (8-48d)$$

where N is the sample size. However, for dependent and nonnormal variables these estimators are biased ([Fernández and Salas 1990](#)). Hence, some corrections are needed before using them for solving the system of Equations (8-47a-d) to estimate the parameters of the GAR(1) model (only the estimator of the expected value can be used without a correction factor).

Wallis and O'Connell (1972) suggest the following correction to obtain an unbiased estimator of ρ_1 for an AR(1) model:

$$\hat{\rho}_1 = \frac{r_1 N + 1}{N - 4} \quad (8-49)$$

in which r_1 is given by Equation (8-48d). Also, Matalas (1966) and O'Connell (1977) show that if the variables follow an AR(1) process, an unbiased estimator of the variance can be obtained by

$$\hat{\sigma}^2 = \frac{N - 1}{N - K} s^2 \quad (8-50)$$

where $K = [N(1 - \hat{\rho}_1^2) - 2\hat{\rho}_1(1 - \hat{\rho}_1^N)]/[N(1 - \hat{\rho}_1)^2]$ and s^2 and $\hat{\rho}_1$ are given by Equations (8-48b) and (8-49), respectively. In addition, Fernández and Salas (1990) suggest the following correction to obtain an unbiased estimator of γ for a GAR(1) process:

$$\hat{\gamma} = \frac{\hat{\gamma}_0}{(1 - 3.12\hat{\rho}_1^{3.7}N^{-0.49})} \quad (8-51)$$

where $\hat{\gamma}_0$ is the skewness coefficient suggested by Bobee and Robitaille (1975) for independent gamma variables as

$$\hat{\gamma}_0 = \frac{Lg_1[A + B(L^2/N)g_1^2]}{\sqrt{N}} \quad (8-52)$$

in which

$$L = \frac{N - 2}{\sqrt{N - 1}}, \quad A = 1 + 6.51 N^{-1} + 20.2 N^{-2}, \quad \text{and} \quad B = 1.48 N^{-1} + 6.77 N^{-2} \quad (8-53)$$

Therefore, the general procedure to estimate the parameters of a GAR(l) model based on available sample series is as follows: (1) estimates of the mean m , variance s^2 , skewness coefficient g_1 , and lag-one autocorrelation coefficient r_1 , are obtained from the sample using Equations (8-48a-d); (2) the unbiased autocorrelation coefficient, $\hat{\rho}_1$, is determined from Equation (8-49) as a function of N and r_1 ; (3) with this value of $\hat{\rho}_1$, the unbiased variance $\hat{\sigma}^2$ is estimated from Equation (8-50); (4) with the values of N , $\hat{\rho}_1$, and g_1 , the unbiased estimate $\hat{\gamma}$ of γ is determined from Equation (8-51); and (5) Equations (8-47a-d) are used to estimate the set of model parameters λ , α , β , and ϕ .

8.5.1.5 The DARMA(1, 1) Model

In Section 8.5.1.1 we discussed the simple Markov chain considering the state zero, in which $Y_t < Y_0$, and state one, where $Y_t \geq Y_0$. For convenience, we can also use an additional symbol, say X , to denote the states zero and one, i.e., X is a discrete random variable where $X = 0$ if $Y_t < Y_0$ and $X = 1$ if $Y_t \geq Y_0$. Saying this another way, a continuous valued process Y_t was censored or clipped at Y_0 leading to a discrete valued process X_t . If the original hydrological process Y_t is autocorrelated, then the clipped process X_t is also expected to be autocorrelated (Salas et al. 2001). What we did in Section 8.5.1.1 was to model the sequence of zeros and ones using a simple Markov chain. We could also say that we modeled the variable X with a simple Markov chain.

In some cases, modeling the X process with a simple Markov chain is adequate, but for cases where the underlying process Y has longer dependence, in other words, an autocorrelation function

that persists for long time, a model with a more flexible correlation structure may be necessary to represent X_t . Thus, we will assume that the autocorrelation of X_t can be represented by a DARMA process. For example, the DARMA(1, 1) model is defined as (Jacobs and Lewis 1977a, b)

$$X_i = U_i Z_i + (1 - U_i) W_{i-1}, \quad i = 1, 2, \dots \quad (8-54)$$

where

U_i = an independent Bernoulli (0,1) process with parameter $P(U_i = 1) = \beta$,

Z_i = another independent Bernoulli (0,1) process with $P[Z_i = 0] = \pi_0$ and $P[Z_i = 1] = \pi_1$, and W_{i-1} is a discrete AR(1) process, in other words, a DAR(1) process with parameters λ and π_0 .

The autocorrelation function of the DARMA(1, 1) model is $\rho_k(X) = c\lambda^{k-1}$, $k \geq 1$ with $c = (1 - \beta)(\lambda + \beta - 2\lambda\beta)$. When $\beta = 0$, X_i becomes the DAR(1) process. In general, the DAR(1) process is defined as

$$X_i = V_i X_{i-1} + (1 - V_i) Z_i \quad i = 1, 2, \dots \quad (8-55)$$

where V_i is an independent Bernoulli (0,1) process with parameter λ , and Z_i is as defined previously. The autocorrelation function of the DAR(1) model is $\rho_k(X) = \lambda^k$, $k \geq 1$.

Example 8-6: Estimation of the 7 Day, 10 Year Low Flow Based on the GAR(1) Model

Table 8-4 gives the 7 day low-flow data for the gauging station Mapocho River at Rinconada de Maipú, Chile, for 1980–2007 (i.e., $N = 28$). Figure 8-8 shows the time series data. The following statistics are obtained directly from historic data using Equations (8-48a–d): $m = 14.30$, $s^2 = 5.57^2$, $g_1 = 0.298$, and $r_1 = 0.358$. Also from Equation (8-49) the unbiased estimate of the lag-1 autocorrelation coefficient is $\hat{\rho}_1 = 0.459$, and Equation (8-50) gives the estimate of the standard deviation $\hat{\sigma} = 5.74$ [refer to Equation (8-50) for the value of $K = 2.59$]. In addition, from Equation (8-53), one obtains $L = 5.004$, $A = 1.258$, and $B = 0.062$ so that Equation (8-52) gives $\hat{\gamma}_0 = 0.355$, the unbiased estimate of γ_0 for independent values. Furthermore, from Equation (8-51) the unbiased estimate of the skewness coefficient (for autocorrelated data) becomes $\hat{\gamma} = 0.368$. Summarizing, the unbiased estimates of the GAR(1) model statistics are $\hat{\mu} = 14.30$, $\hat{\sigma} = 5.74$, $\hat{\gamma} = 0.368$, and $\hat{\rho}_1 = 0.459$. Using these values in Equations (8-47a–d), the estimates of the parameters of the GAR(1) model are obtained as $\hat{\lambda} = -16.9$, $\hat{\alpha} = 0.946$, $\hat{\beta} = 29.5$, and $\hat{\phi} = 0.459$.

Table 8-4. 7 Day Low Flows (m^3/s) of the Mapocho River at Rinconada de Maipú, Chile, for 1980–2007.

Year	Q (m^3/s)	Year	Q (m^3/s)	Year	Q (m^3/s)
1980	18.29	1990	11.26	2000	11.91
1981	8.53	1991	10.80	2001	19.73
1982	9.04	1992	15.90	2002	19.54
1983	11.70	1993	19.41	2003	24.90
1984	13.74	1994	13.87	2004	18.19
1985	12.76	1995	12.31	2005	26.30
1986	16.87	1996	7.11	2006	18.23
1987	22.79	1997	8.75	2007	14.30
1988	2.42	1998	9.91	—	—
1989	12.46	1999	9.42	—	—

Source: Banco Nacional de Aguas, Dirección General de Aguas, Ministerio de Obras Públicas, Chile.

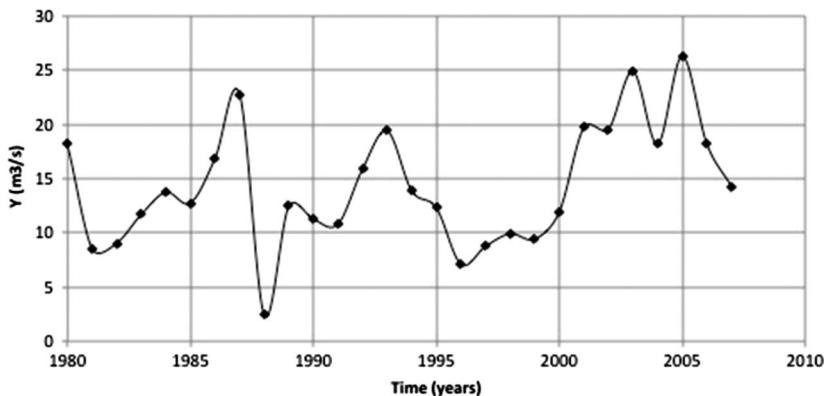


Figure 8-8. Time series data of 7 day low flows of the Mapocho River at Rinconada de Maipú for 1980–2007.

Using these parameters and the generating procedure of Equations (8-42) and (8-44), 1,000 values of 7 day low flows were obtained. Figure 8-9 shows the CDF of these values and the CDF of the historical data. Thus, the 10 year low flow, in other words, the low flow corresponding to 0.1 nonexceedance probability based on the simulated GAR(1) model, gives a value of $6.8 \text{ m}^3/\text{s}$. However, the 10 year low flow obtained from the historical data is $8.53 \text{ m}^3/\text{s}$ (because it corresponds to the third value of the historic series using the Weibull plotting position). For comparison, if a three-parameter gamma distribution function for independent values is also fitted (i.e., $\rho_1 = 0$) using the unbiased statistics $m = 14.30$, $\sigma^2 = 5.57^2$, and $\hat{\gamma}_0 = 0.355$ (from the foregoing calculations) and the parameters of the gamma distribution estimated from Equations (8-47a–c) ($\hat{\lambda} = -17.1$, $\hat{\alpha} = 1.012$, and $\hat{\beta} = 31.7$), the value $7.4 \text{ m}^3/\text{s}$ is obtained for the 10 year, 7 day low flow. Figure 8-9 also shows the CDF of the gamma independent series.

8.5.2 Return Period and Risk of Low Flows

In Section 8.5.1.1, simple Markov chains were introduced as one of the simplest models that can be used to represent the dependence structure of two-state discrete processes. To estimate the return period and risk of low-flow events some additional definitions and concepts are presented here including an example.

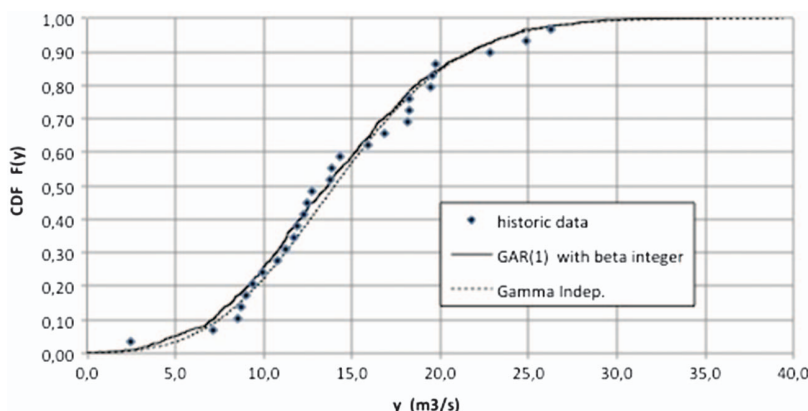


Figure 8-9. CDF of the 7 day low flows of the Mapocho River at Rinconada de Maipú, Chile, obtained from historical data, independent gamma, and the GAR(1) model based on 1,000 generated values.

The return period of a particular event has been generally defined as “the average number of time steps (e.g., years) required to the first occurrence of the event.” For instance in relation to the event $Y_t < Y_0$ the assumption is that such event has occurred in the past, a finite time τ has elapsed since then, and the interest is in the remaining waiting time N for the next occurrence of $Y_t < Y_0$. An alternative definition of return period is “the expected value of the number of time steps between any two successive occurrences of the event.” In this case, the assumption is that an event $Y_t < Y_0$ has just occurred and the interest is in the time of arrival of the next event $Y_t < Y_0$. This definition is equivalent to the previous one when the time past τ , after the occurrence of $Y_t < Y_0$, is equal to zero. In practice, both definitions have been accepted as being equivalent because in simple cases such as those related to independent annual flood events they lead to the same result. But they lead to different results when they are applied to complex hydrological events such as autocorrelated low flows.

To estimate the return period of an event $Y_t < Y_0$, the following probability given in Equation (8-39) is needed:

$$f_{n,Y_0} = P(Y_t < Y_0 \text{ occurs for the first time at the } n^{\text{th}} \text{ time step})$$

where $f_{0,Y_0} = 0$. Let N denote the random variable defining the number of time steps needed to the first occurrence of such an event. Then, considering the first definition of return period given previously, the return period T is the expected value of N :

$$T = E(N) = \sum_{n=0}^{\infty} nf_{n,Y_0}$$

In addition, if a critical low-flow value Y_0 is specified so that the occurrence of the event $Y_t < Y_0$ produces a failure, and L is the project life measured in the same time units as time steps (usually years), then the risk of failure can be defined as

$$R_{L,Y_0} = P(Y_t < Y_0 \text{ occurs at least once in } L \text{ time steps})$$

Furthermore, the following probability is equivalent for evaluating the risk, i.e.,

$$S_{n,Y_0} = P(Y_t < Y_0 \text{ has occurred at or before time step } n)$$

Then the risk of failure of a project with a project life L is S_{L,Y_0} . Note that the foregoing definitions assume that $\tau > 0$ (the time past after the occurrence of a failure event) and the interest is to estimate the probability of the time it will take for the failure event to occur for the first time after the construction of the project. Such time has been denoted by N .

For estimating the return period of a low-flow event, we first need to determine f_{n,Y_0} , the probability that $Y_t < Y_0$ occurs for the first time at the n^{th} time step, in which Y_0 is the critical value. Under the assumption that the sequence of zeros and ones may be modeled by a first-order Markov chain, the probability f_{n,Y_0} may be determined from Equation (8-39). Then, the return period considering the first definition is given by (Fernández and Salas 1999a)

$$T = E(N) = \sum_{n=0}^{\infty} nf_{n,Y_0} = 1 + \frac{1 - p_0}{p_{10}} \quad (8-56)$$

In addition, S_{n,Y_0} , the probability that event $Y_t < Y_0$ occurred at or before time step n , can be determined by

$$\begin{aligned}
S_{0,Y_0} &= 0 \\
S_{1,Y_0} &= p_0 \\
S_{2,Y_0} &= S_{1,Y_0} + f_{2,Y_0} \\
&\dots \\
S_{n,Y_0} &= S_{n-1,Y_0} + f_{n,Y_0}, \quad n \geq 2
\end{aligned} \tag{8-57}$$

Therefore, for $n = L$, the risk of failure becomes (Fernández and Salas 1999a)

$$S_{L,Y_0} = 1 - (1 - p_0)(1 - p_{10})^{L-1} \tag{8-58}$$

Furthermore, for estimating the return period considering the second definition discussed previously, one must calculate f_w , the probability that a failure event occurs after another failure event occurred w time steps earlier, in other words, we are interested in $T = E(W)$. Then considering the sequence of zeros and ones in the following sketch,

States:	0,	1,	1,	1,	1,	1,	1,	0
Time step:	0,	1,	2,	3,	4,	(w-2),	(w-1),	w

illustrates that after the occurrence of zero (i.e., the event $Y_t < Y_0$), it takes w steps for the occurrence of another zero. Then, in this case,

$$\begin{aligned}
f_0 &= 0 \\
f_1 &= p_{00} \\
f_2 &= p_{01}p_{10} \\
&\dots \\
f_w &= p_{01}p_{11}^{w-2}p_{10}, \quad w \geq 2
\end{aligned} \tag{8-59}$$

and the return period is given by (Fernández and Salas 1999a)

$$T = E(W) = \sum_{w=0}^{\infty} wf_w = p_{00} + \frac{p_{01}}{p_{10}}(1 + p_{10}) \tag{8-60}$$

where p_{00} and p_{10} can be obtained from Equations (8-37) and (8-38), respectively.

Example 8-7: Estimating the Return Period and Risk of Low-Flow Events

This example illustrates the procedure for calculating the return period and risk of a low-flow event. The estimation of return period and risk related to low-flow events in the Paraná River at Corrientes, Argentina, is of special interest because of the importance of navigation on that river (Paoli et al. 1994). Figure 8-10 shows the 7 day low-flow time series for 1904–1992. The low-flow values of interest are the minimum observed value that occurred in 1944, the 10 year minimum annual flow, and the 50 year minimum annual flow. We would like to determine the following statistics: (a) return period of the observed minimum 7 day low flow and the risk that a flow equal to or smaller than the historical (observed) value will occur in the next 30 years; (b) 10 year low flow, Q_{10} ; and (c) 50 year low flow, Q_{50} .

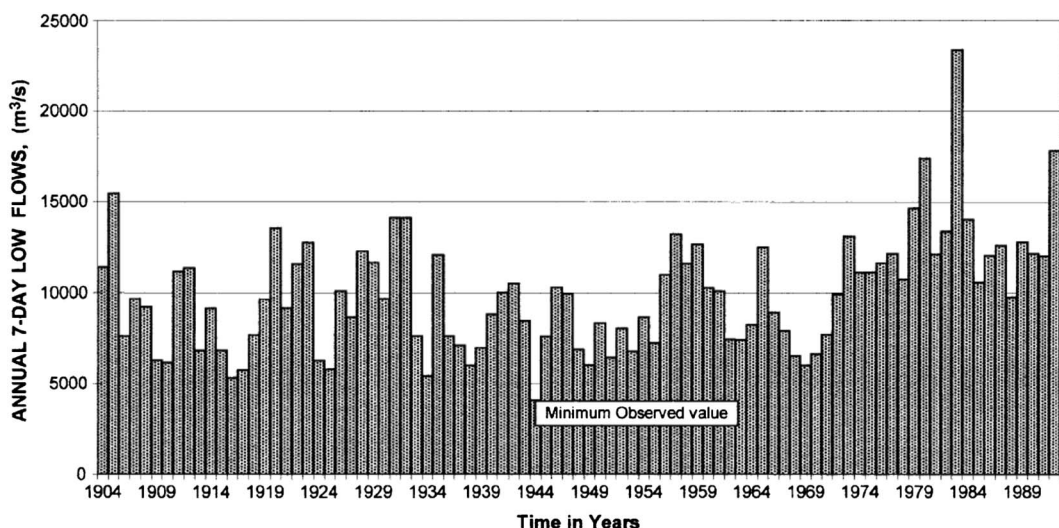


Figure 8-10. Annual 7 day low flows of the Paraná River at Corrientes, Argentina, for 1904–1992.
Source: Fernández and Salas (1999b).

(a) Return period and risk

Table 8-5 shows the basic statistical properties of the series of 7 day low flows. Because the observed time series is skewed (skewness coefficient is 1.024) transforming the original series into Gaussian series is necessary before applying Equation (8-37). Thus, the original data was log-transformed, and Table 8-6 shows some basic properties of the log-transformed series.

Because the minimum low-flow value is $X_0 = 4,070 \text{ m}^3/\text{s}$, the corresponding value in the log-transformed (normal) domain is $Y_0 = 3.610$. Then one can calculate p_0 using the normal distribution function as

$$p_0 = P(Y < 3.61) = P\left(Z < \frac{3.61 - 3.975}{0.138}\right) = 0.0041$$

With this value of p_0 and $\rho = 0.506$ one can determine the value of p_{00} from Equation (8-37) as

Table 8-5. Statistical Properties of the 7 Day Low Flows of the Paraná River at Corrientes, Argentina.

Statistical property	Value
Period of record	1904–1992
Length of record (years)	89
Mean (m^3/s)	9,915
Minimum (m^3/s)	4,070
Standard deviation (m^3/s)	3,208
Skew coefficient	1.024
Lag-1 correlation	0.491

Source: Fernández and Salas (1999b).

Table 8-6. Statistical Properties of the Log-Transformed Series of 7 Day Low Flows of the Paraná River at Corrientes, Argentina.

Statistical property	Transformed value, $Y = \log(X)$
Mean	3.975
Minimum	3.610
Standard deviation	0.138
Skew coefficient	~ 0.0
Lag-1 correlation	0.506

Source: Fernández and Salas (1999b).

$$p_{00} = p_0 + \frac{1}{2\pi p_0} \int_0^{\rho} \frac{\exp[-Y_0^2/(1+z)]}{\sqrt{1-z^2}} dz = 0.00514$$

Then from Equations (8-38) and (8-56) we get

$$p_{10} = \frac{p_0}{(1-p_0)} (1-p_{00}) = 0.0039954 \quad \text{and}$$

$$T = 1 + \frac{1-p_0}{p_{10}} = 1 + \frac{1-0.0041}{0.0039954} \approx 250 \text{ years}$$

Also, the risk of failure for a project life of 30 years can be computed from Equation (8-58) as

$$S_{L,Y_0} = 1 - (1-p_0)(1-p_{10})^{L-1} = 1 - (1-0.0041)(1-0.0039954)^{30-1} = 0.113$$

(b) 10 year low flow

Solving Equations (8-37), (8-38), and (8-56) numerically for values of $T = 10$ and $\rho = 0.506$, one obtains $Y_{10} = 3.7981$. Then, $Q_{10} = 10^{3.798} = 6,282 \text{ m}^3/\text{s}$.

(c) 50 year low flow

Similarly, for $T = 50$ and $\rho = 0.506$ the 50 year low flow discharge is $Q_{50} = 10^{3.6912} = 4,911 \text{ m}^3/\text{s}$.

8.6 STATISTICAL CHARACTERIZATION OF MULTIYEAR DROUGHTS

As indicated in Section 8.1, Yevjevich (1967) introduces the definition of a drought event as the succession of consecutive intervals where the hydrological variable of interest remains below a threshold level x_0 . Thus for a fixed threshold x_0 , the main drought characteristics are drought length L (length of negative run or number of consecutive intervals where $X_t < x_0$ followed and preceded by at least one interval where $X_t \geq x_0$), drought magnitude or accumulated deficit D (sum of the individual deficits $S_t = x_0 - x_t$ over the drought duration L), and drought intensity, defined as the ratio of drought magnitude to the drought length, $I = D/L$.

The probabilistic characterization of drought events is more complex than for low flows. Indeed, the need to consider at least two characteristics (e.g., length and magnitude), which are not mutually independent, coupled with the relatively short hydrologic records that are generally available, makes the traditional inferential approach (i.e., fitting a distribution function to the observed drought characteristic) applicable only when long records are available. However, such difficulties can be circumvented by deriving analytically the probability distributions of drought properties, assuming that a certain stochastic model represents the underlying hydrological series. Then, instead of fitting a probability distribution directly to the historical drought characteristics one may fit a stochastic model to the underlying hydrological series and determine the distribution and the parameters of the drought properties either by analytical methods or by Monte Carlo simulation. In this section we describe alternative statistical methods for characterizing droughts, namely empirical methods based on historical data or based on simulated series and analytical methods based on closed form or approximate equations. [Mishra and Singh \(2011\)](#) is a recent review of drought modeling concepts and methods.

8.6.1 Probability Distributions and Moments of Drought Characteristics

Finding the distribution and moments of droughts can be a complex undertaking because of the multiple variables that are needed to define them. For this reason, we approach the problem by determining the statistical properties of individual variables first, then bringing them together in a joint framework. This procedure is described in the following sections.

8.6.1.1 Probability Distribution and Moments of Drought Length

The properties of run length and its application to drought have been widely investigated in the literature. For example, [Downer et al. \(1967\)](#) study the distribution and the statistical moments of positive and negative run lengths for a sequence of independent identically distributed normal and log-normal random variables. Also, [Llamas and Siddiqui \(1969\)](#) consider the case of a two-state lag-1 Markov process and derive analytical expressions for determining the probabilities of runs of wet and dry years of specified lengths. Since then numerous studies and developments have been reported (e.g., [Sen 1976](#); [Chang et al. 1984a, b](#); [Loaiciga and Leipnik 1996](#); [Salas et al. 2001](#); [Loaiciga 2005](#); [Cancelliere and Salas 2010](#)).

The simplest way to model drought length is assuming that the underlying water supply series is iid. In this case, the probability mass function (PMF) of drought length is geometric:

$$f_L(\ell) = P(L = \ell) = (1 - p_1)^{\ell-1} p_1 \quad (8-61)$$

where $p_1 = P(X_t > x_0)$ is the parameter. The foregoing equation enables computing the probability that a drought will last exactly ℓ time-steps. Then, the CDF, in other words, the probability that a drought has a length equal to or smaller than ℓ time steps, can be computed as

$$P(L \leq \ell) = \sum_{j=1}^{\ell} (1 - p_1)^{j-1} p_1 = 1 - (1 - p_1)^{\ell} \quad (8-62)$$

Consequently, the expected value and the variance of drought length are given respectively by

$$E(L) = 1/p_1 \quad (8-63)$$

$$Var(L) = (1 - p_1)/p_1^2 \quad (8-64)$$

The iid assumption may be acceptable in some cases, for instance when dealing with yearly precipitation where the autocorrelation structure may be negligible. However, when dealing with

streamflows, the time-dependence structure is generally significant and therefore a model that is capable of representing such temporal dependence may be needed. For example, if a Markov model (Markov chain) is adopted for modeling the sequence of deficits and surpluses, the PMF of drought length can be derived analytically. For a stationary simple Markov chain, the PMF of drought length is also geometric:

$$f_L(\ell) = P[L = \ell] = (1 - p_{01})^{\ell-1} p_{01} \quad (8-65)$$

where the parameter p_{01} is the transition probability as defined previously. Equation (8-65) enables computing the probability that a drought will last exactly ℓ time steps. The CDF of L , in other words, the probability that a drought has a length equal to or smaller than ℓ time steps, is given by

$$P[L \leq \ell] = \sum_{j=1}^{\ell} (1 - p_{01})^{j-1} p_{01} = 1 - (1 - p_{01})^{\ell} \quad (8-66)$$

Likewise, the probability that a drought has a length greater than ℓ time steps is

$$P[L > \ell] = 1 - P[L \leq \ell] = (1 - p_{01})^{\ell} \quad (8-67)$$

The expected value and the variance of drought length follow from Equation (8-65) as

$$E(L) = \frac{1}{p_{01}} \quad (8-68)$$

$$Var(L) = \frac{1 - p_{01}}{p_{01}^2} \quad (8-69)$$

Given a sample x_1, x_2, \dots, x_N , where N is the sample size, and the threshold x_0 , the transition probability p_{01} can be estimated using maximum likelihood by counting the number of times a deficit is followed by a surplus N_{01} and the number of times a deficit is followed by a deficit N_{00} . Then

$$\hat{p}_{01} = \frac{N_{01}}{N_{00} + N_{01}} \quad (8-70)$$

Similarly, one can estimate p_1 by counting the number of surpluses N_1 as

$$\hat{p}_1 = N_1 / N \quad (8-71)$$

In practice these equations can be employed only if a sufficient number of transitions N_{00} and N_{01} are observed. However, if the hydrological series is short or the threshold x_0 low, the number of observed transitions may be too small and the estimation of p_{01} by Equation (8-70) and p_1 by Equation (8-71) may be unreliable.

An alternative is to use a parametric approach similar to that shown in Section 8.5. By definition, p_{01} can be written as

$$p_{01} = 1 - p_{00} = 1 - P[X_t \leq x_0 | X_{t-1} \leq x_0] = 1 - \frac{P[X_t \leq x_0, X_{t-1} \leq x_0]}{P[X_{t-1} \leq x_0]} \quad (8-72)$$

where $P[X_t \leq x_0, X_{t-1} \leq x_0]$ is the joint distribution of X_t and X_{t-1} and $P[X_{t-1} \leq x_0]$ is the CDF of X_{t-1} . Assuming a bivariate normal distribution for (X_t, X_{t-1}) , the following expression can be adopted to estimate p_{01} (Cramer and Leadbetter 1967):

$$\hat{p}_{01} = 1 - \hat{p}_0 - \frac{1}{2\pi\hat{p}_0} \int_0^{\rho} \frac{\exp[-x_0^2/(1+z)]}{\sqrt{1-z^2}} dz \quad (8-73)$$

where ρ = lag-1 serial correlation coefficient of X_t , $\hat{p}_0 = 1 - \hat{p}_1$, and \hat{p}_0 can be estimated by

$$\hat{p}_0 = \Phi\left(\frac{x_0 - \hat{\mu}_x}{\hat{\sigma}_x}\right) \quad (8-74)$$

where $\Phi(\cdot)$ represents the standard normal CDF, and $\hat{\mu}_x$ and $\hat{\sigma}_x$ are the sample mean and sample standard deviation of X_t , respectively.

Furthermore, when the underlying series exhibits a strong autocorrelation or serial dependence a better alternative to the lag-1 Markov model for modeling the sequences of deficits and surpluses is the DARMA(1, 1) model of Equation (8-54) in Section 8.5.1.5. Low-order DARMA models, originally introduced by Jacobs and Lewis (1977, 1978), have been applied to daily precipitation (Chang et al. 1984a) and monthly streamflows (Chebaane et al. 1995). Also Chung and Salas (2000) use a DARMA(1, 1) model to derive the return period and risk of droughts. In particular, they show that the DARMA(1, 1) model is better than the simple Markov chain for modeling drought length probabilities where streamflows exhibit strong autocorrelation, as is the case of the Niger River's annual streamflows. The probability distribution of the length L of a run of state $i = 0$ (drought length) for a DARMA(1, 1) model has been derived by Chang et al. (1984b). The expectation of L is

$$E[L] = \frac{\pi_0[1 - \beta\lambda + \beta(1 - \lambda - \beta + 2\beta\lambda)\{1 - \pi_0\}]}{\{1 - \pi_0\}[1 - \lambda(1 - \beta)\{1 - \beta\pi_0\} - \beta\pi_0\{1 - \beta(1 - \lambda)\}]} \quad (8-75)$$

Other properties and applications of DARMA models for modeling drought lengths can be found in the literature (e.g., Chebaane et al. 1995, Salas et al. 2001, Cancelliere and Salas 2010). As an alternative to DARMA models, higher-order Markov chains have been proposed (e.g., Akyuz et al. 2012, Tabari et al. 2015). Also, drought-length properties related to periodic processes such as monthly streamflows have been reported by Cancelliere and Salas (2004).

Example 8-8: Fitting the Probability Distribution of Drought Lengths

Table 8-7 lists 119 years of records (1984–2002) of annual streamflows of the Poudre River at the Mouth of the Canyon gauging station. Because diversions and storage facilities are upstream from the gauging station, the measured flows have been adjusted (naturalized) so as to approximate the natural flows that would have existed at the site. Figure 8-11 shows the time series of annual flows and the threshold $x_0 = 299,000$ ac-ft (equal to the long-term mean). The figure indicates that various drought episodes have occurred on the Poudre River throughout the historical record, such as those of the 1930s and 1950s. In particular, two 8 year droughts occurred in the years 1930–1937 and 1987–1994. The coefficients of variation, skewness, and lag-1 serial correlation are 0.36, 0.98, and 0.153, respectively, which are characteristic of streams in the semi-arid western United States.

Table 8-7. Annual Streamflows (thousands acre-ft) of the Poudre River at Mouth of the Canyon (1884–2002).

Year	Streamflow ft ³ /s						
1884	695	1914	410	1944	236	1974	329
1885	514	1915	230	1945	249	1975	278
1886	338	1916	270	1946	203	1976	206
1887	332	1917	520	1947	336	1977	129
1888	202	1918	320	1948	226	1978	330
1889	224	1919	150	1949	379	1979	372
1890	264	1920	410	1950	205	1980	471
1891	298	1921	437	1951	330	1981	193
1892	236	1922	199	1952	316	1982	298
1893	252	1923	453	1953	202	1983	702
1894	341	1924	481	1954	122	1984	440
1895	392	1925	211	1955	167	1985	261
1896	255	1926	428	1956	242	1986	368
1897	377	1927	264	1957	441	1987	169
1898	221	1928	325	1958	289	1988	287
1899	420	1929	330	1959	251	1989	192
1900	516	1930	227	1960	238	1990	268
1901	368	1931	172	1961	350	1991	295
1902	206	1932	232	1962	312	1992	237
1903	353	1933	272	1963	155	1993	286
1904	395	1934	127	1964	192	1994	190
1905	378	1935	277	1965	340	1995	358
1906	300	1936	263	1966	150	1996	321
1907	410	1937	198	1967	247	1997	366
1908	290	1938	358	1968	264	1998	282
1909	500	1939	212	1969	256	1999	384
1910	290	1940	149	1970	351	2000	198
1911	230	1941	212	1971	367	2001	200
1912	350	1942	360	1972	238	2002	95
1913	230	1943	369	1973	377	—	—

Source: Northern Colorado Water Conservancy District, Loveland, Colorado.

Because the lag-1 autocorrelation coefficient is small, a lag-1 Markov model has been adopted to derive the PMF of drought length. Thus, by counting the number of transitions between states, the following results are obtained: $N_{00} = 39$ and $N_{01} = 27$. Then, applying Equation (8-70), the estimate of the parameter \hat{p}_{01} of the geometric distribution is

$$\hat{p}_{01} = \frac{N_{01}}{N_{00} + N_{01}} = \frac{27}{39 + 27} = 0.41$$

Then, from Equation (8-65) the PMF of drought length is

$$f_L(\ell) = P[L = \ell] = (1 - 0.41)^{\ell-1} 0.41, \quad \ell = 1, \dots$$

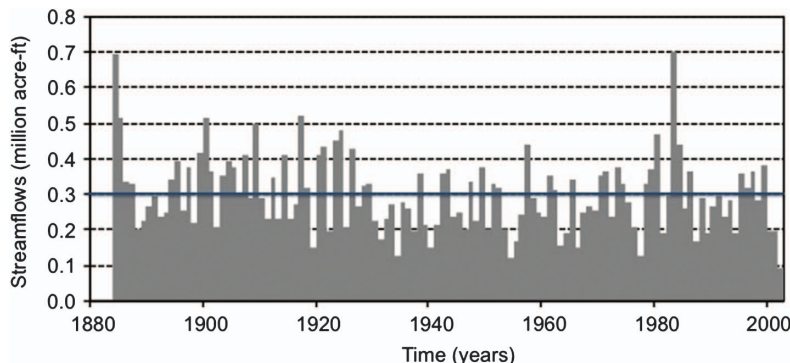


Figure 8-11. Annual flow records of the Poudre River at Mouth of the Canyon (1884–2002) and threshold level x_0 equal to the long-term mean.

Source: Salas et al. (2005).

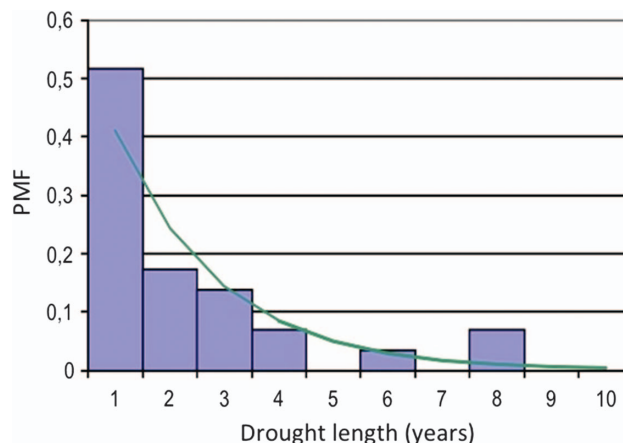


Figure 8-12. Sample PMF of drought length (histogram) and PMF obtained from the fitted simple Markov chain model (continuous line) for the annual flows of the Poudre River at Mouth of the Canyon.

Figure 8-12 shows the derived geometric PMF and the sample frequency distribution of observed drought lengths. The probability of a drought longer than the longest one observed on record can be computed by Equation (8-67) as

$$P[L > 8] = 1 - P[L \leq 8] = (1 - 0.41)^8 = 1.5\%$$

In addition, one can calculate $E(L)$ and $\sigma(L)$ from Equations (8-68) and (8-69), respectively. They give $E(L) = 2.44$ and $\sigma(L) = 1.87$ years, respectively.

If sufficiently long records of the underlying hydrological series are available (as is the case for the data in this example), one may be able to estimate the parameters of the probability distribution of drought length from the observed drought events. For example, assuming that a simple Markov chain represents the underlying series of zeros and ones, Equation (8-68) can be used to estimate p_{01} as

$$\hat{p}_{01} = \frac{1}{\hat{E}(L)} = \frac{1}{\hat{\mu}_L}$$

where $\hat{\mu}_L$ can be estimated from the sample of observed droughts as

Table 8-8. Drought Length (L), Drought Magnitude (D), and Drought Intensity (I) Identified for the Streamflows of the Poudre River at Mouth of the Canyon (1884–2002) Assuming a Threshold $x_0 = \mu_x = 299 \times 10^3$ acre-ft.

Begin year	End year	L (years)	D (10^3 acre-ft)	I (10^3 acre-ft/year)
1888	1893	6	318.07	53.01
1896	1896	1	44.01	44.01
1898	1898	1	78.01	78.01
1902	1902	1	93.01	93.01
1908	1908	1	9.01	9.01
1910	1911	2	78.02	39.01
1913	1913	1	69.01	69.01
1915	1916	2	98.02	49.01
1919	1919	1	149.01	149.01
1922	1922	1	100.01	100.01
1925	1925	1	88.011	88.011
1927	1927	1	35.011	35.011
1930	1937	8	624.09	78.011
1939	1941	3	324.03	108.01
1944	1946	3	209.03	69.678
1948	1948	1	73.011	73.011
1950	1950	1	94.011	94.011
1953	1956	4	463.05	115.76
1958	1960	3	119.03	39.678
1963	1964	2	251.02	125.51
1966	1969	4	279.05	69.761
1972	1972	1	61.011	61.011
1975	1977	3	284.03	94.678
1981	1982	2	107.02	53.511
1985	1985	1	38.011	38.011
1987	1994	8	468.2	58.525
1998	1998	1	17.356	17.356
2000	2002	3	404.01	134.67
Mean		2.39	177.68	72.76
Variance		4.10	25,829.14	1,200.64

$$\hat{\mu}_L = (1/m) \sum_{i=1}^m L_i$$

where m is the number of drought episodes. For example, Table 8-8 gives the durations of the various drought lengths that occurred on the Poudre River. The sample mean of drought length is $\hat{\mu}_L = 2.39$, so that $\hat{p}_{01} = 0.418$. This would be an alternative procedure for estimating the parameter of the geometric distribution as referred to in the first part of this example.

8.6.1.2 Fitting Probability Distributions to Drought Magnitude and Drought Intensity

Long records of hydrologic data may enable fitting the distribution of drought magnitude and intensity. For example, one may assume that the probability distribution of drought magnitude is a two-parameter gamma as

$$f_D(d) = \frac{1}{\beta_D \Gamma(r_D)} \left(\frac{d}{\beta_D} \right)^{r_D-1} e^{-\frac{d}{\beta_D}} \quad (8-76)$$

where β_D and r_D represent the scale and shape parameters, respectively. The moment estimators of β_D and r_D are given by

$$\hat{\beta}_D = \hat{\sigma}_D^2 / \hat{\mu}_D \text{ and } \hat{r}_D = \hat{\mu}_D^2 / \hat{\sigma}_D^2 \quad (8-77)$$

where $\hat{\mu}_D$ and $\hat{\sigma}_D^2$ are the sample mean and variance, respectively, which may be determined from the observations of drought magnitude D_j as

$$\hat{\mu}_D = \frac{1}{m} \sum_{j=1}^m D_j \text{ and } \hat{\sigma}_D^2 = \frac{1}{m-1} \sum_{j=1}^m (D_j - \hat{\mu}_D)^2.$$

Similarly, one may assume a two-parameter gamma distribution for the drought intensity, $f_I(i)$, and use the method of moments for estimating the parameters β_1 and r_1 .

Example 8-9: Fitting the Probability Distribution of Drought Magnitude and Drought Intensity for the Annual Flows of the Poudre River at the Mouth of the Canyon

Table 8-8 gives the drought length, magnitude, and intensity of the droughts identified for the annual flows of the Poudre River at the Mouth of the Canyon (see Example 8-8), assuming a threshold x_0 equal to the mean. One may observe that the drought with the largest magnitude (624.09×10^3 ac-ft) occurred in 1930–1937 and lasted eight years. We would like to determine the probability that droughts larger than the maximum observed drought magnitude will occur on the Poudre River.

Using the sample mean $\hat{\mu}_D$ and variance $\hat{\sigma}_D^2$ obtained in Table 8-8, we apply the moment Equation (8-77) for estimating the parameters of the gamma distribution for drought magnitude as

$$\begin{aligned} \hat{\beta}_D &= \hat{\sigma}_D^2 / \hat{\mu}_D = 25829.14 / 177.68 = 145.37 \text{ and} \\ \hat{r}_D &= \hat{\mu}_D^2 / \hat{\sigma}_D^2 = (177.68)^2 / 25829.14 = 1.22 \end{aligned}$$

Likewise, the corresponding parameter estimates for drought intensity are

$$\hat{\beta}_I = \hat{\sigma}_I^2 / \hat{\mu}_I = 16.5 \text{ and } \hat{r}_I = \hat{\mu}_I^2 / \hat{\sigma}_I^2 = 4.41$$

Replacing the parameters in the corresponding probability distributions, the probability of various drought events can be computed. Alternatively, one may be interested in determining drought magnitude or intensity corresponding to a given probability.

For instance, the probability of a drought magnitude greater than the largest observed value (i.e., $D = 624.09 \times 10^3$ ac-ft) can be computed by integrating the corresponding PDF as

$$P[D > 624.09] = 1 - \int_0^{624.09} \frac{1}{145.37 \Gamma(1.22)} \left(\frac{d}{145.37} \right)^{1.22-1} e^{-\frac{d}{145.37}} dd = 0.02$$

The foregoing integral can be determined using standard routines for computing the gamma integral. For instance, using Matlab, the command $P = \text{gamcdf}(624.09, 1.22, 145.37) = 0.978$ can be used to estimate the required integral. In a similar fashion, one can compute the probability that a drought with intensity greater than a fixed value, say 130×10^3 ac-ft/year, will occur as

$$P[I > 130] = 1 - \int_0^{130} \frac{1}{16.50\Gamma(4.41)} \left(\frac{d}{16.5}\right)^{4.41-1} e^{-\frac{d}{16.50}} dd = 0.067$$

In addition, one may want to determine the drought magnitude for a given exceedance probability, for example, $p = 5\%$, using the inverse of the gamma distribution. This can be achieved numerically by using, for instance, the Matlab function `gaminv(q, r, beta)`, where q is the nonexceedance probability, and β and r are the parameters. In our case, $q = 1 - 0.05 = 0.95$, and the desired drought magnitude is obtained as $D = \text{gaminv}(0.95, 1.22, 145.37) = 496.22 \times 10^3$ ac-ft.

8.6.1.3 Analytical Approximations of Probability Distributions of Drought Magnitude

Drought magnitude (accumulated deficit) may be considered as a random sum of random variables, in other words., the sum of L deficits $S_t = x_0 - X_t$, where drought length L is a random variable. The analytical derivation of the probability distribution of drought magnitude is generally cumbersome and closed-form solutions are feasible only in a few cases (e.g., [Sen 1976](#)). However, analytical approximations have been proposed that overcome the difficulties of applying the inferential approach when a small number of droughts are observed. Such analytical approximations are generally based on deriving the moments of drought magnitude as a function of the moments of the individual deficits and the moments of drought length. Such moments can then be used to estimate the parameters of probability distributions by the method of moments. To this end, several authors have adopted the gamma distribution as the underlying distribution of drought magnitude (e.g., [Guven 1983](#), [Shiau and Shen 2001](#), [Bonaccorso et al. 2003](#), [Gonzalez and Valdes 2003](#), [Salas et al. 2005](#), [Mishra et al. 2009](#)).

More specifically, assuming serial independence for the underlying hydrological variable, the expected value and variance of D are given by the following expressions ([Sen 1977](#)):

$$E(D) = E(L) \quad E(S) = \mu_L \mu_S \quad (8-78)$$

$$Var(D) = E(L) Var(S) + Var(L) E^2(S) = \mu_L \sigma_S^2 + \sigma_L^2 \mu_S^2 \quad (8-79)$$

where

individual deficit S = truncated variable $S = x_0 - X_t$ such that $x_0 > X_t$ and t is any time interval,
 μ_L and μ_S = means of L and S , respectively, and
 σ_L^2 and σ_S^2 = corresponding variances.

The gamma distribution with PDF,

$$f_D(d) = \frac{1}{\beta \Gamma(r)} \left(\frac{d}{\beta}\right)^{r-1} e^{-\frac{d}{\beta}}, \quad (8-80)$$

is assumed as the distribution of drought magnitude D where r and β are the parameters. Then using the method of moments and Equations (8-78) and (8-79), the gamma parameters can be expressed as a function of the moments of deficit S and drought length L as

$$r = \frac{\mu_L^2 \mu_S^2}{\mu_L \sigma_S^2 + \sigma_L^2 \mu_S^2} \quad (8-81)$$

$$\beta = \frac{\mu_L \sigma_S^2 + \sigma_L^2 \mu_S^2}{\mu_L \mu_S} \quad (8-82)$$

The foregoing equations allow expressing the PDF of drought magnitude [Equation (8-80)] as a function of the moments of drought length L and deficit S . The moments of L can be determined based on the procedure outlined in Section 8.6.1.1, while the moments of S can be estimated from the sample mean and sample variance of the observed deficits, in other words,

$$\hat{\mu}_S = \frac{1}{k} \sum_{i=1}^k S_i \quad (8-83)$$

$$\hat{\sigma}_S^2 = \frac{1}{k-1} \sum_{i=1}^k (S_i - \hat{\mu}_S)^2 \quad (8-84)$$

Alternatively, another method can be employed for estimating the moments of the individual deficits S , noting that the expected value and the variance of S can be computed as a function of the probability distribution of the underlying hydrological variable X_t . This method is particularly useful in cases of short records or in cases where the threshold level x_0 is small (lower than the sample mean). In these cases, the number of drought events obtained from the historical records will be small, and consequently the statistics derived from them will be unreliable. Bonaccorso et al. (2003) derive the moments of S for the case of normal, log-normal, and gamma-distributed X_t and the related expressions of the parameters r and β of the gamma distribution for drought magnitude, under the assumption of negligible autocorrelation in the series. Table 8-9 gives the mean μ_S and variance σ_S^2 of the deficits, and Table 8-10 gives the parameters r and β for the three referred distributions, where the threshold is parameterized as (Yevjevich 1967)

$$x_0 = \mu_x - \alpha \sigma_x = \mu_x (1 - \alpha Cv_x) \quad (8-85)$$

where μ_x and Cv_x are the mean and the coefficient of variation of the underlying hydrological variable X_t , and α is a threshold coefficient. For instance, if $\alpha = 0$, then $x_0 = \mu_x$.

Example 8-10: Fitting the Probability Distribution of Drought Magnitude for the Annual Flows of the Salso River at Pozzillo Reservoir (Italy) Based on Analytical Approximations

Table 8-11 shows the annual flows of the Salso River at Pozzillo reservoir (Italy) for 1959–1998 (i.e., 40 years of records). The coefficients of variation and skewness and the lag-1 serial correlation are 0.64, 1.51, and –0.02, respectively. Table 8-12 reports the main characteristics of the droughts identified assuming a threshold $x_0 = 159.89$ mm (the long-term mean). The table shows that only nine droughts occurred during the historical period 1959–1998. We are interested in computing the probability of observing a drought with magnitude larger than the maximum observed. However, the number of identified droughts is inadequate to fit a probability distribution to the observed drought statistics.

Therefore, the previously outlined approach will be adopted for deriving the probability distribution of drought magnitude. Such an approach capitalizes on the statistics of the whole deficit series and therefore leads to more reliable estimation of the probability distribution of drought characteristics, especially when the number of observed droughts is limited. We assume the gamma PDF for drought magnitude D as in Equation (8-80), in which the parameters r and β will be estimated using Equations (8-81) and (8-82), where the moments of the deficit S are replaced by their sample moments, and the moments of L are computed from Equations (8-63) and (8-64). The sample moments of the observed deficits S are

$$\hat{\mu}_S = \frac{1}{k} \sum_{i=1}^k S_i = 51.65 \text{ and } \hat{\sigma}_S^2 = \frac{1}{k-1} \sum_{i=1}^k (S_i - \hat{\mu}_S)^2 = 1,857.3$$

in which $k = 27$ is the number of the observed deficits S_i .

Table 8-9. Mean μ_S and Variance σ_S^2 of the Deficits S for Different Distributions of X_r

Distribution of X_r	μ_S	σ_S^2	Other parameters
Normal (μ_x, σ_x)	$\sigma_x \left[-\alpha + \frac{1}{\rho_0} \Phi(-\alpha) \right]$	$\sigma_x^2 \left\{ \frac{\phi(-\alpha)}{\rho_0} \left[\alpha - \frac{\Phi(-\alpha)}{\rho_0} \right] + 1 \right\}$	$\rho_0 = \Phi(-\alpha)$
Log-normal (μ_y, σ_y)	$\exp(\mu_y + \frac{1}{2}\sigma_y^2) \left(1 - \alpha \sqrt{\exp(\sigma_y^2) - 1} - \frac{\Delta}{\rho_0} \right)$	$\exp(2\sigma_y + \sigma_y^2) \left[\frac{\exp(\sigma_y^2)}{\rho_0} \cdot \Psi - \frac{\Delta^2}{\rho_0^2} \right]$	$\rho_0 = \Phi \left[\frac{\sigma_y}{2} + \frac{\ln(1-\alpha C_{V_x})}{\sigma_y} \right]$ $\Delta = \Phi \left[-\frac{\sigma_y}{2} + \frac{\ln(1-\alpha C_{V_x})}{\sigma_y} \right]$ $\Psi = \Phi \left[-\frac{3\sigma_y}{2} + \frac{\ln(1-\alpha C_{V_x})}{\sigma_y} \right]$
Gamma (r_x, β_x)	$\beta_x r_x \left[1 - \alpha C_{V_x} - \frac{\Theta}{\rho_0} \right]$	$\beta_x r_x \left[\frac{\beta_x(r_x+1)}{\rho_0} \Omega - \frac{\beta_x r_x}{\rho_0^2} \Theta^2 \right]$	$\rho_0 = G \left[r_x, r_x(1 - \alpha C_{V_x}) \right]$ $\Theta = G \left[r_x + 1, r_x(1 - \alpha C_{V_x}) \right]$ $\Omega = G \left[r_x + 2, r_x(1 - \alpha C_{V_x}) \right]$

Note that the symbols $\phi(z)$ and $\Phi(z)$ denote the PDF and CDF of the standard normal variable Z. Also $G(a, x) = \frac{1}{\Gamma(a)} \int_0^x t^{a-1} e^{-t} dt$ is the regularized lower incomplete gamma function.
Source: Bonacorso (2002).

Table 8-10. Parameters of the Gamma Distribution of Drought Magnitude for Different Distributions of X_t .

Distribution of X_t	R	β
Normal (μ_x, σ_x)	$\frac{(-\alpha + \frac{\phi(-\alpha)}{p_0})}{p_0 \left(-\alpha + \frac{\phi(-\alpha)}{p_0} \right)^2 - p_1 \left(\frac{\alpha \phi(-\alpha) + \phi^2(-\alpha)}{p_0^2} - 1 \right)}$	$\sigma_x \frac{\left[\frac{p_0}{p_1} \left(-\alpha + \frac{\phi(-\alpha)}{p_0} \right)^2 - \left(\alpha \frac{\phi(-\alpha)}{p_0} + \frac{\phi^2(-\alpha)}{p_0^2} - 1 \right) \right]}{\left(-\alpha + \frac{\phi(-\alpha)}{p_0} \right)}$
Log-normal (μ_y, σ_y)	$\frac{(1 - \alpha Cv_x - \frac{\alpha}{p_0})^2}{p_0 \left(1 - \alpha Cv_x - \frac{\alpha}{p_0} \right)^2 - p_1 \left(\frac{\alpha^2}{p_0^2} - \exp(\sigma_y^2) \frac{\psi}{p_0} \right)}$	$\mu_x \frac{\left[\frac{p_0}{p_1} \left(1 - \alpha Cv_x - \frac{\alpha}{p_0} \right)^2 - \frac{\alpha^2}{p_0^2} + \exp(\sigma_y^2) \frac{\psi}{p_0} \right]}{\left(1 - \alpha Cv_x - \frac{\alpha}{p_0} \right)}$
Gamma (r_x, β_x)	$\frac{(1 - \alpha Cv_x - \frac{\alpha}{p_0})^2}{\left\{ p_0 \left(1 - \alpha Cv_x - \frac{\alpha}{p_0} \right)^2 - p_1 \left[\frac{\alpha^2}{p_0^2} - \frac{\alpha}{p_0} \cdot (Cv_x^2 + 1) \right] \right\}}$	$\mu_x \frac{\left[\frac{p_0}{p_1} \left(1 - \alpha Cv_x - \frac{\alpha}{p_0} \right)^2 - \frac{\alpha^2}{p_0^2} + \frac{\alpha}{p_0} \cdot (Cv_x^2 + 1) \right]}{\left(1 - \alpha Cv_x - \frac{\alpha}{p_0} \right)}$

Source: [Bonaccorso \(2002\)](#), [Cancelliere et al. \(2003\)](#).

Table 8-11. Annual Flows (mm) of the Salso River at Pozzillo Reservoir (1959–1998).

Year	Streamflows	Year	Streamflows	Year	Streamflows	Year	Streamflows
1959	149.72	1969	245.65	1979	158.23	1989	14.66
1960	147.58	1970	101.45	1980	157.10	1990	15.07
1961	138.91	1971	79.91	1981	172.96	1991	61.45
1962	128.81	1972	282.73	1982	138.54	1992	142.12
1963	209.52	1973	511.62	1983	91.21	1993	124.77
1964	334.31	1974	103.02	1984	144.02	1994	171.48
1965	175.08	1975	68.29	1985	202.29	1995	51.45
1966	198.02	1976	395.02	1986	108.79	1996	372.73
1967	201.72	1977	53.41	1987	153.67	1997	109.29
1968	120.16	1978	132.14	1988	157.31	1998	71.56

Table 8-12. Main Characteristics of the Droughts Identified for the Flows of the Salso River at Pozzillo Reservoir (1959–1998), Assuming a Threshold $x_0 = \mu_x = 159.89$ mm.

Begin year	End year	L (years)	D (mm)	I (mm/year)
1959	1962	4	74.56	18.64
1968	1968	1	39.73	39.73
1970	1971	2	138.43	69.21
1974	1975	2	148.48	74.24
1977	1980	4	138.70	34.67
1982	1984	3	105.91	35.30
1986	1993	8	501.31	62.66
1995	1995	1	108.44	108.44
1997	1998	2	138.94	69.47

Conversely, the mean and the variance of L are determined from Equation (8-63) and (8-64), respectively, as

$$E(L) = \frac{1}{p_1} = 3.08 \text{ years and } Var(L) = \frac{1 - p_1}{p_1^2} = 6.39 \text{ years}^2$$

where $p_1 = 0.325$ has been computed following the same procedure as that outlined in Section 8.6.1.1. Then, the parameters r and β of the gamma distribution are computed from Equations (8-81) and (8-82), respectively, as

$$r = \frac{\mu_L^2 \mu_S^2}{\mu_L \sigma_S^2 + \sigma_L^2 \mu_S^2} = 1.109$$

$$\beta = \frac{\mu_L \sigma_S^2 + \sigma_L^2 \mu_S^2}{\mu_L \mu_S} = 143.23$$

Note that for estimating the parameters r and β , the whole series of 27 deficits has been used, which should lead in principle to more reliable estimates as compared with the case when r and β are estimated directly from the observed nine droughts.

Then the probability of observing a drought with a magnitude greater than the largest observed in the historical record, i.e., $D = 501.31$, is computed by

$$P[D > 501.31] = 1 - \int_0^{501.31} \frac{1}{143.23 \Gamma(1.109)} \left(\frac{d}{143.23} \right)^{1.109-1} e^{-\frac{d}{143.23}} dd = 0.037$$

The foregoing integral is computed using the Matlab gamma function command:

$$\text{gamcdf}(501.31, 1.109, 143.23) = 0.963$$

Example 8-11: Deriving the Probability Distribution of Drought Magnitude for the Annual Flows of the Salso River at Pozzillo Reservoir Using an Alternative Method

In this example, the probability distribution of drought magnitude for the Salso River at Pozzillo Reservoir is derived, using the alternative approach outlined previously. More specifically, we are interested in analyzing drought characteristics considering the threshold level $x_0 = 80$ mm. This threshold represents about 50% of the sample mean, and not many drought events will result from the empirical flow data, as Table 8-13 shows, where only six droughts occurred in 1959–1998. Furthermore, the number of deficits is only eight, which is too small to apply the procedure illustrated in Example 8-10. Therefore, the alternative approach will be applied for deriving the probability distributions of drought magnitude. Such an approach capitalizes on the statistics computed from the whole hydrological series and therefore leads to more reliable estimation of the probability distribution of drought characteristics, especially when the number of observed droughts is small.

Assuming the gamma distribution is the underlying model for drought magnitude, its parameters r and β can be determined from the equations in Table 8-10. We also assume that the distribution of the streamflow series for the Salso River is gamma with parameters r_x and β_x . Because the mean and variance of the historical streamflows are $\hat{\mu}_x = 159.89$ and $\hat{\sigma}_x^2 = 10,397$, respectively, using the method of moments we estimate the parameters r_x and β_x as $\hat{r}_x = \hat{\mu}_x^2 / \hat{\sigma}_x^2 = 2.46$ and $\hat{\beta}_x = \hat{\sigma}_x^2 / \hat{\mu}_x = 65.02$. And the coefficient of variation is $\hat{C}_v = \hat{\sigma}_x / \hat{\mu}_x = 0.64$.

Table 8-13. Main Characteristics of the Droughts Identified for the Flows of the Salso River at Pozzillo Reservoir (1959–1998) Assuming a Threshold $x_0 = 80$ mm.

Begin year	End year	L (years)	D (mm)	I (mm/year)
1971	1971	1	0.09	0.09
1975	1975	1	11.71	11.71
1977	1977	1	26.59	26.59
1989	1991	3	148.82	49.61
1995	1995	1	28.55	28.55
1998	1998	1	8.44	8.44

Also, because the assumed threshold is $x_0 = 80$ mm, the threshold coefficient α can be computed from Equation (8-85) as

$$\alpha = \frac{\mu_x - x_0}{\sigma_x} = \frac{159.89 - 80}{101.96} = .783$$

And the parameters r and β of the gamma distribution of drought magnitude are computed using the equations of the last row of Table 8-10. Thus, the following results are obtained:

$$\begin{aligned} p_0 &= G[r_x, r_x(1 - \alpha C_v)] = 0.23, \quad p_1 = 1 - p_0 = 0.77 \\ \Theta &= G[r_x + 1, r_x(1 - \alpha C_v)] = 0.0736, \quad \Omega = G[r_x + 2, r_x(1 - \alpha C_v)] = 0.0192, \\ \hat{r} &= \frac{\left(1 - \alpha C_v - \frac{\Theta}{p_0}\right)^2}{\left\{p_0\left(1 - \alpha C_v - \frac{\Theta}{p_0}\right)^2 - p_1\left[\frac{\Theta^2}{p_0^2} - \frac{\Omega}{p_0}\left(C_v^2 + 1\right)\right]\right\}} = 1.767, \text{ and} \\ \hat{\beta} &= \frac{\mu_x \left[\frac{p_0}{p_1} \left(1 - \alpha C_v - \frac{\Theta}{p_0}\right)^2 - \frac{\Theta^2}{p_0^2} + \frac{\Omega}{p_0} \left(C_v^2 + 1\right) \right]}{\left(1 - \alpha C_v - \frac{\Theta}{p_0}\right)} = 20.55. \end{aligned}$$

Then, the probability that a drought with magnitude greater than the largest observed drought magnitude is computed as

$$P[D > 148.82] = 1 - \int_0^{148.82} \frac{1}{20.55\Gamma(1.767)} \left(\frac{d}{20.55}\right)^{1.767-1} e^{-\frac{d}{20.55}} dd = 0.004$$

Again, the previous integral can be computed using one of the numerical standard routines for computing the gamma integral.

8.6.1.4 Analytical Approximations for Determining the Joint Probability Distributions of Drought Characteristics

In some practical problems, considering two or more drought characteristics may be necessary. For instance, one may be interested in computing the probability that a drought of magnitude D exceeds a certain value given that the duration of the drought is equal to a given number of years. Because the drought characteristics, L , D , and I are not mutually independent, one must use a multivariate

formulation to model their joint occurrence. For this purpose, one may use bivariate distributions for any pair of drought characteristics or copulas (e.g., Salas et al. 2005, Shiau 2006, Serinaldi et al. 2009, Songbai and Singh 2010). Such an approach, however, requires a rather long series of observations, because it requires estimating the parameters of the distributions that are to be fitted to the observed droughts.

An alternative approach is based on conditional distributions, which capitalizes on the links between D and L and between I and L . For example, the bivariate PDF of D and L , $f_{D,L}(d, \ell)$ can be expressed as the product of the conditional distribution of the two variables as (e.g. Salas et al. 2005)

$$f_{D,L}(d, \ell) = f_{D|L=\ell}(d)f_L(\ell) \quad (8-86)$$

where $f_{D|L=\ell}(d)$ is the distribution of D conditional on a fixed value of L , and $f_L(\ell)$ is the marginal PDF of L . A similar expression can be written for the bivariate distribution of I and L as

$$f_{I,L}(i, \ell) = f_{I|L=\ell}(i)f_L(\ell) \quad (8-87)$$

Thus, the joint distributions $f_{D,L}(d, \ell)$ and $f_{I,L}(i, \ell)$ can be determined once the conditional distributions $f_{D|L=\ell}(d)$ and $f_{I|L=\ell}(i)$ and the marginal distribution $f_L(\ell)$ are known. Some authors have assumed a parametric distribution for $D|L$, and have estimated the parameters from observed droughts (e.g., Guven 1983, Sharma 1995, Shiau and Shen 2001). In some cases, due to the limited number of droughts that can be observed from the available records, synthetic generation (Wang and Salas 1989; Shiau and Shen 2001) or long hydrologic series reconstructed from tree ring records (e.g., Gonzalez and Valdes 2003, Biondi et al. 2005) have been utilized.

Alternatively, an approach similar to that described in Section 8.6.1.3 can be employed for estimating the parameters of the distribution of $D|L$ that capitalizes on analytical expressions of the moments of drought magnitude. More specifically, the approximate moments of drought magnitude computed based on the distribution of the underlying process X_t and on the threshold are used to estimate the parameters by the method of moments. This enables exploiting the available information from the observed series, thus allowing a reliable estimation of the distribution of drought characteristics even for a relatively short sample series.

Assuming the underlying series X_t is iid., the mean and variance of drought magnitude conditional on a fixed drought length $L=\ell$ are given respectively by

$$E(D|L=\ell) = \ell E(S) \quad (8-88)$$

$$Var(D|L=\ell) = \ell Var(S) \quad (8-89)$$

However, the iid assumption is not valid because most hydrologic series exhibit significant autocorrelation. In this case, the computation of the conditional moments of drought magnitude is more involved, and no closed-form solution is available. Nevertheless, some approximations have been suggested (e.g., Salas et al. 2005, Biondi et al. 2005, Cancelliere and Salas 2010). For example, Cancelliere and Salas (2010) provide empirical approximations that enable computing the conditional moments as a function of the skewness coefficient of the underlying variable X_t , the threshold parameter α , and the lag-1 autocorrelation coefficient ρ_1 . The proposed approximations for the mean and the variance of drought magnitude of fixed length ℓ are (Cancelliere and Salas 2010)

$$E(D_\ell) = \mu_S a_m \ell^{b_m} \quad (8-90)$$

$$Var(D_\ell) = \sigma_S^2 a_v \ell^{b_v} \quad (8-91)$$

where $E(D_\ell)$ and $Var(D_\ell)$ are respectively the expected value and variance of the drought magnitude of length ℓ for series that are autocorrelated and skewed; μ_S and σ_S^2 are respectively the expected value and variance of a single-year deficit assuming that the series are skewed but uncorrelated, thus they are functions of the given marginal distribution; and the threshold x_0 , and the parameters a_m , b_m , a_v , and b_v are related to ρ_1 and x_0 through the following expressions:

$$a_m = 1.0 + (.6983\alpha - .5592)\rho_1 + (-.6634\alpha - .3418)\rho_1^2 \quad (8-92a)$$

$$b_m = 1.0 + (-0.1840\alpha + 0.5903)\rho_1 + (0.1865\alpha + 0.0839)\rho_1^2 \quad (8-92b)$$

$$a_v = 1.0 + (0.7415\alpha - 1.0325)\rho_1 + (-0.7969\alpha - 0.0928)\rho_1^2 \quad (8-93a)$$

$$b_v = 1.0 + (-0.4414\alpha + 1.078)\rho_1 + (0.4175\alpha + 0.5707)\rho_1^2 \quad (8-93b)$$

Note that for $\rho_1 = 0$, $E(D_\ell) = \mu_S\ell$ and $Var(D_\ell) = \sigma_S^2\ell$ because $a_m = b_m = a_v = b_v = 1$.

[Cancelliere \(2008\)](#) compares several distributions by simulation, including log-normal, gamma, and beta, among others, for drought magnitude conditioned on a fixed drought length where the underlying series is autocorrelated. In particular, the method of moments has been applied to estimate the parameters of each distribution, using the approximate moments derived in Equations (8-90) and (8-91). The results of the comparisons based on statistical goodness-of-fit tests reveal that the beta distribution is to be preferred, besides it is bounded, as is the case of the drought magnitude.

The beta PDF takes the form ([Johnson et al. 1994](#))

$$f_{D|L=\ell}(d) = \frac{1}{B(p, q)} \frac{(d-a)^{p-1}(b-d)^{q-1}}{(b-a)^{p+q-1}} \quad (a \leq d \leq b) \quad (8-94)$$

where $B(p, q)$ is the complete beta function, and a and b are the lower and upper bounds, respectively. In our case, $a=0$ and $b=\ell x_o$, because a drought of length ℓ cannot have magnitude greater than ℓx_o , and the parameters p and q can be estimated as a function of the first two moments of the drought magnitude $\mu_D = E(D_\ell)$ and $\sigma_D^2 = Var(D_\ell)$ as ([Cancelliere and Salas 2010](#))

$$p = \left(\frac{\mu_D}{\sigma_D} \right)^2 \left(1 - \frac{\mu_D}{\ell x_o} \right) - \frac{\mu_D}{\ell x_o} \quad (8-95)$$

$$q = \frac{\mu_D(\ell x_o - \mu_D)}{\sigma_D^2} - (1 + p) \quad (8-96)$$

where μ_D and σ_D^2 are determined from Equations (8-90) and (8-91), respectively. Then, the bivariate PDF of drought magnitude and length takes the following form:

$$f_{D,L}(d, \ell) = \frac{1}{B(p, q)} \frac{(d)^{p-1}(\ell x_o - d)^{q-1}}{(\ell x_o)^{p+q-1}} f_L(\ell), \quad (0 \leq d \leq \ell x_o) \quad (8-97)$$

where $f_L(\ell)$ is the PDF of drought length (Section 8.6.1.1).

Furthermore, from the conditional distribution of drought magnitude given drought length, the conditional distribution of drought intensity I given drought length L can be obtained. Indeed, because drought intensity is the ratio of drought magnitude and drought length, in other words, $I = D/L$, the conditional PDF of drought intensity I given a fixed length $L = \ell$ can be derived from Equation (8-94) as

$$f_{I|L}(i) = \frac{1}{B(p, q)} \frac{(i)^{p-1} (x_0 - i)^{q-1}}{(x_0)^{p+q-1}}, \quad (0 \leq i \leq x_0) \quad (8-98)$$

where p and q are given by Equations (8-95) and (8-96), respectively. Thus, the bivariate PDF of drought intensity and length can be found as (Cancelliere and Salas 2010)

$$f_{I,L}(i, \ell) = \frac{1}{B(p, q)} \frac{(i)^{p-1} (x_0 - i)^{q-1}}{(x_0)^{p+q-1}} f_L(\ell), \quad (0 \leq i \leq x_0) \quad (8-99)$$

By integrating the bivariate PDFs, the occurrence probability of various drought events can be found (Salas et al. 2005). For example, for specific drought events using the previously described models we have

- (1) for drought event $E = [D > d_0 \text{ and } L = \ell_0 (\ell_0 = 1, 2, \dots)]$:

$$P[D > d_0, L = \ell_0] = \int_{d_0}^{\ell_0 x_0} f_{D,L}(z, \ell_0) dz = f_L(\ell_0) \int_{d_0}^{\ell_0 x_0} \frac{1}{B(p, q)} \frac{(z)^{p-1} (\ell_0 x_0 - z)^{q-1}}{(\ell_0 x_0)^{p+q-1}} dz \quad (8-100)$$

- (2) for drought event $E = [D > d_0 \text{ and } L \geq \ell_0 (\ell_0 = 1, 2, \dots)]$:

$$\begin{aligned} P[D > d_0, L \geq \ell_0] \\ = \sum_{\ell=\ell_0}^{\infty} \int_{d_0}^{\ell_0 x_0} f_{D,L}(z, \ell) dz = \sum_{\ell=\ell_0}^{\infty} \left[f_L(\ell) \int_{d_0}^{\ell_0 x_0} \frac{1}{B(p, q)} \frac{(z)^{p-1} (\ell x_0 - z)^{q-1}}{(\ell x_0)^{p+q-1}} dz \right] \end{aligned} \quad (8-101)$$

- (3) for drought event $E = [I > i_0 \text{ and } L = \ell_0 (\ell_0 = 1, 2, \dots)]$:

$$P[I > i_0, L = \ell_0] = \int_{i_0}^{x_0} f_{I,L}(z, \ell_0) dz = f_L(\ell_0) \int_{i_0}^{x_0} \frac{1}{B(p, q)} \frac{(z)^{p-1} (x_0 - z)^{q-1}}{(x_0)^{p+q-1}} dz \quad (8-102)$$

- (4) for drought event $E = [I > i_0 \text{ and } L \geq \ell_0 (\ell_0 = 1, 2, \dots)]$:

$$\begin{aligned} P[I > i_0, L \geq \ell_0] \\ = \sum_{\ell=\ell_0}^{\infty} \int_{i_0}^{x_0} f_{I,L}(z, \ell) dz = \sum_{\ell=\ell_0}^{\infty} \left[f_L(\ell) \int_{i_0}^{x_0} \frac{1}{B(p, q)} \frac{(z)^{p-1} (x_0 - z)^{q-1}}{(x_0)^{p+q-1}} dz \right] \end{aligned} \quad (8-103)$$

Furthermore, the marginal probability of drought events $E = \{D > d_0\}$ or $E = \{I > i_0\}$ can be obtained from Equations (8-101) or (8-103), respectively, by letting $\ell_0 = 1$. Note that despite the

apparent complexity of the aforementioned expressions, the integrations can be carried out efficiently using numerical tools for the beta PDF that are available in most statistical software.

8.6.2 Return Period of Multiyear Droughts

The return period of a drought event may be defined as the average elapsed time, or mean interarrival time, between two such events (Lloyd 1970, Loaiciga and Mariño 1991, Fernández and Salas 1999a). Shiau and Shen (2001) develop a formulation for determining the return period of droughts with magnitude greater than or equal to a given value. Cancelliere and Salas (2004) extend such a formulation for drought length in periodic series, while Cancelliere et al. (2003), Gonzalez and Valdes (2003), Salas et al. (2005), and Biondi et al. (2005) include other characteristics such as drought length and intensity, under the assumption of lag-1 Markov dependence.

The return period (or mean recurrence time) of droughts for any of the drought scenarios and events E as specified previously, e.g., $E = \{L = \ell_0 \text{ and } D > d_0\}$ may be estimated as the average of the recurrence times as

$$T = \frac{1}{(N_E - 1)} \sum_{j=1}^{N_E-1} T_E(j) \quad (8-104)$$

in which $T_E(j)$ denotes the recurrence time of two successive drought events and N_E is the number of such drought events. Equation (8-104) is particularly useful for determining the return periods of drought events based on a historical sample (particularly for a long record) or a sample generated from a stochastic model. An alternative procedure based on analytical formulations is given in the following.

To derive an analytical expression for estimating T , the formulation proposed by Shiau and Shen (2001) for the case of drought events characterized only by the drought magnitude can be extended to the more general case of drought events jointly defined in terms of drought magnitude and length (or drought intensity and length). For this purpose, the interarrival time $T(E)$ between two droughts events E [e.g., $E = \{D > d_0 \text{ and } L = \ell_0\}$] may be written as (Cancelliere and Salas 2002, Gonzalez and Valdes 2003, Salas et al. 2005)

$$T = \frac{E(L) + E(L_n)}{P(E)} \quad (8-105)$$

where $E(L)$ and $E(L_n)$ are the expected values of the duration of specific drought event and nondrought event, respectively, and $P(E)$ is the joint probability of the specific drought event that may be determined from Equations (8-100)–(8-103) as the case may be. For the case of a lag-1 Markov process, $E(L)$ can be computed from Equation (8-68) and $E(L_n)$ can also be obtained from Equation (8-68) by replacing p_{01} with p_{10} . Alternatively, $E(L)$ and $E(L_n)$ can be estimated from the sample mean of the observed drought length and nondrought length, respectively. Note that although for an autocorrelated process, the independence assumption between drought events is not exactly met, yet Equation (8-105) provides an excellent approximation (e.g., Salas et al. 2005, Cancelliere and Salas 2010).

Example 8-12: Computing the 50 Year Drought Magnitude for the Salso River at Pozzillo Reservoir

In this example, the 50 year (return period) drought magnitude for the Salso River at Pozzillo Reservoir (see Examples 8-10 and 8-11) will be computed assuming a threshold x_0 equal to the mean.

For the drought event $E = \{D > d\}$, i.e., a drought with a magnitude greater than d , the associated return period will be computed by Equation (8-105), in other words,

$$T = \frac{E(L) + E(L_n)}{P(D > d)}$$

In our case, $E(L)$ and $E(L_n)$ will be estimated using the sample means of the observed drought length \bar{L} and nondrought length \bar{L}_n . The desired T year magnitude d can be computed by solving for d in the following equation:

$$P[D > d] = \frac{\bar{L} + \bar{L}_n}{T}$$

where the probability can be computed by making use of the gamma CDF as in Example 8-10. In our case, the following results are obtained:

$$\bar{L} = 3 \text{ years}, \quad \bar{L}_n = 1.5 \text{ years}, \quad \text{and } P[D > d] = \frac{\bar{L} + \bar{L}_n}{T} = 0.09$$

Then, the drought magnitude d can be computed (as in Example 8-10) as the value with exceedance probability 0.09. Recalling from Example 8-10 that the parameters of the gamma distribution of drought magnitude for Salso River at Pozzillo Reservoir are $r = 1.109$ and $\beta = 143.23$ the following Matlab command is used to find the 50 year accumulated deficit d as

$$d = \text{gaminv}(1 - 0.09, 1.109, 143.23) = 372.12 \text{ mm}$$

Example 8-13: Calculating the Return Period of Drought Magnitude and Length for the Annual Flows of the Poudre River at the Mouth of the Canyon (Table 8-7)

In this example, we will analyze drought magnitude and length for the annual flows of the Poudre River at the Mouth of the Canyon. In particular, the return period associated with a drought of length $L = 3$ and magnitude greater than 300,000 ac-ft will be computed using the analytical approximations for the joint distribution of drought length and magnitude illustrated in Section 8.6.1.4. In what follows we will use the threshold $x_0 = 299,000$ acre-ft (the sample mean) and the threshold coefficient $\alpha = 0$ [refer to Equation (8-85)].

The return period of such critical drought will be computed by Equation (8-105), in other words,

$$T = \frac{E(L) + E(L_n)}{P(L = \ell_0, D > d_0)} = \frac{E(L) + E(L_n)}{P(L = 3, D > 300)}$$

where $E(L)$ and $E(L_n)$ are, respectively, the expected values of the durations of specific drought events and nondrought events. These expected values can be estimated as the sample mean of observed drought length \bar{L} and nondrought length \bar{L}_n , which gives $\bar{L} = 2.4$ years and $\bar{L}_n = 1.9$ years. Furthermore, the probability $P(L = 3, D > 300)$ can be computed by Equation (8-100). The parameters p and q of the beta distribution can be estimated by Equations (8-95) and (8-96), in which the mean and standard deviation of drought magnitude $E(D_\ell)$ and $Var(D_\ell)$, are given by the empirical expressions (8-90) and (8-91), respectively.

The coefficients in Equations (8-90) and (8-91) are computed considering that $\alpha = 0$ and $\rho_1 = 0.153$ (Example 8-8) as

$$a_m = 1.0 + (.6983\alpha - .5592)\rho_1 + (-.6634\alpha - .3418)\rho_1^2 = 0.906$$

$$b_m = 1.0 + (-0.1840\alpha + 0.5903)\rho_1 + (0.1865\alpha + 0.0839)\rho_1^2 = 1.092$$

$$a_v = 1.0 + (0.7415\alpha - 1.0325)\rho_1 + (-0.7969\alpha - 0.0928)\rho_1^2 = 0.840$$

$$b_v = 1.0 + (-0.4414\alpha + 1.078)\rho_1 + (0.4175\alpha + 0.5707)\rho_1^2 = 1.178$$

and the moments $\hat{\mu}_s$ and $\hat{\sigma}_s^2$ will be determined from the expressions reported in Table 8-9. For this purpose, we assume that the marginal distribution of the Poudre River annual streamflow series is log-normal, and applying the method of moments, the parameters are estimated as

$$\hat{\sigma}_y = \sqrt{\ln\left(\frac{\hat{\sigma}_x^2}{\hat{\mu}_x^2} + 1\right)} = 0.347 \text{ and } \hat{\mu}_y = \ln(\hat{\mu}_x) - \frac{\hat{\sigma}_y^2}{2} = 5.64$$

in which $\hat{\mu}_x = 299$ and $\hat{Cv}_x = 0.36$. Then the mean $\hat{\mu}_s$ and the variance $\hat{\sigma}_s^2$ of the individual deficits are computed as (Table 8-9)

$$\hat{\mu}_s = \exp\left(\hat{\mu}_y + \frac{1}{2}\hat{\sigma}_y^2\right)\left(1 - \alpha\sqrt{\exp(\hat{\sigma}_y^2) - 1} - \frac{\Delta}{p_0}\right) = 72.401$$

$$\hat{\sigma}_s^2 = \exp(2\hat{\mu}_y + \hat{\sigma}_y^2)\left[\frac{\exp(\hat{\sigma}_y^2)}{p_0} \cdot \Psi - \frac{\Delta^2}{p_0^2}\right] = 2,071.44$$

where

$$p_0 = \Phi\left[\frac{1}{2}\hat{\sigma}_y + \frac{\ln(1 - \alpha\hat{Cv}_x)}{\hat{\sigma}_y}\right] = 0.569, \quad \Delta = \Phi\left[-\frac{1}{2}\hat{\sigma}_y + \frac{\ln(1 - \alpha\hat{Cv}_x)}{\hat{\sigma}_y}\right] = 0.431, \text{ and}$$

$$\Psi = \Phi\left[-\frac{3}{2}\hat{\sigma}_y + \frac{\ln(1 - \alpha\hat{Cv}_x)}{\hat{\sigma}_y}\right] = 0.301.$$

For $\ell = 3$, Equations (8-90) and (8-91) yield, respectively,

$$\hat{\mu}_D = \hat{\mu}_s a_m \ell^{b_m} = 217.89 \text{ and } \hat{\sigma}_D^2 = \hat{\sigma}_s^2 a_v \ell^{b_v} = 6,348.40,$$

and the parameters p and q of the beta distribution are obtained from Equations (8-95) and (8-96), respectively, as

$$p = \left(\frac{\hat{\mu}_D}{\hat{\sigma}_D}\right)^2 \left(1 - \frac{\hat{\mu}_D}{\ell x_o}\right) - \frac{\hat{\mu}_D}{\ell x_o} = 5.419 \text{ and } q = \frac{\hat{\mu}_D(\ell x_o - \hat{\mu}_D)}{\hat{\sigma}_D^2} - (1 + p) = 16.89$$

Therefore, the probability of the drought $E = \{D > d_0 \text{ and } L = 3\}$ is obtained from Equation (8-100) as

$$P[D > d_o, L = 3] = f_L(3) \int_{d_0}^{3x_0} \frac{1}{B(p,q)} \frac{(z)^{p-1}(3x_0 - z)^{q-1}}{(3x_0)^{p+q-1}} dz$$

From Example 8-8, $f_L(3) = (1 - 0.41)^{3-1} 0.41 = 0.143$ and the integral can be computed using, for instance, the Matlab function betacdf as

$$\int_{d_0}^{3x_0} \frac{1}{B(p,q)} \frac{(z)^{p-1} (3x_0 - z)^{q-1}}{(3x_0)^{p+q-1}} dz = 1 - \text{betacdf}[d_0/(3^*x_0), p, q] = 0.155$$

It follows that $P[D > d_0, L = 3] = 0.0222$, and the corresponding return period is

$$T = \frac{\bar{L} + \bar{L}_n}{P[D > d_o, L = 3]} = 194 \text{ years}$$

The foregoing procedure can be repeated for different values of d_0 and L and for different types of drought events, such as those indicated in Equations (8-100)–(8-103). For instance, Figure 8-13 shows the return periods of droughts defined as $E = \{D > d_0 \text{ and } L = \ell_0 (\ell_0 = 1, 2, \dots)\}$, which were obtained from Equation (8-105) for various values of the deficit coefficient $\delta = d_0/x_0$ and threshold $x_0 = \mu_x$.

8.7 REGIONAL ANALYSIS OF DROUGHTS

Drought identification and characterization in a region is an important component of drought mitigation and management studies. While drought analysis at individual sites provides useful information on drought occurrences in a watershed, regional analysis enables identifying droughts that affect a region, considering the duration, magnitude (or intensity), and areal extent of the drought based on data that are available at several sites of the study region (e.g., Tase 1976, Santos 1983, Rossi et al. 1992, Shin and Salas 2000, Rossi and Cancelliere 2003). As presented in this chapter regional analysis of drought differs from regional analysis of low flows. In regional analysis of low flows, the objective is determining low-flow characteristics at sites with short records or at ungauged

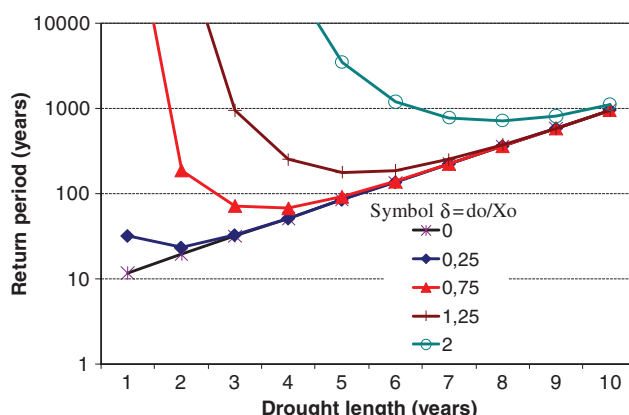


Figure 8-13. Return period of drought events defined by $E = \{D > d_0 \text{ and } L = \ell_0 (\ell_0 = 1, 2, \dots)\}$ for the Poudre River at Mouth of the Canyon annual flows obtained from Equation (8-105) for various values of the deficit coefficient δ and the threshold $x_0 = \mu_x$.

Source: Cancelliere and Salas (2010).

sites, while in regional analysis of drought one would like to identify and characterize the variability of drought as it varies through the region. Presenting regional drought analysis in detail would be too lengthy for this chapter. We simply outline the underlying definitions following the method originally developed by [Tase \(1976\)](#).

Let us consider a region having a total area A and m precipitation stations located within and nearby the area of interest. Station k has an area of influence denoted by $s(k)$ (e.g., defined by the Thiessen polygon), which may be expressed as a fraction $a(k)$ of the total area as

$$a(k) = \frac{s(k)}{\sum_{j=1}^m s(j)} \quad (8-106)$$

in which $A = s(1) + s(2) + \dots + s(m)$. In addition, we will denote by $X_t(k)$ the precipitation at station k at time t , and $x_0(k)$ the threshold level for station k . Then the following indicator variable can be defined for station k :

$$\begin{aligned} I_t(k) &= 0 && \text{if } X_t(k) \geq x_0(k) \\ I_t(k) &= 1 && \text{if } X_t(k) < x_0(k) \end{aligned} \quad (8-107)$$

which indicates that if a deficit occurs at time t at site k , i.e., $X_t(k) < x_0(k)$, then $I_t(k) = 1$. And the fraction of the area affected by deficit in a time t is denoted as *areal coverage of deficit* and is given by the index

$$Ad_t = \sum_{k=1}^m a(k) I_t(k) \quad (8-108)$$

Then a regional deficit occurs at time t if the areal coverage of deficit Ad_t exceeds a given threshold a_c ([Tase 1976](#)). Accordingly, the *areal (regional) deficit* D_t can be determined by

$$D_t = \sum_{k=1}^m a(k) I_t(k) [x_0(k) - X_t(k)] \quad \text{if } Ad_t \geq a_c \quad (8-109)$$

The index Ad_t is a measure of the area affected by deficit, expressed as a fraction of the total area that ranges between 0 and 1, while the index D_t provides a measure of the total amount of deficit in the area (region). It is basically the sum of the deficits at each site weighted by the corresponding influence areas (computed for example by the Thiessen polygons).

Regional drought is defined as a consecutive sequence of regional deficits preceded and succeeded by surpluses. Then the duration of the regional drought can be characterized by

$$L = t_f - t_i + 1 \quad (8-110)$$

where t_i and t_f are such that $D_{t_i-1} = 0$, $D_t > 0$ for $t_i \leq t \leq t_f$, and $D_{t_f+1} = 0$. In addition, *regional drought magnitude* can be determined as

$$DM = \sum_{t=t_i}^{t_f} D_t \quad (8-111)$$

and the *regional drought intensity* by

$$DI = \frac{DM}{L} \quad (8-112)$$

Furthermore, the *mean areal coverage of drought* can be computed by

$$AD = \frac{1}{L} \sum_{t=t_i}^{t_f} Ad_t \quad (8-113)$$

Once the time series of regional deficit D_t and the threshold a_c have been determined, one can apply the drought analysis methods described previously for determining the statistical properties of droughts, such as expected values, variances, distribution, and return period of drought events. Note that the foregoing definitions of regional drought have been illustrated using precipitation as the key hydrological input representing water supply in the study region, and several developments and applications thereof are available (e.g., [Tase 1976](#), [Santos 1983](#), [Rossi et al. 1992](#), [Rossi and Cancelliere 2003](#)). However, the application of regional drought as described previously for hydrological inputs other than precipitation have not been made.

8.8 EFFECTS OF HYDRAULIC STRUCTURES ON LOW FLOWS

Human intervention directly and indirectly alters the natural flow regime of river systems ([Wang and Cai 2009](#)). Indirect effects occur by changes in natural phenomena such as climate and changes in vegetation, land use, soil, and topography. River works such as dams, river diversions, major mining explorations and operational activities, and groundwater pumping for many water supply purposes directly alter the natural flow regime of streams and river systems. For several decades, many studies have been conducted to identify the effects of water development on the natural streamflows. For example, [Dynesius and Nilsson \(1994\)](#) report that 77% of the total flow of the largest rivers in the United States, Canada, Europe, and the former Soviet Union was affected by dams, reservoirs, aqueducts, and irrigation. They estimate that hydrologic alterations have occurred in 60% of rivers all over the world, including more than 85% of US rivers and 60% to 65% of European rivers. In many of those rivers significant changes of the natural flow regime have been observed, such as decreasing flows during the wet season while increasing flows during the dry season. While control of natural flow regime has proper functions for regulating water supply and flood control, it conflicts with other functions of the streams and rivers such as those related to their natural environment and ecology.

The variability of streamflows through time at a given cross-section of a river is called *flow regime*. Natural flow regime refers to the condition before the development of rivers, without controlling the flow regime by hydraulic structures. Rivers have their own natural flow regime characteristics based on the climate, morphology of the river basin, and land use, and these flow regime characteristics maintain the health of the river environment. However, artificial river works such as dams changes the natural flow regime and consequently their various statistical characteristics.

Flow duration curves (FDC) and the *Indicator of Hydrologic Alteration* (IHA) have been useful for identifying the degree of alteration in flow regime resulting from the effects of hydraulic structures. Natural flows vary over the year, and FDC is one of the methods used to identify the flow variability from low flows to floods. An FDC for a given site of a river is a plot of flow against the percentage of time the flow has been equaled or exceeded. Flow records of 10 years or more adequately define the shape of the curve ([Hadley et al. 1987](#), [Maheshwari et al. 1995](#), [Subramanya 1994](#)). In low-flow studies, the main interest is the low-flow section of a FDC. The section may be determined as part of the curve with flows below median flow that corresponds to the discharge equal to or exceeding 50% ([Smakhtin 2001](#)). The Indicators of Hydrologic Alteration (IHA),

developed by The Nature Conservancy ([Richter et al. 1997](#)), are based on 32 indexes that define a series of biologically relevant hydrologic attributes and then quantify hydrologic alterations associated with anticipated perturbations arising from the effect of hydraulic structures by comparing the hydrologic regimes from pre-impact and post-impact time frames. [Poff et al. \(1997\)](#) and [Richter et al. \(1997\)](#) classify flow regime in terms of magnitude of flow, frequency of its occurrence, duration, timing of a specific flow, and rate of change. [Zhang et al. \(2015a, b\)](#) assess temporal and spatial alteration of flow regimes in some reservoir-regulated rivers in China using IHA. During the post-regulation period, they show a decrease in the high-flow magnitudes and an increase in the low flows (relative to those during the pre-regulation period). Table 8-14 shows several flow regime characteristics related to low flows.

Much has been written about the impacts on low flows by hydraulic structure such as dams (e.g., [Homa et al. 2013](#)). The typical differences in the FDCs are that the flows, at the low-flow section of the FDC during the post-impact period, become greater than those for the pre-impact period. However, the opposite occurs for the flows at the high-flow section of the FDC (e.g., [Gippel and Stewardson 1995](#), [Gustard et al. 1989](#), [Hadley et al. 1987](#), [McMahon and Finlayson 2003](#)). Also, the annual minimum flows affected by regulation by dams generally increase compared with the pre-regulation period ([Richter et al. 1997](#), [Magilligan and Nislow 2005](#)).

Figure 8-14 shows the Han River in Korea where several dams have been constructed. The multipurpose dams impound water during the rainy season (June–September) and then the stored waters in the reservoirs are released to be used for water supply in urban areas during the low-flow period (November–March). Likewise, the Geum River has two multipurpose dams that also store the rain waters that are then released to be used downstream during low-flow periods. For illustration, Figure 8-15 shows the comparison of the average daily flows obtained using the flow data for the pre-impact period (1921–1940) and the flows for the post-impact period (1988–2007). Clearly the flows during the low-flow period are generally larger in the post-impact period than in the pre-impact period. Also, Figure 8-16 shows the comparison of the FDCs obtained for the two periods. As expected, the flows in the lower portion of the curve are bigger for the post-impact period than for the pre-impact period. This effect also becomes evident for the 1 day and 30 day minimum flows as shown in Figures 8-17 and 8-18, respectively.

Table 8-14. Low-Flow Hydrologic Parameters Used in the Indicators of Hydrologic Alteration (IHA).

IHA statistics group	Regime characteristics	Low-flow hydrologic parameters
Group 2: Magnitude and duration of annual extreme discharge conditions	Magnitude Duration	Annual minima. 1 day means Annual minima. 3 day means Annual minima. 7 day means Annual minima. 30 day means Annual minima. 90 day means
Group 3: Timing of annual extreme discharge conditions	Timing	Julian date of each annual 1 day minimum discharge
Group 4: Frequency and duration of high and low pulses	Frequency Duration	No. of low pulses each year Mean duration of low pulses within each year
Group 5: Rate and frequency of water condition changes	Rate of change Frequency	Means of all negative differences between consecutive daily values No. of falls

Source: Modified from [Richter et al. \(1997\)](#).

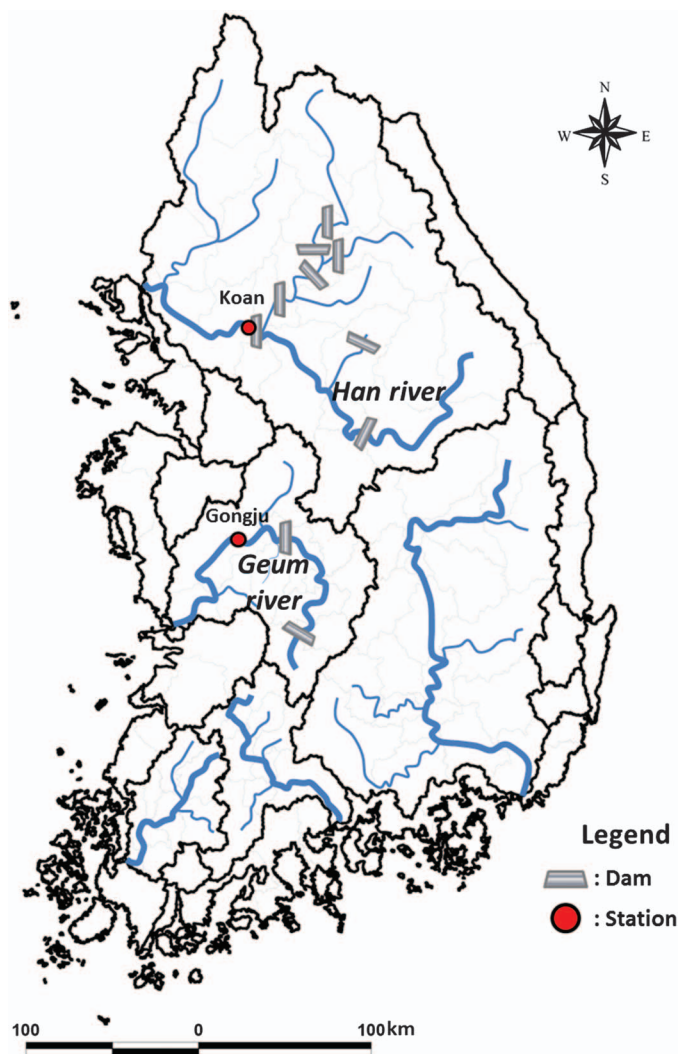


Figure 8-14. The Han and Geum river basins in Korea.

8.9 CLOSING REMARKS

In the statistical analysis of low flows and droughts discussed in this chapter we made the implicit assumption that the underlying data and models thereof are stationary (i.e., the model statistics and parameters remain constant through time). However, this assumption may not be valid in some cases. The basic data used for deriving low flows and droughts may be nonstationary for several reasons such as human intervention in the landscape and water cycle, natural events such as volcanic explosions or forest fires, the effect of low-frequency components of oceanic-atmospheric phenomena, and global warming (Salas et al. 2012). Numerous studies and reports assess changes (e.g., increasing or decreasing trends) in low-flow conditions in individual rivers, regions, and worldwide (e.g., Lins and Slack 1999, Douglas et al. 2000, Yue et al. 2003, Svensson et al. 2005, Hannaford and Marsh 2006), and the results of either significant increases, decreases, or no changes vary depending on the country and region of study and the tests utilized.

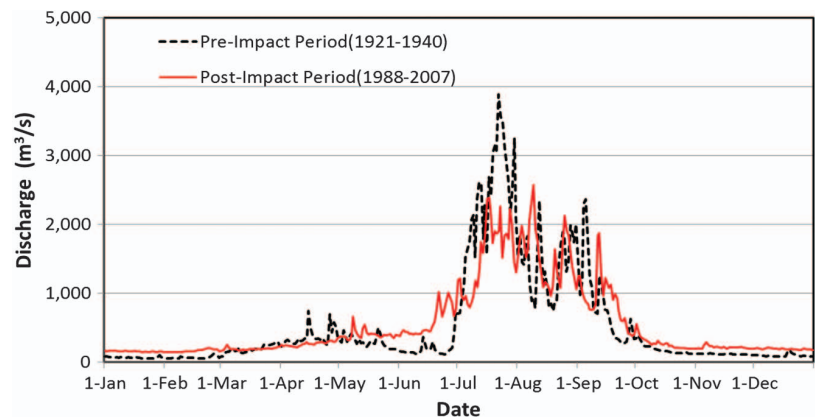


Figure 8-15. The daily average flows for the pre- and post-regulation periods in the Han river at Koan station, Korea.

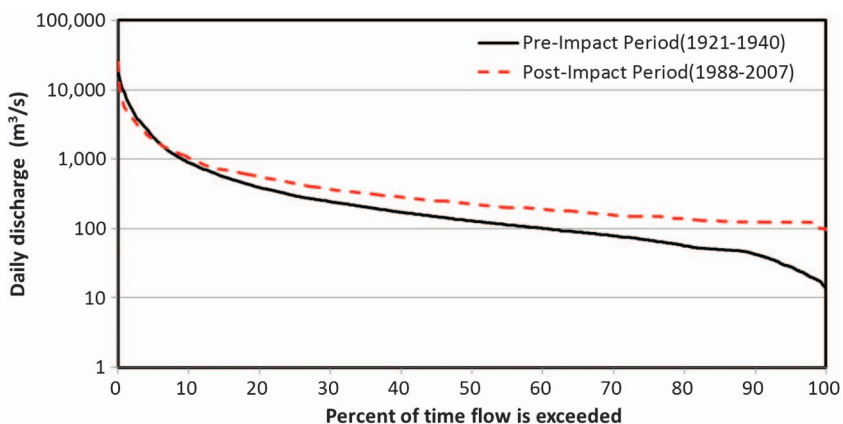


Figure 8-16. Daily flow duration curve in the Han River at Koan, Korea.

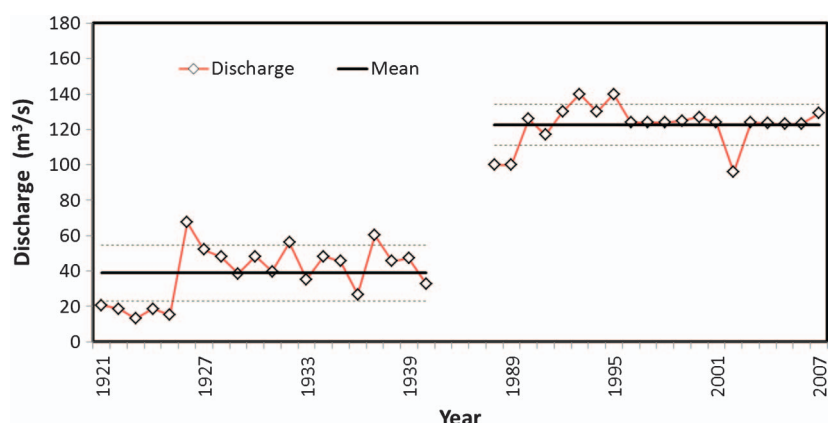


Figure 8-17. 1 day minimum flows for the Han River at the Koan station during the pre-impact and post-impact periods.

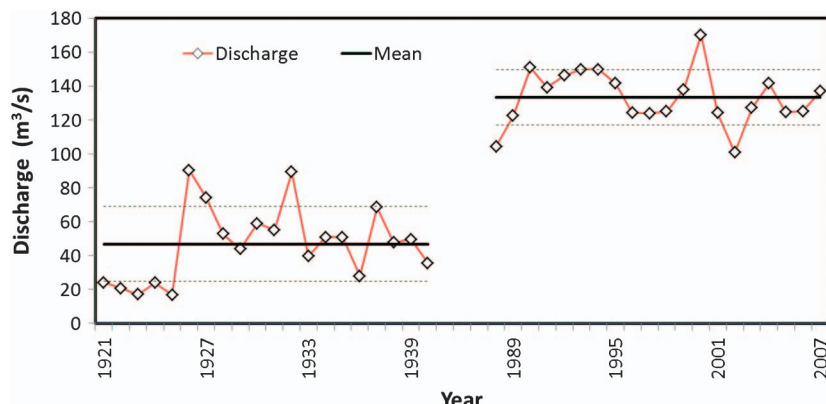


Figure 8-18. 30 day minimum flows for the Han River at the Koan station during the pre-impact and post-impact periods.

In most if not all cases, the justification of such studies has been the concern for the possible effects of anthropogenic global climate change on low flows and droughts. However, determining the cause of any change in low flows is not an easy task. The problem is even more difficult when trying to assess with confidence the impacts of future climate change because of the uncertainties in climate models and the complexity of the relationships of various components of the hydrologic cycle (Hannaford and Marsh 2006). In some cases, such as in the Midwest in the United States, changes in low flows may be related to similar changes in precipitation (e.g., Douglas et al. 2000). However, it has been argued that in some places, such as Iowa (where agricultural lands comprise more than 70% of the land area), increases in precipitation alone do not explain the observed increases in baseflow and most likely result from improvements in land management practices (Schilling and Libra 2003). In addition, studies in the United Kingdom based on a benchmark network of 120 relatively undisturbed catchments indicate no compelling evidence of trends in low flows (Hannaford and Marsh 2006). Furthermore, studies based on 21 daily river flows in many locations worldwide suggest increases in low flows for 10 of the stations (Svensson et al. 2005), and the authors argue that such increases are not consistent with an intensification of the hydrological cycle in a warming climate that would result in more severe droughts and that the cause of such increases may be the increasing number of reservoirs in the basins. The authors conclude that such “modifications to the river flow regime would likely obscure any recent alteration in the hydrological cycle due to climate change.”

Despite the limitations and uncertainties involved in projecting the global climate into the future, many studies aim to determine the impacts of climate change on low flows and droughts at the continental, country, regional, and basin scales (e.g., Ryu et al. 2011, van Lanen et al. 2007). In addition to the difficulty of quantifying the effects of land-use changes on low flows and droughts, distinguishing between the effects of low-frequency components of the oceanic-atmospheric system and those from global warming is not feasible at present. Studies addressing the effect of large-scale low-frequency components of the climate system on the variability of runoff and droughts include, for example, Ozger et al. (2009) and Gudmundsson et al. (2011). Furthermore, some studies (e.g., Dai et al. 2004) have attributed the severity of droughts in the past decades to global warming. However, Sheffield et al. (2012b) argue that several studies and reports, including the IV Assessment Report of the Intergovernmental Panel on Climate Change (IPCC Climate Change 2007), have overestimated the increase of global drought because the computations were made using the Palmer Drought Severity Index (PDSI) based on a temperature-driven potential evapotranspiration (PE). However, the drought estimates using the same PDSI, but where PE is determined based on a more realistic model involving energy, humidity, and wind speed, suggested that minor change in drought occurred in the past decades (Sheffield et al. 2012b).

As reported in Section 8.6, a problem in characterizing multiyear droughts is the limited sample size commonly available from historical instrumental records. For example, based on the 1911–1998 record of the Meuse River, concluding whether drought has become more severe or frequent is not possible (van Lanen et al. 2007). One technique that has been helpful to extend streamflow records is based on tree ring records, which enable streamflow reconstruction back in time (e.g., Loaiciga et al. 1993, Meko et al. 2001, Woodhouse 2001, Biondi and Strachan 2011). Often the reconstructed flow records show that periods of low flows and droughts more severe than those observed from instrumental records have occurred in the past (e.g., Meko et al. 1995, Meko et al. 2001, Gonzalez and Valdes 2003, Gedalof et al. 2004, Tarawneh and Salas 2008). A stochastic nonparametric approach for streamflow generation combining observational and paleoreconstructed data has also been suggested (Prairie et al. 2008). Furthermore, alternative stochastic models capable of generating nonstationary-like changes in streamflow sequences have been developed (e.g., Montanari et al. 2000, Koutsoyiannis 2002, Sveinsson et al. 2003). Data generated based on these models can be utilized for drought analysis using some of the empirical methods included in this chapter. Lastly, recent advances have been made in developing statistical analysis of extreme events under nonstationary conditions (e.g., Villarini et al. 2009, Vogel et al. 2011, Salas and Obeysekera 2014, Lopez and Frances 2013). Although the main applications of those techniques focus on extreme flood and sea level events, some advances have been made to analyze low flows and droughts as well (e.g., Garcia Galiano et al. 2011, Arpita and Mujumdar 2015, Kwon and Lall 2016, Cancelliere and Bonaccorso 2016).

References

- Akyuz, D. E., M. Bayazit, and B. Onoz. 2012. "Markov chain models for hydrological drought characteristics." *J. Hydrometeorol.* **13** (1): 298–309.
- Alley, W. M. 1984. "The Palmer drought severity index: Limitations and assumptions." *J. Clim. Appl. Meteorol.* **23** (7): 1100–1109.
- Arpita, M., and P. P. Mujumdar. 2015. "Return levels of hydrologic droughts under climate change." *Adv. Water Resour.* **75**: 67–79.
- ASCE. 1980. "Characteristics of low flows." *J. Hydraul. Div.* **106** (5): 717–731.
- Biondi, F., T. J. Kozubowski, and A. K. Panorska. 2005. "A new model for quantifying climate episodes." *Int. J. Climatol.* **25** (9): 1253–1264.
- Biondi, F., and S. Strachan. 2011. "Dendrohydrology in 2050: Challenges and opportunities." In *Toward a sustainable water future, visions for 2050*, edited by W. M. Grayman, D. P. Loucks, and L. Saito. Reston, VA: ASCE.
- Bobee, B., and R. Robitaille. 1975. "Correction of bias in the estimation of the coefficient of skewness." *Water Resour. Res.* **11** (6): 851–854.
- Bonaccorso, B. 2002. "Stochastic characterization of drought events." Ph.D. thesis, Univ. of Catania.
- Bonaccorso, B., A. Cancelliere, and G. Rossi. 2003. "An analytical formulation of return period of drought severity." *Stochastic Environ. Res. Risk Assess.* **17** (3): 157–174.
- Bond, N. R., P. S. Lake, and A. H. Arthington. 2008. "The impact of drought on freshwater ecosystem: An Australian perspective." *Hydrobiologia* **600** (1): 3–16.
- Box, G. E. P., and D. R. Cox. 1964. "An analysis of transformations." *J. R. Stat. Soc., Ser. B* **26** (2): 211–252.
- Box, G. E. P., and G. M. Jenkins. 1976. *Time series analysis forecasting and control*. San Francisco: Holden-Day.
- Cancelliere, A. 2008. "Stochastic characterization of droughts in stationary and periodic series." Ph.D. dissertation, Colorado State Univ.
- Cancelliere, A., and B. Bonaccorso. 2016. "A non-stationary analytical framework for the probabilistic characterization of drought events." In *Proc., EWRI World Environmental and Water Resources Congress*. Reston, VA: ASCE.
- Cancelliere, A., B. Bonaccorso, G. Rossi, and J. D. Salas. 2003. "On the probabilistic characterization of drought events." In *Proc., 23rd AGU Hydrology Days*. Fort Collins, CO: Colorado State Univ.
- Cancelliere, A., and J. D. Salas. 2002. "Characterizing the recurrence of hydrologic droughts." In *Proc., AGU Fall Meeting*. San Francisco.

- Cancelliere, A., and J. D. Salas. 2004. "Drought length properties in periodic-stochastic hydrologic data." *Water Resour. Res.* **40** (2).
- Cancelliere, A., and J. D. Salas. 2010. "Drought probabilities and return period for annual streamflows series." *J. Hydrol.* **391** (1–2): 77–89.
- Chang, T., M. Kavvas, and J. Delleur. 1984a. "Daily precipitation modeling by discrete autoregressive moving average processes." *Water Resour. Res.* **20** (5): 565–580.
- Chang, T., M. Kavvas, and J. Delleur. 1984b. "Modeling sequences of wet and dry days by binary discrete autoregressive moving average processes." *J. Clim. Appl. Meteorol.* **23** (9): 1367–1378.
- Chebaane, M., J. Salas, and D. Boes. 1995. "Product periodic autoregressive processes for modeling intermittent monthly streamflows." *Water Resour. Res.* **31** (6): 1513–1518.
- Chung, C. H., and J. D. Salas. 2000. "Return period and risk of droughts for dependent hydrologic processes." *J. Hydrol. Eng.* **5** (3): 259–268.
- CONAGUA (Comision Nacional del Agua). 2016. "BANDAS." Accessed July 9, 2016. <http://www.conagua-gob.mx/CONAGUA07/Contenido/Documentos/Portada%20BANDAS.htm>.
- Condie, R., and G. A. Nix. 1975. "Modelling of low flow frequency distributions and parameter estimation." In *Proc., Int. Water Resources Symp.on Water for Arid Lands*. Madison, WI: International Water Resources Association.
- Cramer, H., and M. Leadbetter. 1967. *Stationary and related stochastic processes*. New York: Wiley.
- Dai, A., K. E. Trenberth, and T. A. Qian. 2004. "A global data set of Palmer Drought Severity Index for 1870–2002: Relationship with soil moisture and effects of surface warming." *J. Hydrometeorol.* **5** (6): 1117–1130.
- Douglas, E. M., R. M. Vogel, and C. N. Kroll. 2000. "Trends in floods and low flows in the United States: Impact of spatial correlation." *J. Hydrol.* **240** (1–2): 90–105.
- Downer, R., M. Siddiqui, and V. Yevjevich. 1967. "Application of runs to hydrological droughts." In *Proc., Int. Hydrology Symp.* Fort Collins, CO: Colorado State Univ.
- Dracup, J. A., K. L. Lee, and E. G. Paulson Jr. 1980. "On the statistical characteristics of drought events." *Water Resour. Res.* **16** (2): 289–296.
- Dynesius, M., and C. Nilsson. 1994. "Fragmentation and flow regulation of river systems in the northern third of the world." *Science* **266** (5186): 753–762.
- Fernández, B., and J. D. Salas. 1990. "Gamma-autoregressive models for streamflow simulation." *J. Hydrol. Eng.* **116** (11): 1403–1414.
- Fernández, B., and J. D. Salas. 1999a. "Return period and risk of hydrologic events. 1: Mathematical formulation." *J. Hydrol. Eng.* **4** (4): 297–307.
- Fernández, B., and J. D. Salas. 1999b. "Return period and risk of hydrologic events. 2: Applications." *J. Hydrol. Eng.* **4** (4): 308–316.
- Frick, D. M., D. Bode, and J. D. Salas. 1990. "Effect of drought on urban water supplies. I: Drought analysis." *J. Hydrol. Eng.* **116** (6): 733–753.
- Garcia Galiano, S. G., J. D. Giraldo, M. A. Urrea, A. Merida, and C. N. Tetay. 2011. "Assessing drought hazard under non-stationary conditions on Southeast Spain." In *Proc., Symp. Risk in Water Resources Management H03*, 85–91. Melbourne, Australia.
- Gaver, D. P., and P. A. W. Lewis. 1980. "First order autoregressive gamma sequences and point process." *Adv. Appl. Probab.* **12** (3): 727–745.
- Gedalof, Z., D. L. Peterson, and N. J. Mantua. 2004. "Columbia river flow and drought since 1750." *J. Am. Water Resour. Assoc.* **40** (6): 1579–1592.
- Gonzalez, J., and J. Valdes. 2003. "Bivariate drought recurrence analysis using tree ring reconstructions." *J. Hydrol. Eng.* **8** (5): 247–258.
- Gudmundsson, L., L. M. Tallaksen, K. Stahl, and A. K. Fleig. 2011. "Low-frequency variability of European runoff." *Hydrol. Earth Syst. Sci.* **15** (9): 2853–2869.
- Gumbel, E. J. 1958. *Statistics of extremes*. New York: Columbia University Press.
- Gustard, A., L. A. Roald, S. Demuth, H. S. Lumadjeng, and R. Gross. 1989. "Flow regimes from experimental and network data (FREND)." In *Hydrological studies*, Vol. I. Wallingford, UK: Institute of Hydrology.
- Guttman, N. B. 1998. "Comparing the Palmer drought index and the standardized precipitation index." *J. Am. Water Resour. Assoc.* **34** (1): 113–121.
- Guven, O. 1983. "A simplified semiempirical approach to probabilities of extreme hydrologic droughts." *Water Resour. Res.* **19** (2): 441–453.

- Haan, C. T. 1992. *Statistical methods in hydrology*. Ames, IA: Iowa State Press.
- Hadley, R. F., M. R. Kalinger, A. W. Burns, and T. R. Eschner. 1987. "Water development and associated hydrologic changes in the Platte River, Nebraska, U.S.A." *Regul. Rivers: Res. Manage.* **1** (4): 331–341.
- Hannaford, J., and T. Marsh. 2006. "An assessment of trends in UK runoff and low flows using a network of undisturbed catchments." *Int. J. Climatol.* **26** (9): 1237–1253.
- Hayes, D. C. 1992. *Low flow characteristics of streams in Virginia: Water supply paper 2374*. Denver: US Geological Survey, Federal Center.
- Heim, R. 2002. "A review of twentieth-century drought indices used in the United States." *Bull. Am. Meteorol. Soc.* **83** (8): 1149–1166.
- Hirsch, R. M., D. R. Helsel, T. A. Cohn, and E. J. Gilroy, 1993. "Statistical analysis of hydrologic data (chapter 17)." In *Handbook of hydrology*, edited by D. R. Maidment. New York: McGraw-Hill.
- Homa, E. S., C. Brown, K. McGarigal, B. W. Compton, and S. D. Jackson. 2013. "Estimating hydrologic alteration from basin characteristics in Massachusetts." *J. Hydrol.* **503**: 196–208.
- Hosking, J. R. M., and J. R. Wallis. 1997. *Regional frequency analysis*. Cambridge, UK: Cambridge University Press.
- IFC (Instream Flow Council). (2002). "Instream flows for riverine resource stewardship." Accessed November 8, 2018. <https://www.instreamflowcouncil.org/>.
- Institute of Hydrology. 1980. *Low-flow studies*. Rep. No. 1. Wallingford, UK: Institute of Hydrology.
- IPCC (Intergovernmental Panel on Climate Change) Climate Change. 2007. *The physical science basis: Contribution of working group i to the fourth assessment report of the intergovernmental panel on climate change*. Edited by S. Solomon, et al. Cambridge, MA: Cambridge University Press.
- Jackson, B. B. 1975. "Markov mixture models for drought lengths." *Water Resour. Res.* **11** (1): 64–74.
- Jacobs, P. A., and P. A. W. Lewis. 1977. "A mixed autoregressive-moving average exponential sequence and point process (EARMA1, 1)." *Adv. Appl. Probab.* **9** (1): 87–104.
- Jacobs, P. A., and P. A. W. Lewis. 1978. "Discrete time series generated by mixtures. I: Correlational and runs properties." *J. R. Stat. Soc. Oxford* **40** (1): 94–105.
- Jennings, M. E., and M. A. Benson. 1969. "Frequency curves for annual flood series with some zero events or incomplete data." *Water Resour. Res.* **5** (1): 276–280.
- Johnson, N., S. Kotz, and N. Balakrishnan. 1994. *Continuous univariate distributions*. Vol. 1. New York: Wiley.
- Kirby, W. 1972. "Computer-oriented Wilson-Hilferty transformation that preserves the first three moments and the lower bound of the Pearson type 3 distribution." *Water Resour. Res.* **8** (5): 1251–1254.
- Kite, G. W. 1988. *Frequency and risk analyses in hydrology*. Littleton, CO: Water Resources Publishing.
- Koutsoyiannis, D. 2002. "The Hurst phenomenon and fractional Gaussian noise made easy." *Hydrol. Sci. J.* **47** (4): 573–595.
- Kroll, C. N., J. G. Luz, T. B. Allen, and R. M. Vogel. 2004. "Developing a watershed characteristics database to improve low streamflow prediction." *J. Hydrol. Eng.* **9** (2): 116–125.
- Kroll, C. N., and J. R. Stedinger. 1998. "Generalized least squares regression procedures revisited." *Water Resour. Res.* **34** (1): 121–128.
- Kroll, C. N., and R. M. Vogel. 2002. "The probability distribution of low streamflow series in the United States." *J. Hydrol. Eng.* **7** (2): 137–146.
- Kwon, H. H., and U. Lall. 2016. "A copula-based nonstationary frequency analysis for the 2012–2015 drought in California." *Water Resour. Res.* **52** (7): 5662–5675.
- Laaha, G., and G. Blöschl. 2006a. "A comparison of low flow regionalisation methods—Catchment grouping." *J. Hydrol.* **323** (1–4): 193–214.
- Laaha, G., and G. Blöschl. 2006b. "Seasonality indices for regionalizing low flows." *Hydrolog. Processes* **20** (18): 3851–3878.
- Laaha, G., and G. Blöschl. 2007. "A national low flow estimation procedure for Austria." *Hydrol. Sci. J.* **52** (4): 625–644.
- Lawrance, A. J. 1982. "The innovation distribution of a gamma distributed autoregressive process." *Scand. J. Stat.* **9** (4): 234–236.
- Lawrance, A. J., and P. A. W. Lewis. 1981. "A new autoregressive time series model in exponential variables [NEAR(1)]." *Adv. Appl. Probab.* **13** (4): 826–845.
- Lins, H. F., and J. R. Slack. 1999. "Streamflow trends in the United States." *Geophys. Res. Lett.* **26** (2): 227–230.

- Llamas, J., and M. Siddiqui. 1969. *Runs of precipitation series: Hydrology paper 33*. Fort Collins, CO: Colorado State Univ.
- Lloyd, E. H. 1970. "Return period in the presence of persistence." *J. Hydrol.* **10** (3): 202–215.
- Loaiciga, H. A. 2005. "On the probability of droughts: The compound renewal model." *Water Resour. Res.* **41** (1): W01009.
- Loaiciga, H. A., L. Haston, and J. Michaelsen. 1993. "Dendrohydrology and long-term hydrological phenomena." *Rev. Geophys.* **31** (2): 151–171.
- Loaiciga, H. A., and R. B. Leipnik. 1996. "Stochastic renewal model of low-flow streamflow sequences." *Stochastic Hydraul. Hydraul.* **10** (1): 65–85.
- Loaiciga, H. A., and M. A. Mariño. 1991. "Recurrence interval of geophysical events." *J. Water Resour. Plann. Manage.* **117** (3): 367–382.
- Lopez, J., and F. Frances. 2013. "Non-stationary flood frequency analysis in continental Spanish rivers, using climate and reservoir indices as external covariates." *Hydrol. Earth Sci.* **17** (8): 3189–3203.
- Loucks, D. P., J. R. Stedinger, and D. A. Haith. 1981. *Water resource systems planning and analysis*. Englewood Cliffs, NJ: Prentice Hall.
- Magilligan, F. J., and K. H. Nislow. 2005. "Changes in hydrologic regime by dam." *Geomorphology* **71** (1–2): 61–78.
- Maheshwari, B. L., K. F. Walker, and T. A. McMahon. 1995. "Effects of regulation on the flow regime of the river Murray, Australia." *River Res. Appl.* **10** (1): 15–38.
- Matalas, N. C. 1966. "Time series analysis." *Water Resour. Res.* **3** (3): 817–829.
- McMahon, T. A., and B. L. Finlayson. 2003. "Droughts and anti-droughts: The hydrology of Australian rivers." *Freshwater Biol.* **48** (7): 1147–1160.
- Meko, D., C. W. Stockton, and W. R. Boggess. 1995. "The tree-ring record of severe sustained drought." *Water Resour. Bull.* **31** (5): 789–801.
- Meko, D., M. Therrell, C. Baisan, and M. Hughes. 2001. "Sacramento river flow reconstructed to A.D. 869 from tree rings." *J. Am. Water Resour. Assoc.* **37** (4): 1029–1039.
- Mishra, A. K., and V. P. Singh. 2010. "A review of drought concepts." *J. Hydrol.* **391** (1–2): 202–216.
- Mishra, A. K., and V. P. Singh. 2011. "Drought modeling—A review." *J. Hydrol.* **403** (1–2): 157–175.
- Mishra, A. K., V. P. Singh, and V. R. Desai. 2009. "Drought characterization: A probabilistic approach." *Stochastic Environ. Res. Risk Assess.* **23** (1): 41–55.
- Montanari, A., R. Rosso, and M. Taqqu. 2000. "A seasonal fractional ARIMA model applied to the Nile River monthly flows at Aswan." *Water Resour. Res.* **36** (5): 1249–1259.
- Nathan, R. J., and T. A. McMahon. 1990. "Identification of homogeneous regions for the purpose of regionalization." *J. Hydrol.* **121** (1–4): 217–238.
- Nathan, R. J., and T. A. McMahon. 1992. "Estimating low flow characteristics at ungauged catchments." *Water Resour. Manage.* **6** (2): 85–100.
- NERC (National Environmental Research Council). 1975. *Flood studies report*. Vol. 1. London: NERC.
- O'Connell, P. E. 1977. "ARIMA models in synthetic hydrology." In *Mathematical models for surface water hydrology*, edited by T. A. Ciriani, V. Maione, and J. R. Wallis, 51–68. New York: Wiley.
- Onöz, B., and M. Bayazit. 2001. "Power distribution for low streamflow." *J. Hydrol. Eng.* **6** (5): 429–435.
- Ozger, M., A. K. Mishra, and V. P. Singh. 2009. "Low frequency drought variability associated with climate indices." *J. Hydrol.* **364** (1–2): 152–162.
- Panu, U. S., and T. C. Sharma. 2002. "Challenges in drought research: Some perspectives and future directions." *J. Hydrol. Sci.* **47**: S19–S30.
- Paoli, C., J. Bolzicco, and P. Cacik. 1994. "Analysis of low flows in the Paraná River." [In Spanish.] In Vol. 4 of *XVI IAHR Congreso Latinoamericano de Hidráulica*, 59–70. Santiago, Chile.
- Pearson, C. P. 1995. "Regional frequency analysis of low streamflows in New Zealand rivers." *J. Hydrol.* **33** (2): 94–122.
- Poff, N. L., et al. 1997. "The natural flow regime: A paradigm for river conservation and restoration." *BioScience* **47** (11): 769–784.
- Prairie, J., K. Nowak, B. Rajagopalan, and U. Lall. 2008. "A stochastic nonparametric approach for streamflow generation combining observational and paleoreconstructed data." *Water Resour. Res.* **44** (6): W06423.
- Raynal-Villasenor, J. A. 2013. "Moment estimators of the GEV distribution for the minima." *J. Appl. Water Sci.* **3** (1): 13–18.

- Reilly, C. F., and C. N. Kroll. 2003. "Estimation of low streamflow statistics using baseflow correlation." *Water Resour. Res.* **39** (9): 1236.
- Richter, B. D., J. V. Baumgartner, R. Wigington, and D. P. Braun. 1997. "How much water does a river need?" *Freshwater Biol.* **37** (1): 231–249.
- Riggs, H. C. 1980. "Characteristics of low flows." *J. Hydraul. Div.* **106** (5): 717–731.
- Rossi, G., M. Benedini, G. Tsakiris, and S. Giakoumakis. 1992. "On regional drought estimation and analysis." *Water Resour. Manage.* **6** (4): 249–277.
- Rossi, G., and A. Cancelliere. 2003. "At site and regional identification by REDIM model." In *Tools for drought mitigation in Mediterranean regions*, edited by G. Rossi, A. Cancelliere, T. Oweis, L. Pereira, M. Shatanawi, and A. Zairi, 37–54. Dordrecht, Netherlands: Kluwer Academic.
- Ryu, J. H., J. H. Lee, S. Jeong, S. K. Park, and K. Han. 2011. "The impacts of climate change on local hydrology and low flow frequency in the Geum River basin, Korea." *Hydrol. Processes* **25** (22): 3437–3447.
- Salas, J. D. 1993. "Analysis and modeling of hydrologic time series." In *Handbook of hydrology*, edited by D. R. Maidment. New York: McGraw-Hill.
- Salas, J. D., C. Chung, and B. Fernández. 2001. "Relating autocorrelations and crossing rates of continuous- and discrete-valued hydrologic processes." *J. Hydrol. Eng.* **6** (2): 109–118.
- Salas, J. D., J. W. Delleur, V. M. Yevjevich, and W. L. Lane. 1980. *Applied modeling of hydrologic time series*. Littleton, CO: Water Resources Publications.
- Salas, J. D., C. Fu, A. Cancelliere, D. Dustin, D. Bode, A. Pineda, and E. Vincent. 2005. "Characterizing the severity and risk of drought in the Poudre River, Colorado." *J. Water Resour. Plann. Manage.* **131** (5): 383–393.
- Salas, J. D., J. H. Heo, J. Obeysekera, M. Arabi, R. A. Smith, and G. Tabios. 2019. *Probability and statistics in water resources*. Fort Collins, CO: Colorado State Univ.
- Salas, J. D., and J. Obeysekera. 2014. "Revisiting the concepts of return period and risk for nonstationary hydrologic events." *J. Hydrol. Eng.* **19** (3): 554–568.
- Salas, J. D., and R. A. Pielke. 2003. "Stochastic characteristics and modeling of hydroclimatic processes." Chap. 32 in *Handbook of weather, climate, and water: Atmospheric chemistry, hydrology, and societal impacts*, edited by T. D. Potter and B. R. Colman. Hoboken, NJ: Wiley.
- Salas, J. D., B. Rajagopalan, L. Saito, and C. Brown. 2012. "Climate nonstationarity and water resources management: Introduction." *J. Water Resour. Plann. Manage.* **138** (5): 385–388.
- Saldarriaga, J., and V. Yevjevich. 1970. *Applications of run lengths to hydrological series: Hydrology paper 40*. Fort Collins, CO: Colorado State Univ.
- Santos, M. 1983. "Regional droughts: A stochastic characterization." *J. Hydrol.* **66** (1–4): 183–211.
- Schilling, K. E., and R. D. Libra. 2003. "Increased baseflow in Iowa over the second half of the 20th century." *J. Am. Water Res. Assoc.* **39** (4): 851–860.
- Sen, Z. 1976. "Wet and dry periods of annual flow series." *J. Hydraul. Div.* **102** (HY10): 1503–1514.
- Sen, Z. 1977. "Run-sums of annual flow series." *J. Hydrol.* **35** (3–4): 311–324.
- Serinaldi, F., B. Bonaccorso, A. Cancelliere, and S. Grimaldi. 2009. "Probabilistic characterization of drought properties through copulas." *Phys. Chem. Earth* **34** (10–12): 596–605.
- Sharma, T. 1995. "Estimation of drought severity on independent and dependent hydrologic series." *Water Resour. Manage.* **11** (1): 35–49.
- Shaw, E. M. 1988. *Hydrology in practice*. London: Chapman and Hill.
- Sheffield, J., B. Livneh, and E. F. Wood. 2012a. "Representation of terrestrial hydrology and large-scale drought of the continental United States from the North American regional reanalysis." *J. Hydrometeorol.* **13** (3): 856–876.
- Sheffield, J., E. F. Wood, and M. L. Roderick. 2012b. "Little change in global drought over the past 60 years." *Nature* **491** (7424): 435–438.
- Shiau, J. T. 2006. "Fitting drought duration and severity with two-dimensional copulas." *Water Resour. Manage.* **20** (5): 795–815.
- Shiau, J. T., and H. Shen. 2001. "Recurrence analysis of hydrologic droughts of differing severity." *J. Water Resour. Plann. Manage.* **127** (1): 30–40.
- Shin, H. S., and J. D. Salas. 2000. "Regional drought analysis based on neural networks." *J. Hydraul. Eng.* **5** (2): 145–155.
- Smakhtin, V. U. 2001. "Low flow hydrology: A review." *J. Hydrol.* **240** (3–4): 147–186.

- Songbai, S., and V. Singh. 2010. "Meta-elliptical copulas for drought frequency analysis of periodic hydrologic data." *Stochastic Environ. Res. Risk Assess.* **24** (3): 425–444.
- Stedinger, J. R., and G. D. Tasker. 1986. "Regional hydrologic analysis. 1: Ordinary, weighted, and generalized least squares compared." *Water Resour. Res.* **22** (5): 844.
- Stedinger, J. R., and W. O. Thomas Jr. 1985. *Low-flow frequency estimation using base-flow measurements*. Open-File Rep. No. 85-95. Reston, VA: USGS.
- Stedinger, J. R., R. M. Vogel, and E. Foufoula-Georgiou. 1993. "Frequency analysis of extreme events." Chap. 18 in *Handbook of hydrology*, edited by D. R. Maidment. New York: McGraw-Hill.
- Subramanya, K. 1994. *Engineering hydrology*. 2nd ed. New Delhi: Tata McGraw-Hill.
- Svensson, C., W. Z. Kundzewicz, and T. Maurer. 2005. "Trend detection in river flow series: 2. Flood and low-flow index series." *Hydrol. Sci. J.* **50** (5): 811–824.
- Sveinsson, O., J. D. Salas, D. C. Boes, and R. A. Pielke Sr. 2003. "Modeling the dynamics of long term variability of hydroclimatic processes." *J. Hydrometeorol.* **4** (3): 489–505.
- Svoboda, M. 2000. "An introduction to the drought monitor." *Drought Networks News* **12** (1): 15–20.
- Tabari, H., R. Zamani, H. Rahmati, and P. Willemans. 2015. "Markov chains of different orders for streamflow drought analysis." *Water Resour. Manage.* **29** (9): 3441–3457.
- Tallaksen, L. M. 1995. "A review of baseflow recession analysis." *J. Hydrol.* **165** (1–4): 349–370.
- Tallaksen, L. M., and H. A. J. van Lanen, eds. 2004. *Hydrological drought— Processes and estimation methods for streamflow and groundwater: Developments in water sciences* 48, 580. Dordrecht, Netherlands: Elsevier.
- Tarawneh, Z. S., and J. D. Salas. 2008. *Extending the streamflows of the Colorado River using tree ring indices and drought analysis*. Fort Collins, CO: Colorado State Univ.
- Tase, N. 1976. "Area-deficit-intensity characteristics of droughts." Ph.D. thesis, Colorado State Univ. Fort Collins, CO.
- Tasker, G. D. 1987. "A comparison of methods for estimating low flow characteristics of streams." *Water Resour. Bull.* **23** (6): 1077–1083.
- Thomas, D. M., and M. A. Benson. 1970. *Generalization of streamflow characteristics from drainage-basin characteristics: USGS Water Supply Paper 1975*. Washington, DC: USGS.
- USACE (US Army Corps of Engineers). 1964. *Low flow frequency analysis*. Technical Rep. No. N1. Tulsa, OK: USACE.
- USACE. 1975. "Hydrologic frequency analysis." In *Hydrologic engineering methods for water resources development: IHD-3*, Vol. 3. Davis, CA: USACE.
- USGS (US Geological Survey). 1958. *Handbook for hydrologists, Chapter VII*. Washington, DC: US Dept. of Interior, USGS.
- USGS. 2010a. "GLSNet: Regional hydrologic regression and NETwork analysis using generalized least squares." Accessed September 10, 2010. <https://water.usgs.gov/software/GLSNet>.
- USGS. 2010b. "Hydrologic unit maps." Accessed September 10, 2010. <https://water.usgs.gov/GIS/huc.html>.
- USIAC (US Interagency Advisory Committee on Water Data). 1982. *Guidelines for determining flood flow frequency*. Bulletin 17B. Reston, VA: USGS.
- van Lanen, H. A. J., L. M. Tallaksen, and G. Rees. 2007. "Droughts and climate change." In *Annex II in Commission Staff Working Document Impact Assessment, Accompanying Document to Communication Addressing the Challenge of Water Scarcity and Droughts in the European Union (COM 2007)*. Brussels, Belgium: Commission of the European Communities.
- Viessman, W., Jr., G. L. Lewis, and J. W. Knapp. 1989. *Introduction to hydrology*. 3rd ed. New York: Harper and Row.
- Villarini, G., J. A. Smith, F. Serinaldi, J. Bales, P. D. Bates, and W. F. Krajewski. 2009. "Flood frequency analysis for nonstationary annual peak records in an urban drainage basin." *Adv. Water Resour.* **32** (8): 1255–1266.
- Vogel, R. M., and C. N. Kroll. 1989. "Low-flow frequency analysis using probability plot correlation coefficients." *J. Water Resour. Plann. Manage.* **115** (3): 338–357.
- Vogel, R. M., and C. N. Kroll. 1991. "The value of streamflows record augmentation procedures in low-flow and flood-flow frequency analysis." *J. Hydrol.* **125** (3–4): 259–276.
- Vogel, R. M., and C. N. Kroll. 1992. "Regional geohydrologic-geomorphic relationships for the estimation of low-flow statistics." *Water Resour. Res.* **28** (9): 2451–2458.
- Vogel, R. M., and C. N. Kroll. 1996. "Estimation of baseflow recession constants." *Water Resour. Manage.* **10** (4): 303–320.

- Vogel, R. M., and I. Wilson. 1996. "Probability distribution of annual maximum, mean, and minimum streamflows in the United States." *J. Hydrol. Eng.* **1** (2): 69–76.
- Vogel, R. M., C. Yaindl, and M. Walter. 2011. "Nonstationarity: Flood magnification and recurrence reduction factors in the United States." *J. Am. Water Res. Assoc.* **47** (3): 464–474.
- Wallis, J. R., and P. E. O'Connell. 1972. "Small sample estimation of r1." *Water Resour. Res.* **8** (3): 707–712.
- Wang, D., and X. Cai. 2009. "Detecting human interferences to low flows through base flow recession analysis." *Water Resour. Res.* **45** (7): W07426.
- Wang, D. C., and J. D. Salas. 1989. "Stochastic modeling and generation of drought." In *Proc., ASCE National Conf. on Hydraulic Modeling*. Reston, VA: ASCE.
- Weiss, G. 1977. "Shot noise models for the generation of synthetic streamflow data." *Water Resour. Res.* **13** (1): 101–108.
- Wilhite, D. A. 2000. "Drought as a natural hazard: Concepts and definitions." In *Drought: A global assessment*. Vol. 1, edited by D. A. Wilhite, 3–18. London: Routledge.
- Wong, G., H. A. J. van Lanen, and P. J. J. F. Torfs. 2013. "Probabilistic analysis of hydrological drought characteristics using meteorological drought." *Hydrol. Sci. J.* **58** (2): 253–270.
- Woodhouse, C. A. 2001. "A tree-ring reconstruction of streamflow for the Colorado front range." *J. Am. Water Resour. Assoc.* **37** (3): 561–569.
- Yevjevich, V. M. 1967. *An objective approach to definitions and investigations of continental hydrologic droughts: Hydrology Paper No. 23*. Fort Collins, CO: Colorado State Univ.
- Yevjevich, V. M. 1972. *Stochastic processes in hydrology*. Fort Collins, CO: Water Resources Publications.
- Young, A. R., C. E. Round, and A. Gustard. 2000. "Spatial and temporal variations in the occurrence of low flow events in the UK." *Hydrol. Earth Syst. Sci.* **4** (1): 35–45.
- Yue, S., P. Pilon, and B. Phinney. 2003. "Canadian streamflow trend detection: Impacts of serial and cross-correlation." *Hydrol. Sci. J.* **48** (1): 51–63.
- Zhang, Z., and C. N. Kroll. 2007a. "The baseflow correlation method with multiple gauged sites." *J. Hydrol.* **347** (3–4): 371–380.
- Zhang, Z., and C. N. Kroll. 2007b. "A closer look at baseflow correlation." *J. Hydrol. Eng.* **12** (2): 190–196.
- Zhang, Q., X. Gu, V. P. Singh, and X. Chen. 2015a. "Evaluation of ecological instream flow using multiple ecological indicators with consideration of hydrological alterations." *J. Hydrol.* **529** (3): 711–722.
- Zhang, Y., X. Zhai, Q. Shao, and Z. Yan. 2015b. "Assessing temporal and spatial alterations of flow regimes in the regulated Huai River Basin, China." *J. Hydrol.* **529** (1): 382–397.

CHAPTER 9

Probabilistic Models for Urban Stormwater Management

Yiping Guo
Daeryong Park
Alfonso Mejia
Jorge Gironás
Larry Roesner

LIST OF SYMBOLS

The following symbols are used in this chapter:

A	area of a roof draining to a storage unit (m^2)
A_{BMP}	surface area of a specific best management practice (BMP; m^2)
A_w	wetted area of channel cross-section (m^2)
B	storage volume of a rain barrel or cistern (l)
B_w	wetted top width of channel cross-section (m)
b	rainfall inter-event time (h)
\bar{b}	average rainfall inter-event time (h)
C	runoff coefficient
C_{in}	influent event-mean concentration (EMC) (mg/l)
C_{out}	effluent EMC (mg/l)
C^*	background EMC or irreducible minimum concentration (mg/l)
c	celerity of kinematic wave through a channel reach (m/s)
E	number of exceedances per year
$E[\cdot]$	expected value of a random variable
$F(\cdot)$	cumulative distribution function
$f(\cdot)$	probability density function
$f(b)$	probability density function of inter-event time
$f(t)$	probability density function of rainfall event duration
$f(v)$	probability density function of rainfall event volume
f_c	ultimate infiltration capacity of soil (mm/h)
G	water use rate from a storage unit for rainwater harvesting (l/day)
G_{\max}	maximum use rate that may be provided by a storage unit for a specified reliability (l/day)
$G_p(0)$	probability per use/load cycle that some spill occurs
g	plotting position parameter in Cunnane formula
h	degree of imperviousness expressed as a fraction (dimensionless)

I	inflow rate to a channel reach (m^3/s)
i	imperviousness ratio, between 0–1
J	rank of the event (in descending order of magnitude) in Cunnane formula
K	Muskingum K value of a channel reach (h)
k	aerial removal rate constant (m/day)
L	number of subintervals in the Latin hypercube sampling method
M	pollutant mass (g/m^2)
m	kinematic ratio of a channel reach
N	number of years of record
O	outflow rate from a channel reach (m^3/s)
P_w	perimeter of the wetted portion of a channel reach's cross section (m)
Q	flow rate (m^3/day)
Q_o	peak discharge rate from a detention pond resulting from a rainfall event falling on the upstream catchment (mm/h)
Q_p	peak discharge rate of a runoff event regarded as a random variable
q	BMP hydraulic loading rate (m/day)
q_o	discharge per unit top width normally determined for half of the peak discharge (m^3/s)
q_p	specific peak discharge rate (m^3/s)
R_a	annual total volume of runoff generated from the roof of a building (l)
R_c	annual total volume of water collected in a rainwater storage unit that is subsequently utilized instead of being spilled (l)
R_e	reliability of a storage unit in supplying water, defined as the fraction of time when use needs are satisfied by water collected in the storage unit (dimensionless)
R_{\max}	maximum reliability that may be achieved given a location, roof area, and use rate (dimensionless)
S_d	area-weighted depression storage of the impervious and pervious areas (mm)
S_{dd}	difference between S_{il} and S_{di} (mm)
S_{di}	depression storage of the impervious area (mm)
S_{dp}	depression storage of the pervious area (mm)
S_{il}	initial loss of the pervious area (mm)
S_{iw}	initial soil wetting infiltration volume (mm)
S_o	channel bottom slope (m/m)
S_{Q_o}	maximum storage volume utilized during the passage of a runoff event through a detention pond that resulted in a peak outflow rate of Q_o (m^3)
(S_q, q)	a pair of storage volume and discharge rate of a detention pond (mm, mm/h)
s	standard error of the regression
T	time since the start of the routing calculation (h)
T_d	annual total length of time when water needs to be withdrawn from a storage unit (h)
T_R	return period of a given peak discharge rate (years)
t	rainfall event duration (h)
\bar{t}	average rainfall event duration (h)
t_c	time of concentration of a catchment (h)
t_{cc}	adjusted time of concentration of a catchment for incorporation of the effects of a downstream channel reach (h)
t_{sd}	storage-delay time of a channel reach (h)
$u(T)$	instantaneous unit hydrograph of a channel reach
V	average flow velocity through a channel reach (m/s)
V_{BMP}	flow volume that passes through the BMP (m^3)
V_R	urban runoff (m^3)
V_o	flow volume that by-passes around the BMP (m^3)

v	rainfall event volume (mm)
\bar{v}	average rainfall event volume (mm)
v_c	runoff from a roof top area that can be collected into a rainwater storage unit as a result of a rainfall event (mm)
v_{ff}	first flush to be diverted away from the rainwater storage unit (mm)
v_r	runoff volume from a catchment per rainfall event (mm)
X	random variable used in describing the derived distribution theory, or the weighting factor used in Muskingum–Cunge channel routing
x	specific value of random variable X
x_p	x value of p percentile
(Y, y)	random variable and a specific value of it
(Z, z)	random variable and a specific value of it, or standard normal quantile corresponding to exceedance probability
ζ	distribution parameter of rainfall event volume (1/mm)
$\delta(T)$	Dirac delta function of time T
σ	standard deviation of the instantaneous unit hydrograph of a channel reach
$\hat{\sigma}$	sample standard deviation
θ	average number of rainfall events per year
ε	random variable
λ	distribution parameter of rainfall event duration (1/h)
ϕ	coefficient used in converting rainfall event volume to volume of runoff that can be collected from a roof to a storage unit (dimensionless)
ω	independent-uniform-random number
ψ	distribution parameter of interevent time (1/h)
$\hat{\mu}$	sample mean

9.0 GENERAL

Urban areas are characterized by the predominance of impervious surfaces (e.g., paved roads and roofs) and the presence of manmade or hydraulically improved drainage systems (e.g., sewers). As a result, the response of an urban catchment to rainfall is much faster than that of a rural catchment of equivalent area, slope, and soils. Stormwater from urban areas is therefore characterized by larger volumes and higher peak flows. In addition, stormwater from urban areas is also heavily polluted. Proper control and management of stormwater from urban areas is needed to reduce downstream flooding, avoid excessive rates of erosion, and improve water quality.

Urban stormwater management is implemented through the adoption of nonstructural practices and the use of structural infiltration, conveyance, and storage facilities designed to control the quantity and improve the quality of runoff from urban areas. Stormwater models are developed to numerically model the rainfall–runoff transformation processes, stormwater transport, detention and overflow processes, and water quality degradation and improvement processes occurring on catchments and through stormwater management systems. Most existing stormwater models are deterministic in nature because neither the input nor the output of these models is described as random variables. These models have been widely and routinely used for the planning, design, and analysis of stormwater management systems. The Storm Water Management Model SWMM ([Rossman 2010](#)) and the Hydrologic Modeling System HEC-HMS ([USACE 2010](#)) are examples of such stormwater models.

However, the random nature of the hydrological processes involved and the uncertainty associated with the variables, model structure, and parameters, must be taken into account in the

analysis, planning, design, and operation of stormwater management systems. Statistical methods have been widely used to model hydrometeorological variables that are considered random variables. One of the major applications of these methods is determining the likelihood of occurrence of events with certain characteristics, by means of frequency analysis or fitting of probability density functions. A traditional outcome of such application is the set of intensity-duration-frequency (IDF) curves, which are graphical representations of the relationship between the average rainfall intensity, duration, and return period ([Akan and Houghtalen, 2003](#)). Other applications include the estimation of flood frequencies, risk analysis, the characterization of pollutant concentrations in runoff, the statistical interpolation and downscaling/upscaling of variables, regional analysis for the estimation of flood peaks from urban areas, and the determination of critical threshold values for design. An example of the latter is the concept of water quality capture volume (WQCV), which corresponds to a certain volume of runoff representative of frequent events that has to be controlled to accomplish specific water quality treatment goals ([UDFCD 2001](#)).

The conventional statistical methods used in urban stormwater management are mainly for rainfall and flood frequency analysis purposes. These methods are usually discussed in ordinary hydrology books; some are also presented in other chapters of this book. In this chapter we introduce two statistical approaches that have recently been developed and applied to urban stormwater systems. In Section 9.1, we present the so called Analytical Probabilistic Stormwater Models (APSWM), which allow estimation of the frequency of several variables relevant to hydrologic analysis and design using closed-form analytical equations. These models are developed based on the probability distributions of the local rainfall event characteristics and the properties of the catchments and drainage elements. The APSWM is a valuable complement to the two conventional approaches used in urban stormwater management (i.e., the design storm approach and the use of continuous simulations).

In Section 9.2, we introduce uncertainty analysis applied to urban catchments, particularly to the performance of best management practices (BMPs), which are widely used to control the quantity and quality of urban runoff. Several methods differing in their assumptions and level of complexity are described and used to demonstrate that designs based only on median conditions cannot provide reliable pollutant removal rates.

9.1 ANALYTICAL PROBABILISTIC STORMWATER MODELS

This section presents a collection of analytical equations that can be used for stormwater modeling and design. This collection of equations is referred to as the APSWM. Following an overview of the general methodology, the APSWM development process is illustrated.

9.1.1 Overview

The probability of occurrence and annual/seasonal averages of some output variables of interest in hydrologic modeling can only be determined through either the use of design storms of various return periods or the use of continuous simulation with long-term observed rainfall data as input followed by frequency analysis on the output. Currently, the design storm approach is widely used in regular stormwater management planning and design studies (WEF and ASCE 2012).

Design storms are hypothetical rainfall events associated with specified return periods. The specified return periods correspond to the desired level of risk that components of a stormwater management system need to be designed for. The basic assumption made in the use of design storms is that the return period of the resulting runoff and peak flow is the same as that of the input design storm. This assumption may result in significant errors in some cases ([Adams and Howard 1986](#)). Research (e.g., [Marsalek 1978](#), [Urbonas 1979](#), [Packman and Kidd 1980](#), [Beaudoin et al. 1983](#),

Marsalek and Watt 1984, Voorhees and Wenzel 1984, Wenzel and Voorhees 1984, Levy and McCuen 1999, Nnadi et al. 1999, and others) has been conducted to understand the limitations of the design storm approach and to ensure its proper use in engineering practice. Most of these studies focus only on flood peak estimation because runoff volume was not the main concern before stormwater quality control was required. Urbonas (1979) concludes that it is possible to develop design storms that, when used together with a stormwater model, can reasonably predict peak flows from small urban basins of various return periods. Comparing design storm and continuous simulation results, Packman and Kidd (1980) point out that the proper selection of design storms and antecedent catchment conditions is of paramount importance if the probabilities of rainfall and runoff are to be considered equal. Studying the applications of the design storm approach for different locations, Beaudoin et al. (1983), Wenzel and Voorhees (1984), Voorhees and Wenzel (1984), and Nnadi et al. (1999) conclude that significant parameter sensitivity does exist and an appropriate choice of design storm parameters is essential to produce peak flows of desired return periods.

Although the basic assumption of the design storm approach is not proven to always be acceptable, due to its simplicity and reproducibility, it is still widely used in planning and design. Thus, the approach commonly taken in stormwater management is that, unless runoff volume is of specific interest or the project is of great importance, continuous simulation is not conducted even though it may provide more accurate estimates of peak discharge frequencies.

The analytical probabilistic approach was developed to provide an alternative to the two conventional approaches (e.g., Guo and Adams 1998a, b; 1999a, b). This approach estimates flood peak and volume frequency distributions using closed-form analytical equations, which are derived from the probability distributions of the local rainfall event characteristics and the properties of the catchments. More recently, the capabilities of the analytical probabilistic approach were expanded with (1) the derivation of additional equations to separately model channel reaches (Guo and Zhuge 2008, Guo et al. 2009); (2) the incorporation of a hydrologic element aggregation strategy and a probabilistic rainfall areal reduction method (Guo and Dai 2009); (3) the application of the analytical probabilistic approach to study low-impact development practices such as rainwater harvesting systems, green roofs, rain gardens, and bioretention systems (Guo and Baetz 2007, Zhang and Guo 2013a, 2013b, 2014); and (4) the consideration of both infiltration and saturation-excess runoff (Guo et al. 2012). Hereinafter, the analytical equations derived in the aforementioned publications that are useful for stormwater modeling and stormwater management purposes are collectively referred to as the analytical probabilistic stormwater models, or simply the APSWM.

Historically, Eagleson (1972) first applies the analytical probabilistic approach for relating flood frequency characteristics with rainfall and catchment characteristics. Afterward, research was conducted to relate runoff and flood frequencies to basin geomorphology and rainfall characteristics (e.g., Hebson and Wood 1982, Cordova and Rodriguez-Iturbe 1983, Diaz-Granados et al. 1984, Sanchez 1986, Wood and Hebson 1986, Bierkens and Puente 1990, Shen et al. 1990, Sivapalan et al. 1990, Cadavid et al. 1991, Raines and Valdes 1993, Kurothe et al. 1997). Similar approaches have been used to study urban stormwater management problems (e.g., Howard 1976, Cha and Bras 1979, Di Toro and Small 1979, Small and Di Toro 1979, Adams and Bontje 1984, Loganathan and Delleur 1984, Di Toro 1984, Loganathan et al. 1985, 1994, Cruise and Singh 1988, Li and Adams 1994, Barbe et al. 1996, Papa and Adams 1997, Papa et al. 1999, Guo and Urbonas 2002, Behera et al. 2006). Adams and Papa (2000) summarize advances made in the application of the analytical probabilistic approach to the urban stormwater management problems. More recently, similar approaches were developed for locations where the rainfall characteristics differ significantly from those observed in Canada and the United States (e.g., Bacchi et al. 2008; Balistrocchi et al. 2009; Andrés-Doménech et al. 2010, 2012; Zegpi and Fernández 2010).

The approach described in this section is essentially statistical. It differs from stochastic approaches used to model soil moisture dynamics and streamflows at the catchment scale

(e.g., Rodriguez-Iturbe et al. 1999, Botter et al. 2007). Those stochastic approaches follow from the theory of continuous stochastic dynamical systems or stochastic differential equations (Rodriguez-Iturbe et al. 1999, Daly and Porporato 2010). For example, Botter et al.'s (2007) approach begins by assuming that the daily rainfall is given by a Poisson process with exponentially distributed rainfall depths. After considering the soil moisture dynamics in the root zone, recharge events are modeled as a filtered Poisson process. This filtered Poisson process has the same distribution as the rainfall events but with a different frequency. The recharge events ultimately drive the groundwater storage, which is modeled as a linear reservoir. Using the linear reservoir and the filtered Poisson process, a stochastic differential equation can be derived. In this case, this amounts to an ordinary differential equation and an additive noise term. The steady-state solution of this stochastic equation results in the probability distribution function of streamflows at the outlet of the catchment.

The analytical probabilistic approach used here has in common with the stochastic approach the representation of rainfall depths and time between rainfall events as exponentially distributed random variables. However, the analytical probabilistic approach models rainfall durations at the hourly timescale using an exponential distribution. Thus, the individual rainfall events have variable durations, whereas the stochastic approach utilizes a fixed daily duration. The analytical probabilistic approach is suitable for urban catchments with small drainage areas, from several to a few hundred hectares. It was mainly developed for stormwater management purposes, whereas the stochastic approach is more appropriate to model soil moisture and streamflow distributions at the catchment scale for an overall lumped hydrologic system.

9.1.2 Rainfall Characterization

Presented here is an alternative way of characterizing local rainfall conditions that can be used in stormwater management planning and design. How natural, individual rainfall events are separated from each other is presented first, followed by the fitting of probabilistic models for rainfall event characteristics.

9.1.2.1 Separation of Rainfall Events

The analytical probabilistic approach begins with the separation and analysis of rainfall events observed at a specific location. A continuous rainfall series recorded at a weather station is separated into individual rainfall events. The criterion for distinguishing between consecutive events is a minimum time period without rainfall, referred to as the minimum interevent time or interevent time definition (IETD). Rainfall periods separated by a dry interval equal to or longer than the selected IETD are considered as separate rainfall events. The IETD chosen should be long enough to ensure the statistical independence between consecutive events. At the same time, the selected IETD should not be so long as to combine meteorologically separate rainfall events into one single event. An objective technique for obtaining an appropriate IETD is by examining the relationship between the IETD and the resulting average annual number of rainfall events observed. When further increases of the IETD beyond a threshold level do not result in significant changes in the average annual number of events, that threshold level can be chosen as the IETD.

An appropriate IETD may also be selected following Cruise and Arora's (1990) strategy for formulating and testing Poisson partial duration models. By assuming that the length of the dry interval between consecutive rainfall events (hereinafter referred to as the interevent time and denoted as b) is exponentially distributed, the occurrence of storm events can be approximated as a Poisson process if the rainfall event duration t is much smaller than b (Restrepo-Posada and Eagleson 1982). Selection of different IETD values will result in different numbers of rainfall events every year. If the occurrence of these events is Poissonian, then the numbers of events occurring during each consecutive year must follow the Poisson distribution. The test suggested by Cruise and Arora (1990), which was first proposed by Cunnane (1979), relies on the well-known fact that the

mean and variance of the Poisson distribution are equal. Therefore, if the ratio $r = \text{Var}[n]/E[n]$ is formed for the annual number of event series, where n is the annual number of events and $\text{Var}[\cdot]$ and $E[\cdot]$ are the variance and expectation operations, respectively, r should approach unity as the IETD is increased. [Ashkar and Rousselle \(1987\)](#) point out that once a series has been accepted as Poisson admissible, the likelihood of correlation between the events is greatly reduced. Therefore, a statistical test may be devised for r based on the approximation that the factor $(N - 1)r$ is χ^2 distributed with $(N - 1)$ degrees of freedom ([Cunnane 1979](#)), where N is the number of years of record. The critical values (denoted as r_c , both the lower and upper bounds) can thus be determined for selected levels of significance ([Cruise and Arora 1990](#)).

Other methods are available to assist in the selection of an appropriate IETD. [Eagleson \(1972\)](#), [Restrepo-Posada and Eagleson \(1982\)](#), [Adams et al. \(1986\)](#), [Adams and Papa \(2000\)](#), and [Andrés-Doménech et al. \(2010\)](#) provide details. Previous research has shown that a six- to twelve-hour IETD is appropriate for most locations in the United States and Canada ([Cordova and Bras 1981](#), [Restrepo-Posada and Eagleson 1982](#), [Bonta and Rao 1988](#), [Guo and Baetz 2007](#)).

9.1.2.2 Probabilistic Models of Rainfall Event Characteristics

For planning and design purposes, urban catchments are often small in size, ranging from several hectares to a few hundred hectares. The development of APSWM assumes that rainfall on catchments of such size is adequately described by a representative point rainfall. Each rainfall event as observed at a point is characterized by its rainfall volume (v), rainfall duration (t), and the interevent time (b) before the rainfall event occurs. After the separation of rainfall events, a historical rainfall record can be viewed as comprising a time series for each of the aforementioned rainfall event characteristics. The individual values of v , t , and b contained in each of their respective time series may be subjected to frequency analyses. Histograms for v , t , and b can be prepared, and probability density functions (PDFs) can be fitted to the histograms. An average annual number of storm events can also be obtained from these statistical calculations. Exponential PDFs have been found to often fit such histograms satisfactorily ([Eagleson 1972, 1978](#); [Howard 1976](#); [Adams and Bontje 1984](#); [Adams et al. 1986](#)). However, in some locations the Weibull distribution is more appropriate for v ([Bacchi et al. 2008](#), [Balistocchi et al. 2009](#)); in some locations the generalized Pareto distribution is more appropriate for v and t ([Andrés-Doménech et al. 2010](#)); and in some locations the two-parameter gamma distribution is more appropriate for v and t ([Zegpi and Fernández 2010](#)).

The development of APSWM employs the exponential distributions for rainfall characteristics (Table 9-1). The joint PDFs of v , t , and b are sometimes also required. In cases where the random variables are statistically independent, the joint PDF is the product of their marginal PDFs. As shown in [Adams and Papa \(2000\)](#), for most Canadian locations, only weak correlations exist between rainfall event volume and duration. Therefore, in this development, the three rainfall event characteristics are treated as statistically independent. For some locations, v and t were found to be closely correlated (e.g., [Rivera et al. 2005](#), [Zegpi and Fernández 2010](#)). For those locations, care should be taken in applying the APSWM.

Table 9-1. Probabilistic Models of Local Rainfall Characteristics.

<i>Rainfall characteristic</i>	<i>Exponential PDF</i>	<i>Distribution parameter estimation</i>
Volume, v (mm)	$f(v) = \zeta \exp(-\zeta v)$	$\zeta = \frac{1}{v}$
Duration, t (h)	$f(t) = \lambda \exp(-\lambda t)$	$\lambda = \frac{1}{t}$
Interevent time, b (h)	$f(b) = \psi \exp(-\psi b)$	$\psi = \frac{1}{b}$
Average annual or seasonal number of rainfall events		θ

Table 9-1 shows that ζ , λ , and ψ are distribution parameters, while θ is the annual or seasonal total number of rainfall events. The parameters ζ , λ , and ψ may be estimated from, respectively, \bar{v} , the average event volume, \bar{t} , the average event duration, and \bar{b} , the average interevent time of the rainfall record. For locations throughout Canada, estimates of the values of these parameters may be found in Adams and Papa (2000), and for locations throughout the United States, they can be found in Driscoll et al. (1989) or Wanielista and Yousef (1993). More up-to-date values of these parameters may be obtained by conducting rainfall event separation and statistical analysis using local and up-to-date rainfall data.

Using probabilistic models of storm events to represent local rainfall conditions is advantageous. First of all, the complete spectrum of the frequency distributions of the two major storm event characteristics (i.e., v and t) are properly described and represented. This is important for the design of water quality and erosion control facilities. Second, the actual durations of storm events are studied and characterized as opposed to subjectively selected durations in the development and specification of design storms. Third, by describing and including the frequency distribution of interevent times, the impact of dry periods and consecutive storms may be considered as well.

In processing some rainfall data, many rainfall events were found to have volumes less than a very low threshold level, and the total volume of these small events contributes a very low percentage to the total rainfall volume (Guo and Adams 1998a, Bacchi et al. 2008). To ensure that moderate to large events are properly represented by the fitted theoretical distributions, storms with a volume less than a threshold level may be omitted in the frequency analyses to determine the statistics of rainfall event characteristics. The omission of small events can be justified given that such events result in negligible amount of runoff on most urban catchments.

9.1.3 Event-Based Rainfall-Runoff Transformation

Rainfall-runoff transformation employed in the APSWM is similar to that used in the design storm and continuous simulation approaches but on a rainfall event-by-event basis. In this subsection, the rainfall-runoff transformations over the impervious and pervious areas of an urban catchment are characterized first, followed by a description of the combination of runoff generated from impervious and pervious areas.

9.1.3.1 Impervious Areas

Using the analytical probabilistic approach, the input storm event and the output runoff event are both treated as a whole and no time-step-by-time-step calculations are made within individual events. A runoff event is characterized by runoff event volume, runoff event duration, and peak discharge rate. The runoff event volume is calculated as the difference between the volume of the input rainfall event and the total volume of hydrologic losses.

Interception and depression storage losses are lumped together; the sum of the two losses is referred to as depression storage losses. In developing the probabilistic models, surface depressions are assumed to be filled before any runoff occurs for each rainfall event and the dry period that follows is always assumed to be long enough that water accumulated in the depression storage areas is completely evaporated (or infiltrated for pervious areas) and surface depressions are empty at the beginning of each rainfall event.

Like many numerical hydrologic models, in calculating the total rainfall losses, an urban catchment is divided into impervious (subscript i) and pervious (subscript p) areas. For impervious areas, the infiltration loss is assumed to be zero and the input rainfall volume is totally converted to runoff volume after filling the impervious area depression storage, S_{di} (in mm). Thus, runoff volume generated from impervious areas, v_{ri} (in mm), can be calculated as follows:

$$v_{ri} = \begin{cases} 0, & v \leq S_{di} \\ v - S_{di}, & v > S_{di} \end{cases} \quad (9-1)$$

9.1.3.2 Pervious Areas

For pervious areas, the input rainfall volume fills the pervious area depression storage, S_{dp} , and infiltrates into the soil; the rainfall volume remaining after the filling of depression storage and infiltration into the soil becomes surface runoff. The units of S_{di} and S_{dp} are mm of water over the entire impervious area and the entire pervious area, respectively. The duration of infiltration is essentially the same as the rainfall duration, because runoff from the pervious surfaces is assumed to take negligible time to reach the impervious portions of the catchment or the sewer system. Thus, infiltration on the pervious portions of an urban catchment ceases soon after the rainfall event ends. The total infiltration losses within a runoff event are considered as the combination of two parts, namely, losses due to initial wetting of the soil and losses as a result of infiltration at a constant rate, f_c , throughout the duration of the runoff event. That is

$$S_{mf} = S_{iw} + f_c t \quad (9-2)$$

where

S_{mf} = maximum possible infiltration losses during a rainfall event,

S_{iw} = initial soil wetting infiltration volume, which is assumed to be the same for all rainfall events,

f_c = the ultimate infiltration capacity of the catchment soils.

Guo and Adams (1998a) show that the value of S_{iw} can be estimated based on the infiltration parameters of the soils and climatic conditions of the region. The runoff volume from the pervious areas of an urban catchment, v_{rp} (in mm), can then be calculated as

$$v_{rp} = \begin{cases} 0, & v \leq S_{dp} + S_{iw} + f_c t \\ v - S_{dp} - S_{iw} - f_c t, & v > S_{dp} + S_{iw} + f_c t \end{cases} \quad (9-3)$$

To simplify expressions, the sum of S_{dp} and S_{iw} is denoted as S_{il} hereafter and is referred to as pervious area initial losses. Equation (9-3) implies that for runoff to occur on a pervious area, the input rainfall event volume must be greater than the sum of the pervious area depression storage and the maximum possible infiltration volume within the rainfall event.

9.1.3.3 Combination of Impervious and Pervious Areas

The overall runoff generation of the urban catchment is the area-weighted combination of the runoff from the pervious and impervious portions of the catchment. In an urban catchment, S_{di} is usually less than S_{dp} . Therefore, if v is less than S_{di} , then v must be less than $(S_{il} + f_c t)$. If the fraction of the impervious area of the urban catchment is h , then combining Equations (9-1) and (9-3) gives the following equation for urban catchments:

$$v_r = hv_{ri} + (1-h)v_{rp} = \begin{cases} 0, & v \leq S_{di} \\ h(v - S_{di}), & S_{di} < v \leq S_{il} + f_c t \\ v - S_d - f_c(1-h)t, & v > S_{il} + f_c t \end{cases} \quad (9-4)$$

where $S_d = hS_{di} + (1-h)S_{il}$, which is the area-weighted depression storage of the impervious areas and the initial losses of the pervious areas of the urban catchment.

Many continuous or event simulation models employ similar rainfall-runoff transformation mechanisms but on a time-step-by-time-step basis, with a determination of rainfall losses for each time step. In contrast, the rainfall-runoff transformation considered here for the development of probabilistic models is based on individual events, calculating total runoff volume for each individual event. Nevertheless, the same physical processes (i.e., interception, depression storage, and infiltration losses) are considered and mathematically represented.

9.1.4 Derived Probability Distributions of Runoff Characteristics

The general theory underlying the APSWM development is described here first. Based on this theory, the probability distributions of runoff characteristics from small catchments are then derived. Also illustrated here is the development of APSWM for three different stormwater management planning and design purposes: the design of detention ponds for flood control, the routing of flood waves through channel reaches, and the evaluation of the performance of low-impact development practices.

9.1.4.1 Derived Probability Distribution Theory

The derived probability distribution theory states that the probability distribution of a dependent random variable is fundamentally related to, and may be derived from, those of the independent random variables using the functional relationship between the dependent and independent random variables.

Consider a one-to-one and monotonic functional relationship, $y = g(x)$, which transforms values of an independent random variable X to values of a dependent random variable Y . The inverse of this function is $x = g^{-1}(y)$. The cumulative distribution function (CDF) of Y is

$$\begin{aligned} F_Y(y) &= P[Y \leq y] \\ &= P[X \leq g^{-1}(y)] \\ &= F_X(g^{-1}(y)) \\ &= \int_{-\infty}^{g^{-1}(y)} f_X(x) dx \end{aligned} \quad (9-5)$$

where $P[\cdot]$ = probability that the condition specified inside the brackets is satisfied, $F_X(g^{-1}(y))$ is the CDF of X , because $g^{-1}(y) = x$, $f_X(x)$ is the PDF of X . The interval $(-\infty, g^{-1}(y))$ defines the range of X such that the corresponding values of Y is less than a specific value y .

If $f_X(x)$ and $g^{-1}(y)$ are both known, the CDF of Y , $F_Y(y)$, can be obtained by carrying out the integration shown in Equation (9-5). The PDF of Y is the first derivative of $F_Y(y)$ with respect to y .

If a dependent random variable Z is a function of multiple random variables, the theory can also be applied to derive the PDF of Z . For instance, consider Z a function of two random variables X and Y given by

$$z = g(x, y) \quad (9-6)$$

where z , x , and y are, respectively, specific values of Z , X , and Y . The joint PDF of X and Y is denoted as $f_{X,Y}(x, y)$. The domain of X and Y such that the corresponding Z values are less than or equal to a specific value z is denoted as R_z . Following the same logic as for the case of a single independent random variable, the CDF of Z is determined by integrating the joint PDF of X and Y over the domain of X and Y values included in R_z . That is,

$$\begin{aligned} F_Z(z) &= P[Z \leq z] \\ &= \iint_{R_z} f_{X,Y}(x, y) dx dy \end{aligned} \quad (9-7)$$

The domain R_z is expressed in terms of x , y , and z and is determined based on the functional relationship expressed in Equation (9-6). The integration in Equation (9-7) will make x and y disappear, and the CDF of Z , $F_Z(z)$, may be obtained as a function of z only. The PDF of Z can then be determined by differentiating its CDF with respect to z :

$$f_Z(z) = \frac{d}{dz} \iint_{R_z} f_{X,Y}(x,y) dx dy \quad (9-8)$$

The previously described procedure constitutes the fundamentals of the derived probability distribution theory, which may be applied to derive the PDF of a random variable that is a function of other random variables. Success of such a derivation depends upon the determination and integration of the joint probability density function of the independent random variables. Adams and Papa (2000) provide more details about the derived probability distribution theory.

9.1.4.2 Runoff Event Volume

Equation (9-4) describes the functional relationship between the dependent random variable v_r and independent random variables v and t . (In describing random variables, a capital letter is conventionally used to represent the random variable itself, whereas the corresponding lower case letter is used to represent a particular value that the random variable may take. Throughout this chapter, this convention is followed as much as possible, but at the same time, as long as no risk of confusion exists, capital letters representing random variables are not introduced to reduce the total number of symbols used). Guo and Adams (1998a) derive the probability distribution of V_R using the derived probability distribution theory and this functional relationship. The probability per rainfall event that the generated runoff volume is greater than v_r was also determined. This probability, denoted as $P[V_R > v_r]$, represents the exceedance probability of V_R and is given by the following equation:

$$P[V_R > v_r] = \begin{cases} \exp(-\zeta S_{di}), & v_r = 0 \\ \exp(-\zeta S_{di} - \frac{\zeta}{h} v_r), & 0 < v_r \leq hS_{dd} \\ \frac{\lambda}{\lambda + \zeta f_c - \zeta f_c h} \exp(-\zeta S_d - \zeta v_r) \\ + \frac{\zeta f_c (1-h)}{\lambda + \zeta f_c - \zeta f_c h} \exp\left[-\zeta S_{di} + \frac{\lambda}{f_c} S_{dd} - \frac{1}{h} \left(\zeta + \frac{\lambda}{f_c}\right) v_r\right], & v_r > hS_{dd} \end{cases} \quad (9-9)$$

In Equation (9-9), $S_{dd} = S_{il} - S_{di}$.

The CDF of V_R can be easily determined from Equation (9-9), from which its PDF can also be determined. Knowing the PDF of V_R , Guo and Adams (1998a) determine the expected value of V_R per rainfall event. This expected value can be expressed as follows:

$$E(V_R) = \frac{h}{\zeta} \exp(-\zeta S_{di}) + \frac{\lambda(1-h)}{\zeta(\zeta f_c + \lambda)} \exp(-\zeta S_{il}) \quad (9-10)$$

The average annual runoff volume is the product of $E(V_R)$ and θ . Equations (9-9) and (9-10) are the first part of the APSWM. Using these equations, the average annual runoff volume and the probability distribution of runoff event volume from an urban catchment can be analytically determined.

9.1.4.3 Runoff Event Peak Discharge Rate

The rising and recession shapes of runoff hydrographs are approximated by triangular shapes. The time base of a runoff hydrograph, or the duration of a runoff event, is estimated through the use of

the catchment time of concentration. For this purpose, the term time of concentration, denoted t_c , is defined as the time required for runoff to travel from the most remote portion (time-wise) of the catchment to its outlet. The duration of the runoff event can then be estimated as $t + t_c$ (i.e., the duration of the rainfall event plus the catchment time of concentration). This can be drawn from the observation that runoff at the outlet starts at the beginning of the corresponding rainfall event if the delay caused by the time needed to fill the depressions of the catchment is negligible, and that it takes time t_c for the last drop of water falling on hydraulically the most remote part of the catchment to contribute flow to the outlet.

The catchment time of concentration is treated as a constant independent of rainfall characteristics for the determination of flood frequencies. In this regard, the catchment time of concentration can be viewed as a parameter combining the effects of catchment slope, roughness, length, shape, and topology. The peak discharge rate, Q_p , of a triangular hydrograph with runoff volume v_r and time base ($t + t_c$) is determined from the hydrograph geometry as

$$Q_p = \frac{2v_r}{t + t_c} \quad (9-11)$$

Note that this expression for peak discharge rate is independent of the ratio between the time to peak and the time base of a hydrograph. Arguably, Equation (9-11) may provide good estimates of peak discharge rates for some runoff events, but poor estimates for other events. When the interest is not in the determination of the peak discharge rate of a specific event, but in the determination of the exceedance probability of peak discharge rates from thousands of independent runoff events, the triangular hydrograph assumption for individual events may be justified.

Combining Equation (9-11) with Equation (9-4), the peak discharge rate Q_p resulting from a rainfall event with volume v and duration t can be expressed as

$$Q_p = \begin{cases} 0, & v \leq S_{di} \\ \frac{2h(v - S_{di})}{t + t_c}, & S_{di} < v \leq S_{il} + f_c t \\ \frac{2[v - S_d - f_c(1 - h)t]}{t + t_c}, & v > S_{il} + f_c t \end{cases} \quad (9-12)$$

Equation (9-12) describes the functional relationship between the dependent random variable Q_p and independent random variables v and t . Based on this relationship and the derived probability distribution theory, [Guo and Adams \(1998b\)](#) derive the probability distribution of Q_p . For two types of catchments, the exceedance probability per rainfall event, $P[Q_p > q_p]$, can be summarized as follows. For catchments with $f_c < S_{dd}/t_c$,

$$P[Q_p > q_p] = \begin{cases} \frac{2h\lambda}{2h\lambda + \zeta q_p} \exp\left(-\zeta S_{di} - \frac{\zeta t_c}{2h} q_p\right), & q_p < 2f_c h \\ \frac{2\lambda\zeta(1-h)(q_p - 2f_c h)}{(2h\lambda + \zeta q_p)(2\lambda + \zeta q_p + 2f_c \zeta - 2hf_c \zeta)} \exp\left[-\frac{(\zeta S_{il} - \lambda t_c - f_c \zeta t_c)q_p - 2f_c \zeta h S_{di} + 2\lambda h S_{dd}}{q_p - 2f_c h}\right] \\ + \frac{2h\lambda}{2h\lambda + \zeta q_p} \exp\left(-\zeta S_{di} - \frac{\zeta t_c}{2h} q_p\right), & 2f_c h \leq q_p < \frac{2hS_{dd}}{t_c} \\ \frac{\lambda}{\lambda + \zeta(\frac{q_p}{2} + f_c - f_c h)} \exp\left(-\zeta S_d - \frac{\zeta t_c}{2} q_p\right), & q_p \geq \frac{2hS_{dd}}{t_c} \end{cases} \quad (9-13)$$

For catchments with $f_c \geq S_{dd}/t_c$,

$$P[Q_p > q_p] = \begin{cases} \frac{2h\lambda}{2h\lambda + \zeta q_p} \exp\left(-\zeta S_{di} - \frac{\zeta t_c}{2h} q_p\right), & q_p < \frac{2hS_{dd}}{t_c} \\ \frac{2\lambda\zeta(1-h)(2f_c h - q_p)}{(2h\lambda + \zeta q_p)(2\lambda + \zeta q_p + 2f_c \zeta - 2hf_c \zeta)} \exp\left[-\frac{(\zeta S_{il} - \lambda t_c - f_c \zeta t_c)q_p - 2f_c \zeta h S_{di} + 2\lambda h S_{dd}}{q_p - 2f_c h}\right] \\ + \frac{2\lambda}{2\lambda + \zeta(q_p + 2f_c - 2f_c h)} \exp\left(-\zeta S_d - \frac{\zeta t_c}{2} q_p\right), & \frac{2hS_{dd}}{t_c} \leq q_p < 2f_c h \\ \frac{\lambda}{\lambda + \zeta\left(\frac{q_p}{2} + f_c - f_c h\right)} \exp\left(-\zeta S_d - \frac{\zeta t_c}{2} q_p\right), & q_p \geq 2f_c h \end{cases} \quad (9-14)$$

Equations (9-13) and (9-14) also form part of the APSWM.

9.1.4.4 Runoff Routing through Detention Ponds

For the sizing of urban flood control detention ponds, regulatory agencies often require that for a series of return-period design storm events up to and including the most severe one, peak discharges for developed conditions with flood control in place shall not exceed peak discharges under existing land-use conditions or some other specific values (Walesh 1989). The design storm approach has therefore naturally been used for designing flood control detention facilities to satisfy this type of continuous probability criteria (Akan 1989, WEF and ASCE 2012). Inherent in the design storm-based approach is the assumption that the return period of a design storm equals the return period of the peak discharge rate from the catchment resulting from the input design storm and the consequent peak outflow rate from the flood control pond. Continuous simulation involves the use of long-term historical precipitation records together with a simulation model to evaluate the simulated historical response of a proposed detention pond. The design is modified so as to produce an acceptable statistical performance of the system, consistent with the specified continuous probability criteria for flood control. The disadvantage of the continuous simulation approach is that it involves many more computational steps, and depending on how frequency analysis is performed on the continuous simulation results, the final design results may not be as reproducible as those from the design storm approach. As a result, continuous simulation is not commonly used in sizing flood control detention facilities.

Guo and Adams (1999b) develop probabilistic models to approximate continuous simulation results for the sizing of flood control detention facilities. Assuming that (1) the inflow hydrograph is triangular in shape, (2) the detention facility is empty at the start of any flood-producing runoff event, and (3) the outflow hydrographs have a linear rising limb, then Figure 9-1 may be used to represent the routing of the hydrograph through a detention facility for each runoff event. Figure 9-1 shows that the time base of the inflow hydrograph is $(t + t_c)$, where t is the duration of the causal rainfall event and t_c is the catchment time of concentration. The outflow occurs immediately after the start of the inflow hydrograph. Because the outflow at an instant of time is directly proportional to the storage volume reached at that time, the highest storage volume is reached only when the inflow and outflow hydrographs intersect, and afterward the outflow rates would always be greater than the inflow rates. That is why the outflow hydrograph intersects with the inflow hydrograph at the peak of the outflow hydrograph and along the recession limb of the inflow hydrograph. The volume of the runoff event, v_r , in mm of water over the catchment, entering the detention facility equals the area enclosed by the inflow hydrograph. The shaded area in Figure 9-1, denoted S_{Q_o} (mm), equals the maximum storage volume utilized during the passage of the runoff event. Hence, the peak outflow rate, Q_o , is the discharge rate of the detention facility at storage volume S_{Q_o} .

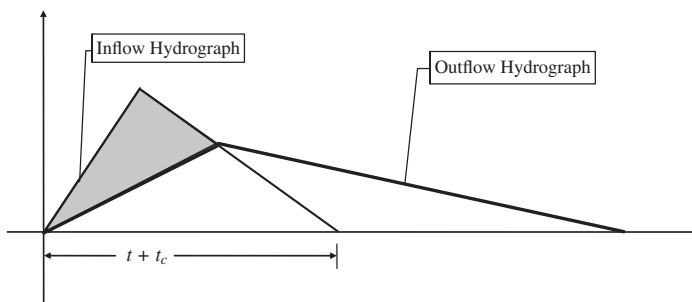


Figure 9-1. Routing of hydrographs through a flood control detention facility.

Figure 9-1 shows that

$$S_{Q_o} = \frac{1}{2}(Q_i - Q_o)(t + t_c) \quad (9-15)$$

where Q_i is the peak inflow rate and has the units of Q_o , (mm/h), and t and t_c are both in h.

Rearranging Equation (9-15), and noting that $v_r = \frac{1}{2}Q_i(t + t_c)$, the following is obtained:

$$Q_o = \frac{2(v_r - S_{Q_o})}{t + t_c} \quad (9-16)$$

Substituting Equation (9-4) for the expression of v_r into Equation (9-16) results in the following:

$$Q_o = \begin{cases} 0, & v \leq S_{di} \\ \frac{2[h(v - S_{di}) - S_{Q_o}]}{t + t_c}, & S_{di} < v \leq S_{il} + f_c t \\ \frac{2[v - S_d - f_c(1 - h)t - S_{Q_o}]}{t + t_c}, & v > S_{il} + f_c t \end{cases} \quad (9-17)$$

To use Equation (9-17), the relationship between S_{Q_o} and Q_o must be known. In the case where the storage–discharge relationship of a pond can be expressed in a functional form, this functional form can be substituted into Equation (9-17), and Q_o may be expressed as an explicit function of v , t , catchment hydrologic parameters, and constants/coefficients included in the functional storage–discharge relationship. However, the storage–discharge relationships of actual detention facilities are often only available in a tabular form, with pairs of storage–discharge values corresponding to various water levels in the detention facility. In these cases, if the storage–discharge table is not replaced with a fitted analytical function, Equation (9-17) can only be solved iteratively by trial and error using the storage–discharge table of the detention facility.

In developing the probabilistic model, the solution of Equation (9-17) is not explicitly sought, but rather interest resides in the probability per rainfall event that Q_o exceeds a given value q , denoted $P[Q_o > q]$. If S_q is the storage volume of the detention facility at which the routed discharge rate from the facility equals the given value q , then this S_q value can be used as the S_{Q_o} value in Equation (9-17) to derive $P[Q_o > q]$ based on Equation (9-17) and the probability distributions of v and t . For any given value q , the corresponding S_q value can be determined from the storage–discharge table of the detention facility, through interpolation if necessary.

In a typical design scenario, the values for storage volume in the storage–discharge table are estimated from the grading plan of the detention facility, and discharge values are determined from the selected orifice size and the hydraulic head over the orifice at the corresponding storage volume. Due to natural terrain conditions or the installation of an orifice and weir combination as the outflow control device, the storage–discharge relationship may be discontinuous. As a result, devising an analytical function for the storage–discharge relationship may be problematic. Thus, the strategy used in Guo and Adams's (1999b) derivation is that the storage–discharge relationship is treated as comprising discrete combinations of (S_q, q) . For each of these combinations, $P[Q_o > q]$ is derived. The ordered combinations of $P[Q_o > q]$ for all possible discrete values of q , which are of interest in planning and design, forms the probability distribution of the peak outflow rate Q_o . This strategy greatly simplifies the derivation that would be required if the storage–discharge relationship is treated as a function and substituted into Equation (9-17).

Following that simplifying strategy and utilizing the functional relationship between dependent random variable Q_o and independent random variables v and t as described in Equation (9-17), Guo and Adams (1999b) derive an analytical expression for the exceedance probability of $P[Q_o > q]$ as a function of contributing catchment hydrologic parameters, parameters reflecting local climatic conditions, and q and the corresponding S_q values. The $P[Q_o > q]$ results presented in the following are different for four possible types of (S_q, q) combinations.

For Type 1 (S_q, q) combinations with $q < 2f_c h$ and $S_q < hS_{dd} - qt_c/2$,

$$P[Q_o > q] = \frac{2h\lambda}{2h\lambda + \zeta q} \exp\left[-\zeta\left(\frac{qt_c}{2h} + S_{di} + \frac{S_q}{h}\right)\right] \quad (9-18)$$

For Type 2 (S_q, q) combinations with $q < 2f_c h$ and $S_q \geq hS_{dd} - qt_c/2$,

$$\begin{aligned} P[Q_o > q] = & \frac{\lambda}{\lambda + \zeta\left(\frac{q}{2} + f_c - f_c h\right)} \exp\left[-\zeta\left(\frac{qt_c}{2} + S_d + S_q\right)\right] \\ & + \frac{2\lambda\zeta(1-h)(2f_c h - q)}{(2h\lambda + \zeta q)(2\lambda + \zeta q + 2f_c \zeta - 2hf_c \zeta)} \exp\left[-\frac{(\zeta S_{il} - \lambda t_c - f_c \zeta t_c)q - 2f_c \zeta(hS_{di} + S_q) + 2\lambda(hS_{dd} - S_q)}{q - 2f_c h}\right] \end{aligned} \quad (9-19)$$

For Type 3 (S_q, q) combinations with $q \geq 2f_c h$ and $S_q < hS_{dd} - qt_c/2$,

$$\begin{aligned} P[Q_o > q] = & \frac{2h\lambda}{2h\lambda + \zeta q} \exp\left[-\zeta\left(\frac{qt_c}{2h} + S_{di} + \frac{S_q}{h}\right)\right] \\ & + \frac{2\lambda\zeta(1-h)(q - 2f_c h)}{(2h\lambda + \zeta q)(2\lambda + \zeta q + 2f_c \zeta - 2hf_c \zeta)} \exp\left[-\frac{(\zeta S_{il} - \lambda t_c - f_c \zeta t_c)q - 2f_c \zeta(hS_{di} + S_q) + 2\lambda(hS_{dd} - S_q)}{q - 2f_c h}\right] \end{aligned} \quad (9-20)$$

For Type 4 (S_q, q) combinations with $q \geq 2f_c h$ and $S_q \geq hS_{dd} - qt_c/2$,

$$P[Q_o > q] = \frac{\lambda}{\lambda + \zeta\left(\frac{q}{2} + f_c - f_c h\right)} \exp\left[-\zeta\left(\frac{qt_c}{2} + S_d + S_q\right)\right] \quad (9-21)$$

With the upstream catchment characterized by its area, h , S_{di} , S_{il} , f_c , and t_c , and the downstream detention pond described by the ordered pairs of (S_q, q) values, the probability of the outflow

from the detention pond exceeding each q value can therefore be evaluated analytically using Equation (9-18) through (9-21). Through interpolation and extrapolation of the ordered pairs of (S_q, q) values, the pond storage volume corresponding to any specific pond outflow value of interest may be obtained, the probability that the pond outflow exceeding that specific outflow value can also be analytically evaluated using Equations (9-18) through (9-21). In a design situation, the q values and their exceedance probabilities will be given according to the flood control criteria, and the required corresponding S_q values may be obtained through trial-and-error calculations using Equations (9-18) through (9-21). These equations form the part of the APSWM that facilitates the probabilistic routing of runoff through flood control detention ponds and the hydrologic design of detention ponds to satisfy continuous probability criteria.

[Guo and Adams \(1999a\)](#) also derive analytical equations that can be used for the analysis of detention ponds for stormwater quality control purposes. Those equations are not presented here because the format of the design criteria for stormwater quality control is not that uniform across jurisdictions, whereas equations derived in [Guo and Adams \(1999a\)](#) can only be used to estimate the stormwater capture efficiency and average detention time provided by quality-control detention ponds. Although inappropriate, some jurisdictions still specify stormwater quality control criteria in terms of design storms.

9.1.4.5 Runoff Routing through Channel Reaches

A channel reach, such as a stream segment, drainage ditch, or sewer pipe, usually attenuates and translates runoff peaks. In stormwater management studies, runoff routing through channel reaches is often conducted not to provide detailed real-time flood wave behavior, but to determine flood frequency distributions at downstream locations of interest. The design storm approach, as used in stormwater management, properly models only changes (attenuation and translation) to individual hydrographs; the quantification of the associated shift or statistical transformation of peak inflow as a random variable is not attempted.

[Guo et al. \(2009\)](#) propose a probabilistic channel-routing method and derive analytical equations that can be used to determine the changes to the entire probability distribution of flood peaks induced by channel reaches. The analytical equations eliminate a major deficiency of the design storm approach by appropriately following not only the key hydrologic changes that a channel reach typically makes to individual inflow hydrographs, but also the transformations in the probability distribution taking place from the upstream to the downstream cross-sections of a channel reach.

Similar to any time-step-by-time-step channel routing method, the probabilistic channel-routing method was developed by first considering the physical characteristics of a channel reach and the equations governing flood flows. The difference is that the probabilistic approach needs a more concise way of representing the effect of a channel reach on the reduction of flood peaks. To understand this concise representation, the following brief review of conventional channel routing calculations is provided first.

Probabilistic channel routing is based on the widely used Muskingum–Cunge channel routing method ([Fread 1993](#)), which employs the equation of continuity:

$$I - O = \frac{dS}{dT} \quad (9-22)$$

where I is the inflow rate to the reach, O is the outflow rate from the reach, and S is the storage of water within the entire reach at time T . [McCarthy \(1938\)](#) first expresses S as

$$S = K[IX + O(1 - X)] \quad (9-23)$$

where K is a routing coefficient and X is a weighting factor.

Cunge (1969) shows that X can be related to the reach characteristics as follows:

$$X = \frac{1}{2} \left(1 - \frac{q_o}{S_f c \Delta x} \right) \quad (9-24)$$

where q_o is the discharge per unit top width of the channel, c is the celerity of a kinematic (or diffusive) wave, and Δx is the length of the reach. The friction slope S_f may be approximated as the initial slope of the energy grade line (Fread 1993), or simply by the slope of the channel reach. The value of c is estimated as a function of the average velocity V by

$$c = mV \quad (9-25)$$

where m is the kinematic ratio, which depends on the shape of the cross-section of the reach (Fread 1993). It can be estimated using

$$m = \frac{5}{3} - \frac{2}{3} \frac{A_w}{B_w P_w} \frac{dP_w}{dy} \quad (9-26)$$

where

B_w = top width of the channel,

A_w = cross-sectional area,

P_w = shear perimeter, and

y = water depth of the channel cross-section.

Alternatively, a diffusive wave celerity equation (Jain 2001) may be used to estimate c , in which case the ratio between wave celerity and flow velocity may be different from m . The kinematic wave celerity is often used in practice, for the sake of simplicity. A more recent alternative for computing X was presented by Dooge (1982).

The value of K is commonly estimated as the travel time of the wave through the reach:

$$K = \frac{\Delta x}{c} \quad (9-27)$$

Thus, both K and X values can, to some extent, be related to the physical characteristics of the reach. Routing can be done using either constant m and c parameters (i.e., using a single average discharge and velocity) or variable parameters (i.e., estimated for each new discharge and velocity during the routing process). Equations (9-22) through (9-27) form the basis of the Muskingum–Cunge channel-routing method. It blends the greater predictive ability of the diffusion wave method with the simplicity of hydrologic routing, resulting in one of the most commonly used general techniques.

The probabilistic channel-routing method presented in Guo et al. (2009) is made possible by concisely representing the major effect that channel reaches have on event hydrographs. With distributed lateral inflows into a channel reach treated as outflows from adjacent catchments joining at the downstream end of the channel reach, the translation and storage effects on the upstream inflow hydrographs exerted by the channel reach are considered separately in the development of the probabilistic channel-routing method. If rain falling on a catchment is viewed as inflow to it, then in terms of flow routing, a lumped catchment also exerts translation and storage effects on inflow hydrographs. Therefore, only for the purpose of calculating the flood peak reduction caused by a channel reach, the channel reach may be viewed as equivalent to a catchment. Nevertheless, physical and functional differences exist between a catchment and a channel reach. In the development of the probabilistic channel-routing method, with appropriate attention paid to the differences between a

channel reach and a catchment, a channel reach is treated as an equivalent catchment for quantifying its flood peak reduction effects.

Because unit hydrographs of catchments are commonly used to combine and represent all the effects catchments exert on incoming effective rainfall hyetographs, a unit-hydrograph-like mathematical analogy was made and obtained for a channel reach, with the potential to represent all the effects that channel reaches exert on inflow hydrographs. To this end, Equations (9-22) and (9-23) are used to solve for O in response to a unit impulse inflow into the reach at time zero, which results in the instantaneous unit hydrograph (IUH) from the channel reach:

$$u(T) = \frac{e^{\frac{-T}{K(1-X)}}}{K(1-X)^2} - \frac{X\delta(0)}{(1-X)} \quad (9-28)$$

In Equation (9-28), $u(T)$ is the IUH of the channel reach and $\delta(0)$ is the Dirac delta function at time $T = 0$. The IUH of a channel reach shows a negative impulse at $T = 0$ and exponential recession afterward. Other than the initial negative impulse, it is similar to the response of a single linear reservoir to an instantaneous but unit input.

With Equation (9-28) as the IUH of a channel reach, the channel reach can in fact be treated as a catchment for flow-routing purposes. In essence, channel reaches transform inflow hydrographs in a manner similar to the way catchments transform effective rainfall hyetographs: by attenuating and translating the input. Because the time base of a runoff hydrograph is assumed to be equal to the duration of the causal rainfall event plus the catchment t_c , the latter should explicitly include the translation time over the catchment and the storage-induced delay time by the catchment. The longer the catchment t_c , the greater the degree of peak attenuation. In probabilistic channel-flood routing, the flood peak reduction effect of a channel reach is accounted for by increasing the t_c of the upstream catchment that discharges into the channel reach.

The difference between a channel reach and a catchment is that pure translation (which does not occur in nature but occurs in calculation if $X = 0.5$ when the Muskingum–Cunge channel-routing method is used) of water occurring in a channel reach does not attenuate incoming flood peaks, whereas translation of water on a catchment always results in attenuation of peak rainfall input. This is because pure translation of water inside a spatially confined channel may not cause diffusion of water and hence does not change the temporal shape of the inflow hydrograph, whereas translation of water on a catchment surface facilitates concentration of spatially distributed rainfall and simultaneously diffuses the incoming rainfall hyetograph in time. This difference necessitates that the additional delay time that should be added to the t_c of the upstream catchment, to account for the flood attenuation effect of a downstream channel reach, should only be the storage-induced delay time of the channel reach, not the translation time of flood waves through the channel reach; although the two occur in nature simultaneously and may be proportional to each other.

Temporary storage of water causes the storage-induced delay time of both a catchment and a channel reach. The functional effects are the same: the spreading in time of inflow hydrographs and the reduction of inflow peaks. The physical difference is that storage over a catchment includes surface depression, distributed pond/reservoir storage, and valley storage of river flows. These are lumped, as being a part of the catchment. Whereas the storage a channel reach provides includes only its valley storage. The concept of storage-induced delay time (simply referred to as storage-delay time) is introduced for the purposes of separating translation from storage and accounting for the flood attenuation effect of a channel reach.

To estimate the storage-delay time t_{sd} of a channel reach, the moments of the IUH of the channel reach are examined. The first moment of the IUH about the origin is found to be equal to K . The second moment of the IUH about the mean (σ^2) is found to be (Guo et al 2009)

$$\sigma^2 = K^2(1 - 2X) \quad (9-29)$$

The first moment about the origin is a measure of the average time it takes for a unit impulse inflow to pass through a reach and become a flood wave in the process. The standard deviation σ , i.e., the square root of the second moment about the mean, characterizes the increase in the duration (temporal width) of the flood wave as it travels through the reach.

The functional difference between a catchment and a channel reach results in the fact that, unlike a catchment, the mean of the IUH of a channel reach, which measures the wave translation time through the reach, does not change the shape of an inflow hydrograph and does not directly contribute to the storage-induced delay time of the channel reach. The standard deviation of the IUH, however, does characterize the increase in the width or duration of a flood wave as it travels through the reach. The t_{sd} of the channel reach should approximately equal the amount of increase in the duration of a flood wave as it travels through the reach and should therefore be proportional to the standard deviation of the IUH.

Assuming that the t_{sd} of a channel reach is directly proportional to the standard deviation of its IUH, the special case with $X = 0$ (level-surface storage) may be considered, so as to determine the value of the proportionality between t_{sd} and σ . Equation (9-24) shows that short flat reaches, or short reaches with rough surfaces, have X close to zero. These reach characteristics make them behave more like a catchment with little storage. Because the time of concentration of a catchment without storage effects equals the longest time of travel of a wave through the catchment, the t_{sd} of a reach with $X = 0$ can therefore be equated to the time of travel through the reach. The time of travel for water droplets through the reach is mK , where K is the wave travel time through the reach and m is the kinematic ratio, which is the ratio between wave celerity and flow velocity. Because $\sigma = K$ when $X = 0$, the proportionality between t_{sd} and σ is thus m for the special case of $X = 0$. The duration of the causal rainfall event may affect the proportionality constant as well. Longer rainfall events may be associated with slightly smaller proportionality constants. However, to achieve an accuracy that is normally expected for planning and design purposes, these details can be neglected, and it is assumed that when $X = 0$, $t_{sd} = m\sigma$ for all rainfall events.

Generalizing this reasoning to cases with nonzero X values, the t_{sd} of a channel reach is then $mK\sqrt{1 - 2X}$, and the time base of any flood hydrograph will increase by $mK\sqrt{1 - 2X}$ after passing through the channel reach. Because the K , X , and m values of a reach provide sufficient information about the reach for Muskingum–Cunge routing calculations, $mK\sqrt{1 - 2X}$ captures and condenses this information. If t_{sd} is not too long, as compared with the t_c of the upstream catchment, the channel reach can be lumped with the upstream catchment for routing purposes, and the time of concentration of the lumped equivalent catchment is:

$$t_{cc} = t_c + t_{sd} = t_c + mK\sqrt{1 - 2X} \quad (9-30)$$

This t_{cc} combines the rainfall–runoff routing effect of the upstream catchment and the peak attenuation effect of the downstream channel reach. The other parameters of this equivalent catchment are the same as those of the catchment upstream of the inflow cross-section of the channel reach. Using t_{cc} as the t_c in Equations (9-13) and (9-14), the exceedance probability distribution of peak flows from the reach can be analytically determined. Separate calculation of t_{sd} based on the physical characteristics of the channel reach makes its flood peak attenuation effect explicit and accountable.

9.1.4.6 Conversion from Event-Based Exceedance Probability to Return Period

The previously presented derived probability distribution results comprise the main part of the APSWM. The majority of them are expressed in the form of the exceedance probability of a quantity

of interest per rainfall event. The conversion from exceedance probability per rainfall event to return period is as follows:

$$T_R = \frac{1}{\theta P} \quad (9-31)$$

where

T_R = return period (in years) of the quantity of interest,

θ = average number of rainfall events per year, and

P = exceedance probability per rainfall event.

If the quantity of interest is the runoff event volume from a catchment, then P is $P[V_r > v_r]$ as shown in Equation (9-9); if the quantity of interest is the peak outflow rate from a detention pond as a result of a runoff event, then P is $P[Q_o > q]$ as shown in Equations (9-18) through (9-21). Thus, a simple inversion of the previously derived exceedance probabilities can convert the APSWM results to return periods. To apply APSWM for a specific location, event-based analysis of precipitation records must be conducted to obtain the values of θ and the other three distribution parameters (i.e., ζ , λ , and ψ).

9.1.4.7 Sizing of Storage Units for Rainwater Harvesting

The analytical probabilistic approach can also be effectively used for the study of low-impact development (LID) practices such as rain gardens, green roofs, and rainwater harvesting systems. As an example, derived equations that can be used for sizing storage units for rainwater harvesting are presented here.

Advocated by green building design principles is the use of rainwater storage units to collect roof runoff during nonwinter seasons for nonpotable uses (Kibert 2005). Depending on the type, design, and construction of roofs, some may collect 100% of rainfall and convert it to runoff, while some may convert only a fraction of rainfall to runoff. As a general case, a factor ϕ may be applied to convert rainfall to runoff. In climates where evaporation during rainfall events is high and cannot be neglected, the ϕ values may be further reduced to account for this loss of evaporation during rainfall events. In some green building applications, diverting the first flush of each event away from the rainwater storage unit may be desirable. If this is required, the volume of runoff that can be collected in the storage unit from a rainfall event is

$$v_c = \begin{cases} 0, & v \leq v_{ff} \\ \phi(v - v_{ff}), & v > v_{ff} \end{cases} \quad (9-32)$$

where

v = depth or volume of the rainfall event,

v_{ff} = designated first flush depth, and

v_c = runoff that can be collected into the storage unit; these variables are all measured in depth (mm) of water over the rooftop area.

Given the marginal PDF of v (Table 9-1) and the functional relationship between v_c and v as shown in Equation (9-32), the probability distribution of v_c can be obtained by using the derived probability distribution theory. The expected value of v_c per rainfall event, $E[v_c]$, can then be determined as well. The annual total volume of runoff (denoted as R_a) generated from the roof after diverting first flush is the product of $E[v_c]$ and θ . It can be expressed as

$$R_a = A \frac{\theta \phi}{\zeta} e^{-\zeta v_{ff}} \quad (9-33)$$

where A is the area of the vertical projection of the roof (hereafter referred to as the rooftop area) and θ is the average number of rainfall events per year when the storage unit is in operation. With ζ expressed in 1/mm, A in m^2 , and v_{ff} and v_c in mm over the rooftop area, the R_a calculated using Equation (9-33) has the unit of liters (L). If other unit systems are used, proper unit conversion needs to be applied. [Guo and Baetz \(2007\)](#) provide detailed derivations.

Water collected in the storage unit during rainfall events is used for landscaping, hardscape cleaning, and/or maintenance purposes during dry periods between successive rainfall events. Within the duration of individual rainfall events, no water needs to be taken from the storage unit. Thus, the annual total length of time when water needs to be withdrawn from the storage unit is

$$T_d = \theta E[b] = \theta \int_{b=0}^{\infty} b \psi e^{-\psi b} db = \frac{\theta}{\psi} \quad (9-34)$$

where $E[b]$ is the expected value of interevent time b .

Depending on the size of the storage unit, the local climate, and the use rate, water may not be available when it is needed. The reliability of the storage unit in supplying water is defined as the fraction (or percentage) of time when use needs are satisfied by water collected in the storage unit. This reliability is denoted as R_e (dimensionless). The average daily rate of water use from the storage unit is denoted as G (L/day), and G is considered as a constant. If G varies significantly from month to month or season to season, the following equations may be used separately for individual seasons within which G remains relatively constant.

A first-hand estimate of the maximum use rate that may be provided by a storage unit with a reliability of R_e is

$$G_{\max} = \frac{R_a}{T_d R_e} = \frac{A \phi \psi}{\zeta R_e} e^{-\zeta v_{ff}} \quad (9-35)$$

This maximum rate can only be provided when the storage unit is large enough to capture and store 100% of collectable runoff from all rainfall events. In reality, spills from the storage unit may occur when it is full while more rain water is still draining to it. Even if the storage unit is large enough for individual rainfall events, when one rainfall event is followed closely by another, spills may still occur because the storage unit is not empty when the next event occurs.

To estimate the required storage volume for a desired use rate and reliability, the amount of rain water that can be actually collected and subsequently used has to be determined. This is done by determining the total volume that is spilled from the storage unit. To determine the annual total spill volume, a use/load cycle (referred to as the current cycle or the cycle) starting from the beginning of a dry period, or the end of the last rainfall event, is analyzed. The interevent times, durations, and depths of rainfall events comprising each use/load cycle are treated as statistically independent, exponentially distributed random variables. The probability per cycle of a spill volume equaling or exceeding a given value is derived using the derived probability distribution theory by [Guo and Baetz \(2007\)](#). As a part of this probability, the probability per cycle that some spill occurs (denoted $G_P(0)$, where the argument 0 indicates that the spill is greater than zero) is derived to be

$$G_P(0) = \left(\frac{A \phi \psi}{A \phi \psi + \zeta G} + \frac{\zeta G}{A \phi \psi + \zeta G} e^{-\zeta B / (A \phi) - \psi B / G} \right) e^{-\zeta v_{ff}} \quad (9-36)$$

where B is the size of the storage unit in L.

The annual total spill volume is simply the product of the annual number of cycles and the expected value of spill per cycle. The annual total volume collected into the storage unit and utilized

subsequently is denoted as R_c . R_c can be calculated as the annual total volume of runoff collected from the roof with diversion of first flush (i.e., R_a) minus the annual total spill volume, or (Guo and Baetz 2007)

$$R_c = \frac{A\phi\theta}{\zeta} [e^{-\zeta v_{ff}} - G_p(0)] \quad (9-37)$$

The length of time that this captured volume sustains various uses is simply R_c divided by the use rate G . Because the annual total length of dry periods when water is required is θ/ψ [from Equation (9-34)], the reliability of having water in the storage unit when needed is

$$R_e = \frac{R_c/G}{\theta/\psi} = \frac{A\phi\psi}{A\phi\psi + \zeta G} e^{-\zeta v_{ff}} [1 - e^{-\zeta B/(A\phi) - \psi B/G}] \quad (9-38)$$

Equation (9-38) may be used to determine the reliability for a given location, roof area, storage unit size, and use rate. Equation (9-38) shows that given a location, roof area, and use rate, the maximum reliability that can be achieved is

$$R_{e\max} = \frac{A\phi\psi}{A\phi\psi + \zeta G} e^{-\zeta v_{ff}} \quad (9-39)$$

This maximum reliability can only be achieved when B approaches infinity. Similarly, given a desired reliability R_e and infinite storage volume, the maximum sustainable use rate can be obtained by solving Equation (9-38) for G . The result is

$$G_{\max} = \frac{A\phi\psi}{\zeta} \left(\frac{e^{-\zeta v_{ff}}}{R_e} - 1 \right) \quad (9-40)$$

The most common application is to determine the required storage volume knowing the desired reliability, roof area, and average water use rate. This required storage volume is obtained by solving Equation (9-38) for B :

$$B = \frac{A\phi G}{\zeta G + A\phi\psi} \ln \left[\frac{A\phi\psi e^{-\zeta v_{ff}}}{A\phi\psi e^{-\zeta v_{ff}} - R_e(A\phi\psi + \zeta G)} \right] \quad (9-41)$$

In using Equation (9-41), care must be taken to ensure that the desired R_e is less than or equal to the maximum that may be achieved.

9.1.5 Example 9-1: Flood Quantile Estimation and Flood Control Detention Pond Design in Chicago, Illinois

Guo and Baetz (2007) give example applications of the sizing equations for rainwater harvesting for two locations: Chicago, Illinois and Phoenix, Arizona. Presented here are example applications of flood quantile estimation and flood control analysis using the APSWM; Guo (2001) provides more details about these example applications, whereas Quader and Guo (2006) and Guo and Markus (2011) report additional example applications of the APSWM for real watersheds in Ontario, Canada, and the Chicago area, respectively.

As a first step in using the APSWM, the event-based local rainfall statistics must be obtained. To represent the climate in the Chicago area, a 50-year hourly historical rainfall record (from 1948 to

1997) from the Midway Airport in Chicago was analyzed. A minimum inter-event time of 12 h was used to separate the continuous hourly record into individual events, and rainfall events with volumes less than 0.5 mm were omitted from statistical analysis. To avoid snowfall events, data from November through March were not included in the analysis. The average rainfall event volume, average rainfall event duration, and average interevent time were found to be 13.3 mm, 8.62 h, and 90.9 h, respectively. With these mean values and using the method of moments, exponential distributions may be fitted to rainfall event volume, duration, and inter-event time (see Table 9-1). The annual average number of rainfall events was determined to be 45.

For flood control analysis and design, the purpose of conducting design storm modeling or continuous simulations and applying the analytical probabilistic approach is to determine peak flood discharge rates of various return periods from a catchment of interest and to design flood control structures to satisfy flood control requirements. In the example study, the continuous hourly rainfall data from the Midway Airport in Chicago, the fitted exponential distributions, and the design storms developed for the Chicago region were used for comparison purposes.

A hypothetical urban catchment in the Chicago area has an area of 259 hectares and an imperviousness of 35%. The average slope of the catchment is 0.005 m/m. The US Environmental Protection Agency's Stormwater Management Model, Version 4, or SWMM4 ([Huber and Dickinson 1988](#)) was used for continuous simulation. Table 9-2 lists the other hydrologic parameters input to the SWMM4 model to represent the catchment.

The peak discharge rates of individual runoff events were determined from the simulated continuous flow series. These individual peak discharge rates were then ranked in descending order. The peak discharge rate exceedance probability is determined using the Weibull plotting position formula. This exceedance probability is then converted to a corresponding return period according to Equation (9-31). Plotting of these peak discharge rates versus their corresponding return periods in a graph facilitates the estimation of peak discharge rates of desired return periods from simulated continuous flow series.

For design storm modeling, both SWMM4 and the Hydrologic Engineering Center–Hydrologic Modeling System (HEC-HMS) developed by the US Army Corps of Engineers ([USACE 1998](#)) were used. The HEC-HMS model allows the choice of several precipitation loss calculation methods and several runoff routing methods. The “initial and uniform loss rate” method was selected because it closely resembles the method used in the analytical probabilistic approach. The Clark unit hydrograph method was chosen for catchment runoff routing calculations. The Clark unit hydrograph method requires the input of the catchment time of concentration and storage coefficient, which were estimated by comparing the peak discharge rates simulated using the SWMM4 model with those simulated using the HEC-HMS model under the same input design storms. This estimation procedure ensures that the same test catchment is represented both in the SWMM4 model and in the HEC-HMS model.

Table 9-2. Hydrologic Parameters of Test Catchment Used in SWMM4.

<i>Manning's n</i>								
S_{di} (mm)	S_{dp} (mm)	f_m (mm/h)	f_c (mm/h)	k (h^{-1})	R	Impervious areas	Pervious areas	Catchment width (m)
0.0	4.6	76.2	3.6	4.14	0.01	0.05	0.25	9144

Source: [Guo \(2001\)](#).

Notes: This application of SWMM4 uses the Horton infiltration model where f_m is the maximum infiltration capacity of the soil; f_c is the ultimate infiltration capacity of the soil; k is the infiltration capacity decay coefficient; and R is a constant, considered to be much less than one, used in $k_d = Rk$ for the determination of k_d , where k_d is the decay coefficient for the infiltration capacity recovery curve.

Using the HEC-HMS model with the “initial and uniform loss rate” option, all rainfall is treated as lost until the volume of initial loss is satisfied, and then rainfall is lost at a constant rate. The constant loss rate is taken as the minimum ultimate infiltration rate used with the Horton infiltration equation in the SWMM4 model. The initial loss volume is the sum of pervious area depression storage and pervious area initial soil wetting infiltration volume. The pervious area initial soil wetting infiltration volume S_{iw} was used in the APSWM and is defined in [Guo and Adams \(1998a\)](#). The value of S_{iw} for this example was estimated using a procedure outlined in [Guo and Adams \(1998a\)](#), based on the Horton infiltration parameter values input to the SWMM4 model.

Design storms with return periods from two months to 100 years were obtained from [Huff and Angel \(1992\)](#) for the Chicago region. Peak discharges computed using these design storms are extremely sensitive to storm duration. Although some stormwater management ordinances specify the use of 24 h design storms regardless of the size of the catchment, shorter-duration design storms are deemed appropriate for small urban catchments. Given that the time of concentration and storage coefficient of the catchment were estimated to be 1.9 and 0.25 h, respectively, the 6 h duration design storms were chosen initially. To verify the appropriateness of this choice and demonstrate the effect of the duration of design storms, the 3 h and 24 h design storms were also simulated.

[Huff and Angel \(1992\)](#) classify the rainstorms depending on which quartile of the storm period received the heaviest rainfall. Design storms of a specified duration and return period can have four different temporal distributions: peaking in the first, second, third, and fourth quartile. These different temporal distributions will affect the peak discharge as well. To demonstrate this effect, for the 6 h design storms, two types of temporal distributions were used: one peaking in the first quartile and the other peaking in the third quartile within the duration of the storm. Two types of temporal distributions were used for the 3 h duration storms: one peaking in the first quartile and the other peaking in the second quartile. For the 24 h design storms, only one temporal distribution peaking in the third quartile was used because storms of durations from 12 to 24 h most often peak in the third quartile ([Huff and Angel 1992](#)).

Two continuous SWMM4 simulation runs were performed, one with detention storage to reduce peak flow by 50% for return periods from two to 100 years and the other without detention storage. In applying the analytical probabilistic approach, Equations (9-13) and (9-14) were used to calculate peak flow exceedance probabilities for the case of a catchment without downstream detention pond; and Equations (9-18) through (9-21) were used to calculate the peak outflow exceedance probabilities from the detention pond servicing the upstream catchment. Figure 9-2

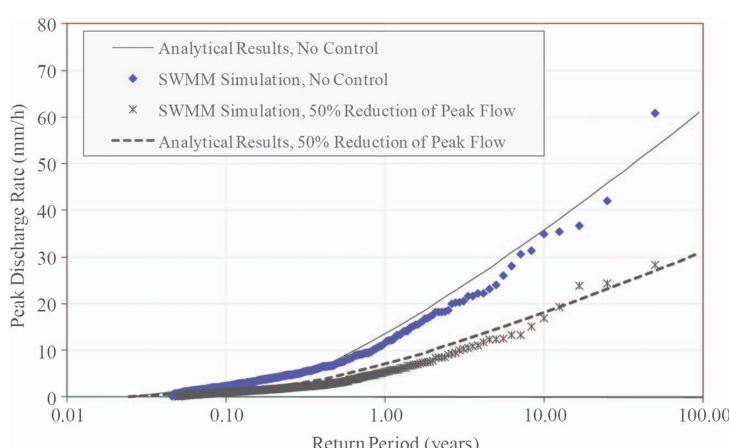


Figure 9-2. Comparison of SWMM4 continuous simulation and analytical probabilistic results.
Source: [Guo \(2001\)](#).

Sizing of Flood Control Detention Facilities Using the Analytical Probabilistic Approach			
Chicago Midway Airport Meteorological Parameters			
$\zeta =$	0.075	1/mm	(The inverse of the mean rainfall event volume.)
$\lambda =$	0.116	1/h	(The inverse of the mean rainfall event duration.)
$\theta =$	45	events	(The average number of rainfall events per year.)
Catchment Hydrological Parameters			
User Input Parameters			
Catchment Area, $A =$			259 hectares
Fraction of Impervious Areas, $h =$			0.35
Impervious Area Depression Storage, $S_{di} =$			0 mm
Pervious Area Depression Storage, $S_{dp} =$			4.6 mm
Pervious Area Ultimate Infiltration Capacity, $f_c =$			3.6 mm/h
Pervious Area Initial Soil Wetting Infiltration, $S_{iw} =$			13.2 mm
Catchment Time of Concentration, $t_c =$			1.9 hours
Calculations Using the Analytical Equations			
Required Storage-Discharge Table		Resulting Peak Discharge Rate Return Period	
Storage Volume (m ³)	Discharge Rate (m ³ /s)	Return Period (years)	
0	0.000	0.0	
42000	6.853	2.0	
60900	9.137	5.0	
91200	13.706	25.0	
96650	17.361	50.0	
98690	21.929	100.0	

Return Period (years)	Peak Discharge Rate (cms)
2.0	6.853
5.0	9.137
25.0	13.706
50.0	17.361
100.0	21.929
0.0	0.000
42000	6.853
60900	9.137
91200	13.706
96650	17.361
98690	21.929

Figure 9-3. Sample spreadsheet application of the analytical probabilistic approach.

Source: Guo (2001).

compares the analytical probabilistic and continuous simulation results for the two cases. The case without a detention pond is referred to as “No Control” and the one with a detention pond is referred to as “50% Reduction of Peak Flow.” Figure 9-3 shows the storage–discharge relationship of the pond. In fact, Equations (9-18) through (9-21) were coded into the spreadsheet shown in Figure 9-3 to determine, through trial and error, the required storage volume to satisfy the flood control criterion. In this case, the criterion is to reduce peak discharge rates by approximately 50% for return periods from two to 100 years. Figure 9-2 indicates that for the two cases, the analytical probabilistic approach generates very similar peak discharge–frequency relationships to those generated from SWMM continuous simulations.

For design storm modeling, the same two cases were modeled using the HEC-HMS model and the SWMM4 model under single-event mode. For the case of urban catchment without flood control, Figure 9-4 presents the comparison, which shows that the 24 h design storms produced much lower peak discharges for all return periods. The 3 h design storms were found to produce peak discharges similar to those generated from the 6 h storms for the test catchment. To avoid overcrowding, Figure 9-4 does not show peak discharges generated from 3 h design storms. Examining Figures 9-2 and 9-4 together, the peak discharge–frequency relationship generated by the 6 h duration design storms is clearly in close agreement with that generated from continuous

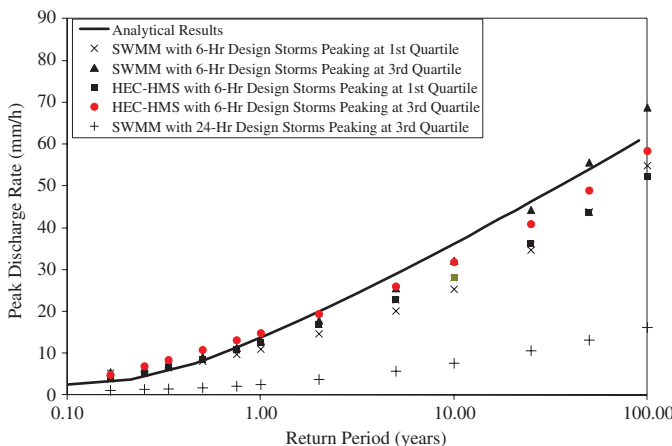


Figure 9-4. Comparison of design storm modeling and analytical probabilistic results for the test catchment without flood control.

Source: Guo (2001).

simulation. This suggests that the choice of design storm durations on the order of 3 to 6 h is appropriate for the test catchment. Figure 9-4 also shows that the use of different types of 6 h duration design storms resulted in different peak discharge rates and that the differences are larger for higher-return periods.

For the case of an urban catchment serviced by a downstream detention pond, comparisons similar to those in Figure 4 were observed. The 24 h storms produced much lower peak discharge rates, while the 3 h and 6 h storms resulted in similar peak discharges. For the sake of clarity, Figure 9-5 contains only the six-h storm results. Again, Figure 9-5 shows that, using the design storm approach, the difference in peak discharge rates due to the use of different models and different types of design storms becomes larger for higher-return periods. For return periods of 25 years, 50 years, or 100 years, when only 6 h design storms are used, the maximum difference in peak discharge rates can be as high as 45% of the average predicted peak discharge rates for the same frequency but using

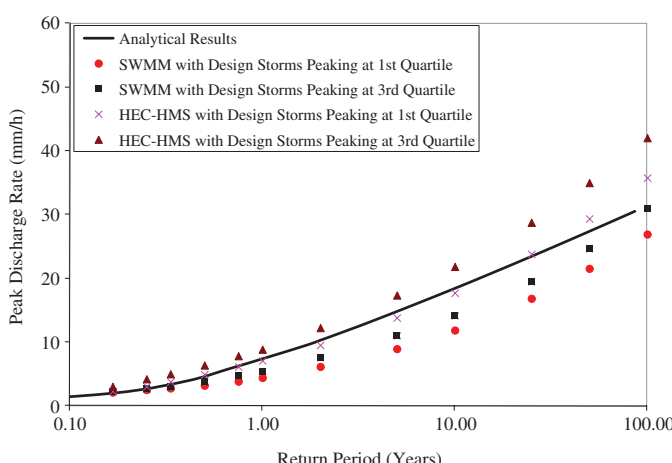


Figure 9-5. Comparison of design storm modeling and analytical probabilistic results for the test catchment serviced by a flood control detention pond.

Source: Guo (2001).

different models or different input design storms. Figures 9-4 and 9-5 show that the analytical probabilistic approach generated similar results to those generated from using the design storm approach with 6 h duration design storms. Input parameters for the analytical probabilistic approach were not in any way calibrated but were simply taken from the same parameters or calculated from related parameters used in the other two approaches.

In a design situation, the main objective is to find the required storage volume. To compare results, two levels of control criteria were investigated. Level 1 requires that the peak discharge rate from the detention pond with a return period of 100 years not exceed 0.028 m³/s per hectare of upstream catchment area. Level 2 requires that the peak discharge rate from the detention pond with a return period of 100 years not exceed 0.042 m³/s per hectare of upstream catchment area. Using the design storms with a return period of 100 years, through trial and error, the storage volume required to satisfy a control criterion can be determined using the SWMM4 model or the HEC-HMS model. The required storage volume determined from the design storm approach will obviously vary depending on which model or which type of design storm is used. This storage volume will also conceivably vary if different durations of the design storms are used. To demonstrate this variability, the 3 h, 6 h, and 24 h design storms were all used to determine the required storage volume. Table 9-3 presents results of these modeling runs. The storage volume determined from the analytical probabilistic approach was obtained by using the spreadsheet shown in Figure 9-3 where Equations (9-18) through (9-21) are embedded. Only one storage volume value can be obtained for each control level from the analytical probabilistic approach.

Table 9-3 shows that the storage volume determined using the design storm approach can vary significantly depending on which model and design storm are used. In fact, for control level 1, the maximum difference can be 75% of the average value, while for control level 2, the maximum difference can be about 130% of the average value. The 24 h design storm resulted in much lower storage volume requirements as compared with those resulting from the 3 and 6 h storms. This is a result of the combination of the much less intense 24 h storm and the small test catchment. As shown previously, 24 h storms are not appropriate for the test catchment that has a time of concentration of 1.9 h. When the results from the 24 h storms are excluded, Table 9-3 shows that for control level 1, the maximum difference can be 41% of the average value, whereas for control level 2, the maximum

Table 9-3. Comparison of Flood Control Detention Volume Requirements Determined Using Different Methods.

Approach (method) used	Vol. required to satisfy level 1 control (×1,000 m ³)	Vol. required to satisfy level 2 control (×1,000 m ³)
SWMM with 3-h storm peaking in 1 st quartile	170	144
SWMM with 3-h storm peaking in 2 nd quartile	178	155
SWMM with 6-h storm peaking in 1 st quartile	173	144
SWMM with 6-h storm peaking in 3 rd quartile	211	184
SWMM with 24-h storm peaking in 3 rd quartile	113	26
HEC-HMS with 3-h storm peaking in 1 st quartile	211	185
HEC-HMS with 3-h storm peaking in 2 nd quartile	226	207
HEC-HMS with 6-h storm peaking in 1 st quartile	212	186
HEC-HMS with 6-h storm peaking in 3 rd quartile	254	229
HEC-HMS with 24-h storm peaking in 3 rd quartile	136	49
Analytical probabilistic approach	175	154

Source: Guo (2001).

difference can be 47% of the average value. The storage volume determined from the analytical probabilistic approach is within the range determined from the design storm approach with storm durations of 3 or 6 h.

Results presented in this example indicate that design storm modeling can provide results for the estimation of peak discharge frequency relationships similar to those generated from the other two approaches when appropriate design storm types and durations are chosen. At the same time, this example also shows that significantly different results may be obtained if different design storms are used. This is a result of the theoretical deficiencies associated with the design storm approach. In this example study, quantification of the magnitude of the differences resulting from the use of different design storms was for the purpose of discouraging their use in planning and design studies. When applied properly, continuous simulation is expected to provide the most accurate results because it does not require any simplifying assumptions. This example shows that the analytical probabilistic approach can generate results similar to continuous simulation but with much less effort. The analytical probabilistic approach may therefore serve as a complement for use in urban stormwater management planning and design.

9.2 PERFORMANCE MODELING FOR BMP POLLUTANT REMOVAL WITH UNCERTAINTY ANALYSIS

This section presents a collection of methods for uncertainty assessment applied to the performance of BMP's in terms of total suspended solid removal. These methods can serve as a complement to the tools traditionally used in the design of these drainage practices. Following an overview of the topic of interest and the BMP's modeling strategy, the different methods and their sensitivities are described and then applied in an example.

9.2.1 Overview

Most of the urban hydrologic models are deterministic and ignore uncertainty, despite the fact that uncertainty analysis can lead to diverse results, offering the decision maker more information and options. In the case of water quality modeling, uncertainties can be even larger, and systems and/or facilities can be very unpredictable. This includes uncertainties in models representing pollutant removals in stormwater BMPs, which are widely used to reduce nonpoint-source pollutants. Much information on the performance of hydrologic infrastructures has been published (Chow et al. 1988; ASCE and WEF 1992; Urbonas and Roesner 1993; Guo and Adams 1999a; Guo and Urbonas, 1996, 2002). However, BMP performance in the treatment of pollutants remains a popular research topic. Currently, the most common approach is to treat BMPs as deterministic systems characterized by a percent-concentration reduction. Percent removal concentrations of pollutants for BMP evaluation are strongly discouraged. They can be problematic because the cleaner the input runoff, the more difficult its treatment becomes. To overcome the previous, the performance of BMPs can be represented by an effluent concentration independent of inflow concentration (Strecker et al. 2001, Huber 2006). In this section we describe the construction of a BMP performance model with uncertainty analysis and evaluate this model's performance by comparing its results with observed data from Park et al. (2011) and Park and Roesner (2012).

9.2.2 BMP Performance Modeling

The classical model for water treatment is the first-order decay model, widely used to describe pollutant removal in treatment plants, wetlands, swales, etc. (Carleton et al. 2001, Braskerud 2002, Wong et al. 2006). The performance of volumetric BMPs for stormwater is closely related to water

treatment in wetlands; it uses variables such as geometric storage shape, inflow and outflow rates, and influent and effluent concentrations. One of the models used in modeling both systems is the $k\text{-}C^*$ model. The model has been applied to constructed wetland performance, which has resulted in good reproducibility of real situations (Kadlec 2000, 2003; Rousseau et al. 2004, Stone et al. 2004). It incorporates “irreducible minimum concentration” to the first-decay equation, where the observed effluent concentration converges to a constant value. Assumptions of steady-state and plug flow conditions, typical of flow hydrodynamics within wetland systems (Kadlec and Knight 1996), are adopted. The model is defined by

$$C_{out} = C^* + (C_{in} - C^*)e^{-k/q} \quad (9-42)$$

where

C_{in} and C_{out} = influent and effluent event mean concentration (EMC) (mg/l),

C^* = background EMC or irreducible minimum concentration (mg/l),

k = aerial removal rate constant (m/day),

$q = Q/A_{BMP}$ = BMP hydraulic loading rate (m/day),

Q = average inflow rate (m^3/day), and

A_{BMP} = surface area of the BMP (m^2).

Although the model assumes steady-state flow conditions, the BMP fills quickly and drains over a long period (24 to 72 h) at an essentially constant rate. For that reason, the assumption is reasonable for BMPs. The $k\text{-}C^*$ model has been used to model wetland performance, and many studies have verified that this model characterizes the removal of pollutants by wetlands very well (Kadlec and Knight 1996; Kadlec 2000, 2003; Braskerud 2002; Rousseau et al. 2004; Lin et al. 2005). Wong et al. (2002, 2006) and Huber et al. (2006) use the $k\text{-}C^*$ model to simulate stormwater BMPs because the characteristics of wetlands, detention basins and retention ponds are similar.

Uncertainty in the BMP performance to be discussed here includes (1) the uncertainty in the input pollutant concentration of the runoff, C_{in} , which can be calculated using a log-normal distribution of EMC from field data or literature, and (2) the uncertainty in BMP treatment effectiveness, which is accounted for by associating the uncertainty with the key performance parameters of the $k\text{-}C^*$ model.

9.2.2.1 Uncertainty of C_{in}

BMP performance data from the International Stormwater BMP Database (www.bmpdatabase.org) maintained by ASCE and the US Environmental Protection Agency (USEPA) can be used for characterizing uncertainty in C_{in} . For example, Table 9-4 lists the locations, number of datasets, and

Table 9-4. Examples of Detention Basins.

BMP type	BMP name, location	BMP size			
		Number of datasets	Volume (m^3)	Surface area (ha)	Length (m)
Detention basin	15/78, Escondido, CA	17	1,122.54	0.0977	60.96
	5/605 EDB, Downey, CA	2	364.66	0.0598	47.24
	605/91 edb, Cerritos, CA	5	69.57	0.0114	22.86
	Manchester, Encinitas, CA	12	252.79	0.0304	22.86

Source: Park et al. (2011).

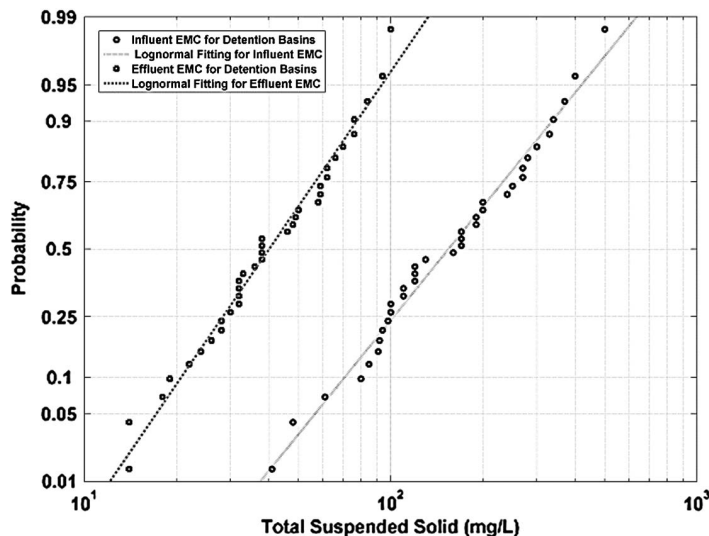


Figure 9-6. Log-normal probability plots of observed C_{in} and C_{out} in detention basins.

Source: Park et al. (2011).

Table 9-5. Results of Goodness-of-Fit Tests; Observed C_{in} and C_{out} from Figure 9-6.

Test	Critical value ($\alpha = 0.10$)		Decision
	C_{in}	C_{out}	
Chi-square	0.663	0.860	Accept
Kolmogorov-Smirnov	0.789	0.852	Accept
Anderson-Darling	0.567	0.685	Accept

Source: Park et al. (2011).

sizes of four dry detention BMPs for retrieved total suspended solids (TSS) data, a representative nonpoint-source pollutant. TSS distributions for both C_{in} and C_{out} in these locations are well represented as log-normal probability plots (Figure 9-6). Table 9-5 shows the results of three goodness-of-fit tests using the well-known chi-squared, Kolmogorov-Smirnov, and Anderson-Darling tests. To apply these tests for normality, all C_{in} and C_{out} values were transformed using the natural logarithm (D'Agostino and Stephens 1986, Kotegoda and Rosso 1997). All tests at a significance level of 0.1 showed that a log-normal distribution can be accepted for both observed C_{in} and observed C_{out} .

9.2.2.2 Uncertainty of Parameter k

The parameter k is related to q with a power function in the k -C* model (Schierup et al. 1990, Lin et al. 2005). However, the variance of C_{out} simulated with the k -C* model, changes dramatically depending on k . Therefore, applying a prediction interval in the k versus q regression line is necessary. A prediction interval focuses on the variance of individual data, whereas a confidence interval focuses on the variance of a regression line. The prediction is calculated as (Kutner et al. 2004)

$$\text{Mean} \pm t_{0.025} s \sqrt{1 + \frac{1}{n} + \frac{(X - \bar{X})^2}{\sum_{i=1}^n (X_i - \bar{X})^2}} \quad (9-43)$$

where

- t = critical value of the t distribution for the appropriate degree of freedom ($n - 2$),
- n = number of total data,
- s = standard error of the regression,
- X = average q at which the confidence interval is calculated,
- \bar{X} = mean of observed q from monitoring data, and
- X_i = individual observed q from monitoring data.

For TSS in BMPs, Figure 9-7 exhibits a power regression relation given by $k = 1.4841q^{0.9721}$, similar to the ones identified by Schierup et al. (1990) and Lin et al. (2005). A regression of estimated k using Equation (9-42) versus observed q for each storm event was performed with a 95% prediction interval of 0.4370. Then, the vertical distribution generating k depending on q is considered a two-parameter log-normal distribution.

9.2.2.3 Estimation of C^*

This approach assumes a known constant value of C^* because its uncertainty is less relevant than the uncertainty of C_{in} or k . This also helps with reducing the number of parameters needed in the uncertainty analysis. From the minimum C_{out} in the dataset and the range of C^* suggested in the literature (Table 9-6), we choose a value of $C^* = 10 \text{ mg/L}$.

What follows is the uncertainty analysis considering three cases, which require specific information (Table 9-7): uncertainty in C_{in} , uncertainty in k , and uncertainty in both. For example,

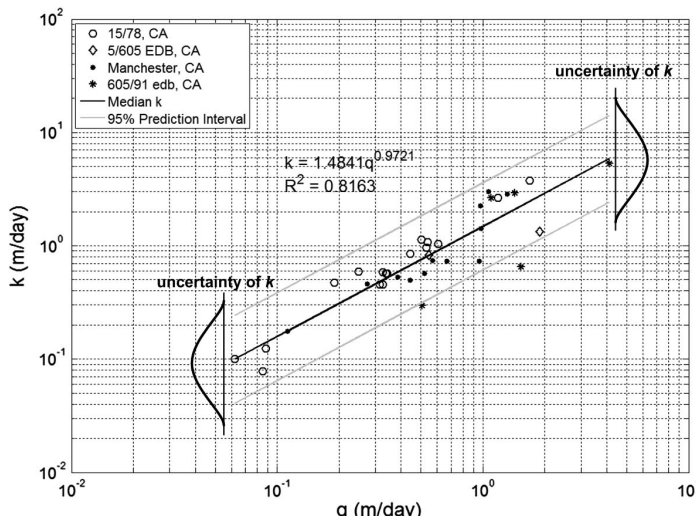


Figure 9-7. Estimated k versus q using individual storm events for detention basins.
Source: Park et al. (2011).

Table 9-6. Typical Background Concentration Values Proposed in Literature.

Literature	TSS (mg/L)
Kadlec and Knight (1996)	$5.1 + 0.16 C_{in}$
Barrett (2004)	5 ~ 20
Crites et al. (2006)	6

Source: Park et al. (2011).

Table 9-7. Required Parameters Information of C_{in} and k for Uncertainty Analyses.

Input parameters	C_{in}		K	
	Mean = 5.038	Std. dev. = 0.6083	Mean = $\log(1.4841q^{0.9721})$	Std. dev. = 0.437
Uncertainty in C_{in}	C_{in}	✓	✓	✓
	k (with constant C_{in})	✓	—	✓
	k (with constant q)	✓	—	✓
	C_{in} and k	✓	✓	✓

Source: [Park et al. \(2011\)](#).

✓ = required information for uncertainty computation.

to analyze the uncertainty in C_{in} , the required information is the log-transformed standard deviation of C_{in} and the log-transformed means of C_{in} and k . The standard deviation of k can be estimated from the distance of the prediction interval between the median k and the 95% prediction interval shown in Figure 9-7.

9.2.3 Methods for Uncertainty Analysis

Three methods, the derived distribution method (DDM) for the analytical method, the first-order second moment (FOSM) for the approximation method, and the Latin hypercube sampling (LHS) for the Monte Carlo simulation, are applied for estimating uncertainty of C_{out} in the k - C^* model.

9.2.3.1 Derived Distribution Method

In the DDM, the PDF of a variable $Y=g(X)$ can be obtained given the PDF of X , $f_x(x)$. The transformation from the PDF of X to that of Y entails the substitution of the inverse function of Y solved for X in the PDF of X . Then, the PDF of Y is ([Salas et al. 2004](#))

$$f_Y(Y) = \left| \frac{dg^{-1}(Y)}{dy} \right| f_x[g^{-1}(Y)] \quad (9-44)$$

In our case, the variable Y is C_{out} , and the variable X would be either C_{in} or k .

9.2.3.2 First-Order Second Moment

In cases where analytical methods such as DDM are cumbersome to apply, approximate methods have been suggested. For example, FOSM uses a Taylor-series expansion of the performance function and enables estimating the mean and variance of the performance function as

$$E(Y) = E[g(X_1, \dots, X_n)] \approx g(\mu_1, \dots, \mu_n) \quad (9-45)$$

$$Var(Y) = Var[g(X_1, \dots, X_n)] \approx \sum_{j=1}^n \left(\frac{\partial g}{\partial X_i} \right)_\mu^2 Var(X_i) + \sum_{i=1}^n \sum_{j=1}^n \left(\frac{\partial g}{\partial X_i} \right)_\mu \left(\frac{\partial g}{\partial X_j} \right)_\mu Cov(X_i, X_j) \quad (9-46)$$

Assuming that the X_i 's are independent variables, $\text{Cov}(X_i, X_j) = 0$. Then the variance of Y is

$$\text{Var}(Y) = \text{Var}[g(X_1, \dots, X_n)] \approx \sum_{j=1}^n \left(\frac{\partial g}{\partial X_i} \right)_\mu^2 \text{Var}(X_i) \quad (9-47)$$

where $\hat{\mu}_{\ln x}$ and $\hat{\sigma}_{\ln x}$ can be calculated from the sample mean and standard deviation of log-transformed X . Finally, the inverse of the CDF is calculated to quantify the percentile of the log-normal distribution using the estimated parameters (Salas et al. 2004):

$$X_p = \exp(\mu_{\ln x} \pm Z\sigma_{\ln x}) \quad (9-48)$$

where Z is the standard normal quantile corresponding to exceedance probability, and X_p is the X value of p percentile.

9.2.3.3 Latin Hypercube Sampling

LHS is a stratified sampling method to reduce variance and sampling error. The steps to apply the method are as follows (Tung and Yen 2005):

1. Select the number of subintervals, L , and divide the range $[0, 1]$ into L equal intervals.
2. For each subinterval, define ω_l as independent-uniform-random numbers from $\omega_l \sim U\left(\frac{0,1}{L}\right)$ for $l = 1, 2, \dots, L$. Then, a sequence of probability values u_m is generated as
 - a. $u_i = \frac{l-1}{L} + \omega_l \quad l = 1, 2, \dots, L$
3. Compute $Z_l = F^{-1}(u_l)$, in which $F(\cdot)$ is the CDF of the random variable of standard normal distribution.
4. Compute mean and standard deviation from log-transformed C_{in} or k .
5. Compute generated C_{in} or k assuming log-normal distribution as $X_l = \exp(\mu_{\ln x} + Z_l\sigma_{\ln x})$.
6. Apply generated C_{in} or k to the k - C^* model.

9.2.4 Sensitivity Results

The distribution of C_{out} for the k - C^* model is then estimated with the two identified distributed input parameters, C_{in} and k . Results of uncertainty in C_{in} , uncertainty in k , and uncertainty in both C_{in} and k can be computed. These results assume that geometric (A_{BMP}) and hydrological parameters (Q) don't have uncertainty. In addition, the background concentration (C^*) is fixed at 10 mg/L because the minimum value of the observed data used was close to that concentration. C_{in} and k were represented as log-normal distributions because their observed distributions are very close to log-normal (Figure 9-6).

9.2.4.1 Sensitivity of Uncertainty in C_{in}

The following log-normal distribution $f_{C_{in}}(C_{in})$ for C_{in} is assumed with a mean value $\mu_{\ln C_{in}}$ and standard deviation $\sigma_{\ln C_{in}}$ from the selected TSS of detention basins in the BMP database (see also Figure 9-6):

$$f_{C_{in}}(C_{in}) = \frac{1}{\sqrt{2\pi}C_{in}\sigma_{\ln C_{in}}} \exp\left[-\frac{1}{2}\left(\frac{\ln(C_{in}) - \mu_{\ln C_{in}}}{\sigma_{\ln C_{in}}}\right)^2\right] \quad (9-49)$$

According to Equation (9-44), the PDF for C_{out} , $f(C_{out})$ is given by

$$f_{C_{out}}(C_{out}) = \left| \frac{dg^{-1}(C_{out})}{dC_{out}} \right| f_{c_{in}}[g^{-1}(C_{out})] \quad (9-50)$$

where,

$$g^{-1}(C_{out}) = C^* + (C_{out} - C^*) \exp(k/q) = C_{in} \quad (9-51)$$

$$\left| \frac{dg^{-1}(C_{out})}{dC_{out}} \right| = |\exp(k/q)| = \exp(k/q) \quad (9-52)$$

Substituting Equation (9-51) and Equation (9-52) into Equation (9-50), the resulting PDF for the effluent EMC, $f_{out}(C_{out})$, is

$$f(C_{out}) = \frac{1}{\sqrt{2\pi} \left[C_{out} - C^* \left\{ 1 - \frac{1}{\exp(\frac{k}{q})} \right\} \right] \sigma_{lnC_{in}}} \exp \left[-0.5 \left(\frac{\ln \left[C_{out} - C^* \left\{ 1 - \frac{1}{\exp(\frac{k}{q})} \right\} \right] - (\mu_{lnC_{in}} - (\frac{k}{q}))}{\sigma_{lnC_{in}}} \right)^2 \right] \quad (9-53)$$

Adopting the relationship $k = 1.4841q^{0.9721}$ (Figure 9-8), we obtain

$$f(C_{out}) = \frac{1}{\sqrt{2\pi} \left[C_{out} - C^* \left\{ 1 - \frac{1}{\exp(1.481q^{-0.0279})} \right\} \right] \sigma_{lnC_{in}}} \exp \left[-0.5 \left(\frac{\ln \left[C_{out} - C^* \left\{ 1 - \frac{1}{\exp(1.481q^{-0.0279})} \right\} \right] - (\mu_{lnC_{in}} - 1.4841q^{-0.0279})}{\sigma_{lnC_{in}}} \right)^2 \right] \quad (9-54)$$

Equation (9-54) shows that $f(C_{out})$ is a three-parameter log-normal distribution, whose scale parameter ($1.481q^{-0.0279}$) and location parameter ($C^* \{1 - 1/\exp(1.481q^{-0.0279})\}$) vary with q . $f(C_{out})$ is very sensitive to the value of $\exp(1.481q^{-0.0279})$ when it is a function of q and becomes closer to the two-parameter log-normal distribution as $\exp(1.481q^{-0.0279})$ approximates to 1. However, $f(C_{out})$ changes to the three-parameter log-normal distribution for values of $\exp(1.481q^{-0.0279})$ much greater than 1.

Figure 9-8a shows comparisons of the PDFs for the three methods: DDM, LHS, and FOSM. DDM is derived from Equation (9-54) with constant q . C_{out} assumes a two-parameter log-normal distribution. The PDF obtained using FOSM differs from the DDM and the LHS when q is both 0.01 and 5 m/day. Conceptual differences among the three methods explain this discrepancy. No assumptions regarding the distribution of C_{out} are required by DDM and LHS methods. In contrast, a known PDF must be assumed for C_{out} when using the FOSM method. This assumption makes the method simpler but introduces error. DDM is the most accurate method, but defining the exact value corresponding to a specific percentile is difficult because an extra computation is needed to estimate the percentile from the PDF matched with C_{out} . With LHS, estimating the precise value of a specific percentile is relatively easy.

For $q = 0.01$ and 5 m/day, $\exp(1.481q^{-0.0279})$ is 5.41 and 4.13, respectively. Both values are much greater than 1, and the PDF in Equation (9-54) differs from the log-normal distribution to a large extent. This creates the differences observed between the DDM and LHS PDFs and the log-normal PDF obtained using FOSM. Thus, LHS gives the correct representation rather than FOSM because the LHS PDFs coincide with the DDM PDFs.

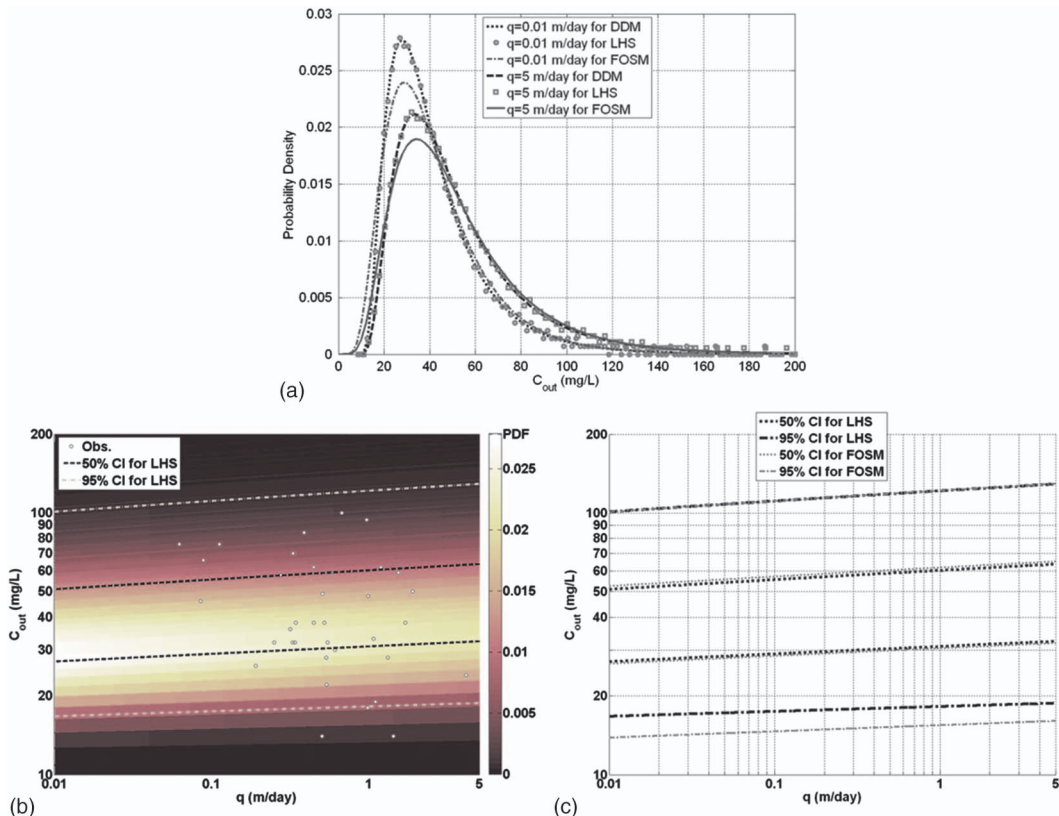


Figure 9-8. Uncertainty in C_{in} : (a) PDFs comparison of $f(C_{out})$ among DDM, LHS, and FOSM; (b) PDFs of LHS, including confidence intervals (CIs) and observed data; and (c) comparison of CIs between LHS and FOSM.

Source: Park et al. (2011).

The obtained PDFs of C_{out} represent the observed data well (Figure 9-8b). The 95% and 50% confidence intervals represent the high variability of the data, with C_{out} values being higher and more scattered for large values of q . Most of the observed data are placed out of the 50% confidence interval and two points (5% of the total data) are located outside of the 95% confidence interval. Figure 9-8c compares the 50% and 95% upper and lower confidence intervals obtained using LHS and FOSM. With the exemption of the lower 95% confidence limits, the rest of the limits are very similar. Hence, the distributed C_{out} is essentially identical for LHS and FOSM.

9.2.4.2 Sensitivity of Uncertainty in k with Constant q

A constant value of q must be adopted to determine the effect of C_{in} on the uncertainty of C_{out} with respect to k . In this case, we use $q = 0.1$ m/day. The mean and standard deviation of the log-transformed k are obtained from Table 9-7. The uncertainty in k with constant C_{in} for DDM can be simplified as follows:

$$f(C_{out}) = \frac{1}{\sqrt{2\pi} \ln\left(\frac{C_{in}-C^*}{C_{out}-C^*}\right) \sigma_{lnk} |(C_{out} - C^*)|} \exp\left[-\frac{1}{2} \left(\frac{\ln\left[0.1 \ln\left(\frac{C_{in}-C^*}{C_{out}-C^*}\right)\right] - \mu_{lnk}}{\sigma_{lnk}}\right)^2\right] \quad (9-55)$$

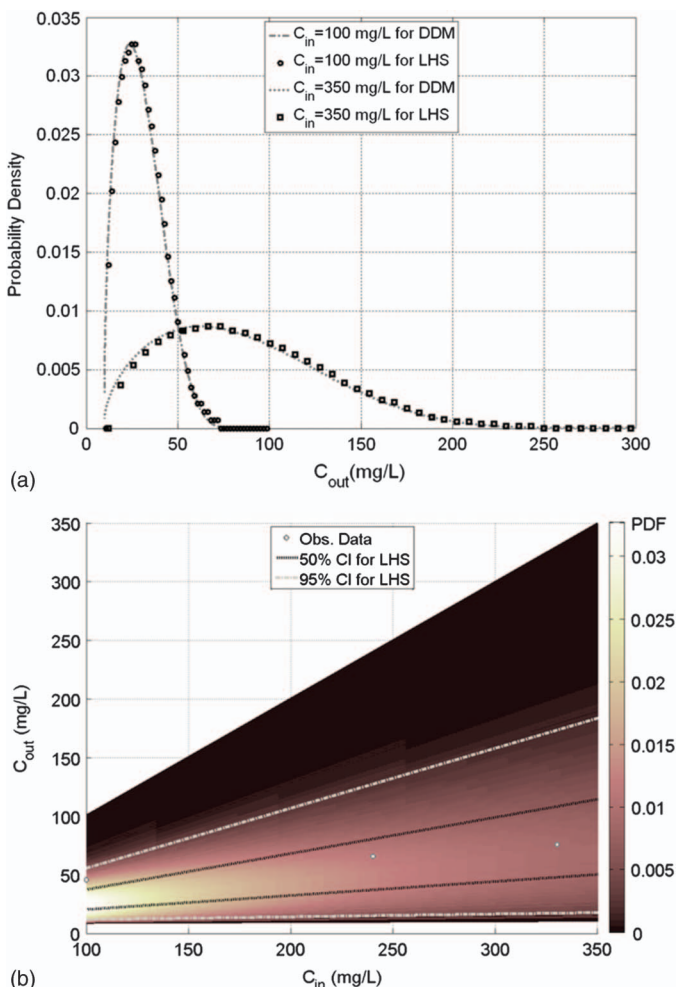


Figure 9-9. Uncertainty in k with constant q : (a) PDFs comparison of $f(C_{out})$ as a function of C_{in} using $q = 0.1$ m/day between DDM and LHS and (b) PDFs from LHS, including confidence intervals (CIs) and observed data.

Source: Park et al. (2011).

Figure 9-9a shows both PDFs for values of $C_{in} = 100$ mg/L and 350 mg/L. In this case, only DDM and LHS are used for the uncertainty analysis. FOSM cannot be used because the C_{out} distribution of Equation (9-55) is difficult to define. Both methods produce very similar distributions and represent a higher variability in C_{out} as C_{in} increases. In other words, predicting C_{out} is more difficult for a high C_{in} at a constant q . Figure 9-9b shows the PDFs of C_{out} for the observed data when q is restricted to 0.1 m/day. This figure shows the PDF computed using LHS, but almost identical results are obtained with the PDFs using DDM, as Figure 9-9a illustrates. The 95% and 50% confidence intervals become wider as q increases. For this analysis, only three observed data points from Table 9-7 were available as $q = 0.1$ m/day; two of the three points lie within the 50% confidence interval and the third is within the 95% confidence interval.

9.2.4.3 Sensitivity of Uncertainty in k with Constant C_{in}

A constant value of $C_{in} = 170$ mg/L is assumed to determine the effect of q on the uncertainty of k . In this case, the mean and standard deviation of log-transformed k are obtained from Table 9-7. Figure 9-10a shows PDFs for values of $q = 0.01$ m/day and 5 m/day. Then, the DDM is given by

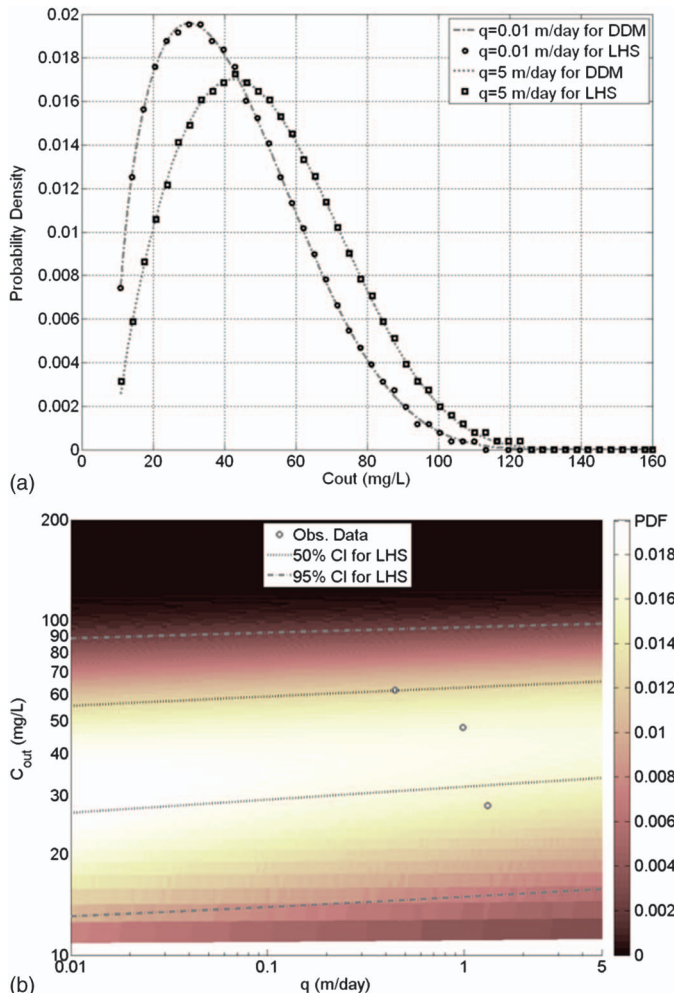


Figure 9-10. Uncertainty in k with constant C_{in} : (a) comparison of $f(C_{out})$ as a function of q using $C_{in} = 170$ mg/L between DDM and LHS and (b) PDFs from LHS, including confidence intervals (CIs) and observed data.

Source: Park et al. (2011).

$$f(C_{out}) = \frac{1}{\sqrt{2\pi} \ln\left(\frac{170-C^*}{C_{out}-C^*}\right) \sigma_{lnk} |(C_{out} - C^*)|} \exp\left[-\frac{1}{2} \left(\frac{\ln\left[q \ln\left(\frac{170-C^*}{C_{out}-C^*}\right)\right] - \mu_{lnk}}{\sigma_{lnk}} \right)^2\right] \quad (9-56)$$

Again, we use only DDM and LHS for the uncertainty analysis for the same reason given in the previous subsection. Both the DDM and LHS methods produce very similar distributions and represent higher variability in C_{out} as q increases. In other words, the shapes of the PDFs of C_{out} demonstrate a more positive skew with decreasing q . As a result, predict C_{out} for high q is more difficult at a constant C_{in} .

Figure 9-10b shows PDFs of C_{out} for the observed data obtained from Table 9-4 when C_{in} is restricted to 170 mg/L. The 95% and 50% confidence intervals are plotted as well. These intervals indicate that C_{out} values are higher and a little more scattered for larger values of q . Two of the three observed datasets are scattered within the 50% confidence interval, and a third point is located within

the 95% confidence interval. Although having only three datasets available for comparison, they do validate that PDFs of the $k\text{-}C^*$ model describe the behavior of observed data. Based on the previous results, the shape of the PDF as a function of C_{in} was found to show more change of variance than as a function of q . It can be concluded that C_{in} is a more sensitive variable than q for the uncertainty in k when the $k\text{-}C^*$ model is considered with TSS.

9.2.4.4 Sensitivity in Both C_{in} and k

This section assumes no correlation between C_{in} and k to simplify the calculations. Because of mathematical complexities, the DDM cannot be applied to derive $f(C_{out})$ when uncertainties in both C_{in} and k are simultaneously applied to the $k\text{-}C^*$ model. Thus, we use the FOSM method and the LHS method, which have been shown to generate similar distributions as the DDM method.

Figure 9-11a shows a comparison of both PDFs for $q = 0.01$ and $q = 5$ m/day. Both distributions are relatively similar for $q = 5$ m/day, but differences are observed in the peak values for $q = 0.01$ m/day. The distribution of C_{out} is skewed to the right for both values of q . As mentioned previously, the FOSM assumes a log-normal distribution. Thus, the shapes of the PDFs generated by the LHS and FOSM methods are expected to differ. Figure 9-11b shows the PDFs obtained with LHS, their confidence intervals of 50% and 95%, and the observed data. About two-thirds of the total data

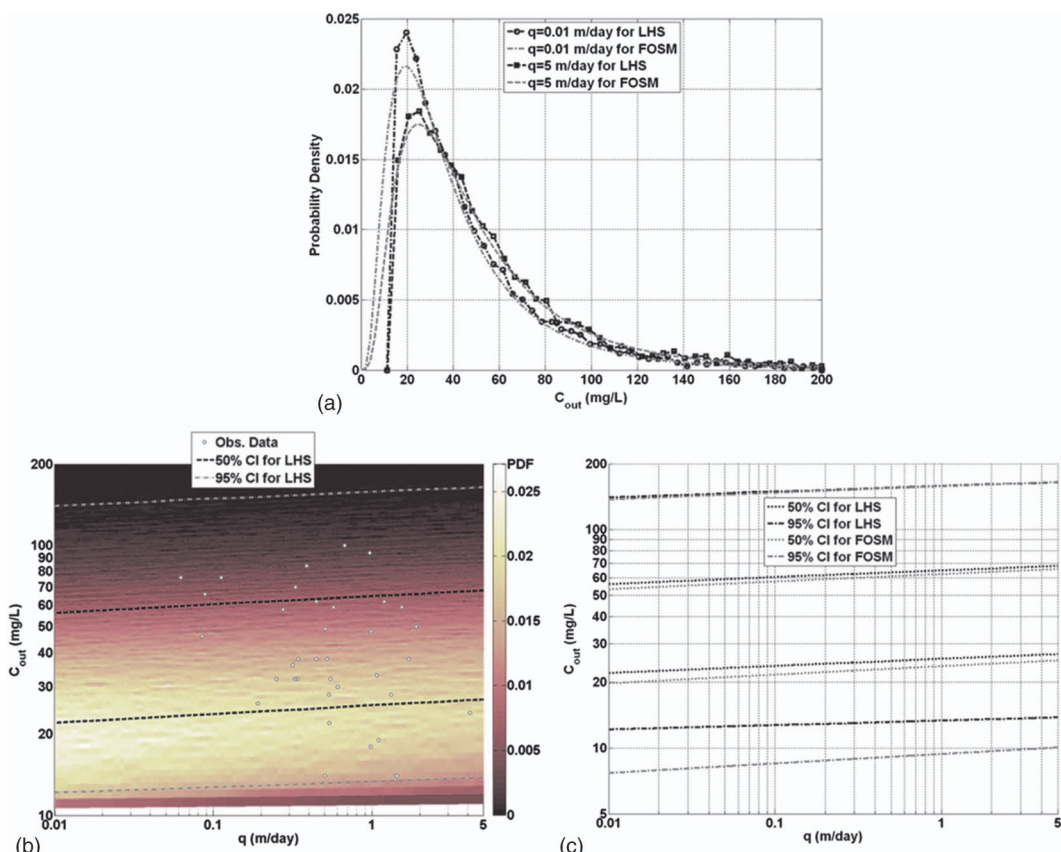


Figure 9-11. Uncertainty in both C_{in} and q : (a) PDFs comparison of $f(C_{out})$ as a function of q between LHS and FOSM; (b) PDFs from LHS, including confidence intervals (Cl) and observed data; and (c) comparison of Cls between LHS and FOSM.

Source: Park et al. (2011).

are located within the 50% confidence interval, and all observed data are located within the placed 95% confidence interval.

Figure 9-11c compares the 50% and 95% confidence intervals obtained using LHS and FOSM when uncertainties in C_{in} and k are considered. These methods produce different distributions because the FOSM analysis ensures a log-normal distribution for C_{out} , whereas the LHS method does not. Nevertheless, confidence intervals between LHS and FOSM are not substantially different. Thus, the assumption of a log-normal distribution for C_{out} seems to be practical for estimating the variance of C_{out} .

9.2.5 Example 9-2: Uncertainty Analysis of BMP Performance for TSS Removal in Los Angeles, California

The following example, adapted from Park and Roesner (2012), illustrates how the BMP performance model and the FOSM uncertainty analysis previously discussed can be applied to a given catchment. To create the example, 60 years of continuous hourly rainfall data for Los Angeles International Airport (LA) were obtained from the National Climatic Data Center (NCDC) and input into the storage, treatment, overflow, and runoff model (STORM) (USACE 1977) to simulate the volumes involved. This location was chosen because all of the detention basins shown in Table 9-4 are located in the area, and the sampling duration is the minimum time unit used by STORM. The rain gauge NCDC Cooperative Observer Program (COOP) ID number is 045114, and the records span the period from January 1, 1950, to December 31, 2009. Event-based urban runoff quality data used to develop the statistical characteristics C_{in} and k were taken from Sections 9.2.2.1 and 9.2.2.2. An IETD of 6 h and a minimum threshold runoff depth of 0.01 in. (0.254 mm) were specified to separate the flow data into individual events. For this example, the catchment has an area of 1 acre ($4,045 \text{ m}^2$), imperviousness of 40%, a BMP volume of 0.2 in. ($\approx 5.0 \text{ mm}$), and a BMP surface area to watershed area ratio of 0.01. Uncertainty in the imperviousness is not considered. Table 9-8 summarizes these and other relevant data.

The runoff coefficient for STORM was calculated using the catchment imperviousness ratio (i) between 0 and 1, by means of the following expression widely used in many US municipalities (Urbonas et al. 1990):

$$C = 0.85i^3 - 0.78i^2 + 0.774i + 0.04 \quad (9-57)$$

Further, for this example, urban runoff (V_R) is introduced to the BMP at a rate equal to the lowest inflow value or the average drawdown rate specified for the BMP. When the BMP is full, the flow is bypassed around the BMP and discharged directly to the receiving water. The total volume of storm flow that passes through the BMP is designated as V_{BMP} . The difference ($V_R - V_{BMP}$) is V_O , the volume of runoff that bypasses the BMP (see Figure 9-12). The total pollutant load from any storm is

Table 9-8. Values Employed for STORM Parameters.

Parameters	Value
Area (acre)	1 (= $4,046.86 \text{ m}^2$)
Depression storage (in.)	0.1 (= 2.54 mm)
Evaporation (in./day)	0.18 (= 4.57 mm)
Interevent time (h)	6
First flush depth (in.)	0
Time of concentration (h)	0.1

Source: Park and Roesner (2012).

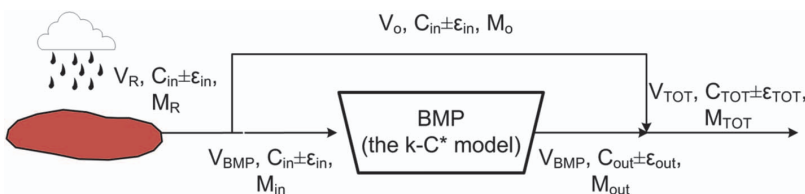


Figure 9-12. Schematic of an urban stormwater system.

Source: Park and Roesner (2012).

calculated as the sum of pollutant load discharged from the BMP plus the pollutant load bypassed directly to the receiving water. As discussed previously, a storm is defined as a period of rainfall that is preceded and succeeded by a period equal to or longer than the selected IETD.

9.2.5.1 Load Frequency Curve Approach

Load duration curves (LDCs) have been suggested by Stiles (2001). Several researchers (Stiles 2001; Cleland 2002, 2003; Bonta and Cleland 2003; O'Donnell et al. 2005) have utilized LDCs to estimate the total maximum daily load (TMDL), because this method is capable of identifying daily loads that account for the time variability of water quality. A maximum concentration standard and a hydrologic flow duration curve (FDC) can identify a TMDL appropriate for the full range of streamflow conditions, and the maximum daily load can be verified for any given day (USEPA 2007). Although LDCs have become more widely used and accepted for pollutant loads estimation, considering the pollutant-reducing physical model is necessary. The current LDC method only accounts for flow variables and does not consider other variables because it does not incorporate all relevant physical processes (Shen and Zhao 2010). In this example, we adopt an approach for estimating the pollutant load exceedance frequencies resulting from BMPs with their estimates of the certainties (or uncertainties). If a target water quality standard is specified as an average load and an upper limit on that load, which is not to be exceeded more than n times per year, the algorithm presented will assist in the design of a BMP that will meet the criteria with 95% certainty. The method is simple, but it is a step forward in linking BMP performance to receiving water quality.

This study used the load frequency curve (LFC) instead of the LDC. As water quality regulations containing exceedance frequency criteria of storm events for instream concentrations and/or BMP loads are more commonly used, the certainty (or uncertainty) of meeting these criteria becomes important, and the proper design point on the load exceedance frequency curve becomes an issue.

The following steps demonstrate the method for computing a pollutant-load frequency curve on an event basis according to Figure 9-12:

1. STORM simulates V_R for an event.
2. The pollutant mass in the runoff (M_R) is computed by multiplying V_R and the TSS EMCs in the runoff from the catchment $C_{in} = (\bar{C}_{in} \pm \epsilon_{in})$, where \bar{C}_{in} is the average inflow concentration and ϵ_{in} is a random variable taken from the log-normal distribution of C_{in} from Figure 9-6.
3. V_R is divided into V_{BMP} and V_o by STORM.
4. The pollutant mass that bypasses the BMP (M_o) is computed by multiplying M_o and C_{in} .
5. The pollutant mass that leaves the BMP (M_{out}) is computed by multiplying V_{BMP} and the C_{out} estimated by the k - C^* model for the situation of uncertainties in both C_{in} and k as in Section 9.2.4.4. Note that C^* is estimated to be 10 mg/L as shown in Table 9-6.
6. The total pollutant mass discharged to the receiving waters for the event (M_{TOT}) is computed by adding M_o and M_{out} .

7. A long-term hourly rainfall record is input to STORM to generate a time series of the mass loads identified in steps 2 to 6.
8. The exceedances per year are computed by ranking the TSS event loads. LFCs are plotted using the plot-position formula proposed by Cunnane (1978):

$$T_R = \frac{N + 1 - 2g}{J - g} \quad (9-58)$$

where

T_R = return period, which indicates a fraction of a year (years),

N = number of years of record,

J = rank of the event (in descending order of magnitude), and

g = plotting position parameter (0.4 in this case).

The number of exceedances per year E can be calculated from the return period T_R as follows:

$$E = \frac{1}{T_R} \quad (9-59)$$

To develop the statistical characteristics of the mass loads for an event, the median, 95% upper confidence limit (UCL) and lower confidence limit (LCL) for TSS loads in the runoff (M_R) and in the bypass (M_o) are computed as

$$M_{in,median} = C_{in,median} V \quad (9-60)$$

$$M_{95\%UCL} = C_{in,95\%UCL} V \quad (9-61)$$

$$M_{95\%LCL} = C_{in,95\%LCL} V \quad (9-62)$$

where M and V correspond to M_R and V_R and M_o and V_o , for runoff and bypass calculations. To compute 95% confidence limits (CLs) for C_{out} , we must estimate $\mu_{lnC_{out}}$ and $\sigma_{lnC_{out}}$. The 95% CLs of C_{out} are then

$$C_{out,95\%UCL} = \exp(\mu_{lnC_{out}} + 1.96\sigma_{lnC_{out}}) \quad (9-63)$$

$$C_{out,95\%LCL} = \exp(\mu_{lnC_{out}} - 1.96\sigma_{lnC_{out}}) \quad (9-64)$$

The TSS load that leaves the BMP and its 95% CLs are determined also using Equation (9-60) through Equation (9-62). In this case, M and C correspond to M_{out} and C_{out} . Finally, the uncertainty in M_{TOT} can be determined by means of Monte Carlo simulations.

The FOSM method was applied to the k - C^* model with parameters defined according to the aforementioned protocol, assuming that the two variables C_{in} and k are independent because the correlation coefficient between k and C_{in} computed from the observed data is small enough to allow for C_{in} and k to be regarded as independent.

9.2.5.2 Application Results

Figure 9-13 shows the LFCs of TSS event loads resulting from the 60 year simulation. Each point is a storm event load computed using the procedure described in the previous subsection. The blue points and curves result from simulations of the catchment loads without BMPs. Because no

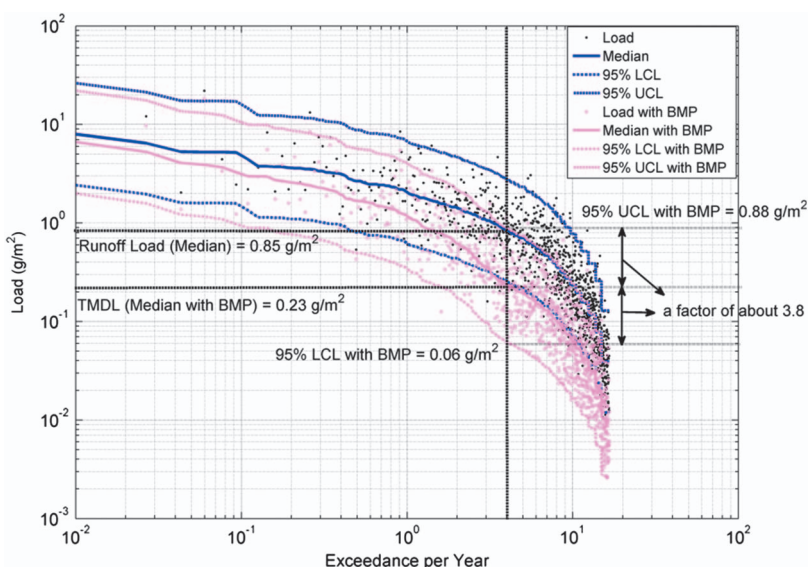


Figure 9-13. Load frequency curves, including confidence limits, for the requirements of load and exceedance.

Source: Park and Roesner (2012).

treatment occurs, the scatter in the event loads is entirely due to the uncertainty in the TSS concentration in the runoff. Moreover, Figure 9-13 reveals interesting information regarding the design of BMPs. For example, suppose that the target water quality standard for this example requires the TSS load from the catchment not to exceed $0.23 \text{ g}/\text{m}^2$ more than four times per year. In that case, the median untreated catchment runoff load that is exceeded four times per year (i.e., $0.85 \text{ g}/\text{m}^2$) would have to be reduced 73% by the BMP to be implemented. The figure also shows that the median pollutant concentration discharged from the BMP designed with the parameter values adopted in this study will be equal to the allowable target water quality standard. However, 50% of the time the target water quality standard will be exceeded by as much as a factor of approximately 3.8 (the value of the 95% UCL). Thus, to be 95% certain that we will not exceed the target water quality standard, the BMP must be designed so that the 95% UCL meets the target, which means that the median value must be approximately $0.06 \text{ g}/\text{m}^2$. Conceptually, by sizing the BMP such that its 95% CLs meet the target criteria, the load-frequency target value for the watershed TSS load is likely to be met. However, for the case illustrated here, an extended detention BMP able to meet this target water quality standard seems unlikely, because the median TSS load reduction would need to be about 94%. Such a performance level far exceeds the capability of traditional current BMPs. Overall, it seems certain that sizing BMPs based on median EMCs of runoff will not provide reliable pollutant removal from stormwater discharges to receiving waters.

9.3 SUMMARY

Stormwater management is a growing concern in many parts of the globe. Alongside the more traditional problems of water supply and distribution, as well as sewage collection, stormwater management has become a relevant topic in urban hydrology. In accordance with the overall theme of this monograph, we have described and illustrated the use of probability distributions in stormwater modeling and design. We presented two approaches for stormwater management

modeling and analysis where probability distributions can be of great utility. Section 9.1 describes the first approach, which resulted in a package of tools named APSWM. Section 9.2 describes the second approach, which deals with uncertainty in the performance of BMPs.

In summary, the APSWM is a collection of analytical equations that can be used for stormwater modeling and design. In terms of accuracy, the APSWM may provide a good compromise between the simple design storm approach and the more laborious continuous simulation approach. Section 9.1.4.1 describes the general theory underlying the APSWM development. The development of APSWM was then illustrated with three different stormwater management planning and design purposes. The first purpose is the design of detention ponds for flood control. Closed-form analytical equations were obtained that can be used to select the appropriate sizes of detention ponds. In Section 9.1.4.5, a probabilistic channel-routing method was developed to explain the effect of channel routing on the probability distribution of flood peaks. Subsection 9.1.4.7 demonstrates the use of APSWM equations to study the performance of low-impact development practices. Specifically, this demonstration focused on the sizing of storage units for rainwater harvesting. Section 9.1 ends with an application example, which illustrates the use of APSWM for flood quantile estimation and flood control detention pond design in Chicago. The example subsection also includes references to additional case studies using APSWM. All these case studies show that, for a location of interest, with the completion of the rainfall event-based analysis and quantification of the distribution parameter values representing the climate conditions of the location, the application of APSWM is computationally more efficient than either the design storm or the continuous simulation approaches.

The second part of this chapter, Section 9.2, shows the importance and utility of incorporating uncertainty analysis when examining the performance of BMPs. This is demonstrated using the k - C^* model and TSS as the representative pollutant. Three different methods were used to estimate uncertainty: DDM, FOSM, and LHS. The methods differ in their assumptions. For example, FOSM can be used as an alternative to DDM when the functional relationship involved in the DDM transformation is too complex and hence difficult to handle analytically. As a sampling technique, LHS generally offers a wider applicability than DDM and FOSM. The three methods rely on the same statistical representation of the uncertainty in the k - C^* model. This representation uses a log-normal distribution to quantify the distribution of the influent event mean concentration. This distribution together with DDM can be used to obtain the distribution of the effluent event mean concentration. Uncertainty in the parameter k is also taken into consideration. k is modeled using a log-normal distribution as well but conditioned on the value of the BMP hydraulic loading rate. Section 9.2.4.1 examines the effect of influent concentration uncertainty alone on BMP performance. Sections 9.2.4.2 and 9.2.4.3 examine the effect of uncertainty in k on BMP performance, whereas Section 9.2.4.4 examines the joined effect of uncertainties in both variables. For the latter, the input concentration and k are treated as being statistically independent. Lastly, in Subsection 9.2.5, the application of the uncertainty analysis method FOSM is illustrated in detail using an example of TSS load reduction by an extended detention pond in Los Angeles.

The application of uncertainty analysis to BMP performance evaluation not only serves to illustrate the application of probabilistic methods in stormwater management, but more important, it highlights the need to account for uncertainty in the design and evaluation of stormwater infrastructure for water quality control. The computational efficiencies provided by the APSWM can facilitate wider applications of uncertainty analysis in stormwater management planning and design.

ACKNOWLEDGMENTS

The authors thank Dr. Wayne C. Huber, Dr. James P. Heaney, and Dr. Veronica L. Webster, for their valuable comments and suggestions that helped to improve initial versions of this chapter. Some of

the authors acknowledge the financial support provided by the Harold H. Short endowed fund for the Civil Infrastructure System Laboratory at Colorado State University. Finally, Jorge Gironás thanks Conicyt/Fondap/15110017 and 15110020, and Daeryong Park thanks the NRF Grant 2016R1C1B1013711.

References

- Adams, B. J., and J. B. Bontje. 1984. "Microcomputer applications of analytical models for urban stormwater management." In *Emerging computer techniques in stormwater and flood management*, edited by W. James, 138–162. New York: ASCE.
- Adams, B. J., H. G. Fraser, C. D. D. Howard, and M. S. Hanafy. 1986. "Meteorologic data analysis for drainage system design." *J. Environ. Eng.* **112** (5): 827–848.
- Adams, B. J., and C. D. D. Howard. 1986. "Design storm pathology." *Can. Water Resour. J.* **11** (3): 49–55.
- Adams, B. J., and F. Papa. 2000. *Urban stormwater management planning with analytical probabilistic models*. Toronto: Wiley.
- Akan, A. O. 1989. "Detention pond sizing for multiple return periods." *J. Hydraul. Eng.* **115** (5): 650–664.
- Akan, A. O., and R. J. Houghtalen. 2003. *Urban hydrology, hydraulics and stormwater quality*. Hoboken, NJ: Wiley.
- Andrés-Doménech, I., A. Montanari, and J. B. Marco. 2010. "Stochastic rainfall analysis for storm tank performance evaluation." *Hydrol. Earth Syst. Sci.* **14** (7): 1221–1232.
- Andrés-Doménech, I., A. Montanari, and J. B. Marco. 2012. "Efficiency of storm detention tanks for urban drainage systems under climate variability." *J. Water Resour. Plann. Manage.* **138** (1): 36–46.
- ASCE and WEF (Water Environment Federation). 1992. *Design of urban stormwater controls*. ASCE/EWRI Manuals and Reports on Engineering Practice No. 87. Reston, VA: ASCE.
- Ashkar, F., and J. Rousselle. 1987. "Partial duration series modeling under the assumption of a Poissonian flood count." *J. Hydrol.* **90** (1–2): 135–144.
- Bacchi, B., M. Balistrocchi, and G. Grossi. 2008. "Proposal of a semi-probabilistic approach for storage facility design." *Urban Water J.* **5** (3): 195–208.
- Balistrocchi, M., G. Grossi, and B. Bacchi. 2009. "An analytical probabilistic model of the quality efficiency of a sewer tank." *Water Resour. Res.* **45** (12): W12420.
- Barbe, D. E., J. F. Cruise, and X. Mo. 1996. "Modeling the buildup and washoff of pollutants on urban watersheds." *Water Resour. Bull.* **32** (3): 511–519.
- Barrett, M. E. 2004. "Retention pond performance: Examples from the international stormwater BMP database." In *Proc., World Environmental and Water Resource Congress*. Reston, VA: ASCE.
- Beaudoin, P., J. Rousselle, and G. Marchi. 1983. "Reliability of the design storm concept in evaluating runoff peak flow." *Water Resour. Bull.* **19** (3): 483–487.
- Behera, P. K., B. J. Adams, and J. Y. Li. 2006. "Runoff quality analysis of urban catchments with analytical probabilistic models." *J. Water Resour. Plann. Manage.* **132** (1): 4–14.
- Bierkens, M. F. P., and C. E. Puente. 1990. "Analytically derived runoff models based on rainfall point processes." *Water Resour. Res.* **26** (11): 2653–2659.
- Bonta, J. V., and B. Cleland. 2003. "Incorporating natural variability, uncertainty, and risk into water quality evaluations using duration curves." *J. Am. Water Resour. Assoc.* **39** (6): 1481–1496.
- Bonta, J. V., and A. R. Rao. 1988. "Factors affecting the identification of independent storm events." *J. Hydrol.* **98** (3–4): 275–293.
- Botter, G., A. Porporato, E. Daly, I. Rodriguez-Iturbe, and A. Rinaldo. 2007. "Probabilistic characterization of base flows in river basins: Roles of soil, vegetation and geomorphology." *Water Resour. Res.* **43**: W06404.
- Braskerud, B. C. 2002. "Factors affecting phosphorus retention in small constructed wetlands treating agricultural non-point source pollution." *Ecol. Eng.* **19** (1): 41–61.
- Cadavid, L., J. T. B. Obeysekera, and H. W. Shen. 1991. "Flood-frequency derivation from kinematic wave." *J. Hydraul. Eng.* **117** (4): 489–510.
- Carleton, J. N., T. J. Grizzard, A. N. Godrej, and H. E. Post. 2001. "Factors affecting the performance of stormwater treatment wetlands." *Water Res.* **35** (6): 1552–1562.
- Chan, S.-O., and R. L. Bras. 1979. "Urban storm water management: Distribution of flood volumes." *Water Resour. Res.* **15** (2): 371–382.

- Cleland, B. 2002. "TMDL development from the 'bottom up'—Part II: Using duration curves to connect the pieces." In *Proc., Water Environment Federation, National TMDL Science and Policy*, 687–697. Alexandria, VA: Water Environment Federation.
- Cleland, B. 2003. "TMDL development from the 'bottom up'—Part III: Duration curves and wet-weather assessments." In *Proc., Water Environment Federation, National TMDL Science and Policy*, 1740–1766. Alexandria, VA: Water Environment Federation.
- Cordova, J. R., and R. L. Bras. 1981. "Physically based probabilistic models of infiltration, soil moisture, and actual evapotranspiration." *Water Resour. Res.* **17** (1): 93–106.
- Cordova, J. R., and I. Rodriguez-Iturbe. 1983. "Geomorphologic estimation of extreme discharge probabilities." *J. Hydrol.* **65** (1–3): 159–173.
- Crites, R. W., S. C. Reed, and E. J. Middlebrooks. 2006. *Natural wastewater treatment systems*. Boca Raton, FL: Taylor and Francis/CRC Press.
- Cruise, J. F., and K. Arora. 1990. "A hydroclimatic application strategy for the Poisson partial duration model." *Water Resour. Bull.* **26** (3): 431–442.
- Cruise, J. F., and V. P. Singh. 1988. "Design of sewage lagoons using stochastic streamflow sequences." *J. Water Resour. Plann. Manage.* **114** (3): 353–364.
- Cunge, J. A. 1969. "On the subject of a flood propagation computation method (Muskingum method)." *J. Hydraul. Res.* **7** (2): 205–230.
- Cunnane, C. 1978. "Unbiased plotting positions—A review." *J. Hydrol.* **37** (3–4): 205–222.
- Cunnane, C. 1979. "A note on the Poisson assumption in partial duration series models." *Water Resour. Res.* **15** (2): 489–494.
- D'Agostino, R. B., and M. A. Stephens. 1986. *Goodness-of-fit techniques*. New York: Marcel Dekker.
- Daly, E., and A. Porporato. 2010. "Effect of different jump distributions on the dynamics of jump processes." *Phys. Rev. E* **81** (6): 061133.
- Diaz-Granados, M. A., J. B. Valdes, and R. L. Bras. 1984. "A physically based flood frequency distribution." *Water Resour. Res.* **20** (7): 995–1002.
- Di Toro, D. M. 1984. "Probability model of stream quality due to runoff." *J. Environ. Eng.* **110** (3): 607–628.
- Di Toro, D. M., and M. J. Small. 1979. "Stormwater interception and storage." *J. Environ. Eng.* **105** (EE1): 43–53.
- Dooge, J. C. I. 1982. "Hydrodynamic derivation of storage parameters of the Muskingum model." *J. Hydrol.* **54** (4): 371–387.
- Driscoll, E. D., G. E. Pallegui, E. W. Strecker, and P. E. Shelley. 1989. *Analysis of storm event characteristics for selected rainfall gauges throughout the United States*. Report. Washington, DC: EPA.
- Eagleson, P. S. 1972. "Dynamics of flood frequency." *Water Resour. Res.* **8** (4): 878–898.
- Eagleson, P. S. 1978. "Climate, soil, and vegetation, 2, the distribution of annual precipitation derived from observed storm sequences." *Water Resour. Res.* **14** (5): 713–721.
- Fread, D. L. 1993. "Flow routing." In *Handbook of hydrology*, edited by D. R. Maidment, 10.1–10.36. New York: McGraw-Hill.
- Guo, J. C. Y., and B. Urbonas. 1996. "Maximized detention volume determined by runoff capture ratio." *J. Water Resour. Plann. Manage.* **122** (1): 33–39.
- Guo, J. C. Y., and B. Urbonas. 2002. "Runoff capture and delivery curves for storm-water quality control designs." *J. Water Resour. Plann. Manage.* **128** (3): 208–215.
- Guo, Y. 2001. "Hydrologic design of urban flood control detention ponds." *J. Hydrol. Eng.* **6** (6): 472–479.
- Guo, Y., and B. J. Adams. 1998a. "Hydrologic analysis of urban catchments with event-based probabilistic models. 1: Runoff volume." *Water Resour. Res.* **34** (12): 3421–3431.
- Guo, Y., and B. J. Adams. 1998b. "Hydrologic analysis of urban catchments with event-based probabilistic models. 2: Peak discharge rate." *Water Resour. Res.* **34** (12): 3433–3443.
- Guo, Y., and B. J. Adams. 1999a. "Analysis of detention ponds for storm water quality control." *Water Resour. Res.* **35** (8): 2447–2456.
- Guo, Y., and B. J. Adams. 1999b. "An analytical probabilistic approach to sizing flood control detention facilities." *Water Resour. Res.* **35** (8): 2457–2468.
- Guo, Y., and B. W. Baetz. 2007. "Sizing of rainwater storage units for green building applications." *J. Hydrol. Eng.* **12** (2): 197–205.
- Guo, Y., and J. Dai. 2009. "Expanded analytical probabilistic stormwater models for use in watershed and master drainage planning." *Can. J. Civil Eng.* **36** (6): 933–943.

- Guo, Y., D. Hansen, and C. Li. 2009. "Probabilistic approach to estimating the effects of channel reaches on flood frequencies." *Water Resour. Res.* **45** (8): W08404.
- Guo, Y., S. Liu, and B. W. Baetz. 2012. "Probabilistic rainfall-runoff transformation considering both infiltration and saturation excess runoff generation processes." *Water Resour. Res.* **48** (6): W06513.
- Guo, Y., and M. Markus. 2011. "An analytical probabilistic approach for estimating design floods of small watersheds." *J. Hydrol. Eng.* **16** (11): 847–857.
- Guo, Y., and Z. Zhuge. 2008. "Analytical probabilistic flood routing for urban stormwater management purposes." *Can. J. Civil Eng.* **35** (5): 487–499.
- Hebson, C., and E. F. Wood. 1982. "A derived flood frequency distribution using Horton order ratios." *Water Resour. Res.* **18** (5): 1509–1518.
- Howard, C. D. D. 1976. "Theory of storage and treatment plant overflows." *J. Environ. Eng.* **102** (EE4): 709–722.
- Huber, W. C. 2006. "Use of EPA SWMM5 for generation of BMP effluent EMC distribution." In *Proc., World Environmental and Water Resource Congress*. Reston, VA: ASCE.
- Huber, W. C., L. Cannon, and M. Stouder. 2006. *BMP modeling concepts and simulation*. EPA/600/R-06/33. Washington, DC: USEPA.
- Huber, W. C., and R. E. Dickinson. 1988. *Stormwater management model, version 4: User's manual*. EPA/600/3-88/001a (NTIS PB88-236641/AS). Athens, GA: EPA.
- Huff, F. A., and J. R. Angel. 1992. *Rainfall frequency atlas of the Midwest*. Bulletin 71. Champaign, IL: Illinois State Water Survey.
- Jain, S. C. 2001. *Open-channel flow*. New York: Wiley.
- Kadlec, R. H. 2000. "The inadequacy of first-order treatment wetland models." *Ecol. Eng.* **15** (1–2): 105–119.
- Kadlec, R. H. 2003. "Effects of pollutant speciation in treatment wetlands design." *Ecol. Eng.* **20** (1): 1–16.
- Kadlec, R. H., and R. L. Knight. 1996. *Treatment wetlands*. Boca Raton, FL: Lewis Publishers.
- Kibert, C. J. 2005. *Sustainable construction: Green building design and delivery*. New York: Wiley.
- Kotegoda, N. T., and R. Rosso. 1997. *Statistics, probability, and reliability for civil and environmental engineers*. New York: McGraw-Hill.
- Kurothe, R. S., N. K. Goel, and B. S. Mathur. 1997. "Derived flood frequency distribution for negatively correlated rainfall intensity and duration." *Water Resour. Res.* **33** (9): 2103–2107.
- Kutner, M. H., C. J. Nachtsheim, and J. Neter. 2004. *Applied linear regression models*. Homewood, IL: Irwin.
- Levy, B., and R. McCuen. 1999. "Assessment of storm duration for hydrologic design." *J. Hydrol. Eng.* **4** (3): 209–213.
- Li, J. Y., and B. J. Adams. 1994. "Statistical water quality modeling for urban runoff control planning." *Water Sci. Technol.* **29** (1–2): 181–190.
- Lin, Y. F., S. R. Jing, D. Y. Lee, Y. F. Chang, Y. M. Chen, and K. C. Shih. 2005. "Performance of a constructed wetland treating intensive shrimp aquaculture wastewater under high hydraulic loading rate." *Environ. Poll.* **134** (3): 411–421.
- Loganathan, G. V., and J. W. Delleur. 1984. "Effects of urbanization on frequencies of overflows and pollutant loadings from storm sewer overflows: A derived distribution approach." *Water Resour. Res.* **20** (7): 857–865.
- Loganathan, V. G., J. W. Delleur, and R. I. Segarra. 1985. "Planning detention storage for stormwater management." *J. Water Resour. Plann. Manage.* **111** (4): 382–398.
- Loganathan, G. V., E. W. Watkins, and D. F. Kibler. 1994. "Sizing storm-water detention basins for pollutant removal." *J. Environ. Eng.* **120** (6): 1380–1399.
- Marsalek, J. 1978. "Research on the design storm concept." In *Urban water resources research program: Technical memorandum No. 33*. Reston, VA: ASCE.
- Marsalek, J., and W. E. Watt. 1984. "Design storms for urban drainage design." *Can. J. Civil Eng.* **11** (3): 574–584.
- McCarthy, G. T. 1938. "The unit hydrograph and flood routing." In *Proc., Conf. on North Atlantic Division*. Washington, DC: USACE.
- Nnadi, F. N., F. X. Kline, H. L. Wray Jr., and M. P. Wanielista. 1999. "Comparison of design storm concepts using continuous simulation with short duration storms." *J. Am. Water Resour. Assoc.* **35** (1): 61–72.
- O'Donnell, K. J., D. F. Tyler, and T. S. Wu. 2005. "TMDL report: Fecal and total coliform TMDL for the New River (WBID 1442)." In *Proc., 3rd Conf. Watershed Management to Meet Water Quality Standards and Emerging TMDL (Total Maximum Daily Load)*. St. Joseph, MI: American Society of Agricultural Engineers.
- Packman, J. C., and C. H. R. Kidd. 1980. "A logical approach to the design storm concept." *Water Resour. Res.* **16** (6): 994–1000.

- Papa, F., and B. J. Adams. 1997. "Application of derived probability and dynamic programming techniques to planning regional stormwater management systems." *Water Sci. Technol.* **36** (5): 227–234.
- Papa, F., B. J. Adams, and Y. Guo. 1999. "Detention time selection for stormwater quality control ponds." *Can. J. Civil Eng.* **26** (1): 72–82.
- Park, D., J. C. Loftis, and L. A. Roesner. 2011. "Modeling performance of storm water best management practices with uncertainty analysis." *J. Hydrol. Eng.* **16** (4): 332–344.
- Park, D., and L. A. Roesner. 2012. "Evaluation of pollutant loads from stormwater BMPs to receiving water using load frequency curves with uncertainty analysis." *Water Res.* **46** (20): 6881–6890.
- Quader, A., and Y. Guo. 2006. "Peak discharge estimation for urban catchments using analytical probabilistic and design storm approaches." *J. Hydrol. Eng.* **11** (1): 46–54.
- Raines, T. H., and J. B. Valdes. 1993. "Estimation of flood frequencies for ungaged catchments." *J. Hydraul. Eng.* **119** (10): 1138–1154.
- Restrepo-Posada, P. J., and P. S. Eagleson. 1982. "Identification of independent rainstorms." *J. Hydrol.* **55** (1–4): 303–319.
- Rivera, P., J. Gironás, J. P. Montt, and B. Fernández. 2005. "An analytical model for hydrologic analysis in urban watersheds." In *Proc., 10th Int. Conf. Urban Drainage*. Madrid, Spain: International Association for Hydro-Environment Engineering and Research.
- Rodriguez-Iturbe, I., A. Porporato, L. Ridolfi, V. Isham, and D. Cox. 1999. "Probabilistic modelling of water balance at a point: The role of climate, soil and vegetation." *Proc. R. Soc. London Ser. A* **455** (1990): 3789–3805.
- Rossman, L. A. 2010. *Storm water management model user's manual. Version 5.0*. Rep. No. EPA/600/R-05/040. Cincinnati: USEPA.
- Rousseau, D. P. L., P. A. Vanrolleghem, and N. De Pauw. 2004. "Model-based design of horizontal subsurface flow constructed treatment wetlands: A review." *Water Res.* **38** (6): 1484–1493.
- Salas, J. D., R. A. Smith, G. Q. Tabios, and J.-H. Heo. 2004. *Statistical techniques in water resources and environmental engineering*. Fort Collins, CO: Colorado State Univ.
- Sanchez, L. 1986. "Flood frequency analysis of ungauged watersheds using a derived kinematic wave model." M.Eng. thesis, Univ. of Toronto.
- Schierup, H. H., H. Brix, and B. Lorenzen. 1990. "Wastewater treatment in constructed reed beds in Denmark—State of the art." In *Proc., Int. Conf. Use of Constructed Wetlands in Water Pollution Control*, edited by P. F. Cooper and B. C. Findlater. Oxford: Pergamon Press.
- Shen, H. W., G. J. Koch, and J. T. B. Obeysekera. 1990. "Physically based flood features and frequencies." *J. Hydraul. Eng.* **116** (4): 494–514.
- Shen, J., and Y. Zhao. 2010. "Combined Bayesian statistics and load duration curve method for bacteria nonpoint source loading estimation." *Water Res.* **44** (1): 77–84.
- Sivapalan, M., E. F. Wood, and K. Beven. 1990. "On hydrologic similarity, 3, A dimensionless flood frequency model using a generalized geomorphologic unit hydrograph and partial area runoff generation." *Water Resour. Res.* **26** (1): 43–58.
- Small, M. J., and D. M. Di Toro. 1979. "Stormwater treatment systems." *J. Environ. Eng.* **105** (EE3): 557–569.
- Strecker, E. W., M. M. Quigley, B. R. Urbonas, J. E. Jones, and J. K. Clary. 2001. "Determining urban storm water BMP effectiveness." *J. Water Resour. Plann. Manage.* **27** (3): 144–149.
- Stiles, T. C. 2001. "A simple method to define bacteria TMDLs in Kansas." In *Proc., ASIWPCA/ACWF/WEF TMDL Science Issues Conf. On-Site Program*, 375–378. Washington, DC: Water Environment Federation and Association of State and Interstate Water Pollution Control Administrators.
- Stone, K. C., M. E. Poach, P. G. Hunt, and G. B. Reddy. 2004. "Marsh-pond-marsh constructed wetland design analysis for swine lagoon wastewater treatment." *Ecol. Eng.* **23** (2): 127–133.
- Tung, Y. K., and B. C. Yen. 2005. *Hydroystems engineering uncertainty analysis*. New York: McGraw-Hill.
- UDFCD (Urban Drainage and Flood Control District). 2001. *Urban storm drainage criteria manual, revised August 2006*. Denver: UDFCD.
- Urbonas, B. 1979. "Reliability of design storms in modeling." In *Proc., Int. Symp. Urban Storm Runoff*, 27–35. Lexington, KY: Univ. of Kentucky.
- Urbonas, B. R., J. C. Y. Guo, and L. S. Tucker. 1990. "Optimization of stormwater quality capture volume." In *Proc., Urban Stormwater Quality Enhancement-Source Control, Retrofitting and Combined Sewer Technology*. Reston, VA: ASCE.

- Urbonas, B. R., and L. A. Roesner. 1993. "Hydrologic design for urban drainage and flood control." In *Handbook of hydrology*, edited by D. R. Maidment. New York: McGraw-Hill.
- USACE (US Army Corps of Engineers). 1977. *Storage, treatment, overflow, runoff model 'STORM' user's manual*. Davis, CA: Hydrologic Engineering Center.
- USACE. 1998. *HEC-HMS hydrologic modeling system user's manual—Version 1.0*. Davis, CA: Hydrologic Engineering Center.
- USACE. 2010. *HEC-HMS hydrologic modeling system user's manual—Version 3.5*. Davis, CA: Hydrologic Engineering Center.
- USEPA (US Environmental Protection Agency). 2007. *An approach for using load duration curves in the development of TMDLs*. Washington, DC: USEPA.
- Voorhees, M. L., and H. G. Wenzel Jr. 1984. "Urban design storm sensitivity and reliability." *J. Hydrol.* **68** (1–4): 39–60.
- Walesh, S. G. 1989. *Urban surface water management*. New York: Wiley.
- Wanielista, M. P., and Y. A. Yousef. 1993. *Stormwater management*. New York: Wiley.
- WEF (Water Environment Federation) and ASCE. 2012. *Design of urban stormwater controls: WEF manual of practice no. 23, ASCE/EWRI manuals and reports on engineering practice no. 87*. New York: McGraw Hill.
- Wenzel, H. G., Jr., and M. L. Voorhees. 1984. "An evaluation of urban design storm sensitivity." *Water Sci. Technol.* **16** (8–9): 219–236.
- Wong, T. H. F., T. D. Fletcher, H. P. Duncan, J. R. Coleman, and G. A. Jenkins. 2002. "A model for urban stormwater improvement conceptualization." In *Proc., 9th Int. Conf. on Urban Drainage*. Den Haag, Netherlands: International Water Association.
- Wong, T. H. F., T. D. Fletcher, H. P. Duncan, and G. A. Jenkins. 2006. "Modeling urban stormwater treatment—A unified approach." *Ecol. Eng.* **27** (1): 58–70.
- Wood, E. F., and C. S. Hebson. 1986. "On hydrologic similarity, 1. Derivation of the dimensionless flood frequency curve." *Water Resour. Res.* **22** (11): 1549–1554.
- Zegpi, M., and B. Fernández. 2010. "Hydrological model for urban catchments—Analytical development using copulas and numerical solution." *Hydrol. Sci. J.* **55** (7): 1123–1136.
- Zhang, S., and Y. Guo. 2013a. "An analytical probabilistic model for evaluating the hydrologic performance of green roofs." *J. Hydrol. Eng.* **18** (1): 19–28.
- Zhang, S., and Y. Guo. 2013b. "An explicit equation for estimating the stormwater capture efficiency of rain gardens." *J. Hydrol. Eng.* **18** (12): 1739–1748.
- Zhang, S., and Y. Guo. 2014. "Stormwater capture efficiency of bioretention systems." *Water Resour. Manage.* **28** (1): 149–168.

CHAPTER 10

Analysis of Water Quality Random Variables

Jim C. Loftis

GLOSSARY

Alpha (α): Level of significance or tail area associated with a statistical interval or hypothesis test

Box plot or box-and-whiskers plot: Graphical representation of distribution of subpopulation consisting of 25th and 75th percentiles (box), median, extremes (whiskers whose value depends on software package), and usually outliers

Censored observation: Reported laboratory measurement that has been altered by the laboratory, typically a nondetect or trace value reported as less than a certain numerical value

Coliform: Large class of bacteria found in water and soil; specific types, *E-coli* and fecal coliforms are used as indicators of human or livestock pollution

Confidence interval: Statistical interval computed to contain the true value of a population parameter with specified probability or confidence level, $1 - \alpha$

Continuous distribution: Distribution of a random variable that can take on any value within a certain range, for example, all real numbers

Cryptosporidium: Genus of protozoans that can cause gastrointestinal illness

Cumulative distribution function (cdf): Nonexceedance probability associated with a given value of a particular random variable

Detection limit: For a given laboratory method, the lowest concentration that is statistically different from zero, for example three times the standard deviation of repeated measurements at zero concentration

Discrete distribution: Distribution of a random variable that can take on only certain values, typically integers

Empirical distribution function (edf): Estimated value of cdf obtained from observed data

Enterococcus A genus of bacteria common in human intestinal tracts

Event mean concentration: Mass-averaged mean concentration of a particular constituent for a particular storm or runoff event

Geometric mean: n th root of the product of n observations

Geosmin: Organic compound, produced by blue-green algae, that imparts an earthy taste and odor to drinking water at parts per trillion level

Giardia: Genus of protozoans that can cause gastrointestinal illness

Maximum likelihood estimate: A parameter estimate that maximizes a likelihood function that then makes what has actually been observed as probable as possible

Most probable number (MPN): An estimate of microbial concentration based on fermentation and test for presence or absence in successive dilutions

Nondetect (ND): Laboratory measurement below the detection limit, typically reported as "less than" the detection limit

Nonparametric method: Statistical method that does not depend upon the distribution of the sampled population

Order statistic: Observation corresponding to a given rank. The n th order statistic is the smallest observation and has rank 1

Outlier: Observation that is apparently inconsistent with the distribution of other similar observations

Parameter (of a distribution): A defining numerical characteristic of a population or distribution, such as mean and variance for the normal distribution

Parametric method: Statistical method that assumes a particular probability distribution for the sampled population

Percentile: The specific value of a distribution such that a given percentage of the distribution is equal to or below that value

Population: The set of all possible sampling units for a given situation (see *target population* and *sampled population*)

Practical quantification limit (PQL or QL): Lowest concentration level for a specific laboratory method that results in acceptable precision (standard deviation of repeated measurements at that concentration); also called the reporting limit (RL)

Precision: Statistical measure of repeatability, usually expressed as a standard deviation

Prediction interval: Statistical interval constructed from background data to contain a future sample or samples with specified probability if no change has occurred

Probability: Measure (zero to one) of likelihood of a certain outcome of a chance experiment

Probability density function (pdf): Mathematical description of a probability distribution, from which specific probabilities are derived by integration between appropriate limits

Probability distribution: Mathematical or graphical description of the frequency of particular events, such as drawing successive samples from a given population

Proportion: Fraction of a given population that has a certain attribute

Quantile: The specific value of a distribution such that a given fraction of the distribution is equal to or below that value

Random variable: Mathematical variable whose value depends to some extent on the outcome of a chance experiment

Sampled population: Set of all sampling units that can actually be sampled in a given sampling program

Sampling unit: In environmental statistics, a physical quantity of an environmental medium, such as air, water, or soil, that could be analyzed in the laboratory or field

Seasonality: Annual cyclic pattern in population parameters, such as mean and variance

Serial correlation: In a time series, carryover of information, redundancy, or tendency of successive observations to remain above or below the mean

Standard error: Sample standard deviation of an estimate of a parameter, such as the standard error of the sample mean; the standard error is a measure of precision of a parameter estimate

Reporting limit (RL): Lowest concentration level for a specific laboratory method that results in acceptable precision (standard deviation of repeated measurements at that concentration); also called the practical quantitation limit (PQL)

Resource Conservation and Recovery Act (RCRA): Federal legislation that regulates disposal of solid and hazardous wastes

Target population: Set of all possible sampling units of interest in a given sampling program

Time series plot: Graphical plot of measurements over time

Total organic carbon (TOC): Laboratory measurement of total organic constituent concentration in water

Trace: Common term for a laboratory measurement falling above the detection limit and below the practical quantitation limit

Unbiased: Descriptor for a statistical method for which the average result tends to the true value over a large number of repeated applications for the same population

10.0 GENERAL

The topic of water quality distributions is as large as the topic of water quantity distributions. So treating the subject in a single chapter is very difficult, and we must therefore limit the discussion to a few characteristics that are of particular interest and importance to practitioners and that are different in some way from water quantity. Of course, much of the discussion of water quantity distributions can be applied to water quality as well.

This chapter will briefly discuss the following topics:

- Special characteristics and practical applications of water quality random variables,
- Most commonly used distributions—both continuous and discrete,
- Transformations and testing for goodness of fit,
- Nonparametric characterization using quantiles,
- Censored observations,
- Probability sampling versus stochastic processes/serial correlation,
- Seasonal and flow effects, and
- Multivariate characterization.

10.1 SPECIAL CHARACTERISTICS OF WATER QUALITY RANDOM VARIABLES

Water quality random variables have several important characteristics that strongly affect their distributions and that, to some extent at least, differ from water quantity random variables:

1. While both water quality and quantity are multivariate, a very large number of random variables of different types characterize water quality. These include physical, chemical, and

biological measurements, with as many as 20, 50, or more measurements from field instruments and multiple laboratories required to characterize a single water sample.

2. Obviously, opportunities exist for many types of error to creep into measurements in the field, during handling and transport, or in the laboratory. Not surprisingly then, data quality is frequently lacking.
3. At the same time, laboratory techniques are constantly being developed and improved, and methods or laboratories are often changed for cost or other reasons. Measuring certain low-level constituents at the level of nanograms per liter (ng/L) or parts per trillion is now possible—and sometimes necessary. The taste and odor compound, geosmin, for example, is detectable by sensitive humans at about 5 ng/L. As measurement methods change over time, so does the measurement error variance of water quality observations. The variance may change from sample to sample, particularly for biological measurements, and does not always decrease over time.
4. Water quality data from low-level measurements, particularly organics, also frequently include nondetects (recorded for example as <5.0 µg/L), which result from censoring of measured values by the laboratory. The presence of nondetects obviously complicates statistical analysis of data, particularly when the detection limit or censoring level changes over time.
5. Water quality datasets are not often symmetrically distributed for several reasons, including the presence of nondetects, relationships with precipitation and/or streamflow, and the importance of biological variables and processes.
6. And finally, characterizing water quality random variables in a rigorous sampling context—which requires that the population of interest, or target population, is specified in advance of sampling—may be difficult or impossible. As a simple example, if one is interested in studying the effects of fire on water quality, the sampling program is limited by the fact that one does not know in advance when and where the fire will occur.

Helsel and Hirsch (2002, p. 2) provide a similar list of special characteristics for water resources data in general.

Note at the outset that characteristic 6 is probably the most important. Consequently, data users often waste a great deal of time arguing about whether or not the data are normally distributed, when the far more important question is whether or not the data adequately represent the real population of interest.

10.2 PRACTICAL APPLICATIONS OF WATER QUALITY DISTRIBUTIONS

The distribution of a water quality random variable depends on the particular population of interest, which in turn depends upon the intended use of the data for a particular application. The following describes three of the more common broad categories of monitoring, and then the next sections discuss the probability distributions that have been most useful for those applications.

First, routine, fixed-station monitoring of streams and lakes is important for assessing compliance with stream standards and suitability for intended uses such as drinking water, contact recreation, and aquatic habitat. Routine monitoring should be accompanied by the production of routine reports, which generally include statistical summaries and some type of trend analysis. Sound network design and data analysis are critical for getting the most from limited and usually shrinking budgets for routine monitoring, but many routine monitoring programs produce more data than useful information (Ward et al. 1986). Furthermore, a sound statistical foundation is often lacking when stream standards and compliance criteria are established.

Second, limited-duration intensive surveys are needed to augment routine monitoring when evaluating the impacts of certain human activities or rare events such as fires or floods, particularly when a large suite of constituents and a high level of spatial and temporal resolution are required. Multivariate methods and mapping may be particularly important for characterizing the impact of pollution sources. Unless the results of similar surveys are available, the probability distributions of variables of concern may not be known until after the study is complete.

And third, regulatory monitoring for compliance with permits is somewhat different from routine monitoring to assess use-based standards compliance, although the ultimate purpose of protecting beneficial uses is the same. Monitoring for permit compliance focuses on the known location of discharge into a receiving water, for example the outfall of a wastewater treatment plant or the entire area covered by a landfill overlying an aquifer. For this type of monitoring detailed requirements for monitoring and statistical analysis of data are often needed to assess compliance. A notable example is Resource Conservation and Recovery Act (RCRA) compliance monitoring of groundwater at landfills and other waste disposal facilities. Guidance for this type of monitoring includes a recommendation for evaluating the distribution of constituents of concern ([EPA 2009](#)).

The following paragraphs briefly discuss the parametric distributions, both continuous and discrete, that are most commonly used in water quality. The mathematical formulae for the probability density functions (pdfs) and parameters are widely available in texts on probability theory (e.g., [Wackerly et al. 2008](#)). With the exception of the Weibull distribution, all are discussed in [McBride \(2005\)](#) within the context of water quality management. [Note: Chapter 10 of [McBride \(2005\)](#) requires an important correction. On p. 220 in the caption to Table 10.3 and in Example 10.3 on page 221, “for a 3×10 mL, 3×1 mL, and 3×0.1 mL” should be replaced with “for a 3×100 mL, 3×10 mL, and 3×1.0 mL.” Personal communication from the author.]

10.3 THE NORMAL DISTRIBUTION

To begin the discussion of continuous distributions, the normal distribution is generally the most widely used. Because the normal distribution is well covered in all statistical texts and elsewhere in this monograph, the normal distribution needs no general description here.

As discussed earlier, many water quality random variables are not normally distributed unless they are transformed, and even then transformations are not always successful in achieving normality. Parametric representations of water quality distributions are of limited utility, and most practitioners should rely most heavily on nonparametric (also referred to as distribution-free) approaches. For most routine water quality data analysis, nonparametric approaches can be used without any pretesting to evaluate the form of the distribution. This approach reduces work, costs, and complexity of the resulting report without compromising the validity or value of the information produced.

Nevertheless, the normal distribution is of central importance in water quality statistics for several reasons. First, in some cases the normal distribution is a good fit to water quality data. As one example, [Nakano et al. \(2015\)](#) find that the normal distribution is a good fit for nitrate concentrations in groundwater on the main island of Okinawa in Japan. And in other cases, transformations of the data can often be used to achieve normality, as discussed later. Second, sample means tend to be normally distributed, regardless of the underlying distribution, via the central limit theorem ([Wackerly et al. 2008](#)). The number of samples required to achieve normality of the sample mean depends on the type and degree of departure from normality. Means—taken over days, months, or even years—are often analyzed statistically. Sample size calculations for estimation of means with a desired error and confidence level are generally based on the approximate normality of the sample mean ([Gilbert 1987](#), p. 31). Third, measurement errors and instrument noise tend to be normally

distributed. Finally, the normal distribution is very commonly used in nonparametric statistical methods because the test statistic is often approximately normally distributed for larger sample sizes.

10.4 TESTS FOR NORMALITY AND TRANSFORMATIONS

Whether necessary or not, testing water quality data for normality and attempting transformations before employing nonparametric methods is fairly common practice. [EPA \(2009\)](#) states that “Testing of normality is ubiquitous in environmental statistical analysis,” and certainly a parametric model based on a particular distribution is useful in several applications. Therefore, in keeping with the major theme of this monograph, assume that we have water quality data that are collected from a target population of interest by an appropriate sampling scheme, such as simple random sampling or systematic sampling of the entire population of interest ([Gilbert 1987](#)). Furthermore, we wish to select an appropriate distribution as the foundation for a statistical model. In many cases, experience with similar datasets will provide sufficient or at least some guidance. If more guidance is needed, the traditional approach involves inspection of probability plots (usually for linearity or presence of outliers) for alternative distributions and/or hypothesis testing, for example, using a null hypothesis that the given set of data comes from a normal (or other specified) distribution.

This is in fact the approach that the U.S. Environmental Protection Agency advocates ([EPA 2009](#)). The recommended approach is to test first for normality by an appropriate test of hypothesis and then to attempt Box–Cox transformations using the “ladder of powers” described in [Helsel and Hirsch \(2002\)](#). The form of those transformations is

$$y_k = \begin{cases} x^\lambda & \text{for } \lambda \neq 0 \\ \log x & \text{for } \lambda = 0 \end{cases} \quad (10-1)$$

where λ can be any real number, but for the ladder of powers is taken as

$$\lambda = 0, \frac{1}{4}, \frac{1}{3}, \frac{1}{2}, 1, 2, 3, 4$$

If an acceptable degree of normality is not achieved, then nonparametric methods would be used. In [EPA \(2009\)](#) and elsewhere, “acceptable” is defined in terms of failure to reject a null hypothesis of normality based on an appropriate hypothesis test, but the conclusion may depend on the sample size as noted later.

In applying [EPA \(2009\)](#), the most common use of the transformed observations is construction of prediction limits using the formula for normally distributed data. Valid limits can be obtained, even though the backtransformed mean of the transformed data (logs, for example) is not the mean of the original data. (It is the geometric mean in the preceding example.)

An obvious problem with this approach, and with testing for normality or other distributions in general, is that the hypothesis test is more sensitive (powerful) as the sample size increases. Thus, larger datasets are more likely to result in a rejection of the null hypothesis of normality or transformed normality and therefore in the use of nonparametric prediction limits. However, nonparametric prediction limits can be no wider than the difference between the largest and smallest observation and have significance levels no smaller than $1/(n - 1)$, where n is the number of observations. Therefore, parametric tests, when appropriate, have an advantage for small sample sizes in both the achievable significance level and the power at a given significance level.

However, unless one has additional evidence (from a similar monitoring program perhaps) to support an assumption of some particular distribution, conclusively determining the distribution

when sample sizes are small is not possible. Thus, when the choice of a parametric method is based primarily on normality testing using a small sample size, the assumed significance level for the chosen parametric method may be incorrect. Therefore, both parametric and nonparametric approaches have limitations, especially for small sample sizes, and the best choice will depend upon the application.

For applications in which hypothesis tests for distribution fit are needed, [EPA \(2009\)](#) recommends and describes the Shapiro–Wilk procedure for sample sizes of 50 or less and the Shapiro–Francia procedure for larger sample sizes. [EPA \(2009\)](#) also recommends Filliben’s probability plot correlation coefficient as the logical test to accompany visual inspection of the normal probability plot and as having similar power to the Shapiro–Wilk procedure. [Gilbert \(1987, pp. 158–162\)](#) describes the Shapiro–Wilk W test for samples sizes of 50 or smaller and D’Agostino’s test for sample sizes of 50 or larger. Many other tests, such as the popular chi-squared goodness of fit and Kolmogorov–Smirnov are available in statistical texts, for example [Zar \(1999\)](#), and statistical software packages, and testing may be applied to other distributions as well.

The EPA software package ProUCL provides routines for distribution fitting, outlier analysis, and many statistical procedures that are widely applied in water quality data analysis. In particular, the package includes most of the procedures for the analysis of censored data that are described later in this chapter. The software and accompanying documentation, including user and technical guides, are free to download at <https://www.epa.gov/land-research/proucl-software>.

The ProUCL technical guide ([Singh and Singh 2015, p. 18](#)) makes the important point that observations that appear to be either outliers or high values from the population of interest may actually represent a different population altogether—a contaminated area of soil or a water quality contamination event, for example. The total group of observations, including the high values, may appear to be adequately modeled by a log–normal distribution, when in fact two different distributions are present. In practice, separating out the high values and modeling them separately or as a mixture may or may not be advisable, depending on the actual population of interest and associated information needs. However, if the actual target population is carefully defined, as discussed elsewhere in this chapter, a logical approach to distribution fitting should become apparent.

10.5 THE LOG–NORMAL DISTRIBUTION

The log–normal distribution, also discussed in other chapters, is probably the most widely applicable distribution for modeling water quality variables of all types given that it has a lower bound of zero and positive skewness. The latter is extremely common in water quality observations, especially but not limited to microbiological variables, which are prone to include a few values that are much larger than the rest. As just a few examples, [Masago et al. \(2002\)](#) find that a log–normal distribution was acceptable for *Cryptosporidium* levels in the Sagami River, Japan, based on goodness-of fit-testing at a significance level of 0.05, and provides a better fit than a normal distribution or negative binomial distribution. [Çelo et al. \(1999\)](#) find that heavy metal concentrations were log–normally distributed in sediments along the Albanian coast. [Mujeriego and Peters \(2008\)](#) find that microbial quality of reclaimed water was “adequately interpreted” by a log–normal distribution. [Wang et al. \(2007\)](#) observe a log–normal distribution for event mean concentrations of total phosphorus in surface runoff from multiple land uses in a hilly area around Taihu Lake in eastern China. [Dolgonosov and Korchagin \(2014\)](#) find that a seasonal log–normal model provides a good description of the distribution of stream flow and several water quality variables for the Moskova River in Russia. The water quality variables were turbidity, color index, alkalinity, permanganate oxidability, chloride, total microbial count, total coliforms, and fecal streptococci.

And, in a principal component analysis (PCA; to be described further in this chapter) of water quality variables from the Illinois River Basin in Arkansas and Oklahoma, Olsen et al. (2012) find that all 26 chemical and biological variables included in the PCA were right-skewed and better described by a log-normal distribution than by a normal distribution.

The log-normal distribution is extremely easy to use because the logs of the observations are normally distributed. Thus standard normal tables can be used to make probability statements. Gilbert (1987, Chapter 13) presents a particularly thorough discussion of the log-normal distribution with environmental applications, from which a few key concepts are repeated here:

- Parameters of the distribution are the mean and variance of the logs.
- Mean and variance of the untransformed observations are obtained from transformation equations that include both of these parameters (Gilbert 1987, p. 167).
- Antilog of the mean of the logs is the median (equal to the geometric mean) of the untransformed observations.
- Other percentiles correspond to normal percentiles of the logs and are obtained by exponentiation thereof.
- Therefore, a confidence interval for the median may be obtained by computing a confidence interval for the mean of the logs and exponentiating (Gilbert 1987, p. 173; Helsel 2012, p. 119).
- Gilbert (1987, pp. 165–166, 172) presents the best (minimum-variance unbiased) estimators for the mean and median of the untransformed log-normal distribution and for the corresponding variance of those estimates. These estimators require the use of a function denoted as $\Psi()$ for which the first few terms of an infinite series are presented and can easily be computed via spreadsheet. Simpler estimators perform well only for large sample sizes (Gilbert 1987, pp. 167–168, 171–172).

Helsel (2012, pp. 115–118) discusses several options for computing confidence intervals for the mean of the log-normal distribution, including a bootstrapping approach. Bootstrapping involves repeated sampling with replacement from the original dataset to obtain many (hundreds or thousands) of estimates, from which a confidence interval is obtained by computing the desired percentiles.

10.6 OTHER CONTINUOUS DISTRIBUTIONS: GAMMA, WEIBULL, AND BETA

Other continuous distributions that are sometimes used in modeling water quality random variables are the gamma, Weibull, and beta. Gilbert (1987, p. 157) presents their density functions. Wackerly et al. (2008, pp. 185–200) discuss the gamma and beta distributions, while McBride (2005, pp. 31–33) provides additional discussion of the gamma and beta distributions regarding water quality applications and states that the beta distribution is particularly useful as a prior distribution in Bayesian analysis. A few example applications from the literature follow.

Behera et al. (2000) studied the distribution of event mean concentrations of 15 urban runoff quality constituents representing chemical and bacteriological pollutants, nutrients, and heavy metals. Using a Kolmogorov-Smirnov test to assess goodness of fit, the authors conclude that the log-normal, gamma, and exponential distributions were all useful for describing runoff quality constituents. The exponential distribution is actually a special case of the gamma distribution (McBride 2005, p. 32).

In a study of the distributions applicable at three stages (settled water, filtered water, and final water) within a water treatment plant, Nwaiwu and Bitrus (2005) also use a Kolmogorov-Smirnov test to evaluate goodness of fit of alternative distributions. In the words of the authors, “For the

settled water, colour and turbidity are lognormally distributed while pH is normally distributed; filtered water has colour, turbidity, free chlorine and total chlorine log normally distributed while pH has gamma distribution for best fit. The log normal distribution fitted all the parameters undertaken for the final water.”

Thompson et al. (2000) analyzed polycyclic aromatic hydrocarbon (PAH) sediment and oyster contamination data collected at Murrells Inlet, South Carolina. They find that the Weibull distribution generally provides an adequate fit (and better fit than the log-normal distribution) to the data considered. The authors also explore several methods of estimating Weibull parameters from censored (nondetect) data, to be discussed in a later section. EPA (2009) mentions prediction limits based on the gamma distribution (Bhaumik and Gibbons 2006) and Weibull distribution (Cameron 2007).

10.7 THE BINOMIAL AND HYPERGEOMETRIC DISTRIBUTIONS

Moving now to discrete distributions, the binomial is most broadly applicable. The binomial distribution gives the probability of x successes in n independent trials, each with probability of success p . p and n are the parameters of this distribution (McBride 2005, p. 143; Wackerly et al. 2008, p. 100.) Thus any dichotomous variable is always binomially distributed if sampling is random or samples are otherwise independent.

The binomial is an extremely important discrete distribution for water quality applications because of its applicability for setting and evaluating stream standards and because it is the basis for many nonparametric methods. Because any distribution is adequately characterized by a sufficient number of quantiles, the binomial distribution can be used to develop any required probability of occurrence within any interval when those quantiles are known. In that sense, the binomial distribution is ultimately the only distribution that one would ever need. Or, more realistically, the binomial distribution can be used to develop probability statements about order statistics, on which nonparametric methods are based. Those probability statements then form the basis for nonparametric interval estimates and hypothesis tests (Conover 1980). The binomial and cumulative binomial distributions are conveniently evaluated with statistical software (including statistical functions in Microsoft Excel).

As a practical application of the binomial distribution, suppose that one wishes to evaluate the performance of an effluent standard and monitoring strategy designed to indicate compliance when the effluent is below a fixed limit (of say 1 mg/L biochemical oxygen demand, BOD) at least 90% of the time. The discharge permit requires 20 samples per month with no more than two (10%) exceeding 1 mg/L BOD.

Now suppose that the effluent is actually above the limit 15% of the time. What is the probability that the monitoring program will correctly conclude that the discharger is out of compliance? The desired probability is the probability of obtaining more than two samples above the limit (successes) out of 20 when $p = 0.15$. This probability is 1 minus the cumulative binomial distribution with $x = 2$, $n = 20$, and $p = 0.15$, which turns out to be 1.0–0.405 or about 0.6. Thus a 60% chance exists of correctly concluding the effluent standard is violated, and a 40% chance exists of erroneously concluding that the discharger is in compliance.

Given that this type of analysis is extremely simple to perform, that it is not more widely used in setting compliance criteria and designing monitoring strategies for permit compliance is somewhat surprising. McBride (2005, p. 183–192) expands upon this discussion, using the binomial distribution and “classical approach” to determine the number of allowable exceedances to control risk to both “producer” (discharger) and “consumer” (beneficial use) and then extends the discussion to the development of such rules using a Bayesian approach. The binomial distribution is also applicable to

evaluating probabilities of a given number or proportion of samples being recorded above or below one or more threshold levels and thus for answering “several relevant questions about censored data” (Helsel 2012, p. 142–152).

A variation of the binomial distribution, the hypergeometric distribution, provides the probability of obtaining x successes in sampling without replacement in a finite population of N trials containing exactly D successes (McBride 2005, p. 147; Wackerly et al. 2008, p. 125). Helsel (2012, p. 147) provides an example application for determining the largest expected number of exceedances, y , (of a standard or detection limit), for a confidence level of $1 - \alpha$, in a given future number of samples, m , after observing zero exceedances in the first n samples. First define $H(x; n, D, N)$ as the cumulative hypergeometric distribution giving the probability of x or fewer exceedances out of n samples drawn without replacement from N total samples, of which D are exceedances. Note that in this example $N = n + m$. The largest expected number of future exceedances, y , is therefore the smallest value of D for which the probability of $x = 0$ exceedances in the first n trials is less than α ; or in the aforementioned notation, the smallest value of y for which

$$H(0; n, y, n + m) < \alpha \quad (10-2)$$

Helsel (2012, p. 147) gives a numerical example and the required Minitab commands.

Note that this example does not include estimation of the proportion of exceedances, p , in the overall population. However, p can be estimated from the same data and is simply the number of nonconforming samples over the total number of samples. Confidence intervals for p are discussed later in this chapter.

10.8 OTHER DISCRETE DISTRIBUTIONS AND MICROBIOLOGICAL VARIABLES

For biological monitoring, parametric descriptions of other discrete distributions are often applicable. McBride (2005) presents an excellent discussion of the applicable distributions and includes chapters on “Microbial Water Quality and Human Health” (Chapter 9) and “MPNs and Microbiology” (Chapter 10; see correction in Section 10.2). MPN refers to “most probable number” in microbial assays that use fermentation of successive dilutions in which presence should be indicated if at least one cell is present. Chapter 9 of McBride (2005) discusses statistical approaches to analysis of exposure assessment, dose response, risk profiling, and risk communication.

10.8.1 The Poisson Distribution

The Poisson distribution (McBride 2005, p. 144; Wackerly et al. 2008, p. 131) is commonly used to model microbial counts in water. The single parameter of this distribution is both the mean and variance, which are identical. The mean and variance are counts, not concentrations, and scale directly with the sample volume (Loftis et al. 1999).

Young and Komisar (1999) use the Poisson distribution to model variability of *Cryptosporidium* oocysts and *Giardia* cysts in water. Haas and Rose (1996) find that the distribution of *Cryptosporidium* oocysts is consistent with the Poisson distribution. Gale et al. (2002) find that total coliforms were Poisson distributed in 5,000 volumes of treated water. McBride (2005) notes that the standard tables for MPNs are all based on random sampling from Poisson distributions. However, some “untidy aspects of MPN tables and their usage” are discussed at length in McBride (2005, Chapter 10).

10.8.2 The Negative Binomial Distribution

Another relative of the binomial distribution, the negative binomial distribution, provides the probability associated with a given number of trials, n , required to achieve the k th success when each trial has a success probability p (Wackerly et al. 2008, p. 121). The possible values of n are $k, k + 1, k + 2, \dots$, and the parameters of the distribution are k and p . McBride (2005, pp. 36, 145) describes the distribution as applicable for describing the distribution of *Cryptosporidium* oocysts in water bodies (Gale 1998). The distribution is always overdispersed, meaning that the variance is always greater than the mean. The variance increases with the value of k , which is therefore called the dispersion parameter.

In Young and Komisar (1999), cited previously regarding the Poisson distribution, the negative binomial distribution is used to model situations in which clumping of the (oo)cysts occurs. Petterson (2001) finds that virus counts on salad crops irrigated with wastewater were best fitted by a negative binomial distribution rather than Poisson, indicating overdispersion and viral clumping. Crohn and Yates (1997) assume a negative binomial distribution of virus densities and use a volume-varying version of the negative binomial distribution to develop a one-sided confidence interval for the mean virus concentration in treated water. The dispersion parameter, k , is estimated from data collected prior to water treatment.

10.8.3 The Multinomial Distribution

The multinomial distribution is a generalization of the binomial distribution in which there are m possible outcomes to each trial with probabilities p_1, p_2, \dots, p_m , which sum to 1. McBride (2005, pp. 148, 222–224) describes the multinomial distribution and its use in developing exact MPNs.

10.9 NONPARAMETRIC REPRESENTATIONS

Continuing the discussion from Section 10.4, many, if not most, water quality random variables are not well described by either the normal distribution or log-normal distributions, thus greatly reducing the applicability of many classical statistical methods. And, certainly, many water quality data sets are not well described by any common parametric distribution. Therefore, nonparametric methods have become an (if not yet “the”) accepted norm for water quality data analysis. Most data analysis tasks can be accomplished by nonparametric methods that are easy to understand and implement in statistical software, perform nearly as well (in terms of power and validity of significance level) as parametric alternatives when the data are normally distributed, and perform much better as the data depart from normality.

In a nonparametric view, the distribution is characterized only by the data themselves, that is, order statistics, and their associated quantiles (or percentiles). Any distribution is adequately characterized by a sufficiently large number of quantiles, each corresponding to a left-tail (nonexceedance) probability, p , and therefore representing a binomial distribution with parameter p . Thus the basis for many nonparametric methods is the binomial distribution and its normal approximation (Conover 1980, pp. 52, 95–142).

We shall briefly discuss both point and confidence interval estimates of quantiles and of nonexceedance probabilities, p , with more attention to the former because the estimation of nonexceedance probabilities is central to flood frequency analysis, discussed elsewhere in this monograph.

10.9.1 Nonparametric Estimation of Quantiles and Proportions

For common values of p and confidence level $1 - \alpha$, tables are readily available for nonparametric confidence intervals on quantiles. The tables give the ranks of the observations that form the

confidence interval (Hahn and Meeker 1991, p. 82). Alternatively, and for other situations, one can use the cumulative binomial distribution as described in Conover (1980, p. 112) or Hahn and Meeker (1991, p. 83). Briefly, the procedure is as follows for sample size n , probability level p^* , and confidence level $1 - \alpha$ (Iyer 2000):

1. Define $B(x,m,p)$ as the cumulative binomial probability of x or fewer successes in m trials with probability of success p .
2. For each integer $x = 0, 1, \dots, n$, compute $B(x,n,p^*)$.
3. Select a value of $B(x,n,p^*)$ that is approximately equal to $\alpha/2$. Denote this entry as α_1 and the corresponding value of x as $r - 1$.
4. Select another value of $B(x,n,p^*)$ that is approximately equal to $1 - \alpha/2$. Denote this entry as $1 - \alpha_2$ and the corresponding value of x as $s - 1$.
5. A confidence interval for the p^* th quantile with confidence level greater than or equal to $1 - \alpha_1 - \alpha_2$ is given by the interval $[x(r), x(s)]$ where $x(r)$ and $x(s)$ are the order statistics of rank r and s , respectively.

The required cumulative binomial probabilities are conveniently evaluated in Microsoft Excel with the statistical function, BINOM.DIST.

Gilbert (1987, p. 141) gives the following approximate formula (appropriate for $n > 20$), where l and u define the ranks of the lower and upper limits, respectively, and $Z_{1-\alpha/2}$ is the standard normal random variable with left-tail probability $1 - \alpha/2$.

$$l = p^*(n + 1) - Z_{1-\alpha/2}[np^*(1 - p^*)]^{1/2} \quad (10-3)$$

$$u = p^*(n + 1) + Z_{1-\alpha/2}[np^*(1 - p^*)]^{1/2} \quad (10-4)$$

Because l and u are not integers, the limits are usually approximated by interpolation between the appropriate order statistics.

As in flood frequency analysis, the value of p corresponding to a given observation (and equivalently, proportion or cumulative distribution function, cdf) is most commonly the Weibull plotting position, $p = m/n + 1$, where m is the rank of the observation and n is the total number of observations.

A similar concept is the proportion of the distribution that lies below a fixed level, x_0 , not corresponding to an actual observation. That proportion is estimated as $p = x/n$, where x is the observed number of observations ("successes") that lie below the fixed limit, x_0 , out of a total number of observations ("trials") n .

In regulatory applications, in particular, confidence intervals both for quantiles and proportions (equivalently, cdfs) are often useful. Such intervals can help determine whether a given dataset or sample size is adequate either for setting standards or assessing compliance (McBride 2005, pp. 179–185).

As was the case for quantiles, nonparametric confidence intervals on a proportion are readily available in tables and graphs (Gilbert 1987, p. 257; Hahn and Meeker 1991, pp. 104–107). Alternatively a "conservative two-sided 100(1 – α) % confidence interval for p " is given by Hahn and Meeker (1991, p. 104) as follows,

$$[p1, p2] = \left[\left\{ 1 + \frac{(n - x + 1)F1}{x} \right\}^{-1}, \quad \left\{ 1 + \frac{n - x}{(x + 1)F2} \right\}^{-1} \right] \quad (10-5)$$

where

x = observed number of “successes” in n trials; thus, the point estimate of $p = x/n$;

p_1, p_2 = lower and upper confidence limits, respectively;

F_1 = quantile of the F distribution with left-tail probability of $1 - \alpha/2$ and degrees of freedom $n_1 = 2n - 2x + 2$ and $n_2 = 2x$; and

F_2 = quantile of the F distribution with left-tail probability of $1 - \alpha/2$ and degrees of freedom $n_1 = 2x + 2$ and $n_2 = 2n - 2x$.

The F distribution quantiles can be evaluated using the Microsoft Excel function F.INV.

The following gives a large-sample approximate formula for situations in which both np and $n(1 - p)$ are greater than 5 (according to [Gilbert 1987](#), p. 143) or 10 (according to [Hahn and Meeker 1991](#), p. 106).

$$[p_1, p_2] = p \pm Z_{1-\alpha/2} \left[\frac{p(1-p)}{n} \right]^{1/2} \quad (10-6)$$

where

p = point estimate of the desired probability = x/n , and

$Z_{1-\alpha/2}$ = standard normal random variable with left-tail probability $1 - \alpha/2$.

10.9.2 Box-and-Whisker Plots

The estimated quartiles (25th and 75th percentiles) of a distribution define the interquartile range, which along with the median, form the basis of the box-and-whisker plot (boxplot), the most widely used graphical representation of water quality distributions. The quartiles are shown as a box, median within the box, and upper and lower extreme values as whiskers. Most statistical software packages can produce these plots with various options for defining the whiskers and plotting outlying values beyond the whiskers, along with additional information such as sample size. In the default options of Minitab, for example, the whiskers extend to the actual data point that lies just inside a point defined as 1.5 times the interquartile range beyond the end of the box. The values outside the whiskers are plotted as asterisks. Minitab, with default options, was used to create Figure 10-1.

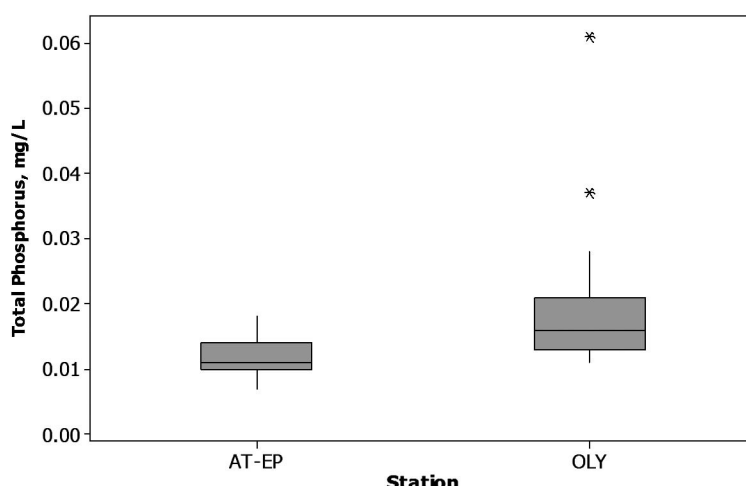


Figure 10-1. Boxplot of total phosphorus concentrations for 2009–2011 at two monitoring stations in the Colorado-Big Thompson Project operated by Northern Water. Stations are Adams Tunnel (AT), East Portal (EP), and Olympus Tunnel (OLY).

Source: Data provided by [Northern Water \(2012\)](#), Berthoud, Colorado.

Box-and-whisker plots are found in essentially all US Geological Survey (and many other) publications on water quality and are perhaps the best way to succinctly describe the distribution of data for a given subpopulation and to compare subpopulations across locations, seasons, or years. The example boxplot in Figure 10-1 compares total phosphorus concentrations at two surface water stations in the Colorado-Big Thompson Project near Estes Park, Colorado.

The upstream station, AT-EP, is located at the east portal of the Adams Tunnel, which transports water from Grand Lake, west of the Continental Divide. The downstream station, OLY (Olympus Tunnel), is located at an outlet from Lake Estes, which receives additional phosphorus inputs from the city of Estes Park and thus exhibits slightly higher total phosphorus concentrations.

10.10 CENSORED OBSERVATIONS

The sensitivity of laboratory methods has limits, and most laboratories will record low-level measurements as nondetect (ND) or less-thans (e.g., $< 10.0 \mu\text{g/L}$) when the measured concentration in the sample has a signal-to-noise ratio that is deemed to be unacceptably small. The critical level, called the detection limit, is derived statistically from the standard deviation of multiple blanks or laboratory spikes and is both laboratory and method specific. The data record is censored by the laboratory at the detection limit. The record may be censored again at a higher level called the practical quantitation limit or PQL, with observations between the detection limit and PQL recorded as a “trace.” Obviously the presence of NDs complicates data analysis, particularly when the fraction of NDs is large and/or when the detection limit changes over time. The fraction of NDs is frequently at or close to 100% for low-level constituents, such as volatile organic compounds in groundwater.

By far the most common method of dealing with NDs in data analysis is simply to substitute a numerical value for the ND. Usually this value is zero, the detection limit, or half the detection limit. Any of these simple substitution methods introduces some level of error into the analysis. Substituting the detection limit or half the detection limit is particularly problematic when the detection limit changes over time due to changes in analytical techniques or simply recalculation of the limit by the laboratory.

Finding observations as different as < 0.5 and < 50.0 within the same data record for the same constituent is not uncommon. Furthermore, all too common is to see higher (sometimes much higher) reporting limits (RLs) later in the record when analytical methods and sensitivity should be improving and detection limits decreasing. This is a strong indication that a data quality problem is associated with the laboratory, and the issue should be addressed as soon as the results are received. As Helsel (2012, pp. 86–87) notes, a very few high nondetects can greatly affect the results of data analysis, particularly when simple substitution is used, and nondetects that have higher RLs than any uncensored observation in the dataset have no useful information content and may be dropped from the dataset.

Many methods improve upon simple substitution for estimating population parameters. Because of the great significance of this issue in groundwater quality data analysis, the aforementioned RCRA guidance (EPA 2009, Chapter 15) devotes considerable attention to the issue and summarizes important findings from several researchers. The ultimate goal of RCRA monitoring is to detect changes in groundwater quality at regulated facilities. Therefore, the discussion in EPA (2009) primarily concerns the effects of alternative methods for handling nondetects on the results of statistical tests—prediction limits in particular. Much broader in scope is Helsel’s (2012) extremely thorough discussion of the problem in general and of the available methods for dealing with it (including statistical software applications).

For the present purpose of discussing statistical distributions, four approaches are mentioned in particular. The first is application of nonparametric methods when the censored values can be

assigned appropriate ranks. If multiple censoring levels or uncensored values are below the reporting limit, the data are postcensored at the highest reporting limit (Helsel 2012, p. 13).

The second is maximum likelihood estimation (MLE) techniques assuming a particular distribution such as normal or log-normal. An example is Cohen's table adjustment method for estimation of the mean and variance (Gilbert 1987, p. 182; EPA 2009, Chapter 15; Helsel 2012, p. 65) or the more versatile and accurate maximum likelihood methods afforded by statistical software (Helsel 2012, pp. 67–70). The statistical software approach easily accommodates multiple censoring levels (with uncensored values in between). Furthermore, this approach incorporates both detection limits and quantitation limits by coding separate intervals for nondetects and trace-level measurements. Helsel (2012, p. 65) notes that MLE approaches are generally appropriate only for sample sizes greater than 30 or 50 to 70 for skewed populations.

The third approach is regression on order statistics (ROS), which involves computing a linear regression equation relating the observed uncensored concentrations, or logs thereof, to their corresponding normal scores. This approach is described and recommended in EPA (2009, Chapter 15). Helsel (2012, pp. 79–86) discusses alternative ROS approaches and the supporting literature, stating that the method is appropriate for smaller sample sizes ($n < 30$) than is MLE.

A fourth alternative is the Kaplan Meier (KM) approach. Like ROS, EPA (2009, Chapter 15) describes and recommends this approach, and Helsel (2012, pp. 70–79) provides a thorough discussion and supporting literature.

Most approaches to dealing with censored data are either nonparametric or assume a normal or transformed normal distribution. An exception is the study by Thompson et al. (2000), mentioned previously in discussing the Weibull distribution. The authors explore several methods of estimating Weibull parameters from censored (nondetect) data for PAHs in sediment and oysters in a South Carolina estuary. The methods include simple substitution of half the detection limit, maximum likelihood, and regression of the linearized distribution function based on noncensored observations only. In tests on artificially censored simulated Weibull data, the latter two methods provide good agreement with the full dataset, while simple substitution provided large root mean squared errors in one of two simulated datasets used in the study.

10.10.1 Empirical Distribution Functions and Summary Statistics for ROS and KM

Both the ROS and KM approaches involve computing empirical (cumulative) distribution functions (edfs), using both censored and uncensored data. The KM approach computes conditional “survival probabilities” for each RL and uncensored observation, while the ROS approach computes plotting positions for each RL and then distributes the uncensored observations evenly below, between, and above the RLs as appropriate.

ROS can be accomplished in either fully parametric or “robust” forms (Helsel 2012, pp. 79–86). In the fully parametric form (also in Gilbert 1987, p. 181), the regression line itself is used to obtain estimates of the mean and standard deviation. The censored values are not used directly, but of course play a role in establishing plotting positions for the uncensored values. In the robust form, the regression line is used to impute values for censored measurements, and summary statistics are then computed using both uncensored observations and imputed values for censored observations. Thus, while the specified distribution is assumed for censored values, the goodness of fit of that distribution to uncensored values will not affect the results, hence the term “robust.” EPA (2009, pp. 15–15 to 15–20) includes a step-by-step procedure and a numerical example.

To obtain summary statistics via KM, Helsel (2012, pp. 73–76) presents nonparametric approaches using the KM edf. EPA (2009, pp. 15–9 to 15–13) includes a step-by-step procedure and numerical example for obtaining the KM edf and estimates of the mean and variance based on a normal distribution of the data or transformed data.

10.10.2 Quantiles and Boxplots Using Censored Data

Helsel (2012, pp. 126–136) discusses nonparametric confidence limits on the median and other quantiles for censored data, which are based on binomial probabilities and the KM approach. Another alternative for estimating distribution parameters and their confidence intervals is bootstrapping or repeated sampling from the observed data with replacement. Helsel (2012, pp. 136–140) discusses this approach, with particular attention to censored data.

The manner in which nondetects are handled can significantly affect the boxplot. If the highest reporting limit is less than the 25th percentile, the use of simple substitution would not affect the box but would affect the whiskers. Helsel (2012, pp. 44–46) recommends plotting the maximum RL as a horizontal line on the boxplot. Portions of the box above the limit are drawn with solid lines. Portions of the box below the limit may be blanked out or computed by KM or ROS and drawn with dashed lines.

Overall, many options are available for dealing with censored data in computing percentiles and other summary statistics, and no single accepted best approach exists. Helsel (2012, pp. 87–92) reviews 15 papers that compare alternative procedures, 14 of which use simulated data and one uses two levels of analytical procedures and real data. A set of detailed recommendations for specific circumstances is presented as well. Briefly, though, for 50% or fewer censored observations, either the KM or an imputation method like robust ROS, is recommended. Both KM and robust ROS are included in the ProUCL software package mentioned previously.

10.10.3 Avoidance of Censoring by Using All Measurements

In some cases, the problem of censored data can be avoided altogether by requiring the laboratory to provide both the actual measurement obtained (including negative values) and either the detection limit and/or an estimate of the precision (standard deviation) of the measurement (Porter et al. 1988). Then one would have the option of censoring or using all measurements without censoring and would be able to interpret individual observations in light of the measurement error. Helsel (2012, p. 33) notes that potential problems exist with reporting of all laboratory instrument readings without supplementary information about instrument error, citing a study by Antweiler and Taylor (2008), in which censored data techniques were compared with using all instrument readings in measurement of a series of trace-level constituent concentrations. Important to note is that this study used actual measurements—44 distinct datasets ranging in size from 34 to 841 samples—whereas most other comparisons, including 14 of those in the aforementioned review, are based on simulated data. The latter allows for more thorough and fully controlled comparisons.

Nevertheless, in the Antweiler and Taylor (2008) study the nonparametric KM technique was the best overall performer, followed by three “acceptable” techniques: robust ROS, substituting half the detection limit, and assigning a random number between zero and the detection limit. Somewhat surprisingly, use of laboratory-generated data below the detection limit was no better than the acceptable procedures. Maximum likelihood techniques performed poorly.

10.11 WATER QUALITY POPULATIONS OF INTEREST DEFINED

When we use a probability distribution, such as a normal distribution with a specified mean and variance, to model a particular water quality (or quantity) random variable, we are referring to a particular water quality population. In a rigorous sense, that population must consist of a defined and countable number of sampling units (such as 1 L samples of water). Clearly, most water quality monitoring programs do not fully define the population of interest.

Examples of complete definitions would be “the total mass of water that flows past a certain stream cross-section over a 10 year period” or “the total mass of water contained in a reservoir (or aquifer) at a particular point in time.” However, if we say simply that the population of interest is the water represented by a group of wells or several locations in a reservoir sampled over a 2 year period, defining a corresponding set of discrete sampling units is not possible. The latter case is almost universal in practice; thus, we rarely find good correspondence between applied probability distributions and real water quality populations. To repeat a statement made at the beginning of this chapter, we may spend a lot of time arguing about whether or not the data are normally distributed, when the far more important problem is to define the real population of interest and to ensure that the data adequately represent that population.

10.12 PROBABILITY SAMPLING

To obtain valid estimates of the parameters of a particular distribution, a probability sampling approach must be employed ([Gilbert 1987](#), pp. 20–23). From a valid probability sample, one can obtain unbiased estimates of the mean and/or other distribution parameters. The precision of those estimates is expressed by the corresponding standard error, from which, in turn, a confidence interval for the parameter of interest may be obtained.

As mentioned previously, the population of interest or target population must consist of a countable number of physical sampling units. Furthermore, the sampled population must be the same as the target population, and every sampling unit in the target/sampled population must have an equal (or at least known) probability of being sampled. Thus, the samples must be drawn at random, or there must at least be a random start followed by fixed-interval (systematic) sampling with additional requirements and concerns ([Gilbert 1987](#), Chapter 8).

Therefore, as just one example, obtaining valid estimates of long-term means of water quality at a given location is impossible from short-term monitoring because the target and sampled populations are not the same. Obviously, achieving these requirements for probability sampling and for obtaining valid estimates of population (distribution) parameters is frequently impossible. However, if these basic requirements and the limitations of not achieving them are carefully noted, then a great deal of confusion and unnecessary argument can be avoided, leading to more effective monitoring programs and more meaningful interpretation of data therefrom.

10.13 TIME SERIES AND STOCHASTIC PROCESSES

Let us now consider sampling at a single location of interest over time. For most water quality data records, the order and time of observations are important. Thus, the data from a particular location consist of a time series. Stochastic hydrologists often define a time series as a segment of a realization of a stochastic process ([Box and Jenkins 1976](#), p. 24). While useful for many purposes and essential for studying long-term patterns and behavior, this interpretation of time series has a few important consequences with regard to our discussion of distributions. First and foremost, valid probability sampling (according to our earlier definition) of a stochastic process is impossible because a stochastic process can have more than one realization, yet we can observe only one of those. Even if we believe that a given process is ergodic (representable by a single realization over a sufficiently long time period), that the target and sampled population would be the same in practical situations is highly unlikely. A “very long” record of a water quality process that is stationary (not changing in fundamental process parameters over time) could represent an exception, if such a thing exists.

In most instances, therefore, distinguishing between a probability sampling view of data analysis and a stochastic process view will be necessary. The two types of models are quite different, and the same terminology (for example the “mean”) can have quite different interpretations in each model type. This is not to say, however, that both types of models cannot be applied to the same (reasonably long) dataset—only that the data analyst should be clear about which type of model underlies a given conclusion. Such conclusions would include the statistical significance of trend or width of a confidence interval for the mean or median.

10.14 IMPORTANCE OF SERIAL CORRELATION

In general, both deterministic patterns, such as seasonality, and/or long-term trend and serial correlation or redundancy are present in water quality processes. We shall discuss seasonality and trend in subsequent sections and so focus here on serial correlation. Serial correlation appears in the form of random short-term trends or “runs” in a time series. What is classified as short or long term is arbitrary and will depend on the time scale of interest (Loftis et al. 1991). Essentially all water quality variables are serially correlated if sampled systematically on a short enough time interval. As automated, nearly continuous monitoring becomes more common, serial correlation becomes more of a concern, at least potentially.

When considering serial correlation in water quality data and appropriate distributions, distinguishing between probability sampling models and stochastic process models as discussed previously is critical. Characterizing serial correlation or redundancy in information from one observation to the next is at the heart of modeling stochastic processes, and so in the stochastic processes view of water quality, we know how to handle serial correlation. However, in random probability sampling, serial correlation has no meaning (with an exception noted in the later “aside”), because the samples have no particular order. We have no problem there either.

The in-between case of systematic (fixed-interval) sampling of a specified target population (e.g., monthly, weekly, or daily sampling over a given year of interest) is where things can get a bit confusing. In systematic probability sampling, obtaining valid estimates of the target population mean or other parameters is possible if one has or assumes a random start and the entire population is sampled; that is, the period of interest equals the period of sampling.

Systematic sampling is often more practical and is often better than random sampling. Obviously monthly sampling is more practical than collecting 12 random samples over the course of the year. And in general, systematic sampling is better than random sampling when patterns over time or space are present in the target population, both for mapping and for estimating population parameters. Those patterns may be either deterministic (seasonality or trend) or random (serial correlation). In fact, spatial correlation is the basis for contour mapping and any type of spatial interpolation, such as kriging. [As an aside, samples that are collected more or less at random over space or time can be indexed spatially and temporally as they are collected and then analyzed for temporal or spatial correlation using geostatistical approaches (semivariograms), which then facilitate interpolation with error estimates by the process of kriging. However, systematic sampling is better suited for this purpose.]

The main problem with systematic sampling lies in the difficulty of obtaining a valid standard error for the quantity being estimated when serial correlation is present. Gilbert (1987, Chapter 8) presents several methods (such as multiple systematic samples or Yates’ method) of doing this, and geostatistical approaches (kriging) may be useful as well. But this is not a simple task, and no simple, broadly applicable approaches exist. Remember that we are talking about target population parameters here, not stochastic process parameters.

10.14.1 Serial Correlation and Probability Sampling

However, in the case of probability sampling, the effect of serial correlation in a systematic sample is the same as that of sampling a significant fraction of the population. As the level of correlation increases, the effective fraction of the population sampled increases as well, and at some point we approach a complete census, where the standard error of the mean or other parameter of interest approaches zero. Thus we would obtain a nearly identical and perfect estimate of the parameter every time we sampled the same population at the same frequency.

10.14.2 Serial Correlation and Stochastic Processes

The effect of serial correlation on estimates of stochastic process parameters is just the opposite. Suppose that we are interested in the long-term mean of some water quality variable at a particular location but we have only a few years of monthly data. The long-term mean can be viewed as the mean of an (infinitely long) stochastic process that adequately models the time series of data that we have. The mean of the available time series is probably our best estimate of the process mean. It is also the best estimate of the population mean of continuous measurements of water quality at that location over the period of record. However, the period-of-record mean and the long-term process mean are not the same parameter. Consequently, the estimates of the two parameters have different standard errors even though the point estimates are the same. As noted previously, the standard error of the sample mean of the specific period will decrease with increasing serial correlation, while the standard error of the estimated process mean will increase with increasing serial correlation. Both of these are true because more serial correlation implies more information about the neighborhood of each observation and less information about the long term.

So specifying the type of model to apply in a given situation based on what type of information is needed, specific period or long term, is critical. And, again, for specific-period parameters, simply ignoring the effect of serial correlation is “safe” or “conservative” in the sense that the actual standard error will be smaller than that resulting from independent observations. (This might not be safe, of course, if the actual standard error would result in a different statistical conclusion, for example, a significant difference between two groups.) For long-term means, it is possible to correct for the effect of serial correlation using available formulas ([Gilbert 1987](#), pp. 38–40).

10.14.3 Trend and Serial Correlation

Most water quality monitoring programs are as much or more concerned with detecting and estimating trends as with estimating annual or seasonal means. And here again the interpretation depends on the time period of interest and the corresponding view of the target population from either probability sampling or stochastic process standpoints ([Loftis et al. 1991](#)). If the period of interest is the same as the period of monitoring, then a probability sampling view is appropriate, while if the period of interest is long term compared with the period of monitoring, then a stochastic process view is appropriate. The meaning of trend is different between the two views. In the stochastic process view, a trend is usually defined as a change in the underlying mean of the process, continuing into the future. In the probability sampling view, a trend usually means that a pattern exists of increasing or decreasing observations from earlier times to later times with no concern for what happens in the future. As discussed earlier, the distinction between serial correlation and trend is subjective in either view. Generally, long-term changes, or changes associated with a particular influence such as land use or climate change, would be regarded as trends, while short-term, apparently random, changes would be modeled as serial correlation.

However, the effect of serial correlation on the precision of estimates of model parameters, such as trend magnitude, is opposite in the two views. In the probability sampling view, little, if any, need exists to distinguish between serial correlation and trend. Both are simply patterns in the population, and as the density of sampling increases, the precision of the pattern description or associated

parameter estimates improves, and with continuous (well-calibrated) monitoring, the description is essentially perfect.

In the probability sampling view, if one computes, for example, a linear trend magnitude using linear regression (assuming the model is otherwise appropriate), then the computed *p*-value will be conservative (too large) in the presence of serial correlation. In this view, the *p*-value associated with a given set of *n* (equally spaced) observations is loosely interpreted as the probability of getting as large a slope as the computed one from a random set of *n* observations (same spacing and located in the same period of record) when the computed slope for a continuous record of the same period is actually zero. Of course, the best way to model trends in this view is probably not a straight line through the data. See Helsel and Hirsch (2002, pp. 285–292) for discussion of various smooths.

However, in the stochastic process view, only so much information about the underlying process can be obtained from any period of monitoring, and the more serial correlation is present, the less long-term information is present in short-term data. So, as in the case of estimating means in the stochastic process view, considering serial correlation is necessary when testing for trend or estimating trend magnitudes of stochastic processes as well. In this case, the *p*-value would be interpreted as the probability of getting as large a slope as the computed one from a randomly chosen set of *n* observations with the same spacing starting at any point in the process, not necessarily anywhere close to the period of record. In this case, the computed *p*-value will be too small, unless corrected for serial correlation (Hirsch and Slack 1984).

10.14.4 Automated Sampling, Nearly Continuous Monitoring

The aforementioned arguments and distinctions between the two views become most important with automated samplers producing high-frequency, nearly continuous records and very large sample sizes. In the probability sampling view, which requires that the entire target population is sampled, serial correlation can be “safely” (but perhaps not optimally) ignored. Estimates of population parameters will be better than computed precisions imply, and standard errors will approach zero as a complete census of the population is approached. When a complete census is achieved, a probability distribution model is not really needed because any desired frequency of a given event can be computed directly from the data.

In the stochastic process view, serial correlation must be considered as part of the model and accounted for or removed by averaging over large enough time periods so that the resulting averages are nearly independent. In many cases of course the choice of view is not clear cut, requiring creativity, multiple interpretations perhaps, and most certainly great care in explanation of assumptions underlying data analysis.

10.15 SEASONALITY AND FLOW EFFECTS

For most surface water quality random variables, the distribution varies with streamflow/runoff properties. Because the latter generally exhibit somewhat predictable seasonal patterns, water quality varies seasonally as well. For some variables, temperature or diurnal variation is important. Weekly cycles may be introduced by weekly patterns in human activity.

There are many approaches to characterizing seasonal and/or flow effects. The simplest approach is simply to divide the year into appropriate seasons or flow ranges and treat each season as a separate population. Of course, choosing the number of separate seasons and how to define them “appropriately” may be difficult, especially because the timing and magnitude of spring runoff, storm events, or other patterns may vary greatly from year to year.

Other approaches may involve building seasonality, flow, and other effects into models for the analysis of water quality time series. The current state of the art is represented by a method called

weighted regressions on time, discharge, and season (WRTDS) described in Hirsch et al. (2010). The approach is suitable for the analysis of long-term time series of surface water quality data and allows for “maximum flexibility in representations of long-term trend, seasonal components, and discharge-related components of the behavior of the water-quality variable of interest.”

The general form of the WRTDS equation follows:

$$\ln(c) = \beta_0 + \beta_1 t + \beta_2 \ln(Q) + \beta_3 \sin(2\pi t) + \beta_4 \cos(2\pi t) + \varepsilon \quad (10-7)$$

where

- \ln = natural log transform,
- β 's = fitted regression coefficients,
- c = concentration,
- Q = discharge,
- t = time in years, and
- ε = unexplained variation or noise.

The weighted regression approach allows the regression coefficients, and thus the concentration versus discharge relationship, seasonal patterns, and trend components, to vary over time. In the regression estimation of the coefficients, each actual observation is weighted according to distance from the point being estimated, and the distance has three components: time, season, and flow. Obviously, observations closer to the estimation point are more relevant and will therefore have larger weights.

The WRTDS method is now incorporated into a package called EGRET, Exploration and Graphics for RivEr Trends: An R-package for the analysis of long-term changes in water quality and streamflow. A user guide for EGRET is available at <http://pubs.usgs.gov/tm/04/a10/> (Hirsch and Di Cicco 2015).

10.16 MULTIVARIATE CHARACTERIZATION

Because water quality at a particular location in time and space is characterized by a large number of measurements—chemical, physical, and biological—reducing the number of dimensions using a multivariate approach is often desirable. The most common of these is principal component analysis (PCA). The details of PCA may be found in many texts. Manly (1994) provides a very readable introduction, while Johnson and Wischern (1998) provide more mathematical detail. In PCA, correlation among n variables is used to replace the original set of variables with a new set of n variables, each of which is a linear combination of the original set. The sum of variances of the original and new variables is the same, but the new variables are ordered such that the first has the largest variance, the next has the second largest variance, and so on.

Most commonly, the original variables are initially standardized by subtracting the mean and dividing by the standard deviation, so that all are dimensionless, the variance of each is one, and the sum of variances is n . Thus variables of different types, units, and orders of magnitude may be combined. If the original variables are normally distributed, the standardized variables will be standard normal deviates, Z . Each new variable is called a principal component (PC). The variance of each principal component is the corresponding eigenvalue of the correlation matrix. The coefficients of the standardized original variables in the linear combination that defines a given PC (called PC coefficients) are the elements of the corresponding eigenvector.

If the correlation among the original variables is strong, the first two (or at most three) PCs will contain much (more than 50%) of the variance of the original set, in which case a two- or

three-dimensional characterization of water quality may be possible. Because the magnitude of the PC coefficients defines the importance of each original variable in a given PC, relating each of the first two or three PCs for a given water quality dataset to a particular pollution source or natural driver of water quality is often possible.

Mapping of the first few principal components can be used both to establish a relationship of a principal component to a particular pollution source and to map the effect of a given source on water quality. For example, in a principal component analysis of water quality data from the Illinois River Watershed in Oklahoma (Olsen et al. 2012), the first two principal components were clearly related to land application of poultry waste and municipal waste treatment discharges, respectively. In PC1, the important variables were aluminum, arsenic, copper, *E-coli*, *Enterococcus*, fecal coliform, iron, potassium, nickel, total coliform, TOC, total phosphorus, and zinc. These variables are strongly associated with poultry feed or poultry waste. In PC2, the important variables were chloride, sodium, and sulfate, which are associated with wastewater treatment effluent.

The spatial patterns of the first two principal components were also aligned with the same association between PCs and contaminant sources. PC1 had the highest values immediately downstream of the greatest concentration of poultry houses, and the values decreased as one moved downstream. Because the largest coefficients in PC1 also corresponded with the constituents that are present in poultry waste, a clear relationship was established between PC1 and land application of poultry waste. A similar spatial pattern and relationship were found between PC2 and municipal waste treatment discharges.

The same paper discusses alternatives for data preparation prior to PCA, based on a literature review of 49 articles, many of which also relate principal components to specific pollution sources. Of particular interest here is the distribution of original variables, prior to PCA. The development of principal components does not require a multivariate normal distribution. However, nonnormality will affect the correlation matrix and distribution of the standardized variables. Johnson and Wischern (1998, p. 459) state that “inferences can be made from the sample components when the population is multivariate normal,” and Legendre and Legendre (1998) state that ensuring that the distributions are “reasonably unskewed” is important. In the Illinois River case study, all the 26 variables (chemical and bacterial) included in the PCA were right skewed, and a log transform resulted in “more normal” data based on visual inspection of probability plots. Therefore, the data were log transformed prior to PCA.

Many other multivariate methods are employed in water quality studies, including factor analysis (which is similar to and may begin with PCA), discriminant function analysis, multivariate ANOVA, and cluster analysis. Manly (1994) and Johnson and Wischern (1998) are good references for these methods, as well as for PCA. Helsel (2012, Chapter 13, pp. 269–296) discusses multivariate methods for censored data. Other than cluster analysis, all these methods depend on the correlation matrix and are thus affected by nonnormality of the data. Cluster analysis is most commonly based on Euclidian distance between observation vectors.

10.17 SUMMARY

For modeling chemical concentrations, the log-normal distribution is the most useful parametric option. Other transformations in addition to the log are sometimes used, and several other distributions may be appropriate, particularly discrete distributions for microbiological monitoring. The binomial distribution is necessary for setting water quality standards that are based on percentiles and for establishing permit monitoring requirements and compliance criteria that include an allowable number of exceedances in a given number of samples. The binomial distribution also forms the basis for nonparametric descriptions of the distribution in terms of percentiles. For most routine

applications, such descriptions are generally more appropriate than parametric distribution models. Interval estimates of quantiles and cumulative probabilities are needed to assess the adequacy of a given monitoring program or dataset to provide the needed precision in nonparametric characterization. Several alternatives for such estimates were presented or referenced.

One of the most important and challenging aspects of characterizing water quality distributions is the interpretation of censored or nondetect observations. The usual alternative of substituting half the detection limit has many shortcomings, especially when the detection limit changes over time and/or when a few large nondetect observations are present. Many options exist for interpreting censored observations, the most promising of which appear to be the Kaplan-Meier approach and robust regression on order statistics.

The problem of selecting an appropriate distribution for water quality data is generally less difficult and less important than the problem of carefully defining the population of interest. Two alternatives exist: probability sampling of a target population for the purpose of estimating population parameters and sampling to create a time series for estimating parameters of a stochastic process model. Either or both approaches may be appropriate, depending on the time scale of interest. However, the interpretation of model parameters, such as the mean, and the importance of serial correlation is very different between the two approaches. With a few exceptions, serial correlation can be ignored in probability sampling, but is, of course, the basis for stochastic process models.

Seasonality and flow effects are key drivers that determine water quality distributions. The simple alternative of partitioning observations into multiple subpopulations according to season or flow is often appropriate. However, for long records in particular, statistical models may be used to describe seasonal patterns, flow effects, and trend. The new modeling package called EGRET, being developed by USGS, provides a great deal of flexibility for incorporating these effects into a weighted regression approach that can be useful for interpreting changes in water quality over time.

Finally, because water quality is often described in terms of dozens of separate measurements of chemical, physical, and biological measurements, multivariate approaches are often used to reduce the number of variables and to investigate and map the overall impact of particular land use changes or contaminant sources. Of the available multivariate techniques, PCA has been most widely applied. An assumption of a multivariate normal distribution is not a requirement of PCA. However, because the correlation matrix is generally the starting point for PCA, nonnormality will affect the results of this and most other multivariate methods.

References

- Antweiler, R. C., and H. E. Taylor. 2008. "Evaluation of statistical treatments of left-censored environmental data using coincident uncensored data sets. I: Summary statistics." *Environ. Sci. Technol.* **42** (10): 3732–3738.
- Behera, P. K., J. Y. Li, and B. J. Adams. 2000. "Characterization of urban runoff quality: A Toronto case study." In *Applied modeling of urban water systems*, 225–248. Guelph, Canada: CHI Publications.
- Bhaumik, D. K., and R. D. Gibbons. 2006. "One-sided approximate prediction intervals for at least p of m observation from a gamma population at each of r locations." *Technometrics* **48** (1): 112–119.
- Box, G. E. P., and G. M. Jenkins. 1976. *Time series analysis, forecasting and control*. San Francisco: Holden-Day.
- Cameron, K. 2007. "Weibull prediction limits with retesting." In *Proc., Joint Statistical Meetings*, 2343–2349. Alexandria, VA: American Statistics Association.
- Çelo, V., D. Babi, B. Baraj, and A. Çullaj. 1999. "An assessment of heavy metal pollution in the sediments along the Albanian coast." *Water Air Soil Pollut.* **111** (1–4): 235–250.
- Conover, W. J. 1980. *Practical nonparametric statistics*. 2nd ed. New York: Wiley.
- Crohn, D. M., and M. V. Yates. 1997. "Interpreting negative virus results from highly treated water." *J. Environ. Eng.* **123** (5): 423–430.
- Dolgonosov, B. M., and K. A. Korchagin. 2014. "Seasonal variations of the distribution of water quality." *Water Resour.* **41** (1): 46–54.
- Gale, P. 1998. "Simulating cryptosporidium exposures in drinking water during an outbreak." *Water Sci. Technol.* **38** (12): 7–13.

- Gale, P., R. Pitchers, and P. Gray. 2002. "The effect of drinking water treatment on the spatial heterogeneity of micro-organisms: Implications for assessment of treatment efficiency and health risk." *Water Resour.* **36** (6): 1640–1648.
- Gilbert, R. O. 1987. *Statistical methods for environmental pollution monitoring*. New York: Wiley.
- Haas, C. N., and J. B. Rose. 1996. "Distribution of cryptosporidium Oocysts in a water supply." *Water Resour.* **30** (10): 2251–2254.
- Hahn, G. J., and W. Q. Meeker. 1991. *Statistical intervals: A guide for practitioners*. New York: Wiley.
- Helsel, D. R. 2012. *Statistics for censored environmental data using Minitab and R*. 2nd ed. New York: Wiley.
- Helsel, D. R., and R. M. Hirsch. 2002. "Statistical methods in water resources." Techniques of water resources investigations, Book 4, Chapter A3. Reston, VA: USGS. <https://water.usgs.gov/pubs/twri/twri4a3/>.
- Hirsch, R. J., and J. R. Slack. 1984. "A nonparametric trend test for seasonal data with serial dependence." *Water Resour. Res.* **18** (1): 107–121.
- Hirsch, R. M., and L. A. De Cicco. 2015. "User guide to exploration and graphics for RivEr trends (EGRET) and data retrieval: R packages for hydrologic data (version 2.0, February 2015)." Techniques and methods, Book 4, Chapter A10. Reston, VA: USGS.
- Hirsch, R. M., D. L. Moyer, and S. A. Archfield. 2010. "Weighted regressions on time, discharge, and season (WRTDS), with an application to Chesapeake Bay river inputs." *J. Am. Water Resour. Assoc.* **46** (5): 857–880.
- Iyer, H. 2000. *Class notes for statistics for environmental monitoring*. Fort Collins, CO: Colorado State Univ.
- Johnson, R. A., and D. W. Wischern. 1998. *Applied multivariate statistics*. 4th ed. Englewood Cliffs, NJ: Prentice Hall.
- Legendre, L., and P. Legendre. 1998. *Numerical ecology*, 853. 2nd ed. Dordrecht, Netherlands: Elsevier.
- Loftis, J. C., H. K. Iyer, and H. J. Baker. 1999. "Rethinking Poisson-based statistics for ground water quality monitoring." *Ground Water* **37** (2): 275–281.
- Loftis, J. C., G. B. McBride, and J. C. Ellis. 1991. "Considerations of scale in water quality monitoring and data analysis." *Water Resour. Bull.* **27** (2): 255–264.
- Manly, B. F. J. 1994. *Multivariate statistical methods: A primer*. 2nd ed. New York/Boca Raton, FL: Chapman and Hall/CRC.
- Masago, Y., Katayama, H., Hashimoto, A., Hirata, T., and Ohgaki, S. (2002). "Assessment of risk of infection due to cryptosporidium parvum in drinking water." *Water Sci. Technol.* **46** (11–12), 319–324.
- McBride, G. B. 2005. *Using statistical methods for water quality management*. New York: Wiley.
- Mujeriego, R., and K. Peters. 2008. "Process reliability and significance of reclaimed water quality parameters." *Water Sci. Technol.* **57** (5): 667–674.
- Nakano, T., J. Yasumoto, H. Terasawa, and N. Nawa. 2015. "Distribution and influent factors of nitrate concentration in groundwater." *Trans. Jpn. Soc. Irrig. Drain. Rural Eng.* **81** (4): 283–291.
- Northern Water. 2012. "Water quality monitoring program data retrieval." Accessed November 14, 2012. <http://www.northernwater.org/WaterQuality/WaterQualityData.aspx>.
- Nwaiwu, E. N., and A. Bitrus. 2005. "Fitting probability distributions to component water quality data from a treatment plant." *Global J. Environ. Sci.* **4** (2): 151–154.
- Olsen, R., R. Chappell, and J. Loftis. 2012. "Water quality sample collection, data treatment and results presentation for principal components analysis—Literature review and Illinois River Watershed case study." *Water Res.* **46** (9): 3110–3122.
- Petterson, A. N. J. 2001. "Viral risks associated with wastewater reuse: Modeling virus persistence on wastewater irrigated salad crops." *Water Sci. Technol.* **43** (12): 23–26.
- Porter, P. S., R. C. Ward, and H. F. Bell. 1988. "The detection limit." *Environ. Sci. Technol.* **22** (8): 856–861.
- Singh, A., and A. K. Singh. 2015. "Statistical software for environmental applications for data sets with and without non-detect observations." ProUCL version 5.1.00 technical guide, EPA/600/R-07/041. <https://www.epa.gov/land-research/proucl-software>.
- Thompson, R. E., E. O. Voit, and G. I. Scott. 2000. "Statistical modeling of sediment and oyster PAH contamination data collected at a South Carolina estuary (complete and left-censored samples)." *Environmetrics* **11** (1): 99–119.
- USEPA (US Environmental Protection Agency). 2009. *Statistical analysis of groundwater monitoring data at RCRA facilities, unified guidance*. EPA 530/R-09-007. Washington, DC: USEPA.
- Wackerly, D. D., W. Mendenhall, and R. L. Scheaffer. 2008. *Mathematical statistics with applications*. 7th ed. Belmont, CA: Thomson Brooks/Cole.

- Wang, P., C. Gao, Q. Yao, and X. Shen. 2007. "Characteristics of agricultural phosphorous losses with surface runoff under different land uses in hilly area around Taihu Lake." *J. Agro-Environ. Sci.* **26** (3): 826–830.
- Ward, R. C., J. C. Loftis, and G. B. McBride. 1986. "The data-rich but information poor syndrome in water quality monitoring." *Environ. Manage.* **10** (3): 291–297.
- Young, P. L., and S. J. Komisar. 1999. "The variability introduced by partial sample analysis to numbers of cryptosporidium Oocysts and Giardia cysts reported under the information collection rule." *Water Res.* **33** (11): 2660–2668.
- Zar, J. H. 1999. *Biostatistical analysis*. 4th ed. Englewood Cliffs, NJ: Prentice-Hall.

CHAPTER 11

Multivariate Frequency Distributions in Hydrology

Hemant Chowdhary, M.ASCE
Vijay P. Singh, Dist. M.ASCE

11.0 GENERAL

Hydrological variables are characterized by a significant stochastic component and therefore most hydrological planning strategies and designs are based on frequency analysis of the pertinent variables. Owing to the dominant role of single variables, these plans and designs are typically based on univariate frequency analysis. Being multidimensional in nature, a fuller description of hydrological processes is, however, given in terms of more than one variable. For example, knowing the intensity, duration, and/or areal coverage of a storm event together with the amount of precipitation itself may be important. Similarly, for a flood event, along with knowing the peak flow, its duration and/or volume may also be useful. Likewise, while severity is the main feature, the duration and/or areal extent of drought are important factors to be considered simultaneously. Water quality variables are normally considered one at a time when assessing the quality of water. Simultaneous consideration of two or more variables is, however, required for certain adverse impacts that different pollutants may collectively have on aquatic life and/or in impairing a water body for specific designated uses, for example, even though survival of fecal coliforms in seawater mainly depends on the presence of sunlight, intensity of solar radiation, temperature, salinity, and pH also significantly affect the dynamics of the survival rate. To develop better risk management strategies and emergency preparedness plans, simultaneous consideration of two or more hydrological variables may be beneficial in various situations. The realization that hydrological design and risk management procedures can benefit from the multivariate consideration of the processes involved is growing. Multivariate analyses provide a comprehensive view of the associated stochastic processes and render greater efficiency to hydrological design and management strategies.

Considerable research has addressed the hydrological frequency analyses of precipitation and flow variables owing to their dominant role in most hydrologic engineering designs. Flood frequency analysis is traditionally done by fitting univariate distributions to peak flows observed at the location of interest along a river or stream. The main objective of various drainage designs, for example, dam spillways or bridges, has been to estimate a flow that will have an average interarrival period larger than a specified design return period. Although such designs have been based on flood peaks, associated flood volume and duration constitute important hydraulic design factors in flood management programs and in analyzing the risk of damage due to floods. It is intuitive to expect that severity of damage to residential and commercial properties, crops, hydraulic infrastructure, rural or urban utilities, and traffic interruptions on highways due to flooding are all functions of the combined effects of peak flow, volume, and duration of a flood event. Thus, multivariate analysis,

rather than univariate analyses of only flow peaks, may be beneficial and can result in the improvement of management strategies and better assessment of potential risk ([De Michele et al. 2005](#), [Salvadori and De Michele 2004](#)).

In the past, bivariate and multivariate frequency analyses in hydrology have been done on a limited basis. These applications employed bivariate or trivariate normal, log-normal, exponential, Gumbel, and general extreme value distributions. Most of these studies involved multivariate normal distribution, which has elegant statistics and well-established inference procedures. In some instances, marginals were transformed to normal distribution before using multivariate normal distribution. However, at times, the constituent marginals may be non-Gaussian or may not necessarily result in multivariate normality even when they are normally distributed individually. Furthermore, individual processes may comprise different marginals that cannot be represented by the conventional bivariate or multivariate distributions, which require that the marginals have to be of the same type. The copula-based multivariate frequency analysis methods overcome this limitation and thus have greater potential for numerous hydrological applications. The copula-based multivariate frequency analysis is a fairly new approach, and its applicability and usefulness in the field of hydrology are being actively researched. This chapter presents multivariate hydrological frequency analysis, elaborating the copula approach, as employed for rainfall, flood, and drought processes. Section 11.1 below provides a brief review of application of multivariate distributions in hydrology. Section 11.2 presents the conventional distribution functions that have been traditionally used for the purpose. Section 11.3 elaborates the copula concept and the various types of copula models that are used in hydrology. Because various copulas are capable of characterizing a broad range of dependence, the selection of appropriate copulas for different hydrological applications becomes a nontrivial task. This section on bivariate copula fitting gives details of the procedures for selection and estimation of copula parameters. Section 11.4 illustrates the use of the copula method by presenting a few examples wherein potential copulas for multivariate extreme rainfall, flood, and regional flood management processes are identified.

11.1 MULTIVARIATE DISTRIBUTIONS IN HYDROLOGY

From time to time, some studies have emphasized the importance and usefulness of simultaneous consideration of dominant and associated variables. Most of these studies have involved various important features of storms or floods, such as storm depth, duration, average intensity, maximum intensity, time to peak, interarrival period, and number of storms in a specified period; flood volume, duration, and peak flow and time to peak flow; or drought severity and duration, among others. Studies involving storm characteristics have had different objectives, such as simulation of rainfall field, rainfall-runoff modeling, and derivation of frequency distributions for flood peak, urban storm volume, or annual precipitation. Similarly, studies with flow variables have been conducted for various purposes, such as checking the adequacy of dam spillway, floodplain zoning, risk assessment of levees and embankment, retention basin design, derivation of flood frequency distribution at a station downstream of a confluence, and improvement of the efficiency of parameter estimates of frequency distributions.

While most earlier studies consider independence among variables, many of the latter studies incorporate dependence features inherent among associated variables being analyzed simultaneously. A brief account of these studies done in the past, employing conventional and copula-based approaches, is presented here.

11.1.1 Hydrometeorological Applications

One of the earliest works on frequency distributions for rainfall variables is that of [Grace and Eagleson \(1966\)](#), which studied storm depth, storm duration, and interstorm time duration. [Todorovic and Yevjevich \(1969\)](#) investigate the probability distributions of precipitation intensities

considering six descriptors: (1) number of storms in a fixed interval of time, (2) number of storms producing a given amount of precipitation, (3) time elapsed between a reference time and the end of a storm, (4) total precipitation of a given number of storms, (5) precipitation of a particular storm from a sequence of storms, and (6) total precipitation in a specified time interval. While deriving the peak flood frequency distribution from climatic and catchment variables together with the functional relationships provided by the kinematic wave method of hydrograph forecasting, [Eagleson \(1972\)](#) fits univariate exponential distributions to storm intensity, depth, and duration. Although [Grace and Eagleson \(1966\)](#) consider storm depth and duration strongly correlated, [Eagleson \(1972\)](#) considers these two variables to be independent. [Carlson and Fox \(1976\)](#) adapt the derived flood frequency distribution (DFFD) model of [Eagleson \(1972\)](#) for a snowmelt–flood frequency model.

In another interesting study, [Eagleson \(1978\)](#) derives the distribution of annual precipitation from the joint distribution of storm interarrival time and storm depth. Even a few years of storm event data was noted as being sufficient for obtaining the distribution of annual precipitation and for having lesser variance as compared with one obtained using a long-term annual precipitation record. [Eagleson \(1978\)](#) also emphasizes the linkages of evapotranspiration with interstorm duration, start and end of infiltration process with storm duration, and infiltration and runoff with storm depths. The derived distribution technique of [Eagleson \(1972\)](#) was also employed by [Chan and Bras \(1979\)](#) for obtaining a probability distribution of urban storm volume above a specified threshold. [Cordova and Bras \(1981\)](#) employ this same technique to derive the probability distribution of the infiltration volume. Similarly, [Diaz-Granados et al. \(1984\)](#) use the same storm characteristics for deriving flood frequency distribution based on geomorphoclimatic instantaneous unit hydrograph (GcIUH) theory.

Contrary to the common perception of mutual independence among storm intensity and duration, [Cordova and Rodriguez-Iturbe \(1985\)](#), while obtaining the probabilistic structure of storm surface runoff, conclude that the correlation between the two variables has an important effect. The storm intensity and duration are considered bivariate exponentially distributed as per [Nagao and Kadoya's \(1971\)](#) proposed distribution. Significant correlation between storm intensity and duration, at higher soil moisture content, increases the probability of occurrence of storm surface runoff. [Bacchi et al \(1994\)](#) employ a bivariate exponential model, earlier proposed by [Gumbel \(1960a\)](#), for modeling extreme storm intensity for given durations. However, only one set of model parameters was obtained for each rainfall station by pooling the data of a few specific durations (1, 3, 6, 12, and 24 h), which was mentioned as one of the limitations of the study. In a study similar to that of [Cordova and Rodriguez-Iturbe \(1985\)](#), [Kurothe et al. \(1997\)](#) also employ the bivariate exponential model for rainfall intensity and duration, while deriving flood frequency distribution using GcIUH theory. This bivariate exponential distribution, proposed earlier by [Gumbel \(1960a\)](#) and applied later by [Bacchi et al. \(1994\)](#), admitted only negatively correlated random variables.

[Goel et al. \(2000\)](#) extend the work of [Kurothe et al. \(1997\)](#) on the DFFD model by employing the model proposed by [Nagao and Kadoya \(1971\)](#) that admitted both positive and negative correlation among rainfall intensity and duration. Extending the works of [Sackl and Bergmann \(1987\)](#) and [Goel et al. \(1998\)](#), [Yue \(1999\)](#) satisfactorily models daily peak storm intensity and storm volume from two rainfall stations from different climatic regions in Japan using bivariate normal distribution by first transforming the marginals to normality. In other studies, [Yue \(2000a, 2001a, 2002\)](#) employ bivariate mixed Gumbel, Gumbel logistic, and log–normal models, respectively, for the same two variables.

In all of these studies, either the same types of distributions had been assumed for the marginals, or they had been transformed to normal distributions. In hydrological literature, bivariate distribution with different marginals, as given by [Finch and Groblicki \(1984\)](#), was first applied by [Singh and Singh \(1991\)](#) for the weakly associated rainfall intensity and depth variables with product-moment correlation $|\rho| \leq 1/3$. For a wider range of dependency (with Spearman's correlation of $-7/12 \leq \rho_s \leq 1$), [Long and Krzysztofowicz \(1995\)](#) construct a newer family of bivariate probability density functions with specified marginals. The dependence structure serves as a density weighting function that describes the dependence within the Fréchet bounds and involves probability integral

transforms of the two variates. The ability to control the shape of bivariate density independently of the degree of association is cited as the advantage of the method. Furthering this work, Kelly and Krzysztofowicz (1997) construct a meta-Gaussian bivariate density involving the normal quantile transform (NQT) of the two variates that can belong to any arbitrary marginals and have any possible dependence. This work was among the first in bivariate frequency analysis that considered different marginal distributions with flexible covariance structures. In fact, Moran et al. (1970) propose such use of meta-Gaussian bivariate density much earlier, while designing experiments to ascertain if average rainfall in an area increases by cloud seeding. Herr and Krzysztofowicz (2005) also derive the bivariate distribution of point or areal precipitation amounts at two stations or areas using a meta-Gaussian distribution and demonstrate its application in real-time forecasting.

11.1.2 Hydrological Applications

Following the development of univariate functions for largest flood exceedances, Todorovic (1971) introduces another important feature of times of occurrence of extreme floods. This may be regarded as the beginning of the bivariate or multivariate consideration in the field of flood frequency analysis. Todorovic and Woolhiser (1972) highlight the significance of the time of occurrence of an extreme flood event during any year, linking it to the variable within-year flood damage function. Gupta et al. (1976) present a synthesis of the aforementioned approach, in which distributions of largest exceedances and the corresponding times of occurrences are obtained as marginals of their joint distribution, assuming the two variables are independent. The use of this methodology for two rivers in the United States demonstrated the applicability of the bivariate approach but did not show a significant improvement over the approach presented by Todorovic (1971) and applied by Todorovic and Woolhiser (1972). In further development and generalization of his and his coworkers' work, Todorovic (1978) highlights various properties of flood events, such as peak flow and corresponding duration and volume and times of occurrence of the peaks, arising from a partial duration series (PDS). Distributions of peak flood flow, its time of occurrence, and flood volume were derived on the basis of characteristics of these processes rather than by assuming any standard forms.

Ashkar and Rousselle (1982) utilize the multivariate nature of the flood process for deriving distributions of flood duration and flood volume for three river stations in Canada. Kavvas (1982) models the time of flood occurrence and peak flow using a two-dimensional nonhomogeneous stochastic trigger model by considering flood occurrences as primary events that trigger flood peaks at a secondary level. Using the principle of maximum entropy (POME), Krstanovic and Singh (1987) derive bivariate Gaussian and exponential distributions for flood peak and volume, with constraints specified in terms of variance, covariance, and cross-covariance. Consideration of flood volume and duration for flood risk assessment, in conjunction with the flood peak flow, was also advocated by Correia (1987). Providing a practical example, Sackl and Bergmann (1987) indicate the usefulness of a bivariate model of direct runoff flood peak and volume for the design of retention basins. They propose that the design volume could be obtained by modeling normalized flood peak and volume as a bivariate normal distribution. In an indirect approach, Rosbjerg (1987) obtains the frequency distribution of annual maximum flood from successive peak floods, employing the Marshall-Olkin bivariate exponential distribution (Marshall and Olkin 1967) that considered Poissonian occurrence times and admitted positive dependence only.

Haan and Wilson (1987) demonstrate applicability of the method of derived distributions for flood volume and flood peak using the Soil Conservation Service (SCS) and rational methods, respectively. It was opined that better estimates of design quantiles can be obtained by such a derived distribution method and establishing the viability of such an alternative procedure can also be important for its application for ungauged regions. In an interesting study Raynal-Villasenor and Salas (1987) employ logistic and mixed bivariate extreme value distributions, as given by Gumbel (1960b), for estimating parameters of the underlying extreme value marginals with better efficiency.

The approach was used for extending shorter extreme value data with the help of longer periods of other associated data. Further, the approach was applied for obtaining a flood frequency distribution downstream of a confluence, based on the flood information from two upstream stations in the form of a convolution equation given by Woodroffe (1975). Extending the work of Escalante and Raynal-Villasenor (1994) and Raynal-Villasenor and Salas (1987), Escalante and Raynal-Villasenor (1998) demonstrates the suitability of a multivariate extreme value distribution with mixed Gumbel marginals for modeling marginals in incomplete multivariate datasets from 42 gauging stations in northern Mexico.

Stating the importance of understanding flood events as a whole, Goel et al. (1998) study the bivariate distribution of normalized flood peak and volume data of a partial duration series for an Indian river also. For the risk assessment of levees and embankments, the US Army Corps of Engineers (USACE 1999) studied the conditional probability of failure function based on flood peak and duration. Adopting an approach similar to that taken by Goel et al. (1998), Yue et al. (1999) employ a bivariate Gumbel mixed model, originally proposed by Gumbel (1960b), for obtaining pairwise joint and conditional probabilities for flood peak, volume, and duration data from a Canadian river. Yue (2000b, 2001b) also applies the bivariate log-normal distribution and bivariate extreme value distribution for multivariate flood frequency analysis.

Overall, bivariate normal, log-normal, exponential, or Gumbel (called mixed Gumbel) distributions have typically been applied for hydrologic variables, such as flood peak, and associated volume and duration. Extensive efforts, spanning decades of research in the area of flood frequency analysis, have resulted in the identification of some plausible candidate distribution functions. The lack of multivariate distributions featuring marginals from different distributions restricts the ability to utilize and fit such suitable univariate distributions directly. Choulakian et al. (1990) note that such restriction makes migration from univariate to multivariate flood frequency analysis suboptimal. Another disadvantage of using conventional multivariate formulations is of association measure, directly or indirectly, linked to the Pearson linear correlation measure. The Pearson coefficient is not invariant to nonlinear monotonic transformations and depicts linear correlation rather than the functional association and may also not even be estimable in certain situations, involving heavy-tailed distributions (Genest and Favre 2007). The copula concept, which overcomes some of the restrictions posed by the conventional multivariate distributions, has been emerging as a new way of multivariate frequency distribution analysis.

Multivariate distribution modeling, through joint and conditional distributions, characterizing different dependence structures, is an active area of research (Kotz et al. 2000, Sarabia Alzaga and Go'mez De'niz 2011) encompassing various applications in hydrology and water resources, such as frequency analysis, streamflow or rainfall simulation, geostatistical interpolation, bias correction, and downscaling. Owing to the intuitive nature of its construction mechanism, the copula approach has been increasingly applied in recent years for hydrological applications, and its applicability and advantages are being studied in greater detail. Various dependence models in hydrology and water resources include topics such as frequency analysis (Favre et al. 2004, Salvadori and De Michele 2010, Hao and Singh 2013a), streamflow simulation or disaggregation (Hao and Singh 2013b, Li et al. 2013), drought characterization (Kao and Govindaraju 2010, Khedun et al. 2012, Hao et al. 2014, Hao and Singh 2015a), geostatistical interpolation (Bardossy and Li 2008), bias correction (Piani and Haerter 2012, Vogl et al. 2012, Mao et al. 2014), error or uncertainty analysis (Villarini et al. 2008, Chowdhary and Singh 2010, AghaKouchak et al. 2010a, b), downscaling (Laux et al. 2011, Van den Berg et al. 2011, Verhoest et al. 2015), and statistical forecasting (Khedun et al. 2014).

Extreme events involving joint occurrences, in particular, that lead to serious economic damage have attracted a lot of attention recently (Dutfoy et al. 2014, Davison and Huser 2015). The provision of copulas as viable alternative has resulted in heightened activity in formulating multivariate distributions to model the nonlinear dependence of hydroclimatic variables in a suite

of applications (Salvadori and De Michele 2007, Schoelzel and Friederichs 2008, Jaworski et al. 2010, Hao and Singh 2015b). These methods illustrate different ways of modeling dependence structures and have advantages and disadvantages. Chowdhary et al. (2011) outline the process of selecting suitable copulas to model the dependence structure, which is an important task and a continuing challenge. The following text about conventional and copula-based multivariate distribution methods will help the reader understand the important facets of these highly useful hydrologic analyses.

11.2 CONVENTIONAL MULTIVARIATE DISTRIBUTIONS USED IN HYDROLOGY

Traditionally, bivariate normal, log-normal, exponential, or Gumbel (called mixed Gumbel) distributions have been applied for hydrological variables, such as flood peaks and associated flood volume and duration. Alternatively, marginals are transformed to normal distributions, using the Box-Cox transformation or two-step power transformation, before using bivariate normal distribution for fitting the data. The random bivariate (X, Y) is used henceforth for bivariate frequency analysis. Multivariate distributions are also used, but on a very limited basis. The joint density functions of the bivariate distributions employed in hydrological studies are presented here in the following subsections.

11.2.1 Bivariate Normal Distribution

The joint probability density function (pdf) and cumulative distribution function (cdf) for a bivariate normal random vector (X, Y) are given by

$$f_{X,Y}(x, y) = \frac{1}{\sigma_X \sigma_Y} \phi_{BVN}(z_X, z_Y; \rho) \quad (11-1)$$

where $Z_X = \frac{X - \mu_X}{\sigma_X}$, $Z_Y = \frac{Y - \mu_Y}{\sigma_Y}$,
and

$$\phi_{BVN}(z_1, z_2; \rho) = \frac{1}{2\pi\sqrt{1-\rho^2}} \exp\left[-\frac{1}{2(1-\rho^2)}(z_1^2 - 2\rho z_1 z_2 + z_2^2)\right] \quad (11-2)$$

where

$-\infty < z_x, z_y < \infty$, $-1 < \rho < 1$, $\sigma_X, \sigma_Y > 0$, $-\infty < x, y < \infty$, and μ_X, μ_Y are real valued,

μ_X and σ_X \Rightarrow mean and standard deviation of X ,

μ_Y and σ_Y \Rightarrow mean and standard deviation of Y , and

ρ \Rightarrow the measure of linear association.

Pearson's linear coefficient of correlation is given by

$$\rho = \text{Corr}(X, Y) = \frac{\text{E}[(X - \mu_X)(Y - \mu_Y)]}{\sigma_X \sigma_Y} \quad (11-3)$$

The joint pdf for a bivariate normal random vector (X, Y) is given by

$$F_{X,Y}(x, y) = \Phi_{BVN}(z_X, z_Y; \rho) \quad (11-4)$$

with

$$\Phi_{\text{BVN}}(z_1, z_2; \rho) = \int_{-\infty}^{z_2} \int_{-\infty}^{z_1} \phi_{\text{BVN}}(r, s; \rho) dr ds \quad (11-5)$$

Figure 11-1 shows joint and marginal distribution characteristics of a bivariate normal distribution, $(X, Y) \sim \text{BVN}[(100, 50), (100, 40; 40, 25)]$, that is, having $\rho = 0.8$. The numbers within parentheses here are the means vector and the covariance matrix of the depicted bivariate normal distribution.

11.2.2 Bivariate Log-Normal Distribution

A bivariate log-normal density function can be obtained through the transformation of the aforementioned normal bivariate density function. Two positive variates $(W_1, W_2) \sim \text{BVLNOR}$ if $(\log W_1, \log W_2) = (X, Y) \sim \text{BVNOR}$. The joint distribution $f_{W_1, W_2}(w_1, w_2)$ can be written as

$$f_{W_1, W_2}(w_1, w_2) = \frac{1}{w_1 w_2 \sigma_X \sigma_Y} \phi_{\text{BVN}}\left(\frac{\log w_1 - \mu_X}{\sigma_X}, \frac{\log w_2 - \mu_Y}{\sigma_Y}; \rho\right), \quad w_1, w_2 > 0 \quad (11-6)$$

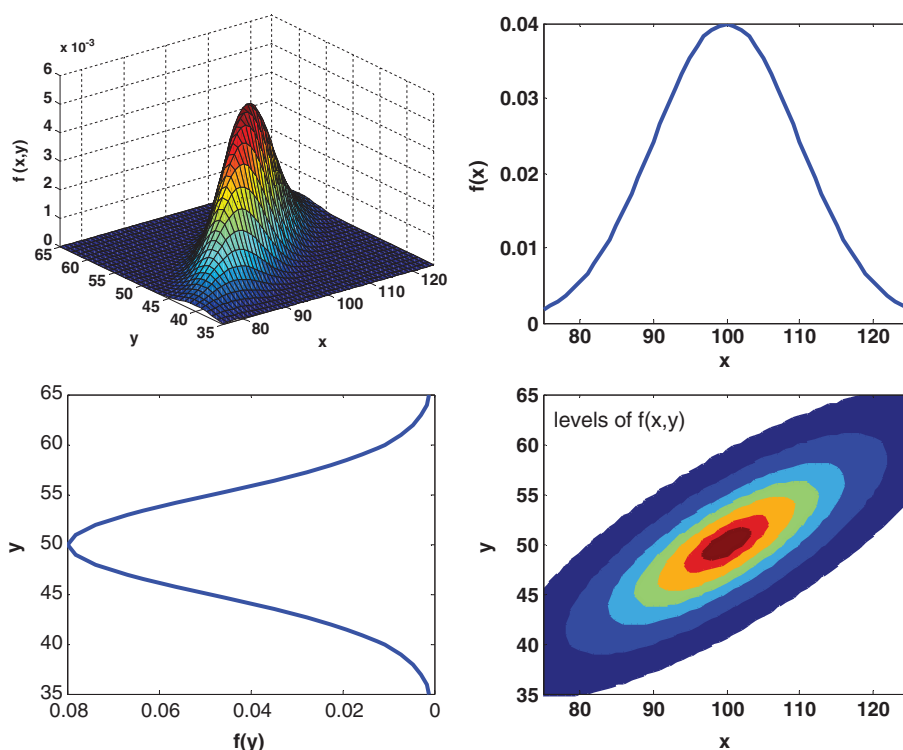


Figure 11-1. Joint and marginal distribution for a bivariate normal random vector.

The cdf $F_{U,V}(u, v)$ is given by

$$F_{U,V}(u, v) = \Phi_{\text{BVN}}\left(\frac{\log u - \mu_X}{\sigma_X}, \frac{\log v - \mu_Y}{\sigma_Y}; \rho\right), \quad u, v > 0 \quad (11-7)$$

This distribution is restricted for variates that can only take positive values. Here μ_X, σ_X are the mean and standard deviation of X . Similarly, μ_Y, σ_Y are the mean and standard deviation of Y .

11.2.3 Bivariate Exponential Distribution

The joint probability distribution function $F_{X,Y}(x, y)$ and the density function $f_{X,Y}(x, y)$ for a bivariate exponential random vector (X, Y) are given by

$$F_{X,Y}(x, y) = 1 - \exp\left(-\frac{x}{\eta_X}\right) - \exp\left(-\frac{y}{\eta_Y}\right) + \exp\left(-\frac{x}{\eta_X} - \frac{y}{\eta_Y} - \theta \frac{x}{\eta_X} \frac{y}{\eta_Y}\right) \quad (11-8)$$

and

$$f_{X,Y}(x, y) = \left[\left(\frac{1}{\eta_X} + \theta y \right) \left(\frac{1}{\eta_Y} + \theta x \right) - \theta \right] \exp\left(-\frac{x}{\eta_X} - \frac{y}{\eta_Y} - \theta \frac{x}{\eta_X} \frac{y}{\eta_Y}\right), \quad (11-9)$$

where $x, y \geq 0$, $\eta_X, \eta_Y \geq 0$, and $0 \leq \theta \leq \frac{1}{\eta_X \eta_Y}$.

The marginal densities and cdfs for X and Y are

$$f_X(x) = \frac{1}{\eta_X} \exp\left(-\frac{x}{\eta_X}\right) \text{ and } f_Y(y) = \frac{1}{\eta_Y} \exp\left(-\frac{y}{\eta_Y}\right) \quad (11-10)$$

and

$$F_X(x) = 1 - \exp\left(-\frac{x}{\eta_X}\right) \text{ and } F_Y(y) = 1 - \exp\left(-\frac{y}{\eta_Y}\right) \quad (11-11)$$

The domain of θ is obtained by observing that the joint probability evaluated at any (x, y) is always less than or equal to the corresponding marginal probability. That is,

$$\begin{aligned} F_{X,Y}(x, y) &= 1 - \exp\left(-\frac{x}{\eta_X}\right) - \exp\left(-\frac{y}{\eta_Y}\right) + \exp\left\{-\frac{x}{\eta_X} - \frac{y}{\eta_Y} - \theta \frac{x}{\eta_X} \frac{y}{\eta_Y}\right\} \\ &\leq F_X(x) = 1 - \exp\left(-\frac{x}{\eta_X}\right), \end{aligned} \quad (11-12)$$

which implies that

$$-\frac{x}{\eta_X} \left(1 + \theta \frac{y}{\eta_Y}\right) \leq 0 \quad \text{or} \quad \left(1 + \theta \frac{y}{\eta_Y}\right) \geq 0 \quad \text{or} \quad \theta \geq 0$$

because $0 \leq y < \infty$ and $\frac{1}{\eta_Y} > 0$.

And $f(x, y) \geq 0$ for $x, y \geq 0$ implies that

$$f_{X,Y}(0,0) = \left(\frac{1}{\eta_X} \frac{1}{\eta_Y} - \theta \right) \geq 0 \quad \text{or} \quad \theta \leq \frac{1}{\eta_X \eta_Y}$$

Thus, the range of possible values for θ is $0 \leq \theta \leq \frac{1}{\eta_X \eta_Y}$.
 X and Y are independent if and only if

$$F_{X,Y}(x,y) = F_X(x)F_Y(y) = \left[1 - \exp\left(-\frac{x}{\eta_X}\right) \right] \left[1 - \exp\left(-\frac{y}{\eta_Y}\right) \right] \quad (11-13)$$

This relationship is true if and only if $\theta = 0$. Consequently, a nonzero value of θ implies dependence between X and Y . Further, the correlation between X and Y is always negative and is bounded by 0 on the upper end (Gumbel 1960a). Figure 11-2 shows a probability density of a typical bivariate exponential distribution, $(X, Y) \sim \text{BVEXP}(\frac{1}{\eta_X} = 0.05, \frac{1}{\eta_Y} = 1.2, \theta = 0.06)$, given by the aforementioned joint distribution.

11.2.4 Bivariate Largest Extreme Value or Gumbel Distribution

The joint probability density function for a bivariate extreme value (or Gumbel) random vector (X, Y) is given by

$$F_{X,Y}(x,y) = F_X(x)F_Y(y) \exp\left[-\theta\left(\frac{1}{\ln F_X(x)} + \frac{1}{\ln F_Y(y)}\right)^{-1}\right], \quad 0 \leq \theta \leq 1 \quad (11-14)$$

where $-\infty < x, y < \infty$.

The marginals $F_X(x)$ and $F_Y(y)$ are Gumbel distributed, and the probability distribution and density function are, respectively, of the form

$$F_X(x) = \Phi_{\text{LEV}}\left(\frac{x - \gamma_X}{\alpha_X}\right) \quad (11-15)$$

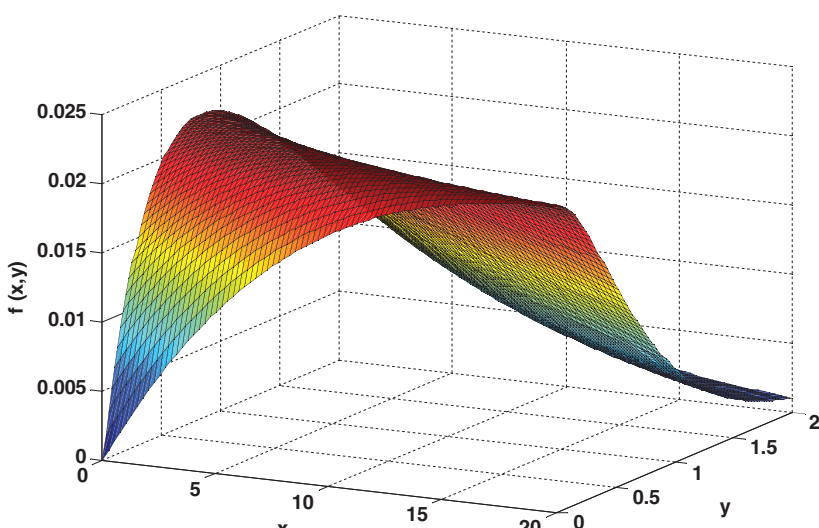


Figure 11-2. Example of a bivariate exponential pdf.

$$f_X(x) = \frac{1}{\sigma} \phi_{LEV} \left(\frac{x - \gamma_X}{\alpha_X} \right) \quad (11-16)$$

with

$$\begin{aligned}\Phi_{LEV}(z) &= \exp[-\exp(-z)] \\ \phi_{LEV}(z) &= \exp[-z - \exp(-z)]\end{aligned}$$

The parameter θ is related to the Pearson correlation coefficient ρ through the relationship

$$\theta = 2 \lfloor 1 - \cos(\pi\sqrt{\rho/6}) \rfloor \quad \text{for } 0 \leq \rho \leq 2/3$$

Note that the bivariate Gumbel distribution is defined only for random variables that are positively correlated with $0 \leq \rho \leq 2/3$. Double differentiation of the joint cdf in (11-14) yields the probability density function as

$$f_{X,Y}(x, y) = f_X(x)f_Y(y) \exp(-\theta A) \left[\left(1 - \frac{\theta A^2}{B_X^2} \right) \left(1 - \frac{\theta A^2}{B_Y^2} \right) - \frac{2\theta A^3}{(B_X B_Y)^2} \right] \quad (11-17)$$

where A , B , and C are given by

$$A = \left(\frac{1}{B_X} + \frac{1}{B_Y} \right)^{-1}; \quad B_X = \ln[F_X(x)]; \quad B_Y = \ln[F_Y(y)]$$

when $\theta = 0$, $F_{X,Y}(x, y) = F_X(x)F_Y(y)$ and $f_{X,Y}(x, y) = f_X(x)f_Y(y)$, which implies that X and Y are independent.

Figure 11-3 illustrates the characteristics of a bivariate Gumbel distribution for $\rho = 0.4$ (or $\theta = 0.623$), $\gamma_X = 100$, $\alpha_X = 5$, $\gamma_Y = 50$, and $\alpha_Y = 2$.

11.3 COPULA METHOD AND ITS USE IN HYDROLOGY

Copulas are functions that “couple” marginal probabilities or standard uniform probabilities to their joint probability distributions. Benefiting from the key invariance property of the copula $C_\theta(\mathbf{u})$, of a d -dimensional uniformly distributed random vector $\mathbf{U} = (U_1, U_2, \dots, U_d)$, the joint probability distribution function $F_{\mathbf{X}}(\mathbf{X})$ of arbitrarily distributed random variables $X_i \forall i = 1:d$ can be expressed through the inverse probability integral transformation $X_i = F_X^{-1}(U_i)$, in terms of its respective marginal probability distributions as $F_{\mathbf{X}}(\mathbf{X}) = C_\theta[F_{X_i}(X_i)]$. Here, θ is the association parameter vector that characterizes the dependence structure of \mathbf{U} or \mathbf{X} . Figure 11-4 shows this conceptualization of a copula, adapted from Favre et al. (2004). The parameters of copula-based distributions are related to the nonparametric dependence measures Spearman’s rho and Kendall’s tau, which represent functional association among the random variables under consideration. Several copula classes exist, and a multitude of families reside within each class. Although not every copula family is comprehensive enough to admit the whole range of dependence space, availability of many copula types provides the scope for representing any dependence structure through one or more alternatives. As copulas allow arbitrary marginals, including complex mixture distributions, generation of

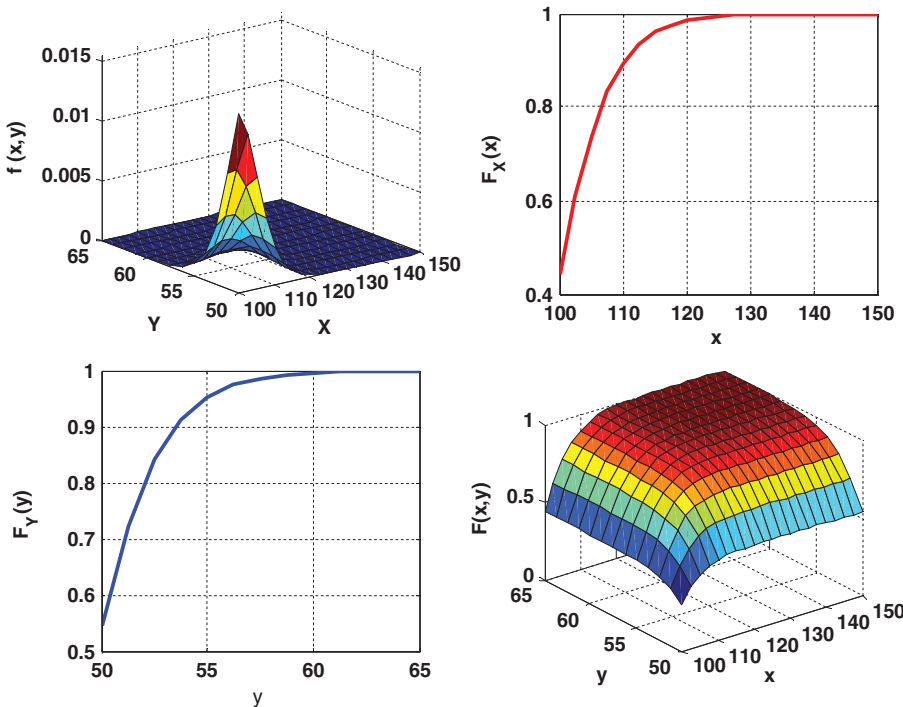


Figure 11-3. Example of a bivariate Gumbel distribution.

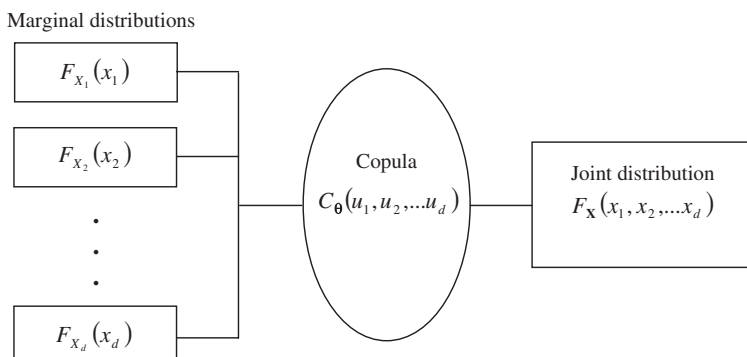


Figure 11-4. Schematization of copula concept.

any combination of associated random variables is a comparatively easier process. Thus, copulas overcome many of the limitations of conventional distributional forms and offer new possibilities for various multivariate hydrological applications that were hitherto restricted by the constraints of available distributions.

The copula theory has been in vogue for some time now, especially with respect to actuarial science and finance applications (Frees and Valdez 1998), but its application to hydrological engineering is recent (Genest and Favre 2007). Though many available copula families provide a wide choice of dependence structure, selecting appropriate copulas for different hydrological applications becomes a nontrivial task. Graphical and analytical statistical inference procedures for ascertaining the suitability of copula models are beginning to evolve and are being developed and

tested, and presently experience of their usage is limited. Overall, the topic of copula is still in the initial phase of development in general, its usage in hydrological engineering, in particular, is an area of active research.

11.3.1 Copula Concept

Unlike conventional multivariate frequency distributions, copula-based distributions are expressed in terms of the constituent marginal probabilities and more advantageously in terms of uniform marginals. Although the development and application potential of copulas is a topic of current research, it is rooted in the theorem due to [Sklar \(1959\)](#). According to this theorem, the joint distribution function of any randomly distributed pair (X, Y) may be written as

$$H(x, y) = C[F(x), G(y)], \quad x, y \in R \quad (11-18)$$

Here, $F(x)$ and $G(y)$ are marginal probability distributions and take $I = [0,1]$. $C: I \times I \rightarrow I$, a mapping function, is the “copula.” It also means that a valid probabilistic model for (X, Y) is obtained whenever the three constituents, C , F_X , and G_Y , are chosen from given parametric families, namely

$$F(x; \delta), \quad G(y; \eta), \quad C(u, v; \theta)$$

where

δ and η \Rightarrow parameter vectors of the marginal distributions,

θ \Rightarrow dependence parameter vector, and

u and v \Rightarrow quantiles of the uniformly distributed variables $U = F(X)$ and $V = G(Y)$, respectively.

A copula surface has an important property of being bounded by the Fréchet–Hoeffding bounds, corresponding to the perfect negative and positive dependence, respectively. The Fréchet–Hoeffding lower and upper bounds, usually denoted by $\check{W}(u, v)$ and $M(u, v)$, for every (u, v) , satisfy the inequality

$$\check{W}(u, v) \leq C(u, v) \leq M(u, v)$$

The product copula, denoted by $\Pi(u, v)$, is another important copula that corresponds to the independence between (u, v) and lies between the Fréchet–Hoeffding bounds. These three special copulas are given as

$$\check{W}(u, v) = \max(u + v - 1, 0), \quad M(u, v) = \min(u, v), \quad \text{and} \quad \Pi(u, v) = uv$$

The copula families that allow for the representation of a full range of dependence, from perfectly negative to perfectly positive, are termed comprehensive copulas. The range of dependence parameter θ in real-valued parameter bivariate copulas corresponds to the range of dependence it can represent. Figure 11-5 shows graphs of cdfs of these copulas in three-dimensional form and as level curves. The property of copula level curves to correspond to u or v values at their intersection with the upper axis or the right axis, respectively, allows omitting their labeling.

11.3.2 Copula Classes

Copula types are broadly categorized in four classes: Archimedean, extreme value, elliptical, and other miscellaneous class. Copulas can also be categorized as single-parameter or vector-parameter copulas, depending on the comprehensiveness with which the dependence structure is defined. Furthermore, for any copula, three more copulas can be derived by using simple relationships, and these are called associated copulas. [Joe \(1997\)](#) and [Nelsen \(2006\)](#) provide a theoretical background

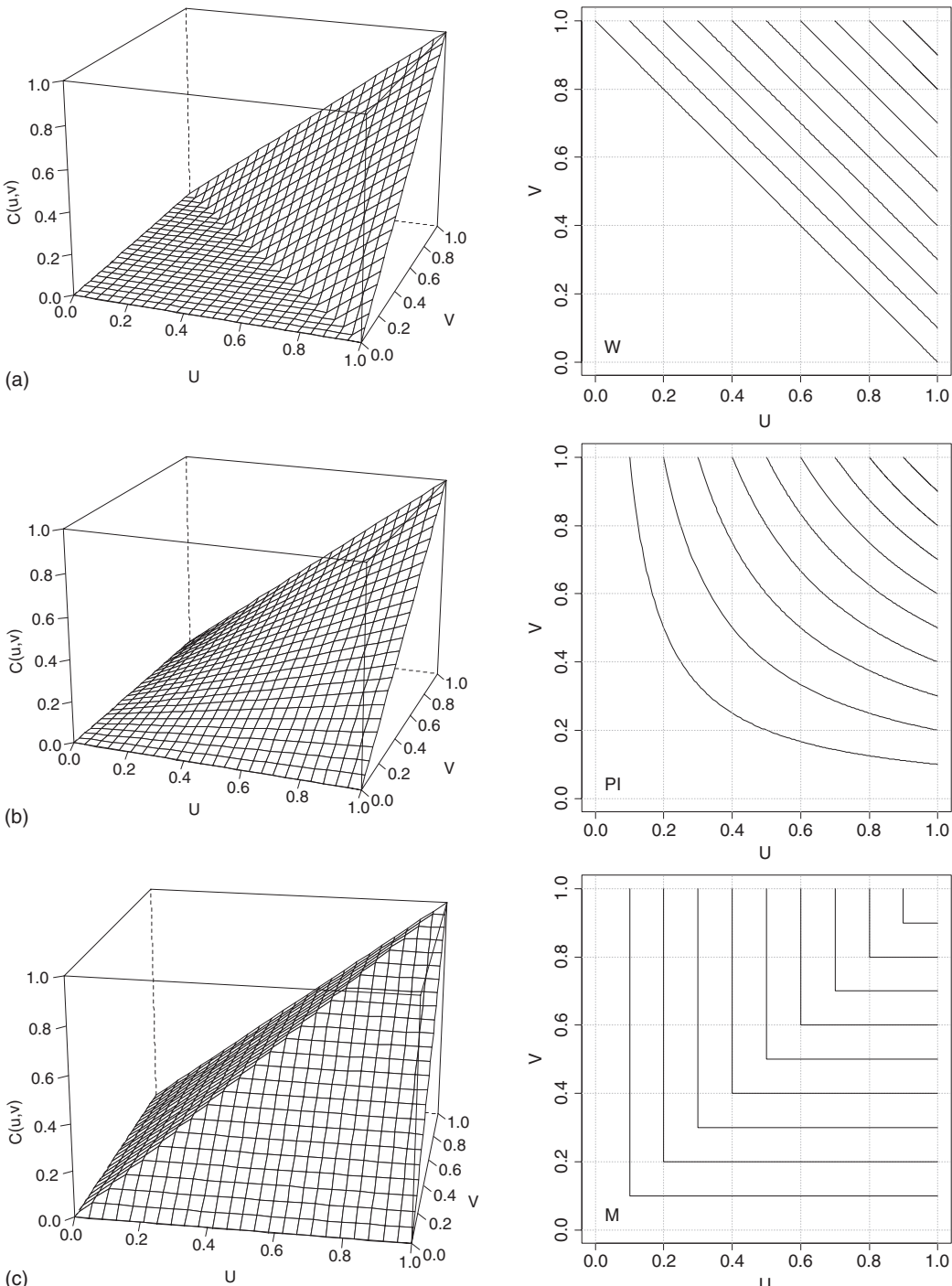


Figure 11-5. Cumulative distribution functions of (a) minimum \check{W} , (b) product \prod , and (c) maximum M copulas in three-dimensional form (left panel) and as level curves (right panel).

and properties of many copula types. [Salvadori et al. \(2007\)](#) is a useful reference for working on copula applications in the field of hydrology. [Genest and Favre's \(2007\)](#) overview of copula estimation and inference procedures provides details of several important aspects of copula

modeling, including the recently proposed goodness-of-fit tests. This chapter makes substantial use of these sources.

11.3.2.1 Archimedean Copulas

The Archimedean copulas have been widely employed owing to their easy construction, wider range, and various admissible dependence and several other nice properties (Nelsen 2006). Of the several copula families, the Archimedean family has also been frequently applied in the field of hydrology. This copula family has the form

$$\phi[C(u, v)] = \phi(u) + \phi(v)$$

where a continuous, strictly decreasing, and convex mapping function $\phi(t): I \rightarrow [0, \infty]$, with $\phi(1) = 0$, is called a generating function. This, in turn, satisfies the requirement of convexity of the cdf level curves and results in a valid copula. The copula probability is obtained as

$$C(u, v) = \phi^{[-1]}\{\phi(u) + \phi(v)\} \quad (11-19)$$

Here, function $\phi^{[-1]}(t): [0, \infty] \rightarrow I$ is the pseudo-inverse of the generating function. It is continuous and nonincreasing on $[0, \infty]$ and strictly decreasing on $[0, \phi(0)]$ and is given by

$$\phi^{[-1]}(t) = \begin{cases} \phi^{-1}(t) & \forall 0 \leq t \leq \phi(0) \\ 0 & \forall \phi(0) \leq t < \infty \end{cases} \quad (11-20)$$

The generator is termed “strict,” and the resulting copula is a strict copula when $\phi(0) = \infty$. The dependence parameter θ is hidden in the generating function $\phi(t)$, e.g., for the Frank copula, which has been employed for several hydrological applications, the generating function involves θ in the form

$$\phi(t) = -\ln\left(\frac{1 - e^{-\theta t}}{1 - e^{-\theta}}\right), \quad \theta \in (-\infty, \infty) \setminus \{0\}$$

The inverse of this strict generating function is given by

$$\phi^{-1}(t) = -\frac{1}{\theta} \ln[1 - (1 - e^{-\theta})e^{-t}]$$

Employing this generating function, its inverse, and the form of the Archimedean copulas given in Equation (11-19), the bivariate cdf $C_\theta(u, v)$ for the Frank copula is obtained as

$$C_\theta(u, v) = -\frac{1}{\theta} \ln\left[1 - \frac{(1 - e^{-\theta u})(1 - e^{-\theta v})}{1 - e^{-\theta}}\right] \quad (11-21)$$

Double differentiating this copula probability, the copula density is obtained as

$$c_\theta(u, v) = \frac{\partial^2 C_\theta(u, v)}{\partial u \partial v} = \frac{\theta e^{-\theta(u+v)}}{(1 - e^{-\theta})[\exp(-\theta C_\theta)]^2} \quad (11-22)$$

For Archimedean copulas, the joint probability function for the bivariate random variable (X, Y) in its original domain, using Equations (11-18) and (11-19), can be written as

$$H(x, y) = C_0(u, v) = C[F(x), G(y)] = \phi^{[-1]}\{\phi[F(x)] + \phi[G(y)]\} \quad (11-23)$$

The joint pdf for (X, Y) , taking $f(x)$ and $g(y)$ as marginal densities, can be obtained as

$$\begin{aligned} h(x, y) &= \frac{\partial^2 C_0(u, v)}{\partial u \partial v} \frac{\partial u}{\partial x} \frac{\partial v}{\partial y} = \frac{\partial^2 C_0(u, v)}{\partial u \partial v} \frac{\partial F(x)}{\partial x} \frac{\partial G(y)}{\partial y} \\ &= f(x)g(y) c_0(u, v) \end{aligned} \quad (11-24)$$

For the Frank copula, the joint cdf for (X, Y) , using Equations (11-21) and (11-23), is obtained as

$$H(x, y) = -\frac{1}{\theta} \ln \left[1 - \frac{(1 - e^{-\theta F_X(x)})(1 - e^{-\theta F_Y(y)})}{1 - e^{-\theta}} \right]$$

Similarly, its joint pdf, using Equations (11-22) and (11-24), is obtained as

$$h(x, y) = f(x)g(y) \frac{\theta e^{-\theta[F(x)+G(y)]}}{(1 - e^{-\theta})[\exp(-\theta C_0)]^2}$$

The Archimedean copula is a fairly large class, owing to easier evolution of newer copulas by coining valid generating functions as defined by Equation (11-19). Nelsen (2006) enumerates 22 single-parameter bivariate Archimedean copulas along with their generating functions, probability distribution functions, and admissible dependence ranges. Ali-Mikhail-Haq (AMH), Clayton, Frank, Genest-Ghoudi (GG), Gumbel-Barnett (GB), Gumbel-Hooggaard (GH), and Joe are some of the commonly used Archimedean copulas. Figure 11-6 illustrates GH, Frank, and Clayton copulas using 500 randomly generated pairs of (u, v) for three different dependence strengths, equivalent to Kendall's tau of 0.25, 0.50, and 0.75. These three values indicate increasing strength of association between u and v , which is apparent from the scatter plots. Perceiving the difference in the nature of the three copulas for low-dependence values such as 0.25 is graphically difficult. For higher values of Kendall's tau such as 0.50 and 0.75 the difference becomes increasingly apparent, and the scatter plots start depicting features that are specific to these copulas. Table 11-1 gives expressions for the generating function, copula probability, and parameter space for a few copula families.

11.3.2.2 Extreme Value Copulas

Extreme value copulas are suitable when associated random variables of interest are formed by component-wise maxima. A copula C_* is considered an extreme value copula if a copula C exists such that

$$C_*(u, v) = \lim_{n \rightarrow \infty} C^n(u^{1/n}, v^{1/n})$$

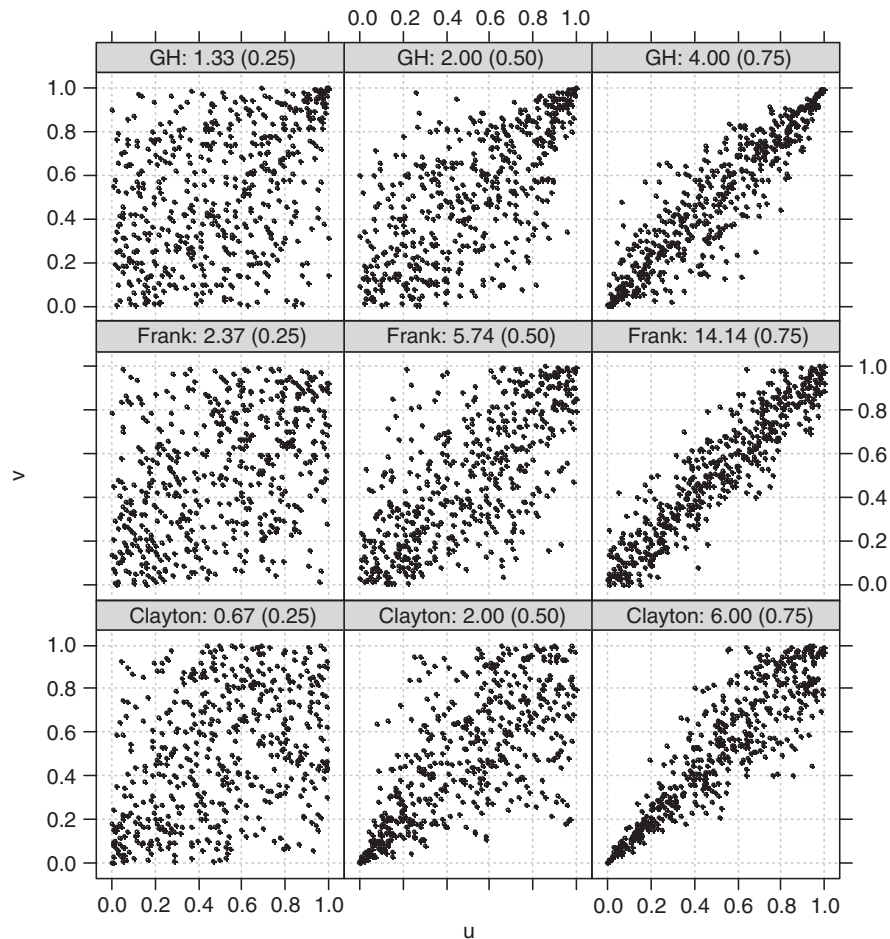


Figure 11-6. Illustration of GH, Frank, and Clayton copulas through 500 random bivariate (U, V) samples for increasing strengths of association. The left, middle, and right panels correspond to Kendall's tau τ values of 0.25, 0.50, and 0.75, respectively. The numbers following copula names are dependence parameter θ and corresponding τ values.

Table 11-1. Generating Function, Probability Function, and Parameter Space for a Few Copula Families. $\tilde{u} = -\ln u$ and $\tilde{v} = -\ln v$ Have Been Used in a Few Expressions.

Copula	Generator $\phi(t)$	$C_\theta(u,v)$	Parameter space
AMH	$\ln \frac{1-\theta(1-t)}{t}$	$\frac{uv}{1-\theta(1-u)(1-v)}$	$[-1, 1)$
Clayton	$\frac{1}{\theta}(t^{-\theta} - 1)$	$[\max(u^{-\theta} + v^{-\theta} - 1, 0)]^{-1/\theta}$	$[-1, \infty) \setminus \{0\}$
FGM	n.a.	$uv[1 + \theta(1-u)(1-v)]$	$[-1, 1]$
Frank	$-\ln \frac{e^{-\theta t} - 1}{e^{-\theta} - 1}$	$-\frac{1}{\theta} \ln [1 - \frac{(1-e^{-\theta u})(1-e^{-\theta v})}{(1-e^{-\theta})}]$	$(-\infty, \infty) \setminus \{0\}$
Galambos	n.a.	$uv \exp[(\tilde{u}^{-\theta} + \tilde{v}^{-\theta})^{-1/\theta}]$	$[0, \infty)$
GG	$(1 - t^{1/\theta})^\theta$	$\{\max(1 - [(1 - u^{1/\theta})^\theta + (1 - v^{1/\theta})^\theta]^{1/\theta}, 0)\}^\theta$	$[1, \infty)$
GB	$\ln(1 - \theta \ln t)$	$uv \exp(-\theta \ln u \ln v)$	$(0, 1]$
GH	$(-\ln t)^\theta$	$\exp[-(\tilde{u}^\theta + \tilde{v}^\theta)^{1/\theta}]$	$[1, \infty)$
Joe	$-\ln[1 - (1 - t)^\theta]$	$1 - [(1 - u)^\theta + (1 - v)^\theta - (1 - u)^\theta(1 - v)^\theta]^{1/\theta}$	$[1, \infty)$

Here C implies a copula representing a set of independent and identically distributed random variables $(X_i, Y_i); i = 1:n$, and C_* is the joint distribution of their component-wise maxima $X_{(n)}$ and $Y_{(n)}$. GH and Galambos and Husler-Reiss (HR) are commonly used extreme value copulas. Note that GH is also an Archimedean copula, besides being an extreme value copula. Table 11-1 gives expressions for the copula probability and parameter space for GH and Galambos copulas. The generating function is not applicable for the Galambos copula as it does not belong to the Archimedean copula class.

11.3.2.3 Meta-Elliptic Copulas

Elliptical copulas are elliptically contoured distributions, such as normal, Student-t, and Cauchy copulas. The marginals of these distributions are also from the same distribution families and elliptical in nature. When marginals of different types and possibly non-elliptic nature are used with multivariate elliptical copulas then they are termed meta-elliptical copulas. Denoting the inverse normal probability transform by Φ^{-1} and with $\theta \in [-1, 1]$, the bivariate Gaussian copula is given as

$$C(u, v) = \int_{-\infty}^{\Phi^{-1}(u)} \int_{-\infty}^{\Phi^{-1}(v)} \frac{1}{2\pi\sqrt{1-\theta^2}} \exp\left[-\frac{s^2 - 2\theta st + t^2}{2(1-\theta^2)}\right] ds dt \quad (11-25)$$

Similarly, the bivariate Student-t copula for $\nu > 2$ degrees of freedom, taking its probability transform as t_ν^{-1} and with $\theta \in [-1, 1]$, is given by

$$C(u, v) = \int_{-\infty}^{t_\nu^{-1}(u)} \int_{-\infty}^{t_\nu^{-1}(v)} \frac{1}{2\pi\sqrt{1-\theta^2}} \left[1 + \frac{s^2 - 2\theta st + t^2}{\nu(1-\theta^2)}\right]^{-(\nu+2)/2} ds dt \quad (11-26)$$

11.3.2.4 Miscellaneous Copulas

The Farlie–Gumbel–Morgenstern (FGM), Plackett, and Raftery copulas fall under the miscellaneous copula class. Table 11-1 gives the copula probability and parameter space for the FGM copula. The generating function is not applicable for FGM copulas, as it does not belong to the Archimedean copula class. The FGM copula is not comprehensive, as copulas of this family only have a dependence range of Kendall's tau of $-2/9 \leq \tau \leq 2/9$ or Spearman's rho of $-1/3 \leq \rho_s \leq 1/3$. The limited range of admissible dependence restricts the use of this family for hydrologic applications to only weakly associated variables. The Plackett family of copulas were proposed by [Plackett \(1965\)](#), based on the assumption of a constant cross-product ratio $\theta \geq 0$ for a given (u, v) as

$$\begin{aligned} \theta &= \frac{P[U \leq u, V \leq v]P[U > u, V > v]}{P[U > u, V \leq v]P[U \leq u, V > v]} \\ &= \frac{C(u, v)[1 - u - v + C(u, v)]}{[u - C(u, v)][v - C(u, v)]} \end{aligned} \quad (11-27)$$

Considering a contingency table with (u, v) as the point of demarcation, the numerator in this equality represents the product of probabilities of occurrence in the positive diagonal quadrants, whereas the denominator is the product of probabilities of occurrence in the negative diagonal quadrants. Thus, values of $\theta > 1$ indicate positive dependence, and values of $\theta < 1$ represent negative dependence. This is a comprehensive copula, as values of $\theta = 0$ and $\theta = \infty$ represent perfectly negative and positive dependence, respectively. A value of $\theta = 1$ indicates independence. The copula probability can be expressed explicitly by solving Equation (11-27) as

$$C(u, v) = \frac{1 + (\theta - 1)(u + v)}{2(\theta - 1)} - \frac{\sqrt{[1 + (\theta - 1)(u + v)]^2 - 4uv\theta(\theta - 1)}}{2(\theta - 1)} \quad (11-28)$$

11.3.2.5 Associated Copulas

Three more associated copulas can be derived for any copula family from any of the aforementioned copula classes (Michiels and Schepper 2008). These are obtained as

$$C'(u, v) = u - C(u, 1 - v) \quad (11-29a)$$

$$C''(u, v) = v - C(1 - u, v) \quad (11-29b)$$

$$\bar{C}(u, v) = u + v - 1 + C(1 - u, 1 - v) \quad (11-29c)$$

The first two transformations reverse the nature of dependence in positive and negative quadrants and can be employed for obtaining a positive quadrant dependent (PQD) copula from a negative quadrant dependent (NQD) copula and vice versa. The third copula is known as the survival copula, as it involves a joint distribution of $(1 - U, 1 - V)$ that appears related to the survival probabilities $\bar{F}(x) = P(X > x) = 1 - F(x)$ and $\bar{G}(y) = P(Y > y) = 1 - G(y)$, respectively. Such associated copulas greatly enhance the variety of available copulas.

Salvadori et al. (2007) provide definitions and construction of other copulas in the Archimedean, extreme value, meta-elliptical, and miscellaneous copula classes.

11.3.3 Dependence through Copulas

Pearson's correlation coefficient, which is invariably linked to the dependence parameter of the conventional multivariate distributions, is not invariant to nonlinear monotonic increasing transformations. In contrast, copulas bring out intervariable dependence among multivariate random variables and possess useful properties of invariance with respect to strictly monotonically increasing transformations.

11.3.3.1 Invariance Property of Copulas

Considering any monotonically increasing transformation of (X, Y) , such as $Z_1 = \xi(X)$ and $Z_2 = \psi(Y)$, and taking $H^*(z_1, z_2)$, $F_{Z_1}^*(z_1)$, and $G_{Z_2}^*(z_2)$ as the new joint and marginal distributions of the transformed variables (Z_1, Z_2) , the joint distribution in terms of an assumed copula C^* , using Equation (11-18), is given as

$$H^*(z_1, z_2) = C^*[F_{Z_1}^*(z_1), G_{Z_2}^*(z_2)], \quad z_1, z_2 \in R \quad (11-30)$$

Because the transformations are monotonically increasing, the marginals of the transformed variables can also be expressed as

$$F_{Z_1}^*(z_1) = P(Z_1 \leq z_1) = P[\xi(X) \leq z_1] = P[X \leq \xi^{-1}(z_1)] = F_X[\xi^{-1}(z_1)]$$

and similarly,

$$G_{Z_2}^*(z_2) = \Pr.(Z_2 \leq z_2) = P[\psi(Y) \leq z_2] = P[Y \leq \psi^{-1}(z_2)] = G_Y[\psi^{-1}(z_2)]$$

From first principles and using the copula definition given in Equation (11-18), the joint distribution of (Z_1, Z_2) may be obtained as

$$\begin{aligned} H^*(z_1, z_2) &= P[(Z_1 \leq z_1), (Z_2 \leq z_2)] = P\{[X \leq \xi^{-1}(z_1)], [Y \leq \psi^{-1}(z_2)]\} \\ &= H[\xi^{-1}(z_1), \psi^{-1}(z_2)] = C\{F_X[\xi^{-1}(z_1)], G_Y[\psi^{-1}(z_2)]\} \\ &= C[F_{Z_1}^*(z_1), G_{Z_2}^*(z_2)] \end{aligned} \quad (11-31)$$

Equations (11-30) and (11-31) show that $C = C^*$; in other words, the copula associated with random variables (X, Y) is invariant to any monotonically increasing transformation of the marginals. Further, because the copula characterizes the dependence between X and Y , a faithful graphical representation of dependence should exhibit the same invariance property. Among various possible statistics, the pair of ranks of the two variables, say (R_i, S_i) , is the statistic that retains the maximum amount of information. Rescaling by a factor of $1/(n+1)$ gives a set of points in the unit square $[0, 1]^2$, forming the domain of the “empirical copula” and formally defined as

$$C_n(u, v) = \frac{1}{n} \sum_{i=1}^n \mathbf{1}\left(\frac{R_i}{n+1} \leq u, \frac{S_i}{n+1} \leq v\right) \quad (11-32)$$

Here, $\mathbf{1}(A)$ denotes the indicator function of the (U, V) set. The random variables (U, V) can be considered just another monotonically increasing transformation of (X, Y) by their respective scaled rankings. In fact, this is also equivalent to transforming (X, Y) by their respective empirical probability integrals, say $F_n(X)$ and $G_n(Y)$, given as

$$U = \frac{\text{Rank}(X)}{n+1} = F_n(X), \quad V = \frac{\text{Rank}(Y)}{n+1} = G_n(Y) \quad (11-33)$$

11.3.3.2 Nonparametric Measures of Association

In view of the invariant property of the rank-based dependence structure, the two well-known nonparametric measures, namely Spearman’s rho and Kendall’s tau, are employed. Spearman’s rho is based on the correlation between pairs of ranks of the bivariate random vector (X, Y) . In that sense it is identical to Pearson’s product-moment correlation coefficient of ranks of (X, Y) . Considering (R, S) to be of length n , the sample version of Spearman’s rho, after algebraic simplification, is given by

$$\rho_s^n = \frac{\text{Cov}(R, S)}{\sqrt{\text{Var}(R)} \sqrt{\text{Var}(S)}} = \frac{12}{n(n+1)(n-1)} \sum_{i=1}^n R_i S_i - 3 \frac{n+1}{n-1} \quad (11-34)$$

Under the null hypothesis of independence, $H_0: C = \Pi$, ρ_s^n has a normal distribution with zero mean and variance $1/(n - 1)$. Thus, for the α significance level and with $z_{\alpha/2}$ as normal $\alpha/2$ quantile, $\sqrt{n-1}|\rho_s^n| > z_{\alpha/2}$ would indicate significant dependence. The population version of Spearman's rho, as $n \rightarrow \infty$, is given by

$$\begin{aligned}\rho_s &= 12 E \left[\frac{R_i}{(n+1)} \frac{S_i}{(n+1)} \right] - 3 = 12 E[u v] - 3 \\ &= 12 \int_{[0,1]^2} u v c_0 du dv - 3 \\ &= 12 \int u v dC(u, v) - 3 \\ &= 12 \int C_0(u, v) du dv - 3\end{aligned}\tag{11-35}$$

Any of the latter three equalities in Equation (11-35) provides a means of obtaining the relationship between the dependence parameter θ and the measure of association ρ_s .

Similarly, the association measure Kendall's tau is based on the notion of concordance and discordance among the pairs of random vectors (X, Y) . Two pairs (X_i, Y_i) and (X_j, Y_j) , for $i, j \in 1:n$, are concordant when $(X_i - X_j)(Y_i - Y_j) > 0$ and discordant when $(X_i - X_j)(Y_i - Y_j) < 0$. Considering P_n and Q_n as the number of concordant and discordant pairs of (X, Y) , the empirical version of Kendall's tau is the proportion of the difference of concordant and discordant pairs and is obtained as

$$\tau_n = \frac{P_n - Q_n}{\binom{n}{2}} = \frac{4}{n(n-1)} P_n - 1 = 4 \frac{n}{n-1} \bar{W}_n - \frac{n-3}{n-1}\tag{11-36}$$

Here $\bar{W}_n = \frac{1}{n} \sum_{i=1}^n W_i$ and W_i is the bivariate probability integral transform (BIPIT) variate given by

$$W_i = \frac{1}{n} \#\{j: X_j \leq X_i, Y_j \leq Y_i\} = C_n \left(\frac{R_i}{n+1}, \frac{S_i}{n+1} \right)\tag{11-37}$$

Under the null hypothesis of independence, $H_0: C = \Pi$, τ_n has a normal distribution with zero mean and variance $2(2n+5)/\{9n(n-1)\}$. Thus, for the α significance level, significant dependence is indicated when $\sqrt{9n(n-1)/\{2(2n+5)\}}|\tau_n| > z_{\alpha/2}$. The population version of Kendall's tau, as $n \rightarrow \infty$, is given by

$$\begin{aligned}\tau &= 4 E[W_i] - 1 \\ &= 4 \int C(u, v) dC(u, v) - 1 \\ &= 4 \int C_0 c_0 du dv - 1\end{aligned}\tag{11-38}$$

The latter two equalities provide relationships between dependence parameter θ and the measure of association τ . For Archimedean copulas, Genest and Mackay (1986), alternatively, show that

$$\tau = 1 + 4 \int \frac{\phi(t)}{\phi'(t)} dt \quad (11-39)$$

For some copulas these relationships are derivable in closed form, while a numerical solution could be obtained in other cases. Table 11-2 provides a few examples of closed-form solutions for relationships between the dependence parameter θ and Spearman's rho or Kendall's tau coefficients. Note that specific levels of association invariably correspond to a different dependence parameter θ for different copula types owing to the difference in their construction. For this reason, dependence parameter θ is not suitable for comparison of association level among different copulas.

11.3.3.3 Qualitative Assessment of Dependence

A qualitative graphical assessment and reaffirmation of the level of association can be done by plotting chi-plots and Kendall or K-plots as proposed by [Fisher and Switzer \(2001\)](#) and [Genest and Boies \(2003\)](#), respectively. Whereas chi-plots are akin to chi-square statistics for independence in a two-way contingency table, K-plots are similar to Quantile-Quantile or QQ-plots. Conceptually, a chi-plot is a scatter plot of the measure of distance between an observation and the center of all observations and the chi-square test statistic for independence in a two-way frequency table generated for the four regions delineated by the observation under consideration. Formally, this is a plot of (λ_i, χ_i) , where

$$\chi_i = \frac{H_i - F_i G_i}{\sqrt{F_i(1-F_i)G_i(1-G_i)}} \text{ and } \lambda_i = 4 \operatorname{sign}(\tilde{F}_i \tilde{G}_i) \max(\tilde{F}_i^2, \tilde{G}_i^2) \quad (11-40)$$

where $\tilde{F}_i = F_i - 1/2$, $\tilde{G}_i = G_i - 1/2 \forall i \in 1:n$ and

$$H_i = \frac{1}{n-1} \#\{j \neq i : X_j \leq X_i, Y_j \leq Y_i\} = \frac{nW_i - 1}{n-1}, \quad (11-41)$$

$$F_i = \frac{1}{n-1} \#\{j \neq i : X_j \leq X_i\}, \text{ and } G_i = \frac{1}{n-1} \#\{j \neq i : Y_j \leq Y_i\} \quad (11-42)$$

Table 11-2. Relationships between Dependence Parameter θ and the Nonparametric Association Measures, Kendall's Tau τ and Spearman's Rho ρ_s , for Six Copula Families.

Copula	Kendall's tau τ	Spearman's rho ρ_s
AMH	$\frac{3\theta-2}{3\theta} - \frac{2(1-\theta)^2}{3\theta^2} \ln(1-\theta)$	$\frac{12(1+\theta)}{\theta^2} \operatorname{dilog}(1-\theta) - \frac{24(1-\theta)}{\theta^2} \ln(1-\theta) - \frac{3(\theta+12)}{\theta}$
Clayton	$\theta/(\theta+2)$	Closed form n.a.
FGM	$2\theta/9$	$\theta/3$
Frank	$1 + \frac{4}{\theta} [D_1(\theta) - 1]$	$1 - \frac{12}{\theta} [D_2(-\theta) - D_1(-\theta)]$
Galambos	Closed form n.a.	Closed form n.a.
GH	$1 - 1/\theta$	Closed form n.a.
Plackett	Closed form n.a.	$\frac{(\theta+1)}{(\theta-1)} - \frac{2\theta}{(\theta-1)^2} \ln(\theta)$
Raftery	$2\theta/(3-\theta)$	$\theta(4-3\theta)/(2-\theta)^2$

The plot may also include control limits at ordinates of $\pm c_p / \sqrt{n}$. A scatter of the chi-plot predominantly within these control limits indicates independence among the variables and vice versa. Based on a simulation study, Fisher and Switzer (2001) provide values of $c_p = 1.54, 1.78$, and 2.18 corresponding to p-values of $0.90, 0.95$, and 0.99 , respectively. When the scatter is largely on the upper side of the control limit, it indicates a positive dependence, whereas when it is on the lower side of the limits, it indicates a negative dependence. The authors also recommend avoiding outliers by plotting only those points that satisfy

$$|\lambda_i| \leq 4 \left(\frac{1}{n-1} - \frac{1}{2} \right)^2$$

Figure 11-7 gives the chi-plots for the random samples from the GH, Frank, and Clayton copulas, considered in Section 11.3.2.1. Because these samples pertain to positive dependence, they

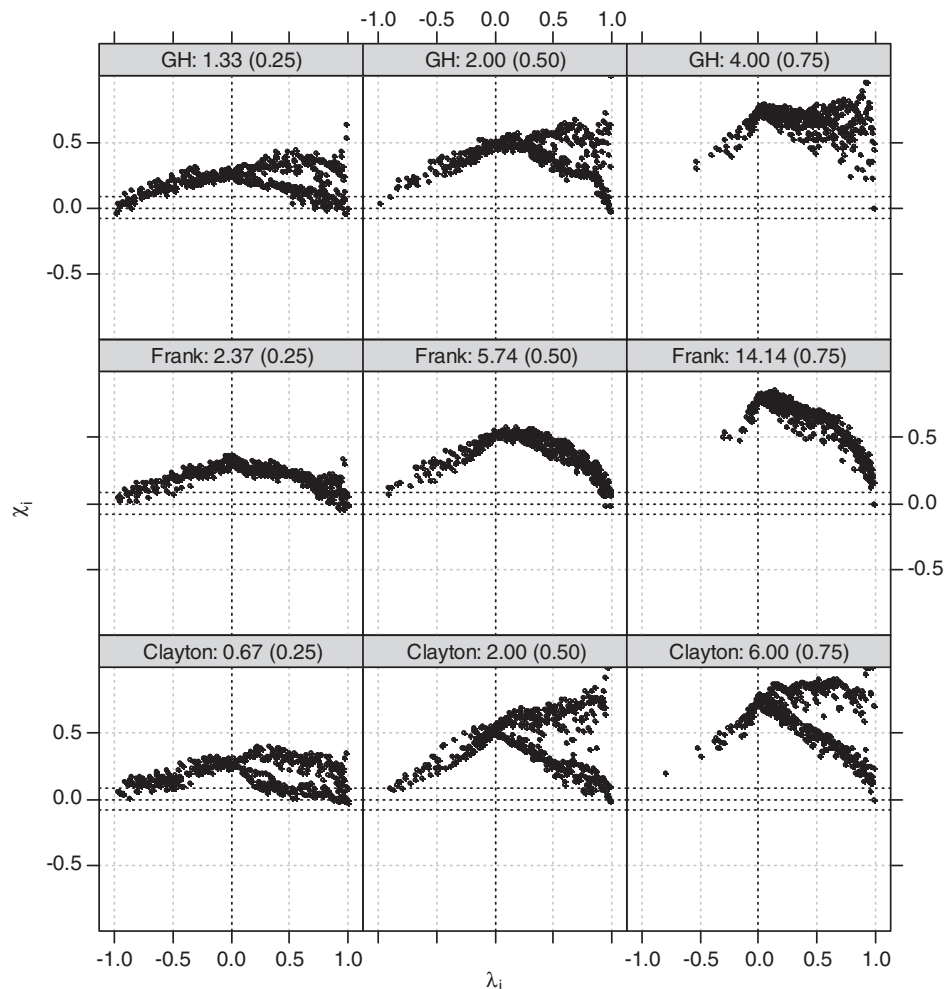


Figure 11-7. Chi-plots for random bivariate samples of (U, V) of size 500 from GH, Frank, and Clayton copulas for increasing strengths of association. The left, middle, and right panels correspond to Kendall's tau τ values of 0.25, 0.50, and 0.75, respectively. The numbers following copula names are dependence parameter θ and corresponding τ values.

all appear on the upper half of the chi-plots and plot increasingly farther from $\chi_i = 0$ for Kendall's tau equal to 0.25, 0.50, and 0.75, respectively. Two distinct groupings of points on the right side are apparent for the GH and Clayton copulas, and these characterize differences in upper- and lower-tail dependence features of these copulas. This is elaborated in the next section.

K-plots, however, are scatter plots of observed and expected order statistics of the BIPIT variable $W = H(X, Y) = C(U, V)$ of the same size, under the null hypothesis of independence between its components X and Y or U and V . Formally, Genest and Boies (2003) suggest plotting the pairs $(W_{i:n}, H_{(i)})$ for $i \in 1:n$, where

$$H_{(1)} < H_{(2)} < \dots < H_{(n)}$$

are the order statistics associated with H_i defined for the chi-plot in Equation (11-40). $W_{i:n}$ is the expected value of the i^{th} statistic of the variable W from a random sample of size n under the assumption of independence between X and Y or U and V . Assuming the cdf and pdf of W to be $K_0(w)$ and $k_0(w)$ under the assumption of independence, the pdf of its i^{th} order statistic, say $f_{w_{(i)}}(w_{(i)})$, is given as

$$f_{w_{(i)}}(w_{(i)}) = n \binom{n-1}{i-1} k_0(w) K_0(w)^{i-1} [1 - K_0(w)]^{n-i}$$

The expected value of $w_{(i)}$, as reported by Genest and Favre (2007), is given as

$$E[w_{(i)}] = W_{i:n} = n \binom{n-1}{i-1} \int_0^1 w k_0(w) K_0(w)^{i-1} [1 - K_0(w)]^{n-i} dw \quad (11-43)$$

where

$$\begin{aligned} K_0(w) &= P[UV \leq w] = \int_0^1 P\left[U \leq \frac{w}{v}\right] dv \\ &= \int_0^w 1 dv + \int_w^1 \frac{w}{v} dv = w - w \log(w) \end{aligned}$$

and

$$k_0(w) = -\log(w)$$

The diagonal line $H_{(i)} = W_{1:n}$ on the K-plot indicates independence, whereas the curve given by $K_0(w) = w - w \log(w)$ corresponds to a perfect positive dependence. In case of a perfect negative dependence, all the points would lie on the x -axis as all $H_i = 0$. Figure 11-8 gives K-plots for the random samples from the GH, Frank, and Clayton copulas, considered in Section 11.3.2.1. Because these samples pertain to positive dependence, they all plot on the left side of the diagonal line and are increasingly closer to the perfect positive dependence curve for the three cases of Kendall's tau equal to 0.25, 0.50, and 0.75, respectively.

11.3.3.4 Tail Dependence Characteristics

The nonparametric association measures, Spearman's rho and Kendall's tau, provide an idea of the overall dependence, considering all regions of the domain I. However, such generalized measures fail

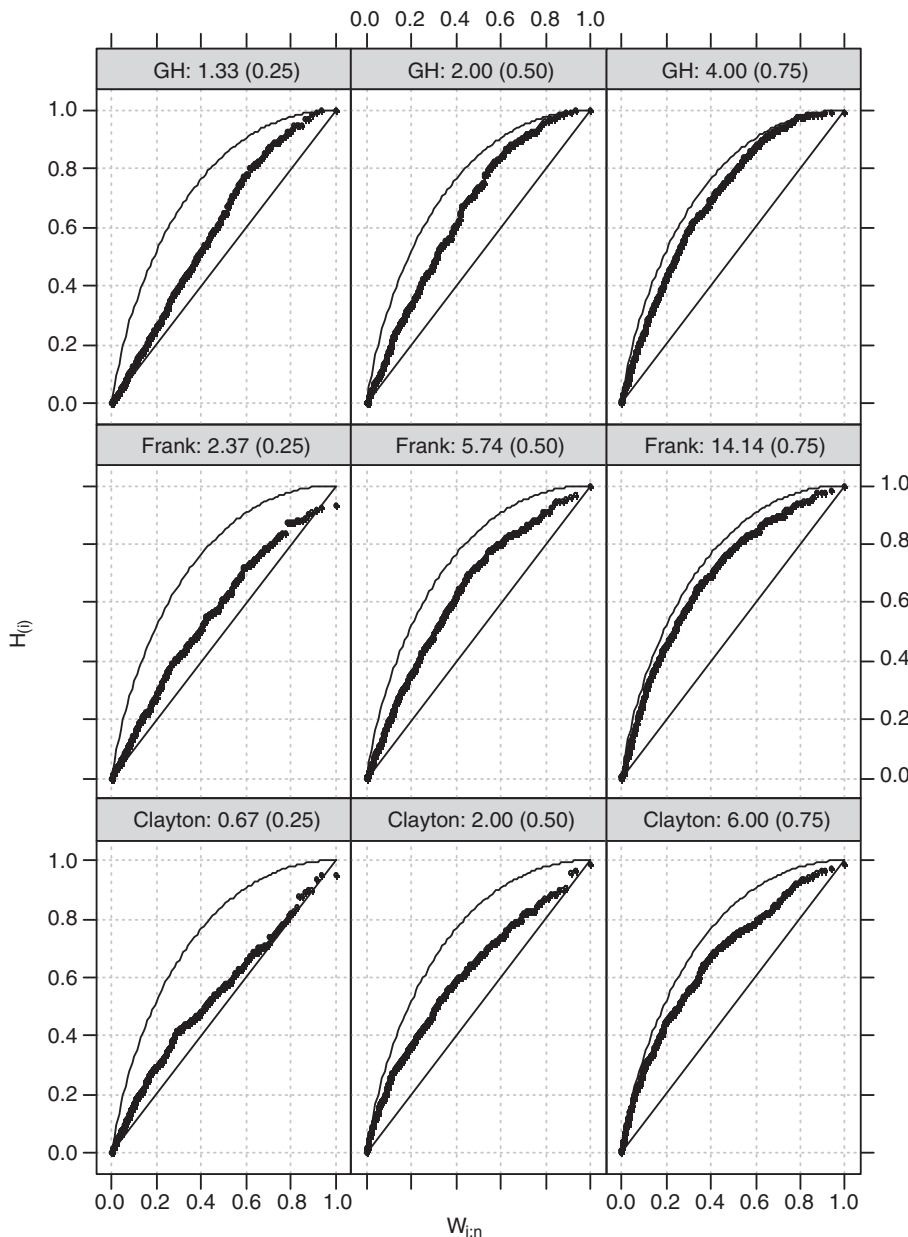


Figure 11-8. K-plots for random bivariate samples of (U, V) of size 500 from GH, Frank, and Clayton copulas for increasing strengths of association. The left, middle, and right panels correspond to Kendall's tau τ values of 0.25, 0.50, and 0.75, respectively. The numbers following copula names are dependence parameter θ and corresponding τ values.

to differentiate among varying dependence strengths in different regions of the domain. Information on the dependence strength in the tails, upper right and lower left, may be important from the perspective of modeling of extremes. For this, the dependence in the upper-right and lower-left quadrants of I, denoted by upper-tail dependence λ_U and lower-tail dependence λ_L , are quantified. Conceptually, tail dependence quantifies the probability of a variable attaining an extreme value

given that the other variable occurred with an extreme value. Formally, the upper-tail dependence is defined as the conditional probability that Y is greater than or equal to the 100t-th percentile of F_Y given that X is greater than the 100t-th percentile of F_X as t approaches 1 ([Nelsen 2006](#)). This can be expressed and obtained in terms of copula probability as

$$\begin{aligned}\lambda_U &= \lim_{t \rightarrow 1^-} P[Y > F_Y^{-1}(t) | X > F_X^{-1}(t)] = \lim_{t \rightarrow 1^-} P[F_Y(Y) > t | F_X(X) > t] \\ &= \lim_{t \rightarrow 1^-} P[V > t | U > t] = \lim_{t \rightarrow 1^-} \frac{P[V > t, U > t]}{P[U > t]} \\ &= \lim_{t \rightarrow 1^-} \frac{1 - 2t + C(t, t)}{1 - t} = 2 - \lim_{t \rightarrow 1^-} \frac{1 - C(t, t)}{1 - t}\end{aligned}\quad (11-44)$$

The lower-tail dependence λ_L is defined analogously and is given as

$$\begin{aligned}\lambda_L &= \lim_{t \rightarrow 0^+} P[Y \leq F_Y^{-1}(t) | X \leq F_X^{-1}(t)] = \lim_{t \rightarrow 0^+} P[F_Y(Y) \leq t | F_X(X) \leq t] \\ &= \lim_{t \rightarrow 0^+} P[V \leq t | U \leq t] = \lim_{t \rightarrow 0^+} \frac{P[V \leq t, U \leq t]}{P[U \leq t]} \\ &= \lim_{t \rightarrow 0^+} \frac{C(t, t)}{t}\end{aligned}\quad (11-45)$$

These expressions are evaluated when the limits exist, providing values of upper- and lower-tail dependences. [Nelsen \(2006\)](#) and [Salvadori et al. \(2007\)](#) provide expressions of tail dependence for most of the available copula types. Table 11-3 gives these values for some of the copulas.

[Abberger \(2005\)](#) indicates that the significance of tail dependence can also be qualitatively established by employing chi-plots. For this, only those (λ_i, χ_i) pairs that come from either the upper-right or the lower-left quadrant are plotted. Figures 11-9 and 11-10 illustrate such chi-plots for upper and lower tails for the random samples from three copulas considered in Section 11.3.2.1. A falling trend leading to extreme points within the control limit indicates insignificant tail dependence. Such is the case for the upper tail for the Clayton copula and for both lower and upper tails for the Frank copula. For the lower tail of the Clayton copula and both lower and upper tails of the GH copula, a significant tail dependence is apparent. The significant tail dependence is also stronger for the increasing value of Kendall's tau and is indicated by higher χ_i values in the extreme region near $\lambda_i = 1$.

11.3.4 Parameter Estimation Methods

The copula dependence parameters can be estimated using methods such as (1) moment-like method (MOM), based on inversion of nonparametric dependence measures; (2) canonical or maximum pseudo-likelihood (MPL) method; and (3) exact maximum likelihood (EML) method. The first two methods completely rely on the relative ranks of joint variates and thus render the determination of dependence structure completely independent of the choice of marginals. These three methods are outlined as follows.

11.3.4.1 Moment-Like Method Based on Inversion of Dependence Measures

This approach is based on the assumption that bivariate dependence structure is fully defined by the relative ranks of the constituent variables. The nonparametric estimates of θ based on Spearman's rho ρ_s or Kendall's tau τ , are obtained from Equations (11-35) or (11-36). For some

Table 11-3. Copula Test Space Based on Admissible Dependence Range and Tail Dependence Characteristics. The Shaded Cells Imply Admissibility of Corresponding Dependence Range.

Copula family/copula	Admissible dependence range in terms of Kendall's Tau		Tail dependence coefficients	
	λ_L	λ_U	λ_L	λ_U
Archimedean				
AMH	0	(0.3333, 1]	0	0
Clayton	0.3333	(0.2222, 0.3333)	$2^{-1/\theta}$	0
Frank	0.2222	(0, 0.2222]	0	0
GG	0	(-0.1817, 0)	0	$2 - 2^{1/\theta}$
Joe	-0.2222	[-0.2222, -0.1817)	0	$2 - 2^{1/\theta}$
Extreme Value				
GH	-0.3613	(-0.3613, -0.3333)	0	0
Galambos	-0.4674	(-0.4674, -0.3613)	0	$2^{-1/\theta}$
Meta-Elliptical				
Normal	-0.5649	(-0.5649, -0.4674)	0	0
Miscellaneous				
FGM	-1	(-1, -0.6109)	0	0
Plackett	-0.6109		0	0

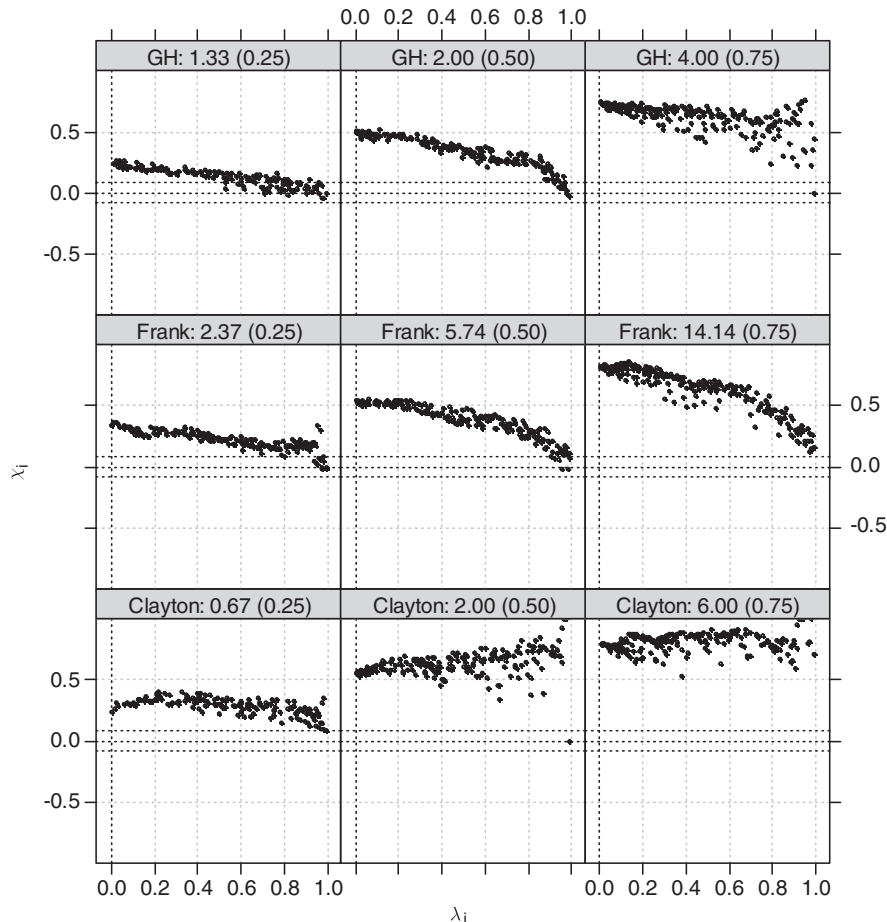


Figure 11-9. Upper-tail characteristics depicted by chi-plots for only the upper-right quadrant samples of the random bivariate samples of size 500 from GH, Frank, and Clayton copulas for increasing strengths of association. The left, middle, and right panels correspond to Kendall's tau τ values of 0.25, 0.50, and 0.75, respectively. The numbers following copula names are dependence parameter θ and corresponding τ values.

copula families, these relationships are obtained in closed form. For example, for the FGM copula, these relationships are

$$\rho_s = \frac{\theta}{3} \text{ and } \tau = \frac{2\theta}{9} \text{ and for } -1 \leq \theta \leq 1$$

This results in a restricted admissible dependence space of $-0.3333 \leq \rho_s \leq 0.3333$ or $-0.2222 \leq \tau \leq 0.2222$. Based on these, the sample-based estimates of θ , much like a moment-based estimate, are obtained, respectively, as

$$\check{\theta}_n = 3\rho_s^n \text{ and } \tilde{\theta}_n = \frac{9\tau_n}{2}$$

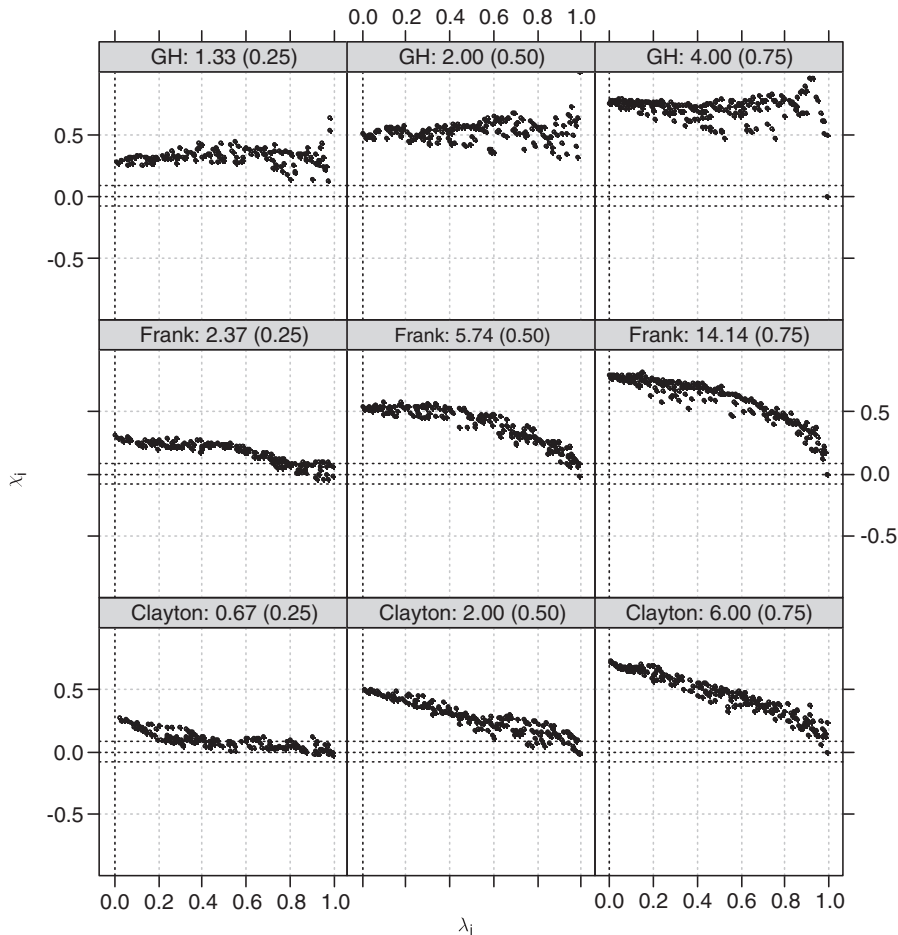


Figure 11-10. Lower-tail characteristics depicted by chi-plots for only the lower-left quadrant samples of the random bivariate samples of size 500 from GH, Frank, and Clayton copulas for increasing strengths of association. The left, middle, and right panels correspond to Kendall's tau τ values of 0.25, 0.50, and 0.75, respectively. The numbers following copula names are dependence parameter θ and corresponding τ values.

Table 11-2 gives these relationships for a few copula families. For the cases in which closed forms are not available, numerical integration can be followed for relating the dependence parameter θ with τ and/or ρ_s . These relationships also define the dependence space for each copula, corresponding to the domain of dependence parameter θ . Note, however, that this method is applicable to the single-parameter copula families only.

Considering general relationships $\theta = g(\tau)$ and $\theta = h(\rho)$, which could be established for various copula families, the approximate $100(1 - \alpha)\%$ confidence intervals can be computed for $\tilde{\theta}_n$ and $\check{\theta}_n$, respectively, following Genest and Rivest (1993) and Borkowf (2002), as

$$\tilde{\theta}_n \pm z_{\alpha/2} \frac{1}{\sqrt{n}} 4 S |g'(\tau_n)| \quad \text{and} \quad \check{\theta}_n \pm z_{\alpha/2} \frac{1}{\sqrt{n}} \sigma_n |h'(\rho_s^n)| \quad (11-46)$$

with

$$S^2 = \frac{1}{n} \sum_{i=1}^n (W_i + \tilde{W}_i - 2\bar{W})^2 \quad \text{and} \quad \sigma_n^2 = 144(-9A_n^2 + B_n + 2C_n + 2D_n + 2E_n)$$

where

$$\begin{aligned}\tilde{W}_i &= \frac{1}{n} \#\{j : X_i \leq X_j, Y_i \leq Y_j\}, \\ A_n &= \frac{1}{n} \sum_{i=1}^n \frac{R_i}{n+1} \frac{S_i}{n+1}, B_n = \frac{1}{n} \sum_{i=1}^n \left(\frac{R_i}{n+1}\right)^2 \left(\frac{S_i}{n+1}\right)^2, \\ C_n &= \frac{1}{n^3} \sum_{i=1}^n \sum_{j=1}^n \sum_{k=1}^n \frac{R_i}{n+1} \frac{S_i}{n+1} 1(R_k \leq R_i, S_k \leq S_j) + \frac{1}{4} - A_n, \\ D_n &= \frac{1}{n^2} \sum_{i=1}^n \sum_{j=1}^n \frac{S_i}{n+1} \frac{S_j}{n+1} \max\left(\frac{R_i}{n+1}, \frac{R_j}{n+1}\right),\end{aligned}$$

and

$$E_n = \frac{1}{n^2} \sum_{i=1}^n \sum_{j=1}^n \frac{R_i}{n+1} \frac{R_j}{n+1} \max\left(\frac{S_i}{n+1}, \frac{S_j}{n+1}\right)$$

Values of $\tilde{\theta}_n$ and $\check{\theta}_n$ likely differ significantly, and in such a case either an average value or the one with least variance is selected.

11.3.4.2 Maximum Pseudo-Likelihood (MPL) Method

In this method, one tries to keep the dependence structure completely independent of the margins that are represented nonparametrically by the respective scaled ranks. Only the dependence parameter is obtained by maximizing the likelihood function. The log-likelihood function, assuming that C_θ is absolutely continuous with density c_θ , is of the form

$$l(\theta) = \sum_{i=1}^n \log \left[c_\theta(\tilde{F}_X(x_i), \tilde{F}_Y(y_i)) \right] = \sum_{i=1}^n \log \left[c_\theta \left(\frac{R_i}{n+1}, \frac{S_i}{n+1} \right) \right] \quad (11-47)$$

where $\tilde{F}_X(x) = R_i/(n+1)$ and $\tilde{F}_Y(y) = S_i/(n+1)$ are rank-based nonparametric marginal probabilities. In other words, the maximum likelihood estimates of only θ are obtained in this method.

11.3.4.3 Exact Maximum Likelihood (EML) Method

In this classical or exact maximum likelihood method, all parameters appearing in the log-likelihood function given by

$$l(\theta, \delta, \eta) = \sum_{i=1}^n \log \{c_\theta[F_X(x; \delta), F_Y(y; \eta)]\} \quad (11-48)$$

are simultaneously estimated. Here, δ and η are parameters of the marginals $F_X(x; \delta)$ and $F_Y(y; \eta)$, and θ is the dependence parameter vector. Another variant of this approach is referred to as the inference from margins (IFM) method, wherein univariate maximum likelihood estimates of δ and η are first obtained separately, and then the estimate of θ is obtained by maximizing the likelihood function. The log-likelihood function for this can be expressed as

$$l(\theta) = \sum_{i=1}^n \log \{c_\theta[\check{F}_X(x; \delta), \check{F}_Y(y; \eta)]\} \quad (11-49)$$

where $\check{F}_X(x; \delta)$ and $\check{F}_Y(y; \eta)$ indicate marginals having parameters δ and η , which are obtained on a univariate basis. The IFM approach is advocated for multivariate copulas of larger dimensions when estimation through the classical approach becomes computationally unwieldy. By this method all

inferences that are made on a univariate level can be taken forward while performing multivariate analysis. Furthermore, [Joe \(2005\)](#) finds the IFM method to be nearly as efficient as the EML method. However, caution has to be exercised while employing the IFM method, as misspecification of marginals may affect the dependence estimation. Interesting to note is that although the classical maximum likelihood approach is more general, smaller mean squared errors were reported for the MPL method in a simulation study reported by [Tsukahara \(2005\)](#).

11.3.5 Copula-Based Random Generation

Copulas facilitate multivariate random number generation, as the procedure based on the conditional distribution is easily extendable to larger dimensions. The conditional bivariate probability $c_u(v) = C(u, v|U = u)$ considered for generating copula-based bivariate random numbers is given as

$$\begin{aligned} c_u(v) &= C(u, v|U = u) = P(V \leq v|U = u) \\ &= \lim_{\Delta u \rightarrow 0} \frac{C(u + \Delta u, v) - C(u, v)}{\Delta u} = \frac{\partial C(u, v)}{\partial u} \end{aligned} \quad (11-50)$$

This conditional probability is itself a cumulative distribution function, and therefore the transformation $V^* = c_u(V)$ results in $V^* \sim U(0, 1)$, which does not depend on U . Thereby, v may be obtained as $V = c_u^{-1}(V^*)$. Utilizing this, the following steps may be used to generate bivariate random numbers for (X, Y) ([Nelsen 2006](#)):

1. Generate two sets of n standard uniform random numbers as u_i and v_i^* for $i = 1:n$.
2. As the copula for (X, Y) , $H_{X, Y}(x, y) = C[F_X(x), F_Y(y)] = C(u, v)$ is known, an expression for $c_u(v) = \frac{\partial C(u, v)}{\partial u}$ is obtained. From this, an inverse expression $c_u^{-1}(v^*)$ can also be obtained.
3. Then, the corresponding v_i is obtained from $v_i = c_u^{-1}(v_i^*)$. The set (u, v) comprising (u_i, v_i) is the randomly generated pairs from copula $C(u, v)$.
4. The bivariate random numbers in the original domain (X, Y) is then obtained as $(x_i, y_i) \forall i = 1:n$, where $x_i = F_X^{-1}(u_i)$ and $y_i = F_Y^{-1}(v_i)$.

11.3.6 Copula Selection Process

The main objective in the copula selection process is to represent the dependence structure of the data under consideration adequately. A popular notion claims that the copula method overcomes various limitations faced by functional distributional forms, including those with restricted dependence space and difficulty in having their multivariate extensions. However, this is not entirely true, as most copulas also are not comprehensive and cover a limited dependence space individually. Their multivariate extensions also invariably come with various additional restrictions; for example, extension to multivariate single-parameter copulas entails all pairwise dependence to be equal, and fully nested Archimedean copulas require certain dependence compatibility conditions to be met. Another important aspect in copula selection is ensuring suitability in terms of tail dependence characteristics. Certain copulas may exhibit similar overall dependence features, while possessing different lower- and/or upper-tail dependence characteristics. The compatibility of copula tail dependence characteristics with that exhibited by the process under consideration thus becomes an important goal. Furthermore, while the forms of functional multivariate distributions lack in terms of variety, a problem of a different nature exists with copulas, and that is of a vast solution space ([Michiels and Schepper 2008](#)). Numerous classes and types of copulas exist, making the identification of suitable ones a nontrivial task.

Intuitively, the copula selection process can be split in two parts. In the first stage, the plausible copula types can be screened from the pool of all available copulas on the basis of admissible dependence ranges and tail dependence characteristics of individual copula types vis-à-vis the dependence characteristics of the data under consideration. Parameter estimation and goodness-of-fit

tests for only those copulas that are screened in the first stage can then follow as a second stage to select a final set of suitable copulas.

Michiels and Schepper's (2008) inventory of admissible dependence space for 29 copulas comes in handy when screening for plausible copulas in the first stage. Each of these copula types may have three additional associated copulas, making the inventory even richer. Table 11-3 gives an adapted and abridged version of this inventory for 10 commonly used copula types. The shaded cells in the table imply admissibility of corresponding dependence ranges for different copula types. The table also lists lower- and upper-tail dependence coefficients λ_L and λ_U as defined in Equations (11-27) and (11-28). On the basis of strength of dependence and tail dependence characteristics of the data under consideration, a short list of plausible copula types can be made. An assessment of dependence, along with p-values, can be made by computing the values of Spearman's rho ρ_s and/or Kendall's tau τ based on observed data. The tail dependence characteristics of the process under consideration can be known from the expert knowledge about that process. The chi-plots for the upper and lower tails, as suggested by Abberger (2005), also help corroborate the values of tail dependence coefficients λ_L and λ_U .

Generally, more than one feasible copula structure may constitute the copula test space. In the second stage, parameters of all the short-listed copula families are estimated using one or more parameter estimation methods. Ascertaining the adequacy of the hypothesized copulas is then imperative. This can be normally accomplished in three ways: (1) graphical methods, (2) error statistics, and (3) formal goodness-of-fit statistics. A randomly generated test dataset from the Clayton copula, with Kendall's tau $\tau = 0.5$, is used to illustrate these goodness-of-fit tests. Figure 11-11 plots this test dataset.

11.3.6.1 Graphical Goodness-of-Fit Methods

Several graphical approaches can be employed that utilize different features for making comparisons. Graphical comparison of the superimposed scatter plots of observed and simulated data is an

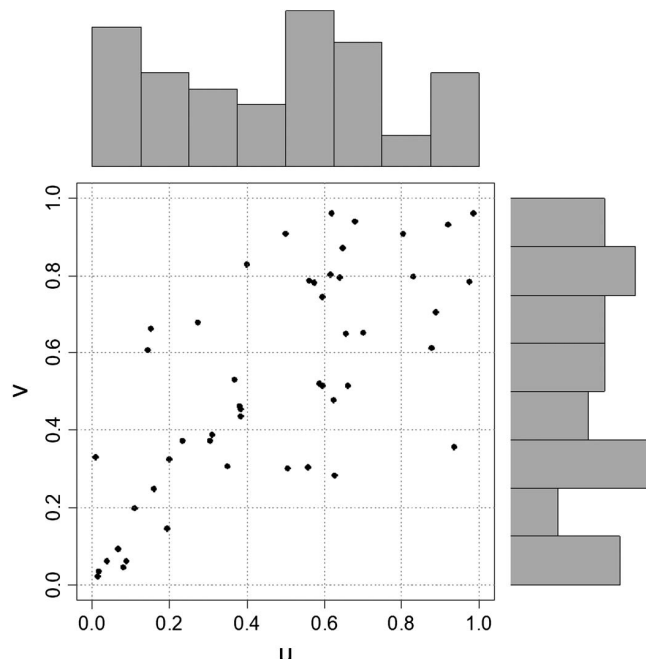


Figure 11-11. Scatter plot of a random test dataset of size 50 of the Clayton copula with Kendall's tau of 0.5 or dependence parameter $\theta = 2.0$. The marginal histograms on the sides are nearly uniformly distributed.

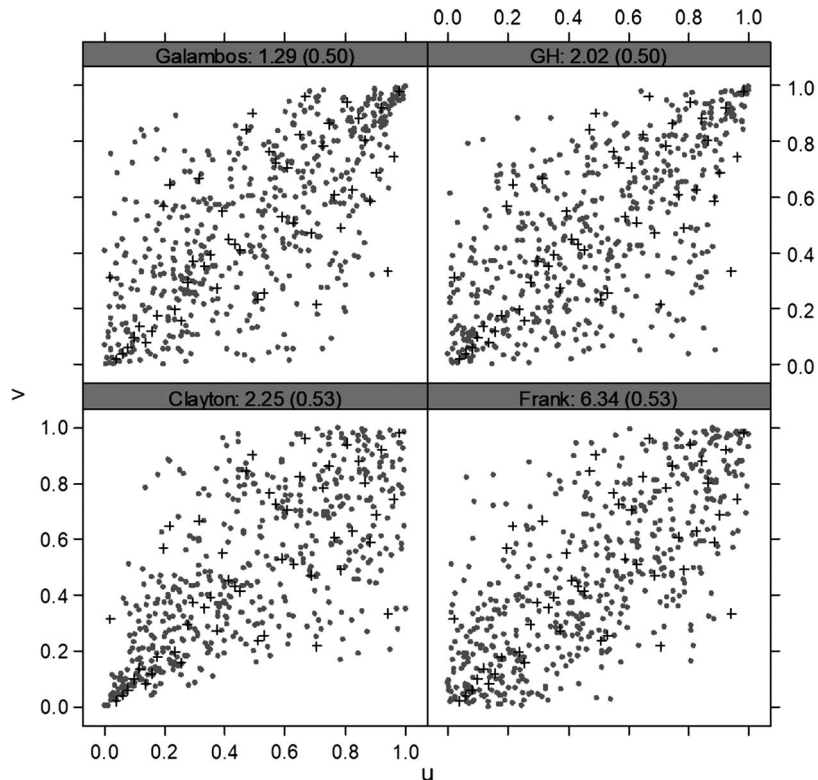


Figure 11-12. Comparison of Clayton copula test data with sets of 500 generated random samples based on dependence parameters obtained by the MPL method. Solid circles in gray are the random samples, whereas plus symbols represent test data. The numbers following the copula names are dependence parameter θ and corresponding τ values.

intuitive way of qualitatively assessing the suitability of the hypothesized copulas. Important to note here is that both very small and very large generated sample sizes can provide misleading comparisons. Figure 11-12 illustrates such comparison of the Clayton copula test dataset with four copula families: Galambos, GH, Clayton, and Frank. The figure shows that the conspicuous lower tail in the test data is better represented by the random data from the Clayton copula as compared with the other copulas. This method, however, is better suited for bivariate cases only, as similar comparisons in higher dimensions become difficult. Furthermore, comparison of the ordered empirical probabilities with corresponding computed probabilities can be made, revealing the extent to which the copula surface fits the scaled ranks of observed data. Figures 11-13 and 11-14 provide this comparison in two ways. In the former case, the empirical and computed probabilities are plotted against the observation numbers that are ranked as per the empirical probabilities. In the latter case, the empirical probabilities are plotted against the computed probabilities, making the vicinity of the diagonal line the desirable region. Both of these comparative plots show that the Clayton copula performs better for the test dataset. The other two graphical options are related to the K-plots. In one option, the empirical and theoretical probability distributions, $K_n(w)$ and $K_{\theta_n}(w)$, of the BIPIT variate $W = C(U, V)$ can be compared—with their closeness supporting nonrejection of the hypothesized copula. Figure 11-15 illustrates this plot for the test dataset, showing that the theoretical probability distributions of W for the Clayton copula better matches the empirical distribution, especially in the lower-tail region. The second option is much like a QQ-plot—a scatter plot between the observed order statistics $W_{(1)} \leq W_{(2)} \leq \dots \leq W_{(n)}$ of W and the corresponding

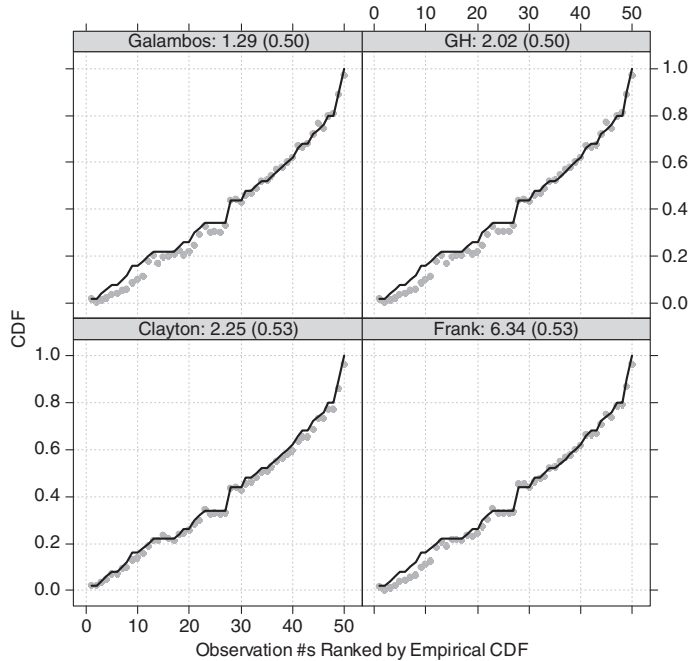


Figure 11-13. Comparison of empirical and MPL method-based computed probabilities for the Clayton copula test data. Lines in black and solid gray circles are empirical and computed probabilities, respectively. The numbers following copula names are dependence parameter θ and corresponding τ values.

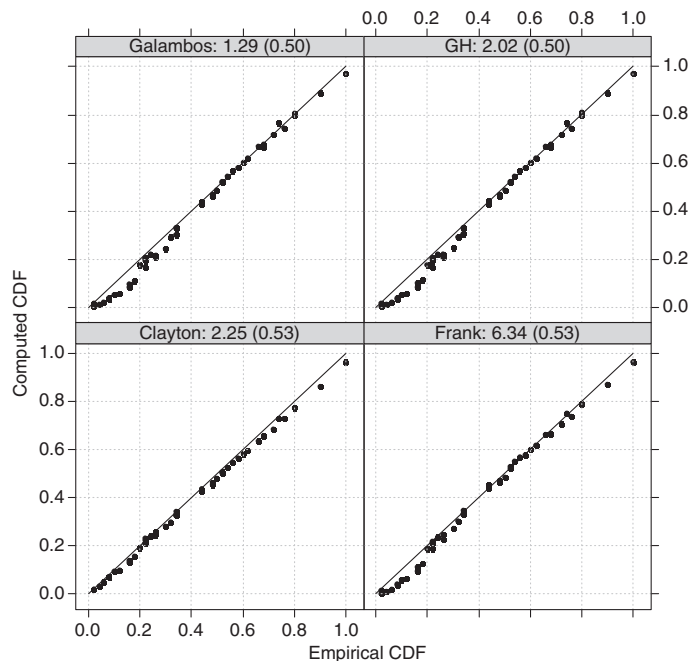


Figure 11-14. Comparison of empirical and MPL method-based computed probabilities for the Clayton copula test data. The diagonal lines represent equivalence of empirical and computed probabilities.

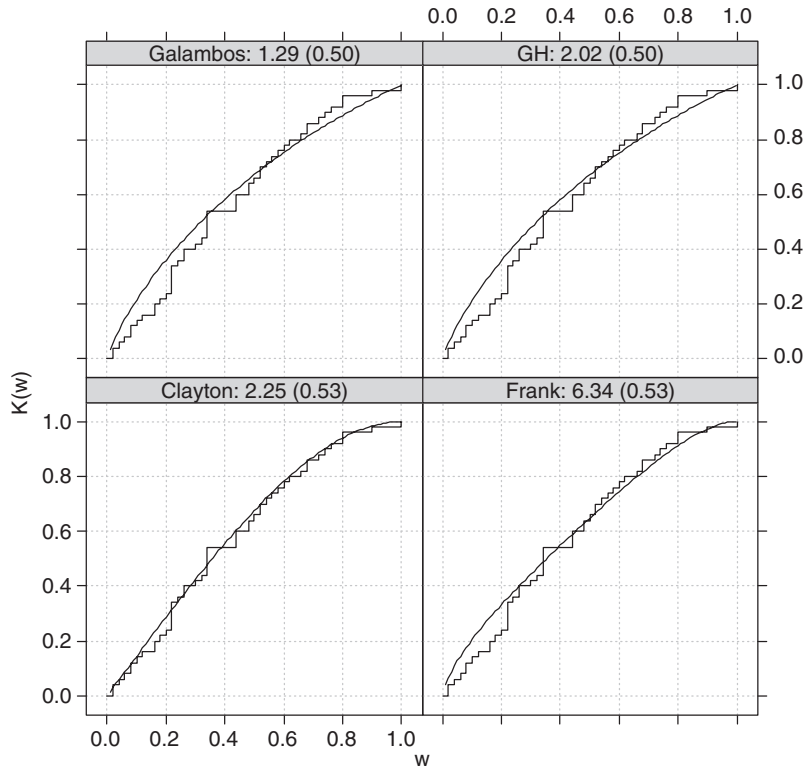


Figure 11-15. Comparison of empirical $K_n(w)$ and theoretical $K_{\theta_n}(w)$ probability distribution functions of the bivariate integral transform variable $W = C(U, V)$ for various copulas. The step functions are empirical distributions, and the curves are the MPL method-based theoretical distributions.

expected order statistics based on the hypothesized copula. Again, conformation to the line from origin and having unit slope suggest nonrejection of the hypothesized copula. Figure 11-16 illustrates this comparison for the test dataset, again showing that the Clayton copula provides the best match as compared with the other three copulas. This plot is also referred to as the “generalized K-plot.”

11.3.6.2 Error Statistics of Fit

A quantitative assessment of the performance of various copula families can be made by comparing the maximized log-likelihood or Akaike information criterion (AIC) values. Various error statistics, such as the root mean square error (RMSE), mean absolute error (MN-A-ERR), and maximum absolute error (MX-A-ERR), reflect other important characteristics of comparison of empirical and computed probabilities. Considering the empirical and computed bivariate probabilities as w_i^o and w_i^c for $i=1:n$ in a sample of size n , respectively, these error statistics are obtained as

$$\text{RMSE} = \sqrt{\frac{1}{n} \sum_{i=1}^n (w_i^o - w_i^c)^2} \quad (11-51a)$$

$$\text{MN-A-ERR} = \frac{1}{n} \sum_{i=1}^n |(w_i^o - w_i^c)| \quad (11-51b)$$

$$\text{MX-A-ERR} = \max_{i=1:n} |(w_i^o - w_i^c)| \quad (11-51c)$$

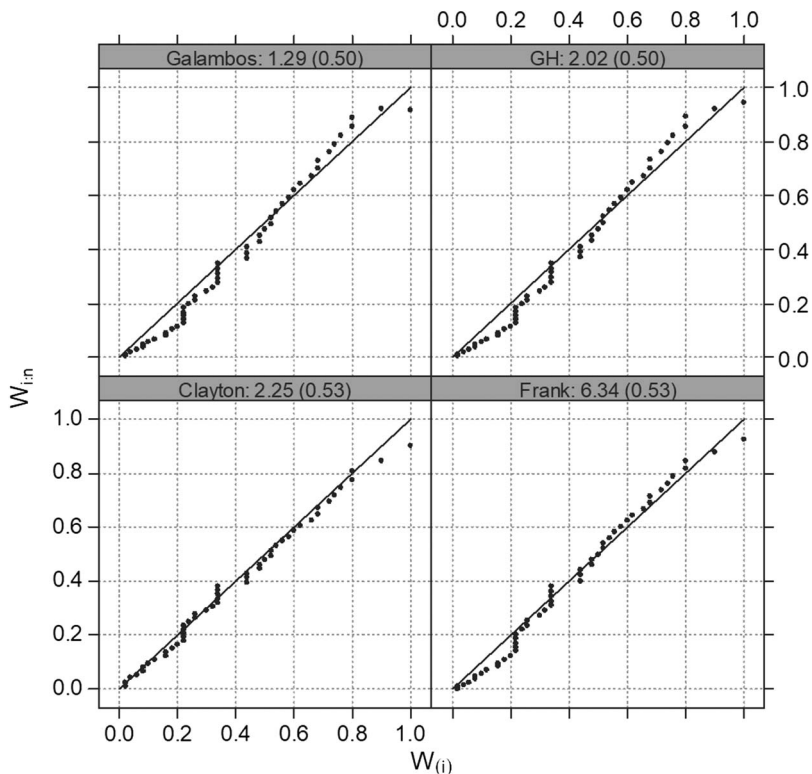


Figure 11-16. Generalized K-plots between observed $W_{(i)}$ and corresponding expected $W_{i:n}$ order statistics of the MPL method-based bivariate probability integral transform variable $W = C(U, V)$ for various copulas. The line through the origin with unit slope indicates equivalence between the two order statistics. The numbers following copula names are dependence parameter θ and corresponding τ values.

Table 11-4 gives these error statistics for the test dataset with respect to the MPL method. As expected, the least errors correspond to the Clayton copula because the test dataset was generated based on the Clayton copula.

11.3.6.3 Analytical Goodness-of-Fit Tests

Genest et al. (2009) present a review of the available analytical goodness-of-fit tests for copulas, including those proposed by Wang and Wells (2000), Fermanian (2005), and Genest et al. (2006),

Table 11-4. Three Error Statistics for Fitting Four Copulas to Clayton Copula Test Dataset with Respect to the MPL Method.

Copula family	MPL-based copula model		
	RMSE	MN-A-ERR	MX-A-ERR
Clayton	0.0185	0.0156	0.0398
Frank	0.0244	0.0186	0.0645
Galambos	0.0302	0.0226	0.0743
GH	0.0296	0.0223	0.0733

among others, and recommend a few Cramer–von Mises type test statistics based on Rosenblatt's transformation. The validity of the parametric bootstrap procedure, proposed by Genest et al. (2006), and for the empirical copula-based test statistics, proposed by Fermanian (2005), has since been formally established by Genest and Remillard (2008). Three goodness-of-fit test statistics, proposed by Fermanian (2005) and Genest et al. (2006), are discussed here to test the adequacy of the hypothesized copulas formally. The first one is the Cramer–von Mises type statistic proposed by Fermanian (2005), which is based on the comparison of empirical and parametric copula probabilities given by the process $\sqrt{n}(C_n - C_{\theta_n})$ and can be obtained as

$$\begin{aligned} CM_n &= n \sum_{i=1}^n \left[C_n \left(\frac{R_i}{n+1}, \frac{S_i}{n+1} \right) - C_{\theta_n} \left(\frac{R_i}{n+1}, \frac{S_i}{n+1} \right) \right]^2 \\ &= n \sum_{i=1}^n \left[W_i - C_{\theta_n} \left(\frac{R_i}{n+1}, \frac{S_i}{n+1} \right) \right]^2 \end{aligned} \quad (11-52)$$

Genest et al. (2006) give the other two Cramer–von Mises and Kolmogorov type statistics as variants of those that Wang and Wells (2000) propose. Providing an objective comparison of the empirical and theoretical probabilities of the BIPIT variate W , these are based on the process $\mathbb{K}_n(w) = \sqrt{n}\{K_n(w) - K_{\theta_n}(w)\}$ and can be obtained as

$$\begin{aligned} S_n &= \int_0^1 |\mathbb{K}_n(w)|^2 k_{\theta_n}(w) dw \\ &= \frac{n}{3} + n \sum_{j=1}^{n-1} K_n^2 \left(\frac{j}{n} \right) \left[K_{\theta_n} \left(\frac{j+1}{n} \right) - K_{\theta_n} \left(\frac{j}{n} \right) \right] \\ &\quad - n \sum_{j=1}^{n-1} K_n \left(\frac{j}{n} \right) \left[K_{\theta_n}^2 \left(\frac{j+1}{n} \right) - K_{\theta_n}^2 \left(\frac{j}{n} \right) \right] \end{aligned} \quad (11-53)$$

and

$$\begin{aligned} T_n &= \sup_{0 \leq w \leq 1} |\mathbb{K}_n(w)| \\ &= \sqrt{n} \max_{i=0,1; 0 \leq j \leq n-1} \left\{ \left| K_n \left(\frac{j}{n} \right) - K_{\theta_n} \left(\frac{j+i}{n} \right) \right| \right\} \end{aligned} \quad (11-54)$$

Tables 11-5 and 11-6 give these three goodness-of-fit test statistics for the test dataset with respect to MOM and MPL methods, respectively. Higher p-values for the Clayton copula for all three statistics indicate that it is most viable among the four copulas considered for the test dataset. This is expected because the test dataset came from the Clayton copula. The p-values for the CM_n statistic for the Frank copula are also comparatively higher and may be owing to the fact that both the Clayton and Frank copulas have insignificant upper-tail dependence. In that sense these statistics may not have a desirable discriminatory power between the Clayton and Frank copulas. The extremely low p-values of all three statistics rule out the Galambos and GH as plausible copulas.

Overall, the copula selection process can be summarized in the following steps:

1. Get an initial idea of the dependence level from the scatter plot of scaled ranks.
2. Quantify the strength of dependence by computing nonparametric dependence measures, such as Spearman's rho and Kendall's tau.
3. Reaffirm the significance of dependence using the chi-plot and/or the K-plot.

Table 11-5. Goodness-of-Fit Statistics for Fitting Four Copulas to the Clayton Copula Test Dataset with Respect to the Inversion of Dependence Measure (MOM) Method.

Statistic	Copula	Observed statistic	Critical test statistic S* and P-value for a run of N =					
			100		1,000		10,000	
			S*	P-val	S*	P-val	S*	P-val
CM_n	Clayton	0.777	1.725	0.980	1.877	0.956	1.887	0.960
			2.070	0.990	1.925	0.971	1.903	0.962
		1.430	2.080	0.280	2.009	0.240	1.957	0.235
	Frank		1.982	0.240	1.964	0.239	1.968	0.234
		1.780	1.816	0.070	1.878	0.074	–	–
			1.655	0.040	1.876	0.076	–	–
	GH	1.768	1.862	0.060	1.862	0.070	1.843	0.063
			1.981	0.100	1.896	0.063	1.890	0.070
		0.034	0.112	0.920	0.121	0.912	0.123	0.892
	S _n		0.130	0.930	0.131	0.910	0.122	0.901
		0.122	0.132	0.060	0.120	0.048	0.119	0.044
			0.119	0.050	0.127	0.062	0.118	0.045
	Galambos	0.204	0.150	0.010	0.158	0.007	–	–
			0.157	0.010	0.159	0.012	–	–
		0.174	0.122	0.020	0.120	0.011	0.117	0.005
T_n	Clayton	0.503	0.837	0.820	0.876	0.862	0.880	0.856
			0.884	0.860	0.894	0.843	0.880	0.864
		0.864	0.889	0.090	0.849	0.044	0.839	0.035
	Frank		0.842	0.020	0.841	0.042	0.835	0.034
		0.973	1.098	0.460	1.129	0.486	–	–
			1.102	0.440	1.118	0.468	–	–
	GH	0.955	1.033	0.060	0.855	0.019	0.857	0.014
			0.800	0.000	0.850	0.013	0.861	0.016

Note: S* implies the critical value of the test statistic at a significance level of 5%, and P-val indicates the p-values of the observed test statistic.

4. Observe the significance of tail dependence by using the chi-plot and compare this with the available expert knowledge about the process under consideration.
5. Preselect one or more copula types that offer the dependence level and the tail dependence under consideration.
6. Estimate copula parameters by one or more methods.
7. Assess the adequacy of hypothesized copulas on the basis of graphical diagnostic plots.
8. Assess the adequacy of hypothesized copulas on the basis of one or more analytical goodness-of-fit test statistics.
9. Identify suitable copula models on the basis of the aforementioned assessment.

11.4 ILLUSTRATIVE EXAMPLES

Many studies emphasize the importance of multivariate hydrological frequency analysis. These studies have involved storm or flood variables, such as storm depth, duration, average intensity,

Table 11-6. Goodness-of-Fit Statistics for Fitting Four Copulas to the Clayton Copula Test Dataset with Respect to the MPL Method.

Statistic	Copula	Observed statistic	Critical test statistic S^* and P-value for a run of $N =$					
			100		1,000		10,000	
			S^*	P-val	S^*	P-val	S^*	P-val
CM_n	Clayton	0.855	2.404	0.780	2.552	0.736	2.651	0.753
			2.332	0.690	2.550	0.753	2.665	0.751
		1.493	1.844	0.210	2.033	0.219	1.997	0.210
	Frank		2.162	0.200	1.959	0.207	1.994	0.211
		2.271	1.833	0.040	1.952	0.028	–	–
			1.754	0.010	1.909	0.020	–	–
	Galambos	2.191	1.949	0.040	1.940	0.023	1.915	0.022
			2.126	0.040	1.880	0.020	1.932	0.025
	S_n	Clayton	0.038	0.131	0.840	0.132	0.843	0.137
				0.123	0.800	0.132	0.834	0.139
		Frank	0.126	0.105	0.030	0.120	0.040	0.120
	Galambos	0.248	0.114	0.040	0.117	0.034	0.121	0.042
			0.190	0.000	0.184	0.009	–	–
			0.169	0.000	0.189	0.009	–	–
	GH	0.209	0.141	0.000	0.131	0.004	0.130	0.005
				0.134	0.000	0.127	0.003	0.132
								0.007
T_n	Clayton	0.526	0.851	0.770	0.902	0.817	0.911	0.809
				0.841	0.730	0.931	0.801	0.917
	Frank	0.880	0.822	0.020	0.841	0.034	0.835	0.029
				0.815	0.020	0.833	0.029	0.847
	Galambos	1.036	1.136	0.340	1.148	0.340	–	–
				1.107	0.270	1.156	0.334	–
	GH	1.028	0.918	0.010	0.904	0.007	0.895	0.010
				0.866	0.000	0.890	0.011	0.895
								0.012

Note: S^* implies the critical value of a test statistic at a significance level of 5%, and P-val indicates the p-values of the observed test statistic.

maximum intensity, time to peak, interarrival period, and number of storms in a specified period; or flood volume, duration and peak flow, and time to peak flow; among a few others. Studies involving storm characteristics have been carried out for purposes such as simulation of rainfall field, rainfall-runoff modeling, and derivation of frequency distributions for flood, urban storm volume, or annual precipitation. Similarly, studies with flow variables have been done for various applications, including checking the adequacy of dam spillways, carrying out risk assessments of levees and embankments, designing retention basins, deriving flood frequency distributions at a station downstream of a confluence, and improving the efficiency of parameter estimates of frequency distributions. Fitting the joint distribution is central to all such applications. The following examples illustrate fitting of copula-based bivariate distributions to flood and rainfall variables that would be required for designing structures that involve risk of failure due to multiple rainfall or flow variables.

11.4.1 Example 11-1: Peak Flow and Volume

The annual peak and average daily flows of the Greenbrier River at Alderson station (USGS Station #03183500) located in West Virginia are considered in this application for obtaining their joint distribution. The Greenbrier River is a tributary of the New River in the southeastern part of the state

and is approximately 165 mi (265 km) long. Through the New, Kanawha, and Ohio Rivers, it is part of the Mississippi River watershed. A river-gauging station is located at Alderson at latitude $37^{\circ}43'27''$ and longitude $80^{\circ}38'30''$, commanding a drainage area of $1,364 \text{ mi}^2$. This analysis considers 110 years of data, from 1896 to 2005. The preparation of annual maximum flood data is an important first step as the selection of maximal events for bivariate data becomes slightly ambiguous. Extreme flood events with respect to the safety of drainage systems are invariably primarily associated with peak flows that cause overtopping of crests of dams or levees, or inundation of floodplains. Any high volume or long duration of flow by itself may not be any cause for concern when flows are lesser than the design capacity of the system. Detrimental effects of high volume and/or duration of flow are also important, but they typically only come into play when a primary failure occurs due to higher peak flows. Annual maximum flood events have therefore been considered in this study on the basis of annual peak flows, and the associated volumes have been obtained from the record of average daily flows. A base flow of $2.5 \times 10^3 \text{ ft}^3/\text{s}$ has been subtracted to obtain flood volumes. The flood duration is taken as the period associated with the annual maximum flow when average daily flows contiguously remained above the base flow. Figure 11-17 gives time series of these two datasets, Q_p in $10^3 \text{ ft}^3/\text{s}$ and V_p in $10^3 \text{ ft}^3/\text{s}\cdot\text{days}$. Figures 11-18a and 11-18b show the scatter plots of these bivariate data and of their scaled ranks, along with the respective histograms. As scaled ranks are empirical probabilities, they are roughly uniformly distributed between 0 and 1.

11.4.1.1 Potential Marginal Distributions

Several candidate distributions, such as two- and three-parameter log-normal (LN2 and LN3), two-parameter gamma (G2), Pearson type III (P3), log-Pearson type III (LP3), and largest extreme value (LEV), are considered for fitting annual peak flow and volume data on a univariate basis. On the basis of Kolmogorov-Smirnov, Anderson Darling, and chi-squared fit statistics and the overall fit of the QQ plots, P3 and three-parameter Weibull (W3) distributions were selected as marginal distributions for the two variables, respectively. The pdfs for P3 and W3 distributions $f_X(x)$ and $f_Y(y)$ for flood peak flow $X = Q_p$ and volume $Y = V_p$, respectively, are given as

$$f_X(x) = \frac{1}{|\alpha_X|} \frac{1}{\Gamma(\beta_X)} \left(\frac{x - \gamma_X}{\alpha_X} \right)^{\beta_X - 1} \exp\left(-\frac{x - \gamma_X}{\alpha_X}\right)$$

where $-\infty < \gamma_X < \infty$, $-\infty < \alpha_X < \infty$, and $\beta_X > 0$ are location, scale, and shape parameters, respectively; $x \geq \exp(\gamma_X) \forall \alpha_X > 0$ and $x \leq \exp(\gamma_X) \forall \alpha_X < 0$;

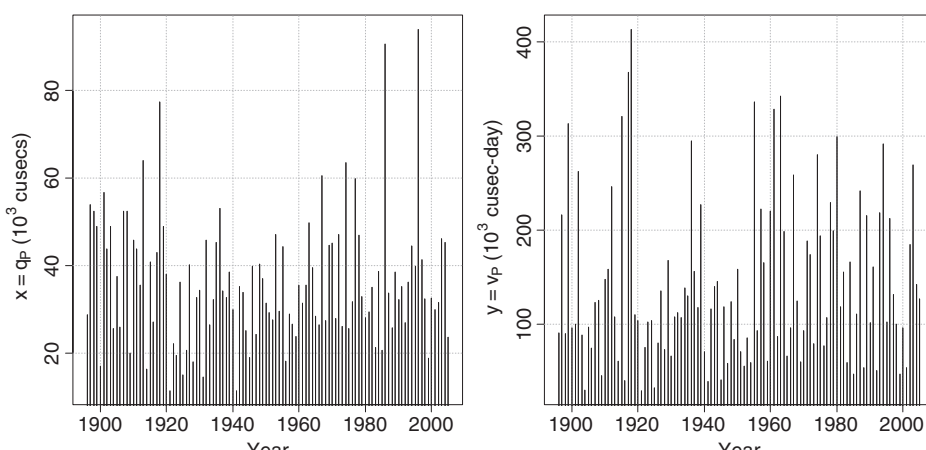


Figure 11-17. Time series of annual peak flows Q_p , in $10^3 \text{ ft}^3/\text{s}$ (or cusec) and corresponding flood volumes V_p , in $10^3 \text{ ft}^3/\text{s}\cdot\text{day}$ (or cusec-day) at Alderson on Greenbrier River.

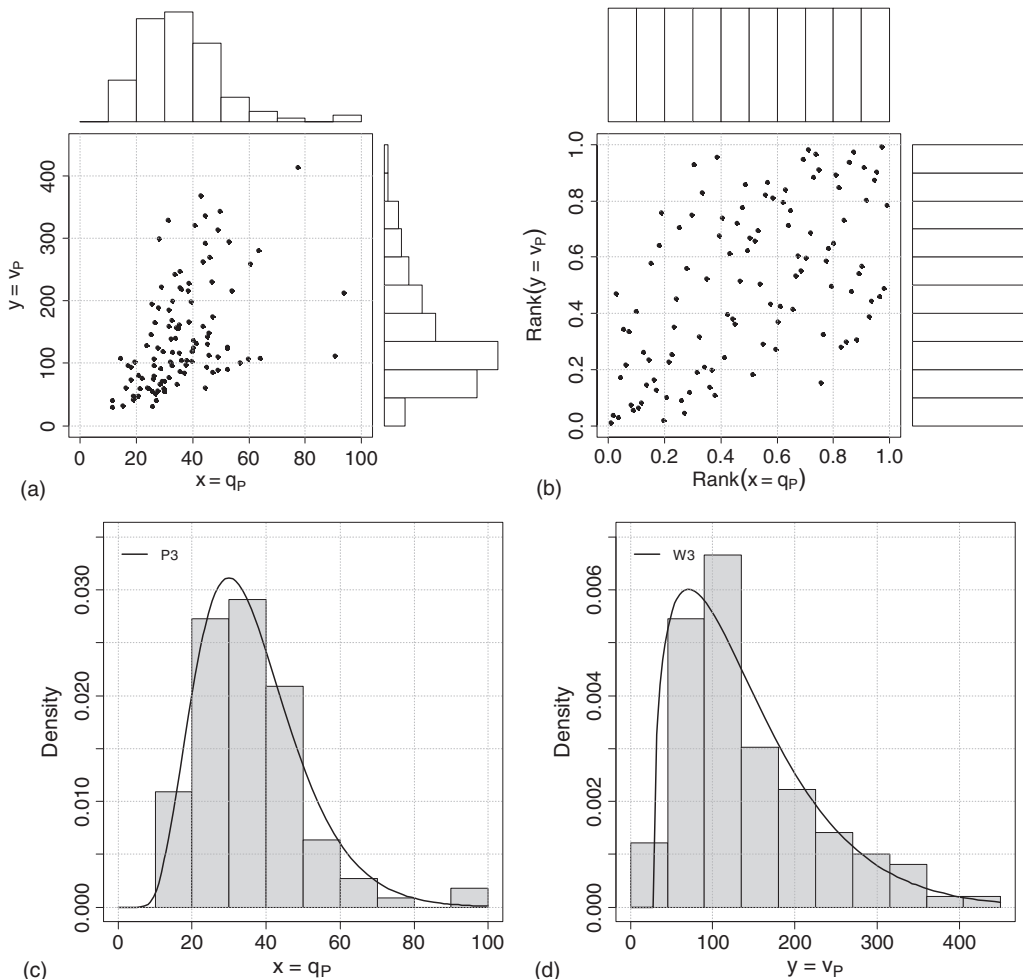


Figure 11-18. Characteristics of observed bivariate annual peak flow (Q_P , in $10^3 \text{ ft}^3/\text{s}$) and corresponding flood volumes (V_P , in $10^3 \text{ ft}^3/\text{s-day}$) at Alderson on Greenbrier River: (a and b) scatter plot and histograms in original domain and of ranks; (c and d) histograms with Pearson type III and three-parameter Weibull pdfs for Q_P and V_P , respectively.

and

$$f_Y(y) = \frac{\beta_Y}{\alpha_Y} \left(\frac{y - \gamma_Y}{\alpha_Y} \right)^{\beta_Y - 1} \exp \left[- \left(\frac{y - \gamma_Y}{\alpha_Y} \right)^{\beta_Y} \right]$$

where $-\infty < \gamma_Y < \infty$ and $\alpha_Y, \beta_Y > 0$ are location, scale, and shape parameters, respectively, and $\gamma_Y \leq y < +\infty$.

The MLEs of parameters for these two marginals are obtained as $\hat{\gamma}_X = 4.601$, $\hat{\alpha}_X = 6.197$, $\hat{\beta}_X = 5.101$, and $\hat{\gamma}_Y = 28.361$, $\hat{\alpha}_Y = 122.185$, $\hat{\beta}_Y = 1.326$. The corresponding standard errors are $Se_{\hat{\gamma}_X} = 4.332$, $Se_{\hat{\alpha}_X} = 1.365$, $Se_{\hat{\beta}_X} = 1.715$, and $Se_{\hat{\gamma}_Y} = 1.907$, $Se_{\hat{\alpha}_Y} = 6.093$, $Se_{\hat{\beta}_Y} = 0.107$. Figures 11-18c and 11-18d show the overlay of probability density curves of these distributions and the corresponding histograms, respectively. Figure 11-19 shows the corresponding QQ plots, along with 95%

confidence intervals. The narrow confidence bands indicate comparatively lesser uncertainty in parameter estimation which is expected for a 110 years dataset.

11.4.1.2 Dependence Structure and Copula Test Space

The scatter plots in Figure 11-18a and b indicate a positive association between annual peak flow and volume data. The sample estimates of Pearson's correlation coefficient, Kendall's tau, and Spearman's rho, 0.466, 0.391, and 0.557, with corresponding p-values of 2.9e-07, 1.78e-09, and 3.0e-10, respectively, corroborate this assertion. Figure 11-20 shows that a significant positive dependence is also indicated by both chi- and K-plots. Considering data exclusively from the lower-left and upper-right quadrants, as suggested by Abberger (2005), the chi-plots in Figure 11-21 exhibit lower- and upper-tail dependence features. Figure 11-21a clearly indicates that evidence exists of lower-tail dependence as a few points close to $\lambda_i = 1$ show significance. More important, Figure 11-21b indicates upper-tail independence, as points in the end zone are within the control limits for the p-value of 0.95. Based on sample Kendall's tau value of 0.391 and the features of lower- and upper-tail

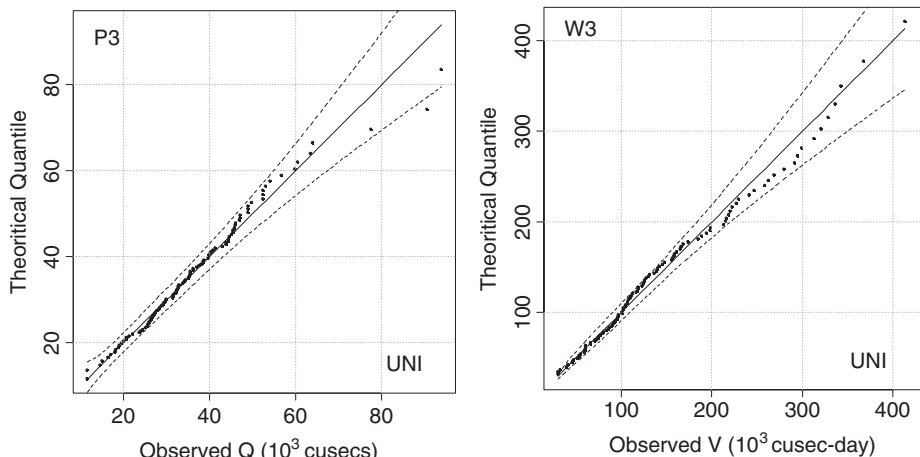


Figure 11-19. QQ plots for Example 11-1 for peak flow (Q_p) and volume (V_p) data fitted with P3 and W3 distributions, respectively.

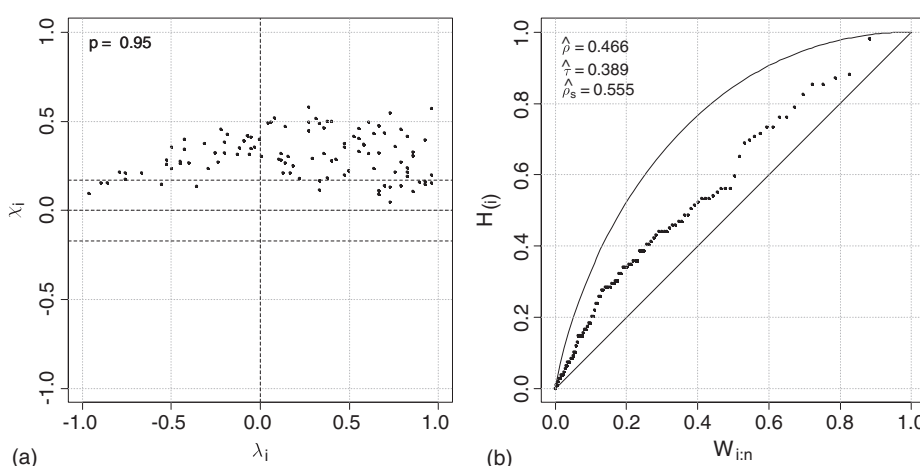


Figure 11-20. Characterization of dependence between annual flood peak flow and volume for Example 11-1 using (a) chi-plot and (b) K-plot.

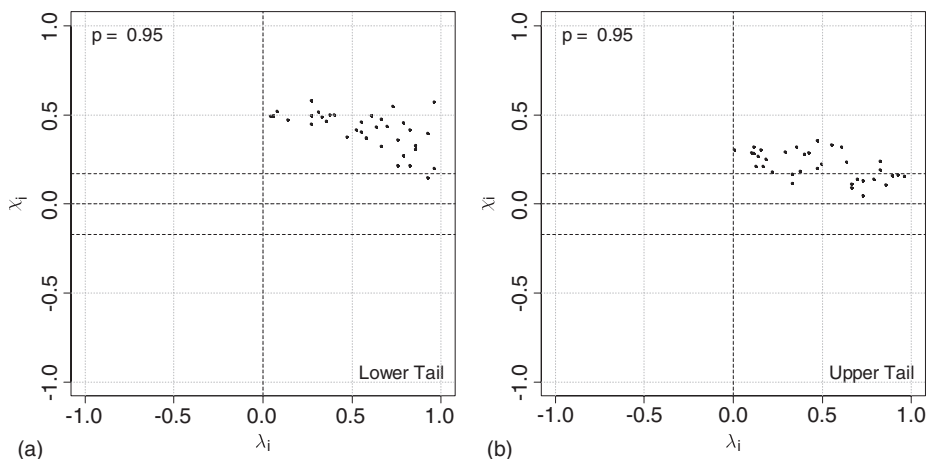


Figure 11-21. Characterization of (a) lower- and (b) upper-tail dependence between annual flood peak flow and volume for Example 11-1 using chi-plots.

dependence, two Archimedean copulas, Clayton and Frank, and two extreme value copulas, Galambos and GH, are selected. To appreciate the problems that arise due to misspecification, two more copulas, AMH and FGM, are also short-listed, noting that the sample dependence is beyond the admissible ranges for these copulas. Although more copulas could have been considered at this initial screening stage, only these six are included in the copula test space, primarily to keep the process shorter.

11.4.1.3 Estimation of Dependence Parameter

The dependence parameters for the six copula families under consideration are estimated by (1) MOM inversion of dependence measures and (2) MPL and IFM methods. These point estimates along with standard errors and the interval estimates, corresponding to a coverage probability of 0.95, are given for these methods in Table 11-7. The estimates for AMH and FGM copulas are not obtainable for this dataset, as the values of τ are beyond the admissible limits. The AMH copula requires τ to be between -0.1817 and 0.3333 , and for the FGM copula τ must be in the range of $-2/9$ to $2/9$ (or -0.222 to 0.222). This illustrates the limitations of these copula families, similar to that faced by some of the conventional functional distributions.

Table 11-7 includes the maximized log-likelihood values (LL_{max}) for the six copula families. These results show that the standard errors of the dependence parameter estimates from this method are much lower than those for the MOM method. For the AMH and FGM copulas the optimal values of dependence parameters lie at the end of the parameter space and correspond to much lower values of τ than those obtained from the sample dataset. The maximum log-likelihood value for the Clayton copula is the largest among them all. Even though the sample Kendall's tau is much higher than the maximum permissible value for the AMH copula, the maximized log-likelihood value for this copula is less by only a small amount as compared with the Clayton copula.

Except for the AMH and Clayton copulas, the standard errors for dependence parameter estimates from the IFM estimation method are similar to those for the MPL method. For the AMH and Clayton copulas the standard errors are substantially less for the MPL method. For the FGM copula the optimal value lies at the end of the parameter space and corresponds to a much lower value of τ than that obtained from the sample dataset. The maximized log-likelihood value for the AMH copula is highest and is even slightly greater than that of the Clayton copula. Thus, from the point of view of maximum log-likelihood values the Clayton copula can be said to perform better for the MPL method, whereas the AMH copula is marginally better for the IFM method.

Table 11-7. Point and Interval Dependence Parameter Estimates for Example 11-1 for the Six Copulas under Consideration with Respect to the Three Estimation Methods. Interval Estimates Correspond to a Coverage Probability of 0.95.

Method/ copula family	Theta ($\hat{\theta}$)	Lower confidence limit	Upper confidence limit	Standard error	Confidence width	LL_{max}
MOM						
Clayton	1.283	0.722	1.844	0.286	0.561	–
Frank	4.036	2.631	5.441	0.717	1.405	–
Galambos	0.917	0.631	1.202	0.146	0.286	–
GH	1.642	1.361	1.922	0.143	0.281	–
MPL						
AMH	0.995	0.900	1.090	0.049	0.095	24.490
Clayton	1.220	1.031	1.409	0.097	0.189	25.451
FGM	0.995	0.823	1.167	0.088	0.172	14.811
Frank	3.970	3.807	4.133	0.083	0.163	19.646
Galambos	0.800	0.665	0.935	0.069	0.135	16.367
GH	1.529	1.388	1.670	0.072	0.141	16.118
IFM						
AMH	0.988	0.852	1.124	0.070	0.136	23.708
Clayton	1.059	0.605	1.513	0.231	0.454	23.417
FGM	0.995	0.826	1.164	0.086	0.169	14.533
Frank	4.043	3.882	4.204	0.082	0.161	19.754
Galambos	0.739	0.603	0.875	0.070	0.136	14.636
GH	1.478	1.336	1.620	0.072	0.142	15.089

Comparison of standard errors and confidence intervals among different copulas is not appropriate, as the dependence parameter has different scaling and sensitivity with respect to the association measures for various copulas. The MPL method, followed by the IFM method, may be preferable over the MOM method as they result in significantly lower standard errors for respective copulas.

11.4.1.4 Assessment of Copula Fitting

The relative suitability of plausible copula families is ascertained in multiple ways by employing (1) graphical methods, (2) error statistics, and (3) formal goodness-of-fit statistics.

Graphical Goodness-of-Fit Tests

First, the observed data are compared with a large number of generated random samples. For this application, a set of random samples of size 500 is generated for each of the six copula families under consideration, utilizing MOM, MPL, and IFM method-based parameters. As the AMH and FGM copulas do not cover the expected dependence range for the MOM method, they are not included in these plots. Figures 11-22 to 11-24 show this comparison of observed and randomly generated samples and that the general nature of the spread of observed data matches with that of random samples. However, a closer look reveals that the Galambos and GH copulas exhibit upper-tail dependence that does not have similar representation in the observed data. Also, very high flows with moderate volumes are not represented by the simulated set. The simulated sets of the other four copulas provide adequate representation, except for the differences around the lower tail where the AMH and Clayton copulas seem to be performing better.

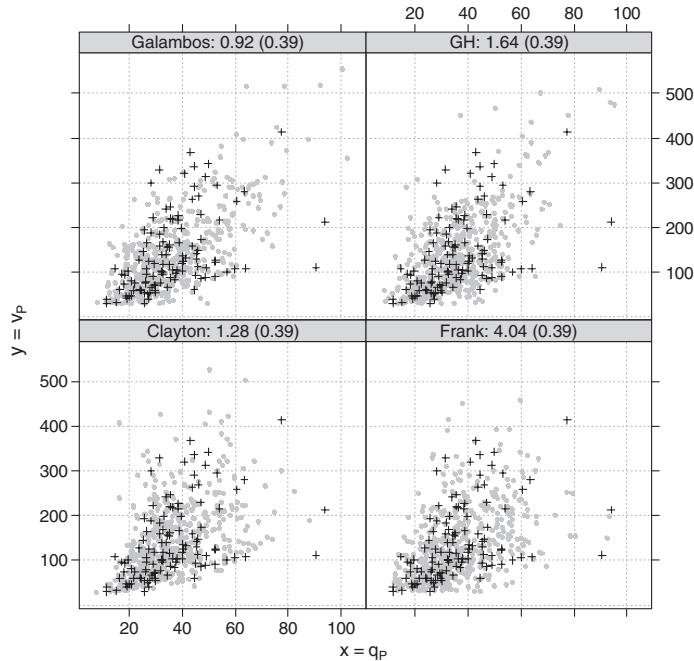


Figure 11-22. Comparison of observed and MOM method-based random samples for Example 11-1 for various copulas. Solid circles are random samples (size 500), whereas plus symbols represent observed data. Numbers in name strips are dependence parameter estimates with corresponding Kendall's tau values in parenthesis.

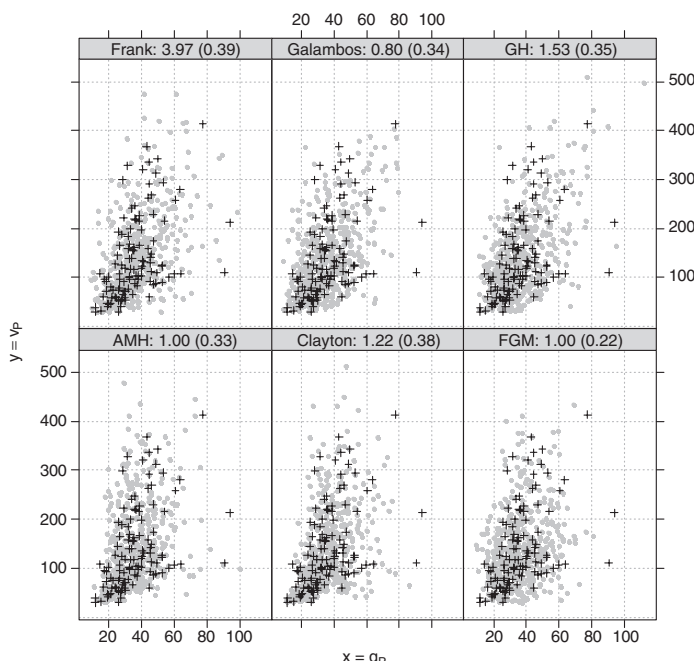


Figure 11-23. Comparison of observed and MPL method-based random samples for Example 11-1 for various copulas. Solid circles are random samples (size 500), whereas plus symbols represent observed data. Numbers in name strips are dependence parameter estimates with corresponding Kendall's tau values in parenthesis.

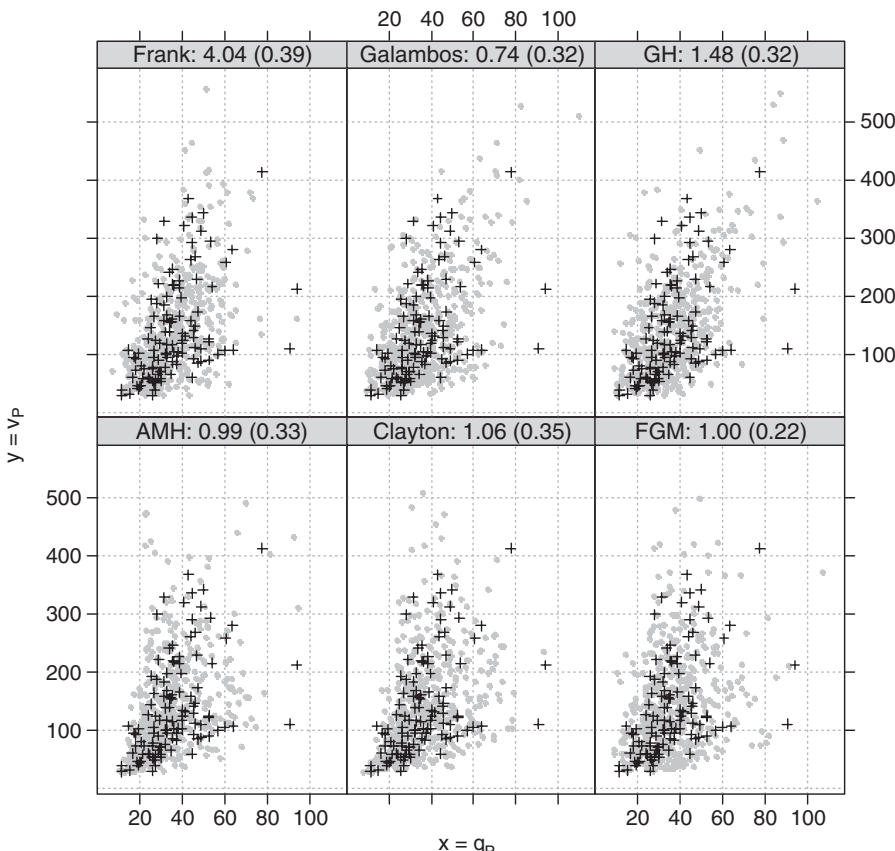


Figure 11-24. Comparison of observed and IFM method-based random samples for Example 11-1. Solid circles are random samples (size 500), whereas plus symbols represent observed data. Numbers in name strips are dependence parameter estimates with corresponding Kendall's tau values in parenthesis.

Second, comparison of empirical probabilities with computed probabilities, which Figures 11-25 to 11-27 depict for the three-parameter estimation methods, reveals the extent to which the computed copula surface would fit the empirical copula surface of the scaled ranks of observed data. This comparison is shown in two ways: (1) as scatter plots with diagonal lines signifying equivalence, as in the top panels of these figures, and (2) as plots with respect to the ranked observation numbers, as in the lower panels. The matching for the AMH and Clayton copulas, followed by the Frank copula, is better than for the other three copulas, with differences between computed and empirical probabilities being minimal for the Clayton copula.

Third, comparison of empirical and computed probability distributions of the BIPIT variate $K_n(w)$ and $K_{\theta_n}(w)$, given in Figures 11-28 to 11-30 for the three methods, shows that the matching is best for the Clayton copula, followed by the AMH and Frank copulas. Finally, the generalized K-plots in Figures 11-31 to 11-33 provide comparison of observed and expected order statistics of the BIPIT variate. Again, the figures show that the matching is best for the Clayton copula, followed again by the AMH and Frank copulas. The graphical fit for the Clayton copula is clearly the best in all the four graphical methods, among the six copulas considered. The relative superiority can, however, be further established by looking at error statistics and results of the formal statistical tests.

11.4.1.5 Various Error Statistics of Fit

A quantitative assessment of the performance of various copula families is made by comparing the maximized log-likelihood values. As all the copulas considered in this study involve fitting a single

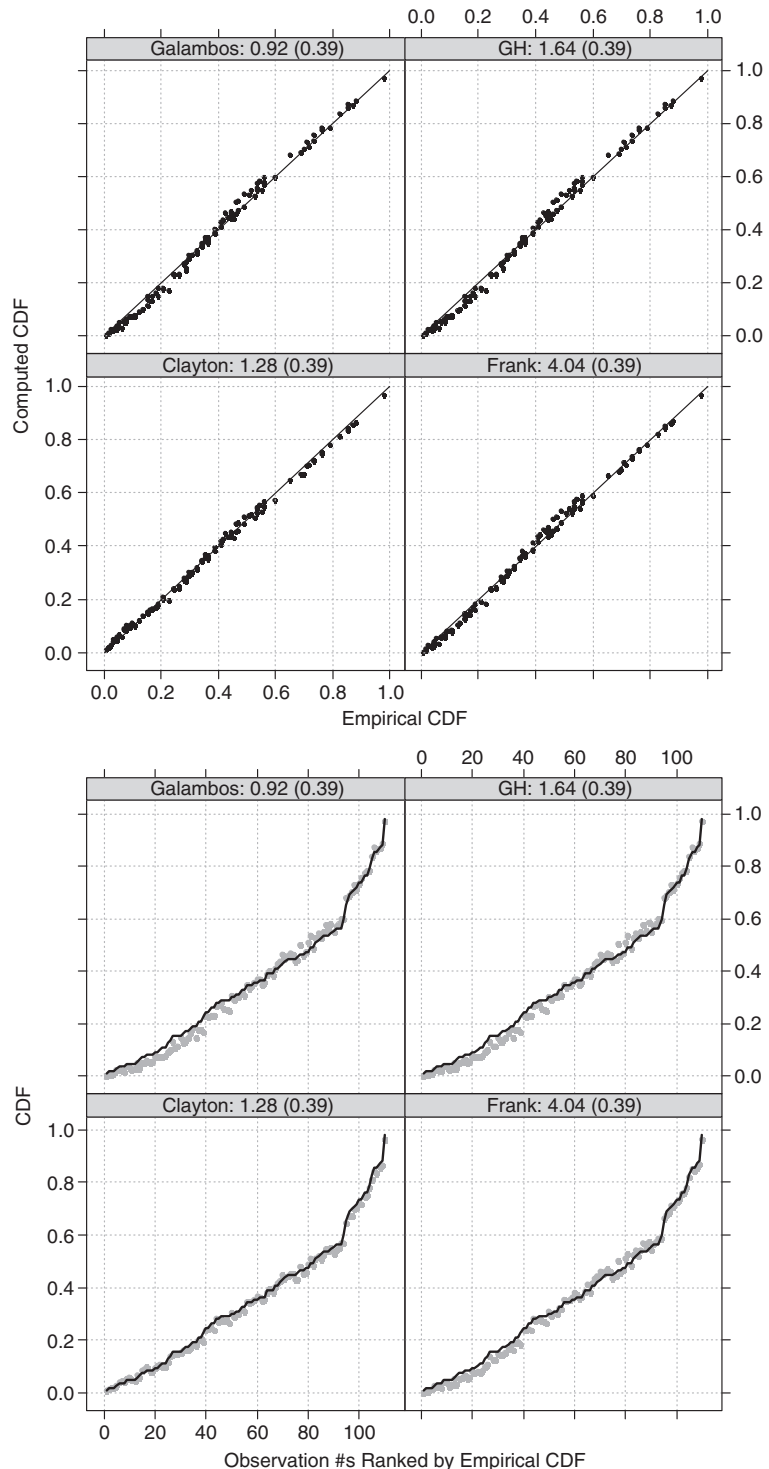


Figure 11-25. Comparison of empirical and MOM method-based computed probabilities for Example 11-1 for various copulas. In the top panel, the comparison takes the form of a scatter plot with a diagonal line signifying equivalence. In the lower panel, the comparison is with respect to ranked observation numbers with solid circles for empirical probabilities and solid lines for the computed probability. Numbers in name strips are dependence parameter estimates with corresponding Kendall's tau values in parenthesis.

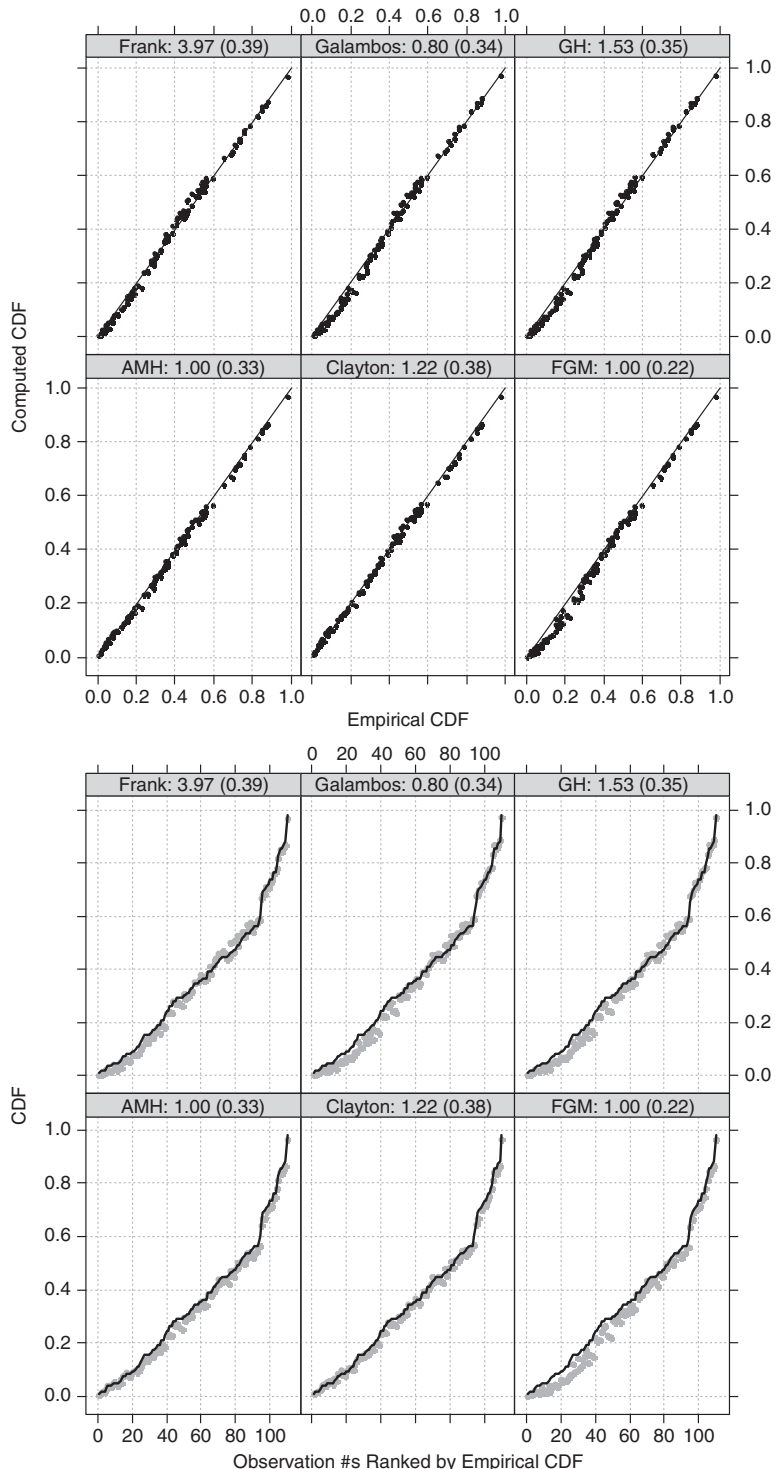


Figure 11-26. Comparison of empirical and MPL method-based computed probabilities for Example 11-1 for various copulas. In the top panel, the comparison takes the form of a scatter plot with diagonal lines signifying equivalence. In the lower panel, the comparison is with respect to ranked observation numbers with solid circles for empirical probabilities and solid lines for the computed probability. Numbers in name strips are dependence parameter estimates with corresponding Kendall's tau values in parenthesis.

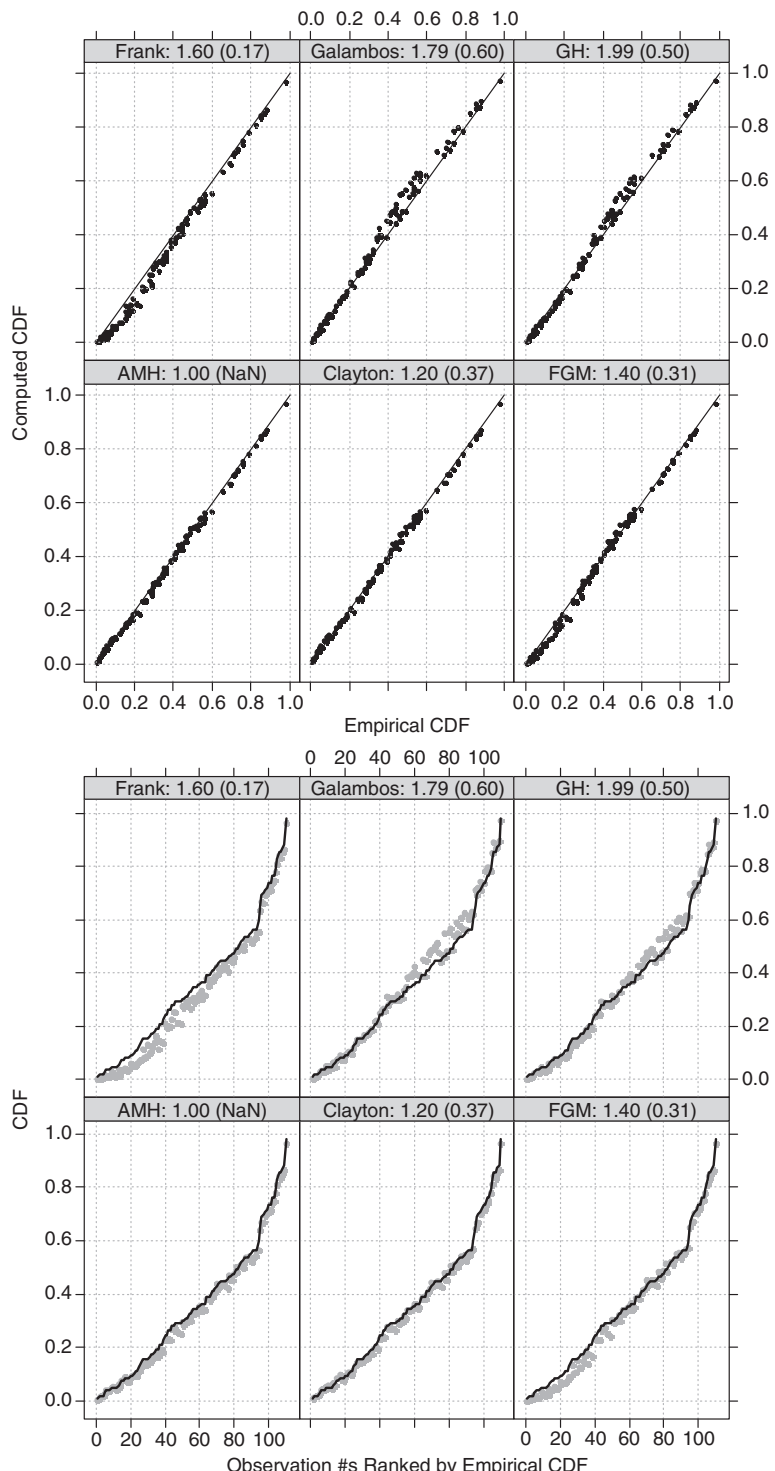


Figure 11-27. Comparison of empirical and IFM method-based computed probabilities for Example 11-1 for various copulas. In the top panel, the comparison takes the form of a scatter plot with diagonal lines signifying equivalence. In the lower panel, the comparison is with respect to ranked observation numbers with solid circles for empirical probabilities and solid lines for the computed probability. Numbers in name strips are dependence parameter estimates with corresponding Kendall's tau values in parenthesis.

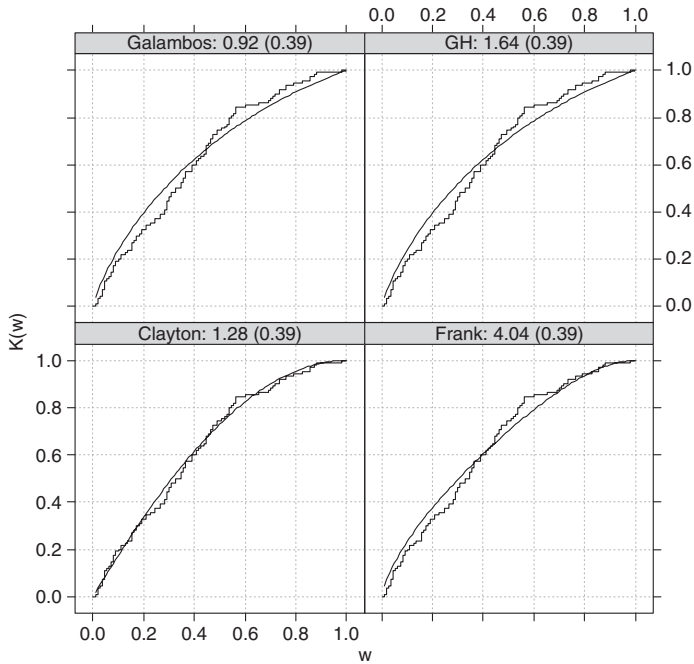


Figure 11-28. Graphical goodness-of-fit test using K-plots for MOM method-based estimation for Example 11-1 for various copulas. Step functions are empirical distributions $K_n(w)$, and curves are theoretical distributions $K_{\theta_n}(w)$ of the bivariate integral transform variable $W = C(U, V)$. Numbers in name strips are dependence parameter estimates with corresponding Kendall's tau values in parenthesis.

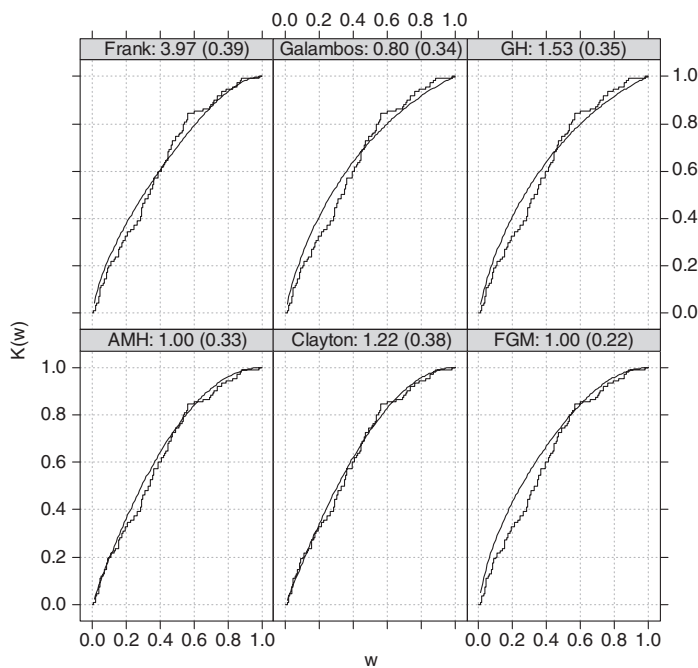


Figure 11-29. Graphical goodness-of-fit test using K-plots for MPL method-based estimation for Example 11-1 for various copulas. Step functions are empirical distributions $K_n(w)$, and curves are theoretical distributions $K_{\theta_n}(w)$ of the bivariate integral transform variable $W = C(U, V)$. Numbers in name strips are dependence parameter estimates with corresponding Kendall's tau values in parenthesis.

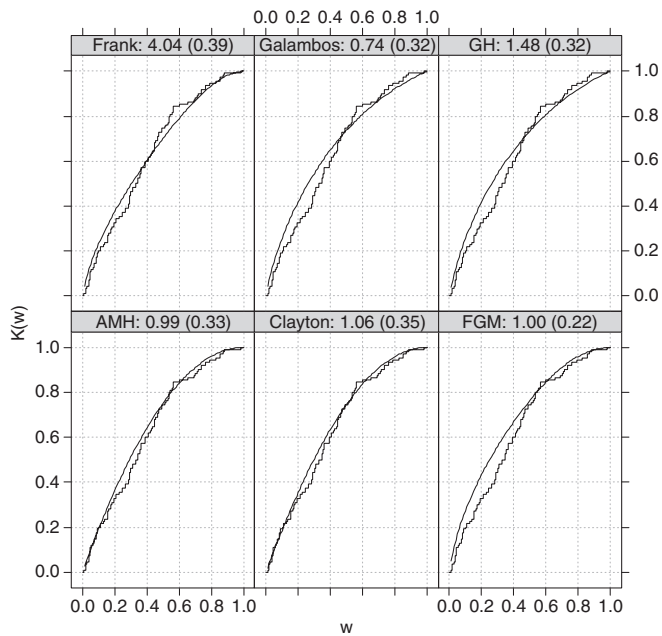


Figure 11-30. Graphical goodness-of-fit test using K-plots for IFM method-based estimation for Example 11-1 for various copulas. Step functions are empirical distributions $K_n(w)$, and curves are theoretical distributions $K_{\theta_n}(w)$ of the bivariate integral transform variable $W = C(U, V)$. Numbers in name strips are dependence parameter estimates with corresponding Kendall's tau values in parenthesis.

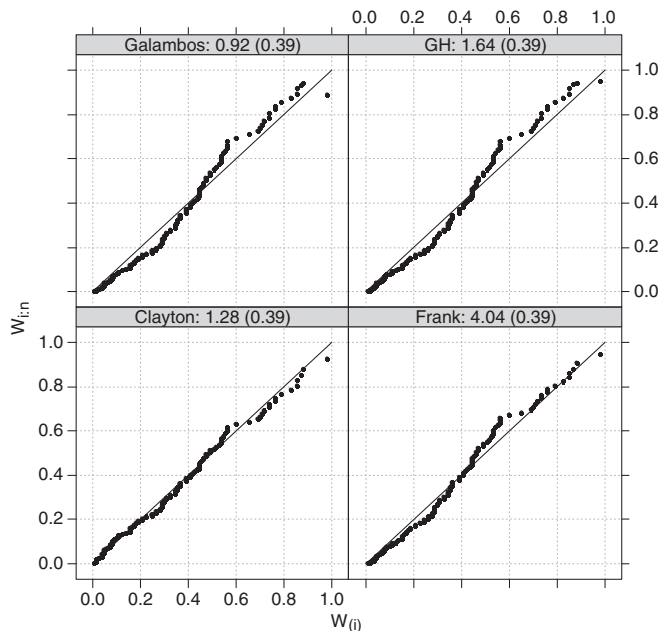


Figure 11-31. Graphical goodness-of-fit test using generalized K-plots for MOM method-based estimation for Example 11-1 for various copulas. The diagonal line indicates equivalence between observed $W_{(i)}$ and corresponding expected $W_{i:n}$ order statistics of the bivariate probability integral transform variable $W = C(U, V)$. Numbers in name strips are dependence parameter estimates with corresponding Kendall's tau values in parenthesis.

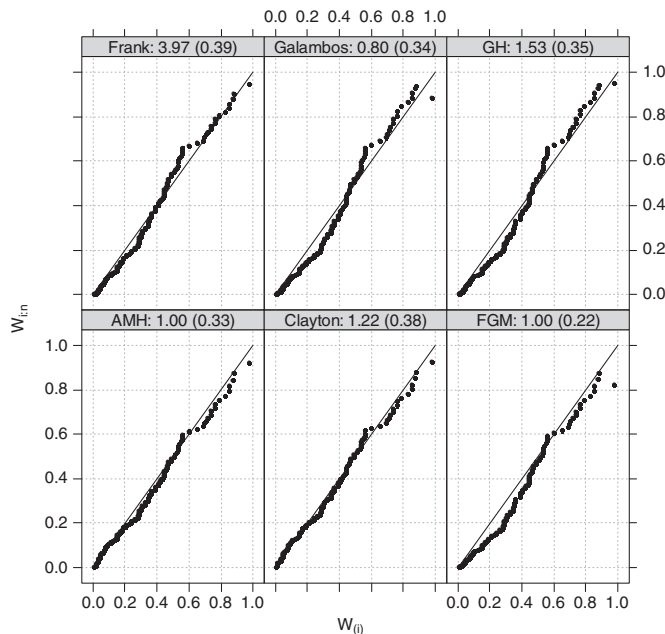


Figure 11-32. Graphical goodness-of-fit test using generalized K-plots for MPL method-based estimation for Example 11-1 for various copulas. The diagonal line indicates equivalence between observed $W_{(i)}$ and corresponding expected $W_{i:n}$ order statistics of the bivariate probability integral transform variable $W = C(U, V)$. Numbers in name strips are dependence parameter estimates with corresponding Kendall's tau values in parenthesis.

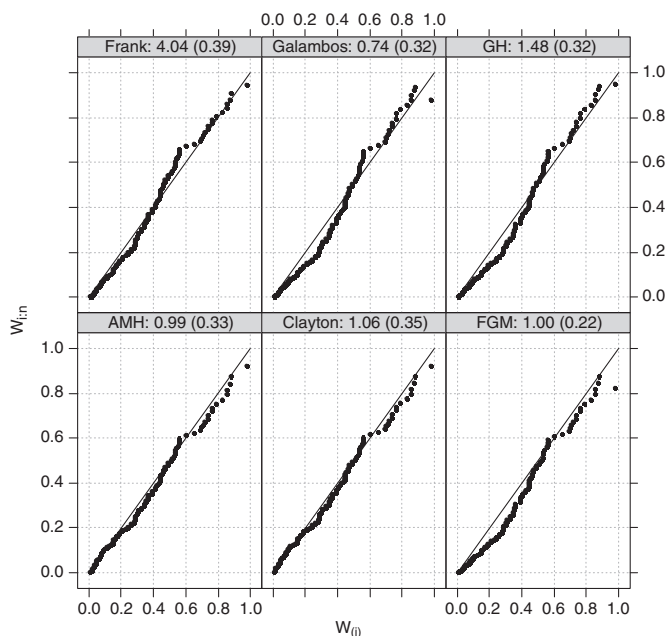


Figure 11-33. Graphical goodness-of-fit test using generalized K-plots for IFM method-based estimation for Example 11-1 for various copulas. The diagonal line indicates equivalence between observed $W_{(i)}$ and corresponding expected $W_{i:n}$ order statistics of the bivariate probability integral transform variable $W = C(U, V)$. Numbers in name strips are dependence parameter estimates with corresponding Kendall's tau values in parenthesis.

Table 11-8. Various Error Statistics for Example 11-1 for the Six Copulas under Consideration with Respect to the Three Estimation Methods.

Method/copula family	RMSE	MN-A-ERR	MN-ERR	MX-A-ERR
MOM				
Clayton	0.013	0.011	0.007	0.034
Frank	0.019	0.016	0.007	0.047
Galambos	0.022	0.018	0.007	0.059
GH	0.022	0.018	0.007	0.059
MPL				
AMH	0.018	0.015	0.014	0.047
Clayton	0.014	0.012	0.008	0.036
FGM	0.034	0.029	0.029	0.082
Frank	0.019	0.016	0.007	0.048
Galambos	0.025	0.020	0.012	0.068
GH	0.024	0.020	0.012	0.067
IFM				
AMH	0.018	0.015	0.014	0.046
Clayton	0.014	0.012	0.009	0.037
FGM	0.024	0.020	0.017	0.064
Frank	0.040	0.035	0.035	0.091
Galambos	0.032	0.022	-0.017	0.086
GH	0.024	0.018	-0.006	0.064

parameter, comparing the maximized log-likelihood value or AIC value would be equivalent. The maximized log-likelihood values for the AMH and Clayton copulas, as given in Table 11-7, are greatest among the six copulas considered and support the conclusions drawn from the previous graphical goodness-of-fit tests. Table 11-8 shows other error statistics RMSE, MN-A-ERR, and MX-A-ERR, showing that the errors for the MOM method are lesser as those of the MPL and IFM methods. The Clayton copula yields the lowest errors in all cases except two of the three methods of parameter estimation. For the MOM method, the FGM copula yields the largest errors in all these error categories. The reasoning for the poor performance of the FGM copula is obvious, as this copula admits τ up to 0.222 only, whereas the sample estimate is much higher at 0.391. A comparatively better performance of the AMH copula than the FGM copula may be attributed to the fact that although this copula also does not cover the desired range of τ , the shortfall from the largest permissible value of 0.333 is not that large. Thus, from the point of view of all these error statistics the Clayton copula may be taken to have performed better than all others, which is consistent with the inference from graphical results.

11.4.1.6 Analytical Goodness-of-Fit Tests

The formal goodness-of-fit tests are carried out for the three-parameter estimation methods by evaluating the Cramer-von Mises type statistics CM_n , S_n , and T_n . For this, a parametric bootstrap procedure is employed for simulating random samples of sizes 100; 1,000; and 10,000. The values of these three statistics, their p-values, and the critical values at the 5% significance level are computed. Simulations are run for each combination of sample size, copula, and method of estimation, except for the Galambos copula for which only the 100 and 1,000 sample size runs were made due to large computational time requirements. [Chowdhary et al. \(2011\)](#) present results from another set of three simulations for each of these cases for sample sizes 100; 1,000; 10,000; and 100,000. An important observation in all these cases is that values of these statistics stabilize sufficiently, even when the

sample size is 10,000, which is also in agreement with the observations made by Genest and Favre (2007). Tables 11-9 to 11-11 list the simulation results for the three methods of parameter estimation. These tests were not carried for the AMH and FGM copulas for the MOM and MPL methods and for

Table 11-9. Goodness-of-Fit Statistics for Example 11-2 for the MOM Method.

Statistic	Copula	Observed statistic	Critical test statistic S^* and P-value for a run of $N =$					
			100		1,000		10,000	
			S^*	P-val	S^*	P-val	S^*	P-val
CM_n	Clayton	2.115	3.448	0.480	3.779	0.541	3.828	0.522
	Frank	4.228	3.582	0.010	3.820	0.034	3.838	0.030
	Galambos	6.095	3.431	0.000	3.839	0.003	–	–
	GH	6.051	4.111	0.000	3.583	0.003	3.687	0.001
S_n	Clayton	0.065	0.148	0.510	0.150	0.511	0.153	0.526
	Frank	0.226	0.155	0.000	0.149	0.002	0.156	0.005
	Galambos	0.331	0.155	0.000	0.157	0.000	–	–
	GH	0.329	0.165	0.000	0.152	0.000	0.153	0.000
T_n	Clayton	0.706	0.993	0.420	0.958	0.414	0.976	0.429
	Frank	0.964	1.039	0.480	1.040	0.483	1.038	0.506
	Galambos	1.141	1.022	0.000	1.026	0.009	–	–
	GH	1.136	1.011	0.000	1.026	0.009	1.029	0.007

Note: S^* implies critical value of the test statistic at a significance level of 5%, and P-val indicates the p-values of the observed test statistic.

Table 11-10. Goodness-of-Fit Statistics for Example 11-1 for the MPL Method.

Statistic	Copula	Observed statistic	Critical test statistic S^* and P-value for a run of $N =$					
			100		1,000		10,000	
			S^*	P-val	S^*	P-val	S^*	P-val
CM_n	AMH	4.290	6.228	0.220	7.133	0.230	7.259	0.227
	Clayton	3.402	4.906	0.240	5.693	0.244	5.563	0.257
	Frank	4.223	4.141	0.050	3.855	0.032	3.981	0.035
	Galambos	8.488	4.900	0.000	–	–	–	–
S_n	GH	8.165	4.428	0.000	4.751	0.001	4.718	0.002
	AMH	0.167	0.240	0.170	0.251	0.179	0.259	0.183
	Clayton	0.123	0.170	0.240	0.191	0.227	0.192	0.226
	Frank	0.225	0.158	0.010	0.152	0.003	0.159	0.005
T_n	Galambos	0.499	0.226	0.000	–	–	–	–
	GH	0.483	0.183	0.000	0.190	0.000	0.196	0.001
	AMH	1.011	1.109	0.080	1.106	0.121	1.137	0.126
	Clayton	0.917	1.012	0.140	1.061	0.143	1.044	0.145
	Frank	0.964	1.032	0.480	1.033	0.483	1.033	0.495
	Galambos	1.409	1.087	0.000	–	–	–	–
	GH	1.389	1.080	0.000	1.082	0.001	1.089	0.001

Note: S^* implies critical value of the test statistic at a significance level of 5%, and P-val indicates the p-values of the observed test statistic.

Table 11-11. Goodness-of-Fit Statistics for Example 11-1 for the IFM Method.

Statistic	Copula	Observed statistic	Critical test statistic S^* and P-value for a run of $N =$					
			100		1,000		10,000	
			S^*	P-val	S^*	P-val	S^*	P-val
CM_n	Clayton	2.356	4.299	0.410	4.900	0.423	4.831	0.428
	Frank	4.277	3.485	0.020	3.915	0.028	3.767	0.026
	Galambos	7.309	5.007	0.020	—	—	—	—
	GH	7.206	3.586	0.000	3.955	0.000	3.984	0.001
S_n	Clayton	0.076	0.132	0.350	0.158	0.393	0.156	0.401
	Frank	0.230	0.156	0.000	0.159	0.005	0.153	0.005
	Galambos	0.425	0.184	0.000	—	—	—	—
	GH	0.421	0.165	0.000	0.181	0.000	0.177	0.000
T_n	Clayton	0.762	0.857	0.240	0.967	0.270	0.967	0.283
	Frank	0.968	1.048	0.490	1.039	0.481	1.040	0.486
	Galambos	1.310	1.062	0.000	—	—	—	—
	GH	1.304	1.053	0.010	1.066	0.000	1.066	0.001

Note: S^* implies critical value of the test statistic at a significance level of 5%, and P-val indicates the p-values of the observed test statistic.

the FGM copula for the IFM method as the dependence range did not include the sample estimates in these cases. The results for all three statistics from any of the three methods do not provide any evidence for rejecting the hypothesis of the Clayton copula as a valid model for the peak flow and volume data under consideration. For the IFM method, the results for the AMH copula also do not provide any evidence for rejection. At the same time, the basis for rejecting the hypothesis of the Frank, Galambos, and GH copulas being viable models at the 5% significance level is overwhelming. Barring a partial support for the Frank copula in terms of the T_n statistic, this inadequacy of support for these three copulas is based on the results of all three statistics for all three methods.

Thus, all the graphical and analytical goodness-of-fit test results indicate nonrejection of the Clayton copula as a suitable copula for the flood peak flow and volume data under consideration. The AMH copula may also be considered equally competitive for this specific dataset when IFM method is considered but may not be preferable in general as it admits a limited positive dependence only. At the same time, these results also provide sufficient basis for rejecting the Frank, Galambos, and GH copulas as viable options, at least for this dataset. Taking the MPL method-based Clayton copula as the finalized copula model for the joint distribution of peak flow and volume data under consideration, Figure 11-34 gives the joint probabilities and densities in the original domains of the variables. The left panel provides a perspective view of joint probability and density, while the right panel gives the corresponding contours. Figure 11-34a illustrates a close match between computed and empirical probabilities, wherein the observed data are plotted over the joint probability surface.

11.4.2 Example 11-2: Storm Duration and Depth

This example uses the hourly rainfall data from the Baton Rouge metropolitan airport station in Louisiana, USA, for 60 hydrological years from 1947 to 2006 for obtaining their joint distribution. A period of 6 h of rainfall hiatus is considered for defining rainfall events to enhance mutual independence of various rain events. A minimum of one tenth of an inch of rainfall qualifies to be counted as a rainfall event. The yearly extreme event is selected on the basis of the storm that has the largest rainfall volume (i.e., rainfall depth), resulting in identification of 60 rain storms. From the

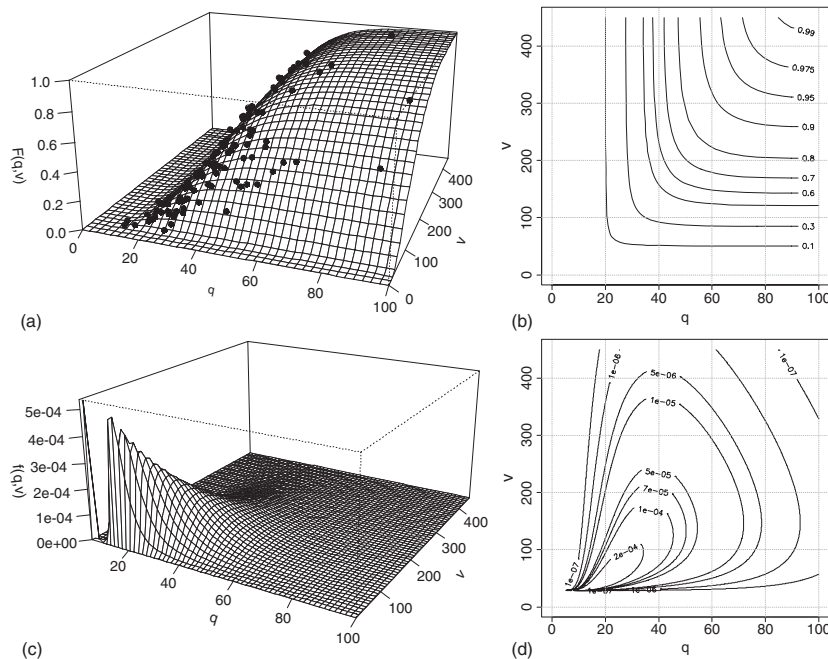


Figure 11-34. Three dimensional and contour plots of joint probability functions for Example 11-1 along with superimposed empirical probabilities in the three-dimensional plot (subplots a and b); and joint density functions as three dimensional and contour plots (subplots c and d).

hourly observations of these annual maximum storms, storm depth (i.e., volume per unit area) V_p in in. and storm duration D_p in hours are obtained. The left-side panel of Figure 11-35 shows the time series of these two variables.

Several candidate distributions, such as normal, LN2 and LN3, G2, P3, LP3, LEV, and two- and three-parameter Weibull are considered for fitting the annual maximum storm depth, duration, average intensity, and maximum intensity on a univariate basis. Based on the Kolmogorov-Smirnov, Anderson Darling, and chi-squared fit statistics and the overall fit of the QQ plots, LP3 and W3 distributions were selected as marginal distributions for these four variables, respectively. Table 11-12 gives the MLEs and corresponding standard errors for the parameters of these marginals. The right-side panel of Figure 11-35 shows the overlay of probability density curves of these distributions and the corresponding histograms. The corresponding QQ plots, along with 95% confidence intervals, are shown in Figure 11-36. The confidence bands indicate comparatively moderate uncertainty in parameter estimation, which is expected for a 60 year dataset.

11.4.2.1 Dependence Structure and Copula Test Space

Figure 11-37 shows the scatter plots of the bivariate data of annual maximum storm duration ($X = D_p$) and depth ($Y = V_p$), of their scaled ranks, and of the computed probabilities (\hat{F}_X, \hat{F}_Y), along with the respective histograms. Being empirical probabilities, scaled ranks are roughly uniformly distributed between 0 and 1. The histograms for computed probabilities are not nearly as uniform as those of the scaled ranks, as observed data are not sufficient to match the expected frequency of occurrence in all ranges satisfactorily. These scatter plots indicate a moderate positive association between storm duration and depth. The sample estimates of Pearson's correlation coefficient, Kendall's tau, and Spearman's rho of 0.445, 0.238, and 0.351, with corresponding p-values of 3.0e-04, 0.007, and 0.006, respectively, corroborate this assertion. Both chi- and K-plots also indicate a weak positive dependence (Figures 11-38a and 11-38b). Considering data exclusively

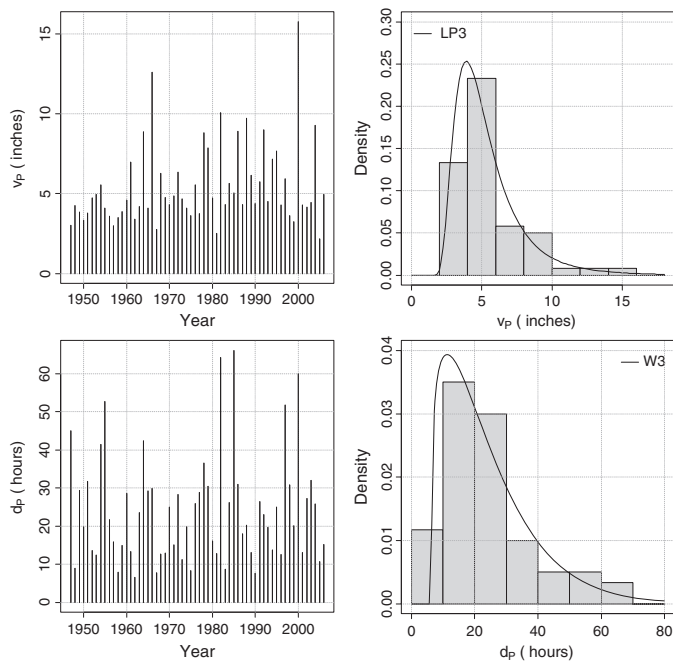


Figure 11-35. Time series (left-side panel) and histograms (right-side panel) of annual maximum storm depth V_p (in in.) and duration D_p (in hours) for Baton Rouge rainfall station. The fitted probability density functions of LP3 and W3 distributions are plotted over the respective histograms.

Table 11-12. Maximum Likelihood Parameter Estimates for the Selected Distributions for Annual Maximum Storm Depth V_p and Storm Duration D_p for Baton Rouge Rainfall Station.

Variable	Finalized distribution	Parameter estimates			Standard errors		
		Location	Scale	Shape	Location	Scale	Shape
V_p	LP3	0.281	0.116	11.432	0.493	0.053	9.268
D_p	W3	6.383	18.891	1.238	0.306	2.137	0.144

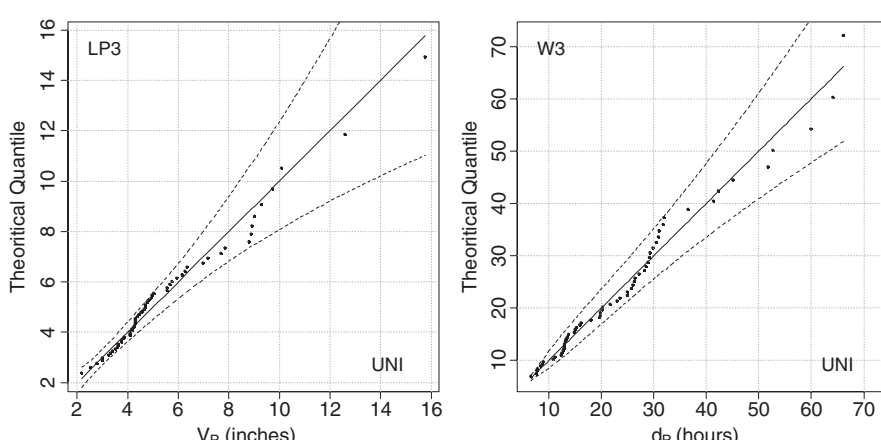


Figure 11-36. QQ plots for annual maximum storm depth V_p and storm duration D_p for Baton Rouge rainfall station data fitted with LP3 and W3 distributions, respectively.

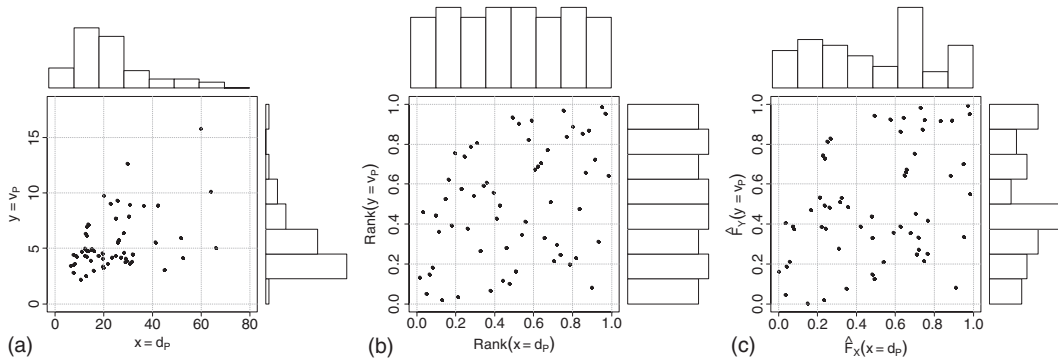


Figure 11-37. Scatter plots and histograms of observed bivariate annual maximum storm duration ($X = D_p$) and corresponding storm volume ($Y = V_p$) data of Baton Rouge rainfall station in (a) original domain, (b) as ranks, and (c) as W3 and LP3 computed probabilities, respectively.

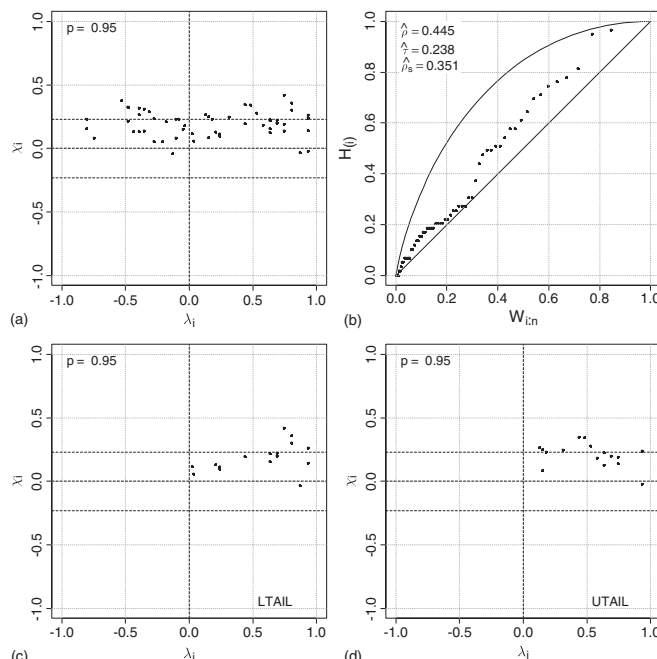


Figure 11-38. Characterization of dependence between annual maximum storm duration and depth for Example 11-2, using (a) chi-plot, (b) K-plot, (c) chi-plot for lower tail, and (d) chi-plot for upper tail.

from the lower-left and upper-right quadrants, as suggested by Abberger (2005), the chi-plots in Figures 11-38c and 11-38d exhibit lower- and upper-tail dependence features. Figure 11-38c clearly shows no evidence of the lower-tail dependence as none of the points close to $\lambda_i = 1$ are significant. Figure 11-38d does not indicate upper-tail dependence convincingly as only one point in the end zone is barely beyond the control limits corresponding to a p-value of 0.95. Based on a sample Kendall's tau value of 0.238 and features of lower- and upper-tail dependence, six copulas—AMH, Clayton, FGM, Frank, Galambos, and GH—are selected. Although the FGM copula admits a Kendall's tau value of up to 2/9 only, it is also short-listed because sometimes the estimated value by optimization may be lower than this limiting value. Although more copulas could have been considered at this initial screening stage, only these six are included in the copula test space to keep the process shorter.

11.4.2.2 Estimation of Dependence Parameter

The dependence parameters for the six copula families under consideration are estimated by the (1) MOM inversion of dependence measures and (2) MPL and IFM methods. Table 11-13 gives these point estimates along with standard errors and the interval estimates, corresponding to a coverage probability of 0.95. The estimate for the FGM copula is not obtainable for this dataset, as the value of τ is beyond the admissible limits of $-2/9$ to $2/9$ (or -0.222 to 0.222).

Table 11-13 includes the LL_{max} for the six copula families. These results show that the standard errors of the dependence parameter estimates from this method are much lower than those for the MOM method. Note that for the FGM copula, the optimal value of dependence parameter lies at the end of the parameter space and corresponds to a marginally lower value of τ than that obtained from the sample dataset. For the MPL method, the maximum log-likelihood value for the Galambos copula is largest among them all, followed by that of the GH copula. For the IFM method, the values for the Galambos copula followed by the GH copula are also higher. Except for the Clayton copula, the standard errors for the dependence parameter estimates from this method are similar to those for the MPL method. For the Clayton copula, the standard errors are substantially lesser for the MPL method, which corresponds to the much lower value of dependence parameter and consequently Kendall's tau value that is returned by the IFM method.

Thus, from the point of view of maximum log-likelihood values, the Galambos copula followed by the GH copula may be stated to be better for both the MPL and the IFM methods. Comparison of standard errors and confidence intervals among different copulas is not appropriate as the

Table 11-13. Point and Interval Dependence Parameter Estimates for Example 11-2 for the Six Copulas under Consideration with Respect to the Three Estimation Methods. Interval Estimates Correspond to a Coverage Probability of 0.95.

Method/ copula family	Theta ($\hat{\theta}$)	Tau ($\hat{\tau}_n / \hat{\tau}_0$)	Lower C.L.	Upper C.L.	Standard error	Conf. width	LL_{max}
MOM							
AMH	0.811	0.238	0.422	1.201	0.390	0.199	–
Clayton	0.626	0.238	0.064	1.188	0.562	0.287	–
Frank	2.251	0.238	0.559	3.943	1.692	0.863	–
FGM	0.580	0.238	0.264	0.897	0.316	0.161	–
GH	1.313	0.238	1.032	1.594	0.281	0.143	–
MPL							
AMH	0.802	0.235	0.574	1.030	0.228	0.117	3.918
Clayton	0.543	0.214	0.360	0.726	0.183	0.093	3.937
FGM	0.995	0.221	0.800	1.190	0.195	0.100	3.778
Frank	2.290	0.242	2.042	2.538	0.248	0.126	3.929
Galambos	0.633	0.268	0.417	0.849	0.216	0.110	5.369
GH	1.351	0.260	1.126	1.576	0.225	0.115	5.130
IFM							
AMH	0.804	0.236	0.582	1.026	0.222	0.113	4.546
Clayton	0.385	<u>0.161</u>	0.067	0.703	0.318	0.162	3.244
FGM	0.995	0.221	0.808	1.182	0.187	0.096	4.466
Frank	2.491	0.261	2.246	2.736	0.245	0.125	4.717
Galambos	0.593	0.248	0.397	0.789	0.196	0.100	5.868
GH	1.315	0.240	1.102	1.528	0.213	0.109	5.473

dependence parameter has different scaling and sensitivity with respect to the association measures for various copulas. The MPL and IFM methods may be preferable over the MOM method as they result in significantly lower standard errors for the respective copulas.

11.4.2.3 Assessment of Copula Fitting

The relative suitability of plausible copula families is ascertained by employing (1) graphical methods, (2) error statistics, and (3) formal goodness-of-fit statistics.

11.4.2.4 Graphical Goodness-of-Fit Tests

First, the observed data are compared with a large number of generated random samples. For this application, a set of random samples of size 500 is generated for each of the six copula families under consideration, utilizing the MOM, MPL, and IFM method-based parameters. As the FGM copula does not cover the expected dependence range for the MOM method, it is not included in these plots. The Galambos copula is also dropped to maintain evenness in the figure. Figures 11-39 to 11-41 show this comparison of observed and randomly generated samples for the three-parameter estimation methods. These plots show that the general nature of the spread of observed data matches with that of the random samples. However, a closer look reveals that the AMH, Clayton, and FGM copulas do not represent higher-duration higher depth data well enough. The Frank copula also fails to represent the observed data with respect to the IFM method. The Galambos and

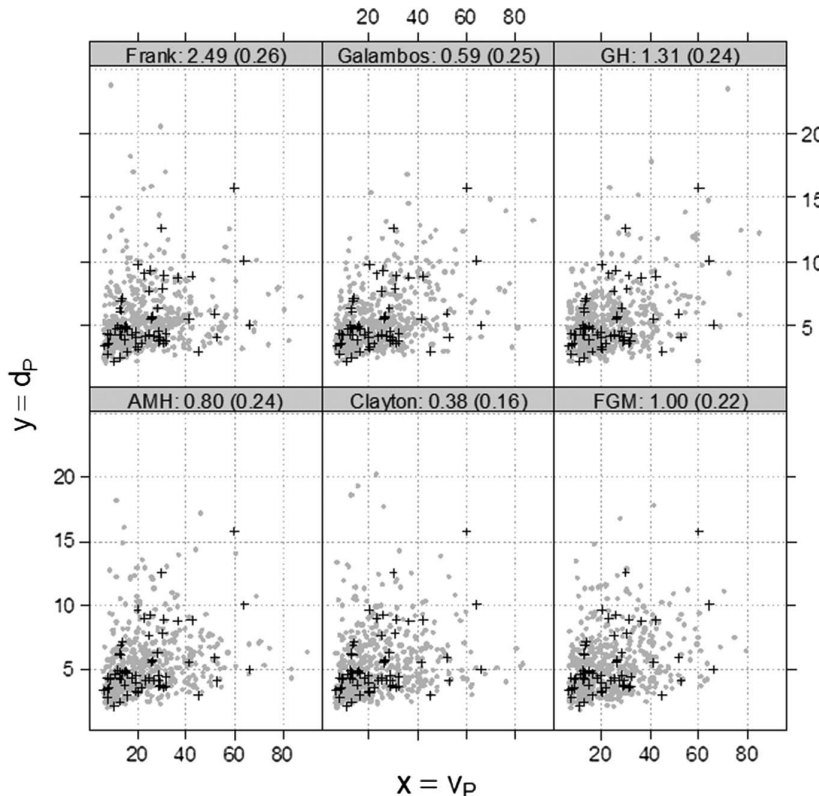


Figure 11-39. Comparison of observed and MOM method-based random samples for Example 11-2 for various copulas. Solid circles are random samples (size 500) and plus symbols are observed data. Numbers in name strips are dependence parameter estimates with corresponding Kendall's tau values in parenthesis.

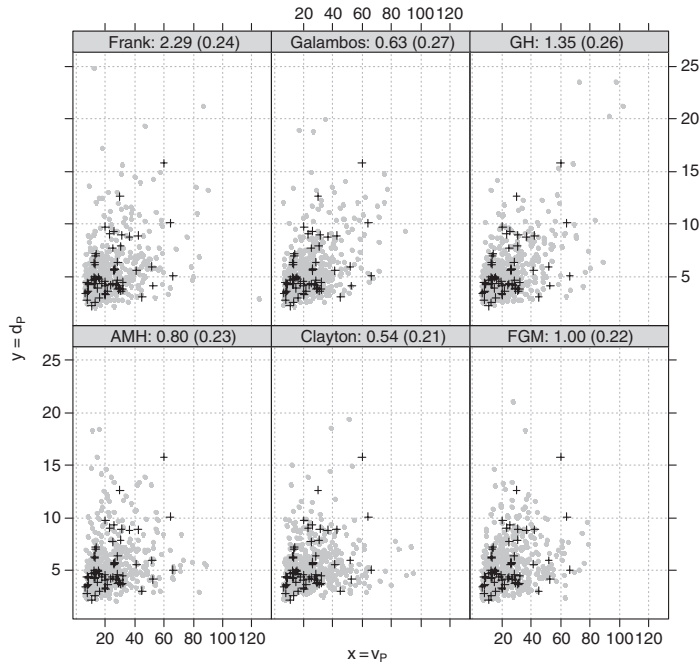


Figure 11-40. Comparison of observed and MPL method-based random samples for Example 11-2 for various copulas. Solid circles are random samples (size 500), and plus symbols are observed data. Numbers in name strips are dependence parameter estimates with corresponding Kendall's tau values in parenthesis.

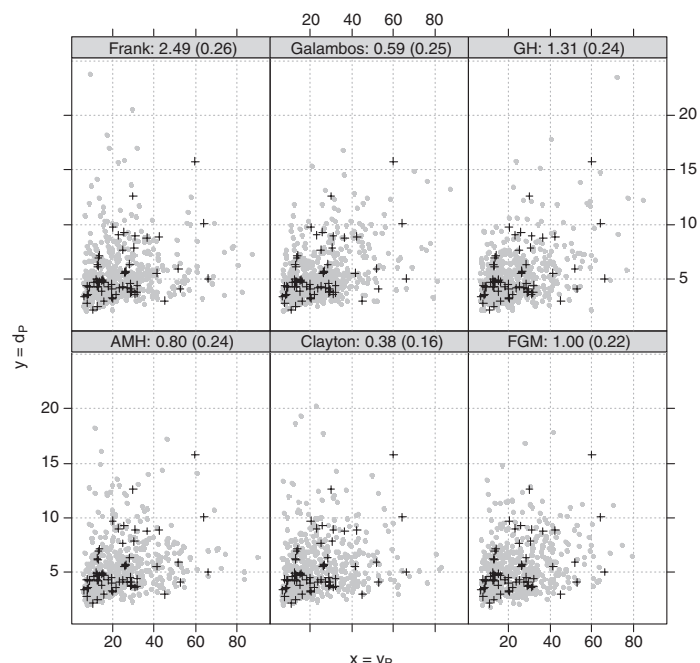


Figure 11-41. Comparison of observed and IFM method-based random samples for Example 11-2 for various copulas. Solid circles are random samples (size 500), and plus symbols are observed data. Numbers in name strips are dependence parameter estimates with corresponding Kendall's tau values in parenthesis.

GH copulas represent these extreme values better and indicate the possibility of a dataset possessing the upper-tail dependence.

Second, comparison of empirical probabilities with computed probabilities, as depicted in Figures 11-42 to 11-44 for the three methods of parameter estimation, reveals the extent to which the computed copula surface would fit the empirical copula surface of the scaled ranks of observed data. This comparison is shown in two ways: (1) as scatter plots with diagonal lines signifying equivalence, as in the top panels of these figures, and (2) as plots with respect to the ranked observation numbers, as in the lower panels. The matching for the GH copula is better than others for the MOM method, especially in the higher joint probability region. For the MPL and IFM methods, both the Galambos and GH copulas are better than all others, even when the differences in the lower region of probability are not significant. For the Clayton copula for the IFM method, in which a significant underestimation of dependence strength is present, the differences are not perceivable to that extent.

Third, the comparison of empirical and computed probability distributions of the BIPIT variate $K_n(w)$ and $K_{\theta_n}(w)$, given in Figures 11-45 to 11-47 for the three methods, shows that the matching is best for the Galambos and GH copulas, especially in the higher ranges of w . The matching for Clayton copula for the IFM method is most inferior, which may again be attributed to the underestimation of the dependence parameter. Finally, the generalized K-plots in Figures 11-48 to 11-50 provide comparison of observed and expected order statistics of the BIPIT variate. This comparison reveals the differences more effectively, clearly showing that the matching for the Galambos and GH copulas is much better and is worst for the Clayton copula.

11.4.2.5 Various Error Statistics of Fit

The maximized log-likelihood values for the Galambos and GH copulas (Table 11-13) are maximum among the six copulas considered and support the conclusions based on the previous graphical goodness-of-fit tests. Table 11-14 shows a comparison of other error statistics, RMSE, MN-A-ERR, and MX-A-ERR. The errors for all three methods are comparable with the exception of the Clayton copula for the IFM method. The reasoning for the poor performance of the Clayton copula for IFM is rooted in its inefficiency in capturing the correct dependence of the sample. Thus, from the point of view of these error statistics, all copulas perform about the same.

11.4.2.6 Analytical Goodness-of-Fit Tests

The formal goodness-of-fit tests are carried out for the three-parameter estimation methods by evaluating the Cramer-von Mises type statistics CM_n , S_n , and T_n . For this, a parametric bootstrap procedure is employed for simulating random samples of sizes 100; 1,000; and 10,000. The values of these three statistics, their p-values, and the critical values at the 5% significance level are computed. Two simulations are run for each combination of sample size, copula model, and method of estimation, except for the Galambos copula for which runs are not made owing to large time requirements, and the FGM for which the dependence parameter is out of the desirable range. An important observation in all cases is that the values of these statistics stabilize sufficiently when the sample size is 10,000, which is in agreement with the observations made by [Genest and Favre \(2007\)](#). Tables 11-15 to 11-17 list these results for the three methods of parameter estimation. The results for all the three statistics from any of the three methods do not provide any evidence for rejecting any of the copulas, except that the Clayton copula is on the verge of rejection on the basis of a few instances. Significantly higher p-values of the Galambos and GH copulas support the inferences made on the basis on graphical results and error statistics.

Thus, all the graphical and analytical goodness-of-fit test results indicate nonrejection of the Galambos and GH copulas and indicate their suitability for the annual maximum storm duration and depth data under consideration. Other copulas, even when they do not result in rejection by formal tests may not be preferred for this dataset as they do not fare well with respect to matching with random samples. Most comparisons being similar for the Galambos and GH copulas, those

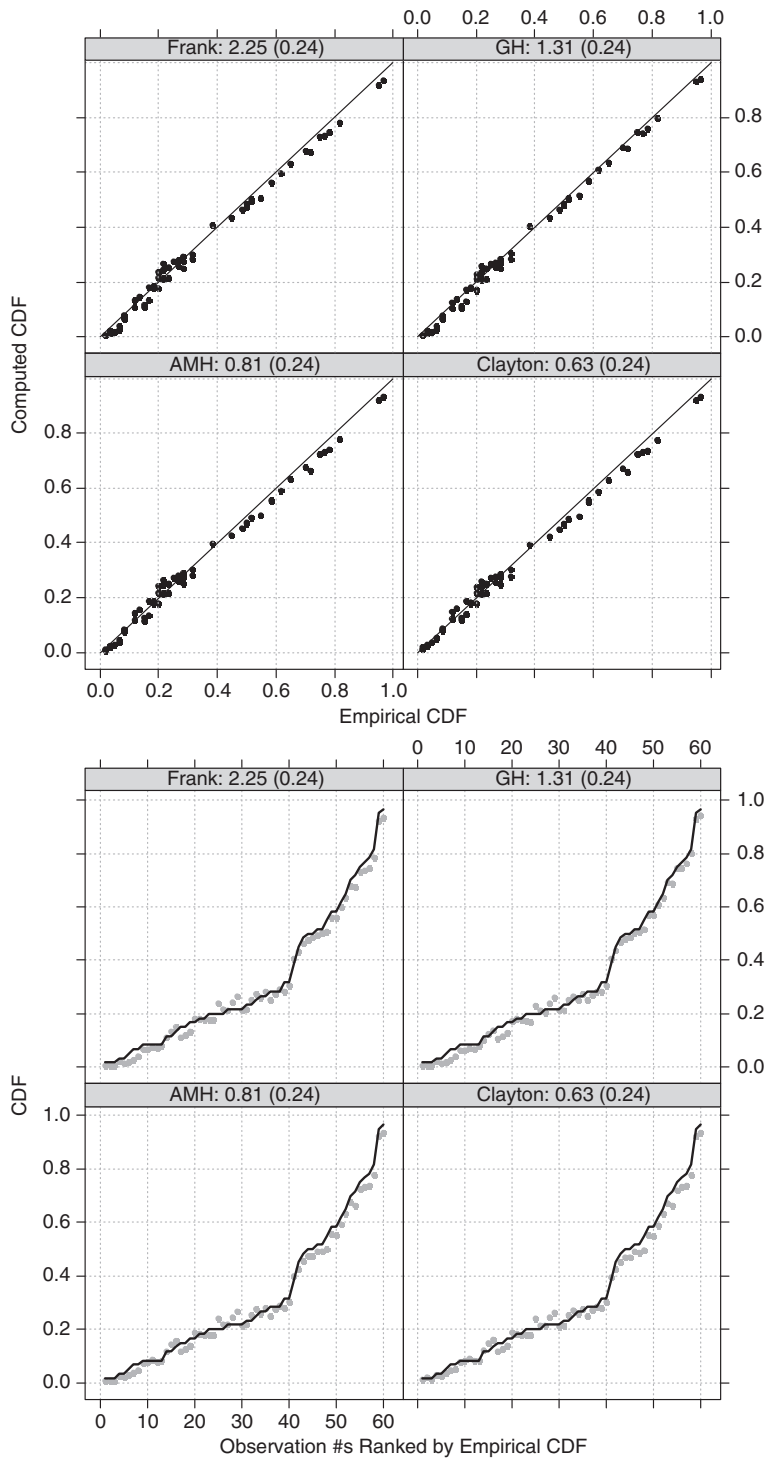


Figure 11-42. Comparison of empirical and MOM method-based computed probabilities for Example 11-2 for various copulas. In the top panel, the comparison takes the form of a scatter plot with diagonal lines signifying equivalence. In the lower panel, the comparison is with respect to ranked observation numbers, with solid circles for empirical probabilities and solid lines for computed probabilities. Numbers in name strips are dependence parameter estimates with corresponding Kendall's tau values in parenthesis.

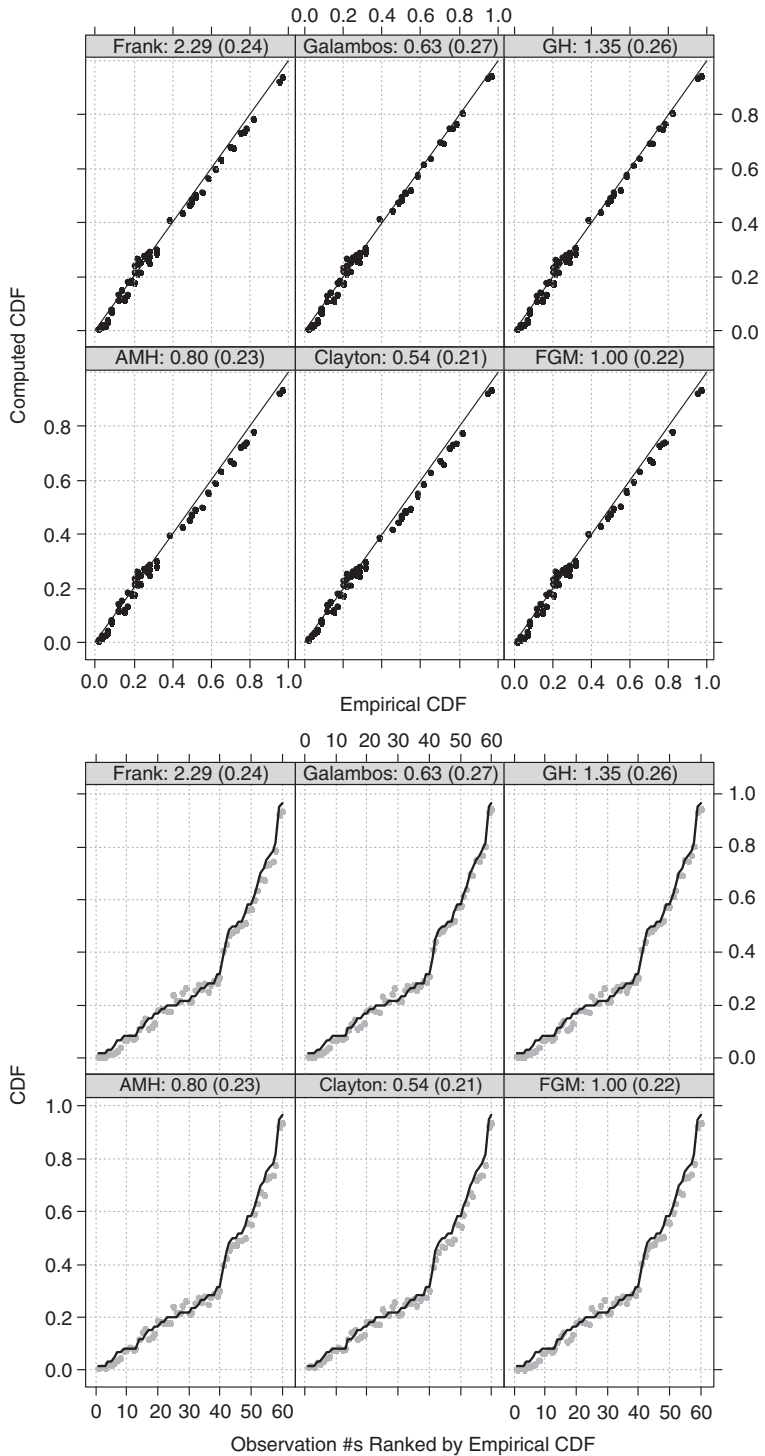


Figure 11-43. Comparison of empirical and MPL method-based computed probabilities for Example 11-2 for various copulas. In the top panel, the comparison takes the form of a scatter plot with diagonal lines signifying equivalence. In the lower panel, the comparison is with respect to ranked observation numbers, with solid circles for empirical probabilities and solid lines for computed probabilities. Numbers in name strips are dependence parameter estimates with corresponding Kendall's tau values in parenthesis.

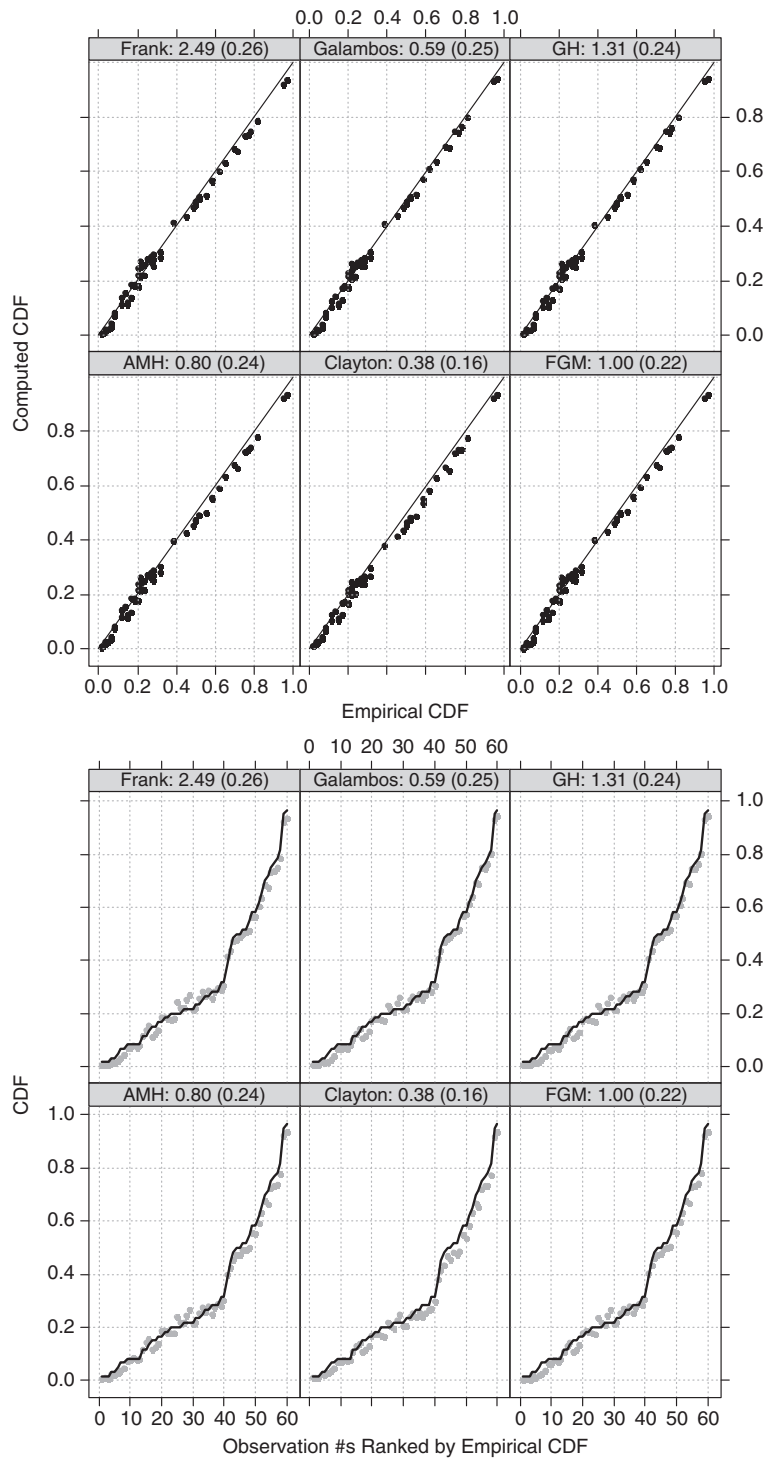


Figure 11-44. Comparison of empirical and IFM method-based computed probabilities for Example 11-2 for various copulas. In the top panel, the comparison takes the form of a scatter plot with diagonal lines signifying equivalence. In the lower panel, the comparison is with respect to ranked observation numbers, with solid circles for empirical probabilities and solid lines for computed probabilities. Numbers in name strips are dependence parameter estimates with corresponding Kendall's tau values in parenthesis.

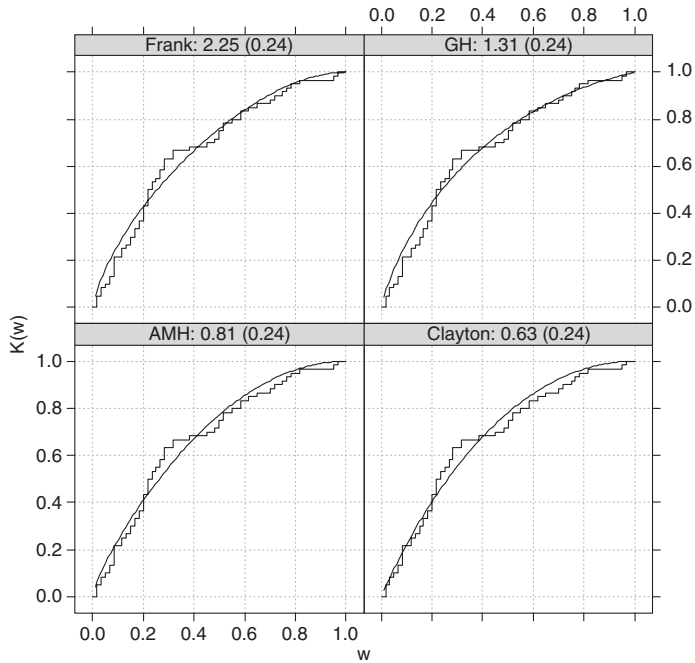


Figure 11-45. Graphical goodness-of-fit test using K-plots for MOM method-based estimation for Example 11-2 for various copulas. Step functions are empirical distributions $K_n(w)$, and curves are theoretical distributions $K_{\theta_n}(w)$ of the bivariate integral transform variable $W = C(U, V)$. Numbers in name strips are dependence parameter estimates with corresponding Kendall's tau values in parenthesis.

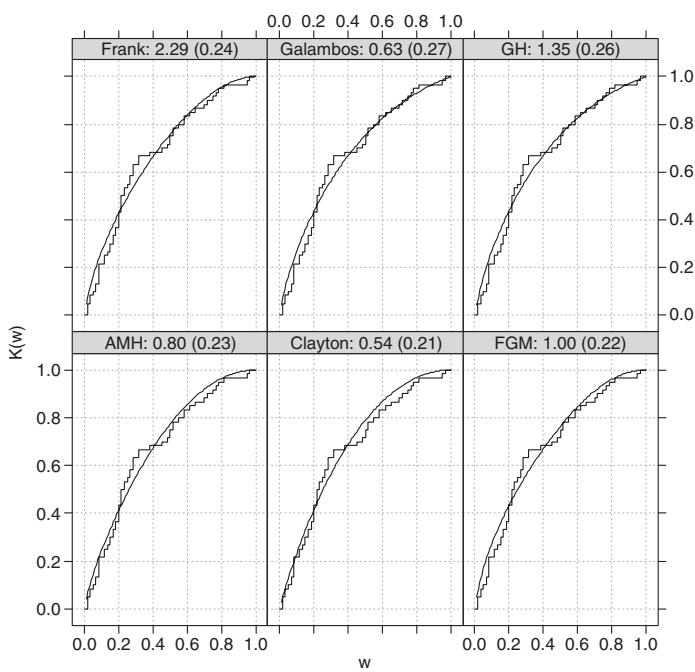


Figure 11-46. Graphical goodness-of-fit test using K-plots for MPL method-based estimation for Example 11-2 for various copulas. Step functions are empirical distributions $K_n(w)$, and curves are theoretical distributions $K_{\theta_n}(w)$ of the bivariate integral transform variable $W = C(U, V)$. Numbers in name strips are dependence parameter estimates with corresponding Kendall's tau values in parenthesis.

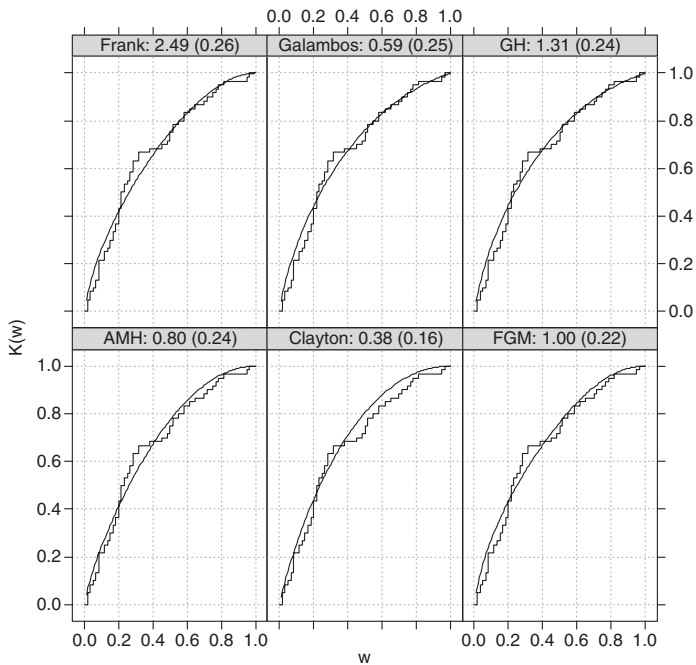


Figure 11-47. Graphical goodness-of-fit test using K-plots for IFM method-based estimation for Example 11-2 for various copulas. Step functions are empirical distributions $K_n(w)$, and curves are theoretical distributions $K_{\theta_n}(w)$ of the bivariate integral transform variable $W = C(U, V)$. Numbers in name strips are dependence parameter estimates with corresponding Kendall's tau values in parenthesis.

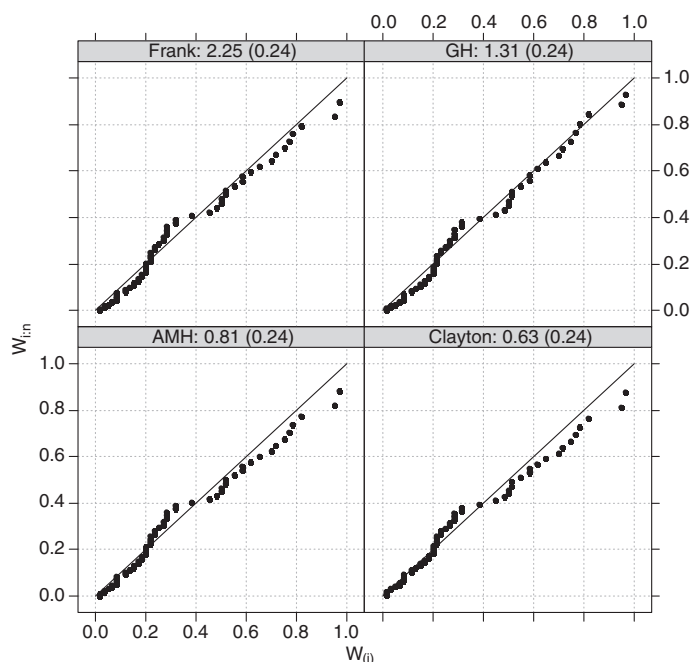


Figure 11-48. Graphical goodness-of-fit test using generalized K-plots for MOM method-based estimation for Example 11-2 for various copulas. The diagonal line indicates equivalence between observed $W_{(i)}$, and corresponding expected W_{in} order statistics of the bivariate probability integral transform variable $W = C(U, V)$. Numbers in name strips are dependence parameter estimates with corresponding Kendall's tau values in parenthesis.

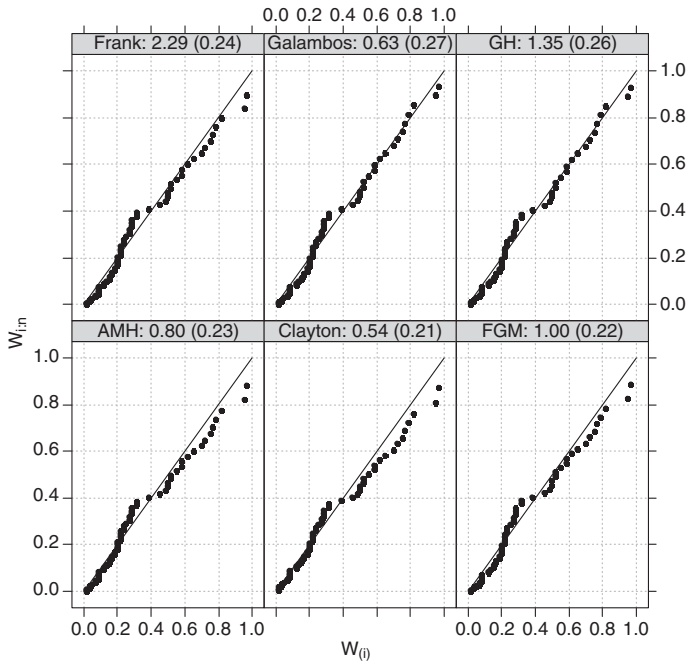


Figure 11-49. Graphical goodness-of-fit test using generalized K-plots for MPL method-based estimation for Example 11-2 for various copulas. The diagonal line indicates equivalence between observed $W_{(i)}$, and corresponding expected $W_{i:n}$ order statistics of the bivariate probability integral transform variable $W = C(U, V)$. Numbers in name strips are dependence parameter estimates with corresponding Kendall's tau values in parenthesis.

obtained from the IFM method may be preferred because the association parameter Kendall's tau returned by this method is closer to the sample estimate.

11.4.3 Example 11-3: Regional Flood Risk Management

With respect to flood hazard, the regional emergency management service is sized so as to provide adequate services to different affected areas within its jurisdiction. Optimal sizing is ascertained on the basis of likelihood of joint occurrence of floods in different regions. If less likelihood exists of simultaneous flooding of different subregions, then a smaller facility may suffice. However, owing to mutual dependence in risk of flooding in neighboring subregions, the likelihood of experiencing simultaneous flooding is usually more than their product likelihood. Furthermore, conditional probabilities of flooding in one subregion, given that the neighboring subregion experiences a certain level of flooding, is also different as compared with when the two processes are independent. This aspect is illustrated by considering annual peak flow data from two adjacent subbasins within Kanawha basin in West Virginia. The two subbasins considered are the Greenbrier and the Gauley subbasins. For the Greenbrier subbasin, the annual peak flow data at Hildale station (USGS ID #03184000) is considered, while for the Gauley subbasin, the annual peak flows at Mt. Outlook station on Meadow River (USGS ID #03190400) is considered. The Hildale station, at latitude $37^{\circ} 38' 24''$ and longitude $80^{\circ} 48' 19''$, has a drainage area of $1,619 \text{ mi}^2$, while the Mt. Outlook station, at latitude $38^{\circ} 11' 23''$ and longitude $80^{\circ} 56' 49''$, has a drainage area of 365 mi^2 . Hildale has 75 years of data from 1936 to 2011, while the Mt. Outlook station has 42 years of data from 1966 to 2011. The joint probability analysis, accomplished on the basis of 42 years of concurrent data at the two stations, attempts to answer the following three questions: (1) which copula(s) can adequately

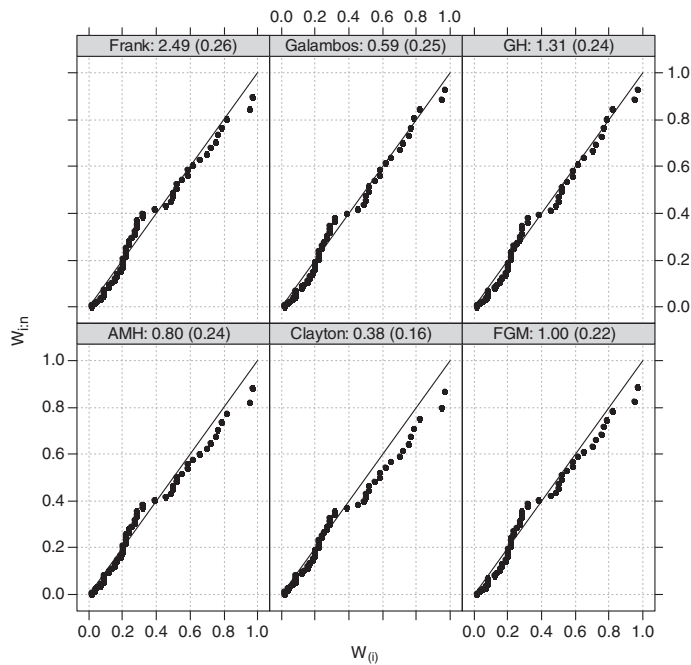


Figure 11-50. Graphical goodness-of-fit test using generalized K-plots for IFM method-based estimation for Example 11-2 for various copulas. The diagonal line indicates equivalence between observed $W_{(i)}$, and corresponding expected $W_{(i:n)}$ order statistics of the bivariate probability integral transform variable $W = C(U, V)$. Numbers in name strips are dependence parameter estimates with corresponding Kendall's tau values in parenthesis.

represent the simultaneous occurrence of annual peak flows in the two subbasins, (2) what is the return period of simultaneous occurrence of 100 year return period flows at both Hilldale and Mt. Outlook stations, and (3) what is the conditional probability of exceedance of 100 year return period flow in one subbasin, given that 100 year flow has been exceeded in the other subbasin?

The time series of annual peak flows at Hilldale (Qp_{HD}) and at Mt. Outlook (Qp_{MO}) obtained from the website of the National Water Information System of the USGS are shown in the left-side panel of Figure 11-51. Of the several candidate distributions considered, the LP3 and P3 are selected for the annual maximum peak flows at these two stations, respectively. Table 11-18 gives the MLEs and corresponding standard errors for parameters of these marginals. The overlay of probability density functions of these distributions and the corresponding histograms are shown in the right-side panel of Figure 11-51. The distribution fits are indicated by the corresponding QQ plots, along with 95% confidence intervals (Figure 11-52).

11.4.3.1 Dependence Structure and Copula Test Space

Figure 11-53 shows the scatter plots of the bivariate data of annual peak flow at Hilldale ($X = Qp_{HD}$) and Mt. Outlook ($X = Qp_{MO}$), of their scaled ranks, and of the computed probabilities (\hat{F}_X, \hat{F}_Y), along with the respective histograms. These scatter plots indicate a moderate positive association between the two peak flow series. The sample estimates of Pearson's correlation coefficient, Kendall's tau, and Spearman's rho of 0.489, 0.469, and 0.660 with corresponding p-values 0.001, 1.25e-05, and 2.0e-06, respectively, corroborate this assertion. A positive dependence is also indicated by both chi and K-plots (Figures 11-54a and 11-54b). Considering data from the lower-left and upper-right quadrants exclusively, chi-plots in Figures 11-54c and 11-54d exhibit lower- and upper-tail dependence

Table 11-14. Various Error Statistics for Example 11-2 for the Six Copulas under Consideration with Respect to the Three-Parameter Estimation Methods.

Method/Copula family	RMSE	MN-A-ERR	MN-ERR	MX-A-ERR
MOM				
AMH	0.025	0.021	0.012	0.052
Clayton	0.025	0.021	0.012	0.056
Frank	0.023	0.021	0.012	0.049
GH	0.021	0.018	0.012	0.045
MPL				
AMH	0.025	0.021	0.012	0.052
Clayton	0.026	0.022	0.015	0.058
FGM	0.024	0.021	0.013	0.048
Frank	0.023	0.020	0.011	0.050
Galambos	0.020	0.016	0.008	0.049
GH	0.020	0.017	0.009	0.048
IFM				
AMH	0.025	0.021	0.012	0.052
Clayton	0.029	0.024	0.021	0.062
FGM	0.024	0.021	0.013	0.048
Frank	0.023	0.020	0.009	0.053
Galambos	0.020	0.017	0.010	0.046
GH	0.021	0.018	0.011	0.045

Table 11-15. Goodness-of-Fit Statistics for Example II for MOM Method.

Statistic	Copula	Observed statistic	Critical test statistic S^* and P-value for a run of $N =$					
			100		1,000		10,000	
			S^*	P-val	S^*	P-val	S^*	P-val
CM_n	AMH	2.199	2.769	0.106	2.520	0.104	2.572	0.110
			2.205	0.067	2.512	0.113	2.540	0.109
		Clayton	2.275	2.460	0.100	2.503	0.083	2.514
			2.709	0.100	2.568	0.102	2.481	0.080
		Frank	1.974	2.616	0.220	2.454	0.153	2.405
			2.284	0.150	2.377	0.170	2.436	0.153
		GH	1.550	2.579	0.465	2.385	0.432	2.460
			2.317	0.490	2.376	0.409	2.442	0.432
	S_n	AMH	0.165	0.296	0.353	0.251	0.266	0.265
			0.261	0.292	0.269	0.306	0.266	0.287
		Clayton	0.132	0.210	0.300	0.224	0.297	0.246
			0.218	0.330	0.225	0.310	0.238	0.310
		Frank	0.207	0.251	0.150	0.234	0.095	0.240
			0.243	0.070	0.236	0.120	0.235	0.107
		GH	0.216	0.258	0.131	0.235	0.094	0.242
			0.253	0.140	0.250	0.095	0.243	0.103

(Continued)

Table 11-15. Goodness-of-Fit Statistics for Example II for MOM Method. (Continued)

Statistic	Copula	Observed statistic	Critical test statistic S* and P-value for a run of N =					
			100		1,000		10,000	
			S*	P-val	S*	P-val	S*	P-val
T_n	AMH	1.104	1.418	0.576	1.405	0.552	1.414	0.565
			1.422	0.551	1.423	0.575	1.410	0.567
	Clayton	0.911	1.308	0.510	1.242	0.515	1.268	0.535
			1.220	0.420	1.233	0.515	1.268	0.535
	Frank	1.260	1.423	0.520	1.418	0.454	1.418	0.487
			1.422	0.480	1.412	0.490	1.420	0.485
	GH	1.271	1.485	0.475	1.427	0.485	1.436	0.483
			1.426	0.520	1.428	0.510	1.437	0.482

Note: S* implies critical value of the test statistic at a significance level of 5%, and P-val indicates the p-values of the observed test statistic.

Table 11-16. Goodness-of-Fit Statistics for Example 11-2 for the MPL Method.

Statistic	Copula	Observed statistic	Critical test statistic S* and P-value for a run of N =					
			100		1,000		10,000	
			S*	P-val	S*	P-val	S*	P-val
CM_n	AMH	2.211	3.072	0.210	3.555	0.281	3.861	0.274
			3.777	0.270	3.844	0.297	3.873	0.278
	Clayton	2.417	3.848	0.150	3.932	0.223	3.734	0.214
			3.970	0.220	3.509	0.215	3.626	0.206
	Frank	1.959	2.509	0.250	2.494	0.230	2.615	0.229
			2.606	0.210	2.617	0.236	2.606	0.225
	GH	1.435	2.541	0.560	2.972	0.666	3.033	0.627
			2.888	0.650	2.932	0.616	3.043	0.627
S_n	AMH	0.167	0.224	0.280	0.239	0.275	0.240	0.291
			0.216	0.210	0.249	0.302	0.243	0.286
	Clayton	0.137	0.241	0.360	0.252	0.421	0.242	0.396
			0.210	0.370	0.236	0.410	0.237	0.392
	Frank	0.206	0.213	0.070	0.238	0.117	0.237	0.116
			0.239	0.110	0.236	0.123	0.238	0.119
	GH	0.201	0.255	0.140	0.269	0.197	0.267	0.189
			0.259	0.150	0.254	0.166	0.265	0.189
T_n	AMH	1.114	1.439	0.570	1.366	0.513	1.376	0.508
			1.321	0.500	1.367	0.524	1.378	0.512
	Clayton	0.960	1.264	0.490	1.267	0.559	1.247	0.544
			1.233	0.500	1.245	0.536	1.235	0.536
	Frank	1.256	1.429	0.420	1.396	0.470	1.401	0.492
			1.368	0.430	1.398	0.496	1.403	0.489
	GH	1.246	1.389	0.580	1.391	0.501	1.392	0.486
			1.400	0.510	1.377	0.490	1.389	0.486

Note: S* implies critical value of the test statistic at a significance level of 5%, and P-val indicates the p-values of the observed test statistic.

Table 11-17. Goodness-of-Fit statistics for Example 11-2 for the IFM Method.

Statistic	Copula	Observed statistic	Critical test statistic S^* and P-value for a run of $N =$					
			100		1,000		10,000	
			S^*	P-val	S^*	P-val	S^*	P-val
CM_n	AMH	2.208	3.704	0.210	3.919	0.282	3.882	0.283
			2.987	0.220	3.659	0.269	3.798	0.281
		Clayton	3.031	0.130	3.836	0.123	3.715	0.109
			3.834	0.110	3.612	0.109	3.719	0.107
		Frank	1.918	0.210	2.566	0.251	2.588	0.246
			2.575	0.280	2.542	0.235	2.586	0.247
	GH	1.543	3.492	0.650	3.042	0.530	3.038	0.555
			2.887	0.550	2.983	0.562	3.063	0.560
	S_n	AMH	0.167	0.218	0.239	0.303	0.240	0.297
			0.215	0.250	0.227	0.257	0.238	0.282
		Clayton	0.185	0.268	0.280	0.229	0.250	0.219
			0.243	0.180	0.239	0.225	0.249	0.220
		Frank	0.200	0.223	0.230	0.118	0.232	0.121
T_n	AMH	1.112	1.309	0.430	1.383	0.506	1.375	0.514
			1.335	0.470	1.362	0.514	1.369	0.510
		Clayton	1.076	1.390	0.630	1.389	0.511	1.390
			1.374	0.520	1.390	0.488	1.390	0.507
		Frank	1.236	1.394	0.580	1.387	0.494	1.378
			1.351	0.600	1.378	0.475	1.378	0.489
	GH	1.270	1.421	0.510	1.416	0.490	1.412	0.501
			1.405	0.550	1.411	0.498	1.415	0.493

Note: S^* implies critical value of the test statistic at a significance level of 5%, and P-val indicates the p-values of the observed test statistic.

features. The latter two figures clearly show no evidence of lower- or upper-tail dependence as none of the points close to $\lambda_i = 1$ show significance. Based on a sample Kendall's tau value of 0.469 and features of lower- and upper-tail dependence, six copulas—Clayton, Frank, GH, N12, N13, and N14—are selected. The latter three copulas refer to even-numbered copulas listed in Table 4.2 of [Nelsen \(2006\)](#). Although more copulas could have been considered at this initial screening stage, only six were included to keep the selection process shorter.

11.4.3.2 Estimation of Dependence Parameter

The dependence parameters for the six copulas under consideration are estimated by the MPL method. Table 11-19 gives the point estimates along with standard errors and the interval estimates, corresponding to a coverage probability of 0.95. This table also includes LL_{max} values for the six copulas. The LL_{max} value for the Frank copula is largest of them all, followed by that of the N13 and N14 copulas. Thus, from the point of view of maximum log-likelihood values, it may be stated that these three copulas are better.

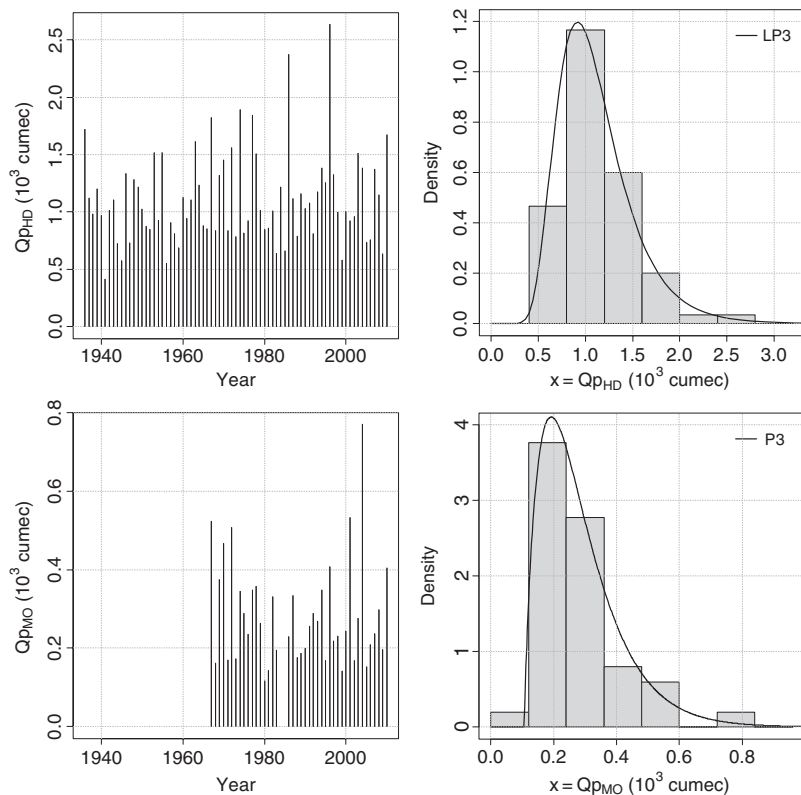


Figure 11-51. Time series (left-side panel) and histograms (right-side panel) of annual peak flows at Hilldale ($X = Q_{p_{HD}}$) and Mt. Outlook ($Y = Q_{p_{MO}}$). The fitted probability density functions of LP3 and P3 distributions are plotted over the respective histograms.

Table 11-18. Maximum Likelihood Parameter Estimates for the Selected Distributions for Annual Peak Flows $Q_{p_{HD}}$ and $Q_{p_{MO}}$ at Hilldale and Mt. Outlook Stations, Respectively.

Variable	Finalized distribution	Parameter estimates			Standard errors		
		Location	Scale	Shape	Location	Scale	Shape
$Q_{p_{HD}}$	LP3	5.823	0.020	291.679	7.828	8.47E-05	71964.64
$Q_{p_{MO}}$	P3	0.106	0.092	1.948	0.0003	0.0008	0.512

11.4.3.3 Assessment of Copula Fitting

The relative suitability of plausible copula families is ascertained in multiple ways by employing (1) graphical methods, (2) error statistics, and (3) formal goodness-of-fit statistics.

11.4.3.4 Graphical Goodness-of-Fit Tests

First, the observed data are compared with a set of randomly generated samples of size 500. Employing the MPL method, Figure 11-55 shows this comparison of observed and randomly generated samples. These plots indicate that although the general nature of the spread of observed

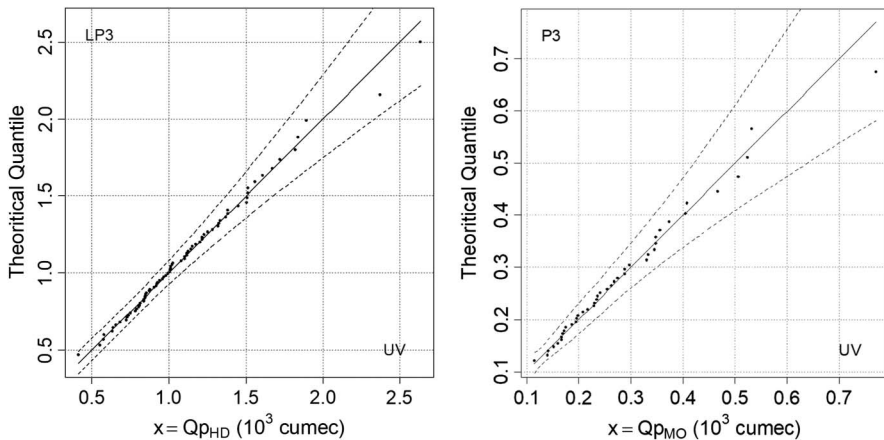


Figure 11-52. QQ plots for annual peak flows at Hilldale ($X = QP_{HD}$) and Mt. Outlook ($Y = QP_{MO}$) data fitted with LP3 and P3 distributions, respectively.

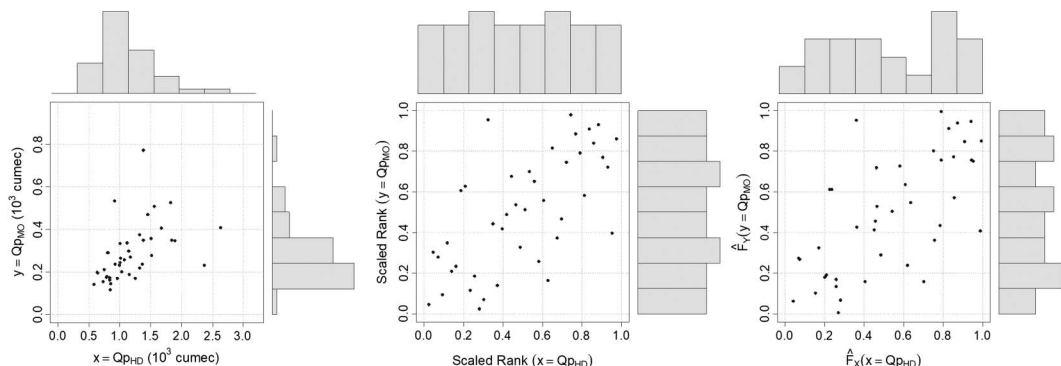


Figure 11-53. Scatter plots and histograms of observed bivariate annual peak flows at Hilldale ($X = QP_{HD}$) and Mt. Outlook ($Y = QP_{MO}$) stations in original domain (left), as ranks (middle), and as LP3 and P3 computed probabilities (right), respectively.

data somewhat matches that of the random samples, the match in the lower and upper tails is not satisfactory except for the Frank and N13 copulas.

Second, comparison of empirical probabilities with computed probabilities (Figure 11-56) reveals the extent to which the computed copula surface would fit the empirical copula surface of the scaled ranks of observed data. This comparison is shown as probabilities plotted with respect to the ranked observation numbers. Although matching for all copulas appears satisfactory, it is comparatively better for the Frank and N13 copulas. Third, comparison of empirical and computed probability distributions of the BIPIT variate $K_n(w)$ and $K_{\theta_n}(w)$ (Figure 11-57) shows that the matching is again comparatively better for the Frank copula, followed by the N13 copula.

11.4.3.5 Error Statistics and Analytical Goodness-of-Fit Tests

The maximized log-likelihood values for the Frank and N13 copulas, as given in Table 11-19, are the two largest among the copulas considered and support the conclusions based on the previous graphical goodness-of-fit tests. Table 11-20 provides other error statistics, RMSE, MN-A-ERR, and MX-A-ERR, showing that the Frank copula has three of the four errors lowest among all copulas. Thus, from the point of view of these error statistics, the Frank copula performs better than the

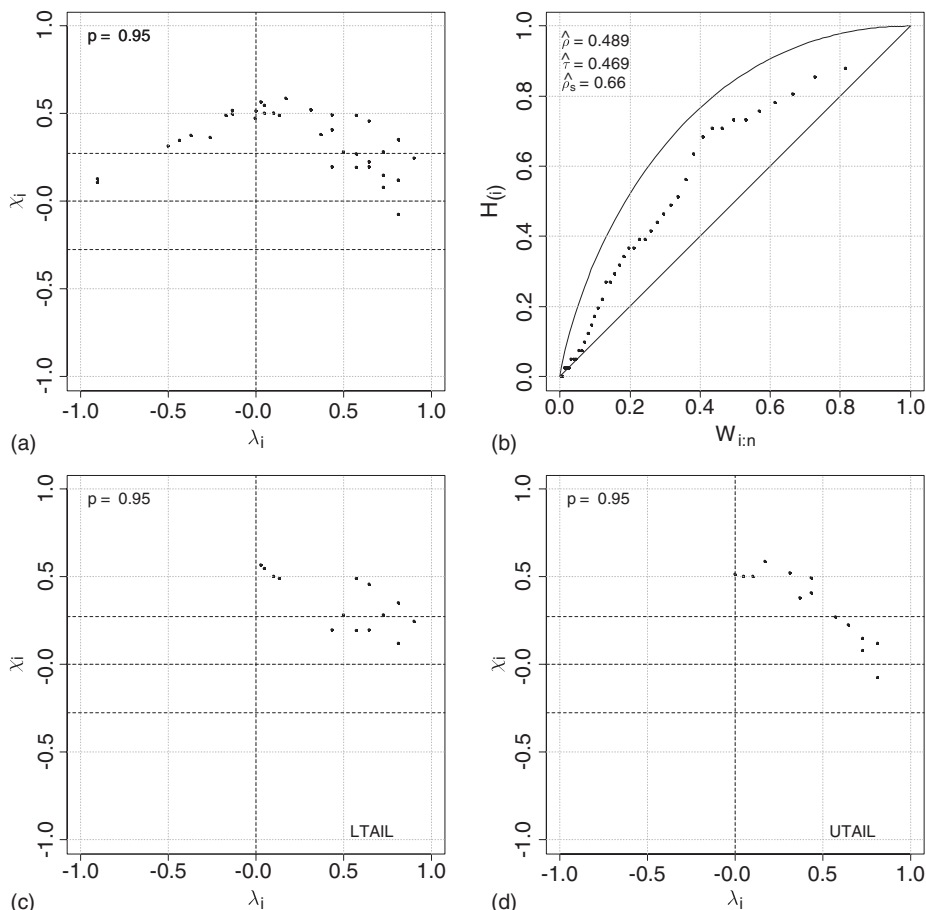


Figure 11-54. Characterization of dependence between annual peak flows at Hilldale and Mt. Outlook stations using (a) chi-plot, (b) K-plot, (c and d) chi-plots for lower and upper tails.

Table 11-19. Point and Interval Estimates of the Dependence Parameter for Example 11-3 for the Six Copulas under Consideration Using the MPL Estimation Method. Interval Estimates Correspond to a Coverage Probability of 0.95.

Method/ copula family	Theta ($\hat{\theta}$)	Tau ($\hat{\tau}_n/\hat{\tau}_0$)	Lower C.L.	Upper C.L.	Standard error	Conf. width	LL_{max}
MPL							
Clayton	1.220	0.379	0.936	1.504	0.284	0.145	8.999
Frank	5.338	0.477	5.058	5.618	0.280	0.143	11.346
GH	1.773	0.436	1.504	2.042	0.269	0.137	9.186
N12	1.200	0.444	0.878	1.522	0.322	0.164	9.646
N13	3.758	0.451	3.496	4.020	0.262	0.134	10.693
N14	1.353	0.460	1.041	1.665	0.312	0.159	9.988

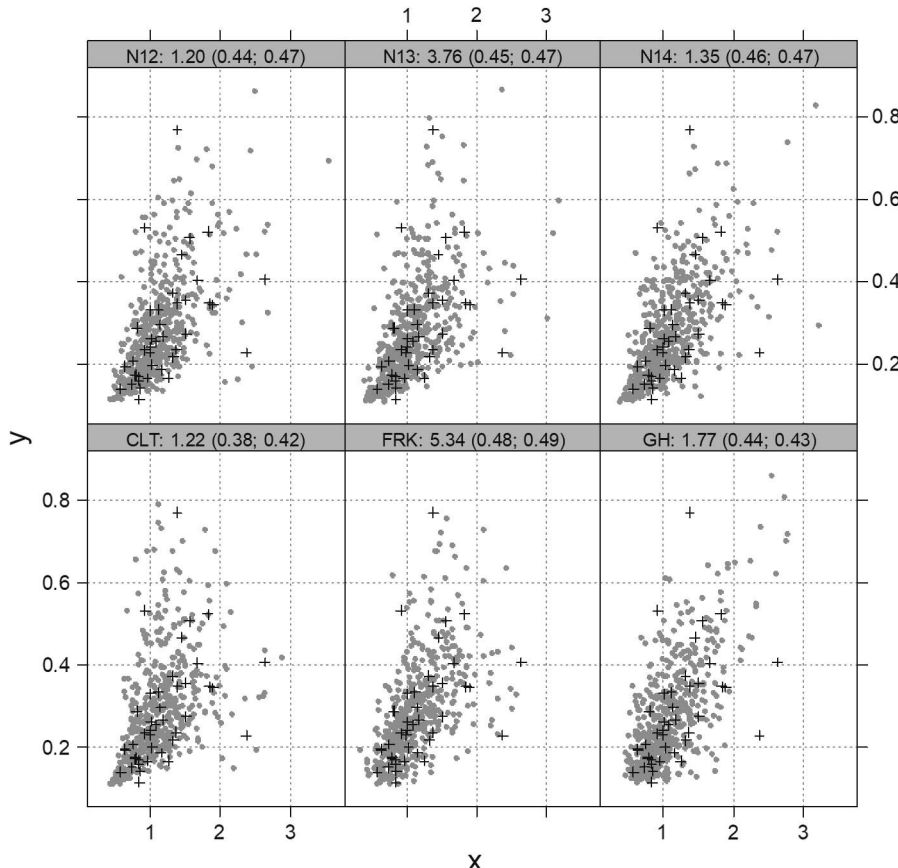


Figure 11-55. Comparison of observed and MPL method-based random samples for annual peak flows at Hilldale and Mt. Outlook stations. Solid circles are random samples (size 500), and plus symbols are observed data. Numbers in name strips are dependence parameter estimates with corresponding Kendall's tau values in parenthesis.

others. The formal goodness-of-fit tests are carried out for the three-parameter estimation methods by evaluating the Cramer–von Mises type statistics CM_n , S_n , and T_n . For this, a parametric bootstrap procedure is employed to simulate 10,000 sets of random samples of size 42, equivalent to the size of the observed dataset. Table 11-21 gives the values of these three statistics, their p-values, and the critical values at the 5% significance level. Results of the three statistics indicate that sufficient ground exists for rejection of the Clayton copula, as the p-value for one statistic is less than 0.05 and is quite low for the other two statistics. However, the p-values for the Frank copula are very high and largest among them all. The p-values for all other copulas are moderate and thus do not immediately disqualify them as viable options.

Thus, all the graphical and analytical goodness-of-fit test results indicate nonrejection of the copulas other than the Clayton copula. However, considering relative suitability, the Frank copula appears most suitable and has been considered further for the joint modeling of annual maximum peak flows at Hilldale and Mt. Outlook stations.

11.4.3.6 Information from Joint Distribution Modeling

As discussed previously, the Frank copula is considered representative of the bivariate data under consideration and copula-based joint and conditional distributions are obtained. Figure 11-58 shows

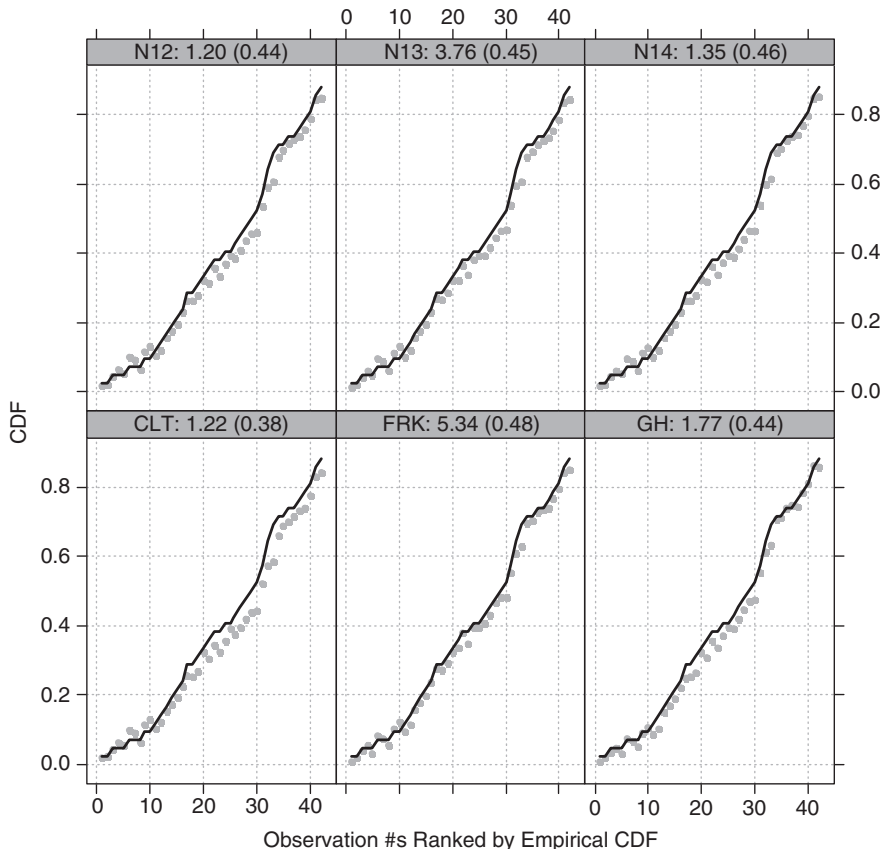


Figure 11-56. Comparison of empirical and MPL method-based computed probabilities of annual peak flows at Hilldale and Mt. Outlook stations. The comparison is with respect to ranked observation numbers, with solid circles for empirical probabilities and solid lines for computed probabilities. Numbers in name strips are dependence parameter estimates with corresponding Kendall's tau values in parenthesis.

the return periods in years corresponding to the exceedance probability of two types of joint events. The left panel corresponds to “OR” events, that is, when flows at either any one or at both of the stations exceed certain threshold flows. The right panel corresponds to “AND” events, that is, when flows at both of stations exceed certain threshold flows simultaneously. These joint return period plots could be used for answering questions such as, “What is the return period of events when flows in (1) either one or both rivers and, in (2) both rivers simultaneously exceed their respective 100 year floods?” Considering the LP3- and P3-based estimated 100 year flood values for Hilldale and Mt. Outlook stations as $2,400 \text{ m}^3/\text{s}$ and $705 \text{ m}^3/\text{s}$, respectively, the return period for exceedance of either one or both of these flows in respective rivers can be read from the “OR” events plot as about 50 years. Similarly, the return period for simultaneous exceedance of these flows in the two rivers is about 2,000 years. Simple probability computations yield computed values for these “OR” and “AND” return periods as 51 years and 1,970 years respectively. This is very useful information for establishing flood management services in the region. For example, as the “AND” return period is very large (2,000 years), the chance that a 100 year flood will occur in both subbasins in the same year is virtually insignificant. In other words, not establishing two separate services that are individually capable of managing flood management and relief services in these two subbasins would be prudent. Instead, only one such service or two services with reduced capacities in each area should be able to

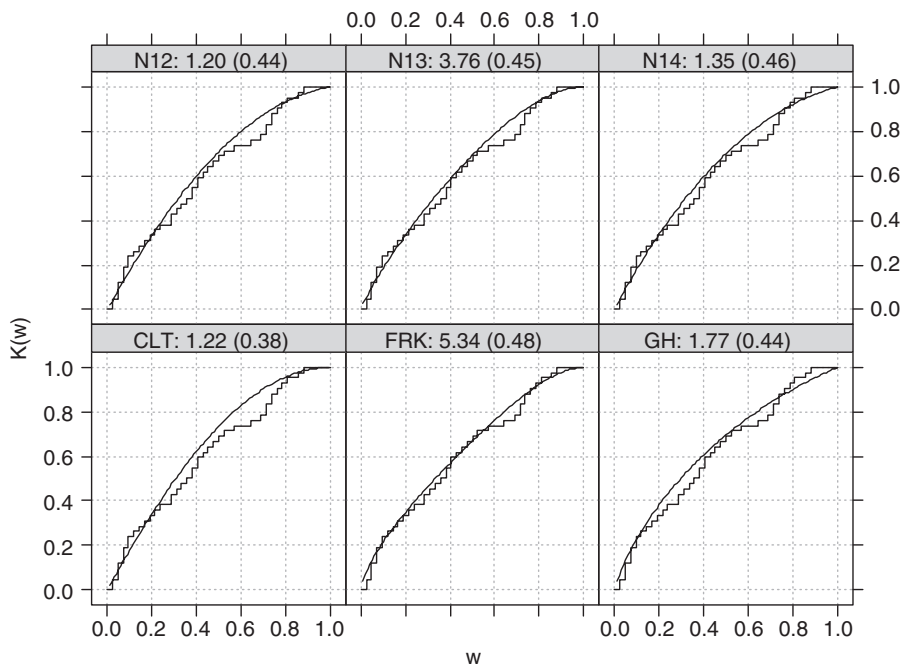


Figure 11-57. Graphical goodness-of-fit test using K-plots for the MPL method-based estimation for Example 11-3. Step functions are empirical distributions $K_n(w)$, and curves are theoretical distributions $K_{\theta_n}(w)$ of the bivariate integral transform variable $W = C(U, V)$. Numbers in name strips are dependence parameter estimates with corresponding Kendall's tau values in parenthesis.

Table 11-20. Various Error Statistics for Example 11-3 for the Six Copulas under Consideration.

Method/Copula Family	RMSE	MN-A-ERR	MN-ERR	MX-A-ERR
MPL				
Clayton	0.041	0.034	0.029	0.106
Frank	0.021	0.018	0.015	0.063
GH	0.027	0.022	0.020	0.060
N12	0.031	0.026	0.020	0.085
N13	0.028	0.024	0.019	0.081
N14	0.028	0.023	0.017	0.075

jointly manage the flood menace in the two areas. Furthermore, the “OR” return period of 51 years indicates that flood management services in support of a 100 year flood will on average be required once in 50 years, in one of the two subbasins. This discounts for the negligible chances of a 100 year flood occurring in the two rivers simultaneously.

Figure 11-59 plots the conditional probabilities. The left panel shows the probability of flows at Hilldale station exceeding a certain value given that flood flow at Mt. Outlook station is more than a certain value. Similarly, the right panel provides the probability of flows at Mt. Outlook station exceeding a certain value given that flood flow at Hilldale station is more than a certain value.

Table 11-21. Goodness-of-Fit Statistics for Example 11-3 for the MPL Method.

Statistic	Copula	Observed statistic	S^*	P-val
CM_n	Clayton	2.940	2.835	0.042
	Frank	0.777	1.944	0.906
	GH	1.263	2.241	0.449
	N12	1.693	2.375	0.203
	N13	1.422	2.291	0.325
	N14	1.336	2.390	0.391
S_n	Clayton	0.191	0.250	0.142
	Frank	0.109	0.207	0.859
	GH	0.165	0.247	0.357
	N12	0.123	0.225	0.402
	N13	0.112	0.201	0.562
	N14	0.109	0.228	0.523
T_n	Clayton	0.919	1.140	0.355
	Frank	1.108	1.228	0.479
	GH	1.152	1.299	0.488
	N12	0.821	1.079	0.634
	N13	0.908	1.088	0.537
	N14	0.860	1.074	0.586

Note: S^* implies critical value of the test statistic based on 10,000 simulation runs at a significance level of 5%, and P-val indicates the p-values of the observed test statistic.

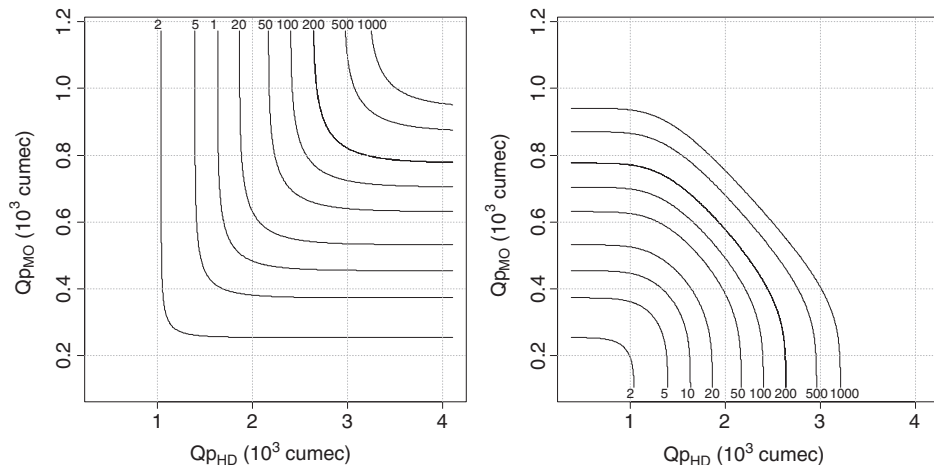


Figure 11-58. Contours of return periods in years corresponding to joint events of exceedances at Hilldale or Mt. Outlook stations. The left panel correspond to "OR" events when flows exceed certain values at either any one or at both stations. The right panel corresponds to events when flows exceed certain values at both stations simultaneously. Units for flows plotted on both axes in both the panels is $10^3 \text{ m}^3/\text{s}$ (or cubic meter per second, or cumec).

Considering the thresholds in two rivers as their 100 year flood, the probability of a flood at Hilldale exceeding its 100 year value of $2,400 \text{ m}^3/\text{s}$, given that a flood at Mt. Outlook exceeded its 100 year flood value of $705 \text{ m}^3/\text{s}$, is read from the left panel as about 5%. Similarly, the probability of a flood at

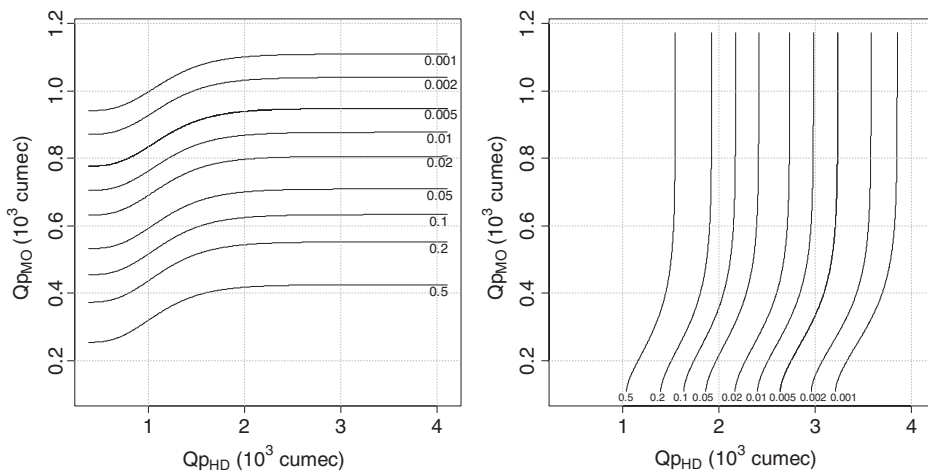


Figure 11-59. Contours of conditional probability corresponding to events of flow exceedances at one station, given that flows exceed certain value at the other station. The left panel corresponds to flow exceedance at Hilldale station, given that flows exceed certain values at Mt. Outlook station. The right panel corresponds to flow exceedance at Mt. Outlook station, given that flows exceed certain values at Hilldale station. Units for flows plotted on both the axes is $10^3 \text{ m}^3/\text{s}$ (or cubic meter per second).

Mt. Outlook exceeding its 100 year value of $705 \text{ m}^3/\text{s}$, given that a flood at Hilldale station exceeded its 100 year flood value of $2,400 \text{ m}^3/\text{s}$, is read from the left panel as about 5%. Computed values of these probabilities are 5.08% and 5.09%, respectively. These conditional probability estimates should help in making management decisions during a flood in one of the rivers in that it provides a chance estimate if the other river will also get flooded and may need flood relief assistance. This shows that when one of the rivers experiences a 100 year flood, about a 5% chance exists that the other river will also experience a 100 year flood. This requires caution to avoid exhausting all resources in the subbasin experiencing a 100 year flood as a 5% chance, which is significant, exists that the other subbasin may also see flooding. A better scheme may be to keep some reserve capacity or arrange for additional support in such situation.

References

- Abberger, K. 2005. "A simple graphical method to explore tail-dependence in stock-return pairs." *Appl. Financial Econ.* **15** (1): 43–51.
- AghaKouchak, A., A. Ba'r'odossy, and E. Habib. 2010a. "Copula-based uncertainty modelling: Application to multisensor precipitation estimates." *Hydrol. Proc.* **24** (15): 2111–2124.
- AghaKouchak, A., E. Habib, and A. Bardossy. 2010b. "Modeling radar rainfall estimation uncertainties: Random error model." *J. Hydrol. Eng.* **15** (4): 265–274.
- Ashkar, F., and J. Rousselle. 1982. "A multivariate statistical analysis of flood magnitude, duration and volume." In *Statistical analysis of rainfall and runoff*, edited by V. P. Singh, 651–669. Littleton, CO: Water Resources Publication.
- Bacchi, B., G. Becciu, and N. T. Kottekoda. 1994. "Bivariate exponential model applied to intensities and durations of extreme rainfall." *J. Hydrol.* **155** (1–2): 225–236.
- Bardossy, A., and J. Li. 2008. "Geostatistical interpolation using copulas." *Water Resour. Res.* **44** (7): W07412.
- Borkowf, C. B. 2002. "Computing the non-null asymptotic variance and the asymptotic relative efficiency of Spearman's rank correlation." *Comput. Stat. Data Anal.* **39** (3): 271–286.
- Carlson, R. F., and P. Fox. 1976. "A northern snowmelt-flood frequency model." *Water Resour. Res.* **12** (4): 786–794.

- Chan, S. O., and R. L. Bras. 1979. "Urban storm water management: Distribution of flood volumes." *Water Resour. Res.* **15** (2): 371–382.
- Choulakian, V., N. El-Jabi, and J. Moussi. 1990. "On the distribution of flood volume in partial duration series analysis of flood phenomena." *Stochastics Hydrol. Hydraul.* **4** (3): 217–226.
- Chowdhary, H., L. A. Escobar, and V. P. Singh. 2011. "Identification of suitable copulas for bivariate frequency analysis of flood peak and flood volume data." *Hydrol. Res.* **42** (2–3): 193–216.
- Chowdhary, H., and V. P. Singh. 2010. "Reducing uncertainty in estimates of frequency distribution parameters using composite likelihood approach and copula-based bivariate distributions." *Water Resour. Res.* **46** (11): W1116.
- Cordova, J. R., and R. L. Bras. 1981. "Physically based probabilistic models of infiltration, soil moisture, and actual evapotranspiration." *Water Resour. Res.* **17** (1): 93–106.
- Cordova, J. R., and I. Rodriguez-Iturbe. 1985. "On the probabilistic structure of storm surface runoff." *Water Resour. Res.* **21** (5): 755–763.
- Correia, F. N. 1987. "Multivariate partial duration series in flood risk analysis." In *Hydrologic frequency modeling*, edited by V. P. Singh. Dordrecht, Netherlands: Springer.
- Davison, A. C., and R. Huser. 2015. "Statistics of extremes: Annual review of statistics and its application." *Ann. Rev. Stat. Appl.* **2** (1): 203–235.
- De Michele, C., G. Salvadori, M. Canossi, A. Petaccia, and R. Rosso. 2005. "Bivariate statistical approach to check adequacy of dam spillway." *J. Hydrol. Eng.* **10** (1): 50–57.
- Diaz-Granados, M. A., J. B. Valdes, and R. L. Bras. 1984. "A physically-based flood frequency distribution." *Water Resour. Res.* **20** (7): 995–1002.
- Dutfoy, A., S. Parey, and N. Roche. 2014. "Multivariate extreme value theory—A tutorial with applications to hydrology and meteorology." *Depend. Model.* **2** (1): 30–48.
- Eagleson, P. S. 1972. "Dynamics of flood frequency." *Water Resour. Res.* **8** (4): 878–898.
- Eagleson, P. S. 1978. "Climate, soil, and vegetation. II: The distribution of annual precipitation derived from observed storm sequences." *Water Resour. Res.* **14** (5): 713–721.
- Escalante-Sandoval, C. 1998. "Multivariate extreme value distribution with mixed Gumbel marginals." *J. Am. Water Resour. Assoc.* **34** (2): 321–333.
- Escalante-Sandoval, C., and J. A. Raynal-Villasenor. 1994. "A trivariate extreme value distribution applied to flood frequency analysis." *J. Res. Nat. Inst. Stand. Technol.* **99** (4): 369–375.
- Escalante-Sandoval, C., and J. A. Raynal-Villasenor. 1998. "Multivariate estimation of floods: The trivariate Gumbel distribution." *J. Stat. Comput. Simul.* **61** (4): 313–340.
- Favre, A.-C., S. El Adlouni, L. Perreault, N. Thiemonge, and B. Bobee. 2004. "Multivariate hydrological frequency analysis using copulas." *Water Resour. Res.* **40** (1): 1–12.
- Fermanian, J.-D. 2005. "Goodness-of-fit tests for copulas." *J. Multivar. Anal.* **95** (1): 119–152.
- Finch, P. D., and R. Groblicki. 1984. "Bivariate probability densities with given margins." *Found. Phys.* **14** (6): 549–552.
- Fisher, N. I., and P. Switzer. 2001. "Statistical computing and graphics—Graphical assessment of dependence: Is a picture worth a 100 tests?" *Am. Stat.* **55** (3): 233–239.
- Frees, E. W., and E. A. Valdez. 1998. "Understanding relationships using copulas." *North Am. Actuarial J.* **2** (1): 1–25.
- Genest, C., and J.-C. Boies. 2003. "Detecting dependence with Kendall plots." *Am. Stat.* **57** (4): 275–284.
- Genest, C., and A.-C. Favre. 2007. "Everything you always wanted to know about copula modeling but were afraid to ask." *J. Hydrol. Eng.* **12** (4): 347–368.
- Genest, C., and J. Mackay. 1986. "The joy of copulas: Bivariate distributions with uniform marginals." *Am. Stat.* **40** (4): 280–283.
- Genest, C., J.-F. Quessy, and B. Remillard. 2006. "Goodness-of-fit procedures for copula models based on the probability integral transformation." *Scand. J. Stat.* **33** (2): 337–366.
- Genest, C., and B. Remillard. 2008. "Validity of the parametric bootstrap for goodness-of-fit testing in semiparametric models." *Probab. Stat.* **44** (6): 1096–1127.
- Genest, C., B. Remillard, and D. Beaudoin. 2009. "Goodness-of-fit tests for copulas: A review and a power study." *Insurance: Math. Econ.* **44** (2): 199–213.
- Genest, C., and L.-P. Rivest. 1993. "Statistical inference procedures for bivariate Archimedean copulas." *J. Am. Stat. Assoc.* **88** (423): 1034–1043.

- Goel, N. K., R. S. Kurothe, B. S. Mathur, and R. M. Vogel. 2000. "A derived flood frequency distribution for correlated rainfall intensity and duration." *J. Hydrol.* **228** (1–2): 56–67.
- Goel, N. K., S. M. Seth, and S. Chandra. 1998. "Multivariate modeling of flood flows." *J. Hydraul. Eng.* **124** (2): 146–155.
- Grace, R. A., and P. S. Eagleson. 1966. *The synthesis of short-time-increment rainfall sequences*. Boston: MIT.
- Gumbel, E. J. 1960a. "Bivariate exponential distributions." *J. Am. Stat. Assoc.* **55** (292–707): 698–707.
- Gumbel, E. J. 1960b. "Multivariate extreme distributions." *Bull. Int. Stat. Inst.* **39** (2): 471–475.
- Gupta, V. K., L. Duckstein, and R. W. Peebles. 1976. "On the joint distribution of the largest flood and its time of occurrence." *Water Resour. Res.* **12** (2): 295–304.
- Haan, C. T., and B. N. Wilson. 1987. "A bivariate flood model and its application." In *Hydrologic frequency modeling*, edited by V. P. Singh. Dordrecht, Netherlands: Springer.
- Hao, Z., A. AghaKouchak, N. Nakhjiri, and A. Farahmand. 2014. "Global integrated drought monitoring and prediction system." *Sci. Data* **1**: 140001.
- Hao, Z., and V. P. Singh. 2013a. "Entropy-based method for bivariate drought analysis." *J. Hydrol. Eng.* **18** (7): 780–786.
- Hao, Z., and V. P. Singh. 2013b. "Modeling multi-site streamflow dependence with maximum entropy copula." *Water Resour. Res.* **49** (10): 7139–7143.
- Hao, Z., and V. P. Singh. 2015a. "Drought characterization from a multivariate perspective: A review." *J. Hydrol.* **527** (8): 668–678.
- Hao, Z., and V. P. Singh. 2015b. "Integrating entropy and copula theories for hydrologic modeling and analysis." *Entropy* **17** (4): 2253–2280.
- Herr, H. D., and R. Krzysztofowicz. 2005. "Generic probability distribution of rainfall in space: The bivariate model." *J. Hydrol.* **306** (1–4): 234–263.
- Jaworski, P., et al., eds. 2010. *Copula theory and its applications: Proceedings of the workshop held in Warsaw, 25–26 September 2009*, 327. New York: Springer.
- Joe, H. 1997. *Multivariate models and dependence concepts*. New York: Chapman and Hall.
- Joe, H. 2005. "Asymptotic efficiency of the two-stage estimation method for copula-based models." *J. Multivariate Anal.* **94** (2): 401–419.
- Kao, S. C., and R. S. Govindaraju. 2010. "A copula-based joint deficit index for droughts." *J. Hydrol.* **380** (1–2): 121–134.
- Kavvas, M. L. 1982. "Stochastic trigger model for flood peaks: 1. Development of the model." *Water Resour. Res.* **18** (2): 383–398.
- Kelly, K. S., and R. Krzysztofowicz. 1997. "A bivariate meta-Gaussian density for use in hydrology." *Stochastics Hydrol. Hydraul.* **11** (1): 17–31.
- Khedun, C. P., A. K. Mishra, H. Chowdhary, and R. Giardino. 2012. "Water deficit duration and severity analysis based on runoff derived from noah land surface model." *J. Hydrol. Eng.* **18** (7): 817–833.
- Khedun, C. P., A. K. Mishra, V. P. Singh, and J. R. Giardino. 2014. "A copula based precipitation forecasting model: Investigating the interdecadal modulation of ENSO's impacts on monthly precipitation." *Water Resour. Res.* **50** (1): 580–600.
- Kotz, S., N. Balakrishnan, and N. L. Johnson. 2000. *Continuous multivariate distributions: Models and applications*, 752. New York: Wiley.
- Krstanovic, P. F., and V. P. Singh. 1987. "A multivariate stochastic flood analysis using entropy." In *Hydrologic frequency modeling*, edited by V. P. Singh. Dordrecht, Netherlands: Springer.
- Kurothe, R. S., N. K. Goel, and B. S. Mathur. 1997. "Derived flood frequency distribution for negatively correlated rainfall intensity and duration." *Water Resour. Res.* **33** (9): 2103–2107.
- Laux, P., et al. 2011. "Copula-based statistical refinement of precipitation in RCM simulations over complex terrain." *Hydrol. Earth Syst. Sci.* **15** (7): 2401–2419.
- Li, C., V. P. Singh, and A. K. Mishra. 2013. "A bivariate mixed distribution with a heavy-tailed component and its application to single-site daily rainfall simulation." *Water Resour. Res.* **49** (2): 767–789.
- Long, D., and R. Krzysztofowicz. 1995. "A family of bivariate densities constructed from marginals." *J. Am. Stat. Assoc.* **90** (430): 739–746.
- Mao, G., S. Vogl, P. Laux, and S. Wagner. 2014. "Stochastic bias correction of dynamically downscaled precipitation fields for Germany through copula-based integration of gridded observation data." *Hydrol. Earth Syst. Sci. Discuss.* **11** (7): 7189–7227.

- Marshall, W. M., and I. Olkin. 1967. "A multivariate exponential distribution." *J. Am. Stat. Assoc.* **62** (317): 30–44.
- Michiels, F., and A. D. Schepper. 2008. "A copula test space model: How to avoid the wrong copula choice." *Kybernetika* **44** (6): 864–878.
- Moran, P. A. P., M. Schuepp, L. D. Calvin, W. A. O. N. Waugh, A. C. Atkinson, and A. M. Walker. 1970. "The methodology of rain-making experiments." *Rev. Int. Stat. Inst.* **38** (1): 105–119.
- Nagao, M., and M. Kadoya. 1971. "Two-variate exponential distribution and its numerical table for engineering application." *Bull. Disaster Prev. Res. Inst. Kyoto Univ.* **20** (3): 183–215.
- Nelsen, R. B. 2006. *An introduction to copulas*. New York: Springer.
- Piani, C., and J. Haerter. 2012. "Two dimensional bias correction of temperature and precipitation copulas in climate models." *Geophys. Res. Lett.* **39** (20): L20401.
- Plackett, R. L. 1965. "A class of bivariate distributions." *J. Am. Stat. Assoc.* **60** (310): 516–522.
- Raynal-Villasenor, J. A., and J. D. Salas. 1987. "A probabilistic model for flooding downstream of the junction of two rivers." In *Hydrologic frequency modeling*, edited by V. P. Singer. Dordrecht, Netherlands: Springer.
- Rosbjerg, D. 1987. "On the annual maximum distribution in dependent partial duration series." *Stochastics Hydrol. Hydraul.* **1** (1): 3–16.
- Sackl, B., and H. Bergmann. 1987. "A bivariate flood model and its application." In *Hydrologic frequency modeling*, edited by V. P. Singer. Dordrecht, Netherlands: Springer.
- Salvadori, G., and C. De Michele. 2004. "Frequency analysis via copulas: Theoretical aspects and applications to hydrological events." *Water Resour. Res.* **40** (12): 1–17.
- Salvadori, G., and C. De Michele. 2007. "On the use of copulas in hydrology: Theory and practice." *J. Hydrol. Eng.* **12** (4): 369–380.
- Salvadori, G., and C. De Michele. 2010. "Multivariate multiparameter extreme value models and return periods: A copula approach." *Water Resour. Res.* **46** (10): W10501.
- Salvadori, G., C. De Michele, N. T. Kottegoda, and R. Rosso. 2007. *Extremes in nature: An approach using copulas*. Dordrecht, Netherlands: Springer.
- Sarabia Alzaga, J. M., and E. Gómez-Déniz. 2011. "Construction of multivariate distributions: A review of some recent results (with discussions)." *Stat. Oper. Res. Trans.* **32**: 3–36.
- Schoelzel, C., and P. Friederichs. 2008. "Multivariate nonnormally distributed random variables in climate research-Introduction to the copula approach." *Nonlinear Proc. Geophys.* **15** (5): 761–772.
- Singh, K., and V. P. Singh. 1991. "Derivation of bivariate probability density functions with exponential marginals." *Stochastics Hydrol. Hydraul.* **5** (1): 55–68.
- Sklar, A. 1959. "Fonctions de répartition à n dimensions et leurs marges." [In French.] *Publ. Inst. Stat. Univ. Paris* **8**: 229–231.
- Todorovic, P. 1971. *On extreme problems in hydrology*. Fort Collins, CO: Joint Statistics Meeting American Statistical Association and the Institute of Mathematical Statistics.
- Todorovic, P. 1978. "Stochastic models of floods." *Water Resour. Res.* **14** (2): 345–356.
- Todorovic, P., and D. A. Woolhiser. 1972. "On the time when the extreme flood occurs." *Water Resour. Res.* **8** (6): 1433–1438.
- Todorovic, P., and V. Yevjevich. 1969. *Stochastic process of precipitation: Hydrology Paper 35*. Fort Collins, CO: Colorado State Univ.
- Tsukahara, H. 2005. "Semiparametric estimation in copula models." *Can. J. Stat.* **33** (3): 357–375.
- USACE. 1999. *Risk-based analysis in geotechnical engineering for support of planning studies*. Rep. No. ETL 1110-2-556. Washington, DC: USACE.
- Van den Berg, M., et al. 2011. "Copula-based downscaling of spatial rainfall: A proof of concept." *Hydrol. Earth Syst. Sci.* **15** (5): 1445–1457.
- Verhoest, N. E., et al. 2015. "Copula-based downscaling of coarse-scale soil moisture observations with implicit bias correction." *IEEE Trans. Geosci. Remote Sens.* **53** (6): 3507–3521.
- Villarini, G., F. Serinaldi, and W. F. Krajewski. 2008. "Modeling radar-rainfall estimation uncertainties using parametric and non-parametric approaches." *Adv. Water Resour.* **31** (12): 1674–1686.
- Vogl, S., P. Laux, W. Qiu, and G. Mao. 2012. "Copula-based assimilation of radar and gauge information to derive bias-corrected precipitation fields." *Hydrol. Earth Syst. Sci.* **16** (7): 2311–2328.
- Wang, W., and M. T. Wells. 2000. "Model selection and semiparametric inference for bivariate failure-time data." *J. Am. Stat. Assoc.* **95** (449): 62–72.

- Woodroffe, M. 1975. *Probability with applications*. New York: McGraw-Hill.
- Yue, S. 1999. "Applying bivariate normal distribution to flood frequency analysis." *Water Int.* **24** (3): 248–254.
- Yue, S. 2000a. "The Gumbel mixed model applied to storm frequency analysis." *Water Resour. Manage.* **14** (5): 377–389.
- Yue, S. 2000b. "The bivariate lognormal distribution to model a multivariate flood episode." *Hydrol. Processes* **14** (14): 2575–2588.
- Yue, S. 2001a. "The Gumbel logistic model for representing a multivariate storm event." *Adv. Water Resour.* **24** (2): 179–185.
- Yue, S. 2001b. "A bivariate extreme value distribution applied to flood frequency analysis." *Hydrol. Res.* **32** (1): 49–64.
- Yue, S. 2002. "The bivariate lognormal distribution for describing joint statistical properties of a multivariate storm event." *Environmetrics* **13** (8): 811–819.

CHAPTER 12

Hydrologic Record Events

Richard M. Vogel
Attilio Castellarin
N. C. Matalas
John F. England, Jr.
Antigoni Zafirakou

GLOSSARY

AM: Annual maximum series, which is the series of the largest value observed in each year; this series is often used in computations of flood frequency

Bivariate (multivariate) distribution: The joint distribution for two (n) random variables X_1 and X_2 (X_1, \dots, X_n) defined on the same probability space, which describes the probability of events defined in terms of both X_1 and X_2 (defined in terms of X_1, \dots, X_n)

Bivariate (multivariate) record (after [Nagaraja et al. 2003](#)): Let $\mathbf{X} = (X_1, X_2)$ [$\mathbf{X} = (X_1, \dots, X_n)$] be a bivariate (multivariate) random variable with an absolutely continuous cumulative distribution function or cdf, F and probability density function or pdf, f . Let F_j and f_j be the marginal cdf and pdf of X_j , $j = 1, 2$ ($j = 1, \dots, n$). Also let $\mathbf{X}(i) = [X_1(i), X_2(i)]$ [$\mathbf{X}(i) = [X_1(i), \dots, X_n(i)]$], with $1 \leq i \leq m$, denote a random sample of size m from F

DEFINITION 1: a bivariate (multivariate) record of *first kind* is said to occur at time k if both of $X_1(k)$ and $X_2(k)$ [$\text{all } X_1(k), \dots, X_n(k)$] exceed—or are smaller than— $X_1(i)$ and $X_2(i)$ [$X_1(k), \dots, X_n(k)$], with $i < k$

DEFINITION 2: a bivariate (multivariate) record of *second kind* is said to occur at time k if at least $X_j(k)$, with $j = 1, 2$ ($j = 1, \dots, n$) exceeds—or is smaller than—all preceding $X_j(i)$, with $i < k$

EEPE: Expected exceedance probability of an envelope; EEPE is the most appropriate summary measure if one's concern is with making a probabilistic statement regarding the single envelope based on historical observations

EPEE: Exceedance probability of the expected envelope; EPEE is the most appropriate summary measure if one's concern is with making a probabilistic statement regarding the envelope expected to occur for a group of sites of given characteristics (i.e., number of sites, record lengths, cross-correlation, etc.)

Exceedance probability: The likelihood or probability that a random variable will be exceeded

EXP: Exponential probability distribution

GEV: Generalized extreme value probability distribution

GPA: Generalized Pareto probability distribution

GUM: Gumbel probability distribution

HU: Hydrologic unit

Lower record: Smallest observed value of a random variable during a particular time period

Monte Carlo experiment: An experiment in which a series of random variables are generated and that series is then used to compute a particular statistic; by repeating the experiment over and over, one may generate a large sample of the particular statistic of interest whose behavior can then be explored

Parametric properties: Properties pertaining to a random variable when that random variable is assumed to follow a particular probability distribution

Plotting position: An empirical estimate of the nonexceedance probability associated with an observation of a random sample from a (possibly unknown) probability distribution

POT: Peaks over threshold, which denotes the series that results from removing all values of the original series below some threshold value

Quantile: Value of a random variable that is exceeded by some probability p , often denoted as x_p , where x is the random variable and p is the exceedance probability

Record: Largest or smallest observed value of a random variable during a particular time period

Record of the first kind: See Section 12.2.4

Record of the second kind: See Section 12.2.4

Record of the third kind: See Section 12.2.4

Record of the fourth kind. See Section 12.2.4

Recurrence interval. Length of time between two events such as the length of time between two floods

T: Average return period or time or recurrence interval between the occurrence of two events, or in the context of floods, the average time one must wait until the occurrence of the next flood event

Upper record: Largest observed value of a random variable during a particular time period

12.0 GENERAL

A record event is defined as an event whose magnitude exceeds, or is exceeded by, all previous events. One thing is certain: a record event, no matter how large or long standing, will eventually be broken (Glick 1978). Thus, the probability that the largest observed flood discharge on a river will be exceeded is 1, and this is true even if the flood's magnitude has an upper bound. However, we do not know the magnitude of the next record flood, other than that it will be greater than the current record flood, that is, the largest observed flood on record. Also, we do not know when the next record flood will occur. The same ideas apply to droughts, or to any other hydrologic flux. Other hydrologic records of interest might include the largest 24-hour rainfall on record, the lowest 7-day streamflow on record, the lowest value of soil moisture on record, and so on. Historically, engineers have always shown particular interest in such records. For example, most hydrology textbooks and manuals list record rainfall amounts that have occurred for various durations. Similarly, for flood discharges, envelope curves based on record floods have been drawn to bound our experience on floods for a particular region, and such curves have found widespread usage in engineering practice for the design of dams and other important facilities in the vicinity of rivers such as nuclear power plants. What is missing from our historical interest in hydrologic records is a theory that enables us to make probabilistic statements about their future occurrence. The purpose of this chapter is to provide such a theoretical framework for describing the probabilistic behavior of hydrologic record events.

The largest or smallest event exhibited within a sequence is a statistical property of a sequence that has long attracted the attention of hydrologists in dealing with floods and droughts through extreme value theory. However, study of record hydrologic events through the formal theory of records has only recently been undertaken, particularly studies of record floods. See [Vogel et al. \(2001\)](#) and [Castellarin et al. \(2005\)](#).

Surely all extraordinary floods are record floods, though not all record floods are extraordinary floods. What distinguishes an extraordinary flood from a flood of record, from a probable maximum flood, or from a 10,000-year flood? The theory of records can provide us with both a mathematical framework for dealing with such questions and a methodology for estimating the probability of occurrence associated with record floods. This chapter combines a theoretical framework for applying the theory of records to flood and other hydrologic processes, while simultaneously documenting numerous recent studies and approaches that have used the theory of records to assign probabilistic statements to extraordinary floods for the purpose of flood management and planning.

Since the pioneering work of [Chandler \(1952\)](#), a rich theory on the mathematics of record events has been developed leading to several summary texts ([Ahsanullah 1995, 2004](#); [Arnold et al. 1998](#); [Nevzorov 2001](#); [Arnold et al. 2008](#)). Within the context of the theory of order statistics, [Arnold et al. \(2008\)](#) provide a pedagogic treatment of the theory of records, suited for teaching the material in this chapter from the point of view of a mathematician. Mathematical interest in the theory of records seems to parallel general human interest in records, since the *Guinness Book of World Records* was first introduced in 1955. By 1974, the *Guinness Book of World Records* became the top-selling copyrighted book in publishing history and has become the authoritative source of records in nearly all fields of human and nonhuman endeavor ([Roberts 1991](#)).

The theory of records relies heavily upon the theory of order statistics ([David and Nagaraja 2003](#)) and extreme order statistics, as well as on the theory of extremes ([Gumbel 1958](#)). The theory of extremes has received a great deal of attention since its introduction by [Gumbel \(1958\)](#), with many advances occurring in the field of hydrology (see [Katz et al. 2002](#), for a recent overview of the field within the context of hydrology). Given the close association between the theory of records and water resource applications, surprisingly few water resource studies have applied the theory of records ([Vogel et al. 2001](#), [Nagaraja et al. 2003](#), [Castellarin et al. 2005](#), [Douglas and Vogel 2006](#), [Serinaldi and Kilsby 2018](#)).

Consider the following definition of record events. Let X_1, X_2, \dots, X_n represent a sequence of annual maximum (AM) flood observations, where n is the total number of time periods for which observations are available. The observation X_i is the n year record flood, which is denoted as Y , if X_i exceeds all previous records in the sequence of length n , or when $Y = \max(X_1, X_2, \dots, X_n)$. [Ahsanullah \(1995, 2004\)](#), [Arnold et al. \(1998, 2008\)](#), and [Nevzorov \(2001\)](#) introduce the entire upper record value sequence as follows. The observation X_j is called an upper record if $X_j > X_i$ for every $i < j$. The times at which these records occur are termed the record time sequence T_m , where the first observation is a record so that $T_0 = 1$, the second record occurs at time $t = j$, so that the record time is $T_1 = j$, and so on. The record value sequence is then $R_m = X_{T_m}$ where $m = 1, 2, \dots$. One can also define the interrecord time sequence as $\Delta_m = T_m - T_{m-1}$, $m = 1, 2, 3, \dots$. The number of upper records N_n in a series of n observations can also be tracked. For example, given the following sequence of $n = 6$ observations (50, 30, 60, 10, 80, 70), the upper record event is $Y = 80$, the resulting upper record time sequence ($T_0 = 1, T_1 = 3, T_2 = 5$), the resulting upper record value process ($R_1 = 50, R_2 = 60, R_3 = 80$), the interrecord time sequence [$\Delta_1 = T_1 - T_0 = 2, \Delta_2 = T_2 - T_1 = 2$], and the number of records in this series of $n = 6$ values is $N_n = 3$ records. All of these record value statistics apply to flood series and resulting flood management problems as described here.

The theory of records centers on probability distributions that are expressible in density, cumulative, and inverse closed forms. It is in this context that the adaptation of the theory of records to hydrologic studies is discussed. Note that in hydrologic studies, distributions expressible only in closed density form, such as the log-normal, and log-Pearson distributions, are used extensively, particularly in studies of floods. The theory of records does not per se exclude probability distributions that are not expressible in cumulative and inverse closed forms, but the current literature does not draw

attention to the use of simulation and Monte Carlo techniques to address properties of record events in terms of distributions that are not expressible in cumulative and inverse closed forms.

Much of the hydrologic literature assumes flood events are independent and identically distributed (*iid*). Interestingly, as we show in this chapter, much of the theory of records depends only on the *iid* assumption. Unfortunately, the *iid* assumption, underlying much of the theory of records, is hydrologically questionable. Though observations of flows lend some credence to the assumption of *iid* in the case of floods, the same cannot be said in reference to droughts. In the case of droughts, persistence, measured by serial correlation, is generally accepted and addressed primarily by assuming low flows are generated by stationary stochastic processes. The general acceptance of climate change by the scientific community has prompted increased attention in dealing with nonstationarity of hydrologic stochastic processes. It remains to be seen to what extent and in what manner properties of record events predicated on the assumption of *iid* would be affected by accounting for variations in the tail weights of probability distributions and nonstationarity. [Arnold et al. \(2008\)](#) briefly consider the case of “records in improved populations” for the case when the process of interest X , is stochastically ordered, so that the process is nonstationary.

This presentation of the theory of records follows the classical theory of record-breaking processes. Thus an objective frequency-based approach that assumes stationary extreme value processes is adopted. It is well documented in several places that the theory of records has a connection to both the theory of extremes and to the theory of order statistics. There are numerous recent developments in the theory of extremes and the theory of order statistics. Given that these three theories are connected, considering connections among extreme value theory, order statistics, record-breaking theory, and other complications due to nonstationarity, along with Bayesian-based statistical analyses, is important. It is anticipated that future work on record processes in hydrology will address these and other issues.

The following summarizes our current knowledge of the theory of record events, along with some new results directed to hydrologic studies. The chapter is broken into three sections: (1) parametric results, (2) nonparametric results, and (3) applications of the theory of record events to envelope curves. In the section on parametric results, we summarize the distributional properties of the flood of record Y and the entire upper record sequence R_m , corresponding to various commonly used probability distributions for X . In the section on nonparametric results, we summarize the statistical properties of the recurrence time (or return period) of the records Y and the nonparametric properties of record-breaking processes, such as the distribution of the number of records in an n year sequence termed N_n . The last section summarizes a few recent case studies that have applied the theory of records to estimate the exceedance probability associated with envelope curves and have tested the theory of records for evaluating the independence of flood records.

12.1 PARAMETRIC PROPERTIES OF HYDROLOGIC RECORDS

All statistical methods can be classified as either parametric or nonparametric. Parametric methods are generally based on an underlying assumption regarding the distribution of the random variable of interest, whereas nonparametric methods generally do not require such assumptions. For example, all of the expressions for the first two moments of X and Y for various assumed probability density functions (pdfs) given in Tables 12-1 and 12-2 are parametric results. Nonparametric methods tend to focus on the ranked or ordered observations because ordered observations have various theoretical properties that are independent of the distribution of the random variable of interest. In the following sections we review both parametric and nonparametric properties of record events.

12.1.1 The Probability Distribution, Quantile Function, and Moments of Record Floods

In this section we consider some probability distributions that arise in the theory of extremes ([Beirlant et al. 2004](#)) and are commonly used in flood frequency analysis, such as the exponential

Table 12-1. The Properties of the Random Variable X and Its Record Process Y for a Gumbel and a Generalized Extreme Value Distribution.

	<i>Gumbel distribution</i>	<i>Generalized extreme value distribution</i>
cdf of X	$F_X(x) = \exp\left\{-\exp\left(-\frac{(x-\xi)}{\alpha}\right)\right\}$	$F_X(x) = \exp\left(-\left[1 - \kappa \cdot \frac{(x-\xi)}{\alpha}\right]^{1/\kappa}\right)$ for $\kappa \neq 0$
Mean of X	$\mu_x = \xi + \gamma\alpha$	$\mu_x = \xi + \alpha[1 - \Gamma(1 + \kappa)]/\kappa$
Variance of X	$\sigma_x^2 = (\pi\alpha)^2/6$	$\sigma_x^2 = \alpha^2\{\Gamma(1 + 2\kappa) - [\Gamma(1 + \kappa)]^2\}/\kappa^2$
Quantile of X	$x(p_x) = \xi - \alpha \ln(-\ln(p_x))$	$x(p_x) = \xi + \frac{\alpha}{\kappa}[1 - (-\ln(p_x))^\kappa]$
Quantile of Y	$y(p_y) = \xi - \alpha \ln\left(-\frac{\ln(p_y)}{n}\right)$	$y(p_y) = \xi + \frac{\alpha}{\kappa}\left[1 - \left(\frac{-\ln(p_y)}{n}\right)^\kappa\right]$
Mean of Y	$\mu_y = \xi + \alpha(\gamma + \ln(n)) = \mu_x + \alpha \ln(n)$	$\mu_y = \xi + \frac{\alpha}{\kappa}\left[1 - \frac{\Gamma(1+\kappa)}{n^\kappa}\right]$
Variance of Y	$\sigma_y^2 = \sigma_x^2 = \frac{\pi^2\alpha^2}{6}$	$\sigma_y^2 = \left(\frac{\alpha}{\kappa \cdot n^\kappa}\right)^2\{\Gamma(1 + 2\kappa) - [\Gamma(1 + \kappa)]^2\}$

Note: cdf = cumulative density function.

Table 12-2. Properties of the Random Variable X and Its Record Process Y for the Exponential and Generalized Pareto Distributions.

	<i>Exponential distribution</i>	<i>Generalized pareto distribution</i>
cdf of X	$F_X(x) = 1 - \exp(-\beta(x - \xi))$	$F_X(x) = 1 - [1 - \beta(x - \xi)]^{1/\kappa}$
Mean of X	$\mu_x = \xi + (1/\beta)$	$\mu_x = \xi + [1/(\beta(1 + \kappa))]$
Standard deviation of X	$\sigma_x = 1/\beta$	$\sigma_x = (1/\beta)\sqrt{\Gamma[1 + (2/\kappa)] - \Gamma^2[1 + (1/\kappa)]}$
Quantile of X	$x(p_x) = \xi - (\ln(1 - p_x)/\beta)$	$x(p_x) = \xi + [1 - (1 - p_x)^\kappa]/(\kappa\beta)$
Quantile of Y	$y(p_y) = \xi - \frac{\ln(1 - p_y^{1/n})}{\beta}$	$y(p_y) = \xi - \frac{(1 - p_y^{1/n})^\kappa}{\beta \cdot \kappa}$
Mean of Y	$\mu_y = \xi + \frac{1}{\beta} \sum_{v=1}^n \frac{1}{v}$	Not available
Variance of Y	$\sigma_y^2 = \frac{1}{\beta} \sum_{v=1}^n \frac{1}{v^2}$	Not available

Note: cdf = cumulative density function.

(EXP) and generalized Pareto (GPA) distributions used in the analysis of flood peaks over a threshold (POT), and the Gumbel (GUM) and generalized extreme value (GEV) distributions used for modeling AM flood series. Further, we only consider exact results, so that in instances when only asymptotic results are available, we do not report them, because in the field of hydrology flood samples are usually not nearly long enough for asymptotic results to apply. We begin by summarizing the pdf, cumulative density function (cdf), quantile function, and moments (where possible) of a record flood drawn from these distributions and the moments of the record process R_m .

Suppose the *iid* annual maximum flood series X has a known cdf $F_X(x)$. The cdf for the record flood Y is then

$$F_Y(y) = [F_X(y)]^n \quad (12-1)$$

where n is the length of the series of annual maximum floods. Similarly, the pdf of Y can be obtained by differentiation of Equation (12-1):

$$f_Y(y) = dF_Y(y)/dy \quad (12-2a)$$

or in terms of the original pdf and cdf of X ([Ang and Tang 1984](#)):

$$f_Y(y) = n[F_X(y)]^{n-1}f_x(y) \quad (12-2b)$$

All of the extreme value pdfs considered here have quantile functions that can be expressed analytically, hence we found it useful to derive moments of Y using the fact that

$$\mu_r = \int_0^1 y^r(p)dp \quad (12-3)$$

where μ_r denotes the r^{th} moment of Y about the origin, and $p = F_Y(y)$ and $y(p)$ are the quantile functions of the record floods Y . The quantile function is also sometimes referred to as the inverse of the cdf. All the results in the following section regarding the properties of Y are derived from Equations (12-1)–(12-3).

We begin by summarizing the properties of record floods drawn from GUM and GEV distributions, followed by a summary of the properties of record floods drawn from EXP and GPA distributions. Further details on all four of these distributions, including their product moments, L-moments, parameter estimators, and goodness-of-fit tests, can be found in [Hosking and Wallis \(1997\)](#) and [Stedinger et al. \(1993\)](#). [Gumbel \(1958\)](#) provides a comprehensive treatment of the GUM and EXP distributions.

12.1.2 The Gumbel Distribution

If X arises from a GUM distribution, then its cdf is

$$F_X(x) = \exp\left\{-\exp\left(-\frac{(x-\xi)}{\alpha}\right)\right\} \quad (12-4)$$

where ξ is the location parameter and α is the scale parameter. The location parameter ξ is equal to the mode of x , which can be determined by setting $df_x(x)/dx = 0$ and solving for $x_{\text{mode}} = \xi$ where $f_x(x) = dF_x(x)/dx$. The mean and variance of X are $\mu_x = \xi + \gamma\alpha$ and $\sigma_x^2 = (\pi\alpha)^2/6$ respectively, where $\gamma = 0.5772$ is the Euler number. The quantile function of a GUM variable is given by

$$x(p_x) = \xi - \alpha \ln(-\ln(p_x)) \quad (12-5)$$

where $p_x = F_X(x)$. The range of x in Equations (12-4) and (12-5) is unbounded both above and below so that $-\infty < x < \infty$.

Substitution of Equation (12-4) into Equations (12-1) and (12-2) leads to the cdf and pdf of the record flood series Y generated from GUM samples of length n . Inversion of the cdf of Y leads to the quantile function for the record flood Y drawn from a GUM sample of length n :

$$y(p_y) = \xi - \alpha \ln\left(-\frac{\ln(p_y)}{n}\right) = \xi - \alpha \ln(-\ln(p_y)) + \alpha \ln(n) \quad (12-6)$$

where $p_y = F_Y(y) = F_X(y)^n$. Note that the quantile functions of the Y series and the X series differ only by the constant term $\alpha \ln(n)$, and for the special case when $n = 1$, the quantile function of the Y series is identical to the quantile function for the X series in Equation (12-5). Therefore, if the distribution of annual maximum floods follows a GUM distribution, the distribution of the record

flood Y will also be Gumbel. This is consistent with the findings of [Gumbel \(1958\)](#), [Ang and Tang \(1984\)](#), [Lambert and Li \(1994\)](#), and others.

Exact expressions for the mean, μ_y , and variance, σ_y^2 , of record floods drawn from a GUM series of length n were first introduced by [Gumbel \(1958\)](#) and may be derived by substitution of Equation (12-6) into Equation (12-3) and using the fact that $\mu_y = \mu_1$ and $\sigma_y^2 = \mu_2 - \mu_1^2$, leading to

$$\mu_y = \xi + \alpha(\gamma + \ln(n)) = \mu_x + \alpha \ln(n) \quad (12-7a)$$

$$\sigma_y^2 = \sigma_x^2 = \frac{\pi^2 \alpha^2}{6} \quad (12-7b)$$

where $\gamma = 0.5772$ is the Euler number. As expected, all moments of Y reduce to the moments of X when $n = 1$, and Y always has exactly the same variance as X , regardless of n . Because both X and Y are Gumbel, they also both have skewness of 1.1396. Arnold et al. (1998, Equations 2.7.15 and 2.7.16) also report the mean and variance of Y ; however, their expressions were found to be in error because they do not reduce to the moments of X when $n = 1$, nor do they reproduce the expected moments when we performed Monte Carlo experiments to check Equation (12-7). The mode of Y , also given by [Gumbel \(1958\)](#), is easily derived by setting $df_y(y)/dy = 0$ and solving for y , where $f_y(y)$ is given by Equation (12-2), resulting in

$$y_{mode} = \xi + \alpha \ln(n) \quad (12-8a)$$

Thus, the mean record event μ_y is always greater than its mode y_{mode} by an amount equal to $\gamma\sigma_x\sqrt{6}/\pi = 0.45\sigma_x = 0.45\sigma_y$. Similarly, the mean of x is also always greater than its mode by the same amount, $0.45\sigma_x$. [Gumbel \(1958\)](#) also reports the median of Y as

$$y(0.5) = \xi + \alpha(0.36651 + \ln(n)) \quad (12-8b)$$

which always lies between the mode and mean. Figure 12-1 compares the exceedance probability [$1 - F_x(\bar{y})$] of the mean $\bar{y} = \mu_y$, median $y(0.5)$, and mode y_{mode} of y with the expected exceedance probability $1/(n+1)$, illustrating that all three measures of central tendency of the flood of record y tend to be exceeded more frequently than one would expect, on average, for a given sample size n . Note that the sample estimator of the nonexceedance probability of the i^{th} observation in a sample ordered in ascending order, $i/(n+1)$, known as the Weibull plotting position, yields unbiased

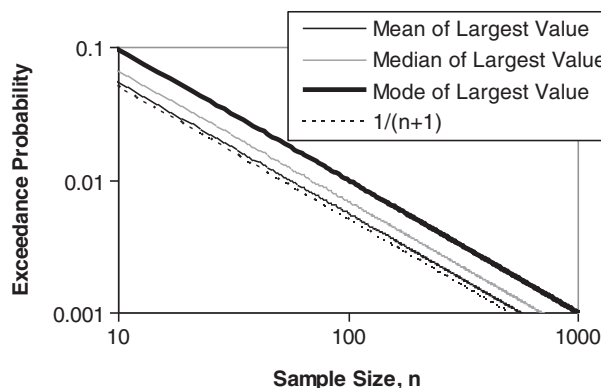


Figure 12-1. Exceedance probability of various measures of central tendency associated with the flood of record from a Gumbel distribution.

estimates of the exceedance probability of any random variable, regardless of its underlying distribution.

L-moments are often preferred over ordinary moments, for parameter estimation and goodness-of-fit evaluation (Hosking and Wallis 1997, Stedinger et al. 1993). The first L-moment of Y is equal to the first ordinary moment of Y given in Equation (12-7a). The second L-moment of Y , denoted $\lambda_2(y)$, is identical to the second L-moment of X , denoted $\lambda_2(x)$, which are both given by

$$\lambda_2(y) = \lambda_2(x) = \alpha \ln(2) \quad (12-9)$$

The L-skew of both X and Y is equal to 0.1699, and the L-kurtosis of both X and Y is equal to 0.1504.

Arnold et al. (1998) document that the upper record process (i.e., the time sequence of record events in a series of extremes; see Section 12.1) for the case when X follows a Gumbel pdf is defined by

$$R_m = \xi + \alpha \ln(R_m^*) \quad (12-10)$$

where R_m^* is a gamma ($m + 1, 1$) random variable, so that the mean and variance of the upper record process is given by

$$E[R_m] = \xi - \alpha\gamma + \alpha \sum_{j=1}^m \frac{1}{j} \quad (12-11)$$

$$Var[R_m] = \alpha^2 \left[\frac{\pi^2}{6} - \sum_{j=1}^m \frac{1}{j^2} \right] \quad (12-12)$$

where again $\gamma = 0.5772$ is the Euler number.

12.1.3 The Generalized Extreme Value Distribution

Douglas and Vogel (2006) first derived the cumulative distribution function, quantile function, moments, and L-moments of the record floods Y for the case when the flood series X_i follows a GEV distribution. The origins of the GEV distribution can be traced to a paper by Fisher and Tippett (1928), which seems to be the first account of what today is referred to as the GEV model. Later the GEV model was discussed by Mises (1936) and subsequently applied by Jenkinson (1955) and is now perhaps the most widely accepted distribution for modeling flood series in the world (see Table 1 of Vogel and Wilson 1996). Its cdf is

$$F_X(x) = \exp \left(- \left[1 - \kappa \cdot \frac{(x - \xi)}{\alpha} \right]^{1/\kappa} \right) \quad \text{for } \kappa \neq 0 \quad (12-13)$$

where ξ is the location parameter, α is the scale parameter, and κ is the shape parameter (Jenkinson 1955). As the shape parameter κ approaches zero, the GEV distribution approaches a GUM (or extreme value type I) distribution. The mean and variance of x are given by $\mu_x = \xi + \alpha[1 - \Gamma(1 + \kappa)]/\kappa$ and $\sigma_x^2 = \alpha^2 \{ \Gamma(1 + 2\kappa) - [\Gamma(1 + \kappa)]^2 \} / \kappa^2$. The range of x in Equation (12-13) is $-\infty < x < \xi + \frac{\alpha}{\kappa}$ for $\kappa > 0$ and $\xi + \frac{\alpha}{\kappa} \leq x < \infty$ for $\kappa < 0$, so that both X and Y will have an upper bound when $\kappa > 0$, as Enzel et al. (1993) and others suggest. Chowdhury et al. (1991) provide goodness-of-fit tests and hypothesis tests for the GEV distribution.

The quantile function for the original flood series X is obtained by solving Equation (12-13) for x which yields

$$x(p_x) = \xi + \frac{\alpha}{\kappa} [1 - (-\ln(p_x))^{\kappa}] \quad (12-14)$$

where $p_x = F_X(x)$. Substitution of Equation (12-13) into Equations (12-1) and (12-2) leads to the cdf and pdf of the record flood series Y generated from GEV samples of length n . The inverse distribution of Y leads to the quantile function for the record flood Y , drawn from a GEV sample of length n :

$$y(p_y) = \xi + \frac{\alpha}{\kappa} \left[1 - \left(\frac{-\ln(p_y)}{n} \right)^{\kappa} \right] \quad (12-15)$$

where $p_y = F_Y(y) = F_X(y)^n$. When $n = 1$, the quantile function of Y in Equation (12-15) reduces to the quantile function for the X series in Equation (12-14). Note that Equation (12-15) is similar in form to the quantile function for the original GEV variate X , given in Equation (12-14). Douglas and Vogel (2006) use the quantile function in Equation (12-14) to derive the moments and L-moments of Y when X arises from a GEV pdf. The mean, μ_y , and variance, σ_y^2 , of Y are

$$\mu_y = \xi + \frac{\alpha}{\kappa} \left[1 - \frac{\Gamma(1 + \kappa)}{n^\kappa} \right] \quad (12-16a)$$

$$\sigma_y^2 = \left(\frac{\alpha}{\kappa \cdot n^\kappa} \right)^2 \{ \Gamma(1 + 2\kappa) - [\Gamma(1 + \kappa)]^2 \} \quad (12-16b)$$

Similar to the quantile function, the first two moments of Y differ in form from those of X , only by the additional term, n^κ . Figure 12-2 compares the exceedance probability [$1 - F_x(\mu_y)$] of the mean record flood from a GEV distribution, for various values of the shape parameter, with the expected exceedance probability $1/(n+1)$. Figure 12-2 documents that the mean record flood (in real space) from a GEV distribution tends to be exceeded less frequently than one would expect for a given sample size n when the shape parameter is negative.

The first L-moment of Y is identical to the mean of Y in Equation (12-16a). The second L-moment of Y is

$$\lambda_2(y) = \frac{\alpha \Gamma(1 + \kappa)}{\kappa n^\kappa} (1 - 2^{-\kappa}) \quad (12-17)$$

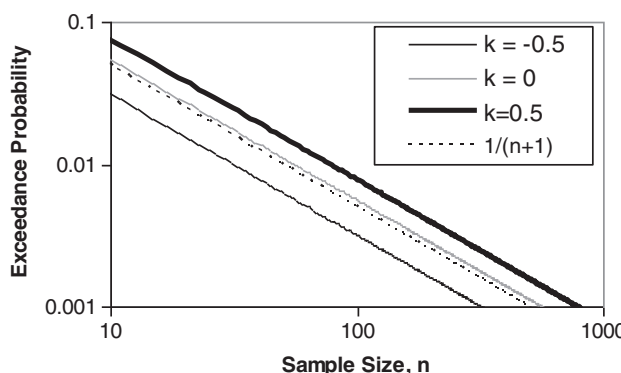


Figure 12-2. Exceedance probability of the mean flood of record μ_y from a GEV distribution for various values of the shape parameter.

The mode of Y is easily derived by setting $df_y(y)/dy=0$ and solving for y , where $f_y(y)$ is given by Equation (12-2), resulting in

$$y_{\text{mode}} = \xi + \frac{\alpha}{\kappa} \left[1 + \left(\frac{\kappa - 1}{n - \kappa} \right)^k \right] \quad (12-18)$$

The L-skew and L-kurtosis of Y are the same as for the original X series given by Stedinger et al. (1993), Hosking and Wallis (1997), and others. Thus, if X follows a GEV distribution, then Y is also GEV with the same shape parameter κ . Only their means and coefficients of variation differ. We are unaware of any previous work summarizing the pdf or moments of the upper record process for the GEV case, analogous to the results for the Gumbel distribution in Equations (12-10)–(12-12).

12.1.4 The Exponential Distribution

For an AM series of floods distributed as a GUM distribution, Stedinger et al. (1993) and others show that the POT flood series will follow an EXP distribution with pdf, cdf, and quantile function given by $f_X(x) = \beta \exp(-\beta(x - \xi))$, $F_X(x) = 1 - \exp(-\beta(x - \xi))$, and $x(p_x) = \xi - (\ln(1 - p_x)/\beta)$, respectively, with mean and standard deviation given by $\mu_x = \xi + (1/\beta)$ and $\sigma_x = 1/\beta$, respectively. Here ξ is generally the threshold value above which flood peaks are reported, hence it is given or assumed, along with the flood series. Substitution of the EXP cdf into Equation (12-1) yields the cdf of the maximum value, which is easily inverted to obtain the quantile function of the record flood for an EXP variable:

$$y(p_y) = \xi - \frac{\ln(1 - p_y^{1/n})}{\beta} \quad (12-19)$$

where $p_y = F_Y(y)$. Gumbel (1958) and Arnold et al. (1998) report exact expressions for the mean and variance of Y (as well as other properties) when X arises from a standard exponential distribution that assumes $\xi = 0$ and $\beta = 1$. Those expressions can be generalized for the exponential distribution introduced here, leading to expressions for the mean and variance of the record flood:

$$\mu_y = \xi + \frac{1}{\beta} \sum_{\nu=1}^n \frac{1}{\nu} \quad (12-20a)$$

$$\sigma_y^2 = \frac{1}{\beta} \sum_{\nu=1}^n \frac{1}{\nu^2} \quad (12-20b)$$

Raqab (2004) derives recurrence relations for the moments of order statistics from a generalized EXP distribution. Numerical integration also provides exact estimates of the moments of Y by substitution of Equation (12-19) into Equation (12-3). Parameter estimates ξ and β obtained from the X series may be used in Equation (12-19) to generate series of record floods or to characterize the pdf or cdf of the Y series using Equations (12-1) and (12-2).

12.1.5 Generalized Pareto Distribution

In the case where an AM series of floods follows a GEV distribution, Stedinger et al. (1993) and others show that the POT flood series follows a GPA distribution with pdf, cdf, and quantile function given by $f_X(x) = \beta[1 - \exp(-\kappa\beta(x - \xi))]^{(1-\kappa)/\kappa}$, $F_X(x) = 1 - [1 - \beta(x - \xi)]^{1/\kappa}$, and

$x(p_x) = \xi + [1 - (1 - p_x)^\kappa]/(\kappa\beta)$, respectively, with the mean and standard deviation given by $\mu_x = \xi + [1/(\beta(1 + \kappa))]$ and $\sigma_x = (1/\beta)\sqrt{\Gamma[1 + (2/\kappa)] - \Gamma^2[1 + (1/\kappa)]}$. Here again, ξ is the threshold value above which flood peaks are reported. Applying Equation (12-1) to the GPA cdf yields the cdf of Y , which is easily inverted to obtain the quantile function of the record flood for a GPA process:

$$y(p_y) = \xi - \frac{(1 - p_y^{1/n})^\kappa}{\beta\kappa} \quad (12-21)$$

where $p_y = F_Y(y)$. Balakrishnan and Ahsanullah (1994) derive recurrence relations for the moments of order statistics for a GPA distribution, but we were unable to obtain closed-form solutions to either the moments or L-moments of Y for the GPA distribution. Arnold et al. (1998) report exact expressions for the mean and variance of Y when X arises from a Pareto model, which is parameterized quite differently from the GPA model. Numerical integration provides exact estimates of the moments of Y by substitution of Equation (12-21) into Equation (12-3). Estimates of ξ , κ , and β obtained from the X series may be used in Equation (12-21) to generate series of record floods or to characterize the pdf or cdf of the Y series using Equation (12-1) and Equation (12-2).

Tables 12-1 and 12-2 summarize the parametric properties of hydrologic records.

12.2 NONPARAMETRIC STATISTICAL PROPERTIES OF HYDROLOGIC RECORDS

For a discussion of the distinction between parametric and nonparametric approaches to summarizing the statistical properties of hydrologic records, see Section 12.1.

12.2.1 The Recurrence or Waiting Time of Record Floods

Interestingly Wilks (1959) and Gumbel (1961) show that the probability distribution of the unconditional waiting or recurrence time to the next record flood has no moments, thus other measures are needed to define the waiting time to the next record flood. That this important yet paradoxical result has received so little attention in the water resources literature is surprising. The only publication we could find in the field of water resources that cited either of these papers is Castellarin et al. (2005). Chandler (1952) and Gumbel (1961) give the pdf of the waiting time T to exceed the m^{th} largest observation in a sample of size n as

$$f_T(t) = \binom{n}{m} mt^{-m-1} \left(1 - \frac{1}{t}\right)^{n-m} \quad \text{for } t \geq 1 \quad (12-22)$$

For example, the expected value of the waiting time T is given by $E[T] = n/(m - 1)$, which is clearly infinite for the record flood ($m = 1$), but finite for all other order statistics. Similarly, all upper moments of T corresponding to the record flood are infinite.

Equation (12-22) written from $m = 1$ gives the pdf of the waiting time to exceed the record flood, which yields

$$f_T(t) = \frac{n}{t^2} \left(1 - \frac{1}{t}\right)^{n-1} \quad \text{for } t \geq 1 \quad (12-23)$$

Figure 12-3 illustrates the pdf of the recurrence time for the three cases $n = 10, 50$, and 100 .

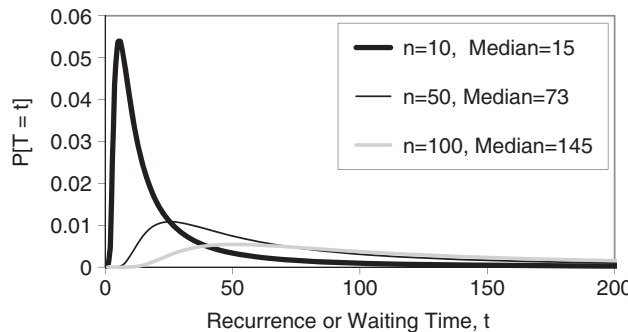


Figure 12-3. Probability distribution of the recurrence time to the next record flood for a sample of size $n = 10, 50$, and 100 years, after just having observed a record flood.

Gumbel (1961) also gives the cdf of the waiting time to exceed the record flood as

$$F_T(t) = \left(1 - \frac{1}{t}\right)^n \quad (12-24)$$

The quantile function for the waiting time to exceed the record flood is easily obtained from Equation (12-24) as

$$T(p) = \frac{1}{1 - p^{1/n}} \quad (12-25)$$

where $p = F_T(t)$.

In addition to the expectation of the recurrence time of the record flood, other measures of central tendency such as the mode, median, and geometric mean of the recurrence time exist for the record flood. Because the moments of the recurrence times do not exist, one could use the mode, median, quantiles, and possibly upper L-moments to describe the recurrence time of the record flood distribution in lieu of the moments.

Gumbel (1961) gives the geometric mean T_G , median T_{median} , and mode T_{mode} of the waiting time to the next record flood as

$$T_G = \exp\left[\sum_{j=1}^n \frac{1}{j}\right] \cong \gamma + \ln(n) = 1.78n \quad (12-26)$$

$$T_{median} = \frac{2^{1/n}}{(2^{1/n} - 1)} \cong \frac{n}{\ln(2)} + \frac{1}{2} = 1.44n + 0.5 \quad (12-27)$$

$$T_{mode} = \frac{n+1}{2} \quad (12-28)$$

Note that in general $T_{mode} < n < T_{median} < T_G$. Clearly these measures of central tendency of the waiting time to the next record flood vary over a significant range from roughly $0.5n$ to $1.8n$.

12.2.2 The Probability Distribution of the Number of Record Events

The time of occurrence at which record highs occur in the original sequence may be expressed as the series of binary variates:

$$Y_i = \begin{cases} 1 & \text{if } X_i = \max(X_1, X_2, \dots, X_i) \\ 0 & \text{otherwise} \end{cases} \quad (12-29)$$

Let R denote the number of record-breaking events in an n year period where

$$R = \sum_{i=1}^n Y_i \quad (12-30)$$

If the *max* function in Equation (12-29) is replaced by *min*, one obtains the lower record events. Alternatively, one can switch from upper- to lower-record events, by replacing the original sequence with $-X_1, -X_2, \dots, -X_n$. Some initial theoretical results are taken from the mathematics literature, and others are introduced here for the first time.

[David and Barton \(1962\)](#) first introduce an expression, using Stirling numbers, for the exact probability mass function (pmf) for the number of upper- and lower-record events in an n year period. A much simpler yet identical expression for the exact pmf of R , denoted $P_n[R=r]$ (see [Vogel et al. 2001](#)), is defined by the recursion

$$P_j[R=r] = \left(1 - \frac{1}{j}\right) P_{j-1}[R=r] + \left(\frac{1}{j}\right) P_{j-1}[R=r-1] \quad (12-31)$$

for $r \geq 1$ and $j \geq 2$ with the initial values $P_1[R=0]=0$ and $P_1[R=1]=1$. [Glick \(1978\)](#) also reports the asymptotic result for large sample sizes:

$$P_n[R=r] = \frac{[\ln(n)]^{r-1}}{n \cdot (r-1)!} \quad (12-32)$$

Combining the definition of the cmf $P[R \leq r] = \sum_{k=1}^r P[R=k]$ with the asymptotic result in Equation (12-32), and after algebra, we obtain

$$P[R \leq r] = \frac{\Gamma(r, \ln(n))}{\Gamma(r)} \quad (12-33)$$

where $\Gamma(x, y)$ is the incomplete gamma function defined by $\Gamma(a, b) = \int_b^\infty t^{a-1} e^{-t} dt$. Note that the gamma function is a special case of the incomplete gamma function whereby $\Gamma(a) = \Gamma(a, 0)$. Figure 12-4 illustrates the agreement between the asymptotic approximation of the cmf and the exact result for $n = 10$ and 100 . We recommend the use of the exact result.

12.2.3 Moments of the Number of Record-Breaking Events

The first observation is defined to be a record event. The following results for the mean and variance of R are due to [Glick \(1978\)](#):

$$\mu_R = \sum_{i=1}^n 1/i \quad (12-34)$$

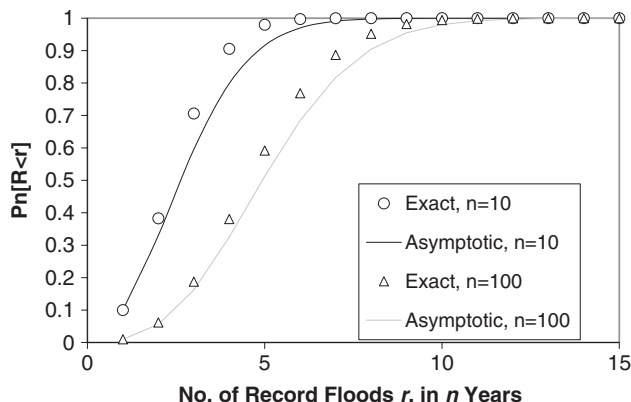


Figure 12-4. Comparison of exact and asymptotic cmfs for the number of record floods in 10- and 100 year periods.

and

$$\sigma_R^2 = \sum_{i=1}^n 1/i - \sum_{i=1}^n 1/i^2 \quad (12-35)$$

Zafirakou-Koulouris (2000, p. 26) derived an exact expression for the skewness of R :

$$\gamma_R = \frac{\sum_{i=1}^n 1/i - 3 \sum_{i=1}^n 1/i^2 + 2 \sum_{i=1}^n 1/i^3}{\left(\sum_{i=1}^n 1/i - \sum_{i=1}^n 1/i^2 \right)^{3/2}} \quad (12-36)$$

as well as an approximation to the kurtosis of R

$$\kappa_R \cong 3.19 - \frac{1.42}{n} - \frac{5.43}{n^2} - 0.00419\sqrt{n} \quad (12-37)$$

The approximation in Equation (12-37) is accurate to at least three decimal places for $4 \leq n \leq 100$.

Vogel et al. (2001) use moment diagrams based on Equations (12-34) to (12-37) to show that in spite of the central limit theorem, the tail behavior of the distribution of R differs significantly from other common distributions even for large sample sizes. Among distribution functions commonly used, the distribution of R closely resembles the normal distribution, though only approximately. Table 12-3 summarizes the moments and moment ratios of the number of record-breaking events in a series of length n .

12.2.4 Multivariate Record Events

Hydrologists have a long-standing and continuing interest in reducing the sampling errors associated with the estimates of specific statistical properties of hydrologic sequences, for example, the parameters of distributions presumed to provide a good probabilistic description of the sequences, or more generally, the moments of the distributions determined from the sequences. Achieving reduction in sampling error via the transfer of information from sequences at nearby sites to a sequence at a particular site is referred to as regionalization, which is a means of augmenting time averages through spatial averages. Collectively the sites comprise a region. Techniques of

Table 12-3. Moments and Moment Ratios of the Number of Record Breaking Events, R.

Moment or moment ratio	Theoretical expression
Mean	$\mu_R = \sum_{i=1}^n \frac{1}{i}$
Variance	$\sigma_R^2 = \sum_{i=1}^n \frac{1}{i} - \sum_{i=1}^n \frac{1}{i^2}$
Skewness	$\gamma_R = \left(\sum_{i=1}^n \frac{1}{i} - 3 \sum_{i=1}^n \frac{1}{i^2} + 2 \sum_{i=1}^n \frac{1}{i^3} \right) / \left(\sum_{i=1}^n \frac{1}{i} - \sum_{i=1}^n \frac{1}{i^2} \right)^{3/2}$
Kurtosis	$\kappa_R = 3.19 - 1.42 \frac{1}{n} - 5.43 \frac{1}{n^2} - 0.00419 \sqrt{n}$
Coefficient of variation	$C_v(R) = \sqrt{\sum_{i=1}^n \frac{1}{i} - \sum_{i=1}^n \frac{1}{i^2}} / \sum_{i=1}^n \frac{1}{i}$

regionalization must contend with the structure of dependence exhibited by the set of m regional sequences. In the following discussions, the lengths of the sequences are assumed to be the same, n , at all sites unless otherwise noted. Further assumed is that the sequences are realizations of a stationary multivariate stochastic process.

The dependence structure may be expressed in terms of the matrix of pairwise product-moment correlations between the sequences:

$$R = \begin{bmatrix} 1 & r_{1,2} & r_{1,3} & r_{1,4} & r_{1,m} \\ r_{2,1} & 1 & r_{2,3} & r_{2,4} & r_{2,m} \\ r_{3,1} & r_{3,2} & 1 & r_{3,4} & r_{3,m} \\ r_{4,1} & r_{4,2} & r_{4,3} & 1 & r_{4,m} \\ r_{m,1} & r_{m,2} & r_{m,3} & r_{m,4} & 1 \end{bmatrix} \quad (12-38)$$

As is well known, R is a symmetric matrix: $r_{j,k} = r_{k,j}$, $\forall j, k$, and $r_{j,k} = 1$ for $j = k$, where $r_{j,k} \rightarrow p_{j,k}$ as $n \rightarrow \infty$. If $r_{j,k}(p_{j,k}) = 0$ and $\forall j \neq k$, then $R \equiv I$, where I is the identity matrix. In general, the effectiveness of regionalization in transferring information to a site of interest from nearby sites diminishes as $p_{j,k} \rightarrow 1$. The univariate probability distributions describing the sequences at each of the m sites are the marginal distributions of the multivariate distribution defining the structure of dependence between the m sequences.

Little hydrologic attention has been directed to multivariate distributions, apart from the multivariate normal distribution, in particular the bivariate normal distribution. Among recent publications on multivariate distributions in hydrology are Kallache et al. (2013), Bardossy and Horning (2016), and Salvadori et al. (2016). Transformations of hydrologic sequences to provide better descriptions by specific univariate distributions do not ensure that a multivariate distribution having those univariate distributions as its marginal distributions will satisfactorily describe the sequences collectively. Multivariate normal distributions have normal marginal distributions, but multivariate distributions other than multivariate normal distributions may have nonnormal marginals. Moreover, product moment correlations are not invariant to transformation.

Flood experience is often summarily reported in terms of flood envelope curves as suggested by Jarvis (1926). The record floods at sites within a specified region, paired with the drainage areas at the sites, are plotted relative to a specified enveloping line, that is, a line below which all paired points lie. The enveloping line is a basis of regionalization, as the line is defined by the flood experience as a function of drainage area at the various sites. The probability that a flood at a specific site will exceed the flood defined by the envelope line for that site provides a regional basis for assessing the flood risk at that site. The probability of exceeding the envelope line at a particular site depends upon the degree of dependence among the record floods at the regional sites, and that dependence is a

function of the dependence structure of the sequences from which the record floods are derived and upon the length of the sequences. However, the dependence between sequences is not a major determinant, as that correlation tends to zero as the length of the sequences increases.

The dependence among the record flows may be expressed by the symmetric matrix of the product-moment correlations between the record flows:

$$W = \begin{bmatrix} 1 & w_{1,2} & w_{1,3} & w_{1,4} & w_{1,m} \\ w_{2,1} & 1 & w_{2,3} & w_{2,4} & w_{2,m} \\ w_{3,1} & w_{3,2} & 1 & w_{3,4} & w_{3,m} \\ w_{4,1} & w_{4,2} & w_{4,3} & 1 & w_{4,m} \\ w_{m,1} & w_{m,2} & w_{m,3} & w_{m,4} & 1 \end{bmatrix} \quad (12-39)$$

If $|\rho_{j,k}| < 1$ and $\forall j \neq k$, then

$$\lim_{n \rightarrow \infty} W \rightarrow I \quad (12-40)$$

where I denotes the identity matrix—the correlation between record values is asymptotically zero. If $|\rho_{j,k}| = 1$, then $|w_{j,k}| = 1$ and $\forall j, k$. See Sibuya (1960) and Husler and Reiss (1989). Two general properties of the distribution of record events within sequences are suggestive of Equation (12-40). First, record events tend to be sparsely distributed over a sequence. For example, from Equations (12-34) and (12-35), the expected number of records in sequences of length $n = 10$ is approximately 2.93 with standard deviation equal to about 1.17. For $n = 10^6$, the mean number of record events is about 14.39 with standard deviation equal to about 3.57. See, for example, Glick (1978). Second, record events tend to occur early in a sequence. Unlike the correlation between sequences that can be estimated directly from the sequences, the correlation between records must be inferred from the $r_{j,k}$ given the length of the sequences, n .

In an unpublished manuscript, Matalas and Olsen (personal communication) provided values of w corresponding to values of ρ and n . Table 12-4 illustrates that given ρ , w decreases as n increases. As ρ increases, w decreases at a slower rate as n increases. The correlations between record events reported by Matalas and Olsen were obtained via simulation of bivariate normal sequences of length n , $\{x_t : t = 1, \dots, n\}$, and $\{y_t : t = 1, \dots, n\}$:

$$x_t = \varepsilon_t \quad (12-41a)$$

$$y_t = \rho \varepsilon_t + \sqrt{1 - \rho^2} \delta_t \quad (12-41b)$$

where $\forall t$, x_t , y_t , ε_t , and δ_t are each distributed as $N(0, 1)$, and ε_t and δ_t are mutually independent. For each specified value of the couple (ρ, n) , $M = 50,000$ paired sequences $\{x\}$ and $\{y\}$ were generated, and from each of the paired sequences, the record values of the sequences were obtained. The correlation w was given by the correlation between the $M = 50,000$ paired record values.

Table 12-4. Correlation Between Records, w , Corresponding to Correlation Between Sequences, ρ , Given n .

$n \setminus \rho$	0.1	0.2	0.4	0.6	0.8	0.9
50	0.009	0.028	0.099	0.238	0.490	0.690
100	0.014	0.027	0.080	0.200	0.446	0.657
200	0.004	0.013	0.055	0.159	0.395	0.616

In a real-world context, the relation between w and ρ given n may be viewed in terms of Walker's (1999) partition of 423 sites in the United States into three regions, an eastern region consisting of 189 sites, a midwestern region consisting of 120 sites, and a western region consisting of 114 sites. At each site, sequences of annual floods were of length $n = 50$. The average correlations, \bar{r} , among the sequences were 0.212 for the eastern region, 0.177 for the midwestern region, and 0.420 for the western region. Under the assumption that floods at a given site are independently and identically distributed, the mean correlations between the record floods, \bar{w} , inferred from the \bar{r} 's, are 0.03 in the eastern region, less than 0.03 in the midwestern region, and about 0.10 in the western region.

If the number of sites in a region is M , the mean distance between the sites would increase as the area of the region increases, and the mean correlation between the sequences would decrease. In a small region where the distances between the sites are small, the correlation between sequences would tend to be large. Orographic effects on meteorological attributes of a region would render the mean correlation between the sequences smaller than they would be in the absence of those effects, whatever the area of the region may be. Moreover, if the length of each of the M sequences is n , the correlations between the sequences would be less if the sequences are nonconcurrent than if the sequences are concurrent. Thus, in general hydrologic settings of orographic effects and nonconcurrency of sequences, the mean correlation between record events would be smaller than they would otherwise be if the orographic effects were absent and if the sequences were all concurrent.

In the previous discussions, the dependence between sequences and the dependence between the record events within the sequences were expressed in terms of the correlations between the sequences and between the record events. Dependence is defined by the multivariate distribution underlying the m regional sequences. Unless dependence is linear, correlation may grossly misrepresent the degree of dependence. If the marginal distributions associated with the m dimensional distribution function for the region are assumed to be of a certain form, then the correlations purporting to define the degree of dependence between sequences may not be able to attain their full mathematical range ($-1, 1$). For example, the marginal distributions of the bivariate Farlie–Gumbel–Morgenstern distribution yield a dependence structure marked by $|\rho| < 1/3$, whatever the marginal distributions are. Schucany et al. (1978) give the upper bound on $|\rho|$ for various marginal distributions, and Butkiewicz and Hys (1977) give a detailed account of the dependence structure in the case of Weibull marginal distributions of the bivariate Farlie–Gumbel–Morgenstern distribution and of its multivariate extension.

Bivariate distributions, such as the Farlie–Gumbel–Morgenstern distribution, for which the dependence structure is marked by correlations considerably less than their full mathematical range, have limited hydrologic utility because the distribution is itself limited to accommodating absolute values of cross-correlations equal to or less than $1/3$. However, such distributions are potentially useful in dealing with situations of low-level dependence structure, situations that arise in studies of regions of large spatial scope. In reference to the record events within sequences, the dependence structure tends to low-level dependence as the sequence lengths n increases. The current dependence structures of record events within hydrologic sequences is a lower level than in the past, and it is a higher level than it will be in the future.

The statistics regarding the number of records within a sequence has been dealt with extensively. For a summary account refer to Arnold et al. (1998). To determine the number of record events within a region, the multivariate structure underlying the observed sequences—at least the dependence structure of the sequences—must be accounted for (see Vogel et al. 2001).

At present the literature on the statistics of records from several sequences is relatively sparse. Several definitions have been proposed for bivariate records. Arnold et al. (1998) list four definitions of bivariate records and note where others may be found in the literature. In reference to random variables X and Y , the four definitions are

1. A record of the first kind occurs at time k , if X_k exceeds all preceding X_i or Y_k exceeds all preceding Y_i , or both;
2. A record of the second kind occurs at time k , if X_k exceeds the current record value X^* or Y_k exceeds the current record value Y^* , or both;
3. A record of the third kind occurs at time k , if X_k exceeds X^* and Y_k exceeds Y^* ; and
4. A record of the fourth kind occurs at time k , if X_k exceeds all preceding X_i and Y_k exceeds all preceding Y_i .

Nagaraja et al. (2003) account for bivariate records of the second and fourth kinds assuming the underlying distribution to be the Farlie–Gumbel–Morgenstern and the normal bivariate distributions. The correlation between the number of records in each of two sequences, both of length n , and the means and standard deviations of the total number of records in the sequences are given. The hydrologic shortcoming of the Farlie–Gumbel–Morgenstern distribution, restriction to low-level dependence, is noted. Transformation of observed flood sequences at two sites on the upper Mississippi river to correspond to normally distributed marginal distributions facilitates estimation of the expected number of future record flows at the sites.

12.3 FLOOD ENVELOPE CURVES: APPLICATION OF THE THEORY OF RECORDS

We begin this section by introducing one of the most common applications of the theory of records to hydrology: envelope curves. A flood envelope curve (Figure 12-5) represents an upper bound on our flood experience in a region and is formed by the record floods for all sites in a region. This section reviews the historical (nonprobabilistic) applications of envelope curves and follows with some recent research and applications that describe how to provide a probabilistic interpretation of envelope curves. Because envelope curves provide an upper bound on our flood experience, they are

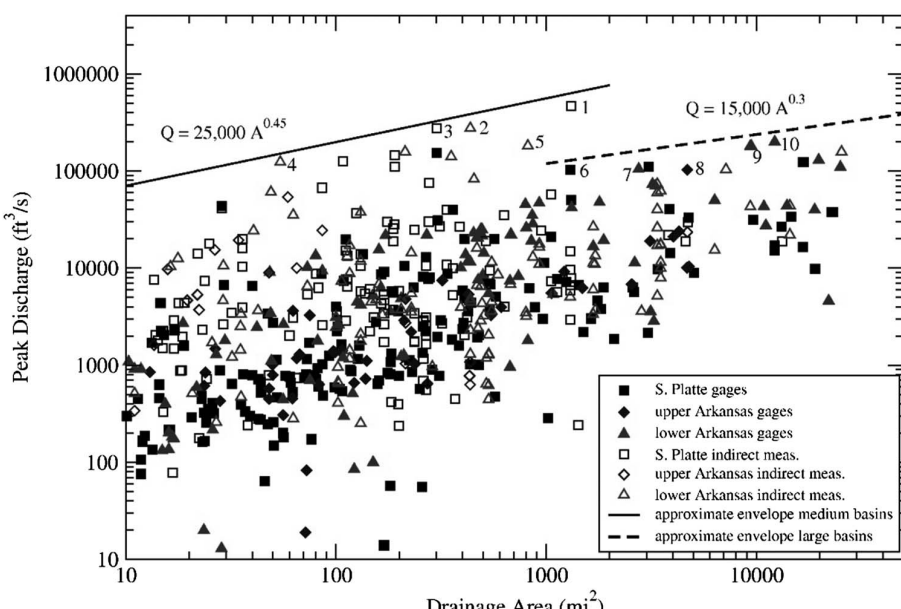


Figure 12-5. Example maximum peak discharge data, Q , and drainage area, A , envelope curve for observations within the Arkansas and South Platte River Basins in Colorado.

often compared loosely to other estimates of extraordinary floods such as the probable maximum flood. A goal of this section is to enable hydrologists to make such comparisons among extraordinary floods more objective, by including a probabilistic interpretation of all such estimates of extraordinary floods.

12.3.1 Envelope Curves: Historical Background

Envelope curves are relatively simple empirical relationships between the maximum peak flow experienced in a region and drainage area. Peak flow data are one of the most important measures of extreme floods (e.g., [Dalrymple 1964](#)). Figure 12-5 shows an example envelope curve, with the points that control the envelope summarized in Table 12-5. Figure 12-5 plots peak flow versus drainage area. Table 12-5 and Figure 12-5 show that the two flood events in June of 1921 (points 1–5) and 1965 (points 8–10) are responsible for the records that define both envelopes depicted.

The most basic envelope curve formula is that attributed to Myers ([Jarvis et al. 1936](#), [Creager et al. 1945](#)):

$$Q = CA^n \quad (12-42)$$

where

Q = peak discharge (ft^3/s),

C = coefficient,

A = drainage area (mi^2), and

n = exponent less than unity.

As Creager et al. (1945, p. 125) note, values assigned to n by various investigators have ranged from 0.3 to 0.8. Based on the data for the Arkansas and South Platte Rivers (Figure 12-5), a change appears to occur in the envelope curve parameters C and n that may be scale dependent.

12.3.1.1 Traditional Envelope Curve Applications

Envelope curves have a long history in flood hydrology studies ([Fuller 1914](#), [Meyer 1917](#), [Alvord and Burdick 1918](#), [Mead 1919](#), [Linsley et al. 1949](#), [Dalrymple 1964](#)). In flood hydrology studies, regional peak discharge envelope curves are useful for four main purposes: (1) to expand the flood database for the watershed of interest with data from nearby streams, (2) to portray extreme flood potential in a region of interest, (3) to gain an understanding of the regional hydrometeorology corresponding to the largest floods on record, and (4) as a basis for comparison of probabilistic estimates of peak discharge and/or design floods. Peak flow envelope curves have traditionally been used to examine maximum floods in many locations such as the United States ([Crippen and Bue 1977](#), [O'Connor and Costa 2004](#)), Puerto Rico ([Smith et al. 2005](#)), Italy ([Marchetti 1955](#)), and globally ([Costa 1987a](#), [Herschy 2003](#)). They have also been used to examine physical causes of extraordinary floods on small basins (e.g., [Costa 1987b](#)) and for differentiation between rainfall and snowmelt floods ([Jarrett 1990](#)).

Flood envelope curves provide an upper bound on the maximum peak streamflow that might be expected at a site of interest based on data from the surrounding region. Usually, a record flood that lies near the envelope curve may be two or three times larger than a flood of record from a particular site within that region ([Crippen and Bue 1977](#)). Envelope curves for a region are often used as a guide to making rule-of-thumb estimates of the magnitude of high flood discharges that may be expected at a given site on a stream. For example, envelope curves have been used for comparing design flood discharges for new and existing dams ([Creager et al. 1945](#), [Bureau of Reclamation 1987](#), [Cudworth 1989](#)). Envelope curves are routinely used by hydrologic and hydraulic engineers to judge the adequacy of probable maximum flood (PMF) estimates ([Cudworth 1989](#), p. 177). They provide a useful empirical comparison of maximum observed floods within a region to the flood behavior at a particular site described by a design flood, PMF, or quantile estimate from a frequency curve. The

Table 12-5. Largest Observed Instantaneous Peak Discharge Estimates that Define the Record Flood Envelope Relation for the Arkansas and South Platte River Basins Up to Year 2005.

Point no. (fig. 12-5)	Station name	Drainage area (mi ²)	Date	Peak discharge (ft ³ /s)	Measurement type	Meas. rating	Flood type
1	Bijou Creek near Wiggins, CO	1,314.0	06/18/1965	466,000	slope-area at misc. site	poor	general storm
2	Rule Creek near Toonerville, CO	435.0	06/18/1965	276,000	slope-area at misc. site	fair	general storm
3	East Bijou Creek at Deer Trail, CO	302.0	06/17/1965	274,000	slope-area at misc. site	fair	general storm
4	Jimmy Camp Creek near Fountain, CO	54.3	06/17/1965	124,000	slope-area at misc. site	fair	general storm
5	Two Buttes Creek near Holly, CO	817.0	06/17/1965	182,000	slope-area at misc. site	good	general storm
6	South Fork Republican River near Idalia, CO	1,300.0	05/31/1935	103,000	slope-area at gauge	unknown	general storm
7	Purgatoire River at Ninemile Dam, near Higbee, CO	2,752.0	06/18/1965	105,000	estimated flow over dam at gauge	unknown	general storm
8	Arkansas River near Pueblo, CO	4,686.0	06/03/1921	103,000	slope-area at gauge	unknown	general storm
9	Arkansas River near Nepesta, CO	9,345.0	06/04/1921	180,000	slope-area at gauge	unknown	general storm
10	Arkansas River at La Junta, CO	12,29.0	06/04/1921	200,000	slope-area at gauge	unknown	general storm

largest historic peaks within a region are also used for PMF comparisons (Bullard 1986). Our probabilistic analysis of envelope curves, which is provided later on in this chapter, makes such comparisons more objective than using an envelope curve without a probabilistic basis.

Envelope curves can be used in research studies that seek to improve our understanding of the mechanisms that give rise to extraordinary floods. For example, one could explore flood seasonality, flood process (snowmelt, thunderstorms, general storms, rain on snow, etc.), and flood hydrometeorology (storm type, duration, areal extent, etc.) for each of the largest floods. This information can then be used to enhance our understanding and prediction of floods in the future. Matthai (1990) describes several limitations of envelope curves, including data quality problems, partial area rainfall/runoff representation, and the curve's nonrepresentativeness of the geologic and climatic conditions at one's point of interest.

12.3.1.2 Envelope Curve Relationships

In addition to the most commonly used envelope curve relation in Equation (12-42), several others have been proposed. Myers and Jarvis (Jarvis 1926, Jarvis et al. 1936) recommend $n = 0.5$ and use a modified form of Equation (12-42) as (see Linsley et al. 1949, p. 574):

$$Q = 100b\sqrt{A} \quad (12-43)$$

with Q and A defined as previously, and b a constant that ranges from about 1 to 300 based on data in Table 12-11 of Linsley et al. (1949). Linsley et al. (1958, p. 211) make the following remarks regarding the Myers formula [Equation (12-43)]: "Only luck will permit the selection of the correct value of b for a basin. Formulas of this type should never be used for engineering design."

Based on the data they had at the time for the United States and at other locations around the world, Creager et al. (1945) recommend a modified form of Equation (12-42):

$$Q = 46CA^{0.894(A^{-0.048})} \quad (12-44)$$

However, they note that this envelope relation did not bound the 1940 storm in North Carolina or the May–June 1935 Texas storm. A more flexible form of an envelope curve formula with five parameters was presented by Crippen (1982):

$$Q = K_1 A^{K_2} (A^{C_1} + C_2)^{K_3} \quad (12-45)$$

where C and K are empirical constants. Meyer (1994) uses Equation (12-45) to estimate maximum flood flows in northern and central California. In addition to the aforementioned equations, many other formulas have been proposed (Jarvis et al. 1936, Creager et al. 1945, Linsley et al. 1949).

An equivalent form of Equation (12-42) with peak flow expressed as a unit discharge q (where $q = Q/A$) is (Creager et al. 1945)

$$q = CA^{n-1} \quad (12-46)$$

Figure 12-6 shows this common relationship, using the data from Figure 12-5. The relation in Equation (12-46) yields a straight line in log space (e.g., Jarvis 1926; Creager et al. 1945; Matalas 1997, 2000; Castellarin et al. 2005). We recommend the use of Equation (12-46), which we employ in Section 12.3.2 for developing a probabilistic interpretation of envelope curves.

Unit discharge envelope curves can be based on other variables, such as elevation (e.g., Figure 12-7), in addition to drainage area. Castellarin et al. (2007) introduce a multivariate approach to the development of probabilistic regional envelope curves, including both geomorphologic factors and climatic factors.

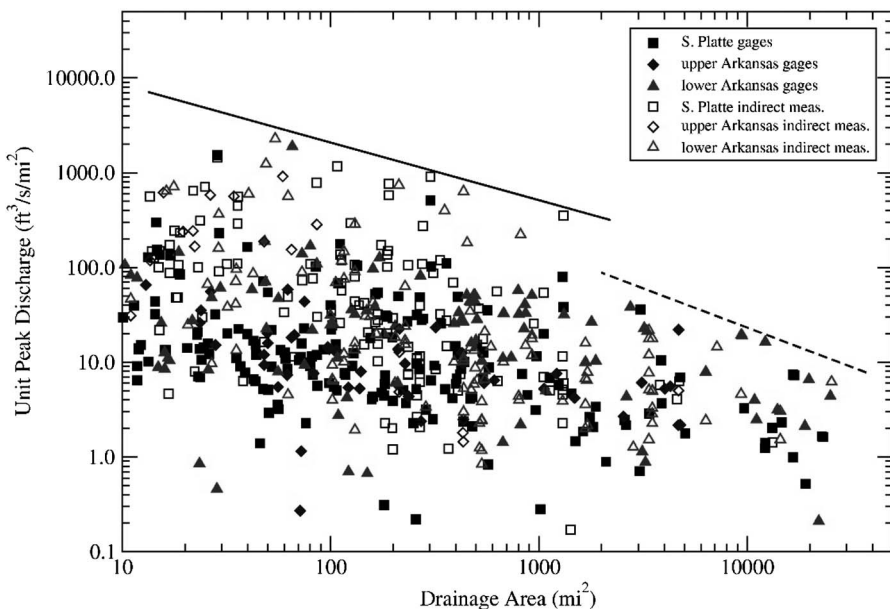


Figure 12-6. Example of maximum unit peak discharge data, q , and drainage area, A , envelope curve for observations within the Arkansas and South Platte River basins in Colorado.

Some early empirical efforts attempted to provide a probabilistic interpretation to record floods. Fuller (1914) presents three equations that relate mean annual floods, drainage area, return period, and maximum floods:

$$\bar{Q} = CA^{0.8} \quad (12-47)$$

$$Q = \bar{Q}(1 + 0.8 \log_{10} T) \quad (12-48)$$

$$Q_{max} = Q(1 + 2A^{-0.3}) \quad (12-49)$$

where

\bar{Q} = mean annual flood,

Q = greatest 24 h discharge during a period of years T (maximum 1 day flood),

Q_{max} = maximum peak flow based on the 1 day maximum, and

C = coefficient that is assumed to be constant for the river at the point of observation.

Fuller (1914) as cited in Meyer (1917) was the first to define a regional flood probability in the context of an envelope curve.

After the mid-1950s in the United States, envelope curves did not typically have any probability or frequency associated with them (Crippen and Bue 1977, Crippen 1982). As IACWD (1986, p. 71) notes, "This magnitude is unqualified by any statement of probability or frequency of occurrence. For this reason, and because the relationship between the envelope curve and the observational data is not prescribed by any specific hydrologic theory, the proper usage and interpretation of the envelope curve are not clear." For envelope curves to be most useful, a probabilistic interpretation is needed and was recently proposed by Castellarin et al. (2005) and Vogel et al. (2007).

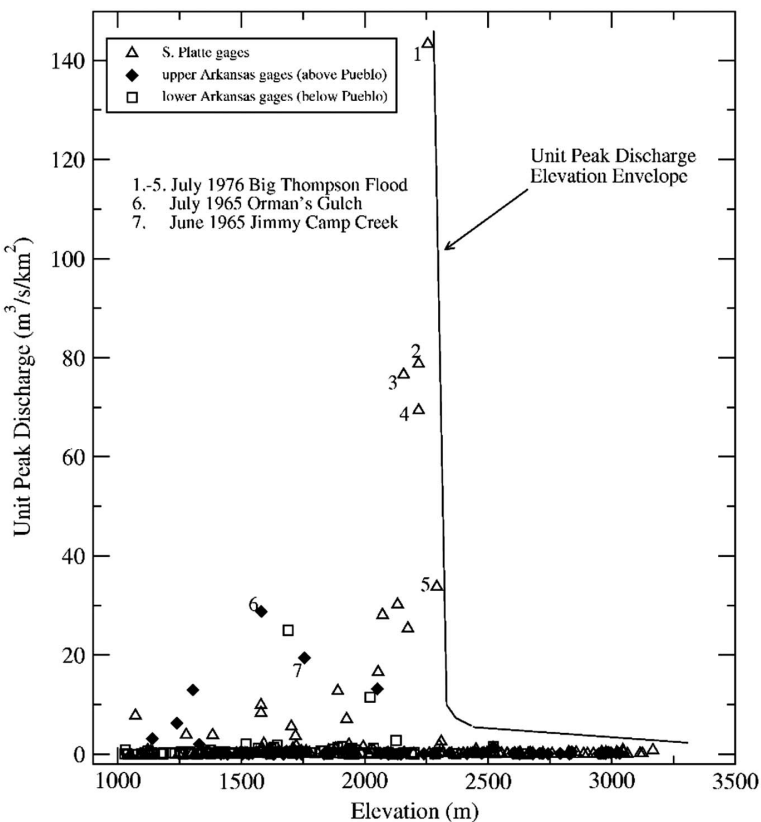


Figure 12-7. Example of flood envelope curve based on watershed elevation for observations within the Arkansas and South Platte River basins, Colorado.

Source: [England et al. \(2010\)](#).

12.3.2 Probabilistic Interpretation of Envelope Curves

Consider an envelope curve that plots the logarithm of the ratio of the record flood to the drainage area, $\ln(Q/A)$, versus $\ln(A)$ as was shown earlier in Figure 12-6 and Equation (12-46). We term such an envelope curve a “regional envelope curve” (REC) because it reflects our regional experience of record floods. Consider the REC in Figure 12-8 ([Jarvis 1926](#)) along with the envelope curve described by

$$\ln\left(\frac{Q}{A}\right) = a + b \ln(A) \quad (12-50)$$

If the envelope curve is assumed to be linear (in log space) with a given slope b , the intercept a in Equation (12-50) may be estimated by forcing the REC to bound all record floods to the present, say up to the year n . See [Castellarin et al. \(2005\)](#) as well as Equation (12-53) and (12-54) and associated discussion for further information on how to estimate the slope term b for a region. Let X_j^i denote the annual maximum flood in year $i = 1, 2, \dots, n$ at site $j = 1, 2, \dots, M$, where M is the number of sites in the region. Let $X_j^{(i)}$ denote the flood flow of rank (i) at site j , where ranking is from smallest (1) to largest (n). The REC’s intercept up to the year n can then be expressed as

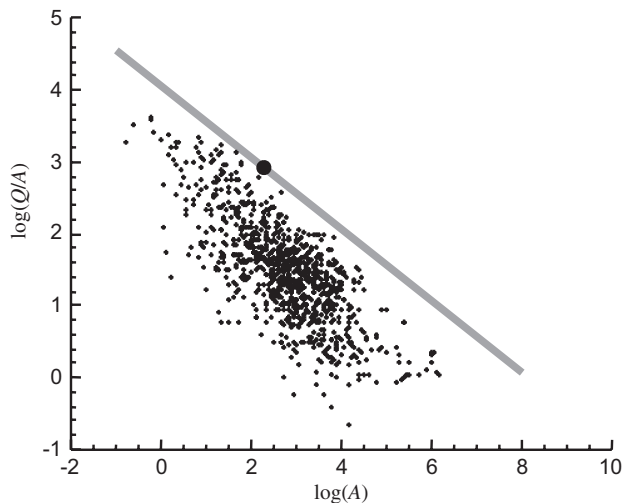


Figure 12-8. Flood experience accrued prior to 1925, discharge, Q in ft^3/s , and drainage area, A in mi^2 ; elements of experience (+) and element of experience (•) defining the intercept of the envelope curve (thick gray line).

Source: [Jarvis \(1926\)](#).

$$a^{(n)} = \max_{j=1, \dots, M} \left\{ \ln \left(\frac{X_j^{(n)}}{A_j} \right) - b \ln(A_j) \right\} \quad (12-51)$$

where A_j is the area of site $j = 1, 2, \dots, M$.

[Castellarin et al. \(2005\)](#) propose a probabilistic interpretation of an REC defined by Equation (12-50) that is based on the following assumptions:

The study region is homogeneous in the sense of the index-flood hypothesis (see, e.g., [Dalrymple 1960](#)) and therefore, the probability distribution of standardized annual maximum peak flows is the same for all sites in the region (or in the pooling group of sites; e.g., [Burn 1990](#), [Castellarin et al. 2001](#)). The standardized annual maximum peak flow, X' , is defined for a given site as the annual maximum peak flow, X , divided by a site-dependent scale factor, μ_X (i.e., the index flood), assumed in this study to be equal to the at-site mean of X . Under this assumption, the flood quantile with exceedance probability p , denoted as x_p , is given by

$$x_p = \mu_X x'_p \quad (12-52)$$

where x'_p is the regional dimensionless flood quantile with exceedance probability p .

The relationship between the index flood μ_X and basin area A is of the form

$$\mu_X = C A^{b+1} \quad (12-53)$$

where C is a constant and b is the same as in Equations (12-50) and (12-51).

Combining Equations (12-52) and (12-53) leads to a relation between $\ln(x_p/A)$ and $\ln(A)$ that is analogous to Equation (12-50):

$$\ln \left(\frac{x_p}{A} \right) = \ln \left(\frac{\mu_X x'_p}{A} \right) = \ln(C x'_p) + b \ln(A) \quad (12-54)$$

The formal analogy between Equations (12-51) and (12-54) originates from the simplifying assumptions and implies that if the index flood scales with the drainage area, then the slope of the REC for a region can be identified from this scaling relationship. More importantly, Castellarin et al. (2005) show that the assumptions also imply that (1) a probabilistic statement can be associated with the intercept $a^{(n)}$ of Equation (12-50), which is determined from the largest standardized annual maximum peak flow observed in the region [here standardization is achieved via the index-flood method using Equation (12-53) to express the index flood], and (2) the exceedance probability (p -value) of the REC is equal to the p -value of the standardized maximum flood (hereafter referred to as regional record flood, Y).

The following two sections illustrate how, under these fundamental assumptions, the problem of estimating the exceedance probability of an REC can be placed within the context of the theory of records and the actual estimation of the exceedance probability of an REC can be addressed.

12.3.2.1 Envelope Curves and the Theory of Records

The REC provides an upper bound on record-breaking flood experiences to date and therefore is closely connected with the theory of records (Vogel et al. 2001, 2007). Castellarin et al. (2005) analyze the gains in regional flood experience summarized by the REC in the context of record-breaking events and evaluate the behavior of sequences of regional record floods for cross-correlated regions through repeated Monte Carlo simulations. See Castellarin et al. (2005) for a description of how those experiments were performed. According to the authors, the regional gain in flood experience that causes an upward shift in the REC involves all sites in the region in a “competition” to break the upper bound that forms the REC. In a region with M sites, a new record event (hereafter referred to as envelope record) occurs when *at least one site* experiences a record flood event *and* the magnitude of that flood also exceeds the upper bound identified by the current REC. When a new envelope-record event is experienced, the REC is shifted upward, with the slope b held constant, to bound the new gain in regional flood experience.

Under the hypotheses adopted here [see Equations (12-52) to (12-54)], which are identical to those described by Castellarin et al. (2005, Section 2.1), the temporal dynamics of the REC coincides with the temporal dynamics of the record-breaking process of the series of maxima of the M standardized annual floods, which is always a univariate *iid* sequence even in the presence of intersite correlation.

Figure 12-9 compares the theoretical average number of records μ_R for a univariate *iid* sequence [Equation (12-34)] with the average number of envelope records obtained from Monte Carlo

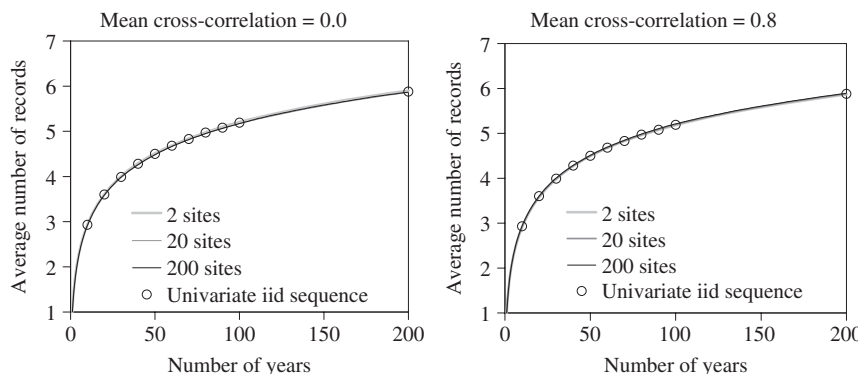


Figure 12-9. Values of $f\mu_R$ for a univariate iid sequence of record-breaking events and average number of envelope records obtained through Monte Carlo experiments for different cross-correlated regions.

experiments. Figure 12-9 considers regions with $M = 2$ to 200 sites, each with sample lengths $n = 1$ to 200 years both with and without cross-correlation. All curves reported in Figure 12-9 are nearly coincident, and analogous outcomes can be obtained for the variance of the number of record events σ_R^2 [Equation (12-35)], showing the equivalence between the temporal dynamics of the record series for a realization of an *iid* sequence of random variables and of an REC.

Even though the moments of the number of envelope-record breaking events depend neither on the regional parent distribution of flood flows, nor on the degree of cross-correlation among flood sequences (see, e.g., Figure 12-9), these aspects are critical when estimating the exceedance probability of the envelope, as detailed in the next subsection.

12.3.2.2 Exceedance Probability of Envelope Curves

We describe how to estimate the exceedance probability of an REC under the hypotheses given in Equations (12-52) to (12-54), which are the same hypotheses as in Castellarin et al. (2005). Let the variables x_i , y_i , and z_i represent three different random variables related to the annual maximum flood at site i , the flood of record (FOR) at site i and the ordinate of the point on the envelope curve corresponding to site i , respectively. Also, let A_i denote the drainage area at site i . The scatter diagram of $\ln(y_i)$ versus $\ln(A_i)$, where $y_i \equiv x_i^{(n)}$ (FOR at site i), is an expression of our flood experience over the period $t = 1$ to $t = n$. Our experience may be bound by an enveloping line, that is, a line below which all our experience, expressed in terms of FORs and their relation to drainage area, lies (see the gray line in Figure 12-8). The enveloping line is set with a slope, b , and passes through that observation, such that all other points lie below the line, hence the name, envelope line. The envelope line [Equation (12-50)] may also be rewritten as

$$\ln(z_i) = a + b \ln(A_i) \quad (12-55)$$

Consider the derivation of the probability of exceeding the envelope curve at a particular site i at time $t = n + 1$, where, perhaps, a water project is envisaged at the site. Vogel et al. (2007) address this problem by considering a hypothetical region consisting of M sites where the sequence length n at each site is sufficiently long (in the limit as $n \rightarrow \infty$), such that the matrix of the correlations between record values may be represented by an identity matrix, $W \approx I$ [see Equations (12-39) and (12-40)]. At time $t = n + 1$, the flood at site i will be a flood of record, R_i at that site with probability

$$P(R_i) = (n + 1)^{-1}; \forall i \quad (12-56)$$

Given that the flood of record event R_i occurs at site i , the record flood will exceed the envelope value at that site, E_i with probability given by

$$P(E_i|R_i) = \int_{z_i}^{\infty} dG_{(n)}(Y_i) \quad (12-57)$$

where z_i denotes the ordinate of the point on the envelope line given in Equation (12-55) corresponding to the abscissa, $\ln(A_i)$, whereas

$$G_{(n)}[Y_i] = F^n[X_i] = \Pr[Y_i > y_i] \quad (12-58)$$

is the distribution of the FOR in a sequence of length n .

Of interest here is the occurrence of both events E_i and R_i , at time $t = n + 1$, that is, having observed at time $t = n + 1$ a record flood at site i that also exceeded the envelope. This particular event, which we term $E_i R_i$, will occur with exceedance probability given by

$$\begin{aligned} P(E_i R_i) &= P(R_i)P(E_i | R_i) \\ &= (n+1)^{-1} \int_{z_i}^{\infty} dG_{(n)}(Y_i) \end{aligned} \quad (12-59)$$

Note that all sites are not equal because site $i = i'$ is the site that defines the current ($t = n$) envelope and for which the record flood, $z_{i'} = x_{i'}^{(n)}$, falls on the envelope curve. All future record floods at that site will exceed the envelope line, so that

$$P(E_{i'} | R_{i'}) = \int_{z_i = x_{i'}^{(n)}}^{\infty} dG_{(n)}(y_{i'}) = 1 \quad (12-60)$$

whereby

$$\begin{aligned} P(E_{i'} R_{i'}) &= P(R_{i'})P(E_{i'} | R_{i'}) \\ &= P(R_{i'}) \\ &= (n+1)^{-1} \end{aligned} \quad (12-61)$$

If a water project is contemplated at site i , then of particular interest at that site is the local exceedance probability in year ($n + 1$) of the envelope line defined in year n , that is, the probability that the flow in year ($n + 1$) at site i will exceed the envelope line defined in year n (see [Vogel et al. 2007](#)):

$$\begin{aligned} \Phi_i(z_i) &= \begin{cases} P(E_{i'} R_{i'}); & \text{if } i = i' \\ P(E_i R_i); & \text{if } i \neq i' \end{cases} \\ &= \begin{cases} (1+n)^{-1}; & \text{if } i = i' \\ (1+n)^{-1} \int_{z_i}^{\infty} dG_{(n)}(Y_i); & \text{if } i \neq i' \end{cases} \end{aligned} \quad (12-62)$$

Equation (12-62) yields an exceedance probability corresponding to the ordinate of the point on the envelope line z_i corresponding to the abscissa, $\ln(A_i)$, based on M samples, each of length n . Hence the probability $\Phi_i(z_i)$ is a random variable with a distribution and moments that depend upon the distributional properties of both the ordinate of the envelope line z_i as well as the flood series at site i .

[Vogel et al. \(2007\)](#) consider two summary measures of $\Phi_i(z_i)$: (1) its expectation $E[\Phi_i(z_i)]$, which we term the expected exceedance probability of an envelope (EEPE), and (2) $\Phi_i(E[z_i])$, which we term the exceedance probability of the expected envelope (EPEE). The EEPE is defined by

$$E[\Phi_i(z_i)] = \begin{cases} (1+n)^{-1}; & \text{if } i = i' \\ \int_0^{\infty} \left[(1+n)^{-1} \int_{z_i}^{\infty} G_{(n)}(Y_i) dz \right] g_{(Mn)}(z_i) dz; & \text{if } i \neq i' \end{cases} \quad (12-63)$$

where $g_{(Mn)}(z_i) = \frac{dG_{(Mn)}(z_i)}{dz}$ and $\Phi_i(z_i)$ is given in Equation (12-62). Here $g_{(Mn)}(z_i)$ represents the pdf associated with the value of the envelope curve at a particular site i . Because the envelope is defined by flood series at M independent sites, each of length n , the record length associated with the pdf of z , $g_{(Mn)}(z_i)$, is equal to Mn . Similarly, the EPEE is defined by

$$\Phi_i(E[z_i]) = \begin{cases} (1+n)^{-1}; & \text{if } i = i' \\ (1+n)^{-1} \int_{\mu_z}^{\infty} dG_{(n)}(Y_i); & \text{if } i \neq i' \end{cases} \quad (12-64)$$

where μ_z denotes the expectation of z .

The summary measures EPEE and EEPE represent two different probabilistic statements regarding an envelope curve. If one's concern is with making a probabilistic statement regarding the single envelope based on historical observations, then EEPE is an appropriate summary measure, whereas if one's concern is with making a probabilistic statement regarding the expected envelope, then EPEE is an appropriate summary measure.

For example, if flood series x arises from a GUM model with cumulative distribution function given in Equation (12-4), and the envelope curve is based on Mn iid GUM observations, according to Equation (12-7a) the expectation of the envelope curve is given by

$$\mu_z = \xi + \alpha(\gamma + \ln(Mn)) \quad (12-65)$$

where ξ is the GUM location parameter, α is the GUM scale parameter, M is the number of sites, each with sample size n , and γ is the Euler number.

Substitution of Equation (12-65) into Equation (12-64) yields the cdf of the record flood at site i denoted as $G_{(n)}(Y_i)$, whereby the exceedance probability of the envelope given in Equation (12-64) becomes

$$\Phi_i(z_i) = \frac{1 - G_{(n)}(z_i)}{n+1} = \frac{1 - \exp\left(-n \exp\left(-\frac{z_i - \xi}{\alpha}\right)\right)}{n+1}; \quad \text{for } i \neq i' \quad (12-66)$$

The EPEE is obtained by substitution of $z_i = \mu_z$ from Equation (12-65) into Equation (12-66), which, after subsequent algebra, leads to

$$\Phi_i(\mu_z) = \text{EPEE} = \frac{1 - \exp\left(-\frac{\exp(-\gamma)}{M}\right)}{n+1}; \quad \text{for } i \neq i' \quad (12-67)$$

where $\Phi_i(\mu_z)$ denotes the exceedance probability associated with the expected envelope curve μ_z , at site i , when flows are iid as Gumbel.

The EEPE for the GUM case is obtained by substitution of $\Phi_i(z_i)$, given by Equation (12-66), and $g_{(mn)}(z_i) = \frac{dG_{(mn)}(z_i)}{dz}$ into Equation (12-63), which leads to

$$\begin{aligned} E[\Phi_i(z_i)] = \text{EEPE} &= \int_0^{\infty} \frac{1 - \exp\left(-n \cdot \exp\left(-\frac{z - \xi}{\alpha}\right)\right)}{n+1} \frac{dG_{(mn)}(z_i)}{dz} dz \quad \text{for } i \neq i' \\ &= \frac{1}{n+1} \left[1 - \frac{M}{M+1} \left(1 - \exp\left(-n(M+1) \cdot \exp\left(\frac{\pi}{C_v \sqrt{6}} - \gamma\right)\right) \right) \right] \\ &\approx \frac{1}{(n+1)(M+1)} \end{aligned} \quad (12-68)$$

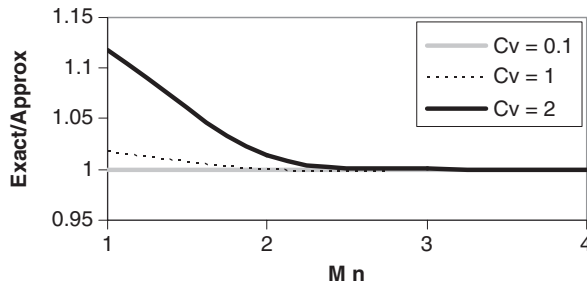


Figure 12-10. Comparison of the exact and approximate expressions for EEPE given in Equation (12-68).

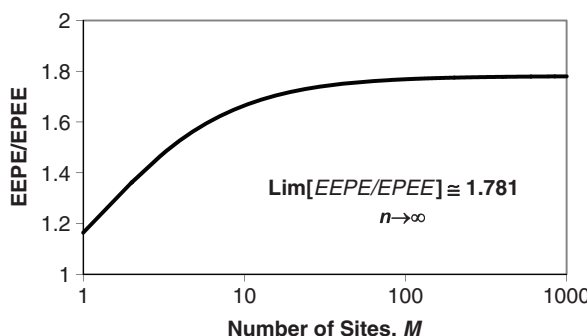


Figure 12-11. Comparison of the ratio of EEPE (Equation (12-68)) to EPEE [Equation (12-67)] for the Gumbel case (M = no. of sites and n = sample size at each site).

where C_v is the coefficient of variation of the annual maximum flood flows x . Figure 12-10 illustrates the ratio of the exact and approximate expressions for EEPE given in Equation (12-68) as a function of M , n , and C_v . Figure 12-10 (see also Vogel et al. 2007) illustrates that the approximation is generally excellent whenever the product $M n > 3$, regardless of the value of C_v .

Figure 12-11 (Vogel et al. 2007) provides a comparison of the values of EPEE and EEPE for the Gumbel case and illustrates that the values of EEPE are always greater than those of EPEE. Figure 12-11 illustrates that over the range of values of M considered, the increase in the ratio of EEPE to EPEE as M increases strongly indicates that the ratio converges to a value equal to approximately 1.781. Vogel et al. (2007) prove the correctness of the analytic expressions of EPEE and EEPE for the *iid* GUM case through a series of Monte Carlo simulation experiments and provide a close analytical expression of the EPEE for the *iid* GEV case, which using the usual notation reads

$$\Phi_i(\mu_z) = EPEE = \frac{1 - \exp\left[-\frac{(\Gamma(1+\kappa))^{1/\kappa}}{M}\right]}{n + 1}; \quad \text{if } i \neq i' \quad (12-69)$$

where $\Gamma(\cdot)$ is the gamma function and κ is the shape parameter of the GEV distribution. As expected, EPEE for the GEV case in Equation (12-69) reduces to EPEE for the GUM case in Equation (12-67) as κ approaches zero.

12.3.3 Exceedance Probability of Empirical Envelope Curves

In most practical applications, the datasets that can be used to construct empirical envelope curves consist of a limited number of years (i.e., the hypothesis that in the limit $n \rightarrow \infty$ cannot be applied).

In addition, actual flood records in neighboring watersheds often exhibit significant values of the cross-correlation coefficient. Nonetheless, it is exactly under these circumstances that an estimation of the exceedance probability of the envelope curve is needed for the design and operation of large dams. Recall that if one's concern is with making a probabilistic statement regarding the single envelope curve based on historical observations, then *EEPE* is an appropriate summary measure, whereas if one's concern is with making a probabilistic statement regarding the expected envelope curve, then *EPEE* is an appropriate summary measure. This subsection illustrates how to estimate *EPEE* for envelope curves constructed from real-world datasets that exhibit limited flow records of varying length and are cross-correlated. We are unaware of any efforts as of yet to estimate *EEPE* from such real-world datasets.

[Castellarin et al. \(2005\)](#) show under two fundamental hypotheses (see beginning of Section 12.3.2) the problem of estimating the *EPEE* reduces to estimating the exceedance probability of the largest value in a regional sample of standardized annual maximum peak flows (i.e., observed peak flows divided by the mean annual flood). Their work's primary challenge involves estimation of the regional information content of concurrent cross-correlated flood series of equal length. [Castellarin et al. \(2005\)](#) use results from [Matalas and Langbein \(1962\)](#) and [Stedinger \(1983\)](#) to quantify the regional information content using the concept of the equivalent number of independent annual maxima. [Castellarin et al. \(2005\)](#) express the equivalent number of independent observations, or number of effective observations n_{eff} , as n times the equivalent number of independent sequences M_{EC} , which can be estimated from

$$\hat{M}_{EC} = \frac{M}{1 + \overline{\rho^\beta}(M - 1)}, \text{ with } \beta = 1.4 \frac{(n M)^{0.176}}{(1 - \rho)^{0.376}} \quad (12-70)$$

where $\overline{\rho^\beta}$ and $(1 - \rho)^{0.376}$ are average values of the corresponding functions of the correlation coefficients [i.e., $\overline{\rho^\beta}$ is the average of the $M(M - 1)/2$ values of $\rho_{k,j}^\beta$, where $\rho_{k,j}$ is the correlation coefficient between annual maximum floods at sites k and j , with $1 \leq k < j \leq M$]. Although here we assume that $\rho_{k,j}$ is the linear correlation between the annual maximum floods, one could also define it as the linear correlation between the logarithms of the annual maximum floods (see, e.g., [Stedinger 1981](#)). [Castellarin \(2007\)](#) presents an algorithm that relaxes the need for concurrent series, enabling the estimation of n_{eff} for real-world datasets.

For a regional dataset consisting of M annual maximum series (AMS) that span n years, the actual distribution of the flood series in time (e.g., missing data, different installation years for different gauges, etc.) can be taken into account as follows. First, one identifies the number of years, n_1 , for which the original dataset includes only one observation of the annual maximum discharge, that is $M - 1$ observations are missing (for example, some gauges may not be operational, or may not be installed yet). These n_1 observations are effective by definition. Second, the dataset containing the $n - n_1$ remaining years is subdivided into $N_{sub} \leq (n - n_1)$ subsets; each one of them (say subset s) is selected in such a way that all its $L_s \leq M$ sequences are concurrent and of equal length l_s and are therefore suitable for the application of the estimator proposed by [Castellarin et al. \(2005\)](#). Using this splitting criterion, the effective number of observations n_{eff} can be calculated as the summation of the effective sample years of data estimated for all N_{sub} subsets,

$$\hat{n}_{eff} = n_1 + \sum_{s=1}^{N_{sub}} \hat{n}_{eff,s} = n_1 + \sum_{s=1}^{N_{sub}} \frac{L_s l_s}{1 + \left[\overline{\rho^\beta} \right]_{L_s} (L_s - 1)}, \text{ with } \beta = 1.4 \frac{(L_s l_s)^{0.176}}{\left[(1 - \rho)^{0.376} \right]_{L_s}} \quad (12-71)$$

For a description of the development of Equation (12-72), see [Castellarin et al. \(2005\)](#), Equation 19).

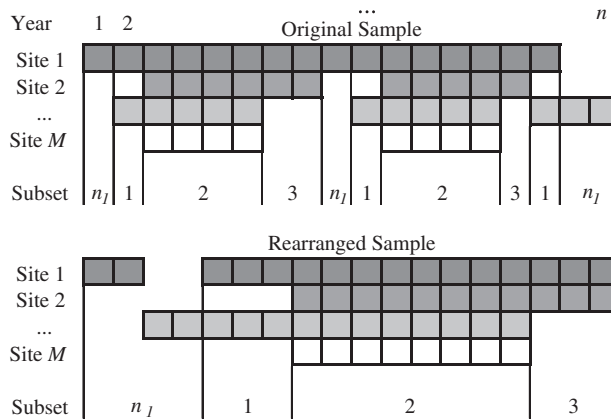


Figure 12-12. Subdivision of a descriptive example of M annual maximum series of flood flows that globally span n years (each square represents one observation) into n_1 single observations and three subsets (i.e., 1, 2, and 3) containing only concurrent sequences of equal length. The rearranged sample highlights the subdivision.

As described previously, n_1 represents the number of times annual floods were observed at one site only (and possibly single observations or indirect measurements at miscellaneous sites), that is, the total number of years in which $L_s = 1$. The notation $[.]^{L_s}$ in Equation (12-71) indicates that the average terms ρ^β and $(1 - \rho)^{0.376}$, which have the same meaning as in Equation (12-70), are to be computed with respect to the $L_s > 1$ annual flood sequences that form subset s . The β exponent in Equation (12-70) coincides formally with β in Equation (12-71). This is consistent with the fact that the L_s sequences forming each subset s are concurrent and of equal length (l_s) (e.g., see Figure 12-12), which was the condition adopted for the identification of the empirical relationship in Equation (12-71).

The EPEE value can be estimated by representing the intersite correlation from a suitable model of cross-correlation versus distance between sites (see, e.g., Tasker and Stedinger 1989, Troutman and Karlinger 2003) and by using an appropriate plotting position with the overall sample years of data set equal to \hat{n}_{eff} . Castellarin (2007) shows that the selection of the cross-correlation model has limited impact on the reliability of EPEE values and recommends the use of the model introduced by Tasker and Stedinger (1989) to approximate the true annual peak cross-correlation function $\rho_{i,j}$ as a function of the distance $d_{i,j}$ among sites i and j ,

$$\rho_{i,j} = \exp\left(-\frac{\lambda_1 d_{i,j}}{1 + \lambda_2 d_{i,j}}\right) \quad (12-72)$$

where $\lambda_1 > 0$ and $\lambda_2 \geq 0$ are the regional parameters that may be estimated by either ordinary or weighted least squares procedures.

Castellarin (2007) addresses the problem of selecting a suitable plotting position for estimating EPEE. Cunnane (1978) introduces the general plotting position:

$$\hat{p}_{EE} = 1 - \frac{\hat{n}_{eff} - \eta}{\hat{n}_{eff} + 1 - 2\eta} \quad (12-73)$$

where η is the plotting position parameter, and \hat{n}_{eff} is the empirical estimate of n_{eff} given in Equation (12-71). Each plotting position is characterized by a particular η value (see, e.g., Table 12-6

Table 12-6. Parameterization of a Probabilistic Regional Envelope Curve (p).

Name	Description*	η	T_{EC}
Weibull	Probability unbiased for all distributions	0.00	$n_{eff} + 1$
Cunnane	Approximately quantile unbiased	0.40	$1.67 \cdot n_{eff} + 0.3$
Gringorten	Optimized for Gumbel distribution	0.44	$1.79 \cdot n_{eff} + 0.2$
Hazen	A traditional choice	0.50	$2 \cdot n_{eff}$
GEV	Quantile unbiased for the maximum of a GEV sample	$0.44 - 0.46 \cdot \kappa$	$\frac{n_{eff} + 0.12 + 0.92\kappa}{0.56 + 0.46\kappa}$

*See also [Stedinger et al. \(1993\)](#).

Note: Plotting positions: η is the parameter of the plotting position as in Equation (12-75); κ is the shape parameter of the GEV distribution; n_{eff} is the effective sample years of data; and $T_{EC} = 1/EPEE$ is the recurrence interval assigned to n_{eff} .

for selection criteria). The results reported in [Castellarin \(2007\)](#) indicate that, among several possible options, a quantile-unbiased plotting position should be used for estimating EPEE. [Castellarin \(2007\)](#) derives a quantile-unbiased plotting position for use with the GEV distribution. The proposed plotting position is a very compact and easy to apply asymptotic formula for the estimation of the exceedance probability of the largest value in a GEV sample, in which the parameter η of Equation (12-73) depends on the shape parameter κ of the fitted GEV distribution,

$$\eta(k) = \frac{\exp(\gamma) - 1}{\exp(\gamma)} - \frac{\pi^2}{12 \exp(\gamma)} \kappa; \quad \eta(\kappa) = 0.44 - 0.46 \kappa \quad (12-74)$$

where, as usual, $\gamma = 0.5772$ is Euler's constant. Equation (12-74) should only be applied when $n_{eff} \geq 10$ and $-0.5 < \kappa < 0.5$.

12.4 APPLICATIONS OF THE THEORY OF RECORDS: CASE STUDIES

The following sections provide three case studies. The first two case studies derive probabilistic regional envelope curves based on (1) annual maximum flood observations in north central Italy and (2) precipitation observations in Austria. The third case study examines the record-breaking properties of flood observations for the continental United States.

12.4.1 Application of Probabilistic Regional Envelope Curves

This section summarizes two real-world applications of the theory of records. In both cases, an estimate of the average recurrence interval $T_{EC} = EPEE$ associated with the expected regional envelope curve is obtained. The first example assesses the applicability of probabilistic regional envelopes of flood flows for design-flood estimation in ungauged basins over a wide geographical region in north central Italy (see [Castellarin 2007](#)). The second example refers to the construction of probabilistic envelope curves for record rainfall events of various durations that were observed in Tyrol (Austria). The second example also provides an assessment of the resulting probabilistic envelope curve using a very long synthetic rainfall series generated through a stochastic rainfall model ([Viglione et al. 2012](#)). Other practical applications of probabilistic regional envelopes of record floods may be found in [Guse et al. \(2009, 2010\)](#) for the region of Saxony, Germany, and in [Padi et al. \(2011\)](#) for the African continent, while probabilistic envelopes of extreme rainstorms are also developed in [Castellarin et al. \(2009\)](#) for north central Italy.

12.4.1.1 Probabilistic Regional Envelope Curves for Flood Flows in North Central Italy

We briefly summarize an application of probabilistic regional envelope curves performed by Castellarin (2007). The study considers flood discharge data for 33 unregulated catchments in north central Italy, which are illustrated in Figure 12-13. The discharge data were collected by the National Hydrographic and Hydrometric National Service of Italy. The record length at the stations varies from a minimum of 15 years to a maximum of 74 years with a mean value of 32 years.

Previous studies indicate that the flood frequency regime presents only a limited degree of heterogeneity over the whole study area and proposes a subdivision of the area into three subregions with an acceptable degree of homogeneity. Also, the GEV distribution was shown to be a suitable regional parent distribution for the annual maximum flood flow sequences in the study area (Castellarin 2007 and references therein).

Figure 12-13 reports three subregions (regions W, western; C, central; and E, eastern), which mainly reflect climatic differences existing in the study area. Table 12-7 lists some characteristics of the study area, such as the number of sites, the overall sample years of data, the number of years for

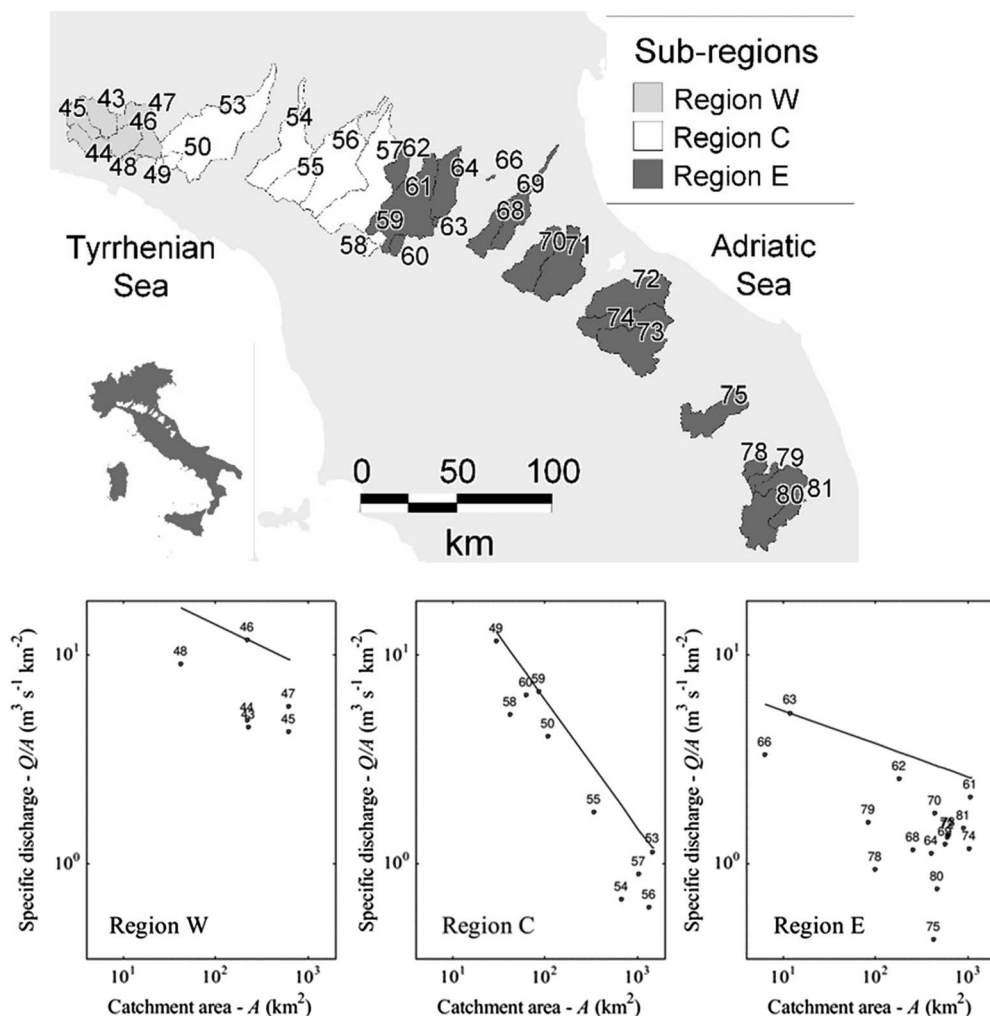


Figure 12-13. North central Italy: 33 basins, grouped into three homogeneous regions (top panel), and empirical regional envelope curves for the three subregions of the study area (bottom panel).

Table 12-7. Characteristics of Regions W, C, and E in N Italy.

Characteristics	Region W	Region C	Region E
Number of sites	6	10	17
Number of observations	159	339	572
Number of single observations (n_1)	12	0	11
Estimated shape parameter κ	-0.34	-0.09	-0.11
Estimated envelope slope [see Equation (12-55)], \hat{b}	-0.21	-0.61	-0.16
Calculated envelope intercept [see Equation (12-55)], a	3.61	4.62	2.05
Parameter λ_1 (km^{-1}) of the correlation model (see Equation 12-72)	For all 3 regions: $4.052 \cdot 10^{-5}$		
Parameter λ_2 (km^{-1}) of the correlation model (see Equation 12-72)	For all 3 regions: $1.606 \cdot 10^{-5}$		
Parameter of the GEV plotting position, $\eta(k)$ of (see Equation 12-74)	0.596	0.481	0.490
Recurrence interval, T_{EC} (years)	258	412	751

which annual floods are available at one site only [i.e., n_1 in Equation (12-71)], and a regional estimate of the shape parameter κ of the GEV estimated as described in Hosking and Wallis (1997).

Figure 12-13 illustrates envelope curves constructed for regions W, C, and E. Table 12-7 reports the estimates of the parameters λ_1 and λ_2 of the cross-correlation model in Equation (12-72) obtained for the entire study area. The estimates were obtained by applying a weighted least squares regression algorithm that weights each sample cross-correlation coefficient between two sequences (sites) proportionally to the number of concurrent annual floods. Table 12-7 also reports the estimates of the envelope slopes \hat{b} , obtained by regressing the empirical values of the index-flood (i.e., at-site estimates of mean annual flood) against the drainage areas of the corresponding basins, along with the values of the intercept a , computed as follows,

$$a = \max_{j=1, \dots, M} \left\{ \ln \left(\frac{Q_j}{A_j} \right) - \hat{b} \ln(A_j) \right\} \quad (12-75)$$

where Q_j denotes the maximum flood observed at site $j = 1, 2, \dots, M$, and M is the number of sites in the region, while A_j is the area of site j . Recall that Equation (12-75) is based on the index flood assumption as was discussed earlier in Section 12.3.2. Finally, Table 12-7 lists the coefficients η of the plotting position estimator calculated using the asymptotic relation of Equation (12-74) as a function of the κ values, and the resulting estimate of the expected recurrence interval, $T_{EC} = 1/EPEE$. Recall that T_{EC} is the expected recurrence interval associated with our estimate of the effective record length n_{eff} associated with the expected envelope. The probabilistic envelope curves in Figure 12-13 can be used to obtain a graphical estimate of the T_{EC} year flood (envelope flood quantile) at any ungauged site within each region as a function of the catchment area alone (T_{EC} values are indicated in Table 12-7).

Castellarin (2007) assesses the reliability of estimates of envelope flood quantiles for ungauged sites through a comprehensive cross-validation procedure. Those experiments illustrate that the accuracy of envelope quantiles are comparable to the reliability of regional predictions produced by the application of the index-flood approach. In summary, envelope flood quantiles are attractive because they (1) can be easily determined for ungauged sites graphically as a function of the catchment area alone, (2) do not require any extrapolation of an assumed flood frequency distribution, and (3) were shown to be conservative by Castellarin (2007) in that overestimation tends to prevail due to the possible presence of regional heterogeneities.

9.4.1.2 Probabilistic Regional Envelope Curves for Record Rainfall Events in Tyrol, Austria

[Castellarin et al. \(2009\)](#) first introduced depth–duration envelope curves (DDECs), which, analogous to RECs for flood flows, are graphical representations of the maximum observed point rainfall depth (or record rainfall depth) for a given duration over a region. Of interest here is the probabilistic interpretation of DDECs which [Castellarin et al. \(2009\)](#) introduces, which is analogous to the probabilistic interpretation of RECs for flood flows. The probabilistic interpretation of DDECs relies on the assumption that the spatial variability of rainfall annual maxima for a given duration τ can be described by the variability of mean annual precipitation (MAP). [Viglione et al. \(2012\)](#) show that if (1) the L-moment ratios of rainfall extremes can be assumed to be constant in space and (2) a nondecreasing scaling law holds between the mean annual maximum rainfall depth m_τ (for duration τ) and MAP, an analytical relationship results between the local MAP value and the T year rainfall depth quantile associated with duration τ , $h_{\tau,T}$. When L-moment ratios can be assumed to be constant in space and the scaling law between m_τ and MAP assumes the form

$$m_\tau = a_\tau \cdot \text{MAP}^{b_\tau} \quad (12-76)$$

the relationship between $h_{\tau,T}$ and MAP becomes

$$\frac{h_{\tau,T}}{\text{MAP}} = k_{\tau,T} \cdot \frac{m_\tau}{\text{MAP}} = k_{\tau,T} \cdot a_\tau \cdot \text{MAP}^{(b_\tau-1)} \quad (12-77)$$

where a_τ and b_τ are regional coefficients, whereas $k_{\tau,T}$ is a growth factor depending on duration τ and recurrence interval T . Probabilistic DDECs were applied and validated in north central Italy ([Castellarin et al. 2009](#)) and in the Austrian district Tyrol ([Viglione et al. 2012](#)). A brief illustration of the Austrian application is reported here below.

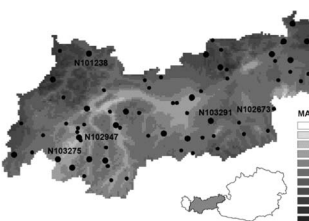
Tyrol is located in the western part of Austria within the Alpine region and has an area of about 10,600 km². Table 12-8 describes the study area and the available raingauge network.

An envelope of the record rainstorms observed in the study area for the durations of interest can be fit using a mathematical relationship analogous to Equation (12-77), in which $k_{\tau,T}$ is replaced by a coefficient, which we term $k_{\tau,\text{MAX}}$, whose meaning is analogous to the intercept a in Equation (12-75) for the REC of flood flows and that can be computed from the observed rainfall data as

$$k_{\tau,\text{MAX}} = \max_{j=1, \dots, M} \left\{ \frac{h_{\tau,\text{MAX},j}}{\hat{a}_\tau \cdot \text{MAP}_j^{b_\tau}} \right\} \quad (12-78)$$

Table 12-8. The 73 Rain Gauges in Tyrol (Austria) Considered in [Viglione et al. \(2012\)](#), the 22 Stations Used for the Comparison are Highlighted in Black; the Gray Scale Shows the Mean Annual Precipitation (MAP).

No. of gauges	73		
Altitude (m a.s.l.)	493 (min)	1,297 (mean)	2,850 (max)
MAP (mm)	548 (min)	1,110 (mean)	1,732 (max)
Series length (years)	1 (min)	10 (mean)	31 (max)
Station-years of data		695	



Note: a.s.l. = above sea level.

Table 12-9. Characteristics of the Annual Maximum Rainfall Depths for Different Durations, Calibrated Coefficients of the Cross-Correlation Formula [Equation (12-72)], Empirical DDEC Parameters, and Estimated Recurrence Interval (the Number of Stations Considered Is 73 for a Total of 695 Observations for All Durations).

Duration τ (hours):	0.25	1	3	6
Estimate of b_τ in Equation (12-77)	0.682	0.518	0.440	0.433
Estimate of a_τ in Equation (12-77)	0.091	0.490	1.15	1.59
Calculated $k_{\tau,\text{MAX}}$ in Equation (12-78)	3.80	3.51	3.49	2.94
Parameter $\lambda_1 (10^{-4} \text{ km}^{-1})$ of the correlation model, Equation (12-72)	5.99	8.87	4.57	5.40
Parameter $\lambda_2 (10^{-4} \text{ km}^{-1})$ of the correlation model, Equation (12-72)	2.05	2.84	1.41	3.38
Number of effective observations \hat{n}_{eff} in Equation (12-71)	663.9	679.5	665.0	484.1
Recurrence interval, T (years)	1,328	1,359	1,330	968

where estimates of a_τ and b_τ of Equation (12-78) are obtained through a regression analysis; $h_{\tau,\text{MAX},j}$ in Equation (12-78) denotes the maximum rainfall depth observed for duration τ at site $j = 1, 2, \dots, M$, and M is the number of sites in the region; and MAP_j is the local value of the mean annual precipitation.

RECs for flood flows and DDECs for rainfall are analogous concepts that share an identical probabilistic interpretation. An estimated recurrence interval can be associated with $k_{\tau,\text{MAX}}$. The empirical estimator of the number of effective observations [Equation (12-71)] yields an estimate of the exceedance probability of the empirical DDECs. Table 12-9 reports the estimates of the parameters of the model [Equation (12-77)] for the durations of interest, together with the estimates of the number of effective observations and the corresponding estimated recurrence intervals obtained by applying a suitable plotting position.

Viglione et al. (2012) assess the validity of the recurrence intervals estimated for each empirical DDEC by comparing the envelope curves with quantiles of rainfall depth associated with the same recurrence intervals retrieved from very long series of synthetic rainfall series generated through an adaptation of the stochastic rainfall model presented in Sivapalan et al. (2005). Viglione et al.'s (2012) stochastic rainfall model was calibrated locally (i.e., site by site) for a subset of 22 gauges spanning the entire range of empirical MAP values (see Figure 12-14) and evenly scattered over the study region (see Table 12-8). Figure 12-15 illustrates the results of this comparison, showing a good agreement between DDECs and rainfall quantiles retrieved from long synthetic series, thus supporting the meaningfulness of the proposed DDECs and the reliability of their probabilistic interpretation. For further details, the interested reader is referred to Viglione et al. (2012).

12.4.2 Record-Breaking Properties of Floods in the United States

The theory of records offers a framework for understanding the probabilistic behavior of extreme events, which is nearly independent of the theory of extremes. Thus examining probabilistic properties of floods is possible without resorting to assumptions regarding a probability distribution. Other than a probability distribution, the other common assumption is that floods are *iid* events. Because the *iid* assumption is the only assumption required for most theoretical results pertaining to record events, the theory of records has been suggested for testing the *iid* assumption (Foster and Stuart 1954). This is a very unique aspect of the theory of records, that is, many of the theoretical results only depend on the single *iid* assumption. Thus an evaluation of whether or not samples behave as expected under the theory of records may be considered a test of the *iid* assumption. In the

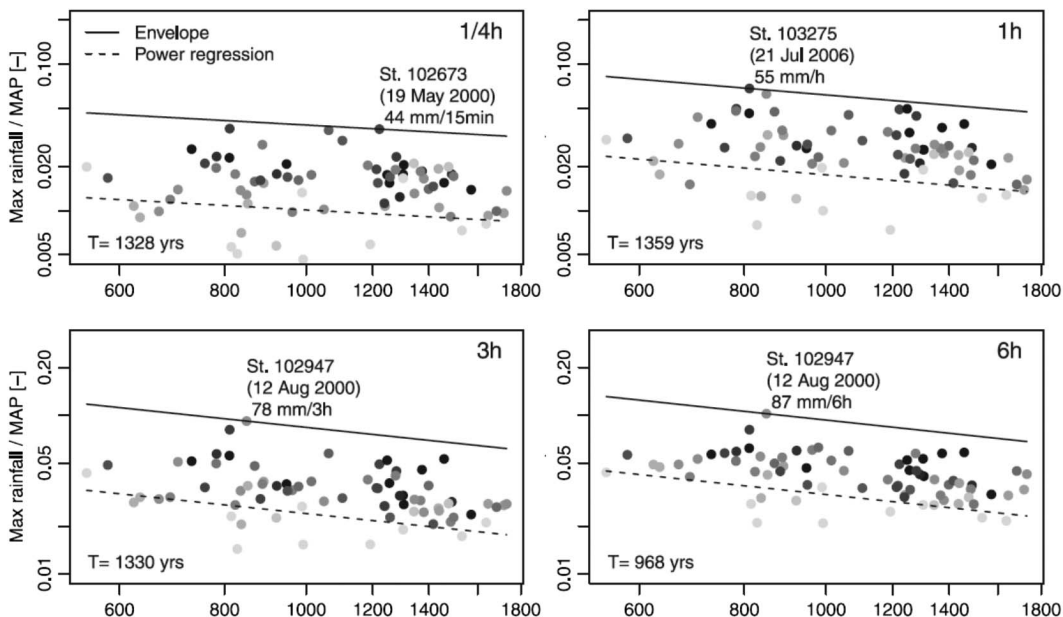


Figure 12-14. DDECs for different durations (0.5 to 6 h) in Tyrol, Austria. The circles represent MAP versus the rescaled maximum recorded rainfall depth for the 73 rainfall stations. The grayscale is proportional to the sample lengths. The envelope curve of Equation (12-77) is shown by the continuous line. The dashed line represents the scaling relation between (m_r/MAP) and MAP of Equation (12-76).

following example from [Vogel et al. \(2001\)](#), the record-breaking properties of historical annual maximum flood records in the United States were examined to determine whether or not they behave like serially independent events.

To perform these experiments, the Hydro-Climatic Data Network (HCDN) compiled by [Slack et al. \(1993\)](#) was employed, which comprises average streamflow values recorded on a daily, monthly, and annual basis in the entire United States spanning the time period 1874–1988. For the purpose of this study, only data pertaining to the 48 conterminous states were considered, which correspond to 18 water resources regions. To enable an effective summary of our results, three meta-regions of the United States were employed: the east, midwest, and west. Respectively, these consist of two-digit HUs 1–6, 7–12, and 13–18. This analysis does not consider regions outside of the continental, conterminous United States of America.

Observations of floods in a region are correlated in space, which influences the sampling properties of the moments of the number of record events, R , given in Equations (12-34 to 12-37). The record-breaking properties were derived for serially independent but spatially correlated events, as in Section 12.2.3. To detect any serial dependence of the record-breaking floods in the United States, the record-breaking frequency of actual floods was compared with their theoretical counterparts.

In Figures 12-16 to 12-18, theoretical and sample estimates of the mean, standard deviation, and coefficient of variation of the number of record floods in an n year period were compared for the eastern, midwestern, and western regions of the United States, respectively. Sample estimates of skewness and kurtosis are known to be significantly biased, so they were not calculated ([Wallis et al. 1974](#), [Vogel and Fennessey 1993](#)). The vertical lines (with the small horizontal lines at the end) on either side of the theoretical values denote approximate 89% Chebyshev 3σ error bars for each statistic ([Ross 1994](#)). Chebyshev's inequality for any random variable X with mean μ and variance σ^2 is given by

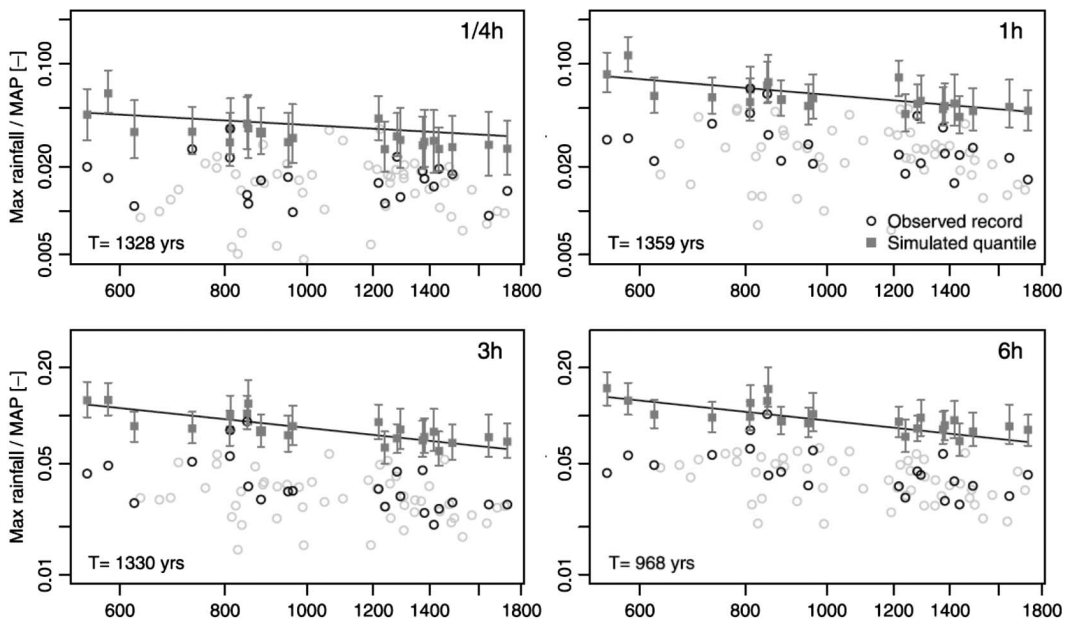


Figure 12-15. Comparison between empirical DDECs and synthetic rainfall quantiles for the return period given by the DDEC procedure. The figure is analogous to Figure 12-14 but only the 22 stations used for the comparison are highlighted (open black circles). The rainfall quantiles, resulting from the stochastic generation of 1 million years of rainfall, are indicated by solid gray squares. The 90% confidence bounds are also indicated in gray.

$$P[|X - \mu| \geq c] \leq \frac{\sigma^2}{c^2} \quad (12-79)$$

where c is a constant equal to half the width of the confidence interval; which here is set equal to 3σ , which implies that $P[|X - \mu| \geq 3\sigma] \leq 0.11$, or else $P[|X - \mu| \leq 3\sigma] \geq 0.89$, which is a crude approximation, but very convenient here as it can be easily parameterized to document the influence of spatial correlation on the width of the derived intervals. Analogous confidence intervals are constructed for the statistics s_R and $C_v[R]$. The heavy confidence intervals denote intervals based on the assumption of spatial independence ($\rho = 0$) of the flood observations. The light-weight confidence intervals (shown only for μ_R) are based on the assumption that the cross-correlation of the flood observations is equal to the average cross-correlation of flow records for all sites in the region. According to Walker (1999), average cross-correlations of the annual maximum flow records in the eastern, midwestern, and western regions of the United States are 0.23, 0.19, and 0.42, respectively. These sample estimates of the average spatial correlation of the annual maximum flood series were computed for all possible pairs of observations, which had at least 10 years of record in common. Employing the regional average value of cross-correlation is the simplest approach to describe the distribution of spatial correlations in a region.

Stedinger (1983), Hosking and Wallis (1988), and Douglas et al. (2000) also use regional average values of cross-correlation to describe the dependence between flow series at different sites. Douglas et al. (2000) compare the use of regional trend tests of US flood records based on (1) regional average spatial cross-correlations and (2) the boot-strap approach for preserving the empirical regional distribution of the spatial dependence of flood observations. They find good agreement between these two approaches. Nevertheless, our use of a regional average spatial cross-correlation is a gross simplification, because the complex spatial and temporal climatic mechanisms, which give rise to

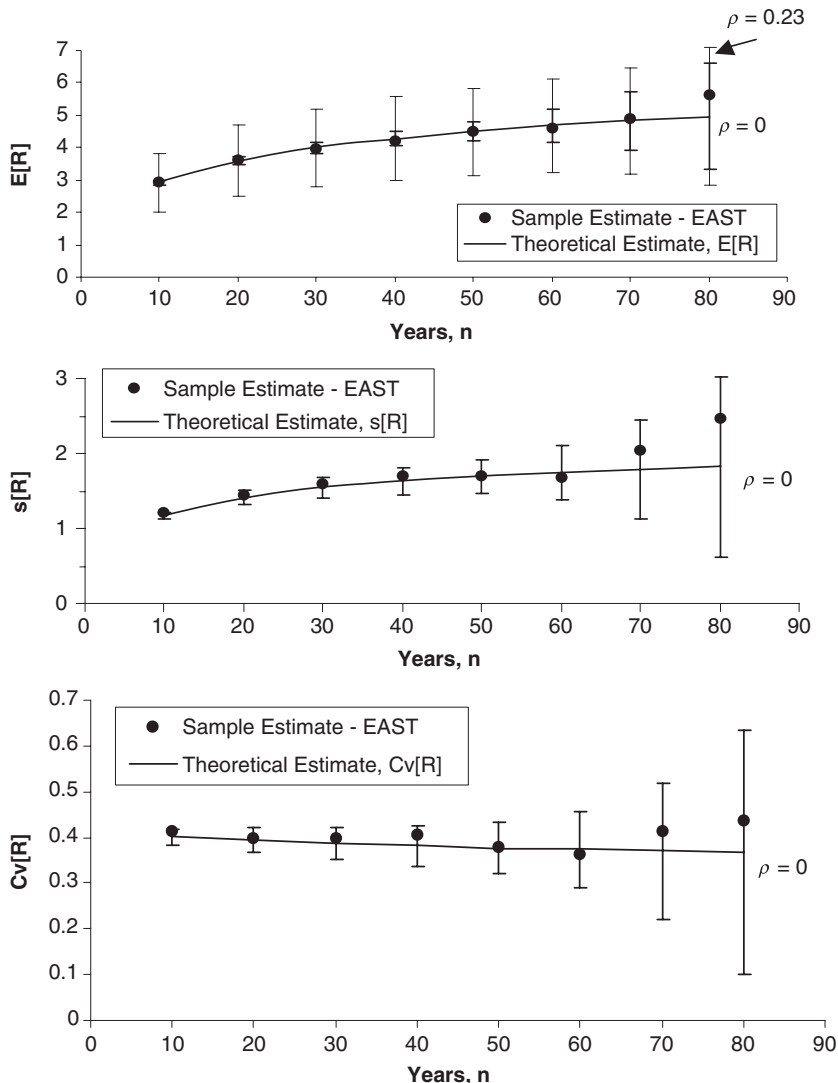


Figure 12-16. Comparison of the sample and theoretical estimates of $E[R]$, $s[R]$, and $C_v[R]$ as a function of n for the eastern region.

flood observations, will lead to spatial correlation structures, which in turn depend strongly upon how the regions are defined.

In computing the moments of the number of record events, R , all possible overlapping sets of n year periods within the HCDN database were considered. Table 12-10 reports the number of such nonoverlapping n year periods available in each region. The reason that confidence intervals widen as n increases is due to the fact that in each region the number of nonoverlapping sets of n year samples decreases as n increases. The confidence intervals reflect the increasing uncertainty associated with our ability to determine properties of record-breaking events as n increases. If smaller regions were used, the confidence intervals would have widened. If the sample estimates of mean R , reported in top graph of Figures 12-16 to 12-18, fall within the reported 89% confidence intervals for μ_R (which account for cross-correlation), it can be concluded that the flood series in that region are serially independent, because that was the only assumption required for the theoretical

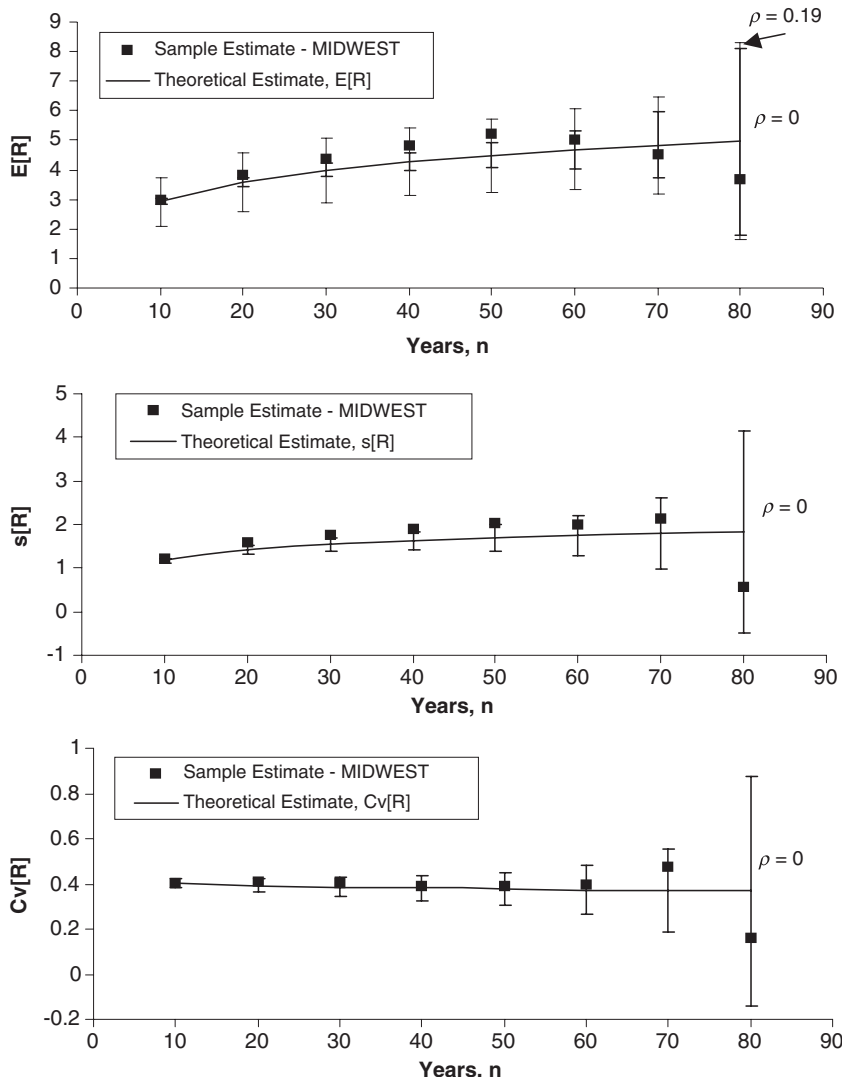


Figure 12-17. Comparison of the sample and theoretical estimates of $E[R]$, $s[R]$, and $C_v[R]$ as a function of n for the midwestern region.

analysis. Note that the confidence intervals for μ_R , which account for the spatial correlation of the flood observations, are much wider than the confidence intervals that assume spatial independence.

In general, Figures 12-16 to 12-18 illustrate that when one accounts for the spatial correlation of the flood observations, the observed regional mean R falls within the 89% confidence intervals for μ_R for all three US regions. However, if the flood observations are assumed to be spatially independent (which they are not), we would mistakenly conclude that flood observations in the midwestern and western regions of the United States are serially dependent. Hence our results indicate that flood observations in the eastern United States are consistent with the theory of record-breaking phenomena for serially independent processes. This example shows that the theory of record-breaking processes provides a comprehensive mathematical framework for evaluating the frequency and magnitude of extreme events and can be applied to identifying nonstationarity in hydrological records.

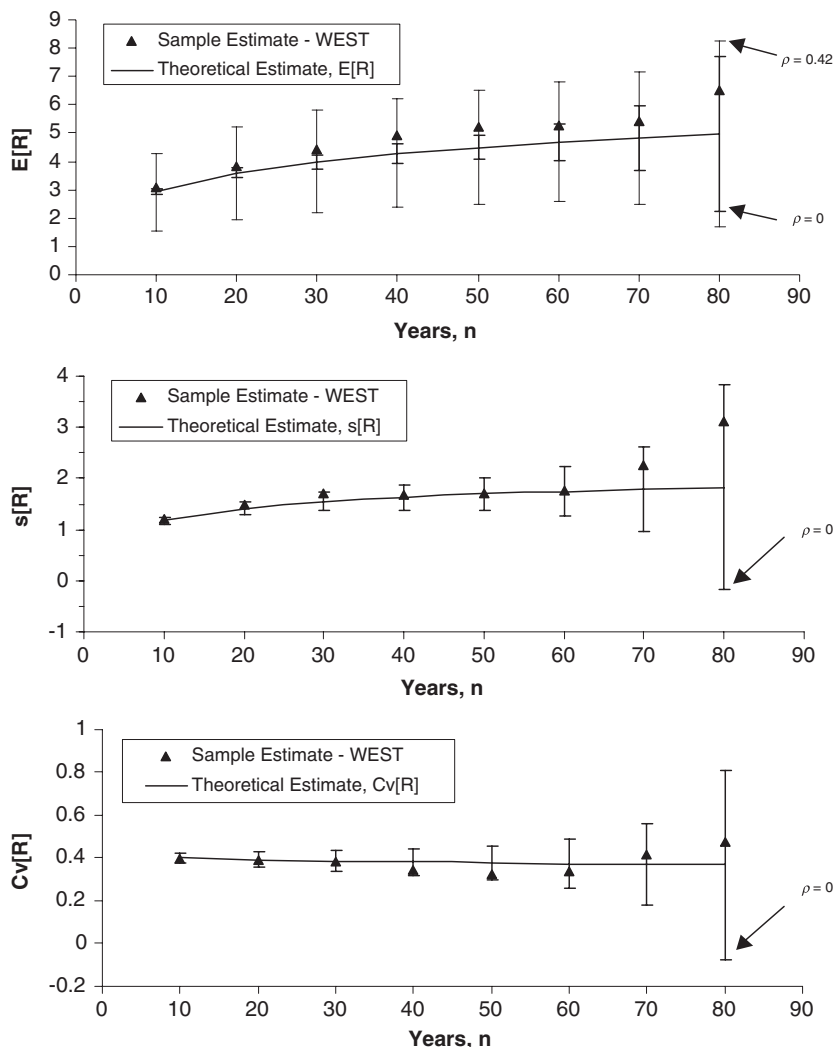


Figure 12-18. Comparison of the sample and theoretical estimates of $E[R]$, $s[R]$, and $C_v[R]$ as a function of n for the western region.

Table 12-10. Number of Nonoverlapping n -Year Periods in Each Region.

Record Length, n	East	Midwest	West
10	2,680	1,919	1,561
20	1,164	838	665
30	650	432	350
40	418	278	200
50	270	151	136
60	112	66	63
70	36	23	22
80	11	3	4
Total	5,341	3,710	3,001

12.5 CONCLUSIONS

We have reviewed various theoretical properties associated with the record-breaking behavior of a single time series or many sets of such observations. While our focus has been on flood and extreme rainfall events, the theory described here applies to many other natural hazards, including droughts, landslides, earthquakes, wind loads, sea levels, temperatures and others. We have discussed parametric record-breaking properties, which generally depend on assumptions concerning the probability distribution of the observations. We have also discussed nonparametric record-breaking properties, which generally only depend on the assumption that the series is independent and identically distributed.

The theory of records relies heavily upon the theory of order statistics (David and Nagaraja 2003) and extreme order statistics, as well as on the theory of extremes (Gumbel 1958). Interestingly, much of the theory of records is independent of the theory of extremes. Remarkably, only recently was the theory of records first applied to water resources data (Vogel et al. 2001), thus many opportunities exist for new avenues of research concerning record processes. We have summarized two recent case studies, which have applied the theory of records to assign an exceedance probability associated with an envelope curve of extreme hydrological events (i.e., floods and rainstorms)—a task that was thought to be impossible before Vogel et al.'s (2007) work. We have also summarized a case study that explored the nonparametric record-breaking properties of flood events in the continental United States. Given ever-increasing concerns over the degree of change associated with the future frequency and magnitude of natural hazards, developments and applications associated with the theory of records are likely to play an increasingly important role.

Because a fundamental assumption associated with much of the theory of records involves an assumption of stationarity, extensions to the theory may be needed to account for nonstationary record processes. For example, many examples now extend the stationary theory of extremes into the nonstationary domain (e.g., Furrer et al. 2010, Sankarasubramanian and Lall 2003, Towler et al. 2010, Vogel et al. 2011; Serago and Vogel, 2018; Salas et al. 2018). Similar extensions are needed to enable the theory of records to account for nonstationary processes.

As it has been emphasized, an attractive property of the theory of records is that much of the theory only depends upon the assumption that flood sequences are *iid*. Two properties under the *iid* assumption in the theory of records complicate the task of determining the extent to which observed sequences yield record events that accord with the theory. First, the expected number of records reflected by a sequence of length n is very sparse. For “long” hydrologic sequences, $n \sim 100$, the expected number of record events is about 5. For long surrogate hydrologic sequences (e.g., tree rings and mud varves, $n \sim 1,000$), the expected number of record events is about 7.5. For sequences of geologic length, $n \sim 1,000,000$, the expected number of record events is about 14.4. The longer a sequence is, the more pronounced is the degree of sparsity of record events. Second, regardless of the length of a sequence, record events tend to occur early in the sequence. The longer the sequence is, the more apparent is the “earliness.” As put by Arnold et al. (1998), “we shall never see the 50th record-breaking event, for in expectation, we will all be dead”. These two factors and others render the task of detecting evidence counter to the *iid* assumption quite challenging.

Many fundamental hydrologic problems depend critically upon an understanding of the theory of extremes, records, and order statistics. We expect that combining these three theories, along with developments in nonstationarity and Bayesian statistics, may lead to numerous extensions to the results presented here. For example, the traditional concepts of the probable maximum precipitation (PMP) and the probable maximum flood (PMF) are used widely in the design of hydraulic structures, yet have never been fully analyzed within the domain of the theory of record processes. Only recently has a rigorous theoretical approach to a probabilistic assessment of the PMP (Koutsoyiannis 1999, Salas et al. 2013) and PMF (Vogel et al. 2007, Salas et al. 2013) been given.

Tremendous opportunities remain associated with the application of the theory of records to estimation of extreme rainfall and flood probabilities, including traditional deterministic criteria, such as the PMP and PMF.

References

- Ahsanullah, M. 1995. *Record statistics*, 227. Hauppauge, NY: Nova Science Publishers.
- Ahsanullah, M. 2004. *Record values—Theory and applications*, 314. Dallas: University Press of America.
- Alvord, J. W., and C. B. Burdick. 1918. *Relief from floods*, 175. New York: McGraw-Hill.
- Ang, A. H-S., and W. H. Tang. 1984. *Probability concepts in engineering planning and design: Volume II Decision, risk and reliability*. New York: Wiley.
- Arnold, B. C., N. Balakrishnan, and H. N. Nagaraja. 1998. *Records*, 312. New York: Wiley.
- Arnold, B. C., N. Balakrishnan, and H. N. Nagaraja. 2008. "Record values." Vol. 54 in *First course in order statistics, classics in applied mathematics*, 241–257. Philadelphia, PA: SIAM.
- Balakrishnan, N., and M. Ahsanullah. 1994. "Recurrence relations for single and product moments of record values from generalized Pareto distribution." *Commun. Stat.-Theor. Methods* 23 (10): 2841–2852.
- Bardossy, A., and S. Horning. 2016. "Gaussian and non-Gaussian inverse modeling of groundwater flow using copulas and random mixing." *Water Resour. Res.* 52 (6): 4504–4526.
- Beirlant, J., Y. Goegebeur, J. Segers, and J. Teugels. 2004. *Statistics of extremes*, 490. Hoboken, NJ: Wiley.
- Bullard, K. L. 1986. *Comparison of estimated probable maximum flood peaks with historic floods*, 165. Denver: Bureau of Reclamation, Hydrology Branch.
- Bureau of Reclamation. 1987. *Design of small dams*. 3rd ed., 860. Denver: US Dept. of Interior, Bureau of Reclamation.
- Burn, D. H. 1990. "Evaluation of regional flood frequency analysis with a region of influence approach." *Water Resour. Res.* 26 (10): 2257–2265.
- Butkiewicz, J., and E. Hys. 1977. "On a Class of Bi- and Multivariate Distributions Generated by Marginal Weibull Distributions." In Vol. 7A *Transaction of the 7th Prague Conf on Information Theory, Statistical Decision Functions, Random Processes and of the 1974 European Meeting of Statisticians*, edited by J. Koženík. Dordrecht, The Netherlands: Springer.
- Castellarin, A. 2007. "Application of probabilistic envelope curves for design-flood estimation at ungaged sites." *Water Resour. Res.* 43 (4): W04406.
- Castellarin, A., D. H. Burn, and A. Brath. 2001. "Assessing the effectiveness of hydrological similarity measures for regional flood frequency analysis." *J. Hydrol.* 241 (3–4): 270–285.
- Castellarin, A., R. Merz, and G. Blöschl. 2009. "Probabilistic envelope curves for extreme rainfall events." *J. Hydrol.* 378 (3–4): 263–271.
- Castellarin, A., R. M. Vogel, and N. C. Matalas. 2005. "Probabilistic behavior of a regional envelope curve." *Water Resour. Res.* 41 (6): W06018.
- Castellarin, A., R. M. Vogel, and N. C. Matalas. 2007. "Multivariate probabilistic regional envelopes of extreme floods." *J. Hydrol.* 336 (3–4): 376–390.
- Chandler, K. N. 1952. "The distribution and frequency of record values." *J. R. Stat. Soc. Ser. B.* 14 (2): 220–228.
- Chowdhury, J. U., J. R. Stedinger, and L.-H. Lu. 1991. "Goodness-of-fit tests for regional generalized extreme value flood distributions." *Water Resour. Res.* 27 (7): 1765–1776.
- Costa, J. E. 1987a. "A comparison of the largest rainfall-runoff floods in the United States with those of the People's Republic of China and the world." *J. Hydrol.* 96 (1–4): 101–115.
- Costa, J. E. 1987b. "Hydraulics and basin morphology of the largest flash floods in the conterminous United States." *J. Hydrol.* 93 (3): 313–338.
- Creager, W. P., J. D. Justin, and J. Hinds. 1945. *Engineering for dams. Vol. I. General design*, 99–140. New York: Wiley.
- Crippen, J. R. 1982. "Envelope curves for extreme flood events." *J. Hydraul. Eng.* 108 (HY10): 1208–1212.
- Crippen, J. R., and C. D. Bue. 1977. *Maximum flood flows in the conterminous United States: US Geological Survey Water-Supply Paper 1887*. Washington, DC: US Printing Office.
- Cudworth, A. G. Jr. 1989. *Flood hydrology manual*, 243. Denver: US Dept. of Interior, Bureau of Reclamation.
- Cunnane, C. 1978. "Unbiased plotting positions—A review." *J. Hydrol.* 37 (3–4): 205–222.
- Dalrymple, T. 1960. *Flood frequency analyses: US Geological Survey Water Supply Paper 1543-A*. Reston, VA: USGS.

- Dalrymple, T. 1964. "Hydrology of flood control. Part I: Flood characteristics and flow determination." In *Handbook of hydrology*, edited by V. T. Chow. New York: McGraw-Hill.
- David, F. N., and D. E. Barton. 1962. *Combinatorial chance*. New York: Hafner, 178–183.
- David, H. A., and H. N. Nagaraja. 2003. *Order statistics*. 3rd ed. New York: Wiley.
- Douglas, E. M., and R. M. Vogel. 2006. "The probabilistic behavior of floods of record in the United States." *J. Hydrol. Eng.* **11** (5): 482–488.
- Douglas, E. M., R. M. Vogel, and C. N. Kroll. 2000. "Trends in floods and low flows in the United States: Impact of spatial correlation." *J. Hydrol.* **240** (1–2): 90–105.
- England, J. F., Jr., J. E. Godaire, R. E. Klinger, and T. R. Bauer. 2010. "Paleohydrologic bounds and extreme flood frequency of the Arkansas River Basin, Colorado, USA." *Geomorphology* **124** (1–2): 1–16.
- Enzel, Y., L. L. Ely, P. K. House, V. R. Baker, and R. H. Webb. 1993. "Paleoflood evidence for a natural upper bound to the flood magnitudes in the Colorado River basin." *Water Resour. Res.* **29** (7): 2287–2297.
- Fisher, R. A., and L. H. C. Tippett. 1928. "Limiting forms of the frequency distributions of the largest and smallest members of a sample." In *Mathematical Proc., Cambridge Philosophical Society*.
- Foster, F. G., and A. Stuart. 1954. "Distribution-free tests in time-series based on the breaking of records, with discussion." *J. R. Stat. Soc. Ser. B.* **16**: 1–22.
- Fuller, W. E. 1914. "Flood flows." *Trans. Am. Soc. Civ. Eng.* **1293** (77): 564–617. 618–694.
- Furrer, E. M., R. W. Katz, M. D. Walter, and R. Furrer. 2010. "Statistical modeling of hot spells and heat waves." *Clim. Res.* **43** (3): 191–205.
- Glick, N. 1978. "Breaking records and breaking boards." *Am. Math. Mon.* **85** (1): 2–26.
- Gumbel, E. J. 1958. *Statistics of extremes*, 375. New York: Columbia University Press.
- Gumbel, E. J. 1961. "The return period of order statistics." *Ann. Inst. Stat. Math.* **12** (3): 249–256.
- Guse, B., A. Castellarin, A. H. Thielen, and B. Merz. 2009. "Effects of intersite dependence of nested catchment structures on probabilistic regional envelope curves." *Hydrol. Earth Syst. Sci.* **13** (9): 1699–1712.
- Guse, B., A. H. Thielen, A. Castellarin, and B. Merz. 2010. "Deriving probabilistic regional envelope curves with two pooling methods." *J. Hydrol.* **380** (1–2): 14–26.
- Herschy, R. 2003. *World catalogue of maximum observed floods: IAHS-AISH Publication No. 284*. Oxfordshire, UK: International Association of Hydrological Sciences.
- Hosking, J. R. M., and J. R. Wallis. 1988. "The effect of intersite dependence on regional flood frequency-analysis." *Water Resour. Res.* **24** (4): 588–600.
- Hosking, J. R. M., and J. R. Wallis. 1997. *Regional frequency analysis: An approach based on L-moments*. Cambridge, MA: Cambridge University Press.
- Husler, J., and R.-D. Reiss. 1989. "Maxima of normal random vectors: Between independence and complete dependence." *Stat. Probab. Lett.* **7** (4): 283–286.
- IACWD (Interagency Advisory Committee on Water Data). 1986. *Feasibility of assigning a probability to the probable maximum flood*. Washington, DC: US Interagency Advisory Committee on Water Data, Hydrology Subcommittee.
- Jarrett, R. D. 1990. "Paleohydrologic techniques used to define the spatial occurrence of floods." *Geomorphology* **3** (2): 181–195.
- Jarvis, C. S. 1926. "Flood flow characteristics." *Trans. Am. Soc. Civ. Eng.* **89** (1): 985–1032.
- Jarvis, C. S., et al. 1936. *Floods in the United States, magnitude and frequency*. US Geological Survey Water-Supply Paper 771. Reston, VA: USGS.
- Jenkinson, A. F. 1955. "The frequency distribution of the annual maximum (or minimum) values of meteorological elements." *Q. J. R. Meteorol. Soc.* **81** (348): 158–171.
- Kallache, M., P. Naveau, and M. Vrac. 2013. "Spatial assessment of precipitation deficits in the Duero basin (central Spain) with multivariate extreme value statistics." *Water Resour. Res.* **49** (10): 6716–6730.
- Katz, R. W., M. B. Parlange, and P. Naveau. 2002. "Statistics of extremes in hydrology." *Adv. Water Resour.* **25** (8–12): 1287–1304.
- Koutsoyiannis, D. 1999. "A probabilistic view of Hershfield's method for estimating probable maximum precipitation." *Water Resour. Res.* **35** (4): 1313–1322.
- Lambert, J. H., and D. Li. 1994. "Evaluating risk of extreme events for univariate-loss functions." *J. Water Resour. Plann. Manage.* **120** (3): 382–399.
- Linsley, R. K., M. A. Kohler, and J. L. H. Paulhus. 1949. *Applied hydrology*, 689. New York: McGraw-Hill.
- Linsley, R. K., M. A. Kohler, and J. L. H. Paulhus. 1958. *Hydrology for engineers*, 340. New York: McGraw-Hill.

- Marchetti, G. 1955. "Sulle massime portate di piena osservate nei corsi d'acqua italiani a tutto il 1953." [In Italian.] *Giorn. Genio* **104** (93): 3–4.
- Matalas, N. C. 1997. "Stochastic hydrology in the context of climate change." *Clim. Change* **37** (1): 89–101.
- Matalas, N. C. 2000. *Note on the envelope curve*. Vienna, VA.
- Matalas, N. C., and W. B. Langbein. 1962. "Information content of the mean." *J. Geophys. Res.* **67** (9): 3441–3448.
- Matthai, H. F. 1990. "Floods." In *Surface water hydrology*, edited by M. G. Wolman and H. C. Riggs. Boulder, CO: Geological Society of America.
- Mead, D. W. 1919. *Hydrology, the fundamental basis of hydraulic engineering*. New York: McGraw-Hill, 647.
- Meyer, A. F. 1917. *Elements of hydrology*, 487. New York: Wiley.
- Meyer, R. W. 1994. *Potential hazards from floodflows within the John Muir House National Historic Site, Franklin Creek drainage basin, California*. US Geological Survey Water-Resources Investigations Rep. No. 93-4009. Reston, VA: USGS.
- Nagaraja, H. N., P. K. Choudhary, and N. C. Matalas. 2003. "Number of records in a bivariate sample with application to Missouri River flood data." *Methodol. Comput. Appl. Probab.* **4** (4): 377–391.
- Nevzorov, V. B. 2001. *Records: Mathematical theory*. Providence, RI: American Mathematical Society, 164.
- O'Connor, J. E., and J. E. Costa. 2004. "Spatial distribution of the largest rainfall-runoff floods from basins between 2.6 and 26, 000 km² in the United States and Puerto Rico." *Water Resour. Res.* **40**: W01107.
- Padi, P. T., G. Di Baldassarre, and A. Castellarin. 2011. "Floodplain management in Africa: Large scale analysis of flood data." *Phys. Chem. Earth* **36** (7–8): 292–298.
- Raqab, M. Z. 2004. "Generalized exponential distribution: Moments of order statistics." *Stat. J. Theor. Appl. Stat.* **38** (1): 29–41.
- Roberts, W. C. 1991. "Human records and a tribute to the Guinness Book of World Records." *Am. J. Cardiol.* **68** (2): 288–289.
- Ross, S. 1994. *A first course in probability*. Englewood Cliffs, NJ: Prentice-Hall.
- Salas, J. D., G. Gavilan, F. R. Salas, P. Julien, and J. Abdullah. 2013. "Uncertainty of the PMP and PMF." Vol. 2 of *Handbook of engineering hydrology: Modeling, climate changes and variability*. Boca Raton, FL: CRC Press.
- Salas, J. D., J. Obeysekera, and R. M. Vogel. 2018. "Techniques for assessing water infrastructure for nonstationary extreme events: A review." *Hydrol. Sci. J.* **63** (3): 325–352.
- Salvadori, G., F. Durante, C. De Michele, M. Bernardi, and L. Petrella. 2016. "A multivariate copula-based framework for dealing with hazard scenarios and failure probabilities." *Water Resour. Res.* **52** (5): 3701–3721.
- Sankarasubramanian, A., and U. Lall. 2003. "Flood quantiles in a changing climate: Seasonal forecasts and causal relations." *Water Resour. Res.* **39** (5): 1134.
- Schucany, W. R., W. C. Parr, and J. E. Boyer. 1978. "Correlation structure in Farlie-Gumbel-Morgenstern distributions." *Biometrika* **65** (3): 650–653.
- Serago, J., and R. M. Vogel. 2018. "Parsimonious nonstationary flood frequency analysis." *Adv. Water Resour.* **112**: 1–16.
- Serinaldi, F. Kilsby. 2018. "Unsurprising surprises: The frequency of record-breaking and overthreshold hydrological extremes under spatial and temporal dependence." *Water Resour. Res.* **54** (9): 6460–6487.
- Sibuya, M. 1960. "Bivariate extreme statistics." *Ann. Inst. Stat. Math.* **11** (3): 195–210.
- Sivapalan, M., G. Blöschl, R. Merz, and D. Gutknecht. 2005. "Linking flood frequency to long-term water balance: Incorporating effects of seasonality." *Water Resour. Res.* **41** (6): W06012.
- Slack, J. R., A. M. Lumb, and J. M. Landwehr. 1993. *Hydro-climatic data network (HCDN): Streamflow data set 1874–1988*. Water Resource Investigations Rep. No. 93-4076. Reston, VA: USGS.
- Smith, J. A., P. Sturdevant-Rees, M. L. Baeck, and M. C. Larsen. 2005. "Tropical cyclones and the flood hydrology of Puerto Rico." *Water Resour. Res.* **41** (6): W06020.
- Stedinger, J. R. 1981. "Estimating correlations in multivariate streamflow models." *Water Resour. Res.* **17** (1): 200–208.
- Stedinger, J. R. 1983. "Estimating a regional flood frequency distribution." *Water Resour. Res.* **19** (2): 503–510.
- Stedinger, J. R., R. M. Vogel, and E. Foufoula-Georgiou. 1993. "Frequency analysis of extreme events." In *Handbook of hydrology*, edited by D. R. Maidment. New York: McGraw-Hill.
- Tasker, G. D., and J. R. Stedinger. 1989. "An operational GLS model for hydrologic regression." *J. Hydrol.* **111** (1–4): 361–375.

- Towler, E., B. Rajagopalan, E. Gilleland, R. S. Summers, D. Yates, and R. W. Katz. 2010. "Modeling hydrologic and water quality extremes in a changing climate: A statistical approach based on extreme value theory." *Water Resour. Res.* **46** (11): W11504.
- Troutman, B. M., and M. R. Karlinger. 2003. "Regional flood probabilities." *Water Resour. Res.* **39** (4): 1095.
- Viglione, A., A. Castellarin, M. Rogger, R. Merz, and G. Blöschl. 2012. "Extreme rainstorms: Comparing regional envelope curves to stochastically generated events." *Water Resour. Res.* **48** (1): W01509.
- Vogel, R. M., and N. Fennessey. 1993. "L moment diagrams should replace product moment diagrams." *Water Resour. Res.* **29** (6): 1745–1752.
- Vogel, R. M., N. C. Matalas, J. F. England Jr., and A. Castellarin. 2007. "An assessment of exceedance probabilities of envelope curves." *Water Resour. Res.* **43** (7): W07403.
- Vogel, R. M., and I. Wilson. 1996. "The probability distribution of annual maximum, minimum and average streamflow in the United States." *J. Hydrol. Eng.* **1** (2): 69–76.
- Vogel, R. M., C. Yaindl, and M. Walter. 2011. "Nonstationarity: Flood magnification and recurrence reduction factors in the United States." *J. Am. Water Resour. Assoc.* **47** (3): 464–474.
- Vogel, R. M., A. Zafirakou-Koulouris, and N. C. Matalas. 2001. "Frequency of record breaking floods." *Water Resour. Res.* **37** (6): 1723–1731.
- Von Mises, R. 1936. "La distribution de la grande de n valeurs." [In French.] *Rev. Math. Union Interbalcanique* **1**: 141–160. Reproduced in Selected papers of Richard von Mises, II, 1964. Providence, RI: American Mathematical Society, 271–294.
- Walker, F. R. Jr. 1999. "Long term variability in flood arrival rates: The presence of annual flood event clustering." Ph.D. dissertation, Cornell Univ.
- Wallis, J. R., N. C. Matalas, and J. R. Slack. 1974. "Just a moment!" *Water Resour. Res.* **10** (2): 211–219.
- Wilks, S. S. 1959. "Recurrence of extreme observations." *J. Aust. Math. Soc.* **1** (1): 106–112.
- Zafirakou-Koulouris, A. 2000. "Statistical methods for floods and droughts." Ph.D. dissertation, Tufts Univ.

Index

- Downloaded from ascelibrary.org by 94.231.217.115 on 09/03/19. Copyright ASCE. For personal use only; all rights reserved.
- advection limit for ET, 75–76, 75*e*
analytical probabilistic stormwater models (APSWM): conversion from exceedance probability to return period, 351–352; derived probability distribution theory, 342–343; flood control analysis, 354–360, 355*t*, 356*f*–358*f*, 359*t*; overview, 336–338; rainfall characterization, 338–340; rainfall event characteristics, 339–340, 339*t*; rainfall-runoff transformation, 340–341; runoff event peak discharge rate, 343–345; runoff event volume, 343; runoff routing through channel reaches, 348–351; runoff routing through detention ponds, 345–348, 346*f*
annual extremes for different durations, 24*t*–25*t*, 24–26, 26*f*, 50–51, 69*f*–70*f*
APSWM. *see* analytical probabilistic stormwater models
aquifers. *see* groundwater hydrology
Archimedean copulas, 420–421, 422*f*, 422*t*
ARMA modeling: low flow analysis, 290–294; streamflow analysis, 210–212
ASCE Standardized Reference ET Equation (ASCE05), 102, 102*e*
Atlas 14 (NOAA), 29, 29*f*
atmospheric evaporative demand (E_0): complementarity with ET, 81–83, 82*f*, 129–133; concept of, 71–73; drivers and limits, 74–78, 125–129; evaporation paradox and, 133–134; as limit to ET, 78–79; measurement of, 73–74; models of, 78–101; observations, 96–101; physics of, 73–78; temperature-based formulations, 93–95, 94*f*; trend decomposition, 130–132, 131*f*; trends, 124–129
autocorrelation: evapotranspiration, 117–120, 118*f*, 119*f*; low flows, 288–299; soil properties, 162–163; streamflow time series, 204, 205*f*
automated sampling, 400
autoregressive moving average (ARMA) models: low flow analysis, 290–294; streamflow, 210–212
Back Creek, West Virginia, flood frequency analysis, 252–255, 253*t*, 254*t*, 255*f*
basin water balance estimates for ET, 83–85, 83*e*–84*e*, 91
Baton Rouge, Louisiana, storm duration and depth analysis, 460–461, 462*f*–463*f*, 462*t*, 463–465, 464*t*, 465*f*–466*f*, 467, 468*f*–474*f*, 473, 475*t*–477*t*
Bayesian methods, 234
best management practices (BMP) for pollutant removal, 360–374, 361*t*–364*t*, 362*f*–363*f*, 367*f*–370*f*, 371*t*–372*t*, 374*f*
beta distribution, 388–389
binomial distribution, 389–390
bivariate exponential distribution, 414–415, 415*f*
bivariate extreme value type I distribution, 415–416, 417*f*
bivariate log-normal distribution, 413–414
bivariate normal distribution, 412–413, 413*f*
bootstrap sampling, 46–49, 47*f*, 48*e*, 48*f*
box-and-whisker plots, 393–394, 393*f*, 396
Budyko framework for ET, 79–81, 80*e*–81*e*, 80*f*
Bulletin 13, Methods of Flow Frequency Analysis (IACWR 1966), 235
Bulletin 15, A Uniform Technique for Determining Flood Flow Frequencies (WRC 1967), 235
Bulletin 17B, Guidelines for Determining Flood Flow Frequency (IACWD 1982), 234–236, 246–247, 249–252, 257
Bulletin 17C, Guidelines for Determining Flood Flow Frequency (IACWD), 255–257
capillary pressure head, 150, 150*f*
CDFs. *see* cumulative distribution functions
censored water quality data, 394–396
channel reaches, 348–351
Chicago, Illinois, flood control analysis, 354–360, 355*t*, 356*f*–358*f*, 359*t*
chi-squared test, 193–194, 194*t*, 195*f*

- climate change: flood frequency analysis and, 257–261; low flows and drought and, 325; precipitation frequency analysis and, 51–52
- coefficient of skew: defined, 183, 183e; gamma PDF, 187; log-gamma PDF, 189; log-normal PDF, 185
- coefficient of variation: gamma PDF, 187; log-gamma PDF, 189; log-normal PDF, 185
- complementarity of regional ET and E_0 , 81–83, 82f, 129–133, 131f, 132t
- complex river system modeling, 222–228
- conditional probability adjustment (CPA), 250, 253
- copulas: analytical goodness-of-fit tests, 441–443, 443t–444t, 458–460, 459t–460t, 461f, 467, 473, 475t–477t, 479, 481, 484t; Archimedean, 420–421, 422f, 422t; assessment of fitting, 449, 451, 458–460, 465, 467, 473, 478–479, 481; concept of, 417f, 418; dependence and, 424–436; dependence structure and test space, 446f–448f, 447–448, 461, 463, 463f, 474, 477, 480f; derivation of associated copulas, 424; error statistics of fit, 440–441, 441t, 451, 458, 458t, 467, 475t, 479, 481, 483t; estimation of dependence parameter, 431–436, 448–449, 449t, 464–465, 464t, 477, 480t; exact maximum likelihood method of estimation, 435–436; extreme value, 421, 423; graphical goodness-of-fit methods, 437–438, 438f–441f, 440, 449, 450f–457f, 451, 465, 465f–466f, 467, 468f–474f, 478–479, 481f–483f; invariance property, 424–425; maximum pseudo-likelihood method of estimation, 435; meta-elliptic, 423; miscellaneous, 423–424; moment-like method of estimation, 431, 433–435; nonparametric measures of association, 425–427, 427t; overview, 416–418; peak flow and volume analysis, 444–449, 445f–448f, 449t, 450f–458f, 451, 458–460, 458t–460t, 461f; potential marginal distributions, 445–447, 446f; qualitative assessment of dependence, 427–429, 428f, 430f; random number generation and, 436; regional flood risk analysis, 473–474, 478–479, 478t, 480t, 481–485, 483t–484t; selection process, 436–443, 437f; storm duration and depth analysis, 460–461, 462f–463f, 462t, 463–465, 464t, 465f–466f, 467, 468f–474f, 473, 475t–477t; tail dependence characteristics, 429–431, 432t, 433f–434f; types of, 418–424
- correlation coefficient, 181, 181e
- correlation scale, 181
- CPA (conditional probability adjustment), 250, 253
- crop ET (ET_c). *see reference crop ET*
- cumulative distribution functions (CDFs): copulas, 418, 419f; empirical frequency analysis and, 273–274, 273e, 395; precipitation frequency analysis, 10–11, 11t, 34f
- cumulative probability plots, 10–11, 69f–70f
- daily precipitation time series, 22–23, 22f–23f
- dam effects on low flows, 321–323
- Darcy's Law, 150, 150e
- DARMA modeling: drought length, 302; low flows, 293–294
- decision making aids for infiltration and soil water processes, 172
- derived distribution method, uncertainty analysis, 364
- derived probability distributions: runoff characteristics, 342–354; runoff event peak discharge rate, 343–345; runoff event volume, 343; runoff routing through channel reaches, 348–351; runoff routing through detention ponds, 345–348, 346f; theory, 342–343
- descriptive indexes for precipitation extremes, 53–54, 53t
- deseasonalization, 213–214, 213e–214e
- design storms, 336–337
- detention ponds: flood control analysis, 354–360, 355t, 356f–358f, 359t; runoff routing, 345–348, 346f
- dimensionless relationships in infiltration, 160–162, 161f
- dimming, 126–128
- disaggregation models, 224–228
- discrete ARMA modeling: drought length, 302; low flows, 293–294
- diversion effects on low flows, 321–323
- droughts: climate change and, 325; DARMA modeling, 302; defined, 272, 273f; intensity, 305–307, 320; length, 300–305, 303t, 304f, 305t; magnitude, 305–308, 310–312, 320; overview, 2–3, 269–270; probability distributions, 300–308, 310–316; regional analysis, 319–321; return period,

- 316–319, 319f; statistical characterization, 299–319
- duration: of drought, 272, 273f; of low flow, 271, 271f; of storm, 460–461, 462f–463f, 462t, 463–465, 464t, 465f–466f, 467, 468f–474f, 473, 475t–477t
- Durbin-Watson test, 40, 40e
- E_0 . *see* atmospheric evaporative demand
- eddy covariance technique, 85–88, 85e, 87e
- effective saturation, 150, 150e, 150f
- El Niño southern oscillation (ENSO), 257–261, 260t, 261t, 262f
- EMA. *see* expected moments algorithm
- EML (exact maximum likelihood) method, 435–436
- empirical analysis: low flows, 273–274; precipitation frequency analysis, 10–11; water quality variables, 395
- energy balance modeling, 88–93, 89f, 92f, 93f
- ENSO (El Niño southern oscillation), 257–261, 260t, 261t, 262f
- enteric bacteria, spring water quality modeling, 198–200, 200f
- envelope curves. *see* flood envelope curves
- E_{pan} . *see* pan evaporation
- EQRM (equi-ratio quantile matching), 36–37, 36f, 37e
- ET. *see* evapotranspiration
- ET_c (crop ET). *see* reference crop ET
- ETCDI (Expert Team on Climate Change Detection and Indexes), 53–54, 53t
- (ET^{WB}). *see* water balance-derived ET
- evaporation. *see* evapotranspiration (ET)
- evaporation paradox, 133–134
- evapotranspiration (ET): advective limit, 73–74, 73e; atmospheric evaporative demand (*see* atmospheric evaporative demand); autocorrelation, 117–120, 118f, 119f; Budyko framework, 79–81, 80e–81e, 80f; complementarity with E_0 , 81–83, 82f, 129–133; defined, 71; dimming and, 126–128; drivers and limits, 74–78, 125–129, 132–133, 132t; eddy covariance estimation, 85–88, 85e, 86f, 87e; energy and water limits, 79–81; energy balance modeling, 88–93, 89f, 92f, 93f; estimation of, 72; evaporation paradox and, 133–134; GCM modeling and, 122; global observations, 121–122; Mann-Kendall test, 117–120, 119f; measurement of, 73–74; models, 78–101; moisture availability limit, 74–75, 74e; overview, 2; Penman-Monteith approach, 101–102, 102e; physics of, 73–78; radiative driver, 76–78, 76e–77e, 76f; reference crop ET (*see* reference crop ET); regional trends across CONUS, 123–125, 123f; remote sensing and, 88–93, 89f, 92f, 93f; stilling and, 128–129; trend analysis, 116–134; utilization of concept, 71–72; water balance estimates, 83–85, 83e–84e, 91
- exact maximum likelihood (EML) method, 435–436
- exceedance probability of envelope curves, 516–522, 519f, 521f, 522t
- expected moments algorithm (EMA), 252, 253–255, 254t, 255f, 256–257, 263–264
- expected value: gamma PDF, 186; log-gamma PDF, 188; log-normal PDF, 184
- Expert Team on Climate Change Detection and Indexes (ETCDI), 53–54
- exponential distribution: bivariate, 414–415, 415f; groundwater hydrology, 186; hydraulic conductivity data, 195–196, 196t; precipitation data, 13; record events, 495t, 500
- extreme events: droughts (*see* droughts); floods (*see* flood frequency analysis); precipitation (*see* precipitation extremes); record events (*see* record events)
- extreme value copulas, 421, 423
- extreme value type I distribution: hydrologic analysis, 415–416, 417f; precipitation extremes, 12; record events, 495t, 496–498, 497f
- extreme value type III distribution: low flow frequency analysis, 279–280, 280f; precipitation data, 12; water quality variables, 388–389
- FARMA (fractionally differenced autoregressive moving average) models, 218–220
- FDCs (flow duration curves), 321–322, 324f
- first-order gamma-autoregressive modeling, 291–295, 295f, 295t
- first-order second moment, uncertainty analysis, 364–365
- flood control. *see* urban stormwater management
- flood envelope curves: basic formula, 509, 509e; empirical, 519–522, 521f, 522t; exceedance probability, 516–522, 519f, 521f, 522t;

- historical background, 508f, 509, 510t, 511; overview, 508–509; probabilistic interpretation of, 513–519, 514f, 522–526, 523f, 524t, 525f, 526t, 527f–528f; relationships, 511–512, 512f, 513f; theory of records and, 515–516, 515f; traditional applications, 509, 511
- flood frequency analysis: annual flood series model, 240–243; block adjustment, 257–258; case studies of record events, 522–532; copula-based analysis, 473–474, 478–479, 478t, 480t, 481–485, 483t–484t; envelope curves (*see* flood envelope curves); estimation procedures, 245–257; expected moments algorithm, 252, 253–255, 254t, 255f, 256–257, 263–264; historical information and, 250–252, 251f, 256–257, 262; log-Pearson type III distribution and, 234, 236–238, 240–244; low outliers, 249–250, 252–253, 256, 262; method of moments (MOM), 245–248; moments of number of record events, 503–504, 505t; multivariate distributions, 410–412, 504–508, 506t; nonparametric properties of record events, 501–508; overview, 2, 233–234; parametric adjustment, 257–258; parametric properties of record events, 494–501; parametric relationships, 258–259; probability distribution of number of record events, 503, 504f; recommendations under development, 255–257; record theory and, 491–533; recurrence time for record event, 501–502, 502e; regional risk analysis, 473–474, 478–479, 478t, 480t, 481–485, 483t–484t; runoff routing through channel reaches, 348–351; theory of records and, 526–531, 529f–531f, 531t; waiting time for record event, 501–502, 502e
- Florida: annual precipitation extreme, example, 24t–25t, 24–26, 26f; climate cycles and rainfall, 51–52, 52f; intensity-duration-frequency curve for rainfall, 26–28, 27f
- flow duration curves (FDCs), 321–322, 324f
- FLUXNET, 85, 86f
- fractional Gaussian noise model, 217–218
- fractionally differenced autoregressive moving average (FARMA) models, 218–220
- frequency analysis: of floods (*see* flood frequency analysis); of low flows, 273–274
- frequency distributions, 28–29, 29f
- frequency factors, 18–19
- gamma distribution: drought magnitude, 307, 309t–310t; groundwater hydrology, 185–188; precipitation data, 13; residence time and age of groundwater, 196–198, 197f; spring water quality modeling, 198–200, 200f; water quality variables, 388–389
- Gauley subbasin, West Virginia, regional flood risk analysis, 473–474, 478–479, 478t, 480t, 481–485, 483t–484t
- Gaussian distribution. *see* normal distribution
- general circulation model (GCM) simulations: evapotranspiration and, 122; precipitation extremes and, 56
- generalized extreme value (GEV) distribution: low flow series, 280–282, 281f; precipitation data, 13; record events, 495t, 498–500, 499f
- generalized Pareto distribution, 495t, 500–501
- geometric mean, 182, 182e
- geostatistical scaling methods, 162–163, 163f, 164f
- Geum River basin, Korea, low flow analysis, 322, 323f
- GEV distribution. *see* generalized extreme value distribution
- glossaries: record events, 491–492; water quality variables, 381–383
- goodness-of-fit tests: annual extremes for different durations, 24t–25t, 24–26, 26f; copula selection, 437–438, 438f–441f, 440–443, 443t–444t, 449, 450f–457f, 451, 458–460, 459t–460t, 461f, 465, 465f–466f, 467, 468f–474f, 473, 475t–477t, 478–479, 481, 481f–483f, 484t; daily precipitation time series, 22–23, 22f–23f; hydraulic conductivity data, 193–194, 194t, 195f; L-moment diagrams, 21; normal distributions, 20; quantitative measures, 21
- gravity drainage, 152
- Greenbrier River, West Virginia, peak flow and volume analysis, 444–449, 445f–448f, 449t, 450f–458f, 451, 458–460, 458t–460t, 461f
- Greenbrier subbasin, West Virginia, regional flood risk analysis, 473–474, 478–479, 478t, 480t, 481–485, 483t–484t
- green building design principles, 352–354
- ground-based measurements of precipitation, 6–7
- groundwater hydrology: coefficient of skew, 183, 183e; geometric mean, 182, 182e;

- notations for aquifer properties, 182; overview, 2; probability density functions, 183–190; probability distributions, 179–201; residence time and age, 196–198, 197f; sample average, 182, 182e; spring water quality modeling, 198–200, 200f; standard deviation, 182–183, 182e–183e; statistical definitions, 180–181; variance, 182
- Guidelines for Determining Flood Flow Frequency**, Bulletin 17 series (IACWD), 234–236, 246–247, 249–252, 255–257
- Gumbel distribution**. *see* extreme value type I distribution
- Han River basin, Korea, low flows analysis, 322, 323f–325f
- historical information: flood frequency analysis and, 250–252, 251f, 256–257, 262; precipitation frequency analysis and, 31–32
- homogeneity: E_{pan} data, 99–101; precipitation extremes, 42–44; statistical, 181
- homogeneous region selection for low flow analysis, 284–285
- Hortonian overland flow, 151
- Hurst effect, 162, 207–208, 217–221
- hydraulic conductivity: aquifers, 179, 180f; exponential PDF application, 195–196, 196t; infiltration and, 150–151; log-gamma PDF application, 192–194, 193f, 194t, 195f; log-normal PDF application, 191–192, 191f–192f; temporal variability, 158–160; vertical soil heterogeneity, 156
- HYDRO-35**, 28–29
- hydrologic analysis: bivariate exponential distribution, 414–415, 415f; bivariate extreme value type I distribution, 415–416, 417f; bivariate log-normal distribution, 413–414; bivariate normal distribution, 412–413, 413f; copula method, 416–443 (*see also* copulas); flood events, 410–412; hydrometeorological applications, 408–410; multivariate distributions, 408–416; overview, 3, 407–408
- hydrologic cycle: evapotranspiration (*see* evapotranspiration); floods (*see* flood frequency analysis); groundwater (*see* groundwater hydrology); infiltration (*see* infiltration); multivariate frequency distributions in (*see* hydrologic analysis); precipitation extremes (*see* precipitation extremes); record events (*see* record events); soil water (*see* soil water); stormwater management and (*see* urban stormwater management); streamflow (*see* streamflow)
- hydrologic design: future data sources, 52–53; future of, 57
- hypergeometric distribution, 390
- IDF (intensity-duration-frequency) curves: precipitation extremes, 26–28, 27f
- IDWM** (inverse distance weighting method), 32–33
- IETD** (interevent time definition), 51
- IHA** (Indicator of Hydrologic Alteration), 321–322, 322t
- impervious areas, 340, 341
- independence: defined, 181; evaluation of, 49–50
- Indicator of Hydrologic Alteration (IHA)**, 321–322, 322t
- infilling methods, 34–35, 34f
- infiltrability. *see* infiltration capacity (f_c)
- infiltration: acronyms and symbols, 172–173; approximation techniques, 153; boundary and initial conditions, 152; capillary pressure head, 150, 150f; cumulative, 151; decision support systems, 172; dimensionless relationships, 160–162, 161f; dynamics of, 151–153; effective parameters of heterogeneous soil, 163–165; effective saturation, 150, 150e, 150f; engineering treatment of, 148; geostatistical scaling, 162–163, 163f, 164f; Hortonian overland flow, 151; hydraulic conductivity and, 150–151; hydrologic process interactions, 145–147, 146f, 148f; local measurement uncertainty, 166–167; local processes, 150–151; numerical solution methods, 152–153; overview, 2; parameter estimation, 167; pedotransfer functions and, 160, 161f; plant canopy and, 148–149, 149f; quantification challenges, 170–171; Richard's Equation, 151, 151e; runoff and, 168–170; scaling and estimation, 160–165; soil-surface sealing and, 153–154; soil-water content measurement, 154, 155f; sorptivity, 156; space-time simulations, 168–172; spatial variability, 156–158, 158f, 159f, 159t; surface flux measurements, 154–156; temporal variability, 158–160; uncertainty, 147, 166–168; variability, 147, 156–160; vertical soil heterogeneity and, 156;

- water transfer process, 150–151; wetting process, 150–151
- infiltration capacity (f_c), 146–147, 151, 160–162, 161^f
- intensity-duration-frequency (IDF) curves, 26–28, 27^f
- interevent time definition (IETD), 51, 338
- intermittent flows, 216–217, 282–283, 283^f
- interpolation methods, 32–37, 34^f
- invariance property of copulas, 424–425
- inverse distance weighting method (IDWM), 32–33
- inverse methods, 167
- joint probability distributions: drought characteristics, 312–316; regional flood risk analysis, 481–485, 484^f–485^f
- Kaplan Meier approach, 395
- k-C* model, 360–371, 361^t–364^t, 362^f–363^f, 367^f–370^f
- kernal density estimation (KDE), 46, 46^e
- k-nearest neighbors resampling (KNNR), 221–222
- LAI (leaf area index), 148–149
- land surface temperature, 93–95, 94^f
- Las Palmas Creek, California, spring water quality, 198–200, 200^f
- Latin hypercube sampling, uncertainty analysis, 365
- leaf area index (LAI), 148–149
- LFCs (load frequency curves), 372–373, 374^f
- linear regression, 39–42
- Little River, North Carolina, flood frequency analysis, 247–248, 248^t, 249^f
- Ljung-Box Q test, 40–42, 41^e
- L-moment analysis: flood frequency analysis, 243–244, 244^f, 244^t; precipitation data, 17–18, 21
- load frequency curves (LFCs), 372–373, 374^f
- log-gamma distribution. *see* log-Pearson type III distribution
- log-normal distribution: bivariate, 413–414; groundwater hydrology, 183–185; hydraulic conductivity data, 191–192, 191^f–192^f; low flow series, 276–278, 278^f, 278^t; precipitation data, 12, 12^e; water quality variables, 387–388
- log-Pearson type III distribution: annual flood series model, 240–243, 242^f; characteristics of, 236–244; defined, 13, 237–238, 237^e, 239^f, 240^t; flood frequency analysis and, 234, 255–256; groundwater hydrology, 188–190; hydraulic conductivity data, 192–194, 193^f, 194^t, 195^f; L-moments, 243–244, 244^f, 244^t; log space characteristics, 236, 240–241; low flow series, 274–276, 276^t; real space characteristics, 237–238, 241–242
- log space method of moments, 245–248
- long memory models, 218–220
- Los Angeles, California, BMP performance for pollutant removal, 371–374, 371^t–372^t, 374^f
- low flows: ARMA modeling, 290–294; autocorrelated flow analysis, 288–299; climate change and, 325; DARMA modeling, 293–294; defined, 270–272, 271^f; empirical frequency analysis, 273–274; extreme value type III distribution, 279–280, 280^f; first-order gamma-autoregressive modeling, 291–295, 294^t, 295^f; fitting of univariate distributions, 274–282; generalized extreme value distribution, 280–282, 281^f; hydraulic structures and, 321–323, 322^t, 323^f–325^f; intermittent flows, 282–283, 283^f; log-Pearson type III distribution, 274–276, 276^t; overview, 2–3, 269–270; probability distribution, 274–283; regional analysis, 283–288 (*see also* regional analysis of low flows); return period and risk, 295–299, 298^f, 298^t–299^t; simple Markov chain modeling, 288–290, 289^f; three-parameter log-normal distribution, 276–278, 278^f, 278^t
- low-impact development practices, 352–354
- LP3 distribution. *see* log-Pearson type III distribution
- MADI (mean absolute deviation index), 21
- Mann-Kendall test: evapotranspiration, 117–120, 119^f; precipitation extremes, 38–39, 38^e–39^e, 41^f
- Mann-Whitney U statistic, 43, 43^e
- Mapocho River, Chile, low flow analysis, 294–295, 294^t, 295^f
- maximum likelihood estimation method, 17
- maximum pseudo-likelihood (MPL) method, 435
- mean absolute deviation index (MADI), 21
- mean square deviation index (MSDI), 21
- measurements: censored water quality data, 394–396; evapotranspiration, 73–74;

- infiltration, 166–168, 171; precipitation, 6–9; soil-water content, 154, 155*f*, 166–168, 171; statistical homogeneity and independence, 181; surface flux, 154–156
- median: gamma PDF, 186; log-gamma PDF, 189; log-normal PDF, 184
- meta-elliptic copulas, 423
- method of moments (MOM): copula dependence parameters, 431–435, 448–449, 449*t*, 464–465, 464*t*; flood frequency analysis, 245–248; precipitation extremes, 16–17; reference crop ET, 106–115, 108*f*–114*f*; with regional skew, 246–248
- Methods of Flow Frequency Analysis, Bulletin 13 (IACWR 1966), 235
- MGBT (multiple Grubbs-Beck outlier test), 256–257
- mode: gamma PDF, 187; log-gamma PDF, 189; log-normal PDF, 184
- model process uncertainty, 167
- moisture availability limit for ET, 74–75, 74*e*
- moments: detection of changes, 44–45, 45*t*; of distributions, 19*t*; drought length, 300–305; estimation of distribution parameters, 17–18; expected moments algorithm, 252, 253–255, 254*t*, 255*f*, 256–257, 263–264; first-order second moment, uncertainty analysis, 364–365; gamma PDF, 187; L-moments approach (*see* L-moment analysis); log-gamma PDF, 189–190; method of moments, 16–17; number of record events, 503–504, 505*t*; record event analysis, 496
- MPL (maximum pseudo-likelihood) method, 435
- MSDI (mean square deviation index), 21
- multinomial distribution, 391
- multiple Grubbs-Beck outlier test (MGBT), 256–257
- multivariate analysis: hydrological variables, 407–485 (*see also* hydrologic analysis); record events, 504–508, 506*t*; time series modeling, 223–224; water quality variables, 401–402
- negative binomial distribution, 391
- New River, Virginia, flood risk forecast, 259–261, 260*t*, 261*t*, 262*f*
- NEXt Generation RADar (NEXRAD), 7–8, 8*f*
- Niger River, 220, 220*e*
- NLDAS (North American Land Data Assimilation System), 106–108
- nonparametric methods: bootstrap sampling, 46–49, 47*f*, 48*e*, 48*f*; copulas and, 425–427, 427*t*; estimation of quantiles and proportions, 391–393; independence evaluation, 49–50; kernel density estimation, 46, 46*e*; precipitation extremes, 45–50; ranked von Neumann test, 50, 50*e*; record event analysis, 501–508; runs test, 48–50, 49*e*–50*e*; streamflow modeling, 221–222; water quality variables, 391–394
- normal distribution: bivariate, 412–413, 413*f*; goodness-of-fit tests, 20; precipitation data, 12, 12*e*; water quality variables, 358–386
- normality testing of water quality, 386–387
- North American Land Data Assimilation System (NLDAS), 106–108
- North Central Italy, probabilistic regional envelope curves, 523–524, 523*f*, 524*t*
- outliers in flood frequency analysis, 249–250, 252–253, 256, 262
- pan evaporation (E_{pan}). *see* E_{pan} : decomposition of trends, 129–130; derivation of E_0 , 94–96; evaporation paradox and, 133–134; observed E_0 , 96–97; trend analysis and, 116, 124–125; uncertainty and limitations, 97–101
- Paraná River, Argentina, low flow return period and risk, 297–299, 298*f*, 298*t*–299*t*
- PARMA streamflow models, 214–216
- partial duration series, 50–51
- PDFs. *see* probability density functions
- Pearson type III distribution: defined, 236, 236*e*, 237*f*; precipitation data, 13
- pedotransfer functions (PTFs), 160, 161*f*
- Penman-Monteith approach to ET, 101–102, 102*e*
- Penns Creek, Pennsylvania, low flow estimation, 275–276, 276*t*
- performance modeling for BMP pollutant removal: description of k-C^{*} model, 360–364; k-C^{*} model, 361*t*–364*t*, 362*f*–363*f*; load frequency curve approach, 372–373, 374*f*; overview, 360; sensitivity, 365–371, 367*f*–370*f*; uncertainty, 361–363, 365–374
- periodic autoregressive moving average (PARMA) models, 214–216
- periodicity of streamflows, 206, 206*f*
- pervious areas, 341

- Philip's infiltration equation, 153, 153*e*, 157, 158*t*
 physics of evapotranspiration, 73–78
 PILFs (potentially influential low floods), 256
 plant canopy interception of rainfall, 148–149, 149*f*
 PMP (probable maximum precipitation), 30–31
 Poisson distribution, 338–339, 390–391
 ponding time, 151, 152, 152*f*
 population of interest, defining, 396–397
 porosity of common rocks, 179, 180*t*
 potentially influential low floods (PILFs), 256
 Poudre River, Colorado: drought intensity analysis, 306–307; drought length analysis, 302–305, 303*t*, 304*f*, 305*t*; drought magnitude analysis, 306–307; drought return period analysis, 317–319, 319*f*; streamflow variability analysis, 208–209, 208*f*–209*f*
 precipitation extremes: annual extremes for different durations, 24*t*–25*t*, 24–26, 26*f*, 50–51, 69*f*–70*f*; bootstrap sampling, 46–49, 47*f*, 48*e*, 48*f*; changes in moments, 44–45, 45*t*; characterization of data, 11–13, 14*t*–16*t*; copula-based analysis, 460–461, 462*f*–463*f*, 462*t*, 463–465, 464*t*, 465*f*–466*f*, 467, 468*f*–474*f*, 473, 475*t*–477*t*; cumulative distribution functions, 10–11; daily precipitation time series, 24, 24*f*, 25*f*; descriptive indexes, 53–54, 53*t*; distribution parameter estimation, 19–20; droughts (*see* droughts); E_{pan} errors, 98–99; errors in measurement, 6; estimation, 7–9; frequency factors, 18–19; GCM simulations, 56; goodness-of-fit tests, 20–26; ground-based measurement, 6–7; homogeneity, 42–44; independence evaluation, 49–50; interevent time definition, 51; kernel density estimation, 46, 46*e*; linear regression, 39–42; Mann-Kendall test, 38–39, 38*e*–39*e*, 41*f*; Mann-Whitney U statistic, 43, 43*e*; measurement, 5–9; monitoring networks, 6–7; nonparametric methods, 45–50; overview, 1, 5; parametric frequency curves, 26–28, 27*f*; partial duration series, 50–51; precipitation frequency analysis (*see* precipitation frequency analysis); probability distributions, 9–13; probable maximum precipitation, 30–31; quantile mapping, 35–37, 36*f*, 37*e*; radar-based measurements, 7–9, 52–53; ranked von Nuemann test, 50; as record events, 492; regional envelope curves, 525–526, 525*f*, 526*t*, 527*f*–528*f*; regional frequency analysis, 21–22; runs test, 48–50, 49*e*–50*e*; satellite-based measurement, 9; Spearman's rank correlation coefficient (ρ) test, 37–38, 37*e*, 39, 40*f*; standard precipitation index, 54–56, 54*e*–55*e*; stationarity issues, 37–42; storm duration and depth analysis, 460–461, 462*f*–463*f*, 462*t*, 463–465, 464*t*, 465*f*–466*f*, 467, 468*f*–474*f*, 473, 475*t*–477*t*
 precipitation frequency analysis: annual extreme value series, 50–51; climate change and, 51–52; cumulative distribution functions, 10–11, 11*t*; estimation in, 32–35; future data sources, 52–53; GCM simulations, 56; length of historical data, 31–32; missing data, 32–36, 34*f*, 36*f*; regional, 21–22; sample adjustment factors, 31; uncertainty and variability, 31–37; for United States, 28–29, 29*f*
 preferential flow, 167
 principal component analysis, 401–402
 probability density functions (PDFs). *see also specific probability distributions*: defined, 180–181; groundwater hydrology, 183–190; maximum likelihood estimation method, 17; precipitation data, 11–13; standard precipitation index, 54–56, 54*e*–55*e*
 probability distributions. *see also specific probability distributions*: annual precipitation extreme, example, 24*t*–25*t*; characterization of precipitation data, 11–13, 14*t*–16*t*; derived, 342–354; drought characteristics, 300–316; drought intensity, 305–307; drought length, 300–305; drought magnitude, 305–308, 309*t*–310*t*, 310–312; evaluation of residuals, 41*t*; flood frequency analysis, 233–234; frequency factors, 18–19; goodness-of-fit tests, 20–26; in groundwater hydrology, 179–201; moments, 17–18, 19*t*, 21; number of record events, 503, 504*f*; overview, 11; parameter estimation, 16–18; precipitation extremes, 9–10, 13; record theory and, 493–494; stormwater modeling, 336–338; water quality variables, 384–403
 probability sampling: serial correlation and, 399; water quality variables, 397
 probability-weighted moments (PWM), 17–18
 probable maximum precipitation (PMP), 30–31

- proportions, nonparametric estimation, 392–393
- ProUCL, 387
- PTFs (pedotransfer functions), 160, 161 f
- PWM (probability-weighted moments), 17–18
- quantile mapping, 35–37, 36 f , 37 e
- quantiles: censored data, 396; log-gamma PDF, 190; log-normal PDF, 185, 187–188; nonparametric estimation, 391–393; record event analysis, 496
- radar-based measurements of precipitation, 7–9, 8 f
- radiative driver for ET, 76–78, 76 f , 126–128
- rainfall: characterization of local conditions, 338–340; conversion from exceedance probability to return period, 351–352; droughts (*see* droughts); extremes (*see* precipitation extremes); frequency analysis (*see* precipitation frequency analysis); infiltration (*see* infiltration); multivariate distributions, 408–410; probabilistic models, 339–340, 339 t ; runoff generation, 340–341; separation of events, 338–339; water harvesting storage unit sizing, 352–354
- rain gauges, 6–7
- random number generation, 436
- ranked von Neumann test, 50, 50 e
- record events: case studies, 522–532; definitions, 491–492; exponential distribution, 495 t , 500; extreme value type I distribution, 495 t , 496–498, 497 f ; flood envelope curves (*see* flood envelope curves); generalized extreme value distribution, 495 t , 498–500, 499 f ; generalized Pareto distribution, 495 t , 500–501; moments of number of events, 503–504, 505 t ; multivariate distributions, 504–508, 506 t ; nonparametric properties, 501–508; overview, 3; parametric properties, 494–501; probability distribution of number of events, 503, 504 f ; properties of United States floods, 526–531, 529 f –531 f , 531 t ; recurrence time, 501–502, 502 e ; theory of, 492–494; waiting time, 501–502, 502 e
- recurrence time for record event, 501–502, 502 e
- reference crop ET (ET_{rc}): approach, 79; ASCE05, 102, 102 e ; concept of, 71–72, 101; derivation of crop ET from reference ET, 102–103; method of moments variability analysis, 106–115, 108 f –114 f ; Penman–Monteith approach to ET, 101–102, 102 e ; sensitivity analysis, 104–106, 105 f ; uncertainty, 103–104
- regional analysis of droughts, 319–321
- regional analysis of low flows: baseflow correlation, 286–288; homogeneous region selection, 284–285; overview, 283; regression model, 285–286
- regional envelope curves, 513–519, 514 f , 522–526, 523 f , 524 t , 525 f , 526 t , 527 f –528 f
- regional frequency analysis of precipitation extremes, 21–22
- regression models, 285–286
- regression on order statistics (ROS), 395
- remote sensing: energy balance modeling of ET and, 88–93, 89 f , 92 f , 93 f ; soil-water content, 171
- reservoirs, 207–209
- residence time and age of groundwater, 196–198, 197 f
- return period: droughts, 316–319, 319 f ; low flows, 295–299, 298 f , 298 t –299 t ; urban stormwater management, 351–352
- Richard's Equation, 151, 151 e
- risk assessment: infiltration and soil water processes, 172; low flows, 295–299, 298 f , 298 t –299 t ; regional flood risk analysis, 473–474, 478–479, 478 t , 480 t , 481–485, 483 t –484 t
- rivers: flood frequency (*see* flood frequency analysis); low flows (*see* low flows); record events (*see* record events); streamflow modeling (*see* streamflow); water quality (*see* water quality)
- ROS (regression on order statistics), 395
- runoff: derived probability distributions, 342–354; detention ponds and, 345–348; infiltration and, 168–170; overview, 3; peak discharge rate, 343–345; rainfall transformation, 340–341; routing through channel reaches, 348–351; saturation excess overland flow, 151; volume, 343
- run-on, 168
- runs test, 48–50, 49 e –50 e
- Salso River, Italy, drought magnitude analysis, 308, 310 t , 311–312, 312 t , 316–317
- sample adjustment factors, 31

- sample average, 182, 182*e. see also* expected value
 San Pedro River, Mexico, low flow estimation, 277–282, 278*f*, 278*t*, 280*f*, 281*f*
 satellite-based measurements of precipitation, 9
 saturated hydraulic conductivity, 150–151, 164–165, 165*f*, 168–170, 169*f*, 170*f*
 scaling, 160–165, 168–170
 seasonality: evapotranspiration, 125; streamflow modeling, 213–216; streamflow time series, 204–206; water quality, 400–401
 SSEB (Simplified Surface Energy Balance) modeling, 89*f*, 92*f*–93*f*
 sensitivity analysis: performance modeling of pollutant removal, 365–371, 367*f*–370*f*; reference crop ET, 104–106, 105*f*
 serial correlation: automated sampling and, 400; nearly continuous monitoring and, 400; probability sampling and, 399; stochastic processes, 399; trend analysis and, 399–400; water quality, 398–400
 shifting mean models, 220–221
 simple Markov chain, 288–290, 289*f*
 Simplified Surface Energy Balance (SSEB) modeling, 88–93, 89*f*, 92*f*–93*f*
 snowfall. *see* precipitation extremes
 software: infiltration and soil water processes, 172; streamflow modeling, 228; water quality data, 387, 389
 soil properties: effective parameters of heterogeneous soil, 163–165; infiltration and, 148; pedotransfer functions and, 160, 161*f*; scaling of, 160–165; soil-surface sealing, 153–154; surface flux measurements, 154–156; temporal variability, 158–160; water content measurement, 154, 155*f*
 soil water. *see also* infiltration: acronyms and symbols, 172–173; hydrologic process interactions, 145–147, 146*f*, 147*f*; local processes, 150–151; measurement methods, 154, 155*f*, 166–168, 171; space-time simulations, 168–172; spatial variability, 156–158, 158*f*, 158*t*, 159*f*, 159*t*; temporal variability, 158–160; uncertainty, 147, 166–168; variability, 147, 156–160
 sorptivity, 156
 spatial correlation, 181
 spatial interpolation methods, 32–37, 36*f*
 spatial variability of infiltration, 156–158, 158*f*, 158*t*, 159*f*, 159*t*
 Spearman's rank correlation coefficient (ρ) test, 37–38, 37*e*, 39, 40*f*
 spring water quality modeling, 198–200, 200*f*
 SSEB (Simplified Surface Energy Balance) modeling, 88–93
 standard deviation, 182–183, 182*e*–183*e*
 standard precipitation index, 54–56, 54*e*–55*e*
 stationarity, 37
 statistical analysis. *see also specific statistical methods*: droughts, 299–319; evapotranspiration, 71–135; precipitation extremes, 5–57
 statistical homogeneity, 181
 statistical inference: aquifer properties, 182–183; infiltration and soil water, 167–168
 stilling, 128–129
 stochastic modeling: serial correlation and, 399; streamflow variability, 203–229; water quality data, 397–398
 storm events. *see* precipitation extremes
 stormwater management. *see* urban stormwater management
 streamflow: ARMA models, 210–212; autocorrelation, 204; complex river system modeling, 222–228; copula-based analysis, 444–449, 445*f*–448*f*, 449*t*, 450*f*–458*f*, 451, 458–460, 458*t*–460*t*, 461*f*; defined, 203; deseasonalization, 213–214, 213*e*–214*e*; disaggregation models, 224–228; flow regime, 321–322; fractional Gaussian noise model, 217–218; Hurst effect, 207–208; intermittent flow models, 216–217; long memory models, 218–220; long-term variability models, 217–221; low flows (*see* low flows); modeling strategies for complex river systems, 226–228; multivariate time series modeling, 223–224; nonparametric modeling, 221–222; overview, 2; peak flow and volume analysis, 444–449, 445*f*–448*f*, 449*t*, 450*f*–458*f*, 451, 458–460, 458*t*–460*t*, 461*f*; periodic models, 214–216; product models for intermittent flows, 216–217; seasonality, 204–206; seasonal series modeling, 213–216; shifting mean models, 220–221; software tools, 228; stochastic features, 203–209; stochastic modeling, 209–222; storage-related statistics, 207–209; variability modeling, 203–229; water quality and, 400–401
 surface energy balance modeling of ET, 88–93, 89*f*, 92*f*, 93*f*

- surface flux measurements, 154–156
 surface infiltration. *see* infiltration
 surface seal, 153–154
 symbols: infiltration and soil water, 172–173;
 urban stormwater management, 333–335
- Technical Paper (TP) 40, 28–29
 temperature-based formulations of E_0 , 93–95,
 94f
 temporal variability of soil properties, 158–160
 tension infiltrometer methods, 155
 three-parameter log-normal distribution: low
 flow series, 276–278, 278f, 278t; precipitation
 data, 12
 time series for streamflow: autocorrelation, 204,
 205f; Hurst effect, 207–208; modeling,
 209–222; seasonality, 204–206; stochastic
 features, 203–209; storage-related statistics,
 207–209
 time series for water quality, 397–398
 TP-40, 28–29
 transformations of water quality data, 386–387
 trend analysis: evapotranspiration, 116–134;
 precipitation extremes, 37–42, 42f; serial
 correlation and, 399–400
 Tropical Rainfall Measuring Mission
 (TRMM), 9
 t-tests, 44–45
 Twelve Mile Creek, North Carolina, low flow
 estimation, 283, 283f
 Tyrol, Austria, probabilistic regional envelope
 curves, 525–526, 525f, 526t, 527f–528f
- uncertainty. *see also* variability: analysis
 methods, 364–365; derived distribution
 method, 364; evapotranspiration, 72; first-
 order second moment, 364–365; infiltration
 and soil water, 147, 166–168; k-C* model and,
 361–363; Latin hypercube sampling, 365;
 pollutant removal BMP performance
 modeling, 361–363, 365–374; precipitation
 frequency analysis, 31–37; reference crop ET
 (ET_{rc}), 103–104; sensitivity, 365–370,
 367f–370f
 Uniform Technique for Determining Flood
 Flow Frequencies, Bulletin 15 (WRC 1967),
 235
 United States: flood frequency analysis,
 233–264 (*see also* flood frequency analysis);
 precipitation frequency analysis, 28–29, 29f;
- record-breaking floods, 526–531, 529f–531f,
 531t
 universal multifractal models, 168–170, 169f,
 170f
 Upper Colorado River basin, disaggregation
 models, 227–228
 urban stormwater management: analytical
 probabilistic models, 336–360; conversion
 from exceedance probability to return period,
 351–352; derived probability distributions for
 runoff characteristics, 342–354; flood control
 analysis, 354–360, 355t, 356f–358f, 359t;
 overview, 3; pollutant removal performance
 modeling, 360–374, 361t–364t, 362f–363f,
 367f–370f, 371t, 372f; rainfall
 characterization, 338–340; rainfall-runoff
 transformation, 340–341; runoff event peak
 discharge rate, 343–345; runoff event volume,
 343; runoff routing through channel reaches,
 348–351; runoff routing through detention
 ponds, 345–348, 346f; symbols, 333–335
- variability. *see also* uncertainty: infiltration and
 soil water, 147; precipitation frequency
 analysis, 31–37; reference crop ET, 106–115,
 108f–114f
 variance: defined, 182; gamma PDF, 187;
 log-gamma PDF, 189; log-normal PDF, 185
 von Neumann's ratio test, 50, 50e
- waiting time for record event, 501–502, 502e
 Wald-Wolfowitz test, 48–50, 49e–50e
 water balance-derived ET (ET^{WB}), 83–85,
 83e–84e, 91, 132–134, 132t
 water management. *see* urban stormwater
 management
 water pollution: BMP performance modeling,
 360–374, 361t–364t, 362f–363f, 367f–370f,
 371t–372t, 374f; microbiological
 contaminants, 390–391
 water quality: analysis of variables, 381–403;
 beta distribution, 388–389; binomial
 distribution, 389–390; box-and-whisker plots,
 393–394, 393f; censored observations,
 394–396; definitions, 381–383; extreme value
 type III distribution, 388–389; gamma
 distribution, 388–389; hypergeometric
 distribution, 390; log-normal distribution,
 387–388; microbiological variables, 390–391;
 multinomial distribution, 391; multivariate

characterization, 401–402; negative binomial distribution, 391; nonparametric representations of data, 391–394; normal distribution, 358–386; normality testing of data, 386–387; overview, 3, 383; Poisson distribution, 390; population of interest, defining, 396–397; practical applications of distributions, 384–385; probability sampling, 397; seasonality, 400–401; serial correlation, 398–400; special characteristics of variables, 383–384; springs, 198–200, 200*f*; stochastic processes, 397–398; streamflow and, 400–401; time series, 397–398; transformation of data, 386–387

Water Resources Council (WRC), 235
Water Resources Planning Act, 235
water table, infiltration and, 152
Watson, Keith, 157
Weather Surveillance Radar 88-Doppler (WSR 88-D), 7–8, 8*f*
Weibull distribution. *see* extreme value type III distribution
WRC (Water Resources Council), 235
WSR 88-D (Weather Surveillance Radar 88-Doppler), 7–8, 8*f*
Z-statistic. *see* Mann-Kendall test